

Matthieu Hamel *Editor*

Plastic Scintillators

Chemistry and Applications

Topics in Applied Physics

Volume 140

Series Editors

Young Pak Lee, Physics, Hanyang University, Seoul, Korea (Republic of)

David J. Lockwood, Metrology Research Center, National Research Council of Canada, Ottawa, ON, Canada

Paolo M. Ossi, NEMAS - WIBIDI Lab, Politecnico di Milano, Milano, Italy

Kaoru Yamanouchi, Department of Chemistry, The University of Tokyo, Tokyo, Japan

Topics in Applied Physics is a well-established series of review books, each of which presents a comprehensive survey of a selected topic within the domain of applied physics. Since 1973 it has served a broad readership across academia and industry, providing both newcomers and seasoned scholars easy but comprehensive access to the state of the art of a number of diverse research topics.

Edited and written by leading international scientists, each volume contains high-quality review contributions, extending from an introduction to the subject right up to the frontiers of contemporary research.

Topics in Applied Physics strives to provide its readership with a diverse and interdisciplinary collection of some of the most current topics across the full spectrum of applied physics research, including but not limited to:

- Quantum computation and information
- Photonics, optoelectronics and device physics
- Nanoscale science and technology
- Ultrafast physics
- Microscopy and advanced imaging
- Biomaterials and biophysics
- Liquids and soft matter
- Materials for energy
- Geophysics
- Computational physics and numerical methods
- Interdisciplinary physics and engineering

We welcome any suggestions for topics coming from the community of applied physicists, no matter what the field, and encourage prospective book editors to approach us with ideas. Potential authors who wish to submit a book proposal should contact Zach Evenson, Publishing Editor:

zachary.evenson@springer.com

Topics in Applied Physics is included in Web of Science (2019 Impact Factor: 0.633), and is indexed by Scopus.

More information about this series at <http://www.springer.com/series/560>

Matthieu Hamel
Editor

Plastic Scintillators

Chemistry and Applications



Springer

Editor

Matthieu Hamel
Université Paris-Saclay, CEA, List
Laboratoire Capteurs et Architectures Electroniques
Palaiseau, France

ISSN 0303-4216
Topics in Applied Physics
ISBN 978-3-030-73487-9
<https://doi.org/10.1007/978-3-030-73488-6>

ISSN 1437-0859 (electronic)
ISBN 978-3-030-73488-6 (eBook)

© Springer Nature Switzerland AG 2021

This work is subject to copyright. All rights are reserved by the Publisher, whether the whole or part of the material is concerned, specifically the rights of translation, reprinting, reuse of illustrations, recitation, broadcasting, reproduction on microfilms or in any other physical way, and transmission or information storage and retrieval, electronic adaptation, computer software, or by similar or dissimilar methodology now known or hereafter developed.

The use of general descriptive names, registered names, trademarks, service marks, etc. in this publication does not imply, even in the absence of a specific statement, that such names are exempt from the relevant protective laws and regulations and therefore free for general use.

The publisher, the authors and the editors are safe to assume that the advice and information in this book are believed to be true and accurate at the date of publication. Neither the publisher nor the authors or the editors give a warranty, expressed or implied, with respect to the material contained herein or for any errors or omissions that may have been made. The publisher remains neutral with regard to jurisdictional claims in published maps and institutional affiliations.

This Springer imprint is published by the registered company Springer Nature Switzerland AG
The registered company address is: Gewerbestrasse 11, 6330 Cham, Switzerland

Foreword

As one looks back over the history of radiation measurements, one finds distinct eras of intense development and progress, sometimes driven by emergent applications or by innovations in other fields. The initial radiation detectors were the gas-filled detectors (ionization chamber, proportional counter, and Geiger–Mueller tube) which stood as the dominant form of radiation detector until ~1950. The inorganic scintillator, introduced by Hofstadter, then revolutionized radiation detection for gamma rays since it offered high efficiency and reasonable energy resolution. The introduction of new inorganic scintillators was slow but steady, driven to meet particular application needs. The focus of detector development was changed by the introduction of the silicon semiconductor (~1970). Even with its small size, the superb energy resolution for charged particles opened advanced measurement possibilities. Larger detector volumes, better energy resolution, and higher efficiency became possible with germanium, which evolved to become today’s gold standard for gamma-ray energy resolution. Such was the general state of our field at the beginning of this millennium.

The September 11, 2001 terrorist attack in New York City heralded a shift in the direction of radiation detector R&D. Coupled with the activity inspired by CERN’s Crystal Clear Collaboration, an intense push was developed to deploy radiation sensors on a large scale for national security. This has led to two decades of development focused almost entirely on **inorganic** scintillators. The goal has been to develop large area, highly efficient, robust, inexpensive, gamma-ray detectors with much better energy resolution and particle discrimination than was previously available. Figure 1 from [1] depicts the productive outcome of this impressive effort.

The point of recalling this history is to show that inorganic scintillators have been the focus of the R&D limelight for decades, garnering the attention for both analytical method and material development. In the meantime, their organic counterparts have quietly evolved and continue to produce some very attractive detector materials.

While the push to improve detector performance has led to a slew of new inorganic scintillators, only a few of these have proven to provide practical solutions to real problems, particularly for the market of security applications. These applications

require large area and volume to subtend and stop incident neutrons and gamma rays coming from afar, have a low cost for widespread deployment, high environmental robustness, and simplicity in execution. Since inorganic scintillators and semiconductors have difficulty in meeting these constraints, attention has now fully swung to explore and exploit the organic scintillators.

Any history of organic scintillators will inevitably include the fiducial works of J. B. Birks [2] and F. D. Brooks [3] (the latter reference provides a nice review of the field up to ~1980). But since then, a small group of dedicated researchers have pushed to improve light yield, understand molecular dynamics and quenching phenomena, improve environmental acceptability, and leverage the ability to discriminate the fast neutrons from the gamma-ray background. What has been lacking is a comprehensive treatise that elucidates the science governing these processes, the existing and new materials and their properties, and the future pathway. This much-needed volume, written by these dedicated researchers, admirably fills this gap.

Whereas inorganic scintillators derive their scintillation capability from their crystalline properties, organic scintillators can function in liquid, plastic, or crystalline form. This obviates the necessity of growing crystals atom-by-atom, which enables larger, cost-effective volumes to be achieved. Since organic scintillators can be acquired for $\sim \$ 1/\text{cm}^3$, as compared to $\sim \$ 50\text{--}100/\text{cm}^3$ for their inorganic counterparts, large volumes strongly favor organics. This property (in addition to their prompt scintillation decay times) has led to their widespread adoption, e.g., for security applications and rare event physics searches [4], despite their inherent disadvantages of low density and efficiency, limited spectral capability, and age-related degradation. But over the last decade, material advances have made these disadvantages less operationally restrictive. This can be seen in the commercially available, larger stilbene detectors with reasonable light yield and particle discrimination capability, and newer plastic scintillator properties that rival the traditional liquid scintillator [5].

By loading scintillators with dopants of heavy metals or neutron absorbers, the effective stopping power of any organic scintillator to gamma rays or neutrons can be dramatically improved, and recent work has led to larger volumes and higher scintillation light yields (likely due to reduced quenching) [6]. If the current light yields of ~ 10 photons/keV can be improved by factors of $\sim 3\text{--}5$, the spectroscopic capability can become competitive with some inorganics without requiring heavy spectral unfolding. Exploiting new work in nanotechnology, nanoparticles have been homogeneously introduced into a matrix and have led to new detector materials that are individually sensitive to slow and fast neutrons, as well as gamma rays. This triple particle discrimination ability could foreshadow a significant advance for homeland security applications [7].

While the past few decades have brought remarkable developments in inorganic scintillators (e.g., LYSO, LaBr₃, SrI₂, CLYC, ...), we are now on the verge of similar breakthroughs in organic scintillators. With a deeper understanding of the underlying

physical and chemical mechanisms in play, coupled with rapid and inexpensive fabrication, one can foresee more affordable, larger volume, and capable fast detectors that can fill critical roles in our most important detection applications. This volume is particularly useful not only for elucidating the current state of the art, but also for highlighting those research areas that will lead to these breakthroughs by our detection community.

Ann Arbor, MI, USA

David K. Wehe

References

1. C. Dujardin, E. Auffray, E. Bourret-Courchesne, P. Dorenbos, P. Lecoq, M. Nikl, A.N. Vasil'ev, A. Yoshikawa, R.-Y. Zhu, IEEE Trans. Nucl. Sci. **65**(8), 1977 (2018)
2. J.B. Birks, *The Theory and Practice of Scintillation Counting* (Pergamon Press, Oxford, 1964)
3. F.D. Brooks, Nucl. Instr. Meth. **162**(1–3), 477 (1979)
4. V.A. Li, T.M. Classen, S.A. Dazeley, M.J. Duvall, I. Jovanovic, A.N. Mabe, E.T.E. Reedy, F. Sutanto, Nucl. Instr. Methods A **942**, 162334 (2019)
5. N. Zaitseva, B.L. Rupert, I. Pawełczak, A. Glenn, H.P. Martinez, L. Carman, M. Faust, N. Cherepy, S. Payne, Nucl. Instr. Methods A **668**, 88 (2012)
6. G.H.V. Bertrand, J. Dumazert, F. Sguerra, R. Coulon, G. Corre, M. Hamel, J. Mater. Chem. C **3**(35), 6006 (2015)
7. C. Frangville, J. Dumazert, E. Montbarbon, R. Coulon, G.H.V. Bertrand, M. Hamel, Mater. Chem. Front. **3**(8), 1574 (2019)

Preface

Cross-disciplinary research is extremely pleasant to open-minded scientists who love to exit from their comfort background, and learn new subjects. The scintillation domain—and more particularly plastic scintillator, which is the subject of this book—is one of those disciplines that require skills in many fields such as organ(ometallic) chemistry, materials chemistry, photophysics of condensed matter, electronics, signal processing, and nuclear physics. All these are linked such as a puzzle, a defective piece leading undoubtedly to scintillating systems of low detection performances. The extensive research that has been performed these last two decades on fast neutron/gamma discriminating plastic scintillators is a living example: chemistry to stabilize the material or to introduce triplet-harvesting fluorophores, high-level photophysical understanding, new digitizers and solutions offering real-time pulse shape discrimination. Since this thematic is scientifically rich, it finds applications in many fields such as fundamental physics, homeland security, radioprotection, and environmental assays.

This book consists of 15 chapters written by leading experts in all the above-mentioned areas. Besides, I am very indebted to all the Authors for the time they have considered writing this wonderful book. It is divided in two main sections: Part I—*materials* is the chemical modifications of plastic scintillator and is composed of eight chapters. Chapter 1 introduces the concept of plastic scintillator and opposes it against another variety of state-of-the-art materials: inorganics scintillators. I am glad to be associated with C. Dujardin (expert scientist in inorganic scintillator) in this chapter. Chapter 2 is a success story from N. Zaitseva and collaborators from Lawrence Livermore National Laboratory about a fast neutron/gamma discriminating plastic scintillator that is now commercially available. Chapters 3 and 4 present the latest application-driven developments in elemental loading for two main applications: first is written by J. Dumazert and C. Frangville on thermal neutron detection, second on gamma spectrometry (and other applications) by G. Bertrand and M. Hamel. In Chap. 5, M. Koshimizu shatters the limits of plastic scintillation to their inorganic counterparts: composite scintillators are materials that merge all advantages of the two worlds. Chapter 6 focuses on a special polymer for scintillation mostly studied and developed by S. Carturan and A. Quaranta. The last two chapters of this first part are proposed by P. Feng and coworkers. The first chapter by Patrick

presents an overview on molecular design considerations for the three main organic scintillators: single crystal, liquid and plastic. The second chapter reports organic glass scintillators as a brand new class of materials that look particularly efficient in terms of scintillation properties.

In Part II—*applications*, standard, or chemically modified plastics are used in particular fields or combined with new possibilities in signal processing. In Chap. 9, B. Liu and X. Ouyang present the use of photonic crystals to mitigate light confinement in these materials. Chapter 10 by M. Thevenin and Y. Moline introduces plastic scintillators to smart algorithms and powerful analog stages to enhance their detection properties, putting at a higher scale new considerations in nuclear instrumentation. Chapter 11 is the application of plastic scintillators to gas detection by two field specialists: P. Cassette and K. Mitev. Then, the leading collaboration around S. Beddar presents the recent advances and clinical applications of plastic scintillators in the field of radiation therapy in Chap. 12. Other experts from the University of Barcelona (A. Tarancón and coworkers) present the use of plastic scintillators for environmental analysis in Chap. 13. This team is one of the few that gathers skills equally in material synthesis and their application to radiation detection. Chapter 14 by P. Laurent and coworkers initiates the readership to a less known application of plastic (and inorganic) scintillators: their use to study the Earth from ground to the magnetosphere. Then large experiments that use these materials are presented by P. B. Cushman and D. M. Poehlmann in Chap. 15.

This book is intended to become a screenshot of what are plastic scintillators in early 2021 (the date of completion of this book) and how they can be used as a simple, yet versatile sensor for nuclear instrumentation. Beginners will find all the definitions of the important parameters (light output, figure of merit, radiation/matter interaction), and experts will have access as well to the most comprehensive state of the art of the chemical modifications of these materials and revisited instruments. I hope the book will deserve the community to a better knowledge in this field.

Last, it is important to mention the “special” conditions the Authors have faced while preparing their chapters. This year 2020 has seen the spread of the COVID-19 disease. Most of our work has been upset due to lockdown(s) or subsequent delays on the project. I am very grateful the Authors succeeded, however, in preparing their manuscript in due time.

“L’important, c’est pas la victoire, mais le combat” Daïtro.

Saclay, France

Matthieu Hamel

Contents

Part I Materials

1	Introduction—Overview on Plastic and Inorganic Scintillators	3
	Christophe Dujardin and Matthieu Hamel	
1.1	History of Scintillators	4
1.2	Plastic Scintillator Chemists	8
1.3	The Scintillation Process in Plastics and Inorganic Materials/Crystals	8
1.4	Typical Preparation Process and Size Possibilities	11
1.5	Main Parameters and Tools for Modification or Improvement	13
1.5.1	Light Yield	14
1.5.2	Decay Time	16
1.5.3	Emission Wavelength	18
1.5.4	Behavior Against External Environment	19
1.5.5	Effective Atomic Number and Density	24
1.6	Summary	25
	References	26
2	Neutron/Gamma Pulse Shape Discrimination in Plastics Scintillators: From Development to Commercialization	35
	Natalia P. Zaitseva, M. Leslie Carman, Andrew M. Glenn, and Andrew N. Mabe	
2.1	Physical Basis for Neutron/Gamma Discrimination in Organic Scintillators	35
2.2	Plastic Scintillators with Efficient Fast Neutron/Gamma Discrimination	39
2.2.1	PPO-Based PSD Plastics	40
2.2.2	PSD Plastics Utilizing Alternative Dyes and Dye Mixtures	52
2.3	PSD Plastics for Combined Detection of Fast and Thermal Neutrons	68
2.3.1	<i>¹⁰B-loaded PSD Plastic Scintillators</i>	68

2.3.2 <i>⁶Li-loaded PSD Plastic Scintillators</i>	74
2.4 Commercialization and Further Directions of Studies	82
References	86
3 The Detection of Slow Neutrons	91
Jonathan Dumazert and Camille Frangville	
3.1 Slow Neutrons: Essential Features	91
3.1.1 The Definition of Slow Neutrons	92
3.1.2 The Origins of Slow Neutrons	93
3.2 Nuclear Reactions of Interest in Slow Neutron Detection	99
3.2.1 Natural Abundance, Reaction Cross Section, Q-Value, and Typology of Reaction Products	100
3.2.2 Main Nuclear Reactions of Interest	101
3.2.3 Size of the Scintillator: Slow Neutron Mean Free Path and the Interaction of Reaction Products	106
3.3 Detection of Reaction Products and n/γ Discrimination	109
3.3.1 Background Radiation	109
3.3.2 Pulse Height Discrimination	110
3.3.3 Pulse Shape Discrimination	112
3.3.4 Compensated Detectors	114
3.3.5 Multiplicity-Gated Detection	115
3.3.6 Capture-Gated Detection	115
3.4 Figures of Merit for Slow Neutron Detectors	117
3.4.1 Figures of Merit About the Response to Neutrons	117
3.4.2 Figures of Merit About the Response to Gamma Rays	119
3.4.3 Figures of Merit About the Response to Neutron Against the Response to Gamma Rays	120
3.5 Incorporation of Neutron Converters into Plastic Scintillator-Based Detectors	122
3.5.1 Homogeneous Incorporation	122
3.5.2 Heterogeneous Incorporation	125
3.6 Applications of Plastic Scintillators to the Detection of Slow Neutrons	130
3.6.1 Homeland Security	131
3.6.2 Neutron Flux Monitoring and Source Characterization	131
3.6.3 Reactor Antineutrino Experiments, Surveillance, and Monitoring	132
References	133
4 Chemical Approach on Organometallic Loading in Plastic Scintillators and Its Applications	139
Guillaume H. V. Bertrand and Matthieu Hamel	
4.1 Introduction/Context	139
4.1.1 Plastic Scintillation	139

4.1.2	Frame of This Chapter	140
4.1.3	Properties Optimization	140
4.1.4	Chemical Design and Material Science, What the Loading Implies	141
4.1.5	Organization of This Chapter: Application Driven	142
4.2	Scintillation Process Enhancement	143
4.2.1	Triplet Harvesting	143
4.2.2	Iridium Complexes	143
4.2.3	Europium Complexes	145
4.3	Photon Detection	146
4.3.1	Theory	146
4.3.2	X-ray Detection	147
4.3.3	Gamma Detection	149
4.4	Neutron Detection	156
4.4.1	Thermal Neutron	156
4.4.2	Lithium Loading	158
4.4.3	Boron Loading	159
4.4.4	Cadmium and Gadolinium Loading	160
4.5	Conclusion	162
4.6	Table by Elements	162
	References	164
5	Polysiloxane-Based Scintillators	169
	Sara Maria Carturan and Alberto Quaranta	
5.1	Foreword	169
5.1.1	Silicon-Based Polymer Properties: Chemistry	170
5.1.2	The Synthesis of Silicones	172
5.2	Optical Properties of Phenyl-Containing Polysiloxanes	174
5.3	Design of Polysiloxane-Based Scintillators	179
5.3.1	Energy Transfer in Organic Polymers	179
5.3.2	Polymeric Scintillators	181
5.3.3	Polysiloxane-Based Scintillators	183
5.4	Polysiloxane Scintillators for Neutron Detection	186
5.4.1	Neutron Detection in Organic Scintillators	186
5.4.2	B and Li Loaded Polysiloxanes for Detection of Thermal Neutrons	190
5.4.3	Design of Polysiloxane Scintillators for n/y Discrimination	194
5.5	Summary	196
	References	197
6	Composite Scintillators	201
	Masanori Koshimizu	
6.1	Introduction to Organic–Inorganic Composites	201
6.1.1	Overview on Fabrication Methods of Nanocomposites	203

6.1.2	Optical Properties Related to the Nanocomposite Structure	206
6.2	Plastic Scintillators Incorporating Non-emitting Inorganic Nanoparticles	208
6.2.1	Sol-gel-Derived Organic-Inorganic Composite Scintillators	209
6.2.2	Nanocomposite Scintillators Fabricated via Two-Step Synthesis	211
6.3	Nanocomposite Scintillators Comprising Luminescent Nanoparticles	214
6.3.1	Nanocomposite Scintillators Comprising Inorganic Phosphor Nanoparticles	214
6.3.2	Nanocomposite Scintillators Comprising Semiconductor Nanocrystals	217
6.4	Summary and Future Prospects	219
	References	220
7	Molecular Design Considerations for Different Classes of Organic Scintillators	223
	Patrick L. Feng	
7.1	Design Considerations for Crystalline, Plastic, and Liquid Scintillators	224
7.1.1	Background on Scintillation Mechanisms	224
7.1.2	Process (1): Direct Excitation into π -Electronic States	225
7.1.3	Process (2): Overview of Direct Ionization and Recombination of π -states	230
7.1.4	Physical and Mechanical Properties of Different Classes of Organic Scintillators	237
7.2	Future Opportunities	239
	References	240
8	Organic Glass Scintillators	243
	Patrick L. Feng, Nicholas R. Myllenbeck, and Joseph S. Carlson	
8.1	Introduction to Organic Glass Scintillators	243
8.2	Glassy State of Matter	244
8.3	Differentiating Characteristics of Organic Molecular Glasses	246
8.4	Design Strategies for Stable Organic Molecular Glasses	246
8.4.1	Nonplanar Structures	248
8.4.2	Increasing Molecular Size	249
8.4.3	Multiple Conformations	250
8.4.4	Physical Mixtures	252
8.5	Fluorescent Molecular Glasses as Organic Glass Scintillators (OGSs)	253
8.6	Organic Glass Scintillators: Case Studies	255

8.7	Organic Glass Thermal and Mechanical Properties	262
8.7.1	Mechanical Strength: Intermolecular Interactions	264
8.7.2	Mechanical Strength: Organic Glass/Polymer Blending	264
8.8	Properties of OGS/Polymer Blends	266
8.8.1	<i>Effect of Small-Molecule Additives on T_g</i>	266
8.8.2	Scintillation Properties of OGS/Polymer Blends	267
8.9	Organic Glass Scintillator Fabrication Methods	269
8.10	Long-Term Stability and Environmental Aging of Organic Glass Scintillators	270
8.10.1	Surface Versus Bulk Diffusion	270
8.10.2	Accelerated Aging of Organic Glasses and Mitigation Methods	271
8.11	Compatibility of OGS with Multi-functional Additives	275
8.11.1	Boron-Loaded OGS for Fast Neutron/Gamma PSD and Thermal Neutron Capture	275
8.11.2	Metal-Loaded OGS for Fast Neutron/Gamma PSD and Gamma-Ray Spectroscopy	277
8.12	Summary and Future Outlook	277
	References	278

Part II Applications

9	Optical Improvements of Plastic Scintillators by Nanophotonics	287
	Bo Liu and Xiaoping Ouyang	
9.1	Introduction	287
9.2	Enhancement of Light Extraction Efficiency of Plastic Scintillators by Photonic Crystals	289
9.2.1	Introduction of Photonic Crystals	289
9.2.2	Enhancement Mechanism of Light Extraction Efficiency by Photonic Crystals	290
9.2.3	Control of Directional Emission by Photonic Crystals	294
9.2.4	Consideration for the Structural Design of Photonic Crystals	296
9.3	Control of Directional Emission of Plastic Scintillators by Plasmonic Lattice Resonances	297
9.4	Patterning Techniques for Plastic Scintillators	298
9.4.1	Self-assembly Lithography	299
9.4.2	Nanoimprint Lithography (NIL)	301
9.4.3	X-Ray Interference Lithography (XIL)	301
9.5	Improved Scintillation Performance of Detectors by Photonic Crystals	302
9.6	Summary and Remark	304

References	305
10 Analog and Digital Signal Processing for Nuclear Instrumentation	309
Mathieu Thevenin and Yoann Moline	
10.1 Introduction	309
10.2 The Light to Electric Signal Conversion	311
10.2.1 Design of PMTs	311
10.2.2 Solid-State Semiconductor Photodetectors	331
10.3 The Signal Acquisition Frontend	344
10.3.1 Charge to Voltage Conversion	344
10.3.2 Gain and Pulse Shaping Stage	346
10.3.3 Voltage Limiters	347
10.3.4 Impedance Matching and Other Effects	348
10.4 The Digitization Stage	349
10.4.1 Signal Digitization Basics	349
10.4.2 Digitizer Architectures	354
10.5 Signal Processing and Feature Extraction	356
10.5.1 Low-Level Digital Stream Processing	357
10.5.2 Digital Pulse Processing	365
10.6 Data and Information Processing	368
10.6.1 Count Rate Analysis	369
10.6.2 Discrimination of the Nature of the Interactions	369
10.6.3 Spectral Unmixing and Radionuclide Identification	372
10.7 Conclusion	373
References	374
11 Radioactive Noble Gas Detection and Measurement with Plastic Scintillators	385
Krasimir Mitev and Philippe Cassette	
11.1 Radioactive Noble Gas Isotopes	385
11.1.1 Kr-85	388
11.1.2 Xe-131m	389
11.1.3 Xe-133	390
11.1.4 Xe-133m	391
11.1.5 Xe-135	392
11.1.6 Ar-37	392
11.1.7 Rn-222 and Progenies	393
11.1.8 Rn-220 and Progenies	395
11.2 Application of Plastic Scintillators to the Detection of Noble Gas	396
11.2.1 Xenon Detection Systems for the CTBT Network	396
11.2.2 Kr-85 Monitors Using Plastic Scintillators	400
11.2.3 Radon and Thoron Detection and Measurement with Plastic Scintillators	402
11.3 RNG-Related Properties of Plastic Scintillators	403

11.3.1	Noble Gas Absorption in Plastic Materials	403
11.3.2	<i>Application of Pulse Shape Discrimination to ^{222}Rn Measurements</i>	410
11.3.3	<i>Description of the Alpha-Particle Peak Shapes in ^{222}Rn Measurements with Plastic Scintillators</i>	414
11.4	Concluding Remarks	419
	References	420
12	Recent Advances and Clinical Applications of Plastic Scintillators in the Field of Radiation Therapy	425
	Sam Beddar, Irwin Tendler, François Therriault-Proulx, Louis Archambault, and Luc Beaulieu	
12.1	Introduction	426
12.2	Basic Dosimetry Properties of Plastic Scintillators	427
12.2.1	Basic Properties of Scintillators Used in Radiation Therapy	427
12.2.2	Relating Scintillation Signal to Absorbed Dose	428
12.2.3	Other Properties	429
12.3	Signal Processing in Plastic Scintillators Dosimeters	430
12.3.1	Cherenkov and Other Sources of Stem Effects	430
12.3.2	Multi-point Radiation Therapy Plastic Scintillator Dosimeters	432
12.4	Clinical Applications and Special Procedures	433
12.4.1	Photon and Electron External Beam Radiation Therapy	433
12.4.2	Proton External Beam Radiation Therapy	440
12.4.3	Brachytherapy	449
12.5	Conclusion	454
	References	454
13	Plastic Scintillators in Environmental Analysis	461
	Alex Tarancón, Héctor Bagán, and José Francisco García	
13.1	Environmental Analysis: Requirements and Characteristics. Contribution of Plastic Scintillators	462
13.2	Preparation of Plastic Scintillators for Environmental α/β Emitting Radionuclide Analysis	467
13.2.1	Fibers and Sheets	468
13.2.2	Plastic Scintillation Particles	468
13.2.3	Stability of Plastic Scintillation Microspheres	474
13.2.4	Plastic Scintillation Resins	476
13.3	Direct Surface and Soil Analysis	477
13.4	Sensors and Online Analysis of Alpha and Beta Emitting Radionuclides	481
13.4.1	Sensors Based on Plastic Scintillation Microspheres (PSm)	482
13.4.2	Sensors Based on Plastic Scintillation Resins	485

13.4.3	Sensors Based on Plastic Scintillation Fibers (PSf)	487
13.4.4	Sensors Based on Plastic Scintillation Sheets	488
13.5	Plastic Scintillators for Beta Emitting Radionuclide Analysis	489
13.6	Plastic Scintillators for Alpha Emitting Radionuclide Analysis	498
13.7	Conclusion	503
	References	504
14	Use of Scintillators to Study the Earth from Ground to the Radiation Belts	509
	Philippe Laurent, Sébastien Célestin, Vincent Maget, Pablo Caron, and François Trompier	
14.1	Survey of Earth Natural Radioactivity and Potential Nuclear Accidents, Citizen Science	509
14.1.1	Source of Terrestrial Natural Radioactivity	509
14.1.2	Sources of Radioactive Pollution in the Environment	512
14.1.3	Nuclear Activities Survey and Alert in Case of Accident: Description of Official and NGO Networks	514
14.1.4	Measuring and Mapping the Radioactivity in the Environment: The Citizen Science Approach	519
14.2	High-Energy Processes in the Atmosphere, Terrestrial Gamma-Ray Flashes (TGFs), and Gamma-Ray Glows	521
14.2.1	Gamma Ray Emissions During Thunderstorms	521
14.2.2	Gamma-Ray Glows	522
14.2.3	Terrestrial Gamma-Ray Flashes (TGFs)	523
14.2.4	TARANIS: A Satellite to Study the Effects of Thunderstorms and Lightning	524
14.2.5	Measure of Gamma Rays and Particles in the Earth Radiation Belts	526
14.2.6	Measure of Gamma Rays/Particles from the Radiation Belts	529
14.2.7	IGOSAT: A Student Nanosat Project to Measure Radiation Belts Gamma Ray/Particles	531
14.3	Conclusion	533
	References	534
15	Plastic Scintillator Detectors for Particle Physics	541
	Priscilla Brooks Cushman and David-Michael Poehlmann	
15.1	Introduction	541
15.2	Principles of Calorimetry in High-Energy Physics	542
15.2.1	Electromagnetic and Hadronic Showers	542
15.2.2	Historical Review of Plastic Scintillating Calorimetry	544

Contents	xix
15.3 Modern Plastic Scintillator Calorimeter Design	559
15.3.1 Experiments at the Large Hadron Collider	559
15.3.2 High-Granularity Calorimeters for Particle Flow Strategies	564
15.3.3 Dual-Readout Solutions	570
15.4 Neutrino Experiments	571
15.4.1 Optimizing Calorimeters for Neutrino Physics	571
15.4.2 Tracking Calorimeters for Neutrinos	572
15.5 Large Plastic Scintillator Detectors in the Future	579
15.5.1 Neutron Sensitivity	579
15.6 Conclusion	583
References	584
Appendix: Molecules Cited in the Book	589
Index	631

Contributors

Louis Archambault Département de physique, de génie physique et d'optique, et Centre de recherche sur le cancer, Université Laval, Quebec, QC, Canada; Service de physique médicale et radioprotection, Service de radio-oncologie et Axe oncologie du CRCHU de Québec, CHU de Québec - Université Laval, Quebec, QC, Canada

Héctor Bagán Department of Chemical Engineering and Analytical Chemistry, University of Barcelona, Barcelona, Spain

Luc Beaulieu Département de physique, de génie physique et d'optique, et Centre de recherche sur le cancer, Université Laval, Quebec, QC, Canada; Service de physique médicale et radioprotection, Service de radio-oncologie et Axe oncologie du CRCHU de Québec, CHU de Québec - Université Laval, Quebec, QC, Canada

Sam Beddar Department of Radiation Physics, The University of Texas MD Anderson Cancer Center, Houston, TX, USA;
The Graduate School of Biomedical Sciences, The University of Texas MD Anderson Cancer Center, Houston, TX, USA

Guillaume H. V. Bertrand Université Paris-Saclay, CEA, List, Palaiseau, France

Joseph S. Carlson Sandia National Laboratories, Livermore, CA, USA

M. Leslie Carman Lawrence Livermore National Laboratory, Livermore, CA, USA

Pablo Caron DPHY - Department of Physics, Instrumentation Environment and Space, ONERA, Toulouse, France

Sara Maria Carturan Dipartimento di Fisica e Astronomia, Università di Padova, Padua, Italy;
INFN – Laboratori Nazionali di Legnaro, Legnaro, PD, Italy

Philippe Cassette Sofia University “St. Kliment Ohridski”, Faculty of Physics, Sofia, Bulgaria

Sebastien Celestin Laboratory of Physics and Chemistry of the Environment and Space (LPC2E), University of Orleans, CNRS, CNES, Orleans, France

Priscilla Brooks Cushman School of Physics and Astronomy, University of Minnesota, Minneapolis, MN, USA

Christophe Dujardin Université de Lyon, Université Claude Bernard Lyon 1, CNRS, Institut Lumière Matière UMR 5306, Villeurbanne, France

Jonathan Dumazert Université Paris-Saclay, CEA, List, Palaiseau, France

Patrick L. Feng Sandia National Laboratories, Livermore, CA, USA

Camille Frangville Université Paris-Saclay, CEA, List, Palaiseau, France

José Francisco García Department of Chemical Engineering and Analytical Chemistry, University of Barcelona, Barcelona, Spain

Andrew M. Glenn Lawrence Livermore National Laboratory, Livermore, CA, USA

Matthieu Hamel Université Paris-Saclay, CEA, List, Palaiseau, France

Masanori Koshimizu Department of Applied Chemistry, Tohoku University, Miyagi, Japan

Philippe Laurent CEA, IRFU, CEA Saclay, Paris, France;
Laboratoire Astroparticule et Cosmologie, Paris, France

Bo Liu School of Physics Science and Engineering, Tongji University, Shanghai, People's Republic of China

Andrew N. Mabe Lawrence Livermore National Laboratory, Livermore, CA, USA

Vincent Maget DPHY - Department of Physics, Instrumentation Environment and Space, ONERA, Toulouse, France

Krasimir Mitev Sofia University “St. Kliment Ohridski”, Faculty of Physics, Sofia, Bulgaria

Yoann Moline Université Paris-Saclay, CEA, List, Palaiseau, France

Nicholas R. Myllenbeck Sandia National Laboratories, Livermore, CA, USA

Xiaoping Ouyang Northwest Institute of Nuclear Technology, Xi'an, People's Republic of China

David-Michael Poehlmann Department of Physics and Astronomy, University of California, Davis, CA, USA

Alberto Quaranta Department of Industrial Engineering, University of Trento, Trento, Italy

Alex Tarancón Department of Chemical Engineering and Analytical Chemistry, University of Barcelona, Barcelona, Spain;
Serra Hunter Fellow, Barcelona, Spain

Irwin Tendler Department of Radiation Physics, The University of Texas MD Anderson Cancer Center, Houston, TX, USA

François Therriault-Proulx Co-Founder, CEO At Medscint Inc., Quebec City, Canada

Mathieu Thevenin Université Paris-Saclay CEA SPEC CEA-CNRS UMR 3680, Gif-sur-Yvette, France

François Trompier IRSN, Fontenay-aux-Roses, France

Natalia P. Zaitseva Lawrence Livermore National Laboratory, Livermore, CA, USA

Part I

Materials

Chapter 1

Introduction—Overview on Plastic and Inorganic Scintillators



Christophe Dujardin and Matthieu Hamel

Abstract Scintillators are materials that are able to emit photons when impinged with ionizing radiations. This family of materials is covered by both organic and inorganic structures, with some similarities but also with different photophysical processes occurring underneath. The scientific fields and communities are in fact rather separated, while it would benefit from more interactions and collaborations. This book is mostly focused on plastic scintillators, which are polymer-based materials, and the purpose of this chapter is to introduce and link them to well-known inorganic scintillators. In addition, hybrids materials are new developments based on inorganic nanocrystals in organic host. In such hybrid materials, a complex interplay occurs along the energy relaxation leading to the emission of light. Thanks to their chemical versatility, plastic scintillators can easily be modified. Whereas the first decades have seen their use as “all-purpose” detectors, the most recent developments afford specialization of the materials toward a given application. Thus, various modification stages are possible: the simplest is to tune its chemical properties. In addition, this material is an optical device, and complicated photophysical phenomena occur in the radiation/matter interaction volume. Finally yet importantly, current developments in artificial intelligence, as well as highly sophisticated algorithms, are used to overcome intrinsic limitations of plastics properties. This chapter thus gives a historical perspective on the development of plastic scintillators with a mention of past and current main actors. Then, a discussion follows on the basic principles in plastic scintillation design. Their main properties are finally presented and compared with inorganic scintillators. Some of these properties will be partially discussed herein since they will be fully explained in dedicated chapters.

C. Dujardin

Institut Lumière Matière, Université de Lyon, Université Claude Bernard Lyon 1, CNRS, 69622 Villeurbanne, France
e-mail: christophe.dujardin@univ-lyon1.fr

M. Hamel

Laboratoire Capteurs Et Architectures Électroniques, Université Paris-Saclay, CEA, 91120 Palaiseau, List, France
e-mail: matthieu.hamel@cea.fr

1.1 History of Scintillators

The first scintillator ever described was BaPt(CN)₄ for X-ray detection in 1895. It was under the form as a powder, now called X-ray phosphor and played a major role in medical x-ray radiography. With the emergence of photomultipliers, the research on scintillating materials has been intensified. Thus, plastic scintillators (PSs) were first depicted in the literature by Marvin G. Schorr and Franklin L. Torney as early as 1950 [1], a few months only after their liquid equivalents were discovered [2, 3]. Regarding inorganic scintillators as single crystals, the main known compositions were discovered after the 1950s as depicted in [4].

This first plastic was composed of *m*-terphenyl dissolved in polystyrene.¹ Rapidly various formulations appeared which highlighted the necessity to add a wavelength-shifter (i.e., a molecule that is able to absorb UV light from the primary fluorophore and emits at longer wavelengths) to the abovementioned binary mixture so as to afford better scintillation external efficiency, including the light extraction as mentioned by Pichat and Pesteil [5]. These discoveries lead to the commercial plastic formulations we currently know. In 1953, the first loading attempts with organometallics in the form of bismuth hexahydrobenzoate or triphenylmethyllead were published by the same French group, already with the aim of increasing the effective atomic number for gamma spectroscopy [6]. This scintillator modification is one of the hottest topics in the context of homeland security [7, 8], the another one is the pulse shape discrimination between fast neutrons and gamma rays [9, 10] which was first described by Frank D. Brooks in 1960 [11]. Concerning thermal neutrons (i.e., with kinetic energy in the range of 25 meV) detection, loading with dedicated elements allowing their capture appeared in the early sixties. Thus, lithium was described in a Russian patent [12] and boron in a British report, later on popularized in a paper from Anisimova [13], thanks to isopropenyl boron carbohydride. Gadolinium appeared a few years later in the form of gadolinium benzoyl acetone at low concentration (typically $\leq 0.2\%$ of Gd) [14]. Gamma spectroscopy and neutron detection with plastics will be fully described in dedicated chapters of this book. Some other application-driven but peculiar developments were also performed: fluorine loading for high-energy neutron detection [15–17], cadmium [18], hafnium [19], various lanthanides and actinides [20], etc. Various elements can thus be loaded into plastics. Selected developments for both inorganic and organic scintillators are summarized in Fig. 1.1.

Later, John B. Birks published the first book on the principle of scintillation counting in 1964, covering notably the latest developments and use of plastics and inorganics [21]. During these first fifteen years, plastics were extensively studied with the aim to find the best composition in terms of scintillation efficiency, decay time, chemical stability, etc. It is noteworthy that the well-known combinations of fluorophores, e.g., *p*-terphenyl/POPOP or PPO/POPOP were discovered at this time,

¹Topological representation and key information of these molecules is given in the Appendix section at the end of the book.

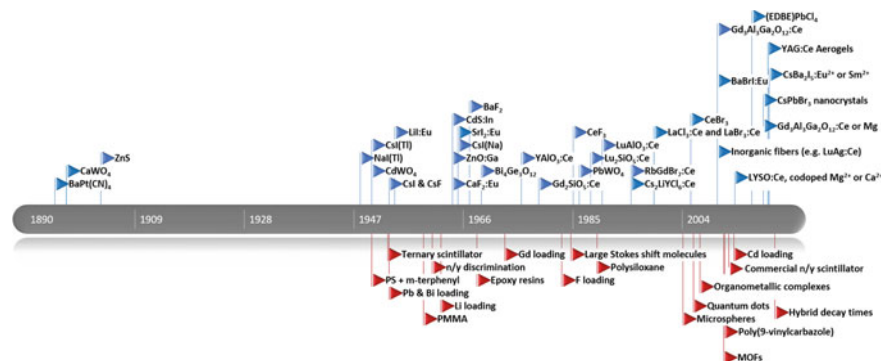


Fig. 1.1 Timeline of the main scintillator developments from 1890 to 2020 (illustrative only; for inorganics rather fast scintillators are considered)

and more details will be given in the following sections. Nowadays important developments are still performed as can be seen in the increasing number of publications talking about plastic scintillator modifications (Fig. 1.2).

Soon after the discovery of plastic scintillators, physics and chemical researches were followed by their industrial production. The Cold War probably took a key role as it involved important needs in the context of nuclear and radiological detection and radioprotection of the workers involved in the preparation of nuclear weapons. The two Blocs thus independently created their own facilities to cover them. Several companies emerged for the Western Bloc: *Pilot Chemicals* (USA, est. 1951), *National Radiac INC.* (Sintilon material, USA, before 1956 [22]), *Bicron* (USA, est. 1969), *Koch Light* (UK and USA, before 1969), and *Nuclear Enterprises Ltd.* (Scotland). Plastic scintillator NE 102 (NE standing for *Nuclear Enterprises*) was cited as early as 1959 [23]. Naton scintillators (*Nash & Thompson*, UK) appeared in the first part

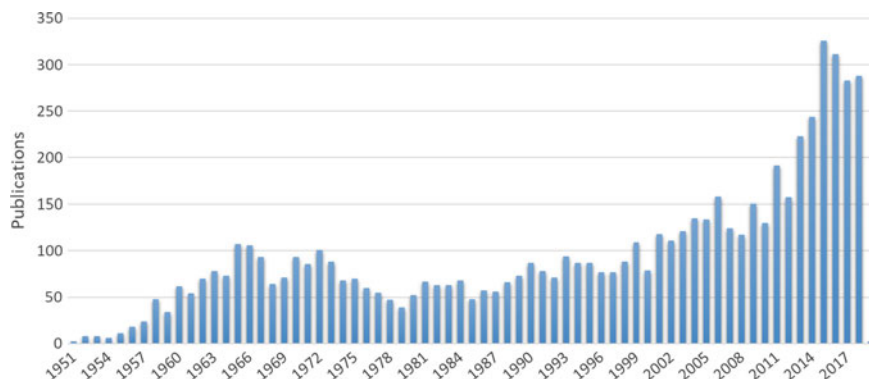


Fig. 1.2 Number of publications referring chemical modifications of plastic scintillators and sorted yearly (source SciFinder[®], as of November 2019)

of the 1960s. Later on, the Pilot-x references appear in the *Nuclear Enterprises* catalog. *Altulor* (France, 1957) and *Polivar* (Italy) were involved in the preparation of PMMA-based PSs, mostly for CERN experiments during the years 1985–1990. Some old catalog front covers can be seen in Fig. 1.3.

From the Eastern Bloc, three main institutes were created. First is the *Institute for High-Energy Physics* (IHEP, USSR, 1963). The research and development program of plastic scintillators was started in the 1970s from the initiative of V. Rykalin. In the beginning, the technology of manufacturing PSs by the method of large-block thermal polymerization (SC-2xx series) followed by mechanical treatment and polishing was settled. Then extruded plastics (SC-3xx series) were extensively studied. Other trade codes from IHEP exist under the form PSM-xxx series. For example, PSM-115 (an injection-molded plastic) was used in HERA-B (a particle physics experiment at the HERA accelerator at DESY, see Chap. 15). These PSM-xxx codes have disappeared from IHEP catalog. The maximum dimensions of the bulk scintillators are $200 \times 50 \times 10$ cm, with a production of up to 100 tons per year. Reference [24] presents all the key developments of IHEP in the field. In Ukraine, the *Institute of Scintillating Materials* (ISMA) was established in 2002 as a part of *Institute for Single Crystals* who found birth as early as 1955. ISMA has extended its inorganic research expertise to several other materials, including thus plastic scintillators. Former Czechoslovakia also has a long history in scintillators, whose research and development work started as early as 1952 in the Research Institute of Electronic Physics. In 1959, research and production were associated with the *TESLA National Corporation*. In the early 1990s, part of this institute was transformed into a private-owned company called *SM&D (Scintillation Materials and Detectors)*. This company was then acquired by *Envinet a.s.* in 2008, then *Nuvia CZ* in 2016.

In 1990, *Bicron* claimed a production capacity of 12 tons of plastic scintillator per month. It seems that *Saint-Gobain Crystals and Detectors* acquired both *Nuclear Enterprises* after 1987 and *Bicron* after April 1993. In 1997, *Eljen Technology*, a subsidiary of *Ludlum Measurements* was created by C. Hurlbut (formerly from *Bicron*) in Texas.

It is also worth mentioning *Kuraray* from Japan, who started the production of scintillating fibers but also some plastics as early as 1982. In 2013, the discovery of the Higgs Boson was achieved in part with the use of these scintillating fibers. Currently, *Kuraray* is a global leader together with *Saint-Gobain Crystals and Detectors* in fibers technology. Table 1.1 inventories current manufacturers as well as some trade characteristics. It seems also that other companies may provide scintillators on-demand, such as *FUJITOK* [25] or *Plaken co., Ltd* [26] in Japan; such companies are not listed in Table 1.1.

Through history, it may be difficult to find reliable data on all commercial scintillators. Table 1.2 lists the various scintillator codes their main property. This table could be useful for further cross-comparison since several materials are now out of commercialization. Some other commercial PSs might incidentally be omitted. Despite this large choice (especially in the case of standard formulation, which is obviously both the most available and the most sold as well), there are still exciting chemical challenges to overcome and new possibilities to be discovered. They will now be described.



Fig. 1.3 Catalog front covers of Nuclear Enterprises (1980), Bicron (1990) and TESLA (late 1970s), and advertisement of National Radiac INC. (this advertisement is reproduced from [22] with permission from the American Chemical Society)

Table 1.1 Main providers of plastic scintillators (in alphabetic order). Some companies may be resellers of other manufacturers

Name	Country	Trade codes	Estimated number of products
Advatech UK Limited	UK	n.d	Amcrys reseller
Amcrys	Ukraine	UPS-xxx	> 10
Beijing Nuclear Instrument Factory	China	ST-4xx	n.d.
Detec-Europe	France	n.d	Amcrys reseller
Eljen Technology	USA	EJ-2xx	21
Epic-Crystal	China	n.d	1
Institute for High-Energy Physics	Russia	SC-2xx (bulk) SC-3xx (molded)	24
Kuraray	Japan	SCSN-xx	3
Nuvia CZ	Czech Republic	NuDET Plastic	2
Perkin-Elmer	UK	Meltilex®	1
Rexon	USA	RP-xxx	3
Saint-Gobain Crystals and Detectors	USA	BC-4xx	21
Shandong Haiqiang Environmental Protection Technology Co., Ltd	China	n.d	n.d.
Win-Trust	China	SPxxx	3

n.d. not determined

1.2 Plastic Scintillator Chemists

Figure 1.4 tries to overview the main teams, laboratories, institutes or companies that are currently or were previously involved in plastic scintillators modification, as well as their period of activity when the information is available. It may be sometimes difficult to judge whether active research is still ongoing in some groups. Only the key laboratories (with two or more publications written in this field) are shown, and collaborations cannot be added, so the publications are granted to the corresponding author.

1.3 The Scintillation Process in Plastics and Inorganic Materials/Crystals

Whatever the liquid or plastic nature, an organic scintillator can be resumed as a matrix that contains one or several organic fluorophores and potentially some dopants for giving special application features. These fluorophores are usually called primary

Table 1.2 Classification of past and current commercial scintillators. Scintillating fibers and prototypes are omitted

Main application	Scintillator code (alphabetical order)
General purpose	BC-400, BC-404, BC-408, BC-412, BC-416, EJ-200, EJ-204, EJ-208, EJ-212, NE 102A, NE 110, NE 114, Pilot F, RP-200, RP-400, RP-408, SC-201, SC-202, SC-205, SC-301, SC-302, SC-304, SC-306, SC-307, SC-308, SC-309, SCSN-38, SCSN-61, SCSN-81, SP32, SP101, ST-401, UPS-89, UPS-90, UPS-96, UPS-923A
Long decay time	BC-444(G), EJ-240, NE 115, UPS-92S
Ultrafast timing	BC-418, BC-420, BC-422(Q), EJ-228, EJ-230, EJ-232(Q), KL 236, Naton 136, NE 104, NE 104B, NE 111A(ZIP), Pilot B, Pilot M, Pilot U, Pilot U2, SC-206, SC-207, SC-305, UPS-91F
Green emitting	BC-428, EJ-260, EJ-262, SC-203, SC-204, SC-303, SP33, UPS-974
Red emitting	BC-430, NE 108*
Lead loading	BC-452, EJ-256, NE 142, SC-223, SC-322
Tin loading	NE 140, SC-221, SC-222, SC-321
Fast neutron/gamma discrimination	EJ-276(G), NE 150, UPS-113NG
Deuterated polymer	BC-436, NE 125
Boron loading	BC-454, EJ-254, SC-231, SC-331
High temperature applications	BC-434, BC-438, BC-440(M), BC-448(M), EJ-244, EJ-248, NE 160
Low energy gamma rays or X-rays	BC-450, NE 105
Radiation hard	PSM-115, SCSN-81 T, UPS-92RH, UPS-98RH

*in Nuclear Enterprises catalog this scintillator is mentioned to emit at $\lambda_{\max} = 538$ nm, despite being classified as “red” plastic. However and according to the CIE rules, 538 nm is “yellowish green”

and secondary fluorophores, this name contracting to their respective role within the organic scintillator. In standard liquids or plastics, the matrix accounts for $\geq 95\%$ of the material, so radiation/matter interactions occur here. What happens afterwards has been extensively described elsewhere [21] and will be introduced in several chapters of this book. In a few words, excitons are created and are transferred from the matrix to the primary fluorophore, usually (but not exclusively) by Förster Resonance Energy Transfer (FRET), which is a non-radiative transfer. The second process is radiative and undergoes emission/absorption between a donor and an acceptor; this is the roles of the primary and the secondary fluorophores, respectively. Ultimately, the emission wavelength and potentially the scintillation decay time are usually governed by the secondary fluorophores. But various exceptions exist.

Similarly, an inorganic scintillator can be seen as a host containing emitting centers. The latter can be a doping ion or a point defect (extrinsic), but can be as



Fig. 1.4 Time and spatial repartition of laboratories and companies engaged in plastic scintillator modifications. Orange color is for active institutes, green for inactive institutes, and grey represents commercial companies

well an intrinsic emitting species such as an exciton. At each level, chemical developments are still under review (e.g., quantum dots, conducting polymers, new loadings, crystal growth, etc.), but one has to admit that the “old” formulations are still particularly efficient and notorious. In the case of plastic scintillators, new formulations have been reviewed from time to time [27–32] and was discussed as well in several books [21, 33, 34]. The case of inorganic scintillators is rather different since they became highly specialized regarding the field of application (γ -ray spectroscopy, fast timing...) [35]. Given the large number of suitable polymers and fluorophores for scintillation as well as their respective concentration within the polymer, numerous formulations are possible, but the chemist has to respect the following fulfilments:

The light yield, which is the number of photons emitted after radiation/matter interaction per unit of deposited energy, must be as high as possible and linear with the broadest absorbed energy range.

Chemical loading gives special properties to the plastic scintillator but must not interfere (or at least to the lowest extent) with its light yield. In addition, it must result in chemically and environmentally stable material since plastic is usually used for several years with expected retention of the global performances.

The material must be highly transparent to its own light (no self-absorption, eventually high Stokes shift²), otherwise it will not be possible to use it at large scale.

²The Stokes shift is the numerical difference between absorption and emission wavenumber maxima of the same electronic transition. It is calculated as $\Delta\nu = 1/\lambda_{\text{abs}}^{\text{max}} - 1/\lambda_{\text{flu}}^{\text{max}}$ in cm^{-1} .

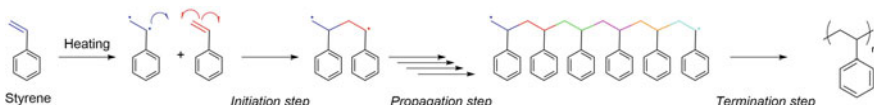
Depending on the application, a fast response might be required.

All these parameters will be fully described in this book.

1.4 Typical Preparation Process and Size Possibilities

Since plastic and inorganic scintillators differ from their chemical nature, their preparation process is not comparable.

All the plastics that are available from commercial suppliers are prepared in the same way, which is the thermally initiated radical polymerization. Two different aromatic polymers are used: either **poly(vinyltoluene)** or **polystyrene**. Whereas the former is currently being used by major companies such as *Eljen Technology* or *Saint-Gobain Crystals and Detectors*, the latter is the choice of *IHEP*, *Nuvia CZ*, and *Amcrys*. Thus, **purified monomers are mixed with fluorophores and heated so that complete polymerization is reached**. Heating breaks the styrene double-bond into two radicals, each of them being able to propagate with other styrene molecules, then creating oligomers and polymers. Scheme 1.1 represents a vulgarized polymerization of styrene, and this reaction being valid for vinyltoluene as well as all other monomers that are able to polymerize under radical polymerization method. Bulk, classical polymerization conditions (100–150 °C for several days) lead to polymers with high molecular weight, more than 200,000 [36], and typically 230,000–500,000 g.mol⁻¹ [37]. Polymers with molecular weights higher than 50,000 have shown to display better light output than scintillators composed of polymers with shorter chains [38]. The correlation between residual styrene and quality of the transmission spectrum at low wavelengths has been experimentally determined [39]. For polymers of molecular weight 50,000, almost 10% of styrene remains, and only 1.4% of styrene is still present in the bulk monolith for molecular weight of 210,000 g.mol⁻¹. Also, residual monomer is pointed as a key cause for scintillator aging. Other production methods than casting are possible: injection molding or extrusion. Here, the quantity of residual monomer is very low but these two methods usually lead to lower performance scintillator in terms of light output [40]. However, this production method has been chosen to equip calorimeters for high-energy physics experiments, as the as-prepared scintillators are prepared at lower cost than molding. On the margin, 3D-printing and digital light processing emerged as a new production possibility but they usually show moderate performances against the standard preparation methods [41–48], but the extensive R&D currently performing in this area should benefit to the scintillation field in the near future. As an example, CERN has recently communicated on a proof of concept of a 3D-printed “super-cube” (two



Scheme 1.1 Polymerization steps to polystyrene: initiation, propagation, and termination

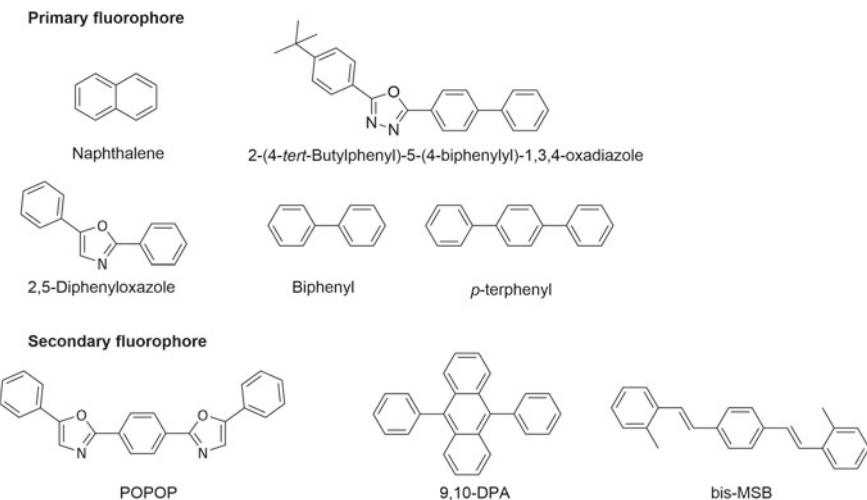


Fig. 1.5 Classical primary and secondary fluorophores used in most plastic (and liquid) scintillators

million cubic scintillators intended to be prepared with this technology) for neutrino oscillation experiments [49].

Since the polymer accounts for 70–97% of the composition of the scintillator, most of the energy released by the impinging ionizing radiation is deposited here. One can understand that the polymer must have fluorescent and scintillating properties. As itself, polystyrene (and poly(vinyltoluene) as well) is a primary scintillator, but due to its high self-absorption at its own emission wavelength (300–350 nm), it is not possible to use it as such [30]. Adding a primary fluorophore to the polymer constitutes the first step toward efficient plastics, but still the attenuation length is below 10 cm. Finally, a secondary fluorophore, usually called wavelength-shifter, is added to the composition leading acceptable attenuation length (typically more than 2 m, even 4 m according to commercial datasheets) and a standard composition of plastic scintillator is found. Figure 1.5 shows classical molecules that act as primary or secondary fluorophores. Probably the most known primary fluorophores are 2,5-diphenyloxazole and p-terphenyl and they can be coupled to 9,10-diphenylanthracene (9,10-DPA), 1,4-bis(2-methylstyryl)benzene (bis-MSB), or 1,4-bis(5-phenyl-2-oxazolyl)benzene (POPOP). Nevertheless, this list is obviously not exhaustive and every year new molecules or luminescent systems are being evaluated. A noticeable limitation of the design of new plastic scintillators is their iterative process: preparation of various formulations, characterization, and ranking according to their performances [31]. This methodology might be time-consuming and costly.

With such procedure, high quality and homogeneous scintillators can be produced with very large sizes as leading suppliers can prepare kg-scale slabs or cylinders. For example, *Saint-Gobain Crystals and Detectors* are able to provide 48 L plastics with dimensions $6 \times 40 \times 200 \text{ cm}^3$ [50] (but it is known that the same company can provide much bigger materials), *Amcrys* can offer up to 144 L plastics, and *Nuvia CZ* mentions the possibility to prepare up to 60 kg of monolith [51]. In fact, the volume

of the final scintillator is limited by the size of the oven used for heating the material while polymerizing. However, light scattering, heterogeneities of light production and collection may affect both light yield and energy resolution³ of the scintillator at such volume.

Inorganic scintillators can be prepared and used in various forms: single crystals, fibers, powders, thin films, aerogels [52], nanocrystals [35], and even hybrids [53], but the description of all the synthesis methods is out of the scope of this chapter. Note nevertheless, that the main difference is the melting point, as illustrated for typical inorganic scintillator (661 °C for NaI and 2050 °C for Lu₂SiO₅:Ce³⁺ (LSO)) rendering the cost productions for equivalent volume significantly higher due to heating.

1.5 Main Parameters and Tools for Modification or Improvement

Neither plastic nor inorganic scintillators can be considered as the “Holy Grail” in terms of radiation detection and price accessibility, so as the ultimate detector does not exist, and a careful choice must be performed when choosing the appropriate detector for the given application. Nonetheless, PSs can cover a broad range of applications, and above all their price compared with inorganic-based detectors can be a strong, even a decisive advantage. For example, PVT- and NaI:Tl-based detectors were compared for vehicle portal monitor applications [54]. Here, the balance is in the favor of plastic scintillator due to large number of traffic lanes that exist at border crossings and need to be equipped with such portal monitors, but the Authors conclude as “neither PVT nor NaI:Tl is a clear “winner” for all portal monitor applications [55].” Overall, the comparison might be tricky to realize since the two scintillators do not compete on the same performance skills and costs (as we will see thereafter).

So, if looking at pros and cons of using plastics versus inorganics, the main parameters are summarized in Table 1.3. It is somehow difficult to reference in an exhaustive way all the parameters that are useful for a radiological sensor, especially due to the versatility and the extreme diversity of both inorganic and plastic scintillators. Table 1.3 tries to reference the main parameters and the behavior of the materials under various external conditions. Here the cost of the scintillator (purchase from a supplier or laboratory production) has not been considered since it is not possible to make a comparison between all scintillators; so only material-related properties are discussed. For the inorganic world of scintillators, a very useful website has been created by Lawrence Berkeley National Laboratory [56]. As of November 2019, it was kept updated with numerous formulations, their main characteristics with suitable references. This is one of the most comprehensive databases freely available for scientists.

³The energy resolution is defined as the full width at half maximum (FWHM) of the full energy peak at a given energy.

Table 1.3 Main parameters for plastic and inorganic scintillators

Property	Plastics	Inorganics
Light yield	Up to 10,000 ph/MeV	Up to 100,000 ph/MeV
Decay time	0.3–280 ns, low afterglow	Down to sub ns
Emission wavelength	580 nm–650 nm	180 nm-IR
Material loading	Multiple elements	Multiple elements
Effective atomic number	Low (mostly H, C and O): 5.7	Can be high (> 60)
Density	1.04–1.56	Up to 9
Radiation hardness	Up to \approx 30 kGy with γ -rays	Depends on impurities
Temperature dependence	Low below 40 °C	Can depend from low to high temperature
Humidity	Partially fogging with moisture	Some are hygroscopic
Magnetic field influence	Light output increase with magnetic field	No studies

1.5.1 Light Yield

When compared to the best inorganics, the light yield of plastics may represent one of their main limitation, and the key to success for better formulations (low density is another limitation, in particular for gamma spectroscopy). It seems that there is an upper limit of 10,000 emitted photons per deposited MeV by the impinging ionizing radiation for regular formulations. Going beyond this limit has been the subject of numerous research projects, since this parameter has a strong impact on the others: energy resolution of the scintillator, sensibility to low incident energies, quality of the pulse shape discrimination. For example, it is difficult to reference how many organic fluorophores were tested to improve the light yield, some of them being chemically speaking highly designed to this field [57–60]. An extension of this work has led some teams to (re)consider unitary scintillators, that is to say composed of only one molecule. Thus, *N*-(2-ethylhexylcarbazole) is a carbazole derivative that affords a liquid scintillator with an intrinsic light output of 6,000 ph/MeV [61, 62]. A 90:10 mixture of two silanes: (bis(9,9-dimethyl-9*H*-fluoren-2-yl)bis(phenyl)silane and tris(9,9-dimethyl-9*H*-fluoren-2-yl)(phenyl)silane can form an organic glass with a light yield that is superior to standard plastic scintillators [63, 64 and Chap. 8].

Various factors can affect the light yield: purity of the starting chemicals, choice of the chemicals (monomers—polymers, fluorophores, the latter being either organic or organometallic), preparation process (e.g., polymerization method), optical improvements, etc. Standard fluorophores display excellent photophysical properties, with

optically-excited quantum yield close to unity, which is not the case for PS or PVT. Since the polymer accounts for the main part of the scintillator formulation, various polymers with potentially better fluorescence quantum yields or properties have been tested: poly(methyl methacrylate) (PMMA) [65], poly(lactic acid) [66], poly(2-vinylnaphthalene) [67], polyimides [68–71], poly(ethylene naphthalate) (PEN) [72, 73], poly(ethylene terephthalate) (PET) [73, 74], poly(vinyl alcohol) (PVA) [75], (Styrene Ethylene/Butadiene Styrene) copolymer (SEBS) [76], poly(9-vinylcarbazole) (PVK) and carbazole derivatives [77, 78], polysiloxanes [79, 80], polycarbonate [81], and poly(phenyl sulfone) [82]. Except that for PVK, improving the light yield with other polymers was unsuccessful. Reference [32] gives more details on these possible polymer modifications, and a focus on polysiloxanes and their applications is available in Chap. 5.

Only a few materials were announced to overcome this 10,000 ph/MeV limitation, but all the reported high light yields were given in a relative way, that is to say against a commercial scintillator. With the exception of organic glasses, all the materials contained organometallic compounds as the photoluminescent probe, with reported light yields of up to 32,000 ph/MeV, so three times the light output of a standard PS.

In addition, optical parameters have a strong influence on the final response of the scintillator: material self-absorption (especially in the case of pulse shape discriminating plastics) [83], global shape [84], nature of the covering layer (if any) [85], photon extraction [86], polishing quality of the surfaces [86], optical interface between the scintillator and the photosensor, surface covered by the photosensor [50], etc. One can see the important contribution performed in this field by the SuperNEMO experiment [86]. These optical questions are somehow the same whatever the nature of the scintillator. Several sections of this book will discuss chemical or optical improvements of the light yield.

As described above, the ideal and universal scintillator does not exist. A trade-off between global performances has always to be found in order to fit the requirements of the targeted uses. Some applications require the highest light yield. In priority, when high spectral resolution is required as for homeland security, the number of detected photons per interaction, i.e., the statistics has a large influence, and halides doped with Eu²⁺ have been developed accordingly. Several compositions with scintillation yield approaching the theoretical limit have been discovered. Several low-bandgap materials are now approaching the 100,000 ph/MeV [87]. These compounds exhibit such properties in the labs but production at large scale is not yet achieved. Among them, SrI₂:Eu²⁺ is probably the most advanced [35]. Noteworthy are also the recent advances of co-doping NaI:Tl leading to an energy resolution below 5% [88]. In addition, non-proportionality also plays a major role, and the highest yield does not always show the best energy resolution. Various factors may affect the yield. In the crude model, the scintillation mechanisms are split into three stages: multiplication, transfer, and luminescence, hence each step has to be efficient. The luminescence yield has to be almost 100% and this is the reason why Ce³⁺ and Eu²⁺ are widely used. They combine a very high luminescence yield approaching unity and a rather fast recombination time. Eu³⁺ and Tb³⁺ are also efficient but show a weak recombination rate leading to millisecond-range decay time. They are used as phosphors

but not as single crystals. The multiplication stage is mostly driven by the forbidden bandgap. Roughly, a small gap is generally preferred to favor the high number of secondary excitations. Regarding the transport stage, defects can be detrimental. A large interplay with the traps occurs in this stage and can lead to strong decrease of the scintillation yield and afterglow.

Noteworthy is the possibility to improve the external light yield of inorganics and plastics by imprinting the surface with photonic crystals. Chapter 9 will extensively present this breakthrough for plastics; reference [89] is the most suitable for inorganics.

1.5.2 ***Decay Time***

1.5.2.1 Main Component

Organic scintillators are known to be fast radiation detectors. In a perfect model, the decay constant can be described as a monoexponential decay: $i(t) \propto e^{-t/\tau}$, with τ being the luminescence decay. However, most of the experimental decays are usually better described as bi-exponential (τ_{fast} and τ_{slow}) or even non-exponential decays.

Most of the known PS decays fall within a range starting around a few hundreds of picoseconds up to almost 300 ns, with the whole range of decay times being covered. Ultrafast plastics are usually intended for use in ultrafast timing and counting [90, 91]. In the past, NE 111 and Naton 136 were very famous fast plastics. These materials are usually prepared from oxadiazoles such as PBD or butyl-PBD as the primary fluorophore (sometimes without wavelength-shifter, limiting therefore their use to cm^3 volume only due to strong self-absorption process), and quenching of the photoluminescence can be performed with internal quenchers such as benzophenone, piperidine, or other amines [92]. Such intermolecular quenching with low molecular weight additives seems to degrade the stability, thus the response of the scintillators [91].

On the opposite side, moderately slow [93] or slow scintillators [94] may find applications in dE/dx applications such as telescopes and phoswiches [95, 96]. It is noteworthy that such multiple-layered scintillator may also combine plastics with inorganics [97]. Only a few publications show the development of long-lived photoluminescent scintillators, and only one refers to the use of the phosphorescence of an organic molecule, namely erythrosin B with a lifetime of 0.64 ms [98], but the material suffered from stability. The second possibility is to benefit from the chemistry of organometallics, such as the ones based on iridium(III) [99–103] or europium(III) complexes [104–106]. For example, Ir(mppy)₃ in PVT or PVK displays a relative light output of 32,000 ph/MeV with a decay time of about 850 ns [99]. Such fluorophore choice has been driven by the spin-metal transition that allows harvesting triplet states, thus possibly performing fast neutron/gamma pulse shape discrimination thanks to triplet state deexcitations. It is therefore not the same decaying pathway than the primary fluorophore high-concentration strategy, which is usually used

Table 1.4 Examples of decay time values in plastics from 0.5 ns up to 370,000 ns

Polymer ^a	Fluorophores ^a	Decay time (ns)	Light yield (ph/MeV)	Ref
PVT	PBD (40 g/L) quenched by acetophenone (5%)	0.5	≈ 900	[89]
PS	EHCz (1–40 wt%)	14.9–22.1	1,230–2,700	[77]
PS	Proprietary mixture of two primary fluorophores	2.5–90	Not given	[93]
PVT	Ir(ppy-F ₂) ₂ (F ₂ -pic) (0.2%)	793	7,300	[100]
EpoTek	2-Naphthoic acid	110,000	Not given	[98]
PS	Eu(phen)(DBM) ₃ (2%)	370,000	5,650 ^b	[104]

^aPVT: poly(vinyltoluene), PS: polystyrene, PBD: 2-((1-biphenyl)-4-yl)-5-phenyl-1,3,4-oxadiazole, EHCz: N-(2-ethylhexyl)carbazole, Ir(ppy-F₂)₂(F₂-pic): (3,5-difluoro-2-pyridinecarboxylato)bis[3,5-difluoro-2-(2-pyridinyl)phenyl]iridium (III), Eu(phen)(DBM)₃: tris(acetylacetonato)(1,10-phenanthroline)europium(III). wt% stands for weight percentage

^bunder alpha irradiation

for fast neutron/gamma pulse shape discrimination [9]. Such organometallic fluorophores (and more generally organometallic loading) will be described in Chap. 4. It is amazing to see that the decay of plastic scintillators can extend on almost six decades (Table 1.4)!

In the case of inorganic scintillators, the primary decay is driven by the radiative rate of the emitting center. It can be accelerated when non-radiative processes occur, but it is detrimental to the light yield. Such situation is not really of interest for scintillation except when pile-up has to be avoided. Note that quite often, non-radiative processes are connected with thermal quenching rendering the decay time and the yield temperature-dependent. The range of decay time is rather wide. Faster scintillators are cross-luminescent materials (such as BaF₂, main decay time being around 0.8 ns in addition to a slow component of 630 ns) but they generally show a slow component and emit in the deep UV. Direct bandgap semi-conductors can be very fast but they generally show a strong self-absorption. ZnO:Ga is, as an illustration very interesting composition with this respect, with a 0.8 ns decay for the purest material [107]. Nanocrystals of semi-conductors are also under deep investigation. They exhibit a very fast emission due to the confined excitonic recombination. Self-absorption is still an issue, but in the case of 2D materials the fast bi-exciton emission is red shifted, and first attempts to use them for fast timing application are emerging [53]. Most common crystals are doped with popular activators such as Ce³⁺ leading to decays in the range of tens of ns, in the microsecond range for Eu²⁺ and Tl⁺, and in the ms range for Eu³⁺ and Tb³⁺. Note that depending on the crystal quality, some afterglow may appear.

1.5.2.2 Afterglow

Contrary to their liquid equivalents, plastic scintillators are not known to display problematic light afterglow. The delayed fluorescence of EJ-200 plastic scintillator has been recently measured in a time window ranging from 1 up to 10 μs [108]. The scintillation decay was expressed under the form of three exponentials with the corresponding weights: 7.8 ns (95.8%), 490 ns (2.2%), and 2,370 ns (2.0%). The exact description of the photon distribution with time is mandatory when plastics are used in experiments with high rates, i.e., when the afterglow may become an issue.

As explained above, afterglow occurs during the transport mechanism. It corresponds to traps acting as intermediate states for free carriers. The sequence of trapping and detrapping prior to the transfer toward the activator delays its emission. The detrapping probability depends on the trap depth, its frequency factor and on the temperature. It is rather impossible to give some typical values, even for a composition since it may vary from a producer to another. Because the afterglow is connected to a competition for the charge carriers to be captured by the activator or by the trap, co-doping is often used to mitigate that effect. Among all the existing commercial compositions, one of the lowest afterglows is observed for CdWO₄.

1.5.3 Emission Wavelength

Intrinsically both families of scintillators are able to emit light in the whole visible domain. In the case of plastics, adding suitable wavelength-shifters allow tuning the emission wavelength, typically with λ_{em}^{max} from 380 nm (polymer with primary fluorophore) up to ca. 640 nm, violanthrone being the last emitting species here [109] (Fig. 1.6).

The violet wavelength ($\lambda_{em}^{max} \approx 420\text{nm}$) is the most referenced since it is the predilection domain of standard photocathodes of photomultiplier tubes. Green-emitting scintillators appeared as a wavelength-optimized coupling for solid sensors such as photodiodes and CCDs, and also as radiation-hard scintillators. Red-emitting scintillators are privileged when Cherenkov residual background strongly interferes with the signal. This effect can become an issue in dosimetry (see Chap. 12) and in fusion experiments (e.g., Laser Mégajoule facility). Interestingly, Boldt and Tsipis used wavelength difference between two plastic scintillators in anticoincidence, with appropriate filters in front of the photomultiplier tubes [110]. When the first scintillator emits at 460 nm (PS + p -T + TPB + POPOP), the second emits at higher energies: 400 nm (PS + p -T). The concept of Spectral-Shape Discrimination was proposed by Feng et al. for fast neutron/gamma discrimination [100]. When excited with 2 MeV protons or 20 keV electrons, a poly(9-vinylcarbazole) scintillator containing Ir(ppy)₂(acac) emits photons at 515 nm and around 420 nm, respectively.

As for the decay time, the wavelength of emission is driven by the activator in inorganic scintillators. It ranges from deep UV down to IR. Some of the activators such as Eu³⁺ (red), Tb³⁺ (green) are rather insensitive to the host, and some others



Fig. 1.6 Raw scintillators with various emission wavelengths

are strongly affected by the crystal field. As an illustration, Ce^{3+} emits in the UV in fluorides while it emits in the red in iodides and sulfides. Some recent research studies with activated materials by both Eu^{2+} and Sm^{2+} show an efficient energy transfer from Eu^{2+} to Sm^{2+} , the latter emitting about 840 nm. These compositions show very good performances for gamma-ray spectroscopy (light yield in the range of 50,000 ph/MeV, energy resolution approaching 3% and a decay time of 2 μs) while emitting in the IR: the material is even visually black [111]!

1.5.4 Behavior Against External Environment

1.5.4.1 Radiation Hardness

Radiation hardness is not an issue for radioprotection or homeland security applications, but it turns to reality when used in large experiments where the fluence is very high such as in Large Hadron Collider at CERN. For example, some calorimeters are composed of alternated slices of plastic scintillators and depleted uranium (DU), and an accelerated loss of transmission was noticed due to the natural radioactivity of DU (see Chap. 15). In the world of plastic scintillators, rad-hard materials have become the specialty of Zorn et al. in the 90s [112–114] and more recently of the Institute for Scintillating Materials, and Amcrys offers a “rad-hard” commercial PS (see Table 1.2). A recent review has been published in this field in 2019 [115].

Three strategies arise: first is to replace polystyrene by polysiloxanes [116]. For example, *p*-terphenyl and bis-MSB were dissolved in HARDSL® (a polysiloxane) and were exposed to a 400 kGy proton radiation dose. The results showed a 7%

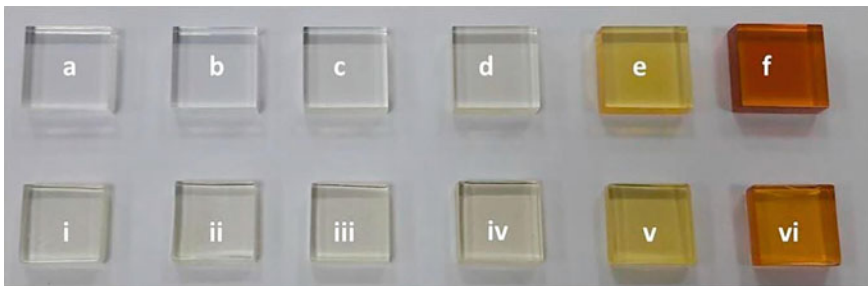


Fig. 1.7 Blue-emitting UPS-923A PS (top, *a*–*f*) and green-emitting PS (bottom, *i*–*vi*) gradually neat, then exposed to 10^{13} , 10^{14} , 10^{15} , 10^{16} , and 10^{17} n/cm² (reproduced from [126] with permission from Elsevier)

only loss of transmission at 400 nm. However, the transmission does not relate to the full story of the scintillation. PET and PEN polymers were also irradiated up to 140 kGy by the same team [117, 118]. Second is the use of fluorophores with exceptional Stokes shift: PMP [119] (although it seems that the same group later on discarded its use for such application a few months later [120]), or 3-HF and fluorinated flavones derivatives [121–124]. After degradation due to radiations, the transmission is reduced but molecules with high Stokes shift seem less affected than regular wavelength-shifters. Third is the use of colored centers diluters. These “diffusion enhancers” are usually aromatic liquid molecules: 4-isopropylbiphenyl, 1-isopropyl- and 1-methylnaphthalene, *p*-xylene and 1,6-dimethylnaphthalene [122, 125]. In addition, the polymer is cross-linked so that it maintains good mechanical properties. Thus, a scintillator composed of 1.5% of 4'-fluoro-3-hydroxyflavone, 8% of 4,4'-divinylbiphenyl and 25% of 4-isopropylbiphenyl as the diffusion enhancer presented an initial light output of 5,200 ph/MeV only but retained 94% of this value when exposed to 33 kGy. However, their mechanical properties might be impacted by the addition of such high amount of liquid in the polymer.

Usually, the radiation hardness is assessed under gamma exposition, but blue and green-emitting PSs have also been studied under a high neutron fluence ranging from 10^{13} to 10^{17} neutrons/cm² [126]. The visual aspect of these scintillators with the neutron dose is impressive with a strong amber-coloration due to the absorbed dose (Fig. 1.7). LEDs allow the scintillator to recover from radiation damage more rapidly [127].

Also of interest, fast neutron/gamma discriminating plastics were exposed to 10 kGy from a ⁶⁰Co source [128]. Several days after exposition, the scintillators were able to recover part of the light output as well as their yellow color vanished (Fig. 1.8). More surprisingly, the authors noticed that the quality of the neutron/gamma discrimination (the Figure of Merit value⁴) was improved after irradiation. ¹H NMR spectroscopy and High Resolution Mass Spectra Studies revealed

⁴The Figure of Merit value (*FoM*) is evaluated thanks to $FoM = \frac{|\mu_n - \mu_\gamma|}{2.35(\sigma_n^2 + \sigma_\gamma^2)}$, where n and γ are the mean positions of the neutron and the gamma-ray contributions, and σ_n and σ_γ are the standard

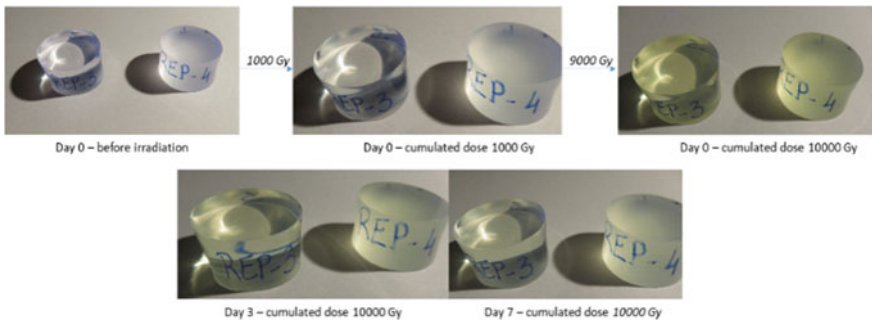


Fig. 1.8 Visual evolution of PSD plastics exposed to 10 kGy of gamma rays with time (reproduced from [128] with permission from the PCCP Owner Societies)

the formation of a formic anhydride derivative of POPOP. This demonstrates that secondary fluorophores have also an impact on the n/ γ discrimination performances (see Chap. 2). A similar study was also performed on EJ-299-33A prototype n/ γ plastic [129]. After irradiation of 28 kGy, no n/ γ discrimination remained visible. The influence of neutrons on the neutron/gamma discrimination performances of EJ-276 was also recently checked [130]. As expected, both light output and FOM value decrease with irradiation.

Regarding inorganic scintillators, the radiation hardness covers many aspects. The high-energy colliders for high energy physics is for sure addressed in order to avoid the transmission losses induced, and the tremendous work regarding PbWO₄ in the frame of CMS benefited from the Crystal Clear collaboration [131]. The radiation hardness nevertheless covers several other aspects in many applications. As an illustration, thin film detectors for imaging or beam monitoring in the next generations of synchrotron facilities will receive significant doses to modify internal mechanisms. Beyond the transmission aspect, radiation induces defects that may affect afterglow and internal yield as well. Even yield enhancement, called bright burn or hysteresis has been observed, such as in Eu²⁺-doped BaAl₄O₇ scintillator [132]. This aspect is detrimental for medical imaging where the X-ray panel is not uniformly irradiated and a small local change of the yield is critical for the image quality. The same effect is really an issue in dosimetry that requires a very good linearity response with respect to the dose. As for the afterglow, traps are strongly involved in these “memory” mechanisms.

1.5.4.2 Temperature Dependence

Plastics are known to be robust detectors against temperature variations, especially in the range -20–20 °C. More than the scintillator itself, the {scintillator—optical transducer—photodetector} whole system has to be considered to temperature variations,

deviations of neutron and gamma lobes. It determines numerically the quality of the neutron/ γ discrimination at a given energy, usually expressed in keVee.

with the photodetector being probably the most sensitive part of the system. In particular, scintillators for dosimetry may present exactly the same light output at room temperature (calibration) and at the temperature of the body (analysis, see Chap. 12). After the pioneering work of Rozman [133], Peralta studied the scintillation response of BC-404 PS and scintillating fibers in the range 0–40 °C [134]. BC-438 is a plastic scintillator that has been specifically designed for well-logging applications, where the temperature can sometimes reach 225 °C [135]. Its relative light output is 24% of NaI:Tl, that is to say $\approx 9,000$ ph/MeV. When heating the material in a dedicated system (with a less optimized optical transducer), the light output goes from $\approx 14\%$ of NaI:Tl at 25 °C down to $\approx 4\%$ at 200 °C, with a reported light output variation slope of $-0.02\%/\text{°C}$ in the range 25–50 °C. Unfortunately, the only information on this PS is its polystyrene base [136]; it means therefore that the scintillator is still usable way beyond its glass transition point (100 °C). BC-438 as well as BC-434 (another scintillator for high temperature experiments) are not anymore available in the *Saint-Gobain Crystals and Detectors* catalog. Cross-linked scintillators are copolymers that are prepared from styrene and another molecule bearing at least two polymerizable double-bonds, such as divinylbenzene or dimethacrylates. Such cross-linked polymers are already known from commercial suppliers (BC-440M, EJ-244) but recent publications have shown that the modified plastic scintillators had better mechanical properties [137, 138] and the light output was preserved when used at high temperatures, such as 120 °C [139], so higher than the T_g of PS or PVT.

Sometimes introducing new molecules may be followed by unexpected features. Sguerra et al. discovered that some organometallic complexes may be able to present thermoluminescent properties [103]. Thus, Ir(pic)₂(acac) doped at 0.05 wt% in a plastic scintillator displays an intense thermoluminescence as a competitive process to scintillation and thus could be misclassified. Thus, charging this scintillator with ambient light at room temperature would lead to the release of the equivalent of 40,000 ph/MeV.

The main mechanism leading to thermal dependence of inorganic scintillator is the so-called thermal quenching, where the luminescent center shows a strong electron-phonon coupling. This effect is not specific to scintillation and occurs under optical excitation as well. Famous scintillators such as PbWO₄ or BGO are fast because of the non-radiative recombination that operates even at room temperature. It affects thus the scintillation yield and the time response and in calorimetry where a stability of the scintillation response is required, the scintillator is thermalized. For oil logging and exploration where γ -spectroscopy is required, the temperature is largely increased at deep underground. At low temperature, afterglow often appears due to stabilization of trapped carriers and even a scintillation yield decrease can be observed. These aspects are of importance in the case of bolometry using scintillators. Another phenomenon is the decrease of the yield at large temperature due to phonon-assisted auto-ionization as observed in YAG:Ce in the frame of LED application [140]. Finally, the scintillation response non-proportionality also depends on the temperature due to the dependence of the migration distances during the thermalization stage.

Fig. 1.9 Example of temporary fogging of PS after hot and humid exposure and rapid cooling performed in a laboratory (reproduced from [145] with permission from Elsevier)



1.5.4.3 Moisture Effect

When mounted in radiation portal monitors, detectors are subjected to both temperature and humidity variations between night and day cycles. As a result, fogging degradation can appear due to water permeation with the material, leading to unscheduled maintenance of the detectors. R&D teams from USA have extensively studied and proposed solutions to avoid this unwanted effect [141–147]. Around 200- μm microcrazes appear throughout the whole volume, leading to useless detectors during months (Fig. 1.9). This is usually the case for both PS- or PVT-based scintillators. More than the humidity itself, the combination with low and ambient temperatures might affect the material. Both internal (i.e., material modification) and external (coating) solutions exist to circumvent this effect.

Sensitivity to moisture is the main chemical instability for inorganics, nevertheless, appropriate packaging is efficient. NaI:Tl and LaBr₃:Ce are illustrative hygroscopic but commercial products.

1.5.4.4 Magnetic Field Influence

At a glance, magnetic fields should be considered as having no or little influence on plastic scintillators' response. This effect is in turn of primary importance due to the strong magnetic induction taking place in colliders, calorimeters, and magnetic resonance imagers.

Magnetic field dependence of the light output has been barely studied. In particular, the theory underneath this evolution is still unclear, without any supporting Monte-Carlo simulations. Rather than detector effects, the way the energy is deposited within the material could be modified with the magnetic field: exciton

diffusion, changed Birks' saturation effect. Three major findings arise [148]: first, the light output increases with the surrounding magnetic field. Thus, up to 20% more photons are created with magnetic fields up to 1.5 T. Most of this light increase is attributed to Cerenkov light production in the clear parts of the detector (e.g., optical fiber); when the signal is corrected, there is still an increase of 2.4% of the light output [149]. Second, various formulations afford different patterns, as can be seen between SCSN-38, NE 102A, and Polivar scintillators [150, 151]. The latter is a PMMA-based material containing 3–10% of naphthalene and 1% of butyl-PBD (and POPOP or BBD as wavelength-shifter) and shows the strongest field dependence. Despite their (small) polymer difference: PVT for NE 102A and PS for SCSN-38, both scintillators behave the same way between 0 and 0.45 T. Last, the results differ if the scintillator is a bulk monolith or a scintillating fiber. Chapter 12 will provide more insight into this effect on plastic scintillators and scintillating fibers.

The influence of magnetic field on inorganics seems poorly studied. At CERN/CMS, PbWO₄ has been installed in a high magnetic field calorimeter and seems safe for use.

1.5.5 Effective Atomic Number and Density

These parameters are essential to perform gamma spectrometry measurements, e.g., for the crucial application of homeland security, or when high-stopping power is required, and by essence inorganics are highly privileged against plastics. Since PSSs are mainly composed of carbon and hydrogen, their effective atomic number Z_{eff} is around 5.7, so mainly Compton scattering occurs after gamma interaction with energies ≥ 100 keV. Here, organometallic chemistry and material engineering are powerful tools to add peculiar elements to plastic scintillators [152]. To increase Z_{eff} , heavy metals such as tin, lead, or bismuth have been extensively studied [7], the main challenge being to load the material with large quantities of metal without affecting both optical transparency and light output. From these three metals, lead seems to quench the scintillation more than the two others do. Thanks to the use of tributyltin methacrylate as the organometallic (with 6 wt% of tin in the scintillator), a pseudo-gamma spectrometry is reachable at incident gamma energies up to the gamma emitted by ²²Na ($E_{\gamma} = 1,274$ keV) [153, 154]. This scintillator was reported to display around 6,600 ph/MeV under γ -rays excitation.

In fact, it is currently difficult to judge on a future substitution of inorganics by metal-loaded plastics. In some cases, the fraction of photopeak against all detected events seems too low to account for an acceptable, key-determining feature allowing determining the nature of the incident gamma ray. However, recent improvement in unfolding algorithms such as ML-EM (standing for Maximum-Likelihood fitting by Expectation Maximization method) appear extremely promising to resolve such spectra [155, 156]. Here as well, Chap. 4 on organometallic addition to scintillators will perform an in-depth understanding of this important loading, and Chap. 10 on new deconvolution algorithms will complete the discussion.

About the density, plastics are obviously driven by the matrix and heavy metal loading, even if high content does not change dramatically the metrics. Poly(pentafluorostyrene) affords scintillators with density 1.56, so 50% higher than polystyrene or PVT [17].

Inorganic crystals are by far performing regarding the density and they are widely used for gamma-ray spectroscopy. The main effect of the density on the scintillation yield, i.e., once the energy is deposited, appears on the so-called alpha/gamma quenching factor. The energy deposition of alpha particle in matter is driven by the Beth-Bloch formula. It means that the density of generated excitation is higher than under gamma-ray excitation. It appears that high spatial density of excitation induces quenching, leading thus to a significant difference of scintillation yield between gamma-ray excitation and alpha particle excitation. The ratio is called the quenching factor. Because dense material leads to higher density of excitation, they will be less favorable to alpha detection with this respect. As an illustration, the quenching factor is 0.12 for LSO (d 7.4, Z_{eff} 66) and 0.15 for BGO (d 7.15, Z_{eff} 75.2) while it is 0.5 for NaI:Tl (d 3.67, Z_{eff} 50.8).

1.6 Summary

After 70 years of paramount discoveries, plastic scintillators cannot be avoided in various applications such as homeland security, nuclear batteries [157], environmental assays, radioprotection, or personal dosimetry. In this chapter, we reviewed on a historical point of view the development of plastic scintillators, the key laboratories and companies and their main properties alongside with inorganics.

All the molecules that are involved in the preparation have been thoroughly investigated: polymer, primary fluorophore and wavelength-shifter. Still, there is a lot of room for improvement due to the large molecular and photophysical diversity. Loading the polymer with additives grants the scintillator with special features: gamma spectroscopy with organometallics, radiation hardness with diffusion enhancers, etc. The photophysical understanding of fast neutron/gamma discrimination is a stunning level. On this basis, it is not difficult to understand why these materials are so popular in the nuclear physics community. As a ultimate proof, the three new plastic scintillators—and probably others—that have been commercialized in the last ten years (EJ-276 from *Eljen Technology*, NuDET Plastic SP33 from *Nuvia CZ*, and UPS-113NG plastic from *Amcrys*) show that undoubtedly the research on new materials and/or new concepts is still challenging for cross-disciplinary teams of chemists and physicists. The chemistry of nanomaterials (e.g., quantum dots, metal-organic frameworks, nanocomposites) has changed several paradigms and composites (mixtures of inorganic and organic materials) or heterostructured scintillators combine the advantages of both families.

In addition to this chapter and the references herein cited, the reader is encouraged to open the following reviews and book chapters that have been published after 2000. For plastic scintillators: reviews [8, 9, 31, 32, 65, 115, 158–167] and book or book

chapters [7, 10, 157, 168, 169]. All these recent reviews undoubtedly demonstrate the high research activity in this field. For inorganics, please refer to these reviews [4, 35, 89, 160, 170], book or book chapters [171, 172]. For composite and hybrid materials please refer to [173–175] and Chap. 6.

Acknowledgements CD would like to thank the Crystal Clear Collaboration as well as the SCINT conference series community. MH would like to thank Hana Burešova, Sergey Kushko and Vladimir Rykalin for their help in the industrial history section. All the scientists that have been involved since 2009 in the development of plastic scintillators at CEA area are also particularly acknowledged. This cross-disciplinary work could not be performed without the collaboration of chemists, physicists, and electronics. This laboratory is one of the few where all this heterogeneous mixture can become a homogenous and efficient blend. National and international collaborators are not forgotten since new methodologies to be learnt always lead to better knowledge for both parties. Last, Stéphane Normand is particularly acknowledged for everything he has given to me: the discovery of nuclear instrumentation and cross-disciplinary science, and above all trust, integrity, friendship.

References

1. M.G. Schorr, F.L. Torney, Phys. Rev. **80**(3), 474 (1950)
2. G.T. Reynolds, F.B. Harrison, G. Salvini, Phys. Rev. **78**(4), 488 (1950)
3. H. Kallmann, Phys. Rev. **78**(5), 621 (1950)
4. M.J. Weber, J. Lumin. **100**(1–4), 35 (2002)
5. L. Pichat, P. Pesteil, Perfectionnements apportés aux corps solides fluorescents, notamment pour le comptage d'événements radio-actifs par scintillation. FR-1071794. Accessed 10 Oct 1952
6. L. Pichat, P. Pesteil, J. Clément, J. Chim. Phys. Phys.-Chim. Biol. **50**, 26 (1953)
7. M. Hamel, F. Carrel, in *New Insights on Gamma Rays*, ed. by A. M. Maghraby (InTech, 2017), pp. 47–66
8. T.J. Hajagos, C. Liu, N.J. Cherepy, Q. Pei, Adv. Mater. **30**(27), 1706956 (2018)
9. G.H.V. Bertrand, M. Hamel, S. Normand, F. Sguerra, Nucl. Instr. Methods A **776**, 114 (2015)
10. P. Zhmurin, in *Engineering of Scintillation Materials and Radiation Technologies. Proceedings of ISMART 2016*, vol. 200, ed. by M. Korzhik, A. Gekhtin (Springer Proceedings in Physics, Cham, 2017), pp. 129–149
11. F.D. Brooks, R.W. Pringle, B.L. Funt, I.R.E. Trans, Nucl. Sci. **7**(2–3), 35 (1960)
12. E.E. Baroni, D.V. Viktorov, I.M. Rozman, V.M. Shoniya, Plastic scintillators for neutron recording, SU 1961-745031. Accessed 16 Sept 1961
13. G.I. Anisimova, L.S. Danelyan, A.F. Zhigach, V.R. Lazarenko, V.N. Siryatskaya, P.Z. Sorokin, Prib. Tekh. Eksp. **1**, 49 (1969)
14. J.B. Czirr, Nucl. Instr. Meth. **108**, 613 (1973)
15. D.V. Viktorov, L.A. Gorbunov, I.M. Rozman, A.M. Sirenko, V.M. Shoniya, At. Energ. **54**, 58 (1983)
16. I.B. Nemchenok, A.A. Shurenkova, V.B. Brudanin, N.A. Gundorin, V.V. Timkin, Bull. Russ. Acad. Sci.: Phys. **76**(11), 1187 (2012)
17. M. Hamel, P. Sibczyński, P. Blanc, J. Iwanowska, F. Carrel, A. Syntfeld-Kažuch, S. Normand, Nucl. Instr. Methods A **768**, 26 (2014)
18. I.B. Nemchenok, A.A. Shurenkova, V.B. Brudanin, N.A. Gundorin, V.V. Timkin, Bull. Russ. Acad. Sci.: Phys. **76**(11), 1187 (2012). Translated from Izv. Ross. Akad. Nauk, Ser. Fiz. **76**(11), 1326 (2012)
19. F. Hiyama, T. Noguchi, M. Koshimizu, S. Kishimoto, R. Haruki, F. Nishikido, T. Yanagida, Y. Fujimoto, T. Aida, S. Takami, T. Adschiiri, K. Asai, Jpn. J. Appl. Phys. **57**(1), 012601 (2018)

20. Z.W. Bell, C. Huei-Ho, G.M. Brown, C. Hurlbut, Method of loading organic materials with group iii plus lanthanide and actinide elements, US6544442. Accessed 22 Sept 1999
21. J.B. Birks, *The Theory and Practice of Scintillation Counting* (Pergamon Press, Oxford, 1964).
22. Anal. Chem. **28**(8), 38A (1956)
23. F.D. Brooks, Nucl. Instr. Meth. **4**(3), 151 (1959)
24. V. Rykalin, V. Brekhovskikh, S. Chernichenko, A. Gorin, V. Semenov, J. Phys. Sci. Appl. **5**, 6 (2015)
25. Y. Morishita, K. Hoshi, T. Torii, Nucl. Instr. Methods A **966**, 163795 (2020)
26. M. Koshimizu, T. Yanagida, R. Kamishima, Y. Fujimoto, K. Asai, Sens. Mater. **31**(4), 1233 (2019)
27. R.C. Sangster, J.W. Irvine Jr., J. Chem. Phys. **24**(4), 670 (1956)
28. I.M. Rozman, S.F. Kilin, Sov. Phys. Usp. **2**, 856 (1960)
29. F.D. Brooks, Nucl. Instr. Meth. **162**(1–3), 477 (1979)
30. S.W. Moser, W.F. Harder, C.R. Hurlbut, M.R. Kusner, Radiat. Phys. Chem. **41**(1/2), 31 (1993)
31. I.G. Britvich, V.G. Vasil'chenko, V.N. Kirichenko, S.I. Kuptsov, V.G. Lapshin, A.P. Soldatov, A.S. Solov'ev, V.I. Rykalin, S.K. Chernichenko, I.V. Shein, Instr. Exp. Techn. **45**(5), 644 (2002). Translated from Prib. Tekhn. Eksp. **45**(5), 66 (2002)
32. G.H.V. Bertrand, M. Hamel, F. Sguerra, Chem. – Eur. J. **20**(48), 15660 (2014)
33. D.L. Horrocks, *Organic Scintillators—Proceedings of the International Symposium on Organic Scintillators, Argonne National Laboratory, June 20–22, 1966*, (Gordon and Breach, New York, 1968)
34. B.M. Krasovitskii, B.M. Bolotin, *In Organic Luminescent Materials* (Wiley, Weinheim, 1988), p. 200
35. C. Dujardin, E. Auffray, E. Bourret-Courchesne, P. Dorenbos, P. Lecoq, M. Nikl, A.N. Vasil'ev, A. Yoshikawa, R.-Y. Zhu, IEEE Trans. Nucl. Sci. **65**(8), 1977 (2018)
36. A. Wieczorek, K. Dulski, S. Niedźwiecki, D. Alfs, P. Bialas, C. Curceanu, E. Czerwiński, A. Danel, A. Gajos, B. Glowacz, M. Gorgol, B. Hiesmayr, B. Jasińska, K. Kacprzak, D. Kamińska, L. Kaplon, A. Kochanowski, G. Korcyl, P. Kowalski, T. Kozik, W. Krzemień, E. Kubicz, M. Kucharek, M. Mohammed, M. Pawlik-Niedźwiecka, M. Palka, L. Raczyński, Z. Rudy, O. Rundel, N.G. Sharma, M. SilarSKI, T. Uchacz, W. Wiślicki, B. Zgardzińska, M. Zieliński, P. Moskal, PLoS ONE **12**(11), e0186728 (2017)
37. M. Hamel, V. Simic, S. Normand, React. Funct. Polym. **68**(12), 1671 (2008)
38. B.L. Funt, A. Hetherington, Int. J. Appl. Radiat. Isot. **4**(3–4), 189 (1959)
39. M.D. Shafranov, L.Y. Zhil'tsova, E.N. Matveeva, A.Y. Klimova, J. Appl. Spectrosc. **20**(1), 130 (1974)
40. Ł. Kaplon, A. Kochanowski, M. Molenda, P. Moskal, A. Wieczorek, T. Bednarski, P. Białas, E. Czerwiński, G. Korcyl, J. Kowal, P. Kowalski, T. Kozik, W. Krzemień, S. Niedźwiecki, M. Pałka, M. Pawlik, L. Raczyński, Z. Rudy, P. Salabura, N. Gupta-Sharma, M. SilarSKI, A. Stłomski, J. Smyrski, A. Strzelecki, W. Wiślicki, M. Zieliński, N. Zoń, Bio-Algorithms and Med-Systems **10**(1), 27 (2014)
41. Y. Mishnayot, M. Layani, I. Cooperstein, S. Magdassi, G. Ron, Rev. Sci. Instrum. **85**(8), 085102 (2014)
42. G. Ron, S. Magdassi, I. Cooperstein, M. Layani, Y. Mishnayot, Methods for fabricating 3-dimentional scintillators, WO215118533. Accessed 04 Feb 2014
43. J. Son, D.G. Kim, S. Lee, J. Park, Y. Kim, T. Schaarschmidt, Y.K. Kim, J. Korean Phys. Soc. **73**(7), 887 (2018)
44. S. Lee, J. Son, D.G. Kim, J. Choi, Y.K. Kim, Nucl. Instr. Methods A **929**, 23 (2019)
45. D.-G. Kim, S. Lee, J. Park, J. Son, T.H. Kim, Y.H. Kim, K. Pak, Y.K. Kim, Nucl. Eng. Technol. **52**(12), 2910 (2020)
46. D.-G. Kim, S. Lee, J. Park, J. Son, Y.H. Kim, Y.K. Kim, EPJ Web. Conf. **225**, 01005 (2020)
47. S. Berns, A. Boyarinsev, S. Hugon, U. Kose, D. Sgalaberna, A. De Roeck, A. Lebedynskiy, T. Sibilieva, P. Zhmurin, J. Instrum. **15**, P10019 (2020)
48. N. Lynch, T. Monajemi, J.L. Robar, Biomed. Phys. Eng. Express **6**(5), 055014 (2020)

49. CERN website. <https://home.cern/news/news/experiments/cern-led-international-collaboration-develops-3d-printed-neutrino-detectors>. Accessed 25 June 2020
50. M.R. Kusner, P.R. Menge, M.T. McLaughlin, Large Plastic Scintillator with Efficient SiPM Readout. Poster presented at the 2017 IEEE Nuclear Science Symposium and Medical Imaging Conference (NSS/MIC), Atlanta, Georgia, USA. Accessed 21–28 Oct 2017
51. NUVIATECH Instruments website. <https://www.nuviatech-instruments.com/product/nudet-plastic/>. Accessed 25 June 2020
52. M. Odziomek, F. Chaput, C. Dujardin, F. Lerouge, P. Cassette, M. Sitarz, S. Parola, A.C.S. Appl. Mater. Interfaces **10**(38), 32304 (2018)
53. R.M. Turtos, S. Gundacker, S. Omelkov, B. Mahler, A.H. Khan, J. Saaring, Z. Meng, A. Vasil'ev, C. Dujardin, M. Kirm, I. Moreels, E. Auffray, P. Lecoq, NPJ 2D Mater. Appl. **3**, 37 (2019)
54. D.C. Stromswold, E.R. Siciliano, J.E. Schweppe, J.H. Ely, B.D. Milbrath, R.T. Kouzes, B.D. Geelhood, I.E.E.E. Nucl. Sci. Symp. Conf. **2**, 1065 (2003)
55. E.R. Siciliano, J.H. Ely, R.T. Kouzes, B.D. Milbrath, J.E. Schweppe, D.C. Stromswold, Nucl. Instr. Methods A **550**(3), 647 (2005)
56. S. Derenzo, M. Boswell, M. Weber, K. Brennan, Lawrence Berkeley National Laboratory website. <https://scintillator.lbl.gov/>. Accessed 25 June 2020
57. S.A. Ponomarenko, N.M. Surin, O.V. Borshchev, Y.N. Luponosov, D.Y. Akimov, I.S. Alexandrov, A.A. Burenkov, A.G. Kovalenko, V.N. Stekhanov, E.A. Kleymuk, O.T. Gritsenko, G.V. Cherkayev, A.S. Kechek'yan, O.A. Serenko, A.M. Muzafarov, Sci. Rep. **4**, 6549 (2014)
58. T.Y. Starikova, N.M. Surin, O.V. Borshchev, S.A. Pisarev, E.A. Svidchenko, Y.V. Fedorov, S.A. Ponomarenko, J. Mater. Chem. C **4**, 4699 (2016)
59. M.S. Skorotetckya, O.V. Borshcheva, G.V. Cherkayeva, S.A. Ponomarenko, Russ. J. Org. Chem. **55**, 25 (2019)
60. S.A. Ponomarenko, N.M. Surin, M.S. Skorotetcky, O.V. Borshchev, S.A. Pisarev, E.A. Svidchenko, Y.V. Fedorov, F. Molins, T. Brixner, J. Mater. Chem. C **7**, 14612 (2019)
61. E. Montbarbon, F. Sguerra, G.H.V. Bertrand, É. Magnier, R. Coulon, R.B. Pansu, M. Hamel, Chem. – Eur. J. **22**(34), 12074 (2016)
62. M. Hamel, G. Bertrand, F. Sguerra, Procédé de mesure en scintillation liquide, utilisation, composition et kit associés, WO2017077241. Accessed 03 Nov 2016
63. J.S. Carlson, P. Marleau, R.A. Zarkesh, P.L. Feng, J. Am. Chem. Soc. **139**(28), 9621 (2017)
64. P.L. Feng, J.S. Carlson, High-efficiency organic glass scintillators, US9845334. Accessed 10 Oct 2016
65. V.N. Salimgareeva, S.V. Kolesov, Instr. Exp. Techn. **48**(3), 273 (2005)
66. M. Hamel, G. Lebouteiller, J. Appl. Polym. Sci. **137**(21), 48724 (2019)
67. I. Sen, D. Penumadu, M. Williamson, L.F. Miller, A.D. Green, A.N. Mabe, IEEE Trans. Nucl. Sci. **58**(3), 1386 (2011)
68. A. Quaranta, S. Carturan, G. Maggioni, P.M. Milazzo, U. Abbondanno, G. Della Mea, F. Gramegna, U. Pieri, IEEE Trans. Nucl. Sci. **48**(2), 219 (2001)
69. A. Quaranta, A. Vomiero, S. Carturan, G. Maggioni, G. Della Mea, Synth. Met. **138**(1–2), 275 (2003)
70. S. Carturan, A. Quaranta, A. Vomiero, M. Bonafini, G. Maggioni, G. Della Mea, IEEE Nucl. Sci. Symp. Conf. **2**, 869 (2004)
71. S. Carturan, A. Quaranta, A. Vomiero, M. Bonafini, G. Maggioni, G. Della Mea, IEEE Trans. Nucl. Sci. **52**(3), 748 (2005)
72. Y. Efremenko, L. Fajt, M. Febbraro, F. Fischer, C. Hayward, R. Hodák, T. Kraetzschmar, B. Majorovits, D. Muenstermann, E. Öz, R. Pjatkan, M. Pohl, D. Radford, R. Rouhana, E. Sala, O. Schulz, I. Štekl, M. Stommel, J. Instrum. **14**, P07006 (2019)
73. H. Nakamura, Y. Shirakawa, H. Kitamura, T. Yamada, Z. Shidara, T. Yokozuka, P. Nguyen, T. Takahashi, S. Takahashi, Radiat. Meas. **59**, 172 (2013)
74. H. Nakamura, Radiation detection element using waste plastic, WO2011067952. Accessed 04 Dec 2009

75. J. Oliveira, P.M. Martins, V. Correia, L. Hilliou, D. Petrovykh, S. Lanceros-Mendez, *Polym. Test.* **69**, 26 (2018)
76. J. Oliveira, V. Correia, P. Costa, A. Francesko, G. Rocha, S. Lanceros-Mendez, *Compos. B* **133**, 226 (2018)
77. E. Montbarbon, F. Sguerra, G.H.V. Bertrand, S. Gaillard, J.-L. Renaud, R.B. Pansu, M. Hamel, *ChemPhotoChem* **1**, 451 (2017)
78. M. Hamel, G. Bertrand, F. Sguerra, Scintillateur plastique, détecteur, procédé de fabrication et procédé de mesure par scintillation associés, FR1652902. 01 Apr 2016
79. A. Quaranta, S.M. Carturan, T. Marchi, V.L. Kravchuk, F. Gramegna, G. Maggioni, M. Degerlier, *IEEE Trans. Nucl. Sci.* **57**(2), 891 (2010)
80. T. Marchi, F. Pino, C.L. Fontana, A. Quaranta, E. Zanazzi, M. Vesco, M. Cinausero, N. Daldosso, V. Paterlini, F. Gramegna, S. Moretto, G. Collazuol, M. Degerlier, D. Fabris, S.M. Carturan, *Sci. Rep.* **9**, 9154 (2019)
81. H. Nakamura, Y. Shirakawa, H. Kitamura, N. Sato, S. Takahashi, *Jpn. J. Health Phys.* **49**(2), 98 (2014)
82. H. Nakamura, Y. Shirakawa, N. Sato, H. Kitamura, S. Takahashi, *Radiat. Meas.* **73**, 14 (2015)
83. E. Montbarbon, Z. Zhang, A. Grabowski, R. Woo, D. Tromson, C. Dehé-Pittance, R.B. Pansu, G.H.V. Bertrand, M. Hamel, *J. Lumin.* **213**, 67 (2019)
84. A.S. Barabash, A. Basharina-Freshville, S. Blot, M. Bongrand, C. Bourgeois, D. Breton, V. Brudanin, H. Burešová, J. Buste, A.J. Caffrey, S. Calvez, M. Cascella, C. Černá, J.P. Cesar, E. Chauveau, A. Chopra, G. Claverie, S. De Capua, F. Delalee, D. Duchesneau, V. Egorov, G. Eurin, J.J. Evans, L. Fajt, D. Filosofov, R. Flack, X. Garrido, H. Gómez, B. Guillon, P. Guzowski, R. Hodák, K. Holý, A. Huber, C. Hugon, A. Jeremie, S. Jullian, M. Kauer, A. Klimentko, O. Kochetov, S.I. Konovalov, V. Kovalenko, K. Lang, Y. Lemière, T. Le Noblet, Z. Lipták, X.R. Liu, P. Loaiza, G. Lutter, J. Maalmi, M. Macko, F. Mamedov, C. Marquet, F. Mauger, I. Moreau, B. Morgan, J. Mott, I. Nemchenok, M. Nomachi, F. Nova, H. Ohsumi, R.B. Pahlka, J.R. Pater, F. Perrot, F. Piquemal, P. Povinec, P. Přidal, Y.A. Ramachers, A. Rebii, A. Remoto, B. Richards, J.S. Ricol, C.L. Riddle, E. Rukhadze, R. Saakyan, R. Salazar, X. Sarazin, J. Sedgebeer, Y. Shitov, F. Šimkovic, L. Simard, A. Smetana, K. Smolek, A. Smolnikov, S. Snow, S. Söldner-Rembold, B. Soulé, M. Špavorová, I. Štekl, J. Thomas, V. Timkin, S. Torre, V.I. Tretyak, V.I. Tretyak, V.I. Umatov, C. Vilela, V. Vorobel, D. Waters, A. Žukauskas, *Nucl. Instr. Methods A* **868**, 98 (2017)
85. M. Janecek, *IEEE Trans. Nucl. Sci.* **59**(3), 490 (2012)
86. E. Chauveau, Dissertation, Université de Bordeaux 1, (2010)
87. P. Dorenbos, *Opt. Mater X* **1**, 100021 (2019)
88. I.V. Khodyuk, S.A. Messina, T.J. Hayden, E.D. Bourret, G.A. Bizarri, *J. Appl. Phys.* **118**(8), 084901 (2015)
89. B. Singh, M.S.J. Marshall, S. Waterman, C. Pina-Hernandez, A. Koshelev, K. Munechika, A. Knapitsch, M. Salomoni, R. Pots, P. Lecoq, V.V. Nagarkar, *IEEE Trans. Nucl. Sci.* **65**(4), 1059 (2018)
90. M. Moszyński, B. Bengtson, *Nucl. Instr. Methods* **158**, 1 (1979)
91. A. Ebran, J. Taieb, G. Belier, A. Chatillon, B. Laurent, J.-F. Martin, E. Pellereau, *Nucl. Instr. Methods A* **728**, 40 (2013)
92. M. Hamel, M. Trocmé, A. Rousseau, S. Darbon, *J. Lumin.* **190**, 511 (2017)
93. M. Hamel, M. Soumaré, H. Burešová, G.H.V. Bertrand, *Dyes Pigm.* **165**, 112 (2019)
94. K.M. Teh, D. Shapira, B.L. Burks, R.L. Varner, J.L. Blankenship, E.J. Ludwig, R.E. Fauber, C.F. Maguire, *Nucl. Instr. Methods A* **254**(3), 600 (1987)
95. F. Lidén, J. Nyberg, A. Johnson, A. Kerek, *Nucl. Instr. Methods A* **253**(2), 305 (1987)
96. F. Lidén, A. Johnson, A. Kerek, E. Dafni, M. Sidi, *Nucl. Instr. Methods A* **273**(1), 240 (1988)
97. A.T. Farsoni, D.M. Hamby, *Nucl. Instr. Methods A* **578**(3), 528 (2007)
98. L.R. Lindvold, A.R. Beierholm, C.E. Andersen, *Radiat. Meas.* **45**(3–6), 615 (2010)
99. I.H. Campbell, B.K. Crone, *Appl. Phys. Lett.* **90**(1), 012117 (2007)
100. P.L. Feng, J. Villone, K. Hattar, S. Mrowka, B.M. Wong, M.D. Allendorf, F.P. Doty, *IEEE Trans. Nucl. Sci.* **59**(6), 3312 (2012)

101. F.P. Doty, M.D. Allendorf, P.L. Feng, Doped luminescent materials and particle discrimination using same, WO2011/060085. Accessed 10 Nov 2010
102. N.J. Cherepy, R.D. Sanner, T.M. Tillotson, S.A. Payne, P.R. Beck, S. Hunter, L. Ahle, P.A. Thelin, IEEE Nucl. Sci. Symp. Conf. 1972 (2012)
103. F. Sguerra, R. Marion, G.H.V. Bertrand, R. Coulon, É. Sauvageot, R. Daniellou, J.-L. Renaud, S. Gaillard, M. Hamel, J. Mater. Chem. C **2**, 6125 (2014)
104. A.F. Adadurov, P.N. Zhmurin, V.N. Lebedev, V.V. Kovalenko, Nucl. Instr. Methods A **621**(1–3), 354 (2010)
105. P.N. Zhmurin, V.N. Lebedev, A.F. Adadurov, V.N. Pereymak, Y.A. Gurkalenko, Radiat. Meas. **62**, 1 (2014)
106. C.D. Bell, N. Bosworth, Fluorescent Compound, EP0913448. Accessed 25 May 1995
107. E.D. Bourret-Courchesne, S.E. Derenzo, M.J. Weber, Nucl. Instr. Methods A **601**(3), 358 (2009)
108. S. Nutter, Y. Amare, T. Anderson, D. Angelaszek, N. Anthony, K. Cheryian, G.H. Choi, M. Copley, S. Couto, L. Derome, L. Eraud, L. Hagenau, J.H. Han, H.G. Huh, Y.S. Hwang, H.J. Hyun, S. Im, H.B. Jeon, J.A. Jeon, S. Jeong, S.C. Kang, H.J. Kim, K.C. Kim, M.H. Kim, H.Y. Lee, J. Lee, M.H. Lee, J. Liang, J.T. Link, L. Lu, L. Lutz, A. Menchaca-Rocha, T. Mernik, J.W. Mitchell, S.I. Mognet, S. Morton, M. Nester, O. Ofoha, H. Park, I.H. Park, J.M. Park, N. Picot-Clémente, R. Quinn, E.S. Seo, J.R. Smith, P. Walpole, R.P. Weinmann, J. Wu, Y.S. Yoon, Nucl. Instr. Methods A **942**, 162368 (2019)
109. A. Sytnik, M. Kasha, Radiat. Phys. Chem. **41**(1/2), 331 (1993)
110. E. Boldt, C. Tsipis, Rev. Sci. Instrum. **32**(3), 280 (1961)
111. W. Wolszczak, K.W. Krämer, P. Dorenbos, J. Lumin. **222**, 117101 (2020)
112. C. Zorn, Nucl. Phys. B **32**, 377 (1993)
113. C. Zorn, S. Majewski, R. Wojcik, C. Hurlbut, W. Moser, IEEE Trans. Nucl. Sci. **37**(2), 487 (1990)
114. C. Zorn, IEEE Trans. Nucl. Sci. **37**(2), 504 (1990)
115. Y.N. Kharzheev, Phys. Part. Nucl. **50**(1), 42 (2019)
116. M. Dettmann, V. Herrig, J. Maldonis, J. Neuhaus, D. Shrestha, P. Rajbhandari, Z. Thune, M. Been, M. Martinez-Szewczyk, V. Khristenko, Y. Onel, U. Akguna, J. Instrum. **12**, P03017 (2017)
117. B. Bilki, Y. Onel, E. Tiras, J. Wetzel, D. Winn, IEEE NSS/MIC Conf. Rec. 1 (2016)
118. B. Bilki, Y. Onel, E. Tiras, J. Wetzel, D. Winn, J. Instrum. **13**, C02052 (2018)
119. M. Bowen, S. Majewski, D. Pettey, J. Walker, R. Wojcik, C. Zorn, IEEE Trans. Nucl. Sci. **36**(1), 562 (1989)
120. S. Majewski, M. Bowen, J. Szaban, C. Zorn, Nucl. Instr. Methods A **281**(3), 497 (1989)
121. Y.A. Gurkalenko, P.N. Zhmurin, V.N. Lebedev, V.N. Pereymak, O.V. Svidlo, Funct. Mater. **23**(1), 40 (2016)
122. E.S. Velmozhnaya, Y.A. Gurkalenko, D.A. Eliseev, P.N. Zhmurin, V.N. Lebedev, V.N. Pereymak, Funct. Mater. **23**(4), 650 (2016)
123. Y.A. Gurkalenko, D.A. Eliseev, P.N. Zhmurin, V.N. Pereymak, O.V. Svidlo, Funct. Mater. **24**(2), 244 (2017)
124. Y.A. Gurkalenko, P.M. Zhmurin, V.M. Pereymak, D.A. Yelisieiev, O.V. Yelisieieva, Funct. Mater. **25**(4), 670 (2018)
125. E.S. Velmozhnaya, Y.A. Gurkalenko, D.A. Eliseev, P.N. Zhmurin, V.N. Lebedev, V.N. Pereymak, Funct. Mater. **22**(4), 494 (2015)
126. V. Baranov, Y.I. Davydov, R. Erasmus, C.O. Kureba, N. Lekalakala, T. Masuku, J.E. Mdhluli, B. Mellado, G. Mokgatitswane, E. Sideras-Haddad, I. Vasilyev, P.N. Zhmurin, Nucl. Instr. Methods B **436**, 236 (2018)
127. J. Wetzel, E. Tiras, B. Bilki, Y. Onel, D. Winn, Nucl. Instr. Methods B **395**, 13 (2017)
128. E. Montbarbon, M.-N. Amiot, D. Tromson, S. Gaillard, C. Frangville, R. Woo, G.H.V. Bertrand, R.B. Pansu, J.-L. Renaud, M. Hamel, Phys. Chem. Chem. Phys. **19**(41), 28105 (2017)

129. S. Baccaro, A. Cemmi, I. Di Sarcina, B. Esposito, G. Ferrara, A. Grossi, M. Montecchi, S. Poddia, F. Pompili, L. Quintieri, M. Riva, IEEE Trans. Nucl. Sci. **65**(8), 2046 (2018)
130. S. Mianowski, K. Brylew, A. Dziedzic, K. Grzenda, P. Karpowicz, A. Korgul, M. Krakowiak, R. Prokopowicz, G. Madejowski, Z. Mianowska, M. Moszynski, T. Szczesniak, M. Ziembia, J. Instrum. **15**, P10012 (2020)
131. The CMS Electromagnetic Calorimeter Group, J. Instrum. **5**, P03010 (2010)
132. G. Patton, F. Moretti, A. Belsky, K. Al Saghir, S. Chenu, G. Matzen, M. Allix, C. Dujardin Phys. Chem. Chem. Phys. **16**(45), 24824 (2014)
133. I.M. Rozman, Bull. Acad. Sci. (USSR) Phys. Ser. **22**, 48 (1958)
134. L. Peralta, Nucl. Instr. Methods A **883**, 20 (2018)
135. C. Rozsa, R. Dayton, P. Raby, M. Kusner, R. Schreiner, IEEE Trans. Nucl. Sci. **37**(2), 966 (1990)
136. C.R. Hurlbut, High-temperature well logging instrument with plastic scintillation element, US4833320. Accessed 02 Mar 1988
137. A. Mahl, A. Lim, J. Latta, H.A. Yemam, U. Greife, A. Sellinger, Nucl. Instr. Methods A **884**, 113 (2018)
138. H.A. Yemam, A. Mahl, A. Lim, A. Sellinger, U. Greife, Use of multi-functional cross-linking agents in manufacture of pulse shape discriminating plastic scintillators, the scintillator, and methods of using the same, US2019/0018150. Accessed 11 June 2018
139. O. Klitting, F. Sguerra, G.H.V. Bertrand, V. Villemot, M. Hamel, Polymer **213**, 123214 (2021)
140. J. Ueda, P. Dorenbos, A.J.J. Bos, A. Meijerink, S. Tanabe, J. Phys. Chem. C **119**(44), 25003 (2015)
141. R.J. Cameron, B.G. Fritz, C. Hurlbut, R.T. Kouzes, A. Ramey, R. Smola, IEEE Trans. Nucl. Sci. **62**(1), 368 (2015)
142. M. Loyd, M. Pianassola, C. Hurlbut, K. Shipp, L. Sideropoulos, K. Weston, M. Koschan, C.L. Melcher, M. Zhuravleva, Nucl. Instr. Methods A **922**, 202 (2019)
143. M. Loyd, M. Pianassola, C. Hurlbut, K. Shipp, N. Zaitseva, M. Koschan, C.L. Melcher, M. Zhuravleva, Nucl. Instr. Methods A **949**, 162918 (2020)
144. M.R. Kusner, P.R. Menge, Scintillation device with moisture barrier, WO2017/106496. Accessed 15 Dec 2015
145. R.T. Kouzes, H.M. Cho, C.C. Cowles, G. Dib, P.E. Keller, J.E. Smart, P.J. Smith, B.J. Tucker, P.L. Feng, N.R. Myllenbeck, S. Payne, Nucl. Instr. Methods A **954**, 161791 (2020)
146. N.P. Zaitseva, L.M. Carman, A.M. Glenn, A.N. Mabe, S.A. Payne, Defect-resistant plastic scintillation radiation detector compositions and fabrication methods, US10647914. Accessed 17 Mar 2017
147. N.P. Zaitseva, A.N. Mabe, M.L. Carman, A.M. Glenn, J.W. Inman, S.A. Payne, Nucl. Instr. Methods A **954**, 161709 (2020)
148. E. Simiele, R.-P. Kapsch, U. Ankerhold, W. Culberson, L. DeWerd, Phys. Med. Biol. **63**(8), 085001 (2018)
149. F. Therriault-Proulx, Z. Wen, G. Ibbott, S. Beddar, Radiat. Meas. **116**, 10 (2018)
150. D. Blömker, U. Holm, R. Klanner, B. Krebs, IEEE Trans. Nucl. Sci. **37**(2), 220 (1990)
151. D. Blömker, U. Holm, R. Klanner, B. Krebs, Nucl. Instr. Methods A **311**(3), 505 (1992)
152. G.H.V. Bertrand, M. Hamel, J. Dumazert, R. Coulon, C. Frangville, Polym. Adv. Technol. **32**(2), 748 (2021)
153. P.L. Feng, W. Mengesha, M.R. Anstey, J.G. Cordaro, IEEE Trans. Nucl. Sci. **63**(1), 407 (2016)
154. P.L. Feng, J.G. Cordaro, W. Mengesha, N.R. Myllenbeck, Metal-loaded plastic scintillators for gamma-ray spectroscopy, US10024983. Accessed 06 Oct 2016
155. M. Hamel, C. Dehé-Pittance, R. Coulon, F. Carrel, P. Pillot, É. Barat, T. Dautremer, T. Montagu, S. Normand, in *IEEE Proceedings of ANIMMA 2013* (2014)
156. F. Carrel, É. Barat, T. Dautremer, M. Hamel, S. Normand, Procédé et dispositif pour détecter des radioéléments, FR1552415. Accessed 24 Mar 2015
157. A.G. Kavetsky, Y.L. Kaminski, G.P. Akulov, S.P. Meleshkov, in *Polymers, Phosphors, and Voltaics for Radioisotope Microbatteries*, ed. by K.E. Bower, Y.A. Barbanel, Y.G. Shrater, G.W. Bohnert (CRC Press, Boca Raton, 2002), pp. 109–189

158. A.J. Peurrung, Nucl. Instr. Methods A **443**(2–3), 400 (2000)
159. A.S. Beddar, Radiat. Meas. **41**(S1), S124 (2007)
160. B.D. Milbrath, A.J. Peurrung, M. Bliss, W.J. Weber, J. Mater. Res. **23**(10), 2561 (2008)
161. L. Beaulieu, S. Beddar, Phys. Med. Biol. **61**(20), R305 (2016)
162. A. Tarancón, H. Bagán, J.F. García, J. Radioanal. Nucl. Chem. **314**, 555 (2017)
163. J. Dumazert, R. Coulon, Q. Lecomte, G.H.V. Bertrand, M. Hamel, Nucl. Instr. Methods A **882**, 53 (2018)
164. H. Al Hamrashdi, S.D. Monk, D. Cheneler, Sensors **19**, 2638 (2019)
165. O.V. Borshchev, N.M. Surin, M.S. Skorotetcky, S.A. Ponomarenko, INEOS OPEN **2**(4), 112 (2019)
166. H. Kang, S. Min, B. Seo, C. Roh, S. Hong, J.H. Cheong, Chemosensors **8**, 106 (2020)
167. N. Zaitseva, A. Glenn, A. Mabe, L. Carman, S. Payne, Int. J. Mod. Phys.: Conf. Ser. **50**, 20600003 (2020)
168. M.F. L'Annunziata, in *Handbook of Radioactivity Analysis (Fourth Edition) Vol. I: Radiation Physics and Detectors*, ed. by M.F. L'Annunziata (Academic Press, 2020), pp. 899–1045
169. P.N. Zhmurin, V.N. Lebedev, V.N. Kovalenko, A.F. Adadurov, V.N. Pereymak, in *New Developments*, in *Chromophore Research*. ed. by A. Molire, E. Vigneron (Nova Science Publishers Inc., New York, 2013), pp. 313–324
170. M. Nikl, A. Yoshikawa, Adv. Opt. Mater. **3**(4), 463 (2015)
171. C. Dujardin, in *Techniques de l'ingénieur Matériaux pour l'optique*, vol. TIB450DUO (Editions T.I., 2017)
172. M. Korzhik, A. Gektin (eds.), *Engineering of Scintillation Materials and Radiation Technologies—Selected Articles of ISMART2018* (Springer Nature, Cham, 2019)
173. D. Cao, G. Yang, Mater. Today Commun. **24**, 101246 (2020)
174. M. Koshimizu, Funct. Mater. Lett. **13**(6), 2030003 (2020)
175. M. Koshimizu, in *Handbook of Sol-Gel Science and Technology*, ed. by L. Klein, M. Aparicio, A. Jitianu (Springer, Cham, 2016) pp. 2273–2300



Christophe Dujardin Christophe Dujardin (55 yo) defended his Ph.D. in physics in 1993 at the University Claude Bernard Lyon1, on the photo-ionization mechanisms. He holds now a full professor position at the University Claude Bernard Lyon 1 in physics. He is an expert in luminescence and scintillation materials and mechanisms. He is the head of the Luminescence group at Institute of Light and Matter. He is the chairman of the International advisory committee of conference series on Inorganic Scintillators and Their Applications (SCINT) and belong to the advisory board of Journal of Luminescence. He is a member of the steering committee for Crystal Clear Collaboration hosted in CERN. In 2020, he is co-author of 204 publications and has a h-index of 37 (ISIWEB).



Matthieu Hamel Matthieu Hamel (41 yo) defended his Ph.D. in organic chemistry in 2005 at the University of Caen Basse-Normandie (France), on the synthesis of ortho-sulfinyl phenylphosphonates. After a first experience in the preparation of plastic scintillators at the French Atomic Energy and Alternative Energies Commission (CEA), he spent a year at the University of Montpellier II (France) working on phosphorylated prodrugs of albitazolium. He obtained a full position at the CEA in 2009, where he developed plastic scintillators and other luminescent materials to the main application of CBRN-E threats. In January 2021, he is the author or co-author of 76 publications, 27 patents, 1 book chapter and 3 reviews, with a h-index 14 according to SciFinder®.

He is the Editor of this book.

Chapter 2

Neutron/Gamma Pulse Shape Discrimination in Plastics Scintillators: From Development to Commercialization



Natalia P. Zaitseva, M. Leslie Carman, Andrew M. Glenn,
and Andrew N. Mabe

Abstract Radiation detection requires instruments which can detect nuclear radiation, having at the same time the ability to discriminate among different types of nuclear particles. For many decades, neutron detection has been based on ${}^3\text{He}$ proportional counters sensitive primarily to thermal neutrons. The most common methods for the detection of fast neutrons have been based on liquid scintillators with pulse shape discrimination (PSD). A decade of studies conducted at Lawrence Livermore National Laboratory (LLNL) led to the development of new materials, among which are the first PSD plastics for fast neutron detection manufactured based on high concentrations of 2,5-diphenyloxazole (PPO) dissolved in aromatic polymers. More advantages were introduced by plastics doped with ${}^{10}\text{B}$ and ${}^6\text{Li}$ that enable combined detection of both thermal and fast neutrons, offering, in addition, a unique “triple” PSD for discrimination between fast neutrons, thermal neutrons, and gamma rays. Studies conducted with these and more recently introduced materials prepared with multiple dyes alternative to PPO produced a deeper understanding of energy transfer and excited state interaction phenomena. Research led to the commercial production of PSD plastics which, due to the deployment advantages and ease of fabrication, create a basis for the replacement of liquid scintillators and widespread use of solid-state scintillators as large-volume and low-cost neutron detectors.

2.1 Physical Basis for Neutron/Gamma Discrimination in Organic Scintillators

Pulse shape discrimination (PSD) techniques used for the detection of neutrons in mixed neutron/gamma radiation fields is based on the two-component decay fluorescence typical for most aromatic compounds [1–3]. Excitation of organic molecules by nuclear radiation produces excited singlet states (S) and triplet states (T). In an excited singlet state, the electron is promoted to the upper level with the same spin

N. P. Zaitseva (✉) · M. L. Carman · A. M. Glenn · A. N. Mabe
Lawrence Livermore National Laboratory, 7000 East Avenue, Livermore, CA 94550, USA
e-mail: zaitseva1@llnl.gov

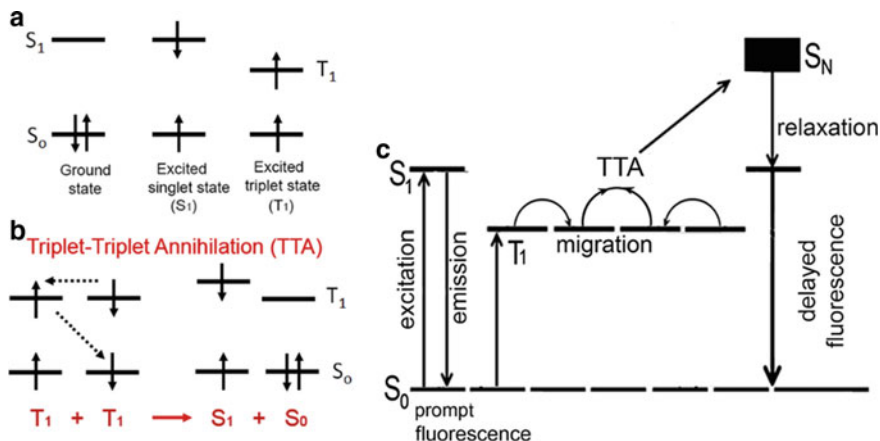
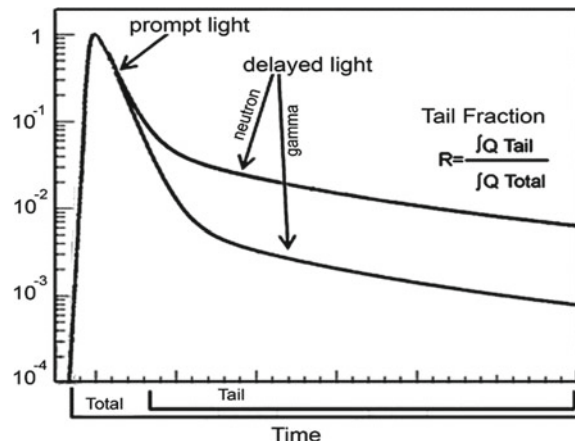


Fig. 2.1 a—Simple molecular orbital representation of singlet and triplet excited states; b—Triplet-triplet annihilation (TTA), and c—Energy level diagram illustrating basic processes leading to the formation of the prompt and delayed light emission

orientation as it had in the ground level (spin paired state). In a triplet state, the excited electron is no longer paired with the ground state electron, so that upper and ground state electrons have a parallel spin orientation (Fig. 2.1a). The majority of the light observed in a scintillation process results from a normal fluorescence emission corresponding to fast de-excitation of singlets in $S_1 \rightarrow S_0$ transition. The direct relaxation of the lowest triplet state T_1 to the ground S_0 state is spin forbidden. However, two molecules in the T_1 state may undergo energy transfer which promotes one molecule to the S_1 state, while the other returns to the S_0 . The process known as triplet-triplet annihilation (TTA) proceeds by the reactions $T_1 + T_1 \rightarrow S_1 + S_0$ and $S_1 \rightarrow h\nu$ resulting in the formation of additionally excited singlets decaying to the ground state over a delayed timescale (Fig. 2.1b and c). The difference in mechanisms of S_1 and T_1 state relaxation determines the shape of scintillation pulses commonly consisting of the fast (prompt) and slow (delayed) components (Fig. 2.2). The prompt component that results from the direct radiative de-excitation of the S_1 state of individual molecules is exponential, while the delayed component that involves excitation migration and interaction between pairs of excited molecules is non-exponential, this is because, in a randomly distributed molecular system, the more closely spaced and the more distant T_1 pairs interact at different time scale [3].

As shown by Fig. 2.2, both neutron- and gamma-induced pulses have prompt and delayed components, but the proportion of the delayed light is higher for neutron excitations. This is because the short range of heavier protons produced from neutron collisions yields a higher concentration of triplets, leading to the enhanced level of delayed emission in neutron-induced pulses in comparison to the pulses produced by the longer range of the electrons from gamma interactions. The resulting difference in the shape of the pulses produced by neutron and gamma interactions gives the basis for the PSD technique. In this technique, the neutron/gamma (n/γ) separation

Fig. 2.2 Schematics of the two-component decay structure indicating different levels of delayed light in neutron and gamma scintillation pulses; ratio of signal integrals, R , collected in two time gates, *Tail* and *Total*, is used for the separation of neutron and gamma pulses (reproduced from [15] with permission from IEEE)



is made based on the value of the ratio of charge, $R = Q_{\text{Tail}}/Q_{\text{Total}}$, for the two time intervals, *Tail* and *Total*, that indicate whether the considered event is likely produced by a neutron or a gamma ray that, respectively, have higher or lower R values (Fig. 2.3a). The method also allows for the quantitative evaluation of PSD by calculation of Figure of Merit $FoM = S/(\delta_{\text{gamma}} + \delta_{\text{neutron}})$, where S is the separation between gamma and neutron peaks, and δ_{gamma} and δ_{neutron} are full widths at half maximum (FWHM) of the corresponding peaks generally extracted from Gaussian fits (Fig. 2.3b).

The PSD properties of organic scintillators were first discovered and demonstrated in a number of early works with unitary systems of organic single crystals (anthracene, *trans*-stilbene, *p*-terphenyl¹), among which *trans*-stilbene became

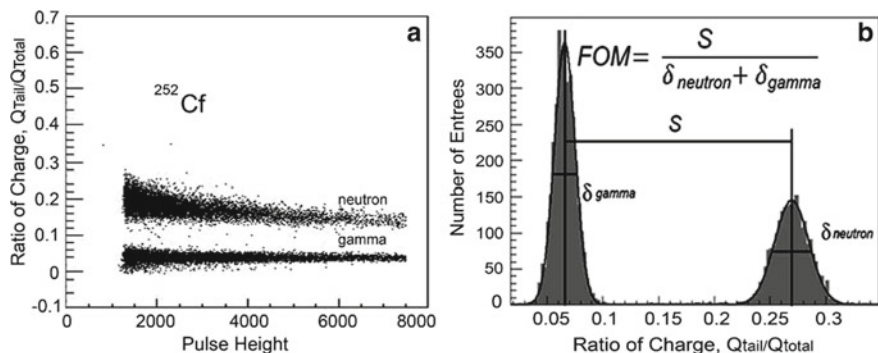


Fig. 2.3 **a**—typical PSD pattern of organic scintillators obtained by digitized separation of neutron and gamma pulses; **b**—PSD profiles of experimental data used for calculation of the PSD figure of merit (FoM) (reproduced from [15] with permission from IEEE)

¹Topological representation and key information of these molecules is given in the Appendix section at the end of the book.

known for its superior discrimination properties [4–6]. Similar properties were also found in liquid scintillators, typically prepared as binary or ternary systems composed of highly efficient fluorescent dyes (e.g., *p*-terphenyl, PPO, PBD, or POPOP) dissolved in aromatic solvents [1, 7]. The level of PSD known for liquid scintillators revealed that the mechanisms of delayed light formation via excitation migration and TTA does not require crystallographic arrangements and may also proceed in amorphous systems. A possibility of obtaining PSD in plastic scintillators was first reported by F. Brooks, in 1960 [8], in a publication describing several plastic mixtures, without any explanation or hypothesis of why only one of them, called “plastic 77” had PSD capability. This plastic was even commercialized by Nuclear Enterprises under reference NE 150 during the early 1960s. The lack of provided mechanism made it difficult for other researchers to reproduce the results or further develop PSD plastic compositions. In addition, instability of these first plastics led to a longtime established opinion about the inherently poor PSD in plastics defined by F. Brooks himself as “consistent with low proportion of delayed component in their scintillation decays” [9].

The low level of the delayed light in traditional plastics, however, is not surprising, considering that, by analogy with liquid scintillators, these plastics have always been prepared with a low concentration of dyes [1], typically not exceeding 1–2% by weight (referred below as wt%). Simple estimations show that, at such concentrations, the typical dye molecules (e.g., *p*-terphenyl, PPO) in plastics are separated by average distances of \approx 30–40 Å. Such distances are sufficiently small for the radiative (emission and reabsorption of a photon) and some fraction of nonradiative Förster dipole–dipole energy transfer (ET) occurring over intermolecular distances of \approx 20–60 Å [1, 10]. However, as established in early theoretical [11] and experimental [11–14] studies, the T_1 - T_1 interactions and triplet ET become possible only at smaller distances of \approx 6–15 Å required for the molecular orbital coupling and Dexter electron-exchange process [3]. In liquids, such distances can be achieved due to the high molecular mobility and collisional migration allowing transfer at relatively low dye concentrations below 1–2%. The situation is different in mixed solid systems, that consist of emitting dye molecules spatially constrained in a solid matrix. An obvious way to decrease intermolecular distances in solid systems is by increasing dye concentrations. Although no connection between PSD and dye concentration was mentioned in the Brooks’ paper, it could be deduced that it was 10% of 4-isopropylbiphenyl (IP) in combination with naphthalene and 3.5% of *p*-terphenyl that, at these elevated concentrations, brought dye molecules to closer distances in the plastic 77, enabling higher probability of TTA and PSD reported in [8]. Another clear effect of the increasing concentration on PSD properties in solid systems was demonstrated in more recent work conducted with the mixed diphenylacetylene (DPAC)—*trans*-stilbene crystals [15]. As shown by results of Fig. 2.4a, the relatively low concentrations typically used for the preparation of traditional plastics with the highest LO correspond exactly to the region of no or negligible n/γ separation that sharply rises above \approx 20% of *trans*-stilbene loads (Fig. 2.4b) when stilbene molecules come to small enough distances required for efficient TTA.

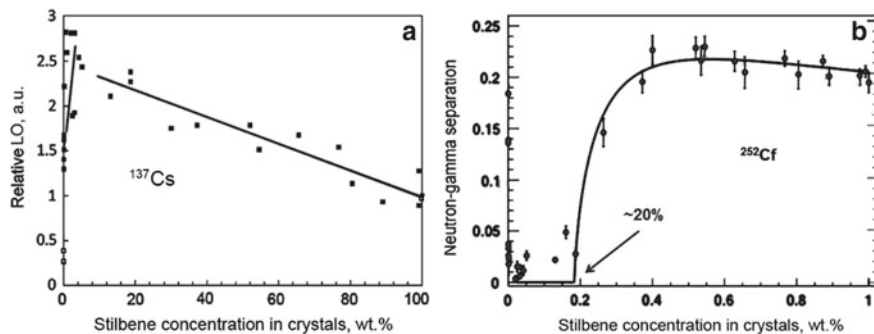


Fig. 2.4 **a**— ^{137}Cs light output (LO) and **b**— ^{252}Cf PSD parameters versus emitting dye (*trans*-stilbene) concentration measured with the mixed DPAC-stilbene crystals (reproduced from [15] with permission from IEEE)

Studies conducted with organic crystals showed that the main reason for the absence of PSD in traditional plastic scintillators results from the triplet excitation traps formed by a lower band gap fluorescent dye present in the host material (polymer matrix) at low concentration. Additional experiments conducted with liquids confirmed that explanations of the conditions leading to the formation of PSD in crystals and liquids can be similarly applied to the mixed plastic systems. This led to the fabrication of the first plastic scintillators that demonstrated that increasing the concentration of the dye can provide conditions suitable for the formation of a network for excitation energy migration and triplet-triplet annihilation and may produce efficient PSD in plastic scintillators.

2.2 Plastic Scintillators with Efficient Fast Neutron/Gamma Discrimination

Depending on the composition, plastic scintillators with PSD can be utilized for the detection of both high-energy (fast) neutrons and low energy (thermal) neutrons. Since neutrons are neutral, they do not interact directly with the electrons in matter. However, their interaction with various nuclei initiate the release of one or more charged particles that can be processed by the detection system. There are two major types of neutron interaction with organic matter, in which the neutron can be either scattered or absorbed by a nucleus. The mechanism of scatter is only efficient for fast neutrons interacting with light nuclei such as hydrogen, while absorption requires the presence of nuclei with a high cross section for neutron capture (e.g., ^6Li , ^{10}B , or Gd) and can be applied only for the detection of thermal neutrons.

High hydrogen content in aromatic compounds and polymers makes hydrocarbon-based plastic scintillators the most suitable materials for fast neutron detection. The close mass of neutrons and hydrogen leads to an efficient elastic scatter, in which

the free neutron transfers part of its kinetic energy to hydrogen nucleus with the production of recoil protons that ionize the material around the point of interaction. The charge produced in the reaction can be collected by conventional methods and detectors traditionally applied for n/γ signal separation using liquid and solid organic scintillators [1, 7, 16].

2.2.1 *PPO-Based PSD Plastics*

2.2.1.1 Preparation and Properties of First PSD Plastics

The first PSD plastics that utilized a high concentration of dyes [17] were prepared as solid solutions of fluorescent dyes 2,5-diphenyloxazole (PPO) and 9,10-diphenylanthracene (DPA) in a polyvinyl toluene (PVT) polymer matrix. The high solubility of PPO in aromatic solvents allowed for easy preparation of liquid and plastic solutions containing high concentrations of dyes up to 30% by weight.

The details of plastic preparation were described in [17]. The n/γ discrimination properties were evaluated using a ^{252}Cf source and charge integration method, as described above (see explanations to Fig. 2.3). It should be noted that to minimize the effects of slight variations in material purity and preparation conditions, a quantitative comparison of results in most cases was made with the samples obtained in one set of polymerizations.

PPO and DPA are well-known fluorescent compounds traditionally used as fluorescent dyes in the composition of different organic scintillators. Measurements made in a PSD survey of many organic crystals [18, 19] showed that both PPO and DPA exhibit neutron/gamma discrimination properties in their pure crystalline state (Fig. 2.5a). To understand the similarities and differences of PSD in plastics versus more traditional liquid scintillators preliminary measurements were made with liquid scintillators prepared with the same dyes. Both DPA and PPO are soluble in *p*-xylene, although at very different solubilities of about 2.5% for DPA and 42% for PPO at room temperature. As shown by Fig. 2.5b, liquid solutions containing DPA or PPO dyes at the concentration close to their solubility limits exhibit high levels of PSD similar to that of single crystals. However, at decreasing concentrations, the separation of the peaks gradually decreases (Fig. 2.5c), leading at the end to a nearly complete overlap of the neutron and gamma pulse distributions in Fig. 2.5d.

Figure 2.6 presents the dependence of PSD on the dye concentration measured in DPA and PPO solutions through the entire range of their solubility in *p*-xylene. As shown by the results, for both types of solutions, there is a region of very low dye concentrations ($< 1 \mu\text{mol/g}$ solution, or $\approx 0.02 \text{ wt\%}$) with negligibly small PSD. Increasing the concentration leads to a gradual enhancement of PSD which, despite the large difference in the solubility, has the same slope for both dyes up to a molecular concentration ($\sim 10 \mu\text{mol/g}$ solution), which corresponds to the maximum in the LO (Fig. 2.6b) for both PPO and DPA.

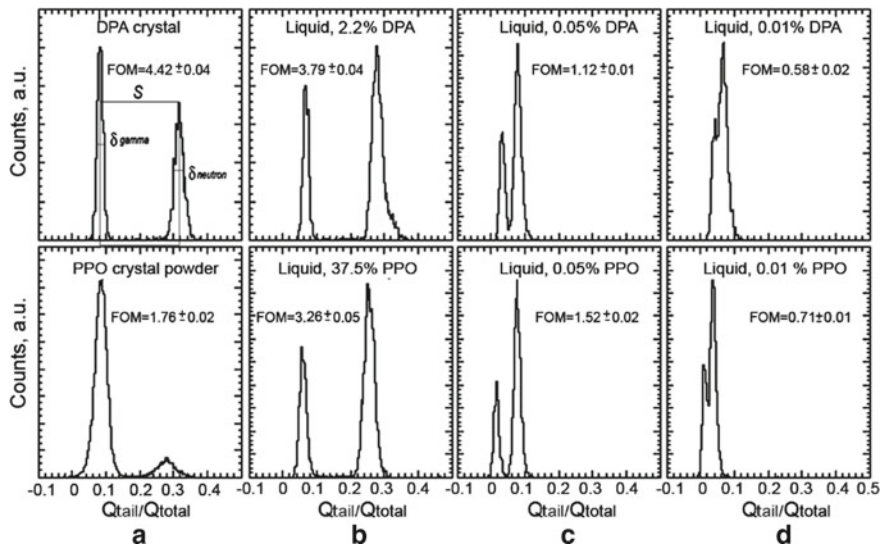


Fig. 2.5 PSD patterns obtained with organic crystals and liquid solutions of DPA and PPO dyes in *p*-xylene: **a**—crystals; **b**—close-to-saturation solutions with excellent PSD; **c**—solutions of intermediate concentration with deteriorating PSD; **d**—low concentration solutions with near complete absence of PSD (reproduced from [17] with permission from Elsevier)

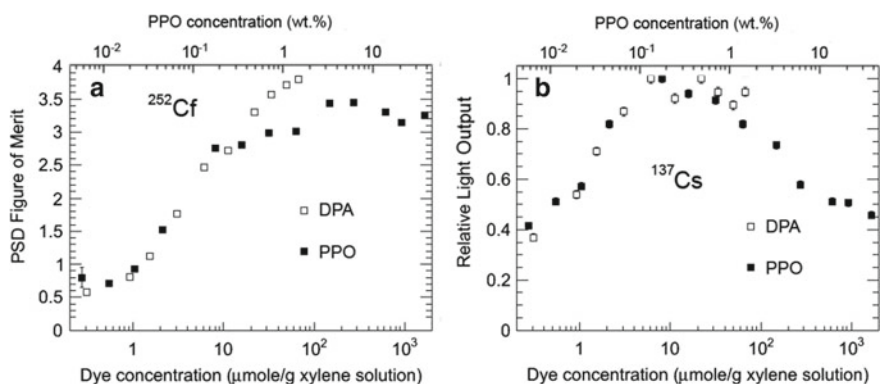


Fig. 2.6 **a**—PSD FoM and **b**— ^{137}Cs LO dependences on the concentration of DPA and PPO in *p*-xylene solutions. FoM statistical errors are within the points (reproduced from [17] with permission from Elsevier)

Since the decrease of the scintillation light efficiency at an increasing concentration (concentration quenching [1]) is typically ascribed to the formation of excimers, S_0S_1 , it can be suggested that the difference in PPO and DPA behavior above this concentration may relate to different kinetics of these processes for different types of the molecules.

The much lower dye concentrations needed for the appearance of PSD in liquid scintillators (0.01–0.02%), in comparison with those found previously in mixed single crystals (~20% in Fig. 2.4) [11], demonstrate once more the high impact of molecular diffusion that facilitates interactions of excited states in liquid solutions. The first experiments conducted with highly loaded PPO-based plastic scintillators confirmed the expectation that in the absence of high molecular mobility, the dye concentrations needed for obtaining efficient PSD are closer to those in crystals rather than in liquid scintillators. Figure 2.7 shows examples of experimental PSD patterns measured in selected PVT-based plastics prepared with increasing concentrations of PPO. The neutron/gamma separation, hardly detectable at low concentrations, becomes clearly pronounced in plastics containing larger fractions of the dye.

More detailed measurements made with a large number of plastic samples prepared with a broad range of PPO concentrations confirmed an increase of the neutron/gamma peak separation in a range of 10–30%, which gives rise to PSD with FoMs >1.27 (Fig. 2.8a) that was a proposed threshold of efficient PSD since it corresponds to 3σ separation between the Gaussian fits of neutron and gamma peaks [17]. As expected, the increase of PSD in plastics occurs at much larger PPO concentrations, more than two orders of magnitude higher than in corresponding liquid solutions. It should be noted that the optimal dye concentration used in the practical preparation of mixed scintillators has been traditionally selected based on the highest scintillation efficiency. The fact that in liquids both the maximum LO and the efficient PSD correspond to the same region of low concentrations (Fig. 2.6) could help explain the easy preparation of liquid scintillators with PSD. In plastics,

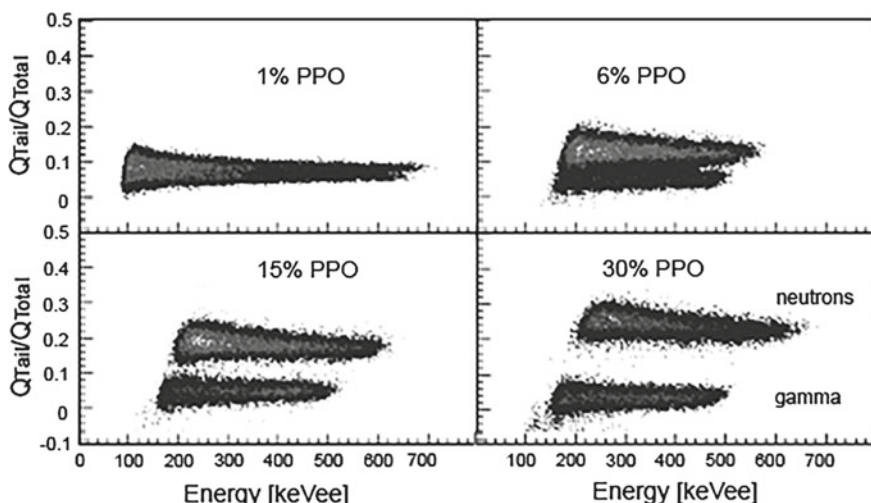


Fig. 2.7 Examples of experimental PSD patterns showing increase of neutron/gamma peak separation at an increasing PPO concentration in PVT (reproduced from [17] with permission from Elsevier)

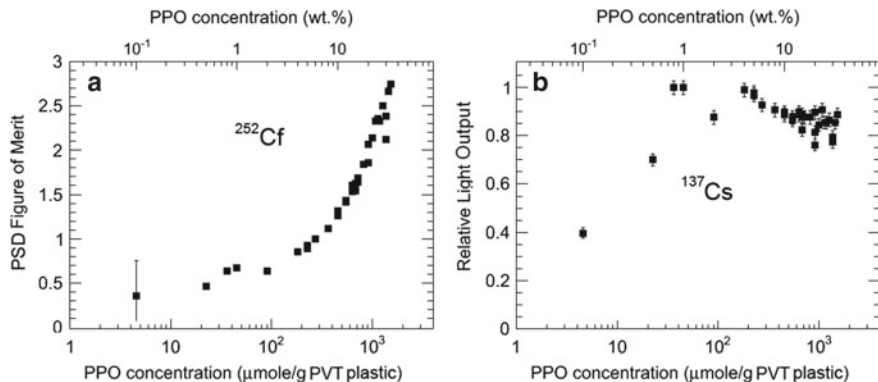


Fig. 2.8 Dependence of neutron/gamma PSD FoM obtained in PPO-PVT plastic scintillators. Comparison to the ¹³⁷Cs LY measured in the same samples shows that the noticeable increase of PSD starts in the region of the declining LY (reproduced from [17] with permission from Elsevier)

on the other hand, the most efficient LO still occurs at relatively low dye concentrations ($\approx 1\%$ in Fig. 2.8b), while efficient PSD appears in a different region, in which increasing PPO concentration leads to about 20% LO loss, due to the concentration quenching. It might be that this decline in the light efficiency contributed to the insufficient exploration of the region of high dye concentration in the previous studies of plastic scintillators.

A noticeable decrease of the LO at high PPO concentrations can negatively influence the final performance of PSD scintillators. The problem was corrected using ternary systems traditionally designed to increase the light efficiency by the addition of secondary dyes with lower band gap and high quantum efficiency. Figure 2.9a

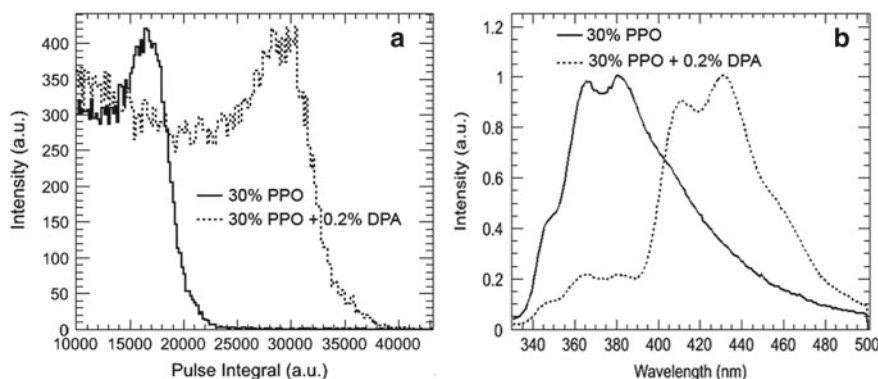


Fig. 2.9 **a**—¹³⁷Cs LO in two $\varnothing 25 \text{ mm} \times 25 \text{ mm}$ PPO-PVT plastic samples showing more than 50% increase upon a small addition of DPA; **b**—corresponding photoluminescence spectra showing that the light emission from PPO molecules in the binary PPO-PVT plastic changes to the spectrum of DPA in the ternary system; $\lambda_{\text{ex}} = 273 \text{ nm}$ (reproduced from [17] with permission from Elsevier)

presents one of the first results showing a more than 50% LO increase obtained with the addition of only 0.2 % DPA, in this case, used as a secondary dye in a PPO-PVT plastic. The concentration of the secondary dye is too low to affect the triplet-triplet interaction, still occurring mainly between the PPO molecules. At the same time, the fact that photoluminescence (PL) of the ternary system is dominated by emission from the DPA molecules (Fig. 2.9b) indicates that singlet excitation is efficiently transferred from PPO to DPA molecules. As a result, the final n/γ peak separation determined by the process of T_1-T_1 annihilation between PPO molecules does not show any noticeable difference in the final PSD patterns of binary and ternary samples. On the contrary, increasing LO determined by the high quantum efficiency and DPA concentration, low enough not to cause any substantial self-absorption, leads to the narrowing of the FWHMs of both peaks, ultimately resulting in the increase of PSD in plastics with the secondary dye. Results obtained with the first PPO-DPA plastics [17] demonstrated a basic principle of how the proportion of the delayed component in decays of mixed organic systems can be enhanced by increasing the concentration of soluble fluorescent dyes in aromatic PS or PVT. Additional studies showed that, at high enough concentrations of dyes, PSD plastics could also be prepared in other polymer matrices, including nonaromatic or mixed aromatic-nonaromatic polymers that can provide higher softening points and enhance the hardness of the materials [20]. Experiments conducted with plastics containing 30% PPO dissolved in a nonaromatic polymethyl methacrylate (PMMA) indicated that the direct excitation of the PPO in the nonaromatic matrix that does not take part in the energy transfer process, still provides efficient LO and PSD that can be adjusted using PS-PMMA copolymers found beneficial in later developments of more diverse compositions.

2.2.1.2 Further Improvement of Composition and PSD Performance

In 2012, the technology of the first PSD plastic preparation was licensed by Eljen Technology [21] for commercial production under the trade name EJ-299-33 (Photo in Fig. 2.10). With no principal differences from the manufacturing methods of standard plastic scintillators, new materials could be easily produced at various size samples comparable to those of the commonly employed liquid scintillators. Comparisons made on small scale ($\approx 2.5 \times 2.5$ cm cylinders) showed that LO and PSD similar to those of commercial liquid scintillators could be obtained with the best selected samples of new plastics (Fig. 2.10b and c). The results looked promising for the widespread replacement of liquid scintillators that suffer from well-known difficulties in handling and field applications. However, when PSD plastics commercially produced as EJ-299-33 cylinders and EJ-299-34 pixelated arrays became available at larger sizes, most studies conducted with new materials reported problems with mechanical and scintillation performance problems that made first PSD plastics inferior to liquid scintillators that they were supposed to replace [22–26].

Among the main mechanical problems negatively affecting first PSD plastic applications were softness and intense dye (PPO) leaching that produced difficulties

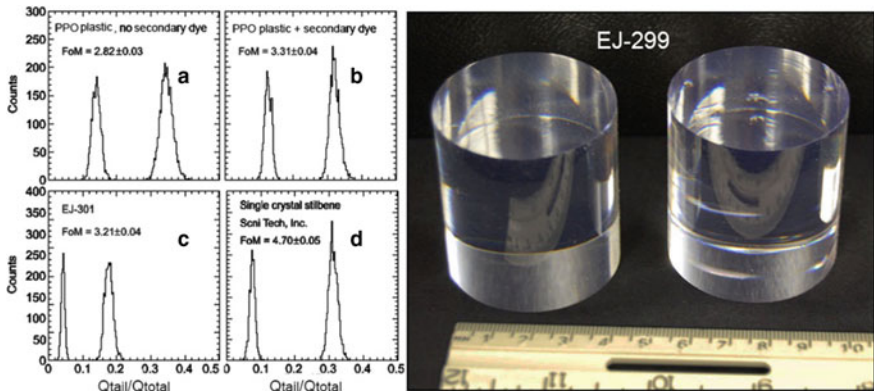
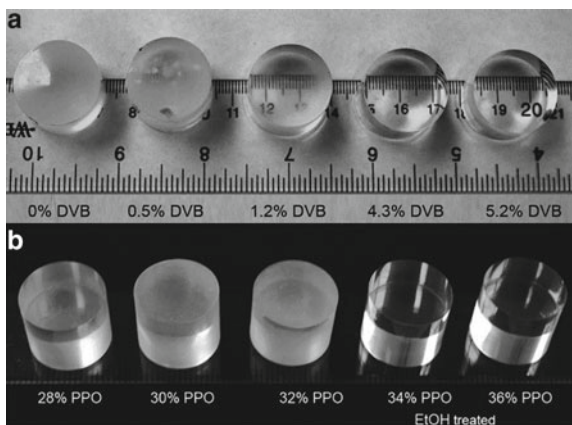


Fig. 2.10 ^{252}Cf n/y PSD FoMs for (480 ± 75) keV_{ee} energy range obtained with **a** binary and **b** ternary plastics in comparison with commercial **c** liquid and **d** single crystal scintillators all prepared as $\varnothing 25 \times 25$ mm cylinders (reproduced from [17] with permission from Elsevier). Right photo shows examples of the first $\varnothing 50 \times 50$ mm commercial PSD plastics EJ-299-33 manufactured by Eljen Technology [21]

in handling [27] and partial degradation of LO and PSD with time. The insufficient performance of the first commercial PSD plastics stimulated further studies on the improvement of physical and scintillation properties of the new materials [28]. In order to eliminate the initial problems, the matrix composition was altered by additions of cross-linking compounds widely used in industrial polymer manufacturing for the enhancement of mechanical properties. Surface treatment of the final machined and polished plastics with ethanol virtually eliminated dye leaching (Fig. 2.11). No specific studies of the effects were conducted, but it was suggested that the positive results were achieved due to the formation of a rigid polymer network by chemical cross-linking tightening and slight surface dissolution by ethanol, both

Fig. 2.11 Photos of one-year-old PSD plastics showing improvement of physical stability:
a—Plastics prepared with different concentrations of a cross-linker, divinylbenzene (DVB); **b**—Slight leaching on the surface of plastics is fully eliminated by the ethanol treatment enabling high PPO loads of 34–36% without any visible degradation (reproduced from [28] with permission from Elsevier)



diminishing free diffusion of PPO molecules in the volume and on the surface of plastics.

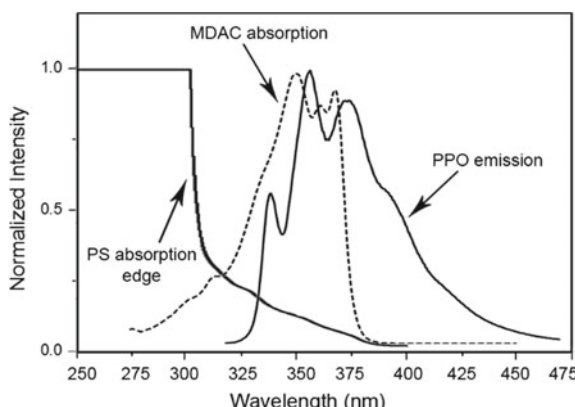
With respect to further PSD performance improvement, initial studies were concentrated on a search for compounds that could produce better efficiency of n/y discrimination. The main requirements considered for the selection of a primary dye are high solubility, bright fluorescence, low self-quenching at increasing concentration, and spectral properties suitable for the efficient transfer of excitation energy from the matrix to the secondary dye. In the assumption that the LO can be diminished by the reabsorption of the primary dye emission by the polymer matrix, the primary dye candidates were considered among the compounds having peak emission outside of PS or PVT absorption region. Noticeable absorption of aromatic matrices starts around 380 nm, sharply increasing below 350 nm, while the wavelength shifters used for most organic scintillators (including PSD plastics) emit around 400–450 nm. In order to stay in the blue region of the optical spectrum, this assumption left a narrow window of \approx 380–400 nm for the optimal peak emission of a potential primary dye alternative to PPO. A complication was introduced by the fact that most of the dyes found to efficiently emit in this region had poor solubility in aromatics. Soluble compounds belonging to the groups of oxazoles (e.g., 2-phenylbenzoxazole), indoles (1,2-diphenylindole, 1-methyl-2-phenylindole), or coumarins (coumarin, 6-methylcoumarin), showed PSD poorer compared to PPO-based plastics. A comprehensive study conducted by Zhmurin et al. [29] with oxadiazoles resulted in a similar conclusion. Other soluble compounds with shorter wavelengths of emission (e.g., biphenyl, bibenzyl, *m*-terphenyl) were considered to be incompatible with PS or PVT due to spectral mismatch. An example of a highly soluble compound rejected in the initial studies was 2”,3,3’,3”-tetramethyl-1,1’:4’1”:4”,1”-quaterphenyl (TMQ, peak emission at 352 nm) that in pure crystalline state has outstanding LO and PSD comparable to crystalline *trans*-stilbene. However, based on a brief study of an inefficient PS—TMQ—bis-MSB system, a conclusion was made that, due to the significant overlay between TMQ emission with the absorption bands of PVT or PS, a large fraction of its light is absorbed back to the matrix, instead of being emitted or transferred to the secondary dyes. The interpretation of these results was that no better performing alternative to PPO could be found at the time of the studies. In addition, PPO, demonstrating the best PSD performance, had an important advantage of commercial availability at high chemical purity for a reasonably low cost. With no alternative primary dyes identified in the experiments, studies continued with elevated concentrations of PPO that, due to the use of the cross-linker and ethanol surface treatment could be raised in laboratory samples up to 40% without the risk of physical degradation or leaching.

A much broader range of selections that could be used for the modification of the initial PSD plastic composition was provided by secondary dyes that, being added to plastics in small quantities (\approx 0.2%) did not require high solubility and low cost. Many efficiently scintillating molecules known to be used as secondary dyes previously were tested in varying plastic compositions. The results showed that the addition of the traditional brightest organic fluorophores like bis-MSB, DPA, and POPOP to plastics containing 30% PPO may produce up to 60% increase of

the LO, compared to the same concentration PPO plastics without a secondary dye. However, the best PSD performance was observed with a less known 7-diethylamino-4-methylcoumarin (MDAC, also known as a laser dye Coumarin 1) that reproducibly exhibited the highest LO. The compound, which is extremely soluble in aromatic solvents (toluene, styrene, vinyltoluene), was shown to be unsuitable for use as a primary dye, because of the tendency to yellow coloration and self-quenching at increasing concentrations. At the same time, having a high scintillation LO confirmed in crystal characterization studies and good spectral overlay with PPO (Fig. 2.12), MDAC was found to be an efficient secondary dye used for the routine preparation of plastics during further developments. An unexpected finding was that, in addition to the best LO efficiency, PPO-MDAC plastics also exhibited slightly better n/γ separation than similar samples prepared with POPOP, or bis-MSB (Fig. 2.13). The specific effect of MDAC can be seen from the comparison of scintillation performance of plastics prepared with the three most efficient secondary dyes at increasing concentration of PPO (Fig. 2.14).

As indicated by the results, the addition of any of the three dyes leads to a significant enhancement of the LO. The effect is well-understood from the basic principle of energy transfer [1, 3], according to which the final emission of a mixed system is produced by secondary dye molecules. With this condition, the LO of plastics is determined by the efficiency of a secondary dye and the overlap of its absorption with the fluorescence emission spectrum of the primary dye. This explains why at the constant low concentration of a secondary dye, the LO is practically unaffected by the PPO concentration (Fig. 2.14a). On the contrary, increasing loads of the primary dye led to the increase of PSD FoM measured with ^{252}Cf source (Fig. 2.14b). In an assumption that the delayed light originates from the interaction of only the primary dye molecules, a similar increase of PSD FoMs at increasing PPO concentration should be expected for plastics with and without secondary dyes. Such expected behavior follows from the same slopes of POPOP and bis-MSB FoM dependences parallel to that of pure PPO plastic shown in Fig. 2.14b. A different behavior of MDAC, as well as its influence of PPO-originated n/γ separation (Fig. 2.13), was

Fig. 2.12 Typical relation between the absorption and emission bands measured with mixed scintillation system consisting of an aromatic matrix(PS), a primary dye (PPO), and a wavelength shifter (MDAC) (reproduced from [28] with permission from Elsevier)



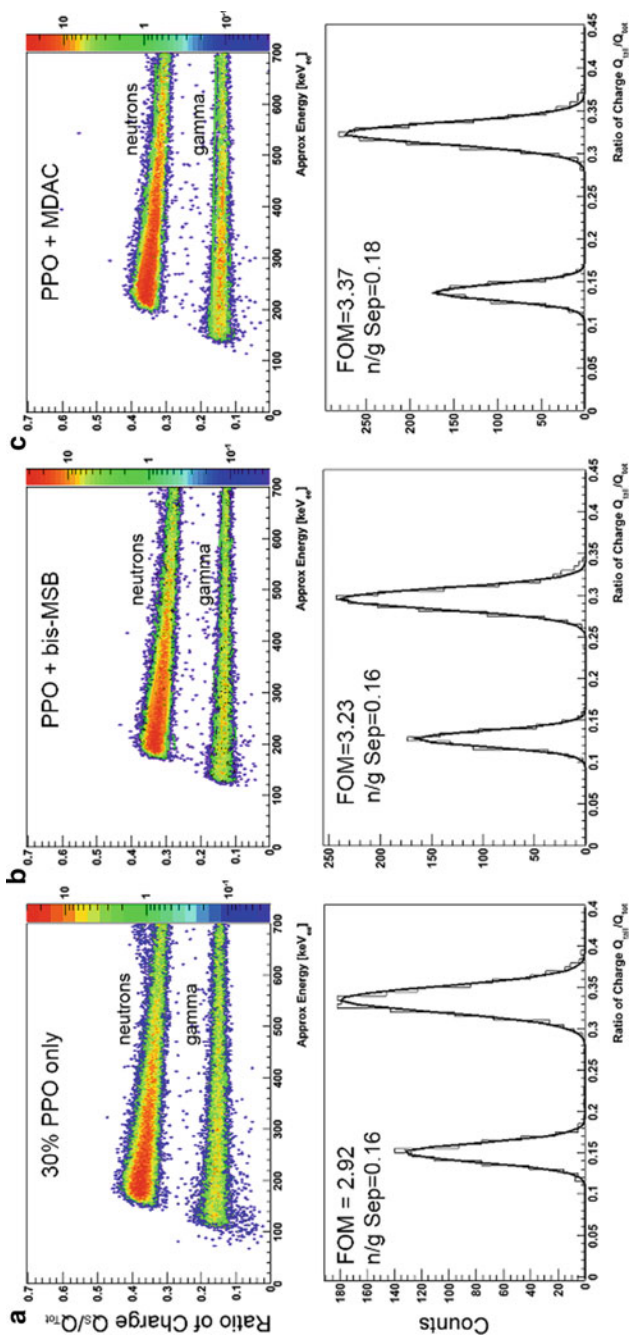
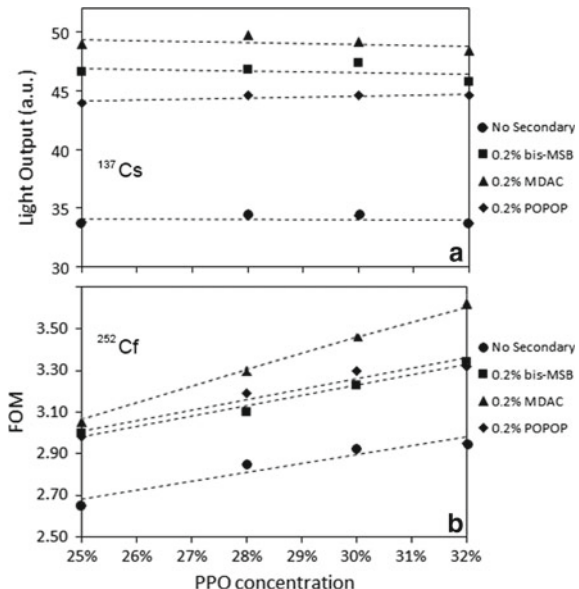


Fig. 2.13 Experimental results obtained with $\varnothing 25 \times 17$ mm long plastic cylinders containing 30% PPO with **a**—no secondary dye, **b**—0.2% bis-MSB, and **c**—0.2% MDAC (reproduced from [28] with permission from Elsevier)

Fig. 2.14 **a**—Change of the LO and **b**—PSD FoM near 480 keV_{ee} measured with plastics prepared at increasing concentrations of PPO and different secondary dyes added at 0.2% (reproduced from [28] with permission from Elsevier)



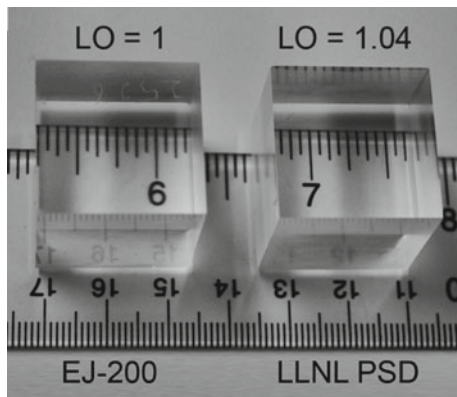
more difficult to explain based on a simple model of one type molecule triplet–triplet interaction, obviously not achievable for secondary dyes at 0.2% concentration. An assumption made at that stage of experiments was that the slightly negative or positive effects of secondary dyes on PSD related to their solubility. It was suggested that the extremely low solubility of POPOP and bis-MSB might produce defects and excitation traps diminishing triplet migration that was not affected by the presence of more soluble MDAC. A much more plausible explanation for the effect was found later in experiments described below in Sect. 2.2.2.

2.2.1.3 Scintillation Performance of Improved Plastics

It is well known that both LO and PSD are size- and shape-sensitive parameters. Therefore, an accurate comparison of the scintillation performance of different materials is best done only with samples having the same dimensions and shape. Small scale measurements made with 1" (25.4 mm) cubes showed that compositional modifications described above could lead to the increase of the LO to the level of the brightest traditional plastics like BC-408 or EJ-200 (Fig. 2.15). According to the data presented by commercial vendors [21], this comparison indicates that scintillation efficiency of about 65% of anthracene, that is, close to $\approx 10,000$ photons/MeV can be achieved with plastic scintillators of small scale.

To evaluate the effects of scaling on attenuation, the characterization of improved PSD plastics was made with larger, 2" (51 mm) diameter samples of 25 to 95 mm in length that were compared to the same size liquid scintillators. Results of the

Fig. 2.15 Comparison of the LO measured with the same size cubes showing that the LO of LLNL-produced PSD plastics containing 30% PPO can be comparable to that of the brightest commercial plastics (reproduced from [28] with permission from Elsevier)



comparison obtained with plastics containing 30% and 36% PPO in combination with 0.2% MDAC are presented in Fig. 2.16. As expected, due to the dye self-absorption, the LO slowly decreases with the increasing length for all scintillators. However, similar slopes of the dependencies do not indicate any different attenuation in plastics compared to commercial liquid scintillators.

An accurate comparison of PSD in different scintillators is more complicated than comparison of the LO. Although the same formula is used for the calculation of the FoMs in majority of publications, the large discrepancy in FoM mean values may be produced by the use of different experimental equipment, digitizers, and algorithms. Even if different samples are compared in the identical laboratory setups, in addition to the equal size and geometry, the same energy range should be considered as one more important criterion for the direct PSD FoMs comparison. Figure 2.17 shows experimental PSD plots obtained with 76 mm (3") long plastic in comparison

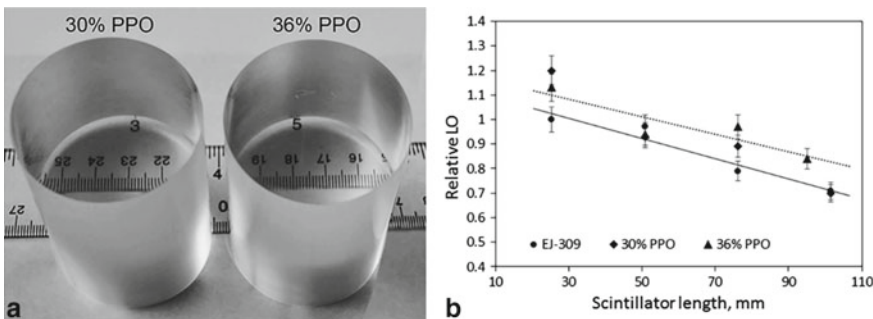


Fig. 2.16 **a**—Plastic scintillators of \varnothing 51 mm \times 95 mm long prepared with 30 and 36% PPO and 0.2% of MDAC; **b**—Relative ^{137}Cs LO of same diameter plastics of different length in comparison to equal size EJ-309 liquid cylinders; the LO of a 25 mm thick EJ-309 cylinder was taken as a unit. The solid and dashed lines correspond to linear fits for EJ-309 and 36% PPO plastic, respectively (reproduced from [28] with permission from Elsevier)

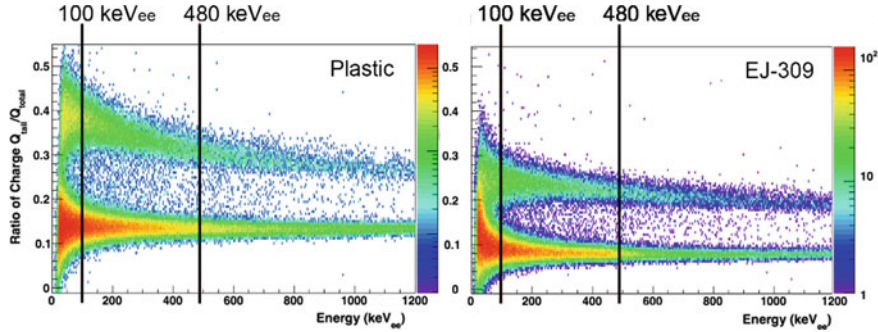


Fig. 2.17 ^{252}Cf n/ γ discrimination plot of a \varnothing 51 and 76 mm long PSD 36% PPO plastic in comparison to the same size liquid scintillator obtained under the same conditions of measurements. Vertical lines define two energies for which FoMs versus scintillator lengths were calculated for all scintillators shown in Fig. 2.18 (reproduced from [28] with permission from Elsevier)

to the equal size liquid scintillator. As indicated by the vertical lines, clear separation of thin peaks in the range of higher energies (480 keV_{ee}) yields higher values of PSD FoMs compared to the broader distributions that produce smaller FoMs at low energies (100 keV_{ee}). A noticeable feature seen from the comparison is the wider separation of the plastic n/ γ peaks extended into the lower electron equivalent energies compared to the liquid. The improvement resulted from the increased PPO concentration and increased LO that determines the corresponding PSD FoMs calculated for scintillators of different lengths at the two selected energies (Fig. 2.18). As shown by the results, for both energies the PSD of 30% PPO plastics is close to that of the liquid scintillators. At the same time, contrary to the previously reported results [22], plastics with increased concentration of PPO (36%) may have noticeably better PSD compared to EJ-309, including in the low energy ranges, as shown by the results of Fig. 2.19a. Good discrimination at lower energy is the most desirable for

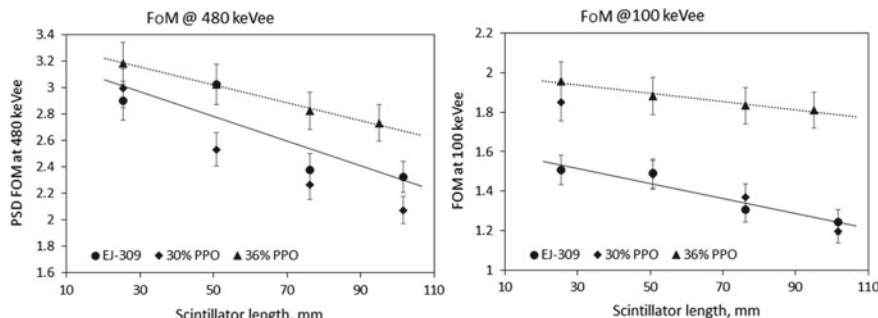


Fig. 2.18 ^{252}Cf PSD FoMs calculated for \varnothing 51 mm diameter plastic and liquid scintillators of different lengths for two electron equivalent energies. The solid and the dashed lines correspond to a linear average of EJ-309 and 36% PPO plastic, respectively (reproduced from [28] with permission from Elsevier)

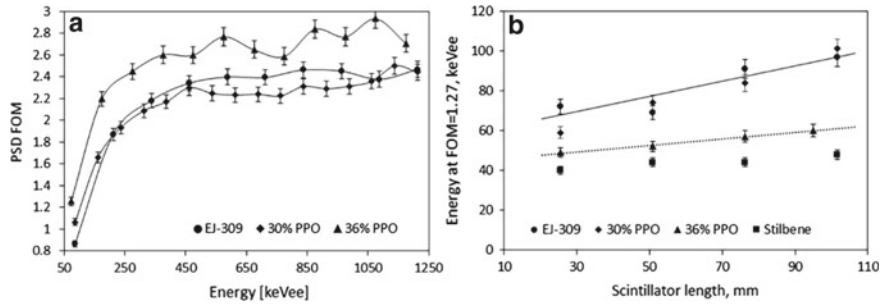


Fig. 2.19 **a**—PSD FoMs versus electron equivalent energy calculated for $\varnothing 51 \times 76$ mm plastic and liquid scintillators; **b**—Low energy cuts obtained with tested scintillators at 3σ neutron/gamma peak separation ($FoM = 1.27$). The solid and the dashed lines correspond to eye-guiding fits of EJ-309 and 36% PPO plastic, respectively (reproduced from [28] with permission from Elsevier)

any PSD material because it substantially widens the energy range and efficiency of neutron detection. The low energy cut at which neutrons and gammas can still be separated at some practically useful degree may be used as a parameter for comparison of different PSD materials. If utilizing $FoM = 1.27$ [17] as such criterion, the corresponding electron equivalent energies are found to be lower for plastics. For example, for the 76 mm long plastic with 36% PPO, the 3σ separation energy will be about 56 keV_{ee} versus 91 keV_{ee} for the same size EJ-309 (Fig. 2.19b). Reported response functions for EJ-299-33 [23, 26, 29, 30] allow only for very approximate evaluations of the respective recoil proton energies. However, based on results of [23] that lists analytical functions for both EJ-299-33 and EJ-309, the better peak separation compensates for the lower neutron-induced LO in plastics, giving for both 76 mm long liquid and plastic the proton energy of about 610 keV_{ee}. It should be noted that such approximate evaluations by no means could be considered accurate, as well as they did not indicate the final point of the plastic development. They rather illustrated the benefits of further scientific studies leading to the enhancement of LO and PSD through the exploration and discovery of new, more efficient plastic compositions. However, the overall results of the development produced a practical impact leading to a new version of commercial PSD plastic scintillator, EJ-276, that replaced previously produced EJ-299-33 [21].

2.2.2 PSD Plastics Utilizing Alternative Dyes and Dye Mixtures

Development of PSD plastics based on highly increased dye concentrations produced new types of plastic scintillators in which the interacting dyes were brought to close

intermolecular distances required for the excited triple states annihilations not achievable in traditional plastics prepared with low dye loads. This opened new opportunities for studies of phenomena involving T_1 energy transfer and TTA mechanisms that may lead to further development and improvement of PSD in solid-state materials. In a one-component system containing a single fluorescent dye, like pure PPO plastics without secondary dyes, the TTA process can be easily explained by the homogeneous interaction between identical PPO molecules. The picture became more complicated in systems containing two or more fluorescent dyes. In the first publication presenting plastics containing a double-dye PPO-DPA combination [17], the high fraction of delayed light and PSD were also explained by the homogeneous TTA between PPO molecules. A possibility of T_1 state interactions between the different molecular species that may also lead to delayed light production was observed in early works with diluted liquid and crystal scintillation systems [11–14]. In applications to the first PSD plastics, such interactions were not considered due to the overwhelmingly low concentrations of the secondary dyes, assumed to be added only as wavelength shifters for the enhancement of LO.

The influence of the secondary dyes on n/γ separation (illustrated by Fig. 2.13) and on PSD FoMs reported in a more recent publication [31] could suggest a possibility of a heterogeneous TTA involving both primary and secondary dye molecules. However, the limitations imposed by using only one primary dye (mainly PPO) combined with a few traditional secondary dyes (bis-MSB, POPOP, DPA) with typical low solubilities, imposed difficulties in detailed consideration of possible TTA mechanisms. To overcome the problem, more extended experiments were conducted with broader variations of primary and secondary dyes that included compounds alternative to PPO and traditional secondary dyes [32]. The focus of the experiments was concentrated on better understanding the energy transfer and triplet state interactions phenomena in new plastics prepared with high dye concentrations not considered in detail in previous works. The scientific aspects of the studies were combined with the practical goals of exploring novel compositions and approaches that may help the design and development of future systems with improved scintillation and PSD performance.

Scintillation dyes selected for the studies are shown in Table 2.1 that lists PPO and biphenyl (BP) already used as primary dyes in PSD developments [17, 28, 31] and newly introduced *m*-terphenyl (*m*-TP) and TMQ insufficiently explored in previous studies. The group of tested secondary dyes also contained traditional bis-MSB, DPA, more recently introduced MDAC, and new, non-traditional dyes from the class of exalites not used previously in bulk plastic scintillator preparations. Different exalites that belong to a group of the oligophenyls are produced by Luxottica/Exciton [33] as efficient laser dyes advertised to have high absorption coefficients at the wavelengths of their peak absorption. The three exalite dyes shown in Table 2.1 were selected based on their spectral characteristics and emission in the blue optical range typical for the traditional plastic scintillators.

The separation of dyes into primary and secondary categories in Table 2.1 is based mainly on the wavelength of emission and solubility. Compounds with high solubility

Table 2.1 Molecular weights (MW), room temperature (RT) solubility in toluene, and scintillation parameters of individual dyes measured in liquid and solid solutions. The data on the fluorescence quantum yield (QY) are cited from literature publications [32]

Compound	MW	RT solubility, wt%	QY	$\lambda_{\text{abs}}^{\text{a}}$, nm	$\lambda_{\text{fluo}}^{\text{a}}$, nm	LO ^b in PS (r.u)	
Primary dye						1%	30%
Biphenyl	154.21	50	0.18 [34]	248	306 + 316	0.02	0.03
<i>m</i> -Terphenyl	230.30	30	0.29 [34]	248	338	0.08	0.28
TMQ	362.52	>60	0.73 [34]	268	352	0.3	0.94
PPO	221.25	42	1.0 [34]	303 + 316	336 + 355 + 370	0.6	0.74
Secondary dye						0.2% in PS	
MDAC	231.30	62	0.99 ^c [35]	350 + 368	394	0.51	
Bis-MSB	310.43	0.57	0.94 [34]	345	395 + 416	0.42	
DPA	330.42	~2	1.0 [34]	354 + 372 + 392	406 + 427	0.42	
E404	659.01	~6	n/a ^d	331	381 + 401	0.55	
E411	650.93	~8	n/a ^d	346	386 + 407	0.52	
E417	831.26	~12	n/a ^d	351	393 + 414	0.52	

^aMajor absorption and emission peak wavelengths in 10^{-6} molar cyclohexane solutions

^b ^{137}Cs LO relative to same size EJ-200 (as in all Figures and Tables below)

^cLiterature data show variations depending on solvents

^dNot measured or reported in literature

(>30%) required for PSD in plastic scintillators are referred to as “primary”. The definition of the “secondary” dye relates more to the longer wavelength compounds used in these studies as wavelength shifters at relatively low concentrations of 0.1–2%. To consider specifics of the transformation of LO and PSD resulting from multiple dye interactions, the choice of highly soluble primary dyes included compounds of different scintillation efficiency. Selection of the tested combinations was based on the largest overlap of fluorescence and absorption spectra. Short wavelength emission BP, *m*-TP, and TMQ were used with E404 added as a wavelength shifter. PPO was tested with both traditional secondary dyes and exalites.

2.2.2.1 Plastics with Single Primary Dyes

The properties of individual compounds were first evaluated in plastics containing a single dye to serve as reference points for consideration of the energy transfer phenomena and effects introduced by interactions of multiple components. As shown

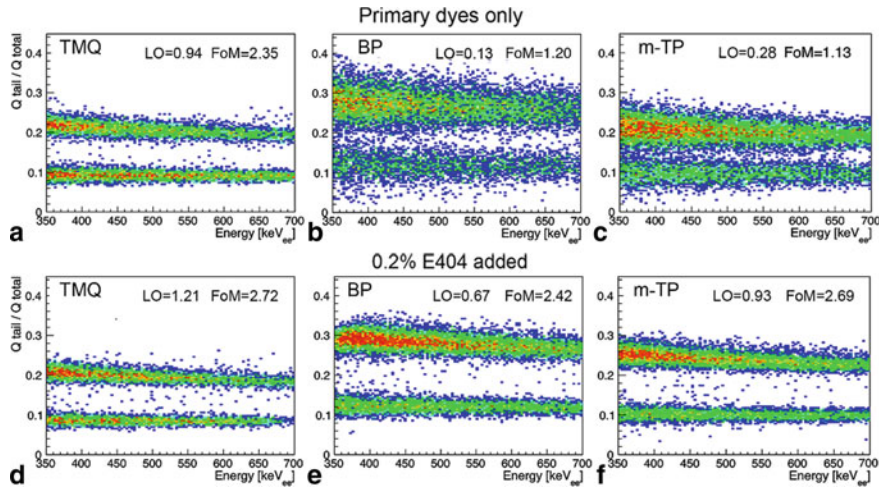


Fig. 2.20 PSD distributions measured with plastics containing 30% of primary dyes without (a, b, c) and with (d, e, f) a secondary dye E404 added at 0.2% concentration. Comparison of results shows the effect of the secondary dye on PSD improvement especially pronounced for BP and *m*-TP because of the high rise of LO (reproduced from [32] with permission from Elsevier)

by the results presented in Table 2.1, at low dye concentrations, there is a correlation between the QY and LO of the plastics. At 1%, low-QY BP and *m*-TP dyes produce the least efficient scintillation compared to the brighter TMQ and PPO. At the increased concentration of primary dyes, the correlation is broken by TMQ that, despite the lower QY, produces higher LO compared to PPO. The disproportionate change of the LO at increasing concentration can be explained by spectral characteristics showing an almost complete lack of BP, *m*-TP, and TMQ self-absorption in comparison to PPO, which loses a fraction of LO due to the overlap of its PL and absorption spectra [34]. All secondary dyes measured at 0.2% concentration show high scintillation efficiency, with slight variations that may also relate to their absorption relatively to the PS fluorescence peak. The QY of the exalites has not been measured, but based on their brightness in comparison to the traditional dyes, can be assumed close to unity.

The importance of the LO for PSD studies is demonstrated by Fig. 2.20a–c showing that in a single dye system, a clear n/γ peak separation can be obtained only with bright compounds like TMQ or PPO [17], while the extremely low LO of BP and *m*-TP produces only negligible PSD problematic for use in accurate studies of the underlying phenomena.

2.2.2.2 Effect of Secondary Dyes

Addition of bright secondary dyes at a small concentration is a typical practice used for the enhancement of LO in all mixed organic scintillators. In a plastic scintillator

consisting of a matrix, a primary dye, and a secondary dye (wavelength shifter), the dyes are selected to satisfy the energetic condition of $S_1(\text{matrix}) > S_1(\text{primary dye}) > S_1(\text{wavelength shifter})$ that allows for the singlet energy transfer from the initially excited matrix to the lowest S_1 of the wavelength shifter that emits the final light. Due to the low concentrations and relatively large intermolecular distances (~32–38 Å at ~1%) in traditional non-PSD plastics, the S_1 energy transfer between the dyes may include a large fraction of the radiative process that is maximized by the fluorescence efficiency of both primary and secondary dyes [3]. In high concentration plastics, the decreasing intermolecular distances (~9–13 Å for 30%) lead to a larger contribution from the nonradiative Förster and Dexter components that increase the overall efficiency of the S_1 energy transfer. Previous studies of PS-based plastics [3, 36] showed that the nonradiative S_1 transfer already becomes dominant at dye concentrations as low as 4% by weight. This is consistent with the results of our calculations showing that at concentrations of 30% and more, as used in the current research, the fraction of nonradiative transfer becomes close to unity (Fig. 2.21d). It is interesting to note that this appears to be true even when dye pairs have a minimal spectral overlay that results in only negligible nonradiative energy transfer at 1% of a primary dye (see example of the m-TP—TMQ in Fig. 2.21). The sharp rise of the energy transfer at the increased concentration indicates that in high concentration plastics, the effect of concentration may become more significant than the degree of the spectral overlay. Under these conditions of the efficient transfer between the dyes, the intensity of the final fluorescence is determined mainly by the secondary dye, which is always selected to have the highest scintillation efficiency.

The results presented in Fig. 2.20d–f illustrate the effects of 0.2% of secondary dye additions that, with proper dye selection, always lead to the increase of PSD, as commonly evaluated by the FoM. With respect to this discussion, it is important to emphasize that FoM evaluation reflects two physical phenomena not necessarily connected to each other. As illustrated by Fig. 2.22a, PSD FoM depends on two types of parameters, which are the n/γ separation and the widths of the corresponding peaks. Increasing LO is a phenomenon determined almost entirely by the singlet S_1 energy

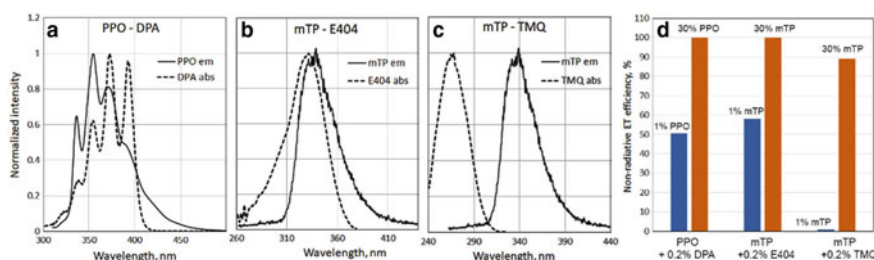


Fig. 2.21 Results illustrating the relationship between the spectral properties, concentration, and calculated Förster energy transfer (ET) efficiency of selected dye pairs: **a–c**—Spectra showing different overlay between the emission of the primary and absorption of the secondary dyes; **d**—Corresponding ET efficiencies showing the domination of the nonradiative ET at 30% primary dye concentration (reproduced from [32] with permission from Elsevier)

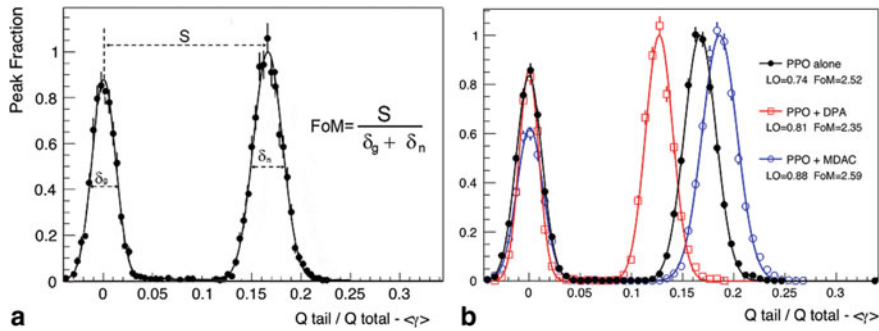


Fig. 2.22 Experimental results for 405–555 keV_{ee} illustrating independent effects of LO and n/γ separation observed upon addition of 1% of secondary dyes to plastics containing 30% PPO: **a**—Normalized charge ratio distribution for a PPO plastic with no secondary dye showing the parameters used for calculation of FoM; **b**—Superposition of PSD profiles showing that at about the same increase of LO the n/γ separation decreases with DPA and increases with MDAC additions (reproduced from [32] with permission from Elsevier)

transfer. Improved photon statistics narrow the FWHM of the distributions leading to the increase of PSD FoMs. Meanwhile, n/γ separation is a function of the dye concentration [17] that affects the triplet T₁ excitation density and the efficiency of the TTA process that determines the delayed light production. A common consideration of double-dye plastics suggests that the molecules of a secondary dye create T₁ excitation traps that cannot participate in the TTA process because of a typical low concentration and large distances between the secondary dye molecules.

In this case, addition of secondary dyes should be expected to decrease the n/γ separation due to the decreasing concentrations of the remaining excited primary dye molecules. On the contrary, in an assumption of a heterogeneous TTA between the molecules of primary and secondary dyes, it could be expected that an increase of the total number of interacting molecules should lead to the increase of the n/γ separation and improvement of PSD. The expected effects are difficult to recognize at typical low ($\approx 0.1\text{--}0.2\%$) secondary dye concentrations, because of the overwhelming influence of the LO. However, the opposite influence of secondary dyes on the n/γ separation in different systems becomes more apparent when some secondary dyes are added at concentrations above $\approx 0.4\text{--}0.5\%$. Examples of systems, in which increased concentration of a secondary dye lead to different effects on the n/γ separation is illustrated by Fig. 2.22b that presents Gaussian fits of n/γ distributions of PPO plastics with two different secondary dyes, DPA and MDAC (to focus on separation comparisons, the peak values of the neutron fits are scaled to one and the distributions are shifted to place the mean of the gamma distribution at zero). As follows from the results, the addition of 1 % DPA leads to increasing LO compared to a PPO plastic prepared without a secondary dye. However, despite this increase, the plastic containing DPA exhibits a lower PSD FoM compared to the initial PPO plastic without a secondary dye. The situation is opposite with a PPO-MDAC pair that, at the same concentration ratio, visibly improves PSD. The comparison shows that, at similar LO of both

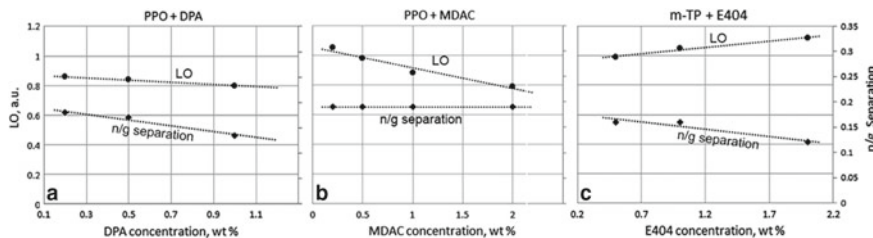


Fig. 2.23 Relationship between the LO and n/γ separation at increasing secondary dye concentration in plastics with different dye combinations: **a**—30% PPO with DPA exhibiting decrease of n/γ separation with the decreasing LO; **b**—30% PPO with MDAC shows no decrease of n/γ separation at visibly decreasing LO; **c**—30% *m*-TP with E404 showing a visible decrease of n/γ separation despite the substantially increased LO (reproduced from [32] with permission from Elsevier)

pairs, the addition of the secondary dyes affects PSD FoM mainly through the change of n/γ separation, independent of LO. More confirmation of distinctively different effects of secondary dyes on the LO and n/γ separation is demonstrated by Fig. 2.23a and b showing that further increasing concentration of both DPA and MDAC dyes leads to the decrease of the LO. However, while with the PPO-DPA combination, the decreasing LO is accompanied by the corresponding decrease of the n/γ separation, the separation in the PPO-MDAC plastics remains unaffected even with higher LO loss. Stronger evidence of the independent change of the LO and n/γ separation is exhibited by plastics containing a pair of new dyes, *m*-TP and E404 (Fig. 2.23c), in which the increasing concentration of E404 leads to the gradual LO enhancement accompanied by the opposite effect of the n/γ separation declining. The change of the LO in all three systems can be easily explained by the difference in self-absorption measured in this work as large for DPA and MDAC and small for E404, and therefore, differently affecting the loss of photons emitted by the relaxation of S_1 states of individual dyes. In the case of less obvious reasons for different n/γ separation behavior, more consideration should be given to the specific properties of dye molecules that may relate to the mutual T_1 - T_1 interactions determining the combinations of dyes that lead to increase or decline of n/γ separation.

2.2.2.3 Effects of Triplet State Energies

Systems of Primary Dyes Participating in Mutual Production of PSD

The energy E_T of the excited T_1 states is among the molecular properties that can be directly attributed to the TTA process and production of the delayed light. To consider the effect of this parameter, experimental results obtained with different dye systems were analyzed using the values of the lowest triplet states E_T available from the literature and calculated for TMQ, which was one of the key compounds used in the tested combinations of dyes (Table 2.2).

Table 2.2 First excited triplet state energies E_T of some compounds of interest [32]

Compound	PS [37]	PPO [38]	MDAC [39]	DPA [40]	Biphenyl [3]	<i>m</i> -Terphenyl [3]	TMQ [32]
E_T , eV	3.2	2.48	2.47	1.77	2.83	2.81	2.75

The first comparison shows that, based on reported data, PPO and MDAC have similar T_1 energy levels separated by $\Delta E_T \approx 0.01$ eV, while PPO and DPA have a much larger energy gap with $\Delta E_T \approx 0.71$ eV. To verify whether the value of ΔE_T is relevant to the selective interactions of dyes in other systems, more experiments were conducted with various mixtures of primary dyes that are highly soluble in PS and in each other. Figure 2.24a shows results obtained with the pair of BP—*m*-TP that have close T_1 energies studied and reported in a number of works [3, 11, 40, 41]. The plastics containing 30% of primary dyes consisting of *m*-TP alone or BP—*m*-TP mixtures were prepared with small additions of E404 that at 0.2% increases LO without producing a significant effect on n/γ separation. Comparison of the results shows that replacement of *m*-TP with an equal mass of BP molecules or vice versa does not lead to any measurable difference in n/γ separation, affecting FoMs only through the slight change in the LO. The result means that in the primary dye mixtures, BP and *m*-TP equally participate in the TTA process behaving like a single dye with the molecules cooperating in the production of PSD determined not by the one individual dye but by the total concentration of both compounds.

Similar examples of primary dyes participating in cooperative production of PSD are the pairs of *m*-TP—TMQ and BP-TMQ presented in Fig. 2.24b. As seen from these results, both mixed samples exhibit a high degree of n/γ separation and PSD not achievable with 20% of any individual dye. It should be noted here that the n/γ separation measured with the mixed samples was also larger than that of 40%

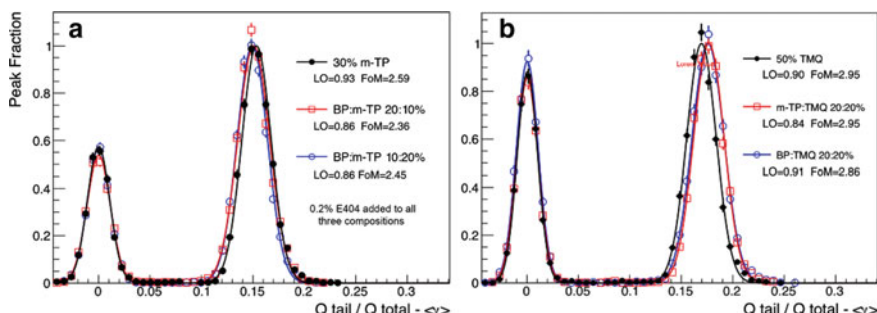


Fig. 2.24 Normalized charge ratio distributions measured with plastics containing primary dyes of close T_1 energy levels separated by $\Delta E_T < \sim 0.1$ eV: **a**—Complete overlay of the distributions shows that in the mixed 30% compositions, BP and *m*-TP act like one dye in producing PSD close to that of the plastic containing 30% of *m*-TP; **b**—Similar results obtained with the 40% of *m*-TP—TMQ and BP—TMQ, mixtures also indicate cooperative interaction of dyes in the production of PSD better than that of 50% of TMQ alone (reproduced from [32] with permission from Elsevier)

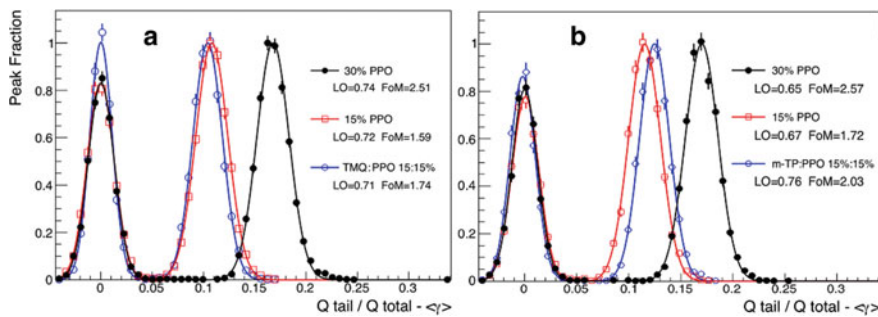


Fig. 2.25 Normalized charge ratio distributions of plastics containing primary dyes of T_1 energy levels separated by $\Delta E_T \approx 0.3$ eV: **a**—LO and PSD of a plastic prepared with 15% TMQ + 15% PPO. Comparison of the distributions shows that PSD of the mixed plastic is more characteristic for 15% rather than for 30% of PPO; **b**—Similar results showing that the plastic containing the total 30% mixture of *m*-TP—PPO exhibits much smaller separation compared to 30% PPO alone (reproduced from [32] with permission from Elsevier)

TMQ alone. The reason may relate to the smaller molecular weights of BP and *m*-TP that, at the same weight concentration, corresponds to a larger total number of dye molecules. To address this concern, mixed samples in Fig. 2.24b are compared to a 50% TMQ that have roughly the same total molar concentration as the mixed *m*-TP—TMQ plastic still producing similar separation and FoM, that would be unlikely to obtain without cooperative dye interactions leading to the rise of PSD.

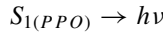
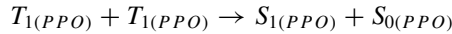
Mixed Primary Dye Systems in which PSD is Produced by one Compound

The experiments conducted with mixtures of BP, *m*-TP, and TMQ shown in Fig. 2.24 clearly demonstrate that, with close E_T levels separated by the $\Delta E_T < \sim 0.1$ eV, all three dyes participate in the mutual production of PSD. Different results were obtained with combinations of dyes having a larger ΔE_T . Figure 2.25a presents PSD distributions measured with plastics containing TMQ and PPO, which have triplet energies separated by $\Delta E_T \approx 0.27$ eV. Comparison of the n/γ separation of the mixed plastic composed of 15% TMQ and 15% PPO to plastics made with 15 and 30% of PPO alone shows that, despite the total 30% concentration, the mixture of two compounds, each capable of PSD production, produces PSD that is characteristic for only 15% PPO. This comparison suggests that in the 30% TMQ—PPO mixture the final PSD is determined only by PPO molecules that are not influenced by the presence of TMQ, as it simply acts as a part of the matrix. Considering the difference between the T_1 energies of PPO and TMQ, it can be concluded that the increasing difference between the T_1 energies of PPO and TMQ, it can be concluded that the increasing difference between the T_1 energies of PPO and TMQ leads to a change in dye interactions that at some certain ΔE_T prevents the participation of dyes in mutual TTA, so that the PSD production process involves only the same type of molecules. The measured outcome can differ depending on the molecular species in the mixture. As indicated by the results, for the case of the TMQ-PPO pair, the n/γ separation produced by 15–15% mixture almost precisely coincides with the n/γ separation that would be produced

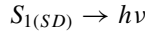
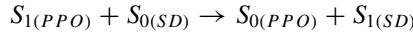
by only 15% PPO. With other combinations, like *m*-TP—PPO shown in Fig. 2.25b, n/γ separation of the mixed plastics can slightly exceed that of the PPO fraction alone. However, considering that with both TMQ—PPO, *m*-TP—PPO pairs the n/γ separation of resulting plastics corresponds more to the PPO concentration rather than to the total concentration of dyes, it can be suggested that, at $\Delta E_T \approx 0.27\text{--}0.33$ eV, the TTA process proceeds homogeneously mainly between the molecules of PPO, which is the lower T_1 component in the mixtures.

2.2.2.4 Discussion of Results

In application to the first PPO-DPA plastics reported in [17], the TTA process that leads to the production of the delayed light was considered as a homogeneous TTA between identical PPO molecules that in the absence of a secondary dye (wavelength shifter) produce a delayed light singlet:



In the case of a secondary dye (SD) presence, a PPO singlet is not emitted, being instead transferred non-radiatively to the lowest excited singlet state of the wavelength shifter that emits the final light:



This process did not suggest the participation of the wavelength shifter in the TTA process. With respect to plastic scintillators, a common approach was that the secondary dye molecules work as energy traps that, being added at low concentrations, cannot participate in the processes of triplet migration and TTA, due to the large intermolecular distances between SD molecules. However, at small intermolecular distances characteristic of the high concentration plastics, there is no reason to eliminate the possibility of the heterogeneous migration and TTA involving both primary and secondary dye molecules. As proposed in early works on the delayed fluorescence studies [13, 14, 42, 43], a mixed donor (D) — acceptor (A) system, in which S_1 and T_1 of A is lower than S_1 and T_1 of D, the delayed fluorescence may consist of at least three kinetic types: D-D homogeneous, A-A homogeneous, and D-A heterogeneous. The former two types proceed according to a regular TTA mechanism between the molecules having equal T_1 levels with the energy difference $\Delta E_T = 0$, while the latter requires nearly equal levels with a small ΔE_T that makes the T_1 energy transfer between D and A molecules reversible [44]. The possible outcomes of the ΔE_T energy difference in mixed systems can be illustrated by the following

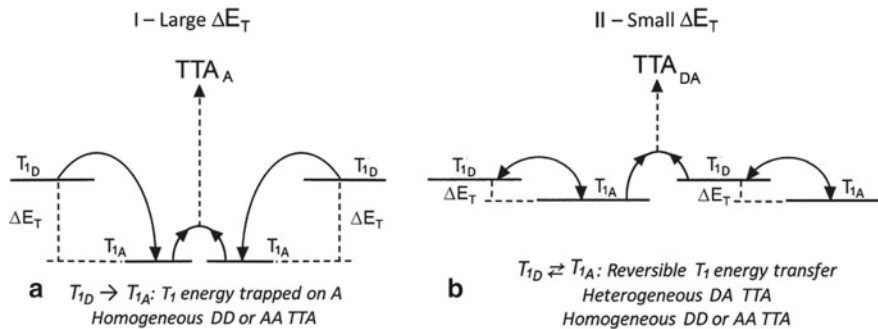


Fig. 2.26 Simplified diagrams illustrating the effect of the donor (D) and acceptor (A) triplet state T_1 energies difference ΔE_T on the possible energy transfer and TTA processes: **a**—Large ΔE_T favoring trapping of initial excitations of the T_1 of the acceptor. The full transfer leads to the TTA of A molecules; **b**—Small ΔE_T allowing for the reversible transfer of excitations between D and A and mixed TTA process involving both D and A molecules (reproduced from [32] with permission from Elsevier)

simplified diagrams (Fig. 2.26). Analysis of the results from different experimental works shows that the accuracy of measured or calculated E_T may vary by 0.05–0.06 eV, being influenced by the experimental methods or molecular environment. However, even with the assumption of low accuracy, there is a visible correlation between the estimated ΔE_T (Table 2.3) experimental effects observed in these studies. As shown by the results, the very small ΔE_T below ~0.1 eV between BP, *m*-TP, and TMQ molecules does not favor the T_1 trapping on one type of molecule, creating conditions for reversible transfer of T_1 excitations that should allow for the energy migration between the molecules of different species and heterogeneous TTA. This leads to the production of PSD not by one type of molecule, but by all dye molecules dissolved in the polymer matrix (Fig. 2.24). From this consideration, the possibility of heterogeneous migration and TTA does not exclude the simultaneous contribution of the homogeneous TTA between identical molecules, so that the final PSD of the mixed-dye system results from both homogeneous and heterogeneous components and is determined by the total concentration of the interacting dyes.

The larger ΔE_T difference between the molecules of different species increases the probability of T_1 excitation trapping on the lower T_1 level molecules. As shown by Fig. 2.25a for an example of a TMQ-PPO pair, at ΔE_T of ~0.27 eV and high enough concentration (~15%) of the lower T_1 level PPO, all initial T_1 excitations may become trapped on PPO molecules, that then participate only in the homogeneous migration and TTA. However, since the distances between the PPO molecules are larger than the average intermolecular distances in a 30% mixture, the homogeneous TTA of excited PPO molecules produces PSD corresponding to its 15% concentration rather than to the total 30% dye concentration of the mixture. With a smaller fraction of the lower E_T molecules, not enough to efficiently accept all initial excitations, the excitations remaining on a higher T_1 energy partner may still contribute to delayed light production by possible TTA. However, with the high probability of trapping, the

Table 2.3 Effect of the energy gap ΔE_T of interacting pairs of dyes on the triplet exciton trapping and type of triplet-triplet annihilation [32]

Dye combination	Primary dyes				Secondary		
	BP- <i>m</i> TP	BP-TMQ	<i>m</i> TP-TMQ	TMQ-PPO	<i>m</i> TP-PPO	PPO-DPA	PPO-MDAC
ΔE_T , eV	0.02	0.08	0.06	0.27	0.35	0.33	0.71
TTA type	Hetero + Homo No trapping	Hetero + Homo No trapping	Hetero + Homo No trapping	Homo (PPO) Traps on PPO	Homo (PPO) Traps on PPO	Homo (PPO) Traps on PPO	Hetero + Homo No trapping

TTA will proceed only between the molecules of the same type. A similar process altered only by the relative concentrations of dyes occurs in systems when small amounts of secondary dyes are added to one primary dye of the overwhelmingly higher concentration. In the case of PPO—DPA systems, due to the very large $\Delta E_T \approx 0.71$ eV between PPO and DPA molecules, a fraction of PPO molecule excitations becomes trapped on the secondary dye, decreasing the total number of PPO T_1 excitations left to participate in the homogeneous TTA of PPO. At the large distances between the DPA molecules added at 0.2–2% concentration, the excitations trapped on DPA are excluded from the TTA process, leading to the observed decrease of n/γ separation and PSD (Fig. 2.23a). On the contrary, the much smaller difference of $\Delta E_T \approx 0.01$ eV in PPO-MDAC T_1 energies, allows for the participation of MDAC molecules in heterogeneous interactions, adding its molecules to the total number of excitations that may produce increasing n/γ separation and PSD. Unfortunately, experimental or calculated data on E_T levels are not available for all secondary dyes used for PSD plastic preparations. However, based on the presented results, the relatively large ΔE_T can be suggested for the traditional combination of PPO—bis-MSB, explaining a slight decrease of n/γ separation typically observed upon additions of small amounts of this secondary dye to PPO. It also can be the case for the newly introduced *m*-TP—E404 pair, in which a large enough ΔE_T should benefit T_1 trapping of excitations from *m*-TP molecules, leading to the decrease of n/γ separation in plastics presented in Fig. 2.23c. A simple logic based on consideration of only T_1 energy levels may be not sufficient to explain all nuances of dye interactions observed in complex systems. An example is the difference of TMQ and *m*-TP effects on the n/γ separation in mixed pairs with PPO (Fig. 2.25). Several sets of samples made with different ratios of TMQ and PPO always showed PSD corresponding only to the PPO concentration, while additions of *m*-TP and BP reproducibly lead to the slightly increased n/γ separations that could not be expected at full and rapid T_1 transfer to PPO molecules. A possible explanation may involve special molecular properties of BP and *m*-TP that can be beneficial for more efficient energy transfer from the initially excited PS to the final emitting dye. Such phenomena studied before with intermediate dyes used to improve singlet transfer efficiency [45] may also take part in the triplet transfer. An explanation offered in this case would be that the better transfer from the initially excited PS provided by *m*-TP or BP molecules increases the T_1 excitation density in the PPO population leading to the observed enhancement of the final n/γ separation. Such assumption, however, requires more investigations with larger combinations of interacting dyes.

Interpretation of scintillation phenomena in plastic systems considered, for the first time, based on the triplet energies of interacting dyes require more verifications in further experimental and modeling works. However, a preliminary summary can be made that, depending on the difference between the energies of the first excited triplet states ΔE_T , the interaction leading to the triplet–triplet annihilation (TTA) and production of delayed light may proceed both homogeneously between identical molecules or heterogeneously between molecules of different species. Based on the obtained results, heterogeneous TTA occurs at $\Delta E_T < 0.1$ eV that is close to the thermal energy kT (0.026 eV at room temperature), allowing for the possibility of

reversible triplet excitation transfer between molecules of different types. The larger difference between the triplet energies, qualified previously [3, 46] as $\Delta E_T \gg kT$, leads to the full flow of the donor-to-acceptor excitations and trapping on the lower T_1 energy level molecules. In quantitative measurements, made with plastic scintillators for the first time in the present work, the full donor-to-acceptor transfer leading to only homogeneous TTA was observed at $\Delta E_T \approx 0.27$ eV. The value agrees with our previous research conducted with the diphenylacetylene-stilbene mixed crystals [15], in which the complete transfer of the excitation energy from diphenylacetylene to the lower T_1 stilbene was observed at $\Delta E_T \approx 0.3$ eV. More remarkable is that the data of these research conducted with solid systems are close to the results obtained more than half a century ago with liquids [42, 43] that showed high rates of the reversible T_1-T_1 energy transfer at ΔE_T of $\sim 0.04\text{--}0.12$ eV. The irreversible transfer to the lower T_1 states observed in those works was also identified close to ΔE_T of ~ 0.3 eV, although results of more recent works conducted with thin organic light-emitting diode (OLED) films [47] indicate that the limit for the heterogeneous TTA may be closer to ~ 0.2 eV. Studies conducted with a larger number of dyes and materials may help to verify or refine the interaction criteria that, in addition to ΔE_T , may be affected by the strength of the molecular orbital coupling or triplet lifetimes not considered in this research. However, the basic understanding of the dye interaction phenomena considered in these experiments can provide useful tools for the design and performance improvement of more advanced plastic scintillators and other materials.

2.2.2.5 Practical Aspects of Multiple Dye Plastic Implementation

One of the important results of these studies shows that the preparation of efficient PSD plastics does not necessarily need to be based on one primary dye with an extremely high solubility of $\geq 30\%$. Considering a complex of physical and scintillation properties (e.g., spectral characteristics, solubility, QY) needed for the preparation of an efficient scintillator, the requirement of such high solubility greatly limits the selection of primary dyes imposing problems on the scintillation performance and preparation process. With no requirement for high QY demonstrated in this work, BP, *m*-TP, or other similar dyes, yet to be found, present broader options for use in efficient PSD plastics. As illustrated by selected examples shown in Table 2.4, LO and PSD similar to or even exceeding that of the current EJ-276 can be obtained with mixtures alternative to PPO. Among the primary dyes, BP used in combination with other dyes can exhibit excellent PSD at high loads, but in this work preparation of stable plastics was found problematic if the concentration of BP exceeded $\sim 20\%$. Plastics with higher BP concentration could be prepared as transparent colorless samples that remained unchanged for a few hours sufficient for the measurements after removing from sealed glass. At longer times, the small size of BP molecules led to intense leaching and a strong chemical odor that could not be prevented by additions of cross-linkers or ethanol surface treatment [28]. TMQ, on the other hand, never showed signs of leaching, even at 50%. Moreover, BP-TMQ or *m*-TP—TMQ

Table 2.4 Examples of mixed-dye combinations with corresponding LO and PSD exceeding that of commercial EJ-276 and previously introduced PPO—MDAC combination [28]. FoM values are for 450–510 keV_{ee}. LO is shown relatively to same size EJ-200 and freshly prepared EJ-276 equal LO of which is taken as a unit [32]

#	Dye composition in PS plastics	LO, r.u	FoM
1	EJ-276	1.00	2.8
2	30% PPO + 0.2% MDAC	1.08	3.3
3	10%BP + 10% <i>m</i> -TP + 10% TMQ + 0.2% E404	1.05	2.8
4	20% BP + 10% TMQ + 0.2% E404	1.02	3.1
5	30% <i>m</i> -TP + 0.5% E404	1.1	3.2
6	10% BP + 20% <i>m</i> -TP + 3% TMQ + 0.2% E404	1	3.2
7	20% BP + 20% TMQ + 0.2% E404	1.2	3.4
8	20% <i>m</i> -TP + 20% TMQ + 0.2% E404	1.4	3.4
9	27% BP + 3% TMQ + 0.2% E404	1.1	3.4
10	20% BP + 20% <i>m</i> -TP + 10% TMQ	0.79	3.5
11	10% BP + 30% <i>m</i> -TP + 1% E404	1.1	3.5
12	10% BP + 30% PPO + 0.5% E417	1.2	3.5
13	20% <i>tert</i> -BBP + 20% TMQ + 0.2% E404	1.2	3.1
14	30% PPO + 2% E417	1.3	3.5
15	30% PPO + 2% E404	1.5	3.7
16	30% PPO + 2% E411	1.5	3.8

r.u. relative units to EJ-276

See main text or Appendix for the molecule abbreviations

mixtures containing 20% TMQ enabled the preparation of a total of 40% primary dye plastics temporarily stable during the observation time (#7 and #8 in Table 2.4).

Unfortunately, the currently high price and low availability of TMQ makes it unsuitable as a primary dye, although it can be used as an intermediate or secondary dye addition in plastics containing BP or *m*-TP (#6 and #10 in Table 2.4). Inexpensive and widely available *m*-TP that produces stable plastics at 30% alone or in 30% mixtures with BP or TMQ is promising for use in compositions where the higher reactivity of oxygen- and light-sensitive PPO [48] may pose problems for long-term stability. This can be also relevant to ⁶Li-loaded plastics where possible complexation between PPO and ⁶Li-salts of carboxylic acids may lead to the loss of LO and PSD (see Sect. 2.3.2 below). Potential options of using two or even three dyes that can produce adequate PSD at the total high concentration diminish the requirement of solubility to smaller levels. As can be seen in Table 2.4 (samples 3, 6, 11, 12), mixed plastics with good PSD can be obtained using only 10% BP that does not produce any leaching. Another approach that can be used in future development is a search for new cooperative primary dyes, among which can be numerous biphenyl derivatives that, according to our crystal characterization studies, always show good PSD. An example is illustrated in Table 2.4 (#13) by the relatively high PSD FoM obtained with

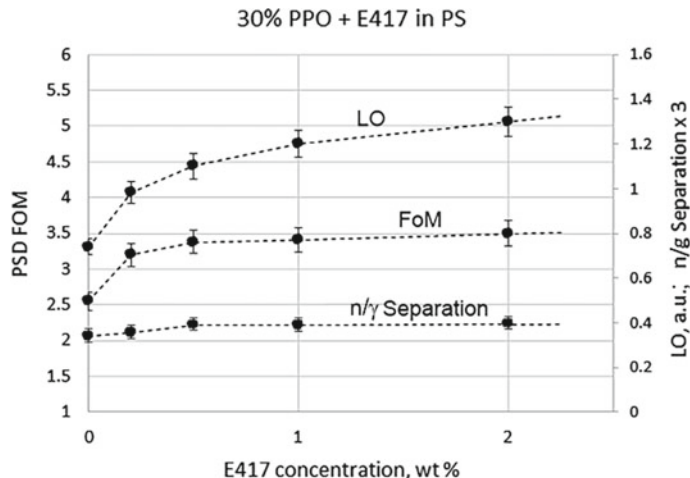


Fig. 2.27 Scintillation and PSD parameters measured with plastics combining 30% PPO and E417 used as a secondary dye (reproduced from [32] with permission from Elsevier)

4-*tert*-butylbiphenyl (*tert*-BBP) that, due to the larger size of branched molecules, does not produce leaching and physical degradation important for applications.

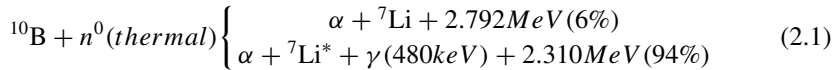
One more practical aspect of the work is the introduction of new secondary dyes. The selection of these dyes is typically based on their brightness and spectral compatibility with primary dyes. As shown in this research, in application to PSD plastics this traditional approach may not be the most efficient at a large difference in T_1 energy levels that may prevent enhancement of PSD otherwise achievable with dyes having smaller ΔE_T . Knowledge of E_T of aromatic compounds would greatly help in the design of better dye combinations. However, with the very wide choice of fluorescent organic compounds, optimal pairs may be found empirically by the simple comparison of results obtained with different mixtures. An example of such an empirical approach is demonstrated by Fig. 2.27 that presents LO and PSD parameters measured with plastics containing 30% PPO combined with E417. The T_1 level of E417 is unknown, but no visible decrease of n/γ separation up to 2% E417 allows for the suggestion that the energies of the PPO and E417 T_1 levels may be close enough to prevent trapping and enable the heterogeneous TTA and cooperation of the partner dyes in PSD production. Similar assumptions can be made with respect to the other tested exalites (E404 and E411) found to increase both n/γ separation and PSD in PPO-based plastics. As shown by the results, PPO combinations with 2% E404 or E411 demonstrate the highest LO and PSD (#15 and 16 in Table 2.4) achieved so far for fast n/γ discrimination with any tested plastic scintillators. An important practical advantage of exalites is that, with the lack of coloration and sensitivity to oxygen, they do not require special precautions and time-consuming purification procedures that prevented the use of MDAC in commercially produced plastic scintillators.

2.3 PSD Plastics for Combined Detection of Fast and Thermal Neutrons

As mentioned above, high hydrogen content in aromatic compounds and polymers makes regular hydrocarbon-based PSD plastic scintillators the most suitable materials for fast neutron detection via the mechanism of elastic (n,p) scattering. Due to their composition, PSD plastics described above can be used only for the detection of fast neutrons with typical energy of 1–20 MeV, leaving undetected low energy and thermal (~0.025 eV) neutrons that do not generate enough light in elastic scatter interactions. Detection of low energy neutrons can be achieved from the presence of special high cross section nuclei, such as ^{10}B or ^6Li that produce heavy charged particles in capture reactions with thermal neutrons. Detection of these particles can also be made based on the different fractions of delayed light in the corresponding scintillation pulses if heavier particles than neutrons are produced in the capture reactions. The phenomenon was first demonstrated many decades ago by the measurements of the decay curves produced by excitation of a *trans*-stilbene crystal by gamma rays, fast neutrons, and alpha particles. The classical triple-curve decay produced in time-of-flight experiments by L. Bollinger and G. Thomas [6] and then widely cited in the literature [1, 3] showed clearly distinctive fractions of the delayed light that suggested that organic PSD materials can be used not only for discrimination between fast neutrons and gamma rays, but also for detection of charged particles, including those produced in thermal neutron capture reactions.

2.3.1 ^{10}B -loaded PSD Plastic Scintillators

The sensitivity of PSD plastic scintillator to thermal neutrons can be achieved by using the capture reaction on a nucleus of ^{10}B , according to Ref. [49]:



^{10}B has an advantage of the high cross-sections for thermal neutron capture (72% of ^3He) and relatively high natural abundance (19.8%). High flash point liquid scintillators with PSD [50–52] were investigated for border monitoring applications and reported to have efficiency comparable to ^3He counters, although with significantly lower gamma-ray rejection levels. On the other hand, solid-state scintillators containing natural boron (glass, plastic, and silicon rubber-based) have been considered mainly as materials without PSD capability [53–55]. Current commercial boron-containing plastic scintillators without PSD (EJ-254, BC-454) use energy deposition pulse height (PH), specific to charged reaction products, to identify neutrons. Such scintillators would benefit from the addition of PSD to provide additional rejection of omnipresent gamma rays events underneath the thermal neutron PH distribution.

2.3.1.1 PSD Properties of Boron-Loaded Plastics

Availability of organo-boron compounds, such as carboranes, soluble in polymers and PPO, allows for easy preparation of PSD plastics of different size and shape [56]. The first examples of ^{10}B -loaded PSD plastics shown in Fig. 2.28 were prepared using a regular PSD composition containing 28% PPO and 0.2 % DPA dissolved in PS or PVT, with the addition of 5% of *m*-carborane that corresponds to ~0.75% of ^{10}B concentration. To enhance the physical stability of plastics, routine preparations also involved the addition of 5% DVB and ~15% of PMMA. PSD performance tests of boron-loaded plastics were performed using a ^{252}Cf source. However, to moderate fast neutrons to thermal neutron energy, measurements were made using 7.5 cm of high-density polyethylene, HDPE, placed between the scintillator and the source.

Identification of scintillator signatures specific to the type of radiation was made by comparison of the PSD distributions of a regular PSD plastic scintillator and its loaded analog containing 5 wt% of *m*-carborane. As illustrated by Fig. 2.29a, a regular PSD plastic exhibits a typical two band response corresponding to fast neutron (proton recoils) and gamma ray (scattered electrons) events, while PSD plastic containing boron provides a response characteristic to thermal neutrons in addition to the typical signatures of gamma rays and fast neutrons. Due to the hydrogen-rich composition and presence of ^{10}B capture nuclei, boron-loaded PSD plastic detects fast neutrons by scattering protons and thermal neutrons by capture reaction products discriminating, at the same time, both types of neutrons against background gamma rays. The scintillator serves dual purposes as a detector and a neutron moderator due to its high hydrogen content. This allows for the accounting of neutrons which are below the detection threshold by protons recoil and above the effective capture by thermal neutron converters. It should be noted that in thermal neutron capture reaction on ^{10}B , two branches are expected according to Eq. (2.1) giving rise to two different signatures (Fig. 2.29b). The first type corresponds to energy deposition by $^7\text{Li} + ^4\text{He}$. Because of the constant energy of the charged reaction products defined by reaction kinematics and their short range of interaction, light output and its delayed

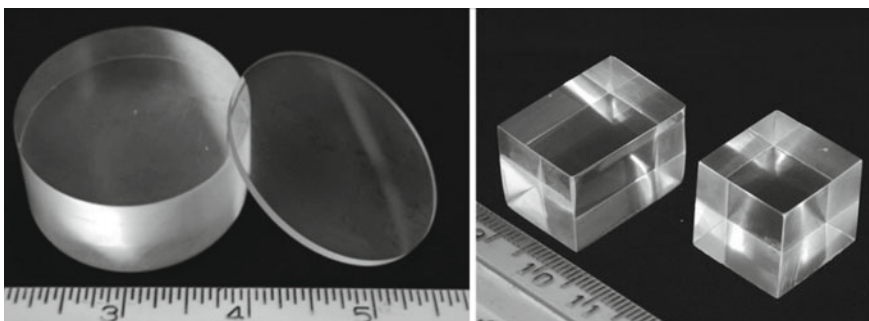


Fig. 2.28 Boron-loaded PSD plastic scintillator samples containing 5 wt% of *m*-carborane with natural boron abundance corresponding to ~0.75 wt% of ^{10}B

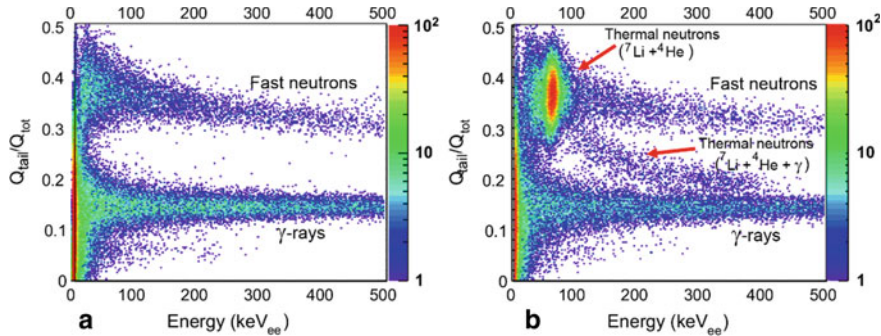


Fig. 2.29 Pulse shape discrimination parameter vs energy in electron equivalent units for **a**—PSD plastic containing 28% PPO and 0.2% DPA exposed to neutron flux from $15\text{-}\mu\text{Ci}^{252}\text{Cf}$ source shielded with 7.5-cm of high-density polyethylene (HDPE) and 5 cm of lead, **b**—Same composition plastic with 5 wt% *m*-carborane of natural boron abundance measured under the same experimental conditions. Both plastic dimensions were $\varnothing 25\text{ mm} \times 10\text{ mm}$ (reproduced from [56] with permission from Elsevier)

fraction is well reproducible as illustrated by a signature with mean values of $72.7 \pm 0.01\text{ keV}_{\text{ee}}$ and 0.387 ± 0.0003 in energy and PSD, respectively. The second type of thermal neutron signature represents events characteristic to energy deposition of $^7\text{Li} + ^4\text{He}$ and a capture γ -ray. Incident gamma rays on the organic scintillator interact mainly by Compton scattering, and their energy deposition depends on scattering angle with maximum characteristic to Compton edge (313 keV for 480 keV capture γ -ray). Since scintillator response time is slower than gamma ray transit time, light output is a convolution due to excitation by charged reaction products and the capture gamma ray. Both, total light output and its delayed fraction vary depending on the capture gamma ray energy deposition. The ratio of delayed light is decreasing as the energy deposition is dominated by the capture gamma rays. Therefore, the second signature, characteristic of thermal neutrons, is shown as a band extending towards typical gamma ray signature. Its maximum energy corresponds to the sum of capture gamma ray Compton edge energy and total energy deposition by charged reaction products (see Fig. 2.29b). Although 480 keV gamma ray is emitted with 94% probability, the vast majority of the capture gamma rays escapes without depositing any energy to the scintillator due to the small sample size (2.5 cm in diameter and 1 cm in thickness), which is consistent with the two orders of magnitude higher intensity observed in the thermal neutron spot than in the band.

PSD parameter distributions in the 50–100 keV_{ee} domain characteristic to thermal neutrons energy are illustrated in Fig. 2.30. Comparison of a PSD plastic (a) and a boron-loaded PSD plastic (b) shows the degree of n/ γ separation and the effect of boron loading on neutron detection efficiency. For each sample in Fig. 2.30, distributions are shown with and without external moderator (Pb+HDPE, and only Pb, respectively). The results indicate comparable scintillator performance in the absence of thermal neutrons. Due to the low energy of the thermal neutron spot position, the n/ γ separation is not as high as in the range corresponding to the Compton

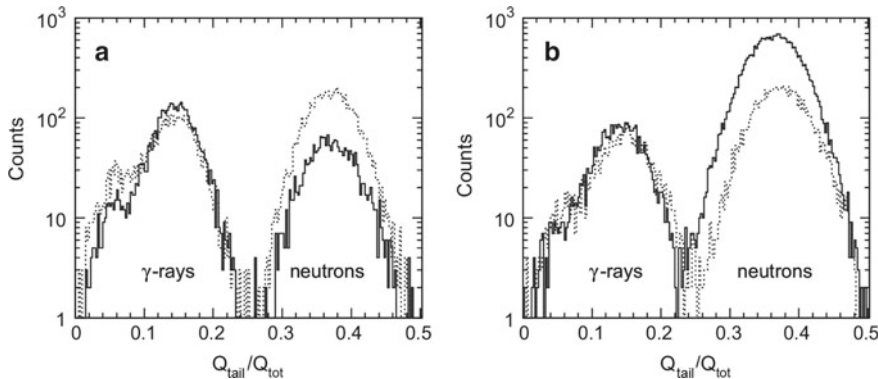


Fig. 2.30 PSD parameter distributions in the energy range of 50–100 keV_{ee} corresponding to data illustrated in Fig. 2.29 for **a**—unloaded PSD plastic, and **b**—PSD plastic containing 5 wt% of *m*-carborane. Dotted line distributions, obtained for samples exposed to 15- μ Ci ²⁵²Cf source without additional moderator, show comparable intensity for both samples. Distributions represented by full lines, obtained with 7.5-cm of HDPE moderator, illustrate a significant increase in neutron counts for boron-loaded plastic compared to PSD plastic sensitive only to fast neutrons (reproduced from [56] with permission from Elsevier)

edge region where PSD of the regular plastics is typically evaluated. However, the results clearly show a significant gain in neutron detection capability in the case of boron-loaded PSD plastic as compared to unloaded PSD plastic exposed to the moderated neutron flux.

2.3.1.2 Effect of Boron Concentration

Incorporation of *m*-carborane into the scintillator requires careful understanding of the effects of a boron-containing compound on the scintillator light collection and pulse shape discrimination properties. The dependence presented in Fig. 2.31a shows a decrease of the LO with increasing *m*-carborane concentration measured in response to ¹³⁷Cs source. Effects of *m*-carborane loading on discrimination properties, n/ γ separation, and FoM values, measured in the 50–100 keV_{ee} energy range containing signatures of both thermal and fast neutrons, are illustrated by Fig. 2.31b. Results show that separation remains constant across the range of *m*-carborane concentrations, which indicates that *m*-carborane does not affect the PSD process. FoM values, on the other hand, slightly decrease with increasing *m*-carborane concentration, from 1.6 without boron loading to 1.4 with 5 wt% of *m*-carborane, respectively. With no change in separation, the reason behind the decrease in the FoM is the widening of neutron and gamma peak distributions due to light losses. PSD properties for scintillators have also been evaluated for events near the Compton edge of ¹³⁷Cs that corresponds mainly to fast neutrons and gamma ray events. Comparison of FOM values denoted by FoM CE in Fig. 2.31c shows that PSD plastic loaded with 5%

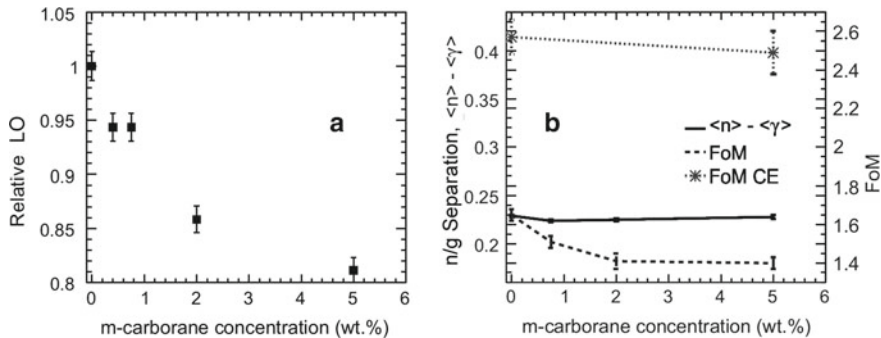


Fig. 2.31 **a**— ^{137}Cs LO of PSD plastic samples containing various concentrations of *m*-carborane relative to a blank unloaded PSD plastic; **b**—n/ γ separation and PSD FoM of events in 50–100 keVee energy range (FoM), and near the Compton edge of ^{137}Cs (FoM CE) vs. *m*-carborane concentration (reproduced from [56] with permission from Elsevier)

of *m*-carborane provides fast n/ γ PSD adequate for applications involving combined detection of both fast and thermal neutrons without the need for moderation.

Scintillator experimental development was combined with Monte Carlo calculations to estimate target ^{10}B concentration based on capture time and thermal neutron capture efficiency. Theoretical calculations made by MCNPX simulations and Neutron Capture Ion Algorithm (NCIA) [56] enable evaluation of thermal neutron capture efficiency versus concentration of ^{10}B and scintillator thickness. As shown by the results presented in Fig. 2.32, simulated thermal neutron capture efficiency on ^{10}B increases with scintillator thickness to reach saturation. With increasing ^{10}B concentration, capture efficiency approaches but does not reach unity, mainly due to thermal neutron escape at detector boundaries. Generally, the results of modeling show that high thermal neutron capture efficiency can be reached with boron loaded plastics of small thicknesses < 1 cm. This result determined by the high thermal neutron capture cross section of ^{10}B provides advantages for potential improvement of boron-loaded plastic performance. The first is the use of the thin samples that substantially reduce the interference of the capture reaction gamma rays, a large fraction of which escape the scintillator due to smaller thickness (Fig. 2.33a). This leads to a higher degree of n/ γ separation and increased PSD FoM (Fig. 2.33b). According to the simulation results of Fig. 2.32, at 5% *m*-carborane load (~0.74% of ^{10}B), the decrease of the thickness from 1 cm to 3 mm should lead to the corresponding loss of thermal capture efficiency from 86 to 48%. A practical performance that can be obtained with boron loaded PSD plastic scintillators was evaluated using an LLNL detector system based on a 12.5 mm thick scintillator tested at Pacific Northwest National Laboratory (PNNL) as part of a Defense Threat Reduction Agency (DTRA) program. The system demonstrated >15% intrinsic detection efficiency for neutrons from a ^{252}Cf source over a wide range of moderator thicknesses with a maximum efficiency exceeding 30%. Further increase of efficiency can be achieved by the use of commercially available ^{10}B enriched carboranes [57] that at 2.5% total

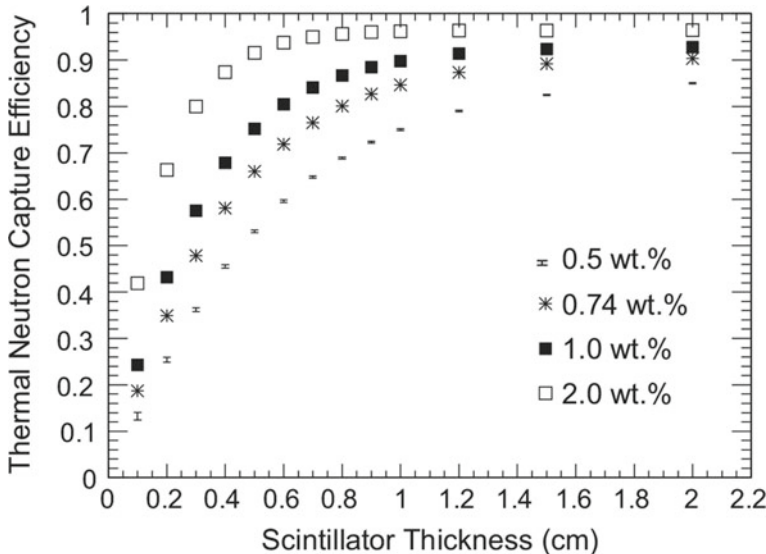


Fig. 2.32 Simulated thermal neutron capture efficiency of ^{10}B versus scintillator thickness for ^{10}B oron loading of 0.5, 0.74, 1.0, and 2.0% by weight. Error bars are within points (reproduced from [56] with permission from Elsevier)

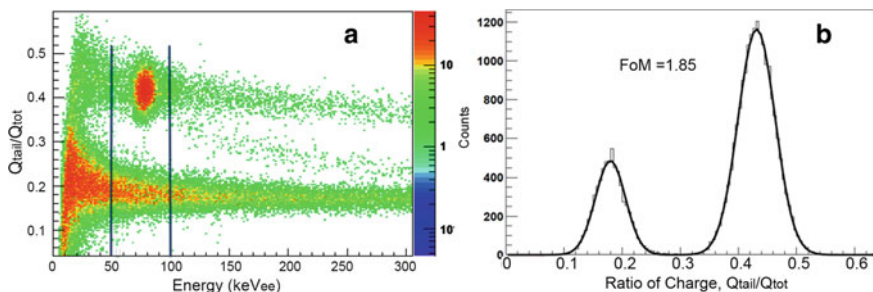


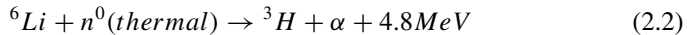
Fig. 2.33 **a**—PSD distributions obtained with a 3 mm thick plastic containing 28% PPO and 0.2% DPA in combination with 5% of *m*-carborane of natural abundance. Comparison to a similar composition plastic illustrated by Fig. 2.29b shows much fewer counts produced by the capture reaction gamma rays, large fraction of which escape the scintillator due to the decreased thickness; **b**—Corresponding PSD showing clear separation of neutron and gamma peak separation

load may produce ~80% efficiency with 3 mm plastic. Another, much less expensive way of PSD improvement is the use of advanced compositions. According to more recent measurements made with 1–2 cm-thick plastics, replacement of DPA by MDAC in 30% PPO plastics may provide PSD and FoMs similar to that of Fig. 2.33b, even when 5% of natural abundance *m*-carborane is used. Another way for potential development is the combination of boron loadings with the new compositions

involving the use of the brightest exalite dyes compatible in triple energies with PPO or alternative primary dyes.

2.3.2 *⁶Li-loaded PSD Plastic Scintillators*

The use of enriched ⁶Li dopant is another alternative for the introduction of thermal neutron sensitivity in plastic scintillators. The interaction of thermal neutrons with ⁶Li proceed via a known capture reaction that has important advantages over ¹⁰B capture (Eq. (2.1)).



Although ⁶Li capture cross section is smaller than that of ¹⁰B (942 vs 3840 barns, respectively [49]), ⁶Li has advantages, among which the most important are higher energy released in the capture reaction and the absence of gamma rays in the final products containing charged particles. The principal drawback that prevented the use of ⁶Li-loaded plastic scintillators in the past related to the difficulties in their preparation due to the lack of solubility of highly polar Li-containing compounds in non-polar aromatic matrices needed for efficient scintillation. Although a few attempts to dissolve inorganic or organic salts of lithium in aromatic liquids were made [58–60], the results were found difficult to apply for preparation of stable and efficient plastics, so that the majority of ⁶Li containing organic scintillators reported in the literature were typically prepared as dispersions of nano- or micro-particles of different Li-compounds in liquid or plastic solutions [61–64].

A potential benefit of ⁶Li incorporation into PSD-capable organic scintillators was demonstrated by the results obtained first with single crystals of ⁶Li salts of some aromatic acids, such as ⁶Li salts of 3-phenylsalicylic acid (Li-3-PSA) [65]. As shown by Fig. 2.34b, the position of the thermal neutron spot shifted to the higher energy range provides a clear separation of fast and thermal neutrons from gamma ray background not mixed, as in case of ¹⁰B, with gamma rays of capture reaction. In addition, ⁶Li containing crystals exhibited a unique feature of “triple PSD” corresponding to discrimination between fast and thermal neutrons, both efficiently separated for gamma radiation (Fig. 2.34c).

To study the possibility of obtaining ⁶Li-loaded plastic scintillators, about 50 different lithium salts of carboxylic acids were tested for compatibility with aromatic polymers. Since none of ⁶Li salts are available commercially, and only a few stable organo-lithium compounds with natural Li abundance containing only ~7.5% of ⁶Li can be purchased from commercial vendors, all tested compounds had to be synthesized via reactions between ⁶LiOH or ⁶Li₂CO₃ and corresponding acids (Fig. 2.35).

None of the tested salts was found soluble in pure aromatic solvents, including toluene, xylene(s), or monomers such as vinyltoluene or styrene used for plastic preparation. However, some of the synthesized compounds, such as Li-3-PSA

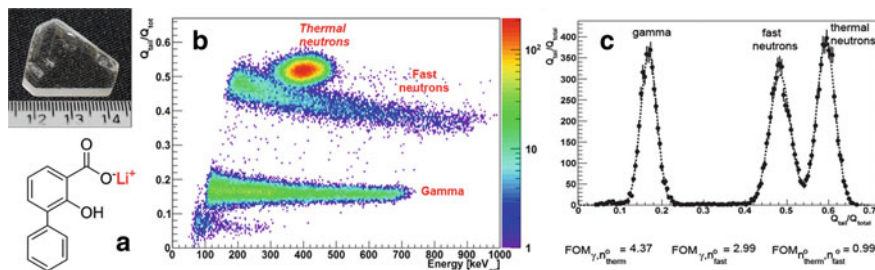


Fig. 2.34 **a**—Crystal of ⁶Lithium salt of 3-phenylsalicylic acid with the corresponding molecular formula; **b**—Experimental PSD plot showing signatures of both fast and thermal neutrons well separated from gamma rays; **c**—“triple” PSD profile with FoMs corresponding to discrimination between fast and thermal neutrons separated for gamma radiation. ²⁵²Cf source with 75 mm HDPE used for measurements (reproduced from [65] with permission from Elsevier)

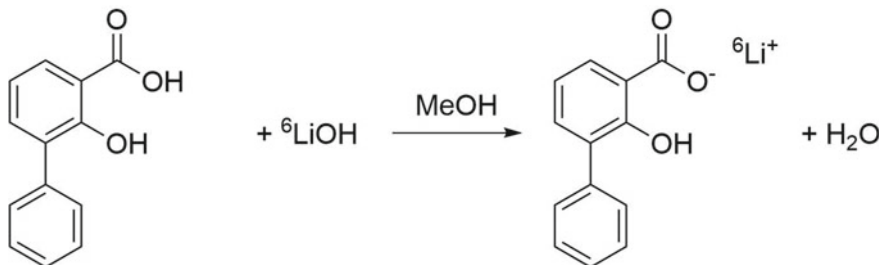


Fig. 2.35 Example of the acid–base reaction of 3-PSA with enriched ⁶Li hydroxide used for the synthesis of ⁶Li-3-PSA salt tested for incorporation into first PSD plastic scintillators

or lithium salt of 3,5-di-*tert*-butylsalicylic acid (Li-BSA) were found to be soluble in PPO or in coordinating solvents, like acetone, methanol, THF, or 1,2-dimethoxyethane (DME) that are miscible with pure aromatics. It should be noted that simple solubility in coordinating solvents is not a sufficient condition for the dissolution of Li-salts in aromatic matrices. More likely is that some Li-salts form molecular complexes with PPO or coordinating solvents diminishing polarity and helping incorporation into organic matrices. More detailed understanding of dissolution chemistry and complex formation processes is still a subject of ongoing investigations. However, conducted studies already led to reproducible preparation of first ⁶Li plastics with properties and efficient PSD performance promising for applications involving simultaneous detection of thermal and fast neutrons without need for traditional moderation.

2.3.2.1 Preparation and Properties of First ${}^6\text{Li}$ -Loaded Plastics

First, ${}^6\text{Li}$ -loaded plastics were prepared with Li-3-PSA added to regular PSD compositions containing 30% of PPO in combination with ~0.2% of secondary dyes, DPA or bis-MSB. ${}^6\text{Li}$ -3-PSA, dissolved in a small amount of DME, was added to precursor mixtures in the amount from 5–10% to the total weight of the scintillator prior to the polymerization conducted according to a standard procedure for PSD plastic production [28]. In the case of a fully enriched ${}^6\text{Li}$ single-isotope compound, this range of concentrations corresponds to 0.135–0.27% of atomic ${}^6\text{Li}$ loads. Highly purified Li-3-PSA is colorless, non-hygroscopic compound that allows for the preparation of optically transparent plastics with hardness or transparency similar to regular PSD plastic scintillators (Fig. 2.36). Measurements of PL spectra showed that they had luminescence typical for organic scintillators, in which the final emission occurs from the molecules of the secondary dyes. Examples of a waveform obtained with the PSD plastics containing DPA as a secondary dye are shown in Fig. 2.37. As follows from the comparison, all measured pulse averages have a shape consistent with having the same prompt component determined by the final emission from the DPA molecules. The relative intensities of the delayed emission, on the other hand, are different in pulses induced by different types of radiation. A regular hydrocarbon-based plastic (Fig. 2.37a) shows a scintillation response typical for organic scintillators with PSD, in which pulses corresponding to fast neutrons have the noticeably higher relative intensity of the delayed component. The addition of ${}^6\text{Li}$ to the composition of this plastic adds one more signature with a respective waveform containing the largest fraction of the delayed emission produced by the heavier alpha and triton particles originating in the capture reaction (Fig. 2.37b). These triple-decay characteristics are qualitatively identical to the classical results of L. Bollinger and G. Thomas [6],



Fig. 2.36 First ${}^6\text{Li}$ -loaded PSD plastics containing PPO (30%) and Li-3-PSA dissolved in polystyrene. Small amounts (~0.2%) of secondary dyes (DPA, bis-MSB) were added as wavelength shifters (reproduced from [65] with permission from Elsevier)

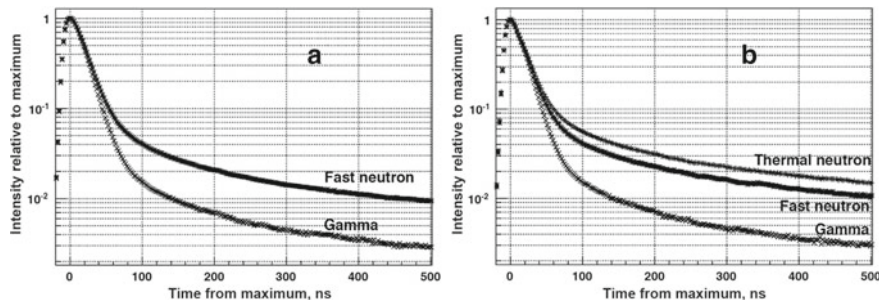


Fig. 2.37 Average ^{252}Cf -moderated waveforms corresponding to the normalized scintillation pulses recorded in the electron equivalent energy range of 351–492 keV_{ee} with **a**—unloaded polystyrene-based PSD plastic containing 30% of PPO and 0.2% DPA, and **b**—plastic of the same composition loaded with 5% of ^6Li -3-PSA (reproduced from [65] with permission from Elsevier)

showing that ^6Li -loaded plastics can be used for direct detection and discrimination of both fast and thermal neutrons in the mixed n/ γ radiation fields.

Figure 2.38 presents experimental PSD patterns obtained with selected samples of Li-loaded plastics irradiated by the mixed fluences of fast neutrons, thermal neutrons, and gamma rays produced by ^{252}Cf source shielded by varying degrees of HDPE. The

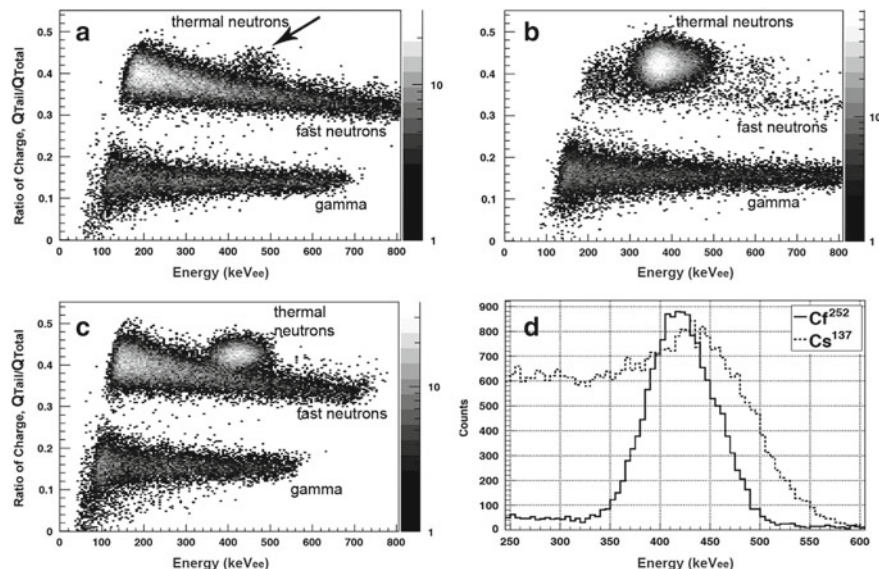


Fig. 2.38 ^{252}Cf PSD patterns obtained with Li-loaded PSD plastics: **a**—5% of $^{6\text{Li}}$ -3-PSA (containing $\sim 0.01\%$ ^6Li), 9 mm HDPE moderation; **b**—7.5% of ^6Li -3-PSA ($\sim 0.27\%$ ^6Li), 7.5 cm of HDPE moderation; **c**—5% of ^6Li -3-PSA ($\sim 0.135\%$ ^6Li) with 9 mm HDPE moderation; **d**— ^{137}Cs and ^{252}Cf spectra corresponding to the pattern **c**, with a sharply pronounced thermal neutron peak (reproduced from [65] with permission from Elsevier)

first pattern (Fig. 2.38a) obtained with a plastic loaded with 5% of natural abundance of ^{6}Li -3-PSA ($\sim 0.01\%$ of ^{6}Li) and a low degree of moderation provided by a 9 mm thick cylinder containing the ^{252}Cf source, is similar to that typical for unloaded PSD plastics irradiated by a ^{252}Cf source that emits only fast neutrons and gammas, with the exception of the small count increase corresponding to thermalized neutrons (shown by the arrow). The intensity of the thermal neutron peak increases with the increase of ^{6}Li load and the use of moderation that leads to the fast-to-thermal neutron conversion (Fig. 2.38b). For the cases corresponding to an intermediate amount of ^{252}Cf moderation or to realistic conditions when both thermal and fast neutrons are present, the “triple” signature of two types of neutrons and gamma rays can be obtained (Fig. 2.38c). It should be noted here that at increasing size additional moderation effects can be introduced by the hydrogen-rich environment of the detector itself. Due to the monoenergetic nature of the alpha and triton particles produced by the capture reaction, the thermal neutron pulses are concentrated in a narrow energy range leading to the appearance of a sharp peak (Fig. 2.38d), with energy resolution (calculated as FWHM/mean) of 13% to 20%, depending on the composition and size of measured plastics.

The ability to simultaneously detect both thermal and fast neutrons discriminated from gamma rays is obviously the most important feature of the new materials. This unique property brings a substantial advantage of lithiated plastics over their regular unloaded counterparts which can be used only for detection of fast neutrons above the low energy threshold for n/γ separation. For most of the known organic scintillators with PSD, the separation threshold falls into the gamma-equivalent energy range of about 50–100 keV_{ee}, which, depending on the type of materials with different quenching factors, may correspond to the neutron energy of 300–700 keV [66]. This means that a large fraction of less energetic neutrons cannot be detected using regular PSD materials. The fact that particles resulting from the capture reaction produce scintillation pulses far above the discrimination threshold allows for the detection of thermal neutrons in the energy range where their signature can be clearly separated from the gamma radiation background. The PSD FoMs with mean values of 3.19 and 2.96 calculated for the first examples of ^{6}Li -loaded plastics in the near-thermal-neutron energy range (Fig. 2.39a and b) correspond to efficient thermal n/γ discrimination. At the same time, as follows from the results, the sensitivity to thermal neutrons does not diminish the ability of the new materials to detect fast neutrons (FoMs equal to 2.47 and 2.33, respectively). As in the case of ^{10}B plastics, simultaneous detection of thermal and fast neutrons increases the total efficiency of neutron detection. As shown by the results of computer simulation in Fig. 2.40, due to the lower capture cross section and poorer solubility, the thermal neutron detection efficiency of ^{6}Li can be lower in comparison with the same loads of ^{10}B . However, substantially better discrimination determined by higher energy and absence of gamma rays released in the capture reaction makes ^{6}Li -loaded plastics more attractive for many applications compared to plastics loaded with ^{10}B . The PSD FoMs corresponding to the fast/thermal neutron discrimination are relatively small in the first tested plastics (0.693 and 0.63 in Fig. 2.39a and b, respectively). However, results obtained with single crystals (Fig. 2.34c) may indicate that, with

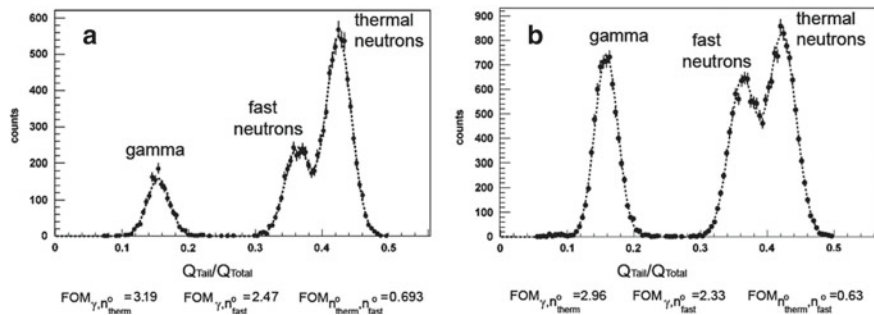


Fig. 2.39 PSD profiles obtained with $\varnothing 2.5 \text{ cm} \times 2.5 \text{ cm}$ -thick plastics containing 30% of PPO, 5% of ^{6}Li -3-PSA, and secondary dyes: **a**—DPA; **b**—bis-MSB. 9 mm of HDPE moderation used to moderate neutrons emitted by ^{252}Cf source. FoMs are calculated in the near thermal neutron spot energy (reproduced from [65] with permission from Elsevier)

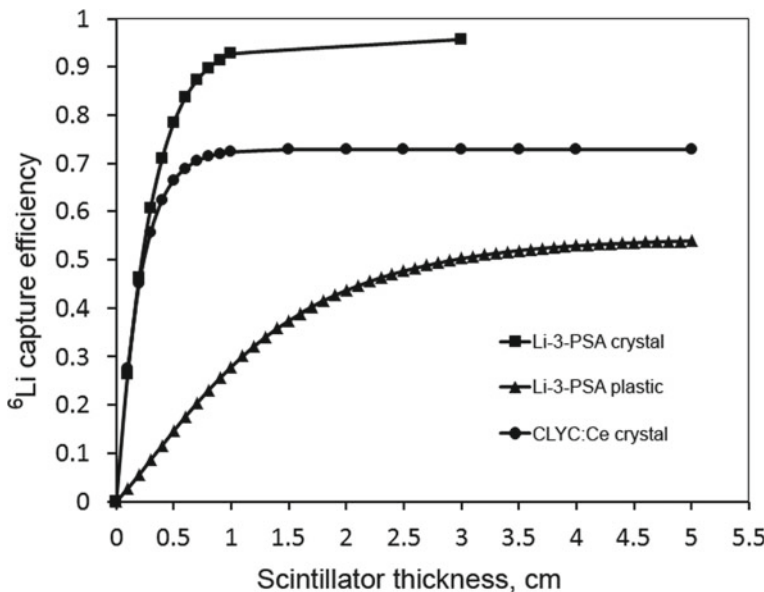


Fig. 2.40 Calculated probability of thermal neutron capture on ^{6}Li atoms in plastics, ^{6}Li -3-PSA single crystals, and CLYC crystals given for comparison. ^{6}Li concentrations and densities used for corresponding calculations: 2.7 wt% and $1.1 \text{ g}/\text{cm}^3$ for Li-3-PSA; 0.2 wt% and $1.1 \text{ g}/\text{cm}^3$ for Li-plastic; 1 wt% and $3.6 \text{ g}/\text{cm}^3$ for CLYC (reproduced from [65] with permission from Elsevier)

further development, this new kind of discrimination may be controlled and improved for potential use in more advanced neutron detection systems.

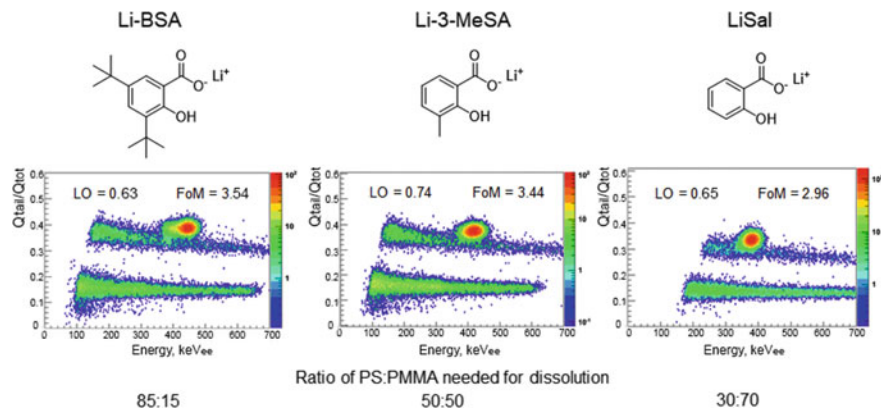


Fig. 2.41 Examples of structures and best triple PSD distributions obtained with three most studied ^{6}Li salts of salicylic acid derivatives dissolved in plastics containing 30% PPO and 0.2% of bis-MSB. Numbers on the pictures show corresponding ^{137}Cs light output relative to that of unloaded PSD plastics measured under the same conditions and thermal neutron/gamma FoMs calculated for the energy range of the thermal neutron spot location. The lower numbers indicate fractions of nonaromatic PMMA added to facilitate dissolution of the corresponding salt amounts containing 0.1% of ^{6}Li

2.3.2.2 Modifications to Improve PSD and Light Output

The first stage of ^{6}Li -loaded plastic development involved studies conducted with ^{6}Li salts of aromatic acids, among which a possibility of dissolution in PS or PVT matrix was found only for few salts of salicylic acid derivatives. Examples of salts that could be dissolved in optically transparent plastics are shown in Fig. 2.41. It should be noted that each of these salts could be incorporated in PS or PVT matrices at the atomic concentrations of ^{6}Li up to 0.4%. However, to decrease difficulties in cost, purification, synthesis, and impurity effects, plastics for the initial studies were typically prepared with 0.1% of atomic ^{6}Li . As indicated by the results, dissolution of each compound requires the addition of the nonaromatic PMMA that negatively affects n/y separation and PSD at increasing concentration. Similar to ^{6}Li -3-PSA, ^{6}Li -BSA is partially soluble in PPO, so that only 15% of PMMA is needed to incorporate the salt into the polymer, and as a result, the ^{6}Li -BSA-loaded plastic has the highest PSD FoM. The decrease of PSD in ^{6}Li -3-MeSA (lithium salt of 3-methylsalicylic acid) and ^{6}Li Sal (lithium salt of salicylic acid [67]) plastics correlates with the increasing concentration of PMMA needed for dissolution. There is no direct correlation between the fraction of PMMA and LO found for all ^{6}Li -loaded plastics to be lower than that of the corresponding unloaded versions. The reason for the LO loss introduced by additions of aromatic salts can be understood from the consideration of the absorption and fluorescent spectra of molecules present in the plastic mixtures. Lithium salts of salicylic acids are low QY fluorescent compounds with the wavelengths of emission close to or longer than the wavelengths of most secondary dyes, such as DPA or bis-MSB. As illustrated by the example of ^{6}Li -3-PSA plastic

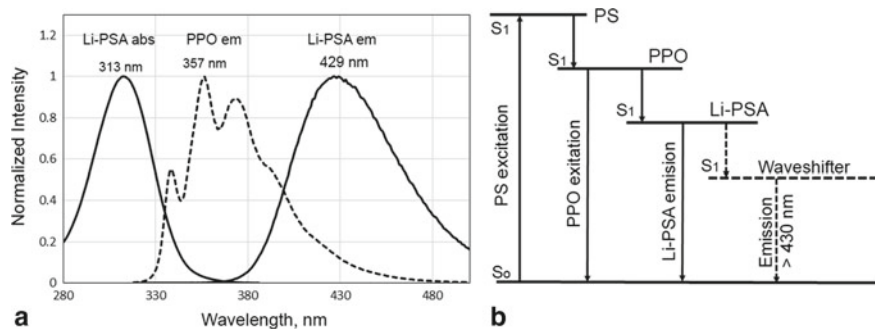


Fig. 2.42 **a**—Superposition of spectra showing that, due to the overlay of the Li-3-PSA absorption with the PPO emission, Li-3-PSA that has a longer wavelength of emission (429 nm) may act as a secondary dye relatively to PPO; **b**—Energy diagram illustrating singlet transfer from PPO to the low QY Li-3-PSA molecules. To obtain the high LO from such a system, highly efficient wavelength shifter with the peak emission longer than ~430 nm is required

(Fig. 2.42a), in PPO-based systems, the lithium compounds may act like inefficient secondary dyes that emit a fraction of the final light. This means that collection of the total light of the whole system requires the use of additional high QY secondary dyes with the longer wavelength of emission that, for the case of Li-3-PSA, should be $> \sim 430$ nm, which is not typical for the most known efficient wavelength shifters (see Table 2.1).

Ideally, the limitations of the spectral incompatibility could be avoided using non-fluorescent aliphatic lithium salts that do not have any absorption in the range of PPO or other common dyes emission. The use of nonaromatic lithium salts of methacrylic and pivalic acids in preparation of plastic scintillators has been reported in previous works [68, 69]. Studies conducted in this research with the broader range of compounds showed that other Li-containing derivatives of short chain aliphatic acids can also be incorporated into plastic compositions (Fig. 2.43a). As follows from the comparison of the results presented in Figs. 2.41 and 2.43b, replacement of

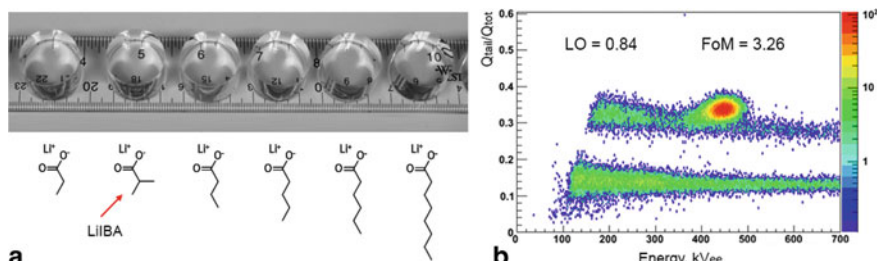
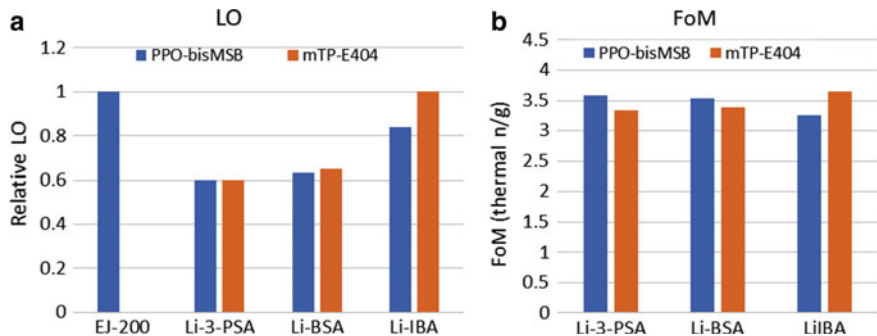


Fig. 2.43 **a**—Plastic scintillators prepared with 30% PPO combined with 0.2% bis-MSB and different ⁶Li salts of aliphatic acids; **b**—Example of PSD obtained with ⁶Li salt of isobutyric acid (⁶LiIBA). The value of FoM corresponds to thermal neutron/gamma discrimination. All plastics were prepared with 0.1% of atomic ⁶Li



aromatic ${}^6\text{Li}$ -salts by the aliphatic versions may lead to a 10–30% increase of LO, decreasing, at the same time, n/γ separation because of the contribution of salts into the total nonaromatic fraction. However, in this tradeoff between increasing LO and decreasing n/γ separation, use of aliphatic salts can still produce relatively high FoM (3.26), close to those obtained with aromatic molecules.

More recent developments of the PSD plastic compositions based on the non-traditional primary and secondary dyes described above (Sect. 2.2.2) open opportunities for further improvement of ${}^6\text{Li}$ -loaded plastics. As shown by the results of Fig. 2.44, replacement of PPO—bis-MSB by the *m*-TP—E404 pair in basic PSD composition leads to the increase of the LO, especially pronounced for plastics loaded with nonaromatic ${}^6\text{Li}$ I_{BA}. It has been long suspected that oxygen- and nitrogen-containing PPO form chemical complexes with polar lithium compounds that, in addition to possible oxidation, may lead to slightly yellow discoloration and LO loss. Use of the pure hydrocarbon *m*-TP in combination with highly efficient exalites may provide better options for the production of ${}^6\text{Li}$ -loaded plastics with decreased self-absorption, especially important for the LO and PSD performance of large-scale scintillators.

2.4 Commercialization and Further Directions of Studies

PSD plastics for fast neutron detection are now produced commercially. According to the website of Eljen Technology [21], the first commercial version, EJ-299-33, has been recently replaced by EJ-276 that offers better physical hardness, enhanced long-term stability, and can be produced with sizes up to ~20 cm in a variety of shapes and configurations requested by users for different applications (Fig. 2.45).

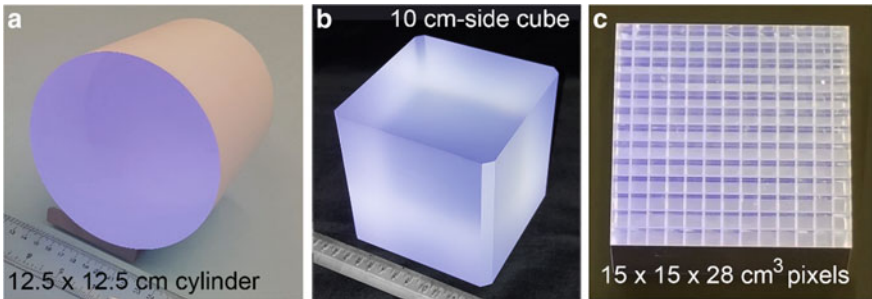


Fig. 2.45 PSD plastics produced by Eljen Technology in different sizes and shapes for fast neutron detection applications (pictures are courtesy of Eljen Technology)

One more important application that soon may require large-scale production of ${}^6\text{Li}$ -loaded plastics is antineutrino detection [70, 71]. The process of identifying an antineutrino is based on the inverse beta-decay (IBD) reaction: $\bar{\nu}_e + p \rightarrow e^+ + n$. According to this reaction, first experimentally determined by F. Reines and C. Cowan [72], an electron antineutrino $\bar{\nu}_e$ interacts with a proton p inside the plastic scintillator medium, producing a positron e^+ and a low energy neutron n . The characteristic time scale between prompt (positron annihilation) and delayed (neutron capture) signals can be used as the primary signature for identifying neutrino events. The IBD event detection efficiency, that critically depends on the neutron capture detection efficiency, is very low with regular liquid or plastic scintillators but can be increased using capture-loaded scintillators. Ideally, both ${}^{10}\text{B}$ and ${}^6\text{Li}$ can be used to facilitate the likelihood of IBD event detection [73, 74]. However, as mentioned above, the reaction of ${}^6\text{Li}$ that produces an alpha and a triton has an advantage of not having gamma rays in the reaction products. Alpha particles cannot travel far, they ionize the scintillator right at the capture locations offering better chances for the localization of the neutron capture events. With new ${}^6\text{Li}$ plastic scintillators, additional advantages are introduced by a distinct “triple” PSD feature that greatly suppresses the background events. Although nuclear reactors produce an enormous number of neutrinos, most of them just pass through any shielding and the detector itself without any interaction, so that large detectors on a scale of ~ 100 kg are potentially needed to get meaningful signals. Initial progress achieved with the first ${}^6\text{Li}$ -loaded plastic scintillators is illustrated by Fig. 2.46 that presents large-scale prototypes manufactured for tests in the segmented antineutrino directional detector (SANDD) [75]. Calculations show that 0.1% ${}^6\text{Li}$ loading is sufficient for the detection of about 40% of IBD events. Higher ${}^6\text{Li}$ loads up to 0.4–0.5% would be greatly beneficial for the enhancement of the detection efficiency. However, to reach these levels, more studies are required to understand lithium interactions with the polymer matrix and dyes that negatively affect LO and attenuation in large-scale scintillators. In this respect, replacement of PPO by less reactive, pure hydrocarbon *m*-TP combined with more efficient exalite wavelength shifters may produce better opportunities for both increasing LO and ${}^6\text{Li}$ loads.

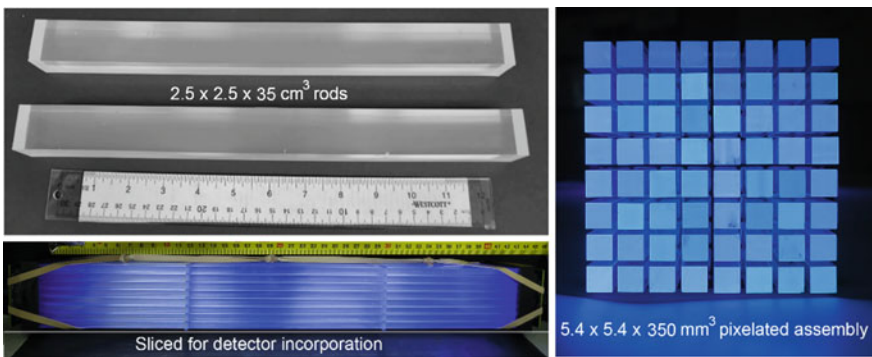


Fig. 2.46 35 cm-scale ^{6}Li -loaded PSD plastic scintillators manufactured for antineutrino detection applications [75]

The use of new compositions based on alternative dyes may also help to resolve another problem of new materials, which is the long-term stability of PSD plastics performance. The overall results described above relate mostly to freshly prepared compositions, without addressing issues of the possible temporal degradation important for the incorporation of scintillators into working detectors. Figure 2.47a presents a photo of the $\varnothing 76 \times 76$ mm cylinder of one of the first commercially produced EJ-276. The LO of this plastic measured shortly after receiving from the company was reported as equal to the same size EJ-309 liquid scintillator [28]. However, as found in further observations, over the 2 years of exposure to the ambient conditions, the same plastic developed a well distinguished yellow discoloration that led to a substantial LO loss of 25% (Fig. 2.47b) accompanied by the respective decrease of PSD (Fig. 2.47c). Development of the yellow discoloration typical for PPO-based PSD plastics can be attributed to relatively high reactivity of PPO known to degrade

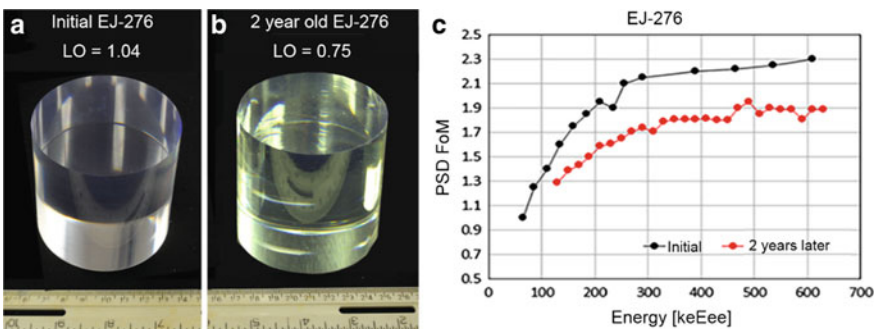
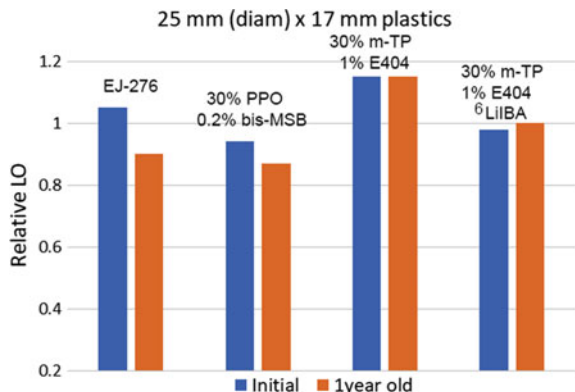


Fig. 2.47 Photos of the same $\varnothing 76$ mm \times 76 mm EJ-276 PSD plastic cylinder taken right, **a**—after receiving from the company and, **b**—after 2 years resulting in the development of the yellow discoloration. **c**—The respective ^{137}Cs LO measured relative to the same size EJ-309 cylinder shows 25 % loss of the LO accompanied by the respective decrease of PSD FoM

Fig. 2.48 Comparison of the LO measured in freshly prepared and one-year-old plastics showing higher performance stability typical for *m*-TP-based plastics in comparison to plastics prepared with PPO



under the effects of heating and oxidation [48]. The effect of yellowing and LO loss could have been also observed with some small-scale plastics containing PPO with traditional secondary dyes like bis-MSB, DPA, or POPOP. At the same time, no change in the performance has been recorded during half a year of observations with any of PPO—E417 plastics, initial LO of which is shown in Fig. 2.27. Measurements made over a year of observations with plastics containing 30% *m*-TP in combination with E404 also showed no degradation in either regular PSD or ${}^6\text{Li}$ -loaded versions (Fig. 2.48). However, more studies should be made with new compositions prepared at larger scales.

Replacement of liquid scintillators by solid-state materials is one of the major goals of PSD plastic developments. With all known advantages of solid scintillators, such replacement can become widespread and realistic only under the condition that plastics can provide equal or better performance compared to liquids traditionally used in PSD detectors. The results of the conducted studies show that high scintillation and PSD performance equal to those of liquid scintillators is possible to achieve with plastics. To maintain this performance, further developments of new compositions should also include studies of the physical and performance stability that will benefit commercial production and application of new materials.

Acknowledgements The work was performed under the auspices of the U.S. Department of Energy by Lawrence Livermore National Laboratory under Contract DE-AC52-07NA27344. This work has been supported by the NA-22 office of the U.S. Department of Energy. Additional support for boron plastic development was provided by the Defense and Thread Reduction Agency (DTRA). We also want to acknowledge Stephen Payne, Benjamin Rupert, Iwona Pawełczak, Paul Martinez, Nerine Cherepy, Michelle Faust for their contribution to this research, and Viacheslav Li, Steven Dazeley, and Nathaniel Bowden for help and discussions related to ${}^6\text{Li}$ -plastics development and applications.

References

1. F.D. Brooks, Nucl. Instr. Methods **4**(3), 151 (1959)
2. J.B. Birks, *The Theory and Practice of Scintillation Counting* (Pergamon Press, Oxford, 1964).
3. J.B. Birks, *Photophysics of Aromatic Molecules* (Wiley-Interscience, London, 1970).
4. G.T. Wright, Proc. Phys. Soc. B **69**(3), 358 (1956)
5. R.B. Owen, I.R.E. Trans, Nucl. Sci. **5**(3), 198 (1958)
6. L.M. Bollinger, G.E. Thomas, Rev. Sci. Instrum. **32**(9), 1044 (1961)
7. D.L. Horrocks, Appl. Spectrosc. **24**(4), 397 (1970)
8. F.D. Brooks, R.W. Pringle, B.L. Funt, I.R.E. Trans, Nucl. Sci. **7**(2–3), 35 (1960)
9. F.D. Brooks, Nucl. Instr. Methods **162**(1–3), 477 (1979)
10. T. Förster, Discuss. Faraday Soc. **27**, 7 (1959)
11. D.L. Dexter, J. Chem. Phys. **21**(5), 836 (1953)
12. A. Terenin, V. Ermolaev, Trans. Faraday Soc. **52**, 1042 (1956)
13. C.A. Parker, C.G. Hatchard, T.A. Joyce, Nature **205**, 1282 (1965)
14. L. Azarraga, T.N. Misra, S.P. McGlynn, J. Chem. Phys. **42**(10), 3720 (1965)
15. N. Zaitseva, L. Carman, A. Glenn, R. Hatarik, S. Hamel, M. Faust, B. Schabes, N. Cherepy, S. Payne, IEEE Trans. Nucl. Sci. **58**(6), 3411 (2011)
16. N. Zaitseva, A. Glenn, L. Carman, H.P. Martinez, R. Hatarik, H. Klapper, S. Payne, Nucl. Instr. Methods A **789**, 8 (2015)
17. N. Zaitseva, B.L. Rupert, I. Pawełczak, A. Glenn, H.P. Martinez, L. Carman, M. Faust, N. Cherepy, S. Payne, Nucl. Instr. Methods A **668**, 88 (2012)
18. G. Hull, N.P. Zaitseva, N.J. Cherepy, J.R. Newby, W. Stoeffl, S.A. Payne, IEEE Trans. Nucl. Sci. **56**(3), 899 (2009)
19. N.P. Zaitseva, J. Newby, S. Hamel, L. Carman, M. Faust, V. Lordi, N.J. Cherepy, W. Stoeffl, S.A. Payne, Proc. SPIE **7449**, 744911 (2009)
20. H.P. Martinez, I. Pawełczak, A.M. Glenn, M.L. Carman, N. Zaitseva, S. Payne, Nucl. Instr. Methods A **771**, 28 (2015)
21. Eljen Technology website, <https://eljentechnology.com>. Accessed 11 Sept 2020
22. S.A. Pozzi, M.M. Bourne, S.D. Clarke, Nucl. Instr. Methods A **723**, 19 (2013)
23. C.C. Lawrence, M.F. Febbraro, T.N. Massey, M. Flaska, F.D. Becchetti, S.A. Pozzi, Nucl. Instr. Methods A **759**, 16 (2014)
24. D. Cester, G. Nebbia, L. Stevanato, F. Pino, G. Viesti, Nucl. Instr. Methods A **735**, 202 (2014)
25. J. Iwanowska-Hanke, M. Moszynski, L. Swiderski, P. Sibczynski, T. Szczesniak, T. Krakowski, P. Schotanus, J. Instrum. **9**, P06014 (2014)
26. R.S. Woolf, A.L. Hutcheson, C. Gwon, B.F. Phlips, E.A. Wulf, Nucl. Instr. Methods A **784**, 80 (2015)
27. T.J. Hajagos, D. Kishpaugh, Q. Pei, Nucl. Instr. Methods A **825**, 40 (2016)
28. N.P. Zaitseva, A.M. Glenn, A.N. Mabe, M.L. Carman, C.R. Hurlbut, J.W. Inman, S.A. Payne, Nucl. Instr. Methods A **889**, 97 (2018)
29. P.N. Zhmurin, V.N. Lebedev, V.D. Titskaya, A.F. Adadurov, D.A. Elyseev, V.N. Pereymak, Nucl. Instr. Methods A **761**, 92 (2014)
30. A. Buffler, A.C. Comrie, F.D. Smit, H.J. Wörtche, IEEE Trans. Nucl. Sci. **62**(3), 1422 (2015)
31. E. Montbarbon, Z. Zhang, A. Grabowski, R. Woo, D. Tromson, C. Dehé-Pittance, R.B. Pansu, G.H.V. Bertrand, M. Hamel, J. Lumin. **213**, 67 (2019)
32. N.P. Zaitseva, A.M. Glenn, M.L. Carman, A.N. Mabe, S.A. Payne, N. Marom, X. Wang, Nucl. Instr. Methods A **978**, 164455 (2020)
33. Luxottica/Exciton website, <https://exciton.luxottica.com>. Accessed 11 Sept 2020
34. I.B. Berlman, *Fluorescence Spectra of Aromatic Molecules* (Academic Press, New York and London, 1971).
35. R.F. Kubin, A.N. Fletcher, Chem. Phys. Lett. **99**(1), 49 (1983)
36. J.B. Birks, K.N. Kuchela, Discuss. Faraday Soc. **27**, 57 (1959)
37. S. Reineke, M.A. Baldo, Sci. Rep. **4**, 3797 (2015)

38. F.S. Dainton, T. Morrow, G.A. Salmon, G.F. Thompson, Proc. R. Soc. London, Ser. A **328**(1575), 457 (1972)
39. K.I. Priyadarsini, D.B. Naik, P.N. Moorthy, J. Photochem. Photobiol. A **54**(2), 251 (1990)
40. J.S. Brinen, J.G. Koren, Chem. Phys. Lett. **2**(8), 671 (1968)
41. A. Kira, J.K. Thomas, J. Phys. Chem. **78**(2), 196 (1974)
42. H.L.J. Bäckström, K. Sandros, Acta Chem. Scand. **14**, 48 (1960)
43. K. Sandros, H.L.J. Bäckström, Acta Chem. Scand. **16**, 958 (1962)
44. K. Sandros, Acta Chem. Scand. **18**, 2355 (1964)
45. M. Furst, H. Kallmann, Phys. Rev. **97**, 583 (1955)
46. H. Sternlicht, G.C. Nieman, G.W. Robinson, J. Chem. Phys. **38**(6), 1326 (1963)
47. A. Lighart, X. de Vries, L. Zhang, M.C.W.M. Pols, P.A. Bobbert, H. van Eersel, R. Coehoorn, Adv. Funct. Mater. **28**(52), 1804618 (2018)
48. M.E. Ackerman, G.H. Daub, F.N. Hayes, H.A. Mackay, in *Organic Scintillators and Scintillation Counting*, ed. by D.L. Horrocks, C.-T. Peng (Academic Press, 1971)
49. G. Knoll, *Radiation Detection and Measurements*, 3rd edn. (Wiley, New York, 1999).
50. M. Flaska, S. Pozzi, Nucl. Instr. Methods A **599**(2–3), 221 (2009)
51. L. Swiderski, M. Moszynski, D. Wolski, T. Batsch, A. Nassalski, A. Syntfeld-Kazuch, T. Szczesniak, F. Kniest, M.R. Kusner, G. Pausch, J. Stein, W. Klamra, IEEE Trans. Nucl. Sci. **55**(6), 3710 (2008)
52. L. Swiderski, M. Moszynski, D. Wolski, T. Batsch, J. Iwanowska, A. Nassalski, A. Syntfeld-Kazuch, T. Szczesniak, F. Kniest, M.R. Kusner, G. Pausch, J. Stein, W. Klamra, P. Schotanus, C. Hurlbut, IEEE Trans. Nucl. Sci. **57**(1), 375 (2010)
53. L.M. Bollinger, G.E. Thomas, R.J. Ginther, Nucl. Instr. Methods **17**(1), 97 (1962)
54. S. Normand, B. Mouanda, S. Haan, M. Louvel, IEEE Trans. Nucl. Sci. **49**(2), 577 (2002)
55. Z.W. Bell, M.A. Miller, L. Maya, G.M. Brown, F.V. Sloop Jr., IEEE Trans. Nucl. Sci. **51**(4), 1773 (2004)
56. I.A. Pawełczak, A.M. Glenn, H.P. Martinez, M.L. Carman, N.P. Zaitseva, S.A. Payne, Nucl. Instr. Methods A **751**, 62 (2014)
57. Katchem website, www.katchem.cz. Accessed 24 Sept 2020
58. H. Kallmann, M. Furst, F. Brown, Nucleonics **14**, 48 (1956)
59. J. Hejwowski, A. Szymanski, Rev. Sci. Instrum. **32**(9), 1057 (1961)
60. L.R. Greenwood, N.R. Chellew, G.A. Zarwell, Rev. Sci. Instrum. **50**(4), 472 (1979)
61. B.M. Fisher, J.N. Abdurashitov, K.J. Coakley, V.N. Gavrin, D.M. Gilliam, J.S. Nico, A.A. Shikhin, A.K. Thompson, D.F. Vecchia, V.E. Yants, Nucl. Instr. Methods A **646**(1), 126 (2011)
62. I. Sen, M. Urfner, D. Penumadu, S.A. Young, L.F. Miller, A.N. Mabe, IEEE Trans. Nucl. Sci. **59**(4), 1781 (2012)
63. S.M. Carturan, M. Vesco, I. Bonesso, A. Quaranta, G. Maggioni, L. Stevanato, E. Zanazzi, T. Marchi, D. Fabris, M. Cinausero, F. Pino, F. Gramegna, Nucl. Instr. Methods A **925**, 109 (2019)
64. C. Frangville, A. Grabowski, J. Dumazert, E. Montbarbon, C. Lynde, R. Coulon, A. Venerosy, G.H.V. Bertrand, M. Hamel, Nucl. Instr. Methods A **942**, 162370 (2019)
65. N. Zaitseva, A. Glenn, H.P. Martinez, L. Carman, I. Pawełczak, M. Faust, S. Payne, Nucl. Instr. Methods A **729**, 747 (2013)
66. S.M. Robinson, R.C. Runkle, R.J. Newby, Nucl. Instr. Methods A **652**(1), 404 (2011)
67. A.N. Mabe, A.M. Glenn, M.L. Carman, N.P. Zaitseva, S.A. Payne, Nucl. Instr. Methods A **806**, 80 (2016)
68. R.D. Breukers, C.M. Bartle, A. Edgar, Nucl. Instr. Methods A **701**, 58 (2013)
69. N.J. Cherepy, R.D. Sanner, P.R. Beck, E.L. Swanberg, T.M. Tillotson, S.A. Payne, C.R. Hurlbut, Nucl. Instr. Methods A **778**, 126 (2015)
70. J. Ashenfelter, A.B. Balantekin, C. Baldenegro, H.R. Band, C.D. Bass, D.E. Bergeron, D. Berish, L.J. Bignell, N.S. Bowden, J. Boyle, J. Bricco, J.P. Brodsky, C.D. Bryan, A. Bykadorova Telles, J.J. Cherwinka, T. Classen, K. Commeford, A.J. Conant, A.A. Cox, D. Davee, D. Dean, G. Deichert, M.V. Diwan, M.J. Dolinski, A. Erickson, M. Febbraro, B.T. Foust, J.K. Gaison, A. Galindo-Uribarri, C.E. Gilbert, K.E. Gilje, A. Glenn, B.W. Goddard, B.T. Hackett, K. Han,

- S. Hans, A.B. Hansell, K.M. Heeger, B. Heffron, J. Insler, D.E. Jaffe, X. Ji, D.C. Jones, K. Koehler, O. Kyzlova, C.E. Lane, T.J. Langford, J. LaRosa, B.R. Littlejohn, F. Lopez, X. Lu, D.A. Martinez Caicedo, J.T. Matta, R.D. McKeown, M.P. Mendenhall, H.J. Miller, J.M. Minock, P.E. Mueller, H.P. Mumm, J. Napolitano, R. Neilson, J.A. Nikkel, D. Norcini, S. Nour, D.A. Pushin, X. Qian, E. Romero-Romero, R. Rosero, D. Sarenac, B.S. Seilhan, R. Sharma, P.T. Surukuchi, C. Trinh, M.A. Tyra, R.L. Varner, B. Viren, J.M. Wagner, W. Wang, B. White, C. White, J. Wilhelmi, T. Wise, H. Yao, M. Yeh, Y.-R. Yen, A. Zhang, C. Zhang, X. Zhang, M. Zhao, Nucl. Instr. Methods A **922**, 287 (2019)
71. C. Lane, S.M. Usman, J. Blackmon, C. Rasco, H.P. Mumm, D. Markoff, G.R. Jocher, R. Dorrill, M. Duvall, J.G. Learned, V. Li, J. Maricic, S. Matsuno, R. Milincic, S. Negrashev, M. Sakai, M. Rosen, G. Varner, P. Huber, M.L. Pitt, S.D. Rountree, R.B. Vogelaar, T. Wright, Z. Yokley, arXiv:1501.06935 (2015)
72. F. Reines, C.L. Cowan Jr., Nature **178**, 446 (1956)
73. V.A. Li, R. Dorrill, M.J. Duvall, J. Koblanski, S. Negrashev, M. Sakai, S.A. Wipperfurth, K. Engel, G.R. Jocher, J.G. Learned, L. Macchiarulo, S. Matsuno, W.F. McDonough, H.P. Mumm, J. Murillo, K. Nishimura, M. Rosen, S.M. Usman, G.S. Varner, Rev. Sci. Instrum. **87**, 021301 (2016)
74. J. Ashenfelter, A.B. Balantekin, H.R. Band, G. Barclay, C.D. Bass, D. Berish, L. Bignell, N.S. Bowden, A. Bowes, J.P. Brodsky, C.D. Bryan, J.J. Cherwinka, R. Chu, T. Classen, K. Commeford, A.J. Conant, D. Davee, D. Dean, G. Deichert, M.V. Diwan, M.J. Dolinski, J. Dolph, M. DuVernois, A.S. Erickson, M.T. Febbraro, J.K. Gaison, A. Galindo-Uribarri, K. Gilje, A. Glenn, B.W. Goddard, M. Green, B.T. Hackett, K. Han, S. Hans, K.M. Heeger, B. Heffron, J. Insler, D.E. Jaffe, D. Jones, T.J. Langford, B.R. Littlejohn, D.A. Martinez Caicedo, J.T. Matta, R.D. McKeown, M.P. Mendenhall, P.E. Mueller, H.P. Mumm, J. Napolitano, R. Neilson, J.A. Nikkel, D. Norcini, D. Pushin, X. Qian, E. Romero, R. Rosero, B.S. Seilhan, R. Sharma, S. Sheets, P.T. Surukuchi, C. Trinh, R.L. Varner, B. Viren, W. Wang, B. White, C. White, J. Wilhelmi, C. Williams, T. Wise, H. Yao, M. Yeh, Y.-R. Yen, G.Z. Zangakis, C. Zhang, X. Zhang, J. Phys. G: Nucl. Part. Phys. **43**(11), 113001 (2016)
75. V.A. Li, T.M. Classen, S.A. Dazeley, M.J. Duvall, I. Jovanovic, A.N. Mabe, E.T.E. Reedy, F. Sutanto, Nucl. Instr. Methods A **942**, 162334 (2019)



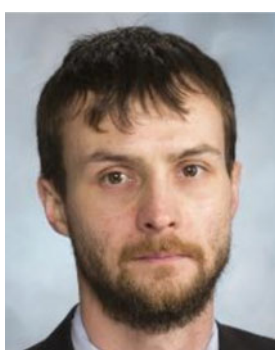
Natalia P. Zaitseva received her Ph.D. from Moscow State University (Russia) in 1989. In 1993 she joined Lawrence Livermore National Laboratory to lead the scientific development of the technology for production of super-large (>50 cm) crystals for the world-largest laser National Ignition Facility (NIF). Dr. Zaitseva led multiple projects on development of new classes of organic scintillators for radiation detection. She and her team conducted extensive studies of new PSD materials that led to development and commercial production of solution-grown stilbene and first plastic scintillators with efficient PSD. She is an author of more than 150 publications and patents.



M. Leslie Carman received a degree in Chemistry from University of California in Santa Barbara in 1969. Since that time, she has been working with Lawrence Livermore National Laboratory, first in the field of biochemistry and then in large-scale crystal growth developments. Her current research interest involves production and characterization of new materials, including organic and inorganic crystals and different types of plastic scintillators for neutron detection. Leslie Carman is author and co-author of more than 60 publications and patents.



Andrew M. Glenn received his Ph.D. in High Energy Nuclear Physics from University of Tennessee in 2004. He is a nuclear scientist currently specializing in neutron detection. He has designed and developed data acquisition systems and algorithms for electronic instrumentation, used for characterization of new liquid, crystalline and plastic scintillators. Dr. Glenn is also an effective modeler and has conducted studies of neutron time correlations in SNM as well as helping develop large-scale detectors. He has 200 publications as a member of large collaborations on nuclear science as well as 28 other publications and patents.



Andrew N. Mabe received his Ph.D. in Polymer Chemistry from University of Tennessee in 2013. He started his work at Lawrence Livermore National Laboratory as a postdoctoral researcher in 2014, becoming a staff scientist with a strong background in synthetic organic, inorganic, and polymer chemistries. He was a major contributor to development of large-scale polymerization technique for production of ^{6}Li -loaded plastic scintillators, working at the same time on multiple projects that, in short time, resulted in 25 publications and patents. Dr. Mabe tragically deceased in June 2020.

Chapter 3

The Detection of Slow Neutrons



Jonathan Dumazert and Camille Frangville

Abstract This chapter introduces the physical concepts that underline the making and characterization of plastic-scintillator-based, slow neutron detectors. For this purpose, we shall introduce the physical concepts behind neutron emission, scattering, and absorption, as well as the interaction of reaction products inside the detection medium. Upon detailing the discrimination techniques between slow neutron-, and background radiation-induced pulses, we shall also be able to motivate the definition of the usual figures of merit for such detectors.

3.1 Slow Neutrons: Essential Features

Neutrons, like protons, are baryons, made of three quarks and fermions with a $\frac{1}{2}$ -spin quantum number. As far as nuclear measurement is concerned, the essential properties of the neutron, labeled n or ${}_0^1n$, are as follows:

- it is a *massive* particle, with a mass $m_n = 939.56542052(54) \text{ MeV}/c^2$ (slightly greater than the one of a proton);
- when free, it is an *unstable* particle with a mean lifetime $\tau_n = 881.5(15) \text{ s}$;
- it is an *electrically neutral* particle.

As it was stated in Chap. 2, neutrons, like gamma and X rays, thus belong to the category of chargeless radiations: when passing through matter, they do not interact by Coulomb force with electrons nor atom nuclei. Nonetheless, the interaction of free neutrons with matter nuclei, either by nuclear scattering or nuclear reaction, generates charged particles or electromagnetic radiations that subsequently induce the release of such particles (such as gamma rays). It is these particles that ionize the detection medium, allowing the collection of a scintillation signal and thereby

J. Dumazert (✉) · C. Frangville
Université Paris-Saclay, CEA, List, 91120 Palaiseau, France
e-mail: jonathan.dumazert@cea.fr

C. Frangville
e-mail: camille.frangville@cea.fr

the detection of incident neutron radiation [1]. Neutron radiation, for this reason, is said to be an *indirectly ionizing* radiation, while the ionization signal, produced by the abovementioned interaction products, may be referred to as the *signature* of the neutron field inside the medium. Now, to understand the specific challenges that the detection of *slow* neutrons poses, especially with respect to the detection of *fast* neutrons, we need, in the first place, to clarify the meaning of this speed-based classification.

3.1.1 The Definition of Slow Neutrons

Free neutrons may be characterized by their velocity, labeled v_n and expressed in m s^{-1} , or their kinetic energy E_n . For non-relativistic neutrons, i.e., neutrons with $E_n < 50 \text{ MeV}$, both physical quantities are simply related as

$$E_n = \frac{1}{2}m_nv_n^2 \quad (3.1)$$

with E_n in joules (J). Given the massive energies at stake in the context of nuclear instrumentation, however, energy E_n is almost always found expressed in multiples of the electronvolt (eV) unit. The term *temperature* is also used to designate kinetic energy E_n .

If neutrons are mostly classified with respect to their kinetic energies, the definitions of the associated classes are subject to variability. For the purpose of our discussion, we shall keep the definition of slow neutrons as these neutrons whose kinetic energy is such that they are usually detected via nuclear reactions. A useful classification criterion is provided by the energy selectivity of neutron absorption by the ^{113}Cd isotope, which drops by two orders of magnitudes between $E_n = 0.2 \text{ eV}$ and $E_n = 0.8 \text{ eV}$. As a result, a so-called *cadmium cutoff* is defined around 0.5 eV, and neutrons with E_n below this cutoff will fall into the category of slow neutrons [2]. Other authors define the slow neutron region by boundary $E_n < 1 \text{ eV}$ [3], and the order of magnitude relevant for our description remains the same.

The generic category of slow neutrons encompasses, e.g., cold or hot neutrons [3]. One essential concept is one of *thermal neutrons*. So-called thermal neutrons are neutrons that have reached thermal equilibrium with their diffusion environment, meaning that, on average, they lose as much kinetic energy as they gain through scattering interactions. The energy distribution $n(E_{n,th})$ of such neutrons is described by Maxwell–Boltzmann distribution as

$$n(E_{n,th})dE_{n,th} = \frac{2\pi}{(\pi k_B T)^{\frac{3}{2}}} \sqrt{E_{n,th}} e^{-\frac{E_{n,th}}{k_B T}} dE_{n,th}, \text{ with } \int_0^{+\infty} n(E_{n,th})dE_{n,th} = 1 \quad (3.2)$$

From Eq. (3.2), we deduce the mean kinetic energy of thermal neutrons $\overline{E_{n,th}} = \frac{3}{2}k_B T = 38 \text{ meV}$ at room temperature ($T = 293.6 \text{ K}$). The speed distribution $n(v_{n,th})$ of thermal neutrons, also described by Maxwell–Boltzmann distribution, allows to calculate their most likely velocity $v_{n,th}^* = \sqrt{\frac{2k_B T}{m_n}} = 2200 \text{ ms}^{-1}$ and the corresponding kinetic energy $E_{n,th}^* = k_B T = 25.3 \text{ meV}$ at room temperature.

Having defined slow neutrons, we must now shed light on their prominent origins in the context of plastic scintillator-based detection.

3.1.2 The Origins of Slow Neutrons

3.1.2.1 Neutron Sources and Emission Spectra

The most obvious source of free neutrons is *nuclear fission* that is either a type of radioactive decay (spontaneous fission) or nuclear reaction (induced fission) in which a heavy nucleus is split into a number of lighter nuclei, along with several prompt neutrons and gamma rays.

Californium 252 (^{252}Cf) is the most commonly used spontaneous fission source to calibrate neutron detectors, yielding as much as $0.0116 \text{ n s}^{-1} \text{ Bq}^{-1}$ of total activity [4]. The kinetic energy distribution of said neutrons may be modeled by a single-variable Maxwell distribution [5] or more realistically by a two-parameter Watt distribution [6], labeled $W(a, b)$ and read as

$$W(a, b) = C(a, b) \cdot e^{-aE_n} \cdot \sinh(\sqrt{bE_n}) \quad (3.3)$$

where $C(a, b)$ is the normalization constant of the distribution. Spontaneously fissioning isotopes typically have Watt parameters [7] lying between $a = 0.847 \text{ MeV}^{-1}$ (^{252}Cf) and $a = 1.542 \text{ MeV}^{-1}$ (^{238}U), as well as between $b = 1.034 \text{ MeV}^{-1}$ and $b = 6.811 \text{ MeV}^{-1}$. As a result, the interpolated mean energies $\overline{E_n}$ carried by prompt neutrons are found within a narrow range, at 1.69 MeV for ^{238}U , 2.07 MeV for ^{239}Pu , and 2.13 MeV for ^{252}Cf . These values are consistent with experimental data, the unfolded spectrum of ^{252}Cf , for instance, showing a mean in the vicinity of 2.3 MeV , while being peaked around 0.7 MeV [8]. The tail of the energy distribution is usually deemed significant up to $10\text{--}15 \text{ MeV}$.

$^{241}\text{Am-Be}$ is the second most commonplace source of free neutrons as *radioisotope alpha-neutron* sources, in which a high- Z , alpha emitter is mixed with a low- Z material, subsequently leading to neutron emission through an (α, n) nuclear reaction. Considering the most popular mix, which is $^{241}\text{Am-Be}$, the said emission process would read as

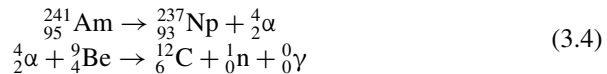
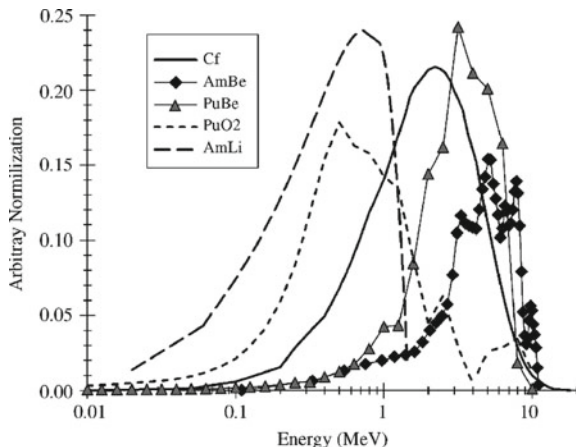


Fig. 3.1 Neutron spectra of ^{252}Cf , $^{241}\text{Am-Be}$, Pu-Be, and Am-Li neutron sources (Reproduced from [12] with permission from Elsevier)



The source strength is governed by the activity of the alpha emitter. Radioisotope (α, n) source spectra, like prompt fission spectra, take the shape of a continuum, in some cases tailing up to 11–14 MeV. The mean neutron energies, however, can be found over a wider range, from 0.5 MeV for $^{241}\text{AmLi}$ [9] up to around 4 MeV for $^{241}\text{AmBe}$ and $^{239}\text{PuBe}$ [10, 11]. Figure 3.1 presents the spectra of various neutron-emitting sources [12].

From this brief overview of neutron sources emission spectra, we see that, though these may range down to the slow energy range, they are essentially fast neutron spectra, with mean kinetic energy above 1 MeV. This property endorses the idea that neutrons are born in the fast energy range [13] and that the slow neutrons we are dealing with in the context of detection appear at the end of a subsequent process of radiation-matter interaction, often called *neutron moderation* [14].

3.1.2.2 Neutron Moderation Through Elastic and Inelastic Scattering

Moderation generally refers to the physical process through which free neutrons lose kinetic energy down to the thermal energy range. This process essentially relies on two nuclear interactions: *elastic neutron scattering* and *inelastic neutron scattering*.

Since neutrons carry no electrical charge, they are likely, when passing through matter, to penetrate atom nuclei and cause nuclear reactions. Scattering is a type of such reaction in which at least one neutron gets reemitted [15]. Elastic scattering, labeled $^A_Z\text{X}(n, n)$, of a neutron by a nucleus ^A_ZX , Z being the atom number and A the mass number, is described by equation



where the scattering nucleus remains in the ground state after the interaction. Elastic scattering may always take place, whatever the neutron kinetic energy or the allowance for other nuclear interactions.

On the contrary, inelastic neutron scattering by nucleus ${}^A_Z X$, labeled ${}^A_Z X(n, n')$ or ${}^A_Z X(n, n'\gamma)$, is described by



where nucleus ${}^A_Z X^*$ is promoted to an excited state as a consequence of the interaction and returns to its ground state through one of the known processes of nuclear deexcitation (gamma-ray emission, internal conversion, or internal pair creation). Inelastic scattering can occur as soon as the incident neutron energy is sufficiently large to excite the nucleus to its first energy level above ground state; it is therefore a *threshold reaction*.

In order to quantify the moderating power of a given material, as well as the respective parts that elastic and inelastic scatterings play in the loss of kinetic energy by the incoming neutron, we introduce *microscopic scattering cross sections*. We recall that the infinitesimal probability dP for an incoming neutron to undergo a given reaction $R({}^A_Z X, n)$ with nuclei ${}^A_Z X$ is related to the infinitesimal range dr traveled by the particle and the atom density $N_{^A_Z X}$ of said nuclei inside the interaction medium as follows:

$$dP = N_{^A_Z X} \sigma_{R({}^A_Z X, n)} dr \quad (3.7)$$

where $\sigma_{R({}^A_Z X, n)}$ is the microscopic cross section of the reaction. The non-SI unit for microscopic cross sections is the barn, labeled b and defined as $1 \text{ b} = 10^{-24} \text{ cm}^2$. Figure 3.2 represents the microscopic cross sections of ${}^1\text{H}$ and ${}^{12}\text{C}$ for elastic scat-

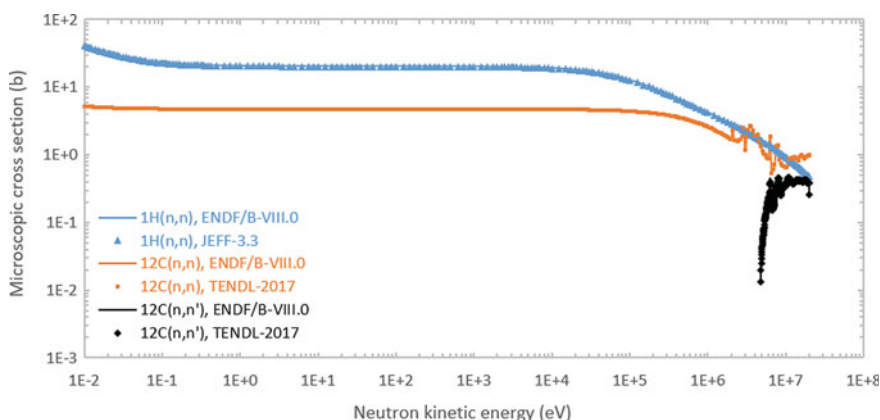


Fig. 3.2 Microscopic scattering cross sections versus neutron kinetic energy for ${}^1\text{H}$ and ${}^{12}\text{C}$

Table 3.1 Main hydrogen-based material for neutron moderation

	HDPE	Paraffin	${}^2\text{H}_2\text{O}$	Plastic scintillator ^a
Density (g cm ⁻³)	0.93–0.97	0.90–0.93	1.11	0.90–1.05
wt% (H)	14.3	14.7	20.1	7.7–8.4
Mean logarithmic reduction (from 2.3 MeV down to 100 meV)	0.82	0.82–0.90	0.51	0.71–0.73

^aFor polystyrene and poly(vinyltoluene)-based plastic scintillators

tering, respectively, labeled $\sigma_{^1\text{H}(\text{n},\text{n})}$ (in blue) and $\sigma_{^{12}\text{C}(\text{n},\text{n})}$ (in orange), as well as the microscopic cross section of ${}^{12}\text{C}$ for inelastic scattering, noted $\sigma_{^{12}\text{C}(\text{n},\text{n}')}$ (in black). These atom nuclei were chosen for being the fundamental components of the most popular neutron moderators, such as polyethylene¹ (C_2H_4)_n, as well as of plastic scintillator matrices (poly(vinyltoluene)(C_9H_{10})_n, or polystyrene (C_8H_8)_n). The cross sections were made available by JANIS 4 database [16] and taken from international libraries ENDF/VIII.0, JEFF-3.3, and TENDL-2017.

Figure 3.2 illustrates several properties of neutron scattering. Firstly, inelastic scattering by ${}^{12}\text{C}$ appears for $E_n > 4.8 \text{ MeV}$ (slightly above the first excited state of the nucleus at 4.439 MeV [17]), hence the interaction only takes place over the last energy half-decade of $E_n < 20 \text{ MeV}$. Secondly, we observe that for $E_n < 20 \text{ MeV}$, the inelastic scattering cross section $\sigma_{^{12}\text{C}(\text{n},\text{n}')} < 1 \text{ b}$, while the elastic scattering cross section $\sigma_{^{12}\text{C}(\text{n},\text{n})} \sim 5 \text{ b}$ over 7 decades ($10^{-2} \leq E_n \leq 10^5 \text{ eV}$). Eventually, the cross section of the lighter ${}^1\text{H}$ nucleus $\sigma_{^1\text{H}(\text{n},\text{n})} \sim 20 \text{ b}$ spans over the same 7 decades, so that hydrogen is the primary contributor to neutron moderation. It follows that, at the energy scales of interest in this discussion, elastic scattering in hydrogen-rich media, such as polyethylene moderators and plastic scintillators, is the main interaction through which free neutrons are slowed down (Table 3.1).

Having identified the nuclear interactions that are responsible for the appearance of slow neutrons when starting from fast fission or radioisotope (α, n) source spectra, we must now quantify the energy loss of neutrons to the medium through the study of kinematics.

3.1.2.3 Kinematics of Neutron Elastic Scattering

Kinematics describes, in a macroscopic mode, the amount of kinetic energy that is expected to be lost by neutrons through elastic scattering. For this purpose, we introduce the *mean logarithmic reduction* of neutron kinetic energy by nuclei with mass number A , labeled ξ_A , and given by [15]

$$\xi_A = 1 - \frac{(A - 1)^2}{2A} \ln\left(\frac{A + 1}{A - 1}\right) \quad (3.8)$$

¹Topological representation and key information of these molecules is given in the Appendix section at the end of the book.

The values of the mean logarithmic reduction for ^1H and ^{12}C are $\xi_{^1\text{H}} = 1$, and $\xi_{^{12}\text{C}} = 0.158$, respectively.

Let us suppose that we study the kinematics of neutron scattering inside a poly(vinyltoluene)-based plastic scintillator matrix. Keeping the marking from Sect. 3.1.2.2, the mean logarithmic reduction ξ_{VT} of this multi-element material can be calculated as

$$\xi_{VT} = \frac{9 \cdot \overline{\sigma_{^{12}\text{C}(n,n)}} \cdot \xi_{^1\text{H}} + 10 \cdot \overline{\sigma_{^1\text{H}(n,n)}} \cdot \xi_{^{12}\text{C}}}{9 \cdot \overline{\sigma_{^{12}\text{C}(n,n)}} + 10 \cdot \overline{\sigma_{^1\text{H}(n,n)}}} \quad (3.9)$$

where $\overline{\sigma_{^1\text{H}(n,n)}}$ and $\overline{\sigma_{^{12}\text{C}(n,n)}}$ are the mean microscopic cross sections of ^1H and ^{12}C for elastic scattering between the initial kinetic energy of an incoming neutron, labeled E_0 , and the final energy of the same neutron E_f . For the sake of demonstration, let us consider that the emitter of neutron radiation is a bare ^{252}Cf source, and thus that the initial energy $E_0 = 2.3$ MeV, corresponding to the mean energy of a prompt fission neutron from this radioisotope. Supposing that this incoming neutron completes its moderation process inside the plastic scintillator volume, it will, by definition, reach the thermal energy range described by Eq. (3.2), with a 95% probability of having kinetic energy below 100 meV. We therefore impose $E_f = 100$ meV. It follows, using the energy distributions reproduced in Fig. 3.2, that $\overline{\sigma_{^1\text{H}(n,n)}} = 5.11$ b and $\overline{\sigma_{^{12}\text{C}(n,n)}} = 2.72$ b. Parametrizing Eq. (3.9) with these factors, we obtain $\xi_{VT} = 0.73$.

The concept of mean logarithmic reduction of neutron energy bears meaning inside an exponential model of neutron kinematics. Inside this model, if E_i refers to the mean expected kinetic energy of the neutron after the i th elastic scattering event, then

$$\forall i > 1, E_i = E_{i-1} e^{-\xi_{VT}} \quad (3.10)$$

From this relation, the mean number of collisions n needed to moderate the incoming neutron inside the plastic scintillator is straightforwardly derived as

$$n = \left\lceil \frac{\ln\left(\frac{E_0}{E_f}\right)}{\xi_{VT}} \right\rceil \quad (3.11)$$

which, with the same parameters as above, yields a mean number $n = 23$ of scattering events to bring the incoming neutron from E_0 to E_f .

Calculations of such type provide us with the first scaling parameters to design neutron moderators and plastic scintillators dedicated to the detection of incoming neutrons of known emission spectra. However, the definition of the electronic treatments that are implemented inside the associated processing chain may also require a study of the kinetics of neutron moderation.

3.1.2.4 Kinetics of Neutron Moderation

Kinetics describes the delay between consecutive elastic scattering events, as well as the expected duration of the complete neutron moderation process inside a medium.

Keeping the notations from Sects. 3.1.2.2 and 3.1.2.3, the mean delay expected between the i^{th} and the $(i + 1)^{\text{th}}$ neutron elastic scattering events is governed by microscopic cross sections $\sigma_{^1\text{H}(\text{n},\text{n})}(E_i)$ and $\sigma_{^{12}\text{C}(\text{n},\text{n})}(E_i)$, as well as neutron scattering angles inside the laboratory frame [15]. The mean cosine of the scattering angle θ upon diffusion by a nucleus with mass number is given by the relation $\overline{\cos(\theta)} = \frac{2}{3A}$. Considering the same scattering nuclei as in the previous paragraphs, we obtain $\overline{\cos(\theta_{^1\text{H}})} = \frac{2}{3}$ for ^1H and $\overline{\cos(\theta_{^{12}\text{C}})} = \frac{1}{18}$ for ^{12}C .

To describe the kinetics of neutron moderation inside a medium that is supposed both infinite and homogenous, we then introduce the *macroscopic transport cross section*, labeled Σ_{tr} and expressed in cm^{-1} . Denoting E_i the neutron kinetic energy after the i^{th} scattering event and considering a hydrogen and carbon-based moderating medium, this cross section reads as

$$\Sigma_{tr}(E_i) = N_{\text{H}} \cdot \sigma_{^1\text{H}(\text{n},\text{n})}(E_i) \cdot (1 - \overline{\cos(\theta_{^1\text{H}})}) + N_{\text{C}} \cdot \sigma_{^{12}\text{C}(\text{n},\text{n})}(E_i) \cdot (1 - \overline{\cos(\theta_{^{12}\text{C}})}) \quad (3.12)$$

where N_{H} and N_{C} are, respectively, the atom concentrations in hydrogen and carbon, given in at cm^{-3} . Eventually, if v_i refers to the neutron velocity after the i^{th} scattering event, the mean expected delay between the i^{th} and the $(i + 1)^{\text{th}}$ scattering events can be estimated as

$$\Delta t_{i(i+1)} = \frac{1}{v_i \cdot \Sigma_{tr}(E_i)} \quad (3.13)$$

Given the complex evolutions of microscopic cross sections $\sigma_{^1\text{H}(\text{n},\text{n})}$ and $\sigma_{^{12}\text{C}(\text{n},\text{n})}$ as a function of E_i , that is illustrated in Fig. 3.1, Eq. (3.13) does not in general yield an explicit dependence on the neutron kinetic energy. Furthermore, the time parameter that is so computed only reflects the average kinetics between elastic scattering events, the actual delay being adequately described as a trial in a random variable whose mean is close to the estimate that is obtained from Eq. (3.13). Eventually, when departing from the infinite medium hypothesis, the expected probability distribution associated with the delay between consecutive scattering events, as well as with the overall neutron moderation process, should be determined by means of a Monte Carlo method.

As an illustration, we assume the moderation medium to a poly(vinyltoluene)-based plastic scintillator matrix and use the atom concentrations N_{H} and N_{C} from the datasheets of commercial equivalents BC-408 [18] and EJ-200 [19]. We consider, like in Sect. 3.1.2.3, that the neutron emitter radiation is a bare ^{252}Cf source and that the mean expected neutron energy after the first elastic scattering event is about $E_1 = 700 \text{ keV}$. Equation (3.13) then yields an expected average delay between the first and second scattering events $\Delta t_{12} \sim 4 \text{ ns}$. To offer a comparison, Liu et al.

[20] estimated, by means of a Monte Carlo-based method, the mean of probability distribution associated with the delay between the same events, when dealing with a large-scale (about 33 dm^3) BC-408 plastic scintillator. This scale making the infinite medium assumption acceptable, the authors found an estimate $\Delta t_{12} \sim 3 \text{ ns}$ in fair agreement with the one we derived *supra* from a macroscopic model. In general, the mean moderation time, labeled $\overline{t_m}$, that results from the succession of such scattering events needs to be estimated with a Monte Carlo approach, notably to account for the impact of the diffusion medium geometry. However, provided that both infinite and homogenous medium assumptions are justified and keeping the notations from Sect. 3.1.2.3, a rough estimate of this time parameter [21] may be given by

$$\overline{t_m} = \frac{2}{v_f \cdot \xi_{VT} \cdot \overline{\Sigma_{tr}}} = \frac{2}{v_f \cdot \xi_{VT} \cdot \left[N_H \cdot \overline{\sigma_{1H(n,n)}} \cdot \left(1 - \overline{\cos(\theta_{1H})} \right) + N_C \cdot \overline{\sigma_{12C(n,n)}} \cdot \left(1 - \overline{\cos(\theta_{12C})} \right) \right]} \quad (3.14)$$

This formula, once again applied to the case of a poly(vinyltoluene)-based plastic scintillator matrix, yields an expected mean moderation time $\overline{t_m} \sim 30 \mu\text{s}$ from $E_0 = 2.3 \text{ MeV}$ down to $E_f = 100 \text{ meV}$.

In this section, we have thus covered the main characteristics of the process bringing neutrons from their originating energies down to the slow energy range. We shall now describe the types of nuclear reactions they undergo upon entering said energy range, as well as the specific reactions that are taken advantage of in the context of plastic scintillator-based neutron detection.

3.2 Nuclear Reactions of Interest in Slow Neutron Detection

Elastic and inelastic scatterings are the nuclear interactions responsible for the slowing down of fast-born neutrons, as well as neutron detection in proton recoil-based modified plastic scintillators [22]. However, once neutrons fall into the slow energy range, upon moderation inside either the sensitive medium or its environment, the kinetic energy carried out by recoil protons becomes insufficient to allow the first-hand detection. Instead, slow neutron detection relies upon two different types of nuclear reactions, namely *neutron absorption* and *neutron capture*. In both types of reactions, no neutrons get reemitted after penetrating inside the involved nucleus. The distinction between them, in the most commonplace terminology, lies in that neutron absorption leads to the breaking of the reacting nucleus, whereas neutron capture results in the formation of a compound nucleus. Now, most natural isotopes interact with neutrons through absorption or capture. In order to select the main nuclear reactions of interest in the context of plastic scintillator-based slow neutron detection, we thus need to identify the factors that are relevant to qualify these reactions.

3.2.1 Natural Abundance, Reaction Cross Section, Q-Value, and Typology of Reaction Products

The interest for slow neutron detection of a stable, naturally occurring isotope and of the associated reaction, is assessed with respect to four main criteria [2]:

- the natural abundance of the reacting isotope (as well as the availability of the element in an enriched form with regard to the concentration in the said element);
- the probability for the nuclear reaction between a nucleus of this isotope and a slow neutron to take place;
- the average energy that is released by this reaction;
- the nature and the energy distribution of the particles that are released after the reaction (so-called *reaction products*).

The reaction probability P is quantified in a similar fashion as the moderating power of material, introducing a *microscopic absorption (or capture) cross section* $\sigma_{R(z^A X, n)}$ for reaction $R(z^A X, n)$ with a nucleus $z^A X$. This microscopic cross section is related to the reaction probability by Eq. (3.7). An isotope of interest must therefore possess a $\sigma_{R(z^A X, n)}$ cross section as high as possible for neutrons in the slow energy range.

The amount of energy released by the reaction, in other words, the difference between the total energies shared by the particles that are present in the final state and the particles that are present in the initial state, is referred to as the Q-value of the reaction and labeled Q . A nuclear reaction is said *exothermal* as soon as it presents a strictly positive Q-value. Now, the indirect detection of slow neutrons will depend on the energy that is laid down by the reaction products inside the sensitive medium. The higher the Q-value of a given absorption or capture reaction $R(z^A X, n)$ will be, the better should thus be the potential exploitability of said reaction.

The amount of energy that is laid down value inside the detection medium by the reaction products sharing the Q-value also depends on the nature and the energy distribution associated with these products. The aim here is to maximize the contrast between the neutron field signature against the interaction of the radiation background with the atoms of the sensor. To this end, the reaction products that transfer the highest amount of kinetic energy to the sensitive medium, i.e. ions, tend to be favorable to slow neutron detection. In cases where the plastic scintillator allows some discrimination of directly ionizing particles based on the shape of collected pulses, such reaction products will be easier to differentiate from the contribution of background radiation to monitored nuclear counting.

It is known that, based on the three latter criteria we enumerated above, ${}^3\text{He}$ is the gold standard isotope in slow neutron detection [23], in such a way that the performance of detectors founded upon competing isotopes is often assessed with respect to the ones of ${}^3\text{He}$ gaseous counters. The compatibility of a given reacting isotope with plastic scintillator technology being, however, an additional criterion in the frame of this discussion, the list of viable isotopes and associated reactions for

the purpose of efficiently detecting slow neutrons may be eventually reduced to a very limited number of entries.

3.2.2 Main Nuclear Reactions of Interest

As we stated in the previous paragraph, the main nuclear reactions in plastic scintillator-based slow neutron detection are few enough to be extensively described here.

3.2.2.1 The $^{10}\text{B}(\text{n},\alpha)$ Reaction

This is an absorption reaction where ^{10}B nuclei, whose isotope abundance is close to 20% in natural boron, are broken into a ^4He nucleus (i.e. an alpha particle) and a ^7Li nucleus upon reacting with a neutron (which itself disappears in the interaction). The reaction is described by Eq. (3.15a) with a 6% probability and by Eq. (3.15b) with a 94% probability [2], depending on whether the ^7Li ion product is created in its fundamental or first excited state:

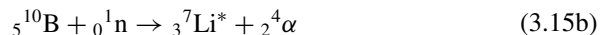


Figure 3.3 represents the evolution of the microscopic cross section of ^{10}B for nuclear absorption, labeled $\sigma_{^{10}\text{B}(\text{n},\alpha)}$, as a function of neutron kinetic energy E_n .

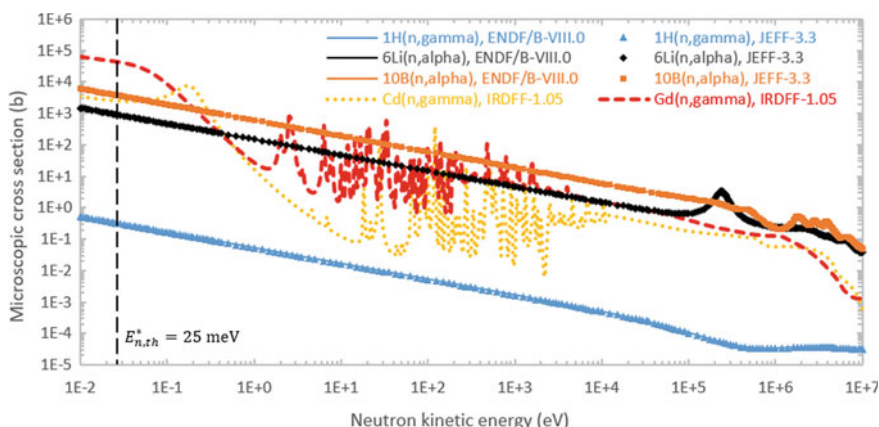


Fig. 3.3 Microscopic reaction cross sections versus neutron kinetic energy for the main reactions of interest in slow neutron detection

The cross sections were made available by JANIS 4 database [16] and taken from international libraries ENDF/VIII.0 and TENDL-2017. We see that, over 7 decades ($10^{-2} \leq E_n \leq 10^5$ eV), logarithm $\log(\sigma_{^{10}\text{B}(\text{n},\alpha)})$ decreases linearly with $\log(E_n)$, according to what is called a typical “ $\frac{1}{v_n}$ dependence”. The cross section given at the kinetic energy of a thermal neutron with its most likely velocity equals $\sigma_{^{10}\text{B}(\text{n},\alpha)}(25.3 \text{ meV}) = 3835 \text{ b}$.

The Q-value associated with the absorption reaction is $Q = 2.31 \text{ MeV}$ in Eq. (3.15a) and $Q = 2.79 \text{ MeV}$ in Eq. (3.15b). In the first case, the Q-value is shared kinematically between both ions, respectively, as $E_{^7\text{Li}} = 0.84 \text{ MeV}$ and $E_\alpha = 1.47 \text{ MeV}$. In the second case, an additional gamma ray with energy $E_\gamma = 0.48 \text{ MeV}$ is emitted upon deexcitation of the ${}^7\text{Li}^*$ nucleus.

3.2.2.2 The ${}^6\text{Li}(\text{n},\alpha)$ Reaction

This is also an absorption reaction where ${}^6\text{Li}$ nuclei, whose isotope abundance is about 7.6% in natural lithium, are broken into an alpha particle and a tritium nucleus upon reacting with a neutron, following equation:



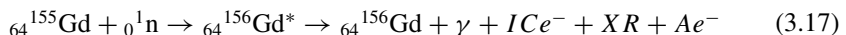
The distribution of the associated microscopic cross section $\sigma_{^{10}\text{B}(\text{n},\alpha)}$ as a function of E_n is superimposed to the one from the previous paragraph in Fig. 3.3 (using the same international libraries ENDF/VIII.0 and TENDL-2017). The figure shows that this absorption reaction also follows a $\frac{1}{v_n}$ trend over six and a half decades ($10^{-2} \leq E_n \leq 5 \cdot 10^4 \text{ eV}$), with a slope about $\frac{1}{4}$ th of the one describing the ${}^{10}\text{B}(\text{n},\alpha)$ reaction. The cross section for thermal neutrons at room temperature is given by $\sigma_{^6\text{Li}(\text{n},\alpha)}(25.3 \text{ meV}) = 940 \text{ b}$.

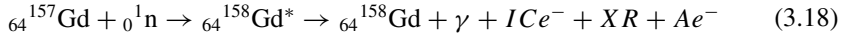
The Q-value reads as $Q = 4.78 \text{ MeV}$ and is shared between both ion products with respective kinetic energies $E_{^3\text{H}} = 2.73 \text{ MeV}$ and $E_\alpha = 2.05 \text{ MeV}$.

In a nutshell, the ${}^{10}\text{B}(\text{n},\alpha)$ and ${}^6\text{Li}(\text{n},\alpha)$ absorptions are two very similar nuclear reactions, with cross sections in the 10^2 – 10^3 b close to the thermal energy range, Q-values in the order of 1 MeV, and essentially ion reaction products.

3.2.2.3 The ${}^{155}\text{Gd}(\text{n},\gamma)$ and ${}^{157}\text{Gd}(\text{n},\gamma)$ Reactions

These capture reactions by ${}^{155}\text{Gd}$ and ${}^{157}\text{Gd}$ nuclei, whose isotope abundances are about 14.8% and 15.7%, respectively, in natural gadolinium, lead to an isotopic change of the nucleus, from one stable to another stable isotope, as described in Eqs. (3.17) and (3.18):





Though stable, the resulting nuclei ${}^{156}\text{Gd}^*$ and ${}^{158}\text{Gd}^*$ are produced in an excited state so that the reaction is promptly followed by a radiative rearrangement of nuclear and atomic structures. The radiative cascade includes the emission of gamma rays (γ) from the nucleus, as well as internal conversion electrons (ICe^-), X rays (XR), and Auger electrons (Ae^-) from the atom.

Figure 3.3 shows the evolution of the microscopic cross section of ${}^{\text{nat}}\text{Gd}$ for radiative capture, labeled $\sigma_{\text{Gd}(n,\gamma)}$, as a function of E_n . The cross sections, also made available by JANIS 4 database, were taken from the international library IRDFF-1.05. We observe that, contrary to ${}^{10}\text{B}$ and ${}^6\text{Li}$, the reaction probability trend of Gd is extremely structured over the energy range of interest. The cross section noticeably drops by more than two orders of magnitude over a single decade of neutron kinetic energy, falling from the order of 10^4 b around $E_n = 50$ meV down to the order of 10^2 b around $E_n = 0.5$ eV. The distribution also presents a wide resonance region between $E_n = 1$ eV and $E_n = 5$ keV, reaching as much as 750 b, followed by a $\frac{1}{v_n}$ region up to $E_n = 1$ MeV. Figure 3.3 shows that the cross section for thermal neutrons, about $\sigma_{\text{Gd}(n,\gamma)}(25.3 \text{ meV}) = 49000$ b, is 10 times higher than the one of ${}^{10}\text{B}$ at the same energy. In ${}^{\text{nat}}\text{Gd}$, approximately 81.5% of this figure is accounted for by the capture cross section $\sigma_{^{157}\text{Gd}(n,\gamma)}(25.3 \text{ meV}) = 254000$ b of ${}^{157}\text{Gd}$, which is the highest among stable and naturally abundant isotopes (the remaining 18.5% being contributed by isotope ${}^{155}\text{Gd}$, with $\sigma_{^{155}\text{Gd}(n,\gamma)}(25.3 \text{ meV}) = 60900$ b).

The Q-values associated with both radiative capture reactions are $Q = 8.54$ MeV for Eq. (3.17) and $Q = 7.94$ MeV for Eq. (3.18), so that the average energy freed by a $\text{Gd}(n, \gamma)$ reaction inside the natural element is found around $Q = 8$ MeV. Most of these energies (99.2% in the case of the ${}^{157}\text{Gd}(n, \gamma)$ reaction [24]) are carried by prompt gamma rays. The deexcitation gamma-ray spectrum of ${}^{156}\text{Gd}^*$ and ${}^{158}\text{Gd}^*$ is modeled as the superimposition of the following:

- A continuous component, lying between 0 and the Q-value, whose probability density function reaches a maximum in the vicinity of 2 MeV (about 10^{-2} per neutron capture for ${}^{158}\text{Gd}^*$). This component originates from a multi-step gamma-ray cascade between the neutron capture state and the ground state, involving a large number of intermediate, unresolvable energy levels. This continuum usually accounts for most of the signature that is experimentally available [25];
- A discrete component, topping the previous one, and whose lines (including prominent rays at 79.510 and 181.931 keV) come mainly from two-step gamma-ray cascades via low-lying energy levels in the excited nuclei [26].

The superimposition of both components [24] is illustrated in Fig. 3.4a in the case of the ${}^{157}\text{Gd}(n, \gamma)$ reaction.

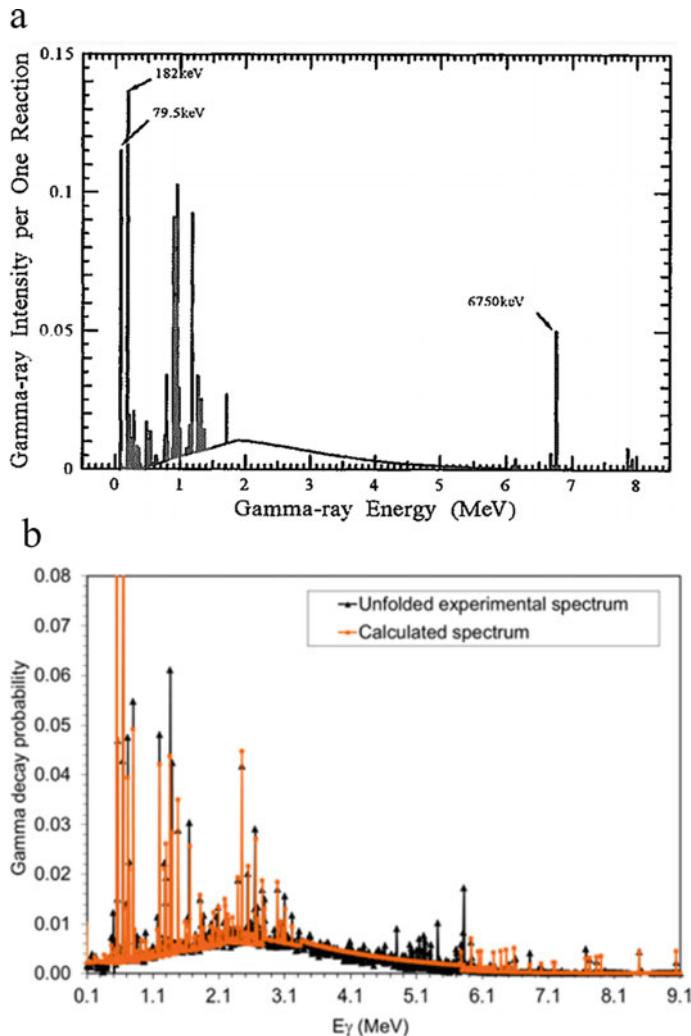
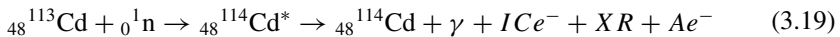


Fig. 3.4 Energy spectra of the prompt gamma rays from **a** $^{157}\text{Gd}(n, \gamma)$ (reprinted from [24] with permission from Taylor and Francis) and **b** $^{113}\text{Cd}(n, \gamma)$ (reprinted from [27] with permission from EDP Sciences) neutron capture reactions

3.2.2.4 The $^{113}\text{Cd}(n,\gamma)$ Reaction

This is another radiative capture reaction, where ^{113}Cd nuclei, whose abundance is about 12.2% in natural cadmium, change isotopy following equation:



The distribution of the microscopic cross section of ^{nat}Cd for radiative capture, labeled $\sigma_{\text{Cd}(n,\gamma)}$, was added to Fig. 3.3 (IRDFF-1.05 library). It shows, like the distribution that was analyzed in the previous paragraph, a non- $\frac{1}{v_n}$ profile with a sharp drop from a maximum about 7300 b at $E_n = 0.2 \text{ eV}$ down to the order of 10^2 b close to $E_n = 0.5 \text{ eV}$ and a large resonance region between $E_n = 10 \text{ eV}$ and $E_n = 15 \text{ keV}$. Figure 3.3 shows that the element reaction cross section for thermal neutrons, about $\sigma_{\text{Cd}(n,\gamma)}(25.3 \text{ meV}) = 2500 \text{ b}$, is in the same order as the one of ^{10}B at that energy and is almost entirely accounted for by the capture cross section of the ^{113}Cd isotope: $\sigma_{^{113}\text{Cd}(n,\gamma)}(25.3 \text{ meV}) = 20600 \text{ b}$, the highest in nature after the ones of ^{155}Gd and ^{157}Gd .

The Q-value associated with reaction Eq. (3.19) reads $Q = 9.04 \text{ MeV}$, also representative of the energy freed by $\text{Cd}(n, \gamma)$ radiative capture all together. The phenomenology of the emission is similar to the one of the previously reviewed $\text{Gd}(n, \gamma)$ reactions, with a deexcitation gamma-ray spectrum of $^{114}\text{Cd}^*$ modeled as the combination [28] of the following:

- A continuum, whose probability density reaches a maximum around 2.2 MeV (again about 10^{-2} per neutron capture). This component would carry approximately 40% of total gamma-ray emission following the capture reaction [27];
- A set of lines, dominated by 558.32-keV gamma ray.

The superimposition of these components [27] is illustrated in Fig. 3.4b, in the case of $^{113}\text{Cd}(n, \gamma)$ reaction, and with an emphasis on the continuous component.

To conclude, the $\text{Gd}(n, \gamma)$ and $\text{Cd}(n, \gamma)$ radiative capture, with cross sections in the 10^3 – 10^4 b at thermal energy, Q-values close to 10 MeV and essentially photon reaction products. As mentioned above, the microscopic cross sections of absorption and capture reactions as a function of E_n are plotted in Fig. 3.3. To provide a reference, the $\frac{1}{v_n}$ cross section of the prominent nuclear reaction inside plastic scintillator, that is the radiative capture of neutrons by ^1H , labeled $\sigma_{^1\text{H}(n,\gamma)}$, was added to the plot. Its relatively slow value ($\sigma_{^1\text{H}(n,\gamma)}(25.3 \text{ meV}) = 333 \text{ mb}$ for thermal neutrons) is indeed susceptible to be compensated by the large atom density of hydrogen inside the detection medium. The said capture results in the emission of a single-line, gamma-ray spectrum at 2.225 MeV. Table 3.2 summarizes the criteria of merit associated with the nuclear reactions of interest in slow neutron detection, including standard isotope abundances [29, 30], as well as cross sections and Q-values made available by the NSR database [31].

Table 3.2 Nuclear reactions of interest in slow neutron detection

Nuclear reaction	Natural isotope abundance (%) [30]	Cross section at 25.3 meV (b) [16, 31]	Q-value (keV) [31]	Reaction products
$^6\text{Li}(\text{n}, \alpha)$	7.59 (4)	940 (4)	4783.47 (0.00)	Alpha, triton
$^{10}\text{B}(\text{n}, \alpha)$	19.9 (7)	3835 (11)	2789.91 (0.02)	Alpha, lithium ion
$^{113}\text{Cd}(\text{n}, \gamma)$	12.22 (12)	20,600 (400)	9042.97 (0.14)	Photons, electrons
^{149}Sm	13.9	42,080 (400)		
^{151}Eu	47.8	9100 (100)		
$^{155}\text{Gd}(\text{n}, \gamma)$	14.80 (12)	60,900 (500)	8536.35 (0.07)	Photons, electrons
$^{157}\text{Gd}(\text{n}, \gamma)$	15.65 (2)	254,000 (800)	7937.39 (0.06)	Photons, electrons
^{164}Dy	28.1	2840 (40)		
^{176}Lu	2.61	2065 (35)		
^{191}Ir	37.3	954 (10)		

3.2.3 Size of the Scintillator: Slow Neutron Mean Free Path and the Interaction of Reaction Products

Suppose a fast-born neutron has been brought to the slow or thermal energy range upon moderation inside either the plastic scintillator medium or an external moderator. The probability for the said neutron to be detected can be bound upwardly by the product of two probabilities:

- the probability P_a that the neutron be absorbed or captured inside the detection assembly;
- the probability P_r that the products of absorption or capture reaction form at least one recordable signal in the plastic scintillator.

Probability P_a strongly depends on the geometry of the diffusion medium, as well as on the way neutron-converting isotopes, such as the ones we listed in the previous paragraph, were incorporated into the said medium. It must therefore be estimated by means of a Monte Carlo-based particle transport code. However, provided that the plastic scintillator medium may be considered infinite and neutron converters may be presumed homogeneously dispersed within this medium, then the probability for a neutron of kinetic energy E_n to be absorbed in a given medium can be quantified by introducing a macroscopic absorption cross section, labeled Σ_a and expressed in cm^{-1} . If N_j is the atom density of neutron-absorbing nuclei j present in the medium, and σ_{R_j} the microscopic cross section for neutron-consuming reaction R_j with said nuclei, then the macroscopic cross section will read as

$$\Sigma_a(E_n) = \sum_j N_j \cdot \sigma_{R_j}(E_n) \quad (3.20)$$

A valuable scaling figure when designing a slow neutron detector is the *slow or thermal neutron mean path*, defined as the average traveled by such neutron before being absorbed and labeled λ_a . Provided that the abovementioned assumptions hold, then λ_a is simply derived as the inverse of Σ_a . The neutron mean free path presents an order of magnitude of the size the scintillator needs to have for a detection-useful neutron reaction to take place inside it. As an illustration, we consider the case of a thermal neutron with kinetic energy $E_{n,th}^* = 25.3 \text{ meV}$. If the diffusion medium is a poly(vinyltoluene)-based matrix, without any additional neutron converter besides hydrogen and carbon, then Eq. (3.20) would yield an estimate for $\lambda_a \sim 57.5 \text{ cm}$, as accounted for by ${}^1\text{H}(n, \gamma)$ and ${}^{12}\text{C}(n, \gamma)$ capture reactions. Upon diffusion within the same plastic matrix, although homogeneously loaded up to 1 wt% with natural Gd, the free path would reduce down to $\lambda_a \sim 0.5 \text{ cm}$.

For neutron absorption or capture to result in a recordable pulse, the associated reaction products need to lay down a higher amount of energy inside the plastic scintillator than the one that corresponds to the triggering threshold, found around 10–50 keV_{ee} at the output of most conventional detection chains. In this regard, the cases of ion products from ${}^{10}\text{B}(n, \alpha)$ and ${}^6\text{Li}(n, \alpha)$ reactions, on the one hand, and photon products from $\text{Gd}(n, \gamma)$, $\text{Cd}(n, \gamma)$, and as well as ${}^1\text{H}(n, \gamma)$ reactions, on the other hand, must be covered separately, due to the distinct radiation–matter interactions that govern their respective energy transfers to the sensitive medium.

Ions are charged and thus directly ionizing particles that lose kinetic energy mostly through Coulomb interactions with atom nuclei. Consequently, their energy transfer is described in a deterministic fashion and quantified by quoting the *mass stopping power* of the propagation medium for the particle type and kinetic energy E . This stopping power, labeled $S(E)$ and usually expressed in MeV cm² g⁻¹, is defined as the infinitesimal amount of energy dE that is laid down by the particle per unit of distance dr traveled inside the medium divided by the density ρ of the said medium

$$S(E) = \frac{1}{\rho} \cdot \frac{dE}{dr} \quad (3.21)$$

The expected range of the particle in the stopping medium is then computed by integrating Eq. (3.21) between the particle initial and rest kinetic energies. Supposing that ${}^6\text{Li}$ or ${}^{10}\text{B}$ are homogeneously incorporated into a poly(vinyltoluene)-based plastic scintillator, with density $\rho = 1.032 \text{ g cm}^{-3}$, the stopping powers and expected ranges associated with the tritium and alpha particle reaction products will be those reported in Table 3.3. The values were calculated using the PSTAR and ASTAR programs [32], made available by the National Institute of Standards and Technology. We observe that, for the Q-value carried by ions to be entirely transferred to the detection medium, the scintillator size needs only to be in the order of 1–10 mm. In cases where the neutron converter is heterogeneously incorporated into the plastic scintillator-based neutron detector, however, the energy loss of the reaction products to the coating material must be taken into account.

Table 3.3 Stopping powers and expected ranges of ion reaction products inside a poly(vinyl toluene)-based plastic scintillator [32]

Particle	Energy (MeV)	Stopping power (MeV cm ² g ⁻¹)	Expected range (mm)
³ H	2.73	$1.273 \cdot 10^2$	22.1
⁴ He	1.47	$1.956 \cdot 10^3$	0.8
⁴ He	2.05	$1.634 \cdot 10^3$	1.3

Contrary to ions, photons are chargeless, and thus indirectly ionizing particles essentially interact with atom nuclei through the photoelectric effect, Compton effect, and (above 1.022 MeV) pair creation. As a result, their energy transfer is described probabilistically. The electrons that are set in motion through the abovementioned processes subsequently transfer their kinetic energy to the detection medium through Coulomb interaction. At a macroscopic scale, the aggregation of all interaction probabilities leading to the formation of directly ionizing electrons is represented by the *mass attenuation coefficient* of the medium associated with photon kinetic energy E , labeled $\mu/\rho(E)$ and usually expressed in g cm⁻². If $dN(E)$ is the infinitesimal number of photons with energy E undergoing such processes over the infinitesimal range dr inside the propagation medium and ρ the mass density, then the meaning of this coefficient is given by the following linear attenuation equation:

$$dN(E) = -\frac{\mu}{\rho(E)} \cdot \rho \cdot N(E) \cdot dr \quad (3.22)$$

When scaling a plastic scintillator to optimize the probability P_r of photons producing a recordable signal, a valuable figure is the *half-value layer* (HVL) of the medium, defined as the thickness where 50% of incoming photons have been attenuated. From Eq. (3.22), we get an explicit derivation of this figure

$$HVL(E) = \frac{\ln(2)}{\frac{\mu}{\rho(E)} \cdot \rho} \quad (3.23)$$

Supposing the same vinyltoluene-based medium we considered above may be deemed infinite compared to the distance traveled by the particles, coefficients μ/ρ and HVL for photons of kinetic energies $E = 0.48$ MeV as released in the ¹⁰B(n, α) absorption reaction, and $E = 2.2$ MeV corresponding to the ¹H(n, γ) line, as presented in Table 3.4. The $E = 2.2$ MeV also matches the most likely energy carried by gamma rays in Gd(n, γ) and Cd(n, γ) radiative captures. The values were obtained from reference [33]. We see that, for a large portion of photon reaction

Table 3.4 Mass attenuation coefficients and HVL of photon reaction products [33]

Energy (MeV)	Mass attenuation coefficient (cm ² g ⁻¹)	HVL (cm)
0.5	$9.443 \cdot 10^{-2}$	7.1
2.2	$4.642 \cdot 10^{-2}$	14.5

products to be recorded inside the detector, the scintillator size this time needs to be in the order of 10–100 cm.

Considering a fixed mass load in any neutron converter, minimizing the scintillator size and associated cost, with respect to probability P_a will tend to favor isotopes with the largest microscopic reaction cross section, namely ^{157}Gd , ^{155}Gd , and ^{113}Cd . Conversely, minimizing that same size with respect to probability P_r will lead to prefer ion-producing isotopes, namely ^{10}B and ^6Li . The tradeoff between both strategies, nonetheless, may only be fully understood upon studying the influence of the radiation background as a function of the scintillator size and content. The phenomenology of said background, as well as the description of the discrimination techniques that are available for the different reaction products we have encountered in this discussion, will thus form the topic of our next section.

3.3 Detection of Reaction Products and n/γ Discrimination

3.3.1 *Background Radiation*

In practical cases, neutron detection and counting must be performed in the presence of background radiations that, as far as plastic scintillator-based slow neutron detectors are concerned, will be mostly accounted for by the following:

- gamma rays from natural radioactivity, essentially emitted by ^{40}K , as well as radionuclides in the disintegration chains of ^{238}U and ^{232}Th . The said gamma-ray background shows a highest-energy, prominent line from ^{208}Tl at 2.614 MeV [34]. Its average energy after multiple diffusions in the environment, however, is typically found between 300 and 400 keV at the detector level. The gamma-ray dose rate induced by natural radioactivity is normally between 50 and 100 nSv h $^{-1}$;
- the products of cosmic rays, mainly muons with a mean energy in the vicinity of 4 GeV at sea level. Based on an average flux of about 0.01 cm 2 s $^{-1}$ sr $^{-1}$ [35] and a stopping power close to 2 MeV cm 2 g $^{-1}$ in plastic matrices, these may induce a significant count rate in large-scale plastic scintillator far above the abovementioned, 2.6–2.7 MeV limit for natural background gamma rays;
- gamma rays from the neutron emitter itself, whether it is a fission or a radioisotope (α , n) source. As an illustration, a sealed ^{252}Cf sample, as widely used to calibrate neutron detectors, is a mixed n/γ source [36] that, together with a mean number of 3.77 neutrons, releases an average of 7–10 gamma rays per spontaneous fission. The associated prompt and delayed gamma-ray spectrum form a continuum ranging up to 10 MeV, thus again far above natural background. The average energy carried by these rays, however, lies close to 0.9 MeV. In any case, characterizing a slow neutron detector with a neutron source often involves the use of a high atom number and high-density gamma-ray shield made of lead (Pb) or tungsten (W);

- gamma rays from an additional radioisotope being present in the vicinity of the neutron emitter. The systematic study of the influence of such interfering sources is usually carried out using ^{137}Cs (662-keV line) as a long-lived radioactive product from neutron-induced fission and ^{60}Co (1.17- and 1.33-MeV lines) as a commonplace neutron activation product in alloy steels.

It follows that, for a plastic scintillator incorporating a high absorption cross section converter to selectively detect neutrons in the presence of background radiations (mainly gamma rays), the registering method must discriminate efficiently the associated reaction products against the said radiations. Such is the purpose of so-called n/γ discrimination techniques that, as we shall discuss in the rest of this section, only come out in a small number, and whose effectiveness strongly depends on the neutron-converting reaction at play inside the plastic scintillator-based detector.

3.3.2 Pulse Height Discrimination

The first type of event filtering dedicated to the discrimination of slow neutron-induced pulses from the gamma-ray and muon background relies upon the measured energy that is itself proportional to the amplitude (hence the denomination of *pulse height discrimination*, PHD) or area of their corresponding pulses. In practice, neutron separation by PHD follows two major strategies.

On the one hand, it is possible that the amount of kinetic energy laid down by neutron reaction products inside the sensitive medium and translated into units of eV electron equivalent (eV_{ee}) exceeds the 2.6-MeV_{ee} limit for natural background gamma rays (as there is no quenching for gamma rays). In this case, an energy-calibrated pulse height lower threshold may foster n/γ discrimination. Now, according to Sect. 3.2.2, Gd(n, γ) and Cd(n, γ) radiative captures yield Q-values between 8 and 9 MeV, which, as they are carried by photons and electrons, are unitarily converted into MeV_{ee}. Provided the plastic scintillator is large enough with respect to the photon high-value layer (HVL) above 2.6 MeV (for instance, about 17.5 cm at 3 MeV in poly(vinyl toluene)-based matrices), this PHD strategy will be implementable in the form of a low-pass energy filter typically found close to 3 MeV_{ee} [37]. Additionally, a high-pass energy filter may be set in place to reject muon events above the Q-value of the neutron-converting reaction or the highest significant spectral signature of said reaction inside the scintillator, thus ranging usually between 5 and 8 MeV_{ee} [37, 38]. However, in most practical applications, the potential presence of high-energy gamma rays from the source or an intense contribution from muons to the signal in large-scale plastic scintillator incorporating Gd or Cd, will prevent low-pass PHD from yielding a robust n/γ discrimination on its own.

We observe that, in the 94% most likely version of the $^{10}\text{B}(\text{n}, \alpha)$ reaction, as well as in the $^{6}\text{Li}(\text{n}, \alpha)$ reaction, Q-values are also superior to 2.6 MeV. The scintillation signal induced by the ion products of said absorption reactions, nonetheless, undergoes severe fluorescence extinction, quantified by a *quenching factor* labeled QF .

This factor, which depends on the particle nature, converts the energy E (in MeV) transferred to the medium into the energy E_{ee} (in MeV_{ee}) available at the output of the measurement chain. If $\frac{dE}{dr}$ refers, like in Sect. 3.2.3, to the linear energy transfer of the particle and kB is the so-called Birks constant (a characteristic of the scintillating material), then Birks formula [39] leads to

$$E_{ee}(E) \propto \int_0^E \frac{dE}{1+kB \cdot (\frac{dE}{dr})} \sim \frac{E}{1+kB \cdot (\frac{dE}{dr})} \quad (3.24)$$

The latter approximation applying when $\frac{dE}{dr}$ may be deemed constant over the energy range of interest. Furthermore, it follows from the Bethe formula that $\frac{dE}{dr} \propto Z^2$, with Z the charge number of the particle. Provided that $kB \cdot (\frac{dE}{dr}) \gg 1$, then Eq. (3.24) yields the approximate dependence

$$QF(E) = \frac{E_{ee}}{E} \propto \frac{1}{Z^2} \quad (3.25)$$

The Bethe formula being independent on the particle mass, the quenching factor $QF_{^3H}$ for tritium ions may be taken equal to one of protons, which is well described in the literature [40] as

$$QF_{^3H}(E) = \frac{E_{ee}}{E} = \frac{0.034 \cdot E^2 + 0.125 \cdot E}{E} \quad (3.26)$$

Applied to the triton particle released in ${}^6Li(n, \alpha)$ reactions, Eq. (3.26) yields $QF_{^3H}(2.73) = 0.218 \text{ MeV}_{ee} \cdot \text{MeV}^{-1}$, hence $E_{ee} = 516 \text{ keV}_{ee}$.

Now, using Eq. (3.25) with $Z = 2$, the quenching factor for alpha particles may be estimated as $QF_{\alpha}(E) \sim \frac{QF_{^3H}(E)}{4}$. Implemented with the products of ${}^{10}B(n, \alpha)$ and ${}^6Li(n, \alpha)$ reactions, said approximation leads to $QF_{\alpha}(1.47) = 0.044 \text{ MeV}_{ee} \cdot \text{MeV}^{-1}$ (hence a spectral signature centered on $E_{ee} = 64 \text{ keV}_{ee}$) and $QF_{\alpha}(2.05) = 0.049 \text{ MeV}_{ee} \cdot \text{MeV}^{-1}$ ($E_{ee} = 100 \text{ keV}_{ee}$), respectively. The first estimate stands in agreement with experimental quenching $E_{ee}(1.47 \text{ MeV}) \sim 60 \text{ keV}_{ee}$ in plastic scintillator incorporating ${}^{10}B$ neutron-absorbing nuclei [41].

Eventually, still based upon Eq. (3.25) with $Z = 3$, an estimate of the quenching factor for lithium ions reads as $QF_{^7Li}(E) \sim \frac{QF_{^3H}(E)}{9}$. Applied to the lithium-ion product in ${}^{10}B(n, \alpha)$ reactions, this approximation yields $QF_{^7Li}(0.84) \sim 0.017 \text{ MeV}_{ee} \cdot \text{MeV}^{-1}$. As such a quenching factor results in $E_{ee}(0.84 \text{ MeV}) \sim 14 \text{ keV}_{ee}$, we see that, in a plastic scintillator incorporating ${}^{10}B$, the 7Li ion product is unlikely to contribute significantly to the signal of interest.

In any case, the positively charged and neutral products from ${}^{10}B(n, \alpha)$ and ${}^6Li(n, \alpha)$ reactions form an exploitable signal between 50 and 500 keV_{ee}, that is within the same spectral range as natural background, and widespread artificial gamma-ray emitters. Neutron counting by peak-area estimation around the energy lines listed in Sects. 3.2.2.1 and 3.2.2.2 may thus be made unreliable by gamma-ray interferences in a mere PHD method. This issue is essentially addressed via two

complementing n/ γ discrimination techniques: pulse shape discrimination and the implementation of a two-sensor compensation scheme.

3.3.3 Pulse Shape Discrimination

When the plastic scintillator chemical formula is purposely modified, the detector may allow some separation between the scintillation signals from ions (tritium, helium, and tritium nuclei in the context of boron- or lithium-based neutron detection) on the one hand and electrons on the other hand, founded upon the difference in time distributions of pulses. Such particle-discrimination method is thus called *pulse shape discrimination* (PSD). This slow n/ γ PSD shares the same physical origin as fast n/ γ PSD with recoil protons, that is the larger stopping power of the plastic medium with respect to ions, favoring the creation of longer-decay-constant, excited triplet states in the scintillator [42]. Along with a modification of the plastic scintillator formulation, PSD requires a sorting algorithm based on the time or frequency characteristics of an average slow neutron-induced pulse and an average gamma-ray-induced pulse (see Chap. 10 for more details on various dedicated algorithms). A popular method involves the ratio of the partial pulse area above an optimized decay time threshold labeled Q_{tail} and the full pulse area Q_{total} . Pulses are then displayed in a two-parameter diagram as a function of both energy E_{ee} and the $\frac{Q_{tail}}{Q_{total}}$ ratio.

The slow n/ γ discrimination power [43] of a plastic scintillator, like its fast n/ γ separation capability, is qualified with a standard, unitless figure of merit, labeled $FoM_{n_{slow},\gamma}$, and estimated as

$$FoM_{n_{slow},\gamma}(E_{ee}) = \frac{\mu_{n_{slow}}(E_{ee}) - \mu_{\gamma}(E_{ee})}{2\sqrt{2 \ln(2)} [\sigma_{n_{slow}}(E_{ee}) + \sigma_{\gamma}(E_{ee})]} \quad (3.27)$$

where $\mu_{n_{slow}}$ and μ_{γ} are the centroids, and $\sigma_{n_{slow}}$ and σ_{γ} the standard deviations of Gaussian distributions fitting the experimental slow neutron (essentially from tritons and alpha particles) and gamma-ray lobes at kinetic energy E_{ee} in two-parameter diagrams. Such signal processing construction is described step by step in Fig. 3.5.

As represented in Fig. 3.6, the directly ionizing signature of $^{10}\text{B}(\text{n}, \alpha)$ and $^{6}\text{Li}(\text{n}, \alpha)$ reactions may be identified more robustly upon combining information on the pulse energy-equivalent area (PHD) and time distribution (PSD). The coupling of PHD and PSD was successfully applied to the detection of slow neutrons based upon plastic scintillator incorporating lithium [43], boron [46], or both [47, 48], with typical $FoM_{n_{slow},\gamma}$ lying around 3 between 350 and 500 keV_{ee} (tritium ion) and around 1.5 between 50 and 100 keV_{ee} (alpha particles).

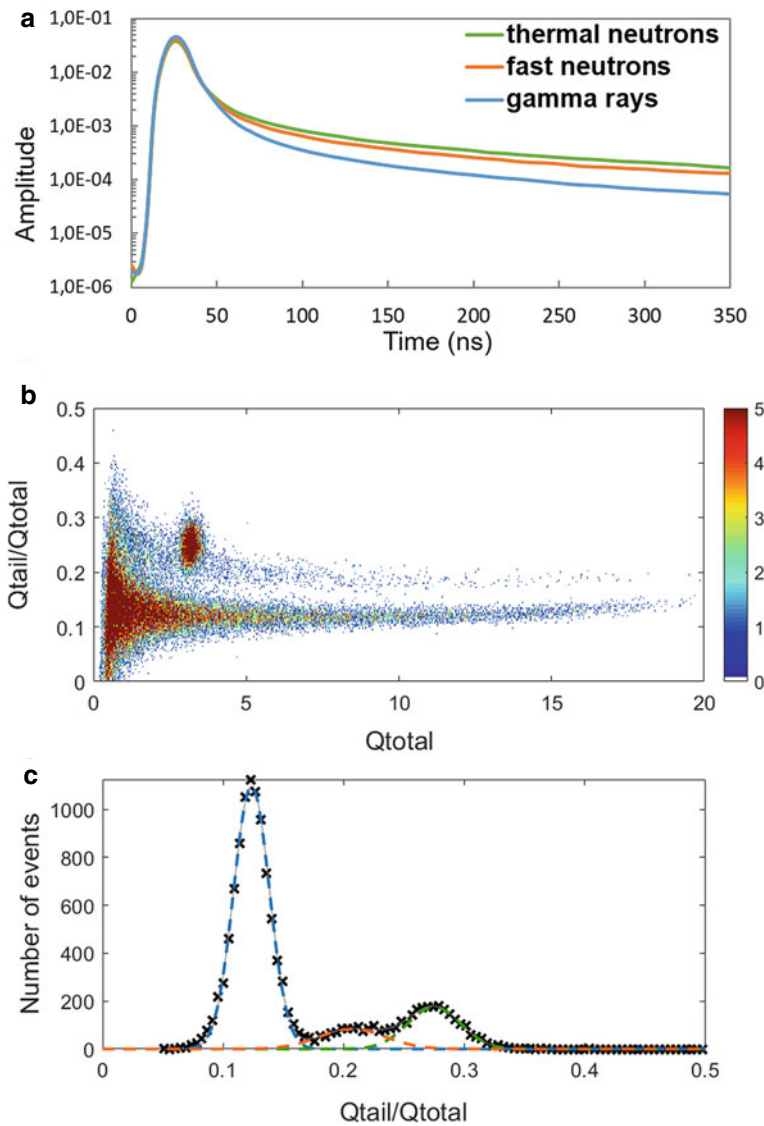


Fig. 3.5 **a** Baseline-subtracted and energy-normalized average pulses from thermal neutron pulses (green curve), fast neutron pulses (orange curve) and gamma-ray pulses (blue curve) (adapted from [44]). **b** Pulse shape discrimination diagram of a ^{6}Li -doped plastic scintillator exposed to a thermalized ^{252}Cf source. **c** Corresponding PSD histogram ($\text{FoM}(n_{\text{thermal}}/\gamma) = 1.75$ and $\text{FoM}(n_{\text{fast}}/\gamma) = 0.83$ above 180 keVee) (reproduced from [45] with permission from the Royal Society of Chemistry)

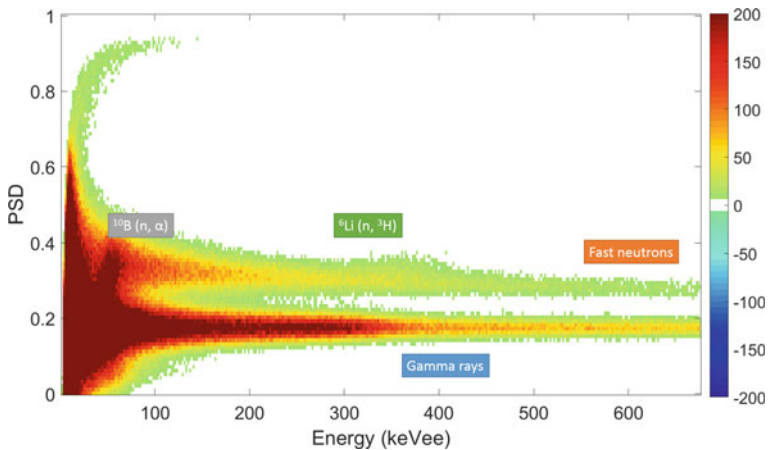


Fig. 3.6 Biparametric spectrum showing ^{10}B and ^6Li neutron absorptions, fast neutrons, and gamma-ray lobes under moderated ^{252}Cf source (Reproduced from [47] with permission from Elsevier)

3.3.4 Compensated Detectors

When no PSD is available, another way to consolidate slow neutron detection against intense or varying gamma-ray backgrounds is to implement a *two-sensor compensation method*. In this detection scheme, two isolated scintillators are used jointly, one being made sensitive to neutrons through the incorporation of a slow neutron converter, the second, as deprived of such incorporation, remaining only significantly sensitive to other radiations (including natural radioactivity, artificial gamma rays, and the fast component of the neutron field). Provided that both twin plastic scintillator are exposed to the same slow neutron fluence, the signature of absorption or capture reactions of interest inside the first scintillator may be isolated by subtracting to its response the response of the second sensor (so-called, for this same reason, the compensation sensor). This subtraction, in order to increase the discrimination power, will be carried out over a spectral range that was previously identified as relevant with respect to the conversion reaction at stake (PHD). Additionally, this difference may need to be weighted by the ratio of the sensitivities of both scintillators to the other components of the incoming radiation field. As a consequence, the stability of this sensitivity ratio against the measured energy distribution of the radiation background, which is always subject to change, is the key to qualify the reliability of the compensated detector. Compensated boron-loaded plastic scintillator [49] proved themselves an efficient alternative to scintillators allowing a PSD when insulating signature from the tritium and helium nuclei over the measured energy ranges that were described in Sect. 3.3.2. Twin scintillator-based compensation between 60 and 200 keV_{ee} was also implemented [50] in order to isolate the

signature of intense gamma-ray lines in $\text{Gd}(n, \gamma)$ capture reactions that, by nature, cannot be discriminated by PSD.

3.3.5 Multiplicity-Gated Detection

As mentioned in Sect. 3.3.2, when putting into play $\text{Gd}(n, \gamma)$ and $\text{Cd}(n, \gamma)$ reactions, PHD founded upon the attenuation of gamma rays with kinetic energy above 2.6 MeV needs to be consolidated to operate in the presence of a high-energy natural or artificial radiation background. One possible method is the so-called *multiplicity-gated detection* or discrimination. The radiative cascade following the abovementioned capture reactions is indeed characterized by a high multiplicity, the Q-values being carried [25, 28] by an average of 4 gamma rays in both natural elements. Such a multiplicity is then likely to cause coincident interaction events inside the detector. Now, this multiple signature can be used to discriminate a neutron-induced event topology provided that the detector possesses the multi-hit capability, i.e., that coincident events occurring inside isolated portions of the segmented plastic scintillator may be registered on separate channels. Multiplicity-gated detection was notably proven efficient in large plastic scintillator incorporating Gd , upon enforcing an event registration multiplicity [51, 52] above 2 to 3, together with PHD thresholds typically in the order of 500 keV_{ee} on said events considered independently.

3.3.6 Capture-Gated Detection

Another powerful method to identify neutron-induced pulse frames is *capture-gated detection* or discrimination that relies on the interarrival delay between two types of physically correlated, recorded events. This discrimination technique aims, more precisely, at discriminating from radiological background some radiation–matter interaction scenarios that involve:

- the first sequence of elastic (n, n) scattering events of a neutron by light nuclei inside the plastic scintillator medium;
- a delayed absorption or radiative capture event of the same neutron after complete or partial moderation, either by a nucleus from the plastic matrix or by an additional neutron-converting isotope.

The detection of the first event sequence is founded upon the excitation signature of recoiling nuclei inside the scintillator, and thus upon the generation of enough photo-electrons to be triggered against electronic noise. Assuming a measuring threshold in the vicinity of 15 keV_{ee} and using Eq. (3.26) in order to account for the fluorescence quenching that affects the signature of protons, the associated signal will be essentially filled by recoil protons from the scattering of fast-born neutrons down to kinetic energy about $E_f = 100$ keV. By applying Eq. (3.14) to this detectable

segment of the neutron moderation process and considering the same poly(vinyl toluene)-based diffusion matrix, we see that the average time lapse of this event sequence is $\bar{t}_m \sim 60$ ns. As this estimate is of the same order as a typical scintillation pulse duration, it follows that the first scattering event sequence is likely to be detected within a single pulse. For a capture-gated detection to operate, we also see that a significant fraction of the incoming neutron field must be found in the fast energy range.

While the amplitude of the delayed event can be identified by PHD, the interevent delay, often called the *capture time*, is governed by the follow-up of the moderation process, as well as by the absorption or radiative capture reaction at play. In turn, the random kinetics of both processes are strongly influenced by the geometry of the detection assembly and the way any additional neutron converter was incorporated into the plastic scintillator-based detector. As a result, the probability distribution that is associated with neutron capture time must in general be investigated through the Monte Carlo simulations. Said distributions, however, may usually be fitted with a combination of exponential functions [20], with time constants related to the macroscopic scattering and absorption cross sections inside the composite medium. Moreover, an order-of-magnitude estimate of the average capture time, labeled \bar{t}_c , may, as soon as the sensor can be deemed both infinite and homogeneous, be explicitly derived [21] as

$$\bar{t}_c = \frac{2}{v_f \cdot \xi_{VT} \cdot \bar{\Sigma}_{tr}} + \frac{1}{v_{n,th}^* \cdot \Sigma_a (E_{n,th}^*)} \quad (3.28)$$

using the notations from Sects. 3.2 and 3.3, and assuming $E_f = 1$ eV as representative of a moderated neutron entering the slow energy range. As an illustration, considering a bare vinyltoluene-based matrix and a slow neutron detection scheme relying upon the sole ${}^1\text{H}(n, \gamma)$ capture reaction, then Eq. (3.28) will yield $\bar{t}_c \sim 265$ μs . Using the same example as in Sect. 3.2.3, the same plastic matrix homogeneously loaded with 1-wt% natural Gd, the estimate would be reduced down to $\bar{t}_c \sim 6$ μs .

In practice, and due to the stochastic nature of the scattering and absorption processes, capture-gated detection implements a temporal correlation gate between the first and second interaction events, typically between the orders of 1 μs and to 10 to 100 μs depending on the natures and mass loads of neutron converters inside the detection assembly. A PHD condition on the energy associated with the delayed event is usually added to the detection procedure, either in the vicinity of the triton and alpha particle lines [53] or above a 3-MeV_{ee} lower threshold [37] when exploiting ${}^{10}\text{B}(n, \alpha)$ and $\text{Gd}(n, \gamma)$ reactions, respectively. Another implementation of capture-gated detection, illustrated with a plastic scintillator-based detector incorporating Cd [20], leans on the definition of two regions of interest in the delay probability distribution: one signal region corresponding to the abovementioned interval, and one *compensation* region of the same extent outside the correlation gate. A neutron count rate is then obtained by subtracting the counts in the compensation region from the ones in the signal region. In any case, the performance of slow n/ γ discrimination by a capture-gated method improves when the width of the temporal gate and thus the average capture time \bar{t}_c get lower.

Having described the way plastic scintillators, used in combination with strong converters, react to a neutron field as well as to a radiation background that is mostly accounted for by gamma rays, we now have grounds to define the figures of merit that will prove relevant to characterize them.

3.4 Figures of Merit for Slow Neutron Detectors

Aside from the figures of merit that are used to qualify all plastic scintillators (such as the light yield or the value of the decay constant), as well as those relating to the way neutron converters are incorporated into plastic scintillator-based detectors (that will form the topic of this Section), there are a number of figures that are estimated specifically to assess the performance of plastic scintillator acting as slow neutron detectors. Such figures, according to the theoretical descriptions in Sects. 3.2 and 3.3, may be broken down into three categories.

3.4.1 Figures of Merit About the Response to Neutrons

These figures describe quantitatively the intensity of a plastic scintillator-based detector to a neutron field, as well as the features of this response that are likely to facilitate n/γ separation. Their list includes the following factors.

3.4.1.1 True Detection Rate of a Neutron Source

The most obvious figure of merit that may be used to assess the performance of a slow neutron detector is the *true detection rate* (TDR) of a neutron source, defined as the number of times the said source is detected over a series of trials. The TDR is an SI-unitless figure, usually expressed as a percentage. For this figure to be exploitable, one needs to state the radioisotope nature and conditioning (bare or moderated) of the source, its activity (Bq), mass (g) or neutron emission rate (neutron per second, $n\ s^{-1}$), and the distance between the source and the detector. The measurement times associated with every trial as well as the number of trials are also relevant to evaluate the uncertainty of the TDR. In order to facilitate the benchmark of neutron detectors, some international standards may be recommended according to the application at hand. As an illustration, the ANSI 42-35-2016 standard, which is used to qualify radiation portal monitors (RPMs) for homeland security [54], would require that the TDR be estimated over 60 trials using a ^{252}Cf source with a $2 \cdot 10^4\ n\ s^{-1}$ emission rate, surrounded by 1 cm steel followed by 0.5 cm lead, and set at a specified distance from the external face of the detector assembly.

3.4.1.2 Absolute Neutron Detection Efficiency

The *absolute neutron detection efficiency*, labeled $\varepsilon_{n,abs}$, is the number of pulses that are recorded per neutron emitted by the source [51]. It is therefore an SI-unitless figure, usually expressed in count per neutron ($c\ n^{-1}$) or, equivalently, in units of count rate ($c\ s^{-1}$, or cps) per unit of source activity (Bq), mass (g), or neutron emission rate ($n\ s^{-1}$). As this figure not only depends on the detector but also on the experimental setup, it only allows a benchmark between different neutron counters in cases where source conditioning and measurement configurations are strictly identical.

3.4.1.3 Intrinsic Neutron Detection Efficiency

In order to compare the responses of neutron counters that have been evaluated in different layouts, one needs to normalize the absolute detection efficiency $\varepsilon_{n,abs}$ by factors that do not depend on the detection assembly and method. The so-obtained figure of merit is called *intrinsic neutron detection efficiency* [55], or *registration efficiency* [56], and represents the number of pulses that are recorded per neutron reaching the detector. Labeled $\varepsilon_{n,int}$, it is usually expressed in $c\ n^{-1}$ or %. Now, the relationship between efficiencies $\varepsilon_{n,abs}$ and $\varepsilon_{n,int}$ is given by

$$\varepsilon_{n,abs} = \varepsilon_{n,int} \cdot \varepsilon_g \cdot \varepsilon_s \quad (3.29)$$

where ε_s refers to the source efficiency (neutrons escaping the source per emitted neutron), and ε_g to the geometrical efficiency (neutrons reaching the detector per neutron escaping the source). Provided that the neutron field attenuation inside the emitting material ($\varepsilon_s = 1$), as well as between the source and the sensitive medium are negligible, then Eq. (3.29) simplifies as

$$\varepsilon_{n,abs} = \varepsilon_{n,int} \cdot \frac{\Omega}{4\pi} \quad (3.30)$$

where Ω is the solid angle (in steradian, sr) subtended by the detector from the stand-point of the source. Assuming that the neutron field inside the detector is essentially in the slow energy range, a maximum for $\varepsilon_{n,int}$ may be explicitly derived as the product of probabilities P_a and P_r , as defined in Sect. 3.2.3.

3.4.1.4 Neutron Detection Sensitivity

The most commonplace figure to describe the performance of a detector with respect to neutron response is *neutron detection sensitivity*, or simply *neutron sensitivity*, defined as the number of pulses that are recorded per unit of neutron flux ($n\ m^{-2}\ s^{-1}$). This sensitivity, labeled S_n , has the SI unit of a surface area, and is expressed in $cps/(n\ cm^{-2}\ s^{-1})$ or equivalently in $c\ n^{-1}\ cm^2$. When dealing specifically with slow

neutron detectors [57], sensitivity S_n is often related to units of thermal neutron flux (nv), in which case it is expressed in cps/nv. Provided that the same assumptions that led to simplifying Eq. (3.29) into Eq. (3.30) hold, neutron detection sensitivity may be made explicit as a function of the intrinsic neutron detection efficiency, according to

$$S_n = \varepsilon_{n,int} \cdot \Sigma \quad (3.31)$$

where Σ is the entrance area (cm^2) of the detector.

Let us underline, eventually, that neutron sensitivity can be translated into a number of recorded pulses per unit of *neutron dose rate* (nano to microsievert, respectively, nSv and μSv) upon using a spectral, neutron-to-dose conversion such as the one that is recommended by International Commission on Radiological Protection [58]. In this case, the sensitivity S_n will typically be expressed in $\text{cps}/(\mu\text{Sv h}^{-1})$.

3.4.1.5 Other Figures

In addition to the abovelisted figures of merit, additional figures relating to specific features of the detector response to the neutron field, used themselves as part of the n/γ discrimination method, are likely to be introduced. Such is the case, for instance, of the presence and spectrometric characteristics (area under peak, full width at half maximum) of an identifiable energy peak inside the spectral response of the plastic scintillator-based detector, corresponding to the interaction of a nuclear reaction product of interest [59].

3.4.2 Figures of Merit About the Response to Gamma Rays

These figures describe quantitatively the vulnerability of plastic scintillator-based detector to gamma rays, which we have said to be the main contributors to the radiation background that are susceptible to impinge n/γ discrimination. They can be listed as follows.

3.4.2.1 Gamma-Ray Induced False Alarm Rate and Count Rate

Once again, the most immediate figure that may be used to quantify the vulnerability of a neutron detector with respect to other radiations is the false alarm rate (FAR) or false detection rate induced by a non-neutron-emitting source defined as the number of times such a source is detected over a series of trials. The FAR, as the TDR we defined earlier, is an SI-unitless figure given in %. As it was explained throughout Sect. 3.3, gamma rays are most often the essential radiations contributing to false

neutron detection, whether that is as part of the natural radiation background or as an additional field. It follows that neutron FAR is usually assessed in the presence of an intense and penetrating gamma-ray emitter, typically ^{137}Cs or ^{60}Co . For the figure of merit to be exploitable, one also needs to mention the activity (Bq) of the source as well as its distance to the detector or alternatively the gamma-ray dose rate (nSv h^{-1} to mSv h^{-1}) it induces on the said detector. As for the evaluation of the TDR, some standards may be applicable to the detector characterization. As an illustration, the above cited ANSI 42-35-2016 standard [54] would recommend the FAR to be evaluated over 20 trials using a ^{137}Cs source inducing a dose rate in the vicinity of $10 \mu\text{Sv h}^{-1}$.

Alternatively, the immunity of the neutron detector against the background may be simply measured by the neutron count rate (c s^{-1}) that is recorded in the absence of any significant neutron field. This mainly gamma-ray induced count rate, labeled $\lambda_{n\gamma}$, can be either associated with the natural radiation background, or to a gamma-ray emitter whose characteristics need to be specified.

3.4.2.2 Intrinsic Gamma-Ray Detection Efficiency and Sensitivity

A more universal figure of merit regarding the vulnerability of a slow neutron detector to gamma rays is the *intrinsic gamma-ray detection efficiency* that represents the number of pulses that are recorded as neutron events per gamma ray reaching the detector [55]. This figure labeled $\varepsilon_{\gamma,int}(E_\gamma)$ is usually expressed in $\text{c } \gamma^{-1}$ or % for gamma rays at a specified energy E_γ . It may thus be described as a spectral function. Alternatively, one may quote the *gamma-ray detection sensitivity* of the neutron counter, usually defined as the number of pulses that are recorded per unit of gamma-ray dose rate, $\text{cps}/(\mu\text{Sv h}^{-1})$.

3.4.3 Figures of Merit About the Response to Neutron Against the Response to Gamma Rays

For the purpose of designing a performant neutron detector, one would aim at maximizing all figures of merit that relate to the neutron response, as well as minimizing the figures of merit that were defined about the response to gamma rays. In practice, both types of figures are often intertwined, in other words, the neutron response can only be increased at the expense of a higher gamma-ray response. It follows that the figures ultimately qualify the merits of a neutron detection assembly and methods encapsulate a tradeoff between homogenous neutron and gamma-ray performance criteria. The most popular figures are listed below.

3.4.3.1 TDR Versus FAR

The most immediate way to describe the performance of a detector that is designed to target a specific type of particles, hereby neutrons, is based upon its FAR/TDR tradeoff. This may be done by quoting the TDR that is reached against a preset, acceptable FAR, like it is usually specified in detection standards [50], or by default, indicating the maximum possible value of the difference between both figures of merit [60]. As indicated in Sects. 3.4.1.1 and 3.4.2.1, TDR/FAR ratios are only interpretable provided all relevant information on neutron and gamma-ray expositions are made explicit. So as to quote a n/γ response number that is not bound to a particular experimental configuration nor to a final application at hand, one needs, however, to turn to the intrinsic figures that were introduced above.

3.4.3.2 Neutron/Gamma Rejection Ratio

The *neutron/gamma intrinsic rejection*, or *discrimination ratio* [52], is defined as the ratio between neutron intrinsic neutron detection efficiency $\epsilon_{n,int}$ and intrinsic gamma-ray detection efficiency $\epsilon_{\gamma,int}$. This ratio, hereby labeled $RR_{n\gamma}$, is a unitless figure, homogenous to a number of accurately counted neutrons to a number of gamma rays that were erroneously recorded as neutrons, $n \gamma^{-1}$. The contrast of gamma-ray to neutron responses may also be quantified by the ratio between neutron and gamma-ray detection sensitivities, expressed in units of neutron flux or dose rate per unit of gamma-ray dose rate. In any case, the rejection ratio of a slow neutron detector must be quoted against a specified gamma-ray emitting radioisotope (^{137}Cs , ^{60}Co) or gamma-ray energy E_γ and needs to be maximized for the detector to operate within a natural or artificial background.

3.4.3.3 Neutron Detection Limit and Minimum Detectable Neutron Flux or Emission Rate

Albeit the n/γ rejection ratio carries information on the detector capability, it does not capture the working of the decision process. Firstly, a detection threshold, labeled $DT_{n,\alpha}(t)$ and expressed as counts (c), is set against a false neutron detection risk noted α as

$$DT_{n,\alpha}(t) = k_{1-\alpha} \cdot \sqrt{2\lambda_{n\gamma} t} \quad (3.32)$$

where t is the measurement time, $\lambda_{n\gamma}$ is the gamma-ray induced count rate, and $k_{1-\alpha}$ is a quantile of the standard normal distribution. Secondly, a neutron detection limit, labeled $DL_{n,\alpha,\beta}(t)$ and expressed in c, is specified against a risk of a non-detection risk noted β . The relation between $L_{n,\alpha,\beta}(t)$ and β must, in general, be computed numerically [61]. However, provided that one imposes $\alpha = \beta$, then the neutron

detection limit can be derived explicitly as

$$DL_{n,\alpha=\beta}(t) = k_{1-\alpha}^2 + 2 \cdot DT_{n,\alpha}(t) \quad (3.33)$$

In case the values for both risks are not quoted, the neutron detection limit is presumed to have been calculated [62] for $\alpha = \beta = 5\%$. Eventually, the detection limit $DL_{n,\alpha,\beta}$ may be converted into a *minimum detectable neutron flux* ($\text{n cm}^{-2} \text{ s}^{-1}$) using sensitivity S_n or alternatively into a *minimum detectable neutron emission rate* (n s^{-1}) using efficiency $\varepsilon_{n,abs}$.

As announced at the beginning of this section, after reviewing the essential figures of merit that are used to qualify all neutron detectors, the discussion needs to be moved to those that specifically relate to the incorporation of neutron converters into the plastic scintillator detection assembly.

3.5 Incorporation of Neutron Converters into Plastic Scintillator-Based Detectors

The incorporation of neutron converters into plastic scintillator-based detectors may involve organic as well as inorganic chemistry. The organic chemistry strategies lay on the synthesis of molecules bearing neutron absorbers as cited in Sect. 3.2 (e.g., ^{6}Li , ^{10}B , $^{155/157}\text{Gd}$ in their natural occurrence or enriched forms), whereas inorganic strategies will consider their crystals or glasses forms, most often with nanometric to micrometric sizes (see Chap. 6). Then, those chemical objects could be homogeneously incorporated in or heterogeneously coated on plastic scintillators depending on multiple parameters such as the ease of fabrication, the signal collection, or the sensor design. The main intent behind homogeneous incorporation is to maximize the detection efficiency yielded by a fixed mass load of neutron-absorbing elements, especially by cutting or limiting the energy loss of reaction products outside the sensitive medium. Conversely, the second strategy pursues the external coating of a bulk or segmented plastic scintillator, favoring the ease in scale-up to the detriment of homogeneity. As we shall discuss in the rest of this section, homogeneous loading on the one hand and heterogeneous coating on the other hand not only rely upon distinct incorporation processes, but are also designed according to different technological priorities. Therefore, each of them will be characterized by specific merit criteria.

3.5.1 Homogeneous Incorporation

The homogeneous incorporation or *loading* of slow neutron converters in the plastic scintillators aims at maximizing probabilities P_a and P_r , as we defined them in Sect. 3.2.3, for a given mass of the incorporated element. The main drawback of

this incorporation strategy is that it modifies the content of the plastic scintillator itself. On the one hand, the solubility of the neutron-absorbing material into the hydrocarbon-based medium will set a limit to the amount that can be embedded. On the other hand, the degradation of the scintillator optical properties, resulting from turbidity, inhomogeneity of the mixture, and luminescence self-extinction [39], will both affect the maximum of mass loading and the feasibility of sensors scaling up. Homogeneously loaded plastic scintillator for slow neutron detection will thus be characterized by factors according to the following:

- the *solubility constant* of the dopant inside the monomer, expressed in g L^{-1} or mol L^{-1} , that quantifies the compatibility between the matrix and the incorporated material;
- the *weight percentage* at which a particular loading will be incorporated in a plastic scintillator, most often expressed as a relative and additional mass percentage (wt %) in which the monomer mass will be raised at 100 wt%;
- the *light yield (LY)* of the detector at a measured energy of interest E_{ee} , given in scintillation photons generated per MeV of deposited energy (ph MeV^{-1});
- the figure of merit $FoM_{n,\gamma}$, as stated in Sect. 3.3.3;
- the *largest volume* of the loaded scintillator that can be achieved for the abovecited optimum mass load.

With these figures of merit in view, two so-called homogeneous incorporation strategies may be followed, that is doping the plastic scintillator via molecular binding or loading the matrix with nano- and micro- particles.

3.5.1.1 Molecular Binding

For a strictly homogeneous loading of the plastic scintillator, the insertion of the converter elements in the form of organometallic compounds is required. The literature results over the past decades will be displayed in the following tables for each chosen element promoting slow neutron detection.

Boron-loaded plastic scintillators form one of the most mature technological solutions in the field, as evidenced by the commercial availability of some scintillators as BC-454, EJ-254, SC-231, and SC-331 from Saint-Gobain Crystals and Detectors, Eljen Technology, and IHEP, respectively (see Chap. 1). The most popular organometallic compound dopants are *closو-carborane* molecules such as *ortho*-carborane (or its *meta*-carborane isomer), with the chemical formula $C_2B_{10}H_{12}$ [63, 46]. The high boron content and good solubility in apolar matrices make these structures easy to incorporate for the given application. The use of pyrene and benzene derivatives (e.g., tetra-borylated benzene) [64] as well as bis(pinacolato)diboron $[(CH_3)_4C_2O_2B]_2$ [41] were also reported, as listed in Table 3.5.

Lithium-loaded plastic scintillator is a challenging topic, essentially due to the extremely low solubility of highly polar Li-ions in apolar aromatic polymers, along with the lower cross section absorption of ^6Li (940(4) b) against ^{10}B (3835(11) b) and isotopic abundance (7.6(4)% versus 19.9(7)%). Most reported samples were

Table 3.5 Boron derivatives in plastic scintillators and characteristics

^{10}B derivative	wt% loading/type of plastic	Sample size	Light output (ph/MeV) ^a	FoM (energy)	References
<i>o</i> -carborane	4	n.d. ^b	8,600	n.d.	[65]
“boron molecule”	5	\varnothing 4 cm, h 15 cm	n.d.	n.d.	[53]
<i>m</i> -carborane	5/PVT	\varnothing 2.5 cm, h 1 cm	80%/non-loaded PS	1.6 (50–100 keV _{ee})	[46]
bis(pinacolato)diboron	11.75 (0.2 ^{10}B)/PVT	\varnothing 5.1 cm, h n.d.	98%/BC-408 (~9,800)	1.04 (100 keV _{ee}) 1.64 (400 keV _{ee})	[41]
tetra-borylated benzene (TBB)	1/PVT	\varnothing 4.7 cm, h 1.1–1.3 cm	84%/EJ-204 (~9,050)	n.d.	[64]
“boron-containing molded PS”	0.9 (^{10}B)/PS	$9 \times 9 \times 5$ mm ³	8,600	n.d.	[66, 67]
4,4,5,5-tetramethyl-2-phenyl-1,3,2-dioxaborolane (MBB)	1 (0.05 ^{10}B)/PVT	\varnothing 4.7 cm, h 1.1–1.3 cm	89%/BC-408 (~ 8,900)	1.04 (100 keV _{ee}) 1.67 (500 keV _{ee})	[68]

^aAccording to their datasheets, BC-408 is 10,000 ph/MeV and EJ-204 is 10,400 ph/MeV

^bn.d. not determined

prepared through ${}^6\text{Li}$ -organometallic complexes such as lithium pivalate [69], lithium 2-methylbutyrate [45], and lithium salicylate [70] compounds. Another homogeneous incorporation strategy implies the use of lithium compounds as co-monomers, e.g., lithium methacrylate [71] or lithium maleate [72]. All their main characteristics are gathered in Table 3.6.

Cd-loading in plastic scintillators remains poorly studied probably due to the extreme toxicity of organocadmium compounds. To the best of our knowledge, only one achievement of Cd-loaded plastic scintillator with hexamethylphosphotriamide [73, 74] has been performed as described in Table 3.7.

Gadolinium-loaded plastic scintillators have been reported with various strategies from Gd-benzoylacetone complex [75], Gd-nitrate with hexamethylphosphotriamide [76], Gd-chloride with hexamethylphosphoramide [73], Gd-nitrate-trisbutylphosphate [59], Gd tris-isopropoxide [77], or Gd tris-tetramethylheptanedionate [78]. The main characteristics of these materials are depicted in Table 3.8.

3.5.1.2 Nano- and Micro-composites for Thermal Neutron Detection

To achieve high mass loading with diversified neutron signature in the plastic scintillator, pseudo-homogeneous doping of the matrix with nano or microcrystals represents another powerful approach. Hence, various lithium- or gadolinium-containing micro- and nanoparticles have been reported as shown in Table 3.9. Lithium nanoparticle loading in polysiloxanes [79] is extensively presented in Chap. 5.

3.5.2 Heterogeneous Incorporation

Aside from homogeneous molecular and small particle composite loading, slow neutron converters may be incorporated inside the detection assembly as layers that are separated from the plastic scintillator. Such a process is usually referred to as *coating* or *lining*. Now, and as we have mentioned earlier, heterogeneous loading is necessarily associated with a coarser grain of the absorbing material inside the sensor, ranging from an equitable sandwich-like scheme up to the extreme case of an external coating surrounding a bulk plastic scintillator. Hence, all radiation–matter interactions and relevant figures of merit (including Σ_a , λ_a , and \bar{t}_c from the previous sections) will, in general, have to be evaluated through Monte Carlo simulations.

We have already mentioned that, as far as an alternative to homogeneous loading is needed, the incorporation of lithium inside a plastic scintillator-based detector forms a hotter topic than one of boron. It can be shown, moreover, that while the shorter range of ${}^{10}\text{B}(n, \alpha)$ reaction products makes them advantageous for boron-lined gas proportional counters [84], ${}^6\text{Li}(n, \alpha)$ absorptions are a preferred option for plastic scintillator-coated detectors, due to the higher light output from the secondary

Table 3.6 Lithium derivatives in plastic scintillators and characteristics

^{6}Li derivative	wt% loading/type of plastic	Sample size	Light output (ph/MeV)	FoM (energy)	References
Li-3-phenylsalicylate	5–7.5 (0.14–0.27 ^{6}Li)/PS	\varnothing 7 cm, h 3 cm	–	2.47 (200 keV _{ee})	[43]
Li-pivalate	20–35 (1.3–2.27 ^{6}Li)/PVT	\varnothing 4.45 cm, h 5.6 cm	–	1.3 (300–1000 keV _{ee})	[69]
Li-salicylate	2.8–5 (0.12–0.21 ^{6}Li)/PS:PMMA	\varnothing 5.1 cm, h 2.5 cm	57–70%/non-loaded PS	2.1–2.5 above 80 keV _{ee}	[70]
Li-3-phenylsalicylate	4.3–7.6 (0.12–0.21 ^{6}Li)/PS:PMMA	\varnothing 5.1 cm, h 2.5 cm	52–57%/non-loaded PS	2.3–2.5 above 80 keV _{ee}	[70]
Li-2-methylbutyrate	3–50 (0.05–1.7 ^{6}Li)/PS	\varnothing 3 cm, h 1.5 cm	4,410–7,790	0.2–1.5 above 180 keV _{ee}	[45]
Li-methacrylate	1.25–10 (0.08–0.63 ^{6}Li)/PS	\varnothing 2 cm, h 1 cm	–	–	[71]
Li-maleate	31.64 (3 ^{6}Li)/PS-co-PLiMAN-co-PVPPO	n.d. ^a	495	–	[72]

^an.d. not determined

Table 3.7 Cadmium derivatives in plastic scintillator and characteristics

^{113}Cd derivative	wt% loading/type of plastic	Sample size	Light output (ph/MeV)	References
HMPTA: CdCl_2	0.5–2/PMMA	\varnothing 2.7 cm; h. 1 cm	65%/non-loaded PS	[73, 74]

particle that they produce. Now, the most commonly implemented neutron-sensitive scintillation detectors incorporating Li are homogeneous matrices of fine particles of lithium-6 fluoride and zinc sulfide phosphor $^6\text{Li:ZnS}$ or $^6\text{Li:ZnS(Ag)}$ compacted in a colorless binder, sandwiched with wavelength shifters [85] and light guide strips [86], or directly painted on the surface of the plastic scintillator [69], allowing an areal density of ^6Li as high as 9 mg cm^{-2} . However, due to the important stopping power (and thus loss of charges) of LiF and light self-extinction inside ZnS, the light output from the incoming particles tends to be quite small. This is the reason why Ianakiev et al. [84] introduced a slow neutron detector based upon 95%-enriched ^6Li metal foils sandwiched between light guide strips that are laminated with films of scintillating plastic. The first prototype of this technology consisted of $20'' \times 2'' \times 0.25''$ thick strips of PMMA light guide with $200\text{-}\mu\text{m}$ plastic films, while the model of the concatenated detection assembly was heterogeneously loaded with 464 mg cm^{-3} density, $50\text{-}\mu\text{m}$ neutron-converting films. Composite detectors including plastic scintillator and ^6Li converters [87] were also studied. Another strategy from Foster et al. involved the use of ^6Li -glass rods pre-treated with a silane-coupling agent (APTES) to enhance their adhesion to a PVT matrix, which will be polymerized around them [88]. This method appears as effortless from a chemical point of view but exhibits remarkable discrimination of the thermal neutrons region from fast neutrons and gamma regions ($\text{FoM}(n_{\text{th}}/\gamma) = 3$ at 500 keVee).

Popular applications of plastic scintillator-based slow neutron detectors incorporating Gd or Cd, as we shall discuss in the next section, often involve high-scale systems [89] that should sometimes allow for shape versatility. Heterogeneous loading, in such cases, appears like the only viable technological option when taking advantage of $\text{Gd}(n, \gamma)$ capture reactions, and the neutron converter is most often incorporated in the form of a $25\text{-}\mu\text{m}$ gadolinium oxide Gd_2O_3 internal coating of Mylar [52] or polyester [37] films in which plastic scintillator bars are subsequently wrapped. The interleaving of the fast-decay plastic scintillator (BC-408) with 1-mm-thick Gd_2O_3 -doped polydimethylsiloxane (PDMS) sheets was also reported [38], for a total 0.5-wt% inhomogeneous Gd load of the sensor. In some cases, such as the one of the PANDA detector series [37], the design can be declined between 100-kg and 1-ton modules as a function of the neutron measurement at hand. Cadmium represents a cheaper and lighter alternative to Gd although, as it was said in Sect. 3.5.1.1, it can almost be incorporated heterogeneously into the plastic scintillator detection assembly. Aiming at developing a sensitive and transportable neutron monitor, Liu et al. [20] thus described a sensor made of four hundred BC-408 plastic scintillator blocks with dimensions $1 \times 1 \times 20 \text{ cm}^3$, each of them being covered by a $100\text{-}\mu\text{m}$ ^{nat}Cd film. After concatenation, the detector reached an active volume of about

Table 3.8 Gadolinium derivatives in plastic scintillators and characteristics

Gd derivative	wt% loading/type of plastic	Sample size	Light output (ph/MeV)	References
Gd-benzoylacetonate	0.1–0.2/PVT	Ø 2.5 cm, h 15 cm	42–15%/non-loaded PS	[75]
Gd(NO ₃) ₃ /HMPTA	1–3/PMMMA	Ø 3 cm, h 1 cm	79–51%/non-loaded PS	[76]
HMPTA-GdCl ₃	0.5–4/PMMA	Ø 2.7 cm, h 1 cm	85–68%/non-loaded PS	[73]
Gd(NO ₃) ₃ (TBP) ₃	0.6–1.5/PVT	Ø 2.5 cm, h 1 cm	60–45%/non-loaded PS	[59]
GdOCH(CH ₃) ₂) ₃	0.5–3/PS	Ø 1.4 cm, h 0.3–1.3 cm	93–75%/non-loaded PS, 10,990–8,200	[77]
Gd-(TMHD) ₃	0–3.6/PS	Ø 1.6 cm, h 12 cm	70–15%/non-loaded PS	[78]

Table 3.9 Nano- and micro-composites for thermal neutron detection

Nano/micro compound	wt% loading/type of plastic	Sample size	Light output (ph/MeV)	FoM	References
${}^6\text{LiF}$ nanocrystals 218 ± 32 nm	– /polysiloxane	$\varnothing \sim 5$ cm, h 500 μm	–	–	[79]
${}^6\text{Li}^{nat}\text{Gd}^{11}\text{B}_3\text{O}_9\text{:Ce}^{3+}$ microcrystals $300\text{--}500$ μm	– /PVT	$\varnothing 5$ cm, h 5 cm	–	–	[80]
${}^6\text{Li}^{nat}\text{Gd}^{11}\text{B}_3\text{O}_9\text{:Ce}^{3+}$ microcrystals	10/PVT	$\varnothing 12.7$ cm, h 10.2 cm	–	–	[81]
${}^6\text{Li}_2{}^{10}\text{B}_4\text{O}_7$ nanoparticles 66 ± 22 nm	0.3/PS	$\varnothing 3.2$ cm, h 1.1 cm	3,750	1.4 (477 keVee)	[48]
${}^6\text{LiF}$ nanoparticles $50\text{--}100$ nm	25/PVA	2.2×2.2 cm^2 , h $100\text{--}200$ μm	–	–	[82]
Gd_2O_3 capped with BMEP ^a nanoplates crystals edge length 9 nm; thickness 1 nm	31–40/PVT	$\varnothing 1$ cm, h 0.3 cm	27,000–22,000	–	[83]

^aBMEP bis(2-(methacryloyloxy)ethyl) phosphate

8 dm³, with a neutron converter granularity close to the one of a homogeneously doped scintillator.

To conclude this section, let us underline that homogeneous and heterogeneous incorporations may be combined to address technical challenges such as low-energy neutron measurement. Kim et al. [90], for instance, described the conception and characterization of a hybrid detector devoted to neutrons with kinetic energies between $E_n = 10$ meV and $E_n = 600$ meV based on plastic scintillator that is loaded up 5.9 wt% with ¹⁰B and uniformly layered by a mixture of Gd₂O₃ powder linseed oil with a thickness equal to 30 ± 5 μm.

3.6 Applications of Plastic Scintillators to the Detection of Slow Neutrons

As we have already stated, ³He is the most commonly used converter in neutron counters found on the market. The inert ³He gas under pressure is contained inside a tube that is itself placed within a hydrogenous moderator, whose dimensions maximize the neutron capture rate inside the gas. Charged particles produced by the reaction (protium and tritium nuclei) directly ionize the gaseous medium, generating a cloud of charge carriers that induce the detected signal. Commercial detectors display a neutron sensitivity within the order of magnitude 1 c nSv⁻¹ against a gamma-ray sensitivity of 10^{-3} c nSv⁻¹, hence yielding a n/γ rejection ratio of 10^3 , consolidated up to 1-mSv h⁻¹ gamma-ray dose rates [58]. Despite the constant improvement in the performance of plastic scintillator-based neutron detectors, such figures of merit remain unchallenged. However, 9/11 attacks have led to the deployment of a rising quantity of special nuclear materials monitors at borders, causing the demand for ³He to skyrocket [91]. The shadow of a worldwide shortage and the strategic stakes weighing on the ³He resource (United States and Russian stocks of nuclear weapons being the main providers of the isotope during the 2000s decade) have severely affected the cost of the detectors [92], from around 100 USD/L in 2008 up to 2000 USD/L in 2013. It is essentially this international context that has been driving the R&D effort on plastic scintillator-based neutron detectors over the past two decades. Among other alternative technologies to ³He proportional counters, plastic scintillators indeed stand as cheap; versatile; easy to scale up, store, and handle; and readily available. The short inventory that we drew in this chapter indicates that the ongoing research on plastic scintillator-based neutron detectors, pursued through academic and industrial collaborations, bears the potential to replace ³He counters in a growing number of applications. In this last section, we shall focus on a few practical applications where these detectors have already established themselves as mature technological solutions.

3.6.1 *Homeland Security*

A prominent application field for plastic scintillator-based slow neutron detectors is homeland nuclear security [93], which encompasses the countering of special nuclear material (low-, and high-enriched U, Pu) proliferation and smuggling, as well as of the threat posed by radioactive dispersal devices (so-called “dirty bombs”). One of the keystones of the civil security response to these missions lies in the display of radiation portal monitors (RPMs) in public places, critical entry checkpoints, and national borders. Against their liquid counterparts, plastics appear more field deployable for being solid-state, mechanically robust, sealed, and non-fusible media, which has been increasingly driving industrial solutions toward plastic scintillator-based monitors. For RPMs to detect weak static or moving neutron radioemitters, however, the scale-up of the sensitive medium is required, up to the order of 10 dm^3 at least, which tends to exclude the homogenous loading of the plastic scintillator with strong neutron absorbers. This is the reason why most proofs of concept in this topic involved multiplicity-, or capture-gated Gd-lined [52, 94], and Cd-lined [20, 95] plastic scintillators, whose figures of merit complied with the applicable standards [54] in RPM qualification.

Aside from large fixed RPMs, transportable neutron detectors may be displayed as part of the homeland security response. Due to their low intrinsic efficiencies, such detectors will prove themselves useful whenever long enough counting times, typically between the orders of 10^2 to 10^3 s, are operationally acceptable [96]. Such plastic scintillator-based slow neutron monitors include, for instance, PHD and multiplicity-gated Bonner sphere-like Gd-lined plastic scintillator [51], as well as PHD and capture-gated boron-loaded plastic scintillator [97].

3.6.2 *Neutron Flux Monitoring and Source Characterization*

Plastic scintillators incorporating neutron converters have also received attention in the field of neutron source flux monitoring and characterization.

An important application of neutron irradiators is boron neutron capture therapy (BNCT), a cancer treatment targeting brain tumors and melanoma. The procedure involves the introduction of ^{10}B into tumor cells and subsequent irradiation with thermal or epithermal neutrons. The absorption reactions taking place in the cells release high-energy ions, whose LET allows for selective destruction of the tumor. In order to monitor in real time the neutron dose that is absorbed by a patient and converted into the said ion products, a compensated boron-loaded plastic scintillator coupled with an optical fiber [49] was introduced. The detector was used as part of two clinical trials at the heavy water neutron irradiation facility of the Kyoto University Reactor (KUR) and delivered estimates of the thermal neutron within a 10% agreement with standard Gd foil activation results (above a $1 \cdot 10^6 \text{-n cm}^{-2} \text{ s}^{-1}$ flux).

Another application relates to the determination of neutron emission properties, especially multiplicity, when dealing with fission or fusion sources with large-scale Gd-lined plastic scintillator [38, 98]. As an example, the above-referenced NSTAR module was applied to the determination of neutron multiplicity in fusion-based neutron generators. The so-called multi-hit capability, in other words, the power of resolving multiple neutrons emitted in a burst, was tested with a 10-Hz pulsed small deuterium–deuterium neutron generator. Mean multiplicities of 3.4 ± 0.5 , 9.5 ± 1.2 , and 13.7 ± 1.7 were estimated for 30, 60, and 80 μA -beam currents, respectively, thus verifying a proportionality relation of about $0.15 \pm 0.03 \mu\text{A}^{-1}$ (under up to a $7 \cdot 10^{-4} \text{n s}^{-1}$ emission rate).

3.6.3 Reactor Antineutrino Experiments, Surveillance, and Monitoring

To conclude, we describe an application of plastic scintillator-based slow neutron detectors that have been gaining momentum over the past decade, namely reactor antineutrino experiments. Neutrino experiments are designed to measure or bound the value of the θ_{13} mixing angle, a neutron oscillation parameter that governs the flavor change of electron antineutrinos. In practical experiments, angle θ_{13} is observed using the antineutrino (labeled) flux emitted as part of beta minus decays in nuclear fission reactors. For neutral electron antineutrinos to be detected, they must firstly interact with a large target that is rich in hydrogen nuclei, according to the inverse beta decay equation



The antineutrino is then detected indirectly through the annihilation of the β^+ -positron and the delayed capture of the neutron, with the time correlation of both signals increasing the rejection ratio between the antineutrino signature and the radiation background signal. Electron antineutrinos being produced along the disintegration chains of ${}^{235}\text{U}$ and ${}^{239}\text{Pu}$, with an average of 6 antineutrinos per fission product beta decay chain [99], they can also be used as a signal of interest for surveilling and monitoring nuclear power plants. As an illustration, these add up to a $2 \cdot 10^{20} \text{s}^{-1}$ electron antineutrino emission rate for an operating 1-GWt power plant. The neutron detectors that are classically used in this context take the form of very-large-scale (>100 tons), homogeneously Gd-loaded liquid scintillators, such as the ones introduced as part of the Double Chooz [100] and Daya Bay reactor antineutrino experiments [101]. Recent work has dealt with the conception of a large, Gd-coated [37], or loaded [102] plastic scintillator aimed at the same application. As an illustration, we may consider the mobile and adaptable PANDA detector that incorporates Gd in a heterogeneous fashion. A 360-kg prototype was built and set at sea level, within 36 m of the 3.4 GWth reactor of Ohi Power Station (Kansai Electric Power

Co., Inc.), as reported by Oguri et al. [103]. A $22 \pm 11 \text{ c day}^{-1}$ count rate difference was obtained experimentally when the reactor went from ON to OFF state, consistent with the theoretical 3.4% intrinsic antineutrino detection efficiency that was calculated by the authors. Laboratory studies were additionally carried out with ^6Li -coated segmented plastic scintillators [104]. The reader can refer to Chap. 15 for other examples.

Acknowledgements The authors would like to thank Dr. Clément Lynde and Dr. Matthieu Hamel, from CEA List, for their decisive help in writing this chapter.

References

1. T.W. Crane, M.P. Baker, Neutron detectors, passive non-destructive assay of nuclear materials, Springfield VA, National Technical Information Service, 379 (1991)
2. G. Knoll, *Radiation Detection and Measurement*, 4th edn. (Wiley, New York, 2010), p. 519
3. J. Byrne, *Neutrons, Nuclei and Matter: An Exploration of the Physics of Slow Neutrons* (Dover Publications Inc., New York, 2011), p. 36
4. G. Knoll, *Radiation Detection and Measurement*, 4th edn. (Wiley, New York, 2010), p. 19
5. J. Terrel, Phys. Rev. **113**(2), 527 (1958)
6. B.E. Watt, Phys. Rev. **87**(6), 1037 (1952)
7. N. Ensslin, W.C. Harker, M.S. Krick, D.G. Langner, M.M. Pickrell, J.E. Stewart, *Application Guide to Neutron Multiplicity Counting, LA-13422-M* (Los Alamos National Laboratory, 1998)
8. B.C. Anderson, K.E. Holbert, H. Bowler, Sci. Technol. Nucl. Install. **12**, 1 (2016)
9. B. Goddard, S. Croft, A. Lousteau, P. Peerani, Nucl. Instr. Methods A **830**, 256 (2016)
10. J.W. Marsh, D.J. Thomas, M. Burke, Nucl. Instr. Methods A **366**(2), 340 (1995)
11. H.R. Vega-Carrillo, E. Manzanares-Acuña, A.M. Becerra-Ferreiro, A. Carillo-Nuñez, Appl. Radiat. Isot. **57**(2), 167 (2002)
12. R.T. Kouzes, E.R. Siciliano, J.H. Ely, P.E. Keller, R.J. McConn, Nucl. Instr. Methods A **584**(2–3), 383 (2008)
13. Y. Peneliau, O. Litaize, P. Archier, C. De Saint Jean, Nucl. Data Sheets **118**, 459 (2014)
14. M. Joyce, *Nuclear Engineering: A Conceptual Introduction to Nuclear Power* (Butterworth-Heinemann, Oxford, 2018), p. 111
15. P. Reuss, *Neutron Physics* (EDP Sciences, Oakland, 2008), p. 97
16. N. Soppera, M. Bossant, E. Dupont, Nucl. Data Sheets **120**, 294 (2014)
17. M.B. Chadwick, L.J. Cox, P.G. Young, A.S. Meigooni, Nucl. Sci. Eng. **123**(1), 17 (1996)
18. Saint-Gobain Crystals website, www.crystals.saint-gobain.com/products/bc-408-bc-412-bc-416. Accessed 07 Oct 2020
19. Eljen Technology website, eljentechnology.com/products/plastic-scintillators/ej-200-ej-204-ej-208-ej-212. Accessed 07 Oct 2020
20. Y. Liu, Y.-G. Yang, Y. Tai, Z. Zhang, Chin. Phys. C **40**(7), 1 (2016)
21. P. Baeten, M. Bruggeman, R. Carchon, Safeguards Project Nuclear Research Centre SCK CEN, Mol, BLG-732, February 1997
22. G.H.V. Bertrand, M. Hamel, S. Normand, F. Sguerra, Nucl. Instr. Methods A **776**, 114 (2015)
23. E.V. Ryabeva, V.V. Kadilin, V.A. Idalov, At. Energy **127**(1), 51 (2019)
24. Y. Sakurai, T. Kobayashi, J. Nucl. Sci. Technol. **39**(S2), 1294 (2002)
25. K. Hagiwara, T. Yano, T. Tanaka, M.S. Reen, P.K. Das, S. Lorenz, I. Ou, T. Sudo, Y. Yamada, T. Mori, T. Kayano, R. Dhir, Y. Koshio, M. Sakuda, A. Kimura, S. Nakamura, N. Iwamoto, H. Harada, M. Wurm, W. Focillon, M. Gonin, A. Ali, G. Collazuol, Progr. Theor. Exp. Phys. **2019**(2), 023D01 (2019)

26. M.A. Ali, V.A. Khitrov, Y.V. Kholnov, A.M. Sukhovoj, A.V. Vojnov, J. Phys. G: Nucl. Part. Phys. **20**(12), 1943 (1994)
27. T. Belgya, L. Szentmiklósi, R. Massarczyk, R. Schwengner, A. Junghans, E. Grosse, EPJ Web Conf. **146**, 05009 (2017)
28. T. Belgya, L. Szentmiklosi, R. Massarczyk, R. Schwengner, G. Schramm, E. Birgersson, A. Junghans, in *Proceedings of the European Research Infrastructures for Nuclear Data Applications (ERINDA) Workshop*, CERN, Geneva, Switzerland, 1–3 Oct 2013
29. V.F. Sears, Neutron News **3**(3), 26 (1992)
30. A.D. Carlson, V.G. Pronyaev, D.L. Smith, N.M. Larson, Z. Chen, G.M. Hale, F.-J. Hambach, E.V. Gai, S.-Y. Oh, S.A. Badikov, T. Kawano, H.M. Hofmann, H. Vonach, S. Tagesen, Nucl. Data Sheets **110**(12), 3215 (2009)
31. B. Pritychenko, E. Bétká, M.A. Kellett, B. Singh, J. Totans, Nucl. Instr. Methods A **640**(1), 213 (2011)
32. M. Berger, J. Coursey, M. Zucker, J. Chang, *ESTAR, PSTAR, and ASTAR: Computer Programs for Calculating Stopping-Power and Range Tables for Electrons, Protons, and Helium Ions (version 1.2.3)* (National Institute of Standards and Technology, Gaithersburg, MD, 2005)
33. S.M. Seltzer, J.H. Hubbell, Tables and graphs of photon mass attenuation coefficient and mass energy-absorption coefficients for photon energies 1 keV to 20 MeV for elements $Z = 1$ to 92 and some dosimetric materials, appendix to invited plenary lecture by J.H. Hubbell “45 Years (1950–1995) with X-ray interactions and applications. Paper presented at the 51st National Meeting of the Japanese Society of Radiological Technology, Nagoya, Japan, 14–16 Apr 1995
34. M.E. Medhat, Y. Wang, Appl. Radiat. Isot. **84**, 13 (2014)
35. N. Ramesh, M. Hawron, C. Martin, A. Bachri, J. Arkansas Acad. Sci. **65**, 67 (2011)
36. A.B. Smith, P.R. Fields, A.M. Friedman, Phys. Rev. **104**(3), 699 (1956)
37. Y. Kuroda, S. Oguri, Y. Kato, R. Nakata, Y. Inoue, C. Ito, M. Minowa, Nucl. Instr. Methods A **690**, 41 (2012)
38. I.A. Pawełczak, J. Töke, E. Henry, M. Quinlan, H. Singh, W.U. Schröder, Nucl. Instr. Methods A **629**, 230 (2011)
39. J.B. Birks, *The Theory and Practice of Scintillation Counting* (Pergamon Press, 1964), p. 185
40. M. Marseguerra, E. Padovani, S.A. Pozzi, Prog. Nucl. Energy **43**(1), 305 (2003)
41. A. Mahl, H.A. Yemam, J. Stuntz, T. Remedes, A. Sellinger, U. Greife, Nucl. Instr. Methods A **816**, 96 (2016)
42. R. Voltz, G. Laustriat, J. Phys. France **29**(2), 159 (1968)
43. N.P. Zaitseva, A.B. Glenn, H.P. Martinez, M.L. Carman, I.A. Pawelczak, M. Faust, S.A. Payne, Nucl. Instr. Methods A **729**, 747 (2013)
44. C. Lynde, E. Montbarbon, M. Hamel, A. Grabowski, C. Frangville, G.H.V. Bertrand, G. Galli, F. Carrel, V. Schoepff, Z. El Bitard, IEEE Trans. Nucl. Sci. **67**(4), 679 (2020)
45. C. Frangville, M. Hamel, E. Montbarbon, G.H.V. Bertrand, A. Grabowski, C. Lynde, Mater. Chem. Front. **3**(8), 1626 (2019)
46. I.A. Pawełczak, A.M. Glenn, H.P. Martinez, M.L. Carman, N.P. Zaitseva, S.A. Payne, Nucl. Instr. Methods A **751**, 62 (2014)
47. C. Frangville, A. Grabowski, J. Dumazert, E. Montbarbon, C. Lynde, R. Coulon, A. Venerosy, G.H.V. Bertrand, M. Hamel, Nucl. Instr. Methods A **942**, 162370 (2019)
48. C. Frangville, A. Grabowski, J. Dumazert, E. Montbarbon, C. Lynde, R. Coulon, A. Venerosy, G.H.V. Bertrand, M. Hamel, Mater. Chem. Front. **3**(8), 1574 (2019)
49. M. Ishikawa, K. Ono, Y. Sakurai, H. Unesaki, A. Uritani, G. Bengua, T. Kobayashi, K. Tanaka, T. Kosako, Appl. Radiat. Isot. **61**, 775 (2004)
50. J. Dumazert, R. Coulon, M. Hamel, F. Carrel, F. Sguerra, S. Normand, L. Méchin, G.H.V. Bertrand, IEEE Trans. Nucl. Sci. **63**(3), 1551 (2016)
51. J. Dumazert, R. Coulon, G. Corre, M. Hamel, Q. Lecomte, V. Kondrasovs, C. Dehé-Pittance, G.H.V. Bertrand, J.-M. Bourbotte, S. Garti, R. Woo, Nucl. Instr. Methods A **954**, 161199 (2020)
52. R. De Vita, F. Ambi, M. Battagliari, M. Osipenko, D. Piombo, G. Ricco, M. Ripani, M. Taiuti, Nucl. Instr. Methods A **617**(1), 219 (2010)

53. S. Normand, B. Mouanda, S. Haan, M. Louvel, IEEE Trans. Nucl. Sci. **49**(4), 1603 (2002)
54. ANSI N42.35-2016, American National Standard for Evaluation and Performance of Radiation Portal Monitors in Homeland Security (2016)
55. R.T. Kouzes, J.H. Ely, A.T. Lintereur, D.L. Stephens, *Neutron Detection Gamma Insensitivity Criteria, Technical Rpt, PNNL-18903* (Pacific Northwest National Laboratory, Richland, 2009)
56. D.A. Abdushukurov, M.A. Abduvokhidov, D.V. Bondarenko, K.K. Muminov, T.A. Toshov, D.Y. Chistyakov, J. Instrum. **2**, P04001 (2007)
57. K.S. McKinnay, T.R. Anderson, N.H. Johnson, in *IEEE Nuclear Science Symposium Conference Record* (2011), p. 553
58. A. Klett, B. Burgkhardt, IEEE Trans. Nucl. Sci. **44**(3), 757 (1997)
59. Z.W. Bell, G.M. Brown, C.H. Ho, F.V. Sloop Jr., Proc. SPIE **4784**, 150 (2002)
60. K. Pritchard, A. Osovitzky, J. Ziegler, E. Binkley, P. Tsai, N. Hadad, M. Jackson, C. Hurlbut, G.M. Baltic, C.F. Majkrzak, N.C. Maliszewskyj, IEEE Trans. Nucl. Sci. **67**(1), 414 (2020)
61. ISO11929-3, Determination of the detection limit and decision threshold for ionizing radiation (2010)
62. G.R. Gilmore, *Practical Gamma-Ray Spectrometry*, 2nd edn. (Wiley, Chichester, 2008), p. 117
63. M. Hamel, G.H.V. Bertrand, F. Carrel, R. Coulon, J. Dumazert, E. Montbarbon, F. Sguerra, in *4th International Conference on Advancements in Nuclear Instrumentation Measurement Methods and their Applications (ANIMMA)*, Lisbon, 20–24 Apr 2015
64. H.A. Yemam, A. Mahl, U. Koldemir, T. Remedes, S. Parkin, U. Greife, A. Sellinger, Sci. Rep. **5**, 13401 (2015)
65. I.G. Britvich, V.G. Vasil'chenko, V.N. Kirichenko, S.I. Kuptsov, V.G. Lapshin, A.P. Soldatov, A.S. Solov'ev, V.I. Rykalin, S.K. Chernichenko, I.V. Shein, Instr. Exp. Techn. **45**(5), 644 (2002)
66. V.V. Porosev, G.A. Savinov, J. Instrum. **14**, P06003 (2019)
67. G.I. Britvich, V.G. Vasil'chenko, Y.V. Gilitsky, A.P. Chubenko, A.E. Kushnirenko, E.A. Mamidzhanyan, V.P. Pavlyuchenko, V.A. Pikalov, V.A. Romakhin, A.P. Soldatov, O.V. Sumaneev, S.K. Chernichenko, I.V. Shein, A.L. Shepetov, Instr. Exp. Techn. **47**(5), 571 (2004)
68. A. Mahl, H.A. Yemam, R. Fernando, J.T. Koubek, A. Sellinger, U. Greife, Nucl. Instr. Methods A **880**, 1 (2018)
69. N.J. Cherepy, R.D. Sanner, P.R. Beck, E.L. Swanberg, T.M. Tillotson, S.A. Payne, C.R. Hurlbut, Nucl. Instr. Methods A **778**, 126 (2015)
70. A. Mabe, A. Glenn, M.L. Carman, N. Zaitseva, S.A. Payne, Nucl. Instr. Methods A **806**, 80 (2016)
71. R.D. Breukers, C.M. Bartle, A. Edgar, Nucl. Instr. Methods A **701**, 58 (2013)
72. A.N. Mabe, M.J. Uffner, D. Penumadu, G.K. Schweitzer, L.F. Miller, Radiat. Meas. **66**, 5 (2014)
73. I.B. Nemchenok, N.A. Gundorin, E.A. Shevchik, A.A. Shurenkova, Funct. Mater. **20**(3), 310 (2013)
74. I.B. Nemchenok, A.A. Shurenkova, V.B. Brudanin, N.A. Gundorin, V.V. Timkin, Bull. Russ. Acad. Sci. Phys. **76**(11), 1187 (2012)
75. J.B. Czirr, Nucl. Instr. Methods **108**(3), 613 (1973)
76. V.B. Brudanin, V.I. Bregadze, N.A. Gundorin, D.V. Filossofov, O.I. Kochetov, I.B. Nemtchenok, A.A. Smolnikov, S.I. Vasiliev, Phys. Part. Nucl. Lett. **109**(6), 69 (2001)
77. L. Ovechnika, K. Riley, S. Miller, Z. Bell, V. Nagarkar, Phys. Procedia **2**(2), 161 (2009)
78. G.H.V. Bertrand, J. Dumazert, F. Sguerra, R. Coulon, G. Corre, M. Hamel, J. Mater. Chem. C **3**, 6006 (2015)
79. S.M. Carturan, M. Degerlier, G. Maggioni, T. Marchi, F. Gramegna, M. Cinausero, L. Stevanato, M. Vesco, A. Quaranta, Acta Phys. Pol. A **134**(1), 405 (2018)
80. A.M. Williams, P.A. Beelev, N.M. Spyrou, Radiat. Prot. Dosim. **110**(1–4), 497 (2004)
81. D.M. Slaughter, C.R. Stuart, R.F. Klaas, D.B. Merrill, IEEE Trans. Nucl. Sci. **63**(3), 1650 (2016)
82. C.L. Wang, L. Gou, J.M. Zaleski, D.L. Friesel, Nucl. Instr. Methods A **622**(1), 186 (2010)

83. W. Cai, Q. Chen, N. Cherepy, A. Dooraghi, D. Kispaugh, A. Chatzioannou, S. Payne, W. Wang, Q. Pei, J. Mater. Chem. C **1**(10), 1970 (2013)
84. K.D. Ianakiev, M.T. Swinhoe, A. Favalli, K. Chung, D.W. MacArthur, Nucl. Instr. Methods A **652**, 417 (2011)
85. M. Katagiri, K. Sakasai, M. Matsubayashi, T. Nakamura, Y. Kondo, Y. Chujo, H. Nanto, T. Kojima, Nucl. Instr. Methods A **529**(1), 274 (2004)
86. H. Friedrich, V. Dangendorf, A. Brauning-Demian, Appl. Phys. A **74**, 124 (2002)
87. K.S. Lee, S.H. Ahn, B. Hong, M. Ito, T.I. Kang, B.I. Kim, H.C. Kim, J.H. Kim, K.B. Lee, S. Park, M.S. Ryu, K.S. Sim, J. Korean Phys. Soc. **48**(4), 846 (2006)
88. A. Foster, A. Meddeb, M. Wonders, M. Flaska, M. Sharma, Z. Ounaises, I. Jovanovic, Nucl. Instr. Methods A **954**, 161681 (2020)
89. J. Dumazert, R. Coulon, Q. Lecomte, G.H.V. Bertrand, M. Hamel, Nucl. Instr. Methods A **882**, 53 (2018)
90. C.E. Kim, R.J. Hu, B. Hong, H.-C. Kim, S. Lee, K.S. Sim, S.J. Hong, Y.J. Kim, J. Korean Phys. Soc. **52**(3), 908 (2008)
91. D.A. Shea, The helium-3 shortage: supply demand and options for Congress, Congressional Research Service (2010)
92. Managing critical isotopes, weaknesses in DOE's management of helium-3 delayed the federal response to a critical supply shortage, GAO-11-472, U.S. Government Accountability Office, Washington D.C. (2011)
93. R.C. Runkle, A. Bernstein, P.E. Vanier, J. Appl. Phys. **108**(11), 1101 (2010)
94. E. Fanchini, IEEE Trans. Nucl. Sci. **33**(1), 392 (2016)
95. G. Sannié, V. Kondrasov, G. Corre, K. Boudergui, B. Perot, in *4th International Conference on Advancements in Nuclear Instrumentation Measurements Methods and their Applications (ANIMMA)*, Lisbon, Portugal, 20–24 Apr 2015
96. P. Holm, K. Peräjärvi, H. Toivonen, J. Nilsson, T. Gäfvert, M. Boucher, J. Dipple, M. Foster, J. Häkkinen, M. Iwatschenko-Borho, NOVE: novel neutron detection methods for nuclear security—dynamic testing, NKS-342, July 2015
97. P. Holm, K. Peräjärvi, S. Ristkari, T. Siiskonen, H. Toivonen, Nucl. Instr. Methods A **751**, 48 (2014)
98. C. Roecker, A. Bernstein, N.S. Bowden, B. Cabrera-Palmer, S. Dazeley, M. Gerling, P. Marleau, M.D. Sweany, K. Vetter, Nucl. Instr. Methods A **826**, 21 (2016)
99. P. Huber, Phys. Rev. C **84**, 024617 (2011)
100. C. Aberle, C. Buck, B. Gramlich, F.X. Hartmann, M. Lindner, S. Schönert, U. Schwan, S. Wagner, H. Watanabe, J. Instrum. **7**(06), 6008 (2012)
101. W. Beriguete, J. Cao, Y. Ding, S. Hans, K.M. Heeger, L. Hu, A. Huang, K.-B. Luk, I. Nemchenok, M. Qi, R. Rosero, H. Sun, R. Wang, Y. Wang, L. Wen, Y. Yang, M. Yeh, Z. Zhang, L. Zhou, Nucl. Instr. Methods A **763**, 82 (2014)
102. S. Ozturk, Nucl. Instr. Methods A **955**, 163314 (2020)
103. S. Oguri, Y. Kuroda, Y. Kato, R. Nakata, Y. Inoue, C. Ito, M. Minowa, Nucl. Instr. Methods A **757**, 33 (2014)
104. S.D. Kiff, N. Bowden, J. Lund, D. Reyna, Nucl. Instr. Methods A **652**, 412 (2011)



Dr. Jonathan Dumazert received his M.Sc. degree in Photonics from Imperial College London (UK) in 2013 and Ph.D. in nuclear physics and instrumentation from the University of Caen Normandie (France) in 2016. Since 2016, he holds a permanent position at the French Atomic Energy Commission (CEA) as a researcher. His work deals with isotopic analysis from activation reactions, the conception of nuclear instruments for the needs of radioprotection and dismantling, as well as signal processing and data treatment for reactor safety and CBRNE applications. He also takes part in the coordination of scientific research on particle-discrimination schemes in mixed fields, through international publications and patent depositions (h-index 7; 21 publications, 8 patents).



Dr. Camille Frangville received her M.Sc. degree in Chemistry and Nano Sciences from Ecole Nationale Supérieure de Chimie de Rennes (France) in 2012 and PhD in Nano Sciences for theranostic in 2015. After 3 years of post-doctoral fellowship at the French Atomic Energy Commission (CEA), she holds now a permanent position. Her work deals with chemical tunability and industrial transfers of plastic scintillators as well as radiophysical monitoring, data processing, and prototyping addressing civil nuclear safety to homeland security. (h-index 4; 15 publications; 3 patents).

Chapter 4

Chemical Approach on Organometallic Loading in Plastic Scintillators and Its Applications



Guillaume H. V. Bertrand  and Matthieu Hamel 

Abstract In this chapter, we present an overview of the field of plastic scintillation through a chemical point of view. More particularly, we focus on their design by the homogenous incorporation of organometallic dopant in the wide sense of the term. This chapter is organized into sections representing the main application and the associated choice of metal dopant. We present and evaluate in these contexts different chemical strategies, focusing on the inherent tradeoff that come with loading a plastic scintillator with organometallics. Examples of applications and successful transfers are also shown to motivate and encourage the community to explore this field.

4.1 Introduction/Context

4.1.1 Plastic Scintillation

Plastic scintillator, as described in this book, is a very powerful tool for radiation measurements. Out of all other technologies, it is the most versatile in terms of shape and available quantity. As with most technologies, there is also tradeoff. Plastic scintillator is among the less efficient in terms of energy resolution, density and energy conversion. Nevertheless, its price and availability makes it the most used conversion material. Since its inception in the 1950s, plastic scintillator research focuses on the amelioration of its properties by several approaches coming from material science, optics, or chemical design. Among this last category, several chemical modifications of the plastic scintillator formulation have produced critical advances for the field [1, 2 and Chap. 1 of this book]. Hence, a new and powerful way of rationalizing plastic scintillator emerged: application-driven chemical design. Especially since 2000s, plastic scintillator formulation and composition were tailored towards a specific use, in order to increase an otherwise poor response. We can notably cite here the early

G. H. V. Bertrand  · M. Hamel
Université Paris-Saclay, CEA, List, 91120 Palaiseau, France
e-mail: guillaume.bertrand@cea.fr

conception of plastic scintillator able to discriminate radiation type (beta/gamma, fast neutron/gamma) and the recent advances made possible by modern chemistry.

Plenty of approaches are viable, but we will detail here only the ones concerning the use of organometallic molecules as a part of the plastic scintillator formulation. Numerous metal nuclei are interesting in nuclear instrumentation and chemists around the world tried to take advantage of their properties to further the performances of plastic scintillators.

4.1.2 Frame of This Chapter

As mentioned above we will focus on the use of organometallic complexes in plastic scintillator. The notion of organometallic is here a wide one as it encompasses also alkali metal (Li) and metalloid (B). We will not treat their use in liquid scintillator, a very close cousin but we will give some examples and references in the last table in Sect. 4.6 of this chapter. We will also restrain this part to homogenous doping, meaning that hybrid organic/inorganic scintillator is out of the scope of this chapter and will be considered in Chap. 6 instead. Nanoparticles are also here excluded but they have already been discussed elsewhere [3, 4].

Other parts of the book will also overlap with this chapter, especially thermal neutron detection, we will try to cover the subject with a more chemical approach in order to give an overview of the subject and to give the reader the keys to understand this field, as more expert and precise developments will be described in these chapters.

4.1.3 Properties Optimization

The two first order parameters in plastic scintillator measurements are the counting rate and the scintillation yields.

Counting rate: It is directly linked to the probability of an interaction between an ionizing particle and the scintillator. In case of alpha and beta, the counting rate is defined by the thickness of the scintillator and any shielding factor (cladding, reflective paint, etc.), generally outside of thin film or scintillating fibers there is no need for optimization here. However, for gamma or neutrons, counting rate in plastic is less than ideal due to various second-order factors.

- Low photoelectric interaction (gamma <0.1 MeV): plastic scintillators are mainly made from low Z atoms such as C and H.
- Compton scattering (gamma): plastic scintillators have a low overall density ($\approx 1.1 \text{ g/cm}^3$) and their low Z composition impacts a lot on their actual electron density.
- Thermal neutron capture: C and H and their natural isotopes do not have an efficient cross section.

- Fast neutron: The high concentration of hydrogen atoms makes them a decent thermalizer. This can be enhanced by using large volume of scintillator. Despite that, measurement is difficult as fast neutron signals are very hard to separate from a gamma signature in plastic scintillators that have not been chemically modified for that purpose.

Scintillation yield: It is characteristic of the scintillator ability to convert energy from an ionization event into a pulse of detectable photons. It is noteworthy that the gold standard in term of scintillation yield is the EJ-200 plastic scintillator with a yield of 10,000 ph/MeV. If we assume an emission centered at 420 nm (2.952 eV), the global energy yield of EJ-200 is below 3%. This implies that the scintillation process is less efficient than other scintillators (liquid, inorganic, single crystal...), and it leads us to second-order parameters responsible for these losses. They are numerous ranging from electronic mobility to photophysical properties.

- Constant ionization thermalization: energy dissipated by heat during the ionization process. This comprises intermolecular kinetic dissipation and intramolecular vibronic dissipation.
- The capacity of the medium (herein the polymer matrix) to efficiently transfer excitons towards a primary fluorophore before they are lost.
- The quantum yields of the primary/secondary fluorophore duet.
- The self-absorption process.
- The photon collection efficiency.
- In the case of fast neutron detection: the ability to perform Triplet-Triplet Annihilation (TTA, see Chap. 2).

For each of these inputs, chemical modifications of the polymeric medium and the fluorophore(s) will have an effect on the overall properties of the plastic scintillator. Through this chapter, we will keep in mind that a design improvement on one of these factors is very hard to obtain alone without altering some other parameters.

4.1.4 Chemical Design and Material Science, What the Loading Implies

Plastic matrices, and especially styrene-based polymers, can incorporate a variety of dopant molecules. Through this book, the loading with 0.01 to 30 weight percent (hereafter abbreviated as wt%) of multiple aromatic fluorophores is the core idea behind plastic scintillation counting. As mentioned earlier, plastic scintillator is not an ideal sensor but often the only one suitable for a designated application. There is a strong incentive to find additives or dopants that will improve its property in a desired direction.

Loading with organometallics is often described as X wt% of atom Y in the scintillator. This is relative to the proportion of mass that represents the metal in

the final material but it does not directly represent the amount of organometallic complex used in the process, since the molecular weight of the metal is a fraction of the organometallic complex. That is why when a loading is described as 1 wt% of atom Y in a plastic scintillator, the dopant itself, the organometallic compound, can represent between 1.5 and 10% of the total mass. This is especially true for lithium, its low atomic number being disadvantageous since large organic moieties may “dilute” the lithium percentage in the global proportion. The reader needs to bear in mind that in most applications researchers are looking for the maximum loading possible sometimes aiming over 10 wt% of an element in a plastic scintillator.

Since plastic scintillators are mainly composed of carbon and hydrogen, there is a strong incentive to look elsewhere in the periodic table to find atoms with interesting properties. This implies for a large majority of the elements an organometallic complex to ensure solubility in polymeric matrices. This is the first major roadblock where chemist input is invaluable as the design of organometallic compounds is a flexible way to incorporate homogeneously the targeted metal in a plastic scintillator. Organometallic solubility in styrene and stability towards temperature and polymerization conditions dictate the technical specifications for the chemist. Nevertheless, on several occasions, the targeted elements incorporation is too weak in classical polystyrene scintillator. This can be circumvented by adding a copolymer to change the polarity of the medium and increase the incorporation of organometallic.

Inclusion of organometallics is often harmful for the scintillation yields for different reasons:

- Organometallics are often non-emissive, they trap excitons due to wide orbital and spin-orbit coupling, this favoring charge separation and non-radiative decay by vibrational mode. Some organometallics on the other hand are designed to be emissive, and are an area of interest that we will treat below.
- Organometallic complexes are often comprised of a charged metal atom stabilized by ligand. This strong local dipole is another trap for charged species and excitons by Coulombian interaction.
- They often present large absorption bands and favor self-absorption.
- Undesired aggregation/non-homogenous dispersion leads to turbidity.

These parameters are also subject to chemical design and fine-tuning. It is a fine line to thread upon to balance improvement in one sector without totally harming the scintillation process. Nevertheless, we will show herein that organometallics are the only way to allow unprecedented features to plastic scintillators that obviously would not be available with regular plastics.

4.1.5 Organization of This Chapter: Application Driven

It is in this spirit of plastic scintillator design for specific application that we will unfold this chapter. The method here is to present the area of interest, its challenge and the solution brought by organometallic loading and the chemical design behind

it. The reader will nonetheless find at the end of this chapter a table by element with significant application.

4.2 Scintillation Process Enhancement

4.2.1 Triplet Harvesting

After an ionization event, the energy is distributed in the medium as ionized molecules recombine with available free charge carriers to form high order excitons. They thermally decay toward a low-energy exciton S_1 or T_1 , respectively the LUMO singlet and triplet exciton, who differ by the spin matching between the HOMO and the LUMO of the excited molecule. Triplet state radiative decay is a forbidden transition so triplet state tends to be long-lived and overall more susceptible to undergo non-radiative decay and thus loss of information [5]. Photophysics of plastic scintillator tells us that between 50 and 75% of the excitation from an ionization event ends up producing triplet states [6]. Research hence focuses to introduce triplet harvesting and emissive organometallics in the matrices in order to increase the scintillation yield.

4.2.2 Iridium Complexes

Triplet harvesting is greatly investigated in various fields of material science. Among all the molecules investigated, phenylpyridine iridium complexes¹ stand out as very efficient triplet stabilizer. The polycyclic aromatic ligand acts as an antenna for exciton and the iridium center stabilizes triplet excited states owing to its strong spin-orbit coupling and rigid complex geometry. Some of the most accessible complexes (Fig. 4.1) were tested as dopant for plastic scintillator with a great scintillation yield.

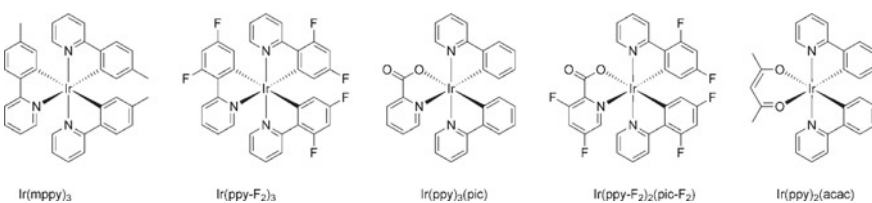


Fig. 4.1 Non-exhaustive examples of iridium complexes used in plastic scintillator for triplet harvesting

¹Topological representation and key information of these molecules is given in the Appendix section at the end of the book.

Overall, the approach is efficient on small-scale sample, with scintillation yields 1.7 times the yields of EJ-208 for 1 cm³ samples [7–10] and only when measured with beta radioluminescence techniques.

The use of iridium complexes also enables an interesting feature in poly(*N*-vinylcarbazole) (PVK)-based scintillator. PVK is intrinsically fluorescent at 420 nm, and the addition of 0.2 wt% of Ir(ppy)₂(acac) creates another emission at 515 nm. It was proven that these two emissions did not show up in same amount when excited by different types of radiation [9]. It is noteworthy to mention this Spectral Shape Discrimination (SSD) that works with other Iridium compounds. The authors of this study mention that the necessary development for this very promising discrimination technique is the use of chromatic sensitive PMT and the creation of dedicated electronics.

There is nonetheless drawback to the use of Iridium complexes. One is its emission lifetime (pulse decay time) around 1 μ s compared to the usual 2 ns from EJ-200 and other organic-based fluorophores. This involves a dedicated electronic to record such long and therefore weak signals. Another drawback is that Iridium complexes adsorb a lot of light and their Stokes shift is not large enough to avoid self-absorption, making samples intensively colored (Fig. 4.2). Despite their high quantum yield, repeated absorptions/re-emissions tend to further lengthen the pulse and decrease the perceived scintillation yield, which is below 7,800 ph MeV⁻¹, when measured with gamma pulse height spectra (Fig. 4.3). This effect is a function of the thickness of the sample and the iridium concentration, which will constrain the range of shape for the scintillator. One last drawback is the presence of constant background



Fig. 4.2 Plastic scintillators loaded with different Iridium complexes and showing different emission wavelength. Top left is the unloaded scintillator

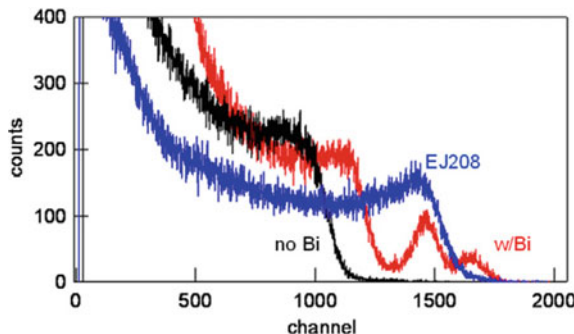


Fig. 4.3 Comparison between a classical plastic scintillator (EJ-208, in *blue*), plastic scintillator loaded with Ir complex (*black*) and plastic scintillator loaded with Ir and Bi (*red*) (reproduced from [8] with permission from IOP)

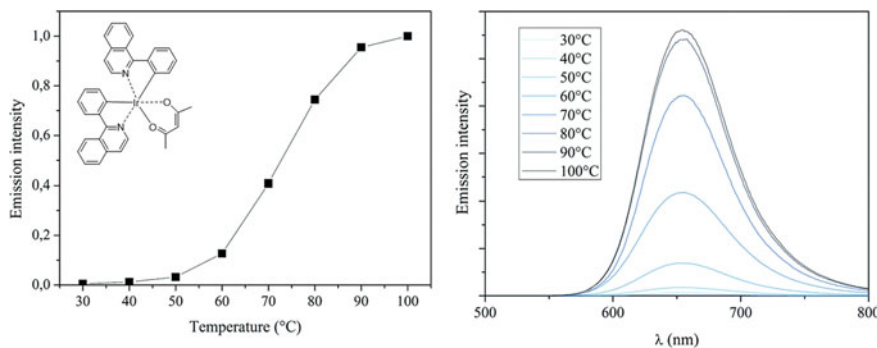


Fig. 4.4 Thermoluminescence of $\text{Ir}(\text{piq})_2(\text{acac})$ loaded plastic scintillator (reproduced from [11] with permission from the Royal Society of Chemistry)

with these complexes as some of them are thermoluminescent (Fig. 4.4) [11]. This makes baseline difficult to evaluate and can artificially increase the perceived scintillation yield. Temperature dependence also implies a temperature-dependent energy calibration.

4.2.3 Europium Complexes

Most of europium complexes have an intrinsic narrow fluorescence at 615 nm due to a 4f–5d transition. This emission has usually a 20% quantum yield but some complexes, and notably the 1,10-phenanthroline based one, have a quantum yield over 50%, which makes them good candidates for scintillation applications. Like the

iridium complexes described above, 1,10-phenanthroline ligand acts as antenna for exciton.

In particular, $\text{Eu}(\text{dbm})_3\text{phen}$ was used at concentrations up to 3 wt% loading in plastic scintillator in order to increase the detection of ionization events with a high density of deposited energy. This application makes sense as excited europium complexes have relatively long lifetimes (around $1 \mu\text{s}$); hence a very stable excited state allows to “flatten” the pulse from an incoming ionization. This was used to detect alpha with a very good light output [12] and also to increase fast neutron/gamma discrimination of plastic scintillator [13]. A book chapter is dedicated to the use of Europium complexes for scintillation counting [14].

4.3 Photon Detection

4.3.1 Theory

Plastic scintillators are inherently not a good choice of material to stop high-energy photons. They are composed mainly of carbon and hydrogen, which implies a low electronic density and hence low probability of Compton interaction. Carbon and Hydrogen are also among the lightest atoms, which make them less susceptible to undergo a photoelectric event with gamma energy over 100 keV. This is often mentioned as a low Z_{eff} material problem, since the highest the average atomic number of the material, the higher its probability to generate Photoelectric (PE) interactions (Fig. 4.5). PE events are particularly interesting in the field of nuclear instrumentation as they reflect the total energy of the incoming radiation, hence

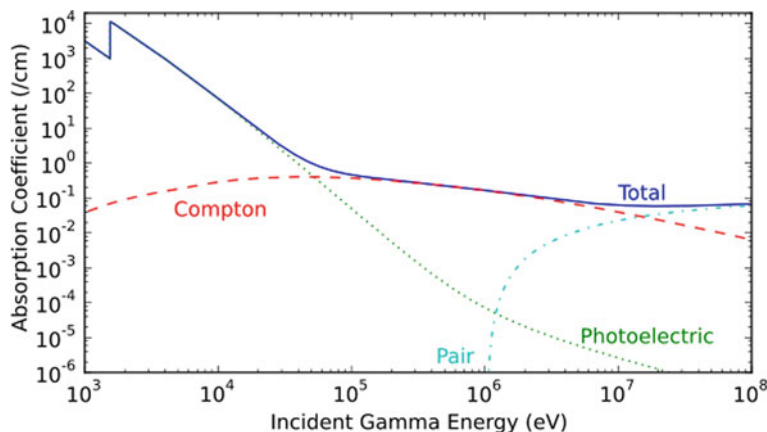


Fig. 4.5 Probability of a photon (gamma)/matter interaction in aluminum and its associated nature: Compton scattering, photoelectric effect and pair production (with permission of Joshua Hykes, CC BY-SA 3.0)

making possible spectrometry analysis. Finally, packing and loose organization of molecules inside a plastic scintillator also affect its density making the two above-mentioned paths of interactions (Compton and PE) even less probable.

These three factors: electronic density, Z_{eff} , and molecular packing are targets of choice to improve the rate of interaction between a scintillator and a photon. Ideas emerged in two different contexts: X-ray detection (high-energy photon from fluorescent or bremsstrahlung phenomenon), and gamma-ray detection: high-energy gamma generated by nuclear phenomena (radioactive decay, fission, etc.).

4.3.2 X-ray Detection

X-rays are typically separated in two sub-categories: soft X-rays (100 eV–10 keV) and hard X-rays (10 keV and over). Sources of X-rays are numerous and correspond to several applications: medical, research (synchrotron), material analysis, etc.... Due to this relatively low range of energy, X-ray detection by plastic scintillation is mainly focused on the identification of PE, and in order to increase this rate of interaction, several approaches were tried. One can also mention the recent development in hybrid scintillator (inorganic/organic) and in nanoparticles doping, both of them embedding zones of heavier atoms (higher Z_{eff}) in the plastic scintillator.

However, the oldest and more common approach in this field is the use of organometallic compounds to dope homogeneously the plastic matrix. This gives access to the whole periodic table, and more particularly towards the heavier and non-radioactive atoms at the bottom of it: Lead and Bismuth, which can more efficiently increase the Z_{eff} of the material.

4.3.2.1 Lead Loading

Lead appeared as the first choice for organometallic loading in plastics [15], and was later on extensively studied. Lead doping was achieved with the use of dicarboxylic acid complexes. This is a perfect example to develop one of the main factors to keep in mind while looking for an organometallic dopant: the atom's weight composition. In order to solubilize the metal in the polymer, matrix ligands are chosen to surround the atom (in its plain form but usually as an ion). This ligand shell can be considered as a layer to help a traditionally polar and charged metallic center to be compatible with the non-polar styrene environment. These ligands are typically chosen in a similar way as surfactant with a mono or bidentate group at one end and an aromatic or alkyl chain at the other. This imposes that fragments of the dopant are part of the problem: the ligand will add low Z_{eff} atoms (C, H, O, N) to the medium and often decreases the properties of the scintillator. It also represents an additional mass to evaluate as described earlier. That is the reason why chemists try to minimize the size of the ligand in order to dope more efficiently the scintillator. In the same way, less charged metallic ions are linked to less ligands hence also maximizing the weight

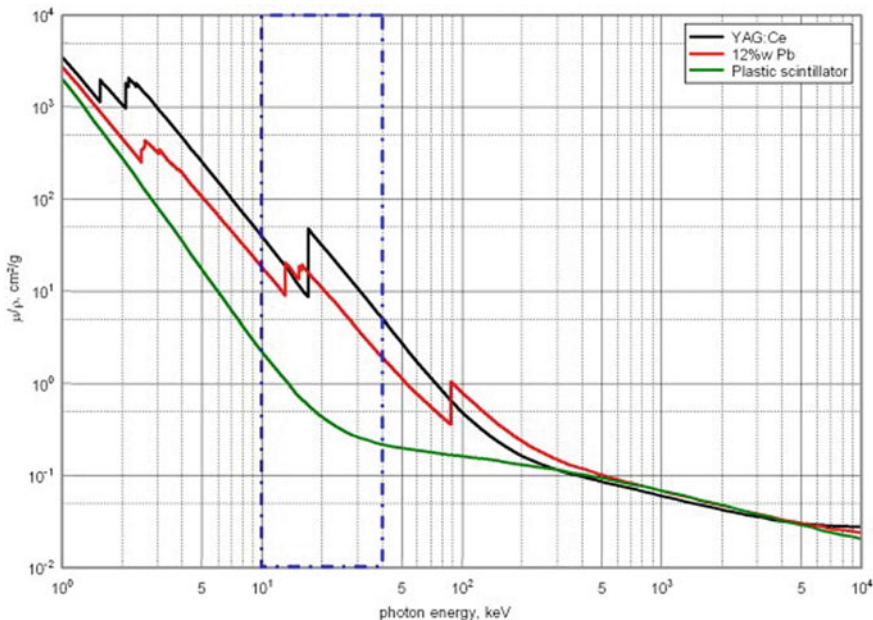


Fig. 4.6 Simulation data on the increase of photoelectric effect due to Pb loading (red) against YAG:Ce (black) inorganic scintillator and standard plastic scintillator (green) (reproduced from [16] with permission from Elsevier)

ratio of the metal. This goes in the same direction as the inherent benefit to have metals with small oxidation degree, as it minimizes the local dipoles and thus charge and exciton trappings.

In the example of lead, loading these considerations work very well to identify good candidates for doping. Scientists quickly converged on lead dimethacrylate as the best candidate, that grants the needed solubility despite its short alkyl chain. Loading up to 27 wt% were achieved [16, 17] and simulation showed (Fig. 4.6) a significant increase of X-ray absorption. This sensor was planned to implement for detection of X-ray burst from a laser-driven fusion event at the Laser Mégajoule Facility in Bordeaux [18, 19].

4.3.2.2 Bismuth Loading

Bismuth is also a potential candidate to increase the Z_{eff} of a material in order to get a higher gamma count rate. As we will develop in the next part, organobismuth compounds represent other challenges in terms of chemical compatibility and design. Bismuth is a very versatile metal that can be used as a salt or a carboxylic complex like a usual metal but also in its bismuthine form. Indeed bismuth can make very stable molecule with C-Bi bonds, and more common of all is triphenylbismuthine:

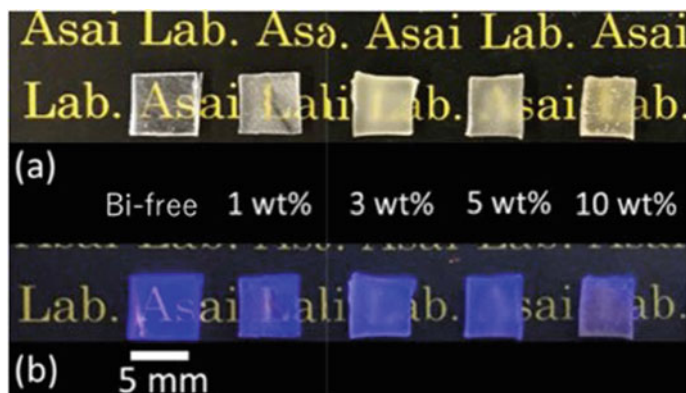


Fig. 4.7 Thin scintillators with BiCl₃ as a dopant **a** under natural light; **b** under UV illumination (reproduced from [21] with permission from Elsevier)

Bi(Ph)₃. All these molecules were tested both in X-ray [20] and in gamma-ray detection [8]. But one research concept stands out here and will shed a new light on a modern approach of metal loading. Koshimizu et al. recently published a paper where BiCl₃ was used to homogeneously load a plastic scintillator. The use of a salt as a doping agent in an apolar matrix like polystyrene is quite a challenge and is usually a discarded strategy. The main reason for that is the low solubility of salt in the apolar monomer. BiCl₃ has nonetheless the huge advantage to have a very high weight content of bismuth (66 wt%), and the Japanese team found an intelligent work around to make it soluble. Instead of synthesizing the material on pot, they dissolved polystyrene and fluorophores in THF and then added a solution of BiCl₃ in highly concentrated HCl. THF is here the perfect intermediate to ensure the miscibility of the entire mixture. They then let the solution evaporate in a controlled temperature environment to obtain the bismuth-loaded scintillator [21]. This ingenious method has nonetheless one drawback as it can only afford relatively small samples ($5 \times 5 \times 1$ mm³) (Fig. 4.7), but it demonstrates very well one elegant approach to metal loading: finding a co-solvent, a co-monomer, or a mediator to ensure the solubility. This method was also applied to a very new entry in the family of metal-doped plastic scintillator: hafnium in polysiloxane matrices [22].

4.3.3 Gamma Detection

Gamma rays cover a large spectrum of energy, ²⁴¹Am is usually the gold standard for low-energy gamma sources at 59 keV, and several common isotope decays produce gamma over 1 MeV (²²Na, ⁶⁰Co, ⁴⁰K, etc.). Traditionally used laboratory sources also encompass ⁵⁷Co (122 keV) and ¹³⁷Cs (daughter at 662 keV). These sources are representative of the typical application for nuclear detection: homeland security,

radioprotection, nuclear fuel cycle, decommissioning, and nonproliferation. This high spectrum of energies implies low to null PE event rate and thus mainly Compton scattering detection, thus precluding any notion of gamma spectrometry. These low interaction rates are what scientists search to bolster by increasing here the Z_{eff} (more PE events and more Compton scattering). It is also worthy to mention here a very closely related strategy aiming at increasing the electronic density, with the replacement of hydrogen atoms by fluorine atoms. Fluorine is the third smallest atom (1st: He, 2nd: Ne), and packed 8 times more electrons than hydrogen. This was implemented to increase the density of the scintillator from 1.05 g cm^{-3} with the associated counting rate efficiency [23]. This density was granted by the use of poly(2,3,4,5,6-pentafluorostyrene).

As for X-rays, lead and bismuth were identified early as an interesting target for this specific application, but historically organotin complexes paved the way to the nowadays understanding of this field. We will develop here the case of tin and bismuth, and the underlying concept behind their usage.

4.3.3.1 Tin Loading

Organotin is a very interesting class of component for organic chemists as it expresses both radical and covalent reactivity. Scientists in the 1960s exploited the family of stable tin compounds that found a new use in plastic scintillation. Similar to bismuth, Sn–C bonds are mostly covalent and their tetravalent nature forces to explore short side chains in order to maximize the weight ratio. Candidates are numerous as described in this survey of 2016 by Sandia National Laboratories at Livermore (Fig. 4.8) [24, 25]. This exploration allowed also to rationalize their use and allow an optimal formulation with 6 wt% of elemental tin and a scintillation yield of 6,700 ph/MeV. These samples (5–10 g) featured PE for ^{241}Am (59.5 keV), ^{137}Cs (662 keV) and even the two gamma emissions of the ^{22}Na (511 keV, 1,274 keV).

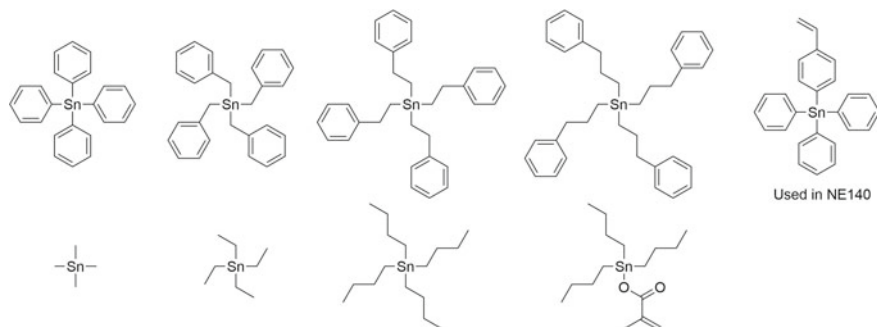


Fig. 4.8 Organotin molecules loaded in plastic scintillators [24] and in NE140 commercial plastic [26, 27]

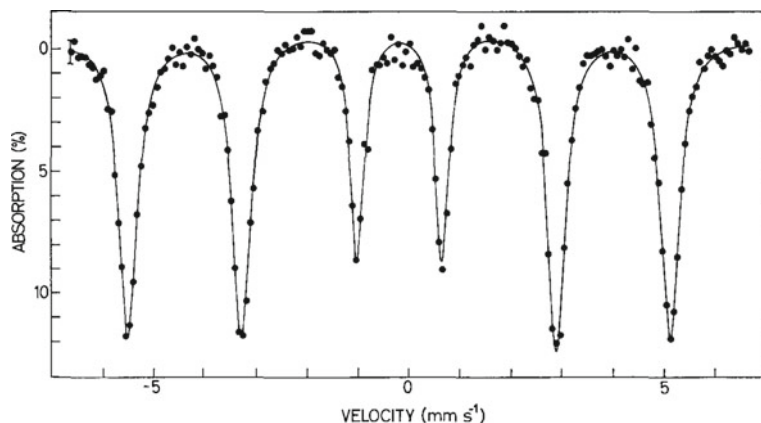


Fig. 4.9 Mössbauer spectrum obtain with a 1 mm thick NE140 plastic scintillator (reproduced from [28] with permission from Elsevier)

These results were built upon the work on tin compound that was made in the late 1960s, early 1970s. These early researches led to the first example of commercial tin-loaded scintillator [26, 27]. In order to ensure the homogenous dispersion and the maximum loading one strategy to dope organometallic compound in a plastic scintillator is to involve it in the polymerization process. This is perfectly represented by the first use of organotin in plastic scintillator. The strategy employed was to add one vinyl group to a side chain of the organotin, and more precisely a styrene group to ensure good incorporation and copolymerization (Fig. 4.8, molecule on the right). This allowed chemists to dope plastic scintillators in the range of 1–10 wt% and observed a large increase of the stopping power towards low-energy gamma rays. This is also the first commercial success of such a scintillator as it was licensed under the trade code NE140 (Nuclear Enterprises), and was widely used in Mössbauer spectroscopy (Fig. 4.9) where it increases the count rate and diminishes the exposition time of samples to gamma radiation [28].

High tin loading was not the perfect solution nonetheless. A major drawback of high metal content in plastic scintillator was discovered then: its nefarious effect on the scintillation yield. It is a compromise that all metal loadings in plastic scintillators need to evaluate, the more you load, the more you increase the count rate but the less your light yield will be. We will cover this phenomenon with our next entry: bismuth loading.

4.3.3.2 Bismuth Loading

As mentioned before in the X-ray section, bismuth is at the same time a very versatile element in terms of chemistry and also the heaviest non-radioactive one, which makes

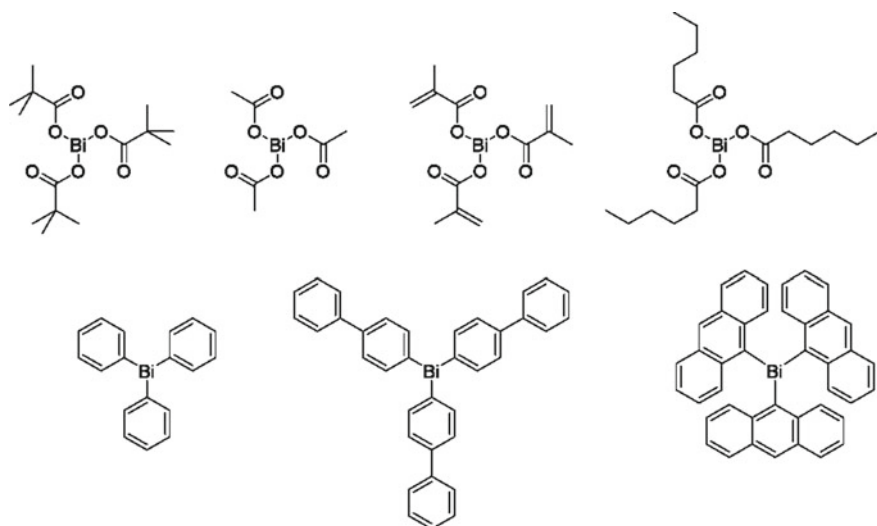


Fig. 4.10 List of organo bismuth compounds tested as dopant in plastic scintillator [8, 29]

it the ideal candidate for increasing the Z_{eff} of a plastic scintillator. Figure 4.10 lists the bismuth-based molecules that were tested for doping plastic matrices.

This large choice gave access to several alleys of experimentation. The goal behind gamma spectroscopy is not only to increase the global counting rate but to gain access to a photoelectric event. As a rule, PE events for gamma energy over 60 keV are not observable for standard plastic scintillator. The ambition of this project is to enable this effect for higher energy gamma rays, more precisely for the detection of ^{57}Co and ^{137}Cs , with, respectively, 122 keV and 662 keV energies. Two separate teams explored this and both indeed observed PE peak in the pulse height spectra (Fig. 4.11) [4, 29, 30].

As shown in Fig. 4.12, loading between 1 and 10 wt% of Bi in a plastic scintillator has the desired proportional effect on the Compton and the PE counting rate validating the concept.

On one hand, bismuth tripivalate and triphenylbismuth are very potent dopants, and on the other hand, a large amount of such molecules has a serious effect on the optical properties of the scintillator. It was explored in depth in order to understand the phenomenon and to find solutions to counteract it. The main effect here and the principal drawback for all metal loadings is the quenching of the luminescence by the introduced metal center. This effect is typically visible in the pulse height spectrum of a loaded scintillator, where the Compton peak is shifted at a lower channel numbers.

The first idea was to combine bismuth loading with iridium metal loading mentioned in Sect. 4.2.2 in order to increase the global light yield and minimize the impact of high bismuth tripivalate loading [7, 31]. As mentioned earlier, this strategy is only viable on small-scale samples. Simple loading with bismuth tripivalate was nonetheless effective and lead to the scale-up of this formulation. They

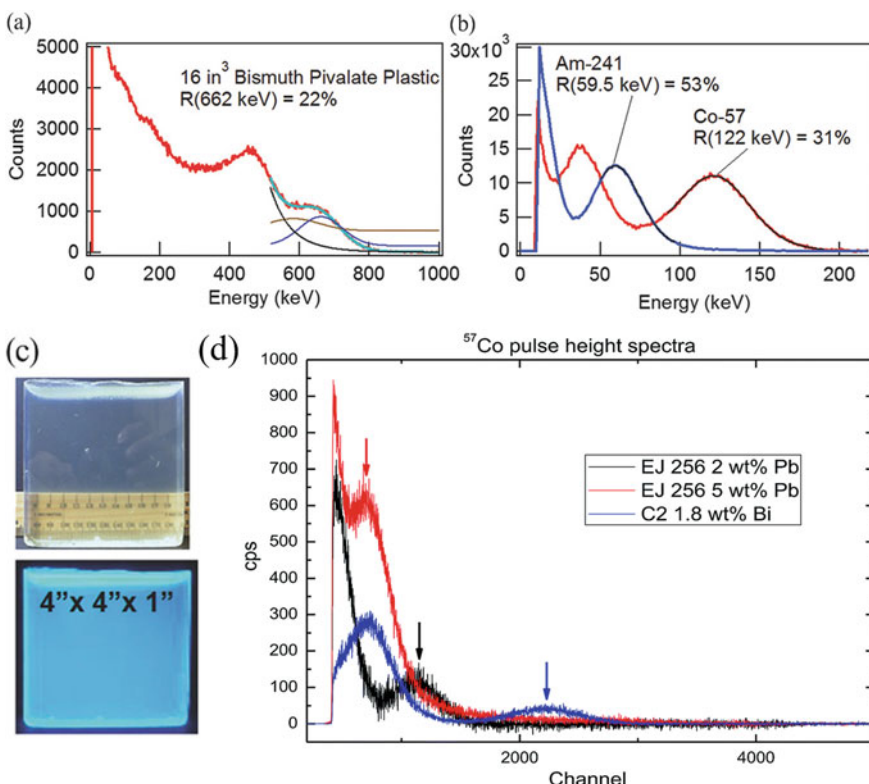


Fig. 4.11 **a** Pulse height spectra of a Bi-loaded scintillator with observation of a photoelectric peak at 662 keV (^{137}Cs). **b** ^{241}Am and ^{57}Co pulse height spectra of the same scintillator. **c** Picture of the material (reproduced from [4] with permission of John Wiley and Sons). **d** Pulse height spectra comparison between commercial Pb loaded scintillators and Bi-loaded scintillator with observation of a photoelectric peak at 122 keV (^{57}Co) (reproduced from [29] with permission from the Royal Society of Chemistry).

produced a 278 cm^3 scintillator containing 8 wt% of elemental bismuth that can be used in a portal monitor set up [32].

The second idea was to adapt the composition of the scintillator to minimize this phenomenon of quenching. Here, we took a page from the tin research presented earlier that focused on tetraphenyltin. Bertrand et al. screened several carboxylic ligands and bismuthane (molecules with a C-Bi bond). The tests turned the research towards triphenylbismuth as a potent candidate, equivalent to the (triphenyl)(*para*-styryl)tin. Like the tin molecules, $\text{Bi}(\text{Ph})_3$ is very similar to the styrene monomer but with three aromatic molecules, making it very soluble and able to reach up to 11 wt% loading. This enables the design of a detector especially sensitive toward gamma rays. This detector is based on a compensation technique, where signal from scintillators with different amount of bismuth are compared to evaluate a proportion of gamma versus a proportion of other ionizing radiation [33].

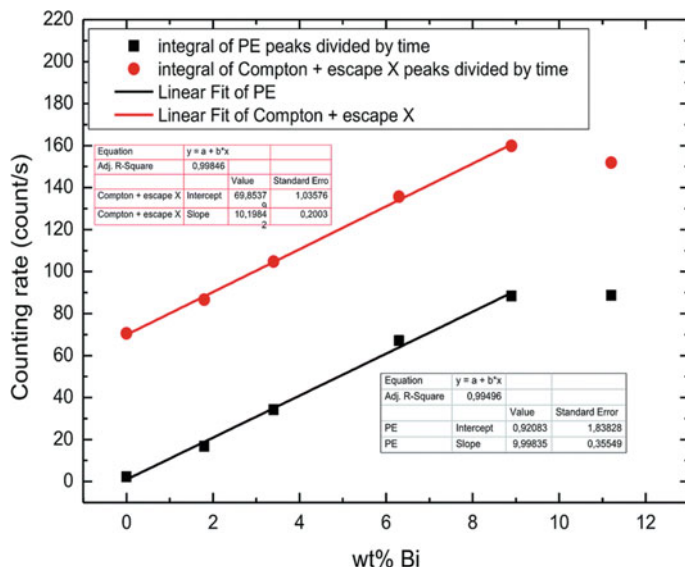


Fig. 4.12 Evolution of the counting rate as a function of the bismuth loading (reproduced from [29] with permission from the Royal Society of Chemistry)

As anticipated, this loading without modification of the matrices has a strong impact on the scintillation yields. $\text{Bi}(\text{Ph})_3$ can become a trap for exciton as it has a very poor photoluminescence quantum yield, hence promoting non-radiative decay of excited state. This was partially overcome by the use of a higher concentration of fluorophores in polystyrene matrices. What is observed is that higher PPO content tends to increase the light output of a loaded scintillator, which is not the case for a pristine one.

In a classic scintillator, optimal PPO content is around 2–3 wt% with no positive effect over 3 wt%. In the case of $\text{Bi}(\text{Ph})_3$ loading, higher concentrations of PPO do increase the scintillation yields (Fig. 4.13), this is attributed to the higher probability to get orbital overlap between a PPO and $\text{Bi}(\text{Ph})_3$ molecule. This favors electronic transfer (Dexter) and “extracts” some of the excitons that were doomed within the $\text{Bi}(\text{Ph})_3$ to give them a chance to decay radiatively. The three phenyl rings play a major role in this approach, as higher concentration of fluorophore was tested with other metal loadings without success. One example of this is the loading with lanthanides that we will discuss in the following section.

4.3.3.3 Lanthanides Loading

Lanthanides complexes have a very peculiar chemistry due to their bonding electronic layer (4f) having a shorter mean radius than already complete orbital (6s), phenomenon known as the lanthanide contraction [34]. This implies a ligand–metal

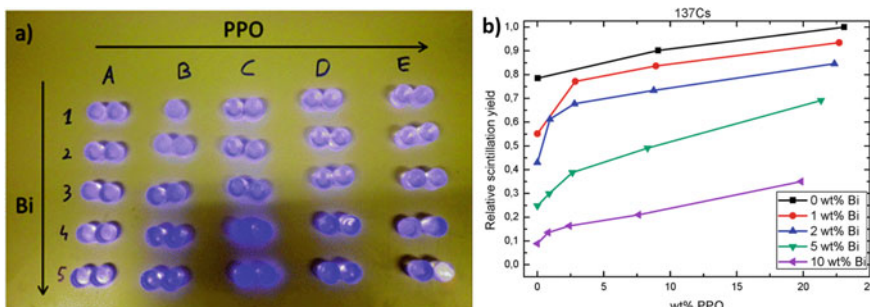
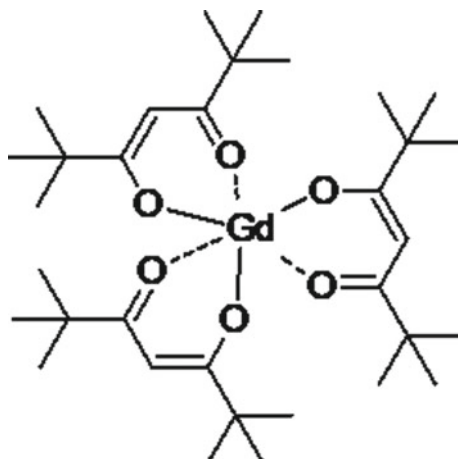


Fig. 4.13 **a** Photo of scintillator with increasing amount of primary fluorophore (PPO) and of bismuth loading. **b** Evolution of the light yield for different amount of Bi loading as a function of the PPO concentration (reproduced from [29] with permission from the Royal Society of Chemistry)

interaction to be mainly governed by Coulombian interaction, which makes their geometry extremely dependent on the ligand steric hindrance. The number of ligands can go from one and up to twelve [35] and have a very dynamic behavior as the geometry is not strongly directed by orbital interactions. This also implies that the ligand chemistry and geometry are almost the same for all lanthanides, which have a stable 3+ oxidation state. The exception is the cerium, which is more stable at its 4+ oxidation state.

Strong of these facts, several ligands were tested and the TetraMethylHeptane-Dionate ligand (TMHD, Fig. 4.14 when complexed with Gd) was identified as a good candidate. It is ubiquitous for all the lanthanides, meaning all $[\text{L}](\text{TMHD})_3$ complexes are synthetically available and also stable in the polymerization conditions. $[\text{L}](\text{TMHD})_3$ are a little soluble in styrene, and afford 0.1 wt% loading. In order to increase this proportion, a copolymer was found essential. 1,4-Butanediol dimethacrylate acted at the same time as a curing agent (cross-linking) and a ligand

Fig. 4.14 Molecule of $\text{Gd}^{\text{III}}(\text{TMHD})_3$



for solubilizing the $[L](\text{TMHD})_3$. After heating under inert atmosphere the starting mixture, a partial ligand exchange occurs and enables a better solvation of the lanthanides complexes. This can afford up to 5 wt% loading in lanthanides atoms [35].

Here, also the more lanthanides complexes the less light output from the scintillator. The same approach as for the bismuth loading was applied, that is to say the increase of the primary fluorophore content (Fig. 4.13). However, increase of PPO content did not affect the light output meaningfully compared to the bismuth loading. An explanation can be the lack of electronic communication between the lanthanides complex and its medium. The three TMHD ligands form an isolation shell that traps the high-energy excitation and allows them to decay, denying them the opportunity to be fed back into the scintillator medium. This is also coherent with the phenyl ring from the triphenylbismuth, enabling such a communication [35].

Nevertheless, this loading technique was applied to check the photoelectric effect in plastic scintillators loaded with all available lanthanides. Results for this series (Fig. 4.15) show a drop in the PE efficiency between the Thulium and the Ytterbium, which is predicted by PE theory and subsequent MCNP6.1 simulation.

As a wrap up for this part, the solutions to load an element in a plastic scintillator are numerous but never perfect. Minimizing tradeoff is the most difficult task for scintillation performance in plastics that are not ideal to begin with, but the potential application is worth the trouble.

Among lanthanides resides one particular atom that is interesting far beyond the scope of gamma detection: gadolinium. It has two abundant and stable isotopes that have a thermal neutron cross section among the highest known. This is a perfect transition that leads us to another powerful application of metal loading for specific application: neutron detection [36].

4.4 Neutron Detection

4.4.1 Thermal Neutron

Alpha, beta, and gamma have a straightforward way of interacting with matter: the denser the better its stopping power. Neutrons on the other hand are a more subtle source of ionization. Their kinetic energy classifies them and dictates their probability of interaction. For example, fast neutron ($E_n > 0.5 \text{ MeV}$) interacts mainly in plastic scintillator with hydrogen atom in a ballistic way, generating a recoil proton. The focus of this part is the other extremum of this range: thermal neutron ($E_n \approx 0.025 \text{ eV}$). This particle mainly interacts via neutron capture. For each element, the affinity for thermal neutron capture is defined by a cross section in Barns, with the high cross section meaning a high rate of neutron capture. This cross section value is depending on the element's isotopes and among the natural elements only a few have an exploitable cross section (Table 4.1).

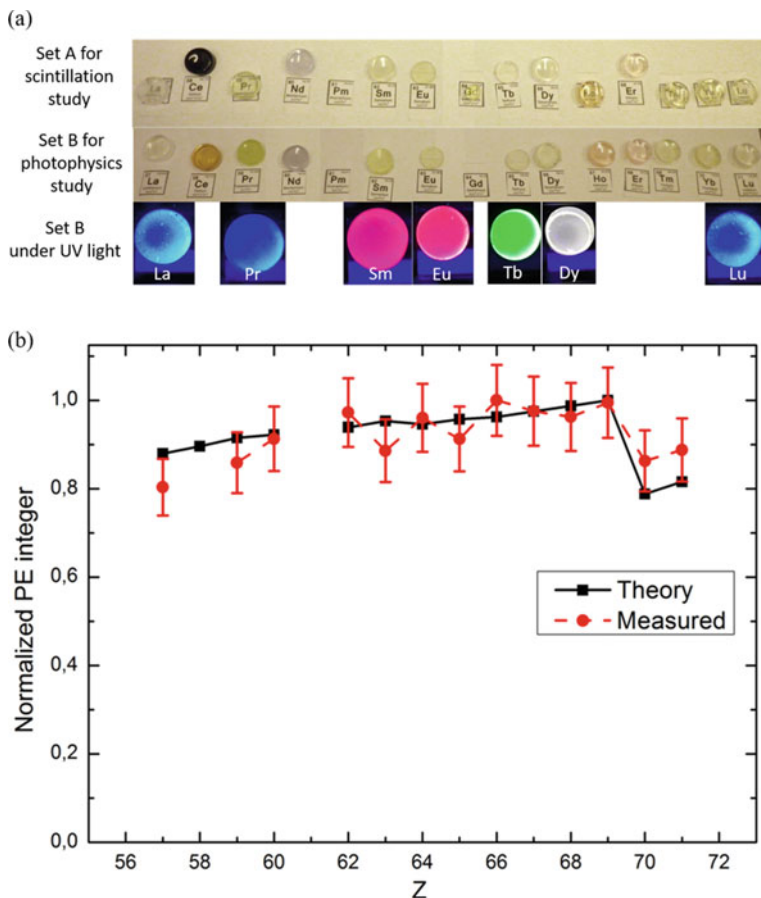


Fig. 4.15 **a** Photos of lanthanides loaded plastic scintillator under ambient and UV light. **b** Intensity of the PE peak as a function of the lanthanide used in the plastic scintillator; comparison between MCNP6.1 simulation and measurement (reproduced from [36] with permission from John Wiley and sons)

Table 4.1 Isotopes of interest for thermal neutron detection

Isotope	Natural abundance	Thermal neutron cross section (barns)
³ He	0.00013%	$5,327 \pm 10$
⁶ Li	7.5%	936 ± 6
¹⁰ B	19.8%	$3,840 \pm 11$
¹¹³ Cd	12.3%	$20,000 \pm 300$
¹⁵⁵ Gd	14.7%	$56,200 \pm 1,000$
¹⁵⁷ Gd	15.7%	$242,000 \pm 4,000$

^3He is given here, as it is today the gold standard for neutron detection in pressurized discharged tubes. Its scarcity and high price are a driving force to find alternatives for neutron detection. Lithium, boron, cadmium, and gadolinium loading in plastic scintillator is hence quite an important topic that we will dissect in this order.

4.4.2 *Lithium Loading*

^6Li reacts with a thermal neutron and generates an alpha and a triton particle, thus a discriminable signal, particularly when using formulations that can perform fast neutron/gamma discrimination. The literature often refers to this scintillator as triple discriminating material. Lithium loading was studied from different angles, some of them presented in other parts of this book. The first mention of its use as a neutron sensitizer was in liquid scintillators in 1979 [37]. We will discuss here the homogenous doping with organic salts. Most groups in the world working on this one have their favorite solution, for example, Zaitseva et al. described extensively the use of lithium salicylate in plastic scintillator (Cf. Chap. 2 of this Book) [38].

Breukers et al. used lithium methacrylate as an easy source of lithium loading, and reported also the incorporation of enriched ^6Li [39]. Cherepy et al. published recently some results with lithium pivalate [7, 30]. A 77 cm³ scintillator containing 1 wt% of elemental 99.5% enriched ^6Li was presented in 2017 and was announced to be commercialized by Eljen Technology as EJ-270 [40]. Unfortunately, at the date of April 2020 this entry is not available in the vendor's product catalogue and no further information or communication since this announcement was made at the time this book was finalized. ^6Li is considered by the IAEA as a nuclear material with high restriction and surveillance as it is one of the primary fuel for fusion bomb, so one can speculate that this could prevent further development as a final product would be subject to hard scrutiny and possibly international market restriction. This might be the reason why no lithium-loaded scintillator is yet to be commercially available.

Frangville et al. did more recently a thorough survey of potent molecules susceptible to incorporate efficiently lithium in plastic matrices. This two-part study is a perfect example of a full-fledge research effort to find a solution for maximizing the loading and minimizing its effect on scintillator behavior [41]. It focused first on a rigorous screening of the potential target molecule regarding their solubility in monomers (Fig. 4.16) identifying lithium alpha-valerate as the best candidate. Lithium is quite a light element and a large organic anion can easily represent 99% of the total mass thus inerting the loaded material in the medium. More than elsewhere, there is a strong incentive here to minimize the size of the organic ligand. As an example, lithium represents 6.42% of the valerate and of the pivalate mass, and 4.82% of the salicylate mass. This can be extended for a particular study case: for a scintillator weighting 10 g, loading with only 1 wt% of elemental lithium represent the insertion of 1.56 g of lithium valerate or pivalate, and 2.38 g of salicylate. This represents in each case a significant part of the total weight (15–24%) and will definitely have an effect on the optical and mechanical properties.

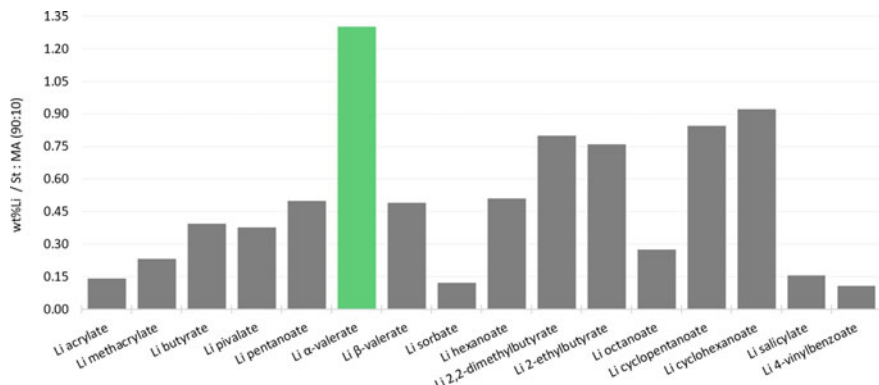
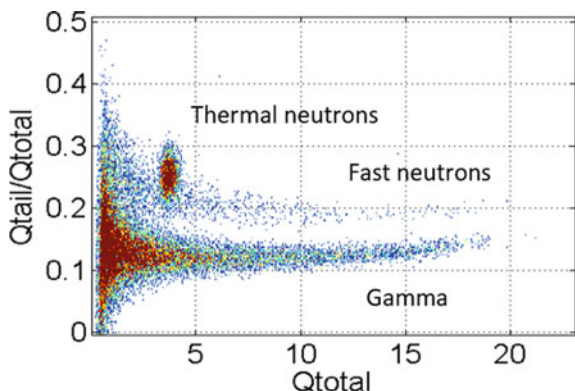


Fig. 4.16 Solubility study of different lithium carboxylates (reproduced from [41] with permission from the Royal Society of Chemistry)

Fig. 4.17 Bidimensional graphic visualization of the triple discrimination capacity of a lithium-loaded plastic scintillator (reproduced from [41] with permission from the Royal Society of Chemistry)



Furthermore, lithium is present as a single charged species (Li^+) which makes the resulting molecule ($\text{RCOO}^- \text{Li}^+$) highly polar. Solubility is not optimal and can vary for molecules of the same family.

This study from Frangville et al. also optimized the formulation, with the help of a co-monomer to maximize lithium alpha-valerate incorporation, and also using enriched lithium-6 to maximize the thermal neutron response (Fig. 4.17). Application [42] and details are also provided in Chap. 3 of this book.

4.4.3 Boron Loading

Not unlike ${}^6\text{Li}$, ${}^{10}\text{B}$ reacts with a thermal neutron to give an alpha particle and a ${}^7\text{Li}$ nucleus.

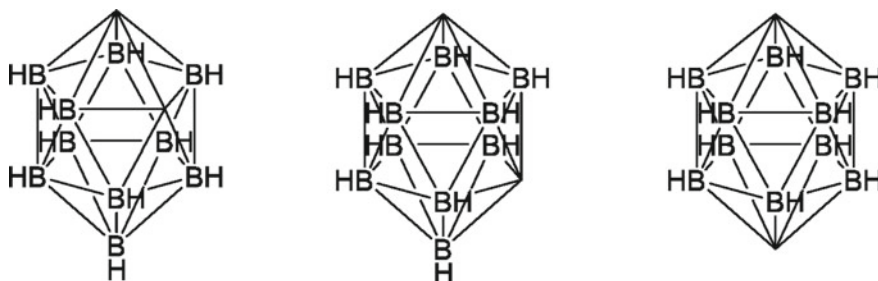


Fig. 4.18 Molecular structures of *ortho*-, *meta*- and *para*-carborane

Boron loading is a very particular topic for the chemist. It cannot be treated as a metal so the approach is drastically different from the rest presented here. Its inclusion in organic molecules could seem as a solution at first but the presence of a missing electron pair on the boron renders them problematic to use as they strongly react with radicals, hence forming degradation products and inhibiting the scintillator polymerization. Nevertheless, some molecular functional groups such as boron pinacol ester provide enough stability to be considered as candidates for scintillator loading. Sellinger et al. made a wide range of these molecules [43, 44]. The composition of these molecules is based around an aromatic unit decorated by several boron pinacol ester groups. This represents unfortunately a small proportion of the molecules mass. A maximum of 0.37 wt% of elemental boron was achieved, which corresponds to 0.074 wt% of ^{10}B . This was enough to observe neutron capture events on 20 g samples.

The more common solution for boron loading is to use stable carborane molecules (Fig. 4.18). They present several advantages: they are composed of multiple boron atom disposed in a cage-like frameworks. Remarkably, the carborane ($\text{C}_2\text{H}_{12}\text{B}_{10}$, with three different position isomers) exhibits a 3D super aromaticity which makes it stable up to 400 °C and resistant to mild radical medium.

This loading was studied very early and the first occurrence of a commercial boron loaded plastic scintillator was BC-454 (now available at Saint-Gobain Crystals). One can note here that Bicron Corporation was pioneer in the fabrication, design and commercialization of doped scintillator in the early 1990s, understandably withholding information about their formulation and components [45, 46]. But in 2000, Normand et al. [47–49] and in 2014, Pawełczak et al. [50] synthesized and reported a carborane doped plastic scintillator with improved performances (Fig. 4.19).

4.4.4 Cadmium and Gadolinium Loading

Cadmium and gadolinium react with a thermal neutron to give gamma burst at different energies. The way to exploit such scintillator is well developed in Chap. 3 of this Book. So it will not be discussed here.

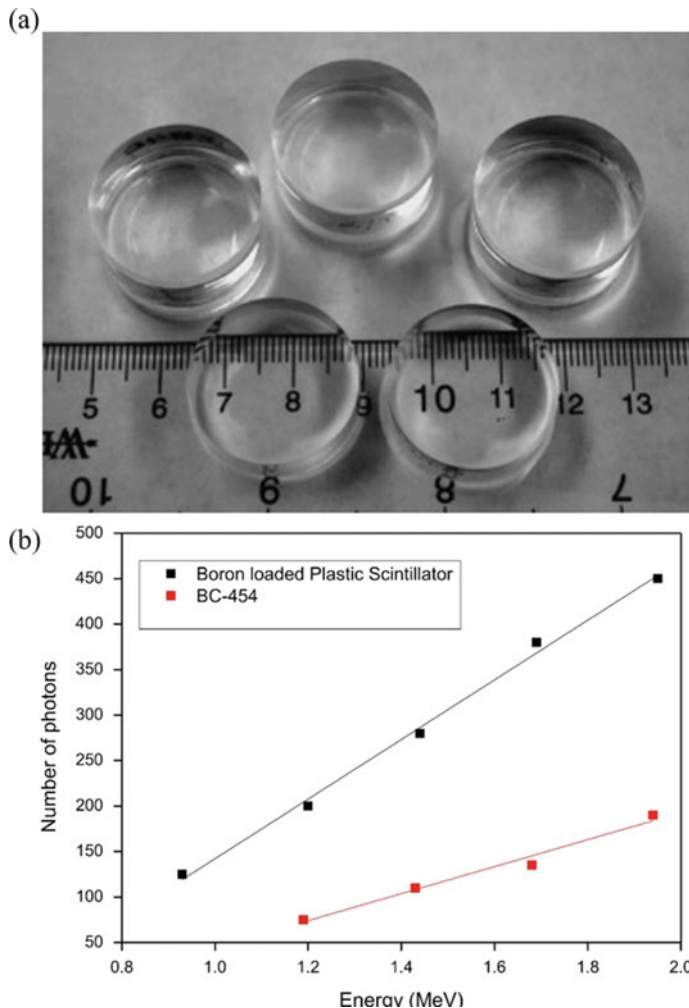


Fig. 4.19 **a** Plastic scintillators with boron loading (reproduced from [50] with permission from Elsevier). **b** Comparison between carborane loaded scintillator and BC-454 commercial alternative (adapted from [49])

Homogenous cadmium loading was, to the best of our knowledge, only studied by Nemchenok et al. in 2012–2013 [51, 52]. The reason for this low interest resides in the extreme toxicity of its organometallic form, which makes it an impractical candidate as it almost guarantees the impossibility to transfer a formulation toward a large-scale chemical facility, for obvious safety reason. They nonetheless made the parallel comparison with gadolinium-loaded scintillator and established in both cases a decrease of the scintillation output as a function of the Cd/Gd loading.

Gadolinium homogenous loading is also a niche subject, because of the difficulty to find a suitable organometallic complex and the difficulty to separate the signal due to neutron interaction from the signal of gamma interaction [51]. But as mentioned in the previous part Gd loading can be achieved and can actually result in relatively large loading with marginal scale-up attempt and proof of concept of neutron detection [53, 54]. Chapter 3 of this book details all the finesse [62] of this application. Outside of Gd(TMHD)_3 , other molecules were tested, an exhaustive list was made by Dumazert et al. [55] and is synthesized in Table 4.2. Two approaches are visible here to tackle the problem of low solubility. On one hand, polar co-dopant were included in the matrices to enable the solvation of gadolinium salts such as GdCl_3 or $\text{Gd(NO}_3)_3$ [52, 56]. On the other hand organometallics such as Gd(TMHD)_3 or $\text{Gd}(i\text{-PrO})_3$ [61]. These last two molecules are very promising as they introduce the least parasite in the scintillator composition but trade performance for high prices. This could evolve if there is a large-scale need of these molecules.

4.5 Conclusion

Plastic scintillator can be viewed as a niche research from a general chemist standpoint but the extent of possible improvement is barely touch as of now. This chapter devoted itself to organometallic chemistry as it covers the vast majority of the Mendeleyev Table in order to satisfy special application need. This lays out the first important takeaway of plastic scintillator loading: ***application-driven design***. With the two striking example of heavy metal loading for possible gamma spectroscopy with Sn, Pb and Bi, and thermal neutron capture with Li, B, or Gd.

These different examples raise a second take-away message: whatever the chosen solution for metal loading, ***there is always a tradeoff between the desired properties to obtain and the optimal behavior of a plastic scintillator***. The heart of the research surrounding organometallic loading is to mitigate this tradeoff in order to optimize the plastic scintillator.

Nevertheless, these developments are worth it as it is sometimes the only way to achieve the desired properties, owing to the flexibility and the wide range of plastic scintillator properties. Research in this field has seen numerous results; some applications even lead to commercial transfers.

4.6 Table by Elements

See Table 4.3.

Table 4.2 List of homogenous gadolinium-loaded plastic scintillators

	Matrix	Dopant	wt% Gd	Dimensions	Light yield	Neutron response
Czirr (1973) [57]	PVT	Gd(HBa) ₃ (homogeneous)	0.1–0.5	2.54 (φ) × 15.24 cm	15–42% of unloaded NE120 (0.1–0.2 wt% Gd)	–
Brudanin et al. (2001) [58]	PMMA	Gd(NO ₃) ₃ (homogeneous)	3	30 (φ) × 10 mm	51% of unloaded plastic scintillator	–
Nemchenok et al. (2013) [52]	PMMA	GdCl ₃ (homogeneous)	4	27 (φ) × 10 mm	67.6% of unloaded plastic scintillator	–
Vel'mozhnaya et al. (2013) [59]	PS	Gd(PhV) ₃ (homogeneous)	4	–	60% of unloaded plastic scintillator	–
Watanabe et al. [60]	Bisphenol-A resin	Unknown	0.1	20 × 200 × 3 mm	56.5% of unloaded plastic scintillator ~700 ph/MeV	–
Ovechnika et al. (2009) [61]	PS	Gd[OCH(CH ₃) ₃] ₃ (homogeneous)	2.5	14 (φ) × 6 mm	76% of unloaded plastic scintillator	Peak at 70 ± 20 keV
Bertrand et al. (2016) [35]	Cross-linked PS	Gd(TMHD) ₃ (homogeneous)	2	16 (φ) × 8 mm	50% of unloaded plastic scintillator ~5000 ph/MeV	Signature distributed between 20 and 200 keV; sensitivity (0.8 wt% Bi-loaded compensator): 3.3 · 10 ⁻¹ cps/nV

Table 4.3 List of elements loaded in organic scintillators with associated application and significant references. Only homogenous loading is presented. Nanoparticles are excluded

Elements	Context	Application	References
Li	Liquid and plastic scintillation	Neutron detection	[40]
B	Liquid and plastic scintillation	Neutron detection	[49, 63, 64]
F	Plastic scintillation	Gamma detection	[23]
Si	Liquid and plastic scintillation	Matrix	Chap. 5
Cl	Plastic scintillator	Adjustment of Z_{eff}	[65]
As	Plastic scintillation	Gamma detection	[64, 66]
Se	Plastic scintillation	Gamma detection	[66]
Sn	Liquid and plastic scintillation	Gamma detection	[24, 66]
Cd	Liquid and plastic scintillation	Neutron detection	[51, 52, 54, 64]
Nd	Liquid scintillation	Double beta decay research, neutrino detection	[67–69]
Mo	Liquid scintillation	Double beta decay research	[70]
In	Liquid scintillation	Solar neutrino detection	[71]
Yb	Liquid scintillation	Solar neutrino detection	[72]
Hf	Plastic scintillation	Gamma detection	[22]
Ln–Lu	Plastic scintillation	Gamma detection	[36]
Gd	Liquid and plastic scintillation	Gamma, Neutron, or neutrino detection	[35, 69]
Hg	Plastic scintillation	Gamma detection	[66, 73]
Pb	Plastic scintillation	Gamma detection	[66, 74]
Bi	Plastic scintillation	Gamma detection	[29, 66]
U	Liquid scintillation	Gamma detection	[54]

References

1. G.H.V. Bertrand, F. Sguerra, M. Hamel, Chem. Eur. J. **20**(48), 15660 (2014)
2. S.W. Moser, W.F. Harder, C.R. Hurlbut, M.R. Kusner, Radiat. Phys. Chem. **41**(1/2), 31 (1993)
3. M. Hamel, F. Carrel, in *New Insights on Gamma Rays*, ed. by A. Maghraby (InTech, 2017), pp. 47
4. T.J. Hajagos, C. Liu, N.J. Cherepy, Q. Pei, Adv. Mater. **30**(27), 1706956 (2018)
5. D.J. Griffiths, D.F. Schroeter, *Introduction to Quantum Mechanics* (Cambridge University Press, 2005)
6. R. Voltz, G. Laustriat, J. Phys. France **29**, 159 (1968)
7. N.J. Cherepy, H.P. Martinez, R.D. Sanner, P.R. Beck, O.B. Drury, E.L. Swanberg, S.A. Payne, C.R. Hurlbut, B. Morris, in *IEEE Nuclear Science Symposium and Medical Imaging Conference (NSS/MIC)* (IEEE, 2017)
8. B.L. Rupert, N.J. Cherepy, B.W. Sturm, R.D. Sanner, S.A. Payne, Europhys. Lett. **97**(2), 22002 (2012)
9. P.L. Feng, J. Villone, K. Hattar, S. Mrowka, B.M. Wong, M.D. Allendorf, F.P. Doty, IEEE Trans. Nucl. Sci. **59**(6), 3312 (2012)
10. F.P. Doty, M.D. Allendorf, P.L. Feng, Doped luminescent materials and particle discrimination using same, WO2011/060085, 10.11.10

11. F. Sguerra, R. Marion, G.H.V. Bertrand, R. Coulon, R. Daniellou, S. Gaillard, M. Hamel, J. Mater. Chem. C **2**(30), 6125 (2014)
12. A.F. Adadurov, P.N. Zhmurin, V.N. Lebedev, V.V. Kovalenko, Nucl. Instr. Methods A **621**(1–3), 354 (2010)
13. P.N. Zhmurin, V.N. Lebedev, A.F. Adadurov, V.N. Pereymak, Y.A. Gurkalenko, Radiat. Meas. **62**, 1 (2014)
14. P.N. Zhmurin, V.N. Lebedev, V.N. Kovalenko, A.F. Adadurov, V.N. Pereymak, in *New Developments, in Chromophore Research*. ed. by A. Moliere, E. Vigneron (Nova Science Publishers Inc., New York, 2013), pp. 313–324
15. L. Pichat, P. Pesteil, J. Clément, J. Chim. Phys. Phys.-Chim. Biol. **50**, 26 (1953)
16. M. Hamel, G. Turk, A. Rousseau, S. Darbon, C. Reverdin, S. Normand, Nucl. Instr. Methods A **660**(1), 57 (2011)
17. M. Hamel, G. Turk, S. Darbon, S. Normand, IEEE Trans. Nucl. Sci. **59**(4), 1268 (2012)
18. M. Hamel, S. Darbon, S. Normand, G. Turk, Scintillateur organique solide dopé par un ou plusieurs éléments chimiques, FR1060977, 21.12.10
19. G. Turk, C. Reverdin, D. Gontier, S. Darbon, C. Dujardin, G. Ledoux, M. Hamel, V. Simic, S. Normand, Rev. Sci. Instrum. **81**(10), 10E509 (2010)
20. M. Koshimizu, G.H.V. Bertrand, M. Hamel, S. Kishimoto, R. Haruki, F. Nishikido, T. Yanagida, Y. Fujimoto, K. Asai, Jpn. J. Appl. Phys. **54**(10), 102202 (2015)
21. K. Kagami, M. Koshimizu, Y. Fujimoto, S. Kishimoto, R. Haruki, F. Nishikido, K. Asai, Radiat. Meas. **135**, 106361 (2020)
22. K. Kagami, M. Koshimizu, Y. Fujimoto, S. Kishimoto, R. Haruki, F. Nishikido, K. Asai, J. Mater. Sci. Mater. Electron. **31**(2), 896 (2020)
23. M. Hamel, P. Sibczyński, P. Blanc, J. Iwanowska, F. Carrel, A. Syntfeld-Kažuch, S. Normand, Nucl. Instr. Methods A **768**, 26 (2014)
24. P.L. Feng, W. Mengesha, M.R. Anstey, J.G. Cordaro, IEEE Trans. Nucl. Sci. **63**(1), 407 (2016)
25. P.L. Feng, J.G. Cordaro, W. Mengesha, N.R. Myllenbeck, Metal-loaded plastic scintillators for gamma-ray spectroscopy, US10024983, 06.10.16
26. S.R. Sandler, K.C. Tsou, Intern. J. Appd. Radn. Isotopes **15**, 419 (1964)
27. Z.H. Cho, C.M. Tsai, L.A. Eriksson, IEEE Trans. Nucl. Sci. **NS-22**(1), 72 (1975)
28. J. Becker, L. Eriksson, L.C. Moberg, Z.H. Cho, Nucl. Instr. Methods A **123**(1), 199 (1975)
29. G.H.V. Bertrand, F. Sguerra, C. Dehé-Pittance, F. Carrel, R. Coulon, S. Normand, E. Barat, T. Dautremer, T. Montagu, M. Hamel, J. Mater. Chem. C **2**(35), 7304 (2014)
30. N. Cherepy, R.D. Sanner, Plastic scintillators with high loading of one or more metal carboxylates, US9234968, 10.10.14
31. N.J. Cherepy, R.D. Sanner, T.M. Tillotson, S.A. Payne, P.R. Beck, S. Hunter, L. Ahle, P.A. Thelin, IEEE Nucl. Sci. Symp. Conf. Rec. **1972** (2012)
32. S. O’Neal, N. Cherepy, S. Hok, S. Payne, IEEE Trans. Nucl. Sci. **67**(4), 746 (2020)
33. J. Dumazert, R. Coulon, G.H.V. Bertrand, S. Normand, L. Méchin, M. Hamel, Nucl. Instr. Methods **819**, 25 (2016)
34. K. Dehnicke, A. Greiner, Angew. Chem. Int. Ed. **42**(12), 1340 (2003)
35. G.H.V. Bertrand, J. Dumazert, F. Sguerra, R. Coulon, G. Corre, M. Hamel, J. Mater. Chem. C **3**(35), 6006 (2015)
36. G.H.V. Bertrand, M. Hamel, J. Dumazert, R. Coulon, C. Frangville, Polym. Adv. Technol. **32**(2), 748 (2021)
37. L.R. Greenwood, N.R. Chellew, G.A. Zarwell, Rev. Sci. Instrum. **50**, 472 (1979)
38. A.N. Mabe, A.M. Glenn, M.L. Carman, N.P. Zaitseva, S.A. Payne, Nucl. Instr. Methods A **806**, 80 (2016)
39. R.D. Breukers, C.M. Bartle, A. Edgar, Nucl. Instr. Methods A **701**, 58 (2013)
40. M.E. Ellis, C. Hurlbut, C. Allwork, B. Morris, in *IEEE Nuclear Science Symposium and Medical Imaging Conference (NSS/MIC)* (IEEE, 2017)
41. C. Frangville, J. Dumazert, E. Montbarbon, R. Coulon, G.H.V. Bertrand, M. Hamel, Mater. Chem. Front. **3**(8), 1574 (2019)

42. C. Frangville, M. Hamel, G.H.V. Bertrand, Scintillateur plastique dopé par des ions métalliques et ses utilisations, FR1856136, 03.07.2018
43. A. Sellinger, U. Greife, H. Yemam, A. Mahl, Boron containing organic/hybrid scintillation materials for gamma and neutron detection, US62/093,136, 17.12.2014
44. H.A. Yemam, A. Mahl, U. Koldemir, T. Remedes, S. Parkin, U. Greife, A. Sellinger, Sci. Rep. **5**, 13401 (2015)
45. Eljen Technology website, <https://eljentechnology.com/>. Accessed 10 Sept 2020
46. Saint-Gobain Crystals website, <https://www.crystals.saint-gobain.com/products/plastic-scintillators>. Accessed 10 Sept 2020
47. S. Normand, P. Delacour, C. Passard, J. Lordin, IEEE Trans. Symp. Conf. Rec. **2**, 787 (2004)
48. S. Normand, B. Mouanda, S. Haan, M. Louvel, Nucl. Instr. Methods A **484**, 342 (2002)
49. S. Normand, B. Mouanda, S. Haan, M. Louvel, in *IEEE Nuclear Science Symposium Conference Record* (2000), p. 6/62
50. I.A. Pawelczak, A.M. Glenn, H.P. Martinez, M.L. Carman, N.P. Zaitseva, S.A. Payne, Nucl. Instr. Methods A **751**, 62 (2014)
51. I.B. Nemchenok, A.A. Shurenkova, V.B. Brudanin, N.A. Gundorin, V.V. Timkin, Bull. Russ. Acad. Sci.: Phys. **76**(11), 1187 (2012)
52. I.B. Nemchenok, N.A. Gundorin, E.A. Shevchik, A.A. Shurenkova, Funct. Mater. **20**(3), 310 (2013)
53. J. Dumazert, R. Coulon, M. Hamel, F. Carrel, F. Sguerra, S. Normand, L. Méchin, G.H.V. Bertrand, IEEE Trans. Nucl. Sci. **63**(3), 1551 (2016)
54. A.R. Ronzion, Int. J. Appl. Rad. Isotop. **4**, 196 (1959)
55. J. Dumazert, R. Coulon, Q. Lecomte, G.H.V. Bertrand, M. Hamel, Nucl. Instr. Methods A **882**, 53 (2018)
56. Z.W. Bell, G.M. Brown, C.H. Ho, F.V. Sloop Jr., Organic scintillators for neutron detection, in *X-Ray and Gamma-Ray Detectors and Applications IV*, vol. 4784, Proceedings of the SPIE, ed. by R.B. James, L.A. Franks, A. Burger, E.M. Westbrook, R.D. Hurst (2002), p. 150
57. J.B. Czirr, Nucl. Instr. Methods **108**(3), 613 (1973)
58. V.B. Brudanin, V.I. Bregadze, N.A. Gundorin, D.V. Filossofov, O.I. Kochetov, I.B. Nemtchenok, A.A. Smolnikov, S.I. Vasiliev, in *Proceedings of the Third International Workshop on Identification of Dark Matter*, (2001), pp. 626–634
59. E.S. Velmozhnaya, A.I. Bedrik, P.N. Zhmurin, V.D. Titskaya, A.F. Adadurov, D.S. Sofronov, Funct. Mater. **20**(4), 494 (2013)
60. M. Watanabe, M. Katsumata, H. Ono, T. Suzuki, H. Miyata, Y. Itoh, K. Ishida, M. Tamura, Y. Yamaguchi, Nucl. Instr. Methods A **770**, 197 (2015)
61. L. Ovechnika, K. Riley, S. Miller, Z. Bell, V. Nagarkar, Phys. Procedia **2**(2), 161 (2009)
62. J. Dumazert, R. Coulon, G.H.V. Bertrand, M. Hamel, F. Sguerra, C. Dehé-Pittance, S. Normand, L. Méchin, in *2015 IEEE Proceedings of the ANIMMA 2015* (2016)
63. L. Swiderski, M. Moszynski, D. Wolski, T. Batsch, A. Nassalski, A. Syntfeld-Kazuch, T. Szczesniak, F. Kniest, M.R. Kusner, G. Pausch, J. Stein, W. Klamra, IEEE Trans. Nucl. Sci. **55**, 3710 (2008)
64. Y. Koike, Nucl. Instr. Methods **97**(3), 443 (1971)
65. A.S. Kirov, C. Hurlbut, J.F. Dempsey, S.B. Shrinivas, J.W. Epstein, W.R. Binns, P.F. Dowkontt, J.F. Williamson, Med. Phys. **26**(8), 1515 (1999)
66. E.E. Baroni, S.F. Kilin, T.N. Lebsadze, I.M. Rozman, V.M. Shoniya, At. Energ. **17**, 1261 (1964)
67. I. Barabanov, L. Bezrukov, C. Cattadori, N. Danilov, A. di Vacri, A. Ianni, S. Nisi, F. Ortica, A. Romani, C. Salvo, O. Smirnov, E. Yanovich, J. Phys.: Conf. Ser. **136**, 042088 (2008)
68. I.R. Barabanov, L.B. Bezrukov, C. Cattadori, N.A. Danilov, A. Di Vacri, A. Ianni, S. Nisi, G.Y. Novikova, F. Ortica, A. Romani, C. Salvo, O.Y. Smirnov, E.A. Yanovich, Instrum. Exp. Tech. **55**(5), 545 (2012)
69. G.Y. Novikova, M.V. Solovyova, E.A. Yanovich, Phys. At. Nucl. **83**(1), 75 (2020)
70. V.M. Gehman, P.J. Doe, R.G.H. Robertson, D.I. Will, H. Ejiri, R. Hazama, Nucl. Instr. Methods A **622**(3), 602 (2010)

71. I.R. Barabanov, L.B. Bezrukov, V.I. Gurentsov, N.A. Danilov, A. di Vacri, C. Cattadori, Y.S. Krylov, G.Y. Novikova, N. Ferrari, E.A. Yanovich, Instrum. Exp. Techn. **53**(4), 513 (2010)
72. N.A. Danilov, Y.S. Krylov, G.V. Korpusov, G.V. Kostikova, I.R. Barabanov, L.B. Bezrukov, V.N. Kornoukhov, N.P. Nesterova, E.A. Yanovich, V.V. Yakshin, N.A. Tsarenko, C. Cattadori, N. Ferrari, A. Falgiani, Radiochemistry **45**, 140 (2003)
73. L.J. Basile, J. Chem. Phys. **27**(3), 801 (1957)
74. M. Hamel, S. Normand, G. Turk, S. Darbon, Highly lead-loaded red plastic scintillators as an X-ray imaging system for the Laser Méga Joule, in *Poster presented at the 2nd International Conference on Advancements in Nuclear Instrumentation, Measurement Methods and Their Applications*, Ghent, Belgium, 06–09 June 2011



Guillaume H. V. Bertrand (36 yo) got his Ph.D. in 2011 at the university Pierre et Marie Curie (Paris VI, France) on the synthesis of semiconductor cobalt complexes with organic photovoltaic application. He then did three post-docs, at MIT (Covalent organic frameworks), CEA Saclay (bismuth loaded plastic scintillator) and IIT Genova (Cd Se/S/Te core crown nanoplatelets), before obtaining a permanent position at CEA Saclay in 2016. His researched focus on the chemical modification of plastic scintillator for specific application. He also take part in decommissioning research and initiated a team effort on scintillating MOFs. As of September 2020 he is the author or co-author of 42 publications and 9 patents, with an h-index of 12.



Matthieu Hamel (41 yo) defended his Ph.D. in organic chemistry in 2005 at the University of Caen Basse-Normandie (France), on the synthesis of *ortho*-sulfinyl phenylphosphonates. After a first experience in the preparation of plastic scintillators at the French Atomic Energy and Alternative Energies Commission (CEA), he spent a year at the University of Montpellier II (France) working on phosphorylated prodrugs of albitazolium. He obtained a full position at the CEA in 2009, where he developed plastic scintillators and other luminescent materials to the main application of CBRN-E threats. In January 2021, he is the author or co-author of 75 publications, 27 patents, 1 book chapter and 3 reviews, with a h-index 14 according to SciFinder®. He is the Editor of this book.

Chapter 5

Polysiloxane-Based Scintillators



Sara Maria Carturan and Alberto Quaranta

Abstract In the following sections, we will describe the main characteristics of scintillators made of polysiloxane, with particular focus on the optical properties of phenyl containing base resins, the energy transfer among added fluorophores and the possibility to achieve not only good scintillation yield but also discrimination between different particles. Moreover, the correlation between the optimal radiation resistance tested for silicone scintillators by several techniques and the physical–chemical properties of the Si–O–Si-based network will be presented. Performances of polysiloxane scintillators as sensors of different radiations, including fast and thermal neutrons, are also presented, and will be described and discussed. Recent results on enhanced light output under proton beam irradiation on thin and flexible siloxane scintillators will be highlighted.

5.1 Foreword

When thinking about soft, pliable matter, you might erroneously consider it as something not very resistant to its usual function, something which is not supposed to last long. On the other hand, when you stroke a fluffy cat, you can eventually grasp its paw and, provided that you do not get scratched by the feline, you might be delighted by the softness and smoothness of the fingertip and, at the same time, amazed by its resistance to scratching, wearing and tearing, which it copes with throughout the pet's life, when it climbs a rough-barked tree, jumps from to the stony field or quickly clammers up coarse walls.

S. M. Carturan ()

Dipartimento di Fisica e Astronomia, Università di Padova e INFN – Laboratori Nazionali di Legnaro, 35020 Legnaro, PD, Italy
e-mail: sara.carturan@lnl.infn.it

A. Quaranta

Department of Industrial Engineering, University of Trento, Via Sommarive 9, 38123 Povo, Trento, Italy
e-mail: alberto.quaranta@unitn.it

In a similar way, elastomeric material such as silicone might be considered as not very useful for applications where tough environments are expected, i.e. high thermal gradients, impinging radiation with high fluxes, vacuum or gas fluxing, flexural, tensile or compressive mechanical stresses, vibrations, humidity variations. These conditions are often encountered when scintillators are needed to reveal ionizing particles, i.e. in nuclear energy generation plants, in homeland security dedicated sites, in radio medical departments, in down-hole gas and oil exploration, in nuclear physics research dedicated plants such as accelerators and cyclotrons. However, we will see in the following paragraphs that this feeling does not apply to the “silicone” case and, once again, “soft” and “pliable” adjectives do not necessarily imply “weak” and “short-lasting”.

The most traditional organic scintillator with widespread use in several of the mentioned applications is poly(vinyltoluene)¹-based, with different additives to achieve desired features. This plastic material, which bears outstanding performances as for light output, attenuation length, response time and machinability, is nevertheless rigid and fragile, it swells in most organic solvents, softens at temperature around 100 °C and undergoes yellowing upon irradiation with high doses of charged particles.

It is extremely exciting to aim at providing researchers and technology community with a scintillating material bearing the most relevant characteristics to be profitably used as particle sensor and, the beneficial mechanical features of flexural and compression strength, together with radiation, thermal and chemical resistance is extremely exciting. This task can be pursued indeed at the cost of jeopardize the maximum light output achievable, which is currently displayed only by poly(vinyltoluene) or polystyrene based plastic scintillators.

5.1.1 *Silicon-Based Polymer Properties: Chemistry*

In everyday life, silicones are found as effective and inexpensive materials to perfectly accomplish various and sometimes challenging tasks. They are used as heat-resistant flexible moulds for baking containers, one-part resin for sealing shower boxes and water pipes, humidity and sun exposure resistant materials for encapsulation and protection of car joints and bearings and sealant in car headlights.

Silicones constitute a unique class of macromolecules in the sense that they do not have natural counterparts, being the artefact of inorganic chemistry evolution. As a matter of fact, these Si–O-based polymers display outstanding features not amenable to C–C based molecules, so that for many applications they remain, as of today, non-replicable materials. This point will be often underlined forward, and reflects the origin of silicone industrial production, i.e. the demand of a grease for aircraft motors with superior thermal stability and absence of carbonaceous by-products in

¹Topological representation and key information of these molecules is given in the Appendix section at the end of the book.

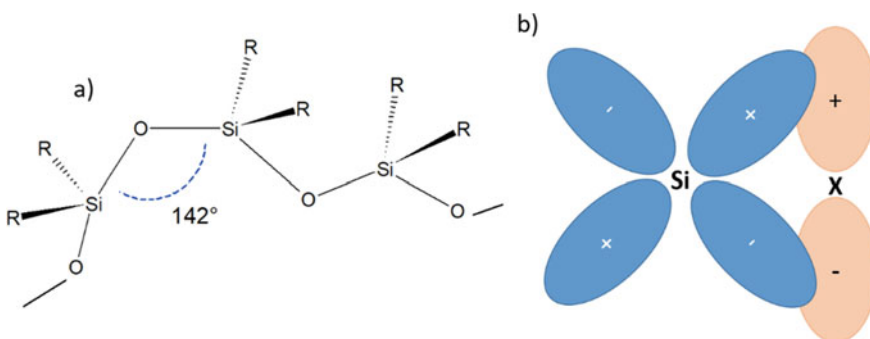


Fig. 5.1 a Conformation of simple silicones. b Scheme of possible ($p \rightarrow d$) π interaction. X = C, N, O with p electron availability

case of breakdown. According to this general view, the still-growing exploitation of silicones evolves in a peculiar framework. The synthesis of silicones requires the availability of elemental Si which is produced by costly high-technology processes, therefore starting R_nSiCl_{4-n} product $-R = -CH_3$ or, in some cases, phenyl or $-H-$, are expensive and produced only by big companies. Moreover, silicone wastes should be processed differently than ordinary C-based polymers either in incinerators or in ordinary plastic recovery plants.

The most striking features of silicones derive from the chemical peculiarity of the $-R_2Si-O-SiR_2-$ moiety. Electronegativity values are C 2.55, Si 1.90, O 3.44 so that a strong polarization of Si–O bond is expected. Bond energies are Si–C 318 kJ/mol, Si–O 452 kJ/mol (bond energy C–H 411 kJ/mol, C–C 346 kJ/mol) [1]. The molecular structure shows Si at the centre of the tetrahedron with two Si–O and Si–C single bonds. Accordingly, the elemental stereochemistry of silicones may be represented as in Fig. 5.1a.

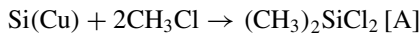
The single tetrahedron presents the side holding oxygen atoms with strong negative polarization which exercises electrostatic repulsion versus the analogous sides of neighbouring tetrahedrons. On the contrary, Si–C bonds present minimal polarization with free rotation of $-R$ groups. These features and the high flexibility of the Si–O–Si chain afford strong intramolecular electrostatic interactions and minor intermolecular ones. Thus, the general structure of silicones, for example, $-(CH_3)_2Si-O$ oils, may be represented as a helical coil with $-R$ groups pointing out towards the external surface.

The consequence of this structure is the extraordinary variety of properties which, in turn, can be tailored by changing the chemical nature of $-R$ groups or by increasing the polymer chain length and, in turn, the number of bridging oxygens.

Thus, silicone oils are used as water-repellent agents in textiles since the polar Si–O units stick to the surface leaving the Si–CH₃ groups exposed to the exterior; this action involves unwinding of the helices. The use of silicones as lubricants, anti-stick materials and surfactants can be similarly accounted for.

As for the influence of $-R$ and of bridging oxygens, it determines the use of silicones as oils, rubbers or resins and the chemical process of monomer synthesis.

For $R = \text{CH}_3$, the direct reaction [2]



gives product [A] as major component and $(\text{CH}_3)_n\text{SiCl}_{4-n}$ as by-products ($n = 3$ or 1). By controlled hydrolysis, product [A] gives the silicone chain terminated by $\text{Si}_2\text{O}(\text{CH}_3)_6$. Substitution of CH_3 by C_6H_5 or other aryl moieties is not simple and involves valuable adjustments of the monomer production. Important features of rubbers and resins will be presented later on.

Besides the structural organization of $-\text{SiOR}_2-$ polymers, the bond strengths of Si–O, Si–C and Si–H constitute important factors to account for the variety and fertility of silicone materials. Indeed, the Si–O bond (452 kJ/mol) is the strongest one among single chemical bonds; in addition, Si–C (318 kJ/mol) and Si–H (318 kJ/mol) also present a valuable bond strength. Accordingly, silicones hold a favourable thermodynamic stability versus thermal flashover and the transparency to visible and near UV spectra. To this concern, the electronic configuration of Si should not be disregarded, particularly as for the availability of empty $3d$ orbitals which make the Si atom capable of ($p \rightarrow d$) π -bonding (Fig. 5.1b), ultimately accounting for the dative π -bonding of Si with p donor ligands.

This fact has been advanced to justify the acid character of $(\text{CH}_3)_3\text{SiOH}$ and the π -electron withdrawing of Si bonded to aromatic moieties. These introductory remarks are surely not exhaustive and merely serve to present the following arguments.

5.1.2 The Synthesis of Silicones

Silicones can be synthesized using different approaches, such as vinyl-addition polymerization, condensation and radical-induced polymerization. For our specific interest concerning organic scintillators, the viable methods are the ones where the variety of chemically reactive functionalities is minimal. This choice is mandatory aiming at the integrity of the additives necessary to achieve a light emission at the maximum yield. As a matter, vinyl or hydroxyl functionalities can be considered harmless for common fluorescent molecules used in scintillation mixtures, where both the primary and secondary dyes are generally polyaromatic molecules, such as *p*-terphenyl (*p*-T), or phenyl-substituted heterocycles, such as 2,5-diphenyloxazole (PPO), 2-(4-*tert*-butylphenyl)-5-(4-phenylphenyl)-1,3,4-oxadiazole (butyl-PBD) and POPOP, the latter behaving as a wavelength shifter. However, the catalyst and the cross-linking compound used to carry out the reticulation reaction in polysiloxanes can interact with the fluorophores, resulting in a detrimental effect either on the optical properties of the dye or in the reactivity and efficiency of the additives for cross-linking.

As an example, one of the pioneering works on the use of silicones to prepare scintillators focuses on the use of 3-hydroxyflavone (3-HF) as unique green-emitting dye, characterized by a large Stokes shift induced by intramolecular proton transfer [3]. The wide interval between absorption and emission of the dye in ideal conditions, such as inhibiting H-bonding of the dye with the medium, hampered reabsorption phenomena. In this case, the presence of silane moieties, Si–H, proved to be detrimental for the attainment of green-emitting scintillator, owing to the H-bonding capability of the reactant with 3-HF. Therefore, peroxide cure was chosen to achieve scintillators with optimal light output, preserving the dye features.

Later on, Zane Bell and co-workers [4–6] doped poly(dimethyl-*co*-diphenylsiloxane) with PPO and adopted an addition-cure system; they prepared scintillators suitable for thermal neutron and gamma-rays detection by loading the precursor mixture either with boron or gadolinium compounds. Thermal neutron detection will be more discussed in Sect. 5.4.2.

As for our research group, since the beginning of this activity related to organic scintillators, two systems have been selected and improved in terms of component ratio and of time and temperature of hardening:

- (i) Platinum-catalyzed vinyl addition,
- (ii) Two-steps Tin-catalyzed condensation.

In case (i), Pt is used in form of Karstedt's catalyst, with Pt^0 coordinated with vinyl-substituted disiloxane, to promote the hydrosilylation between vinyl-terminated linear polysiloxane macromolecules and Si–H cross-linker. The reaction pathway has been studied: critical aspects are the possible formation of Pt metal clusters, causing undesired plasmonic absorption and consequent yellowing [7], and the effect of Pt catalyst poisoning induced by the presence of sulphur or nitrogen heteroatoms in the fluorophore compounds. This reaction has been improved by varying the type of catalyst, i.e. Pt concentration or solvent, and the ratio among base resin, cross-linker and catalyst, as described in detail in the following paragraphs. The vinyl-terminated resins throughout used are schematized in Fig. 5.2. The chemical structures or the molecular weight of these base resins have been changed according to the features demanded for specific application, i.e. aiming at obtaining thin films, a low-viscosity precursor has been chosen or the content and type of substituent have been tailored to enhance additives solubility. Some of these key properties are reported in Table 5.1 of the next section.

The condensation process (ii) involves three crucial reagents: the base resin, which bears silanol terminal groups, the cross-linker, which is usually polydiethoxysilane holding hydrolysable Si–OR groups which react with Si–OH for cross-linking, and the tin-based catalyst, i.e. dibutyltin dilaurate, which promotes a primary hydrolysis and accelerates the condensation. The reagent structures are reported in Fig. 5.3. This type of network leads to minimal shrinkage with the advantage, over addition curing, of exploiting reagents in absence of Si–H bonds, which might attack double bonds of the fluorophores, thus degrading their optical properties.

Irrespectively of the curing system, the process of a preliminary dissolution of fluorophores in suitable media, such as tetrahydrofuran or acetone, followed by

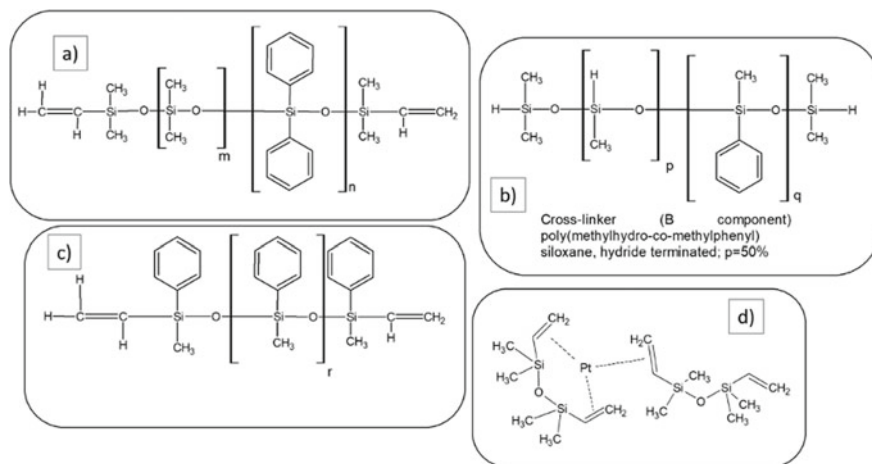


Fig. 5.2 Chemical structures of resins and compounds used in the synthesis of phenyl-containing polysiloxanes by vinyl-addition polymerization. **a** Vinyl terminated copolymer dimethyl-diphenyl with n variable in the range 4–25% as detailed in Table 5.1; **b** chemical structure of the silicon hydride cross-linker; **c** vinyl-terminated homopolymer methyl-phenyl, with $r = 100\%$; **d** chemical structure of Karstedt's Pt catalyst

addition to the siloxane precursor mixture has been pursued. This technique proved to be challenging, owing to further complication to cross-linking arising from the solvent and to the possible presence of residual solvent molecules entrapped into the cross-linked siloxane network. These residues under heating or under impinging particle fluxes may act as radiation or heat-sensitive centres, releasing fragments and producing porosities or creating amber-coloured carbonaceous clusters inside the structure.

Therefore, additives were dissolved directly in the form of powder in the siloxane precursor viscous mixture and left under stirring and mild warming conditions overnight.

5.2 Optical Properties of Phenyl-Containing Polysiloxanes

As mentioned before, phenyl-containing polysiloxane fulfils requirements for an intrinsically fluorescent polymer as matrix for a radiation-responsive material. This fact holds for both solid and liquid systems and it is well known that liquid scintillators, such as the commercial EJ-301 (Eljen Technology), largely employed in nuclear physics experiments for the detection of gamma rays and fast neutrons, belong to the family of benzene derivatives, such as mixed isomers of xylene. These highly flammable and toxic aromatic solvents have the advantage of easily dissolving suitable dyes to achieve optimal scintillation light yield and the capability to discriminate

Table 5.1 Main features of the oligomeric liquid phenyl-siloxanes (first block) and of the siloxane base resins used to prepare organic scintillators, either by addition (second block) or condensation (third block)

Label	Chemical name	Structural unit	Molecular weight (g/mol)	Phenyl mol/l	Refractive index
PM100	poly(methylphenylsiloxane) vinyl terminated	$-\text{OSi}(\text{CH}_3)\text{Ph}-$	2,500–2,700	7.6	1.490
TPTMTS	tetramethyl tetraphenyl trisiloxane	$-\text{OSi}(\text{Ph})_2-\text{OSi}(\text{CH}_3)_2-$	484.8	8.8	1.559
PDPDMS4	poly(diphenyl- <i>co</i> -dimethylsiloxane) vinyl terminated	$-\text{OSi}(\text{Ph})_2-\text{OSi}(\text{CH}_3)_2-$	14,000	0.55	1.430
PDPDMS15	poly(diphenyl- <i>co</i> -dimethylsiloxane) vinyl terminated	$-\text{OSi}(\text{Ph})_2-\text{OSi}(\text{CH}_3)_2-$	19,000	0.71	1.465
PDPDMS22	poly(diphenyl- <i>co</i> -dimethylsiloxane) vinyl terminated	$-\text{OSi}(\text{Ph})_2-\text{OSi}(\text{CH}_3)_2-$	12,500	2.3	1.493
PMPS100	poly(phenylmethylsiloxane) homopolymer vinyl terminated	$-\text{OSi}(\text{CH}_3)\text{Ph}-$	2,000–3,000	6.1	1.537
PDPDMS14	poly(diphenyl- <i>co</i> -dimethylsiloxane) silanol terminated	$-\text{OSi}(\text{Ph})_2-\text{OSi}(\text{CH}_3)_2-$	900–1,000	1.9	1.473

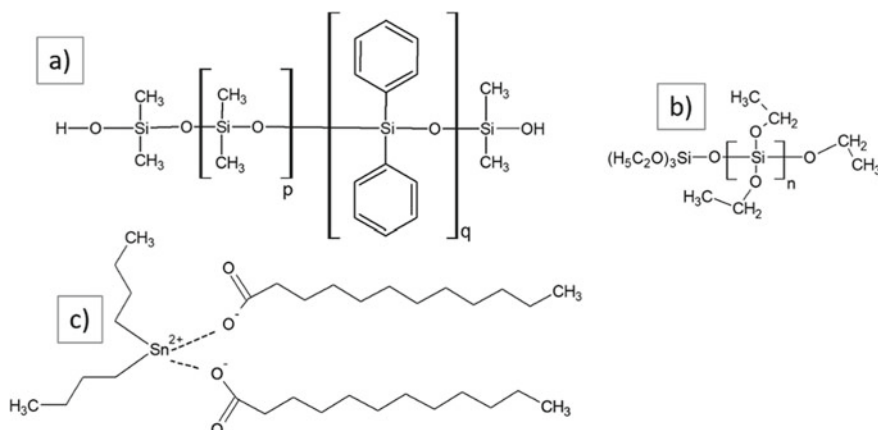


Fig. 5.3 Chemical structures of the reagents used to obtain phenyl-substituted silicones by Sn catalyzed condensation. **a** Poly(dimethyl-*co*-diphenylsiloxane), silanol terminated ($q = 14\text{--}18\text{ mol\%}$); **b** polydiethoxysilane as cross-linker; **c** dibutyltin dilaurate used as catalyst

particles on the basis of the different light pulse shape [8]. Recently, the scintillation performances of new aromatic solvents and water-based emulsions have been investigated in several works [9–11 and references therein], aiming at safer work or handling conditions. Very recently, a non-toxic, non-flammable liquid scintillator has been synthesized with the peculiarity that the solvent itself acts at the same time as matrix to harvest the energy of impinging radiation and as fluorophore to emit scintillation light [12]. Liquid siloxanes should be even safer, owing to their very high flash point, very low volatility, inertness and stability at room temperature. Moreover, waste disposal can be achieved simply by incineration, where evolution of volatile aromatic fragments and formation of powdery silica are the final steps of the oxidative thermal degradation of siloxanes. Within this framework, the profitable use of liquid siloxanes to prepare scintillation mixtures with good detection capability and fast n/γ discrimination characteristics has been demonstrated [13, 14].

In order to point out the basic optical features of siloxane macromolecules bearing phenyl groups, two model compounds have been selected; their structures are depicted in Fig. 5.4, while relevant chemical characteristics are reported in Table 5.1.

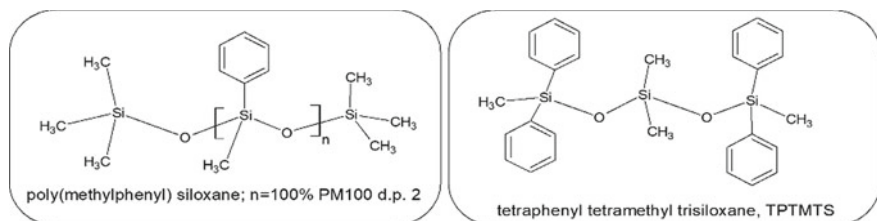


Fig. 5.4 Chemical structure of two siloxane liquids chosen as model compounds

As for the base resin, either *co-* or homo-polysiloxane, with vinyl or silanol termination for the polymer chain, their structures are reported above and main features are in Table 5.1.

Fluorescence measurements of these model compounds are reported in Fig. 5.5. As for the base resins with the structure composed of poly(dimethyl-*co*-diphenylsiloxane) with different amount of phenyl groups, a clear trend can be observed in Fig. 5.5a. The emission spectra exhibit a broad peak at 330 nm with a shoulder at about 285 nm. The lower wavelength shoulder originates from the single phenyl ring, often referred to as “monomer” in literature, while the peak at about 320 nm is characteristic of the excimer formed by two interacting phenyl units within the same macromolecule (intramolecular excimer). This was discussed by Salom and co-workers [15] and, more recently, by Itoh [16], whose fluorescence measurements on linear polysiloxanes block copolymers with either $-\text{Si}(\text{Ph})_2-\text{O}-\text{Si}(\text{CH}_3)_2-$ or $-\text{Si}(\text{Ph})(\text{CH}_3)-\text{O}-\text{Si}(\text{CH}_3)_2-$ units and on oligomers chosen as model compounds revealed the presence of the peak at about 325–330 nm in dilute solutions, where intermolecular interactions are negligible.

The presence of both features, monomer and intramolecular excimer, is typical of aromatic polymers and phenyl-containing siloxanes. The influence of the conformation structure being either block copolymers of dimethyl-diphenyl units or

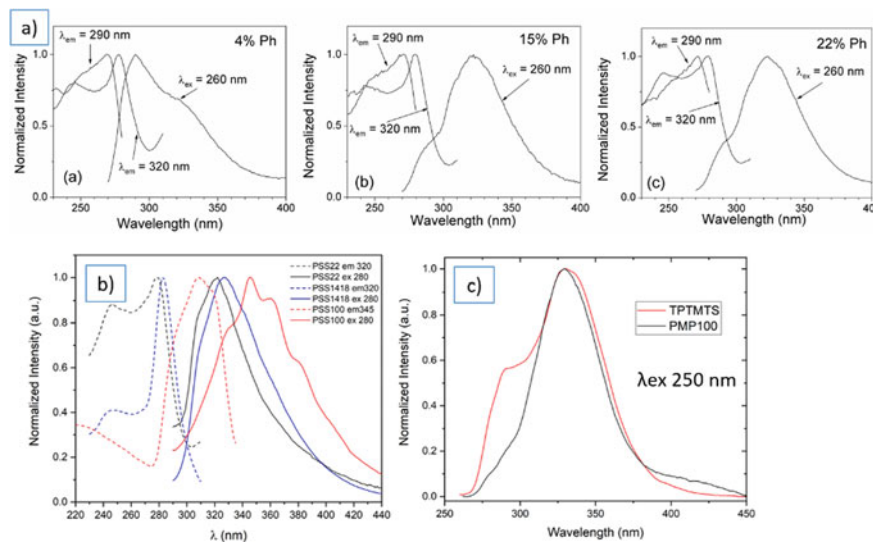


Fig. 5.5 Optical spectra obtained from polysiloxane resins with pendant phenyl groups. **a** Excitation/emission measurements of poly(dimethyl-*co*-diphenylsiloxane) cross-linked resins with increasing amount of phenyl groups; the corresponding vinyl-terminated precursors are labelled as PDPDMS in Table 5.1 (reproduced from [17] with permission from Elsevier). **b** Same as **a** but for resins derived from homopolymer, PMP100, or cross-linked by condensation, PSS1418, derived from PDPDMS14. **c** Emission spectra of two liquid siloxane oligomers, described in Table 5.1, used as model compounds

homopolymer formed by methyl-phenyl repeating units, on the fluorescence features in relation to spectral shape and intensity has been thoroughly studied by our research group [17, 18]. The emission intensity ratio between single phenyl and excimer depends on the possible formation of intramolecular excimers in the different compounds, which is a complex phenomenon, strongly dependent on the structure of the molecule. In carbon-based compounds like vinyl polymers, studied by Hirayama [19], the formation of intramolecular excimers only occurs between adjacent phenyl groups separated by a main chain segment of three carbon atoms (Hirayama's rule), to achieve a face-to-face configuration of the chromophores within a mutual distance of 0.254 nm.

This rule is dictated by the rigid tetrahedral configuration of the main chain carbon atoms. In polysiloxanes, the higher flexibility of the $-\text{Si}=\text{O}-\text{Si}-$ bonds allows for various conformations, where the excimer can be formed between two phenyl groups linked to silicon atoms separated by one oxygen, but also by phenyl units divided by 5 atoms ($-\text{Si}=\text{O}-\text{Si}=\text{O}-\text{Si}-$) [20]. In this framework, long-chain molecules, with high amount of phenyl substituents, give rise to a strong excimer component, as observed by Itoh [16]. In Fig. 5.5a, the increase of diphenyl unit concentration in the dimethyl-*co*-diphenyl polysiloxane base resin leads to a visible decrease in the monomer/excimer ratio. On the other hand, the presence of less bulky $-\text{CH}_3$ group on Si-phenyl unit of the base resin results in higher torsional freedom of the $\text{Si}=\text{O}-\text{Si}$ linkage and, in turn, more probable formation of excimers through facing phenyl rings along the chain. This can be observed in Fig. 5.5b, where the spectrum of PMPS100 derived silicone shows almost pure excimer emission with a remarkable red-shifted component with respect to emission from excimer in diphenyl containing resin (350 nm vs. 330 nm). A further confirmation of the relevance of conformational structure on the occurrence of excimers is given by the fluorescence spectra of model compounds reported in Fig. 5.5c: while the polysiloxane fluid with diphenyl unit alternated to dimethyl along the chain still displays the presence of monomer emission on excitation, the liquid resin with repeating methyl-phenyl substituents at Si displays predominant emission from excimer, whose formation is clearly promoted by the rotational freedom, being the content of phenyl units per gram almost the same in both model compounds.

The possibility to control the amount of phenyl groups in the silicone network is important from two points of view. First of all, by increasing the concentration of phenyl units one can improve the solubility of dye molecules in the network, as mentioned before. Moreover, excimer luminescence features increase both in wavelength and in intensity with the concentration of aromatic groups, owing to the formation of more complex configurations, probably involving more than two phenyl units. The role of the excimer feature in the scintillation process has to be deepened. For instance, in PVT and PS networks, it is known that the energy transfer to the primary dye comes from excimers whose luminescence peaks overlap with the dye absorption spectrum.

The importance of changing the amount of phenyl groups in the base resin is related to dyes solubility, as mentioned before, and can exert a positive effect on the whole luminescence intensity. The enhanced emission from red-shifted excimer

component can reduce efficient energy transfer, as will be shown in the following sections, owing to worse matching between absorption and emission of donor and acceptor in the transfer mechanism.

5.3 Design of Polysiloxane-Based Scintillators

5.3.1 Energy Transfer in Organic Polymers

In organic systems, the scintillation process is based on electronic transitions between π molecular orbitals of conjugated and aromatic molecules. In fact, the energy level difference of these orbitals allows the emission of photons in the visible range, whose frequency (wavelength) decreases (increases) with the size of the conjugated groups.

Independently from the excitation mechanism, the excited state relaxes down to the first singlet excited state, S_1 , and then decays to the singlet ground state, S_0 . This last transition can occur either radiatively, with the emission of a photon, or non-radiatively, converting the excitation energy into heat. The probability to obtain a radiative transition is known as quantum efficiency, Φ . The luminescence intensity decays exponentially with time following the law

$$I(t) = I_o \exp\left(-\frac{t}{\tau}\right) \quad (5.1)$$

where τ is the luminescence decay time, ranging from 1 to some tens of ns for almost all organic fluorophores.

A fraction of excited molecules may undergo a transition to the triplet state, T_1 , through a process known as inter-system crossing. From the triplet state, the molecule may either decay with a long-living transition (in the order of 10^{-4} s) to the ground state, with a very low quantum yield, or go back to the S_1 state, which radiatively decays giving rise to a phenomenon known as delayed fluorescence. Luminescence of organic systems has been extensively treated in fundamental books by Lakowicz and Valeur [21, 22].

Besides the luminescence process, organic scintillation is also based on the energy transfer mechanism between different fluorophores. Following this process, the excitation energy of a fluorophore (donor) D^* is transferred to a second, chemically different, molecule (acceptor) A



which finally decays to the ground state with its characteristic luminescence spectrum and timing resolution.

There are two possible energy transfer mechanisms: radiative energy transfer, and resonant or non-radiative energy transfer. Radiative energy transfer is simply the reabsorption, by the acceptor, A , of a photon emitted from the donor, D^* .

Resonant energy transfer is based on a resonant dipole–dipole interaction, firstly described by Förster [23]. The rate constant k_{RET} of this process is inversely proportional to r^6 , where r is the molecular distance, following the rule:

$$k_{RET} = \frac{1}{\tau_0} \left(\frac{R_0}{r} \right)^6 \quad (5.3)$$

where τ_0 is the donor lifetime in absence of the acceptor, and R_0 is the Förster radius, given by

$$(R_0)^6 = \frac{3 \ln 10 \Phi_F^0}{64 \pi^5 N_A n^4} \int_0^\infty F_D(\lambda) \varepsilon_A(\lambda) \lambda^4 d\lambda \quad (5.4)$$

Here, Φ_F^0 is the donor fluorescence quantum yield in absence of the acceptor, N_A the Avogadro number, n the matrix refractive index, $F_D(\lambda)$ the fluorescence spectrum of the donor and $\varepsilon_A(\lambda)$ the molar absorption of the acceptor. The Förster radius ranges from 1 to few nm and is determined by the overlap between the donor luminescence spectrum and the acceptor absorption spectrum.

In polymeric scintillators, the first energy transfer is a resonant process from the polymer aromatic groups to a dye, known as primary dye, dispersed into the matrix. Since the typical luminescence spectrum of aromatic polymer lies in UV (280–320 nm), the primary dye has to be chosen with an absorption feature in that range. Owing to the Stokes shift, the primary dye luminescence band is typically located around 350–390 nm. Finally, a secondary dye is solubilized in the matrix, whose role is to shift the emission wavelength of the primary one to the visible range (usually around 420 nm) through an energy transfer mechanism which could be either non-radiative or radiative. Other key information of this whole process is also available in Chap. 1.

Aiming at realizing the energy transfer process between the base polymer and dissolved dyes, the study of the fluorescence features of both matrix and dyes is of paramount importance. As for polysiloxane scintillators, to select the proper dye concentration a preliminary study must be carried out on the optical properties of base resins, the energy transfer between matrix and primary dye, and between the latter and the wavelength shifter. Moreover, the transparency of the scintillator to the scintillation light has to be preserved.

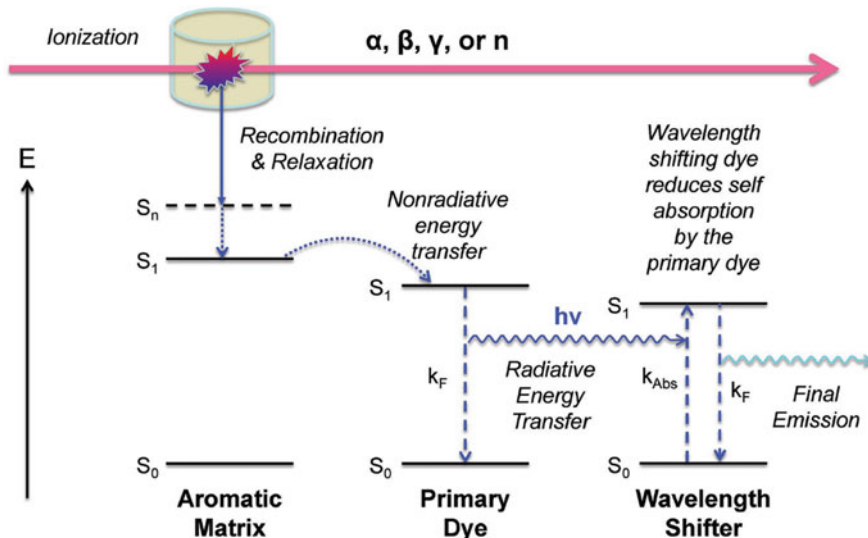
The analysis of the optical properties is surely useful, but the result in terms of scintillation yield is not straightforward. The ionization process induced by impinging radiation leads to exciting the material, either by direct particle interaction or by indirect excitation through secondary electrons; it may be remarkably different from direct UV excitation, used to study multiple fluorophore mixtures in photoluminescence spectroscopy. As an example, the quenching of emitted light due to high density of ionization cannot be foreseen using excitation/fluorescence spectroscopy

techniques. Moreover, it is worth highlighting that the scintillation yield is based on the efficiency of both the conversion of the energy released by the ionizing radiation into electronic excited states and the transfer of this excitation energy to emitting centres with high quantum yield. However, from an operational point of view, the use of these analytical methods can be profitably exploited to optimize a defined three-component system, i.e. matrix, primary dye, wavelength shifter, or even to discard it in case of insufficient response. This strategy has been frequently adopted by our group, taking into account that literature data on optical properties of phenyl containing polysiloxanes are limited and aged 20 years.

5.3.2 Polymeric Scintillators

In polymeric scintillators, the scintillation yield is determined by an efficient interplay between the excited states of different fluorophores. The whole process of scintillation is described in Scheme 5.1.

The impinging radiation interacts with the medium producing ionized or excited molecules. As a result, in the network secondary energetic electrons are produced, causing further electronic excitation in the polymer. A fraction of these excited states involves aromatic groups which, through a non-radiative energy transfer process, donate their energy to the primary dye. In order to enhance the collection of energy from the matrix, the primary dye is typically solubilized at high concentrations,



Scheme 5.1 Description of the process of light emission from a polymer-based scintillator, resulting from radiation-induced ionization

namely around 2.0 wt%. Then, the primary dye transfers its energy to the secondary one, whose concentration is two orders of magnitude lower. Low concentrations are required to avoid both quenching and self-absorption effects. The energy transfer mechanism from the primary to the secondary dye has been typically classified as radiative [24], even if some evidences of non-radiative resonant mechanisms are reported [18]. The dyes are selected on the basis of their solubility, radiation hardness, chemical stability, timing property, exciton nature, price (availability), quantum efficiency and energy transfer capability. To date, the most widely used molecules in commercial plastic scintillators are *p*-terphenyl (*p*-T) and PPO as primary dyes and POPOP as a secondary one (see Chap. 1 for more information).

The scintillation response to gamma rays is essentially the response to scattered Compton electrons. Since organic materials have typically low average Z values, multiple scattering events are unlikely and the result is γ -rays scintillation spectra characterized by a broad Compton edge. Photopeaks at the whole photon energy, created by multiple γ scattering in the solid, are not observed in organic scintillators.

Heavy particles, like protons or ions, release their energy along cylindrical tracks where the most part of the ionization process is localized. The density of ionized states increases with the energy released per path unit dE/dx , also known as linear energy transfer (LET), that is correlated with the mass and the energy of the particle.

The resulting scintillation light yield $L(E)$ is a function of both particle type and energy. Absolute measurements of this parameter are difficult, and relative evaluation with respect to commercial standards is preferred. For instance, the commercial scintillator EJ-212, reproducing NE-102, has a declared light yield of 10,000 photons per electron MeV. This value decreases for protons and ions with the same energy, due to quenching effects in the ionization regions surrounding the tracks.

For very low ionization densities, occurring for electrons, the scintillation yield is proportional to the particle energy E

$$L(E) = SE \quad (5.5)$$

which can be expressed with the differential form

$$\frac{dL}{dx} = S \frac{dE}{dx} \quad (5.6)$$

in order to relate the scintillation intensity to the particle LET.

Heavy particles produce a concentration of ionized and excited molecules along the track proportional to the LET, equal to $B dE/dx$, where B is a constant. So, by assuming a unimolecular quenching characterized by a rate constant k , the specific light yield is expressed by the formula proposed by Birks [24]

$$\frac{dL}{dx} = \frac{S(dE/dx)}{1+kB(dE/dx)} \quad (5.7)$$

where the quenching parameter depends on the scintillator composition. Different models are proposed for this mechanism. Among them, the bimolecular quenching model, holding for high LET particles, has to be cited:

$$\frac{dL}{dx} = \frac{S(dE/dx)}{1+kB'(dE/dx)+C(dE/dx)^2} \quad (5.8)$$

Nonetheless, at present the most used model is Birks' one, owing to its simplicity for calibration procedures.

The main drawback of polymeric scintillators is their low radiation hardness, due to the weakness of carbon bonds with respect to inorganic crystals. The radiation-induced ionization produces molecular radicals and hydrogen loss, leaving unsaturated bonds which absorb the light in a region corresponding to the emission range of secondary dyes [25]. This absorption lowers the scintillation yield of the detector, which decreases with the absorbed dose D following the law [24]

$$I = I_0 e^{-\alpha D} \quad (5.9)$$

where α is a constant depending on the polymer network.

The search of polymeric scintillators with improved radiation resistance is based either on the study of harder networks, such as polysiloxanes tested for the first time by Bowen et al. [26], or on the selection of dyes with a large Stokes shift, like 3-HF, characterized by luminescence bands at wavelengths higher than the residual absorption features [27]. Chapter 1 identifies several suitable compositions for rad-hard scintillators.

For high radiation fluxes, occurring for instance in ion beams, the response of polymeric scintillators dramatically decreases with the fluence due to the damage of both polymer network and emitting dyes, giving rise to secondary luminescence features related to organic by-products [28, 29].

5.3.3 *Polysiloxane-Based Scintillators*

As previously mentioned, pioneering work on polysiloxane as matrices to produce scintillators date back to the 90s [26, 30]. The motivation for searching alternatives to commercial plastic scintillators, i.e. polystyrene- or poly(vinyltoluene)-based, is mainly related to the radiation hardness. Introductory topics of those papers have been indeed focused on the next generation high-energy accelerators for physics research and the need of scintillators suitable to withstand the expected high irradiation doses, up to tens of MRad. In this framework, the use of Si–O–Si containing polymers as skeletal repeating unit is surely promising on the basis of the peculiar chemical properties of the siloxane moiety and of the thermal characteristics of the base polydimethylsiloxane, as discussed previously. As a first attempt, similarly to poly(vinyltoluene) plastics, fluors belonging to the category of polyarylenes have

been used for doping polysiloxane. However, these low polar molecules display minimal solubility in siloxanes and only a limited amount can be added to the matrix so as to avoid precipitation of aggregates. Later on, oxazole derivatives, such as PPO, have been successfully exploited as primary dyes in polysiloxanes [4, 5, 31] in combination with minimal amount of a wavelength shifter, such as triphenylpyrazoline or dimethyl-POPOP. Scintillators produced following this pathway have been proved to be sensitive to alpha particles and gamma rays, with light yield reaching values of 50–65% with respect to the commercial standard EJ-212. Bell and co-workers further widened the application field of these scintillators by adding suitable Boron and Gadolinium compounds as thermal neutron sensitizers. In the case of boron *m*-carborane was used, while Gd was solubilized in the matrix as nitrate salt complexed with tributylphosphate ligand [4, 5]. Addition of carborane into siloxane not simply by dissolution but through generation of covalent bonds has been also pursued by Bell et al. [6].

Our research group has been involved in the search for flexible, radiation resistant, cost-effective detectors, to fulfil the needs of radiation monitor in nuclear physics research plants, such as the SPES project at LNL (Selective Production of Exotic Species) [32]. We have considered the use of siloxanes exploiting different combinations of matrices and fluorophores, as previously described. In particular, the use of polysiloxane copolymers with dimethyl-diphenyl units (22% diphenyl) and poly(methylphenylsiloxane) homopolymer obtained by Pt-catalysed polyaddition has been adopted as most promising. The combination of dyes, both not interfering with the cross-linking reaction and assuring the best levels of light yield, has been found in PPO and Lumogen® Violet 570 (BASF). Alpha particles from ^{241}Am source, γ -rays and He^+ and H^+ ion beams have been detected with these scintillators and a scintillation yield of 65–70% of standard EJ-212 has been recorded under irradiation with alpha and γ -rays [17, 33]. Very recently, a light yield higher than EJ-212 has been measured under irradiation with 5 MeV H^+ (beam current 0.5 fA) at the LABEC accelerator facility (INFN-FI), using 1 mm thin siloxane scintillators, made of homopolymer doped with 1% PPO and 0.02% LV [34]. Pulse height spectra collected from scintillators with the same dyes concentration but different matrix are shown in Fig. 5.6.

It is important to evidence that, for the same energy (about 5 MeV), different impinging particles produce different light response: in the case of alpha from the ^{241}Am source commercial EJ-212 clearly outclasses the siloxane scintillator, irrespectively of the used matrix. On the other hand, using H^+ beam, whose penetration depth in the material is about 10 times higher than alpha with the same energy (see Fig. 5.6b), the response of the siloxane-based scintillators are comparable or even better than 0.5 mm thick EJ-212.

These results point to optimal detection capability of siloxane scintillators, which is limited by self-absorption and surface defects acting as scattering centres, but can be profitably exploited in case of thin layers application, where flexibility and radiation resistance are mandatory.

The possibility to shift the emitted light further to longer wavelengths was realized using a combination of different Lumogen® dyes (BASF), thus obtaining red-emitting

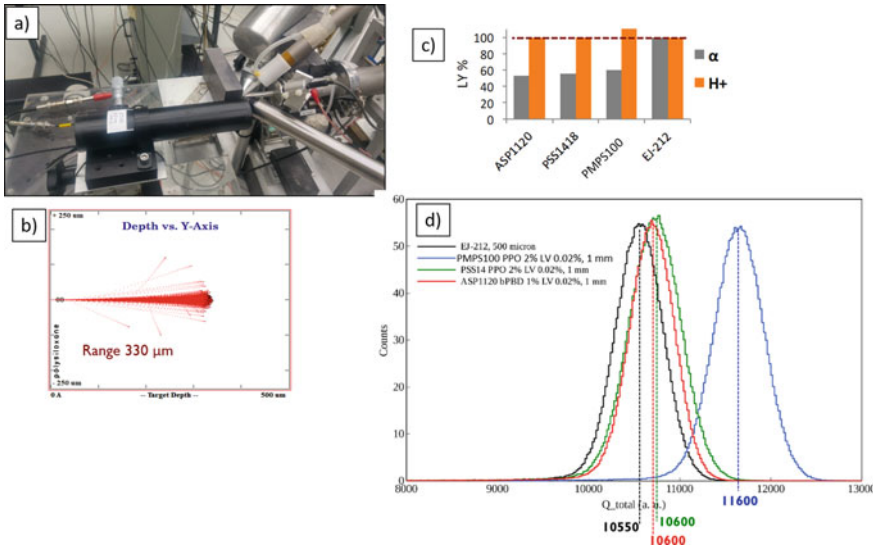


Fig. 5.6 **a** Set-up @LABEC for H^+ irradiation (5 MeV, 0.5 fA, spot 0.5 mm); **b** penetration range of H^+ by SRIM simulation software [35]; **c** light yield of the same sample under different particles with around the same energy, either alpha from source or H^+ from accelerator; **d** pulse-height spectra collected under H^+ beam for EJ-212 and different siloxanes [34]

scintillators as shown in Fig. 5.7a. By adding a selected amount of Lumogen® F Red 300 (LR) in poly(dimethyl-*co*-diphenylsiloxane) and fixing the amount of PPO and Lumogen® F Violet 570 (LV), it is possible to study in detail the energy transfer mechanism between LV (donor) and LR (acceptor), ultimately leading to the optimal composition, as shown in Fig. 5.7b [36].

This approach has been pursued to match the response of the scintillator with the sensitivity of Si photomultiplier or Si avalanche photodiodes (APD), whose sensitivity curve is typically lower in the blue range of the visible spectrum. These devices present several advantages over the traditional photomultiplier tubes, such as higher quantum efficiency, compactness, insensitivity to magnetic fields, low power consumption, durability and good energy resolution. As can be seen in Fig. 5.7c, the response of the scintillator can be enhanced in the range of maximum sensitivity of the tested APD by proper selection of secondary dyes and relative concentrations, so that the light yield of the red-emitting scintillator reaches 85% of the standard EJ-212. To our knowledge, this is the first characterization of a red-emitting polysiloxane scintillator.

In order to carry out an in-depth investigation on the radiation resistance of polysiloxane scintillators with particular reference to the fluorophores decomposition and creation of colour centres, the most useful technique is Ion Beam Induced Luminescence (IBIL) [28]. In the specific case of siloxanes, we have studied both the copolymer with 22 mol% of diphenyl units and blends with the homopolymer,

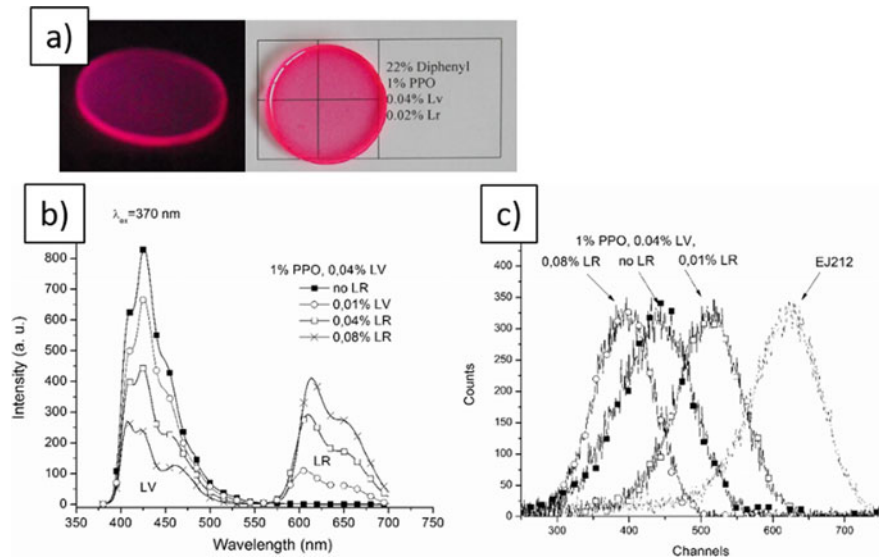


Fig. 5.7 **a** Polysiloxane-based red-emitting scintillator irradiated by UV light (*left*) and in daylight (*right*); **b** emission spectra of LV and LR for samples with 1% PPO, 0.04% LV and variable amount of LR; **c** scintillation spectra of different samples with 1% PPO, 0.04% LV and different amounts of LR (reprinted from [36] with permission from IEEE)

poly(methylphenylsiloxane), added with different fluorophores, either 2,5-bis(5-*tert*-butyl-2-benzoxazolyl)thiophene (BBOT) or LV and PPO [29, 37]. By comparing the degradation rate of the luminescence spectra during ion irradiation, we evidenced that phenyl-containing polysiloxane displayed higher resistance with respect to EJ-212 under 2 MeV H⁺ irradiation. This has been related to the higher bond energy of Si–O–Si moiety and to the presence of bulky diphenyl groups on the same Si atom, acting as protecting shield towards the cleavage of neighbouring Si–O bonds. Moreover, irradiation with γ -rays from intense ⁶⁰Co source with a dose rate of 1,000 Gy/h at doses up to 54 kGy has been performed and again a higher resistance to damage of silicones has been demonstrated with respect to EJ-212 plastic scintillators, both in terms of light yield and in terms of UV–vis transmittance (Fig. 5.8).

5.4 Polysiloxane Scintillators for Neutron Detection

5.4.1 Neutron Detection in Organic Scintillators

Neutron detection in organic scintillators is based on the indirect detection of charged particles resulting from nuclear reactions into the matrix. In particular, two main neutron classes may be proposed, characterized by very different reactions: slow

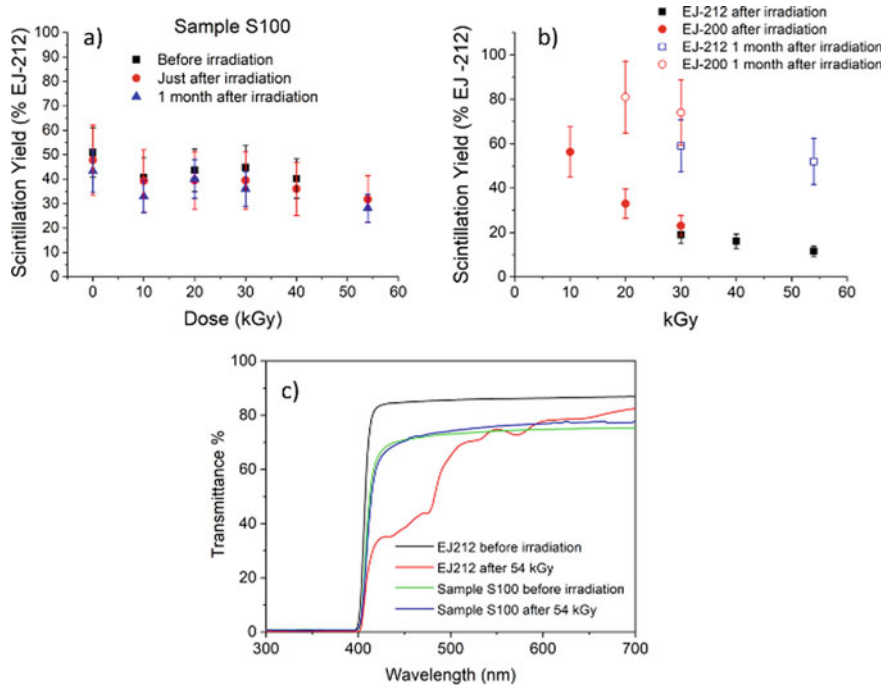
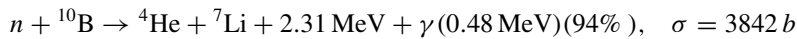
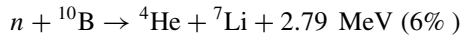


Fig. 5.8 **a** Light response of PDPDMS-22 scintillator to ^{241}Am alpha and one month after γ -rays irradiation; **b** same as **a** but for commercial standards; **c** UV–vis transmittance loss upon irradiation of the standard plastic scintillator (reprinted from [29] with permission from Elsevier)

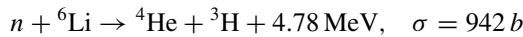
or thermal neutrons and fast neutrons. Chapters 2 and 3 extensively present this important application of organic scintillators.

Slow neutrons, with energies lower than 0.5 eV, are detected through reactions with suitable isotopes, mainly ^{10}B and ^6Li , giving rise to energetic charged particles, like alpha, triton and Li, following the following paths.

For Boron:



For lithium:



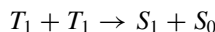
Reaction products are charged particles with low range in matter and can be easily detected by scintillators.

On the other hand, fast neutrons give rise mainly to elastic scattering with protons, whose given energy ranges from 0 to the incident neutron energy. So, the scintillator response is related to the light produced by scattered protons.

The detection of slow neutrons with organic scintillators can be achieved by dispersing suitable compounds enriched with ^{10}B or ^6Li isotopes. From this point of view, ^6Li should be preferred, even if the reaction cross section is low, since the products are lighter and with higher energies, therefore giving rise to a higher scintillation yield. On the other hand, there are no simple ways to dissolve Li-based metal–organic compounds into polymeric matrices, hence the entrapment of ^6Li nuclei in organic scintillators is obtained directly using inorganic powders, such as lithium fluoride, which severely deteriorates the optical transparency of the scintillator. Only quite recently transparent ^6Li containing plastic scintillators have been obtained using Li methacrylate and Li salicylate as precursors [38, 39]. On the other hand, boron can be easily incorporated into organic structures, linked to polymer or dispersed in form of molecules like *o*- or *m*-carborane, preserving the scintillator transparency and it is used since the first attempts to produce scintillators for thermal neutrons [4, 5, 33, 40].

Another approach to incorporate neutron sensitizers isotopes inside a polymer matrix preserving the transparency as much as possible is to synthesize nanoparticles of inorganic compound of ^6Li or ^{10}B or both, thus minimizing light scattering. As for polysiloxane-based scintillators, the topic will be discussed forward. Regarding polyaromatic-based plastic scintillators, very recently, the synthesis of lithium tetraborate nanocrystals with enriched ^6Li and ^{10}B has been pursued and the incorporation of small amounts of nanopowders into polystyrene-based scintillators, formulated for fast neutrons/ γ -rays recognition, allowed to achieve optimal triple discrimination, including thermal neutrons [41].

The detection of fast neutrons is complicated by the presence of γ -rays, which is a background associated with every neutron field. Since both γ -rays and scattered protons are characterized by broad energy spectra, their discrimination cannot be performed by the analysis of the scintillation pulse amplitude. The main approach in organic systems is the Pulse Shape Discrimination (PSD) method. This method is based on the different ionization density produced by the particles scattered by γ -rays, i.e. electrons, and by neutrons, i.e. protons (see Chaps. 2 and 3). Other discrimination techniques are available, and are overviewed in Chap. 10. When ionized molecules capture an electron, they typically form a triplet excited state T_1 [42]. Two very close triplet states can undergo a short-range interaction, called Triplet-Triplet Annihilation (TTA), giving a S_1 excited state and a ground state



where the S_1 state radiatively decays to the ground state. This process is called *delayed fluorescence* and differs from *prompt emission* in displaying decay times of the order of tens of ns, with respect to 1–2 ns, maintaining the same spectral response. From the point of view of the detection, it gives a delayed scintillation, contributing to the

scintillation pulse as a tail extending to longer times. In this framework, protons give rise to a higher density of ionized states along the track with respect to electrons and their scintillation pulses present higher long-time tails with respect to electrons. Suitable analyses of the pulse shape allow to discriminate between the two particles, i.e. between events produced by fast neutrons and γ -rays.

The difficulty of this approach is that the T_1-T_1 interaction is a bimolecular short-range process (less than 1 nm), much shorter than the Förster interaction, exponentially decaying as a function of the intermolecular distance [43]. In other words, molecules in triplet states need to be very close to complete the process.

In liquid scintillators, TTA interaction can be easily accomplished through a diffusion-controlled mechanism. For this reason, the organic detectors of choice able to discriminate at optimal level fast neutrons from γ -rays are traditionally liquid scintillators. In liquids, the molecular diffusivity allows for long-living triplet states to interact even if they are formed far away from each other. In rigid plastic scintillators, typical dye concentrations do not allow a molecular proximity suitable for PSD. Nevertheless, several decades ago, in 1959, Brooks prepared a plastic scintillator, namely NE 150 sold by Nuclear Enterprises, based on polystyrene, showing PSD [44]. The scintillator owes its capability to discriminate different particles to the remarkable presence of either naphthalene or 4-isopropylbiphenyl in high percentage (10 wt%), thus the mechanism of excimer formation is most likely responsible for the observed features. Unfortunately, Brooks found that the plastic scintillator NE 150 was not stable with time, and the research on this topic cooled down for several years, although the need for the substitution of poisoning and flammable liquid scintillators made a comeback from time to time. This fact spurred the research for finding new solid systems capable of PSD, and, since the early 2000s, several research groups published relevant work and experimental results on this topic, although no useful combination of plastics and dyes to achieve PSD was found. In particular, in 2008, M. Hamel synthesized new fluorophores with optimal features as for energy transfer from the polyaromatic matrix and the additive itself, but inefficient regarding pulse shape discrimination [45]. In the same period, the group of Adadurov and Zhmurin [46, 47] focused on the search of high light yield and optimal radiation resistance plastic scintillators, acting on the base structure of the polymer matrix and the concentration of fluorescent additives. The authors worked also on rare-earth-based phosphorescent additives [48] and successfully exploited the difference in decay time of the additives to enable PSD with excellent performance, as detailed in [49]. However, the intuition expressed several years before by Hamel et al. in [45], related to the need of close proximity of triplet states to enable PSD in plastics, owing to the “rigidity” of the matrix hampering diffusion of triplets, proved soundly true few years later, as shown by the work at the Lawrence Livermore Laboratory. The group of N. Zaitseva and co-workers focused their research on pure organic crystals and highly concentrated plastic systems performing optimal PSD for fast neutrons [50, 51]. They found that loading a polyaromatic matrix with high amounts of primary dye, i.e. 2,5-diphenyloxazole, efficiently promotes the triplet-triplet annihilation process, leading to optimal pulse shape parameter for n/γ discrimination. Following this approach, few years later relevant papers appeared of Zhmurin and Adadurov group on the

possibility to increase operational stability and discrimination parameter of the solid scintillator by acting on the chemical structure of the primary dye [52]. In the same period, M. Hamel, P. Blanc and co-workers [53] reformulated the composition of NE 150, improving the cross-linking density of the polymer matrix and, in turn, the long-term resistance, thus producing a PSD plastic scintillator with excellent performance. Moreover, they discovered a patented fluorophore that could respond to the need of optimal PSD, suitable for dissolution in high concentration in plastic aromatic matrices, with no consequence on ageing and minimal cost [54].

In the following paragraphs, results obtained with polysiloxane-based systems will be presented in the case of detection of both slow and fast neutrons.

5.4.2 *B and Li Loaded Polysiloxanes for Detection of Thermal Neutrons*

As previously described, indirect detection of thermal neutrons requires the dissolution of a suitable compound of ^{10}B or ^6Li into the organic scintillator, but the synthesis of precursors fully soluble in siloxane, not interfering with the cross-linking process, is not a trivial task. The use of *ortho*- or *meta*- carborane into the polysiloxane has been pursued, providing optimal results as for detection capability, which resulted comparable to the standard EJ-254 loaded with 5% natural B [5, 33, 38]. The addition of Li compounds has been also attempted, by following the approach of compatibilization of the Li precursor moiety with the organic surrounding medium, as previously pursued by synthesizing lithium salicylate and derivatives as additives in PS-based scintillator [38, 55]. It has to be outlined that the possibility to dissolve thermal neutron sensitive nuclei while preserving optical transparency of the network allows to achieve triple discrimination, i.e. fast neutrons through H- recoil events, γ -rays by Compton events and thermal neutrons by capture on ^6Li nuclei siloxane scintillators.

We adopted two pathways:

- (i) production of fully inorganic nanoparticles of ^6LiF through co-precipitation [56], and
- (ii) synthesis of core–shell oleic acid-capped ^6LiF nanoparticles by high-temperature decomposition of labile Li trifluoroacetate salts in oleic acid medium [57].

Following synthesis (i), it is possible to vary the crystal size down to few tens of nanometres, while adopting route (ii) the oleic acid shell is expected to offer higher affinity with the siloxane matrix [58]. Addition of ^6LiF nanocrystals to one of the well-characterized formulations of siloxane scintillator (PDPDMS22, 1% PPO, 0.02% LV) unavoidably leads to precipitates, with remarkable loss of transparency and, in turn, light output. Therefore, the use of oleic-capped crystals has been pursued as it affords samples with good level of transparency for ^6Li loadings up to 2 wt% in samples of thickness 0.5 mm. Optical transparency is lost if thickness increases, as can be seen in Fig. 5.9 for samples containing 0.5 wt% ^6Li .

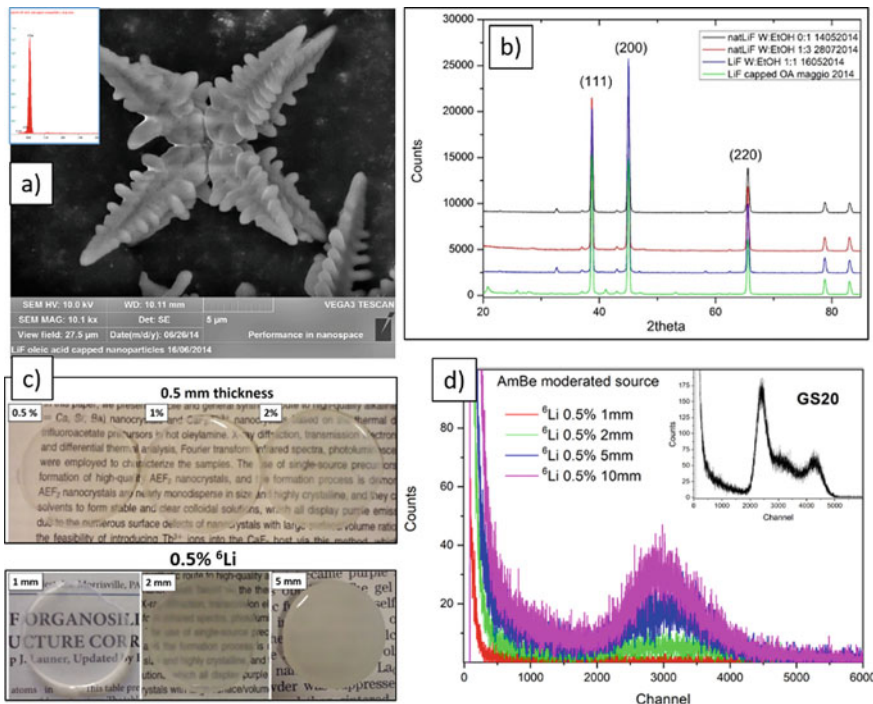


Fig. 5.9 **a** SEM–EDS analysis of oleic acid-capped crystals of LiF. **b** HR-XRD pattern of ^{6}LiF nanocrystals obtained by route (i) and (ii) (see text for details); **c** photos of siloxane samples loaded with varying amounts of ^{6}LiF and different thickness; **d** pulse-height spectra collected from ^{6}Li containing siloxane scintillators under thermal neutrons exposure (reprinted from [58] with permission from IOP Science)

Interestingly, the response to thermal neutrons shown in Fig. 5.9d is quite good in thicker samples, in spite of the low content of absorbing species and poor transparency. This fact is related to the neutron absorption within a scintillating material, described by the exponential attenuation of the impinging neutron beam crossing the material. The attenuation level depends on the absorbing nucleus concentration, its capture cross section and the thickness of the absorbing layer. The neutron absorption length l is defined as the material thickness necessary to attenuate the original fluence of the impinging neutron beam down to a factor $1/e$ (i.e. about 63% absorption). In the case of our 0.5 wt% loaded siloxane samples (corresponding to a ^{6}Li concentration of 5×10^{20} at/cm 3 and to a density of 1.03 g/cm 3) the absorption length is about 20 mm. Hence, thicker samples give higher peak intensity and better signal-to-background ratio in the pulse-height spectrum, as shown in Fig. 5.9d, counteracting the lower transparency.

Considering the detection of thermal neutrons as a task separated from the revelation of fast neutrons and γ -rays, the most popular and effective sensors in the market are EJ-426, in form of white opaque thin layer, and EJ-420 in form of thick grooved

acrylic disc covered by a white composite layer. They are produced by pressing luminescent powders of ZnS activated with Ag (ZnS:Ag) mixed with ^6LiF powder in a plastic binder, acting barely as scaffold; the term “plastic scintillators” might be improper, owing to the inorganic nature of ZnS:Ag. Images of EJ-420 in different sizes are shown in Fig. 5.10a. This type of sensor presents several advantages: the absorption length for thermal neutrons is 0.8 mm, thus a thin layer is enough to stop a large fraction of impinging neutrons, the scintillation yield is one of the highest, 160,000 photons/neutron, and it is almost insensitive to γ -rays, having a low average Z_{eff} [59]. This sensor is white and opaque, hence the maximum thickness to collect light from the side matching the photoconverter is around 0.45 mm. This fact severely limits the detection efficiency to only 20% for EJ-426 and 55% for EJ-420, owing to the reduction of active volume. In the case of thin layer on acrylic baseplate (EJ-426), the composite is hydrophilic and prone to develop cracks (Fig. 5.10b), owing to the excessive amount of solid powders with respect to the binder and to the rigid nature of the binder.

Recently, we have prepared thin and flexible layers composed of fluorescent powders EJ-600 (commercial product of ZnS:Ag) and ^6LiF nanocrystals synthesized according to route i) as previously described, dispersed in polysiloxane matrix with and without phenyl substituents [60]. Different sizes of ^6LiF nanocubes are obtained by varying the solvent as shown in the SEM images of Fig. 5.11a, b. A foldable and compact composite material is obtained in form of self-standing thin layer, as shown in Fig. 5.10c; the capability to detect thermal neutrons is proved by

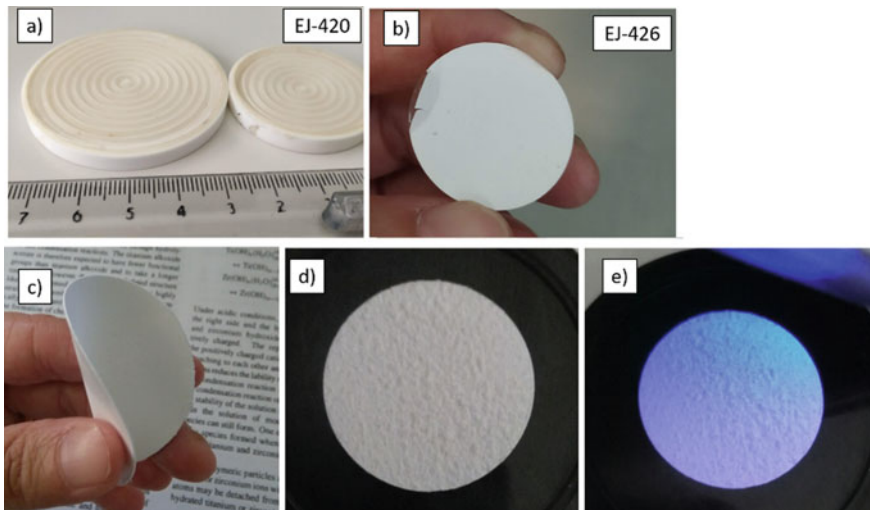


Fig. 5.10 **a** EJ-420 of different sizes; **b** EJ-426 with 0.25 mm sensitive layer on 0.25 mm acrylic plate, showing cracks upon bending; **c** flexible thermal neutron sensor made in PDPDMS22; **d** the polysiloxane sensor in daylight; **e** polysiloxane sensor under UV excitation

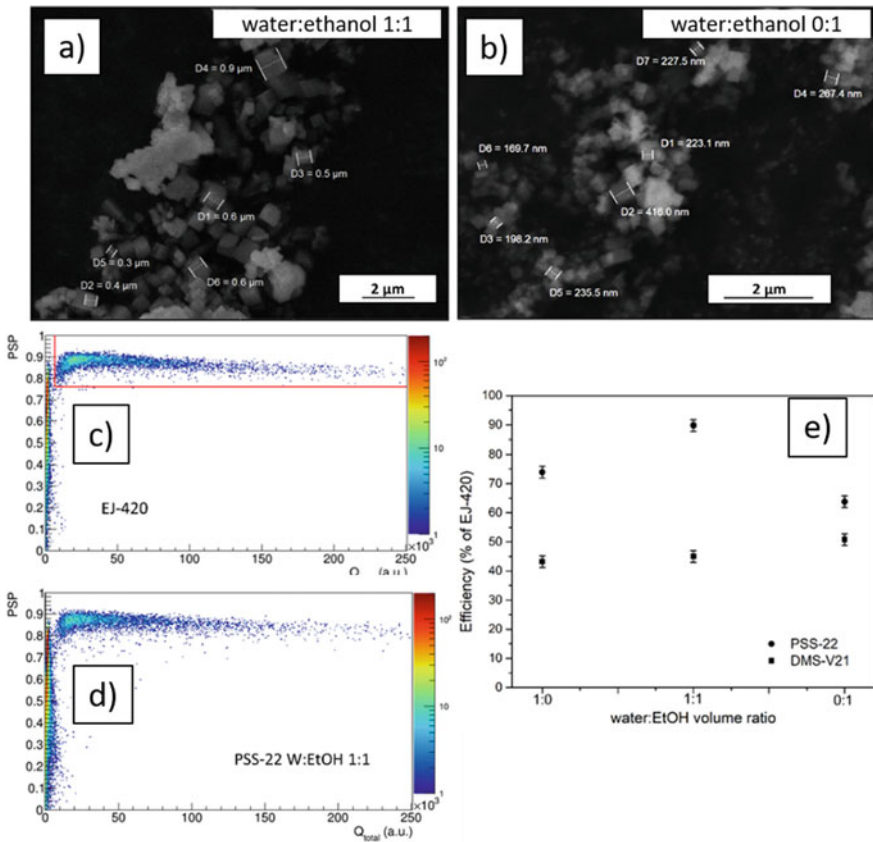


Fig. 5.11 **a** and **b** SEM images of the ${}^6\text{LiF}$ nanocrystals obtained by co-precipitation method in different water/ethanol ratio; **c** and **d** 2D plot of the pulse shape parameter defined in [60] versus total collected charge (red lines in **c**) evidence thermal neutrons-induced events; **e** efficiency of the flex sensors as compared to EJ-420 standard for different siloxane matrices (reprinted from [60] with permission from Elsevier)

the 2D graph (Fig. 5.11c, d) reporting the pulse shape parameter, defined by “sectioning” the light pulse signal in different temporal windows in function of the total charge [60]. This time-related parameter is the basis for particles discrimination, as previously described in Sect. 5.4.1.

Exceedingly high values of detection efficiency have been measured (Fig. 5.11e), approaching the ones of the commercial standard, and the phenyl containing siloxane proved to be the best choice to obtain homogeneous and mechanically stable dispersion of powders into the matrix. The results are quite promising in view of obtaining a soft and pliable pad, able to wrap other detectors with curvature adaptability, thus providing “hybrid” detectors through mechanical coupling, as proposed by Sharma and co-workers [61].

5.4.3 Design of Polysiloxane Scintillators for n/γ Discrimination

The intuition of Brooks [44], the pioneering work of Hamel and co-workers [45, 53], the optimal performance of plastic scintillators obtained by over-doping PVT or PS scintillators with PPO [51] and derivatives [52, 53] to achieve pulse shape discrimination capability spurred the search of systems with similar performances based on polyphenylsiloxanes. The basic principle underlying the successful performance of the formulation proposed by N. Zaitseva has been known for several decades (see Sect. 5.4.1), and is related to the close proximity of fluorophores excited to their triplet states T_1 , which promotes triplet-triplet annihilation (TTA).

In plastic scintillators, TTA is enhanced by increasing the concentration of primary dye well beyond the moderate levels, i.e. 1–2 wt%, needed to achieve optimal light output. This strategy led to outstanding results as for discrimination capability, almost approaching the standard displayed by the best liquid systems as for n/γ discrimination [62]. On the other hand, the intermolecular forces from which the mechanical and thermal properties of PS or PVT are originated are severely weakened by the over-loading of dye molecules; further detrimental effects are due to the interference of the additive on the polymerization process. The point is that the polymer displays remarkably low T_g and the appearance with time of small aggregates on the surface. Further, experimental work led to sensible improvement of the performances of PVT-based plastic scintillator with PSD ability and a very recent commercial formulation, namely EJ-276 Eljen Technology, shows outstanding long-term performance and stability [63]. Chapter 2 highlights in detail this successful story.

We recently demonstrated how the design of polysiloxane scintillators with PSD capability has been examined by our research group [64]. Although the performance level of the scintillator remains below the one displayed by PS and PVT-based sensors, the capability for PMPS100 doped with 6 wt% PPO and 0.02 wt% LV to discriminate fast neutrons from γ -rays has been unambiguously demonstrated. This fact might be surprising, since PPO concentration is 1/5 of the one used in EJ-299–33 and, nevertheless, the TTA mechanism is promoted and accounts for enabled PSD. The close proximity of triplet states is explained by the presence of specific sites where PPO molecules preferentially gather, giving rise on excitation to high local concentration of triplet states. The macromolecule conformation composed of $-\text{PhCH}_3\text{SiO}-$ units has been deeply studied [15] in literature and compared with phenyl-containing vinyl polymers, such as PS and PVT. The Si–O bond length and the wide angle of the Si–O–Si bridge explain the high deformability of the chain and, in turn, the formation of dyads and triads of facing phenyl pendant groups, as schematized in Fig. 5.12a.

The presence of “attraction sites” for PPO composed of stacked phenyl groups promoting PPO excimer formation has been investigated by time-resolved fluorescence spectroscopy and correlated to the PPO concentration. Optical properties account for the results in Fig. 5.12b [64]. Even at very low concentration of PPO,

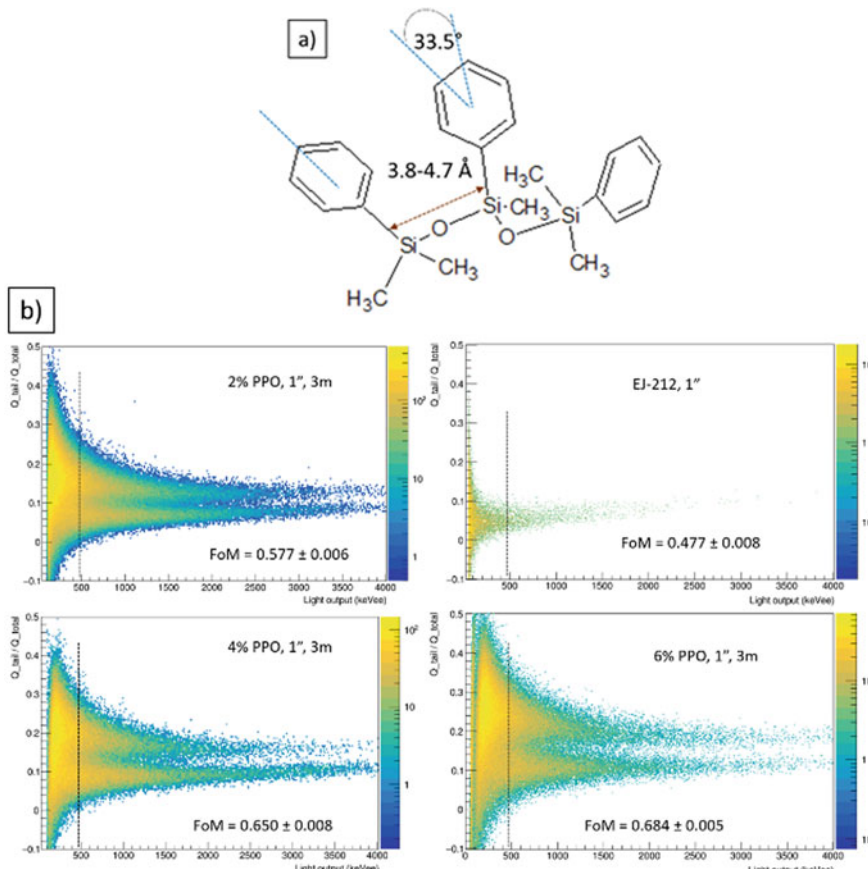


Fig. 5.12 **a** Drawing of the diad conformation in PMPS100 (adapted from [15] with permission from the American Chemical Society); **b** 2D plots reporting pulse shape parameter, defined in [64], versus energy for PPO containing PMPS100 and the standard EJ-212 (reprinted from [64] with permission from Springer Nature)

namely 2 wt%, the PSD is proved to be enabled, in contrast with PS or PVT-based plastic scintillators with similar levels of primary dye, such as EJ-200 and EJ-212.

Our results promoted the experimental work of other research groups with the peculiarity of including organic chemistry experts, thereby making it possible to synthesize in-house primary dyes meeting specific needs:

- (i) excimers (*conditio sine qua non* to enable TTA \rightarrow PSD);
- (ii) solubility in phenyl containing polysiloxane;
- (iii) no involvement with cross-linking;
- (iv) endurance versus medium/high temperature reticulation conditions.

This approach has been followed by Lim and co-workers [65], who succeeded in synthesizing phenyl-containing polysiloxanes doped with either PPO or a fluorene

derivative, whose performances as for light output and discrimination capability not only approach but even exceed those displayed by commercial plastic scintillators.

5.5 Summary

The combination of a scintillator key features, i.e. light output, linearity of response with energy, response time, with additional properties is not mandatory but extremely appealing to widen the application fields. Decades ago, outstanding values for light emission upon irradiation using vinyl aromatic polymers as a base and a carefully studied dyes cocktail have been reached. Later on, nuclear physics, medical physics, homeland security communities urged materials scientists to propose organic scintillators with enhanced properties with regard to their radiation resistance, pulse shape discrimination capability and mechanical strength. The possibility to synthesize a unique material bearing all these features with the best performances ever detected might be considered a mirage. On the other hand, the study of optical properties of each component of the scintillating mixture as the polestar towards the destination is of great importance and can be effective in pursuing the goal. Several groups composed of people with skills on complementary disciplines proved that it is possible to reach optimal results starting from the design of the base material and its additives on the basis of photophysical properties investigation. Within this framework, our research group gave its contribution in preparing elastomeric scintillators, with long-term, high-dose resistance to irradiation, good light output, sensitivity to fast and thermal neutrons and pulse shape discrimination capability. Our work has not been aimed at outperforming commercial scintillators, but at synthesizing siloxane-based particles sensors possessing beneficial extra- properties besides the basic ones, in some cases preserved, in other cases worsened at acceptable levels. In the present chapter, the historical path followed by us has been described. We are pleased to have inspired other groups that showed great chemical and photo-physics skills, creativity and perseverance in producing silicone-based soft but robust scintillators with performances exceeding expectations.

Acknowledgements We deeply acknowledge the Vth Commission of INFN, the Department of Physics and Astronomy, University of Padova, and the Department of Industrial Engineering, University of Trento, for having, in the last decade, trustfully supported the work of our research group, either by providing dedicated funds and by promoting enrolment of final year students, Ph.D. and research fellows. We want to express our gratitude to the Laboratori Nazionali di Legnaro of INFN, in particular to nuclear physics groups that dedicated their knowledge in radiation-matter interaction and in data acquisition and processing during extenuating beam shift for scintillators design and testing. Furthermore, we are deeply indebted to the Laboratori Nazionali di Legnaro technical staff employed in the mechanical workshop and accelerator facilities (AN2000 and CN-7MeV) that provided superior and indispensable skills in supporting our work.

References

1. J.E. Huheey, *Inorganic Chemistry: Principles of Structure and Reactivity*, 3rd edn. (Harper & Row, New York, Cambridge, 1983). Table E1, A32-A40
2. E.G. Rochow, J. Am. Chem. Soc. **67**(6), 963 (1945)
3. J. Harmon, J. Gaynor, V. Feygelman, J. Walker, Nucl. Instr. Methods B **53**(3), 309 (1991)
4. Z.W. Bell, G.M. Brown, C.H. Ho, F.V. Sloop Jr., Organic scintillators for neutron detection, in *X-Ray and Gamma-Ray Detectors and Applications IV*, vol. 4784, Proceedings of SPIE, ed. by R.B. James, L.A. Franks, A. Burger, E.M. Westbrook, R.D. Hurst (2002), p. 150
5. Z.W. Bell, M.A. Miller, L. Maya, G.M. Brown, F.V. Sloop Jr., IEEE Trans. Nucl. Sci. **51**(4), 1773 (2004)
6. Z.W. Bell, G.M. Brown, L. Maya, F.V. Sloop Jr., Boron loaded scintillator. US20090236530, 28.03.2006
7. T.K. Meister, K. Riener, P. Gigler, J. Stohrer, W.A. Herrmann, F.E. Kühn, ACS Catal. **6**(2), 1274 (2016)
8. G. Ranucci, A. Goretti, P. Lombardi, Nucl. Instr. Methods A **412**(2–3), 374 (1998)
9. G. Bentoumi, X. Dai, H. Fritzsché, G. Jonkmans, L. Li, G. Marleau, B. Sur, Nucl. Instr. Methods A **701**, 221 (2013)
10. Z. Chang, N.C. Okoye, M.J. Urfner, A.D. Green, K.E. Childs, L.F. Miller, Nucl. Instr. Methods A **769**, 112 (2015)
11. D.R. Onken, F. Moretti, J. Caravaca, M. Yeh, G.D. Orebi Gannab, E.D. Bourretta, Mater. Adv. **1**, 71 (2020)
12. E. Montbarbon, F. Sguerra, G.H.V. Bertrand, É. Magnier, R. Coulon, R.B. Pansu, M. Hamel, Chem. Eur. J. **22**, 12074 (2016)
13. M. Dalla Palma, S.M. Carturan, M. Degerlier, T. Marchi, M. Cinausero, F. Gramegna, A. Quaranta, Opt. Mater. **42**, 111 (2015)
14. M. Dalla Palma, T. Marchi, S.M. Carturan, C. Checchia, G. Collazuol, F. Gramegna, N. Daldozzo, V. Paterlini, A. Quaranta, M. Cinausero, M. Degerlier, IEEE Trans. Nucl. Sci. **63**(3), 1608 (2016)
15. C. Salom, A. Horta, I. Hernandez-Fuentes, I.F. Pierola, Macromolecules **20**(3), 696 (1987)
16. T. Itoh, Res. Chem. Intermed. **27**, 669 (2001)
17. A. Quaranta, S. Carturan, T. Marchi, M. Cinausero, C. Scian, V.L. Kravchuk, M. Degerlier, F. Gramegna, M. Poggi, G. Maggioni, Opt. Mater. **32**(10), 1317 (2010)
18. A. Quaranta, S.M. Carturan, T. Marchi, V.L. Kravchuk, F. Gramegna, G. Maggioni, M. Degerlier, IEEE Trans. Nucl. Sci. **57**(2), 891 (2010)
19. F. Hirayama, J. Chem. Phys. **42**(9), 3163 (1965)
20. J.J. Freire, I.F. Piérola, A. Horta, Macromolecules **29**(15), 5143 (1996)
21. J.R. Lakowicz, *Principles of Fluorescence Spectroscopy*, 3rd edn. (Springer, Boston, 2006), pp. 443–450
22. B. Valeur, *Molecular Fluorescence: Principles and Applications* (Wiley-VCH, Weinheim, 2001), pp. 72–124
23. T. Förster, Discuss. Faraday Soc. **27**, 7 (1959)
24. J.B. Birks, *Theory and Practice of Scintillation Counting* (Pergamon Press, Oxford, 1964).
25. C. Zorn, IEEE Trans. Nucl. Sci. **37**(2), 504 (1990)
26. M. Bowen, S. Majewski, D. Pettey, J. Walker, R. Wojcik, C. Zorn, IEEE Trans. Nucl. Sci. **36**(1), 562 (1989)
27. A.D. Bross, A. Pla-Dalmau, IEEE Trans. Nucl. Sci. **39**(5), 1199 (1992)
28. A. Quaranta, Nucl. Instr. Methods B **240**(1–2), 117 (2005)
29. A. Quaranta, S. Carturan, M. Cinausero, T. Marchi, F. Gramegna, M. Degerlier, A. Cemmi, S. Baccaro, Mater. Chem. Phys. **137**(3), 951 (2013)
30. V.M. Feygelman, J.K. Walker, J.P. Harmon, Nucl. Instr. Methods A **290**(1–2), 131 (1990)
31. B.V. Grinev, L.A. Andryushchenko, V.M. Shershukov, K.B. Ulanenko, R.A. Minakova, I.V. Sevastjanova, Mat. Res. Soc. Symp. Proc. **348**, 187 (1994)

32. A. Andrichetto, L. Biasetto, M. Manzolaro, P. Benetti, S. Carturan, P. Colombo, F. Gramegna, G. Meneghetti, B. Monelli, G. Prete, P. Zanonato, AIP Conf. Proc. **1099**(1), 728 (2009)
33. S. Carturan, A. Quaranta, T. Marchi, F. Gramegna, M. Degerlier, M. Cinausero, V.L. Kravchuk, M. Poggi, Radiat. Prot. Dosim. **143**(2–4), 471 (2011)
34. S.M. Carturan, F.E. Pino, S. Moretto, C.L. Fontana, E. Zanazzi, R. Raggio, A. Quaranta, manuscript in preparation
35. J.F. Ziegler, M.D. Ziegler, J.P. Biersack, Nucl. Instr. Methods B **268**(11–12), 1818 (2010)
36. M. Dalla Palma, A. Quaranta, T. Marchi, G. Collazuol, S. Carturan, M. Cinausero, M. Degerlier, F. Gramegna, IEEE Trans. Nucl. Sci. **61**(4), 2052 (2014)
37. A. Quaranta, S. Carturan, T. Marchi, A. Antonaci, C. Scian, V.L. Kravchuk, M. Degerlier, F. Gramegna, G. Maggioni, Nucl. Instr. Methods B **268**, 3155 (2010)
38. R.D. Breukers, C.M. Bartle, A. Edgar, Nucl. Instr. Methods A **701**, 58 (2013)
39. A.N. Mabe, A.M. Glenn, M.L. Carman, N.P. Zaitseva, S.A. Payne, Nucl. Instr. Methods A **806**, 80 (2016)
40. A. Quaranta, S. Carturan, T. Marchi, M. Buffa, M. Degerlier, M. Cinausero, G. Guastalla, F. Gramegna, G. Valotto, G. Maggioni, V.L. Kravchuk, J. Non-Cryst. Solids **357**(8–9), 1921 (2011)
41. C. Frangville, A. Grabowski, J. Dumazert, E. Montbarbon, C. Lynde, R. Coulon, A. Venerosy, G.H.V. Bertrand, M. Hamel, Mater. Chem. Front. **3**(8), 1574 (2019)
42. G. Laustriat, Mol. Cryst. **4**(1–4), 127–145 (1968)
43. D.L. Horrocks, Appl. Spectrosc. **24**(4), 397 (1970)
44. F.D. Brooks, R.W. Pringle, B.L. Funt, IRE Trans. Nucl. Sci. **7**(2–3), 35 (1960)
45. M. Hamel, V. Simic, S. Normand, React. Funct. Polym. **68**(12), 1671 (2008)
46. A.F. Adadurov, P.N. Zhmurin, V.N. Lebedev, V.D. Titskaya, Nucl. Instr. Methods A **599**(2–3), 167 (2009)
47. A.F. Adadurov, D.A. Yelyseev, V.D. Titskaya, V.N. Lebedev, P.N. Zhmurin, Radiat. Meas. **46**(5), 498 (2011)
48. A.F. Adadurov, P.N. Zhmurin, V.N. Lebedev, V.N. Kovalenko, Appl. Radiat. Isot. **69**(10), 1475 (2011)
49. P.N. Zhmurin, V.N. Lebedev, A.F. Adadurov, V.N. Pereymak, Y.A. Gurkalenko, Radiat. Meas. **62**, 1 (2014)
50. M.M. Bourne, S.D. Clarke, N. Adamowicz, S.A. Pozzi, N. Zaitseva, L. Carman, Nucl. Instr. Methods A **806**, 348 (2016)
51. N. Zaitseva, B.L. Rupert, I. Pawełczak, A. Glenn, H.P. Martinez, L. Carman, M. Faust, N. Cherepy, S. Payne, Nucl. Instr. Methods A **668**, 88 (2012)
52. P.N. Zhmurin, V.N. Lebedev, V.D. Titskaya, A.F. Adadurov, D.A. Elyseev, V.N. Pereymak, Nucl. Instr. Methods A **761**, 92 (2014)
53. P. Blanc, M. Hamel, C. Dehé-Pittance, L. Rocha, R.B. Pansu, S. Normand, Nucl. Instr. Methods A **750**, 1 (2014)
54. M. Hamel, P. Blanc, S. Normand, C. Dehé-Pittance, Matériaux scintillateurs plastiques, scintillateurs plastiques comprenant ces matériaux et procédé pour discriminer les neutrons des rayons gamma utilisant ces scintillateurs. FR3002945, 07.03.2013
55. N. Zaitseva, A. Glenn, H.P. Martinez, L. Carman, I. Pawełczak, M. Faust, S. Payne, Nucl. Instr. Methods A **729**, 747 (2013)
56. N.D. Alharbi, N. Salah, S.S. Habib, E. Alarfaj, J. Phys. D Appl. Phys. **46**(3), 035305 (2013)
57. Y.-P. Du, Y.-W. Zhang, L.-D. Sun, C.-H. Yan, Dalton Trans. **40**, 8574 (2009)
58. S.M. Carturan, T. Marchi, G. Maggioni, F. Gramegna, M. Degerlier, M. Cinausero, M. Dalla Palma, A. Quaranta, J. Phys. Conf. Ser. **620**, 012010 (2015)
59. C.W.E. van Eijk, A. Bessière, P. Dorenbos, Nucl. Instr. Methods A **529**(1–3), 260 (2004)
60. S.M. Carturan, M. Vesco, I. Bonesso, A. Quaranta, G. Maggioni, L. Stevanato, E. Zanazzi, T. Marchi, D. Fabris, M. Cinausero, F. Pino, F. Gramegna, Nucl. Instr. Methods A **925**, 109 (2019)
61. M. Sharma, J. Nattress, K. Wilhelm, I. Jovanovic, Nucl. Instr. Methods A **857**, 75 (2017)
62. S.A. Pozzi, M.M. Bourne, S.D. Clarke, Nucl. Instr. Methods A **723**, 19 (2013)

63. N.P. Zaitseva, A.M. Glenn, A.N. Mabe, M.L. Carman, C.R. Hurlbut, J.W. Inman, S.A. Payne, Nucl. Instr. Methods A **889**, 97 (2018)
64. T. Marchi, F. Pino, C.L. Fontana, A. Quaranta, E. Zanazzi, M. Vesco, M. Cinausero, N. Daldosso, V. Paterlini, F. Gramegna, S. Moretto, G. Collazuol, M. Degerlier, D. Fabris, S.M. Carturan, Sci. Rep. **9**, 9154 (2019)
65. A. Lim, J. Arrue, P.B. Rose, A. Sellinger, A.S. Erickson, ACS Appl. Polym. Mater. **2**(8), 3657 (2020)



Sara Maria Carturan Born in 1969, Sara Maria Carturan received the Degree in Chemistry in 1993 (University of Padova) and the Ph.D. degree in Chemistry (University of Trento) in 2004. Since 2003 she has held a permanent position as graduated technician at the Department of Physics and Astronomy of the University of Padova, with the main task of providing technological support as for chemistry related aspects to projects and activities funded by DFA and INFN (Laboratori Nazionali di Legnaro). Her research interests have been focused on polymers synthesis and sol-gel derived materials and modification of their optical, electrical and mechanical properties by chemical treatments and/or ion beams interaction for applications covering particles detectors, optical gas sensors, luminescent solar concentrators. She is currently involved as Local Responsible at LNL in the FIRE project, funded by INFN, aiming at the production of fully organic-based radiation detector, where a siloxane scintillator is coupled with flexible Organic Photo Transistor as photo converter.

Sara Maria Carturan has authored more than 100 peer-reviewed articles and is referee of several international journals related to materials science.

h-index: 19, total citations number: 1340 (ISI web of science, July, 2020).

h-index: 23, total citations number: 1927 (Google Scholar, July, 2020).



Alberto Quaranta Born in 1964, Alberto Quaranta is professor of Physics and Physics of Materials at University of Trento, Department of Industrial Engineering. His research interests are focused on scintillation detectors/optical sensors and optical properties of nanostructured glasses and polymers. During last 25 years he was involved in several INFN projects, both as PI and Spokenperson, on radiation detectors. He is chairman of a biennial International School on neutron detectors held in Riva del Garda (Trento). Alberto Quaranta co-authored 166 papers on peer-reviewed journals (h-index 35 on google scholar with 3811 citations).

Chapter 6

Composite Scintillators



Masanori Koshimizu 

Abstract In this chapter, organic–inorganic composite scintillators are introduced with the main focus on nanocomposites. In the field of materials science, organic–inorganic nanocomposites have been used for wide applications. They are designed to offer the advantages of both organic and inorganic counterparts and synergetic effects of the composites. A rich variety of optical materials have been developed based on polymers and inorganic nanoparticles. In spite of the intriguing functionality of the nanocomposites, the fabrication of uniform nanocomposites is challenging in preventing the aggregation of the inorganic nanoparticles. Some strategies to overcome the main issues are introduced in Sect. 6.1.1. Also, two related optical phenomena inherent to nanocomposites are introduced in Sect. 6.1.2: one is the scattering at the interface between the inorganic and organic phases, and the other is the quantum confinement effects of semiconductor nanocrystals, which are attractive inorganic phosphors in nanocomposite scintillators. Subsequently, examples of nanocomposite scintillators prepared by different approaches and design principles are explained. Nanocomposite scintillators have been developed mainly to obtain high detection efficiency for high-energy photons such as X-rays and gamma-rays or thermal neutrons similar to the cases of loaded plastic scintillators. This discussion is complementary to recent review papers and several dedicated chapters of this book [Bertrand et al. in Chem Eur J 20(48), 15660 (2014); Hajagos et al. in Adv. Mater. 30:1706956, 2018; Koshimizu in Mater. Lett. 13:2030003, 2020] [1, 2, 3].

6.1 Introduction to Organic–Inorganic Composites

The development of novel materials based on organic–inorganic composites has attracted considerable attention of materials scientists for decades. Composite materials which contain nano-sized organic and inorganic phases are called nanocomposites. They offer advantages of both organic and inorganic phases and, in some cases, synergetic effects. Many nanocomposites consist of organic (mainly polymer)

M. Koshimizu (✉)

Department of Applied Chemistry, Tohoku University, Miyagi, Japan
e-mail: koshi@qpc.che.tohoku.ac.jp

matrices and inorganic nanoparticles within the matrices, whereas some composites have inorganic matrices in the form of porous solids or glasses. The choice of the matrix depends on the desired flexibility or rigidity of the material. Another characteristic of organic–inorganic nanocomposites is the large area of interface between the organic and inorganic phases. It provides a unique reaction field, whereas hinders good dispersion of inorganic phases.

Nanocomposite materials have been developed for various applications. Enhancement of the mechanical properties such as tensile strength [4] or scratch resistance [5] has been achieved in organic–inorganic nanocomposite materials. Mechanical strength and thermal stability have been enhanced by the incorporation of inorganic nanoparticles in organic–inorganic nanocomposite polymer electrolyte membranes for fuel cell [6, 7] and lithium-ion battery applications [8]. Nanocomposites have also been used for electrodes in lithium-ion batteries [9]. Capacitor nanocomposites have been developed to obtain high power density by utilizing high dielectric permittivity of inorganic nanoparticles and high breakdown strength of polymer matrices [10]. Nanocomposites for gas sensing applications have also been developed to overcome the disadvantages of inorganic materials (high operation temperature and complicated processability) and organic materials (low conductivity and poor stability) [11]. Taking advantage of the large interface area, polymer-based nanocomposites comprising inorganic adsorbent nanoparticles have been fabricated with the aim to remove hazardous heavy metals from wastewater [12, 13]. Also, in organic–inorganic nanocomposite thermoelectric materials, phonon scattering at the interface of inorganic and organic phases enhances the figure of merit of thermoelectric property [14].

Composite scintillators may find applications in the category of optical materials [15]. Hence, materials design and fabrication strategies of nanocomposite optical materials provide profound implications for the design and fabrication of composite scintillators. Some basic physics on the optical properties of nanocomposites are provided in Sect. 6.1.2, with a demonstration of selected examples of nanocomposite optical materials. One of the hot topics on the application of nanocomposite optical materials is on photovoltaic applications, in which conjugated polymer matrices provide flexible and large-area devices easily at low cost as well as high electron mobility, whereas inorganic semiconductor nanocrystals offer tunable optical absorption properties owing to quantum confinement effects [15–17]. Light-emitting diodes based on nanocomposites have extensively been developed using inorganic semiconductor nanocrystals as emitters [15]. Nanocomposite materials for photoelectrochemical water splitting have also been developed on the basis of semiconductor nanocrystals [18]. Nanocomposites have been used for organic polymer-based high refractive index materials because of the high refractive index of the inorganic phase [19]. Photopolymerizable organic–inorganic nanocomposites have been applied as holographic recording media in which refractive index modulation was achieved by the diffusion of monomer and nanoparticles [20].

6.1.1 Overview on Fabrication Methods of Nanocomposites

Contrary to the case of single-phase materials, properties of nanocomposite materials are influenced by the mesoscopic structure and interface state between the organic and inorganic phases, as well as by the intrinsic properties of the organic and inorganic phases. If we assume nanocomposites consisting of polymer host and inorganic nanoparticles, the mean size and size distribution of the nanoparticles and their spatial distribution should be considered as the mesoscopic structure. Additionally, the nature of the interface between the inorganic and organic phases, such as covalent bonding, ionic bonding, or Van der Waals interaction, influences the mesoscopic structure during the synthesis process. The large interface area is the key in the fabrication of nanocomposites. Figure 6.1 shows the various pathways for obtaining organic–inorganic nanocomposites [21]. Depending on the required size of the composites, choice of raw materials, or higher order structure required for the composites, various methods have been developed. Among these are ordered structures or self-assembly [22] as shown in Fig. 6.1 [21], and two methods will be introduced in this subsection: sol–gel method and dispersion of surface-modified inorganic nanoparticles in polymers. The focus is good dispersion of the inorganic nanoparticles, since nanoparticles tend to form aggregates because of the large free energy at the large-area interface, as shown in Fig. 6.2.

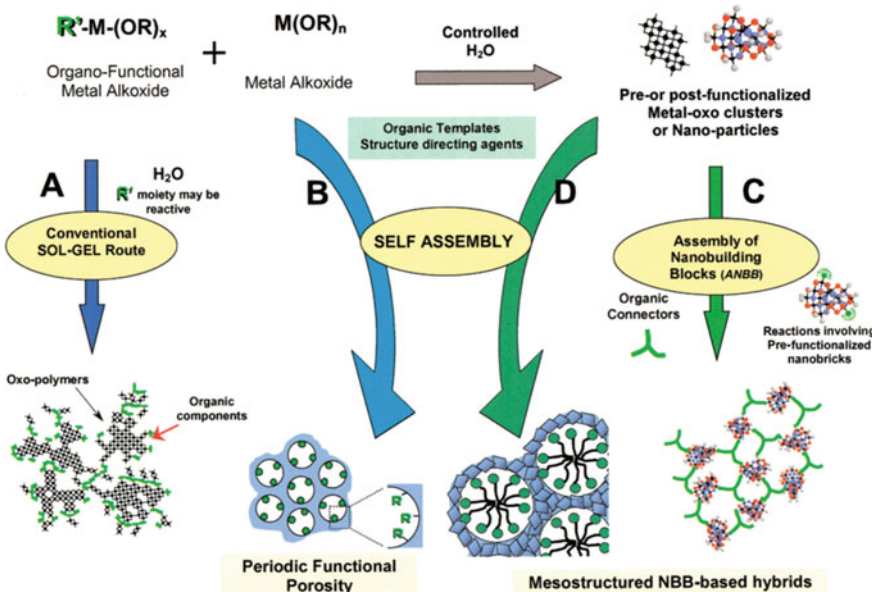


Fig. 6.1 Various pathways for obtaining organic–inorganic nanocomposites (reproduced from [21] with permission from the American Chemical Society)

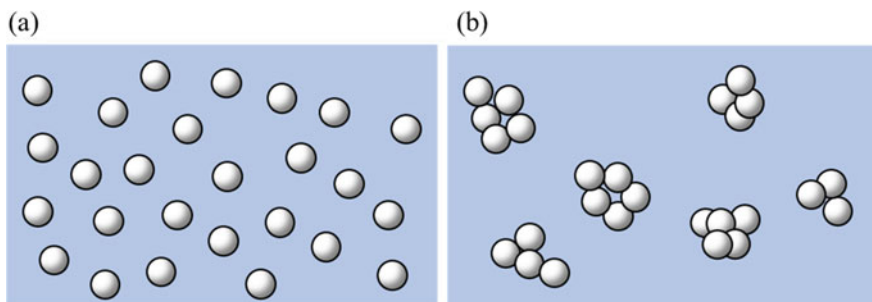
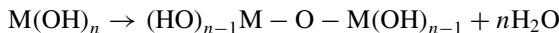
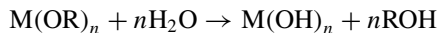


Fig. 6.2 Schematic representations of **a** dispersed and **b** aggregated nanoparticles in an organic matrix

6.1.1.1 Fabrication of Nanocomposites via Sol–gel Method

In sol–gel method, inorganic oxide phases are formed via hydrolysis and polycondensation reactions of the raw materials, mainly metal alkoxides, as follows [23]:



where M is a metal (e.g., Si, Ti, Zr, Al, Hf, etc.) and R is an alkyl group. Oxide nanoparticles can be formed by control of reaction rate via the nature and concentration of catalyst (mainly acids), the concentration of the raw materials, and surfactants as the surface modifiers of the nanoparticles. These reactions occur at relatively low temperature (typically lower than 100 °C), which enables adding organic polymers and molecules. To dissolve organic polymers or molecules, appropriate water-miscible organic solvents are used in addition to water (or acid). After or during the sol–gel reaction, the solutions are dried to obtain solid organic–inorganic nanocomposites. The typical size of the nanocomposites is mm order in thickness. Nanocomposites with good dispersion of inorganic nanoparticles can be obtained by appropriate choice of the conditions for the sol–gel reaction and the drying process.

6.1.1.2 Dispersion of Surface-Modified Inorganic Nanoparticles in Polymers

In this fabrication method, two-step synthesis procedures are necessary: surface-modified nanoparticles are synthesized in the first step, and nanocomposites comprising the surface-modified nanoparticles are synthesized in the second step. Polymer-based nanocomposites can be obtained by polymerization of monomers

containing the dispersion of the surface-modified nanoparticles or drying the dispersion of the surface-modified nanoparticles in which the polymer is dissolved. In both cases, the fabrication of size-controlled inorganic nanoparticles with sufficient surface modification is necessary. In this subsection, fabrication methods of the surface-modified nanoparticles are introduced. The reader is also invited to refer to the main review papers on this field [24–27].

The surface of the nanoparticles can be designed from the viewpoints of surface science and coordination chemistry [28]. Aggregation of inorganic nanoparticles can be avoided by enhancing the affinity of their surface to the host polymers. One method to obtain hydrophobic surfaces is chemical treatment such as silane coupling, in which –OH groups at the surface react with the silane coupling agents to provide hydrophobic nature [29]. Another method to obtain a hydrophobic surface is ligand exchange, in which originally bound surfactants are replaced by other desired ligands. The coverage of the surface with the originally bound and the desired ligands is governed by kinetics of adsorption and desorption of the ligands, which is determined by the concentration of the ligands in the dispersion and the reaction rate constants [26]. The latter depends on the chemical nature of the ligands. Furthermore, hydrophobic surfaces can also be obtained via grafting synthetic polymers to the surface. It should be noted that aggregated nanoparticles can be dispersed in polymer matrices using this technique as shown in Fig. 6.3 [30].

On the contrary to the case of the above surface treatments of the nanoparticles, sub- and supercritical hydrothermal synthesis provide single-step fabrication of organically modified nanoparticles of metal oxides [31]. In sub- and supercritical hydrothermal synthesis, organic ligands can be homogeneously dissolved in water

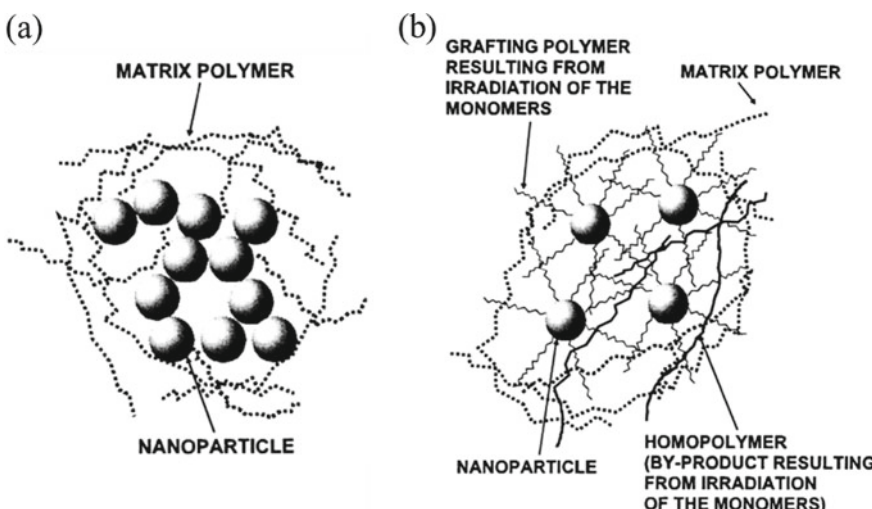


Fig. 6.3 Schematic representations of **a** agglomerated nanoparticles dispersed in a polymer matrix and **b** possible structure of grafted nanoparticles dispersed in a polymer matrix (reproduced from [30] with permission from Elsevier)

owing to a low dielectric constant at high temperature. Metal oxide nanoparticles are formed under a high degree of supersaturation, and the nanoparticle size can further be reduced by the surface modification of the organic ligand molecules via suppression of the particle growth. Additionally, the hot injection approach has been used for the fabrication of monodisperse semiconductor nanocrystals. In this approach, precursors of semiconductors are injected into a hot coordinating solvent such as trioctylphosphine¹ or trioctylphosphine oxide [32]. Rapid addition of the precursors raises the precursor concentration above the nucleation threshold, thereby resulting in nucleation in a short period. The coordinating solvent molecules cap the surface of the nanocrystals to hinder the aggregation. Also, surface capping provides the passivation of the surface localized centers and intrinsic optical (in particular, luminescence) properties of the compound semiconductor nanocrystals.

6.1.2 *Optical Properties Related to the Nanocomposite Structure*

In this subsection, a physical basis on the optical properties of organic–inorganic nanocomposites is provided. One topic is light scattering, which occurs at the interface of the inorganic and organic phases. The relationship between scattering properties and domain size is discussed. The other topic is the quantum confinement effects in semiconductor nanocrystals. Some semiconductor nanocrystals are efficient emitters and have been used as the inorganic part of the nanocomposite scintillators. It should be noted that the emission wavelength of nanocrystals strongly depends on their size in particular for nanocrystals smaller than 10 nm.

6.1.2.1 *Light Scattering Theory*

Contrary to the case of single-phase materials, nanocomposites have multiple phases whose refractive indices may differ. Such difference in the refractive indices causes scattering of the incident light, which results in loss of transparency. The scattering cross-section depends on the size and shape of the domain and the difference in the refractive indices. The scattering cross-sections or transmittance can be estimated in two approaches [33]. For arbitrary domain size, the Mie scattering theory can be applied as the exact solution of the Maxwell equations for the light scattering by a sphere; however, it is not of practical use because the calculation for light scattering by many spheres is tricky [33]. In the case of much smaller domain size, the Rayleigh scattering theory can be used.

In the Rayleigh scattering theory, Transmittance T of the light with wavelength λ in polymer-based nanocomposite comprising spherical inorganic nanoparticles can

¹Topological representation and key information of these molecules is given in the Appendix section at the end of the book.

be estimated with Eq. (6.1) [34]:

$$T = \exp\left\{-\left[\frac{3\phi_p x r^3}{4\lambda^4} \left(\frac{n_p}{n_m} - 1\right)\right]\right\} \quad (6.1)$$

where r is the radius of the inorganic nanoparticles, Φ_p is the volume fraction of the nanoparticles, and x is the optical path length. n_p and n_m are refractive indices of the inorganic nanoparticles and matrix, respectively. As one can deduce from Eq. (6.1), no light scattering occurs when inorganic nanoparticles and polymer hosts show the same refractive index. It should be noted that the nanoparticle size has a significant influence on transparency via the factor r^3 . For the same volume fraction of the inorganic nanoparticles, it is important to reduce the size of the nanoparticles to obtain organic–inorganic nanocomposites with high transparency.

6.1.2.2 Quantum Confinement Effects in Semiconductor Nanocrystals

Semiconductor nanocrystals exhibit size-dependent photophysical properties. Basically, they are governed by the Wannier exciton, which is the bound state of an electron and a hole like a hydrogen atom. The quantum confinement effects originate from the change in the wavefunctions of excitons and electron–hole pairs by boundary condition of the nanocrystal surface. The transition energy of the lowest excited state in the semiconductor nanocrystal becomes higher along with larger exciton binding energy with a reduction in the nanocrystal size [35, 36], resulting in the short wavelength shift of band edge emission from the nanocrystals with reduced size [36]. Also, the continuous electronic structure of bulk semiconductors turns into discrete ones in nanocrystals [35, 36].

Another feature of semiconductor nanocrystal is the involvement of surface states in the emission process; localized centers at the surface easily trap excited states because of the large surface-to-volume ratio of nanocrystals. Surface passivation is necessary to obtain the intrinsic emission of the nanocrystals. Capping of the surface with organic molecules has been widely studied. To enhance the quantum efficiency of luminescence, the nanocrystals are capped with one or multiple shell layers of semiconductors whose bandgap energies are larger than that of the capped semiconductor. Such structure of nanocrystals is called core/shell structure, e.g., CdSe/ZnS or CdSe/CdS [36].

From the viewpoint of potential application in nanocomposite scintillators, colloidal semiconductor nanocrystals are appropriate because they are available on a relatively large scale (order of 0.1–1 g). Core/shell nanocrystals are preferable owing to the higher quantum efficiency of emission. Judged from the appropriate emission wavelengths, core/shell nanocrystals with CdSe or CdS core are commercially available for nanocomposite scintillators. It should be noted that their small Stokes shift results in significant self-absorption in particular for large nanocomposite scintillators. The emission decay time constants of such nanocrystals are on the order of tens of nanosecond, which is slower than the emission of traditional organic

fluorophores but faster than most inorganic scintillators. A wide variety of II-IV semiconductor colloidal nanocrystals including core/shell ones are also commercially available. Recently, nanocrystals lead-based perovskite halide semiconductors have been developed as phosphors having significantly faster emission decay and appropriate emission wavelength [37]. Examples of such composite scintillators are detailed in Sect. 6.3.2.

6.2 Plastic Scintillators Incorporating Non-emitting Inorganic Nanoparticles

In this section, nanocomposite scintillators comprising inorganic nanoparticles with no or negligible emission are introduced. Because part of the energy of impinged radiation is deposited to the inorganic nanoparticles, adding non-emitting inorganic nanoparticles results in a decrease in the scintillation light yield. However, the addition of the non-emitting inorganic nanoparticles has been used to enhance the detection efficiency of the radiation to be detected (e.g., X-rays, gamma-rays, or thermal neutrons). For the detection of high-energy photons such as X-rays or gamma-rays, the effective atomic number of the scintillators should be enhanced to obtain high detection efficiency because the interaction probability steeply increases with the atomic number of the constituent elements. For the detection of thermal neutrons, scintillators loaded with ^6Li , ^{10}B , or Gd isotopes at high concentrations are necessary; neutrons have no electric charge and hence cannot induce electronic excitations or ionizations by themselves. Hence, they are detected via nuclear reactions with ^6Li , ^{10}B , or Gd isotopes to generate high-energy charged particles (with ^6Li or ^{10}B) or gamma-rays (with ^{155}Gd or ^{157}Gd). Chapter 3 of this book is the reference chapter for the detection of thermal neutrons with plastic scintillators.

In the material design of nanocomposite scintillators in this approach, the added nanoparticles should be transparent at the scintillation wavelength. If the nanoparticles absorb the scintillation photons, the scintillation light yield is reduced. Inorganic nanoparticles having large bandgap energy are desirable from this viewpoint. In addition, negligible emission from the inorganic nanoparticles is desirable for applications in which fast response and detection capability at a high counting rate are necessary; emission from the nanoparticles having long scintillation decay component (typically > 10 ns) is undesirable in such applications.

In comparison to loaded plastic scintillators for similar applications, nanocomposite scintillators have several potential advantages. One advantage is higher possible loading concentration in nanocomposites. Loading organometallic compounds in plastic scintillators is a standard procedure for many applications [2, 38, and Chap. 4 of this book]. In this case, the loading concentration is limited by the solubility of the organometallic compound in the host polymer. On the contrary, inorganic nanoparticles can be added without the solubility limit if the aggregation of the nanoparticles can be suppressed by appropriate surface modification. Another possible advantage is the suppression of the quenching by the added compounds or

nanoparticles; many organometallic compounds quench the excited states nearby. If we assume that the quenching occurs via the Förster energy transfer, the energy transfer radius can be up to several nm. In this case, excited states within the large volume of several-nm radius are quenched by only one or two metal atoms. In other words, the addition of organometallic compounds at a small amount significantly reduces the scintillation light yield. In contrast to the case of organometallic compounds, a decrease in the scintillation light yield is caused only by the energy deposition to inorganic nanoparticles in organic–inorganic nanocomposite scintillators and may be smaller than that caused by the quenching by organometallic compounds in loaded plastic scintillators.

6.2.1 Sol-gel-Derived Organic-Inorganic Composite Scintillators

Organic–inorganic nanocomposites fabricated with sol–gel method have inorganic amorphous nanoparticles because the nanocomposites cannot be heated at high temperatures to obtain well-crystallized inorganic nanoparticles. Amorphous inorganic phosphors generally have scintillation light yields significantly smaller than those of crystals. Hence, the inorganic nanoparticles in the nanocomposites fabricated with sol–gel method are used as sensitizers for high-energy photons such as X-rays and gamma-rays or thermal neutrons as well. Detailed description of the scintillators fabricated with sol–gel method can be found elsewhere [39].

For the detection of X-rays and gamma-rays, the effective atomic number of the scintillator should be high to achieve high detection efficiency. In this case, the incorporation of inorganic nanoparticles comprising heavy elements at high concentrations is desired. From this viewpoint, hafnium has been incorporated into polystyrene-based plastic scintillators to enhance the detection efficiency toward synchrotron radiation X-rays [40, 41]. Hafnium was included as complex oxide with silicon to form amorphous nanoparticles, and the hafnium source was HfOCl_2 instead of alkoxide. It should be noted that trimethoxyphenylsilane was used as the silicon source to prepare the organically modified surface of the nanoparticles. Figure 6.4 shows the TEM image of the scintillator [40]. Nanoparticles up to 300 nm were observed within the polystyrene matrix. As shown in the upper left inset of Fig. 6.4, the scintillator was approximately 20 mm ϕ and 0.6-mm thick and seemed translucent because of the relatively large nanoparticles size. The upper right inset of Fig. 6.4 is the EDX spectrum of the nanoparticles, which shows the presence of hafnium as the main constituent of the nanoparticles. Table 6.1 summarizes the scintillation light yield and the detection efficiency of the hafnium-comprising nanocomposite scintillators for 67.4-keV X-rays. These values are benchmarked against a lead-loaded commercially available plastic scintillator, EJ-256 with Pb at 5 wt%. The scintillation light yield gradually decreased with the nanoparticles content up to 25 wt%, which was caused by energy deposition on non-emitting nanoparticles, and the detection

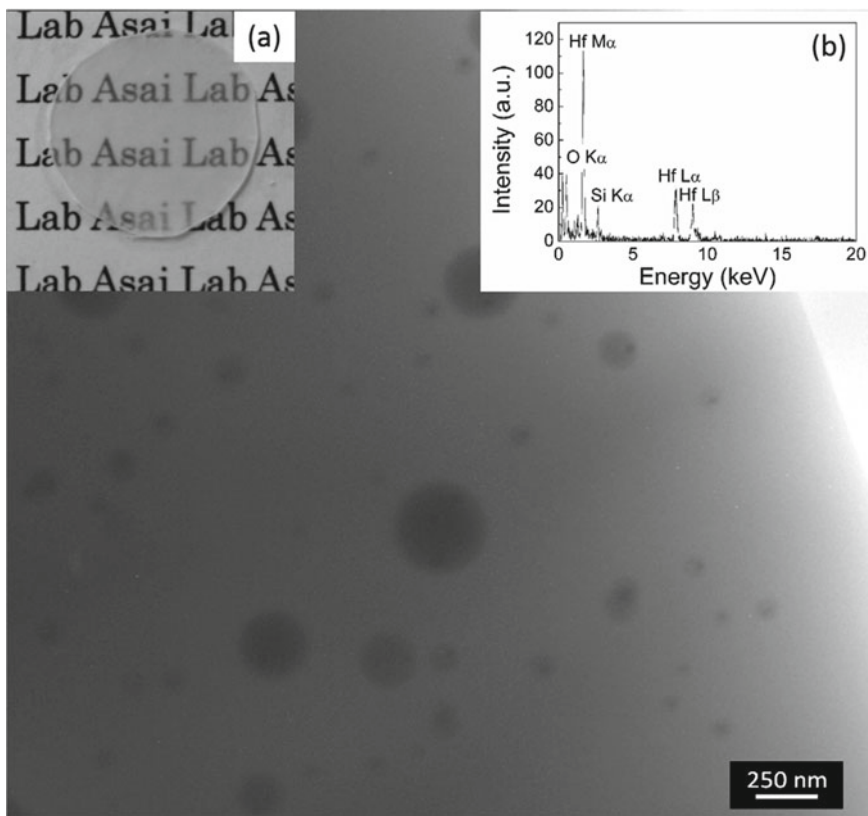
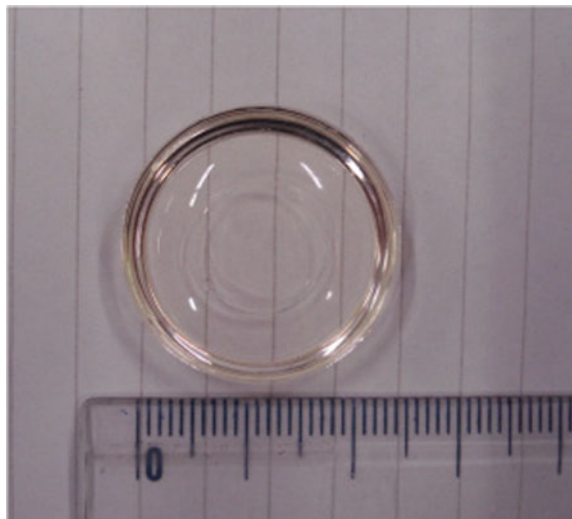


Fig. 6.4 Transmission electron microscopy image of 10 wt% Hf-doped scintillation material. Insets: **a** photograph of 10 wt% Hf-doped organic–inorganic hybrid scintillation material, **b** EDX spectrum of the nanoparticles in the 10 wt% Hf-doped scintillation material (reproduced from [40] with permission from AIP Publishing)

Table 6.1 Scintillation light yield and detection efficiency of nanocomposite scintillators comprising hafnia–silica nanoparticles with different nanoparticles contents and EJ-256 [41]

Sample	Light yield (ph/MeV)	Detection efficiency (%) in 1 mm thickness
Non-doped	11,500	1.7
2.5 wt%	9,300	3.7
5.0 wt%	9,300	4.4
10 wt%	8,100	6.3
15 wt%	6,000	5.4
20 wt%	6,000	5.6
25 wt%	5,200	6.3
EJ-256	5,300	3.4

Fig. 6.5 Photograph of the polyethylene glycol–borosilicate glass nanocomposite (reproduced from [42] with permission from the Japan Society of Applied Physics)



efficiency concomitantly increased. Although the detection efficiency and the scintillation light yield have a complementary relationship, some of the nanocomposite scintillators exceed EJ-256 in both detection efficiency and scintillation light yield.

Nanocomposite scintillators for thermal neutron detection have also been developed [42]. Boron was included in the main constituent of borosilicate glass nanoparticles in poly(ethylene glycol) matrix. A picture of the scintillator is shown in Fig. 6.5. Highly transparent nanocomposite scintillators have successfully been fabricated. Some of the nanocomposite scintillators exhibit 1.2 times higher scintillation light yield than that of BC-454 with B at 5 wt%, which is a commercially available boron-loaded plastic scintillator. Also, the nanocomposite scintillators included B at higher concentrations than that of BC-454.

6.2.2 Nanocomposite Scintillators Fabricated via Two-Step Synthesis

Nanocomposite scintillators have been developed based on plastic scintillators incorporating HfO_2 [43] or Bi_2O_3 [44] nanoparticles synthesized with the subcritical hydrothermal method. The surface of the nanoparticles was modified with 3-phenyl propionic acid to achieve good affinity with the polystyrene host of the nanocomposites. Figure 6.6 shows the TEM image of the HfO_2 nanoparticles [43]. Nanoparticles smaller than 10 nm were observed. The detection efficiency for the 67.4-keV X-rays was enhanced by the addition of the nanoparticles although the scintillation light yield decreased. Some of the nanocomposite scintillators were superior to EJ-256 in the detection efficiency and the scintillation light yield [43]. According to a similar

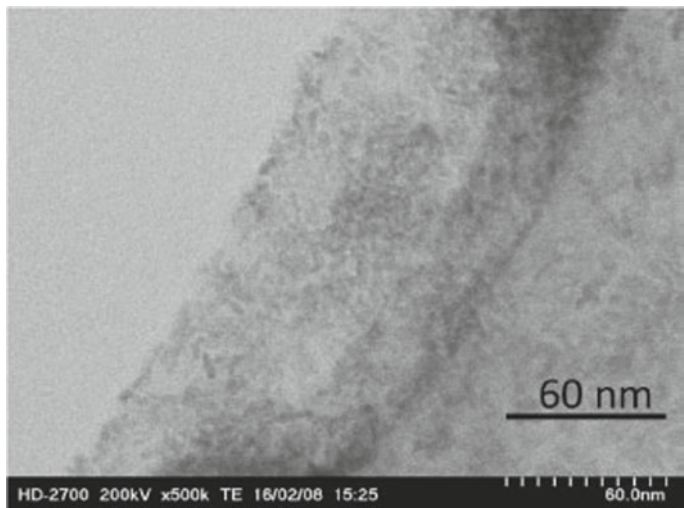


Fig. 6.6 TEM image of HfO₂ nanoparticles to be incorporated in nanocomposite scintillators (reproduced from [43] with permission from the Japan Society of Applied Physics)

procedure, large nanocomposite scintillators comprising ZrO₂ nanoparticles have been developed [45]. Transparent large scintillators up to 3 mm thick were successfully developed with the addition of ZrO₂ nanoparticles up to 60 wt%. This is in contrast to the case of the addition of unmodified ZrO₂ nanoparticles; aggregation of the ZrO₂ nanoparticles resulted in an unclear full-energy peak against 67.4-keV X-rays owing to the inhomogeneity [46].

Nanocomposite scintillators comprising Gd₂O₃ nanoparticles were developed using different synthesizing methods [47]. Gd₂O₃ nanoparticles were synthesized via the thermal decomposition method and subsequently capped with oleic acid or oleylamine. Further, the ligand of the nanoparticles was changed to bis(2-(methacryloyloxy)ethyl)phosphate, which is a coupling agent to copolymerize nanocrystals with methyl methacrylate. Nanocomposite scintillators were obtained by thermally induced radical polymerization of vinyltoluene monomer dispersion of the Gd₂O₃ nanoparticles added with fluorophore molecules. High transparency was achieved owing to the good dispersion of small nanoparticles. Scintillation light yields higher than 20,000 ph/MeV were estimated based on the comparison of beta-induced radioluminescence spectra to that of BC-400. A clear full-energy peak was observed in the pulse height spectra for 662-keV gamma-rays from ¹³⁷Cs with an energy resolution of 11.4%. A similar reaction procedure was applied to the fabrication of nanocomposite scintillators comprising YbF₃ [48] and HfO₂ [49] nanoparticles with scintillation light yields of 8,600 and 7,600 ph/MeV, respectively. A highly transparent nanocomposite scintillator has been successfully obtained. In the former case, a clear full-energy peak was observed in the pulse height spectra although energy resolution was not mentioned owing to the superposition of the full-energy

peak with an escape peak. In the case of HfO_2 nanoparticles, the shape of the superposed peak was deconvolved into the full-energy peak and an escape peak with energy resolutions of 8.0% and 9.0%, respectively. It should be noted that a hypothesis of energy transfer from the Gd_2O_3 nanoparticles to host poly(vinyltoluene) polymer for the high scintillation light yield of the nanocomposite scintillators comprising the Gd_2O_3 nanoparticles was elaborated [47].

Surface stabilization effect on the scintillation light yield has also been researched. GdF_3 nanoparticles derived with precipitation method were modified with different stabilizer molecules and subsequently form nanocomposite scintillators with polystyrene-based host [50]. The difference in the stabilizer molecules results in a significant difference in the scintillation light yields as functions of nanoparticle content. Use of stabilizer molecules having a good affinity to the polystyrene host allowed to introduce nanoparticles at 5 wt% with a decrease of the light yield of only 10% [51].

For thermal neutron detection, the addition of ${}^6\text{LiF}$ nanoparticles to plastic scintillators has been performed. ${}^6\text{LiF}$ nanoparticles synthesized from the thermal decomposition method were capped with oleic acid and compatible with polysiloxane-based scintillators [52]. The nanocomposite scintillators have a clear peak for thermal neutron detection via nuclear reaction with ${}^6\text{Li}$ in the pulse height spectrum. Even smaller ${}^6\text{LiF}$ nanoparticles were prepared with the co-precipitation method; however, they suffered from aggregation [53]. The detection efficiency of the siloxane-based scintillators was enhanced up to 90% that of EJ-420 by further addition of $\text{ZnS}:\text{Ag}$ [54]. An interesting result has been reported on nanocomposite scintillators based on $\text{Li}_2\text{B}_4\text{O}_7$ nanoparticles and polystyrene-based plastic scintillators for neutron detection. The $\text{Li}_2\text{B}_4\text{O}_7$ nanoparticles were fabricated in a colloidal synthesis method in an aqueous solution with poly(*N*-vinylpyrrolidone) as the surface stabilizer [55]. Based on the pulse shape discrimination technique, discrimination of the detection events of fast neutrons, thermal neutrons (via nuclear reactions with ${}^6\text{Li}$ and ${}^{10}\text{B}$), and gamma-rays has been achieved (Fig. 6.7) [56]. Another approach to develop scintillators for fast and thermal neutrons is a combination of $\text{Gd}_2\text{SiO}_5:\text{Ce}$ or $\text{Gd}_2\text{Si}_2\text{O}_7:\text{Ce}$ crystal grains for thermal neutron detection with *trans*-stilbene grains for fast neutron detection [57]. Separate measurements of fast and thermal neutrons and reconstruction of neutron spectrum from ${}^{239}\text{Pu}$ -Be source were achieved. A similar approach was used to obtain composite flexible gel scintillators containing $\text{Gd}_2\text{SiO}_5:\text{Ce}$ or $\text{Gd}_2\text{Si}_2\text{O}_7:\text{Ce}$ crystal grains for thermal neutrons [58]. Detection efficiency of thermal neutrons of 20% was achieved only for a very thin scintillation layer of less than 0.1 mm. High tolerance of the composite scintillators containing $\text{Gd}_2\text{SiO}_5:\text{Ce}$ or $\text{Gd}_2\text{Si}_2\text{O}_7:\text{Ce}$ crystal grains has been shown [59]. They displayed resistance to doses up to 2 MGy.

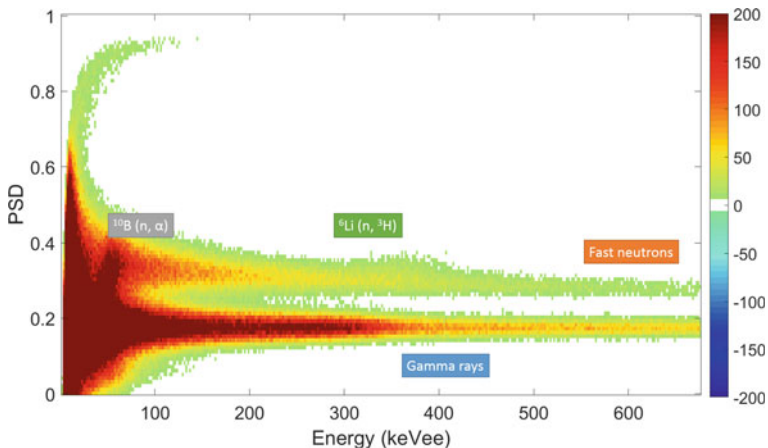


Fig. 6.7 Pulse shape discrimination among detection events of fast neutrons, thermal neutrons reacted with ^6Li or ^{10}B , and gamma-rays (reproduced from [56] with permission from Elsevier)

6.3 Nanocomposite Scintillators Comprising Luminescent Nanoparticles

In contrast to the previous section, nanocomposite scintillators introduced in this section exhibit scintillation from the inorganic nanoparticles. There are two approaches of the material design on this line. One is that the organic host polymer exhibit no or negligible scintillation. In this case, most of the scintillation arises from the inorganic nanoparticles, and the organic polymer provides a transparent host with good workability and scalability. The other approach is the case that the organic host polymers and inorganic nanoparticles both exhibit scintillation. Scintillation from the inorganic nanoparticles in such nanocomposites may be absorbed by the organic host and vice versa. The absorption of the scintillation photons by the scintillators themselves, i.e., self-absorption, may suppress the scintillation light yield and slow down the scintillation decay.

6.3.1 Nanocomposite Scintillators Comprising Inorganic Phosphor Nanoparticles

Nanocomposite scintillators with host polymers showing negligible emission have been developed using a variety of inorganic phosphor nanoparticles. There are two approaches in the development of such nanocomposite scintillators. One is the use of slow emission processes such as 4f-4f transitions of Eu^{3+} ions for current mode

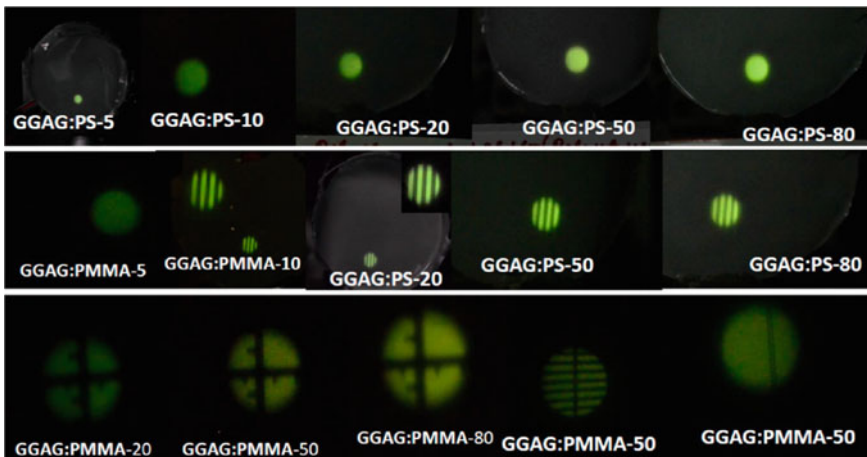


Fig. 6.8 X-ray images on polystyrene (PS) and poly(methyl methacrylate) (PMMA)-based composite scintillators comprising Ce³⁺-doped Gd₃Ga₃Al₂O₁₂ nanoparticles at 10%, 20%, 50%, and 80% showing the full X-ray beam; images formed by a SS line mask of spacing 0.5 mm; images of SS crosswire mask and standard 1p phantom with 10 lp/mm (reproduced from [66] with permission from the American Chemical Society)

applications. Polyvinyl alcohol-based scintillator films comprising Eu³⁺-doped and Eu³⁺ and Li⁺-codoped Y₂HfO₇ nanoparticles have been developed [60]. The transparent films comprised nanoparticles of several tens nm and exhibited clear radioluminescence bands owing to 4f-4f transitions of Eu³⁺. Poly(vinylidene fluoride)-based nanocomposite scintillators comprising Eu³⁺-doped Gd₂O₃ nanoparticles have been developed [61]. The radioluminescence response was improved by using emission from the organic host of polystyrene [62] or poly(vinylidene fluoride) [63] in combination with PPO and POPOP. The other approach is the use of inorganic scintillators with a fast response adequate for pulse counting applications. Nanoparticles of self-activated scintillators exhibiting relatively fast scintillation decay have also been used. Poly(methyl methacrylate)-based nanocomposite scintillator films comprising CdWO₄ nanoparticles of several tens nm were developed for alpha-ray detection [64]. Counting efficiency higher than 40% and resolution of 60–80% was achieved for alpha-rays from ²⁴¹Am in the pulse height spectra. CdWO₄-based nanocomposite scintillators have also been developed using polystyrene host added with fluorophores, in which the scintillation response was mainly obtained from the CdWO₄ nanoparticles [65]. Nanocomposite scintillators have been developed using nanoparticles having a faster emission mechanism, such as 5d-4f transitions of Ce³⁺ ions. Ce-doped Gd₃Ga₃Al₂O₁₂ nanoparticles were used in poly(methyl methacrylate)- and polystyrene-based nanocomposite scintillators [66]. Nanoparticles were synthesized via solid-state sintering and co-precipitation method, and clear X-ray images were successfully obtained using the nanocomposite scintillators

as shown in Fig. 6.8. Polystyrene-based nanocomposite scintillators comprising sol-gel-derived Ce³⁺-doped Lu₂SiO₅ nanoparticles of several tens nm were also developed [67]. Oleic-acid-capped Ce_xLa_{1-x}F₃ nanoparticles were also used in nanocomposite scintillators [68]. They achieved high transparency even at inorganic content of 60 vol% and succeeded in large-scale synthesis. Even faster band edge emission of direct-gap semiconductors was also utilized as the emission mechanism of the inorganic nanoparticles. Ga³⁺-doped ZnO nanoparticles were used as the fluorophores in polystyrene-based nanocomposite scintillators [69, 70]. The nanoparticles were fabricated using the photochemical method [69] or sol–gel method [70]. A non-radiative transfer from the polystyrene host to the Ga³⁺-doped ZnO nanoparticles was quantitatively discussed [69].

Nanocomposites comprising efficiently emitting organic hosts exhibit complicated scintillation processes. Polystyrene-based nanocomposite scintillators comprising 16-nm SrF₂ nanoparticles were synthesized via the chemical precipitation method [71]. The X-ray-excited radioluminescence intensity was enhanced by the addition of the SrF₂ nanoparticles. Two scintillation decay components of 2.8 ns and ~700 ns corresponded to the emission of fluorophores (*p*-terphenyl and POPOP) in the polymer host and self-trapped excitons in SrF₂ nanoparticles, although the emission spectrum was not changed. These results indicate that the emission from the SrF₂ nanoparticles was absorbed by the fluorophores in the polystyrene host, and subsequently, the emission from the fluorophores was obtained. Interesting results were obtained for the nanocomposite scintillators comprising CeF₃ nanoparticles derived via precipitation reactions [72]. The nanocomposite scintillators exhibited only emission from PPO in poly(vinyltoluene) host, and the intensity was significantly enhanced by the addition of CeF₃ nanoparticles, for which energy transfer from the CeF₃ nanoparticles to PPO was hypothesized. Experimental evidence has been obtained for other nanocomposite scintillators comprising 12-nm CeF₃ nanoparticles synthesized in ionic substitution reaction [73]. In the scintillation decay behavior, decay components of fluorophores were only observed. The absence of the slow decay component of the CeF₃ nanoparticles cannot be explained with the absorption of the emission from the CeF₃ nanoparticles by the fluorophores and indicates the non-radiative energy transfer from the nanoparticles to the fluorophores. Clearer evidence on this point has been obtained for polystyrene-based nanocomposite scintillators comprising BaF₂ [74] and Pr³⁺-doped LaPO₄ [75] nanoparticles. As shown in Fig. 6.9 [74], the slow scintillation component of the BaF₂ nanoparticles was suppressed for the nanoparticles less than several tens nm. Quite similar results have been obtained for the Pr³⁺-doped LaPO₄ nanoparticles. These results clearly indicate that a long-range energy transfer on the order of tens of nm occurred from the nanoparticles to the fluorophores.

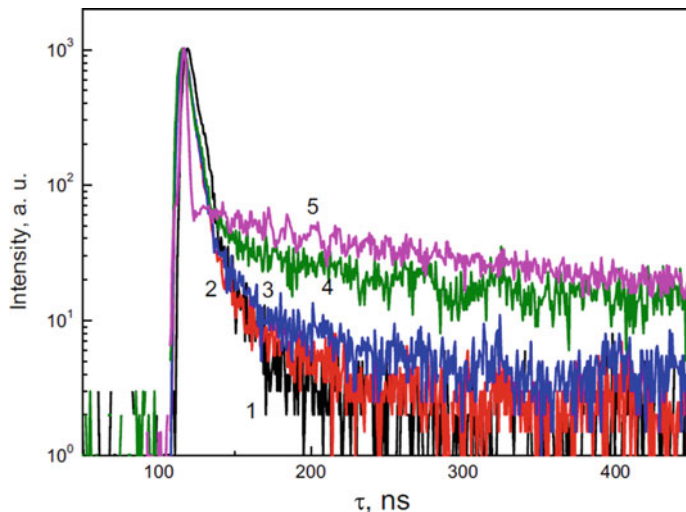


Fig. 6.9 Luminescence decay kinetic curves of polystyrene composites loaded with BaF_2 nanoparticles of different sizes: 1—20 nm; 2—45 nm; 3—65 nm; 4—100 nm; 5— BaF_2 microcrystals ($10 \mu\text{m}$) (reproduced from [74] with permission from Elsevier)

6.3.2 Nanocomposite Scintillators Comprising Semiconductor Nanocrystals

Surface-capped nanocrystals of II–IV compound semiconductors have been used for nanocomposite scintillators. Nanocomposite scintillators comprising CdSe and CdTe nanocrystals have been developed [76]. CdSe nanocrystals in non-aqueous solvent and CdTe nanocrystals in aqueous dispersion have been combined with polystyrene- and poly(vinyl alcohol)-based host polymers, respectively. Alpha particles from ^{241}Am were successfully detected using a nanocomposite scintillator of polystyrene host doped with PPO comprising the CdSe nanocrystals; a clear peak appeared in the pulse height spectrum with the addition of CdSe nanocrystals. Poly(vinyltoluene)-based nanocomposite scintillators comprising CdS nanocrystals have been developed [77]. Gamma-rays and beta-induced scintillation light yields were successfully enhanced from 1.03 to 3.6 times by the addition of the nanocrystals. Nanocomposite scintillators based on CdTe nanocrystals in poly(vinyl alcohol) and poly(methyl methacrylate) have been developed for X-ray imaging [78]. A spatial resolution of 5 lines/mm was successfully achieved. Poly(vinyl alcohol)-based nanocomposite scintillators comprising ZnS nanocrystals in addition to ^6LiF nanoparticles have been developed for thermal neutron detection [79]. A scintillation light yield of ~ 200 ph/neutron, which is comparable to that of BC-704, has been achieved for the scintillator with composition $^6\text{LiF}/\text{ZnS}/\text{PVA} = 0.25:0.5:4.25$ in weight.

In addition to the surface-capped nanocrystals, core/shell nanocrystals have been used as more efficient emitters. Nanocomposite scintillators comprising CdSe/ZnS

nanocrystals were added to PS [80]. Efficient scintillation from the nanocrystals was clearly visible under proton irradiation even at low nanocrystal content of less than 1 wt%. Poly(vinyltoluene)-based nanocomposite scintillators comprising $\text{Cd}_x\text{Zn}_{1-x}\text{S}/\text{ZnS}$ core/shell nanocrystals up to 60 wt% have been developed [81]. The authors expected the energy transfer cascade from the host polymer via the nanocrystals to fluorophores, as shown in Fig. 6.10. CdSe/ZnSe core/shell nanocrystals have also been used in the organic semiconductor host of MEH-PPV [82]. The semiconductor host was used for its lower ionization energy than conventional hosts of plastic scintillators. Enhancement in the cathodoluminescence intensity was successfully achieved by the addition of the core/shell nanocrystals up to 15 vol%. Nanocomposite scintillators based on CdSe/ZnS core/shell nanocrystals in porous Vycor glass have also been developed [83]. An excellent energy resolution of ~15% for 59.5-keV gamma-rays from ^{241}Am was achieved, which is twice better than that of NaI:Tl. The scintillation light yield was significantly enhanced by the addition of the nanocrystals. The addition of perovskite CsPbBr_3 nanocrystals yielded fast response nanocomposite scintillators having 3.4-ns scintillation decay time constant and negligible self-absorption [84].

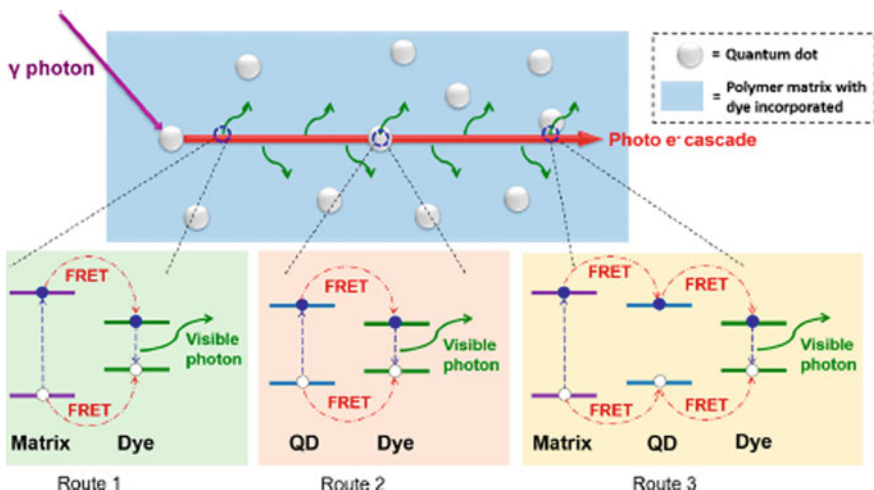


Fig. 6.10 Schematic illustration of the scintillation process and Förster resonance energy transfer (FRET) routes involved in a semiconductor nanocrystal (QD)/dye/polymer ternary system (reproduced from [81] with permission from the American Chemical Society)

6.4 Summary and Future Prospects

In this Chapter, organic–inorganic nanocomposite scintillators are reviewed as an emerging field of scintillator development. Several fabrication approaches are introduced with an emphasis on interface design between organic and inorganic phases. Basis of the optical properties related to nanocomposites is provided. Representative examples of the nanocomposite scintillators are introduced. Among the organic–inorganic nanocomposites fabricated in materials science, the variety of fabricated nanocomposite scintillators have been limited in the choice of organic and inorganic phases and fabrication methods. Nanocomposite materials developed for other applications will provide valuable information on the materials design of nanocomposite scintillators.

The use of nanocomposite scintillators for specific applications has been proposed. For the application to positron emission tomography (PET), nanocomposite scintillators would be an effective alternative to conventional single-crystalline inorganic scintillators [85]. One of the shortcomings of nanocomposite scintillators for the use in PET apparatus is light scattering within the nanocomposites, and optimum thickness of nanocomposite has been proposed on the basis of Monte Carlo simulations [85]. Also, the use of nanocomposites for the detection of radioactive nuclei has been proposed [86]; composite structure enables uptake of radioactive Sr from the seawater in mesoporous silica having high affinity to the radioactive Sr and detection by poly(vinyltoluene)-based scintillator brush grafted on the surface of the mesoporous silica. Nanocomposite scintillators having better performance will be applied to various applications in the near future.

There are several key concepts for innovative nanocomposite scintillators in the future. One is the design and control of energy transfer. If the electronic excitation energy in inorganic nanoparticles as sensitizer transfers to polymer host efficiently, reduction in the scintillation light yield by the sensitizer can be suppressed. In fact, energy transfer from the inorganic nanoparticles to the polymer host has been observed in some nanocomposites comprising small nanoparticles. The second point is the use of highly emissive inorganic nanoparticles with fast emission decay. To develop fast and efficient scintillators based on organic–inorganic nanocomposites, fast emission from the inorganic nanoparticles is necessary. CsPbBr_3 nanocrystals are an appropriate phosphor on this point [87]. The third point is the potential use of photonic structure. The direction of scintillation emission can be controlled using photonic structures [88, and Chap. 9 of this Book], which may enhance the light collection efficiency to the photon detectors.

Acknowledgements This research was supported by a Grant-in-Aid for Development of Systems and Technology for Advanced Measurement and Analysis from the Japan Science and Technology Agency, Grant-in-Aid for Young Scientists (A) (No. 25709088, 2013–2015), a Grant-in-Aid for Scientific Research (A) (No. 18H03890, 2018–2021), and grants from The Kazuchika Okura Memorial Foundation and Nippon Sheet Glass Foundation for Materials Science and Engineering. A part of this research is based on the Cooperative Research Project of the Research Center for Biomedical Engineering, Ministry of Education, Culture, Sports, Science, and Technology.

References

1. G.H.V. Bertrand, M. Hamel, F. Sguerra, *Chem. Eur. J.* **20**(48), 15660 (2014)
2. T.J. Hajagos, C. Liu, N.J. Cherepy, Q. Pei, *Adv. Mater.* **30**(27), 1706956 (2018)
3. M. Koshimizu, *Funct. Mater. Lett.* **13**(6), 2030003 (2020)
4. D. Pinto, L. Bernardo, A. Amaro, S. Lopes, *Constr. Build. Mater.* **95**, 506 (2015)
5. M. Sangermano, M. Messori, *Macromol. Mater. Eng.* **295**(7), 603 (2010)
6. B.P. Tripathi, V.K. Shahi, *Prog. Polym. Sci.* **36**(7), 945 (2011)
7. D.J. Kim, M.J. Jo, S.Y. Nam, *J. Ind. Eng. Chem.* **21**, 36 (2015)
8. L. Yue, J. Ma, J. Zhang, J. Zhao, S. Dong, Z. Liu, G. Cui, L. Chen, *Energy Storage Mater.* **5**, 139 (2016)
9. P. Sengodu, A.D. Deshmukh, *RSC Adv.* **5**(52), 42109 (2015)
10. Q. Wang, L. Zhu, *J. Polym. Sci., Part B: Polym. Phys.* **49**(20), 1421 (2011)
11. A. Kaushik, R. Kumar, S.K. Arya, M. Nair, B.D. Malhotra, S. Bhansali, *Chem. Rev.* **115**(11), 4571 (2015)
12. G. Zhao, X. Huang, Z. Tang, Q. Huang, F. Niu, X. Wang, *Polym. Chem.* **9**, 3562 (2018)
13. C. Su, J. Hazard. Mater. **322**(A), 48 (2017)
14. J. Tang, Y. Chen, S.R. McCuskey, L. Chen, G.C. Bazan, Z. Liang, *Adv. Electron. Mater.* **5**(11), 1800943 (2019)
15. T.-P. Nguyen, *Surf. Coat. Technol.* **206**(4), 742 (2011)
16. L. Zhao, Z. Lin, *Adv. Mater.* **24**(32), 4353 (2012)
17. R. Liu, *Materials* **7**(4), 2747 (2014)
18. S. Singh, H. Chen, S. Shahrokhi, L.P. Wang, C.-H. Lin, L. Hu, X. Guan, A. Tricoli, Z.J. Xu, T. Wu, *ACS Energy Lett.* **5**(5), 1487 (2020)
19. C. Lü, B. Yang, *J. Mater. Chem.* **19**, 2884 (2009)
20. Y. Tomita, E. Hata, K. Momose, S. Takayama, X. Liu, K. Chikama, J. Klepp, C. Pruner, M. Fally, *J. Mod. Opt.* **63**(S3), S1 (2016)
21. C. Sanchez, G.J. de A.A. Soler-Illia, F. Ribot, T. Lalot, C.R. Mayer, V. Cabuil, *Chem. Mater.* **13**(10), 3061 (2001)
22. C. Sanchez, B. Julián, P. Belleville, M. Popall, *J. Mater. Chem.* **15**(35–36), 3559 (2005)
23. P.W. de Oliveira, C. Becker-Willinger, M.H. Jilavi, *Adv. Eng. Mater.* **12**(5), 349 (2010)
24. M.A. Hood, M. Mari, R. Muñoz-Espí, *Materials* **7**(5), 4057 (2014)
25. S. Kango, S. Kalia, A. Celli, J. Njuguna, Y. Habibi, R. Kumar, *Prog. Polym. Sci.* **38**(8), 1232 (2013)
26. J. Jung, M. Chang, H. Yoon, *Appl. Sci.* **8**(8), 1376 (2018)
27. Y. Li, T.M. Krentz, L. Wang, B.C. Benicewicz, L.S. Schadler, A.C.S. Appl. Mater. Interfaces **6**(9), 6005 (2014)
28. M.A. Boles, D. Ling, T. Hyeon, D.V. Talapin, *Nat. Mater.* **15**, 141 (2016)
29. M.J. Owen, in *Adhesion Science and Engineering*, ed. by D.A. Dillard, A.V. Pocius, M. Chaudhury (Elsevier, 2002) pp. 403–431
30. M.Z. Rong, M.Q. Zhang, Y.X. Zheng, H.M. Zeng, R. Walter, K. Friedrich, *Polymer* **42**(1), 167 (2001)
31. T. Adschariri, *Chem. Lett.* **36**, 1188 (2007)
32. C.B. Murray, C.R. Kagan, M.G. Bawendi, *Annu. Rev. Mater. Sci.* **30**, 545 (2000)
33. H.C. van de Hulst, *Light Scattering by Small Particles* (Dover Publications, New York, 1981).
34. H. Althues, J. Henle, S. Kaskel, *Chem. Soc. Rev.* **36**(9), 1454 (2007)
35. G.D. Scholes, G. Rumbles, *Nat. Mater.* **5**, 683 (2006)
36. A.M. Smith, S. Nie, *Acc. Chem. Res.* **43**(2), 190 (2010)
37. K. Tomanová, V. Čuba, M.G. Brik, E. Mihóková, R.M. Turtos, P. Lecoq, F. Auffray, M. Nikl, *APL Mater.* **7**(1), 011104 (2019)
38. M. Hamel, F. Carrel, in *New Insights on Gamma Rays*, ed. by A.M. Maghraby (InTech, 2017), pp. 47–66
39. M. Koshimizu, in *Handbook of Sol-Gel Science and Technology*, ed. by L. Klein, M. Aparicio, A. Jitianu (Springer, Cham, 2016), pp. 2273–2300

40. Y. Sun, M. Koshimizu, N. Yahaba, F. Nishikido, S. Kishimoto, R. Haruki, K. Asai, *Appl. Phys. Lett.* **104**(17), 174104 (2014)
41. K. Kagami, M. Koshimizu, Y. Fujimoto, S. Kishimoto, R. Haruki, F. Nishikido, K. Asai, *J. Mater. Sci.: Mater. Electron.* **31**, 896 (2020)
42. M. Koshimizu, H. Kitajima, T. Iwai, K. Asai, *Jpn. J. Appl. Phys.* **47**(7R), 5717 (2008)
43. F. Hiyama, T. Noguchi, M. Koshimizu, S. Kishimoto, R. Haruki, F. Nishikido, T. Yanagida, Y. Fujimoto, T. Aida, S. Takami, T. Adschari, K. Asai, *Jpn. J. Appl. Phys.* **57**(1), 012601 (2018)
44. F. Hiyama, T. Noguchi, M. Koshimizu, S. Kishimoto, R. Haruki, F. Nishikido, Y. Fujimoto, T. Aida, S. Takami, T. Adschari, K. Asai, *Jpn. J. Appl. Phys.* **57**(5), 052203 (2018)
45. A. Toda, S. Kishimoto, *IEEE Trans. Nucl. Sci.* **67**(6), 983 (2020)
46. Y. Araya, M. Koshimizu, R. Haruki, F. Nishikido, S. Kishimoto, K. Asai, *Sens. Mater.* **27**, 255 (2015)
47. W. Cai, Q. Chen, N. Cherepy, A. Dooraghi, D. Kishpaugh, A. Chatzioannou, S. Payne, W. Xiang, Q. Pei, *J. Mater. Chem. C* **1**(10), 1970 (2013)
48. Y. Jin, D. Kishpaugh, C. Liu, T.J. Hajagos, Q. Chen, L. Li, Y. Chen, Q. Pei, *J. Mater. Chem. C* **4**(16), 3654 (2016)
49. C. Liu, T.J. Hajagos, D. Kishpaugh, Y. Jin, W. Hu, Q. Chen, Q. Pei, *Adv. Funct. Mater.* **25**(29), 4607 (2015)
50. U.U. Sytnik, O.V. Svidlo, P.N. Zhmurin, *Funct. Mater.* **20**, 243 (2013)
51. O.V. Svidlo, P.N. Zhmurin, Y.A. Gurkalenko, *Funct. Mater.* **21**, 414 (2014)
52. S.M. Carturan, T. Marchi, G. Maggioni, F. Gramegna, M. Degerlier, M. Cinausero, M. Dalla Palma, A. Quaranta, *J. Phys. Conf. Ser.* **620**, 012010 (2015)
53. S.M. Carturan, M. Degerlier, G. Maggioni, T. Marchi, F. Gramegna, M. Cinausero, L. Stevanato, M. Vesco, A. Quaranta, *Acta Phys. Pol. A* **134**, 405 (2018)
54. S.M. Carturan, M. Vesco, I. Bonesso, A. Quaranta, G. Maggioni, L. Stevanato, E. Zanazzi, T. Marchi, D. Fabris, M. Cinausero, F. Pino, F. Gramegna, *Nucl. Instr. Methods A* **925**, 109 (2019)
55. C. Frangville, A. Grabowski, J. Dumazert, E. Montbarbon, C. Lynde, R. Coulon, A. Venerosy, G.H.V. Bertrand, M. Hamel, *Mater. Chem. Front.* **3**, 1574 (2019)
56. C. Frangville, A. Grabowski, J. Dumazert, E. Montbarbon, C. Lynde, R. Coulon, A. Venerosy, G.H.V. Bertrand, M. Hamel, *Nucl. Instr. Methods A* **942**, 162370 (2019)
57. N.L. Karavaeva, N.Z. Galunov, E.V. Martynenko, A.V. Kosinova, *Funct. Mater.* **17**, 549 (2010)
58. N.Z. Galunov, B.V. Grinyov, N.L. Karavaeva, Y.V. Gerasymov, O.T. Sidletskiy, O.A. Tarasenko, *IEEE Trans. Nucl. Sci.* **58**(1), 339 (2011)
59. A.Y. Boyarintsev, N.Z. Galunov, I.V. Gerasymov, N.L. Karavaeva, A.V. Krech, L.G. Levchuk, V.F. Popov, O.T. Sidletskiy, P.V. Sorokin, O.A. Tarasenko, *Nucl. Instr. Methods A* **841**, 124 (2017)
60. S.K. Gupta, J.P. Zuniga, M. Abdou, P.S. Ghosh, Y. Mao, *Inorg. Chem. Front.* **7**(2), 505 (2020)
61. P.M. Martins, P. Martins, V. Correia, J.G. Rocha, S. Lanceros-Mendez, *J. Electron. Mater.* **44**, 129 (2015)
62. J. Oliveira, P.M. Martins, P. Martins, V. Correia, J.G. Rocha, S. Lanceros-Mendez, *Appl. Phys. A* **121**, 581 (2015)
63. J. Oliveira, P.M. Martins, P. Martins, V. Correia, J.G. Rocha, S. Lanceros-Mendez, *Composites. Part B* **91**, 610 (2016)
64. H. Ziluei, R. Azimirad, M.M. Larijani, F. Ziae, *Nucl. Instr. Methods A* **852**, 85 (2017)
65. S.M.V. Novais, T.J. Monteiro, V.C. Teixeira, M.A. Gomes, M.E.G. Valerio, Z.S. Macedo, L.B. Barbosa, *J. Lumin.* **199**, 225 (2018)
66. S. Sen, M. Tyagi, K. Sharma, P.S. Sarkar, S. Sarkar, C.B. Basak, S. Pitale, M. Ghosh, S.C. Gadkari, A.C.S. *Appl. Mater. Interfaces* **9**(42), 37310 (2017)
67. M.S.E. Hamroun, K. Bachari, L. Guerbous, A. Berrayah, L. Mechernene, *Optik* **187**, 111 (2019)
68. R.K. Feller, G.M. Purdy, D. Ortiz-Acosta, S. Stange, A. Li, E.A. McKigney, E.I. Esch, R.E. Muenchhausen, R. Gilbertson, M. Bacrania, B.L. Bennett, K.C. Ott, L. Brown, C.S. Macomber, B.L. Scott, R.E. Del Sesto, *J. Mater. Chem.* **21**(15), 5716 (2011)

69. H. Burešová, L. Procházková, R.M. Turtoš, V. Jarý, E. Mihóková, A. Bejtlerová, R. Pjatkan, S. Gundacker, E. Auffray, P. Lecoq, M. Nikl, V. Čuba, *Opt. Exp.* **24**(14), 15289 (2016)
70. S. Alamdari, M.J. Tafreshi, M.S. Ghamsari, *Appl. Phys. A* **125**, 450 (2019)
71. T.M. Demkiv, O.O. Halyatkin, V.V. Vistovskyy, V.B. Hevyk, P.M. Yakibchuk, A.V. Gektn, A.S. Voloshinovskii, *Nucl. Instr. Methods A* **847**, 47 (2017)
72. S. Sahi, W. Chen, K. Jiang, J. Lumin. **159**, 105 (2015)
73. T.M. Demkiv, V.V. Vistovskyy, O.O. Halyatkin, T. Malyi, P.M. Yakibchuk, A.V. Gektn, A.S. Voloshinovskii, *Nucl. Instr. Methods A* **908**, 309 (2018)
74. T.M. Demkiv, O.O. Halyatkin, V.V. Vistovskyy, A.V. Gektn, A.S. Voloshinovskii, *Nucl. Instr. Methods A* **810**, 1 (2016)
75. T.M. Demkiv, O.O. Halyatkin, V.V. Vistovskyy, A.V. Gektn, A.S. Voloshinovskii, *J. Appl. Phys.* **120**(14), 144301 (2016)
76. W.G. Lawrence, S. Thacker, S. Palamakumbura, K.J. Riley, V.V. Nagarkar, *IEEE Trans. Nucl. Sci.* **59**(1), 215 (2012)
77. A.K. Tam, O. Boyraz, J. Unangst, P. Nazareta, M. Schreuder, M. Nilsson, *Rad. Meas.* **111**, 27 (2018)
78. Z. Kang, Y. Zhang, H. Menkara, B.K. Wagner, C.J. Summers, W. Lawrence, V. Nagarkar, *Appl. Phys. Lett.* **98**, 181914 (2011)
79. C.L. Wang, L. Gou, J.M. Zaleski, D.L. Friesel, *Nucl. Instr. Methods A* **622**(1), 186 (2010)
80. J.M. Park, H.J. Kim, Y.S. Hwang, D.H. Kim, H.W. Park, J. Lumin. **146**, 157 (2014)
81. C. Liu, Z. Li, T.J. Hajagos, D. Kishpaugh, D.Y. Chen, Q. Pei, *ACS Nano* **11**(6), 6422 (2017)
82. I.H. Campbell, B.K. Crone, *Adv. Mater.* **18**, 77 (2006)
83. S.E. Létant, T.-F. Wang, *Nano Lett.* **6**, 2877 (2006)
84. M. Gandini, I. Villa, M. Beretta, C. Gotti, M. Imran, F. Carulli, E. Fantuzzi, M. Sassi, M. Zaffalon, C. Brofferio, L. Manna, L. Beverina, A. Vedda, M. Fasoli, L. Gironi, S. Brovelli, *Nat. Nanotechnol.* **15**, 462 (2020)
85. K.J. Wilson, R. Alabd, M. Abolhasan, M. Safavi-Naeini, D.R. Franklin, *Sci. Rep.* **10**, 1409 (2020)
86. V.N. Bliznyuk, A.F. Seliman, S.M. Husson, Y.M. Lvov, T.A. DeVol, *Macromol. Mater. Eng.* **303**, 1700651 (2018)
87. T. Chiba, J. Kido, *J. Mater. Chem. C* **6**(44), 11868 (2018)
88. B. Liu, Q. Wu, Z. Zhu, C. Cheng, M. Gu, J. Xu, H. Chen, J. Liu, L. Chen, Z. Zhang, X. Ouyang, *Appl. Phys. Lett.* **111**(8), 081904 (2017)



Masanori Koshimizu is currently a member of the Department of Applied Chemistry, Graduate School of Engineering, Tohoku University, Japan. He received his B.Eng. (1999), M.Eng. (2001), and Ph.D. (2007) degrees in quantum engineering and systems science from The University of Tokyo. He held the position of Assistant Professor (2004) at the present Department and was promoted to Associate Professor in 2011. His research interests include the development of optical materials for radiation detection including scintillators, storage phosphors, and radiochromic materials. He authored 173 scientific papers, and his h-index is 20.

Chapter 7

Molecular Design Considerations for Different Classes of Organic Scintillators



Patrick L. Feng

Abstract The purpose of this chapter is to review the distinguishing characteristics of different classes of organic scintillators with respect to the performance requirements of typical use cases. Discussion of the relevant physical and photophysical parameters will be provided in the context of the rational design of radiation detection materials. A partial list of these properties is as follows: scintillation light yield, emission wavelength and anisotropy, timing characteristics, ionizing particle discrimination, optical attenuation length, mechanical and environmental robustness, detector volume, and cost. Material design considerations relative to these properties are one of the main objectives of this Chapter. Aromatic materials can produce scintillation light in response to ionizing radiation. This characteristic has been observed in crystalline, liquid, and amorphous scintillators, owing to a process that includes ionization recombination, population of excited electronic states, and radiative de-excitation. Organic scintillators from each category are employed today to satisfy the specific requirements of a wide range of applications. The photophysical and scintillation properties of molecules used in organic scintillators vary across a wide range. This has resulted in over 70 years of research aimed at developing scintillators that possess specific physical and scintillation characteristics. In 1956, Sangster and Irvine Jr. published an in-depth survey describing the scintillation properties of more than fifty organic molecular crystals. This work was significant since it described several important considerations that continue to govern contemporary scintillator development efforts: (1) the scintillation efficiency is dependent upon the electronic structure and fluorescence properties of the constituent molecules, (2) the orientation, shape, and steric properties of the molecule impact the mechanisms of energy transfer giving rise to scintillation, (3) the scintillation efficiency is sensitive to defects and the presence of molecular impurities. Later studies also addressed practical considerations such as detector fabrication/scale-up and the relationship between molecular structure and mechanical properties. These categories provide a general framework from which to approach the development of improved organic scintillators.

P. L. Feng (✉)
Sandia National Laboratories, Livermore, CA, USA
e-mail: plfeng@sandia.gov

7.1 Design Considerations for Crystalline, Plastic, and Liquid Scintillators

7.1.1 Background on Scintillation Mechanisms

The first organic scintillator was discovered in 1947 when Kallman reported that single crystals of naphthalene¹ produced light in response to gamma rays [2, 3]. Anthracene and *trans*-stilbene crystals were later evaluated and found to exhibit similar behavior, yet with a much higher light output response [4, 5]. These observations established the generality of scintillation response in fluorescent organic compounds. In consideration of this finding, the uniform composition and structural order of organic single crystals provided an excellent platform from which to study basic scintillation phenomena. This allowed for systematic studies on the effects of chemical and structural variation. One example is the planar series benzene-naphthalene-anthracene. Another example constitutes the *para*-polyphenyl series: biphenyl, *p*-terphenyl, and *p*-quaterphenyl. In these examples, the scintillation efficiency was found to relate to extent of charge-separation and the corresponding electron transition probabilities, with the more conjugated and larger molecules being more efficient scintillators [1]. Following the initial reports of scintillation in molecular organic crystals, it was later discovered that crystals of *trans*-stilbene could also be used to discriminate between different particle types based on the kinetics of the scintillation pulse, i.e., the method of Pulse-Shape Discrimination (PSD). While methods for the measurement of PSD are discussed in detail elsewhere (see Chaps. 2, 5, and 10), the photophysical processes involved in this capability will be described herein [6–8].

All organic scintillators undergo the same primary processes of excitation and ionization that precedes scintillation light generation. According to seminal work by Birks and others, this includes four processes: (1) excitation into excited π -electron singlet states, (2) ionization of π -electrons, (3) direct excitation of σ -electron and carbon 1s electron excited states, and (4) ionization of electrons other than π -electrons [9]. Processes (1) and (2) account for the scintillation yield, with the majority of light being produced through process (1). Nonradiative pathways (3) and (4) do not contribute to scintillation emission but are instead associated with relaxation via thermalization and molecular damage, respectively. Thus, only the radiative processes (1) and (2) will be discussed here.

Although processes (1) and (2) involve complex theoretical underpinnings that depend on the specific organic medium, it is important to note that nearly the entirety of all organic scintillator developments can be summarized into the optimization of these two light production pathways.

¹Topological representation and key information of these molecules is given in the Appendix section at the end of the book.

7.1.2 Process (1): Direct Excitation into π -Electronic States

7.1.2.1 Process (1): Direct Excitation in Molecular Crystals

In primary (single-component) scintillators such as molecular crystals, process (1) occurs with an efficiency that is roughly proportional to the fraction of aromatic (π) electrons in the molecule and the fluorescence quantum yield (Φ_f). This explains why the scintillation light yield of the polyphenyl series benzene, naphthalene, anthracene, progressively increases in accordance with the respective quantum yields [1]. The Stokes shift is another parameter that must be considered in molecular crystals, due largely to the single-component nature of these scintillators. The Stokes shift is defined as the difference between maximum positions of the absorption and emission spectra corresponding to the same electronic transition (a formula is given in Chap. 1). A more precise description of this consideration from the perspective of scintillator design is the extent of spectral overlap between the electronic absorption and emission spectra. A nonzero spectral overlap will lead to radiative self-absorption, which has several detrimental effects: (1) size-dependent scintillation light yield, (2) shifts in the emission spectrum as a function of interaction position, also known as the ‘inner filter’ effect, (3) slowing down/smearing of the scintillation timing characteristics. One exception to these observations is to introduce an acceptor molecule to reduce or eliminate the spectral overlap. This can be accomplished in crystals by co-crystallizing structurally similar yet photophysically distinct dopant molecules. An example is a mixed crystal of *trans*-stilbene and 1,2-diphenylacetylene, which leads to a larger effective Stokes shift due to energy transfer from the 1,2-diphenylacetylene donor to the *trans*-stilbene acceptor molecules [10]. However, wavelength-shifted molecular crystals are rare due to the lack of suitable dopants that possess the required structural and electronic properties to be co-crystallized at a uniform concentration in the sizes required for practical scintillators. The next two sections describe the practical application of this concept to multi-component solid and liquid scintillator matrices, respectively.

7.1.2.2 Process (1): Direct Excitation in Multi-Component Solid-State Scintillators

In high-viscosity multi-component scintillators such as plastics and organic molecular glasses, process (1) also occurs but with additional energy transfer steps between the π -electron singlet excited states. These processes are dominated by nonradiative (i.e., Förster Resonance Energy Transfer, FRET, see also Chap. 5) but also includes radiative energy transfer via light absorption and reemission. FRET involves the transfer of excited state electronic energy from a donor molecule to an acceptor molecule according to a dipole–dipole coupling mechanism [11]. This process is well-known and proceeds according to the Förster equation:

$$E = \frac{1}{1+(r/R_0)^6} \quad (7.1)$$

with R_0 being the distance between a donor and acceptor molecule at which the energy transfer efficiency is 50%, also known as the Förster distance. Large Förster distances are associated with donor–acceptor pairs that exhibit efficient energy transfer. The Förster distance depends on several factors according to the following equation:

$$R_0^6 = \frac{2.07}{128\pi^5 N_A} \frac{\kappa^2 Q_D}{\eta^4} \int f_D(\lambda) \varepsilon_A(\lambda) \lambda^4 d\lambda \quad (7.2)$$

where Q_D is the fluorescence quantum yield of the donor in the absence of the acceptor, κ^2 is the dipole orientation factor, η is the refractive index of the medium, N_A is the Avogadro constant, and J is the spectral overlap integral. κ is given by:

$$\kappa = \hat{\mu}_A \cdot \hat{\mu}_B - 3(\hat{\mu}_D \cdot \hat{R})(\hat{\mu}_A \cdot \hat{R}) \quad (7.3)$$

where $\hat{\mu}_D$ is the normalized transition dipole moment of each fluorophore, and \hat{R} denotes the normalized inter-fluorophore displacement. Typically, κ^2 is assumed to be $\frac{2}{3}$ for systems where the donor and acceptor molecules are freely rotating and considered to be isotropically oriented during the excited state lifetime. This is true in matrices that comprise liquids, amorphous plastics, and molecular organic glasses. Returning to Eq. (7.2) above, the integral $\int f_D(\lambda) \varepsilon_A(\lambda) \lambda^4 d\lambda$ is associated with the spectral overlap integral, J according to:

$$J = \frac{\int f_D(\lambda) \varepsilon_A(\lambda) \lambda^4 d\lambda}{\int f_D(\lambda) d\lambda} = \int \bar{f}_D(\lambda) \varepsilon_A(\lambda) \lambda^4 d\lambda \quad (7.4)$$

where f_D is the donor emission spectrum, \bar{f}_D is the donor emission spectrum normalized to an area of 1, and ε_A is the acceptor molar extinction coefficient.

The FRET efficiency not only governs the steady-state emission characteristics, but also directly controls the emission timing properties according to Eq. (7.5)

$$k_{ET} = \left(\frac{R_0}{r}\right)^6 \frac{1}{\tau_D} \quad (7.5)$$

where k_{ET} is the rate of energy transfer from the donor to acceptor and τ_D is the fluorescence lifetime of the donor. The donor–acceptor energy transfer rate (k_{ET}) controls the fluorescence/scintillation rise-time (τ_{rise}), whereas the acceptor decay time (τ_A) controls the fluorescence/scintillation decay time (τ_{em}).

With reference to the processes and equations discussed above, it is possible to come up with a set of generalized design rules that guide the development of high light-yield multi-component organic scintillators (Table 7.1). To this end, Berlman tabulated the photophysical characteristics of a large number of donor and acceptor

Table 7.1 Summary of relevant photophysical parameters contributing to the design of high light-yield multi-component organic scintillators

Parameter symbol	Parameter description	Design criteria	Rationale	Strategy
E	FRET Energy Transfer Efficiency	Maximize	Improve scintillation light yield	(See parameter entries below)
R_0	Förster distance	Maximize	Increase E	(See parameter entries below)
Q_D	Donor quantum yield	Maximize	Increase R_0 and E	Select highly fluorescent host matrix
ϵ_A	Acceptor oscillator strength	Maximize	Increase Spectral Overlap	Ensure large acceptor oscillator strength
$\int Q_D(\lambda)\epsilon_A(\lambda)\lambda^4 d\lambda$	Spectral overlap	Maximize	Increase R_0 and E	Match donor emission and acceptor absorption spectra
κ^2	Orientation factor	Maximize	Increase R_0 and E	Impose isotropic molecular orientations
$\int f_A(\lambda)\epsilon_A(\lambda)\lambda^4 d\lambda$	Self-absorption	Minimize	Long optical attenuation length	Maximize acceptor Stokes' shift
τ_D	Donor scintillation decay time	Minimize	Increase R_0 , fast rise-time	Select donor that has short emission lifetime
τ_A	Acceptor scintillation decay time	Minimize	Fast decay time	Select acceptor that has short emission lifetime
Q_A	Acceptor quantum yield	Maximize	Increase scintillation light yield	Select highly fluorescent acceptor(s) (i.e. primary and secondary fluorophores)

molecules, including the Förster Distance (R_0), fluorescence lifetime, and quantum yield [12, 13]. Adadurov et al. performed simulations using these parameters in the above equations to optimize the composition of a plastic scintillator based on polystyrene and 1,5-bis(2-(5-phenyloxazolyl)-benzene (POPOP) [14]. The results showed the effect of wavelength shifter concentration on the light yield and optical attenuation length, as shown in Fig. 7.1.

One notable characteristic of plastic scintillators is that their light yields are lower than the brightest molecular crystals and liquid scintillators by ~50% and ~20%,

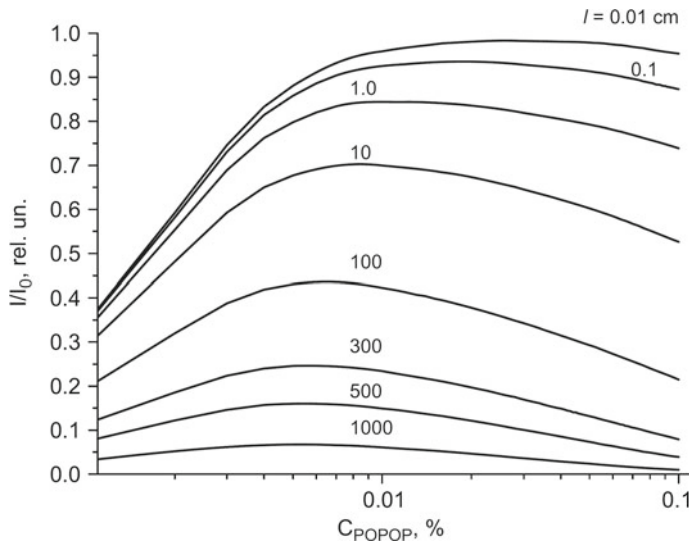


Fig. 7.1 Relative intensity of luminescence for different POPOP concentrations and optical path lengths (l) in polystyrene plastic scintillator (reproduced from [14] with permission from Elsevier)

respectively [15, 16]. This is due in large part to the finite donor quantum yields and maximum achievable FRET efficiency of existing polymer hosts reported to date. Liquid scintillators also possess this limitation but are generally more efficient than plastics due to an enhancement in the energy transfer efficiency via molecular diffusion.

7.1.2.3 Process (1): Direct Excitation in Liquid Scintillators

In low-viscosity multi-component materials such as liquid scintillators, the mechanisms of energy transfer in liquids are similar to that of high-viscosity media such as plastics and glasses but are also influenced by translational diffusion (D). The solvent viscosity controls the diffusion rate to establish a displacement distance (R_D) that occurs on the FRET timescale. The donor–acceptor energy transfer efficiency in liquid solutions thus depends on the relationship between the Förster radius (R_0) and the displacement distance (R_D). In other words, shorter R_0 distances may be overcome by fast diffusion via low viscosity/large R_D , and vice versa. This relationship has been demonstrated in prior work, whereby the solvent viscosity was shown to modulate the efficiency of fluorescence energy transfer [17]. This effect was revealed by studying different donor–acceptor pairs that were subject to cooling or solvent substitution. A summary of the parameters and design considerations controlling the efficiency of donor–acceptor energy transfer in liquids is provided in Table 7.2.

Table 7.2 Summary of photophysical parameters contributing to the design of high light-yield liquid scintillators. Liquid scintillators are generally categorized as multi-component and low-viscosity materials

Parameter symbol	Parameter description	Design criteria	Rationale	Strategy
η	Solvent Viscosity	Minimize	Increase diffusion rate (D) and displacement (R_D)	Select low-viscosity liquid scintillator matrix
D	Diffusion constant	Maximize	Increase R_D	Select low-viscosity liquid scintillator matrix
R_D	Displacement distance	Maximize	Relaxes requirement of large R_0 value	Select low-viscosity liquid scintillator matrix
FRET	Förster Resonance Energy Transfer	Maximize	Increase efficiency of radiation emission on diffusion timescale	Increase Förster Distance (R_0) (See Table 7.1)

7.1.2.4 Summary of Process (1) Effects

The impact of process (1) to the above material categories may be summarized by the following generalizations:

1. Organic single crystals exhibit the highest scintillation light yields due to high fluorescence quantum yields.
2. Multi-component scintillators provide superior optical attenuation lengths due to reduced absorption/emission spectral overlap, as enabled by FRET.

No crystalline, liquid, or plastic scintillator provides an ideal solution towards high light-yield and long attenuation length scintillators, due to the requirements for direct π -excitation (process (1)). Consequently, a key objective constitutes a multi-component scintillator that has high donor fluorescence quantum yield and efficient donor–acceptor FRET.

We may now turn our attention to process (2) to complete the description of light-generation pathways in organic scintillators.

7.1.3 Process (2): Overview of Direct Ionization and Recombination of π -states

While the majority of scintillation light output (e.g., ~80%) occurs due to excitation into excited π -electron singlet states via process (1), ionization of π -electrons via process (2) contributes to an important part of the light pulse that is essential for applications that require particle discrimination. Following ionization of π -electrons, ion recombination leads to the population of both singlet and triplet excited states with a $1/4$ and $3/4$ ratio, respectively. The excited singlets produced by process (2) decay in accordance with the fluorescence decay time and add to the prompt scintillation response produced by process (1). The triplet excited states formally cannot decay to the ground state due to spin-parity selection rules and may either thermalize or annihilate with another excited triplet if the excitation density is sufficiently high. The latter process is called Triplet-Triplet Annihilation (TTA). TTA accounts for the delayed part of the scintillation response and enables pulse-shape discrimination (PSD) techniques to be used.

The efficiency of TTA depends on the mobility and lifetime of the triplet excited states, which correlates closely with the molecular structure and electronic properties of the scintillator. TTA occurs via Dexter energy transfer via triplet wavefunction overlap and is described by Eq. (7.6).

$$k_{ET} \propto J \exp\left[\frac{-2r}{L}\right] \quad (7.6)$$

In this equation, k_{ET} is the Dexter energy transfer rate, J is the spectral overlap integral for triplet states, r is the separation between donor and acceptor, and L is the sum of the Van der Waals radii of the donor and acceptor. k_{ET} determines the efficiency at which TTA can occur, which in turn controls the quantity and kinetics of the delayed scintillation response. Due to the exponential distance dependence in Eq. (7.6), Dexter energy transfer/TTA is a short-range process that is operative at distances of less than 1 nm. This contrasts with the dipolar FRET mechanism that occurs at longer distances of 1–10 nm. Consequently, TTA is more sensitively impacted by the presence of impurities, disorder, or other defects. The relative impact of these considerations will be discussed in the following sections for different classes of organic scintillators.

7.1.3.1 Process (2): Direct Ionization and Recombination in Molecular Crystals

There are several considerations that impact the probability for Dexter energy transfer via TTA in organic molecular crystals. The most fundamental considerations are the electronic structure of the organic compound constituting the crystal. A wide variation in PSD capability was reported in work by Galunov et al. and Hull et al. for a diversity of organic crystals [18, 19]. However, there are additional factors that

impact the TTA efficiency in crystals of a particular compound. These considerations principally include the compositional purity, degree of crystallographic order, and symmetry effects. These properties also affect the electronic properties of the system, namely the presence of triplet trap levels that reside between the HOMO and LUMO of the pure host material.

Purity

Efforts to improve the PSD capabilities of organic crystals have generally focused on decreasing the triplet exciton trap density via extensive purification and higher structural perfection. Arulchakkavarthi studied the scintillation properties of melt-grown *trans*-stilbene crystals of varying degrees of structural order, as assessed by X-ray rocking curve analysis [20]. This study found that an increased concentration of low-angle grain boundary defects decreased the amount of delayed fluorescence and consequently led to poorer PSD. In subsequent work, solution-grown *trans*-stilbene crystals were found to possess better pulse-shape discrimination properties than melt-grown *trans*-stilbene, owing to a higher degree of structural perfection and more efficient TTA [21]. Solution crystal growth methods impose fundamental limitations on the growth rate and mechanical toughness of the crystal (see Sect. 7.1.4.1), which, in turn, influences the maximum practical crystal size, production yield, and cost.

Mixed Crystals

An exception to the ‘purer is better’ approach outlined above comprises co-crystallization of two structurally similar molecules that possess different electronic properties. For example, Zaitseva et al. investigated the scintillation properties of mixed single crystals [10]. 1,2-Diphenylacetylene (‘DPAC’) was co-crystallized with *trans*-stilbene (‘stilbene’) at concentrations of 2–55%. It was discovered that TTA was nearly completely suppressed for a 98:2 crystal of DPAC:stilbene, as might be expected due to the presence of a sufficient trap density to quench the triplet excitons required for TTA. However, TTA was restored in a 63:37 DPAC:stilbene co-crystal such that the PSD capabilities of the mixed crystal exceeded either of the pure constituent crystals. This surprising result was attributed to a sufficient concentration of deep traps in the crystal to facilitate efficient trap-to-trap hopping above the triplet percolation threshold. This result is consistent with earlier work by Robinson, who reported that TTA is maximized in systems that contain a low concentration of shallow traps or a high concentration of deep traps [22]. The distinction between shallow and deep in this context refers to the trap depth with respect to the LUMO and the relative thermal energy of the radiationless transition (kT).

Crystallographic Symmetry

Another strategy that has been employed to increase the efficiency of TTA involves the molecular design of scintillators that crystallize in high-symmetry space groups. As stated previously, TTA is dependent upon the concentration, lifetime, and mobility of triplet excitons. The triplet concentration is established by the ionization event itself, whereas the triplet lifetime is controlled by the electronic properties of the triplet state and purity of the crystal. The remaining factor, triplet mobility, is a second

rank tensor property that is intrinsically symmetry dependent [23]. Higher-symmetry systems exhibit greater triplet mobility relative to their low-symmetry analogs, as previously reported for a series of naphthalene- and salicylate-based organic crystals [24]. In that work, efficient TTA and excellent PSD were observed in crystals of higher symmetry analogs of monoclinic compounds that do not themselves exhibit PSD. Density-functional theory calculations revealed that the intermolecular triplet-excitation energy transfer interactions in a trigonal naphthalene crystal were more than twelve times larger than its lower-symmetry monoclinic analog.

Other studies confirm the role of symmetry on the magnitude and angular dependence of the transport mobility. Vehoff et al. studied the charge-transporting properties of crystallographic polymorphs of benzo[1,2-*b*:4,5-*b'*]bis[*b*]benzothiophene, whereby an order of magnitude larger charge transport mobility was observed for the 3-dimensional versus 1-dimensional molecular network [25]. Separately, the effect of crystallographic symmetry upon the scintillation light yield and PSD anisotropy was evaluated [26, 27]. Angular-dependent neutron measurements on monoclinic *trans*-stilbene crystals revealed uncorrelated angular dependencies for the light output and PSD performance. The extent of variation was ~20% in light output and ~10% in PSD from respective minimum to maximum (Fig. 7.2) [26, 27].

Another property related to symmetry and triplet transport is the percolation threshold. This threshold is a mathematical property that describes the concentration of a dopant or impurity at which an infinite cluster appears for the first time in an infinite lattice. A visual example of the percolation threshold is provided for a 2D square lattice in Fig. 7.3. In this figure, the percolation threshold corresponds to the site occupancy at which connectivity throughout the system is achieved. This concentration is $X \geq 0.6$ for a 2D square lattice. Table 7.3 provides the percolation thresholds for different crystal lattice types, where X refers to the dopant concentrations at which percolation transport is enabled [28]. From these data, it is clear that

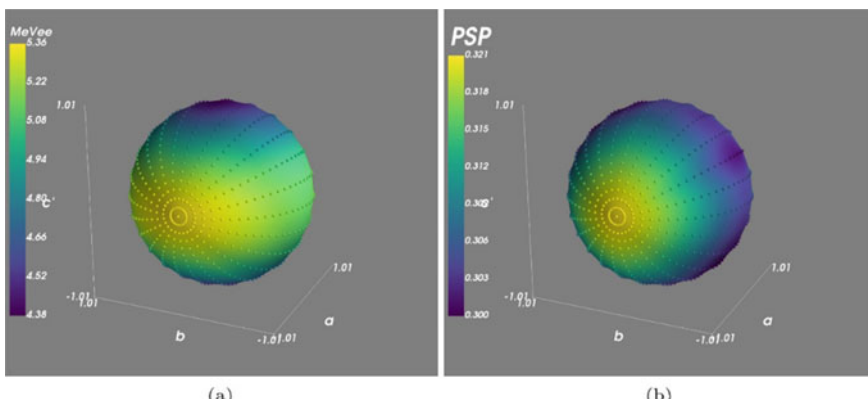


Fig. 7.2 Anisotropy of **a** light output and **b** pulse shape parameter for 10 MeV recoil protons plotted relative to the crystal axes of *trans*-stilbene (reproduced from [26] with permission from Elsevier)

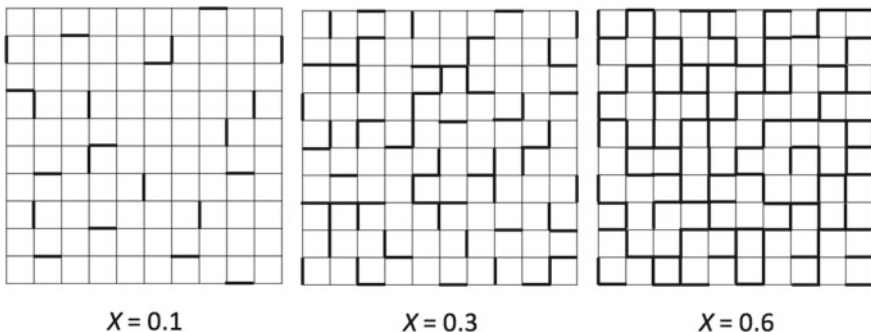


Fig. 7.3 Percolation in a 2D square lattice with occupation probabilities of $X = 0.1$, 0.3 , and 0.6 , respectively. Percolation occurs through the lattice at $X \geq 0.6$ (reproduced from [29] with permission from Elsevier)

Table 7.3 Percolation threshold values for different crystal lattice types [28]

Dimension	Lattice type	Site threshold value (X)
2	Triangle	0.500
2	Square	0.593
2	Honeycomb	0.698
3	Face-centered cubic	0.198
3	Body-centered cubic	0.245
3	Simple cubic	0.311
3	Diamond	0.428

percolation thresholds are lowered in high-symmetry structures, which relaxes the minimum crystal purity and structural order requirements that are needed for TTA. The highest symmetry face-centered cubic (fcc) lattice type corresponds to the lowest percolation threshold concentration due to the largest number of spatially degenerate states. Unfortunately, 80% of known organic crystals are triclinic or monoclinic, with less than 0.1% of known organic crystals belonging to cubic space groups.

Considering this limitation, crystal engineering was evaluated as a strategy for high-symmetry organic scintillator crystals [24]. In 2013, Feng and Foster designed three-fold symmetric organic molecules intended to serve as a structure-directing element for the C_3 symmetry element that is present in trigonal, hexagonal, and cubic crystal systems. Fluorescent naphthalene and salicylic acid chromophore groups were attached to a nonluminescent trialkoxyamine core structure, leading to high-symmetry versions of monoclinic naphthalene and salicylic acid crystals. The result was a ‘turning on’ of PSD capabilities through enhanced triplet-excitation energy transfer, as shown in Fig. 7.4. Density-Functional Theory calculations verified a 12-fold increase in triplet-triplet exchange interactions for tris(1-naphthyoxy)triethylamine, when compared to its low-symmetry parent compound naphthalene.

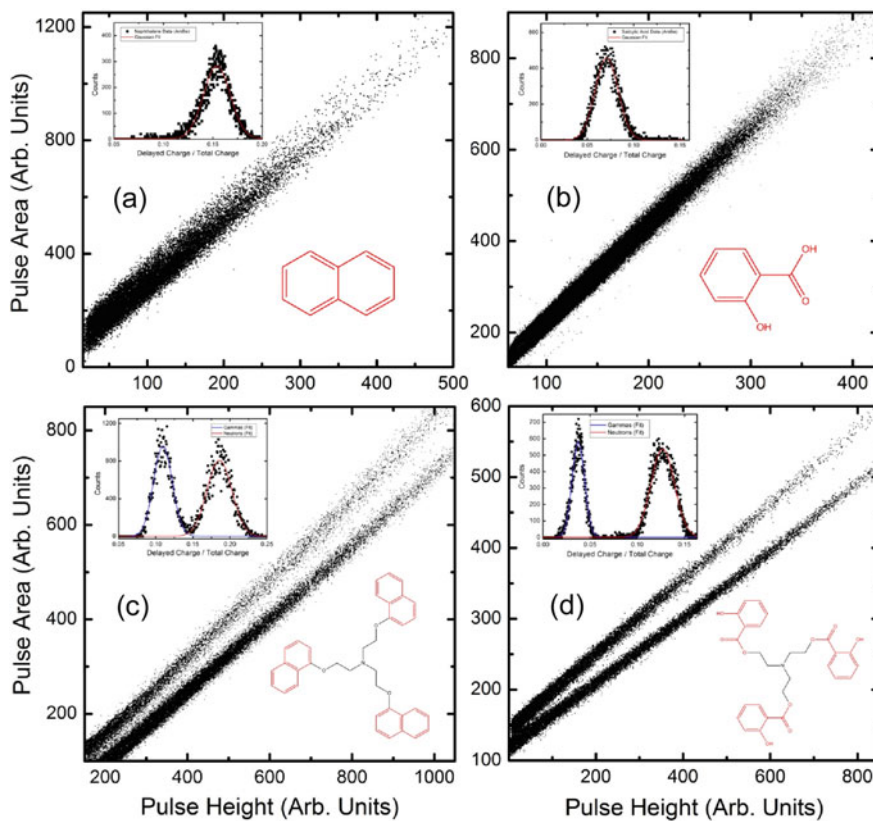


Fig. 7.4 Comparison of the neutron/gamma PSD properties of low-symmetry crystals naphthalene (top left) and salicylic acid (top right) with their high-symmetry trialkoxyamine analogs (bottom left and bottom right), respectively (reproduced from [24] with permission from IEEE)

The three methodologies outlined above (purity, mixed crystals, crystallographic symmetry) represent proven strategies towards improved PSD in crystalline organic scintillators. However, all of these approaches are associated with scientific and practical challenges that generally constrain the use of organic crystals to small-scale applications with scintillator volumes of a few cubic inches or less.

7.1.3.2 Process (2): Direct Ionization and Recombination in Plastic Scintillators

The first plastic scintillators were reported in 1950 by Schorr and Torney and have progressed over the intervening decades to meet the need for low-cost, large-scale, and/or mechanically robust organic scintillators [30 and Chap. 1]. However, even after more than seventy years of development, the scintillation light yield and PSD

properties of commercial plastic scintillators remain inferior to liquid and crystalline scintillators. The reasons for the lower scintillation light yield are related to limitations in process (1), i.e., the FRET energy transfer efficiency. The present section is concerned with a discussion of the reasons for an inefficient process (2) energy conversion that is the root cause of the limited PSD properties of plastics.

Plastic scintillators are based upon an aromatic-containing polymer base in which fluorescent solutes are dissolved (or sometimes covalently linked to the polymer chain). Polystyrene (PS) and poly(vinyltoluene) (PVT) are the most commonly used polymers, due to their high aromatic content, low cost, and favorable thermomechanical properties. These host matrices are linear polymers that are characterized as glassy thermoplastics. Thermoplastic behavior refers to a change in physical properties (e.g., hardness and flow characteristics) above its glass transition temperature without an associated phase change. This behavior is associated with the high molecular weight of PS and PVT used in scintillators, which leads to entanglement of the long polymer chains. Chain entanglement is favorable for promoting good mechanical strength and isotropic optical properties, but it also results in polydispersity with respect to chain length and molecular orientations.

Polydispersity leads to a broad distribution of molecular environments that introduces significant disorder and exciton trapping sites. Chen et al. performed density-functional theory calculations of polystyrene to assess the effect of disorder upon the electronic properties of polystyrene [31]. Those findings revealed that morphological disorder leads to the formation of shallow and deep traps near the band edges of the polymer. This accounts for a significant triplet exciton deactivation pathway due to the intrinsically disordered nature of polystyrene. Another potential triplet trapping pathway comprises excimer formation in PS and/or PVT. Excimers are excited state dimers that form between identical aromatic molecules due to $\pi-\pi$ orbital overlap. Polystyrene is known to exhibit monomer as well as excimer emission depending on the polymerization method and thermal history [32–34]. Excimer formation and TTA have been shown to be competitive in aromatic materials since both pathways serve to depopulate triplet excited states [35–38]. As a result, conventional plastic scintillators based on linear PS and PVT exhibit minimal delayed fluorescence due to TTA and are not capable of any significant PSD.

PSD Plastics

In 1960, Brooks overcame the constraints of triplet trapping in plastic scintillators by incorporating higher concentrations than usual of naphthalene or 4-isopropylbiphenyl in PVT [39]. This behavior has been explained by a similar mechanism as described for mixed organic crystals, namely the introduction of dye molecules to facilitate TTA via trap-to-trap hopping transport [10]. In light of this ground-breaking result, it is surprising that no subsequent work was published on PSD plastics for a period of more than fifty years. This may be due to the limited stability of dissolved small molecules such as naphthalene and 4-isopropylbiphenyl in PVT. In 2012, Zaitseva et al. reported efficient PSD in PVT plastic scintillators that were loaded with 2,5-diphenyloxazole (PPO) at concentrations of up to 30 wt% [40]. The best PSD performance was comparable to EJ-301 liquid and was achieved

for the highest attainable PPO loading of 30 wt%. Initial results indicated that PPO was less susceptible to recrystallization in PVT than other studied molecules such as naphthalene, although later work showed that PPO recrystallization could still occur under ambient conditions [39, 41]. Recrystallization occurred due to the high molecular mobility of PPO in the plasticized PVT matrix, as reflected by the low glass transition temperatures and soft/rubber-like physical characteristics at room temperature [42]. Cross-linking or the co-polymerization of monomeric PPO compounds in PVT were found to be effective in improving the physical characteristics and suppressing PPO recrystallization, although both of these strategies have practical implications for cost, production throughput/yield, and long-term stability [43, 44].

Subsequent work investigated highly soluble small-molecule alternatives to PPO [45], including functionalized *p*-terphenyl and fluorene derivatives [46]. However, results to date show that PPO loading yields the best PSD capabilities [41]. Grodzicka-Kobylka et al. [47] and Sénoville et al. [48] both compared the PSD and light yields of commercial PSD plastic scintillators (Eljen Technology EJ-299-33(G), EJ-299-34(G), and their replacement EJ-276) against EJ-301 liquid scintillator. The results reveal light yield and neutron/gamma PSD discrimination properties that lag behind EJ-301 across the measured energy range. These limitations provide motivation for continued scintillator development efforts.

7.1.3.3 Process (2): Direct Ionization and Recombination in Liquid Scintillators

The mechanism for TTA in liquid scintillators is different from the solid-state materials discussed above in that it involves fast molecular diffusion. Diffusion enables the minimum primary fluorophore concentration in liquids to be low, on the order of 2 wt% for typical scintillation mixtures based on aromatic liquids such as 1,2,4-trimethylbenzene (pseudocumene). This primary fluorophore concentration is roughly an order of magnitude less than in plastic scintillators. At this concentration, the triplet excited state lifetimes and molecular diffusion rate are large enough to facilitate efficient bimolecular recombination via TTA. However, the diffusion rate is inversely proportional to the viscosity and molecular size according to the Stokes–Einstein given in Eq. (7.7),

$$D = \frac{k_B T}{6\pi r\eta} \quad (7.7)$$

where D is the diffusion coefficient, k_B is the Boltzmann constant, r is the radius of a moving particle, and η is the solvent viscosity. It is clear from this relationship that TTA cannot be enhanced by fast diffusion in high-viscosity solid-state scintillator matrices as it is for liquids. Another property of liquid scintillators that reflects the role of fast diffusion towards TTA pertains to the effect of dissolved oxygen. Liquid scintillators must be rigorously deoxygenated since the paramagnetic nature of O_2 quenches triplet excited states. The rate of quenching is competitive with TTA and

results in the loss of PSD capabilities for solutions exposed to oxygen from the atmosphere. Liquids thus possess strict packaging requirements to prevent oxygen ingress and/or solvent egress.

Based on the above considerations for crystals, plastics, and liquids, the ideal organic scintillator matrix is one that has a high fluorescence quantum yield in the ultraviolet range, is molecularly monodisperse, packs isotropically, and is high viscosity/solid-state. These attributes refer specifically to the photophysical and energy transfer properties. We may now turn to a discussion of the physical and mechanical properties of different organic scintillators.

7.1.4 Physical and Mechanical Properties of Different Classes of Organic Scintillators

7.1.4.1 Crystallographic Structure Effects in Molecular Crystals

Virtually all known examples of crystalline organic scintillators crystallize in monoclinic space groups in a herringbone or double herringbone configuration. This commonality supports systematic comparison studies but imposes restrictions on properties that are symmetry-dependent. Second-rank tensor properties are intrinsically symmetry-dependent and include mobility, thermal conductivity, and thermal expansion coefficient, among others. Indeed, the TTA mobility was discussed in the preceding section for low-symmetry versus high-symmetry versions of organic crystals [24]. Stress and strain response are also second-rank tensors, which relate to physical properties such as hardness and fracture toughness.

Prior work has established the relationship between the solid-state packing and the mechanical properties of molecular crystals [49]. The core design requirement for optical materials such as scintillators is that the applied stress (force/unit area) must not exceed the strength of the crystals; otherwise, it leads to deformation or fracture failure. Most organic crystals, including scintillators such as anthracene and *trans*-stilbene, exhibit brittle behavior. This is characterized by failure due to fracture rather than by plastic deformation. In anthracene and *trans*-stilbene, fracture preferentially occurs along the basal crystallographic cleavage plane in response to thermal or mechanical stresses that exceed the crystal's yield strength. One mitigation to this failure mode involves enhanced fracture toughness via plastic flow. This concept was first theorized by Tresca, in 1864, and later developed into a classical theory by Prager and Hill. Their work indicates that plastic flow occurs in molecular crystals via the movement of edge dislocations and grain boundaries [50–52]. Indeed, high dislocation densities in metals and organic crystals have been shown to increase the ductility and fracture toughness of the crystal [53, 54]. Conventionally-grown Bridgman *trans*-stilbene crystals have been shown to have a high density of edge dislocations and low-angle grain boundaries, which toughens the crystal relative to a more defect-free specimen grown via the selective-self seeding vertical Bridgman technique (SSVBT)

or solution-growth methods. Unfortunately, the presence of dislocations and low-angle grain boundary defects have been shown to negatively impact the scintillation properties due to the disruption of intermolecular dipolar and electronic exchange interactions [20, 55]. This observation reveals a trade-off between the scintillation performance of *trans*-stilbene single crystals and their susceptibility to failure due to fracture. To demonstrate this point, we may consider solution-grown *trans*-stilbene. Crystals grown by this method have been shown to provide the highest scintillation performance, owing to their high degree of compositional and structural uniformity [21]. However, solution-grown *trans*-stilbene crystals are susceptible to mechanical and thermal shocks, as evidenced by a maximum manufacturer-recommended thermal gradient of no more than 10 °C/h and 5 °C/hour for 1" × 1" and 2" × 2" cylinders, respectively [56].

7.1.4.2 Physical Properties of Plastic Scintillators

Three of the key physical limitations of organic crystals can be summarized as anisotropic optical/mechanical properties, brittle characteristics, and difficulty in scaling to large sizes. These issues are essentially overcome in plastic scintillators due to a disordered arrangement of covalently-bonded polymer chains. The random tangling of polymer chains used in plastic scintillators results in amorphous character with no preferred molecular orientations. This attribute leads to an isotropic refractive index, which is desirable to achieve uniform detector response and light collection from bulk scintillator elements. The combination of inter-chain entanglement and the covalent nature of polymer bonds also leads to mechanically robust materials. This is reflected in glass transition temperatures that are significantly above room temperature (e.g., ~95 °C for PVT) and mechanical properties that are suitable for large-scale or structural applications [57]. Furthermore, commercial plastic scintillators are produced using thermally-induced radical polymerization of liquid monomer, which is amenable to large-scale production and the incorporation of functional additives such as primary fluorophores and wavelength shifters (see Chap. 1 for more information on the preparation of plastic scintillators).

However, the use of polymers introduces a different set of limitations not observed in crystalline or liquid materials. For example, chain entanglement introduces microscopic void volumes due to packing inefficiencies. This has consequences for applications that are subject to atmospheric moisture and/or gaseous radioactive isotopes. In outdoor deployments such as in radiation portal monitors, water vapor diffuses into plastic scintillators, which leads to temporary and permanent ‘fogging’ following changes in the ambient temperature [58–61]. Similarly, radioactive noble gases produced by nuclear explosions and subject to monitoring within the Comprehensive Nuclear-Test-Ban Treaty (CTBT), may diffuse into plastic scintillators. This leads to an undesired ‘memory effect’ that comprises a rising background level over time [62, 63].

Triplet trapping and the loss of PSD capabilities is another issue with plastic scintillators, as discussed above. This constraint may be mitigated by adding high

concentrations of a primary dye, although this plasticizes the matrix and results in soft/‘rubber-like’ properties. For example, incorporating PPO at concentrations of 15–30 wt% in PVT leads to mechanically deformable materials that possess glass transition temperatures that are near or below room temperature [42, 64]. Lim et al. reported an 88% reduction in the 25 °C Shore D hardness for PVT-based scintillators loaded with ≥20 wt% of PPO [42]. Cross-linking to produce a thermoset polymer has been effective in increasing the mechanical hardness at high dye concentrations, although cross-linked samples retain low glass transition temperature (T_g) values and high attendant molecular mobility/diffusion of dissolved dye molecules [64, 65]. Diffusion of the dissolved scintillator constituents over time may lead to degradation of the scintillation light yield and PSD properties over time [66].

7.2 Future Opportunities

The preceding sections describe the advantages and limitations of different classes of organic scintillators. Existing organic scintillators are characterized by a complex set of trade-offs that must be weighed against the requirements for each intended application. These factors include practicality versus performance considerations associated with each scintillator type. Consideration of the extensive literature to date reveals several landmarks advances towards bright, fast, and PSD-capable crystalline, liquid, and plastic scintillators while providing multiple pathways towards further improvements. For example, scintillation light yields for the brightest plastic and liquid scintillators lag behind crystalline materials such as *trans*-stilbene and anthracene due in large part to the low fluorescence quantum yield of the host material. Consequently, an ongoing objective is to develop high quantum yield host materials as replacements for PVT polymer and existing aromatic solvents, respectively. Furthermore, analysis of the Förster equation reveals opportunities to increase the host–guest energy transfer efficiency that defines the scintillation yield. These include the donor emission lifetime and donor–acceptor spectral overlap, among others. Another opportunity for future improvements pertains to the efficiency of triplet–triplet exchange interactions via Dexter energy transfer. Currently, the highest-performing PSD-capable plastic scintillators are achieved by loading styrenic polymers with high concentrations of small-molecule fluorophores. The required dopant concentration must exceed the percolation threshold of the matrix, and the bimolecular exchange rate must exceed the rate of triplet trapping due to disorder and defects. Thus, ongoing and future work on improved PSD requires increasing the triplet–triplet annihilation efficiency while decreasing the triplet exciton trapping rate. Strategies to this end may involve a combination of compositional purity, monodispersity of the host matrix constituents, and/or higher phase stability of small-molecule fluorophore additives. Other objectives also involve improving the thermomechanical properties and long-term stability of solid-state organic scintillators such as crystals and plastics. Chapter 8 will describe strategies towards improving all of the aforementioned objectives in the context of the first principles discussed here.

References

- R.C. Sangster, J.W. Irvine Jr., *J. Chem. Phys.* **24**(4), 670 (1956)
- H. Kallmann, *Natur und Technik* **13**, 15 (1947)
- I. Broser, H. Kallmann, *Ann. Phys. (Berlin, Ger.)* **438**(3), 317 (1948)
- P.R. Bell, *Phys. Rev.* **73**(11), 1405 (1948)
- S. Niese, *J. Radioanal. Nucl. Chem.* **241**(3), 499 (1999)
- Y. Kaschuck, B. Esposito, *Nucl. Instr. Methods A* **551**(2–3), 420 (2005)
- T.A. King, R. Voltz, *Proc. R. Soc. London, Ser. A* **289**(1418), 424 (1966)
- G. Laustriat, *Mol. Cryst.* **4**(1–4), 127 (1968)
- J.B. Birks, *J. Phys. B: At., Mol. Opt. Phys.* **1**(5), 946 (1968)
- N. Zaitseva, L. Carman, A. Glenn, R. Hatarik, S. Hamel, M. Faust, B. Schabes, N. Cherepy, S. Payne, *IEEE Trans. Nucl. Sci.* **58**(6), 3411 (2011)
- J.R. Lakowicz, *Principles of Fluorescence Spectroscopy* (Springer, 1999)
- I.B. Berlman, *Handbook of Fluorescence Spectra of Aromatic Molecules* 2nd edn. (Academic Press, Inc., 1971)
- I.B. Berlman, *Energy Transfer Parameters of Aromatic Compounds* (Academic Press, Inc., 1973)
- A.F. Adadurov, P.N. Zhmurin, V.N. Lebedev, V.D. Titskaya, *Nucl. Instr. Methods A* **599**(2–3), 167 (2009)
- Eljen Technology website, <https://eljentechnology.com/products/plastic-scintillators>. Accessed 29 Sept 2020
- Saint-Gobain Crystals website, <https://www.crystals.saint-gobain.com/products/plastic-scintillators>. Accessed 29 Sept 2020
- A. Muratsugu, J. Watanabe, S. Kinoshita, *J. Chem. Phys.* **140**(21), 214508 (2014)
- N.Z. Galunov, I.F. Khromiuk, O.A. Tarasenko, *Nucl. Instr. Methods A* **949**, 162870 (2020)
- G. Hull, N.P. Zaitseva, N.J. Cherepy, J.R. Newby, W. Stoeffl, S.A. Payne, *IEEE Trans. Nucl. Sci.* **56**(3), 899 (2009)
- A. Arulchakkavarthi, N. Balamurugan, R. Kumar, P. Santhanaraghavan, S. Muralithar, T. Nagarajan, P. Ramasamy, *Mater. Lett.* **58**(7–8), 1209 (2004)
- N. Zaitseva, A. Glenn, L. Carman, H.P. Martinez, R. Hatarik, H. Klapper, S. Payne, *Nucl. Instr. Methods A* **789**, 8 (2015)
- G.W. Robinson, *Proc. Natl. Acad. Sci. U. S. A.* **49**(4), 521 (1963)
- N. Karl, in *Organic electronic materials*, vol. 41, ed. by R. Farchioni, G. Grossi. Springer Series in Materials Science (Springer, Berlin Heidelberg, 2001), pp. 283–326
- P.L. Feng, M.E. Foster, *IEEE Trans. Nucl. Sci.* **60**(4), 3142 (2013)
- T. Vehoff, B. Baumeier, A. Troisi, D. Andrienko, *J. Am. Chem. Soc.* **132**(33), 11702 (2010)
- R.A. Weldon Jr., J.M. Mueller, C. Awe, P. Barbeau, S. Hedges, L. Li, M. Mishra, J. Mattingly, *Nucl. Instr. Methods A* **977**, 164178 (2020)
- P. Schuster, E. Brubaker, *Nucl. Instr. Methods A* **859**, 95 (2017)
- F. Duan, J. Guojun, *Introduction to Condensed Matter Physics*, vol. 1 (World Scientific Publishing, 2005) p. 109
- B. Ghanbarian, P. Cheng, *J. Power Sources* **307**, 613 (2016)
- M.G. Schorr, F.L. Torney, *Phys. Rev.* **80**(3), 474 (1950)
- L. Chen, R. Batra, R. Ranganathan, G. Sotzing, Y. Cao, R. Ramprasad, *Chem. Mater.* **30**(21), 7699 (2018)
- T. Nishihara, M. Kaneko, *Makromol. Chem.* **124**(1), 84 (1969)
- M.S. Healy, J.E. Hanson, *J. Appl. Polym. Sci.* **104**(1), 360 (2007)
- P. de Sainte Claire, *J. Phys. Chem. B* **110**(14), 7334 (2006)
- J.B. Birks, *Nature* **214**, 1187 (1967)
- R. Casillas, M. Adam, P.B. Coto, A.R. Waterloo, J. Zirzlmeier, S. Rajagopala Reddy, F. Hampel, R. McDonald, R.R. Tykwiński, M. Thoss, D.M. Guldin, *Adv. Energy Mater.* **9**(2), 1802221 (2019)

37. S. Mutsamwira, E.W. Ainscough, A.C. Partridge, P.J. Derrick, V.V. Filichev, Chem. Eur. J. **22**(30), 10376 (2016)
38. C. Ye, V. Gray, J. Mårtensson, K. Börjesson, J. Am. Chem. Soc. **141**(24), 9578 (2019)
39. F.D. Brooks, R.W. Pringle, B.L. Funt, I.R.E. Trans, Nucl. Sci. **7**(2–3), 35 (1960)
40. N. Zaitseva, B.L. Rupert, I. Pawelczak, A. Glenn, H.P. Martinez, L. Carman, M. Faust, N. Cherepy, S. Payne, Nucl. Instr. Methods A **668**, 88 (2012)
41. N.P. Zaitseva, A.M. Glenn, A.N. Mabe, M.L. Carman, C.R. Hurlbut, J.W. Inman, S.A. Payne, Nucl. Instr. Methods A **889**, 97 (2018)
42. A. Lim, G. Hernandez, J. Latta, H.A. Yemam, W. Senevirathna, U. Greife, A. Sellinger, A.C.S. Appl. Polym. Mater. **1**(6), 1420 (2019)
43. Y. Zhu, Y. Chen, L. Zhang, W. Li, B. Huang, J. Wu, Chem. Eng. Res. Des. **104**, 32 (2015)
44. K. Jin, L. Li, J.M. Torkelson, Polymer **115**, 197 (2017)
45. G.H.V. Bertrand, M. Hamel, F. Sguerra, Chem. Eur. J. **20**(48), 15660 (2014)
46. H.A. Yemam, A. Mahl, J.S. Tinkham, J.T. Koubek, U. Greife, A. Sellinger, Chem. Eur. J. **23**(37), 8921 (2017)
47. M. Grodzicka-Kobylka, T. Szczesniak, M. Moszynski, K. Brylew, L. Swiderski, J.J. Valiente-Dobón, P. Schotanus, K. Grodzicki, H. Trzaskowska, J. Instrum. **15**, P03030 (2020)
48. M. Sénoville, F. Delaunay, M. Pärlog, N.L. Achouri, N.A. Orr, Nucl. Instr. Methods A **971**, 164080 (2020)
49. C. Malgrange, C. Ricolleau, M. Schlenker, *Symmetry and Physical Properties of Crystals* (Springer, Dordrecht, 2014).
50. H.-E. Tresca, C.R. Acad. Sci. Paris **59**, 754 (1864)
51. W. Prager, *Introduction to the Mechanics of Continua* (Dover Publications Inc., Mineola, New York, 1961).
52. R. Hill, *The Mathematical Theory of Plasticity* (Clarendon Press, 1950)
53. D.J. Luscher, F.L. Addessio, M.J. Cawkwell, K.J. Ramos, J. Mech. Phys. Solids **98**, 63 (2017)
54. K.M. Davoudi, J.J. Vlassak, J. Appl. Phys. **123**(8), 085302 (2018)
55. M. Li, W. Cui, M.S. Dresselhaus, G. Chen, New J. Phys. **19**, 013033 (2017)
56. Inrad Optics website, <https://inradoptics.com/>. Accessed 29 Sept 2020
57. C. Redding, A. Hackett, M. Laubach, R. Feng, P. Feng, C. Hurlbut, P. Liaw, J.P. Hayward, Nucl. Instr. Methods A **954**, 161448 (2020)
58. R.J. Cameron, B.G. Fritz, C. Hurlbut, R.T. Kouzes, A. Ramey, R. Smola, IEEE Trans. Nucl. Sci. **62**(1), 368 (2015)
59. P.B. Rose Jr., A. Okowita, M.J. Lance, E. Sword, IEEE Trans. Nucl. Sci. **67**(7), 1765 (2020)
60. M. Loyd, M. Pianassola, C. Hurlbut, K. Shipp, L. Sideropoulos, K. Weston, M. Koschan, C.L. Melcher, M. Zhuravleva, Nucl. Instr. Methods A **922**, 202 (2019)
61. N.R. Myllenbeck, S. Payne, P.L. Feng, Nucl. Instr. Methods A **954**, 161782 (2020)
62. K. Takasaki, H. Kobayashi, H. Suzuki, S. Ushigome, J. Nucl. Sci. Technol. **47**(3), 255 (2010)
63. L. Bläckberg, A. Fay, I. Jögi, S. Biegalski, M. Boman, K. Elmgren, T. Fritioff, A. Johansson, L. Mårtensson, F. Nielsen, A. Ringbom, M. Rooth, H. Sjöstrand, M. Klintenberg, Nucl. Instr. Methods A **645**(1), 84 (2011)
64. A. Mahl, A. Lim, J. Latta, H.A. Yemam, U. Greife, A. Sellinger, Nucl. Instr. Methods A **884**, 113 (2018)
65. J.S. Vrentas, C.M. Vrentas, J. Appl. Polym. Sci. **42**, 1931 (1991)
66. T.A. Laplace, B.L. Goldblum, J.E. Bevins, D.L. Bleuel, E. Bourret, J.A. Brown, E.J. Callaghan, J.S. Carlson, P.L. Feng, G. Gabella, K.P. Harrig, J.J. Manfredi, C. Moore, F. Moretti, M. Shinner, A. Sweet, Z.W. Sweger, J. Instrum. **15**, 11020 (2020)



Dr. Patrick Feng is a Principal Member of the Technical Staff at Sandia National Laboratories in Livermore, CA. His research is concerned with the development of novel organic-based scintillator materials. Dr. Feng's relevant contributions include the elucidation of fundamental scintillation phenomena in Metal-Organic Frameworks (MOFs), discovery of triplet-harvesting plastic scintillators for spectrally-resolved particle discrimination, development of metal-loaded plastic scintillators for gamma-ray spectroscopy, aging-resistant plastic scintillators, and melt-cast organic glasses for neutron/gamma discrimination. He has nineteen years of synthetic chemistry experience that includes eleven years of organic scintillator development.

Chapter 8

Organic Glass Scintillators



Patrick L. Feng, Nicholas R. Myllenbeck, and Joseph S. Carlson

Abstract Organic Glass Scintillators (OGSs) have recently been reported as an exciting class of materials that exhibit noteworthy physical and scintillation characteristics. OGSs are based on a stable, amorphous, small-molecule host matrix that contains performance-enhancing additives such as wavelength shifters. This configuration provides a unique set of properties that combines attributes of single crystals, plastic scintillators, and liquid scintillators, respectively. Noteworthy OGS properties include scalable production via melt-casting, scintillation light yields and pulse-shape discrimination properties that are comparable to crystalline *trans*-stilbene, and isotropic optical and mechanical properties that are reminiscent of plastic scintillators. This chapter will describe OGS as a new class of organic scintillators and will review the molecular design considerations that can be utilized to meet the needs of existing and future radiation detection applications. These topics will be presented in the context of the energy transfer pathways and structure–property relationships discussed in detail in the preceding chapter (Chap. 7).

8.1 Introduction to Organic Glass Scintillators

The structure of this chapter begins with a general discussion of amorphous materials and their properties before introducing molecular glasses and OGS. The intent is to highlight the specific attributes of OGS that are amenable to high-scintillation performance. Among these are the photophysical parameters discussed in Chap. 7 that give rise to efficient FRET and intermolecular Dexter energy transfer, respectively. Following a discussion of the performance characteristics of OGS, specific attention will be paid to properties that are of practical interest. Among these are the mechanical properties, long-term stability, and cost/size/manufacturability. The text has thus been organized into the following sections:

- Glassy state of matter;

P. L. Feng (✉) · N. R. Myllenbeck · J. S. Carlson
Sandia National Laboratories, Livermore, CA, USA
e-mail: plfeng@sandia.gov

- Differentiating characteristics of molecular glasses;
- Design strategies for stable molecular glasses;
- Fluorescent molecular glasses as OGS;
- OGS: case studies;
- Organic glass thermal and mechanical properties;
- Properties of OGS/polymer blends;
- OGS fabrication methods;
- Long-term stability and environmental aging of OGS;
- Compatibility of OGS with multi-functional additives.

8.2 Glassy State of Matter

Glasses are nonequilibrium amorphous solids that span a wide range of material classes. Among these are inorganic glasses such as silicate-based oxides (e.g. window glass), polymeric glasses such as PMMA and polystyrene, and metallic glasses. Despite this immense diversity of properties, the unifying characteristic is that all glasses possess a disordered arrangement of the constituent atoms or molecules. A few examples of the importance of glasses in modern society include:

- Glass optical fibers serve as the backbone of modern communication networks due to their isotropic optical properties that are free from grain boundaries. This enables signal transmission over 100 km without amplification.
- Metallic glass alloys are used in applications that require exceptional strength, hardness, resilience, and resistance to wear and corrosion. Metallic glasses are used in critical medical equipment, including surgical pins and stents.
- Glassy polymers can be cross-linked to provide exceptional toughness while maintaining optical transparency. An example is polycarbonate, which is used for eyeglass/safety lenses and is a key component of bulletproof ‘glass’.

Glasses are formed under specific environmental conditions. When a liquid is cooled below its melting temperature, it can crystallize or become supercooled, at which point it can form a disordered glassy solid. This is depicted in Fig. 8.1, where the molar entropy is plotted as a function of temperature. In this plot, the glass transition temperature (T_g) describes a second-order phase transition in which the entropy and free volume are discontinuous from the slope of the supercooled liquid phase. The glass transition is dependent on the history of the material and the rate of temperature change. The slope of the glass phase in Fig. 8.1 may vary depending on the cooling rate and method. Glasses are trapped in local minima on the potential energy landscape, with lower energy states being achieved through molecular rearrangements (Fig. 8.2). Thus, this is a dynamic phenomenon, extending over a range of temperatures and formation conditions. Annealing the supercooled liquid over time allows for structural relaxation of constituent atoms/molecules and a progressive shift to a more stable (lower energy and entropy) state. However, structural relaxation of molecules in the glass can be competitive with recrystallization, which

Fig. 8.1 Molar entropy of *o*-terphenyl in different physical states. The estimated entropy of a liquid-cooled glass is shown in red, whereas the dashed line is an extrapolation of the supercooled liquid to a lower temperature (Reproduced from [1] with permission from the American Institute of Physics)

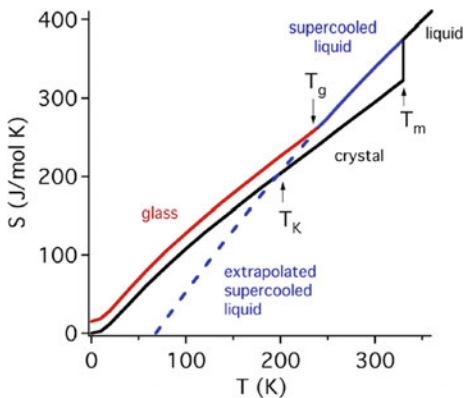
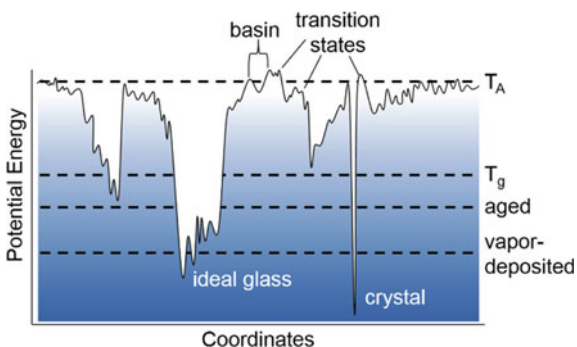


Fig. 8.2 Schematic representation of the potential energy landscape of a glass-forming system (Reproduced from [1] with permission from the American Institute of Physics)



establishes a minimum cooling rate for each glass system formed from the melt. In other words, slow cooling is required to form a high-density and entropically stable glass, although too slow of a cooling rate may lead to the conversion of the glass back into the crystalline phase.

Glass formation via physical vapor deposition can bypass the kinetic restrictions of liquid cooling and can produce exceptionally stable glasses that exhibit unusually high densities. For example, the entropy curves for a vapor-deposited glass of 1,3,5-tri(2-naphthyl)benzene show that vapor deposition leads to a higher glass transition temperature and a lower entropy than ordinary or aged liquid-cooled glasses [2]. Based on aging and diffusion experiments, the authors concluded that it would take more than 40 years of thermal aging for a cast film to reach the packing density and glassy state stability of vapor-deposited 1,3,5-tri(2-naphthyl)benzene. This example reflects the important roles of thermal history and the formation method upon the physical properties of glasses.

As a liquid passes through T_g during cooling, its viscosity increases by as much as 17 orders of magnitude, but the static structural parameters (e.g. the static pressure factor) remain almost unchanged [3]. This leads to behavior that retains traits of both solid and liquid phases. The glass has a long-range structure close to the supercooled

fluid phase, while displaying solid-like mechanical properties on the timescale of practical observation. This ‘practical timescale’ may be defined differently, e.g. 100 s in isothermal dielectric spectroscopy measurements to several years to decades in end-use applications such as organic light-emitting diodes and organic scintillators. Furthermore, glasses and crystals both maintain active vibrational degrees of freedom and rotational motions, but exhibit arrested translational motion of atoms/molecules. These properties impact the energy transfer parameters associated with the Förster and Dexter energy transfer processes discussed in Chap. 7.

8.3 Differentiating Characteristics of Organic Molecular Glasses

Thermoplastic (glassy) polymers represent the most ubiquitous category of organic glasses. These covalently bonded and physically entangled materials possess a distribution of (high) molecular weights and chain orientations. These attributes are associated with the formation of a stable glassy state but lead to polydispersity in various properties that degrade the scintillation performance characteristics [4].

In contrast, molecular glasses, also described as monomeric glasses, refer to the category of organic materials that comprise individual small molecules. The constituents of molecular glasses possess well-defined chemical structures, have molecular weights that are generally less than 1000 g/mol, and are held together by Van der Waal forces. These characteristics have implications for several properties that govern the electronic and physical properties of the material. For example, Wu et al. rationally designed a series of molecular glasses that exhibit well-defined hole-transporting or ambipolar charge-transport properties, as required for use in thin-film Organic Light Emitting Diodes (OLEDs) [5]. The precision at which these molecules can be designed differentiates charge-transporting molecular glasses from glassy polymers. Table 8.1 provides descriptions of several qualities of molecular glasses that are relevant for selected applications.

8.4 Design Strategies for Stable Organic Molecular Glasses

There is significant interest in designing stable molecular glasses, with the required level of stability defined by the intended application. Examples include the shelf life of an amorphous pharmaceutical pill, the operational lifetime of an OLED display, or the deployment lifetime of an ionizing radiation detector (see Table 8.1). Establishing long-term stability of a molecular glass can be challenging since small organic molecules tend to reach thermodynamic equilibrium quickly and convert from amorphous forms into ordered crystalline phases. This challenge is even more difficult in bulk optical materials such as scintillators, which require high transparency across

Table 8.1 Representative application areas and properties of molecular organic glasses

Application	Unique/Desired property	Rationale
Amorphous pharmaceuticals	Solubility	Molecular glass has higher surface mobility than crystalline forms, leading to higher solubility and bioavailability
Photoresists for advanced lithography	Edge/surface roughness	Small molecular size (~1 nm) facilitates high lithographic resolution
Organic LEDs (OLEDs)	Film-forming ability and morphology	Thermal deposition enables precise application of amorphous films for controlled device fabrication and performance
	Electronic and charge-transport properties	Synthetic variation facilitates tunable electronic properties. Monodisperse molecular structure and consistent film properties enable reproducible performance
Organic glass scintillators (OGSs)	Exciton transport	Isotropic structure and well-defined electronic properties facilitate efficient exciton transport
	Optical and mechanical properties	Isotropic structure facilitates uniform light transport properties and improved mechanical properties versus single crystals
	Compositional variability	Molecular glass composition may be varied across a wide range; may serve as a host matrix for functional additives

long optical path lengths, typically of the order of tens of cm. Current efforts to design such glasses are based on generalized principles that inhibit crystallization processes. This includes the incorporation of bulky substituents, lowering symmetry, restricting planarity, increasing molecular size, modifying intermolecular cohesive forces, selecting molecules that exhibit multiple conformations, blending physical mixtures of molecules, or implementing a combination of these strategies [5–11].

Several of the above principles stem from the reversal of insights gained from crystal engineering. For example, it is well known among crystal growers that high compositional purity is a primary prerequisite. In contrast, Molaire and others have shown that stable molecular glasses can be achieved by blending different molecules together to introduce compositional disorder and thus inhibit crystallization [5, 10, 12]. In another example, Lebel et al. showed that it is possible to use hydrogen bonding to induce molecular aggregation in disorganized ways to preclude effective crystalline packing and to slow down diffusion and molecular reorientation in the

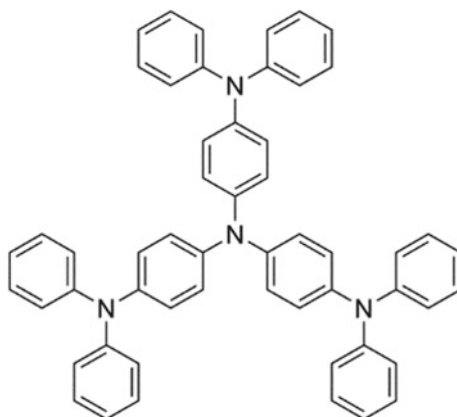
amorphous state [9]. The following sections describe design strategies that have been successfully employed to achieve stable molecular glasses.

8.4.1 Nonplanar Structures

Beginning in 1989, Shirota et al. evaluated nonplanar ‘π-electron starburst’ molecules as organic glass-forming molecules [13–18]. These molecules contain a trigonal structural core and a propeller-like arrangement(s) of peripheral aromatic groups, as shown in Fig. 8.3. The rationale behind this approach was to limit the extent of intermolecular π–π stacking interactions, and thus decrease the propensity of the material to crystallize. The simplest structural congeners, triphenylamine and 1,3,5-triphenylbenzene, were found to readily crystallize under nearly all conditions. However, it was found that further functionalization of the molecule could stabilize the amorphous state under a wide range of melt-cooling conditions. Additional examples of stable glass-forming molecules in this family are shown in Fig. 8.4. Other classes of nonplanar structures have been reported with organic glass formation in mind, including tris(oligophenylenyl)amines [19–22], π-electron systems that contain an oligothiophene group [23–26], π-electron systems that contain an azobenzene moiety [27–29], and others [30–34].

There are two general findings from the above studies: (1) the nonplanar molecular structure is responsible for glass formation, and (2) the glass transition temperature can be increased by the incorporation of a rigid moiety or intermolecular hydrogen bonding sites [9]. These findings provide a starting point for the design of molecular glasses, although it should be noted that not all compounds with nonplanar structures can necessarily form stable glasses. Other factors for glass formation will thus be considered and discussed below.

Fig. 8.3 Molecular structure of ‘π-electron starburst’ compound TDATA



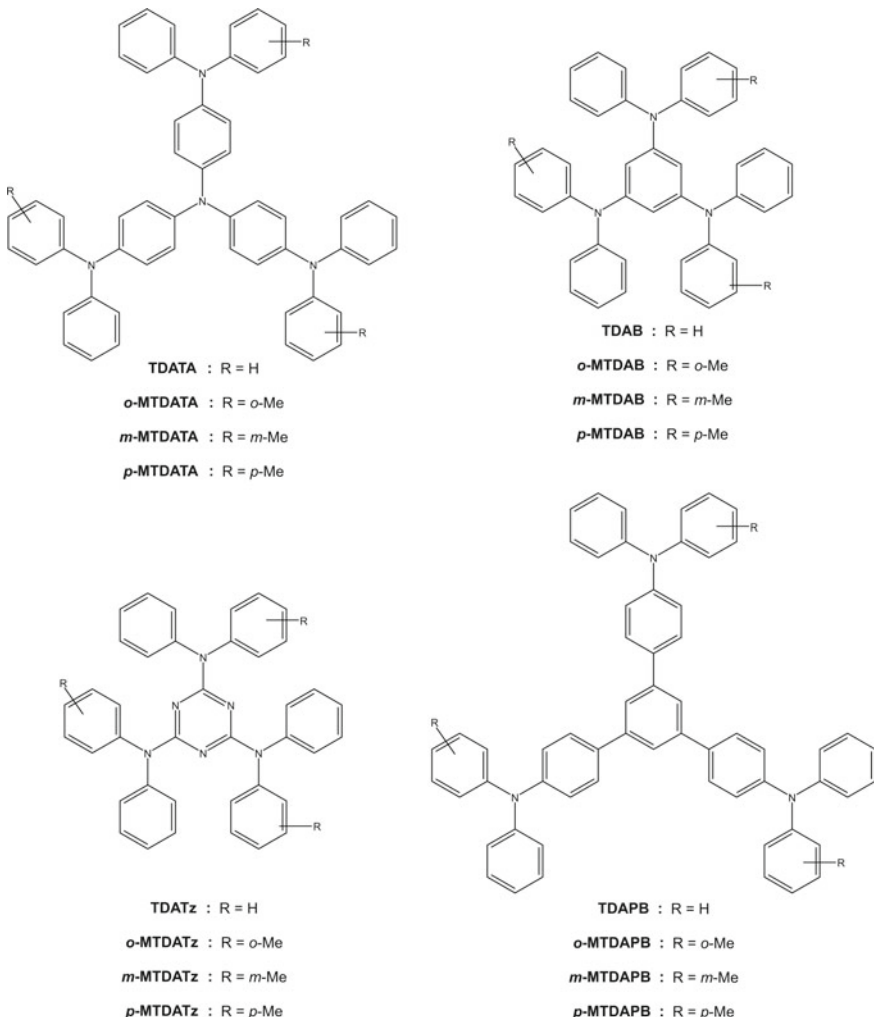


Fig. 8.4 Examples of organic glass-forming ‘ π -electron starburst’ compounds

8.4.2 Increasing Molecular Size

Molecular size has also been shown to directly impact the stability of the glassy state. This has been convincingly demonstrated in the π -electron starburst molecules shown in Fig. 8.4 [35]. For example, ‘*p*-MTDAB’ tends to crystallize over a period of several months at room temperature, whereas a glass of the larger ‘*p*-MTDAPB’ compound does not crystallize even under the most challenging conditions, i.e. heating for prolonged periods above T_g .

Fig. 8.5 Molecular structure of (9,9-dimethylfluoren-2-yl)phenylsilane compounds **P1** ($n = 1$) through **P4** ($n = 4$) [12, 41]

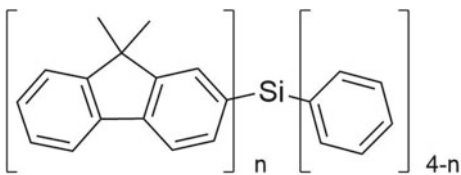


Table 8.2 Glass transition temperatures (T_g) of (9,9-dimethylfluorene)phenylsilane compounds **P1–P4** [41]

Compound name	n	T_g (°C)
(9,9-dimethylfluoren-2-yl)triphenylsilane (P1)	1	45
bis(9,9-dimethylfluoren-2-yl)diphenylsilane (P2)	2	76
tris(9,9-dimethylfluoren-2-yl)phenylsilane (P3)	3	103
tetrakis(9,9-dimethylfluoren-2-yl)silane (P4)	4	126

The addition of alkyl chains is another strategy to higher molecular weights that is widely used in the field of organic electronics. Alkylation has been employed since it may improve the solubility and film-forming properties of target molecules and/or polymers [36, 37]. However, longer alkyl chain length substituents typically lead to a decrease in the glass transition temperature and a corresponding reduction in the tensile modulus [38, 39]. These properties result in a material that is more ‘rubber-like’ at ambient temperatures. This effect is reminiscent of the strong plasticization of PVT by 2,5-diphenyloxazole (PPO) in PSD plastic scintillators [40]. Another consequence of alkylation that is relevant to the design of luminescent materials is a greater average separation distance between chromophores and a lower fractional concentration of aromatic groups. For these reasons, alkylation is generally a disfavored strategy for the design of organic scintillating materials.

Instead, the preferred approach toward increased molecular weight is to increase the number of aromatic chromophores/groups around a central core, as shown for the compounds in Fig. 8.4 [35]. Large and rigid aromatic moieties are particularly preferred for OLED and OGS applications due to the effects of increasing the molecular weight and increasing glass transition temperature, respectively. For example, sequential replacement of phenyl groups by rigid 9,9-dimethylfluorene chromophores in (9,9-dimethylfluoren-2-yl)triphenylsilane leads to stepwise increases in T_g of ~30 °C (Fig. 8.5 and Table 8.2) [12, 41].

8.4.3 Multiple Conformations

The stability of the amorphous state is enhanced in molecules that possess configurational disorder. This can be due to the presence of structural isomers and/or

positional disorder associated with rotational degrees of freedom. These characteristics are evident in characterization studies as line broadening in ^1H nuclear magnetic resonance measurements [42] and X-ray diffraction measurements [43, 44], positional disorder in X-ray structures of crystalline forms of glass-forming molecules [12], and/or the presence of multiple Raman transitions that correspond to different conformational isomers [45]. An effective strategy to this end involves the attachment of planar or asymmetric moieties to the structural core via single bonds. Plante et al. demonstrated this strategy by synthesizing a family of stable molecular glasses with varied functional groups attached to a triazine-based core (Fig. 8.6) [46]. Full-atomistic simulations were employed to investigate the solid-state packing arrangements of these compounds. The molecular dynamics were evaluated computationally, revealing a statistical distribution of conformations across the energy landscape of the system. The relative percentage of each conformer in the solid-state glass is shown in Fig. 8.7. Large activation energy values were determined for inter-conversion between conformers, which indicates difficulty for the phenyl groups to rotate in the solid state below T_g . In another example, Atawa et al. studied the crystallinity and glass-forming behavior of enantiomers of the chiral molecule 5-ethyl-5-methylhydantoin [47]. Mixtures of both enantiomers showed dramatically

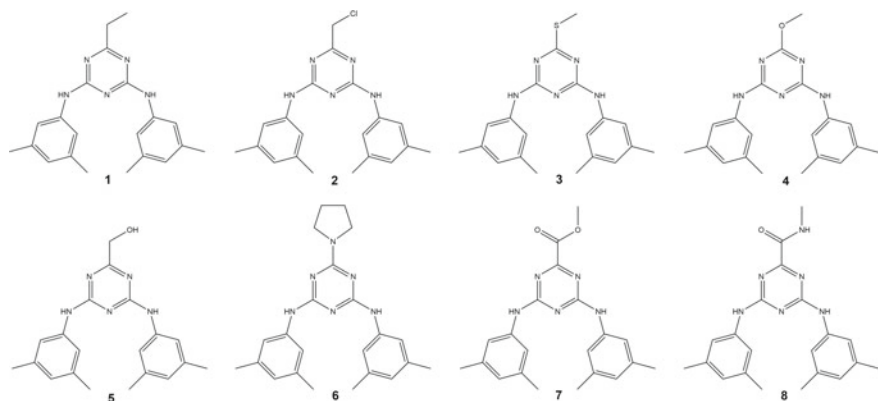


Fig. 8.6 Structures of eight molecular glass-forming compounds based on a triazine core [46]

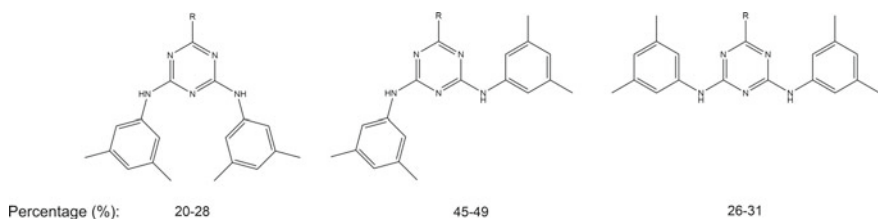
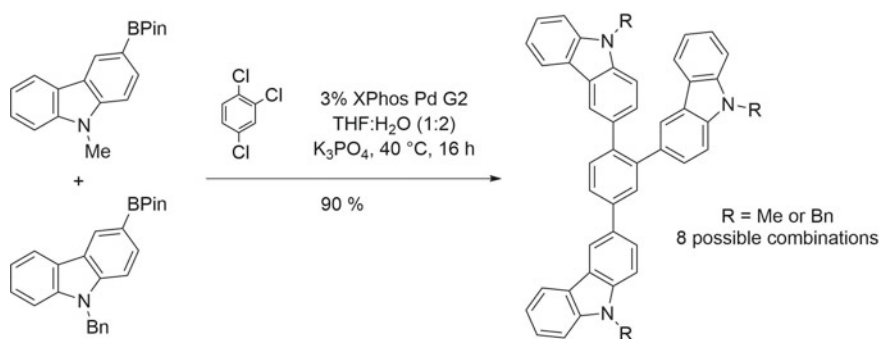


Fig. 8.7 Distribution of calculated molecular conformations in the glassy state of the triazine compounds shown [46]

improved glass-forming ability and glassy state stability compared to specimens of either of the pure enantiomers. This was attributed to the counter-enantiomer in the mixtures acting like an impurity that inhibited crystallization nucleation and growth processes.

8.4.4 Physical Mixtures

The improved glass-forming ability of enantiomeric mixtures introduces a related design concept to stabilize the amorphous state of organic molecules. This strategy involves the introduction of compositional disorder through the purposeful addition of impurity molecule(s) [5, 10, 48]. Molaire and Johnson utilized this strategy to achieve stable molecular glass mixtures for use in OLEDs [10]. The rationale behind this approach is to reduce the concentration of constituent molecules in a mixture to levels that are below their respective crystallization thresholds. The impurity molecule(s) must be rationally selected and/or designed according to three key criteria: (1) a polyfunctional organic nucleus is a common feature of all the molecules in the mixture, (2) the substituents are different enough so that the rate of crystallization is infinitely low, and (3) the substituents are similar enough so that all the molecules in the mixture are completely compatible. These requirements ensure the phase stability of the amorphous state and provide well-defined electronic properties for the mixture. This approach has been effective for physical mixtures of pure constituent compounds or in ‘one-pot’ reactions where multiple reaction products are possible [5, 10, 12, 47, 49]. For example, Wu et al. synthesized a one-pot mixture of eight possible 1,2,4-alkylcarbazole substituted benzene compounds using the Suzuki–Miyaura reaction scheme shown in Scheme 8.1 [5]. The resulting product mixture showed well-defined electronic properties expected of a single molecule but



Scheme 8.1 Reaction scheme for the one-pot formation of eight structurally different but electronically similar reaction products that behave as a stable organic glass [5]. The reagent ‘XPhos Pd G2’ refers to a second-generation palladium catalyst based on the XPhos ligand

formed an exceptionally stable glass that did not crystallize even after accelerated aging above T_g .

8.5 Fluorescent Molecular Glasses as Organic Glass Scintillators (OGSs)

With the general design strategies toward stable molecular glasses defined, we may turn our attention to answering why molecular glasses are suitable matrices for high-performance organic scintillators. Recall from Chap. 7 that the scintillation properties of any organic scintillator are controlled by two key processes: the efficiency of FRET and intermolecular triplet–triplet exchange interactions. The efficiency of these energy conversion mechanisms defines the scintillation light yield and PSD properties, respectively.

Beginning with FRET, there are specific requirements associated with the energy transfer donor compound: high fluorescence quantum yield, short emission decay time, and large spectral overlap with the acceptor absorption spectrum. Values for these parameters are provided in Table 8.3 for representative materials used in different classes of organic scintillators. There are a few notable observations with respect to these data:

- (1) Fluorescence quantum yields proceed from highest to lowest in the order: Organic Glass \approx Crystals > Liquids > Plastics.
- (2) The shortest fluorescence decay times are observed in the organic glass host matrices shown. The organic glass emission lifetimes are significantly faster than the other host matrices, with the exception of 1,2,4-trimethylbenzene liquid, which is nearly as fast.
- (3) Decay times for the (single-component) organic crystals are size-dependent due to the effect of reabsorption and re-emission. This behavior is largely reduced or eliminated in the other scintillator classes due to reduced self-absorption in multi-component mixtures.

It is notable that these trends correlate with the relative scintillation light yields for scintillators based on these materials. In other words, the brightest scintillators have the highest fluorescence quantum yields and the shortest donor emission decay times. These differences largely explain why plastic scintillators have the lowest light yields and organic glass scintillators the highest.

The second energy transfer pathway of interest involves triplet–triplet exchange interactions. This mechanism is responsible for PSD and relies upon bimolecular triplet–triplet annihilation to produce delayed fluorescence. This process can be very efficient in organic crystals, liquids, and organic glasses due to a high degree of uniformity of constituent molecules and their attendant electronic structure(s) [5, 12, 51, 67]. In contrast, TTA is typically disrupted by trapping in non-uniform materials such as organic polymers. The molecular non-uniformity in polymers is due to polydispersity in chain length and packing conformations.

Table 8.3 Fluorescence quantum yields, primary fluorescence decay times, and peak emission wavelengths for luminescent organic materials used in organic scintillators. The crystal entries are reference single-component scintillator materials, whereas the plastic, liquid, and organic glass entries comprise host matrices for multi-component scintillator mixtures

	Quantum yield (Φ)	Decay time (ns)	Peak emission (nm)	Rel. $[^{137}\text{Cs}]$ Scint. light yield ^c [50, 56]
Crystals [49]				
<i>trans</i> -Stilbene [12, 51]	0.62	2.4–8 ^a	385	1.00
Anthracene [51, 52]	0.64	12–26 ^a	440	—
<i>p</i> -Terphenyl [51]	0.67	4.2–11.5 ^a	367	—
Plastics				
Poly(9-vinylcarbazole) [53, 54]	0.076–0.14 ^b	2.5 (monomer) 14 (excimer)	368 (monomer) 425 (excimer)	—
Polystyrene/PVT [51, 55]	0.12–0.18 ^b	12 (monomer) 20 (excimer)	285 (monomer) 332 (excimer)	0.54 (EJ-200)
Liquids				
Toluene [51, 57]	0.14	34	302	—
1-Methylnaphthalene [58–61]	0.25	27.6	337 (monomer) 428 (excimer)	0.30 (BC-501A)
4-Isopropylbiphenyl [56, 62, 63]	0.25	9.7	328	0.10 (BC-501A)
<i>N</i> -(2-ethylhexyl)carbazole [56]	0.30	20.6	368 (monomer) 420 (excimer)	0.50 (BC-501A)
2,6-Diisopropynaphthalene [61, 63]	0.36	30.6	346	—
<i>p</i> -Xylene [51, 64]	0.40	8.2	290	—
1,2,4-Trimethylbenzene (pseudocumene) [65]	0.41	2.15	362	0.63 (EJ-301)
Organic glass				
Bis(9,9'-dimethylfluoren-2-yl)diphenylsilane (P2) [12]	0.66 (glass)	1.7	387	1.14
Tris(9,9'-dipropylfluoren-2-yl)methylsilane [50]	0.78 (crystal) 0.48 (glass)	—	395	1.23
4,4'-Bis((E)-4-(9H-carbazol-9-yl)styryl)biphenyl [65]	0.69	1.6	453	—
Bis(9-phenylcarbazolylbenzofuran), (BPBFC2) [66]	0.87	1.8	427	—

^aDependent on specimen size/thickness [51, 52].

^bDependent on polymerization method and thermal history [55].

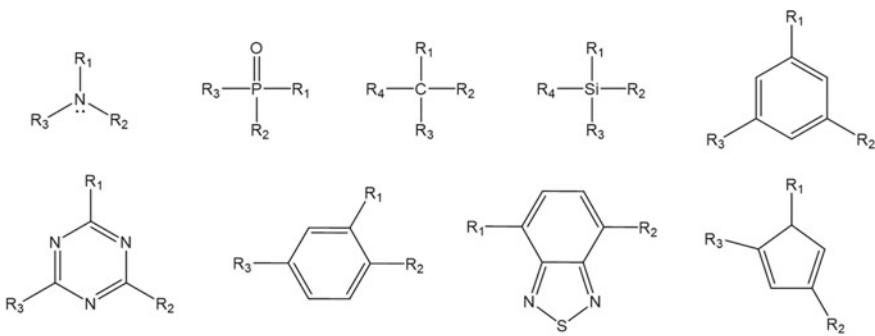
^cNot all materials were evaluated. Results for representative materials are shown

Thus, a requirement of PSD-capable scintillators is that the different molecular conformations and/or components must not confer appreciable variation in the electronic properties. An effective strategy to achieve this goal is to inhibit cofacial overlap between aromatic moieties. This has been previously demonstrated in liquid scintillators, where the branched compound 2,6-diisopropylnaphthalene exhibits a single ‘monomer’ fluorescence emission, whereas the planar compound 1-methylnaphthalene exhibits both monomer and excimer emission (Table 8.3). These insights have been translated to organic glass scintillators, whereby an effective strategy is to attach nonplanar chromophores to a structure-directing molecular core using single bonds. Free rotation around the single bonds introduces disorder in the molecular structure that stabilizes the glassy state and while retaining a consistent electronic structure. The nonplanar individual chromophores attached to each molecule further inhibit cofacial π - π stacking and the formation of deleterious excimers. 9,9'-Dialkylfluorenes [12, 41, 42, 49], 9-phenylcarbazole [66, 68], 2-(4-*tert*-butylphenyl)-5-phenyl-1,3,4-oxadiazole [35, 69], and spirobifluorenes [70, 71] comprise examples of highly fluorescent chromophore groups that have successfully been used to create molecular glass compounds. The molecular structures for these glass-stabilizing groups are shown in the lower portion of Fig. 8.8.

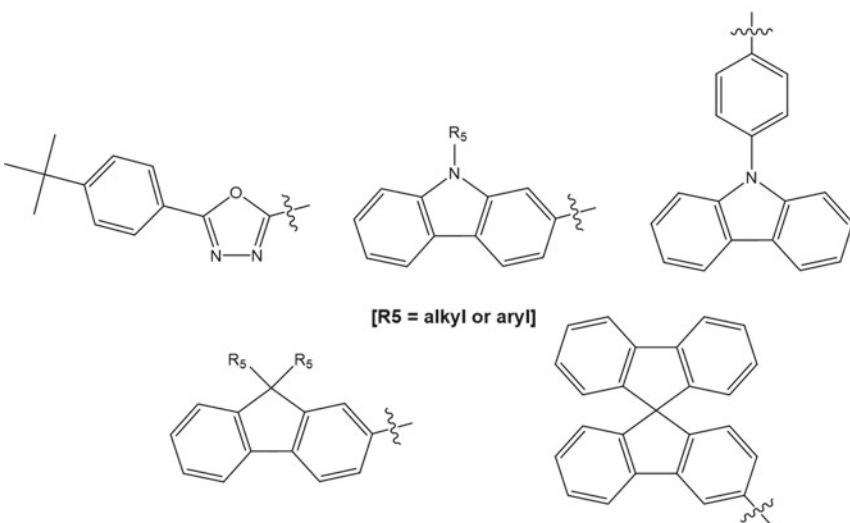
8.6 Organic Glass Scintillators: Case Studies

The first organic glass scintillator was reported in 1958 by Downs and Smith [73]. This OGS was composed of neat triphenyl-*p*-biphenyl-silane, which was transformed into a glass by heating to 120 °C and pouring into a nickel mold to cool. The resulting OGS had a gamma-ray light yield that was 60–75% that of an anthracene reference crystal and a primary scintillation decay time of ~20 ns. Considering these promising results, it is intriguing that there were no subsequent literature reports on OGSs over the following 58 years. One may speculate that this may be due to several factors: (1) widespread availability of PS and PVT that serve as matrices for plastic scintillators (2) plastic scintillator scintillation properties that proved to be better than triphenyl-*p*-biphenyl-silane glass, and (3) superior environmental stability of plastic scintillators in comparison to triphenyl-*p*-biphenyl-silane glass. Indeed, the limited kinetic stability of triphenyl-*p*-biphenyl-silane, when prepared using the literature procedure, limits the practical application of this scintillator. Subsequent work by Carlson et al. showed that triphenyl-*p*-biphenyl-silane organic glass recrystallizes over a period of a few hours at room temperature, as confirmed via PXRD analysis. Figure 8.9 is a photograph of triphenyl-*p*-biphenyl-silane after aging at room temperature for 4 h after casting. The opaque appearance reflects the microcrystalline nature of the devitrified glass.

In 2016, Carlson and Feng reported bulk OGSs based on alkyl- and arylsilane compounds that were functionalized with 9,9'-alkylfluorene chromophores (Figs. 8.10 and 8.11) [12, 49]. These chromophores were selected for a variety of reasons, including high oxidative and thermal stability, high transport mobilities,



Organic Glass Central Core Structures



Organic Glass Chromophore Moieties: (R1-R4)

Fig. 8.8 Representative core and fluorescent chromophore groups for organic glass scintillator compounds [12, 35, 41, 42, 49, 66, 68–72]

UV emission properties suitable as a fluorescence host donor, and a rigid nonplanar structure that leads to high T_g values [74–77]. Similar molecules were previously reported to form stable thin-film organic glass layers in OLED devices [41]. Figure 8.12 provides the structure of one such compound, bis(9,9-dimethylfluoren-2-yl)diphenylsilane (**P2**), along with a photo of crystals of this product obtained from a mixture of dichloromethane and hexanes. The properties of OGSs based on this compound will serve as a representative case study for a discussion of noteworthy OGS scintillation characteristics.

Fig. 8.9 Photograph of a 1 cm diameter disk of 4-biphenyltriphenylsilane organic glass after aging for 4 h at room temperature



Small 1 cm × 1 cm monoliths of bis(9,9-dimethylfluoren-2-yl)diphenylsilane (**P2**) were prepared by heating the purified crystals above their melting temperature and pouring the molten mixture into a room temperature aluminum or silicone mold. Rapid cooling of the compound under these conditions led to the formation of optically transparent organic glasses. However, the birefringence in the left specimen of Fig. 8.13 reveals the presence of internal stress in the sample due to a cooling rate that exceeded the structural relaxation time of the material. Pre-heating the mold and slowly cooling the melt back to room temperature facilitated stress relaxation, as evidenced by the lack of birefringence under cross polarizers for the right specimen in Fig. 8.13.

The obtained pure **P2** glass was an intrinsic scintillator with a gamma-ray light yield comparable to EJ-200 plastic scintillator and 62% that of *trans*-stilbene single crystals [49]. However, the addition of a wavelength shifter to the molten glass matrix led to significantly higher light yields that exceeded solvent-grown *trans*-stilbene single crystals. Table 8.4 summarizes the light yield and key scintillation properties of a **P2**-based OGS doped with 0.05 wt% of *bis*-MSB wavelength shifter. Figure 8.14 compares the energy-dependent fast neutron/gamma pulse-shape discrimination figure-of-merit values of OGS versus two reference scintillators. The results indicate that the OGS PSD-FoM is slightly lower than the solution-grown *trans*-stilbene crystal and significantly greater than EJ-276 plastic across the 0–4 MeVee energy range.

These findings indicate that the OGS has higher light yield, faster emission characteristics, but slightly lower PSD than solution-grown *trans*-stilbene single crystals. Subsequent work by Shin et al. confirmed these results using Cf-252 time-of-flight

Fig. 8.10 Photograph of a 2" × 2" as-cast OGS specimen being removed from its mold



Fig. 8.11 Photograph under UV illumination of a 2.5" × 2.5" × 0.2" OGS scintillator fabricated by net-shape melt-casting in a silicone mold

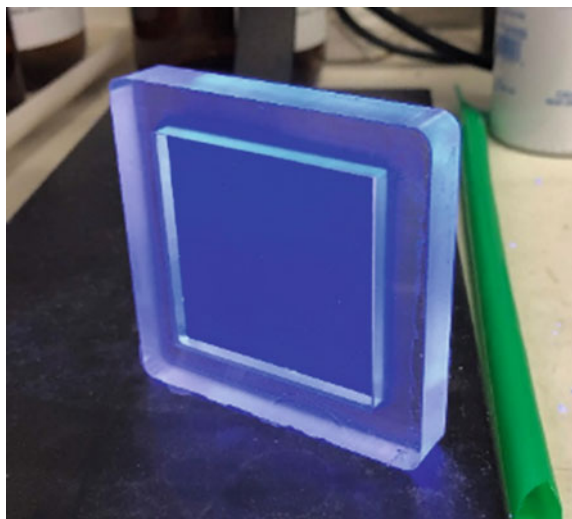




Fig. 8.12 Crystals of bis(9,9-dimethylfluoren-2-yl)diphenylsilane (**P2**) obtained from dichloromethane/hexanes

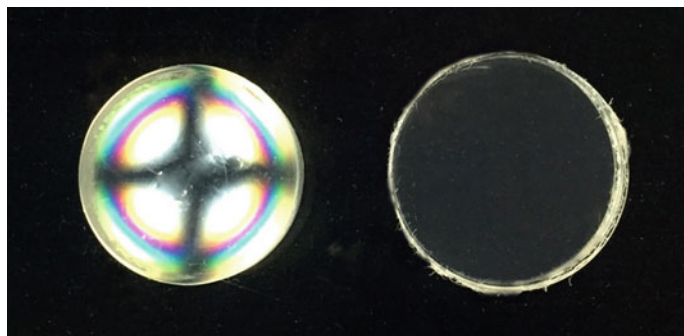
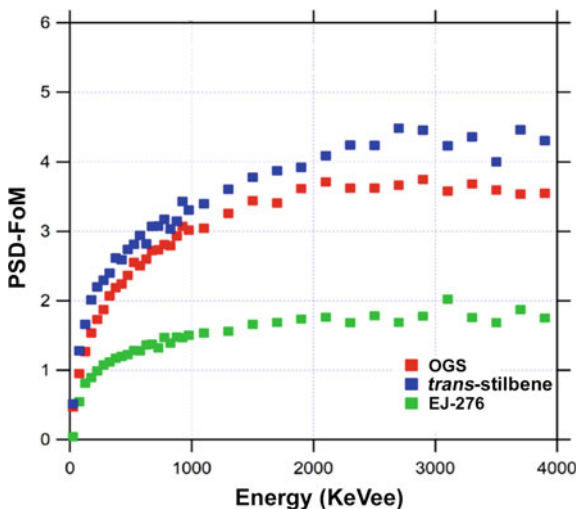


Fig. 8.13 Photographs of 1" diameter quench-cooled (left) and thermally relaxed (right) bis(9,9-dimethylfluoren-2-yl)diphenylsilane (**P2**) OGS specimens under cross-polarized light

Table 8.4 Properties of different organic scintillators [12, 78–80]

Material (1" × 1" cylinders)	Relative ^{137}Cs gamma-ray L.Y. (vs. <i>trans</i> -stilbene crystal)	PSD-FOM at 477 keVee	Primary scintillation decay time (ns)
EJ-200 plastic	0.61	N/A	2.1
EJ-276 plastic	0.53	1.3	13
<i>trans</i> -stilbene crystal	1.00	2.9	4.2
P2 -based OGS	1.14	2.6	1.7

Fig. 8.14 Energy-dependent pulse-shape discrimination figure-of-merit (FoM) values for cylindrical $1'' \times 1''$ specimens of different organic scintillators
(Adapted from [78])



measurements [81]. Comparison of cylindrical $2'' \times 2''$ specimens showed that the OGS provided higher scintillation light output relative to *trans*-stilbene for the evaluated neutron energy range of 0.79–4.57 MeV. The higher pulse height efficiency of the OGS resulted in an 11.92% greater intrinsic neutron detection efficiency than *trans*-stilbene crystal for a light output range of 0.06–2.40 MeVee. This corresponds to a neutron-equivalent energy range of 0.52–4.82 MeV. The greater neutron detection efficiency of OGS is associated with its higher recoil proton light yields, as shown in the proportionality plot in Fig. 8.15. Separate light-yield proportionality measurements by Laplace et al. showed that P2-based OGS has higher relative proton light yields than EJ-276 plastic scintillator across the recoil proton energy range of 0.2–4.5 MeV [82]. It is also notable from that work that the relative proton light yield for OGS is higher than the EJ-309 liquid scintillator from 0.2 to 1 MeV proton energy and comparable from 1 to 20 MeV.

Another relevant property of organic scintillators comprises the scintillation decay kinetics, which defines the photon yield rate and timing resolution. These properties are of critical importance for time-resolved measurements and for use in high-rate environments [83, 84]. The scintillation decay curves for four different organic scintillators are shown in Fig. 8.16 [78]. The results indicate that the OGS has the fastest rise- and decay times among the three reference materials shown. ‘Quenched’ plastic scintillators such as EJ-232Q and BC-422Q exhibit faster rise- and decay times than the OGS, although this comes at the cost of scintillation light output. For example, the 0.7 ns decay time for BC-422Q-1% compares with a 1.7 ns decay time for the OGS, although the light yield for BC-422Q-1% is approximately an order of magnitude less. The Coincidence Timing Resolution (CTR) is a parameter that combines the effects of decay kinetics and scintillation light yield. The CTR values as a function of energy are plotted in Fig. 8.17, illustrating the improved performance of OGS relative to the reference organic scintillators shown [78]. The qualitative interplay

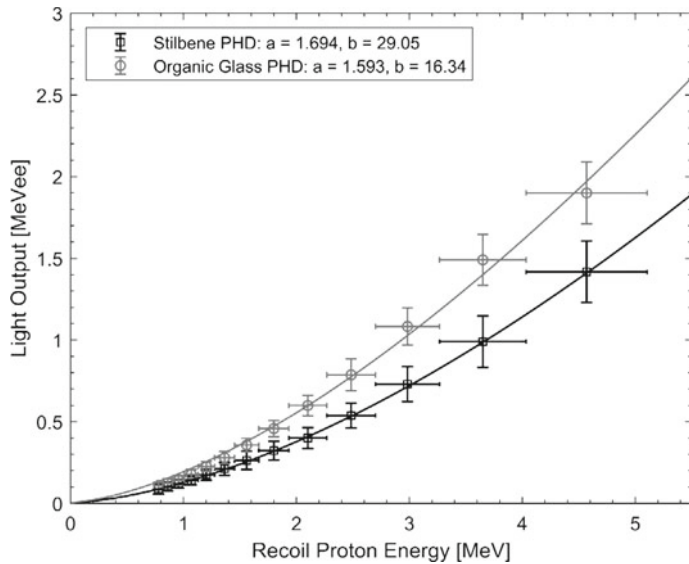
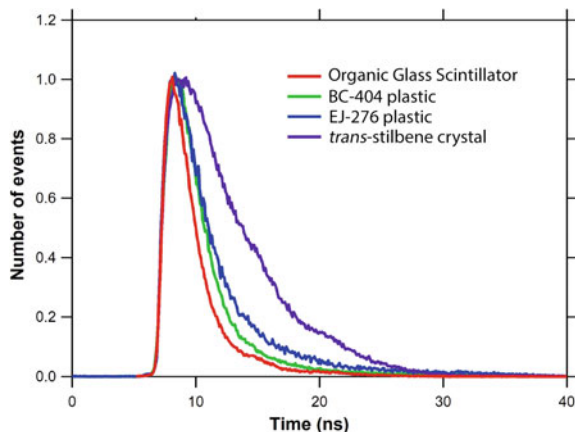


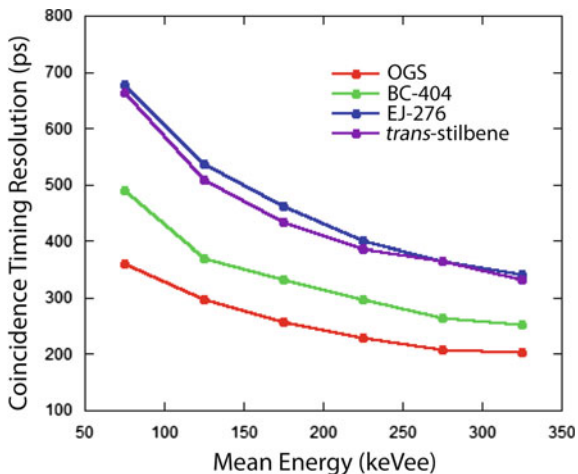
Fig. 8.15 Electron equivalent light yield versus recoil proton light yield proportionality curves for 2" × 2" specimens of OGS (*upper curve*) and solution-grown trans-stilbene crystal (*lower curve*) (Reproduced from [81] with permission from Elsevier)

Fig. 8.16 Scintillation light output curves for different organic scintillators
(Reproduced from [78] with permission from IEEE)



between decay characteristics and light yield is evident in comparing the data for *trans*-stilbene and EJ-276. The CTR values for these two materials are nearly the same despite *trans*-stilbene exhibiting significantly slower scintillation kinetics. This is due to the mitigating effect of *trans*-stilbene's ~1.6 times higher scintillation light yield.

Fig. 8.17 Coincidence timing resolution as a function of electron equivalent energy for OGS and three reference organic scintillators (Reproduced from [78] with permission from IEEE)



8.7 Organic Glass Thermal and Mechanical Properties

The thermal and mechanical properties of solid-state scintillators are properties that impact the ruggedness, production yield/cost, response uniformity, and other attributes related to their practical use. These considerations explain why plastic scintillators based on PS and PVT are preferred for applications that are subject to variable thermal and mechanical environments [85, 86]. However, plastic scintillators have scintillation properties that are inferior to molecular crystals and subject to environmental aging under certain temperature/moisture conditions [87–90]. An ongoing objective is therefore to develop a material that has mechanical properties that are similar to current plastic scintillators, while providing scintillation characteristics that are comparable to or better than crystals such as *trans*-stilbene. This is a challenging task since the material design considerations associated with these goals may involve competing requirements. For example, the favorable tensile and flexural properties of plastic scintillators is due to the physical entanglement of covalently bonded polymer chains [91]. This configuration has the undesired consequence of a distribution of molecular environments that leads to porosity, reduced light yield, and quenched PSD capabilities. Another example of competing requirements is evident in Bridgman- versus solution-grown *trans*-stilbene crystals. Bridgman-grown crystals are mechanically tougher due to a high density of edge dislocations and low-angle grain boundaries, although this leads to inferior PSD properties in comparison to relatively defect-free solution-grown crystals [92, 93].

As described above, organic glasses address the scintillation performance limitations of plastics, while providing a pathway to mechanical properties that are improved over organic crystals. Prior studies on organic glasses reveal thermoplastic behavior that is reminiscent of glassy polymers such as PS and PVT. Figure 8.18 shows the DSC data for the compound tris(9,9'-dimethylfluoren-2-yl)methylsilane, which forms an organic glass after initial crystal melting at 223 °C and subsequent

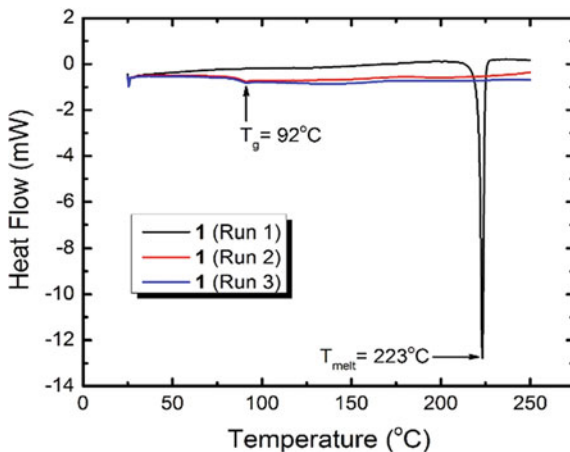


Fig. 8.18 Differential scanning calorimetry (DSC) traces for tris(9,9-dimethylfluoren-2-yl)methylsilane. The crystal melting endotherm at 223 °C was only observed during the first run, being replaced with a glass transition at 92 °C in the second and third runs. These observations indicate the formation of a stable glassy phase after the initial melting and cooling cycle of the starting crystals. Data were collected at a heating rate of 10 °C/min and a quench cooling rate of 300 °C/min following the completion of each run

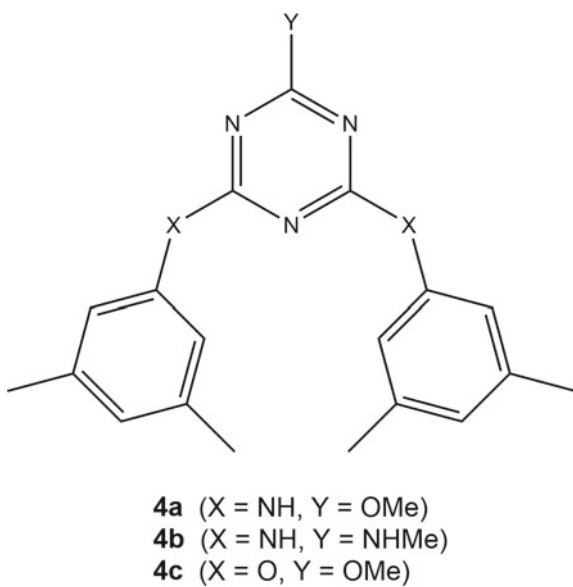
cooling [49]. Re-heating reveals a glass transition temperature (T_g) at 92 °C, which is similar to T_g values that can range from 93 to 118 °C for PVT polymer [94]. Ku et al. further evaluated the thermomechanical properties of organic glasses by studying the rheological properties of a fluorescent organic glass based on a 1,1,4,4-tetraphenylbutadiene (TPB) core [95]. Key observations include a nearly linear relationship between the shear stress and shear rate, and shear thinning above its T_g of 80 °C [95]. These properties indicate that the organic glass behaves like a thermoplastic polymer that melts and flows above a specific temperature and solidifies upon subsequent cooling. Notably, the TPB-based glass has a low viscosity of 0.2 Pa s at a relatively low temperature of 150 °C. Thermoplastic behavior and low melt viscosity are distinguishing characteristics of molecular glasses, making it possible to produce net-shape parts by molding, blowing, and imprinting processes [95, 96].

A comparison of the tensile strength for the TPB-based glass against three reference materials is provided in Table 8.5. These data show that the strength of TPB-based glass is significantly greater than the crystalline materials yet significantly less than polystyrene polymer [95, 97]. This may be explained in the following way: organic glasses and crystals both are held together by Van der Waal forces, although the failure mechanism in crystals occurs at a lower threshold due to shear-strain localization and cleavage fracture along crystallographic slip planes [98]. This is especially true in low symmetry trigonal or monoclinic crystals that comprise nearly all known scintillating organic crystals [51, 99]. Separately, the greater strength of polymers is associated with the entangled configuration of covalently bonded polymer chains.

Table 8.5 Tensile strength of different organic materials

Material	Tensile strength (MPa)
1,1,4,4-tetraphenylbutadiene-based organic glass [95]	2.31
Benzil crystal [97]	0.08
Naphthalene crystal [97]	0.49
Polystyrene polymer [100]	34 ^a

^aAverage value for extrusion grade polystyrene [100]

Fig. 8.19 Triazine organic glass molecules capable of forming multiple hydrogen bonds [9]

8.7.1 Mechanical Strength: Intermolecular Interactions

It is possible to increase the strength of intermolecular interactions and the corresponding cohesive energy density in organic crystals and molecular glasses. One strategy is to functionalize the structure with hydrogen-bonding heteroatoms, which typically have higher binding strength values than $\pi-\pi$ stacking interactions [101]. This approach was applied to enhance the stability of organic glasses based on the series of triazine compounds shown in Fig. 8.19 [9, 102].

8.7.2 Mechanical Strength: Organic Glass/Polymer Blending

A strengthening strategy that is simpler to implement is to blend molecular glasses with miscible polymers, as previously demonstrated in pharmaceuticals and organic

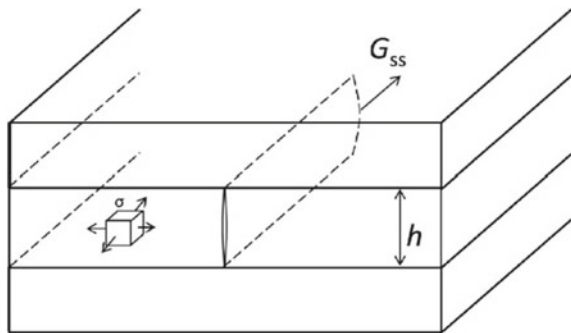


Fig. 8.20 Illustration of the ‘sandwich’ testing configuration for evaluating the fracture properties of glassy organic films. The upper and lower slabs are silicate glass. The sample thickness is h and the steady-state critical energy release value is represented by G_{ss} (Reproduced from [106] with permission from Elsevier)

electronics [103–105]. In 2015, Powell et al. evaluated the fracture properties of molecular glasses/polymer blends, including *o*-terphenyl glasses that were blended with polystyrene [106]. These components are of direct practical significance to scintillators due to their closely related chemical structures and properties to Organic Glass Scintillators [12, 49, 73]. The fracture experiments were evaluated for thin films in the sandwich geometry shown in Fig. 8.20. This configuration was employed to induce stress on the molecular glass that exceeds the viscous relaxation rate near and below T_g . The induced in-plane stress on the film is given by Eq. (8.1),

$$\sigma_{\parallel} = \frac{E}{1-v} \Delta\alpha(T_{set} - T) \quad (8.1)$$

where $\Delta\alpha$ is the difference in linear thermal expansion coefficients between the film and the substrate (silicate glass), E is Young’s modulus of the film, v is Poisson’s ratio, and T_{set} is the temperature at which the liquid begins to behave like an elastic solid. The greater thermal expansion coefficient for the *o*-terphenyl and polystyrene in comparison to the silicate glass substrate results in tensile stress on the specimen upon cooling. Following initial cooling-induced fracture, crack propagation occurs only if the energy release rate G exceeds the material-dependent critical value G_C . In other words, higher G_C values are associated with stronger materials that are more resistant to fracture.

The critical energy release values (G_C) for *o*-terphenyl and several *o*-terphenyl/polystyrene blends are shown in Table 8.6. The results can be summarized by the following statements: (1) the organic glass material is strengthened by factors ranging 2–7 due to the addition of 10% polystyrene of different molecular weights. (2) higher polystyrene molecular weights are correlated with increased fracture toughness. These findings are consistent with an increase of fracture surface area as the crack tip propagates around the permeated volume of each encountered polymer chain [106].

Table 8.6 Critical energy release values (G_c) for the fracture of *o*-terphenyl (OTP) molecular glass and 90:10 OTP:polystyrene polymer blends. The numbers in parentheses are the average polystyrene (PS) molecular weights in g/mol [106]

Material	G_c (J/m ²)
OTP molecular glass	0.64
90% OTP/10% PS (8.4 k)	1.3
90% OTP/10% PS (16 k)	1.7
90% OTP/10% PS (100 k)	3.3
90% OTP/10% PS (1000 k)	4.5

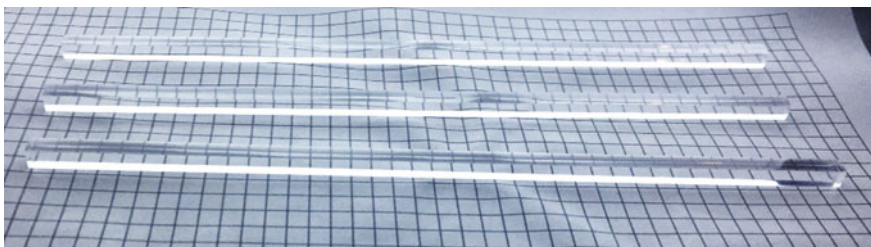


Fig. 8.21 Photograph of 5 mm × 5 mm × 200 mm OGS/polystyrene bars (97:3 wt% composition) prepared via net-shape melt-casting in a trough mold

Polymer blending has been successfully applied to increase the fracture toughness of organic glass scintillators. This enables the straightforward melt-casting preparation of high aspect ratio bars in OGS:polymer blends with polymer content as low as 1–3 wt% (Fig. 8.21).

8.8 Properties of OGS/Polymer Blends

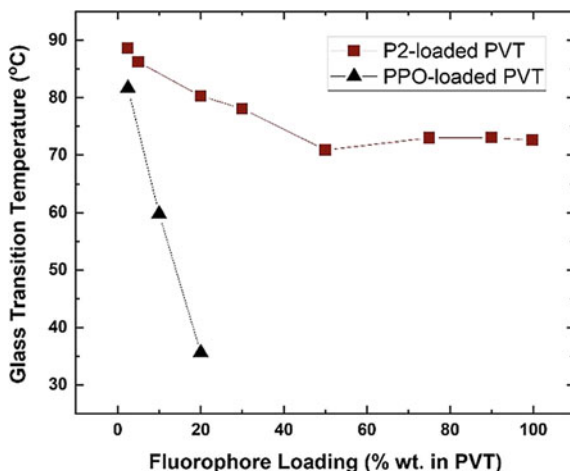
8.8.1 Effect of Small-Molecule Additives on T_g

The physical and scintillation properties of OGS/PVT blends were evaluated across a wide compositional range. Quantities of 2.5–90 wt% of bis(9,9-dimethylfluoren-2-yl)diphenylsilane (**P2**) organic glass were dissolved in a balance of vinyltoluene monomer. The resulting mixtures were heated at ~120 °C for several days, resulting in the transparent monoliths shown in Fig. 8.22. These findings indicate complete miscibility with PVT across the entire compositional range, a result that differs from PPO-loaded PVT used in PSD plastic scintillators. In those materials, the maximum practical PPO concentration is around 30–40 wt% due to limited room-temperature solubility and recrystallization at higher concentrations [40, 107]. Differential scanning calorimetry was performed to investigate the thermomechanical differences



Fig. 8.22 Photographs of $1'' \times 1''$ specimens of mixtures of bis(9,9'-dimethylfluoren-2-yl)diphenylsilane (**P2**) OGS and PVT for OGS concentrations ranging from 2.5 to 90 wt%. A specimen of a 100% OGS mixture is provided at the far right for reference

Fig. 8.23 Glass transition temperature as a function of fluorophore loading in OGS/PVT blends based on **P2** OGS (red squares) and PPO/PVT mixtures (black triangles)



between OGS- and PPO-loaded PVT. The results in Fig. 8.23 indicate that PPO strongly plasticizes the PVT polymer, leading to a $46\text{ }^{\circ}\text{C}$ reduction in T_g at 20 wt% of PPO. In contrast, the addition of **P2** OGS has a significantly smaller effect on T_g that is akin to a physical mixture of non-interacting glassy materials [108]. These results also correlate with observations of consistent material hardness for OGS/PVT blends and rubbery material characteristics of PPO/PVT blends, respectively. The precipitous drop in T_g due to PPO plasticization mirrors a similarly large drop in material hardness, as measured by Lim et al. and shown in Fig. 8.24 [40].

8.8.2 Scintillation Properties of OGS/Polymer Blends

The ^{137}Cs light yields were evaluated for different OGS/PVT blend ratios (Fig. 8.25). The results indicate a steep initial increase in the light yield at OGS concentrations below 2.5 wt% and a gradual increase in the light yield from 2.5 to 90 wt% OGS. It is notable that the light yield of 2.5% OGS in PVT is already greater than that of EJ-200 plastic scintillator. The higher light yields above 2.5 wt% OGS reflect

Fig. 8.24 Shore-D hardness measurements of PPO/PVT mixtures from 2.5 to 30 wt% PPO (Adapted from [40])

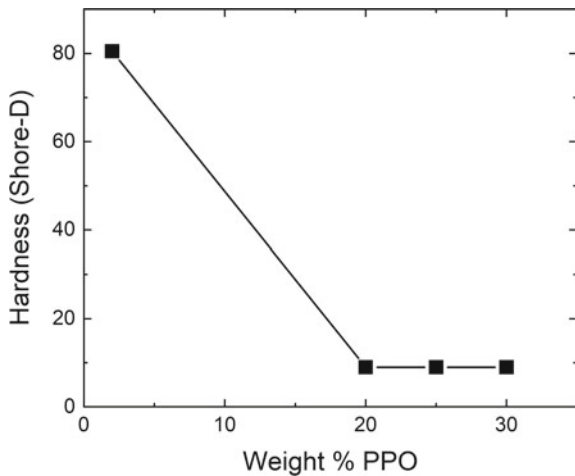
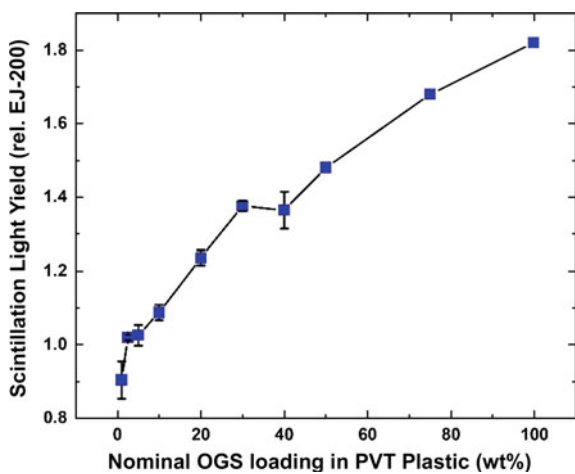


Fig. 8.25 Relative ^{137}Cs light yields for OGS/PVT blends from 2.5 to 100 wt% **P2** OGS



more efficient Förster resonant energy transfer (FRET) between the host matrix and wavelength shifter due to the organic glass molecule.

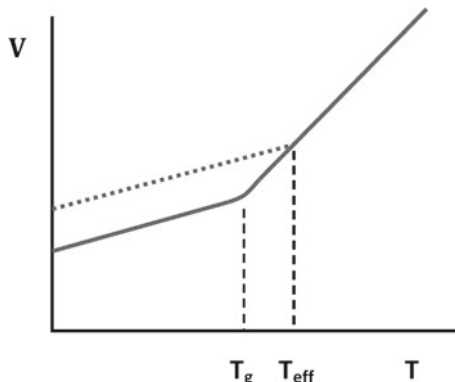
The photophysical and thermal properties studied across the composition range suggest that an important change in the average morphological properties is evident between 30 and 50% **P2** loading. Above this composition range, the glass transition temperature, scintillation lifetime, and ^{137}Cs light yield are consistent with values for the organic glass scintillator. These observations suggest there are emissive units of **P2** in PVT that resemble the pure organic glass scintillator.

8.9 Organic Glass Scintillator Fabrication Methods

Prior work on small-molecule organic glasses has largely focused on thin-film optoelectronic materials and the stabilization of bulk pharmaceuticals. The requirements for OGS are a combination of both fields, i.e. the formation of stable, bulk optical glasses. This has important implications for the fabrication of OGSS due to the limitations in the uniformity of heat transfer and the associated effects upon strain and relaxation. For example, it is unfeasible to produce bulk OGSS using vacuum sublimation processes used in OLED thin films, despite the nearly ideal physical characteristics that this glass formation method provides. This is due to the slow material deposition rate. Similarly, it is unfeasible to produce large-volume OGSS using the rapid quench cooling methods employed in pharmaceuticals. This is due to high strain rates and associated cracking of the optical monolith. Cracking is generally not an issue in pharmaceuticals since there are no optical requirements, and the material is typically reconsolidated or compounded in a pelletization process [44, 96].

To address these issues, a preferred route toward stress-free thermoplastic materials such as molecular glasses and polymers is to allow for thermal relaxation above T_g . This effect is evident in Fig. 8.26, where the free volume of a glass-forming liquid is plotted as a function of temperature. Fast cooling rates lead to higher free volumes and a higher effective glass transition temperature (T_{eff}) due to the effects of internal stress. Reducing the cooling rate above or near T_g leads to higher density materials that are stress-relaxed [109]. Large OGSS specimens (e.g. 5" × 5") can be produced using this method by casting the molten liquid above T_g , holding the temperature steady at ($T_g + 30$ K), and cooling the specimen back to room temperature over a period of several hours.

Fig. 8.26 Temperature dependence of the volume of a liquid through the glass transition temperature (T_g) for slow cooling (solid line) and fast cooling (dotted line). T_{eff} is the effective dynamic transition temperature for fast cooling into the glassy state



8.10 Long-Term Stability and Environmental Aging of Organic Glass Scintillators

The practical significance of a scintillator material depends on the stability of its physical and photophysical properties. For example, organic crystals are generally not suitable for applications that are subject to thermal and mechanical shocks, whereas conventional plastic scintillators may not be suitable for long-term use in humid outdoor environments. A minimum requirement for all of these applications is that the scintillator must exhibit stable properties over time. Accelerated Aging Testing (AAT) was thus employed to evaluate these characteristics for OGSSs.

8.10.1 Surface Versus Bulk Diffusion

Molecular organic glasses typically fail due to devitrification back into their crystalline state [110]. As discussed in Sect. 8.2, the amorphous phase is a kinetically stable state in which the stability timescale may range from seconds to thousands of years. The specific failure mode of interest is crystal nucleation and growth associated with molecular diffusion in the glass [110]. Prior work has shown that the diffusion coefficients on the surfaces of molecular glasses are orders of magnitude faster than the bulk diffusion rate, with a weaker dependence on the temperature and a stronger dependence on the molecular size and intermolecular interactions [111]. The high surface activity of organic molecular glasses explains the higher solubility of amorphous compounds in comparison to their crystalline forms [96].

In a specific example, the surface versus bulk diffusion coefficients for the organic glass *N,N'*-bis(3-methylphenyl)-*N,N'*-diphenylbenzidine (TPD) varies by 14 orders of magnitude for aged glass films [112]. When the material was held below the bulk glass transition temperature (T_g), the surface diffusion coefficient remains fast, has a lower activation energy than the bulk, and is invariant of the bulk dynamics on aged and vapor-deposited glass films. These observations are associated with the devitrification process of the formation and growth of stable crystalline nuclei. Yu showed that the high surface mobility of molecular glasses is directly responsible for fast crystal growth on free surfaces and may also be responsible for crystal growth in the bulk if there is sufficient free volume and microscopic voids throughout [113]. The kinetics of devitrification has been described by Classical Nucleation Theory (CNT), in which the driving force for nucleation is given by the difference in the free energies of the liquid and crystalline phases. In this picture, the kinetic barrier to nucleation is the activation of free energy for molecular motion (i.e. diffusion) in the matrix. The molecular motion is usually expressed in CNT as a function of the viscosity of the matrix and the average distance between crystallizing molecules. The rate of molecular diffusion increases dramatically near T_g due to large changes in the organic glass viscosity, which explains why the glass phase stability can be readily assessed using accelerated aging experiments at temperatures near T_g [3].

8.10.2 Accelerated Aging of Organic Glasses and Mitigation Methods

8.10.2.1 Vacuum Processing

The previous section discussed passivating exterior surfaces of molecular glass specimens to suppress recrystallization. Here, we consider the relationship between free volume and the presence of internal surfaces capable of supporting crystal nucleation. The free volume constitutes an equilibrium property of a glassy system at temperatures above T_g and constitutes structural voids and/or molecular packing imperfections with sizes on the order of 0.02–0.07 nm³ [114]. As shown in Fig. 8.26, cooling rates that are sufficiently fast lead to greater internal free volumes due to the unrelaxed nature of the molecular packing. The unrelaxed nature of the system may be visualized optically using cross-polarized light, as shown by the birefringent stress fields in the left image of Fig. 8.13. The most effective way to achieve a stress-free and high-density glass structure is to use vapor deposition, although this method is generally only practical for film growth. Another approach is to employ a thermal relaxation step, as previously described for 9,9'-dimethylfluoren-2-ylphenylsilane OGSSs [12]. This process produces an ‘aged glass’ with free volume and enthalpy values that are intermediate between a rapidly cooled glass and a vapor-deposited glass (Fig. 8.5). All specimens shown in Fig. 8.27 (see comments on Table 8.7) were aged above T_g for several hours, although the opaque appearances of specimen A1 after 8 days of Accelerated Aging Testing (AAT) indicate glass instability due to recrystallization. The rationale for this observation is complex considering the competition between free-volume reduction during aging and the fast diffusion that occurs near T_g . Free-volume reduction is expected to enhance glass stability, whereas fast diffusion is expected to reduce it. To address this competition, vacuum

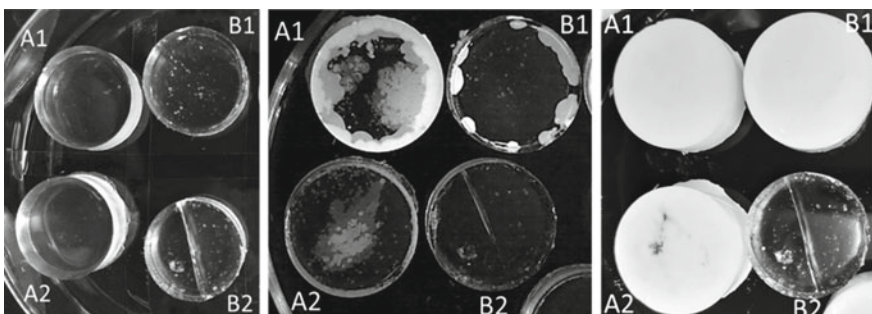


Fig. 8.27 Photograph of 1" × 1" organic glass scintillators during 60 °C accelerated aging experiments at $t = 0$ (*left*), $t = 8$ days (*middle*), and $t = 18$ days (*right*). Preparation details for specimens A1, A2, B1, and B2 are provided in Table 8.7. The minor imperfections in specimens B1 and B2 at $t = 0$ are small bubbles introduced during the casting process. The line bisecting specimen B2 is a casting defect introduced at $t = 0$ and is not associated with aging or recrystallization

Table 8.7 Description of preparation characteristics for OGS specimens A1, A2, B1, and B2

Specimen	Vacuum applied during casting?	PVA coating?
A1		
A2	✓	
B1		✓
B2	✓	✓

was applied during the casting process with the goal of reducing free volume in the bulk. Photos of OGS specimens A1 (no vacuum) and A2 (vacuum) after 8 days of AAT show that this modification was somewhat successful (Fig. 8.27). Specimen A1 shows surface and bulk recrystallization, whereas A2 shows only surface recrystallization. However, it is apparent from the 18 day AAT photo of A2 that vacuum processing alone was not sufficient to preventing recrystallization over this timescale.

8.10.2.2 Surface Coating

Another strategy that was evaluated comprises passivation of the surface using a coating, as previously described by Wu et al. [115]. Initial observation of an amorphous form of the anti-inflammatory drug indomethacin showed that surface recrystallization could be inhibited if the material remained in contact with silicate glass. Indeed, indomethacin below T_g comprises a solid-like interior with low molecular mobility and a liquid-like surface with high mobility. There is also evidence that the highly mobile surface layer is only a few nanometers thick, which suggests that it could be immobilized by contact with a substrate or coating. Indeed, a 10 nm thick gold coating or 3 nm thick polymer coating inhibited the surface crystallization of indomethacin. A surprising result was that the coatings were found to suppress further crystal growth after being applied to specimens that already contained crystalline domains. Also notable was that one 3 nm thick polymer coating was nearly as effective as a 20 nm thick coating.

The surface coating was applied to OGSs using poly(vinyl alcohol) (PVA), and optical grades of epoxy and polyurethane coatings. These materials were selected due to their high optical transparency, low solubility toward OGS, and good film-forming ability. Specimen B1 in Fig. 8.27 is a PVA-coated version of specimen A1. The photo after 8 days of AAT shows that the PVA coating alone reduces the extent of crystallization in OGS, with no surface recrystallization and bulk crystallization being confined to the internal regions near the perimeter of specimen B1. One hypothesis is that these curved regions possess the highest extent of internal free volume and thus provide crystal nucleation sites. To test this notion, specimen B2 was prepared that combines vacuum processing with a surface coating to reduce free volume and passivate the surface mobility, respectively. This approach was very successful, as evident by no change in specimen B2's transparency after 18 days of AAT. Additional AAT on B2 showed that it is stable for more than 6 months at 60 °C. This translates to a room-temperature stability of more than 50 years based on the

time scaling factors observed for other P2-based OGS specimens that were aged to failure at room temperature and 60 °C, respectively. Figure 8.28 quantifies the extent of recrystallization in each sample as a function of time. The y-axis in this plot is the integrated white point of each specimen when viewed against a black background. The data reveal no change in transparency for specimen B2.

An interesting observation related to coating OGS specimens is an improvement in the crack resistance to thermal shocks. This is illustrated in Fig. 8.29, whereby uncoated and coated 1" samples were removed from a 60 °C oven and quench-cooled in air to 22 °C. The uncoated sample cracked due to the high thermal gradient, whereas

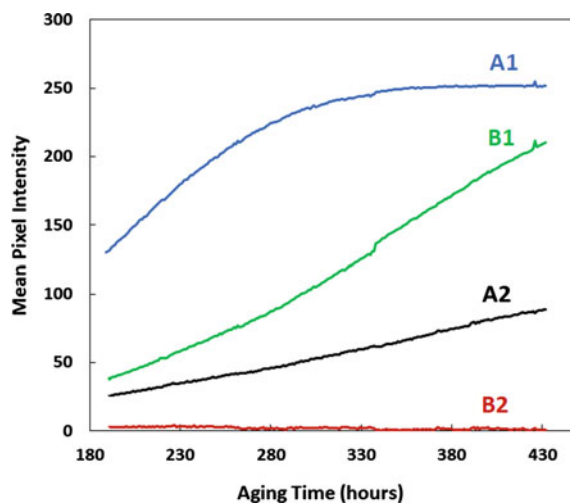


Fig. 8.28 Plot of the integrated white point values for the specimens in Fig. 8.27 as a function of aging time at 60 °C. The y-axis represents opacity and refers to the corrected white point intensity values integrated across the face of each scintillator



Fig. 8.29 Photograph of 1" × 1" OGS specimens before (*left photo*) and after (*right photo*) being rapidly cooled from 60 °C to 22 °C. The left and right specimens in each photo are as-cast (uncoated) OGS and PVA-coated OGS, respectively

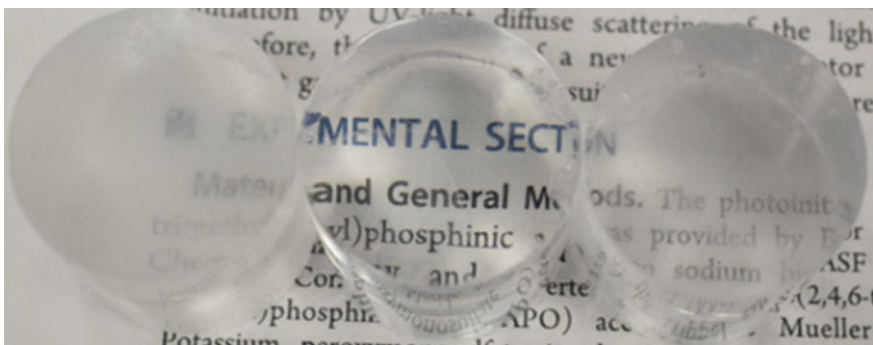


Fig. 8.30 Photograph of 50:50 mixtures of OGS:PVT blends after aging for 45 days. The left specimen is as-cast (uncoated) and was aged at 60 °C. The middle specimen was coated with PVA and aged at 60 °C. The right specimen is as-cast (uncoated) and was aged at 22 °C. Surface clouding is evident in the uncoated samples; no bulk recrystallization is apparent in any specimen

the coated sample did not. As a point of reference, the maximum recommended thermal shock specification for a 1" crystal of *trans*-stilbene is no more than 10 °C/h [116].

8.10.2.3 Physical Blending

Blending glass-forming molecules with other compounds or isomers can significantly enhance the stability of the amorphous state, as discussed in Sects. 8.4.3 and 8.4.4 [5, 10, 12]. This may be due to one or a combination of the following mechanisms: modification of intermolecular interactions, conformational disorder, anti-plasticization effect, and/or a change in energy of the crystal–amorphous interface [117]. Figure 8.30 illustrates the effect of blending **P2** OGS with 50 wt% PVT polymer. The specimens shown were aged for 45 days at either 22 or 60 °C. The results indicate that the OGS/PVT blend is more stable than pure OGS, as evidenced by the lack of any bulk recrystallization in the uncoated 60 °C sample (Fig. 8.30, left). This compares to uncoated OGS specimen A2 in Fig. 8.27, which exhibited surface nucleation after 8 days at 60 °C and extensive bulk crystallization after 18 days. High surface mobility is still reflected by light surface clouding in the uncoated OGS/PVT samples at both temperatures; PVA coating was effective in eliminating this effect (Fig. 8.30, middle).

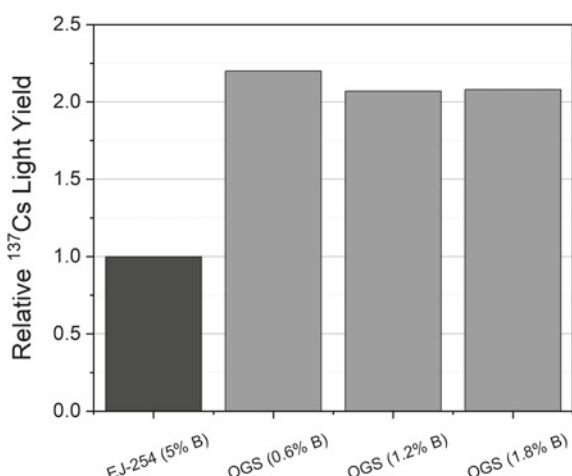
8.11 Compatibility of OGS with Multi-functional Additives

Organic molecular glasses have large positive entropy-of-mixing values and thus serve as good hosts for dissolving organic and/or organometallic additives [10]. Functional additives have been widely investigated for use in plastic and liquid scintillators, including wavelength shifters [118], thermal neutron capture compounds [119, 120], and high atomic number organometallic compounds for increased gamma-ray absorption [121, 122]. However, previously reported materials are based on host matrices with low donor quantum yields, which constrains the achievable light yield for the loaded scintillators. For example, high-Z additives cause relativistic fluorescence quenching that reduces the photon statistics and degrades the energy resolution of organic-based gamma-ray scintillators. Consequently, the 662 keV gamma-ray energy resolution has been limited to ~10% for metal-loaded PS or PVT-based plastic scintillators [121]. The higher baseline light yields for OGS and OGS/polymer blends provide an immediate advantage in designing multi-functional detector materials that are capable of improved detection efficiency.

8.11.1 Boron-Loaded OGS for Fast Neutron/Gamma PSD and Thermal Neutron Capture

Combined fast and thermal neutron discrimination has been demonstrated using boron-loaded OGS. This was achieved by dissolving the molecule tolueneboronic acid 1,3-propanediol ester (TDB) in molten OGS, followed by cooling to room temperature [123]. The resulting scintillator produces more than twice the ^{137}Cs light yield of EJ-254-5% (Fig. 8.31). The light yields are stable across a wide boron loading

Fig. 8.31 Relative ^{137}Cs scintillation light yields for boron-loaded OGS with increased loadings of tolueneboronic acid 1,3-propanediol ester compared to EJ-254-5% as a reference (Adapted from [123])



range, which indicates minimal light-yield quenching due to the boron compound. These attributes produce a neutron capture signal with a light yield equivalent to 120.4 ± 3.7 keVee, which is the highest value reported in the literature for a boron-loaded organic scintillator [124, 125]. PSD histograms for the boron-loaded OGS are shown in Figs. 8.32 and 8.33.

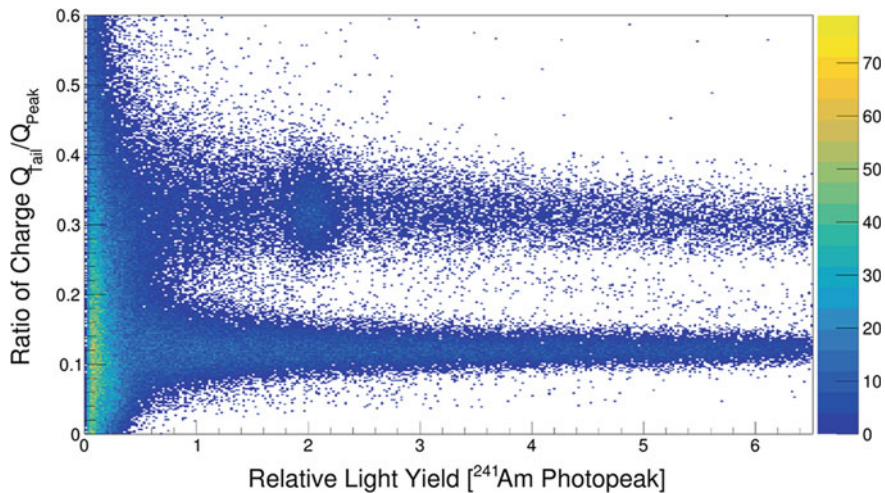


Fig. 8.32 PSD plot for a B-loaded OGS as a function of light output obtained using a time coincidence array (Reproduced from [123] with permission from Elsevier)

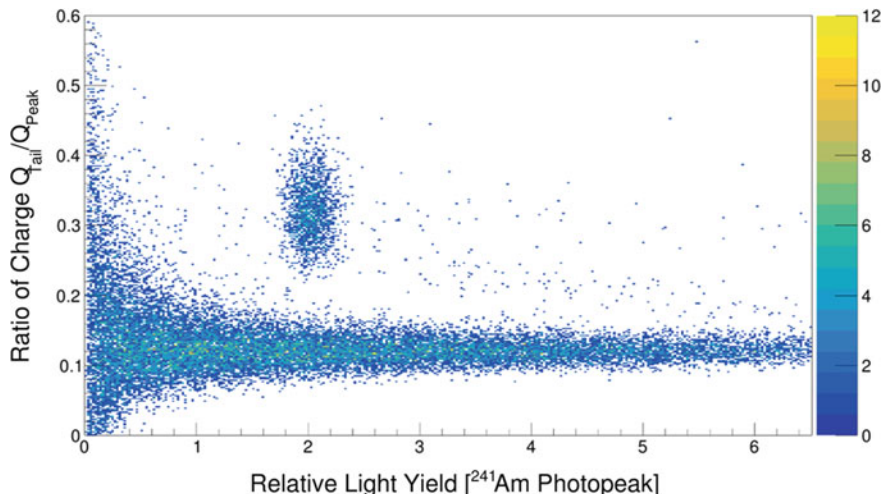
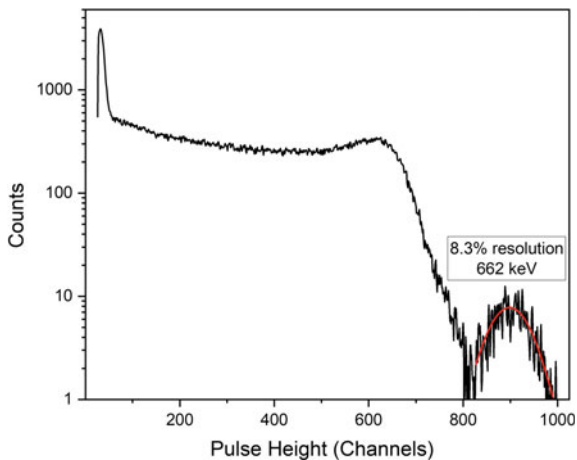


Fig. 8.33 PSD plot for a B-loaded OGS isolating the boron neutron capture response. Coincidence constraints, PSD in the observation detectors, and a minimum pulse integral threshold were applied (Reproduced from [123] with permission from Elsevier)

Fig. 8.34 ^{137}Cs pulse-height spectrum for a 5% tin-loaded OGS scintillator. Scintillator dimensions are 1" diameter \times 0.5" thick



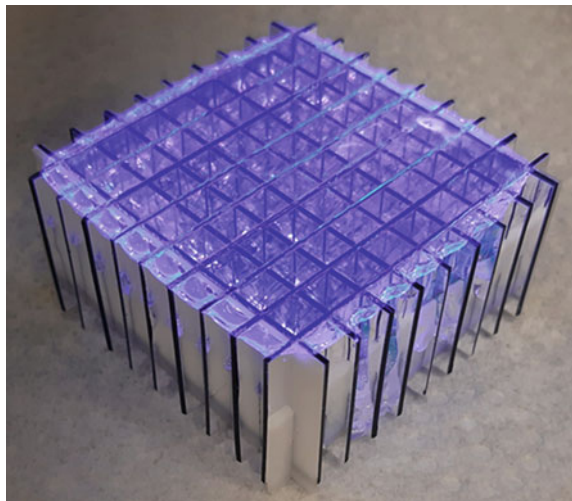
8.11.2 Metal-Loaded OGS for Fast Neutron/Gamma PSD and Gamma-Ray Spectroscopy

The spectroscopic energy resolution of organic scintillators loaded with high-Z elements is fundamentally constrained by the intrinsic light yields of the plastic and liquid host scintillator. The high photon light yield of OGSs is thus advantageous for this purpose. The ^{137}Cs pulse-height spectrum for a prototype (1 cm^3) tin-loaded OGS specimen is shown in Fig. 8.34. The photopeak shows the feasibility of achieving <9% spectroscopic energy resolution for 662 keV gamma-rays. The light yield for 5% tin-loaded OGS is nearly identical to the pure OGS, which indicates minimal light-yield quenching effects.

8.12 Summary and Future Outlook

Characterization of OGS produced to date indicates progress toward addressing the fundamental limitations of crystalline, plastic, and liquid scintillators. The molecular and radiation detection properties of OGS are most similar to crystalline organic scintillators, stemming from identical small molecules that possess high fluorescence quantum yields and exhibit efficient intermolecular triplet-triplet interactions. At the same time, OGSs are similar to liquid and plastic scintillators due to their isotropic nature, ease of fabrication, and compatibility with secondary additives. Examples of such additives include fluorescence wavelength shifters, triplet-harvesting organometallic compounds, Boron-containing molecules, and organometallic compounds. Other attributes of existing OGS include complete miscibility with PS and PVT polymers at all concentrations, and the consequent ability to modify the thermomechanical properties across a wide range. Control over

Fig. 8.35 Photograph under UV illumination of a 50 mm × 50 mm × 30 mm pixelated OGS array fabricated by pouring molten OGS material into an optically segmented mold



the OGS formulation and processing conditions has been shown to stabilize the glassy state, leading to consistent material properties even when subject to extended accelerated aging conditions. The above combination of properties positions OGS as a platform to address contemporary radiation detection needs. One example comprises fabrication of complex neutron detector geometries such as the optically segmented array shown in Fig. 8.35. The use of crystalline and plastic scintillators for such an array is constrained by competing factors such as performance, cost, and production complexity via subtractive cutting/polishing methods. The OGS array in Fig. 8.35 was cast in a single pour, which greatly simplifies the detector manufacturing process. The above combination of properties for OGS-based scintillators provides a pathway to address the performance-limiting characteristics of existing scintillators. Existing work has established notable improvements to several key scintillator properties. However, additional work is required to understand the full breadth of this emerging class of materials.

Acknowledgements This work was supported by the Office of Defense Nuclear Nonproliferation, NA-22, NNSA, U.S. Department of Energy. Sandia National Laboratories is a multimission laboratory managed and operated by National Technology and Engineering Solutions of Sandia, LLC, a wholly owned subsidiary of Honeywell International, Inc., for the U.S. Department of Energy's National Nuclear Security Administration under contract DE-NA0003525.

References

1. M.D. Ediger, J. Chem. Phys. **147**(21), 210901 (2017)
2. S.F. Swallen, K.L. Kearns, M.K. Mapes, Y.S. Kim, R.J. McMahon, M.D. Ediger, T. Wu, L. Yu, S. Satija, Science **315**(5810), 353 (2007)

3. I.M. Kalogeras, H.E.H. Lobland, *J. Mater. Educ.* **34**, 69 (2012)
4. W. Klöpffer, M. Hepp, *Monatsh. Chem.* **125**(1), 25 (1994)
5. Y.-C. Mason Wu, M.F. Molaire, D.S. Weiss, F.A. Angel, C.R. DeBlase, B.P. Fors, *J. Org. Chem.* **80**(24), 12740 (2015)
6. Q. Miao, X. Chi, S. Xiao, R. Zeis, M. Lefenfeld, T. Siegrist, M.L. Steigerwald, C. Nuckolls, *J. Am. Chem. Soc.* **128**(4), 1340 (2006)
7. I. Aujard, J.-P. Baltaze, J.-B. Baudin, E. Cogné, F. Ferrage, L. Jullien, É. Perez, V. Prévost, L.M. Qian, O. Ruel, *J. Am. Chem. Soc.* **123**(34), 8177 (2001)
8. S. Wang, W.J. Oldham, R.A. Hudack, G.C. Bazan, *J. Am. Chem. Soc.* **122**(24), 5695 (2000)
9. O. Lebel, T. Maris, M.-È. Perron, E. Demers, J.D. Wuest, *J. Am. Chem. Soc.* **128**(32), 10372 (2006)
10. M.F. Molaire, R.W. Johnson, *J. Polym. Sci. Part A Polym. Chem.* **27**(8), 2569 (1989)
11. D.M. Walters, L. Antony, J.J. de Pablod, M.D. Ediger, *J. Phys. Chem. Lett.* **8**(14), 3380 (2017)
12. J.S. Carlson, P. Marleau, R.A. Zarkesh, P.L. Feng, *J. Am. Chem. Soc.* **139**(28), 9621 (2017)
13. Y. Shirota, T. Kobata, N. Noma, *Chem. Lett.* **18**(7), 1145 (1989)
14. W. Ishikawa, H. Inada, H. Nakano, Y. Shirota, *Chem. Lett.* **20**(10), 1731 (1991)
15. H. Inada, Y. Shirota, *J. Mater. Chem.* **3**(3), 319 (1993)
16. A. Higuchi, H. Inada, T. Kobata, Y. Shirota, *Adv. Mater.* **3**(11), 549 (1991)
17. W. Ishikawa, H. Inada, H. Nakano, Y. Shirota, *Mol. Cryst. Liq. Cryst. Sci. Technol. Sect. A* **211**(1), 431 (1992)
18. Y. Kuwabara, H. Ogawa, H. Inada, N. Noma, Y. Shirota, *Adv. Mater.* **6**(9), 677 (1994)
19. H. Inada, K. Ohnishi, S. Nomura, A. Higuchi, H. Nakano, Y. Shirota, *J. Mater. Chem.* **4**(2), 171 (1994)
20. J.I. Sam, H. Kageyama, S. Nomura, H. Nakano, Y. Shirota, *Mol. Cryst. Liq. Cryst. Sci. Technol. Sect. A* **296**(1), 445 (1997)
21. A. Higuchi, K. Ohnishi, S. Nomura, H. Inada, Y. Shirota, *J. Mater. Chem.* **2**(10), 1109 (1992)
22. H. Kageyama, K. Ohnishi, S. Nomura, Y. Shirota, *Chem. Phys. Lett.* **277**(1–3), 137 (1997)
23. T. Noda, I. Imae, N. Noma, Y. Shirota, *Adv. Mater.* **9**(3), 239 (1997)
24. T. Noda, H. Ogawa, N. Noma, Y. Shirota, *Adv. Mater.* **9**(9), 720 (1997)
25. T. Noda, Y. Shirota, *J. Am. Chem. Soc.* **120**(37), 9714 (1998)
26. T. Noda, H. Ogawa, N. Noma, Y. Shirota, *J. Mater. Chem.* **9**(9), 2177 (1999)
27. T. Ujike, K. Moriwaki, H. Nakano, Y. Shirota, *J. Photopolym. Sci. Technol.* **11**(1), 33 (1998)
28. Y. Shirota, K. Moriwaki, S. Yoshikawa, T. Ujike, H. Nakano, *J. Mater. Chem.* **8**(12), 2579 (1998)
29. D. Nagahama, T. Ujike, K. Moriwaki, S. Yoshikawa, H. Nakano, Y. Shirota, *J. Photopolym. Sci. Technol.* **12**(2), 277 (1999)
30. K. Nishimura, T. Kobata, H. Inada, Y. Shirota, *J. Mater. Chem.* **1**(5), 897 (1991)
31. M. Yoshihiwa, H. Kageyama, F. Wakaya, M. Takai, K. Gamo, Y. Shirota, *J. Photopolym. Sci. Technol.* **9**(1), 57 (1996)
32. M. Yoshihiwa, H. Kageyama, Y. Shirota, *Appl. Phys. Lett.* **69**(17), 2605 (1996)
33. T. Kadota, H. Kageyama, F. Wakaya, K. Gamo, Y. Shirota, *J. Photopolym. Sci. Technol.* **11**(1), 147 (1998)
34. T. Kadota, H. Kageyama, F. Wakaya, K. Gamo, Y. Shirota, *J. Photopolym. Sci. Technol.* **12**(2), 375 (1999)
35. Y. Shirota, *J. Mater. Chem.* **10**(1), 1–25 (2000)
36. T. Wang, V. Coropceanu, J.-L. Brédas, *Chem. Mater.* **31**(16), 6239 (2019)
37. M. Morisue, I. Ueno, T. Nakanishi, T. Matsui, S. Sasaki, M. Shimizu, J. Matsui, Y. Hasegawa, *RSC Adv.* **7**(37), 22679 (2017)
38. C. Beginn, J.V. Gražulevičius, P. Strohriegl, J. Simmerer, D. Haarer, *Macromol. Chem. Phys.* **195**(7), 2353 (1994)
39. K. Kunal, C.G. Robertson, S. Pawlus, S.F. Hahn, A.P. Sokolov, *Macromolecules* **41**(19), 7232 (2008)
40. A. Lim, G. Hernandez, J. Latta, H.A. Yemam, W. Senevirathna, U. Greife, A. Sellinger, A.C.S. *Appl. Polym. Mater.* **1**(6), 1420 (2019)

41. W. Wei, P.I. Djurovich, M.E. Thompson, *Chem. Mater.* **22**(5), 1724 (2010)
42. X.-M. Liu, C. He, J. Huang, J. Xu, *Chem. Mater.* **17**(2), 434–441 (2005)
43. T. Proffen, S.J.L. Billinge, T. Egami, D.Z. Louca, Z. Kristallogr. **218**(2), 132 (2003)
44. M. Descamps, J.-F. Willart, in *Disordered Pharmaceutical Materials*, ed. by M. Descamps (Wiley-VCH, Weinheim, 2016), pp. 1–56
45. K. Ishii, H. Nakayama, *Phys. Chem. Chem. Phys.* **16**(24), 12073 (2014)
46. A. Plante, S. Palato, O. Lebel, A. Soldera, *J. Mater. Chem. C* **1**(5), 1037 (2013)
47. B. Atawa, N. Couvrat, G. Coquerel, E. Dargent, A. Saiter, *Int. J. Pharm.* **540**(1–2), 11 (2018)
48. K. Grzybowska, M. Paluch, P. Włodarczyk, A. Grzybowski, K. Kaminski, L. Hawelek, D. Zakowiecki, A. Kasprzycka, I. Jankowska-Sumara, *Mol. Pharmaceutics* **9**(4), 894 (2012)
49. R. Katoh, K. Suzuki, A. Furube, M. Kotani, K. Tokumaru, *J. Phys. Chem. C* **113**(7), 2961 (2009)
50. S. Carlson, P.L. Feng, *Nucl. Instr. Methods A* **832**, 152 (2016)
51. R.C. Sangster, J.W. Irvine Jr., *J. Chem. Phys.* **24**(4), 670 (1956)
52. H. Shimura, Y. Ohba, *Jpn. J. Appl. Phys.* **20**(9), 1683 (1981)
53. R. Diana, U. Caruso, S. Piotto, S. Concilio, R. Shikler, B. Panunzi, *Molecules* **25**(6), 1368 (2020)
54. G.E. Johnson, T.A. Good, *Macromolecules* **15**(2), 409 (1982)
55. L.J. Basile, *J. Chem. Phys.* **36**(8), 2204 (1962)
56. E. Montbarbon, F. Sguerra, G.H.V. Bertrand, É. Magnier, R. Coulon, R.B. Pansu, M. Hamel, *Chem. Eur. J.* **22**(34), 12074 (2016)
57. F.H. Quina, F.A. Carroll, *J. Am. Chem. Soc.* **98**(1), 6 (1976)
58. G. Goldstein, W.S. Lyon, *Int. J. Appl. Rad. Isotop.* **15**, 133 (1964)
59. J.B. Aladekomo, J.B. Birks, *Proc. R. Soc. Lond.* **284**(1399), 551 (1965)
60. AAT Bioquest, https://www.aatbio.com/spectrum/1_methyl_naphthalene. Accessed 06 Dec 2020
61. J.A.S.A. Olivera, Dissertation, Universidade do Porto, 2016
62. AAT Bioquest, https://www.aatbio.com/spectrum/monoisopropyl_biphenyl. Accessed 06 Dec 2020
63. A.F.L.O.M. Santos, J.A.S.A. Oliveira, M.D.M.C. Ribeiro da Silva, M.J.S. Monte, *Chemosphere* **146**, 173 (2016)
64. A. Reiser, L.J. Leyshon, *J. Chem. Phys.* **56**(2), 1011 (1972)
65. X. Zhang, Z. Chi, Z. Yang, M. Chen, B. Xu, L. Zhou, C. Wang, Y. Zhang, S. Liu, J. Xu, *Opt. Mater.* **32**(1), 94 (2009)
66. Y. Oyama, M. Mamada, A. Shukla, E.G. Moore, S.-C. Lo, E.B. Namdas, C. Adach, *ACS Mater. Lett.* **2**(2), 161 (2020)
67. F.D. Brooks, *Nucl. Instr. Methods* **162**(1–3), 477 (1979)
68. D. Hu, P. Lu, C. Wang, H. Liu, H. Wang, Z. Wang, T. Fei, X. Gua, Y. Ma, *J. Mater. Chem.* **19**(34), 6143 (2009)
69. Y. Hamada, C. Adachi, T. Tsutsui, S. Saito, *Jpn. J. Appl. Phys.* **31**(6R), 1812 (1992)
70. J. Chen, Q. Hao, S. Wang, S. Li, T. Yu, Y. Zeng, J. Zhao, S. Yang, Y. Wu, C. Xue, G. Yang, Y. Li, *A.C.S. Appl. Polym. Mater.* **1**(3), 526–534 (2019)
71. J. Salbeck, N. Yü, J. Bauer, F. Weissörtel, H. Bestgen, *Synth. Met.* **91**(1–3), 209 (1997)
72. L.C. Brown, A.J. Peloquin, N.P. Godman, G.J. Balach, S.T. Iacono, *J. Org. Chem.* **85**(17), 11116 (2020)
73. J.W. Downs, F.L. Smith, *Nucleonics* **16**, 94 (1958)
74. C.-C. Wu, T.-L. Liu, W.-Y. Hung, Y.-T. Lin, K.-T. Wong, R.-T. Chen, Y.-M. Chen, Y.-Y. Chien, *J. Am. Chem. Soc.* **125**(13), 3710 (2003)
75. L.-Y. Chen, T.-H. Ke, C.-C. Wu, *Appl. Phys. Lett.* **91**(16), 163509 (2007)
76. C.-C. Wu, W.-G. Liu, W.-Y. Hung, T.-L. Liu, Y.-T. Lin, H.-W. Lin, *Appl. Phys. Lett.* **87**(5), 052103 (2005)
77. C.-I. Wu, G.-R. Lee, C.-T. Lin, Y.-H. Chen, *Appl. Phys. Lett.* **87**(24), 242107 (2005)
78. W.K. Warburton, J.S. Carlson, P.L. Feng, A new organic glass scintillator (OGS): property comparisons to stilbene, EJ276 and BC404. Oral presented IEEE Nuclear Science Symposium and Medical Imaging Conference (NSS/MIC), Manchester UK, 26 Oct.–2 Nov 2019

79. S.K. Lee, Y.H. Cho, B.H. Kang, W.G. Lee, J.K. Kim, G.D. Kim, N.Z. Galunov, Y.K. Kim, Prog. Nucl. Sci. Technol. **1**, 292 (2011)
80. Eljen Technology website, Plastic scintillators: pulse shape discrimination EJ-276 & EJ-276G. <https://eljentechnology.com/products/plastic-scintillators/ej-276>. Accessed 30 Sept 2020
81. T.H. Shin, P.L. Feng, J.S. Carlson, S.D. Clarke, S.A. Pozzi, Nucl. Instr. Methods A **939**, 36 (2019)
82. T. Laplace, B. Goldblum, J. Manfredi, J. Brown, J. Carlson, P. Feng, E. Bourret-Courchesne, F. Moretti, J. Bevins, D. Bleuel, E. Callaghan, G. Gabella, K. Harrig, M. Shinner, C. Moore, A. Sweet, Z. Sweger, Comparative scintillation performance of EJ-276, EJ-309 and a novel organic glass. Poster presented IEEE Nuclear Science Symposium and Medical Imaging Conference (NSS/MIC), Manchester UK, 26 Oct.-2 Nov 2019
83. S. Usman, A. Patil, Nucl. Eng. Technol. **50**(7), 1006 (2018)
84. J.A. Brown, B.L. Goldblum, T.A. Laplace, K.P. Harrig, L.A. Bernstein, D.L. Bleuel, W. Younes, D. Reyna, E. Brubaker, P. Marleau, J. Appl. Phys. **124**(4), 045101 (2018)
85. J.S. Schweitzer, Nucl. Geophys. **5**, 65 (1991)
86. E.R. Siciliano, J.H. Ely, R.T. Kouzes, B.D. Milbrath, J.E. Schweppe, D.C. Stromswold, Nucl. Instr. Methods A **550**(3), 647 (2005)
87. R.J. Cameron, B.G. Fritz, C. Hurlbut, R.T. Kouzes, A. Ramey, R. Smola, IEEE Trans. Nucl. Sci. **62**(1), 368 (2015)
88. P.B. Rose Jr., A. Okowita, M.J. Lance, E. Sword, IEEE Trans. Nucl. Sci. **67**(7), 1765 (2020)
89. M. Loyd, M. Pianassola, C. Hurlbut, K. Shipp, L. Sideropoulos, K. Weston, M. Koschan, C.L. Melcher, M. Zhuravleva, Nucl. Instr. Methods A **922**, 202 (2019)
90. N.R. Myllenbeck, S. Payne, P.L. Feng, Nucl. Instr. Methods A **954**, 161782 (2020)
91. C. Redding, A. Hackett, M. Laubach, R. Feng, P. Feng, C. Hurlbut, P. Liaw, J.P. Hayward, Nucl. Instr. Methods A **954**, 161448 (2020)
92. D.J. Luscher, F.L. Addessio, M.J. Cawkwell, K.J. Ramos, J. Mech. Phys. Solids **98**, 63 (2017)
93. K.M. Davoudi, J.J. Vlassak, J. Appl. Phys. **123**(8), 085302 (2018)
94. Ł Kaplon, A. Kochanowski, M. Molenda, P. Moskal, A. Wieczorek, T. Bednarski, P. Białas, E. Czerwiński, G. Korcyl, J. Kowal, P. Kowalski, T. Kozik, W. Krzemień, S. Niedźwiecki, M. Pałka, M. Pawlik, L. Raczyński, Z. Rudy, P. Salabura, N. Gupta-Sharma, M. SilarSKI, A. Ślomski, J. Smyrski, A. Strzelecki, W. Wiślicki, M. Zieliński, N. Zoń, Bio-Algorithms Med-Syst. **10**(1), 27 (2014)
95. K. Ku, J.F. Joung, H. Park, M.-G. Kim, S. Park, W. Kim, Adv. Funct. Mater. **28**(39), 1801394 (2018)
96. B.C. Hancock, G. Zografi, J. Pharm. Sci. **86**(1), 1 (1997)
97. P.S. Bassi, N.K. Sharma, M.K. Sharma, Cryst. Res. Technol. **18**(9), 1191 (1983)
98. S. Manneppalli, K.S.R.N. Mangalampalli, Crystals **7**(11), 324 (2017)
99. P.L. Feng, M.E. Foster, IEEE Trans. Nucl. Sci. **60**(4), 3142 (2013)
100. Overview of materials for polystyrene, Extrusion Grade. <https://www.matweb.com/search/DataSheet.aspx?MatGUID=1c41e50c2e324e00b0c4e419ca780304&ckck=1>. Accessed 30 Sept 2020
101. S. Emamian, T. Lu, H. Kruse, H. Emamian, J. Comput. Chem. **40**(32), 2868 (2019)
102. A. Laventure, A. Gujaral, O. Lebel, C. Pellerin, M.D. Ediger, J. Phys. Chem. B **121**(10), 2350 (2017)
103. U.S. Kestur, L.S. Taylor, CrystEngComm **12**(8), 2390 (2010)
104. J. Kang, N. Shin, D.Y. Jang, V.M. Prabhu, D.Y. Yoon, J. Am. Chem. Soc. **130**(37), 12273 (2008)
105. P.S.K. Amegadze, Y.-Y. Noh, Thin Solid Films **556**, 414 (2014)
106. C.T. Powell, Y. Chen, L. Yu, J. Non-Cryst. Solids **429**, 122 (2015)
107. N. Zaitseva, B.L. Rupert, I. Pawełczak, A. Glenn, H.P. Martinez, L. Carman, M. Faust, N. Cherepy, S. Payne, Nucl. Instr. Methods A **668**, 88 (2012)
108. K.L. Ngai, S. Valenti, S. Capaccioli, J. Non-Cryst. Solids 119573 (2019)
109. B.L. Hammant, Composites **1**(2), 150 (1969)
110. C. Bhugra, M.J. Pikal, J. Pharm. Sci. **97**(4), 1329 (2008)

111. Y. Zhang, Z. Fakhraai, Proc. Natl. Acad. Sci. U. S. A. **114**, 4915 (2017)
112. Y. Zhang, Z. Fakhraai, Phys. Rev. Lett. **118**(6), 066101 (2017)
113. L. Yu, Adv. Drug Delivery Rev. **100**, 3 (2016)
114. D.N. Theodorou, U.W. Suter, Macromolecules **19**(2), 379 (1986)
115. T. Wu, Y. Sun, N. Li, M.M. de Villiers, L. Yu, Langmuir **23**(9), 5148 (2007)
116. Inrad Optics website, <https://inradoptics.com/>. Accessed 29 Sept 2020
117. Y. Wei, B. Dattachowdhury, K.K. Vangara, N. Patel, K. Alexander, S.H.S. Boddu, in *Excipient Applications in Formulation Design and Drug Delivery*, ed. by A.S. Narang, S.H.S. Boddu (Springer, Cham, 2015), pp. 463–495
118. I.B. Berlman, J. Chem. Phys. **34**(3), 1083 (1961)
119. Z. Chang, N.C. Okoye, M.J. Urffer, A.D. Green, K.E. Childs, L.F. Miller, Nucl. Instr. Methods A **769**, 112 (2015)
120. A. Mahl, H.A. Yemam, R. Fernando, J.T. Koubek, A. Sellinger, U. Greife, Nucl. Instr. Methods A **880**, 1 (2018)
121. P.L. Feng, W. Mengesha, M.R. Anstey, J.G. Cordaro, IEEE Trans. Nucl. Sci. **63**(1), 407 (2016)
122. G.H.V. Bertrand, J. Dumazert, F. Sguerra, R. Coulon, G. Corre, M. Hamel, J. Mater. Chem. C **3**, 6006 (2015)
123. L.Q. Nguyen, G. Gabella, B.L. Goldblum, T.A. Laplace, J.S. Carlson, E. Brubaker, P.L. Feng, Nucl. Instr. Methods A, 164898 (2021). <https://doi.org/10.1016/j.nima.2020.164898>
124. Y.K. Sun, H. Zhang, X.K. Zhao, M. Shao, Z.B. Tang, C. Li, Nucl. Instr. Methods A **940**, 129 (2019)
125. L. Swiderski, M. Moszynski, D. Wolski, T. Batsch, J. Iwanowska, A. Nassalski, A. Syntfeld-Kazuch, T. Szczesiak, F. Kniest, M.R. Kusner, G. Pausch, J. Stein, W. Klamra, P. Schotanus, C. Hurlbut, IEEE Trans. Nucl. Sci. **57**(1), 375 (2010)



Dr. Patrick Feng is a Principal Member of the Technical Staff at Sandia National Laboratories in Livermore, CA. His research is concerned with the development of novel organic-based scintillator materials. Dr. Feng's relevant contributions include the elucidation of fundamental scintillation phenomena in Metal–Organic Frameworks (MOFs), discovery of triplet-harvesting plastic scintillators for spectrally-resolved particle discrimination, development of metal-loaded plastic scintillators for gamma-ray spectroscopy, origins of environmental aging in plastic scintillators and melt-cast organic glasses for neutron/gamma discrimination.



Nicholas Myllenbeck is a Senior Member of the Technical Staff at Sandia National Laboratories in Livermore, CA. His research interests are in organic scintillator development and characterization, biomaterial and plastic valorization using synthetic chemistry, and environmental aging of organic materials. Nicholas has developed environmentally aging-resistant plastic scintillators, pulse-shape discriminating organic glass-polymer blends, and advanced processing methods for organic scintillators. He has twelve years of experience in small-molecule and polymer synthesis, including six years of organic scintillator research.



Dr. Joseph Carlson is a Senior Member of the Technical Staff at Sandia National Laboratories in Livermore, CA. Originally trained in the art of natural product synthesis, his research is now focused on innovative ideas for addressing some of the nation's challenges related to renewable transportation fuels, radiation detection, and chemical weapon disposal.

Part II

Applications

Chapter 9

Optical Improvements of Plastic Scintillators by Nanophotonics



Bo Liu and Xiaoping Ouyang

Abstract In this chapter, we discuss the optical improvements of plastic scintillators by nanophotonics, which are mainly focused on the methods to enhance the light extraction efficiency rather than increasing the internal quantum efficiency of plastic scintillators. This is a typical application of the knowledge of nanophotonics, such as photonic crystals and plasmonic lattice resonance on plastic scintillators. Total internal reflection strongly limits light extraction. An important breakthrough can be achieved thanks to nanostructures with wavelength scales on the surface of plastic scintillators, giving rise to directional and wavelength-dependent emission enhancement and thus enhancing the performance of scintillation-based detectors. Underlying physical mechanisms are discussed in detail. Suitable patterning techniques for the surfaces of plastic scintillators, including nanoimprint lithography, self-assembly lithography and X-ray interference lithography are introduced. As an application, we present a typical example of the enhanced ability of neutron detection by photonic crystals on plastic scintillators. It should be emphasized that the application of nanophotonics principles on light output of plastic scintillators could be combined with traditional coupling methods with the aim at the optimization of detection performance.

9.1 Introduction

Plastic scintillators are extensively used in radiation detection systems because of their low cost, easy fabrication process, high efficiency, and fast-timing response (see Chap. 1). In particular, plastic scintillators can play important roles in the

B. Liu ()

School of Physics Science and Engineering, Tongji University, Shanghai 200092, People's Republic of China

e-mail: lbo@tongji.edu.cn

X. Ouyang

Northwest Institute of Nuclear Technology, Xi'an 710024, People's Republic of China
e-mail: oyxp2003@aliyun.com

measurement of mixed neutron/gamma fields based on the pulse shape discrimination technology or the different sensitivity to neutrons and gamma rays [1–3].

Generally, an ideal plastic scintillator should have the following properties: high light output, short decay time, no afterglow, good spectral match to standard photodetectors, and low-cost production. Among these properties, the light output is fundamentally important for the performances, such as sensitivity, signal to noise ratio, detection efficiency and other related performances. For instance, with an improved sensitivity, a lower radiation dose during the medical imaging procedure can be applied. Consequently, cancer-induced risks due to the radiation exposure for patients would be correspondingly decreased [4].

The light yield of scintillators can be defined as the number of photoelectrons generated by radiation interaction with unit energy, which reflects the internal quantum efficiency of scintillators. The light output must take into account the light yield and the light extraction efficiency which determines what proportion of light can radiate into the ambient medium. The ambient medium can be air, optical coupling agents, or receiving windows of detectors.

Refractive indices (RIs) of commonly used plastic scintillators with matrices of poly(vinyltoluene) (PVT) and polystyrene (PS) are in the range 1.58–1.60 at 425 nm, the standard emission wavelength. If the RI of the ambient medium is smaller than these of scintillators, scintillation light would be trapped in the interior of scintillators when the incident angle is larger than the critical angle. Therefore, we can define the light output as

$$LO = \eta_{ex} \cdot LY, \quad (9.1)$$

where LO is the light output, LY is the light yield, η_{ex} is the light extraction efficiency, indicating the percentage of scintillation photons which can radiate into the ambient medium.

Total internal reflection (TIR) is the main reason for the limitation of light extraction efficiency. According to Snell's law, light can radiate out of scintillators when the incident angle is smaller than the critical angle. Neglecting the Fresnel reflection, let us consider an infinite plane scintillator-air interface, the light extraction efficiency from one side face can be determined by

$$\eta_{ex} = \frac{1}{2} \int_0^{\theta_c} \sin \theta d\theta, \quad (9.2)$$

where $\theta_c = \arcsin(n_{air}/n_{sc})$ is the critical angle, n_{air} and n_{sc} are the RIs of air and scintillator, respectively. Assuming $n_{sc} = 1.60$ and thus $\theta_c = 38.68^\circ$, the calculated light extraction efficiency is only about 11.1%. Furthermore, the spatial distribution of light emission follows an approximate Lambertian profile without a specific emission direction, resulting in the poor light collection efficiency in many cases. Directional

emission could be beneficial for the collection efficiency if the scintillation light could be redirected toward the direction of the detectors.

Optical coupling agents, such as silicon grease or oil (typical RIs of 1.5), are often used between the emitting face of scintillators and the window of photodetectors. In addition, wrapping scintillators with diffusive or reflective coating in the non-emitting faces is usually applied [5]. Such steps can certainly improve the light extraction efficiency. However, if the RI mismatch between the scintillators and the windows is not completely eliminated, the TIR still exists and thus decreases the light extraction efficiency. Moreover, in some specific cases, the optical grease or oil cannot be applied, e.g., if the detectors must be placed away from the scintillators for a certain distance in some specific layouts. At extremely low temperatures, the optical grease or oil can be out of function due to freezing. In these situations, the efficient light extraction becomes particularly essential.

Nanophotonics deals with the interaction between light and structured materials at wavelength or subwavelength scales, by which we have the opportunities to control the transition rates of spontaneous radiations and their propagation properties [6]. Typical structures include photonic crystals (PhCs) [7–11], surface plasmonic polariton (SPP) [12], plasmonic lattice resonances (PLRs) [13], optical microcavities [14], and metamaterials [15, 16]. In the following sections, the methods and applications based on the principles of nanophotonics to enhance the light extraction efficiency of plastic scintillators are discussed in details.

9.2 Enhancement of Light Extraction Efficiency of Plastic Scintillators by Photonic Crystals

9.2.1 *Introduction of Photonic Crystals*

Photonic crystals (PhCs) can be defined as one-, two-, or three-dimensional periodic arrangements of materials with different RIs. The photonic band structures of PhCs are analogous to the electronic band structures in quantum mechanics by the periodic potential provided by the atoms in crystals [17]. The characteristic lengths of PhCs are of the order of their operating wavelengths. The propagation properties of photons in PhCs are modulated by their dispersion relations which are determined by the geometric configuration and the RIs of constituent materials. The propagation properties in PhCs are entirely different from those in homogeneous mediums, thus providing a powerful tool to control the propagation of scintillation light as we expect. The concept of PhCs to enhance the light extraction efficiency of scintillators was first proposed for inorganic scintillators in 2008 by M. Kronberger et al. [18].

9.2.2 Enhancement Mechanism of Light Extraction Efficiency by Photonic Crystals

It is natural to consider the so-called band-gap approach of PhCs to enhance the light extraction efficiency. This method requires that the structures of PhCs must penetrate through the luminescence layer and the dispersion relations of PhCs should be tuned into the photonic band-gap to inhibit the in-plane propagation of scintillation light and thus achieve entire light extraction [19]. However, in this case, the scintillators themselves are the constituting materials of PhCs, which leads to a loss of weight compared with full bulk scintillators. In addition, the surface defects caused by the etching of scintillators may lead to an increase of the non-radiative recombination rates and thus decrease the internal quantum efficiency [17]. An alternative scheme is based on the diffraction effect using two-dimensional PhC slabs which are coated on the surface of scintillators without destroying them, therefore avoiding the decrease of internal quantum efficiency [18, 20]. Careful design is necessary for maximizing the light extraction efficiency. Furthermore, the extracted light by PhCs is essentially direction-dependent, which provides a possibility for the control of the directional emission.

The scheme of light extraction process by PhCs for a plastic scintillator is shown in Fig. 9.1a. As a reference, Fig. 9.1b shows the TIR of light in a flat plastic scintillator without PhCs. In the following discussion, the ambient medium is set to be air. For other situations, some necessary comments are addressed.

Fig. 9.1 a Scheme of light extraction process by PhCs for a plastic scintillator.

b Scheme of TIR of light in a flat plastic scintillator without PhCs. Only representative light rays are shown

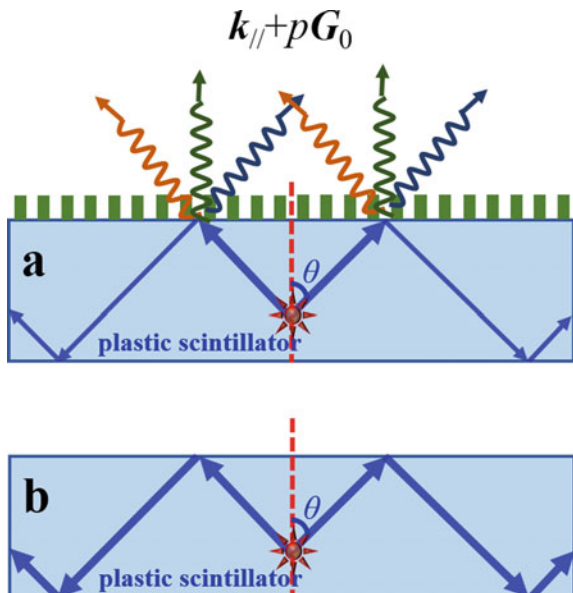
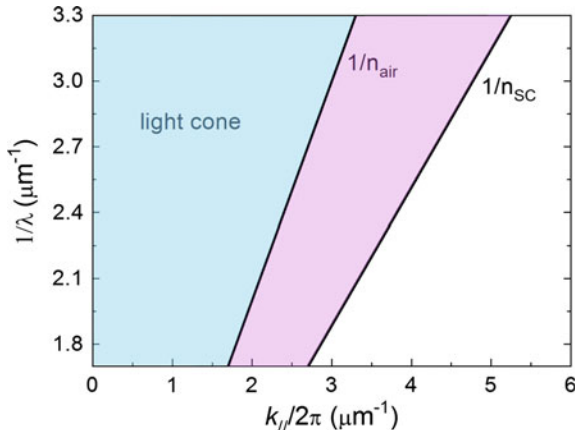


Fig. 9.2 Dispersion relations of a plastic scintillator ($n_{sc} = 1.59$) in air. The blue region denotes the light cone, in which the light can be emitted into air. The red region denotes the light trapped in the scintillator due to TIR



A scintillation light wave with a wave vector k in the interior of a plastic scintillator hits the flat scintillator-air interface. The scintillation light with an incident angle smaller than the critical angle can emit into air, forming a light cone which can be defined by

$$k_{\parallel} = n_{sc} k_0 \sin \theta < n_{air} k_0 \quad \text{for } \theta < \theta_c, \quad (9.3)$$

where k_{\parallel} is the in-plane wave vector, $k_0 = 2\pi/\lambda_0$ is the wave vector of emission wavelength λ_0 in air, θ is the incident angle, θ_c is the critical angle, and n_{air} and n_{sc} are the RIs of air and scintillator, respectively.

The dispersion relations of a plastic scintillator in air are shown in Fig. 9.2. As a typical example, the RI of the plastic scintillator is set to be $n_{sc} = 1.59$, and the range of emission wavelength is set to be 300–600 nm. When $\theta \leq \theta_c$, the scintillation light can be emitted into air, forming the light cone denoted as the blue region in Fig. 9.2. While, when $\theta > \theta_c$, the scintillation light cannot be released into air. The red region in Fig. 9.2 represents the trapping light by TIR.

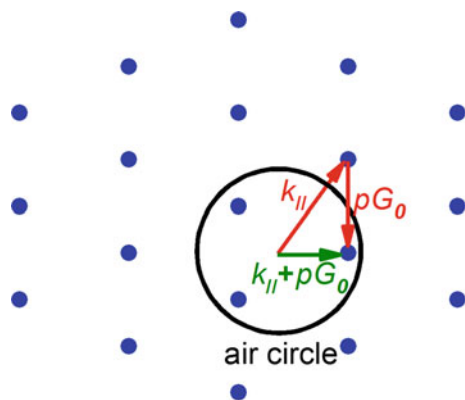
After coating with the PhCs on the emitting face of the scintillator, the wave vector will be split into different harmonics when the incident light hits the periodic structures of the PhCs. The harmonics satisfying the formula (9.4) can emit into air.

$$|k_{\parallel} + pG_0| < \frac{2\pi}{\lambda_0}, \quad (9.4)$$

where p is an integer, $G_0 = 2\pi/a$ with the lattice constant of a , and thus pG_0 is the reciprocal lattice vector. As a result, the emitting light has an emergence angle:

$$\theta_{air} = \arcsin((\lambda_0/2\pi)|k_{\parallel} + pG_0|). \quad (9.5)$$

Fig. 9.3 Physical process of Ewald construction for light propagation controlled by the PhCs



This physical process of light extraction can be illustrated by Ewald construction, as shown in Fig. 9.3 [10]. It shows a top view of a triangular PhC on reciprocal space. The blue dots represent the reciprocal lattice points of the PhC. The air circle describes the air extraction cone. Light in the scintillator having an in-plane wave vector k_{\parallel} cannot couple to air because this k_{\parallel} lies outside the air circle. Due to the presence of the reciprocal lattice vector of PhC, if the new wave vector of $k_{\parallel} + pG_0$ lies within the air circle, the light can emit into air.

PhCs comprising of monolayers of self-assembled hexagonal-close-packed PS nanospheres have been demonstrated to enhance the light extraction efficiency of plastic scintillator (EJ-212 from *Eljen Technology*, $n = 1.58$) [21]. Figure 9.4a is the scheme of light extraction process by PhCs. Figure 9.4b exhibits the top view SEM image of PhCs. Figure 9.4c shows the simulated transmission spectra at 422 nm (emission peak of the plastic scintillator) as a function of incident angle considering a light source inside a scintillator. For a flat reference sample, the transmission completely disappears beyond the critical angle for both s-polarization and p-polarization. However, for the PhC-coated sample, beyond the critical angle, two transmission bands appear for p-polarization, and three transmission bands appear for s-polarization, which implies that the PhCs enable to out-couple the trapped scintillation light. The emission spectra in the normal direction, as shown in Fig. 9.4d, clearly indicate that this enhancement can be observed in the whole range of emission spectra with a wavelength-integrated enhancement of 135%. The enhancement exhibits significant wavelength-dependence with a peak at wavelength of 459 nm due to the diffraction characteristics of PhCs.

An array of periodic nanospheres exhibits whispering gallery modes (WGMs) due to Mie resonance of individual nanospheres and Bragg diffraction arising from the periodic arrangement [22, 23]. Low-order resonances in wavelength-scale dielectric spheres have broadband characteristics of optical responses [24], which is advantageous to the coupling with broadband emission of plastic scintillators. The extraction process involved in WGMs can be understood as follows. When the scintillation light beyond the critical angle hits the interface, the evanescent field near the interface can

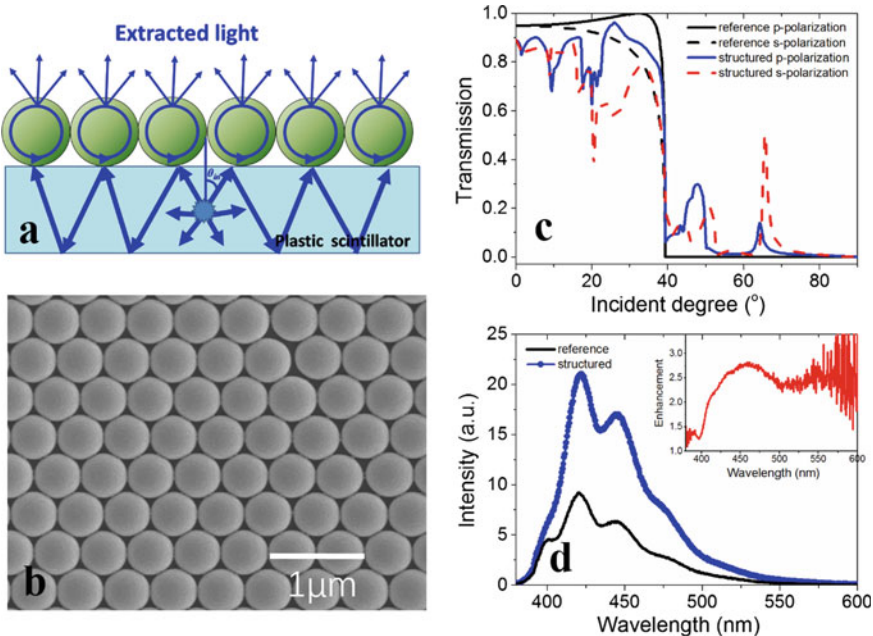
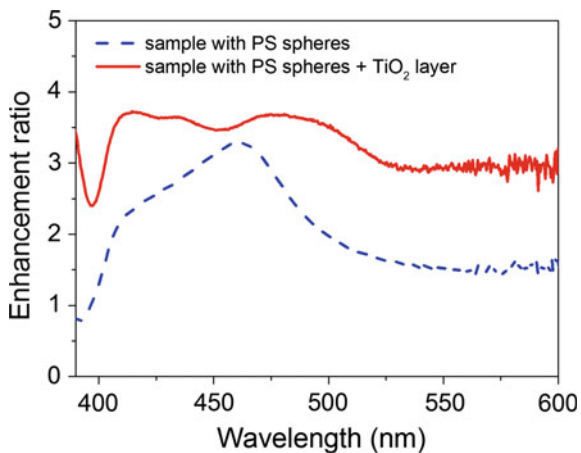


Fig. 9.4 **a** Scheme of light extraction by PhCs formed with the monolayer array of PS nanospheres. **b** Top view SEM image. **c** Simulated transmission spectra at 422 nm as a function of incident angle considering a scintillation light source in the interior of plastic scintillator, with PhCs coated sample and the reference sample for s- and p- polarizations. **d** Luminescence spectra for the PhCs coated sample and the reference sample in the normal direction. The inset represents the enhancement ratio spectrum (Reproduced from [21] with permission from Elsevier)

be coupled into the array of nanospheres forming the WGMs which can propagate in the plane of the layer of nanospheres as a dielectric waveguide due to the coupling among these adjacent nanospheres [25]. The light in the guided modes would be subsequently diffracted by the periodic structures of PhCs into leaky modes. As a consequence, the incident light beyond the critical angle can be finally out-coupled as far-field emission in air. To maximize the extraction efficiency, it is required that the diameter of spheres should be small enough for ensuring that only low-order WGMs can be excited, and at the same time it should be large enough for ensuring that the diffraction can take place effectively. In practical terms, the diameter of nanospheres should be close to the emission wavelength of plastic scintillators. It is necessary to point out that below the critical angle, several dips appear in the transmission spectra due to the diffraction effect of PhCs. These dips result in extra-diffracted light back into the scintillator. However, if the self-absorption of scintillators can be negligible, such back-diffracted light can be reflected by the backside of the scintillators, and then be re-extracted by the PhCs, which could boost the ultimate extraction efficiency. If the self-absorption of scintillators cannot be neglected, these dips have significantly negative impact on the light extraction efficiency.

Fig. 9.5 Enhancement ratio spectra of a plastic scintillator by PhCs with an array of PS nanospheres only, and PS nanospheres coated with a 58.8 nm TiO_2 layer, respectively
(Reproduced from [26] with permission from Elsevier)



The RI of PS nanospheres is 1.59 which is relatively small and thus leads to low RI contrast with air. Increasing RI contrast by coating a thin layer of high RI TiO_2 ($n = 2.8$) on the surface of PS nanospheres can effectively enhance the diffraction efficiency of PhCs, and therefore giving rise to higher light extraction efficiency for plastic scintillators (EJ-212 from *Eljen Technology*), as shown in Fig. 9.5 [26]. Simulations indicate that with the increased RI contrast, the number of modes would thus increase, which renders the coupling between the scintillation light and the PhCs more efficient [27].

9.2.3 Control of Directional Emission by Photonic Crystals

The directivity of emission is dependent on the diffraction of PhCs due to their periodic structures, as indicated by Eq. (9.5). This is an intrinsic characteristic of PhCs. However, the directivity of emission usually is not very evident for the PhCs prepared with self-assembly technique due to a variety of inevitable defects. Especially, for samples with millimeter-scale dimensions or larger, the whole structures are composed of many domains with sizes of several tens of microns with random orientations. Thus, the directivity of emission can be averaged and thus exhibits a similar Lambertian profile. As an alternative technique, hot embossing process using prefabricated molds affords a uniform orientation in the entire region up to several tens centimeters, depending on the areas of molds. Directional enhancement of a plastic scintillator (1 mm thickness, ST-401 from *Beijing Nuclear Instrument Factory*) by PhCs with a triangular lattice has been demonstrated, as shown in Fig. 9.6 [28]. In fact, the target angle of maximal enhancement can be achieved by varying the lattice parameters of PhCs.

For scintillators with a thickness much larger than the emission wavelength, there are a large number of possible values of k_{\parallel} , which leads to many possible emergence

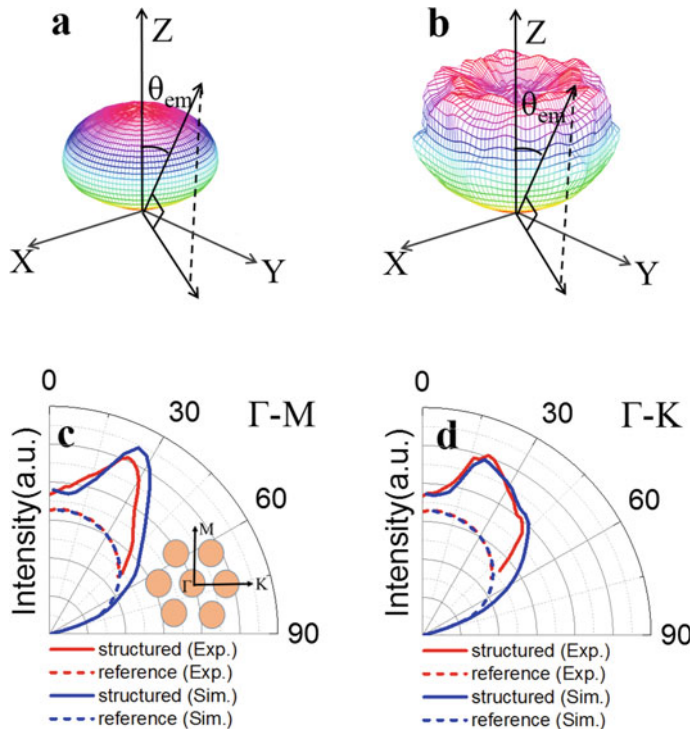
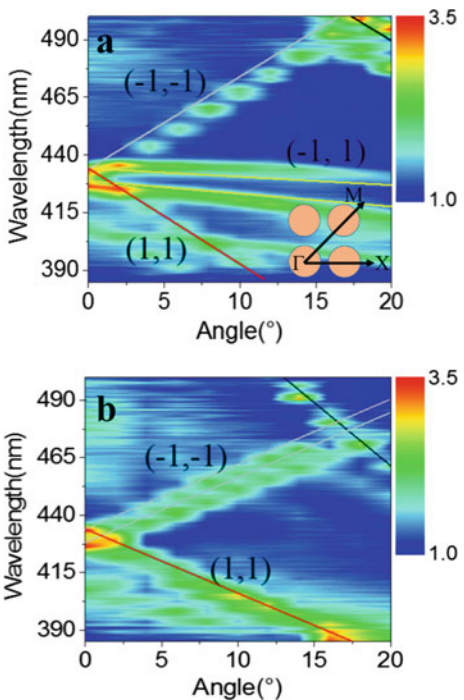


Fig. 9.6 **a, b** Simulated spatial distribution of light emission for a reference plastic scintillator and a PhC-coated plastic scintillator, respectively. **c, d** Experimental and simulated angular profiles of light emission of the reference and PhC-coated plastic scintillators along Γ -M orientation and Γ -K orientation, respectively. Γ -M and Γ -K are the two high-symmetry orientations of the PhC defined by the inset in **c** (Reproduced from [28] with permission from OSA Publishing)

angles. Thus, the angle widths for the directional emission are evidently broadened, as shown in Fig. 9.6. In contrast, when the thickness of scintillator decreases to the scale of emission wavelength, the number of modes for k_{\parallel} becomes very few. In this situation, the directional control could be much more significant, with sharp angular peaks. As shown in Fig. 9.7, the PhCs with a square lattice prepared on a plastic scintillator (ST-401 from *Beijing Nuclear Instrument Factory*) with the thickness of 450 nm have obtained directional emission with sharp angular peaks [29]. Figure 9.7 a and b show the measured angle-dependent emission enhancement spectra along Γ -M and Γ -X orientations, respectively. Spectra in the range 420–440 nm are significantly enhanced in the normal direction. The corresponding diffracted orders are plotted with different colored curves, assuming that the structures were embedded in a homogeneous refractive index medium. The diffracted modes along the Γ -M and Γ -X orientations satisfy Eqs. (9.6) and (9.7), respectively.

Fig. 9.7 a, b

Angle-dependent emission enhancement spectra for the PhC-coated plastic scintillator along Γ -M and Γ -X orientations, respectively. Γ -M and Γ -X are the two high-symmetry orientations of the PhC defined by the inset in **a** (Reproduced from [29] with permission from Springer Nature)



$$\left(\frac{\sqrt{2}}{2} k_0 \sin \theta + m_1 \frac{2\pi}{a} \right)^2 + \left(\frac{\sqrt{2}}{2} k_0 \cos \theta + m_2 \frac{2\pi}{a} \right)^2 = k_1^2 \quad (9.6)$$

$$\left(k_0 \sin \theta + m_1 \frac{2\pi}{a} \right)^2 + \left(m_2 \frac{2\pi}{a} \right)^2 = k_1^2, \quad (9.7)$$

where k_0 is the incident wave number in vacuum, θ is the incident angle, k_1 is the diffractive wave number, a is the lattice constant of PhCs, and m_1 and m_2 are integers defining the diffractive order. Each diffractive order corresponds to a specific emission angle. Additionally, the directional emission is also strongly wavelength-dependent. However, the very thin thickness of plastic scintillators may limit the absorption of radiation or restricts its use to heavy particles with important dE/dx .

9.2.4 Consideration for the Structural Design of Photonic Crystals

The commonly used arrays of PhCs are square and hexagonal lattices which are compatible with most of the preparation techniques. The lattice parameters (periods)

of PhCs determine whether the out-coupling diffraction can occur, which should satisfy Eq. (9.4). As a consequence, the lattice parameters of PhCs are generally in the range of emission wavelength of scintillators.

However, the diffraction efficiency is strongly affected by the constituting units of PhCs. The individual units of PhCs can be nanopillars, nanoholes, nanocones, nanospheres, and so on. Nanopillars and nanoholes are the most common structures which have been used for inorganic [30] and plastic scintillators [28]. Nanocones with subwavelength scale can form gradient index and thus reduce Fresnel reflection of the zero order at a wide range of impinging angles. Therefore, the PhCs consisting of nanocone arrays can simultaneously break through the limitation by TIR and Fresnel reflection, and thus obtain extra enhancement, which has been demonstrated both by simulations and experiments with inorganic scintillators [31, 32]. Nanospheres, as mentioned above, have special WGMs inside of spheres.

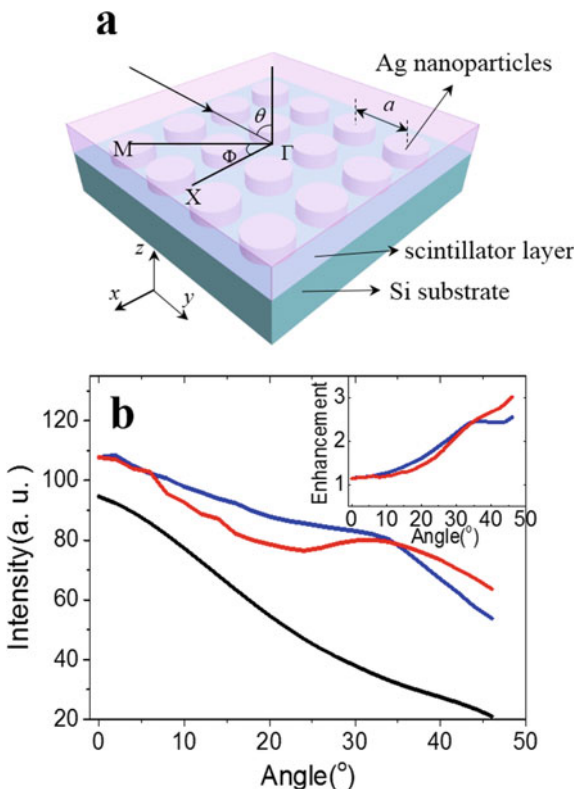
The height of PhC slabs for the light extraction on the surface of scintillators should be approximately one-fold emission wavelength, where the evanescent fields caused by TIR are covered. High RI contrast is preferred in the prior discussion. Finally, the geometric parameters of PhCs for a specific application could be optimized by simulations based on methods such as finite-difference time domain (FDTD) and rigorous coupled-wave analysis (RCWA).

9.3 Control of Directional Emission of Plastic Scintillators by Plasmonic Lattice Resonances

PLRs are collective lattice resonances originating from the radiative coupling among the localized surface plasmon resonances (LSPRs) of individual metallic nanoparticles, which can be significantly enhanced by diffractive orders in the plane of a periodic array. PLRs based on periodic arrays of metallic nanoparticles have been proposed to control the spontaneous radiation of light-emitting materials [13]. PLRs have hybrid photonic-plasmonic natures, exhibiting extended coupling with luminescence centers to several microns [33]. Therefore, PLRs not only take advantage of their high optical mode density of surface plasmons, but also avoid the severe ohmic loss. Such characteristics are beneficial for achieving the directional enhancement of a luminescence layer [34, 35].

PLRs comprising of a square array of Ag nanoparticles have been proposed to directionally enhance the light emission of a plastic scintillator (ST-401 from *Beijing Nuclear Instrument Factory*) on the surface of a silicon substrate [36]. Schematic illustration of the structured plastic scintillator is shown in Fig. 9.8a. An array of Ag nanoparticles with height of 140 nm is embedded in an 800-nm thin plastic scintillator. The array of Ag nanoparticles on the silicon substrate was prepared with nanoimprint lithography and subsequent pattern transfer process. The layer of plastic scintillator was then spin-coated on the prepared array of Ag nanoparticles. Figure 9.8b plots the angle-dependent wavelength-integrated emission intensity in

Fig. 9.8 **a** Schematic illustration of the plastic scintillator with Ag nanoparticle arrays. **b** Angle-dependent wavelength-integrated emission spectra in the range 380–500 nm for the structured sample in the Γ -M (red line) and Γ -X (blue line) orientations and the reference sample (black line). The inset is the enhancement of the structured sample in the Γ -M (red line) and Γ -X (blue line) orientations compared with the reference sample (Reproduced from [36] with permission from the American Institute of Physics)



the range of 380–500 nm for the Γ -M (red line) and Γ -X (blue line) orientations. The enhancement ratios to the reference sample exhibit a monotonous rise with increasing emission angle. It is worth mentioning that the opaque silicon substrate may have an advantage in avoiding the luminescence from transparent substrates, especially for the detection of heavy charged ions.

9.4 Patterning Techniques for Plastic Scintillators

Conventional electron-beam lithography (EBL) uses a beam of electrons to directly generate patterns on a surface [37, 38]. The advantage of this technique is that it can achieve a resolution smaller than 20 nm which is beyond the classical optical diffraction limit. The scanning technique offers a huge flexibility on the patterns but limits the overall throughput due to a serial exposure process, which is thus mostly applicable for low-volume production and especially for research and development. Conventional photolithography technique with ultraviolet is fast due to a parallel

exposure process but restricted to a resolution more than 1 μm by the diffraction limit unless light sources with much shorter wavelengths such as deep ultraviolet or extreme ultraviolet are used [17].

To explore patterning techniques suitable for plastic scintillators, some critical requirements should be taken into account. First, the working wavelength of PhCs should match the emission wavelength of plastic scintillators which is typically in the range 400–500 nm. Therefore, the periods of PhCs should be approximately of the same range. Conventional ultraviolet photolithography is thus not applicable. Second, the patterning techniques should be favorable for large-area preparation because the plastic scintillators in detectors usually have dimensions of several square centimeters or larger. Thus, a slow and costly technique such as EBL is not suitable to directly prepare PhCs on plastic scintillators. However, EBL is often used to fabricate molds with area up to several tens square centimeters which can be applied in nanoimprint lithography. Third, the solvent of resist can dissolve plastic scintillators. For this reason, the step of spin-coating a layer of resist on the surface of plastic scintillators should be avoided. An alternative method is to use non-resist lithography technology such as self-assembled nanospheres. Synthesizing plastic scintillators in structured molds prepared in advance could be another possible method. In the following sections, patterning techniques especially suitable for plastic scintillators are discussed.

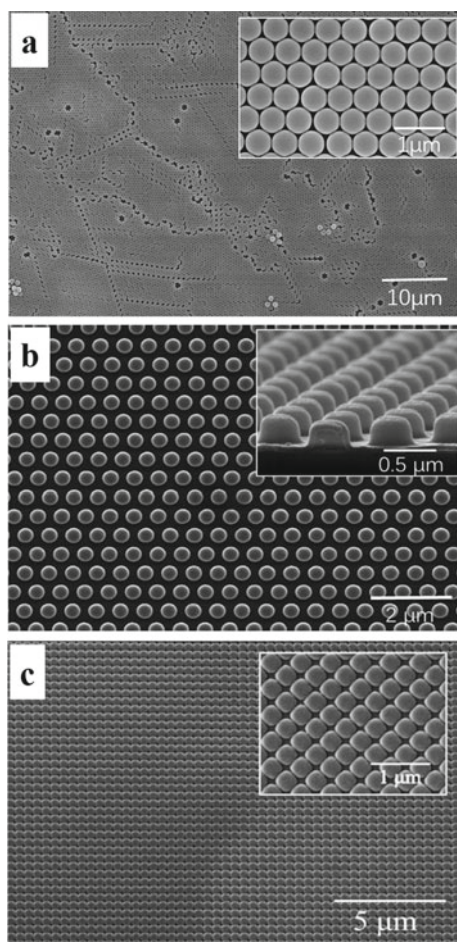
9.4.1 *Self-assembly Lithography*

Nanostructures prepared by self-assembly lithography are pervasive in many areas of nanophotonics [39]. Self-assembly lithography is an important technique to fabricate two-dimensional and three-dimensional PhCs from highly monodisperse colloidal nanospheres, which has been recognized as a facile, inexpensive, efficient, and flexible technique with high controllability and reproducibility. During the preparation process, ordered structures are driven by capillary forces, electrostatic forces, or surface hydrophobicity of the colloidal spheres at the gas-liquid interface [40]. PhCs comprising of a monolayer array of hexagonal-close-packed nanospheres are the most commonly obtained structures since these structures are the thermodynamically stable two-dimensional arrangement of monodisperse isotropic colloidal nanospheres. Self-assembly lithography of colloidal nanospheres can be achieved by using drop-coating, dip-coating, spin-coating, gravity sedimentation, electrophoretic deposition, doctor blading, Langmuir–Blodgett deposition, self-assembly at the gas-liquid interface, crystallization in physically confined cells, and other methods [41–45]. Monodisperse colloidal nanospheres include polymers such as PS and poly(methyl methacrylate) (PMMA), inorganic oxides such as SiO_2 , TiO_2 , and ZnO , core-shell semiconductors, metals, and chalcogenides [39].

Self-assembled colloidal nanospheres can be further modified by post-processes, such as thermal treatment, thin films coating, physical, or chemical infiltration. For example, thermal treatment (for example, heating at softening temperature of PS

nanospheres) can change the shape of the individual polymer nanospheres. Coating with thin shells of different chemical composition (such as TiO_2 , SiO_2 , and Al_2O_3) can control the RI contrast. Figure 9.9a exhibits a typical SEM image of PhCs of self-assembled nanospheres on a plastic scintillator (EJ-228 from *Eljen Technology*). Periodic arrays can be observed in small domains, while the whole structures are composed of many domains with sizes of several tens of microns with random orientations. In addition, some inevitable point defects appear randomly. As mentioned before, these domains with random orientations will be detrimental to the directional control of emission. But the enhancement of light extraction efficiency is still valid. Self-assembled PS nanospheres have been demonstrated to enhance the light extraction efficiency by 120% for plastic scintillators [21]. Moreover, a conformal layer of high RI TiO_2 material coated on the surface of nanospheres by atomic layer

Fig. 9.9 a, b, and c images SEM of PhCs prepared with the methods of self-assembled nanospheres, nanoimprint lithography, and X-ray interference lithography, respectively (c was reproduced from [29] with permission from Springer Nature)



deposition can increase the RI contrast of the PhCs, and thus further enhancing the light extraction efficiency [26].

9.4.2 Nanoimprint Lithography (NIL)

In the mid-1990s, Chou et al. proposed the concept of using a molding process for patterning, which is called Nanoimprint Lithography (NIL) [46, 47]. NIL relies on direct mechanical deformation of the resist and thus obtains resolutions beyond the limitation set by light diffraction or beam scattering, which is different from the conventional EBL and photolithography [48]. By using a prefabricated mold, NIL can replicate features less than 10 nm with long-range order as large as 300 mm in diameter [49]. NIL is fast and low-cost since the mold is reusable.

There are two basic operation procedures for NIL: thermal NIL and UV-NIL. Thermal NIL is also called hot embossing. In the thermal NIL procedure, when the mold is brought into contact with the resist consisting of a thermoplastic polymer, the resist is heated above its glass transition temperature to become a flowable liquid. Exerting a specific pressure, the resist fills the gap of the mold, forming nanopatterns which are subsequently solidified when cooling the sample. After removing the mold, the pattern is finally coated on the substrate. In the UV-NIL procedure, the resist is crosslinked under ultraviolet radiation through the transparent mold after the filling step. UV-NIL can be operated at room temperature and at relatively low imprinting pressure. The low temperature eliminates distortion errors due to the difference in thermal expansion coefficients. The mold for UV-NIL should be transparent to ultraviolet radiation.

However, it is found that the strong ultraviolet radiation would bleach the fluorophores in plastic scintillators, thus degrading the internal quantum efficiency of plastic scintillators. Therefore, UV-NIL is not applicable for plastic scintillators unless the strong radiation resistance of organic luminescence centers is available. Because the matrix of plastic scintillators is usually thermoplastic PS and PVT, thermal NIL is the privileged method [28, 50]. Plastic scintillators can be softened by heat and then pressed with a mold. In this process, coating resist is avoided. NIL can afford PhCs with uniform orientation in the entire region, which is certainly dependent on the structural characteristic of the mold used. Figure 9.9b is a SEM image of a PhC prepared by thermal NIL on the surface of a plastic scintillator (EJ-228 from *Eljen Technology*).

9.4.3 X-Ray Interference Lithography (XIL)

XIL is a newly developed lithography technology for preparing periodic nanostructures with resolution less than 100 nm based on coherent soft X-ray obtained from undulators at synchrotron radiation facility [51]. Coherent multi-beams produced

by masks are used to expose resist. Nanostructures with several square millimeters can be obtained by an individual XIL exposure on inorganic scintillators or other inorganic substrates. Furthermore, multiple exposures enable to obtain nanostructures with several square centimeters or even larger. The throughput of XIL is much higher than that of the EBL, since XIL does not suffer from particulate contamination and residual polymer layer which often appear in the process of NIL. Until now, several XIL beamlines have been built in synchrotron radiation facilities all over the world, such as Swiss Light Source [52], New SUBARU [53], and Shanghai Synchrotron Radiation Facility [54].

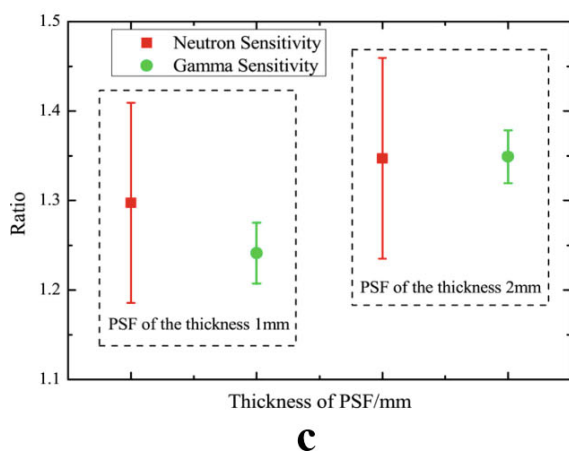
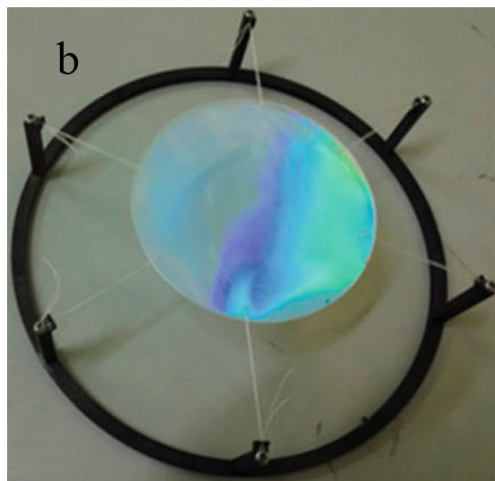
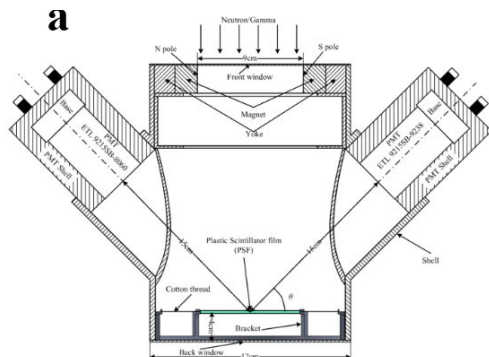
Since the organic solvent in resist can dissolve plastic scintillators, it cannot be spin-coated on their surface. However, an alternative procedure can be applied. Plastic scintillators preliminary dissolved in organic solvent can be spin-coated on a prefabricated mold on a quartz substrate by XIL, as shown in Fig. 9.9c. Using this method, PhC structures are obtained on the bottom surface of the plastic scintillator (ST-401 from *Beijing Nuclear Instrument Factory*) [29]. In fact, XIL has a huge advantage in rapid preparation structures with much smaller dimension than that of PhCs because of the short wavelength of soft X-rays applied. This advantage is expected to play an important role in preparing subwavelength or deep subwavelength structures, such as metamaterials and metasurfaces. However, an unfavorable factor should also be mentioned that XIL depends on expensive synchrotron radiation facilities.

9.5 Improved Scintillation Performance of Detectors by Photonic Crystals

In this section, we present the improvement of scintillation performance by PhCs for a pulsed neutron detector, as a typical example [50]. Pulsed neutron fluxes under strong gamma ray background can be measured based on the different sensitivity of the scintillator to neutrons and gamma rays. To obtain a high ratio of neutron sensitivity to gamma sensitivity, the thickness of plastic scintillators (herein a fast-timing dedicated, 1 or 2 mm thin EJ-228 from *Eljen Technology*) used should be thin enough to reduce the deposited energy of gamma rays. Figure 9.10a shows the schematic illustration of the detector. Figure 9.10b is the picture of the plastic scintillator coated with PhCs used in the detector. Optical coupling grease or oil between the photomultiplier tubes and the scintillator cannot be applied because the photomultiplier tubes were placed far away from the scintillator (15 cm) to avoid undesirable photoelectrons created from the photocathode. In addition, the scintillator cannot be wrapped with reflective layers to avoid the production of scattered neutrons or gamma rays. Therefore, in this severe condition, a large trapping ratio by TIR appears. Enhancement of sensitivity by more than 20% by using PhCs on the surface of the plastic scintillator was obtained, as shown in Fig. 9.10c.

In the above discussion, light enhancement by PhCs on plastic scintillator was demonstrated in the condition of air coupling. However, traditional optical coupling

Fig. 9.10 **a** Schematic illustration of the detector. **b** Picture of the plastic scintillator coated with PhCs used in the detector. **c** Enhancement ratio of neutron sensitivity and gamma sensitivity of the detector with the PhC-coated scintillator to the reference scintillator for different thicknesses: 1 mm (left) and 2 mm (right) (Reproduced from [50] with permission from AIP Publishing)



with grease or oil and wrapping scintillators with diffusive or reflective coating in the non-emitting faces are usually efficient to increase the light collection as well. In fact, such traditional methods can be combined with the methods of nanophotonics, which could obtain better performances of detectors. Bipin Singh et al. demonstrated that the energy resolution of inorganic scintillators can be further enhanced by the combination of PhCs and optical coupling with grease and wrapping with Teflon® tapes [55]. Although inorganic scintillators were used, the principles should be also applicable for plastic scintillators.

9.6 Summary and Remark

Nanophotonics provides powerful tools to enhance the light output and control the directional emission of plastic scintillators. These advantages can directly boost the signal to noise ratio and sensitivity base on the improved photo-statistics. Furthermore, other induced performances such as energy resolution, timing resolution , and ability of particles discrimination are expected to be improved as well.

PhCs can enhance the light extraction efficiency and control the directional emission of plastic scintillators by breaking the limit of TIR based on the diffraction of periodic arrays. Besides the diffraction mechanism of periodic arrays with wavelength scale, subwavelength dielectric arrays such as metafaces may be applied to control the emission of plastic scintillators. Metafaces comprising of dielectric resonant nanoparticles can function the local electromagnetic fields and multiple interferences in resonant nanostructures which can boost many optical effects and offer novel opportunities for the control of light-matter interactions in subwavelength scales [56–58]. For example, dipolar and multipolar Mie-type resonances can be used to control the directional light emission [59]. The concept of metafaces is expected to be introduced into the fields of scintillator-based detectors.

A combination of methods of nanophotonics and traditional coupling is necessary in the structural designs. The critical factors, such as structural parameters, ambient media, interfaces of scintillators, and layouts of detectors, should be fully taken into account in order to satisfy the target performances of detectors.

These patterning techniques discussed above still need further development, with the goals of high-quality, good firmness and friction resistance, low-cost, large-area, and good repeatability, which would be the essential requirements for the extended practical applications of PhCs. Most progresses on the techniques discussed here are still in the stage of research and development in leader laboratories. Although there is no mature product in market so far, the cost for patterning techniques of plastic scintillators is expected to be acceptable compared with the whole cost of scintillation detectors.

It is believed that photonic structures would obtain wide applications in nuclear radiation detectors in the future, benefiting from the fast development on nanophotonics and nanofabricating techniques.

Acknowledgements We express our warm thanks to our colleagues and collaborators who contributed to the development of plastic scintillators with enhanced performances by nanophotonics. They are Chuanwei Cheng and Hong Chen from Tongji University, Liang Chen, Jinliang Liu and Jinlu Ruan from Northwest Institute of Nuclear Technology, Yanqing Wu, Chaofan Xue, Jun Zhao and Renzhong Tai from Shanghai Synchrotron Radiation Facility. These investigations were financially supported by the National Key Research Program of China (Grant No. 2016YFA0301101), the National Natural Science Foundation of China (Grant Nos. 11975168 and 11574230).

References

1. N. Hawkes, G. Taylor, Nucl. Instr. Methods A **729**, 522 (2013)
2. S. Nyibule, E. Henry, W. Schröder, J. Töke, L. Acosta, L. Auditore, G. Cardella, E. De Filippo, L. Francalanza, S. Giani, Nucl. Instr. Methods A **728**, 36 (2013)
3. S.A. Pozzi, M.M. Bourne, S.D. Clarke, Nucl. Instr. Methods A **723**, 19 (2013)
4. D.J. Brenner, E.J. Hall, N. Engl. J. Med. **357**(22), 2277 (2007)
5. M. Janecek, IEEE Trans. Nucl. Sci. **59**(3), 490 (2012)
6. R. Kirchain, L. Kimerling, Nat. Photonics **1**(6), 303 (2007)
7. P. Lodahl, A. Floris van Driel, I.S. Nikolaev, A. Irman, K. Overgaag, D. Vanmaekelbergh, W.L. Vos, Nature **430**(7000), 654 (2004)
8. N. Ganesh, W. Zhang, P.C. Mathias, E. Chow, J.A.N.T. Soares, V. Malyarchuk, A.D. Smith, B.T. Cunningham, Nat. Nanotechnol. **2**(8), 515 (2007)
9. S. Noda, M. Fujita, Nat. Photonics **3**(3), 129 (2009)
10. J.J. Wierer Jr., A. David, M.M. Megens, Nat. Photonics **3**(3), 163 (2009)
11. S. Ogawa, M. Imada, S. Yoshimoto, M. Okano, S. Noda, Science **305**(5681), 227 (2004)
12. K. Okamoto, I. Niki, A. Shvartser, Y. Narukawa, T. Mukai, A. Scherer, Nat. Mater. **3**(9), 601 (2004)
13. S.R.K. Rodriguez, A. Abass, B. Maes, O.T.A. Janssen, G. Vecchi, J. Gómez Rivas, Phys. Rev. X **1**(2), 021019 (2011)
14. H. Yokoyama, Science **256**(5053), 66 (1992)
15. A.A. High, R.C. Devlin, A. Dibos, M. Polking, D.S. Wild, J. Perczel, N.P. de Leon, M.D. Lukin, H. Park, Nature **522**(7555), 192 (2015)
16. A.V. Kildishev, A. Boltasseva, V.M. Shalaev, Science **339**(6125), 1232009 (2013)
17. C. Wiesmann, K. Bergenek, N. Linder, U.T. Schwarz, Laser Photonics Rev. **3**(3), 262 (2009)
18. M. Kronberger, E. Auffray, P. Lecoq, IEEE Trans. Nucl. Sci. **55**(3), 1102 (2008)
19. S. Fan, P.R. Villeneuve, J. Joannopoulos, E. Schubert, Phys. Rev. Lett. **78**(17), 3294 (1997)
20. A. Knapitsch, E. Auffray, C.W. Fabjan, J.-L. Leclercq, P. Lecoq, X. Letartre, C. Seassal, Nucl. Instr. Methods A **628**(1), 385 (2011)
21. J. Liu, Z. Zhu, L. Chen, X. Ouyang, B. Liu, C. Cheng, J. Hu, S. He, Z. Wang, M. Gu, H. Chen, Nucl. Instr. Methods A **795**, 305 (2015)
22. Y. Kurokawa, Y. Jimba, H. Miyazaki, Phys. Rev. B **70**(15), 155107 (2004)
23. H.T. Miyazaki, H. Miyazaki, K. Ohtaka, T. Sato, J. Appl. Phys. **87**(10), 7152 (2000)
24. Y. Yao, J. Yao, V.K. Narasimhan, Z. Ruan, C. Xie, S. Fan, Y. Cui, Nat. Commun. **3**, 664 (2012)
25. Z. Zhu, B. Liu, C. Cheng, H. Chen, M. Gu, Y. Yi, R. Mao, Phys. Status Solidi A **211**(7), 1583 (2014)
26. L. Chen, Z. Zhu, B. Liu, C. Cheng, J. Liu, J. Ruan, Z. Zhang, X. Ouyang, M. Gu, H. Chen, Nucl. Instr. Methods A **871**, 63 (2017)
27. Z. Zhu, B. Liu, H. Zhang, W. Ren, C. Cheng, S. Wu, M. Gu, H. Chen, Opt. Express **23**(6), 7085 (2015)

28. X. Chen, B. Liu, Q. Wu, Z. Zhu, J. Zhu, M. Gu, H. Chen, J. Liu, L. Chen, X. Ouyang, Opt. Express **26**(9), 11438 (2018)
29. Q. Wu, B. Liu, Z. Zhu, M. Gu, H. Chen, C. Xue, J. Zhao, Y. Wu, R. Tai, X. Ouyang, Sci. Rep. **8**, 9254 (2018)
30. A. Knapitsch, E. Auffray, C.W. Fabjan, J.-L. Leclercq, X. Letartre, R. Mazurczyk, P. Lecoq, IEEE Trans. Nucl. Sci. **59**(5), 2334 (2012)
31. A. Knapitsch, E. Auffray, G. Barbastathis, C. Chevalier, C.-H. Hsieh, J.-G. Kim, S. Li, M.S. Marshall, R. Mazurczyk, P. Modrzynski, IEEE Trans. Nucl. Sci. **63**(2), 639 (2016)
32. J.G. Kim, C.H. Hsieh, H.J. Choi, J. Gardener, B. Singh, A. Knapitsch, P. Lecoq, G. Barbastathis, Opt. Express **23**(17), 22730 (2015)
33. S. Murai, M.A. Verschuuren, G. Lozano, G. Pirruccio, S.R.K. Rodriguez, J.G. Rivas, Opt. Express **21**(4), 4250 (2013)
34. M. Ramezani, G. Lozano, M.A. Verschuuren, J. Gómez-Rivas, Phys. Rev. B **94**(12), 125406 (2016)
35. G. Vecchi, V. Giannini, J.G. Rivas, Phys. Rev. Lett. **102**(14), 146807 (2009)
36. B. Liu, Z. Zhu, Q. Wu, C. Cheng, M. Gu, J. Xu, H. Chen, J. Liu, L. Chen, X. Ouyang, Appl. Phys. Lett. **110**(18), 181905 (2017)
37. Y. Chen, Microelectron. Eng. **135**, 57 (2015)
38. T. Oder, J. Shakya, J. Lin, H. Jiang, Appl. Phys. Lett. **83**(6), 1231 (2003)
39. J.F. Galisteo-López, M. Ibáñez, R. Sapienza, L.S. Froufe-Pérez, Á. Blanco, C. López, Adv. Mater. **23**(1), 30 (2011)
40. J. Zhang, Z. Sun, B. Yang, Curr. Opin. Colloid Interface Sci. **14**(2), 103 (2009)
41. J. Yang, M.K. Choi, D.H. Kim, T. Hyeon, Adv. Mater. **28**(6), 1176 (2016)
42. C. López, Adv. Mater. **15**(20), 1679 (2003)
43. X. Ye, L. Qi, Nano Today **6**(6), 608 (2011)
44. V. Kitaev, G.A. Ozin, Adv. Mater. **15**(1), 75 (2003)
45. Y. Xia, B. Gates, Y. Yin, Y. Lu, Adv. Mater. **12**(10), 693 (2000)
46. S.Y. Chou, P.R. Krauss, P.J. Renstrom, Science **272**(5258), 85 (1996)
47. S.Y. Chou, P.R. Krauss, P.J. Renstrom, Appl. Phys. Lett. **67**(21), 3114 (1995)
48. L.J. Guo, Adv. Mater. **19**(4), 495 (2007)
49. M.C. Traub, W. Longsine, V.N. Truskett, Annu. Rev. Chem. Biomol. Eng. **7**, 583 (2016)
50. J. Ruan, X. Ouyang, B. Liu, L. Chen, M. Xu, Z. Zhu, Z. Zhang, S. He, Rev. Sci. Instrum. **89**(12), 123306 (2018)
51. C. Xue, Y. Wu, F. Zhu, S. Yang, H. Liu, J. Zhao, L. Wang, R. Tai, Rev. Sci. Instrum. **87**(4), 043303 (2016)
52. N. Mojarrad, J. Gobrecht, Y. Ekinci, Microelectron. Eng. **143**, 55 (2015)
53. Y. Fukushima, N. Sakagami, T. Kimura, Y. Kamaji, T. Iguchi, Y. Yamaguchi, M. Tada, T. Harada, T. Watanabe, H. Kinoshita, Japan. J. Appl. Phys. **49**(6S), 06GD06 (2010)
54. J. Zhao, Y. Wu, C. Xue, S. Yang, L. Wang, F. Zhu, Z. Zhu, B. Liu, Y. Wang, R. Tai, Microelectron. Eng. **170**, 49 (2017)
55. B. Singh, M.S.J. Marshall, S. Waterman, C. Pina-Hernandez, A. Koshelev, K. Munechika, A. Knapitsch, M. Salomoni, R. Pots, P. Lecoq, V.V. Nagarkar, IEEE Trans. Nucl. Sci. **65**(4), 1059 (2018)
56. S. Liu, A. Vaskin, S. Addamane, B. Leung, M.-C. Tsai, Y. Yang, P.P. Vabishchevich, G.A. Keeler, G. Wang, X. He, Nano Lett. **18**(11), 6906 (2018)
57. A. Vaskin, R. Kolkowski, A.F. Koenderink, I. Staude, Nanophotonics **8**(7), 1151 (2019)
58. I. Staude, T. Pertsch, Y.S. Kivshar, ACS Photonics **6**(4), 802 (2019)
59. A.F. Cihan, A.G. Curto, S. Raza, P.G. Kik, M.L. Brongersma, Nat. Photonics **12**(5), 284 (2018)



Bo Liu was born in 1976. He received his Ph.D. in Nuclear Science and Technology from the University of Science and Technology of China in 2003. Since 2011, he has been a full professor at the School of Physics Science and Engineering, Tongji University. He is a director of the radiation physics branch of Chinese Nuclear Society. His main research activities focus on the applications of nanophotonics on scintillator-based detectors. He has published over 150 peer-reviewed papers, receiving over 2400 citations with h-index of 24. He holds more than 30 patents.



Xiaoping Ouyang was born in 1961. He obtained his Ph.D. in Particle Physics and Nuclear Physics from the Fudan University in 2002. He spent one year at the Oak Ridge National Laboratory as a visiting scholar. He is a full professor at the Northwest Institute of Nuclear Technology. His research interests are centered on the diagnosis technology of pulse radiation fields. He was elected as an academician of the Chinese Academy of Engineering in 2013. He has received many awards including the Qishu Outstanding Youth Award, the Ho Leung Ho Lee Science and Technology Progress Award, and the National Invention and Entrepreneurship Award. He has published over 180 peer-reviewed papers, receiving over 1100 citations with h-index of 13. He holds over 60 patents.

Chapter 10

Analog and Digital Signal Processing for Nuclear Instrumentation



Mathieu Thevenin and Yoann Moline

Abstract The recent integration technologies have provided important computing capacities in all aspects of the signal processing domain. Nuclear science benefits from the advances made in the domain of telecommunication. The most recent analog-to-digital converters can reach several Gigahertz, while heterogeneous designs allow the combination of different technologies enabling fast and real-time signal processing. Nevertheless, most of the nuclear applications today are designed to be executed offline, for example, using MATLAB or Python. This chapter addresses some of the ways to implement nuclear applications in real time using the most recent technologies by combining analog and digital approaches. The contributions of this chapter are as follows: (a) the detailed description of the steps of the signal acquisition chains for organic scintillators to the information processing, including examples from the most recent researches; (b) the provision of design guidelines to make an efficient partitioning between the analog and digital parts of a design. For the digital parts, it provides approaches to split an algorithm between glue logic and state-of-the-art electronics such as Field Programmable Gate Arrays (FPGAs) or ASIC and high-level programs embedded on microcontrollers or microprocessors.

10.1 Introduction

Plastic scintillators are combined with different technologies to form an acquisition chain suitable for measurement and other applications such as Radiation Portal Monitor (RPM). The acquisition chain must be designed carefully to obtain suitable

M. Thevenin

Université Paris-Saclay CEA SPEC CEA-CNRS UMR 3680, F91190 Gif-sur-Yvette, France
e-mail: mathieu.thevenin@cea.fr

Y. Moline

Université Paris-Saclay, CEA, List, Laboratoire Capteurs et Architectures Électroniques,
F-91120 Palaiseau, France
e-mail: yoann.moline@cea.fr

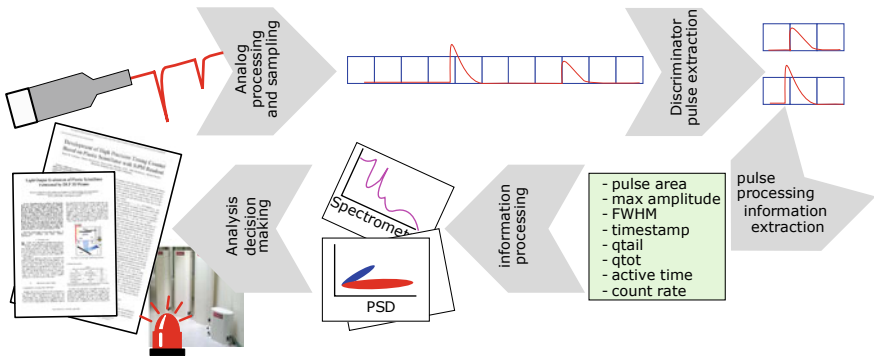


Fig. 10.1 Illustration of the different steps forming an acquisition and information processing chain: first the signal is analog, then it turns to samples after the digitization and the steps of signal processing. Finally, it is dissociated to single pulses that can be analyzed by data processing algorithms. They lead to actual measurements that can be used for decision-making

results. It is the result of decades of research and engineering in different fields such as physics, photonics, analog and digital electronics, and computer science.

The acquisition chain aims at converting the energy deposited into an actual measurement. The organic scintillators are particularly challenging since they can have low rise time and small pulse Full Width at Half Maximum (FWHM). The chain must preserve as much as possible the information (timings, pulse shape, etc.) delivered by the detectors since it can be used by the application. To do this, several steps are needed (Fig. 10.1); the firsts rely on photoelectric devices. Then analog filtering is performed, followed by, in modern acquisition chain, digital processing electronics. The design of the digital processing stages is crucial to achieve good performance and to accurately manage the dead time. Detecting and separating the pulses from the rest of the signal is the base of most of the applications, which is done by discriminators. Thus, each pulse can be analyzed by a digital pulse processing stage. This is where the features are extracted before the end-user application uses them.

This chapter presents the elements of the acquisition chain that can be used for organic scintillators from the light conversion to actual applications. First, Sect. 10.2 depicts the conversion of photons to light to electrical signals. Section 10.3 presents the basics of analog filtering. Section 10.5 explains the digital stream processing challenges. Then, discrimination leads to the pulse processing where information from each interaction (pulse amplitude, timestamp, etc.) is extracted. Finally, Sect. 10.6 gives some example of data processing applications in the domain of the organic scintillation.

10.2 The Light to Electric Signal Conversion

This section introduces the basics of the scintillator-based detector signal readout. It starts with a brief description of the approaches for the conversion of photons to measurable electrical signals. Next, it presents the most common analog signal preprocessing that can be done to achieve basic pulse shaping that matches with digitization requirements.

An acquisition chain for Digital Pulse Processing (DPP) applications where a plastic scintillator is the sensor, and by extension any kind of scintillator can be decomposed into a photosensitive device, an analog conditioning, eventually a shaping step and, depending on the approach, analog discrimination or digital conversion and digital processing. This section starts with the photosensitive device itself. To perform the scintillation light measurement, the scintillator can be coupled to a Photomultiplier (PM) which transforms the scintillation photons into photoelectrons and then into an electrical signal which can be measured by amplification (Fig. 10.2). Two major categories of photosensitive devices are suitable for organic scintillation among those available today: the Photomultiplier Tube (PMT); the Avalanche Photodiode (APD) and its pixelated version called Silicon Photomultiplier (SiPM), which can also be called Multi-Pixel Photon Counter (MPPC). The combination of these two solutions is called Hybrid PhotoDetector (HPD).

10.2.1 Design of PMTs

A typical PMT consists in a photoemissive cathode (photocathode) followed by focusing electrodes, an electron multiplier made of several dynodes, and an electron collector (anode) inside a sealed vacuum tube. To perform the actual conversion of photons into an electric measure, the incident light follows several steps [1] (Fig. 10.3):

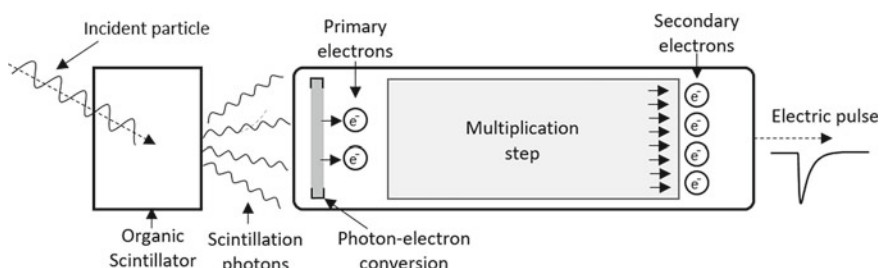


Fig. 10.2 Schematized view of a PM: the organic scintillator (on the left) coupled to a multiplier section which converts the light into an electric signal (on the right)

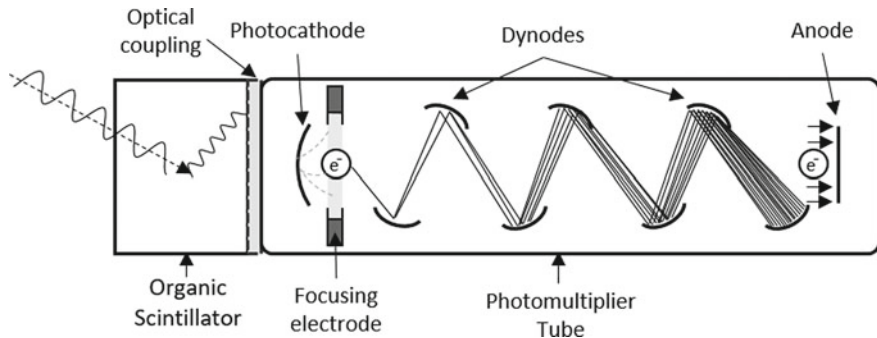


Fig. 10.3 Schematized view of a PMT displaying the focusing electrode, the dynodes, and the anode

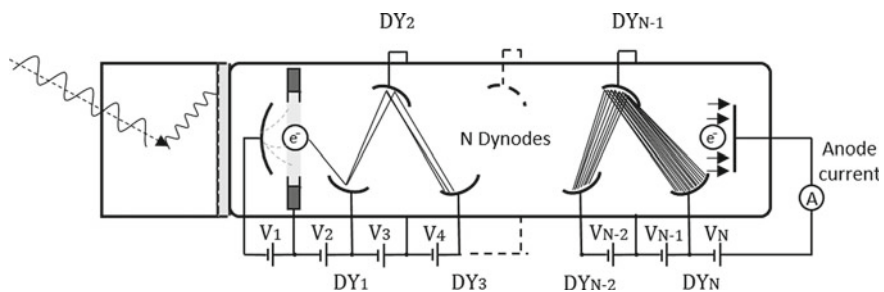


Fig. 10.4 Schematized view on how the voltages are applied to each dynode in order to generate electron multiplication

- the light is converted into current by the photocathode by means of the photoelectric effect. The photons excite electrons, some of which are emitted from the photocathode material surface into the vacuum. The emitted electrons are called photoelectrons;
- the photoelectrons are focused with a focusing electrode onto the first secondary-electron emission surface, called a dynode. The number of photoelectrons is multiplied via the secondary-electron emission effect;
- the secondary emission is repeated several times, indeed, each cascaded dynode emits two to three electrons for received electron. This slightly increases the electric potential and leads to six or seven orders of magnitude amplification;
- the secondary electron emission from the last dynode is finally collected by the anode.

Further discussion about the engineering of PMTs and their usage can be found in the manufacturer technical documentation [2]. To raise the electric potentials on each dynode, the PMT is biased by a High-Voltage (HV) power supply that connects to a voltage divider. The voltage divider applies the biasing to the dynodes (Fig. 10.4).

The choice and the assembly of the PMT are crucial and not trivial due to the wide possibilities offered by the manufacturers. A recent example of how the Pulse-Shape Discrimination (PSD) performance can be influenced by the choice of the PMTs is given in [3].

This section focuses on the electric characteristics and the optimizations of the system for the plastic scintillation applications. For the configuration of the PMT, we have chosen to discuss the following three elements: the photocathode, the type of dynode, and the mounting of the voltage divider circuits. The elements associated with the light collection, the detection surface, the optical coupling, and light guide are discussed in Chap. 9 of this book.

10.2.1.1 The Photocathode

Choosing a correct photocathode is the first of the three important aspects of matching a PMT with its application. The choice is mainly based on the photocathode Quantum Efficiency (QE) and is given by Eq. 10.1 with N_{pe} , the number of photoelectrons created, and $N\gamma$, the number of incident photons. It can simply be described as the ratio between photoelectrons and incident photons. It is expressed as a percentage at a specific wavelength. For example, 100 incident photons impinging a photocathode with a QE of 30% means that it will produce 30 photoelectrons, that is to say, the higher the better.

$$QE[\%] = \frac{N_{pe}}{N\gamma} \approx \frac{Sk[\frac{mA}{W}] \cdot 124}{\lambda} \quad (10.1)$$

The QE of a photocathode is governed by two main parameters: its chemical nature and its operation mode. Photocathodes are generally made of alkali metals or semiconductors activated with alkali. They can operate in two modes: reflection or transmission, depending on the tube configuration [4, 5]. In the reflection mode, the electrons are emitted from the illuminated side of the photocathode. In transmission mode, the photoelectrons are emitted from the backside of the photocathode. The reflective mode is commonly used in side-on PMTs and the transmission mode type is typically used in head-on tubes. Most of the plastic scintillator-based applications use transmissive photocathodes, generally providing a high QE [6], which is why this section focuses mainly on this configuration. Actually, the energy fidelity of a PMT device is more correlated to the cumulus of the QE over the whole spectral range of the PM than the peak QE, which is only given for a specific wavelength. That said, for PSD applications which use timing differences to perform discrimination such as neutron/gamma, one would choose the PMT that provides the best QE.

Instead of using the QE and for more convenience, PMT manufacturers provide the radiant sensitivity (Sk), expressed in mA/W for a given wavelength usually in nanometer. The radiant sensitivity is directly connected to the current by Eq. 10.2 where L_p denotes the incident radiant flux, I_k the measured resulting photocurrent, λ , the wavelength, $c = 3.00 \times 10^8 \text{ m s}^{-1}$, the speed of light, $h = 6.63 \times 10^{-34} \text{ J s}$, Planck's constant, and $qe = 1.6 \times 10^{-19} \text{ C}$ the charge of an electron.

Table 10.1 Photocathode material characteristics in transmission mode, extracted from [6]

Photocathode material	Window material	Spectral response			
		Spectral range (nm)	Peak wavelength		
			Radiant sensitivity (mA/W)	λ (nm)	Quantum efficiency (%)
CsI	MgF ₂	115–200	14	140	13
CsTe	MgF ₂	115–320	29	240	14
Bialkali	Borosilicate	300–650	88	420	27
Bialkali	Quartz	160–650	88	420	27
Multialkali	Borosilicate	300–850	64	420	20
Multialkali	Quartz	160–850	64	420	25
GaAsP(Cs)	Borosilicate	300–720	180	580	40
GaAs(Cs)	Quartz	380–890	85	800	14
InP/InGaAsP(Cs) ^A	Borosilicate	950–1400	21	1300	2.0
					1000–1300

^Arequires cooling down to –80 °C

$$Sk\left[\frac{mA}{W}\right] = \frac{lk}{IP} \approx \frac{Q\epsilon[\%] \cdot \lambda[nm] \cdot qe}{h \cdot c} = \frac{Q\epsilon \cdot \lambda}{124} \quad (10.2)$$

A list of the different materials used for the photocathodes is provided by the manufacturer handbook [6] (Table 10.1). It is organized to display the maximum radiant sensitivity and QE (right columns) and their associated wavelength. Photons at shorter wavelengths carry higher energy than the ones at longer wavelengths. This energy contributes to a higher probability of photo-emission. Therefore, maximum quantum efficiency occurs at a wavelength slightly shorter than the wavelength of maximum radiant sensitivity [1]. For example, for a Bialkali (Borosilicate) photocathode, if 100 pW is the received photo power, then the photocathode would produce 8.8 pA of current, since a radiant sensitivity of 88 mA/W. Similarly, luminous sensitivity is the amount of electrical current produced by a given amount of luminous flux, thus, 10 μlm of incident flux on this photocathode with a sensitivity of 95 μA/lm will produce 950 pA of current.

10.2.1.2 The Uniformity of the Photocathode's Electron Collection

The uniformity is the variation of the PMT response with respect to the incidence of the light when it interacts with the photocathode. The collection efficiency varies according to the position on the photocathode from which the photoelectrons are emitted and influences the spatial uniformity of a PMT. The spatial uniformity is also determined by the uniformity of the surface of the photocathodes themselves.

Although the focusing electrodes of a PMT are designed so that the electrons emitted by the photocathode or the dynodes are efficiently collected by the first or subsequent dynodes, some electrons may deviate from their desired trajectory [7] and the efficiency of the collection is degraded. The area where the sensitivity is uniform

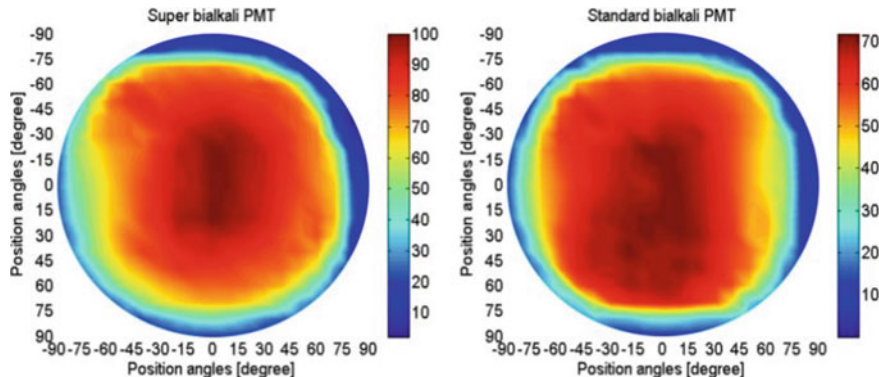


Fig. 10.5 Surface plot representation of the measurements of the detection efficiency of a PMT [9]

is called “useful cathode area” in some papers such as [8]. The photocathode surface uniformity evaluation can be performed by a scan with a laser; in [9], the number of pulses emitted by the laser is counted for each measured point, which leads to surface plots (Fig. 10.5).

Head-on versus side-on PMTs

Head-on PMTs give a better uniformity than side-on PMTs whatever the dynode type, essentially because of the less limited geometry. Logically, for a large-area PMTs like the ones used for neutrino observation experiments, this is an important parameter [9]. Similarly, those used for localization (with position sensitive/matrix sensor) applications must have good spatial uniformity.

10.2.1.3 Dynode Assembly as Electron Multipliers

If the photon-electron conversion is managed by the photocathode (efficiency), the dynode assembly (with voltage biasing) governs the multiplication (gain). It also impacts the signal shape and the temporal characteristics of the PMT output signal. In terms of electronics, it can be considered as the first stage of amplification of the instrumentation chain. As the first amplifier of the chain, the dynodes must raise the electronic signal level above the noise floor. To obtain the global sensitivity of the PMT, at the anode level, the sensitivity of the photocathode must be multiplied by the gain of the dynodes.

A large variety of dynode shapes are commercially available (Fig. 10.6) with different dynode types and characteristics (Table 10.2).

The most conventional types of structures for the dynode assembly are the box-and-grid, linear-focused, and circular types. If their configurations are different, the

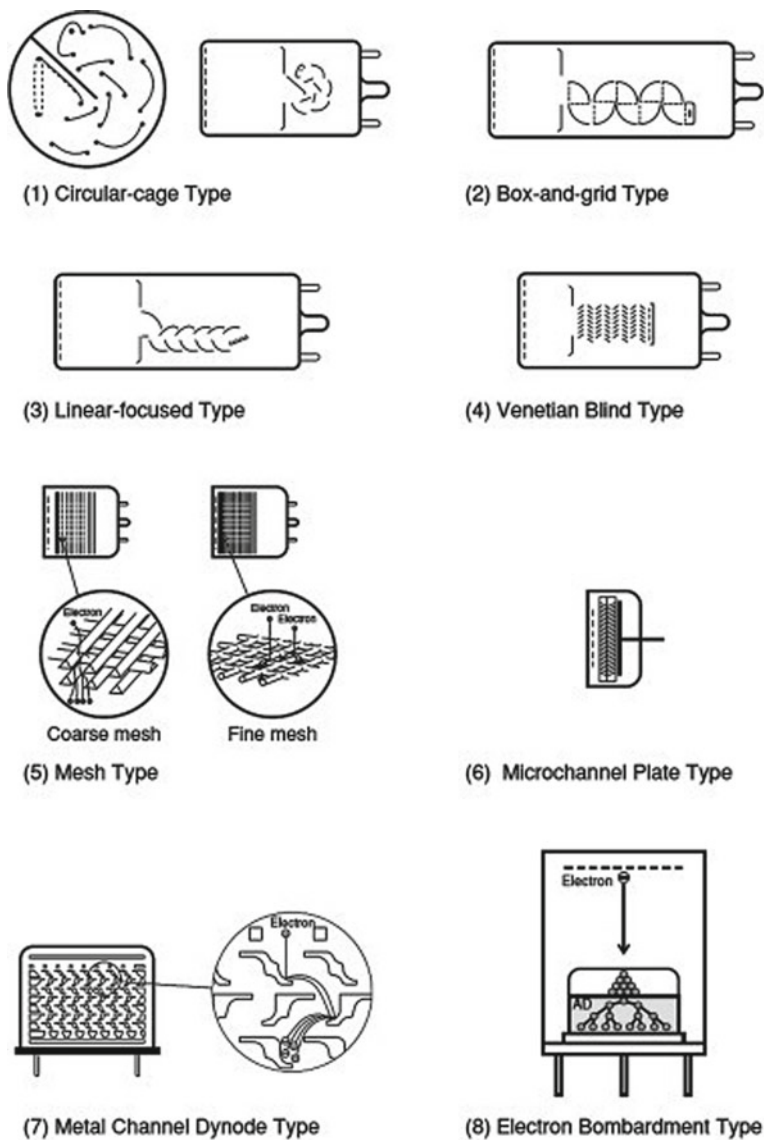


Fig. 10.6 Overview of existing dynode shapes and electron multipliers, obtained with the permission of Hamatasu Photonics from [6]

technique remains the same: the electrons are reflected from one dynode to another. Of course, some electrons may deviate from their favorable trajectories, not contributing to the multiplication, and different dynode arrangements can limit this effect. The circular-cage dynode type features a fast time response, the box-and-grid offers a high detection efficiency and good uniformity, while the linear-focused type offers a

Table 10.2 Dynode geometry characteristics [6]

Dynode type	Rise time (ns)	Pulse linearity at 2% (mA)	Magnetic immunity (mT)	Uniformity	Collection efficiency	Features
Circular-cage	0.9–3.0	1–10	0.1	Poor	Good	Compact, high speed
Box-and-grid	6–20			Good	Very good	High collection efficiency
Linear-focused	0.7–3	10–250		Poor	Good	High speed, high linearity
Venetian blind	6–18	10–40		Good	Poor	Suited for large diameter
Fine mesh	1.5–5.5	300–1000	500–1500 ^A	Good	Poor	High magnetic immunity, high linearity
MCP	0.1–0.3	700	1500 ^A	Good	Poor	High speed
Metal channel	0.65–1.5	30	5 ^B	Good	Good	Compact, high speed
Electron bombardment type	Depends on internal semiconductor		—	Very good	Very good	High electron resolution

^Ain magnetic field parallel to the tube axis

^Bmetal package PMT

combination of fast time response, good time resolution, and excellent pulse linearity. This is because the inner volume of the PMT is filled efficiently, thus, many dynodes can be used. Moreover, it allows the cathode and the anode to be insulated, preventing any feedback.

In the Venetian blind configuration, the dynodes are wide strips of material placed at a 45-degree angle to the electron cascade axis. This technique provides a large entry surface for the incident primary electrons. The dynodes are placed inline, therefore a fraction of the primary electrons can pass directly through them, which reduces the gain and causes variations in transit time.

As far as the four previously mentioned types of architectures are concerned, the linear type seems to offer the best overall performance. However, application specificities must be taken into account. For example, if linearity over a modest current range is desired, then the Venetian blind configuration would do as well as a linear-focus type and at a lower cost.

Mesh type dynodes use mesh electrodes stacked close together. They are mainly developed for tubes used in high magnetic fields and are not detailed here because they are outside the intended field of applications.

Micro Channel Plates (MCPs) can also be used as dynodes with a gain comparable to the conventional ones (up to 10^6). Due to their very small dimensions, their transit times are only a few nanoseconds, compared to a few tens of nanoseconds for the others. Moreover, this small size usually makes PMTs-MCP much less sensitive to magnetic fields. A particular issue when using MCPs is that a cascade in one channel drains the neighboring channels for several milliseconds [10], resulting in non-linearities for counting rates above a few thousand events per second. This kind of issue makes MCPs not suitable for applications where the count rate can be very high (10^5 – 10^6 counts per second).

Metal Channel Dynodes consist in an extremely thin stacked electrodes. As each dynode is very close to the others, the length of the electron path is very short which guarantees excellent timing characteristics and stable gain even under magnetic fields. Generally, they are used in a special multi-anode design to form a position-sensitive sensor. Unfortunately, high crosstalk and non-uniformity across the channels limit their potential, and nowadays SiPMs, which will be introduced further, can easily compete with them [11].

In the electron bombardment-type dynodes, the photoelectrons are accelerated by high voltage and hit a semiconductor; this transfer of the photoelectrons energy to the semiconductor produces a gain. This simple structure presents a low noise, excellent uniformity, and high linearity. HPDs are actually PMTs combining this technology with APDs; they will be detailed further.

The electrical characteristics of a PMT depend not only on the type of dynode but also on the size of the photocathode and the focusing system. The typical performance characteristics of PMTs can be organized according to their dynode types (Table 10.2). Based on these descriptions, three major criteria can be considered to choose the right PMT: timing characteristics (such as transit time), light collection efficiency, and uniformity and linearity.

Hybrid PMTs

Each type of multiplier reflects trade-offs between parameters, hybrid electron multipliers PMTs are designed to optimize these trade-offs. In the case of the box and the linear focusing multiplier, the collection sensitivity and the magnetic immunity of a conventional linear focusing multiplier were improved thanks to a new design of the input optics and the first dynode.

10.2.1.4 Timing Characteristics

In the case of radioactivity measurements made by organic scintillators, good timing characteristics (i.e. fast time response and low spread) are required in many applications, and they actually become crucial for time correlation, time coincidence, and Time-of-Flight (ToF) applications. Indeed, they are based on accurate event datation which cannot suffer from important variations.

When measuring from pulsed light, the output signal of the anode should mimic the native waveform of the incident pulses. The latency time—also called electron transit time—is determined by the time taken by the electrons to pass through the tube from a photocathode to an anode. It varies from one shot to another because photoelectrons and the secondary electron beams can take different paths through a tube (Fig. 10.7). These variations introduce randomness which appears for both the electron transit time and the rise time of the anode pulse.

Generally, extremely short light flashes are used to characterize these timing characteristics. The rise time is the necessary time for the PMT output to go from 10–90% of the maximum amplitude. The electron transit time is the time between the arrival of a pulse and the instant when the anode output reaches its peak value. It is specified at the FWHM of the histogram of the electron transit time. The variations (jitter effect) of the transit time is called the Transit Time Spread (TTS). The typical electrical signal of a PM in response to an optical delta function input, which could be a single photon, forms a pulse (Fig. 10.8).

The time response and biasing voltage correlation

The time response depends on the dynode type, it is tightly coupled to the PMT biasing voltage. Indeed, increasing this voltage improves the electron transit speed and shortens the transit time [1].

Fig. 10.7 Illustration of different electron trajectories causing different transit times (or latency) and affecting the collection efficiency

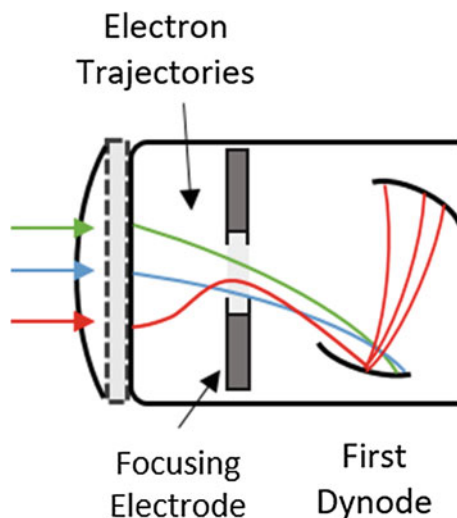
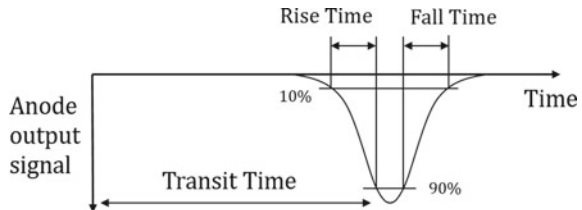


Fig. 10.8 Temporal response of the PMT: an optical delta function input such as a single photon [6]



Fast PMTs

In PMTs the transit time of the electrons is fairly small (between a few nanoseconds and some tens of nanoseconds), and more importantly it exhibits a relatively small spread—depending on the electrode design. In many cases, the distribution of the transit time, and consequently the rise time of the output signal may be larger than 10 ns. However, with optimized electrode designs it can be far below 1 ns. Therefore, the detection bandwidth can be several gigahertz. This is an important parameter to consider for the signal acquisition and processing since the electronics needs to be able to cope with such high frequencies.

10.2.1.5 Dynode Collection Efficiency

The electron multiplication mechanism of a photomultiplier tube is designed taking into account the trajectories of the electrons in order to efficiently multiply the electrons at each stage of the dynode arrangement. In a PMT, the acceleration electric field is created by the application of electric potentials to the dynodes (Fig. 10.3), (Fig. 10.7). However, some electrons may deviate from the favorable trajectories following the electric field; thus, they are lost for the multiplication. The collection efficiency of the first dynode (i.e. the dynode immediately following the photocathode) is the most critical and must be optimized to be higher than 60–90% [1]. It is commonly achieved by focusing the trajectories of the photoelectrons between a photocathode and the first dynode using a focusing electrode. Eventually, the same technique can be found between the different dynodes.

If the objective is to minimize electron transit times, collection efficiency can be sacrificed to get not only shorter distances between dynodes but also higher electric fields. If collection efficiency is probably the first criteria for selecting a PMT, it is important to note that if the cathode's first dynode voltage is low, then the number of photoelectrons entering the effective area of the first dynode is also low, resulting in a slight decrease in collection efficiency.

In addition to the temporal response and to the collection efficiency mentioned above, the spatial and angular uniformities of the detection efficiency depend on the

dynode shape, and will be discussed further. Equation 10.3 gives the photodetection efficiency PDE for a given radiant flux; C_E denotes the collection efficiency.

$$PDE[\%] = Q\epsilon[\%] \cdot C_E[\%] = \frac{Sk[\frac{mA}{W}] \cdot 124}{\lambda} \cdot C_E \quad (10.3)$$

10.2.1.6 Linearity of the Response of a PMT

Linearity can be defined by the proportionality between the quantity of light input and the output current. The proportionality between the incident flux and the anode current is called current linearity. Ideally, the anode output of the PMT varies linearly with the intensity of the incident light. However, non-linearity arises when the light intensity increases to an extent similar to a saturation effect. Both the cathode and the anode affect the linearity. It is commonly accepted that PMTs have good overall linearity [12].

Linearity

On both sides, a rule is always valid, the greater the output current, the greater the error. On the cathode side, the cathode linearity also differs depending on the photocathode materials (Table 10.1), and the constructor gives the low and high current terminals for each type of dynode.

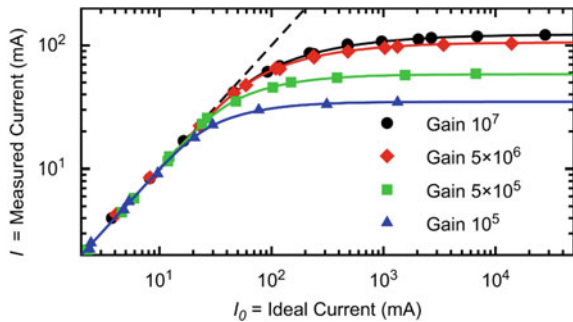
To reduce the effects of photocathode resistivity on the device linearity without degrading the collection efficiency, it is recommended to apply a voltage of 50–300 V between the photocathode and the first dynode, depending on the structure [6]. Linearity is not a significant problem for the reflection-mode photocathodes since they are made of a metal plate whose resistivity is quite low.

On the anode side, in order to keep linearity as high as possible, it is necessary to have a strong magnetic field in the last multiplication stages, where there are more electrons. The linearity is affected by the voltage-divider circuit (HV, current divider and decoupling capacitor) and is described in the next subsection.

To summarize, both cathode and anode linearity characteristics are dependent on the incident light level for a constant voltage, but not to the light wavelength. For PMTs, a strong connection between linearity and gain holds. In general, whatever the dynode type is selected, it provides better pulse linearity when the supply voltage is increased [13] (Fig. 10.9).

Linearity is therefore an important parameter to take into account for applications intended to measure high energies or high rates of interaction/counting which by pile-up also increases quickly the average value of the current produced.

Fig. 10.9 PMT linearity as a function of gain.
Reproduced with permission from [13]



Choosing a PMT

With the view of the different parameters, choosing the right PMT configuration is strongly dependent to the type of dynode. In addition, the characteristics of the PMT may vary depending on the size and shape of the dynode as well as the application context (laboratory or on site with noisy magnetic field) and measurement requirement (timing, energy or count rate)). The most suitable form of dynode should be chosen according to a particular application. There are trade-offs between configurations that minimize TTS and those that maximize collection efficiency or the uniformity of the spatial response. Unfortunately, there is no rule to follow to make the best choice, but we provide some small guidelines.

10.2.1.7 PMT Gain and the Voltage Divider Circuit

As explained before, the dynodes amplify the current by a factor called gain. It depends on the number of dynodes in the multiplier section and on a parameter called the *secondar*. It is defined as the number of secondary electrons emitted per primary electron. δ is a function of the voltage between each stage of the dynodes, V_d , and is given by Eq. 10.4 with A a proportionality parameter, and k is a coefficient determined by the material and the geometric structure of the dynode. It generally has a value in the range 0.7–0.8.

$$\delta = A \cdot V_d^k \quad (10.4)$$

The secondary emission ratio is given by Eq. 10.5 where I_k the current of photoelectrons hits the first dynode, then a current of secondary electrons I_{d1} is emitted. Generalizing for the n^{th} dynode, the secondary emission ratio δ_n can be expressed by Eq. 10.6, where I_{dn} and $I_{d(n-1)}$ denote the emitted current and the incident current of the n^{th} dynode. At the other end of the multiplication cascade, the anode current I_a is given by Eq. 10.7, with CE , the collection efficiency.

$$\delta_1 = \frac{I_{d1}}{Ik} \quad (10.5)$$

$$\delta_n = \frac{I_{dn}}{I_d n - 1} \quad (10.6)$$

$$Ia = Ik \cdot C_E \cdot \delta_1 \cdot \delta_2 \cdot \dots \cdot \delta_n \quad (10.7)$$

The gain of the PMT called G is given by Eq. 10.8. Assuming that a voltage Vd is applied and equally divided between the dynodes, the overall gain G of the PMT can then also be obtained by Eq. 10.9. Therefore, in the case of a PMT that operates with an equally distributed divider, the gain G varies as a function of the bias voltage Vb as given by Eq. 10.10.

$$G = \frac{Ia}{ik} = C_E \cdot \delta_1 \cdot \delta_2 \cdot \dots \cdot \delta_n \quad (10.8)$$

$$G = (A \cdot V_d^k)^n \quad (10.9)$$

$$G = A^n \cdot \left(\frac{V_b}{n+1} \right)^{kn} \quad (10.10)$$

The gain expressed in Eq. 10.10 is proportional to the exponential power kn of the bias voltage. This implies that if the number of dynodes is large, a small change in the bias voltage will result in a large gain difference. To maintain the gain stability, some manufacturers recommend, when selecting the biasing voltage, to pay attention to the line regulation, the load regulation, ripple noise, and the temperature coefficient [6]. Gain fluctuations, and in particular fluctuations in the gain of the first dynode, seriously affects the energy resolution capabilities of the instrument. This, combined with the linearity issues discussed above, may increase the risk of variability in the distribution of the pulse heights.

Biasing with batteries

Ideally, batteries would be the best source of stabilized voltage, but their number makes such a scheme difficult to realize[14].

10.2.1.8 PMT Voltage Divider and Polarity

The design of the divider network is crucial to get the best performance out of the PMT and ideally must follow the datasheet's recommendations. A resistive voltage divider is generally used to obtain all the required voltages from a 1–2 kV high voltage supply. The high voltage supply can be generated from a low supply voltage using

a DC-to-DC converter, or alternatively with a moderately complex power supply at the grid. However, it is important to understand that the inter-electrode voltage distribution is a trade-off between certain performance parameters (a high voltage between cathode and the first dynode is however always recommended). For example, three kinds of voltage divider circuits are given in [14]:

- A is called iterative voltage distribution with the same voltage for all multiplier stages except the first few. This distribution provides the highest gain for a given supply voltage and tends to provide good linearity, which is naturally adapted for nuclear spectroscopy.
- B is called progressive voltage distribution (increasing from the cathode to the anode). This distribution provides the highest linear peak current but with a much lower gain than configuration A.
- C is called intermediate-progressive voltage distribution. It optimizes the time characteristics while providing acceptable gain and linearity. Type C dividers are particularly suitable in physics experiments requiring accurate timing combined with good linearity over a wide dynamic range.

For most scintillation applications, the common method is generally a compromise between A and C. This method uses a stabilized high-voltage power supply in conjunction with a voltage divider (Figs. 10.10, 10.11). This system consists of resistor voltage dividers chosen to provide the desired voltage to each dynode. Variable resistors can also be placed, for example, between the cathode and the focusing electrode, allowing customization of the gain for fine calibrations. To limit the effects of non-linearity and fluctuations, it is important that the current in the resistance chain, known as the bleeder current, remains large compared to the tube current. Equation 10.11 shows the variation of gain with the anode current where I_a is the average anode current and I_{bl} is the bleed current. In order to achieve a high stabilization of the voltage step, the voltage divider must be specially designed to keep the bleeder current I_{bl} as large as possible with regard to the anode current I_a in the tube. This is challenging because the current in the tube can vary on a wide range depending on the frequency of measured events.

$$\frac{\Delta G}{G} = \frac{I_a}{I_{bl}} \cdot \frac{n(1 - \delta) + 1}{(n + 1) \cdot (1 - \delta)} \quad (10.11)$$

For scintillation applications, the PMT operates in pulse mode. In order to maintain the linearity of the PMT in this mode, it is necessary to manage the peak currents, especially in the last stages. There are several solutions to avoid momentary potential drops. For example, the last stages can be kept at a fixed potential by adding decoupling capacitors (Figs. 10.10, 10.11). These capacitors supply the photomultiplier tube with an electrical charge during the formation of the signal pulse and limit the voltage drop between the last dynode and the anode, resulting in a significant improvement in the linearity of the pulse. In other words, they provide the charges required during the duration of the pulse.

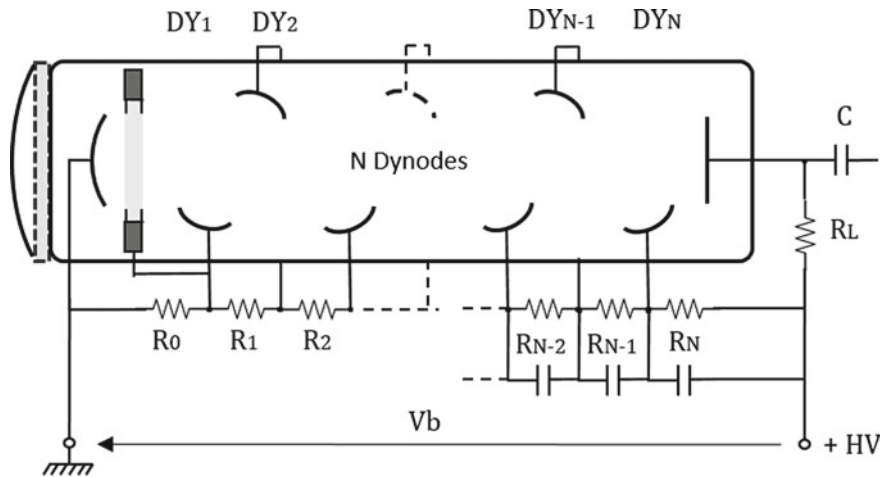


Fig. 10.10 Positive high voltage supply configuration for a PM

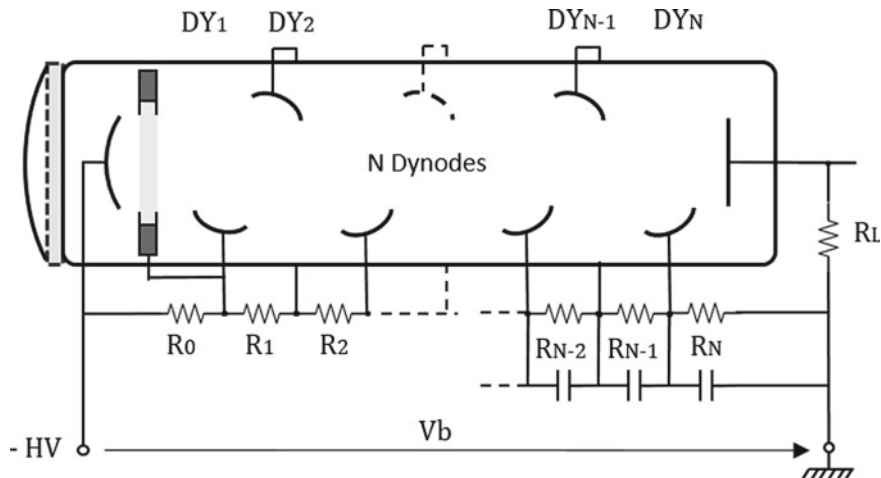


Fig. 10.11 Negative high voltage supply configuration

The literature proposes also solutions based on Zener diodes [14] or transistors [15]. Resistors are replaced, either for maintaining a constant voltage for currents above a minimum threshold (for example, in very high current applications) or for limiting the anode current to a few percent of the divider current, which makes the last inter-stage voltage drops negligible.

10.2.1.9 High Voltage Supply Polarity

PMTs can operate with a high positive or negative voltage, as long as the potential of the dynodes is negative with respect to the photocathode. When the positive biasing is used, the cathode is grounded and the anode is at the high positive potential (Fig. 10.10). When negative biasing is used, the anode is grounded and the cathode is at high negative potential (Fig. 10.11).

If the PMT manufacturers justify the choice of polarity from a practical point of view (for example, magnetic immunity, integration, lifespan, and wiring), their given recommendations considering an application point of view (PSD, time-stamping, photon-counting, etc.) are scarce. For similar applications, one can see a difference in polarity choices in the literature [16–19].

Polarity

Historically, PMTs were all powered by positive high voltage, but nowadays, many of them are also powered by negative high voltage. Each of these two approaches has advantages and disadvantages and, of course, they require a somewhat different design of the voltage divider. In all cases, the polarity of the high voltage supply is a key parameter, and the user must ensure that the correct polarity of the high voltage is applied to ensure that no damage occurs.

Overview of the positive biasing

There are two practical advantages of using positive high voltages. They combine the signal and + high voltage over a single cable, with a splitter. The second is the convenience of positive polarity because it does not require isolating the tube from its environment and thus minimizes the noise level. However, with this grounded cathode scheme, a coupling capacitor (C) must be used to separate the positive high voltage applied to the anode from the signal. Thus, this implies that the anode signal, which is basically negative due to the charge of the electrons, displays a small positive swing (overshoot) above the baseline (Fig. 10.12) as the decoupling capacitor acts as a high-pass filter. Each swing through Zero is called a pole in the signal and can be corrected by analog or digital filtering, the Pole-Zero compensation. In the case of scintillation counting positive high voltage supply, a baseline-offset problem may occur if the count rate increases too much (Fig. 10.13). The value of the decoupling capacitor must be chosen according to the expected pulse duration and load resistance of the amplifier.

Positive high voltage supply makes the system less sensitive to the noise and offers practical wiring advantages. However, the decoupling stage must be designed to keep the signal pulse shape and the baseline integrity, especially at high count rate [20].

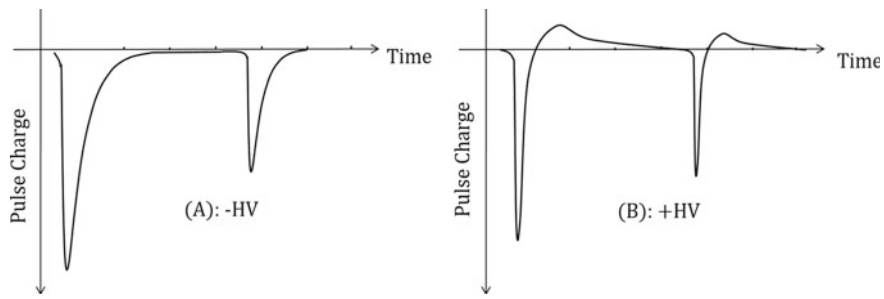


Fig. 10.12 On the left, the signal without a decoupling capacitor; the baseline is set at the positive voltage supply. On the right, the same signal after a decoupling capacitor; the baseline is close to zero Volt

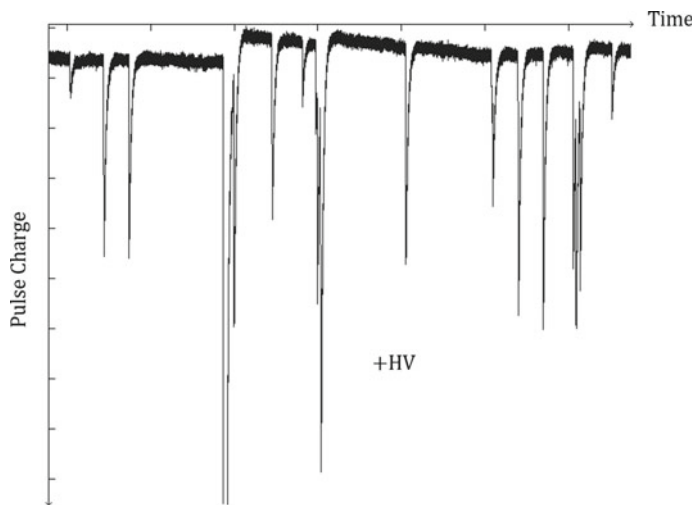


Fig. 10.13 Example of baseline drift due to the presence of overshoots when count rate is important in positive high voltage associated with a decoupling capacitor configuration

Negative high voltage overview

Beside the fact the experiment setup is less immune to the noise in the negative high voltage configuration, there are practical advantages. Since the anode is grounded, it facilitates the connection of the measuring electronics. The second advantage is linked to the absence of the decoupling capacitor since the Direct Current (DC) component of the signal is preserved. Moreover, their shape is not impacted by the decoupling capacitor which may directly benefit to the PSD applications. Moreover, the phase characteristics of the high-pass filter may generate a delay that must be compensated for applications where time resolution is critical.

This polarity is particularly suitable for applications with a high count rate without the risk of too much baseline-offset variation. However, a PMT with a negative high

voltage applied to the photocathode, which is housed in a metal case at ground potential, can cause electrons to strike the inside wall of the bulb, resulting in the production of dark noise [6] (non-thermal contributions) that would lead to dark pulses [17]. Manufacturers use special coating techniques to minimize this effect.

10.2.1.10 Pulses Obtained from a PMT

The output signal at the anode is a current or charge pulse whose total charge is proportional to the initial number of electrons emitted by the photocathode (within the linearity requirements presented). Therefore, the PMT can be represented by a Norton current generator [21] with parallel resistance and a capacitance (Fig. 10.14). R and C are the intrinsic resistance and capacitance which also include the anode load resistance and any external combination of resistors and capacitors in parallel coupled to the output of the photomultiplier (cables, etc.).

The shape of the pulse is determined by the combination of R and C . As presented in Chaps. 1 and 2 of this book, the scintillation phenomenon in a plastic scintillator can be described by a more complex exponential decay. The photoelectron current $I(t)$ is given by Eq. 10.12 with G the gain of PMT previously calculated, Npe the number of photoelectrons created, e the charge of the electron, and τ_s the decay time.

$$I(t) = \frac{G \cdot Npe \cdot e}{\tau_s} \cdot \exp(-t/\tau_s) \quad (10.12)$$

$$V_o(t) = \frac{G \cdot Npe \cdot e}{\tau - \tau_s} \cdot (\exp(-t/\tau_s) - \exp(-t/\tau)) \quad (10.13)$$

Equation 10.13 gives the output voltage with $\tau = R \cdot C$, the resulting curves may be used to predict the output signal (Fig. 10.15). For example, if the photomultiplier is connected to 50Ω impedance measurement circuit, the peak voltage is expected to be 100 mV for $Npe = 100$ photoelectron and $\tau = 1 \text{ ns}$. This model does not take into account the TTS of the photomultiplier which also affects the pulse shape.

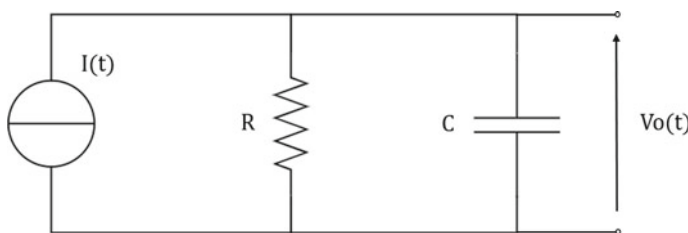
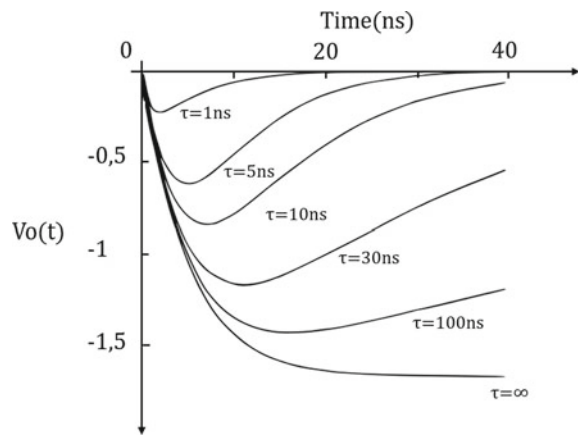


Fig. 10.14 Schematic of the theoretical equivalent circuit of a PMT

Fig. 10.15 Results of Eq. 10.13 for the following parameters
 $Npe = 100$ photoelectrons,
 $G = 10^6$, $\tau_s = 1$ to > 100 ns



Choosing the right constant time τ

The following guidelines can be drawn [21]:

- the output voltage is an accurate reproduction of the input current $I(t)$ only when $\tau \ll \tau_s$;
- the rise time is low and is essentially given by τ of the output circuit;
- for $\tau \gg \tau_s$, the pulse amplitude is larger but the rise time is now approximately given by τ_s while the decay time is essentially determined by the τ of the output circuit; in this mode the current is essentially integrated by C .

Working $\tau \gg \tau_s$ is preferred since it gives a large signal, which is free from fluctuations due to the integration by C . However, the longer decay time of the signal limits counting rates to less than $1/\tau$, after which signal pile-up occurs [14].

10.2.1.11 Source of Pulsed Noise in a PMT

There are several sources of noise in a PMT that can turn to the generation of pulses. The two most important ones are the dark current and the after-pulses. Even when a photomultiplier is not illuminated, a small amount of current still flows. This is the dark current (also called the anode dark current). It leads to the production of pulses when the PMT is under operating high voltage, even in an absolute dark environment [22]. These pulses are considered as noise, and they are a critical factor in determining the lower limit of the light detection. It is admitted to be greatly dependent on the supply voltage [2]. Major sources of dark current may be categorized as follows:

- thermionic emission from the cathode and dynodes;
- leakage currents;

- glass scintillation;
- field emission.

The materials of the photocathode emit tiny quantities of thermionic electrons even at room temperature. Most dark currents originate from the thermionic emissions, especially those from the photocathode since they are successively multiplied by the dynodes. The relation between temperature and thermionic emissions can be described by Eq. 10.14, Richardson's equation, where A denotes a constant, ϕ the work function, T the temperature (in kelvin), and k Boltzmann's constant. Equation 10.14 shows that the noise is strongly temperature-dependent. Therefore, a standard solution consists of cooling the photocathode to reduce thermionic emissions.

$$I = AT^2 \cdot \exp\left(\frac{-e \cdot \phi}{k \cdot T}\right) \quad (10.14)$$

As explained earlier, if the PMT is operated with the cathode at a high voltage and the anode at ground potential (negative bias), the electrons may deviate from their normal trajectories and strike the glass envelope. In this way, scintillation may occur and a dark pulse may result. This does not happen when the PMT is positively biased. If the high voltage is quite high (near the maximum value recommended by the manufacturer), electrons might be emitted from dynodes by the strong electric field and cause dark pulses. A solution is to configure the PM and its voltage divider to set up the high voltage supply to 70–80% of the maximum recommended value. Another source of dark current is the leakage current due to non-perfect electrical isolation. It contributes to the dark current and is predominant when the photomultiplier tube is operated at a low voltage or at low temperatures. Contamination from dust and moisture on the surface of the tube, base, or socket may increase the leakage current. The lowest dark current is achieved when the device has been kept in complete dark conditions for a few hours. It may be substantially higher for some time after exposure of the photocathode to brighter light.

The after-pulses are also dark pulses, but they can be distinguished by the interval that separates the after-pulse from a true pulse which comes from an interaction in the scintillator. Their number cannot be pre-estimated on the opposite of the dark pulses. They often spuriously limit the number of true pulses that can be detected. The effects of after-pulses can be minimized by using coincidence techniques or by the use of a dead time. They principally have two causes [23]:

- After-pulses may be caused by some light emitted by the last few dynodes, which travels to the photocathode. In such cases, after-pulses occurring during 20–100 ns [2] after the true pulse depend on the PM geometry. Since these are usually one-electron events, their amplitudes are generally small.
- The residual gases inside a photomultiplier tube can be ionized by the electrons. In this case, these photoelectrons can strike the photocathode or earlier stages of dynodes and trigger the electron multiplication process. This leads to relative large output noise pulses occurring from 300 ns to 3 μ s after the original pulse [2].

Overview of the PMTs

The PMT family presents many good features for usage in combination with organic scintillators: their ability to detect low light, their high gain, their low noise, and their large area of collection. However they also have several limits.

Due to the distribution of spatial loads on dynodes, linearity decreases as the gain increases. In addition, linearity is affected by not only several factors related to the structure of the device, such as the current divider, but also external factors like the power supply stability (see comment on batteries). The quality of the time and the energy responses requires a high investment in the configuration because it is affected by the transit time of the electrons in the tube, whose deviation depends on the structural characteristics of the device, such as the number of dynodes, the diameter of the photocathode, and again external characteristics like the supply voltage. Actually the high voltage supply and the voltage divider must be chosen and applied very carefully to preserve the useful characteristics of the signal. In addition, there are many sources of noise that can affect the signal and lead to the generation of dark currents and post-pulses even though recent advances made them less noisy. PMTs are highly sensitive to external magnetic fields. Indeed, under the effect of a strong magnetic field, photoelectrons and secondary electrons deviate from their normal trajectory, which affects both the efficiency of photoelectron collection and the gain of the electron multiplier. Finally, PMTs present a high risk of failure due to shocks and vibrations that quickly cause electrical connection failures, critically affecting the internal structure (especially dynodes) and may generate random behavior.

However, if the choice of the PMT and its configuration is carefully done, it is a venerable device usable for all applications based on organic scintillators, especially time-correlated applications and with high counting rate or PSD.

10.2.2 Solid-State Semiconductor Photodetectors

An alternative to PMTs are the solid-state photodetectors. These devices differ from the PMT by their working principle. In their case, the amplification mechanism occurs within a semiconductor material, rather than in a vacuum tube [24]. Silicon devices are based on the simple inverse PN junction. There are three distinct gain regions depending on the bias voltage. Depending on this gain, it is possible to distinguish three regimes and associated families of solid-state photon detectors (Fig. 10.16).

The PIN photodiodes are used in the first zone where the electric field in the avalanche region is too weak to excite the charge carriers to the minimum energy required for impact ionization of the lattice atoms. APDs are monolithic devices made of silicon PN junctions operating in a linear regime. Finally, SiPMs are matrices of Single-Photon Avalanche Diodes (SPADs) working at Geiger regime called. PIN photodiodes have no amplification gain; they totally rely on a charge amplifier. Therefore, this section focuses on APDs and on SiPMs.

Fig. 10.16 Gain regimes versus voltage bias

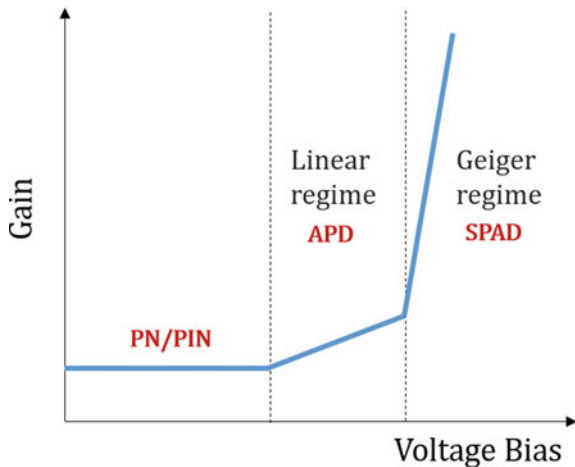
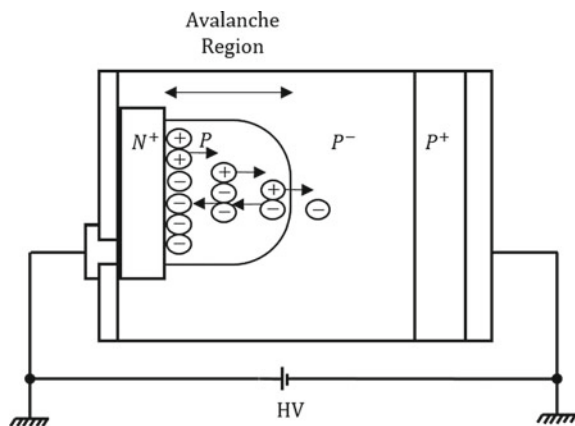


Fig. 10.17 Schematic diagram of APD structure



10.2.2.1 Avalanche Photodiode

APDs (Fig. 10.17) are able to detect light in the whole visible spectrum and are sensitive to even extremely weak signals. This makes them suitable for plastic scintillation application. In a linear regime, the gain is linearly proportional to the bias voltage. Indeed, if the voltage applied to the junction is sufficiently high, the interacting photons are converted into a cascade of electron-hole pairs. The primary charge carriers generated are accelerated and acquire enough energy to generate new pairs by impact ionization due to collisions with the crystal lattice, which in turn are accelerated by the electric field to trigger further events.

The incident photons are absorbed in a large intrinsic or lightly doped region (called p^+) in which they drift by entering into a fine p^-n^+ junction where an electric field can trigger the avalanche effect. The probability of obtaining an ionization for

an impact depends on the strength of the electric field. Either $irate_e$ or $irate_h$ impact-ionization coefficient represents the number of ionization events per unit length for electrons and holes. In silicon (Si), the ionization rate of the electrons ($irate_e$) is higher than the holes ($irate_h$), thus the electrons are the main contributor to the multiplication process. For this reason, the optimal design of an APD is obtained where only electrons are capable of triggering the avalanche process and therefore in which the electron-hole pairs are generated at the p -edge of the depletion layer.

In the impact-ionization avalanche process, each absorbed photon creates a finite number (M) of electron-hole pairs. The value of the multiplication factor M depends on the probability of the impact ionization and is given by Eq. 10.15, where W is the width of the depletion layer. The impact-ionization coefficients are strongly dependent on the reverse bias ($Vbias$), therefore, the multiplication factor can be empirically approximated by Eq. 10.16, with Vbd the breakdown voltage of the device and n a parameter depending on the material [25].

$$1 - 1/M = \int_0^W irate_e \cdot \exp \left[- \int_x^W (irate_e - irate_h) dx' \right] dx \quad (10.15)$$

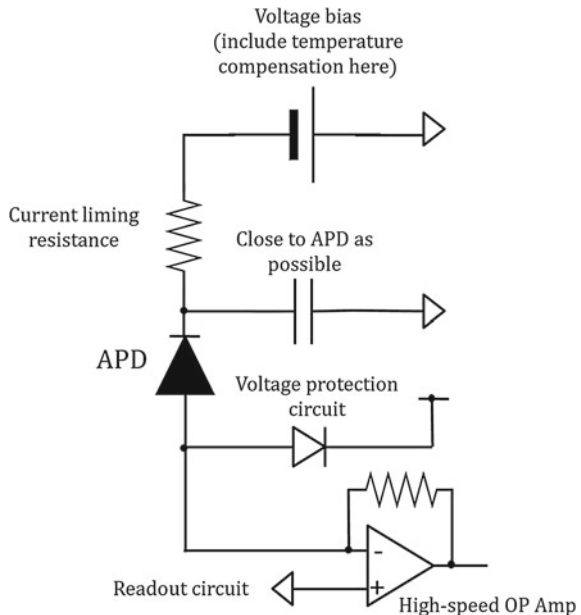
$$M = \frac{1}{1 - (\frac{Vbias}{Vbd}) \cdot n} \quad (10.16)$$

Finally, APDs generates noise in the multiplication process; there are some statistical fluctuations due to non-uniformities in the ionization and they increase with the gain. The noise, like the gain, exhibits a dependence on the energy of the incoming photon and thus its wavelength. At the same time, the photocurrent generated by a light pulse is also amplified by the gain. All these facts are a clear indication that best Signal-to-Noise Ratio (SNR) can be achieved for certain gain values. Despite these drawbacks, the APD is a turnkey component which can easily be used for scintillation applications coupled with organic scintillators as long as the need for energy (due to the low gain) and time resolution is low (scintillation counting). A readout circuit must be used in conjunction with APDs (Fig. 10.18).

10.2.2.2 SPADs and SiPMs

SPADs are APDs operating in the Geiger mode and are more commonly referred to as Geiger-Müller APD (GM-APDs). They operate above the breakdown voltage (Vbd) (seen in the previous section). Under such polarization conditions, the electric field generated in the depletion layer is so high (≈ 105 V/cm) that even a single carrier injected into the space charge region can trigger a self-sustaining Geiger avalanche, amplifying the original photoelectron into a macroscopic current flow. The breakdown voltage Vbd is therefore the minimum (reverse) bias voltage for which a current output pulse can be obtained. However, for $Vbias = Vbd$, the detection efficiency and the gain of the SiPMs are (by definition) always zero. Only for $Vbias > VBD$,

Fig. 10.18 APD circuit use case example: in order to achieve a constant output, the reverse voltage can be adjusted according to the temperature variations [26]



the current output pulses are observed. The overvoltage is the difference between V_{bias} and the breakdown voltage V_{bd} .

$$\Delta v = V_{bias} - V_{bd} \quad (10.17)$$

In principle, the higher Δv is, the higher the performance of the SiPM increases. In order to stop the avalanche current to restore the initial polarization conditions for the detection of new incoming photons, a so-called quenching mechanism is necessary. Quenching is usually performed by means of a passive circuit in which the current is drawn by the photodiode during the Geiger breakdown. It is limited by a high impedance load using a quenching resistor R_q higher than $100\text{ k}\Omega$ (Fig. 10.19).

The breakdown process of a GM-APD is described as follows: in steady state, the capacitance C_d (Fig. 10.20) of the diode is charged at a reverse voltage above the breakdown point (where $V_{bias} > V_{bd}$). When a carrier passes through the high electric field area (switch closed), it triggers an avalanche discharge. The new state of the system can thus be modeled by adding a voltage source V_{bd} with a series resistor R_s in parallel with the diode capacitance. R_s ($\approx 1\text{ k}\Omega$) comprises both the resistance of the neutral regions within the silicon and the resistance of the space charge region.

Therefore, when the avalanche is triggered, C_d discharges through the R_q to the breakdown voltage with a time constant $\tau_D = R_s C_d$, usually of the order of a few hundred picoseconds. As the voltage on C_d decreases, the current I_f flowing through the quenching resistor can then be defined by Eq. 10.20.

Fig. 10.19 A quenching resistor connected to a GM-APD; the use of values over $100\text{ k}\Omega$ is preferable

$$V_{bias} > V_{bd}$$

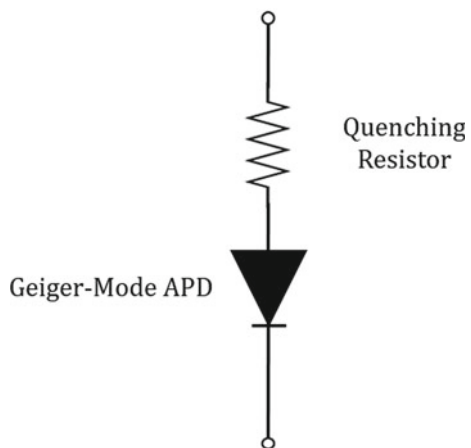
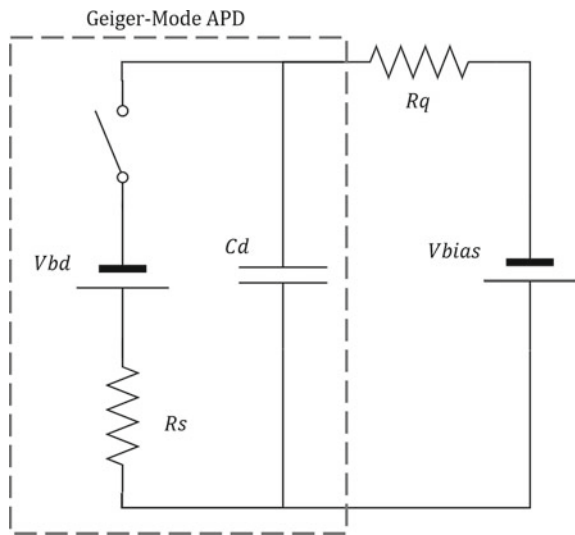


Fig. 10.20 The equivalent circuit of a GM-APD with series quenching resistor and the voltage source



$$I_f = \frac{V_{bias} - V_{br}}{R_q - R_s} \quad (10.18)$$

In the final phase, if R_q is sufficiently high (at least a few hundred $\text{k}\Omega$), the diode current is so low that a statistical fluctuation reduces the instantaneous number of carriers passing through the high-field region to zero, thus extinguishing the avalanche [27]. When the avalanche process is stopped, the switch is opened again and the circuit returns to its original configuration, with the diode capacitance being recharged to V_{br} . Then the capacitor C_d is recharged to the bias voltage with a time constant

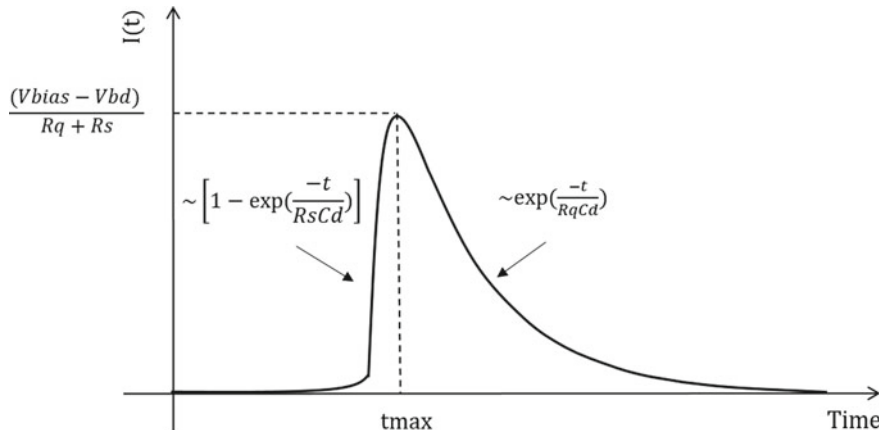


Fig. 10.21 The current pulse produced by a GM-APD in response to a photon absorption

$\tau = C_d \cdot Rq$, and the device becomes ready to detect the arrival of a new photon. Therefore, the output current caused by the Geiger discharge is a pulse with a fast rise time, with a decay time constant τ_R of duration equal to the time it takes for the Geiger discharge to be stopped by the quenching resistor. A characteristic pulse produced by a GM-APD is shown in Fig. 10.21; here, the integral of the current $i(t)$ corresponds to the charge Q produced by the avalanche (Fig. 10.21).

Since the charge is due to a single charge injected into the avalanche region, the gain G for this process can be defined by Eq. 10.19. A typical value for the gain G is between 10^5 and 10^6 . The main limitation of GM-APDs is that the output signal is the same regardless of the number of interacting photons. Indeed, a single photodiode operating in the Geiger mode operates as a photon-triggered switch, with a binary “ON” or “OFF” state, and therefore only provides information on whether a signal is detected or not, without providing an output proportional to the intensity of the incident photon flux (Fig. 10.22).

$$G = Q/e \quad (10.19)$$

SiPMs are designed to counterbalance the “ON/OFF” effect and to obtain a signal proportional to the number of photons emitted (therefore suitable for scintillation, for example). They are composed of GM-APDs (called pixels), all identical, connected in parallel, and arranged in a rectangular array (Fig. 10.23) over a small area, typically a few mm^2 [28]. Unlike APDs, in order to achieve good optical isolation between the micro-cells, the photosensitive surfaces of SiPMs contain certain insulating sections between the pixels that cannot detect light. In addition, all pixels have their own quenching resistance.

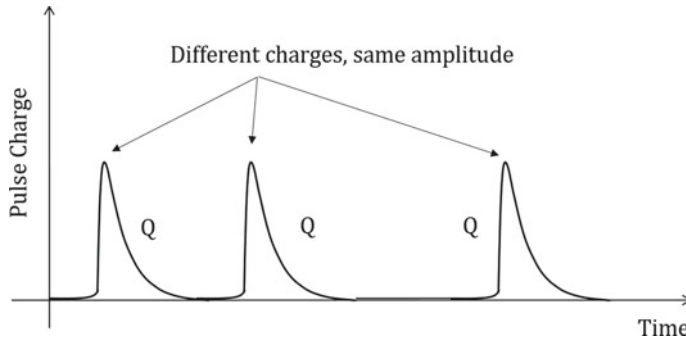


Fig. 10.22 Output charge of a GM-APD is not proportional to the number of incident photons

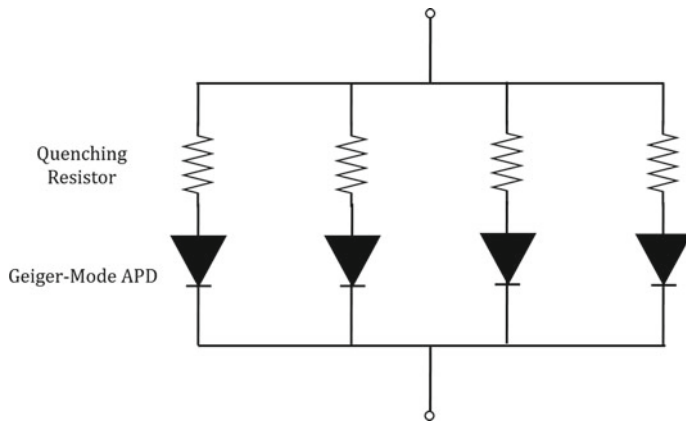
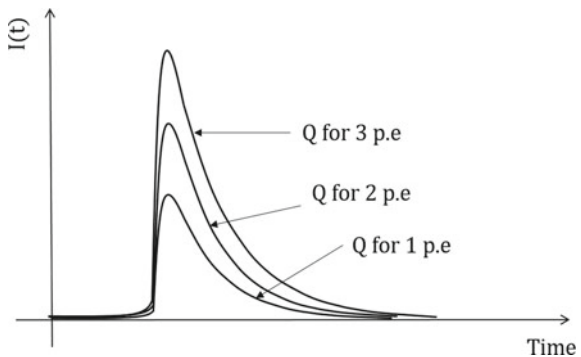


Fig. 10.23 Schematic of the parallel arrangement of GM-APDs with series quenching resistor in SiPMs

Although each cell only offers a binary output, linearity with respect to the number of photons is achieved by summing the cell outputs. If more than one pixel developed an avalanche reaction, the total charge of Q_{tot} became a factor of the number of these cells as presented by Eq. 10.20, where N_f is the number of pixels that nearly simultaneously “fired” or developed avalanches. This equation shows that Q_{tot} is proportional to $(Vbias - Vbd)$. The waveforms (Fig. 10.24) produced by an SiPM in response to a photon for various number N_f are simultaneously “fired” by independent pixels for one photoelectron (called *p.e.* for this example) on 1 pixel, 2 pixels, etc. thus highlighting the excellent photon counting capabilities of SiPMs and their extreme suitability for single photon detection applications.

$$Q_{tot} = N_f \cdot Q = N_f \cdot (Vbias - Vbd) \quad (10.20)$$

Fig. 10.24 Waveforms of current output of a SiPM producing signal when 1, 2, or 3 pixels are fired simultaneously in response to a photon; *p.e.* stands for photoelectron



Gain versus temperature

Due to the Geiger mode of operation, small variations of the biasing voltage or of the temperature can produce high gain variations. The most commonly used method is to use a Gamma spectrum with a scintillator capable of creating a photoelectric effect (usually inorganic...), or with a laser at a known energy [29]. We look at the position of the photoelectric peak at room temperature, in an isothermal environment, oven, or refrigerator. The temperature is measured using a temperature sensor connected to readout electronics to establish a gain correction formula based on the adjustment of these measurement data. Finally, this formula, if linear, can be integrated into an analog or, more easily, into a digital loop to modulate dynamically the bias voltage [30].

10.2.2.3 Photodetection Efficiency (PDE) of the SiPMs

The PDE of a SiPM is the statistical probability that an incident photon will produce a Geiger pulse from one of the SiPM cells. It is defined as the ratio of the number of detected photons to the number of incident photons during photon counting where the pulsed light enters the SiPM. The PDE can be expressed by Eq. 10.21 where $Q\epsilon$ denotes the QE of Silicon, ff the fill factor, and $P_{trigger}$ the avalanche initiation probability (or trigger probability) that takes into account the fact that not all generated photoelectrons are able to initiate an avalanche.

$$PDF = Q\epsilon \cdot ff \cdot P_{trigger} nea \quad (10.21)$$

The intrinsic QE of the silicon has typical values ranging from 80 to 90% and strongly depends on the thickness of topmost layers and of the depletion area. In order to have an element of comparison with the PMT section, the PDE of a SiPM can also be obtained by Eq. 10.22, where R is the responsivity (comparable in principle to the radiant sensitivity of a PMT), G is the gain of the SiPM, h is the Planck constant; c

is the speed of light; e is the charge of the electron, and λ is the wavelength of the incident photons. Reverse voltage increases, while the dependence on wavelength is directly correlated to the responsivity [31].

$$PDE = \frac{R \cdot h \cdot c}{G \cdot \lambda \cdot e} = 1240/\lambda \cdot R/G \quad (10.22)$$

The responsivity of the SiPM is defined as the average photocurrent produced per unit incident optical power. The PDE shows strong dependencies on the biasing voltage and on the wavelength. In particular, it increases with the reverse voltage value, while the dependence on wavelength is directly correlated to the responsivity [31].

Timing performances of the SiPMs

As for PMTs, SiPMs have a TTS, with typical values of the order of $\approx 10^2$ ps which is negligible for the majority of scintillation applications.

In general, the TTS of a SiPM decreases as the applied overvoltage and/or the number of incident photons increase. Some small fluctuations in the avalanche process can arise because of the lateral diffusion of the photons emitted in the avalanche [28]. The time required for the pixels to restore their steady-state conditions is called the recovery time and depends on the photosensitive area and on the pixel size. In particular, it typically ranges from a few tens of nanoseconds (for pitches of ≈ 10 μm) to a few hundreds of nanoseconds (for pitches up to 100 μm) [32]. This last value might become problematic for high scintillation counting rates.

10.2.2.4 Noise in SiPMs

The main source of noise limiting the SiPM performance is dark noise, after-pulses, and crosstalk. Like thermionic emissions of PMT, crosstalk of SiPM is tightly correlated to temperature. Dark noise pulses occur randomly and are due to thermally generated charge carriers reaching the avalanche region. When a pixel is in the “ready” state, the ensuing “dark” pulse is indistinguishable from one due to photon absorption. Such a pulse would be labeled Q for one photoelectron (Fig. 10.24). This means that after calibrating the dark noise of a measuring system, it is possible to find an adequate energy threshold to suppress this noise. However, this means that it is possible to suppress low energy during a scintillation measurement. Dark noise is highly dependent on the applied overvoltage, pixel size, and temperature.

Another important source of noise is the presence of after-pulses. During the Geiger avalanche process, some charge carriers can be temporarily trapped by certain impurities within the crystal lattice and thus generate a new break after their release (an after-pulse). They can be caused by a photo or a dark pulse. Their amplitude depends on how long they start from the original pulse. The closest ones are smaller than the original pulse since the extinction circuit has not yet maintained the capacitor

Cd at the nominal V_{bias} voltage—so the cells are not fully recharged. However, they have the effect of lengthening the recovery time, and that is how they can be detected. In the worst-case situation, if the carrier is released after the recovery time, the time elapses and the after-pulse indistinguishable from a standard pulse is generated by a photon or a dark pulse. However, each new generation of SiPM tends to lower the after-pulse probability, thanks to the use of improved materials and wafer processing technologies.

Some crosstalk may occur when, during a primary avalanche, electron-hole recombination produces ultraviolet photons. If the same pixel reabsorbs the photon, then, the resulting secondary pulse would look like an after-pulse. However, if a nearby pixel absorbs the photon, the secondary correlated avalanche may be close enough in time to the primary that the resulting waveform would be labeled Q for 2 p.e. in Fig. 10.24.

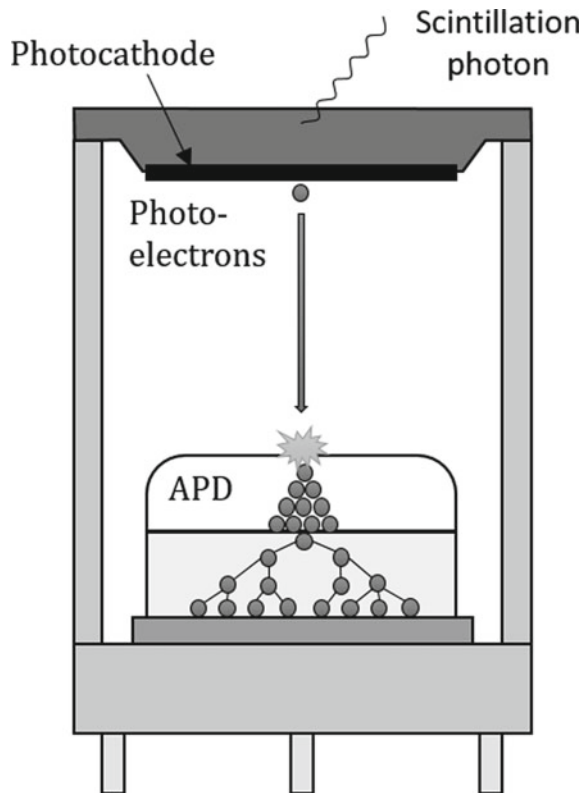
Overview of the SiPMs

As long as small areas are required, the SiPMs are good replacements of the PMTs for counting, spectrometry, and PSD. Thus, SiPMs are compact, work at low bias voltage, typically 40–70 V, have low power consumption, and have a small sensitivity to magnetic fields and to charged particles traversing the device because of the very thin thickness of the silicon wafer (small nuclear counter effect). Finally, SiPMs are very practical to use, tolerate accidental illumination, and have a long lifetime. These features combined with their high internal gain have led to a number of studies aiming at replacing PMTs with SiPMs [33, 34]. Despite their many advantages, they have also some drawbacks. The dark noise cannot be easily (sometimes not at all) discriminated from the signal, the gain strongly depends on temperature, and the size of the device is limited by the dark noise. In addition, the PSD applications based on plastic scintillator still do not achieve the performance of a PMT-based system [33], but future development in this field might reduce the gap between PMT and SiPM (at least for small-sized detectors).

10.2.2.5 Hybrid PhotoDetector

As previously mentioned, an HPD is the combination between a PMT and a solid-state Photodetector (an APD) (Fig. 10.25). As with a PMT, in an HPD, the incident light hits a photocathode, where photoelectric conversion occurs. The photoelectrons thus generated are then accelerated by a high intensity electric field (from a few kilovolts to a 20 kilovolts) applied to the photocathode, and they are then bombarded onto the target APD where electron-hole pairs are generated based on the incident photoelectron energy. This is known as the “electron bombardment gain”. In this configuration, the APD replaces the standard PMT dynode chain as the electron multiplication step, thus reducing fluctuations during the multiplication process and thus achieving better electron resolution.

Fig. 10.25 Schematic of a HPD which comprises the photocathode and an APD which receives the photoelectrons



It has been previously mentioned that the gain of an APD is small compared to the gain of a PMT or of a SiPM. For the HPD, this electron bombardment gain is proportional to the supply voltage of the photocathode (for high voltage values). However, there is actually an energy loss in the electron bombardment due to the insensitive surface layer of the APD. The avalanche photodiode inside an HPD typically generates an electron-hole pair by incident energy of about 3.6 eV [6]. Therefore, the expression of the bombardment gain (G_b) can be obtained by Eq. 10.23 (for high V_{bias} values).

$$G_b = \frac{V_{bias} - V_{thr}}{3.6} \quad (10.23)$$

Taking into account the additional internal multiplication factor provided by the APD (G), the overall gain in an HPD (G_{HPD}) can be expressed by Eq. 10.24 where G denotes the gain of the APD given in Eq. 10.19.

$$G_{HPD} = G_b \cdot G \quad (10.24)$$

This is why the supply voltage of the photocathode and the electron bombardment gain are strongly dependent. For the APD, it is difficult to maintain stable operations if the reverse bias voltage is set close to the breakdown voltage, so typical G values not exceeding one hundred are achieved. In this way, overall APD gains of up to some 10^5 are achievable. This remains less than the gain of a standard PMT but high enough to generate easily measurable output signals than with an APD alone.

Overview of the HPDs

The after-pulses are less present than in a PMT, since there is no dynode, which represents the main source of post-impulses in standard PMTs. In an HPD, the only possible contributions are the thermionic emissions at the photocathode and the ionization of residual gases left in the vacuum. HPDs offer good uniformity. This is because the bombardment gain depends only on the potential difference between the photocathode and the APD (and thus the applied high voltage). This means the photoelectrons generated at each point on the photocathode are accelerated at the same energies, resulting in a uniform response, determined solely by the uniformity of the photocathode sensitivity and the uniformity of the APD gain. Also in the absence of dynodes, the TTS is reduced to typical values in the order of a few hundred picoseconds. This is related to the short response time of the HPD, due to the very low capacity of the APD diode.

The HPDs have many advantages in applications where quantitative properties (energy resolution), reproducibility, and stability are essential factors. In addition to the very good linearity achieved through bombing and the use of an APD, the main source of improvement is the absence of the chain of dynodes. The HPD theoretically produces a better resolution of the pulse height than PMTs, thanks to the very high first gain stage of the HPD. However, the gain does not exceed $\approx 10^4$ – 10^5 . In order to achieve such a gain, a very high voltage must be supplied to the photocathode. The stability of the high voltage is not trivial at values 10–20 kV.

Conclusion

As shown in this section, there are a large number of devices available that can be used as PMs for plastic scintillation applications. In addition, and this is exacerbated for PMT, there are often several possible configurations for the same device. However, among the different systems discussed, several criteria appear to be paramount in the selection of the right device for a given application such as gain, uniformity, and temporal resolution. Moreover, aspects of implementation and embeddedness of the different devices were discussed. In this idea, Table 10.3 represents for each PM of the section, the most representative criteria in order to help the reader to choose the most suitable device for his application.

Table 10.3 Comparison between photomultiplication devices in terms of advantages and drawbacks

	Advantages	Drawbacks
PMT	High gain (up to 10^7) for 1000–2000 V Low noise (depends on the polarity) High quantum efficiency Large detection area As many configurations and types of measurements as possible	Linearity is difficult to maintain as well as response uniformity Sensitive to magnetic field Fragile A few number of manufacturers on the market Not trivial to choose the right configuration for an application
APD	Very good photodetection efficiency Good magnetic immunity Turnkey Noiseless compared to other PM devices	Low gain (up to 10^3) Low sensitivity (10 p.e.) Bad timing resolution
SiPM	High gain (up to 10^6) for < 100 V Single photodetection possible Good timing resolution (TTS < 100 ps) Good magnetic immunity Good PDE Robust	High dark count rate High temperature dependency of the gain Small detection area (but multiple SiPM assembly is possible if suitable electronics are used)
HPD	Many manufacturers Good energy resolution Low probability of after-pulse Good uniformity Good collection efficiency	Moderate gain (up to 10^5) Stable high voltage supply

From the application point of view, the PMT is the most efficient device for low scintillation in the wavelength ranges from ultraviolet to infrared. They are ideally suited for fluorescence spectroscopy and gamma cameras for medical imaging. Despite the low gain, the ease of implementation and low complexity of APDs make them useful for scintillation counting applications such as small embedded measurement systems. The SiPM is essentially between a PMT and an APD, and is best suited for detecting low levels of light in UV to visible wavelength ranges, making it interesting for single photon counting applications. It tends to replace PMT in many applications and is already finding its way into high energy physics, PET, and a large number of handheld detectors. Despite complex implementation, HPDs offer the best compromise between time and energy resolution, making them widely used in high energy physics or ToF measurements.

10.3 The Signal Acquisition Frontend

This section introduces the basics of the scintillator-based detector signal readout. It presents the most common analog signal preprocessing that can be done to achieve basic pulse shaping that matches with digitization requirements.

10.3.1 Charge to Voltage Conversion

In our case, the detector is usually composed of the association of an organic scintillator and a light-to-current converter which is a capacitive device. Therefore, it can be seen as a high-impedance pulsed current source (Fig. 10.26). The weak-charge (low current) pulses obtained are not suitable for most of the processing or transport through a coaxial cable: the charges need to be converted into a voltage and buffered ensuring enough voltage and current to be delivered. This is the job of the first electronic stage that functions as a charge-to-voltage converter.

Since a charge is a current integrated over time, the charge preamplifier is preferred, which is a particular case of TransImpedance Amplifier (TIA). It integrates the weak-charge pulses and converts them into a voltage while providing low-impedance output. Basically, it moves the charge from the input capacitance to another smaller one, named C_F (Fig. 10.27), thus, inducing a voltage variation (Fig. 10.28). It is almost immediately compensated by the negative feedback and can be damped by the bleed resistor R_F . Due to their low-noise characteristics, FET input stage preamplifiers are preferred.

The collected voltage (V_{Col}) can be expressed by Eq. 10.25, with Q_{col} the collected charges, C_D the value of the equivalent capacitor of the detector, and C_L the capacitor of the load. When using a charge preamplifier, Eq. 10.25 leads to Eq. 10.26, where C_f denotes the feedback capacitor (Fig. 10.27), and $\tau = C_F \times R_f$ the time constant involving the feedback resistor R_f (also called the bleed resistor) which damps the pulses.

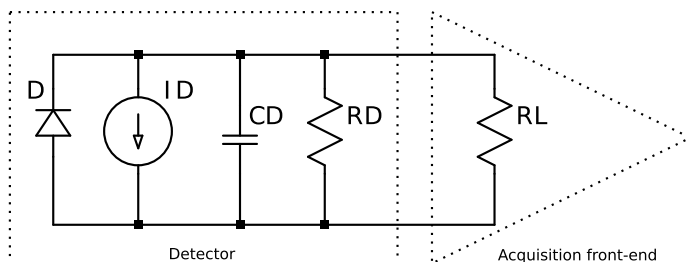


Fig. 10.26 The detector described in the previous section can be modeled by a capacitor C_D with a parallel resistor corresponding to the resistance between the plates

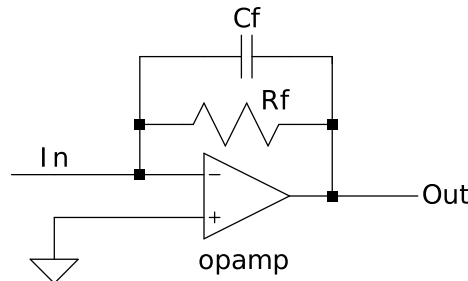


Fig. 10.27 Schematic of a charge preamplifier with a feedback capacitor and resistor, denoted C_f and R_f ; the operational amplifier can be replaced by the equivalent function made of transistor(s); here, the voltage reference connected to the + pin is the 0 V of the ground but any other reference voltage could be used

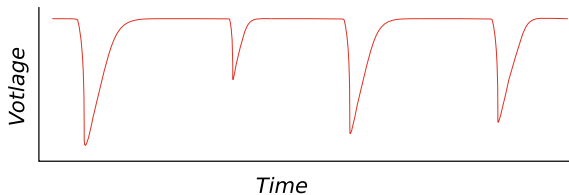


Fig. 10.28 Variations of the voltage across the detector, observed for every single energy deposited in the scintillator; the pulses appear reversed as the PM is biased positively

$$V_{Col} = \frac{Q_{Col}}{C_{detector} + C_L} \quad (10.25)$$

$$V_{out} = -\frac{Q_{Col}}{C_f} \times e^{-t/\tau} \quad (10.26)$$

Obviously, it is important to make sure the acquisition chain corresponds to the characteristics of the pulses which are meant to be observed, typically, the rise time and the fall time given by the specifications of the detectors. The charge-to-voltage, or the current-to-voltage, gain is an essential parameter since it allows the user to set a trigger level expressed in Volt, or eventually to interface it with a digitizer or a multi-channel analyzer. For 1×10^5 electronic charges available at the detector terminal, $1 \cdot 10^5 \times 1.6 \cdot 10^{-19} = 1.6 \cdot 10^{-14}$ Coulomb is the total charge transferred to the feedback the capacitance. If its value is set to 1 pF, then the observed signal amplitude would be 16 mV. A $10 \text{ k}\Omega$ feedback resistor would ensure a time constant of $\tau = 1 \cdot 10^{-12} \times 10 \cdot 10^3 = 10 \text{ ns}$.

10.3.2 Gain and Pulse Shaping Stage

The charge-to-voltage input stage does generally not provide enough gain for further use of the signal, that is why an additional stage is used which also serves as a pulse-shaper and impedance matching for the next stage electronics. Generally, analog pulse-shapers are made of a high-pass filter followed by a low-pass filter. It comes to deriving the signal and then performing an integration (Fig. 10.29). This combination removes the baseline which corresponds to the constant value of the integrator which can be set to zero or to any other value to obtain a vertical offset, visible in Eq. 10.27. The constant times used in the filter will preserve the shape of the pulse or modify it depending on the needs of the application.

$$\text{output}(t) = \int d \frac{ds(t)}{dt} + \text{constant} \quad (10.27)$$

Such filters can be implemented using passive electronics, or active (including amplification) electronics (Figs. 10.30, 10.31). In order to keep the ratio between the pulse amplitude and the deposited energy, it is usually recommended to rely on linear filtering.

In many cases, the designer will want to make the pulses longer. This is done for many reasons, for example, it eases their observation; it also facilitates the interfacing with electronics such as discriminators or multi-channel analyzers. However, if the

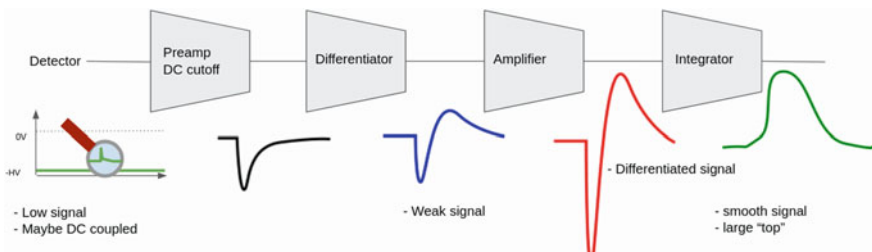


Fig. 10.29 Example of an acquisition chain and the effect of each stage on the signal

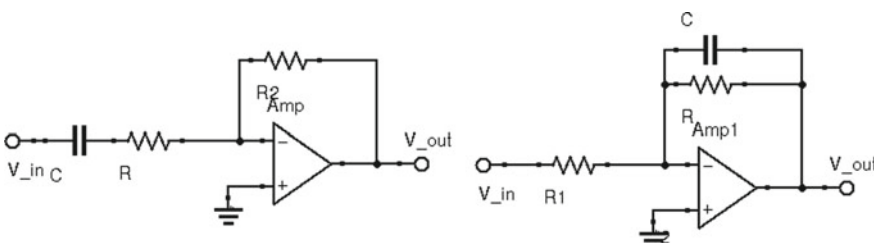
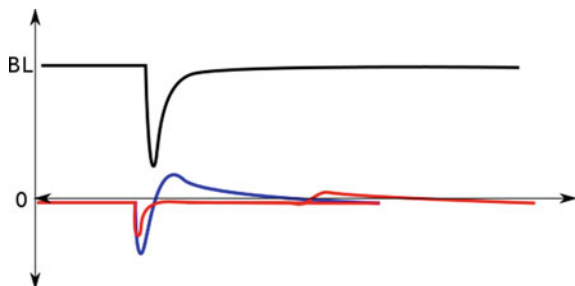


Fig. 10.30 First-order active high-pass (left) (or derivator) and low-pass filter (integrator) (right), with cutting frequency given by $F_c = 1/\tau = \frac{1}{2\pi \cdot R \cdot C}$

Fig. 10.31 Illustration of a high-pass filter used as a derivative filter, also called differentiator. Two time constant τ are illustrated, a short one, in blue, and a long one in red, which delays the overshoot. Note the disappearance of the baseline



count rate is very important, the probability of piling-up rises. On the other hand, if the pulses are too wide, it is possible to shorten their duration by the use of a derivative filter, which is a linear filter. Again, if the simplest implementation using passive filters can be employed, active forms are widely used. As explained before in the chapter, zero-pole compensation [35] may be required to avoid important undershoot or overshoot, depending on the polarity of the signal. The designer has to compromise between the count rate and the pulse duration; here again, it strongly depends on the requirements of the application.

10.3.3 Voltage Limiters

Even if linear filters are preferred, unexpected high energies, especially from cosmic rays, can deposit into the detector causing transient instabilities in the signal acquisition chain leading to inconsistent measurement results. To limit their impact, voltage limiters are used. They can be implemented using two Zener diodes in the feedback net of one of the amplifier stages, but a voltage-limiting operational amplifier can serve the same purpose. This feature can also be implemented in the Analog-to-Digital Converter (ADC) chip itself. It means that any energy corresponding to the voltage over the limit value would appear as a saturation. Of course, further additional electronics such as anti-muon veto signal [36–38] can be implemented.

A simple acquisition chain

As an example, a typical chain (Fig. 10.32) is composed by a low-pass filter followed by a voltage-gain comprising a voltage limiter. The pulse shaping is done by the low-pass filter that would extend the decay time of the pulse to ease its visualization using an oscilloscope or the use of relatively low-speed electronics.

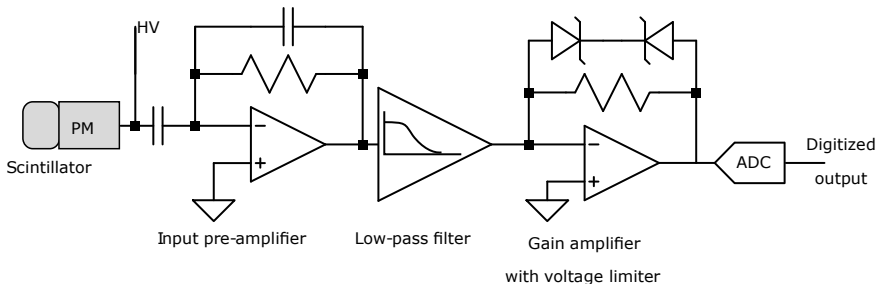


Fig. 10.32 Typical chain to acquire signal from an organic scintillator; the first stage is the charge preamplifier; in this example, the second stage is a low-pass filter that blocks the high frequencies thus reducing aliasing after digitization; this filter can be comprised in the ADC architecture; the voltage limiter stage is not mandatory and may be comprised in the ADC architecture; it generally helps to deal with events that would cause saturation such as high-energy particle deposits in the scintillator. This state can sit anywhere in the chain

10.3.4 Impedance Matching and Other Effects

As a general guideline, to ensure good ElectroMagnetic Compatibility (EMC) and low noise level, particular attention must be paid to the design of the Printed Circuit Boards (PCBs) [39] and particularly to the voltage sources and to the analog and digital ground planes [40]. In the same vein, specific care must be given to impedance matching. Indeed, a mismatch can have multiple detrimental effects which will not be discussed in detail here, and the reader may refer to [41]; one the most common one is the reflection of the pulses (Fig. 10.33). The reflection can be visible when using “T” termination with no load. Another effect is the increase of the pulse length when higher capacitor values are in series with the load termination. For example, by replacing a $50\ \Omega$ termination resistor by a $500\text{ k}\Omega$ resistor, the pulses would appear longer, which is quite understandable since the constant time of the equivalent filter is higher. Moreover, the coaxial cable transporting the signal acts as a transmission line, with parasitic resistance, capacitor, and inductance that must be taken into account (Fig. 10.34). The parameter C_{dx} comes in parallel of the input capacitance of the input stage, both forming, with the serial resistance of the feeding stage and R_{dx} , a low-pass filter that can impact the highest frequencies of the signal.

Fig. 10.33 Illustration of the reflection (on the right) of a primary pulse (on the left) due to impedance mismatch

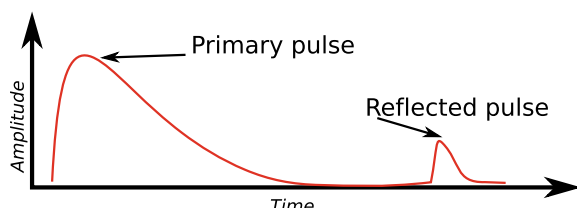
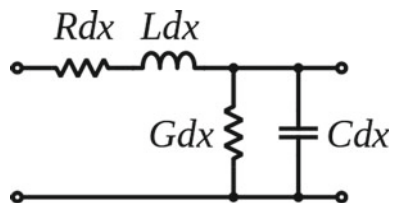


Fig. 10.34 Schematic of a portion of a transmission line where Rdx , Ldx , Gdx , and Cdx are the parameters given per meter of line length for further integration



10.4 The Digitization Stage

This section presents the steps to obtain a digitized signal from an analog electrical signal. First, the basics of digitization such as sampling rate and bit depth are presented. Then, some digitization architectures that can be used for organic scintillation applications are depicted.

10.4.1 Signal Digitization Basics

This subsection introduces the basics related to digitization. It mostly targets the sampling frequency and how it can be determined for pulse processing; then the resolution, expressed in bits or dB , is explained.

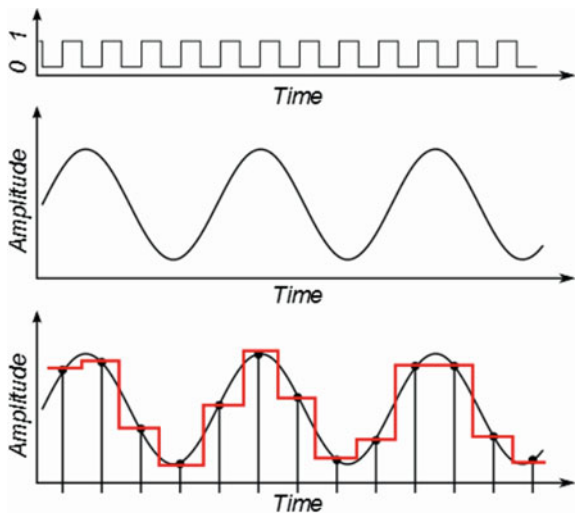
10.4.1.1 Sampling Frequency

Digitization corresponds to the discretization and the quantization of a signal; it is usually performed on a regular time basis. Basically, this corresponds to the encoding of the amplitude (voltage) of a signal into digital numbers at a given sample-rate (Fig. 10.35), expressed either in samples-per-second or in Hertz; it corresponds to the time resolution.

It means that any variation of voltage value falling between two discretization steps would be integrated to be sampled. It may also be ignored, depending on the digitizer technology. Most of the digitizers use a sample-and-hold circuit to integrate the voltage value for a certain time in a capacitor, which is then read out at the following sampling clock cycle. As will be detailed further, the sampling rate must be high enough to ensure that a pulse is properly discretized into a sufficient number of samples to perform a processing (Fig. 10.36). For example, for simple counting application sampling frequency does not need to be as high as that for PSD applications.

The sampling frequency must be chosen according to the highest frequency of the signal that must be preserved in order to comply with the Shannon-Nyquist theorem [42]. That said, it is quite difficult for the experimenter to determine the highest frequency of a pulse obtained by a detector. In general, an empirical and

Fig. 10.35 The analog signal (center graph) is sampled on a time base given by the sampling clock (upper graph). This leads to a digitized signal displayed in red (lower graph)



conservative approach is used. It consists in considering the rise time as the equivalent of half of the period of the highest frequency. We present here a simple and analytical alternative approach that can be easily verified by the experiment. We are going to look for the high cut-off frequency that preserves a certain amount of the pulse energy, for example, 90%. Considering Eq. 10.28, where $\mathcal{F}(p(t))$ is the Fourier transform of the pulse $p(t)$, one need to determine the value of the upper limit of the integral, b , while C is the ratio of the energy of the pulse $p(t)$ that needs to be preserved, a the lowest frequency, and

$$C \cdot \int_a^\infty \mathcal{F}(p(t)) dt \approx \int_a^b \mathcal{F}(p(t)) dt \quad (10.28)$$

Basically, a pulse can be modeled by a two-sided exponential decay equation. The left part (rise time) is given by Eq. 10.29 and the right part (decay time) is given by Eq. 10.30.

$$p_{rise}(t) = e^{t_1 \cdot t} \quad (10.29)$$

$$p_{decay}(t) = e^{t_2 \cdot t} \quad (10.30)$$

The parameter b can be determined either analytically or experimentally by analyzing the pulses priorly digitized using a very high-frequency digitizer. The results we obtained where the pulse frequency that preserves 90% of the pulse energy can be plotted in respect of the pulse FWHM (Fig. 10.37). In this experiment, pulse rise times were the fourth of the decay time, and they were digitized at 2 GHz. For example, FWHM = 10 ns pulses; c = 90% of the energy is contained under 250 MHz.

Fig. 10.36 Illustration of the impact of the acquisition frequency on the resulting signal (red). It is clearly visible that when the acquisition frequency gets lower than the Nyquist frequency, the samples are not close enough to reconstruct the sinus

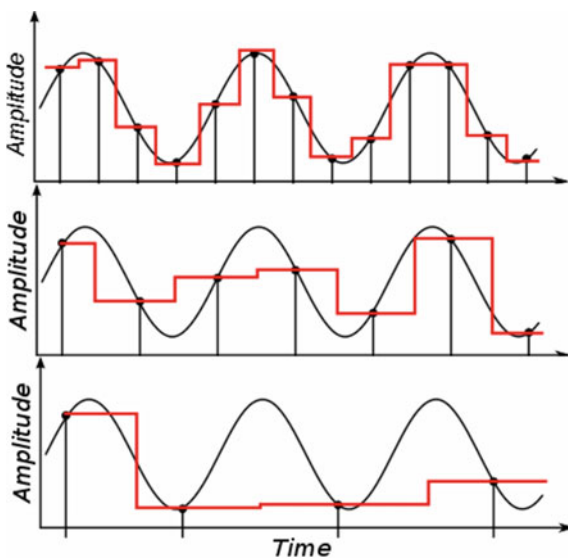
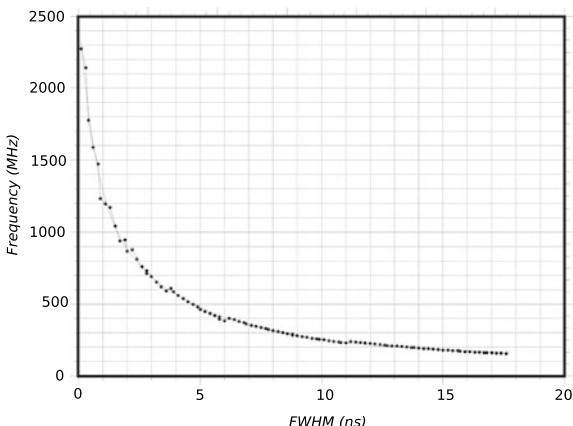


Fig. 10.37 Sampling frequency versus pulse FWHM at $c = 90\%$ of the pulse energy; a 10 ns FWHM pulse requires a 250 MHz digitization to achieve 90% of the energy of the pulse. This plot is obtained from generated pulses with a decay time 4 times longer than the rise time



The aliasing problem

Once the sampling frequency is chosen according to the pulse characteristics, the analog signal must be low-pass filtered in order to avoid aliasing. The effects of aliasing are present in the digitized signal when the analog bandwidth of the signal is greater than two times the ADC sampling rate. As an illustration, this phenomenon is visible in movies when a car wheel is sampled at 25 frames per seconds. If the speed of the car increases, one can see the rotation of the wheel gradually reverses—the signal bandwidth becomes higher than the acquisition bandwidth.

10.4.1.2 The Resolution of a Digitizer

The vertical resolution of a digitizer is usually expressed as a number of bits, and the amplitude values are encoded into power of two as a signed or unsigned integer depending on the ADC features. Practically, it means that the voltage dynamic range of the digitizer (for example, -1 V to 1 V) is divided into 2^N steps, hence, any voltage variation smaller than, in this example, $2/2^N\text{ V}$ cannot be seen (Fig. 10.38).

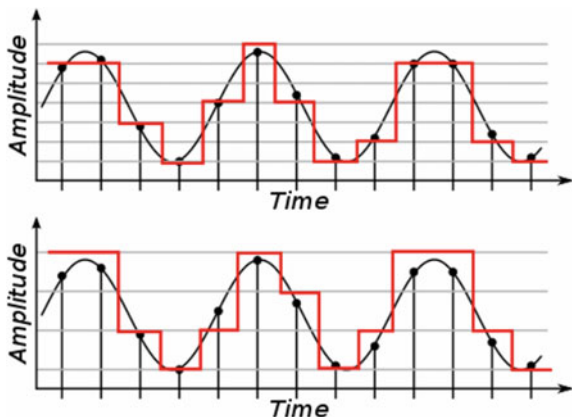
The difference between the analog signal value and the digitized value, corresponding to a voltage step, is called the quantization noise, which is always non-null whatever the ADC resolution is. The SNR of an N-bit ADC is given by Eq. 10.31, which does not take into account the others sources of noise of a system, like thermal noise, amplification noise, etc.

$$\text{SNR} \approx 6.02N + 1.76 \text{ dB} \quad (10.31)$$

The quantization noise caused by the digitization can be simulated (Fig. 10.39). Even for a limited resolution, the quantization noise remains quite low, and thanks to the high sampling rate, the signal is well reproduced. The designer must choose the resolution of the ADC according to the energy resolution requirement of the application.

The designer must choose the front-end analog amplification gain(s) to make sure the expected maximum pulse amplitude matches the input range of the ADC. In the same way, the resolution of the ADC must be chosen according to the expected energy resolution, and they are actually closely related. For example, consider a detector which provides a sensitivity of 22 mV/MeV (0.045 MeV/mV) and a typical gamma-ray application that requires an energy range $0\text{--}8\text{ MeV}$, then output pulse would range from 0 to 176 mV . Digitizing this signal with a 10-bit ADC with a positive $0\text{--}1\text{ Volt}$ input would mean only the first 172 encoding possibilities (quanta) over the 1024 available quanta would be used (less than 8 bits). The actual resolution

Fig. 10.38 Illustration of the impact of the vertical resolution (number of bits); the 3-bit resolution used for the top figure provides better quality signal than the bottom 2-bit resolution used for the bottom one



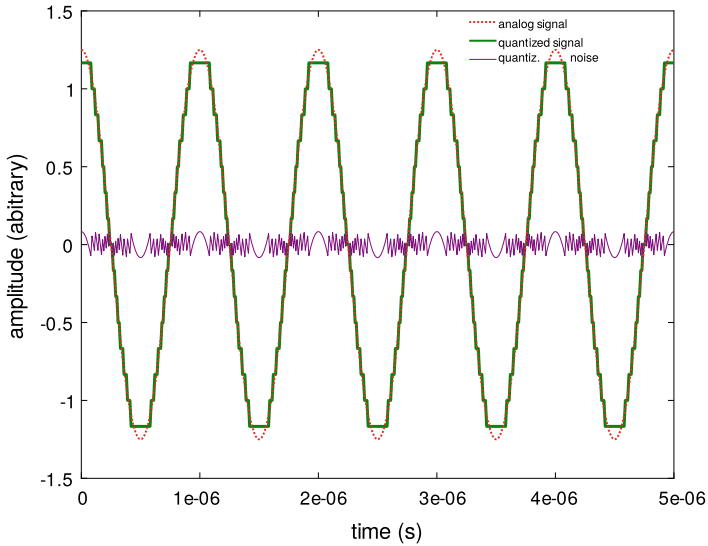


Fig. 10.39 Illustration of quantization error obtained from simulation. The analog signal is displayed in blue, the digitized signal in green, and the delta between them is given in red and corresponds to the quantization error

of the system would be lower (45.45 keV/quantum) than the maximum achievable for 8 MeV range (7.8 keV/quantum)—this comes to the quantization error. Indeed, using a preamplifier of a gain of 5.6 before the digitization would lead to a 123.2 mV/MeV analog signal, the 8 MeV pulses would swing in the 0–985.6 mV range, and the digitizer would make use of almost all the 10 bits and encodes 7.93 keV/quantum. The quantization error automatically stays under this value which is almost the maximum achievable.

Depending on the digitizer architecture, any value out of the dynamic range may cause unexpected result and must be filtered at the analog stage by a voltage limiter.

Effective Number of Bits (ENOB)

A digitizer is supposed to be usable in its whole dynamic, but practically, it never happens. An important figure is called the ENOB, which takes into account the dynamic of the whole circuitry from the input to the output. Thus, not only the raw performance of the ADC is considered but also the impact of the multiplexers and the other analog and digital circuitry which are in the package are considered on the measurement accuracy. Any additional external electronics may affect the ADC performances and must be taken into account in the final design characterization which can have a lower ENOB than the ADC chip itself.

10.4.2 Digitizer Architectures

Through the past decades, many architectures have been designed to convert analog signals to digital codes. The most common are the Successive Approximation Register (SAR), the delta-Sigma ($\delta\Sigma$), and the pipelined ADC architectures. Each of them has specific advantages and disadvantages. Knowing these architectures helps to make the right choice when selecting a component and impacts the ability of the system to perform an accurate measurement. Indeed, ADC generates a latency which is the measure of the delay between a trigger event and the next valid measurement.

10.4.2.1 SAR ADC

The SAR ADCs is one of the most commonly adopted architectures when the sampling rate does not need to be very high. Indeed, their cost is quite low thanks to their simple implementation. It is based on a single comparator (or 1-bit ADC), a Digital-to-Analog Converter (DAC) and some simple control logic (Fig. 10.40).

Basically, this approach consists in capturing and comparing the input voltage with successively smaller references given by a DAC until a precise measurement is achieved, thus, the digitization takes N internal clock cycles for an N -bit depth ADC. This means the internal ADC clock must reach at least N times the sampling frequency. Consequently, the SAR architecture is used for quite slow ADC, typically a few MegaHertz to several dozen of MegaHertz, but this architecture is suitable for integrated synchronous multi-channel ADC since the multiplexing of the inputs remains quite easy. The SAR architecture can be used with organic scintillators combined to slow PM.

10.4.2.2 The Delta-Sigma ($\delta\Sigma$) Architecture

The $\delta\Sigma$ (named $\Sigma\delta$ by some manufacturers) architecture, which strongly relies on oversampling, is widely used for fast digitization and is a particular type of integrative ADC. In general, the fundamental frequency of a digitized signal amplitude divided

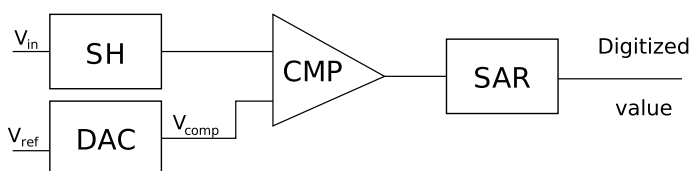


Fig. 10.40 Simplified view of an SAR ADC: the input goes through a sample-and-hold circuit (SH) before being compared with V_{comp} , generated by a DAC. The comparator (CMP) output is then stored in the SAR circuitry. All these modules are driven by a control logic

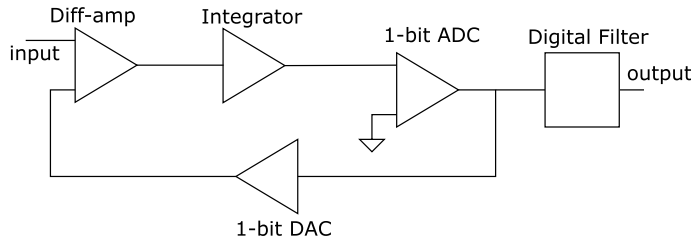


Fig. 10.41 Block diagram of a $\delta\Sigma$ modulator of the first order which comprises a difference amplifier, an integrator, and a comparator. The 1-bit DAC in the feedback loop makes sure the average output of the integrator stays close to the reference level of the comparator

by the Root-Mean-Square (RMS) sum of the other frequencies gives the SNR of an ADC, as given by Eq. 10.31.

Doubling the sampling frequency automatically reduces the noise floor since the noise energy is spread over a wider frequency range. With a simple digital filter designed to reduce the noise, associated with a 1-bit ADC, the $\delta\Sigma$ approach can achieve a wide dynamic range from a very low-resolution ADC, even a single comparator, which is actually a 1-bit ADC. A $4\times$ oversampling increases the SNR by 6 dB, which is equivalent to gaining 1 bit. If a $24\times$ oversampling is used, then a 4-bit ADC can be implemented, a $4^{15}\times$ which corresponds to 16 bits. Oversampling is limited by the switching rate of the digital circuits that implement the ADC, which cannot be higher than a few Gigahertz using today's technologies. For this reason, the $\delta\Sigma$ architecture employs an additional technique called noise shaping. The 1-bit data stream at the (over)sampling rate forms the output of the delta-Sigma modulator. Then, a digital filter (Fig. 10.41) extracts the information and reduces the data rate while improving the resolution and reducing the quantization noise.

10.4.2.3 The Pipelined ADC Architecture

The pipelined ADC architecture is the most widely used for fast acquisition rates, typically over 10 MHz. With the $\delta\Sigma$ architecture, it is likely the one that would be used in the design for organic sensor data acquisition.

Here again, the analog input is first held and sampled. Then, a first flash ADC quantifies its value, generally on a limited number of bits such as four. The quantized value is then given to a DAC whose analog output is subtracted from the held input voltage. The result is a residue that is given to the next stage that operates the same way. Each stage provides a low-resolution quantization of the sample at different times which are aligned using shift registers. An error correction module is implemented to obtain the final sample value. As soon as the first stage has transferred the residue to the next stage, it becomes available to process a new incoming sample, and so on for every stage. Thus, it is literally a pipelined architecture that can reach high data rates, typically over the gigahertz. Such feature makes it perfectly suitable for fast organic scintillators associated with fast PM.

10.4.2.4 Time-to-Digital Converters

For some applications, measuring the date of the arrival of a pulse, the duration of a pulse, the dead time or the active time of a system is important. When long intervals need to be measured with a resolution that is compatible with digital clocks, then simple digital counters can be used. However, their resolutions are generally not better than a few hundreds of picoseconds, and their potential dead time corresponds to the clock period. This approach is generally used for gathering statistics like active and dead times of the system.

More accurate approaches have been proposed; one of the most commonly used is the Vernier interpolator—just as for calipers. It is traditionally implemented using a clock operating at a predefined frequency and a triggerable oscillator operating at another one [43]. Both are associated with a coincidence circuit. The phase between the two oscillators will then be dependent on inducing sliding transitions between each other. The oscillator and the clock rising edge occur at the same time indicating the fraction time that needs to be added to the measurement. Many implementations are used nowadays [44, 45], including some relying on delay lines [46].

Another analog method, which is widely used to measure time intervals lower than 250 ns, is the ramp interpolator. Basically, a capacitor is charged at the start event, then it discharges into a resistor until the stop event. The voltage across the capacitor is measured and digitized giving information about the discharge time. This approach can be more evolved in order to provide better resolution or dynamic range [47, 48].

These last two methods provide excellent sub-picosecond precision but are not suitable alone for long time intervals. Their dead time can be problematic in some implementations.

10.5 Signal Processing and Feature Extraction

While the previous section described how the light produced by an organic scintillator is converted into an electric signal and then can be digitized, this section introduces some of the digital signal processing that can be used in organic scintillation applications. The first part of this section is related to stream processing. It processes discrete samples of the signal in a similar way the analog electronics do on a continuous signal. The second part of this section is devoted to the detection of the events which are the pulses. The discriminator, or event trigger, is used to determine their presence in the signal. The third part of this section is devoted to the pulse processing and the extraction of actual information such as amplitude, duration, shape, and rise time. Then, they can actually be used in the applications; this is going to be presented in the last section of this chapter. Thus, we have two domains (Fig. 10.42): the first which continuously processes the samples, the second that performs the analysis of the pulses themselves to extract the information. Between them stands the discriminator, also named trigger.



Fig. 10.42 Illustration of the different domains that form a digital signal processing chain: before the trigger lays a sample-by-sample stream processing; it is followed by the pulse processing, after the samples of each pulse are extracted

10.5.1 Low-Level Digital Stream Processing

After being digitized, the signal forms a continuous stream of samples, timed by an acquisition clock (Fig. 10.43). The digital chain follows a producer-consumer model [49]. The producer is the ADC and the consumer is the digital processing electronics (Fig. 10.44). Whether the signal is read and processed by an electronic or not, the samples will keep flowing: the consumer has to be able to accept all.

If the processing execution time is too high for the digital processing unit to keep up with the sampling rate, then some data must be dropped (Fig. 10.45). Such a situation would occur when the input buffers are full. This may happen on a regular basis or randomly depending on the architecture and its implementation. The scenario is exactly the same if the saturation comes from a transmission canal, for example, a Universal Serial Bus (USB) that is expected to transmit the data stream to a computer. Of course, the designers would ensure this never happens by a correct sizing of the computing capacities of the digital modules and of the size of their buffers. Nevertheless, the sizing strongly depends on the resources required by the algorithms.

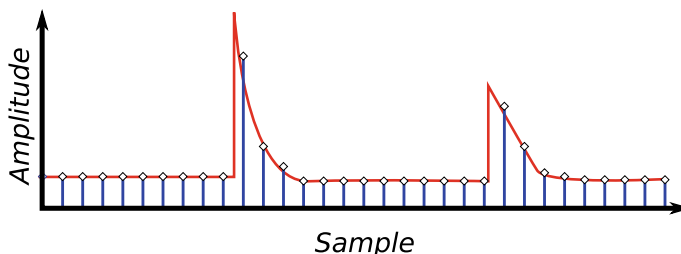
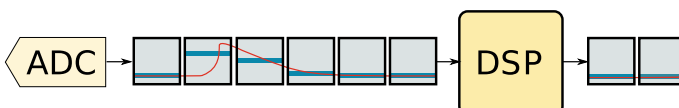


Fig. 10.43 Example of discrete digital samples: the blue vertical lines correspond to the digital samples



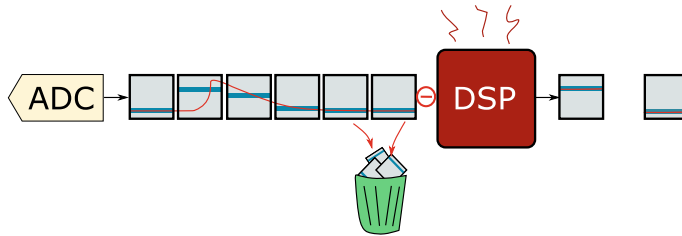


Fig. 10.45 Illustration of a DSP that cannot process the samples. The red lines in the boxes show the analog signal and the blue lines correspond to their sampled values. The DSP cannot accept incoming samples, which leads to dead time; this is illustrated by the samples going to the trash. Since the processing time of a sample may extend because of a too complex calculation, longer delays between samples output can be observed. This is illustrated here by a wider space between the outgoing samples on the right of the DSP

The stream processing is a paradigm that assumes the same compute kernel is applied to each sample [50–52]. Its execution must be done within a given time, typically before the next sample comes. For example, if a 9-tap convolution filter has to be executed on every sample, it would require $9 + 1$ clock cycles to obtain the result if it was executed by a single operation per cycle processor. Even if the processor frequency was quite high, such as 1 GHz, and considering that no clock cycle would be required for the data transfers (which is rarely true), the highest data rates it could process without dead time would be $10^9 / 10 = 100$ MSample/s. Of course, if a dead time was acceptable, for example, 500 ns per event, then the processing time could be long, which would provide more clock cycles for its execution. This can be a choice done by the designers to limit the computing capacity requirements, since no new pulse could come during the dead time, or to make possible the use of traditional processors instead of DSPs. This choice can also be driven by the characteristics of the trigger or the experiment that may require a dead time after every event anyway. This way, the computing capacity can be downsized to use it efficiently. But this leads to the DPP approach, which is going to be detailed further in this chapter.

Generally, in order to increase the number of operations per second that are available to execute a process, the chain of algorithms employed for the stream processing forms a pipeline. The pipelined architecture [53] ensures good performance and flexibility. In the case of stream processing, the pipeline is driven by the acquisition clock—i.e. the arrival of a new sample. Each incoming sample triggers the transmission of the result of the first stage to the second stage (Fig. 10.46). At the same time, each stage processes its new sample, and so on for every stage of the pipeline. This way, the architecture could achieve four 9-tap convolution filters (one per stage) without needing to increase its operating frequency. One could also choose to implement a single pipelined implementation of the convolution filter; thus, it could operate at the same frequency as the data rate, which would allow to reduce the processing frequency to 100 MHz (instead of 1 GHz of the previous example).

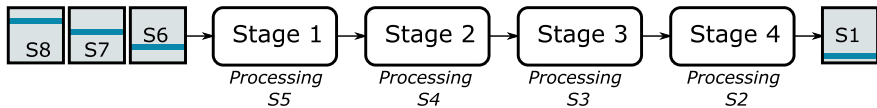


Fig. 10.46 Illustration of a pipelined chain of algorithm that processes samples of a signal; the samples are numbered, from S1 to S8; they are processed by each stage of the pipeline

In a general form, the maximum number of available operations per sample ($NbOPPS$) can be easily obtained using Eq. 10.32 from [54] where $NbPE$ denotes the number of processing elements, $NbPOp$ the number of parallel operations they can individually achieve, F_P the processing element frequencies, and F_S the data rate. This equation can be easily derived to be used on any kind of parallel and pipelined architecture.

$$NbOPPS = NbPOp \times NbPE \times \frac{F_P}{F_S} \quad (10.32)$$

For high sampling rates, typically above 100 MHz, which is the case for organic scintillator data acquisition, the compute kernel must be implemented directly in digital electronics. Using VLSI techniques ensures fast processing with no additional dead time, instead of using programmable processor.

Fixed-point versus Floating-point arithmetic

Even if the digitized samples are encoded by integer values by the ADC, the algorithm designer works using tools like MATLAB/Octave, Python, etc. which operate using the computer Floating Point Unit (FPU). Some real-time embedded hardware do not have FPU, or the resource requirement is too important for the ones which are implemented. For this reason, fixed-point arithmetic is preferred due to its simplicity of implementation using the VLSI approach. Other techniques [55–58] made possible the use of non-floating point computing architectures to achieve similar calculation [59, 60].

10.5.1.1 Digital Filters

Generally, the first digital filters implemented in an acquisition chain are related to the electric noise reduction, but they do not actually target the dark noise introduced earlier in this chapter. Indeed, in addition to the dark pulses that occur in PMs, the signal may be contaminated by different sources of noise. The most common are a) the thermal noise, which is related to the agitation of the electrons through a resistive device (even a wire). It is a white noise distributed all over the frequency spectrum; b) the shot noise, which is caused by some semiconductors [61] like diodes and transistors; it has a Poisson distribution and has a much lower amplitude level than the pulses obtained from a detector.

The noise reduction serves two purposes: first, it prepares the signal for discrimination. Indeed, generally, discriminators use a threshold; thus, they are more accurate if the value of the amplitude of the signal does not randomly fluctuate. Second, it ensures accurate further information extraction. Additional cleaning of the pulses can be performed afterward.

To clean the signal, digital filters [62, 63] have to process all the samples of a stream. It can be done using convolution-based filters, Gaussian filters [64], moving average [65], weighted moving average, and more generally, all Finite Impulse Response (FIR) [66] and Infinite Impulse Response (IIR) [67–69]. Moreover, non-linear filters [70] such as median filters [71], exponential moving average, bilateral filters [72], and Kalman and wavelet filters [73] can also be implemented this way, but they have to be used with caution since they may modify the linearity of the overall energy response of the system. Implementations of filters have been well documented since decades in the domain of nuclear instrumentation [74–76]. They also can be borrowed from other fields related to signal processing such as the audio domain [77] and image processing. Note that the researches not only in biomedical engineering [78], in quantum physics, and in radar engineering [79] but also in the optics and radiotelecommunications require signal processing approaches which are extremely close to the one implemented in nuclear instrumentation. The designer would benefit in studying these domains.

Pulse shaping can be performed after denoising, even if practically they both can be combined in a single algorithm or hardware implementation. Pulse shaping can also deal with the piling-up effects [80, 81]. Again, it facilitates the trigger step and further pulse processing. For high count rates, a double differentiation can be performed, transforming a unipolar pulse into a bipolar pulse, thus reducing the duration of rising part of the pulse. The most commonly implemented pulse-shaper is definitively the trapezoidal filter [82, 83]; pulse deconvolution can also be successful [84, 85].

10.5.1.2 Event Triggers and Discriminators

Naturally, the last step before the actual pulse processing involves in triggering (Fig. 10.47) on the events themselves. This type of algorithm is also called a discriminator. Because each sample can potentially be the first denoting an event, the trigger algorithm cannot afford to miss any sample. This is why their digital implementation relies on stream processing. In some designs, an additional analog trigger can be used in combination with digital processing.

Discrimination is a form of 1-bit digitization of the signal; it generates a strobe when the event is detected (Fig. 10.48). Basically, it is done with an analog comparator built from operational amplifiers or transistors, but this chapter focuses on their digital equivalent. The implementation is similar but comparisons are done on digital values using subtractors instead of using operation amplifiers, the results of a leading-edge discriminator (Fig. 10.49).

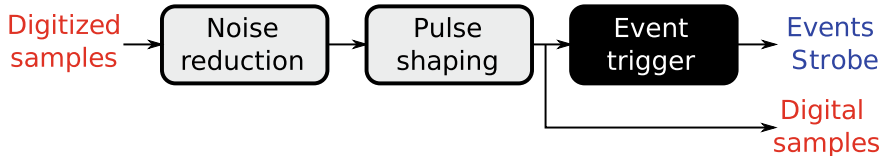


Fig. 10.47 Illustration of the acquisition pipeline that would lead to a result (Fig. 10.48). The first two steps are designed to produce a clean signal (which appears in red in Fig. 10.48), while the last step triggers on the events, the strobes are in blue in Fig. 10.48. Here the event trigger could be a CFD, a Schmitt trigger, or a simple threshold on the sample value

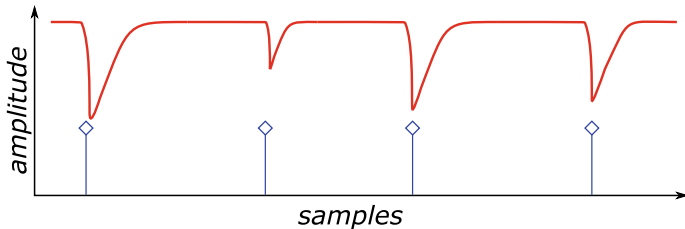


Fig. 10.48 Illustration of event trigger, a class of signal processing that generates strobes (in blue) from a sampled signal (in red)

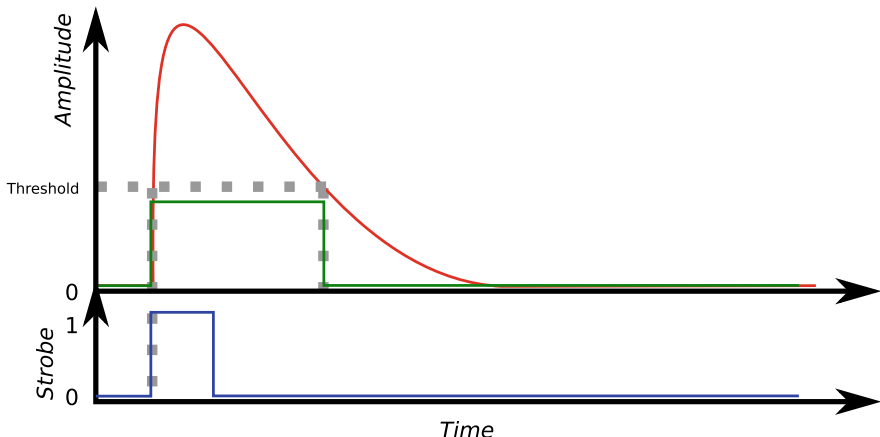


Fig. 10.49 Example of single threshold discrimination made by a simple comparator; the green signal is the result of the comparator, and the blue signal is the strobe generated by the discriminator

The general problem of discrimination is associated with the risk of repeating the detection on pile-ups, after-pulses, or even on some electronic noise. This would lead to the detection of several events, although only one should be considered. This is a situation (Fig. 10.50) where an after-pulse or a pile-up causes the system to trigger twice. A good approach to avoid this effect is by using the Schmitt trigger. It

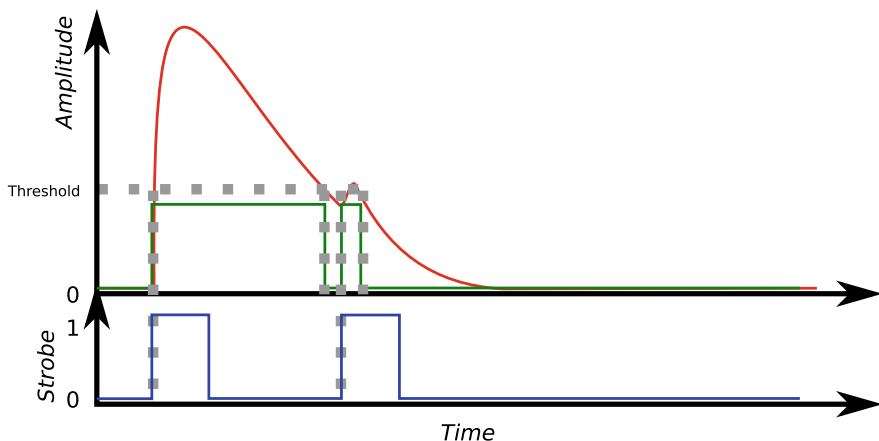
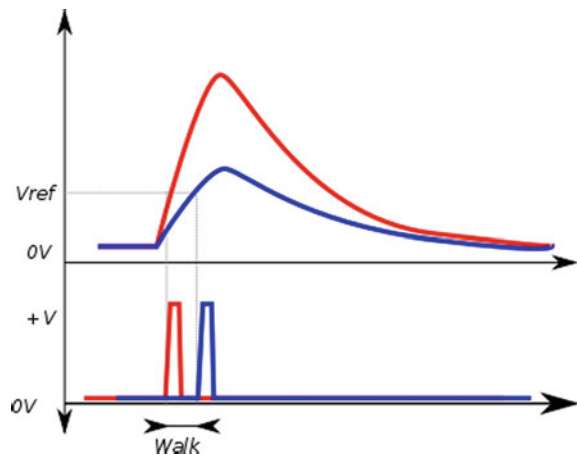


Fig. 10.50 Illustration of the repeated detection of events, here an after-pulse, but the discriminator can also be triggered by electronic noise. The green signal represents the output of the comparator; the blue signal represents the strobe generated by the discriminator

Fig. 10.51 Illustration of walk phenomena and potential imprecise datation of the events



generates a logic “one” when the signal reaches a first threshold (leading-edge) and releases to a “zero” when the signal reaches a second threshold that is set at a much lower value than the first (falling edge).

Another issue caused by the use of simple discriminators is the *walk* (Fig. 10.51). It is the variability in timing corresponding to the detected event. Depending on its maximum amplitude, the pulses may not reach the trigger level at the same instant after their beginning. Moreover, the electronic noise can add more variability. For this reason, leading-edge discriminators are not best suited for applications that require precise time.

Fig. 10.52 Operating principle of the zero-crossing discriminator on two pulses with different amplitude; since the discriminator uses the first derivative of the signal, it always detects the time corresponding to the maximum of amplitude

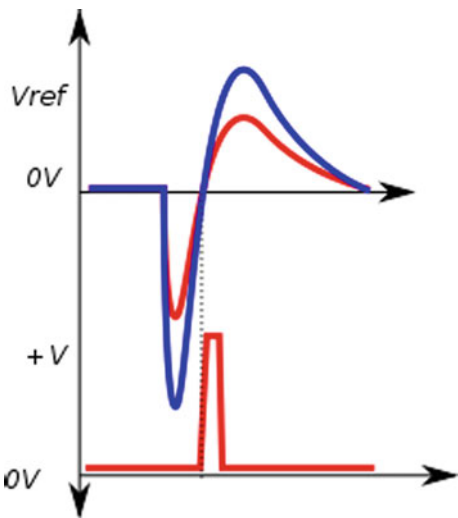
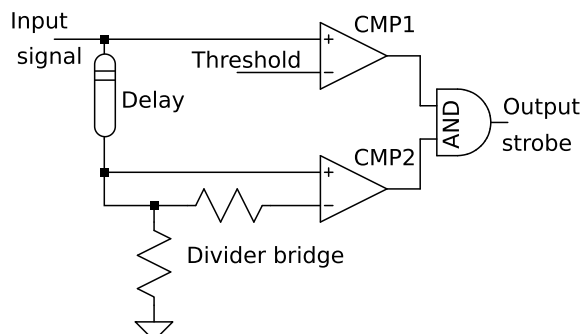


Fig. 10.53 Schematic of a CFD; for more clarity, it represents analog components but a digital implementation follows the exact same layout and functions



To limit the walk effect, the zero-crossing discriminator operates on the derivative of the signal by detecting when its value crosses the zero line. This zero-crossing automatically corresponds to the maximum of amplitude of the pulse (Fig. 10.52). The CFD is probably one of the most commonly used discriminators since it solves most of the issues compared to the others. The internal principle is quite simple; the incoming signal is split into different channels (Fig. 10.53). The first is delayed and inversed and subtracted to the second which is divided by a small value, the constant fraction. Practically, it generates a strobe when the signal reaches a (constant) fraction of its amplitude maximum.

Dead time management

The dead time management is extremely important. Even if nowadays, it is possible to process in real time all the samples generated by ADC, it is easier to impose a dead time than trying to figure out if a pulse is due to an after-pulse or due to an event that must be ignored. A dead time policy must be chosen and associated with accurate dead and active time measurement to provide good results for metrology applications such as in [86, 87]. Then, the dead time can be corrected [88–90] at the application level to provide accurate activity measurement.

Digital pulse pile-up rejection at early steps can be found but conventionally, the pile-up and the after-pulse issue is traditionally solved by correct use of dead time. It also means losing some events. This is why multi-level triggers are more and more implemented in instrumentation. Until recently, they were used only in large instruments [91–93]. However, the advances in digital architectures ease their implementation into small-factor electronics, mostly because it can be done entirely digitally.

They generally operate in parallel on copies of the original signal, which are delayed from each other, and shaped differently. For example (Fig. 10.54), the first trigger level detects as many events as possible; it can drive a counter for further statistics. When it detects a potential pulse, it signals the second-level trigger that a pulse is potentially coming. The second triggering level can evaluate if the pulse is interesting upon various criteria: amplitude, delay after the previous pulse, or many other criteria. It is possible since it operates on a delayed signal. This also allows data reduction since only the portion of the signal containing pulses is considered. If the second trigger decides the pulse is valid, then its samples are copied into a waveform memory [65, 94] or sent to another level. The waveform memory can be used by further pulse processing. Such approach enables much more advanced processing and directly leads to DPP [95, 96]. This way, more advanced pile-up rejection can be designed. Practically and depending on the algorithms, it can be done at the early stages [97] or at the later stages of the acquisition chain [98], and different solutions can also be combined.

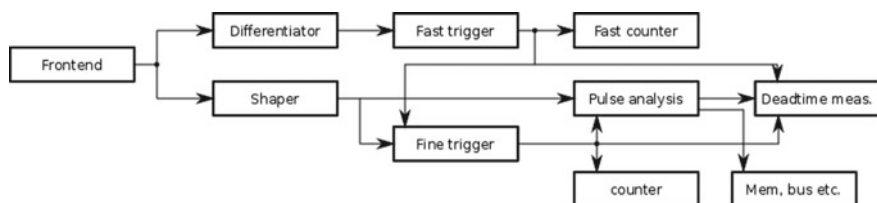


Fig. 10.54 Schematized view of the digital pulse acquisition and information extraction architecture. Two parallel chains appear after the frontend: the top one enables fast counting of the events, and the second analyzes the pulses provided they are not in the dead time imposed by the experimenter

10.5.1.3 Detection of Coinciding Events

To detect coincidences, gates [99] must be opened when an event occurs and then be closed after a certain amount of time (Fig. 10.55). This delay can be customized as required by the application (Fig. 10.56). Moreover, some delay lines can be used to compensate the distance between detectors or to fix any timing issue in relation with the experimental layout. Anti-coincidence can simply be performed by combining logical functions (Fig. 10.57), a “NOT” operation is added to the example given of the Fig. 10.55.

In modern applications, since triggers are digitally implemented and are part of the whole acquisition chain, the events can be timestamped individually, allowing performing time coincidence entirely by the software which handles them as any other data; thus, no delay line is required. For some real-time applications, it is needed to implement coincidence using digital electronics—Complex Programmable Logic Devices (CPLDs) and FPGAs are the perfect parts—in that case, the delay lines are simply replaced by buffers.

10.5.2 Digital Pulse Processing

When it comes to DPP, the entirely discretized pulse is considered as a single object (still composed of discrete samples), thus the methods and the approaches are radically different.

The individual pulses need to be analyzed to extract some features or information that can be used by further algorithms. A correction of the linearity of the chain can be implemented at this stage. For this, a calibration mode would provide the right parameters to this stage. Moreover, some designer can make the choice of providing the energy information in eV and time encoded in seconds to the data

Fig. 10.55 Example of time coincidence using gates; here, a strobe (gray) is generated when the two channels simultaneously receive an event

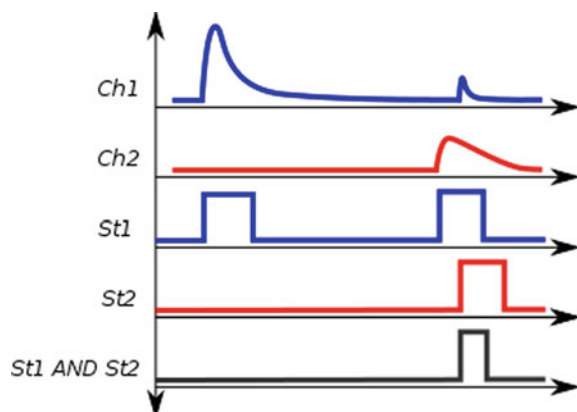


Fig. 10.56 Example of a coincidence application combining a long gate and a short gate; here, a strobe (gray) is generated when the second (red) channel receives an event within a certain amount of time after the first one (blue)

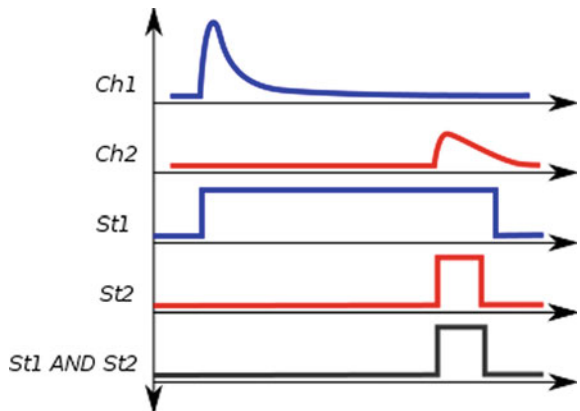
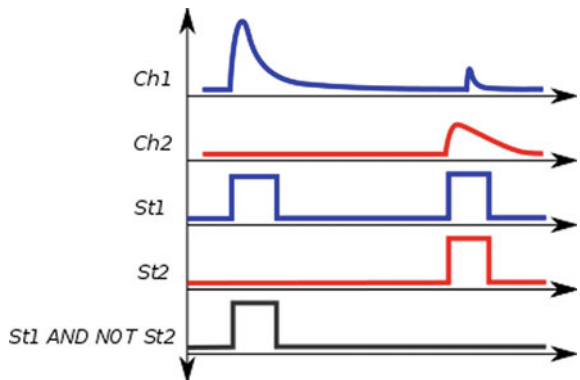


Fig. 10.57 Example of a non-coincidence application that detects events that occur on the first channel (blue) only when the second channel (red) is event free. The resulting strobe is displayed in gray at the lowest part of the graph



processing stage. Among others features, and depending on the final applications, the information that can be extracted are

- the maximum of amplitude;
- the area of the pulse;
- the pulse rise time;
- the pulse falling time;
- the FWHM of the pulse;
- the ToT;
- the centroid of the pulse;
- the area of the tail of the pulse.

As explained earlier, an event forms an electrical pulse which is discriminated. Then, the samples corresponding to the pulses can be saved in a memory or transmitted to a digital pulse processor that can be a workstation [100], multiple embedded processors [101], or FPGAs [102, 103].

Since the pulse processing can take a certain amount of time, a single PP may not be available to process a new incoming pulse, again, leading to dead time. To

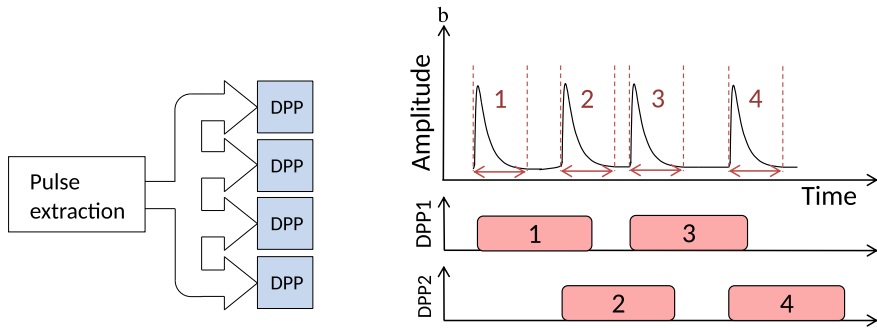


Fig. 10.58 Principle of operation of a pulse processing architecture that statically distributes the pulses to different parallel digital pulse processors, denoted by the DPP boxes

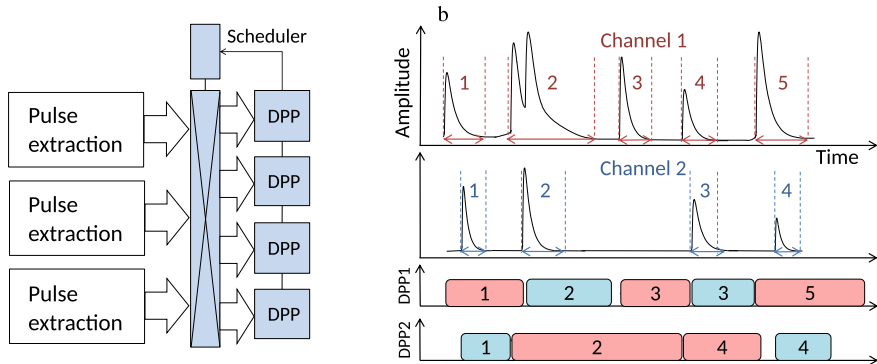


Fig. 10.59 Principle of operation of an advanced multi-channel pulse processing architecture that dynamically distributes the pulses to different parallel software or hardware pulse processors, the DPP squares on the figure

avoid this, multiple parallel PPs can be used [101]. The pulses are then distributed to them (Fig. 10.58). When a huge number of channels and events can occur, this model can be generalized and lead to a more complex DPP architecture [104] (Fig. 10.59) where all the computing resources are shared between several channels. This way, limited computing resources can process a large number of events.

Implementing digital pulse processing with a piece of software makes the system extremely flexible and adaptable to any kind of application. Indeed, the corresponding code can be easily reprogrammed to extract from the pulses any kind of information, even if they were not implemented at the design stage [105].

Depending on the required computing resources and the need for hard real-time processing, the parts that execute the digital signal processing can be of different kinds:

- the Application-Specific Processors (ASICs) are developed using VLSI technology, and usually are devoted to limit a type of processing such as accurate time

measurement or stream filtering. They enable high performance, usually at a low cost if available off-the-shelf. If not, the development of an ASIC requires man-power and thus can be quite expensive;

- the CPLDs and FPGAs are configurable by the user using the VLSI description languages, their performance are lower than the performance of ASICs, and they have relatively high electrical power requirements. They still require VLSI experts to be implemented. They offer a good trade-off as stream processors for organic scintillation applications as they can deal with multiple acquisition channels in real time. They can perform stream processing as well as pulse processing;
- the DSP are well suited for signal processing since they are programmable processors containing specific operators designed to be executed in parallel. They are well suited for pulse processing;
- Graphics Processing Units (GPUs) are designed for stream processing and provide extremely important computational capacities for a good level of flexibility since they can be programmed using standard languages. However, they cannot really be used in embedded environments; they require electrical power and are designed to be used with a workstation, even if embedded GPUs are now available;
- traditional microprocessors and micro-controllers cannot really deal with the real-time requirement of stream processing needed by organic scintillators. However, they are perfect candidates when an application has to handle information, such as searching for peaks in a spectrum, calculating statistics on the signal, and the final steps of a neutron/gamma discrimination. They can be programmed using low-level languages (assembler, C/C++, etc.) as well as high-level languages such as Python when flexibility is required. Microprocessors focus on providing good computing resources compared to the micro-controller family which integrates a large variety of peripherals like memories, ADCs, DACs, and communication modules;
- modern System on Chips (SoCs) are composite parts implementing the different kinds of computing resources listed here into a single package. Modern SoCs that are suitable for organic scintillation application comprise an FPGA, a couple (or more) of microprocessors or micro-controllers, memory and communication resources, eventually some ADCs or DACs.

10.6 Data and Information Processing

After the acquisition of the samples and the extraction of the information from the raw signal, the data processing is strongly related to the end-user application. Usually, and if not done in the previous stage, the encoded values (time, energy, etc.) are converted into physical information. Moreover, the correction of the linearity of the system is performed at this stage. This means the designer has conceived a calibration mode that allows the user to work on the raw data and calculates the correction parameters.

This section gives some examples of data processing based on the information extracted by the acquisition chain. Most of them can either be embedded for a real-time execution or simply run by a workstation after the data acquisition.

10.6.1 Count Rate Analysis

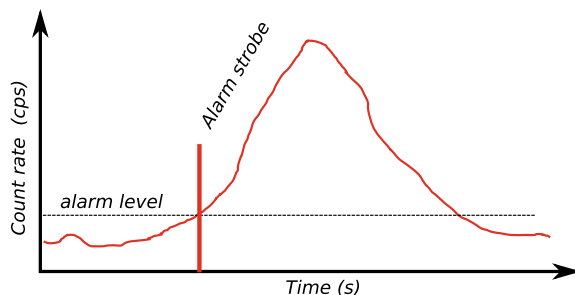
In order to detect illegal transportation of radionuclides, RPMs are installed in harbors, for example, along lanes where semi-trailer trucks move containers. Since an alarm implies the deep inspection of the cargo which requires time and staff, the objective of an RPM is to have a high sensibility with a low number of false alarms.

Basic detection relies on the count rate, eventually corrected of the dead time, to trigger an alarm, basic detection relies on the count rate estimation, which can be corrected of the dead time (Fig. 10.60). More advanced approaches were proposed such as [106] which relies on time-series analysis. Thanks to time analysis combined with algorithms from other fields of researches [107], the count rate over the time provides information on the presence of radionuclides or on their carrier like the speed of displacement [108]. The count rate analysis does not require particularly well-resolved scintillator, but the energy range of the system must match with radionuclides that need to be detected. The fluctuations of the background noise generally require the use of a dynamic threshold [109] if the targeted sensibility must stay low. Generally, the RPMs combine detectors of different nature, such as fission chambers, plastic scintillators to reduce the level of false alarms.

10.6.2 Discrimination of the Nature of the Interactions

When an alarm is triggered, it is important to identify the underlying cause, for example, the transportation of a fissile material like plutonium which is prohibited by the Non-Proliferation Treaty (NPT). Traditionally, ${}^3\text{He}$ fission chambers are used [110], since the neutron/gamma discrimination relies on a simple threshold on the pulses

Fig. 10.60 Example of how the count-rate over time can be used to trigger an alarm; here the threshold is static and represented by the dashed line



amplitude. However, a worldwide shortage of ${}^3\text{He}$ imposes the RPM suppliers to find alternative types of detectors. Because of their sensitivity to neutron and their low cost, the organic scintillators are good candidates [111]. However, the neutron pulses they produce have the same order of amplitude as the gamma pulses. Multiple detector layout enables the use of the ToF [112] approach, with a very good level of discrimination. To be performed, it simply requires the extraction of the timestamp of each pulse, then they are analyzed by a simple algorithm. However, the space required by the detector layout does not make such techniques suitable for ground instruments.

New generation of plastic scintillators were designed to enhance the delayed fluorescence induced by the neutron interactions [113, 114]. Practically, it means that the neutron pulse has more energy in its tail than a gamma one. A simple lot (Fig. 10.61) of the average pulses obtained from a gamma-only mixture of radionuclide and another containing gamma + neutron emitters [115] emphasizes the energy differences between the pulses from the different interactions.

PSD-based methods always proceed in the same way. Features representing specific characteristic of the shape of pulses are extracted. Usually, the total and the delayed energy [18, 116–118] are pertinent since they emphasize the delayed fluorescence. Representations of these features (Figs. 10.62, 10.63) are widely used in the literature [119]. Then, a separation method of the clusters is performed.

$$FOM = \frac{D_{n\gamma}}{FWHM_\gamma - FWHM_n} \quad (10.33)$$

The quality of the separation is evaluated, thanks to the Figure of Merit (FoM) which measures the distance between the two clusters. Typically, the calculation of the FoM involves the distance between the center of the clusters and their FWHM. Other methods appear regularly in the literature such as Pulse Gradient Analysis [120], the ratio between neutron and gamma events [115], or Zero-Crossing [121], but none of them is widely adopted yet. One of the most widely used is given by

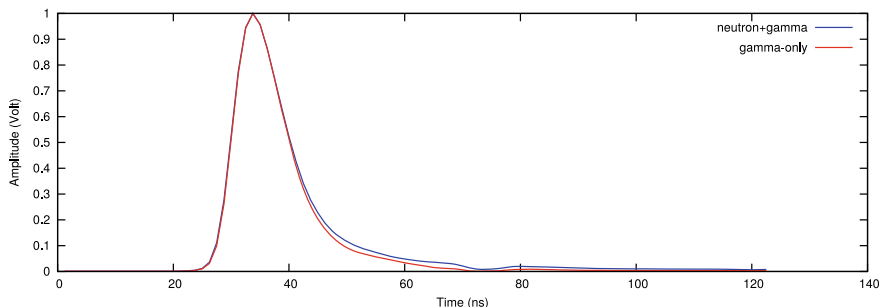


Fig. 10.61 Averaged pulses obtained from gamma-only radionuclide emitters (red) and neutron+gamma emitters (blue); the tail of the pulse contains more energy for the blue one, which is explained by the delayed fluorescence

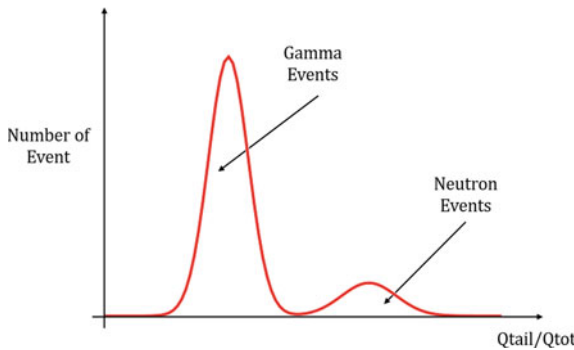


Fig. 10.62 Bins of the number of pulse versus their Q_{tail}/Q_{tot} ; two regions are visible corresponding to the gamma events (left) and to the neutron events (right)

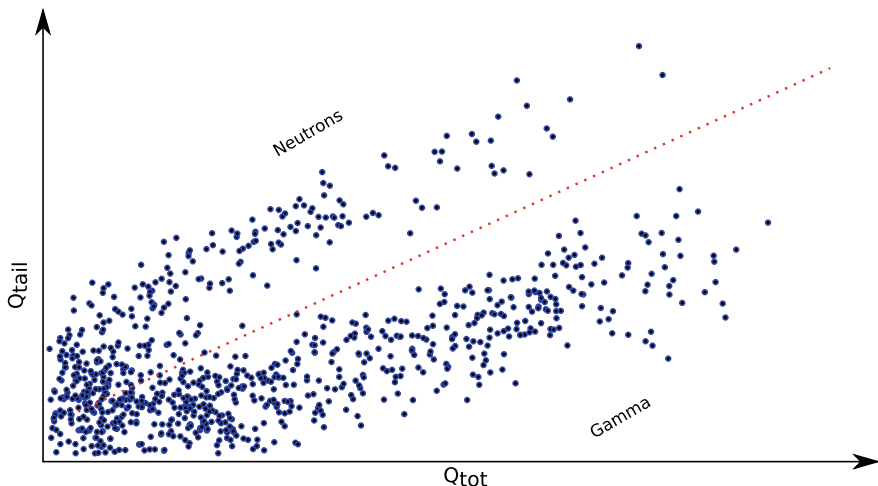


Fig. 10.63 Plot of the Q_{tail} Q_{tot} features; two regions are visible correspond to the gamma events (bottom) and to the neutron events (top)

Eq. 10.33 where D_{ny} is the distance between the center of the clusters (usually the center of Gaussian fit of the clusters), $FWHM_\gamma$ is the FWHM of the gamma cluster (usually, its Gaussian), and $FWHM_n$ the same for the neutron cluster.

Different classification methods exists; due to its simplicity, the Q_{tail}/Q_{tot} ratio is the traditional way to discriminate neutrons from gamma [119]. Different complementary or alternative approaches have been proposed such as the use of pattern recognition algorithms [122] or the combination of the ToF and the PSD [123]. This leads to the general method proposed in [115] that uses different types of feature extracted from the pulses to make a discrimination.

Since discrimination is a classification problem, the use of machine-learning approaches makes sense, and different works are proposed (sometimes on liquid

scintillators) [124–126]. Support-Vector Machine (SVM) [127, 128] and Artificial Neural Network (ANN) [129] are the most employed but, the Gaussian-mixture model [125] and the use of Principal Component Analysis PCA are proposed [130]. When applied to the pulses, they automatically select the right features from the pulses. The user does not need to specify how they need to be extracted (for example, the duration of the charge integration). However, since these approaches are based on training, the training dataset is extremely important, and special care needs to be given to it.

Intrinsic limitation of the traditional FoM

Most of the neutron/gamma discrimination methods rely on the calculation of FoM calculated by Eq. 10.33 and on Gaussian fits. Actually, it is originally designed to provide an assessment of the quality of the delayed fluorescence of a scintillator. Practically, the result quality depends on the acquisition chain. Ultimately, a good neutron/gamma classifier would classify events that are not distinguishable because they would be in the confusion area, which the FoM could not. Another measurement of the quality of the discrimination was proposed in [115].

Discrimination of other types of interaction

PSD can be applied to other problems. The α/β discrimination [131] can be done with coincidence based system [132], the least-square algorithm have also been used [133]. Classification approaches can be done on any kind of event provided that the detector senses them in a different manner. Some techniques combine the properties of the scintillators and the use of algorithms to perform PSD [134], complex detector type can be used such as phoswich (made for instance of the association of organic and inorganic scintillators).

10.6.3 Spectral Unmixing and Radionuclide Identification

Due to their poor photopeak efficiency, the organic scintillators are not good candidates for gamma spectrometry applications. Indeed, radionuclide identification cannot really rely on the energy signature of the radionuclides, especially when they are in complex mixtures. Being able to perform radionuclide identification using plastic scintillators is probably the biggest challenge that could lead to them being even more adopted.

Not only algorithmic [135, 136] and bio-inspired [137, 138] approaches were proposed, but also various machine-learning-based techniques [26, 139–141]. They

actually provide some results that were not expected from the simple analysis of the γ spectra obtained from plastic scintillators.

However, these approaches have some drawbacks especially when the comparison database gets big or if the environmental conditions change. A more recent promising approach [142] where a multiplicative update algorithm based on full-spectrum performs the spectral analysis and provides an estimation of the count rate for each radionuclide potentially present in a mixture. It has been recently successfully tested on plastic scintillator in association with an even more advanced approach [143] which allows robust decision-making, even at low statistics. A sparsity constraint is used with an unbiased count estimation; a single decision threshold is applied for a likelihood ratio test.

10.7 Conclusion

Plastic scintillators are the first elements of an acquisition chain where every single one plays an essential role in obtaining an actual physical measurement. The acquisition chain is the combination of a large number of different technologies associated with nuclear and particle physics, chemistry, photonics, analog and digital electronics, and computer science. This chapter gives some clues for the physicist who wishes to build one. Since it cannot be comprehensive, it focuses on some of the important points that have to be taken into consideration when designing an acquisition chain.

The photomultiplication and current conversion stages must be carefully chosen and must match the characteristics of the scintillator. It must also be perfectly assembled and configured to obtain the expected results. Indeed, the type of components, the materials, and their geometry as well as the polarization voltage strongly impact the amount of light collected and its conversion, as well as the sources of noise. The current obtained at the output of this first conversion stage can therefore be amplified and converted into a voltage to be either observable or be acquired and processed. The voltage/energy ratios must be kept in mind in order to correctly dimension the gains of the first stages. In addition, filtering and voltage limiting are often necessary.

The modern acquisition chains use digital electronics to carry out measurements. They are based on a digitizer that allows the encoding of electrical voltages into digital values. Different digitizer technologies exist and can be used to measure signals from plastic scintillators. It is necessary to choose them carefully to preserve the properties of the signal. Indeed, the choice of the acquisition frequency has an impact on the number of points that form each pulse. Moreover, the resolution in bits, associated with a correct dimensioning of the input gains, directly gives the energy resolution of the system. Digital filters are used not only to clean the signal of different sources of noise, but also to shape the pulses in order to facilitate the discrimination. That kind of digital processing must be performed in real time which is particularly challenging. Indeed, since the organic scintillator may produce short pulses, the electronics must perform calculation within a short amount of time. Again, different technologies can be employed and combined (DSP, FPGA) to build the processing

stage. The discrimination stages are used to separate the useful pulses from the rest of the signal.

Once the pulses are extracted, they can be processed. Essentially, the aim is to extract the characteristics that are used for the application, including maximum amplitude, area (pseudo-energy), rise and fall times, and width at half height. Certain characteristics specific to a particular type application are also extracted, such as the energy of the tail of the pulse, which is widely used in the domain of neutron/gamma discrimination by PSD. Again, this must be done within a limited time to avoid a dead time that could lead to losing some of the pulses. For this, DPP architectures can be implemented.

Finally, the last step is the actual processing of the information. It can be very simple, such as displaying an energy measurement, or associating the count rates of different detectors, or performing time measurements. It can also be complex like neutron/gamma discrimination or radionuclide identification. Some of the most recent approaches combine different techniques involving digital processing, machine learning, artificial intelligence, and relying on a deep knowledge of the nuclear science, physics, and scintillation process. These last two applications are probably the most challenging for the future of plastic scintillators.

References

1. S.V. Polyakov, Photomultiplier tubes. *Exp. Methods Phys. Sci.* **45**, 69 (2013). <https://doi.org/10.1016/B978-0-12-387695-9.00003-2>
2. Hamamatsu Co., Photomultiplier Tubes and Assemblies for Scintillaton Counting and High Energy Physics (2004)
3. M. Grodzicka-Kobylka, T. Szczesniak, M. Moszyński, K. Brylew, L. Swiderski, J.J. Valiente-Dobón, P. Schotanus, K. Grodzicki, H. Trzaskowska, Fast neutron and gamma ray pulse shape discrimination in EJ-276 and EJ-276G plastic scintillators. *J. Instrumen.* **15**(3) (2020). <https://doi.org/10.1088/1748-0221/15/03/P03030>
4. S.V. Polyakov, Single-photon generation and detection, in *Experimental Methods in the Physical Sciences*, vol. 45, ed. by A. Migdall, S.V. Polyakov, J. Fan, J.C. Bienfang (Academic Press, 2013), pp. 69–82. <https://doi.org/10.1016/B978-0-12-387695-9.00003-2>
5. R.J. Brooks, J.R. Howorth, K. McGarry, J. Powell, C. Joseph, *Experimental data on the reflection and transmission spectral response of photocathodes*, vol. 6660 (SPIE, 2007). <https://doi.org/10.1117/12.732349>
6. T. Hakamata (ed.), *Photomultiplier Tubes—Basics and Applications*, 3rd edn. (Hamamatsu Corporation, 2007)
7. T. Koblesky, J. Roloff, C. Polly, J.C. Peng, Cathode position response of large-area photomultipliers under a magnetic field. *Nucl. Instrum. Methods Phys. Res. Sect. A: Accel. Spectrom. Detect. Assoc. Equip.* **670**, 40 (2012). <https://doi.org/10.1016/j.nima.2011.12.054>
8. J.A. Lodge, P. Muff, R.B. Owen, D. Smout, A cross-field photomultiplier with sub-nanosecond risetime suitable for nuclear studies. *IEEE Trans. Nucl. Sci.* **15**(1), 491 (1968). <https://doi.org/10.1109/TNS.1968.4324891>
9. E. Leonora, S. Aiello, D.L. Presti, V. Giordano, *International Workshop on New Photon-detector PhotoDet 2012* (Orsay, 2012)
10. E. Gatti, K. Oba, P. Rehak, Study of the electric field inside microchannel plate multipliers. *IEEE Trans. Nucl. Sci.* **30**(1), 461 (1983). <https://doi.org/10.1109/TNS.1983.4332311>

11. G. Collazuol, M. Bisogni, S. Marcatili, C. Piemonte, A. Del Guerra, Studies of silicon photomultipliers at cryogenic temperatures. *Nucl. Instrum. Methods Phys. Res. Sect. A Accelerat. Spectrom. Detect. Assoc. Equip.* **628**(1), 389 (2011). <https://doi.org/10.1016/j.nima.2010.07.008>
12. D.E. Persyk, *ANSI/IEEE, IEEE Standard Test Procedures for Photomultipliers for Scintillation Counting and Glossary for Scintillation Counting Field* (1972)
13. R. Abbasi et al., Calibration and characterization of the IceCube photomultiplier tube. *Nucl. Instrum. Methods Phys. Res. Sect. A Accel. Spectrom. Detect. Assoc. Equip.* **618**(1–3), 139 (2010). <https://doi.org/10.1016/j.nima.2010.03.102>
14. W.R. Leo, *Techniques for Nuclear and Particle Physics Experiments* (Springer, Berlin Heidelberg, Berlin. Heidelberg (1994). <https://doi.org/10.1007/978-3-642-57920-2>
15. Photonis Co., Photomultiplier tubes (ordering code D-PMT-AB 2002) (2002)
16. F. Luo, Z. Wang, Z. Qin, A. Yang, Y. Heng, *Proceedings of International Conference on Technology and Instrumentation in Particle Physics 2017*, vol. 2 (Springer, 2018), pp. 1–6
17. D. Belver, E. Calvo, C. Cuesta, A. Gallego-Ros, I. Gil-Botella, S. Jiménez, C. Lastoria, T. Lux, C. Palomares, D. Redondo, F. Sanchez, J. Soto-Oton, A. Verdugo, Cryogenic R5912-20Mod photomultiplier tube characterization for the ProtoDUNE dual phase detector. *J. Instrum.* **13**(10) (2018). <https://doi.org/10.1088/1748-0221/13/10/T10006>
18. N.P. Zaitseva, A.M. Glenn, A.N. Mabe, M.L. Carman, C.R. Hurlbut, J.W. Inman, S.A. Payne, Recent developments in plastic scintillators with pulse shape discrimination. *Nucl. Instrum. Methods Phys. Res. Sect. A Accel. Spectrom. Detect. Assoc. Equip.* **889**(2), 97 (2018). <https://doi.org/10.1016/j.nima.2018.01.093>
19. E. Montbarbon, M.N. Amiot, D. Tromson, S. Gaillard, C. Frangville, R. Woo, G.H.V. Bertrand, R.B. Pansu, J.L. Renaud, M. Hamel, Large irradiation doses can improve the fast neutron/gamma discriminating capability of plastic scintillators. *Phys. Chem. Chem. Phys.* **19**(41), 28105 (2017). <https://doi.org/10.1039/c7cp04034b>
20. N. Divani, E. Bayat, M.M. Firoozabadi, Investigation about decoupling capacitors of PMT voltage divider effects on neutron-gamma discrimination investigation about decoupling capacitors of PMT voltage divider effects on neutron-gamma discrimination. *AIP Conf. Proc.* **186**(2) (2018). <https://doi.org/10.1063/1.4903036>
21. A.G. Wright, Electron Tubes Ltd., Design of photomultiplier output circuits for optimum amplitude or response (Technical Reprint R/P065). Bury Street, Ruislip, Middlesex HA4 7TA, UK 1 (NC)
22. IEC, International Electrotechnical Commission (IEC), Measurement of photosensitive devices. IEC 60306-4 (1971)
23. B.H. Candy, Photomultiplier characteristics and practice relevant to photon counting. *Rev. Sci. Inst.* **56**(2), 183 (1985). <https://doi.org/10.1063/1.1138327>
24. B.E.A. Saleh, M.C. Teich, *Semiconductor Photon Detectors* (John Wiley & Sons, Ltd, 1991), chap. 17, pp. 644–695. <https://doi.org/10.1002/0471213748.ch17>
25. S.L. Miller, Ionization rates for holes and electrons in silicon. *Phys. Rev.* **105**, 1246 (1957). <https://doi.org/10.1103/PhysRev.105.1246>
26. M.T. Chughtai, Circuit design for thermal compensation of avalanche photodiode. *Eng. Technol. Appl. Sci. Res.* **9**(1), 3774 (2019). <https://doi.org/10.48084/etasr.2475>
27. G. Barbarino, R. De, G. De, C. Maximiliano, S. Russo, D. Vivolo, *Silicon Photo Multipliers Detectors Operating in Geiger Regime: an Unlimited Device for Future Applications* (InTech open, 2011), pp. 1–46. <https://doi.org/10.5772/21521>
28. P. Buzhan, et al., *the Advanced Study of Silicon Photomultiplier*. January (World Scientific, 2002). https://doi.org/10.1142/9789812776464_0101
29. F. Licciulli, C. Marzocca, An active compensation system for the temperature dependence of SiPM gain. *IEEE Trans. Nucl. Sci.* **62**(1), 228 (2015). <https://doi.org/10.1109/TNS.2015.2388580>
30. A. Gil, J. Rodríguez, V. Álvarez, J. Díaz, J.J. Gómez-Cadenas, D. Lorca, *Proceedings, 2011 IEEE Nuclear Science Symposium and Medical Imaging Conference (NSS/MIC 2011)* (2011), October, pp. 787–790. <https://doi.org/10.1109/NSSMIC.2011.6154298>

31. P. Eckert, H.C. Schultz-Coulon, W. Shen, R. Stamen, A. Tadday, Characterisation studies of silicon photomultipliers. *Nucl. Instrum. Methods Phys. Res. Sect. A Accel. Spectrom. Detect. Assoc. Equip.* **620**(2–3), 217 (2010). <https://doi.org/10.1016/j.nima.2010.03.169>
32. A. Ghassemi, K. Kobayashi, K. Sato, Hamamatsu Co., A technical guide to silicon photomultipliers (MPPC). Overview (2018)
33. K. Kazkaz, T. Stiegler, *Lawrence Livermore National Lab (LLNL)*, Livermore, CA (United States), Replacing photomultiplier tubes with silicon photomultipliers for nuclear safeguards applications, 2020)
34. M.A. Wonders, D.L. Chichester, M. Flaska, Characterization of new-generation silicon photomultipliers for nuclear security applications. *EPJ Web of Conf.* **170**, (2018). <https://doi.org/10.1051/epjconf/201817007015>
35. P. Grybos, R. Szczygiel, Pole-zero cancellation circuit with pulse pile-up tracking system for low noise charge-sensitive amplifiers. *IEEE Trans. Nucl. Sci.* **55**(1), 583 (2008). <https://doi.org/10.1109/TNS.2007.914018>
36. F. Ambrosino, et al., *2009 IEEE Nuclear Science Symposium Conference Record (NSS/MIC)* (2009), pp. 1019–1024. <https://doi.org/10.1109/NSSMIC.2009.5402436>
37. K. Freund, R. Falkenstein, P. Grabmayr, A. Hegai, J. Jochum, M. Knapp, B. Lubsandorzhiev, F. Ritter, C. Schmitt, A.K. Schütz, I. Jitnikov, E. Shevchik, M. Shirchenko, D. Zinatulina, The performance of the Muon Veto of the Gerda experiment. *Eur. Phys. J. C* **76**(5) (2016). <https://doi.org/10.1140/epjc/s10052-016-4140-7>
38. T. Schroettner, M. Schwaiger, P. Kindl, Optimization of an active anti cosmic veto shielding. *Appl. Radiat. Isot.* **61**, 133 (2004). <https://doi.org/10.1016/j.apradiso.2004.03.034>
39. T. Hubing, *2003 IEEE Symposium on Electromagnetic Compatibility. Symposium Record (Cat. No.03CH37446)* (2003), pp. 34–36. <https://doi.org/10.1109/IEMC.2003.1236559>
40. K. Vaesen, R. Jansen, W. De Raedt, H. Kuwabara, T. Kishi, K. Nawa, T. Bessho, *2010 IEEE Radio and Wireless Symposium (RWS)* (2010), pp. 412–415. <https://doi.org/10.1109/RWS.2010.5434136>
41. P. Vizmuller, *RF Design Guide Systems, Circuits and Equations* (Artech House Publishers, 1995)
42. C.E.E. Shannon, Communication in the presence of noise. *Proc. of the IRE* **37**(1), 1021 (1949)
43. R. Barton, M. King, Two vernier time-interval digitizers. *Nucl. Instrum. Methods* **97**(2), 359 (1971). [https://doi.org/10.1016/0029-554X\(71\)90294-1](https://doi.org/10.1016/0029-554X(71)90294-1)
44. J. Mitra, T.K. K. Nayak, An fpga-based phase measurement system. *IEEE Trans. Very Large Scale Integr. (VLSI) Syst.* **26**(1), 133 (2018). <https://doi.org/10.1109/TVLSI.2017.2758807>
45. M. Rashdan, *2017 29th International Conference on Microelectronics (ICM)* (2017), pp. 1–4. <https://doi.org/10.1109/ICM.2017.8268819>
46. P. Dudek, S. Szczepanski, J.V.V. Hatfield, A high-resolution CMOS time-to-digital converter utilizing a vernier delay line. *IEEE J. Solid-State Circuits* **35**(2), 240 (2000). <https://doi.org/10.1109/4.823449>
47. J. Christiansen, Picosecond stopwatches: the evolution of time-to-digital converters. *IEEE Solid-State Circuits Mag.* **4**(3), 55 (2012). <https://doi.org/10.1109/MSSC.2012.2203189>
48. L. Ferreira, M. Moreira, B. Souza, S. Ferreira, F. Baumgratz, S. Bampi, *2020 IEEE 11th Latin American Symposium on Circuits Systems (LASCAS)* (2020), pp. 1–4. <https://doi.org/10.1109/LASCAS45839.2020.9068950>
49. E.W. Dijkstra, Technological University of Mathematics, Eindhoven, Cooperating sequential processes. Technical Report ewd-123 (1965)
50. M. Fragnoulis, P. Carbone, V. Kalavri, A. Katsifodimos. A survey on the evolution of stream processing systems. Arxiv (2020). Preprint
51. P. Carbone, M. Fragnoulis, V. Kalavri, A. Katsifodimos, *Proceedings of the 2020 ACM SIGMOD International Conference on Management of Data* (Association for Computing Machinery, New York, NY, USA, 2020), SIGMOD '20, pp. 2651–2658. <https://doi.org/10.1145/3318464.3383131>
52. R. Stephens, A survey of stream processing. *Acta Inform.* **34**(7), 491 (1997). <https://doi.org/10.1007/s002360050095>

53. C.V. Ramamoorthy, K.H. Kim, *Proceedings of the May 6-10, 1974, National Computer Conference and Exposition* (Association for Computing Machinery, New York, NY, USA, 1974), AFIPS '74, pp. 289–297. <https://doi.org/10.1145/1500175.1500235>
54. M. Thevenin, M. Paindavoine, R. Schmit, B. Heyman, L. Letellier, A templated programmable architecture for highly constrained embedded HD video processing. *J. Real-Time Image Process.* **16**, 143 (2019). <https://doi.org/10.1007/s11554-018-0808-6>
55. C. Jeannerod, J. Jourdan-Lu, *2012 IEEE 23rd International Conference on Application-Specific Systems, Architectures and Processors* (2012), pp. 69–76. <https://doi.org/10.1109/ASAP.2012.12>
56. J. Jourdan, Custom floating-point arithmetic for integer processors: algorithms , implementation , and selection To cite this version. Ph.D. thesis, Ecole normale supérieure de Lyon - ENS LYON (2013)
57. S. Collange, J. Detrey, F. De Dinechin, *Proceedings of the 9th EUROMICRO Conference on Digital System Design: Architectures, Methods and Tools, DSD 2006* (2006), pp. 197–203. <https://doi.org/10.1109/DSD.2006.54>
58. K. Bigou, A. Tisserand, *2014 IEEE 25th International Conference on Application-Specific Systems, Architectures and Processors* (2014), pp. 57–62. <https://doi.org/10.1109/ASAP.2014.6868631>
59. G. Ndour, T.T. Jost, A. Molnos, Y. Durand, A. Tisserand, *ACM International Conference Proceeding Series*, pp. 146–149 (2018). <https://doi.org/10.1145/3229631.3229646>
60. G. Ndour, T.T. Jost, A. Molnos, Y. Durand, A. Tisserand, *ACM International Conference on Computing Frontiers 2019, CF 2019—Proceedings* (2019), pp. 344–349. <https://doi.org/10.1145/3310273.3323159>
61. S. Subramaniam, A. Petr, M. Ong, *2017 International Conference on Noise and Fluctuations (ICNF)* (2017), pp. 1–5. <https://doi.org/10.1109/ICNF.2017.7986022>
62. D. Alberto, M.P. Bussa, E. Falletti, L. Ferrero, R. Garello, A. Grasso, M. Greco, M. Maggiore, Digital filtering for noise reduction in nuclear detectors. *Nucl. Instrum. Methods Phys. Res. Sect. A Accel. Spectrom. Detect. Assoc. Equip.* **594**(3), 382 (2008). <https://doi.org/10.1016/j.nima.2008.06.032>
63. D. Alberto, E. Falletti, L. Ferrero, R. Garello, M. Greco, M. Maggiore, FPGA implementation of digital filters for nuclear detectors. *Nucl. Instrum. Methods Phys. Res. Sect. A Accel. Spectrom. Detect. Assoc. Equip.* **611**(1), 99 (2009). <https://doi.org/10.1016/j.nima.2009.09.049>
64. Q. Ge, L.Q. Ge, H.W. Yuan, A.M. Li, A new digital Gaussian pulse shaping algorithm based on bilinear transformation. *Nucl. Sci. Tech.* **26**(1) (2015). <https://doi.org/10.13538/j.1001-8042/nst.26.010402>
65. Y. Ma, W.J. Fischer, J. Henniger, D. Weinberger, T. Kormoll, System noise of a digital pulse processing module for nuclear instrumentation. *EPJ Web of Conf.* **225**, 01012 (2020). <https://doi.org/10.1051/epjconf/202022501012>
66. Y. Liu, J. Zhang, L. Liu, S. Li, R. Zhou, Implementation of real-time digital CR-RCM shaping filter on FPGA for gamma-ray spectroscopy. *Nucl. Instrum. Methods Phys. Res. Sect. A Accel. Spectrom. Detect. Assoc. Equip.* **906**, 1 (2018). <https://doi.org/10.1016/j.nima.2018.05.020>
67. M. Bogovac, C. Csato, Implementation of a truncated cusp filter for real-time digital pulse processing in nuclear spectrometry. *Nucl. Instrum. Methods Phys. Res. Sect. A Accel. Spectrom. Detect. Assoc. Equip.* **694**, 101 (2012). <https://doi.org/10.1016/j.nima.2012.07.042>
68. T. Thanmai, J. Ravindra, *2020 International Conference on Applied Electronics (AE)* (2020), pp. 1–5. <https://doi.org/10.23919/AE49394.2020.9232853>
69. Y.C. Tsao, K. Choi, Area-efficient parallel fir digital filter structures for symmetric convolutions based on fast fir algorithm. *IEEE Trans. Very Large Scale Integration (VLSI) Syst.* **20**(2), 366 (2010)
70. S. Sajedi, A.K. Asl, M.R. Ay, M.H. Farahani, A. Rahmim, A novel non-linear recursive filter design for extracting high rate pulse features in nuclear medicine imaging and spectroscopy. *Med. Eng. Phys.* **35**(6), 754 (2013). <https://doi.org/10.1016/j.medengphy.2012.08.003>

71. S.A. Fahmy, P.Y. Cheung, W. Luk, Novel FPGA-based implementation of median and weighted median filters for image processing, in *Proceedings—2005 International Conference on Field Programmable Logic and Applications, FPL 2005*, vol. 142 (2005). <https://doi.org/10.1109/FPL.2005.1515713>
72. C. Tomasi, R. Manduchi, *Sixth International Conference on Computer Vision (IEEE Cat. No.98CH36271)* (1998), pp. 839–846. <https://doi.org/10.1109/ICCV.1998.710815>
73. K. Erkan, E.D. D. Bolat, *2005 International Conference on Neural Networks and Brain*, vol. 2 (2005), pp. 951–954. <https://doi.org/10.1109/ICNNB.2005.1614777>
74. G.A. Jullien, *Architectures and Building Blocks for Data Stream DSP Processors* (Springer, US, Boston, MA, 1994). https://doi.org/10.1007/978-1-4615-2762-6_9
75. L. Bardelli, Development of sampling and digital signal processing techniques with applications to Nuclear Physics detectors. Ph.D. thesis, Università degli Studi di Firenze - Dipartimento di Fisica (2005)
76. V. Stoica, Digital pulse-shape analysis and controls for advanced detector systems. Ph.D. thesis, University of Groningen (2012)
77. G. Yu, S. Mallat, E. Bacry, Audio denoising by time-frequency block thresholding. *IEEE Trans. Signal Process.* **56**(5), 1830 (2008). <https://doi.org/10.1109/TSP.2007.912893>
78. D. Bailey, J. Humm, A. Todd-Pokropek, A. van Aswegen, *Nucl. Med. Phys.* (International Atomic Energy Agency, Vienna, 2014)
79. T. Long, T. Zeng, C. Hu, X. Dong, L. Chen, Q. Liu, Y. Xie, Z. Ding, Y. Li, Y. Wang, High resolution radar real-time signal and information processing. *China Commun.* **16**(2), 105 (2019). <https://doi.org/10.12676/j.cc.2019.02.008>
80. P. Žugec et al., Pulse processing routines for neutron time-of-flight data. *Nucl. Instrum. Methods Phys. Res. Sect. A Accel. Spectrom. Detect. Assoc. Equip.* **812**, 134 (2016). <https://doi.org/10.1016/j.nima.2015.12.054>
81. M.R. Mohammadian-Behbahani, S. Saramad, A comparison study of the pile-up correction algorithms. *Nucl. Instrum. Methods Phys. Res. Sect. A Accel. Spectrom. Detect. Assoc. Equip.* **951** (2020). <https://doi.org/10.1016/j.nima.2019.163013>
82. V.T. Jordanov, G.F. Knoll, A.C. Huber, J.A. Pantazis, Digital techniques for real-time pulse shaping in radiation measurements. *Nucl. Inst. Methods Phys. Res. A* **353**(1–3), 261 (1994). [https://doi.org/10.1016/0168-9002\(94\)91652-7](https://doi.org/10.1016/0168-9002(94)91652-7)
83. C. Imperiale, A. Imperiale, On nuclear spectrometry pulses digital shaping and processing. *Measurement* **30**(1), 49 (2001). [https://doi.org/10.1016/S0263-2241\(00\)00057-9](https://doi.org/10.1016/S0263-2241(00)00057-9)
84. W. Xiao, A.T. Farsoni, H. Yang, D.M. Hamby, Model-based pulse deconvolution method for NaI(Tl) detectors. *Nucl. Instrum. Methods Phys. Res. Sect. A Accel. Spectrom. Detect. Assoc. Equip.* **769**, 5 (2015). <https://doi.org/10.1016/j.nima.2014.09.034>
85. M. Nakhostin, M.P. Taggart, P.J. Sellin, A digital pulse shortening method for the mitigation of pulse pile-up effect in scintillation radiation detectors. *J. Instrum.* **14**(4) (2019). <https://doi.org/10.1088/1748-0221/14/04/P04012>
86. B. Chauvenet, C. Bobin, J. Bouchard, A general dead-time correction method based on live-time stamping. *Appl. Meas. Short-Lived Radionucl. Appl. Radiat. Isot.* **130**, 238 (2017). <https://doi.org/10.1016/j.apradiso.2017.10.013>
87. J. Bouchard, MTR2: a discriminator and dead-time module used in counting systems. *Appl. Radiat. Isot.* **52**(3), 441 (2000). [https://doi.org/10.1016/S0969-8043\(99\)00192-X](https://doi.org/10.1016/S0969-8043(99)00192-X)
88. X. Hong, J. Zhou, S. Ni, Y. Ma, J. Yao, W. Zhou, Y. Liu, M. Wang, Counting-loss correction for X-ray spectroscopy using unit impulse pulse shaping. *J. Synchrotron Radiat.* **25**(2), 505 (2018). <https://doi.org/10.1107/S1600577518000322>
89. L. Abbene, G. Gerardi, F. Principato, *2014 IEEE Nuclear Science Symposium and Medical Imaging Conference, NSS/MIC 2014* (Institute of Electrical and Electronics Engineers Inc., 2016). <https://doi.org/10.1109/NSSMIC.2014.7431292>
90. L. Abbene, G. Gerardi, High-rate dead-time corrections in a general purpose digital pulse processing system. *J. Synchrotron Radiat.* **22**, 1190 (2015). <https://doi.org/10.1107/S1600577515013776>

91. E. Pollacco et al., GET: A generic electronics system for TPCs and nuclear physics instrumentation. Nucl. Instrum. Methods Phys. Res. Sect. A Acceler. Spectrom. Detect. Assoc. Equip. **887**, 81 (2018). <https://doi.org/10.1016/j.nima.2018.01.020>
92. M. Aaboud, et al., Performance of the ATLAS trigger system in 2015. Eur. Phys. J. C **77**(5) (2017). <https://doi.org/10.1140/epjc/s10052-017-4852-3>
93. D. Ralet et al., Data-flow coupling and data-acquisition triggers for the PreSPEC-AGATA campaign at GSI. Nucl. Instrum. Methods Phys. Res. Sect. A Acceler. Spectrom. Detect. Assoc. Equip. **786**, 32 (2015). <https://doi.org/10.1016/j.nima.2015.03.025>
94. A.M. Fernandes, R.C. Pereira, J. Sousa, A. Neto, P. Carvalho, A.J.N. Batista, B.B. Carvalho, C.A.F. Varandas, M. Tardocchi, G. Gorini, Parallel processing method for high-speed real time digital pulse processing for gamma-ray spectroscopy. Fusion Eng. Des. **85**(3), 308 (2010). <https://doi.org/10.1016/j.fusengdes.2010.01.004>
95. Y. Moline, M. Thevenin, G. Corre, M. Paindavoine, Auto-adaptive trigger and pulse extraction for digital processing in nuclear instrumentation. IEEE Trans. Nucl. Sci. **62**(2), 480 (2015). <https://doi.org/10.1109/TNS.2015.2411857>
96. R.K. K. Paul, A. Banerjee, P. Dhara, P. Maity, 2020 11th International Conference on Computing, Communication and Networking Technologies (ICCCNT) (2020), pp. 1–5. <https://doi.org/10.1109/ICCCNT49239.2020.9225678>
97. A.P.I. I. Siddavatam, P.P. P. Vaidya, J.M. M. Nair, in 2017 International Conference on Intelligent Computing, Instrumentation and Control Technologies (ICICICT) (2017), pp. 531–535. <https://doi.org/10.1109/ICICICT1.2017.8342619>
98. G. Blaj, C.J. Kenney, A. Dragone, G. Carini, S. Herrmann, P. Hart, A. Tomada, J. Koglin, G. Haller, S. Boutet, M. Messerschmidt, G. Williams, M. Chollet, G. Dakovski, S. Nelson, J. Pines, S. Song, J. Thayer, Optimal pulse processing, pile-up decomposition, and applications of silicon drift detectors at LCLS. IEEE Trans. Nucl. Sci. **64**(11), 2854 (2017). <https://doi.org/10.1109/TNS.2017.2762281>
99. N. Ensslin, D. Reilly, H.J. Smith (eds.), *Principles of Neutron Coincidence Counting* (U.S. Nuclear Regulatory Commission, 1991), pp. 457–491
100. G. Gerardi, L. Abbene, A digital approach for real time high-rate high-resolution radiation measurements. Nuclear Instruments and Methods in Physics Research, Sect. A: Acceler. Spectrom. Detect. Assoc. Equip. **768**, 46 (2014). <https://doi.org/10.1016/j.nima.2014.09.047>
101. J.M. Cardoso, J.B. Simões, C.M. Correia, Dead-time analysis of digital spectrometers. Nucl. Instrum. Methods Phys. Res. Sect. A Accel. Spectrom. Detect. Assoc. Equip. **522**(3), 487 (2004). <https://doi.org/10.1016/j.nima.2003.11.389>
102. A. Fernandes et al., FPGA code for the data acquisition and real-time processing prototype of the ITER radial neutron camera. IEEE Trans. Nucl. Sci. **66**(7), 1318 (2019). <https://doi.org/10.1109/TNS.2019.2903646>
103. N. Cruz, B. Santos, A. Fernandes, P.F. Carvalho, J. Sousa, B. Goncalves, M. Riva, C. Centoli, D. Marocco, B. Esposito, C.M. Correia, R.C. Pereira, The design and performance of the real-time software architecture for the ITER radial neutron camera. IEEE Trans. Nucl. Sci. **66**(7), 1310 (2019). <https://doi.org/10.1109/TNS.2019.2907056>
104. Y. Moline, M. Thevenin, G. Corre, M. Paindavoine, 2015 4th International Conference on Advancements in Nuclear Instrumentation Measurement Methods and their Applications (ANIMMA), pp. 1–4 (2015). <https://doi.org/10.1109/ANIMMA.2015.7465559>
105. L. Barbot, D. Fourmentel, G. De Izarra, C. Destouches, J.F. Villard, Y. Moline, H. Hamrita, MONACO v2: multipurpose and integrated data acquisition system for on-line neutron and gamma measurements. EPJ Web of Conf. **225**, 03012 (2020). <https://doi.org/10.1051/epjconf/202022503012>
106. S.M. Robinson, S.E. Bender, E.L. Flumerfelt, C.A. LoPresti, M.L. Woodring, IEEE Transactions on Nuclear Science vol. 56-6, pp. 3688–3693 (2009). <https://doi.org/10.1109/TNS.2009.2034372>
107. R. Coulon, J. Dumazert, V. Kondrasovs, S. Normand, Implementation of a nonlinear filter for online nuclear counting. Radiat. Meas. **87**, 13 (2016). <https://doi.org/10.1016/j.radmeas.2016.02.007>

108. R. Coulon, V. Kondrasovs, K. Boudergui, S. Normand, Moving sources detection algorithm for radiation portal monitors used in a linear network. *IEEE Trans. Nucl. Sci.* **61**(4), 2189 (2014). <https://doi.org/10.1109/TNS.2014.2299872>
109. R. Coulon, J. Dumazert, *Ionizing Radiation Effects and Applications* (InTech Open, 2018). <https://doi.org/10.5772/intechopen.71233>
110. R.T. Kouzes, E.R. Siciliano, J.H. Ely, P.E. Keller, R.J. McConn, Passive neutron detection for interdiction of nuclear material at borders. *Nuclear Instruments and Methods in Physics Research Sect. A: Accel. Spectrom. Detect. Assoc. Equip.* **584**(2), 383 (2008). <https://doi.org/10.1016/j.nima.2007.10.026>
111. P. Peerani, A. Tomanin, S. Pozzi, J. Dolan, E. Miller, M. Flaska, M. Battaglieri, R. De Vita, L. Ficini, G. Ottonello, G. Ricco, G. Dermody, C. Giles, Testing on novel neutron detectors as alternative to 3He for security applications. *Nucl. Instrum. Methods Phys. Res. Sect. A Accel. Spectrom. Detect. Assoc. Equip.* **696**, 110 (2012). <https://doi.org/10.1016/j.nima.2012.07.025>
112. P.L. Reeder, A.J. Peurrung, R.R. Hansen, D.C. Stromswold, W.K. Hensley, C.W. Hubbard, Detection of fast neutrons in a plastic scintillator using digital pulse processing to reject gammas. *Nucl. Instrum. Methods Phys. Res. Sect. A Accel. Spectrom. Detect. Assoc. Equip.* **422**(1–3), 84 (1999). [https://doi.org/10.1016/S0168-9002\(98\)01068-7](https://doi.org/10.1016/S0168-9002(98)01068-7)
113. P. Blanc, M. Hamel, C. Déhé-Pittance, L. Rocha, R.B. Pansu, S. Normand, Neutron/gamma pulse shape discrimination in plastic scintillators: Preparation and characterization of various compositions. *Nucl. Instrum. Methods Phys. Res. Sect. A Accel. Spectrom. Detect. Assoc. Equip.* **750**, 1 (2014). <https://doi.org/10.1016/j.nima.2014.02.053>
114. G. Bertrand, M. Hamel, S. Normand, F. Sguerra, Pulse shape discrimination between (fast or thermal) neutrons and gamma rays with plastic scintillators: State of the art. *Nucl. Instrum. Methods Phys. Res. Sect. A: Accel. Spectrom. Detect. Assoc. Equip.* **776**, 114 (2015). <https://doi.org/10.1016/j.nima.2014.12.024>
115. R.M. French, M. Thevenin, M. Hamel, E. Montbarbon, A histogram-difference method for neutron/gamma discrimination using liquid and plastic scintillators. *IEEE Trans. Nucl. Sci.* **64**(8), 2423 (2017). <https://doi.org/10.1109/TNS.2017.2720798>
116. N. Zaitseva, A. Glenn, L. Carman, R. Hatarik, S. Hamel, M. Faust, B. Schabes, N. Cherepy, S. Payne, Pulse shape discrimination in impure and mixed single-crystal organic scintillators. *IEEE Trans. Nuclear Sci.* **58**(6 PART 2), 3411 (2011). <https://doi.org/10.1109/TNS.2011.2171363>
117. N. Zaitseva, B.L. Rupert, I. PaweŁczak, A. Glenn, H.P. Martinez, L. Carman, M. Faust, N. Cherepy, S. Payne, Plastic scintillators with efficient neutron/gamma pulse shape discrimination. *Nucl. Instrum. Methods Phys. Res. Sect. A: Acceler. Spectrom. Detect. Assoc. Equip.* **668**, 88 (2012). <https://doi.org/10.1016/j.nima.2011.11.071>
118. C. Lynde, E. Montbarbon, M. Hamel, A. Grabowski, C. Frangville, G.H.V.V. Bertrand, G. Galli, F. Carrel, V. Schoepff, Z. El Bitar, Optimization of the charge comparison method for multiradiation field using various measurement systems. *IEEE Trans. Nucl. Sci.* **67**(4), 679 (2020). <https://doi.org/10.1109/TNS.2020.2966886>
119. P. Blanc, M. Hamel, L. Rocha, R.B.B. Pansu, F. Gobert, I. Lampre, S. Normand, Intrinsic evaluation of n/γ discrimination in plastic scintillators. *IEEE Trans. Nucl. Sci.* **61**(4), 1995 (2014). <https://doi.org/10.1109/TNS.2014.2327292>
120. B. D'Mellow, M.D. Aspinall, R.O. Mackin, M.J. Joyce, A.J. Peyton, Digital discrimination of neutrons and γ -rays in liquid scintillators using pulse gradient analysis. *Nucl. Instrum. Methods Phys. Res. Sect. A: Accel. Spectrom. Detect. Assoc. Equip.* **578**(1), 191 (2007). <https://doi.org/10.1016/j.nima.2007.04.174>
121. E. Bayat, N. Divani-Vais, M.M. Firoozabadi, N. Ghal-Eh, A comparative study on neutron-gamma discrimination with NE213 and UGLLT scintillators using zero-crossing method. *Radiat. Phys. Chem.* **81**(3), 217 (2012). <https://doi.org/10.1016/j.radphyschem.2011.10.016>
122. N. Kehtarnavaz, *Real-Time Digital Signal Processing Based on the TMS320C6000* (Wiley, 2013)

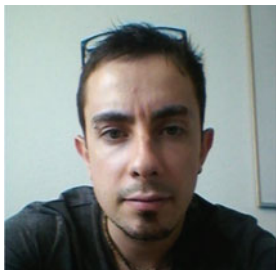
123. L. Stuhl, M. Sasano, K. Yako, J. Yasuda, H. Baba, S. Ota, T. Uesaka, PANDORA, a large volume low-energy neutron detector with real-time neutron-gamma discrimination. *Nucl. Instrum. Methods Phys. Res. Sect. A: Accel. Spectrom. Detect. Assoc. Equip.* **866**, 164 (2017). <https://doi.org/10.1016/j.nima.2017.06.015>
124. J. Griths, S. Kleinegesse, D. Saunders, R. Taylor, A. Vacheret, Pulse shape discrimination and exploration of scintillation signals using convolutional neural networks. *Mach. Learn. Sci. Technol.* **1**(4) (2020). <https://doi.org/10.1088/2632-2153/abb781>
125. A.D. Kaplan, B. Blair, C. Chen, A. Glenn, J. Ruz, R. Wurtz, A neutron-gamma pulse shape discrimination method based on pure and mixed sources. *Nucl. Instrum. Methods Phys. Res. Sect. A: Accel. Spectrom. Detect. Assoc. Equip.* **919**, 36 (2019). <https://doi.org/10.1016/j.nima.2018.11.136>
126. S. Akkoyun, Time-of-flight discrimination between gamma-rays and neutrons by using artificial neural networks. *Annals Nucl. Energy* **55**, 297 (2013). <https://doi.org/10.1016/j.anucene.2013.01.006>
127. X. Yu, J. Zhu, S. Lin, L. Wang, H. Xing, C. Zhang, Y. Xia, S. Liu, Q. Yue, W. Wei, Q. Du, C. Tang, Neutron-gamma discrimination based on the support vector machine method. *Nucl. Instrum. Methods Phys. Res. Sect. A: Accel. Spectrom. Detect. Assoc. Equip.* **777**, 80 (2015). <https://doi.org/10.1016/j.nima.2014.12.087>
128. H. Arahmane, A. Mahmoudi, E.M. Hamzaoui, Y. Ben Maissa, R. Cherkaoui El Moursli, Neutron-gamma discrimination based on support vector machine combined to nonnegative matrix factorization and continuous wavelet transform. *Meas. J. Int. Meas. Confed.* **149** (2020). <https://doi.org/10.1016/j.measurement.2019.106958>
129. X. Fabian et al., Artificial neural networks for neutron/ γ discrimination in the neutron detectors of NEDA. *Nucl. Instrum. Methods Phys. Res. Sect. A: Accel. Spectrom. Detect. Assoc. Equip.* **986**, (2021). <https://doi.org/10.1016/j.nima.2020.164750>
130. Z. Zhang, C. Hu, Y. Zhang, B. Liao, J. Zhu, X. Fan, Y. Li, L. Zhang, The combined application of principal component analysis and decision tree in nuclear pulse shape discrimination. *Nucl. Instrum. Methods Phys. Res. Sect. A Accel. Spectrom. Detect. Assoc. Equip.* **943**, (2019). <https://doi.org/10.1016/j.nima.2019.162425>
131. H. Bagán, A. Tarancón, G. Rauret, J.F. García, Alpha/beta pulse shape discrimination in plastic scintillation using commercial scintillation detectors. *Anal. Chimica Acta* **670**(1–2), 11 (2010). <https://doi.org/10.1016/j.aca.2010.04.055>
132. C. Bobin, C. Thiam, B. Chauvenet, J. Bouchard, On the stochastic dependence between photomultipliers in the TDCR method. *Appl. Radiat. Isot.* **70**(4), 770 (2012). <https://doi.org/10.1016/j.apradiso.2011.12.035>
133. J. Wen, D. Dou, J. Zhu, Z. Zeng, T. Xue, J. Li, J. Li, Y. Liu, *22nd Virtual IEEE Real Time Conference* (2020)
134. R. Panahi, S.A. Feghhi, S.R. Moghadam, S.M. Zamzamian, Simultaneous alpha and gamma discrimination with a phoswich detector using a rise time method and an artificial neural network method. *Appl. Radiat. Isot.* **154**, (2019). <https://doi.org/10.1016/j.apradiso.2019.108881>
135. M.G. Paff, M.L. Ruch, A. Poitrasson-Riviere, A. Sagadevan, S.D. Clarke, S. Pozzi, Organic liquid scintillation detectors for on-the-fly neutron/gamma alarming and radionuclide identification in a pedestrian radiation portal monitor. *Nucl. Instrum. Methods Phys. Res. Sect. A: Accel. Spectrom. Detect. Assoc. Equip.* **789**, 16 (2015). <https://doi.org/10.1016/j.nima.2015.03.088>
136. G.N. Ninh, P. Phongphaeth, C. Nares, Q.N. Hao, *AIP Conference Proceedings*, vol. 1704-1 (American Institute of Physics Inc., 2016), p. 050005. <https://doi.org/10.1063/1.4940101>
137. M. Thevenin, O. Bichler, C. Thiam, V. Lourenço, C. Bobin, in *Proceedings of SPIE—The International Society for Optical Engineering*, vol. 9455 (2015). <https://doi.org/10.1117/12.2177032>
138. C. Bobin, O. Bichler, V. Lourenço, C. Thiam, M. Thévenin, Real-time radionuclide identification in γ -emitter mixtures based on spiking neural network. *Appl. Radiat. Isot.* **109**, 405 (2016). <https://doi.org/10.1016/j.apradiso.2015.12.029>

139. B. Jeon, J. Kim, E. Lee, M. Moon, G. Cho, Pseudo-gamma spectroscopy based on plastic scintillation detectors using multitask learning. *Sensors* **21**(3) (2021). <https://doi.org/10.3390/s21030684>
140. J. Kim, K. Park, G. Cho, Multi-radioisotope identification algorithm using an artificial neural network for plastic gamma spectra. *Applied Radiation and Isotopes* **147**, 83 (2019). <https://doi.org/10.1016/j.apradiso.2019.01.005>
141. B.T. Koo, H.C. Lee, K. Bae, Y. Kim, J. Jung, C.S. Park, H.S. Kim, C.H. Min, Development of a radionuclide identification algorithm based on a convolutional neural network for radiation portal monitoring system. *Radiat. Phys. Chem.* **180** (2021). <https://doi.org/10.1016/j.radphyschem.2020.109300>
142. H. Paradis, C. Bobin, J. Bobin, J. Bouchard, V. Lourenço, C. Thiam, R. André, L. Ferreux, A. de Vismes Ott, M. Thévenin, Spectral unmixing applied to fast identification of γ -emitting radionuclides using NaI(Tl) detectors. *Appl. Radiat. Isot.* **158**, 109068 (2020). <https://doi.org/10.1016/j.apradiso.2020.109068>
143. R. André, C. Bobin, J. Bobin, J. Xu, A. de Vismes Ott, Metrological approach of γ -emitting radionuclides identification at low statistics: application of sparse spectral unmixing to scintillation detectors. *Metrologia* **58**(1), 015011 (2021). <https://doi.org/10.1088/1681-7575/abcc06>



Mathieu Thevenin (ORCID 0000-0002-9962-1135) obtained his B.S. (computer science, 2003), his Master of engineering and his Master's degrees (in Computer science, Embedded systems and Instrumentation, 2006) from the University of Burgundy (France). His Ph.D. (University of Burgundy, 2009) focused on the design of a programmable, small silicon footprint Digital Signal Processor (DSP) for real-time video enhancement with the French Atomic Energy Commission (CEA). Since this time, he has focused on the development of new approaches for data acquisition and processing, from the analog front-end to the data processing and the end-user application including machine learning. His main research interests are the design of programmable hardware architectures for real-time stream signal processing, for various applications like nuclear instrumentation and CBRN-E, spectrometry, digital signal compression and more recently quantum bit readout and stimulation.. He currently holds a permanent senior scientist position at the (CEA)

Iramis institute and he is the head of the electronics and signal processing laboratory. To this date and with a h-index of 7 (according to google scholar), he has co-authored 12 peer-reviewed international journal papers, as much conference papers, 14 patents and 1 book chapter. He also co-managed 3 Ph.D. students and 2 postdoctoral researchers.



Yoann Moline (34 yo) defended his PhD in Computer Engineering at the University of Dijon Burgundy (France), on Digital Pulse Processing architectures for Nuclear Instrumentation at the French Atomic Energy and Alternative Energies Commission (CEA). After a first experience as Design Engineer in Bertin Technologies (France). He obtained a full position at the CEA in 2016, as a research engineer and project manager specializing in the design of architecture and systems for nuclear instrumentation addressing the adequacy between analog/digital electronics, signal processing and instrumentation. Its work is oriented towards the transfer and industrialization of devices dimensioned directly by the needs of the field and the end-user. In January 2021, he is the author or co-author of 8 publications and 3 patents.

Chapter 11

Radioactive Noble Gas Detection and Measurement with Plastic Scintillators



Krasimir Mitev and Philippe Cassette

Abstract Radioactive noble gas isotopes considered in this chapter are fission products of uranium and plutonium, neutron activation products of calcium or radon isotopes belonging to the natural decay chains of uranium and thorium. The measurement of radon isotopes and decay products is important as these radionuclides represent a significant health hazard. The measurement of the other noble gas is of paramount interest for the detection or monitoring of both civil and nuclear activities. The decay data of the main noble gas radionuclides of interest are reported, and noble gas absorption phenomena in plastic polymers are described in detail. Then general applications of plastic scintillators in noble gas atmospheric measurement systems are described. Eventually, specific aspects of radon measurement using plastic scintillators are detailed. This concerns the shape of alpha peaks and the application of alpha/beta discrimination to the measurement of radon and their radioactive progenies.

11.1 Radioactive Noble Gas Isotopes

Radioactive noble gas (RNG) isotopes are good tracers of both civil and military nuclear activities like nuclear reactors, fuel reprocessing plants and nuclear explosions. During the fission of uranium and plutonium, various isotopes of krypton and xenon are formed. In case of intense neutron production, isotopes of argon can also be produced from nuclear reactions with calcium.

In nuclear power plants, short-lived noble gas isotopes decay into non-gaseous elements which are trapped in the fuel, but a few isotopes are sufficiently long-lived to stay in the fuel rods and can be released into the primary coolant, and after, in the environment in case of fuel cladding failure. Because radioactive noble gases

K. Mitev · P. Cassette

Faculty of Physics, Sofia University “St. Kliment Ohridski”, 5 James Bourchier Blvd, 1164 Sofia, Bulgaria

e-mail: kmitev@phys.uni-sofia.bg

P. Cassette

e-mail: philippe.cassette@phys.uni-sofia.bg

cannot be separated by the primary coolant purification system, these noble gases are eventually released into the atmosphere. The activities released from individual reactors may vary over a wide range, depending on the cladding integrity, and thus the atmospheric concentration of noble gases shows large local variations.

To give orders of magnitude, the average annual RNG activity released by French PWR reactors was between 0.9 and 2.2 GBq in 2003 [1]. This is only a very small amount compared to the ^{85}Kr released by reprocessing plants. In 2017, the ^{85}Kr activity release from La Hague reprocessing plant (France) was 285 PBq, which corresponds to about 60% of the release authorization given by the nuclear regulation body [2]. The present average concentration in the atmosphere of the northern hemisphere is about 1 Bq/m³, with higher local concentrations around nuclear facilities. In the European Union, ^{85}Kr and ^{133}Xe are key reporting nuclides for emissions from nuclear power plants and ^{85}Kr is a key reporting nuclide for the emissions from reprocessing facilities.

From a study by Nitta [3], the amount of ^{85}Kr released from the Fukushima Daiichi nuclear power plant accident in 2011 was estimated to be 6.1×10^{16} Bq, which represents about one-third of the ^{85}Kr discharge from La Hague reprocessing plant in 2011.

The behavior of xenon is different, as most of the isotopes produced by fission decay within seconds, but a few isotopes could remain for several days and are produced in such amounts that they can be detected at large distances from their source. The xenon isotopes relevant for environmental sampling are $^{131\text{m}}\text{Xe}$, ^{133}Xe , $^{133\text{m}}\text{Xe}$ and ^{135}Xe .

The fission yields of noble gas can be found in Table 11.1, adapted from [4].

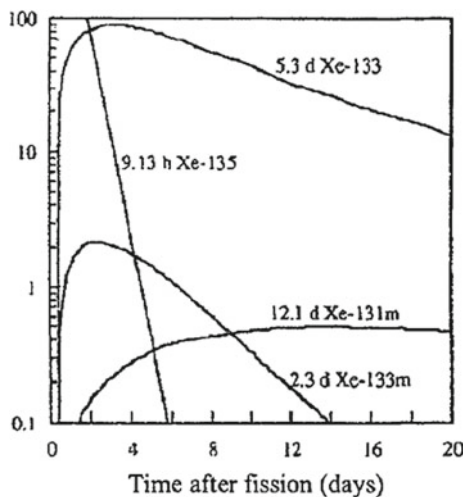
Considering nuclear tests, underground nuclear explosions are likely to vent the chemically inert noble gases into the atmosphere through the ground. This makes the detection of radioactive noble gases in general, and radioxenon in particular, an attractive tool for the survey of clandestine tests of nuclear weapons.

To monitor the compliance with the Comprehensive Nuclear-Test-Ban Treaty (CTBT) which is now signed by 184 countries and ratified by 168 countries, an international network of stations was set up and provides seismic, radionuclide, hydroacoustic and infrasound measurements. The radionuclide part of the network consists

Table 11.1 Cumulative fission yields (%) for different fission types for some krypton and xenon isotopes [4]

	Isotope					
	Fission type	^{85}Kr	$^{131\text{m}}\text{Xe}$	^{133}Xe	$^{133\text{m}}\text{Xe}$	^{135}Xe
^{235}U	Thermal neutrons	2.83×10^{-1}	4.05×10^{-2}	6.70	1.89×10^{-1}	6.54
^{235}U	Fission neutrons	2.75×10^{-1}	4.51×10^{-2}	6.72	1.92×10^{-1}	6.60
^{238}U	Fission neutrons	1.49×10^{-1}	4.61×10^{-2}	6.76	1.90×10^{-1}	6.97
^{239}Pu	Thermal neutrons	1.23×10^{-1}	5.40×10^{-2}	7.02	4.65×10^{-2}	7.61
^{239}Pu	Fission neutrons	1.28×10^{-1}	5.43×10^{-2}	6.96	2.40×10^{-1}	7.54

Fig. 11.1 Evolution of the activity of noble gas with time after fission
(reproduced from [5] with permission from Elsevier)



of 80 stations worldwide, and 40 of these are scheduled to report measurements of radioxenon.

The evolution of the activity of the four radioactive xenon isotopes after fission can be observed in Fig. 11.1 from [5], assuming that these radionuclides are produced by thermal fission of ^{235}U and that there is no fractionation among the three mass chains.

The activity of ^{135}Xe decreases exponentially to become negligible after about 5 days. The ^{133}Xe activity remains at relatively large values for several weeks after the release, and the activity of $^{131\text{m}}\text{Xe}$, which is also produced by the decay of ^{131}I , increases several days after fission and reaches a maximum after about 10 days before decreasing after 2 weeks. The $^{133\text{m}}\text{Xe}$ activity reaches a maximum after about 2 days, and then decreases exponentially.

When monitoring the xenon gas release from a subsurface nuclear detonation, the most important background is the release from nuclear power plants. An inventory was made from the information available from nuclear power plants in North America and Europe in the 1995–2005 period, which concluded that a total of 1.3 PBq of radioxenons are released from nuclear power plants as continuous or pulsed emission in a generic year [1]. It is nevertheless possible to differentiate a nuclear power plant xenon release from the one originating in a nuclear explosion by inspecting the ratio between the different xenon isotopes. The ratio $^{135}\text{Xe}/^{133}\text{Xe}$ is expected to be four orders of magnitudes larger for a subsurface nuclear explosion compared to a reactor release, and the value for $^{133\text{m}}\text{Xe}/^{133}\text{Xe}$ will differ by about two orders of magnitude for the two release types.

Nevertheless, nuclear power plant accidents can potentially make inoperative the very sensitive noble gas monitors of the CTBT network.

The Three Mile Island nuclear power plant accident in 1979 led to a release in the atmosphere of 90–370 PBq [6], and 80% of the activity was due to ^{133}Xe . Another evaluation [7] gave a significantly higher activity release of 820 (70) PBq.

The global ^{133}Xe activity release from the Chernobyl accident in 1986 was estimated to be between 133 and 6500 PBq [8].

In the case of the Fukushima Daiichi disaster, the release of ^{133}Xe was observed at Pacific Northwest National Laboratory, based near Seattle (WA, USA), located more than 7000 km from Fukushima. The first detections of ^{133}Xe were made, starting 4 days following the earthquake with maximum concentrations in excess of 40 Bq/m^3 , which is more than 40,000 times the average concentration of this isotope in this part of the United States [9]. The global ^{133}Xe inventory in the fuel of the Fukushima Daiichi reactors was estimated at 12.2 EBq, from the nuclear fuel burn-up calculations. Measurements and dispersion simulations seem to indicate that 61% of this inventory was released during the accident, with the addition of 2 EBq due to the decay of ^{133}I [10, 11].

Radioxenons are also released by facilities producing these isotopes for medical uses: ^{133}Xe is mainly used for lung perfusion tests and $^{131\text{m}}\text{Xe}$ is the decay product of ^{131}I which is used in medical diagnosis. There are a few facilities in the world producing xenon for medical use, in Canada, the Netherlands, Belgium and South Africa. Air concentration significantly above the normal background can be found in the vicinity of these production centers [12].

Radon-222, on the other hand, is a naturally occurring radioisotope, which is considered to be the second cause of lung cancer after smoking [13]. More than half of the exposure of the public to natural sources of radiation is due to ^{222}Rn and its short-lived decay products. Rn-220 is a short-lived isotope of radon, which may also be present indoors in some regions, and which has received significant attention in the last decade due to the fact that it may impede or bias indoor radon measurements.

The decay schemes and main decay data of the noble gas isotopes of interest are described thereafter.

11.1.1 Kr-85

The ^{85}Kr decays by beta minus transition mainly toward the ground level of ^{85}Rb , with a half-life of 10.752(23) a. The decay scheme is presented in Fig. 11.2. A faint beta transition (probability 0.438%) populates an excited level of ^{85}Rb with $1.015 \mu\text{s}$ lifetime, leading to a weak gamma emission of 513.99 keV. The gamma-ray measurement of ^{85}Kr is possible but with two major difficulties: the emission intensity is low (0.435%) and the energy is close to the positron annihilation energy (511 keV) which is always present in the background spectrum. Thus, the most efficient measurement method is through the detection of the main beta emission (99.562%) with a maximum energy of 687.1 keV and mean energy of 251.4 keV. The use of beta-gamma coincidence detection techniques is made difficult by the low gamma emission intensity and the long half-life of the ^{85}Rb excited state.

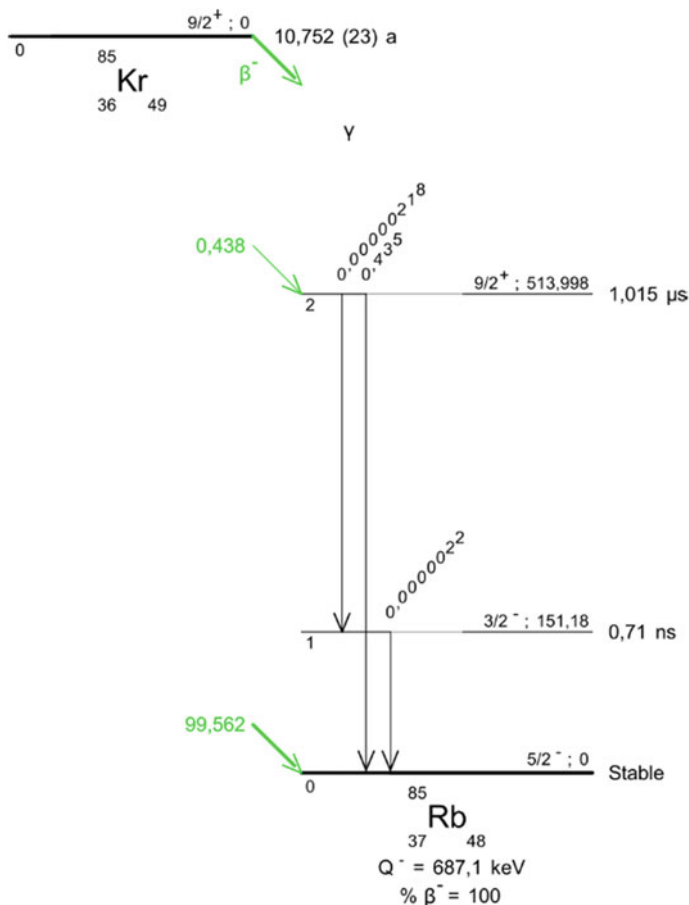


Fig. 11.2 Decay scheme of ^{85}Kr [14]

11.1.2 Xe-131m

The ^{131}mXe de-excites to the stable ^{131}Xe by highly converted gamma transition, with a half-life of 11.962(20) d. The decay scheme is presented in Fig. 11.3. The de-excitation leads to the emission of conversion electrons (97.9% intensity) in the 129.4–163.9 keV energy range, in Auger K electrons in 23.5–34.5 keV energy range, in Auger L electrons in 2.5–5.4 keV energy range and X-ray emission in the 29.5–34.6 keV energy range. The 163.930 keV gamma-ray emission intensity is 1.942%.

Xenon-131 m can be measured by gamma-ray spectrometry or through its electron emission. Electron-X coincidence counting is possible between the conversion electrons and the X-rays following the atomic re-arrangement.

Fig. 11.3 Decay scheme of ^{131m}Xe [14]



11.1.3 Xe-133

Xe-133 disintegrates by beta minus emissions to the excited levels of ^{133}Cs , with $5.2474(5)$ d half-life. The decay scheme is presented in Fig. 11.4. The main beta transition, 99.12% probability, has a maximum energy of 346.4 keV and mean energy of 106.6 keV. It is followed by a gamma de-excitation resulting in 80.9979 keV gamma-ray emission with 37% intensity, or conversion electrons with 45.01–80.99 keV energy range with a total intensity of 62.8%. Xe-133 can be measured with gamma-ray spectrometry or through its beta and conversion electrons. Beta-gamma coincidence measurement techniques can also be used.

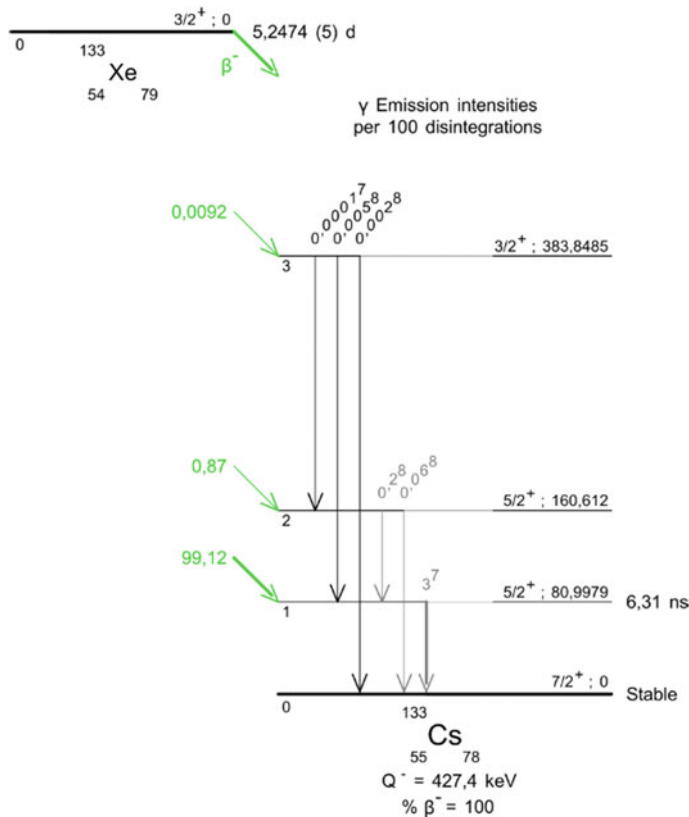


Fig. 11.4 ^{133}Xe decay scheme [14]

11.1.4 Xe-133m

Xe-133m decays by a single highly converted gamma transition to the ground state of ^{133}Xe with a half-life of 2.198(13) d. The decay scheme is presented in Fig. 11.5. Conversion electrons in the 198.655–233.207 keV energy range are emitted with a total intensity of 89.88%, and the 233.219 keV gamma-ray emission is emitted with an intensity of 10.12%. Auger and X-ray in the 23.5–34.5 keV energy range are emitted in coincidence with the conversion electrons.

Xenon-133m can be measured by gamma-ray spectrometry or through its electron emission. Electron-X coincidence counting is possible between the conversion electrons and the X-rays following the atomic re-arrangement.

Fig. 11.5 Decay scheme of ^{133m}Xe [14]



11.1.5 Xe-135

Xe-135 decays by beta minus transitions to excited levels of ^{135}Cs with a half-life of 9.143(29) h. The decay scheme is presented in Fig. 11.6. The main beta emission, with an intensity of 96.1%, has maximum beta energy of 915.2 keV and mean energy of 310.2 keV. It is followed by a 249.794 keV gamma-ray emission, with an intensity of 89.6%, or by the emission of conversion electrons in the 214–250 keV energy range with a total intensity of 6.6%. Xe-135 can be measured by gamma-ray spectrometry, or by the detection of beta electrons, with or without coincidence with the gamma emission.

11.1.6 Ar-37

Ar-37 decays by electron capture to the ground state of ^{37}Cl with a half-life of 35.01(2) d. The decay scheme is presented in Fig. 11.7. The Auger and X-ray emission

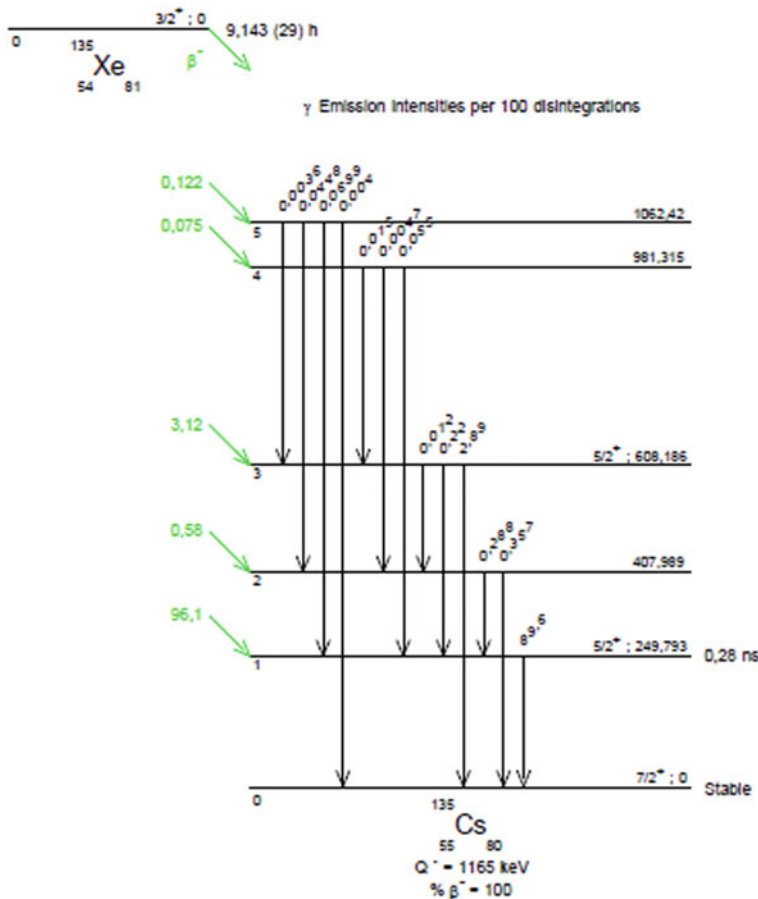


Fig. 11.6 Decay scheme of ^{135}Xe [14]

following the atomic re-arrangement are in the 2.2–2.8 keV energy range. The low-energy emission makes the measurement of this radionuclide quite challenging.

11.1.7 Rn-222 and Progenies

Rn-222, generally called radon, is a radioactive noble gas and its decay leads to the formation of solid progenies. The simplified decay chain is presented in Fig. 11.8.

Rn-222 decays by an alpha transition to ^{218}Po with a half-life of $3.8232(8) \text{ d}$. The main energy of the alpha emission is at 5590.3 keV . The first solid daughter, ^{218}Po , also decays by an alpha transition to ^{214}Pb , with a half-life of 3.071 min , with the main emission of 6002.35 keV alpha-particle. Pb-214 decays by beta transition to ^{214}Bi

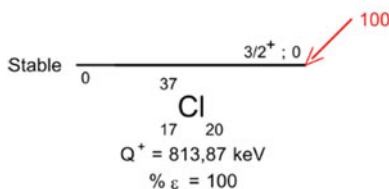
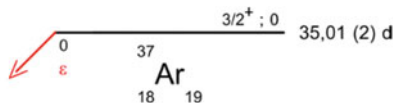
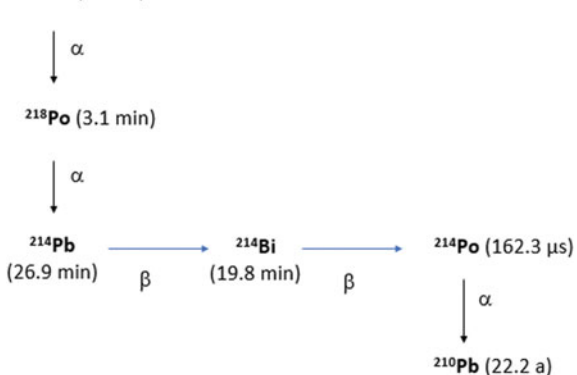


Fig. 11.7 Decay scheme of ^{37}Ar [14]

Fig. 11.8 ^{222}Rn simplified decay chain [14]



with a half-life of 26.916 min. The maximum beta-particle energy is at 1019 keV. Bi-214 mainly decays by multiple beta transitions with a half-life of 19.8 min to the excited and the ground level of ^{214}Po . The maximum beta energy of these transitions is 3270 keV. Po-214 decays by an alpha transition to ^{210}Pb , with a half-life of 162.3 μs . The main alpha emission energy is 7686.82 keV. Pb-210 mainly decays by beta transition with a half-life of 22.23 a. The secular equilibrium between ^{222}Rn and its

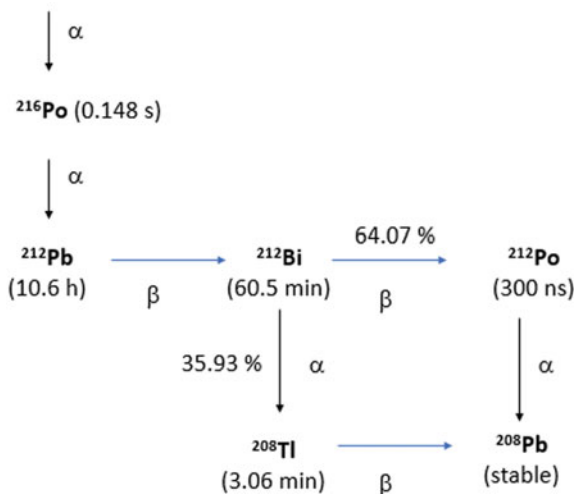
solid daughters, up to ^{214}Po , is reached within about 4 h. In places where there is no long-term radon accumulation, there is no equilibrium between radon and ^{210}Pb and thus, this radionuclide and its daughters can generally be neglected.

Rn-222 is the radioactive daughter of ^{226}Ra and is part of the ^{238}U natural decay series. Thus, its presence is ubiquitous and could present a health hazard. Moreover, it can also be an interfering radionuclide during the measurement of other noble gases.

11.1.8 Rn-220 and Progenies

Rn-220, also called thoron, is a radioactive noble gas decaying through alpha transition with a half-life of 55.8 s to ^{216}Po . Its simplified decay chain is presented in Fig. 11.9. The main alpha emission is at 6288.22 keV. Po-216 decays mainly by an alpha transition to the ground level of ^{212}Pb , with a half-life of 0.148 s. The main alpha emission is at 7678.4 keV. Pb-212 disintegrates by beta minus transitions to excited and ground states of ^{212}Bi with a half-life of 10.64 h. The maximum beta energy is about 415 keV but conversion electrons in the 24–300 keV energy range are also present. Bi-212 decays with a half-life of 60.54 min by alpha transitions to ^{208}Tl (probability 35.93%) or by beta minus transitions to ^{212}Po (probability 64.07%). The alpha energy is in the 5302–6090 keV energy range. The maximum beta energies are in the 446–2252 keV energy range. Tl-208 decays by beta minus transitions to excited levels of ^{208}Pb , with a half-life of 3.058 min. The maximum beta energies are in the 518–1801 keV energy range, and the beta emission can be coincident with

Fig. 11.9 ^{220}Rn decay chain
[14]



high-energy gamma emission or conversion electrons. Po-212 decays by an alpha transition to the ground state of ^{208}Pb , with a half-life of 300 ns. The energy of the alpha-particles is 8785 keV. Rn-220 is part of the ^{232}Th natural decay series and can be found in the environment or indoors. The health hazard presented by ^{220}Rn is generally lower than the one of ^{222}Rn , due to the short half-life of the former but it cannot be neglected, as it could interfere with the measurement of ^{222}Rn .

From the decay properties of these radioactive noble gases of interest, it can be observed that all of them, except ^{37}Ar , emit sufficiently energetic electrons (both beta and conversion electrons), to be detected by beta detectors like plastic scintillators. Rn-222 and ^{220}Rn can also be measured using plastic scintillators, through their high-energy alpha or beta emissions.

Important notice

In this chapter, the abbreviation “PS” refers to “plastic scintillator”.

11.2 Application of Plastic Scintillators to the Detection of Noble Gas

11.2.1 Xenon Detection Systems for the CTBT Network

Four types of noble gas monitoring systems were developed for noble gas monitoring in the frame of the CTBT network [15], namely ARSA, ARIX, SAUNA and SPALAX, and the three latter systems are now integrated into the network. These monitoring devices are mostly composed of an air sampling system, a gas purification unit, and a noble gas detector. These devices aim at detecting xenon radioisotopes, with a detection limit lower than 1 mBq/m³. The air sampling system allows the processing of large air volumes to increase the sensitivity. The purification system is devoted to the elimination of gas which could interfere with the measurement, like water vapor, CO₂, oxygen and radon. After these steps, the purified gas is trapped in a detection cell, associated with beta and gamma detectors, generally arranged as beta-gamma coincidence systems, in order to drastically increase the signal-to-noise ratio and to allow discrimination between the xenon isotopes. Except for the SPALAX device, which uses a combination of a silicon detector for the electrons and a germanium detector for the photons, the others systems make use of a plastic scintillator as the beta and electron detectors and are briefly described hereafter.

11.2.1.1 ARSA

An automated radioxenon sampler and analyzer, ARSA, has been developed at Pacific Northwest National Laboratory in support of the CTBT [16]. This system uses a beta-gamma coincidence counting detector: beta and conversion electrons are detected in a cylindrical plastic scintillation cell, and gamma- and X-rays are detected in a surrounding NaI(Tl) scintillation detector.

The beta cells are made of 1.2 mm thick plastic scintillator (BC-404) and are 5 cm long hollow cylinders with a diameter of 1.25 cm. The cell ends are made of the same scintillator material. Each cell has a small tube glued with optical epoxy on one side for the transfer of the xenon gas into and out of the cell.

The beta cells are surrounded by two NaI(Tl) scintillators coupled to four photomultiplier tubes.

The whole detector is placed inside a 50 mm thick lead shielding lined with a 0.6 mm thick copper plating in order to reduce the detector background. The signal processing allows the detection in coincidence of the plastic and NaI(Tl) leading to a bidimensional beta/gamma spectrum. From the decay properties of each xenon nuclide, several regions of interest can be selected.

The coincidence detection system also allows the detection of radon progenies, like ^{214}Pb , which could interfere with the xenon measurement.

Tests of this system gave minimum detectable concentrations (MDC) of 0.12 mBq/m³ for ^{133}Xe and 0.52 mBq/m³ for ^{135}Xe . An increase of the MDC to 0.39 mBq/m³ for ^{133}Xe was observed after the measurement of an atmosphere containing 110 mBq/m³ of this nuclide, revealing a memory effect due to the diffusion of xenon inside the plastic scintillator cell.

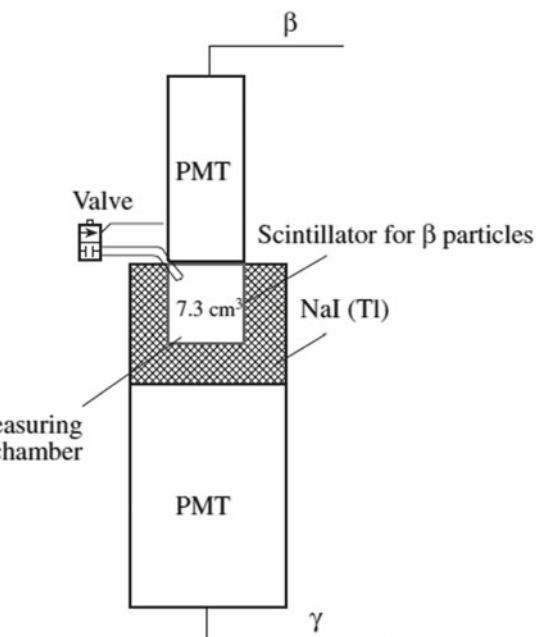
11.2.1.2 ARIX

The development of the ARIX system started in 1996 at Khlopin Radium Institute in St. Petersburg [16], aiming at detecting low volume activities of radioxenons. Further development led to the ARIX-01 system now in use in the CTBT network [17, 18]. A mobile version, ARIX-03, was then developed [19].

The detector unit (Fig. 11.10) consists of the association of two detectors: a NaI(Tl) detector for photons and a plastic scintillator for electrons. The NaI(Tl) crystal has a diameter of 40 mm, a height of 37 mm and a well 18 mm in diameter and 28 mm in depth. The electron detector is a polystyrene-based plastic scintillator applied to the walls of the measuring chamber which is a 0.3 mm thick aluminum barrel (17 mm diameter and 27 mm height). The 0.1 mm thick plastic scintillator covers the inner surface of the barrel.

The aluminum barrel is covered with a transparent organic-glass plug also coated with a plastic scintillator layer. The measuring chamber, transparent for X- and gamma-rays, is located in the well of the NaI(Tl) crystal. Both scintillation units are placed in a vertical position inside a demountable 50 mm thick lead shielding.

Fig. 11.10 Detector unit used in the ARIX-01 system [17]



The two detectors are processed in coincidence, allowing a good rejection of the background and discrimination between the xenon isotopes. The minimum detectable concentration of ^{133}Xe is 0.5 mBq/m³ for 10 hour measurement, which complies with the requirements of the sensitivity of this type of measuring system.

11.2.1.3 SAUNA

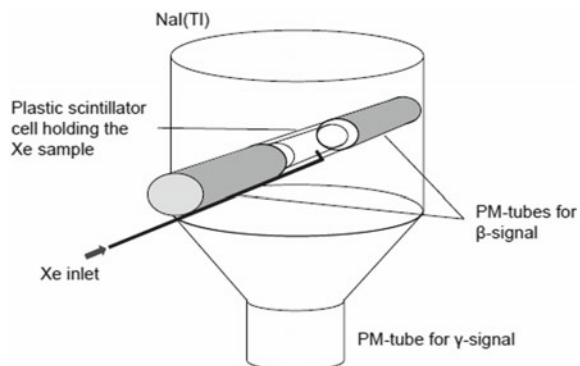
Almost half of the radioxenon detection systems used within the CTBT network are SAUNA systems. Initially developed by the Swedish Defence Research Agency (FOI) [20], the system was commercialized in 2004, and the current version, SAUNA II, is manufactured by the Gammadata SAUNA Systems company [21].

In the sampling and processing units, a xenon sample of typically 1.3 cm³ is extracted from around 15 m³ of air. The xenon sample is then introduced into a detector where the activities of $^{131\text{m}}\text{Xe}$, $^{133\text{m}}\text{Xe}$, ^{133}Xe and ^{135}Xe are measured during 11 h.

The detector is a beta-gamma coincidence spectrometer consisting of a 6.2 cm³ cylindrical plastic scintillator cell, inserted into a drilled hole in a NaI(Tl) crystal, as illustrated in Fig. 11.11.

The beta-particles and conversion electrons are detected by the plastic scintillator cell, and the gamma- and X-rays by the NaI(Tl) crystal. The thickness of the walls of the plastic scintillator cell is 1 mm, assuring that the beta electrons from ^{133}Xe are fully stopped. The NaI(Tl) is read out by one PM-tube, and the plastic

Fig. 11.11 The SAUNA detector. The xenon sample is located inside the plastic scintillator cell during the measurement. The signal from the NaI(Tl) crystal is read out by one PM-tube and the signal from the plastic scintillator by two PM-tubes (adapted from [20])

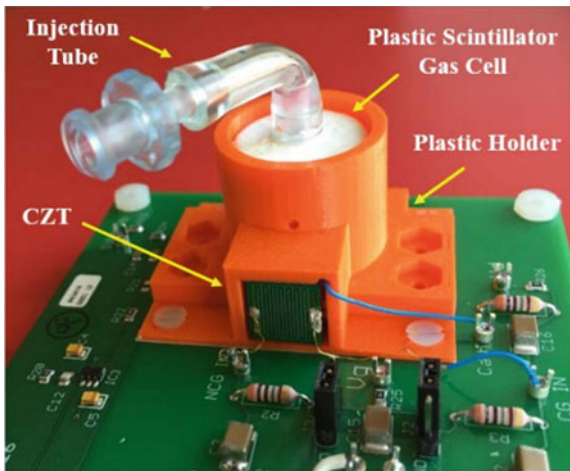


scintillator cell by two (one at each end). An event is recorded in the 2D histogram if a signal is measured in all three PM-tubes in coincidence. The system contains 2 identical detector units working in parallel where one detector measures the gas background in the empty detector while the other one measures a sample, and vice versa. The background measurement is needed to correct for residual activity left in the detector from previous samples, as part of the xenon sample diffuses into the plastic scintillator material of the beta cell during the measurements (memory effect). This memory effect is compensated for by measuring a gas background measurement of the evacuated cell, prior to each sample measurement. The residual activity in the gas background measurement can then be subtracted from the sample activity. For this reason, the SAUNA system contains two detectors working in parallel to allow for continuous monitoring. However, this leads to an elevation of the system detection limit and another approach was investigated, consisting of coating the surface of the plastic scintillator to prevent gas diffusion into it. Several coating materials were tested but the deposition of a 425 nm thick layer of Al_2O_3 lead to the attenuation of the memory effect by a factor of 1000, without introducing a significant degradation of the resolution of the detector [22]. An open problem is the integrity of the coating with time and long-term evaluation of the evolution of the properties of the plastic-coated scintillator which are under investigation.

11.2.1.4 Other System Under Development

An innovative miniature xenon detection system was developed at the Oregon State University [23]. The detector is composed of a 1 cm^3 CZT crystal for gamma- and X-ray detection, associated with an EJ-212 plastic scintillator gas cell (Fig. 11.12). The coplanar CZT crystal was selected for its good energy resolution at room temperature. The plastic scintillator is coupled to a 3×3 array of SiPM detectors, as a rugged alternative to photomultiplier tubes. The two detectors are connected to an FPGA-based electronic system allowing the real-time processing of the coincidences. The minimum detectable concentration of the prototype complies with the CTBT

Fig. 11.12 The CZT/plastic scintillator detection system (reproduced from [23] with permission from Elsevier)



requirements for xenon isotopes except for ^{135}Xe . An increase of the size of the CZT crystal is proposed to improve the MDC for ^{135}Xe , making this detector competitive with the SAUNA and ARIX detection systems.

11.2.2 Kr-85 Monitors Using Plastic Scintillators

As ^{85}Kr is a fission product, it is present in nuclear facilities, especially in the fuel reprocessing plants. Two kinds of monitors are then needed: monitors of ^{85}Kr inside the nuclear facility, including a measurement system in the stack, and monitors in the environment around the nuclear facilities. In each case, the measurement range is different: in the stack of a reprocessing plant, it is in the $10^{-3}\text{--}10^2 \text{ Bq}/\text{cm}^3$ range, in the environment it should cover a much lower range, between less than $1 \text{ Bq}/\text{m}^3$ to a few hundred Bq/m^3 . Many commercial noble gas monitors can be found in the market, but they are generally based on ionization chambers or germanium gamma detectors. A few ones use plastic scintillators and examples are described hereafter.

11.2.2.1 Wide Range Krypton Gas Monitor

Takasaki et al. [24] described a wide range krypton monitor using a thin plastic scintillator as a detector. This scintillator is 50.8 mm in diameter and 0.5 mm thick, covered with a thin polymeric resin film and is protected by an aluminized polyester film. The first film acts as a protection against the memory effect caused by the diffusion of krypton inside the scintillator and the second film as a light shade. A schematic diagram is shown in Fig. 11.13.

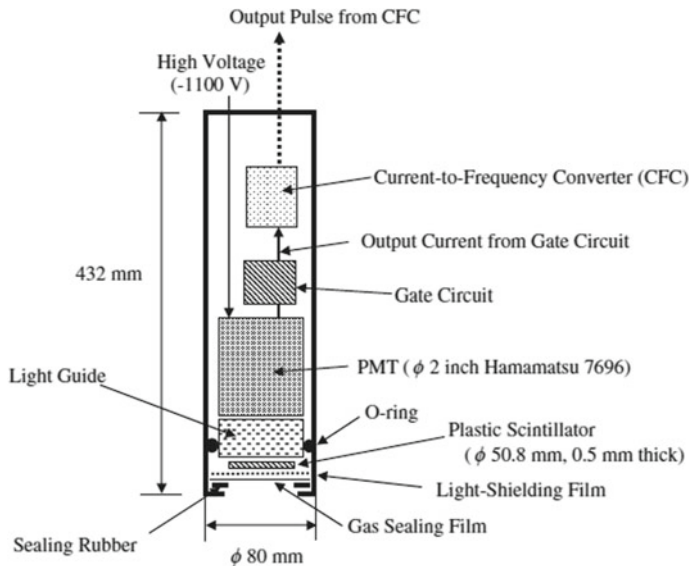


Fig. 11.13 Schematic diagram of the plastic scintillator detector (reproduced from [24] with permission from Taylor & Francis)

The acquisition system is composed of a gating and integrating system, including a discriminator to reject the influence of the dark current of the photomultiplier tube. The pulses are processed by a current to frequency converter. The influence of the temperature was studied, showing an increase in the background counting rate over 30 °C and leading to the conclusion that it is preferable to operate this system at a nearly constant temperature. The relation between the counting rate and the ^{85}Kr concentration was found to be linear from 5.7×10^{-2} to 1.8×10^3 Bq/cm 3 (5.7×10^4 – 1.8×10^9 Bq/m 3). The detection limit for one-minute measurement and 95% confidence level was evaluated to be 4.7×10^{-3} Bq/cm 3 . This performance is similar to the one of a gas detector operating in Geiger-Müller mode, but the operational range of the plastic scintillator detector is three orders of magnitude larger, allowing a much better measurement dynamic.

11.2.2.2 Noble Gas Monitor Station

A noble gas monitor station devoted to the measurement of beta-emitting noble gas is commercially available from the Lab Impex Systems company [25]. This monitor is for indoor use in a –10 to 50 °C temperature range. The system uses a 750 mL measurement chamber and a specially designed plastic scintillator sensor (*sic*). No details are given on the nature of this scintillator but the datasheet mentions that it is a 65 mm diameter and 110 mm long rod. The measurement range for ^{85}Kr is between 10^4 and 10^{10} Bq/m 3 .

11.2.2.3 Environmental ^{85}Kr Monitors

Measurement systems for monitoring ^{85}Kr activity in air are under development worldwide, especially to detect clandestine nuclear fuel reprocessing activities. A commercial system was developed by Bundesamt für Strahlenschutz (Germany) [26], composed of air sampling, purification and detection units, using a proportional counter as a detector. A coincidence detection system based on a plastic scintillator and a gamma- and X-ray detector, similar to the ones previously described for the detection of radioxenons, can be used but with two additional difficulties. First, the gamma emission intensity of ^{85}Kr is low, as mentioned in Sect. 11.1.1 and the energy is close to the annihilation energy which is always present in the background. Second, the standard air concentration in natural krypton is 1.14 cm^3 per cubic meter of air, to be compared with the natural concentration of xenon, which is 0.086 cm^3 per cubic meter of air, and thus corresponds to a dilution of krypton by a factor of more than ten compared to xenon. Thus, the operation of a low-activity detection system for ^{85}Kr based on plastic scintillator is still questionable.

11.2.3 Radon and Thoron Detection and Measurement with Plastic Scintillators

The interest in the development of ^{222}Rn detectors based on plastic scintillators comes mainly from the fact that they are relatively low cost, can be made with large surfaces and can be used in flow-through concepts with liquids and gases.

In some of the first designs of radon detectors with plastic scintillators, the ^{222}Rn decay products are collected electrostatically on thin plastic scintillator foils [27, 28]. Such detectors detect mainly the alpha-particles emitted from the short-lived decay products of ^{222}Rn [29]. The concept finds applications for ^{222}Rn decay product detection as well as to detect the decay products of ^{219}Rn (a radon isotope with a 4 s half-life), exhaled from patients during ^{223}Ra alpha radionuclide therapy [30].

Another type of the early approaches was to produce a radon sensor from a bundle of glass scintillation fibers and to allow ^{222}Rn to flow between the fibers [31]. This gives the alpha-particles of ^{222}Rn and its decay products immediate access to the scintillators [32]. In these studies, it was observed that ^{222}Rn was trapped on the oxide glass surfaces [33], and the method is applicable to the measurement of indoor radon concentrations [34]. A similar approach with direct contact of the scintillator with the ambient media is the developed plastic scintillator doped with NaI(Tl) for underwater radon sensing in oceanographic applications [35].

Other studies have shown that ^{222}Rn can be absorbed in the volume of plastic scintillators, plastic scintillation fibers and plastic scintillation microspheres. Moreover, these materials have alpha/beta-pulse shape discriminating characteristics, which, combined with the ^{222}Rn absorption ability, can be used for ^{222}Rn detection and

measurement [36]. General-purpose plastic scintillators were found also to be applicable to thoron (^{220}Rn) detection [37]. Plastic scintillation microspheres (PSm) [38], which appear to be an alternative to liquid scintillators in certain applications (e.g. continuous monitoring, measuring samples with high salt content, etc.), were found to absorb radon, to possess good pulse shape discrimination characteristics and to be applicable to ^{222}Rn detection and measurement [39]. These PSms are extensively presented in Chap. 13. These properties of the plastic scintillators led to the design of detectors for ^{222}Rn in soil-gas measurements [40], which can be applied for continuous radon in soil-gas monitoring [41].

Recent studies also explore the applicability of PS developed for neutron/gamma-pulse shape discrimination to alpha/beta PSD and radon measurements (see, for example, [42]). Another example is the comparative study of the pulse shape discrimination properties of *trans*-stilbene and EJ-299-33 PS for alpha/beta discrimination [43]. *Trans*-stilbene was found to have superior PSD capabilities, and a compact alpha/beta spectrometer based on stilbene with silicon photomultiplier was proposed for ^{222}Rn measurements [44].

Overall, plastic scintillators possess some important properties which make them an interesting alternative for the development of ^{222}Rn detectors and motivate the research efforts in this direction:

- their absorption ability to radon (and noble gases in general);
- their alpha/beta-pulse-shape discrimination properties; and
- the possibility to analyze their alpha spectra after PSD in case of ^{222}Rn measurements.

These properties are discussed in more detail hereafter.

11.3 RNG-Related Properties of Plastic Scintillators

11.3.1 Noble Gas Absorption in Plastic Materials

When plastic materials are exposed to a medium (e.g. air or water that contains radioactive noble gases (RNGs)), the atoms of the noble gases can penetrate the volume of plastic. The absorption and transport of RNGs in the plastic materials can be described quantitatively by the diffusion equation taking into account the radioactive decay [45]:

$$\frac{\partial c}{\partial t} = D \left[\frac{\partial^2 c}{\partial x^2} + \frac{\partial^2 c}{\partial y^2} + \frac{\partial^2 c}{\partial z^2} \right] - \lambda c \quad (11.1)$$

where c is the RNG atom concentration in the plastic, λ is the RNG decay constant and D is the diffusion coefficient of the RNG in the plastic material. Equation (11.1) can be solved for plastic specimens with different shapes (e.g. plate and cylinder)

and different boundary conditions (e.g. constant or exponentially decreasing RNG concentration in the air) [45].

For example, in thin plate-parallel plastic specimens, the processes are described by the one-dimensional form of Eq. (11.1) [45]:

$$\frac{\partial c(x,t)}{\partial t} = D \frac{\partial^2 c(x,t)}{\partial x^2} - \lambda c(x, t) \quad (11.2)$$

If the above specimen is exposed to air containing constant RNG concentration for exposure time t_s and then left to desorb in a radon-free air for desorption time t_d , then the solution of Eq. (11.2) is [45]:

$$c(x, t_s, t_d) = \frac{4DKc_{out}}{L} \sum_{k=0}^{\infty} \frac{\frac{(2k+1)\pi}{L}}{\lambda_{2k+1}} \left(1 - e^{-\lambda_{2k+1}t_s}\right) e^{-\lambda_{2k+1}t_d} \sin\left(\frac{(2k+1)\pi}{L}x\right) \quad (11.3)$$

where L is the thickness of the specimen, D and K are the diffusion coefficient and the partition coefficient of the RNG in the plastic material and c_{out} is the outside RNG atom concentration. The RNG activity in the specimen is given by [45]:

$$A(t_s, t_d) = \frac{8KA_VV\lambda L_D^2}{L^2} \sum_{k=0}^{\infty} \frac{1-e^{-\lambda_{2k+1}t_s}}{\lambda_{2k+1}} e^{-\lambda_{2k+1}t_d} \quad (11.4)$$

where V is the volume of the specimen, A_V is the outside RNG activity concentration, L_D is the diffusion length of the RNG in the plastic material and $\lambda_{2k+1} = \lambda \left(1 + \left(\frac{(2k+1)\pi L_D}{L}\right)^2\right)$. Solutions of Eq. (11.1) for specimens with plate-parallel or cylindrical geometry are given in [45] and for spherical geometry in [39].

The diffusion length L_D is a measure of the average distance traveled by the RNG atoms in the specimen before they decay. It is given by

$$L_D = \sqrt{\frac{D}{\lambda}} \quad (11.5)$$

The partition coefficient K is defined as

$$K = \frac{A_{V,p}}{A_V} \quad (11.6)$$

where A_V is the RNG activity concentration in the ambient media and $A_{V,p}$ is the RNG concentration just at the inner surface of the specimen. The partition coefficient K can be regarded as an analogue of the equilibrium solubility of stable gases in plastic materials. The partition coefficient K and the diffusion length L_D fully characterize the absorption properties of a plastic material for a given RNG. They both depend on the temperature. The permeation of gases in polymers is sometimes also described with the permeability P , defined as

$$P = KD \quad (11.7)$$

The knowledge of K and L_D allows modeling the kinetics of the RNG absorption in the polymers and evaluating the distribution of the absorbed RNG within the polymer volume, the absorbed RNG activity and its temporal behavior. Therefore, dedicated methods have been developed for the determination of K and L_D [46–48], and these have been tested for different RNGs and various materials [48–53]. Figure 11.14 depicts some instructive examples of the application of the model related to the RNG measurements with plastic scintillators. As can be seen from Fig. 11.14 (left), the absorption of ^{222}Rn in the plastic scintillators introduces transient delay during the exposure as well as some memory effect after the end of the exposure.

Depending on the application, it could be desirable to minimize or account for the transient or memory effects introduced by the radon diffusion in the PS. In both cases, it is important to know K and L_D . Table 11.2 summarizes some available K and L_D data for ^{222}Rn in plastic scintillators, plastic scintillation microspheres (PSm) and plastic scintillation foils (PS foils).

Other plastic materials, notably polycarbonates, were found to have remarkably high absorption ability to radon (^{222}Rn) [57]. Methods for the measurement of RNG

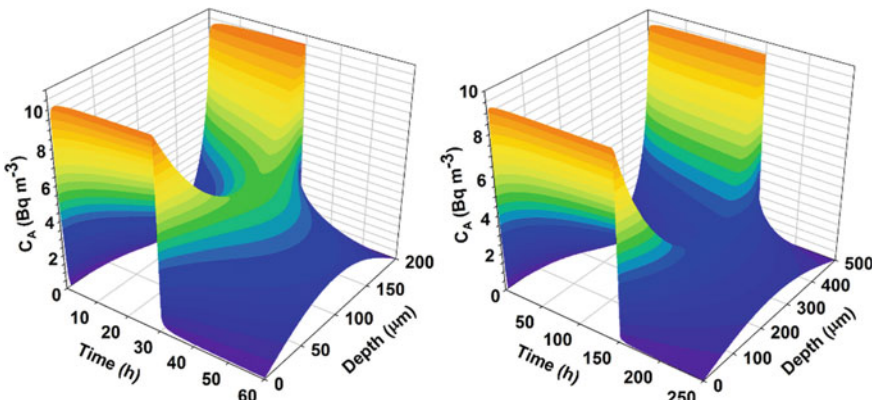


Fig. 11.14 Radon absorbed in plastic scintillators. In-depth activity concentration distribution (C_A) as a function of the sorption and desorption times. (Left) $C_A(t_s, t_d, x)$ for ^{222}Rn absorbed in 200 μm thick BC-400 PS, with exposure time $t_s = 30$ h and desorption in radon-free air followed for 30 h. (Right) $C_A(t_s, t_d, x)$ for ^{222}Rn absorbed in 500 μm thick EJ-212 PS, with exposure time $t_s = 150$ h and desorption in radon-free air followed for 100 h. The K and L_D data used in the model for both materials are taken from Table 11.2

Table 11.2 K and L_D data for ^{222}Rn in different plastic scintillation materials

Type of PS	K from air	L_D , μm	Temperature, °C	References
EJ-212	9.6(12)	141.0(55)	21	[54]
BC-400	10.7(13)	131.5(38)	21	[54]
Polystyrene PSm	5.8(15)	97.0(23)	20	[55]
Polystyrene PS foils	14.9(30)	259(61)	21	[56]

concentration in the environment (air or water) were proposed, which rely on this high absorption ability and use the polycarbonates as RNG samplers [58–61]. The RNG activity absorbed in the sampler can be measured by gamma spectrometry (e.g. [58, 60]), gross beta-counting [62], etching alpha tracks [63] or liquid scintillation counting [64–66]. The ambient RNG concentration is then deduced from the measured RNG activity concentration by applying the model describing the RNG sorption in plastic materials shown above (for more details, see, for example, [49]). The high ^{222}Rn absorption ability of polycarbonates is also the basis of the method for retrospective ^{222}Rn measurements based on home-stored CDs and DVDs (see, for example, [67] and references therein). For the application of the abovementioned methods, it is important to know the K and L_D data of the RNG for the particular polycarbonate. Table 11.3 summarizes available K and L_D values for ^{85}Kr , $^{131\text{m}}\text{Xe}$ and ^{222}Rn in Makrofol® DE and Makrofol® N polycarbonates (Makrofol® is a registered trademark of Bayer AG, Leverkusen, Germany).

Data in Table 11.3 allow modeling the processes of sorption and desorption of ^{85}Kr , $^{131\text{m}}\text{Xe}$ and ^{222}Rn in polycarbonates. For example, Fig. 11.15 shows the dynamics of ^{85}Kr absorption in Makrofol N polycarbonate plates with two different thicknesses and two different sorption/desorption scenarios. Figure 11.16 shows the dynamics of $^{131\text{m}}\text{Xe}$ absorption in Makrofol N polycarbonate plates with two different thicknesses and different sorption/desorption regimes. Notice that due to its larger diffusion length L_D , ^{85}Kr penetrates fast the volume of the specimens and after a relatively short time reaches uniform distribution (Fig. 11.15). In contrast, $^{131\text{m}}\text{Xe}$ with its smaller diffusion length and half-life penetrates slowly the volume of the polymer and stays mostly near the ends of the specimen (Fig. 11.16). Similar behavior is observed also for ^{222}Rn (Fig. 11.14). It should be pointed out that if the partition coefficient K is larger than 1, this means that the polymer can concentrate the noble gas from the environment near its surface (or in its volume, depending on L_D).

The transport of small and stable gas molecules in polymers has received significant attention in the past due to the need for gas separation membranes that find applications in protective coatings, food packing and other industries [68–70]. The solution-diffusion mechanism is typically used to characterize the gas uptake in the polymers, where the dissolution of the gas in the polymer is characterized by the

Table 11.3 K and L_D data for different RNGs in Makrofol® N and DE polycarbonates

Isotope	Polycarbonate	K from air	L_D , μm	Temperature (°C)	References
^{85}Kr	Makrofol N	1.322(65)	9140(910)	22	[51]
	Makrofol DE	0.81(5)		25	[49]
			9180(920)	22	[51]
$^{131\text{m}}\text{Xe}$	Makrofol N	17.2(13)	132.4(32)	22	[51]
	Makrofol DE	5.93(45)	145.1(37)	22	[51]
^{222}Rn	Makrofol N	112(12)	38.9(13)	20	[51]
	Makrofol DE	26.2(25)	52.1(10)	20	[51]

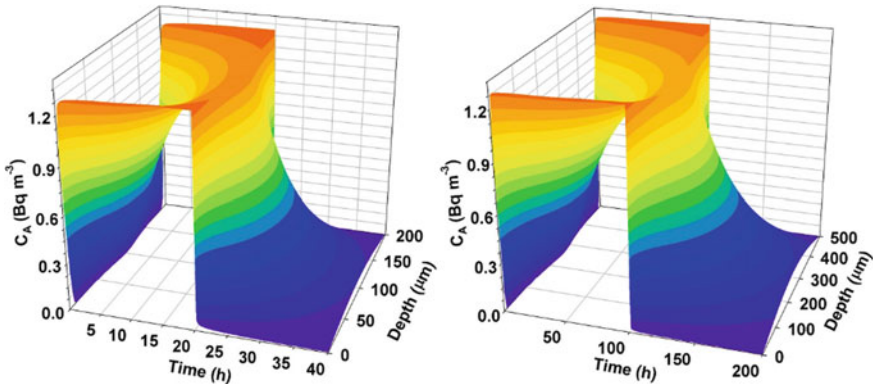


Fig. 11.15 Dynamics of ^{85}Kr absorption in Makrofol N plates exposed to air with constant ^{85}Kr concentration. In-depth activity concentration distribution (C_A) as a function of the sorption and desorption times. (Left) $C_A(t_s, t_d, x)$ for ^{85}Kr absorbed in 200 μm thick Makrofol N plate, exposed for exposure time $t_s = 20$ h and desorbed in ^{85}Kr -free air for $t_d = 20$ h. (Right) $C_A(t_s, t_d, x)$ for ^{85}Kr absorbed in 500 μm thick Makrofol N plate, with exposure time $t_s = 100$ h and desorption in ^{85}Kr -free air for $t_d = 100$ h

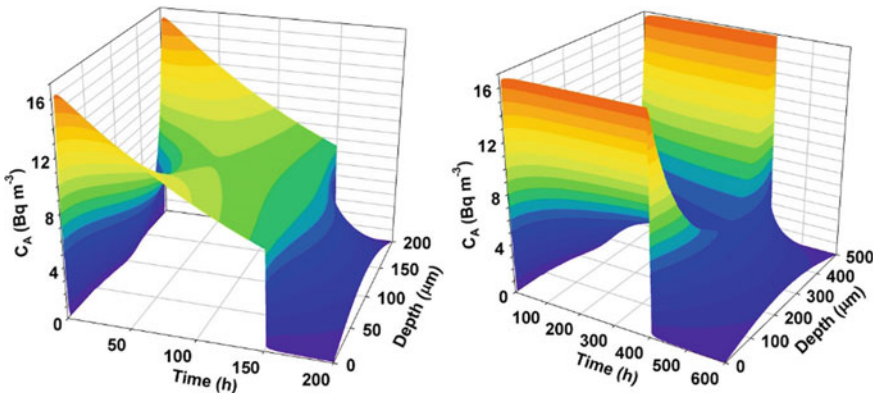


Fig. 11.16 Dynamics of $^{131\text{m}}\text{Xe}$ absorption in Makrofol N plates exposed to air with $^{131\text{m}}\text{Xe}$ concentration. In-depth activity concentration distribution (C_A) as a function of the sorption and desorption times. (Left) $C_A(t_s, t_d, x)$ for $^{131\text{m}}\text{Xe}$ absorbed in 200 μm thick Makrofol N plate, exposed to exponentially decreasing $^{131\text{m}}\text{Xe}$ concentration for exposure time $t_s = 150$ h and desorbed in $^{131\text{m}}\text{Xe}$ -free air for $t_d = 50$ h. (Right) $C_A(t_s, t_d, x)$ for $^{131\text{m}}\text{Xe}$ absorbed in 500 μm thick Makrofol N plate, exposed to constant $^{131\text{m}}\text{Xe}$ with exposure time $t_s = 400$ h and desorption in $^{131\text{m}}\text{Xe}$ -free air for $t_d = 200$ h

partition coefficient K , and the diffusion inside the polymer matrix is characterized by the diffusion coefficient D . The same concept is adopted in the model above (Eq. 11.6). Theories were developed to describe the solubility [71] and diffusion [72] of gases in polymers. These theories evolved in a model, known as the dual sorption theory (see [73] and references therein), which postulates that there are

two concurrent modes of sorption of inert gases in polymers: normal dissolution, which is described by Henry's law and trapping of gas molecules in microvoids that may exist in the polymers. The trapping is described by the Langmuir adsorption model. Both sorption modes combine together to characterize the gas uptake of the polymer, i.e. the immobilization of the penetrant in immobilizing sinks accompanies the normal dissolution processes. The dual sorption theory proposed in [73] requires microvoids or, more generally, free volume within the polymer, in which the immobilization can occur. According to [74], "the free volume can be visualized as a dynamic angstrom-sized voids, cavities, or holes, with a distribution of sizes and shapes, dispersed inside the polymeric matrix". The concepts of free volume, total free volume, excessive free volume [75] and available free volume [76] have been proposed, and attempts were made to describe the gas transport in the polymers (see, for example, [77]). In [78], it was shown that the free volume in the polymer can be related to the diffusion coefficient by a simple exponential relation, an approach that was largely used in later studies. A large study of the solubility of six stable gases in 105 polymers performed in [79] showed that the effective fractional free volume in a given polymer is not the same for different gases, i.e. depends on the type of the penetrating gas. The study of the absorption of ^{85}Kr , $^{131\text{m}}\text{Xe}$ and ^{222}Rn in Makrofol N or DE polycarbonates performed in [51] demonstrated substantially different diffusion coefficients between the three gases. In particular, the results obtained in [51] (see Fig. 11.17) support the proposition in [72] that the diffusion coefficient D and the gas molecular diameter d can be related through:

$$\ln D = A - bd^2 \quad (11.8)$$

where A and b are parameters.

However, in [81] it is shown that the free volume concepts alone cannot explain the gas transport mechanism in polycarbonates, and in [74] it was shown that the

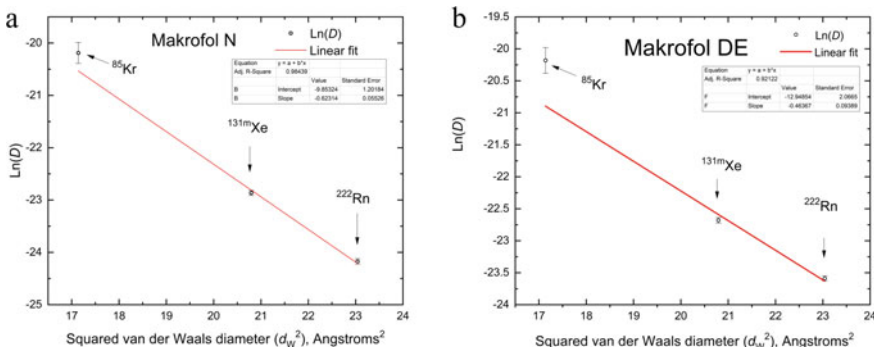


Fig. 11.17 Dependence of the diffusion coefficient on the gas molecular diameter for **a** Makrofol N and **b** DE polycarbonates. The van der Waals molecular diameters are taken from [80]. The error bars indicate the estimated standard uncertainties

local chain dynamics of a glassy polymer is very important for the diffusion coefficient of the penetrating gas. In a more recent study, the non-equilibrium thermodynamics for the glassy polymers (NET-GP) approach was used in combination with the lattice fluid model to develop a non-equilibrium lattice fluid model (NELF) for the prediction of vapor solubility and volume dilation in glassy polymers [82]. The model described well the effect of polymer pre-treatment and its prior history (e.g. annealing or conditioning by pre-swelling) on the resulting gas solubility of glassy polymers. As summarized in [83], the properties of a glassy polymer may depend on the vitrification procedure (cooling rate), filming procedure (melt extrusion or solvent casting), the use of different solvents (solvent volatility), conditioning of the sample (e.g. thermal annealing) or aging effects (see [83] and the references therein). Thus far, it is clear that there are many different factors which affect the noble gas absorption ability of the polymers.

Given the high noble gas absorption ability of polycarbonates and the suitability of plastic scintillators for noble gas measurements, attempts were made to produce a plastic scintillator with high RNG absorption ability. The first attempt was to produce plastic scintillation microspheres (PSm) with high radon absorption properties by producing them from polycarbonate or polystyrene/polycarbonate mixture. As PSms made from polystyrene were shown to be applicable to ^{222}Rn measurements [39], the same production method (i.e. the evaporation/extraction method) was tested to produce PSm with mixed polystyrene-polycarbonate content [55]. The study revealed that it is possible to produce PSm from polycarbonate or a mixture of polycarbonate and polystyrene. In the latter case, polycarbonate and polystyrene are not miscible in each other and remain segregated in the PSm particles. The usage of polycarbonate in the PSm leads also to increased quenching compared to pure polystyrene-based PSms. The ^{222}Rn absorption capacity of the PSm synthesized with polycarbonate is found to be comparative and not superior to that of PSm made of polystyrene [55]. The second attempt to produce PSs with high noble gas absorption ability was to make plastic scintillating foils with mixed polystyrene/polycarbonate content using the solvent evaporation method [56]. Results show that it is possible to produce foils from polystyrene, polycarbonate and polystyrene/polycarbonate mixtures, but the same non-miscibility occurred between polystyrene and polycarbonate, thus leading to the same issues encountered with PSm. The study revealed that the partition coefficient K does not depend too much on the polycarbonate/polystyrene ratio, while the diffusion length L_D decreases with the increase of the polycarbonate content, and the polycarbonate foils have 5 times smaller L_D compared to the polystyrene ones. The results of these studies suggest that not only the material content but also the production method of a plastic scintillator is of paramount importance for the noble gas absorption ability.

Whatever future developments may occur, it seems likely that the RNG absorption in plastic scintillators will be important in two lines of application: to characterize and potentially decrease the memory effect caused by the noble gas absorption and to produce plastic scintillators with high noble gas absorption ability which may be useful for detection and measurement of RNGs.

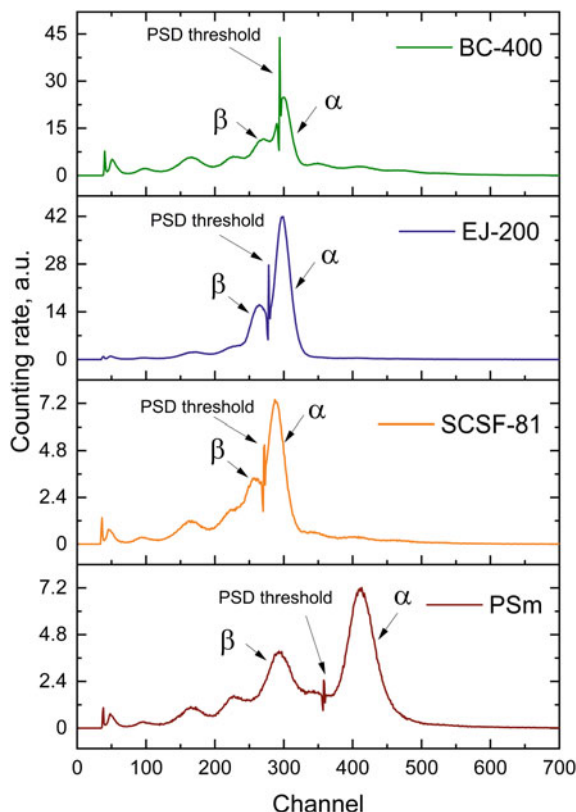
11.3.2 Application of Pulse Shape Discrimination to ^{222}Rn Measurements

Plastic scintillators are known to have pulse shape discrimination capabilities (see, for example, [84–87], Chaps. 2 and 5 in this volume and references therein). As previously mentioned, when PSs are exposed to ^{222}Rn , the gas can penetrate their volume and thus the alpha- and beta-particles of ^{222}Rn and its progeny are emitted directly in the active volume of the scintillator. This increases the detection efficiency for these particles and motivates studies on the applicability of pulse shape discrimination (PSD) techniques. The main objective of these studies is to discriminate the signal from the alpha-particles from that of the beta-particles of the radon progeny.

Various general-purpose PSs were tested for application to PSD measurements of ^{222}Rn [36, 54], such as BC-400 (Saint-Gobain Crystals), EJ-212, EJ-200 (Eljen Technology), plastic scintillating fibers produced by Kuraray (SCSF-81) and PSm (University of Barcelona). In these tests, PS specimens were exposed to ^{222}Rn containing air and afterwards measured on a Photon-Electron Rejecting Alpha Liquid Scintillation Spectrometer (PERALS®, ORDELA). The PERALS spectrometer allows to acquire simultaneously the pulse height and the decay time distribution of the light output with the decay time distribution being acquired with a built-in time-to-pulse-height converter [88]. Figure 11.18 shows typical decay time distributions obtained with the general-purpose PSs. The BC-400 and EJ-200 specimens have imperfect pulse-shape discrimination capabilities with the distribution of the beta- and alpha-pulse decay times being largely superimposed. Notably, plastic scintillating fibers produced by Kuraray (SCSF-81) also possess some PSD capabilities, which are comparable to those of the general-purpose PS. Interestingly, the plastic scintillation microspheres (PSm; for synthesis information, see [38] or Chap. 13) exhibit good PSD properties, with relatively well-separated alpha- and beta-populations. This is despite the multiple scattering of the light between the microspheres prior to its escape from the source.

Figure 11.19 shows the pulse height (PH) spectra, acquired with the PERALS spectrometer simultaneously with the spectra shown in Fig. 11.18. The alpha peaks of ^{222}Rn (5.48948(30) MeV), ^{218}Po (6.00235(9) MeV) and ^{214}Po (7.68682(6) MeV) are clearly seen on the BC-400 and EJ-200 spectra. The continuum below the alpha peaks is an indication of the imperfect pulse shape discrimination of the scintillators. The observed energy resolution of BC-400 and EJ-200 is not sufficient to fully separate the ^{222}Rn and ^{218}Po peaks, but allows full separation of the ^{214}Po peak from the rest of the spectrum. The PH spectra of the plastic scintillating fibers (SCSF-81) exhibit poor energy resolution. This is likely to be due to poor light collection efficiency in these measurements as the ends of the fibers were not directed to the PMT, but were placed vertically in the instrument optical chamber. It can be anticipated that better results will be obtained with a design of a detection system in which the fibers are optically coupled to the PMTs. The energy resolution obtained with the PSm samples is slightly better than that with scintillating fibers, but worse than the one obtained with EJ-200 or BC-400. The ^{222}Rn , ^{218}Po and ^{214}Po peaks can be identified in the spectrum but

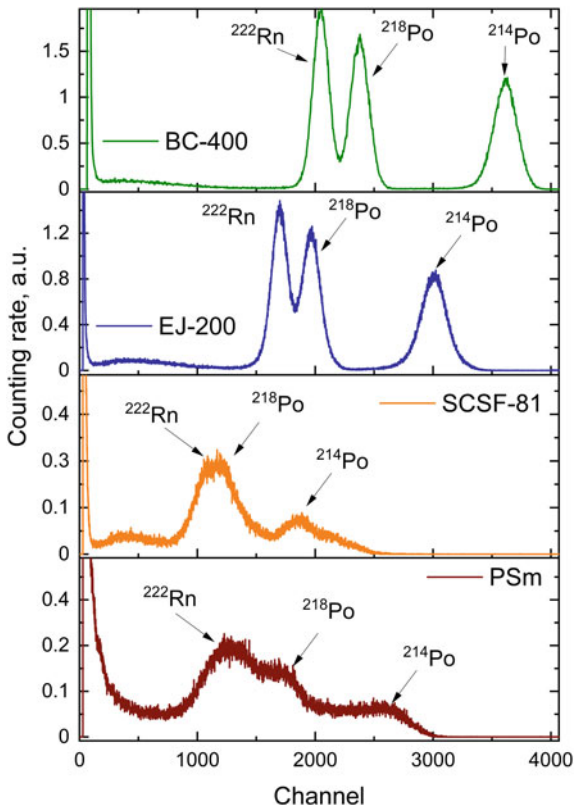
Fig. 11.18 Examples of pulse decay time spectra of various PSs exposed to ^{222}Rn . The measurements are performed with the PERALS spectrometer. The indicated threshold levels are set to discriminate the beta-particles for the acquisition of the PH spectra shown in Fig. 11.19



are largely superimposed. This is also attributed to poor light collection efficiency as the light experiences multiple scattering between the microspheres prior to its escape from the sample. This leads to an increase of the light collection variability and to a decrease of the energy resolution. More details about the pulse shape and pulse height results obtained with common general-purpose plastic scintillators are presented in [36] (BC-400, EJ-200, PSW-51, SCSF-81, PSm), [39] (PSm) and [54] (EJ-212, BC-400).

The next step in the hunt for the optimal plastic scintillator for ^{222}Rn measurements with PSD was to test plastic scintillators developed for neutron/gamma discrimination that have enhanced n/ γ PSD characteristics. In [43], the performance of EJ-299-33 (Eljen Technology) plastic scintillator for alpha/beta-pulse shape discrimination was compared to that of a *trans*-stilbene crystal. The experimental system consists of the scintillator, coupled to a silicon photomultiplier (SiPM, MicroFJ-60035-TSV, SensL) and a waveform digitizer (DT5730, CAEN). Both scintillators were found suitable for α/β PSD, based on the figure-of-merit (FOM) observed (the FOM is the distance between the alpha and beta peaks divided by the sum of the FWHM values of the distributions; see Chap. 1 or 2). Stilbene was found to have better performance

Fig. 11.19 Examples of pulse height spectra of various PSs exposed to ^{222}Rn . The measurements are performed with the PERALS spectrometer with the rejection of the pulses below the threshold level shown in Fig. 11.18. Spectra are acquired simultaneously with those shown in Fig. 11.18. The alpha peaks of ^{222}Rn (5.48948(30) MeV), ^{218}Po (6.00235(9) MeV) and ^{214}Po (7.68682(6) MeV) can be identified in the PH spectra



(FOM = 1.61) compared to EJ-299–33 (FOM = 0.56) [44]. Then, a compact radon measurement device based on stilbene crystal coupled to a SiPM and waveform digitizer was proposed and tested for indoor radon measurements [44].

In another study [42], a plastic scintillator originally developed for n/γ discrimination at CEA was also tested for α/β pulse-shape discrimination and ^{222}Rn measurements. As mentioned, this scintillator (hereafter named CEA-plastic) was purposely designed for Pulse Shape Discrimination between fast neutrons and gamma-rays with a highly concentrated primary fluorophore approach. To circumvent material degradation (bleaching, deformation, etc.; see [87] and Chap. 2), the polymer is cross-linked. The experimental system consists of the plastic scintillator mounted on an optical chamber in front of a PMT (Hamamatsu R7600U-200). The output of the PMT is directly fed to a nanoPSD digital spectrometer (labZY), which has PSD capabilities. The nanoPSD analyzer allows digital real-time pulse processing and analysis, acquisition of time-invariant pulse signature (TIPS) spectra and separation of the incoming pulses in two different spectra according to their TIPS signature [89]. This feature of the nanoPSD device, which is not available in PERALS, allows to visually investigate the beta-to-alpha cross talk and the alpha-to-beta cross talk as

well. An example of a measurement of the CEA-plastic scintillator with this system is shown in Fig. 11.20. The scintillator shows excellent α/β discrimination (FOM = 1.61) with practically no β -pulses in the α -channel and no α -pulses in the β -channel.

The CEA-plastic scintillator was also studied with the PERALS spectrometer. Figure 11.21 shows the pulse decay time and pulse height spectra obtained with the CEA-plastic scintillator and the RadonS® liquid scintillator (ORDELA, USA), which

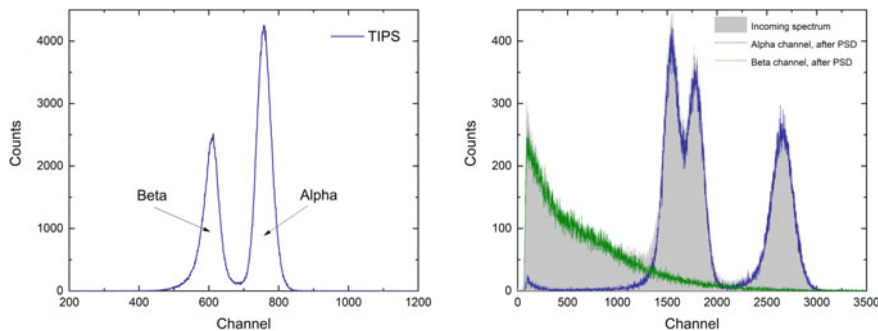


Fig. 11.20 Spectra of a nanoPSD measurement of the CEA-plastic scintillator exposed to ^{222}Rn . (Left) The TIPS spectrum. (Right) The incoming spectrum, and the α - and β -channels after PSD

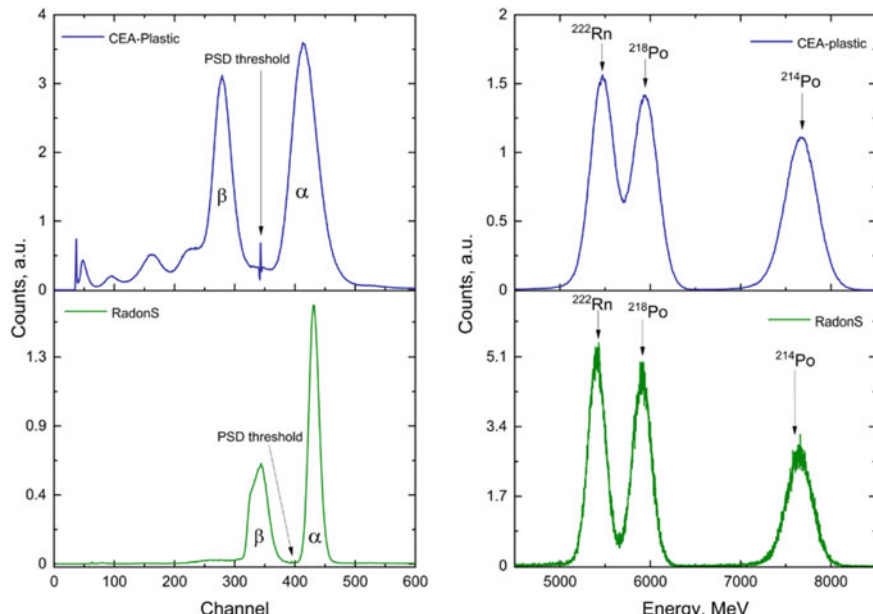


Fig. 11.21 PERALS measurements of CEA-plastic scintillator exposed to ^{222}Rn in air (blue) and ^{222}Rn dissolved in RadonS® liquid scintillator (green). (Left) Pulse decay time spectra. (Right) Pulse height spectra

is recommended for ^{222}Rn counting [88]. Notably, the plastic scintillator provides excellent α/β discrimination, which is comparable to that of the liquid scintillator. Both beta spectra are practically free from beta-pulses in the region of alpha peaks after the pulse shape discrimination. The energy resolution of CEA-plastic scintillator is slightly inferior compared to that of RadonS®.

Overall, plastic scintillators seem capable of α/β -pulse shape discrimination. This property, combined with the ^{222}Rn absorption properties makes them an interesting alternative for ^{222}Rn measurement. In particular, some plastic scintillators developed for neutron/gamma discrimination seem to provide excellent α/β discrimination capabilities. This opens directions for low-background, sensitive ^{222}Rn measurements with PSD, alpha-counting and analysis of the alpha spectra.

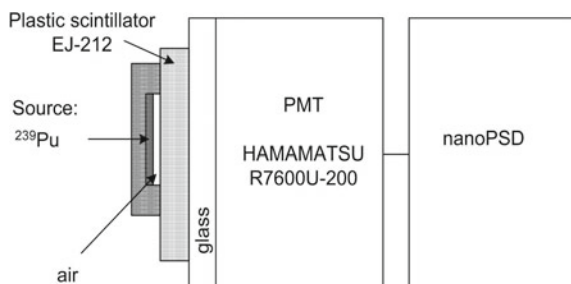
11.3.3 Description of the Alpha-Particle Peak Shapes in ^{222}Rn Measurements with Plastic Scintillators

The good pulse shape discrimination capabilities of plastic scintillators allows to separate the signals from the α - and β -particles and thus to acquire α - and β -pulse height spectra. It is then interesting to analyze the α spectra and try to apply methods developed for α -spectrometry to the problem of ^{222}Rn measurements with plastic scintillators.

Alpha-particle spectroscopy has been the subject of many experimental and theoretical investigations, and a vast body of data and methods were obtained and developed (see, for example, [86, 90] and references therein). Various approaches for line shape fitting were proposed (e.g. [91–94]; reviews of the methods available in [86, 90]). In the context of ^{222}Rn measurements with plastic scintillators, it has to be noted that the ^{222}Rn or its progeny can be outside or on the surface of the plastic scintillator (α source outside the detector) or ^{222}Rn can be absorbed in the volume of the plastic scintillator (α source in the active volume of the detector). These two situations deserve separate attention.

The experimental setup used in the studies of the response of the plastic scintillators to an external source of alpha-particles is shown in Fig. 11.22. It consists

Fig. 11.22 Schematic view of the setup used to test the response of PS to external α sources



of a ^{239}Pu source facing the plastic scintillator with some small distance between the source and the scintillator which is filled with air. The PS is optically coupled to a glass and then to the PMT. The signals from the PMT are processed with the nanoPSD analyzer.

An example of an α -spectrum acquired with the setup from Fig. 11.22 is shown in Fig. 11.23. The spectrum exhibits a broad, asymmetrical peak with significant left tailing. Several reasons can contribute to the observed tailing of the peak:

- energy loss of the α -particles in the source and in the air between the source and the plastic scintillator,
- energy loss in a potentially existing thin, less-effective, layer at the surface of the scintillator, or
- imperfect light collection efficiency of the optical chamber of the setup.

In [91], it was proposed to characterize the alpha peaks of silicon surface barrier detector with a convolution of a one-sided exponential factor $f(x)$ and a Gaussian function $g(x)$:

$$F(x) = (f * g)(x) = A \int_{-\infty}^{\mu} e^{\lambda(u-\mu)} e^{-\frac{(x-u)^2}{2\sigma^2}} du \quad (11.9)$$

where A is a normalization constant, λ describes the slope of the exponential distribution, μ corresponds to the position of the maximum energy of the alpha-particles and σ^2 is the variance of the Gaussian distribution. Performing the integration, one gets

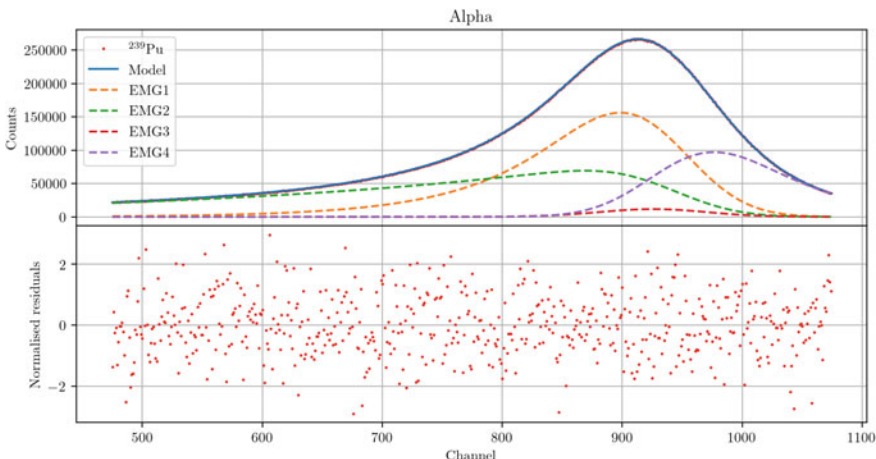


Fig. 11.23 Spectrum of a ^{239}Pu α -source measured with EJ-212 PS. The lines indicate the contribution of the different exponents and the entire fitting function

$$F(x) = (f * g)(x) = \tilde{A} e^{\lambda(x-\mu)+\frac{\lambda^2\sigma^2}{2}} \operatorname{erfc}\left(\frac{x-\mu+\lambda\sigma^2}{\sqrt{2}\sigma}\right) \quad (11.10)$$

where \tilde{A} is another normalization constant and erfc is the complementary error function. A more sophisticated model to describe the peak-shape function measured with ion-implanted silicon detectors was proposed in [92]. There, the spectrum was pre-treated to reduce the long tails, and a convolution of a Gaussian function and a weighted sum of two left-sided exponentials was proposed to improve the tail approximation. In a later study [94], a convolution of a Gaussian function with a normalized sum of three left-sided exponentials was proposed for $F(x)$, abolishing the pre-treatment of the spectrum. More recently, a fitting function with up to 10 left-handed and four right-handed exponentials was proposed for an alpha peak model function $F^*(x)$ [95]:

$$F^*(x) = \sum_{i=1}^{10} \eta_i F(x - \mu_i; \sigma_i; \lambda_i) + \sum_{i=-3}^0 \eta_i F(\mu_i - x; \sigma_i; \lambda_i) \quad (11.11)$$

where λ_i , μ_i , σ_i , and η_i are fitting parameters, and η_i must obey the normalization condition:

$$\sum_{i=-3}^{10} \eta_i = 1 \quad (11.12)$$

Explicitly, for a spectrum containing n alpha lines, the fitting function $F^{**}(x)$ has the form:

$$F^{**}(x) = \sum_{k=1}^n A_k \left(\begin{array}{l} \sum_{i=1}^{10} \eta_i \frac{\lambda_i}{2} e^{\lambda_i(x-\mu_k)+\frac{\lambda_i^2\sigma_k^2}{2}} \operatorname{erfc}\left(\frac{x-\mu_k+\lambda_i\sigma_k^2}{\sqrt{2}\sigma_k}\right) \\ + \sum_{i=-3}^0 \eta_i \frac{\lambda_i}{2} e^{\lambda_i(\mu_k-x)+\frac{\lambda_i^2\sigma_k^2}{2}} \operatorname{erfc}\left(\frac{\mu_k-x+\lambda_i\sigma_k^2}{\sqrt{2}\sigma_k}\right) \end{array} \right) \quad (11.13)$$

where A_k is the fit parameter which corresponds to the area of the k^{th} peak.

The problem of fitting of alpha peaks in spectra obtained with plastic scintillators was studied in [96]. In this study, the alpha peaks obtained with the setup shown in Fig. 11.22 were fitted with a function of the type of $F^*(x)$, using non-linear least squares minimization with the Levenberg-Marquardt algorithm. The approach adopted in [96] was to not only use the function proposed in [95] (Eq. 11.11), but to also start with a pure Gaussian function and increase subsequently the number of the left and right exponents in $F^*(X)$ (Eq. 11.11) until an acceptable value of the χ^2 goodness-of-fit test is obtained. The results of this approach showed that the acceptance criteria of the χ^2 test can be met with $F^*(x)$ with two left and two right exponents [96]. Further studies have shown that the χ^2 acceptance criteria can be also met with a fitting function $F^+(x)$ with three left and one right exponents:

$$F^+(x) = A \eta_0 \frac{\lambda_0}{2} e^{\lambda_0(\mu-x)+\frac{\lambda_0^2 \sigma^2}{2}} \operatorname{erfc}\left(\frac{\mu-x+\lambda_0 \sigma}{\sqrt{2} \sigma}\right) + A \sum_{i=1}^3 \eta_i \frac{\lambda_i}{2} e^{\lambda_i(x-\mu)+\frac{\lambda_i^2 \sigma^2}{2}} \operatorname{erfc}\left(\frac{x-\mu+\lambda_i \sigma}{\sqrt{2} \sigma}\right) \quad (11.14)$$

An example of such a fit is shown in Fig. 11.23. The fitting function describes well the points (reduced $\chi^2 = 1.008$), and no apparent systematic pattern can be identified in the graph of the normalized residuals. The correlation matrix shows significant correlations between the fitted parameters (Table 11.4). Overall, it seems that a fitting function with three left and one right exponents may describe well the peaks obtained with alpha sources which are outside the plastic scintillator. The studies of the fitting of the peak shapes of ^{222}Rn absorbed in the volume of the plastic scintillators were performed with the PERALS and the nanoPSD systems described above. An example of a typical spectrum in the alpha-channel acquired after optimal pulse shape discrimination is shown in Fig. 11.24 (the ^{222}Rn is absorbed in the volume of the PS and is in secular equilibrium with its short-lived decay products). As the ^{222}Rn and its decay products are in the volume of the scintillator, there is no energy loss between the source and the detector and the alpha peaks of ^{222}Rn , ^{218}Po and ^{214}Po are much more symmetrical compared to the case with the source outside the PS (compare Fig. 11.24 to Fig. 11.23).

However, the peaks cannot be fitted with pure Gaussian distributions because significant left tailing can still be observed (Fig. 11.24). This left tailing is currently attributed to possible light absorption in the volume of the PS or to alpha-particles, which are emitted near the surface of the scintillator (see Fig. 11.14) and escape without depositing their full energy in the PS. Interestingly, the alpha peaks of ^{222}Rn absorbed in the volume of the PS can be well-fitted with the same function ($F^+(x)$, Eq. (11.14)) as that used for the fits in the case of alpha sources which are outside the detector. This is illustrated in Figs. 11.25 and 11.26, where PERALS and nanoPSD spectra obtained with ^{222}Rn absorbed in CEA-plastic PS are well fitted with $F^+(x)$.

Table 11.4 Correlation matrix of the parameters of $F^+(X)$ for the fit shown in Fig. 11.23

Parameters	A	μ	σ	λ_1	λ_2	λ_3	λ_0	η_1	η_2	η_3
A	1	0.63	-0.46	-0.92	-0.98	-0.68	0.20	0.77	-0.96	-0.23
μ	0.63	1	-0.93	-0.84	-0.72	-0.99	0.61	0.97	-0.51	-0.84
σ	-0.46	-0.93	1	0.69	0.58	0.93	-0.84	-0.90	0.34	0.96
λ_1	-0.92	-0.84	0.69	1	0.97	0.88	-0.41	-0.92	0.89	0.47
λ_2	-0.98	-0.72	0.58	0.97	1	0.77	-0.34	-0.85	0.95	0.34
λ_3	-0.68	-0.99	0.93	0.88	0.77	1	-0.64	-0.99	0.58	0.81
λ_0	0.20	0.61	-0.84	-0.41	-0.34	-0.64	1	0.60	-0.15	-0.82
η_1	0.77	0.97	-0.90	-0.92	-0.85	-0.99	0.60	1	-0.67	-0.76
η_2	-0.96	-0.51	0.34	0.89	0.95	0.58	-0.15	-0.67	1	0.07
η_3	-0.23	-0.84	0.96	0.47	0.34	0.81	-0.82	-0.76	0.07	1

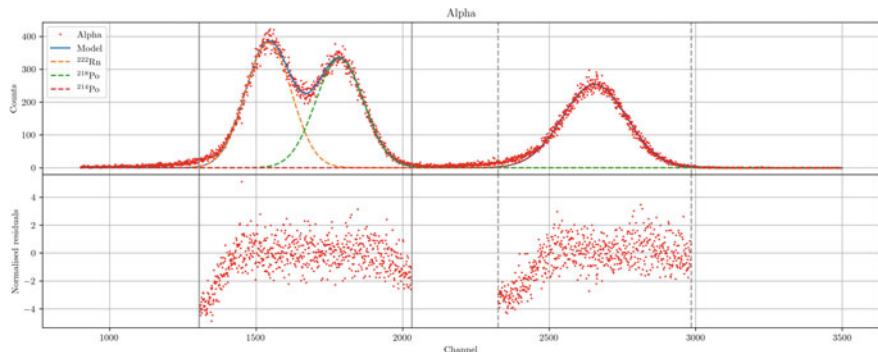


Fig. 11.24 Pulse height spectrum of ^{222}Rn absorbed in CEA-plastic scintillator. The spectrum is that of the alpha-channel after optimal PSD and is acquired with the nanoPSD analyzer. The spectrum is fitted with a sum of three Gaussian distributions, one for each peak. The graph of the normalized residuals shows significant left tailing of the peaks. The reduced χ^2 for the regions with overlapping peaks and the single peak are 2.054 and 2.25, respectively

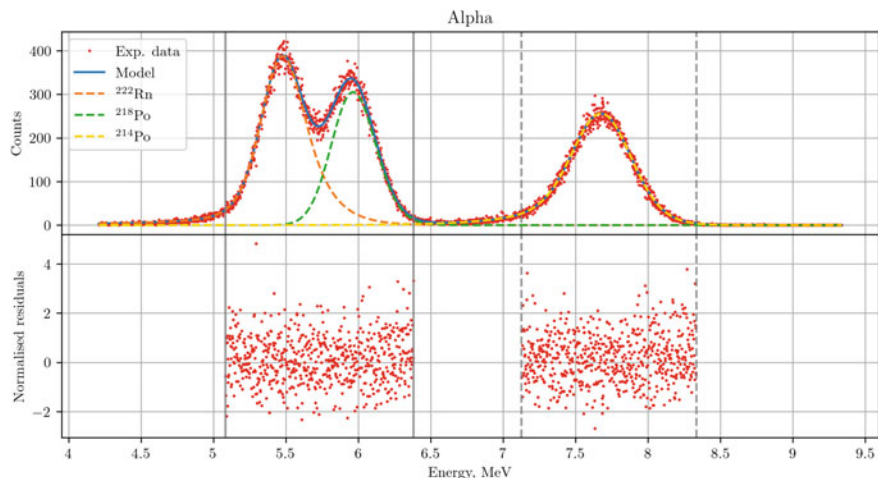


Fig. 11.25 Same spectrum as in Fig. 11.24, but each peak is fitted with the function $F^+(x)$, which has three left and one right exponents. A good description of the data is observed with the reduced χ^2 for the two regions being equal to 1.01 and 1.07, respectively. No apparent systematic pattern is identified in the graph of the normalized residuals

Thus, it appears that the peaks in the alpha spectra of PS, which are acquired after pulse shape discrimination, can be characterized with the function of the type $F^+(x)$ which is obtained from a convolution of a Gaussian function with the sum of three left and one right exponents.

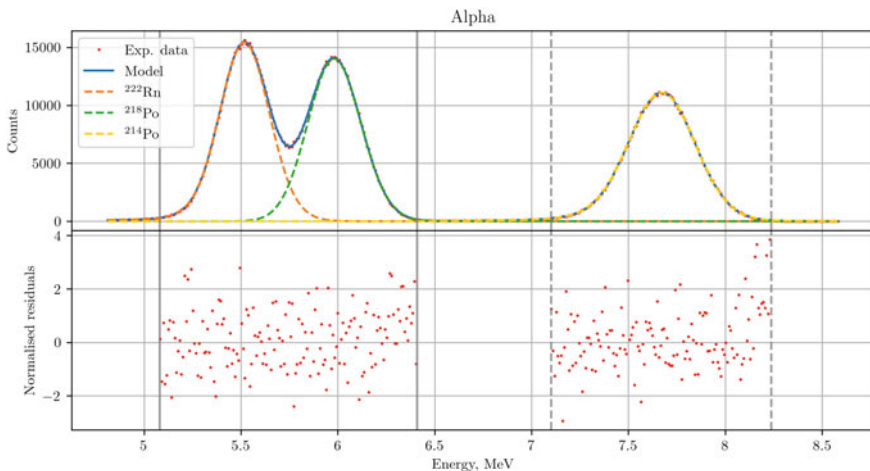


Fig. 11.26 Pulse height spectrum of ^{222}Rn absorbed in CEA-plastic scintillator acquired with PERALS. The spectrum is of the alpha-channel after optimal PSD. The fit of each peak is with the $F^+(x)$ function (Eq. 11.14). A good description of the data is observed with reduced χ^2 values for the two regions 1.41 and 1.37, respectively

11.4 Concluding Remarks

New developments in the field of radon measurement using plastic scintillators are likely to appear in the near future, due to their interesting properties like their absorption properties and the possibility to discriminate between alpha and beta radiation by pulse shape discrimination. These developments will be facilitated by the knowledge of the physical phenomena governing the gas diffusion into the polymers, which are now well established.

For the detection of other noble gases, the absorption inside the plastic scintillator could be a drawback leading to a memory effect. Nevertheless, studies showed that coating these scintillators with various barriers could efficiently suppress the diffusion without altering the detection properties. Thus, the use of plastic scintillators in xenon and krypton monitors is likely to be continued, due to their good detection efficiency for electrons and their low atomic number and low density allowing their use in beta-gamma coincidence systems in association with gamma detectors like inorganic scintillators or semiconductors.

On the other hand, recent progress made in new photon detectors like silicon photomultipliers and the dramatic improvement of the performances of digital electronics allow the possibility to achieve online data processing and pulse shape discrimination. This, combined with future possible developments in the chemistry of plastic scintillators will allow designing compact and flexible detection units for the development of light and portable equipment for the onsite measurement of noble gases.

References

1. M.B. Kalinowski, M.P. Tuma, J. Environ. Radioact. **100**(1), 58 (2009)
2. Legifrance. <https://www.legifrance.gouv.fr/jorf/id/JORFTEXT000031832595>. Accessed 15 Dec 2020
3. W. Nitta, T. Sanada, K. Isogai, C. Schlosser, J. Nucl. Sci. Technol. **51**(5), 712 (2014)
4. T.R. England, B.F. Rider, *Los Alamos National Laboratory Report LAUR-94-3106*, (October 1994)
5. W.R. Schell, M.J. Tobin, D.J. Marsan, C.W. Schell, J. Vives-Batlle, S.R. Yoon, Nucl. Instr. Methods A **385**(2), 277 (1997)
6. P.H. Gudiksen, M.H. Dickerson, *Lawrence Livermore National Laboratory UCRL-JC-104077* (1990)
7. J. Beyea, J. De Cicco. Reestimating the noble gas release from the Three Mile Island accident. Final report. National Audubon Society, prepared for the Three Mile Island Public Health Fund (1992)
8. Chernobyl's legacy: health, environmental and socio-economic impacts and recommendations to the governments of Belarus, the Russian Federation and Ukraine. IAEA (2005)
9. T.W. Bowyer, S.R. Biegalski, M. Cooper, P.W. Eslinger, D. Haas, J.C. Hayes, H.S. Miley, D.J. Strom, V. Woods, J. Environ. Radioact. **102**(7), 681 (2011)
10. A. Stohl, P. Seibert, G. Wotawa, J. Environ. Radioact. **112**, 155 (2012)
11. UNSCEAR 2013 Report, annex A
12. P. Achim, P. Gross, G. Le Petit, T. Taffary, P. Armand, Contribution of isotopes production facilities and nuclear power plants to Xe-133 worldwide atmospheric background, in *Poster presented at the Science and Technology 2011 (SnT 2011)* (Vienna, 8–11 June 2011)
13. World Health Organization. <https://www.who.int/news-room/fact-sheets/detail/radon-and-health>. Accessed 29 Nov 2020
14. Laboratoire National Henri Becquerel. <https://www.lnb.fr/donnees-nucleaires/donnees-nucleaires-tableau>. Accessed 29 Nov 2020
15. Comprehensive Nuclear-Test-Ban Treaty Organization. <https://www.ctbto.org/map/>. Accessed 29 Nov 2020
16. J.I. McIntyre, K.H. Abel, T.W. Bowyer, J.C. Hayes, T.R. Heimbigner, M.E. Panisko, P.L. Reeder, R.C. Thompson, J. Radioanal. Nucl. Chem. **248**(3), 629 (2001)
17. Y. Popov, *Kompleks apparatury K-522-D. TUSHK.412.123.312RE* (K-522-D Complex of Equipment) (St. Petersburg: Radievyi institut, 1996)
18. Y.S. Popov, N.M. Kazarinov, V.Y. Popov, Y.M. Rykov, N.V. Skirda, Instrum. Exp. Tech. **48**(3), 380 (2005). Translated from *Prib. Tekh. Eksp.* **3**, 115 (2005)
19. V.V. Prelovskii, N.M. Kazarinov, A.Y. Donets, V.Y. Popov, I.Y. Popov, N.V. Skirda, Instrum. Exp. Tech. **50**(3), 393 (2007)
20. A. Ringbom, T. Larson, A. Axelsson, K. Elmgren, C. Johansson, Nucl. Instr. Methods A **508**(3), 542 (2003)
21. Sauna Systems, Sauna-II. https://www.saunasystems.se/_resources/file/sauna_web.pdf. Accessed 28 Nov 2020
22. L. Bläckberg, Dissertation, Uppsala universitet (2011)
23. S.A. Czyz, A.T. Farsoni, L. Ranjbar, Nucl. Instr. Methods A **884**, 64 (2018)
24. K. Takasaki, H. Kobayashi, H. Suzuki, S. Ushigome, J. Nucl. Sci. Technol. **47**(3), 255 (2010)
25. PEO Radiation Technology, CMS Noble Gas Monitor. [https://www.peo-radiation-technology.com/en/product/cms-noble-gas-monitor-lab-impex-systems/..](https://www.peo-radiation-technology.com/en/product/cms-noble-gas-monitor-lab-impex-systems/) Last accessed 28 Nov 2020
26. Y.G. Ko, H. Kim, J.Y. Park, S.D. Choi, J.M. Lim, G.S. Choi, W. Lee, Monitoring of Kr-85 by using BfS-IAR system, in *Paper Presented at Transactions of the Korean Nuclear Society Spring Meeting* (Jeju, Korea, 17–18 May 2018)
27. S. Yamamoto, K. Yamasoto, T. Iida, IEEE Trans. Nucl. Sci. **46**(6), 1929 (1999)
28. S. Yamamoto, K. Yamasoto, T. Iida, Development of a real-time radon monitoring system for simultaneous measurements in multiple sites, in *Paper presented at IEEE Nuclear Science Symposium and Medical Imaging Conference* (Toronto, Canada, 8–14 Nov. 1998)

29. S. Yamamoto, T. Iida, Nucl. Instr. Methods A **418**(2–3), 387 (1998)
30. S. Yamamoto, K. Kato, N. Fujita, M. Yamashita, T. Nishimoto, H. Kameyama, S. Abe, Sci. Rep. **8**, 10976 (2018)
31. I.S. Kim, I.J. Lee, A. Appleby, E.A. Christman, M.J. Liepmann, G.H. Sigel Jr., Nucl. Instr. Methods A **356**(2–3), 537 (1995)
32. I.S. Kim, I.J. Lee, A. Appleby, E.A. Christman, M.J. Liepmann, G.H. Sigel Jr., Radiat. Prot. Dosim. **61**(1–3), 77 (1995)
33. I.S. Kim, A. Appleby, G.H. Sigel Jr., Nucl. Instr. Methods A **390**(3), 419 (1997)
34. A. Appleby, I.S. Kim, Radiat. Phys. Chem. **55**(5–6), 749 (1999)
35. K. Shitashima, K. Miyakawa, K. Karasawa, Development and oceanographic applications of underwater in-situ radon sensor using plastic scintillator, in *Paper Presented at IEEE Sensors* (Christchurch, New-Zealand, 25–28 Oct. 2009)
36. K.K. Mitev, Appl. Radiat. Isot. **110**, 236 (2016)
37. K.K. Mitev, Thoron (^{220}Rn) detection with plastic scintillators, in *Paper presented at IEEE Nuclear Science Symposium and Medical Imaging Conference* (San Diego, USA, 31 Oct.–7 Nov. 2015)
38. L.M. Santiago, H. Bagán, A. Tarancón, J.F. Garcia, Nucl. Instr. Methods A **698**, 106 (2013)
39. K. Mitev, I. Dimitrova, A. Tarancón, D. Pressyanov, L. Tsankov, T. Boshkova, S. Georgiev, R. Sekalova, J.F. Garcia, IEEE Trans. Nucl. Sci. **63**(2), 1209 (2016)
40. K.K. Mitev, L.T. Tsankov, M.G. Mitev, C.C. Dutsov, S.B. Georgiev, S.T. Kolev, N.M. Markov, T.H. Todorov, Design and tests of a detector for ^{222}Rn in soil-gas measurements based on ^{222}Rn absorbing scintillating polymers, in *Paper Presented at IEEE Nuclear Science Symposium and Medical Imaging Conference (NSS/MIC)* (Atlanta, USA, 21–28 Oct. 2017)
41. K.K. Mitev, C.C. Dutsov, L.T. Tsankov, S.B. Georgiev, M.G. Mitev, N.M. Markov, T.H. Todorov, Design and field tests of scintillation spectrometer for continuous radon in soil-gas monitoring, in *Paper presented at IEEE Nuclear Science Symposium and Medical Imaging Conference Proceedings (NSS/MIC)* (Sydney, Australia, 10–17 Nov. 2018)
42. K. Mitev, V. Jordanov, M. Hamel, C. Dutsov, S. Georgiev, P. Cassette, Development of a portable scintillation spectrometer with alpha-/beta- and neutron-/gamma- pulse-shape discrimination capabilities, in *Paper presented at IEEE Nuclear Science Symposium and Medical Imaging Conference Proceedings (NSS/MIC)* (Sydney, Australia, 10–17 Nov. 2018)
43. Y. Morishita, A. Di Fulvio, S.D. Clarke, K.J. Kefratt, S.A. Pozzi, Nucl. Instr. Methods A **935**, 207 (2019)
44. Y. Morishita, Y. Ye, L. Mata, S.A. Pozzi, K.J. Kefratt, Radiat. Meas. **137**, 106428 (2020)
45. D. Pressyanov, K. Mitev, S. Georgiev, I. Dimitrova, Nucl. Instr. Methods A **598**(2), 620 (2009)
46. D. Pressyanov, S. Georgiev, I. Dimitrova, K. Mitev, T. Boshkova, Radiat. Prot. Dosim. **145**(2–3), 123 (2011)
47. K. Rovenská, M. Jiránek, Appl. Radiat. Isot. **70**(4), 802 (2012)
48. K. Rovenska, M. Jiránek, Radiat. Prot. Dosim. **145**(2–3), 127 (2011)
49. D. Pressyanov, K. Mitev, I. Dimitrova, S. Georgiev, Nucl. Instr. Methods A **629**(1), 323 (2011)
50. K. Mitev, P. Cassette, S. Georgiev, I. Dimitrova, B. Sabot, T. Boshkova, I. Tartès, D. Pressyanov, Appl. Radiat. Isot. **109**, 270 (2016)
51. K. Mitev, P. Cassette, I. Tartès, S. Georgiev, I. Dimitrova, D. Pressyanov, Appl. Radiat. Isot. **134**, 269 (2018)
52. M. Jiránek, V. Kačmařková, J. Environ. Radioact. **208–209**, 106019 (2019)
53. S. Georgiev, K. Mitev, C. Dutsov, T. Boshkova, I. Dimitrova, Int. J. Environ. Res. Public Health **16**(22), 4523 (2019)
54. K. Mitev, C. Dutsov, S. Georgiev, L. Tsankov, T. Boshkova, IEEE Trans. Nucl. Sci. **64**(6), 1592 (2017)
55. E. Pelay, A. Tarancón, K. Mitev, C. Dutsov, S. Georgiev, L. Tsankov, J.F. García, J. Radioanal. Nucl. Chem. **314**(2), 637 (2017)
56. R. Merín, A. Tarancón, K. Mitev, S. Georgiev, C. Dutsov, H. Bagán, J.F. García, J. Radioanal. Nucl. Chem. **319**(1), 135 (2019)
57. H. Møre, L.M. Hubbard, Radiat. Prot. Dosim. **74**(1–2), 85 (1997)

58. D.S. Pressyanov, K.K. Mitev, V.H. Stefanov, Nucl. Instr. Methods A **527**(3), 657 (2004)
59. K. Mitev, D. Pressyanov, I. Dimitrova, S. Georgiev, T. Boshkova, V. Zhivkova, Nucl. Instr. Methods A **603**(3), 491 (2009)
60. D. Pressyanov, I. Dimitrova, S. Georgiev, E. Hristova, K. Mitev, Nucl. Instr. Methods A **574**(1), 202 (2007)
61. K. Mitev, S. Georgiev, I. Dimitrova, D. Pressyanov, Radiat. Meas. **92**, 32 (2016)
62. S. Georgiev, K. Mitev, D. Pressyanov, I. Dimitrova, T. Boshkova, Radiat. Meas. **47**(4), 303 (2012)
63. I. Dimitrova, K. Mitev, D. Pressyanov, S. Georgiev, T. Boshkova, Radiat. Meas. **46**(1), 119 (2011)
64. K. Mitev, S. Georgiev, D. Pressyanov, I. Dimitrova, V. Zhivkova, T. Boshkova, Radiat. Prot. Dosim. **160**(1–3), 188 (2014)
65. K. Mitev, I. Dimitrova, V. Zhivkova, S. Georgiev, G. Gerganov, D. Pressyanov, T. Boshkova, Nucl. Instr. Methods A **677**, 31 (2012)
66. K. Mitev, V. Zhivkova, D. Pressyanov, S. Georgiev, I. Dimitrova, G. Gerganov, T. Boshkova, Appl. Radiat. Isot. **93**, 87 (2014)
67. D. Pressyanov, I. Dimitrova, K. Mitev, S. Georgiev, *Handbook of Radon: Properties, Applications, And Health (Chemistry Research And Applications)*, ed. by C. Feng, Z. Li (Nova Science Publishers Inc., New York, 2012) pp. 101–129
68. R.W. Baker, B.T. Low, Macromolecules **47**(20), 6999 (2014)
69. O.V. Malykh, A.Y. Golub, V.V. Teplyakov, Adv. Colloid Interface Sci. **164**(1–2), 89 (2011)
70. E.M. Renkin, J. Gen. Physiol. **38**(2), 225 (1954)
71. A.S. Michaels, W.R. Vieth, J.A. Barrie, J. Appl. Phys. **34**(1), 1 (1963)
72. A.S. Michaels, W.R. Vieth, J.A. Barrie, J. Appl. Phys. **34**(1), 13 (1963)
73. W.R. Vieth, J.M. Howell, J.H. Hsieh, J. Membr. Sci. **1**, 177 (1976)
74. C.M. Laot, E. Marand, B. Schmittmann, R.K.P. Zia, Macromolecules **36**(23), 8673 (2003)
75. R.P. White, J.E.G. Lipson, Macromolecules **49**(11), 3987 (2016)
76. S. Putta, S. Nemat-Nasser, Mater. Sci. Eng. A **317**(1–2), 70 (2001)
77. C.-C. Hu, C.-S. Chang, R.-C. Ruaan, J.-Y. Lai, J. Membr. Sci. **226**(1–2), 51 (2003)
78. M.H. Cohen, D. Turnbull, J. Chem. Phys. **31**(5), 1164 (1959)
79. J.Y. Park, D.R. Paul, J. Membr. Sci. **125**(1), 23 (1997)
80. J. Vogt, S. Alvarez, Inorg. Chem. **53**(17), 9260 (2014)
81. C.M. Laot, Dissertation, Virginia Polytechnic Institute and State University (2001)
82. M. Minelli, F. Doghieri, Fluid Phase Equilib. **381**, 1 (2014)
83. M. Minelli, F. Doghieri, Fluid Phase Equilib. **444**, 47 (2017)
84. F.D. Brooks, R.W. Pringle, B.L. Funt, I.R.E. Trans, Nucl. Sci. **7**(2–3), 35 (1960)
85. J.B. Birks, *The Theory and Practice of Scintillation Counting* (Elsevier, 1964)
86. M.F. L'Annunziata (ed.), *Handbook of Radioactivity Analysis*, 4th edn. (Academic Press, 2020)
87. G.H.V. Bertrand, M. Hamel, S. Normand, F. Sguerra, Nucl. Instr. Methods A **776**, 114 (2015)
88. ORDELA, Perals[®] Spectrometer Instruction Manual. ORDELA Model 8100AB-HV (1998)
89. labZY. <https://www.labzy.com/products/nanopsd/>. Accessed 29.11.2020
90. E. García-Torano, Appl. Radiat. Isot. **64**(10–11), 1273 (2006)
91. A. L'Hoir, Nucl. Instr. Methods **223**(2–3), 336 (1984)
92. G. Bortels, P. Collaers, Int. J. Appl. Radiat. Isot. Part A **38**(10), 831 (1987)
93. S. Ihantola, A. Pelikan, R. Pöllänen, H. Toivonen, Nucl. Instr. Methods A **656**(1), 55 (2011)
94. S. Pommé, G. Sibbens, Acta Chim. Slov. **55**(1), 111 (2008)
95. S. Pommé, B. Caro Marroyo, Appl. Radiat. Isot. **96**, 148 (2015)
96. S. Kolev, Annual of Sofia University St. Kliment Ohridski. Fac. Phys. **110**, 121 (2017)



Krasimir Mitev (45 yo) graduated from Sofia University (SU, Bulgaria) with a master's degree in nuclear and particle physics. He defended his Ph.D. thesis in 2005 at the Université Paul Sabatier, Toulouse III (France) on the numerical modeling of proportional counters used for metrology of radioactive noble gases. He then obtained a full position at the Faculty of Physics, SU where he performs research and teaches in the fields of radionuclide metrology, Monte Carlo modeling, radiation measurements and their applications. In December 2020, he is an associated professor and a head of the Department of Atomic Physics at the Faculty of Physics, SU. He is the author or co-author of 98 publications and 2 book chapters, with a h-index 13 according to Scopus®.



Philippe Cassette (67 yo) defended his Ph.D. on the production of hydrogen during PWR accidents, in 1981, at the Université Pierre et Marie Curie, Paris VI, France. Then, he worked until 1990 for nuclear reactor safety at the French Atomic Energy commission (CEA). In 1991, he joined the Laboratoire National Henri Becquerel of CEA, in the field of radionuclide metrology. His activities concerned the development of activity measurement methods for the standardization of radionuclides, including noble gas internal proportional counters and liquid scintillation counters. He retired from CEA in 2020 and is now visiting professor at the University of Sofia (Bulgaria). He is the author or co-author of more than 120 publications, 2 books, with a h-index 16 according to Scopus®.

Chapter 12

Recent Advances and Clinical Applications of Plastic Scintillators in the Field of Radiation Therapy



Sam Beddar , Irwin Tendler , François Therriault-Proulx,
Louis Archambault , and Luc Beaulieu

Abstract Within the last three decades, a lot of interest focused on the development of plastic scintillators as new detectors for clinical applications for radiation therapy. During the period of 1990–2000, following the thesis work of Beddar (A.S. Beddar, Dissertation, University of Wisconsin, 1990) [1], most of the studies focused on a further and deeper characterization of these new detectors, including optical light guides and the mechanisms of the light generated in these media. Between 2010–2020, the interest shifted to refining the designs of these detectors for specific application geared toward radiotherapy treatment machine calibrations, small field dosimetry, low and high dose rate brachytherapy and small field dosimetry. During this decade most of these studies were led by two groups, one at the University of Texas MD Anderson Cancer Center (Sam Beddar) and l’Université Laval (Luc Beaulieu) collaborating with each other and carrying the work in their labs with the hope to bring these detectors to the market. During the last decade (2010–2020), the medical physics community witnessed an explosion of interest in the use of plastic scintillators in the field and many groups all over the world started studying and utilizing plastic scintillation detectors (PSDs) for additional applications which included in vivo dosimetry for brachytherapy, external beam radiation therapy, and proton therapy. In this chapter, the authors tried to cover the most important work

S. Beddar · I. Tendler

Department of Radiation Physics, The University of Texas MD Anderson Cancer Center,
Houston, TX 77030, USA

e-mail: abeddar@mdanderson.org

S. Beddar

The Graduate School of Biomedical Sciences, The University of Texas MD Anderson Cancer
Center, Houston, TX 77030, USA

F. Therriault-Proulx

Co-Founder, CEO At Medscint Inc., Quebec City, Canada

L. Archambault · L. Beaulieu

Département de physique, de génie physique et d’optique, et Centre de recherche sur le cancer,
Université Laval, Quebec, QC, Canada

Service de physique médicale et radioprotection, Service de radio-oncologie et Axe oncologie du
CRCHU de Québec, CHU de Québec - Université Laval, Quebec, QC, Canada

and phase that PSDs witnessed with an emphasis on the latest advances that occurred in the field of radiation therapy. We also predict that inorganic plastic scintillators (ISDs) will gain interest in the next decade, especially in brachytherapy applications.

12.1 Introduction

The earliest mention of using plastic scintillators as a tissue equivalent dosimeter was indicated in a 1964 manuscript by the Japanese group of Murai et al. [2]. It was nearly three decades that a seminal set of papers by Beddar et al. providing a systematic investigation of plastic scintillator response under megavoltage photon and electron therapy beams was published [3, 4]. That work paved the way for increasing research activities in the following two decades [5], culminating in Standard Imaging commercializing the W1 [6, 7] and W2 [8] dosimetry systems. In the last ten years, the use of both plastic [9] and inorganic scintillators [10] for radiation therapy dosimetry applications has seen an increased interest by the medical physics community. According to PubMed,¹ there were only 14 such manuscripts in the 1990–1994 period while there are over 180 since 2015. A key aspect of this increased interest is related to the fact the scintillation dosimetry, and in particular plastic scintillation dosimetry, tackles important limitations of current dosimetry systems used in radiation oncology [9].

In this chapter, we are looking at the latest developments in plastic scintillation dosimetry over the past 5–6 years across three radiation therapy segments, namely external beam photon and electron radiation therapy, proton therapy, and brachytherapy. After a review of the basic physics and dosimetric properties of plastic scintillators (including tackling the Cherenkov stem effect), recent implementations and applications for special external beam treatments are presented, in particular small field photon dosimetry, GammaKnife radiosurgery as well as total body irradiation and total skin electron irradiation dosimetry. A full section is dedicated to the use of scintillators, solid and liquid, for proton dosimetry from point dose measurements to 3D volumetric dosimetry. New results with regards to the challenge of scintillation light quenching for proton beams is also covered. Finally, the latest work on brachytherapy dosimetry, in particular for in vivo dosimetry is presented for low energy, low dose rate brachytherapy, and higher energy high dose rate brachytherapy dosimetry. A recent opening for the use of inorganic scintillators in brachytherapy is concluding this chapter.

¹Using search criteria: scintillation AND dosimetry AND ((radiation therapy) OR (brachytherapy)).

12.2 Basic Dosimetry Properties of Plastic Scintillators

12.2.1 Basic Properties of Scintillators Used in Radiation Therapy

Scintillators are mainly used in radiation therapy to measure the dose delivered by ionizing radiation (i.e., the energy deposited per unit mass) delivered at a certain location in a volume representative of a radiotherapy patient. Measurements can be performed either *in vivo*, in which case the scintillator is placed on the surface or inside the patient, or *ex vivo*, in which case the scintillator is placed inside a patient surrogate called a phantom.

A radiation therapy plastic scintillation detector (PSD) is generally comprised of 3 main components: the scintillator itself, which forms the sensitive region of the detector, the light guide that transports the light produced following irradiation of the sensitive volume and a photodetector that converts this light in a numerical signal. A generic PSD is shown in Fig. 12.1, but numerous variations of this simple design can be found in the literature.

To optimize their spatial resolution, PSDs use small volume scintillators, typically below 5 cubic millimeters. Due to the low stopping power of plastic scintillators, most incident particles will not deposit all their energy. Furthermore, the high instantaneous dose rate produced by medical linear accelerators (linacs) or clinical brachytherapy sources can make it difficult to resolve single events. Therefore, most scintillator detectors employed in radiation therapy use an integrating photodetector instead of event-counting electronics.

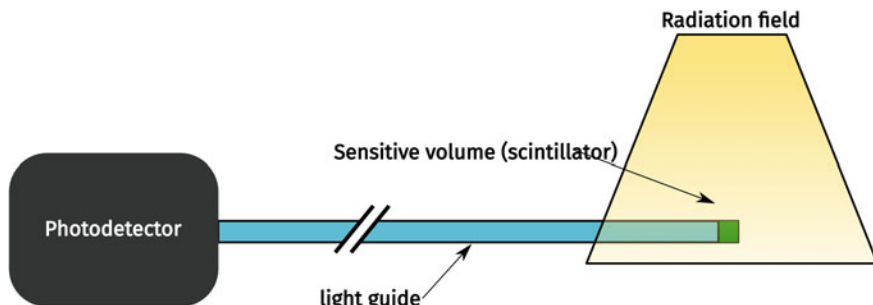


Fig. 12.1 Schematic showing a common measurement setup of a scintillator coupled to an optical fiber

Important notice

Within the context of this chapter, please note that the abbreviation PSD is used to represent Plastic Scintillator Dosimeter.

12.2.2 Relating Scintillation Signal to Absorbed Dose

In most radiation therapy measurements, the number of emitted scintillation photons will be proportional to the dose absorbed by the scintillator, D . Thus, it is possible to determine D by measuring the light output of the scintillator. With detailed knowledge of the scintillator light yield, the transmission of the entire optical chain and the spectral response of the photodetector, it could theoretically be possible to perform absolute dose measurements with a PSD. If a given scintillator has an absolute emission spectrum of $S_a(\lambda)$ photons emitted at wavelength between λ and $\lambda + d\lambda$ per unit energy deposited, the measured signal, M , can be represented as

$$M = \int_0^{\infty} \frac{D}{m_{scint}} S_a(\lambda) W(\lambda) QE(\lambda) d\lambda \quad (12.1)$$

where m_{scint} is the mass of the scintillator, $W(\lambda)$ is the optical attenuation of whole optical chain and $QE(\lambda)$ is the quantum efficiency of the photodetector.

In practice, it is impossible to know $W(\lambda)$ with sufficient accuracy to determine D directly by isolating it from Eq. (12.1). PSD must thus be used as relative dosimeters. Another challenge of PSD comes from Cherenkov radiation [11]. Cherenkov emission is produced in every clear component of the detector. The spectral overlap between scintillation and Cherenkov creates a significant stem effect that needs to be corrected [12, 13]. Even if Cherenkov emission is much lower than scintillation per unit dose, the volume of light guide irradiated can be 10–30 times more than the volume of the scintillator (see Fig. 12.1 for a simple illustration). Methods for dealing with Cherenkov light will be discussed in Sect. 12.3.1.

For dosimetry, the goal is to relate the dose measured at a given point inside a phantom by a dosimeter to the dose that would be received at the same point given the same irradiation, but in the absence of the dosimeter. This conversion can be achieved by applying cavity theories that are valid under specific conditions (e.g., presence of charged particle equilibrium) or by Monte Carlo simulations [14]. The magnitude and complexity of the conversion from the dose measured by the dosimeter to the dose received by the medium in the absence of the detector will be minimized if the composition of the detector closely matches the composition of the medium (i.e., if both have similar stopping power ratios and mass energy attenuation coefficients). Because the reference medium in radiation therapy is water, detector materials that have stopping power ratios and mass energy attenuation coefficients similar to that

of water are desirable. This property is called water equivalence and it one of the main advantages of plastic scintillators [15].

12.2.3 Other Properties

In addition to water equivalence, several properties of PSD were identified and tested when plastic scintillators where first introduced in radiotherapy [3, 12].

12.2.3.1 Linearity to Dose and Dose Rate Independence

Radiation therapy covers a wide range of dose delivery methods from low dose rate, continuous irradiations by permanent implant brachytherapy sources to high dose rate, pulsed irradiation from linacs. PSD have shown to be independent of the dose rate over the whole range of clinically relevant dose rate [3, 15].

12.2.3.2 Response to Particle Type and Energy

The vast majority of radiation treatments are delivered using photons or electrons. Electron beams are produced by linacs and energies between 4 and 20 MeV are routinely used in clinics. Photons beams are produced by bremsstrahlung and use accelerating potential between 6 and 25 MV. Thus, most dose delivered in radiation therapy will be done by electrons between 1 and 25 MeV either directly (electron beams) or indirectly (photon beams). Within this energy range, plastic scintillator response can be considered independent of the particle type and energy [3, 6]. There are, however, some cases of radiation therapy where a PSD response can be affected by the particle type and energy, especially for particle with high linear energy transfer (LET). This can occur in superficial treatment with X-rays of 200 kVp (peak kilovoltage) or less that put low energy electrons in motion or with heavier particles such as protons and ions [16–18]. In such cases, scintillators will exhibit quenching and the light output will be a function of the particle LET. Applying quenching corrections or combining the readout of different type of scintillators can be used to correct for quenching [19, 20].

Nearly three decades after the first use of plastic scintillators in radiation therapy, the field has evolved significantly. There are new and rising treatment modalities for which current radiation therapy dosimeters are not well suited. Adapting PSD for this new paradigm is at the core of current research and development.

Scintillator response to ultra-high dose rates must be characterized to evaluate how PSD could be used with FLASH radiotherapy [21]. FLASH is a new paradigm where dose is delivered in ultra-short pulses of ultra-high dose rate that could lead to significant biological advantages. FLASH requires over 40 Gy/s, while conventional radiation treatments uses dose rates of about 0.05 Gy/s. Using such high dose rates

could alter the performance of a PSD for several reasons. It might be possible to reach a point where a saturation of the light emission process similar to the quenching observed with particles of high LET.

For better targeting cancer, linacs are increasingly combined with magnetic resonance imaging (MRI) devices [22]. Because of this, there is a current need for detectors that are not affected by magnetic fields. Early studies have found that the presence of magnetic field could impact the scintillation process [23, 24]. More recent studies have focused on magnetic fields closer to those encountered in for MRI-linac machine (i.e., 1–1.5 T) and with the specific purpose of assessing the performance of PSD for measurements of MRI-linacs.

It was found that PSDs tend to overrespond in such environment by up to 7–20%, but this apparent overresponse could be explained by change in the Cherenkov light emitted in the detector as well as an actual increase of dose caused by the impact on magnetic field on electron tracks [25, 26]. Detailed study of the emission spectra of plastic scintillators and clear optical fibers in various configurations seem to support that hypothesis [27, 28]. Thus, with proper removal of Cherenkov light, PSD might be a detector of choice for measurements of MRI-linac.

Finally, another application that has been increasing in recent years is *in vivo* measurements. To use a PSD on or within a radiotherapy patient, the detector must be independent of the surrounding temperature. A detector calibrated at room temperature must still provide a valid measurement at body temperature. While plastic scintillators commonly used in PSD do exhibit a small (on the order of 0.7–1.0% for a temperature change of 40 °C), but non-negligible temperature dependence, it is possible to correct it and retain accuracy over a clinical range of temperature [29, 30].

12.3 Signal Processing in Plastic Scintillators Dosimeters

Measurements performed in radiation therapy with any type of detector must typically be accurate to within 5% to be clinically useful. Some applications, such as beam commissioning require an even higher accuracy because any dose measurement errors at this point could become a systematic offset in dose calculation that could potentially affect a large number of patients. High accuracy and precision are therefore needed for PSD.

12.3.1 Cherenkov and Other Sources of Stem Effects

In addition to common source of errors such as readout noise and statistical variations, PSD are strongly affected by Cherenkov radiation. Because Cherenkov is strongly directional and emitted in all clear components of the detector exposed to ionizing radiation, it does not correlate directly with the dose delivered to the sensitive volume of the detector. It must, therefore, be removed from the signal. One method of doing

so is by using a reference optical fiber with no scintillator attached [3]. Scintillation can be isolated by subtracting the signal from both fibers. This technique works well given that both fibers receive the same dose. Unfortunately, modern radiation therapy frequently uses strong dose gradient making it unlikely to have the same dose delivered to both fibers. Another strategy first proposed by Fontbonne et al. is to exploit the spectral difference between Cherenkov and scintillation to decouple them [31]. This spectral separation technique has been shown to work for a wide range of radiotherapy applications [15]. However, Cherenkov light might not be the only source of stem effect. In fact, fluorescence may be present in some measurements [32].

The spectral separation technique may be generalized to account for an arbitrary number of undesired light sources. Assuming a linear superposition of N sources, we can express to overall spectrum, S_{tot} as

$$S_{tot}(\lambda) = x_1 S_1(\lambda) + x_2 S_2 + \cdots + x_n S_n \quad (12.2)$$

where S_i is the relative emission spectrum (i.e., the spectrum with a unit integral value) and x_i the factor to convert for a relative spectrum to an absolute emission (i.e., the total number of photons emitted between λ and $\lambda + d\lambda$). For the scintillator, this is proportional to the dose received. To separate the contribution of each light source, it is necessary to measure the output of the light guide at multiple wavebands. This can be achieved by dividing this output in multiple channels or by using a spectrometer [33].

Going from a continuous spectrum to a discrete sampling at L specific wavelength channels, we can rewrite Eq. (12.2) for a linear superposition of sources in waveband ℓ

$$M_\ell = \sum_{n=1}^N A_n S_n W_\ell \quad (12.3)$$

The product of S_n by W_ℓ represents the response, $R_{\ell,n}$ of the system for the source n in channel ℓ . This can be written in matrix form

$$M = R \cdot x \quad (12.4)$$

where M is a vector of length L , R a matrix of size L by N and x a vector of length N . Assuming that the scintillator corresponds to $n = 1$, the goal is to determine x_1 which will be proportional to the dose. To perform relative dose measurements, the scintillator must first be exposed to a known dose in reference condition to obtain x_1^{ref} . Then the dose relative to that reference for any other measurement will simply be x_1/x_1^{ref} .

To determine x following a measurement M , it is necessary to know R . Then it is straightforward to compute the pseudo inverse R^+ and obtain x from:

$$x = R^+ M \quad (12.5)$$

R^+ is often referred to as the $N \times L$ calibration factor F . Numerically, it is more robust and efficient to compute R^+ through singular value decomposition (SVD) rather than the algebraic form.

Different strategies can be used to determine R . One simple way is to measure the response of the system to each individual light source. In such case, a sequence of measurements is performed where only one of the x_n are nonzero at a time, this allows us to determine R row by row. While conceptually simple, this method may not always be possible experimentally because it may not be possible to isolate some source of stem effects.

Another approach is to use a sequence of K measurements, where the x_k is known in each case. Then the following equation can be solved for R :

$$X = R^+ M \quad (12.6)$$

where X is now a $N \times K$ matrix and M a $L \times K$ matrix. This strategy avoids the need to isolate each emitter but nevertheless requires that the intensity of undesired light sources is known precisely.

In practice, only the light output of the scintillator is often sought. To avoid requiring the intensity of every emitter during the calibration, it is possible to determine R^+ *row by row*

$$f_1 M = x_1 \quad (12.7)$$

where f_1 is a row vector of length L representing the first row of R^+ and x_n is a vector of length K representing the first row of X . This way, for $K \geq L \geq N$, the scintillator can be calibrated without a priori knowledge of the dose received by the other emitters.

12.3.2 Multi-point Radiation Therapy Plastic Scintillator Dosimeters

Once a method for spectrally unmixing the superposed established spectra (one for the scintillator and the others for the sources of stem effect), it is possible to further generalize the system by considering multiple scintillating elements [33]. Indeed, it is possible to place multiple scintillators, each having a distinct emission spectrum on a single light guide and resolve each of them with techniques described in Sect. 12.3.1. These multi-point PSD offer significant advantages for *in vivo* measurements because the dose at multiple locations can be measured simultaneously [34]. By placing small (i.e., sub-millimeter) scintillator elements directly on top of each other, it is

also possible to measure a radiation field with a high spatial resolution and with no sampling gap. This could be a valuable tool for measuring dose distributions with numerous high dose gradients.

12.4 Clinical Applications and Special Procedures

12.4.1 *Photon and Electron External Beam Radiation Therapy*

Dose measurements using plastic scintillators for photon and electron therapeutical beams have been covered extensively in prior publications, from point dose measurements to volumetric dosimetry [5, 9]. Thus, in this section we will cover three specific clinical application cases, namely small field dosimetry, GammaKnife Radiosurgery, and total body irradiation (TBI).

12.4.1.1 Small Field Dosimetry

Modern external beam photon-based radiation therapy treatments are now commonly delivered using a superposition of tens to hundreds of fields that can often be as small as 0.4 mm in diameters. These fields are delivered through techniques such as intensity modulated radiation therapy (IMRT), volumetric arc therapy (VMAT), stereotactic radiosurgery (SRS), and stereotactic body radiotherapy (SBRT). These approaches differ significantly from the standard primary laboratory calibration condition, as well as the usual large field quality assurance (QA) of radiation therapy equipment, typically from $5 \times 5 \text{ cm}^2$ to $40 \times 40 \text{ cm}^2$ [35, 36]. Major issues for dosimetry in these conditions are the signal averaging over the volume of the dosimeter, loss of electronic equilibrium (CPE/PCPE), beam penumbra, and non-water equivalence of the dosimeters [37]. For flattening filter free (FFF) small beams, dose rate can also be an issue [38].

It turns out that plastic scintillators have numerous properties that make them ideal for this task as discussed previously: water-equivalent response to MV photon beams, energy, and dose rate independence, they can be machined to very small sizes and already exist commercially in the form of optical fibers of 0.5, 1.0, and 2.0 mm diameters. The use of scintillators for small field dosimetry was first demonstrated by Létourneau et al. However, the most convincing demonstration based on a modern delivery technology (a CyberKnife) was made by Morin et al. [39], who showed that not only output factors [40] of small fields could be extracted within the accuracy of a Monte Carlo prediction without any correction factors, a first for small field dosimeters, but they were also able to accurately extract experimentally the correction factors of numerous other dosimeters without making any assumption on the details

of the irradiation beam characteristics. These details are needed to use MC-derived, dosimeter-specific correction factors.

A number of subsequent studies further reinforced this result, showing that plastic scintillators are expected to have very small to no correction factors [41–43]. Furthermore, in the past few years, these results were reproduced by numerous clinical end-users worldwide using commercially available plastic scintillator dosimetry systems, namely the W1 [44–48] and W2 systems. The latter was evaluated in relation to the IAEA TRS-438 guidelines. It was concluded that the dosimeter was an ideal detector for commissioning of SRS and SBRT techniques due to the fact that correction factors were not needed [8]. A new study further suggested that plastic scintillators could be used as a transfer detector for traceable measurements in small field dosimetry [49].

12.4.1.2 Gamma Knife Radiosurgery

For the treatment of brain cancer and neurological diseases, Gamma Knife radiosurgery represents an increasingly attractive alternative to traditional brain surgery and whole-brain radiation therapy. A Gamma Knife irradiator uses up to 201 beams of gamma irradiation generated by Cobalt-60 sources and converging to a point in space called the focus or the shot. Characterization and quality assurance of Gamma Knife radiosurgery irradiator represent a challenge and does not only depend on the detector, but also on the necessity to implement special protocols and apparatus to account for the geometry of beam delivery and limited space inside the irradiator. The use of plastic scintillation detectors in conjunction with water-equivalent spherical phantoms show great promises for quality assurance of the shots coming from different size of collimators (4, 8, and 16 mm) [50]. Indeed, Therriault-Proulx et al. have validated the use of a plastic scintillation detector with a sensitive area of 1 mm diameter × 3 mm length (Exradin W1 Standard Imaging, Wisconsin, USA) inside a spherical water-equivalent phantom (Lucy, Standard Imaging). Profiles and output factors were measured using the plastic scintillation detector and compared to measurements obtained with an ion chamber (Exradin A16, Standard Imaging, Wisconsin, USA) and radiochromic films as well as the system data provided by the vendor. For reference, the following report provides a detailed description and performance evaluation of the commonly used Exradin W1 detector [7].

Table 12.1 Output factor for 4-mm and 8-mm collimators as measured by different detectors and compared to the nominal value. Values are normalized to the measurement with 16-mm collimators [50]

	Output factor	
	4-mm collimator	8-mm collimator
Nominal	0.814	0.900
Plastic Scintillator	0.795 (−2.3%)	0.892 (−0.9%)
EBT3	0.793 (−2.6%)	0.881 (−2.1%)
A16	0.727 (−10.7%)	0.883 (−1.9%)

Table 12.1 shows that both the scintillation detector (Exradin W1) and radiochromic film (EBT3) agreed well with nominal values for all collimator sizes, while the ion chamber became particularly subject to volume averaging effect with the 4-mm collimator. This was to be expected based on the spatial resolution of each detector and the fact that the diameters of the sphere where the dose was within 0.5% of the dose at the center of the shot were of 8, 3 and 1 mm for collimator sizes of 16 mm, 8 mm, and 4 mm, respectively. It was also shown as part of this work that a configuration in which the shot moves while the detector remains fixed is equivalent to the opposite (i.e., moving the detector instead of the shot), therefore, validating the possibility to move the table in order to obtain dose profiles using a solid spherical phantom. Validation of a 3D-printed plastic scintillation detector for Gamma Knife dosimetry was recently performed by Lee et al. [51]. The validation was limited to collimator sizes of 16 mm but showed great dose rate linearity ($R = 0.999$) and reproducibility ($\pm 0.56\%$).

12.4.1.3 Total Body Irradiation (TBI) and Electron Skin Total Irradiation (TSEI)

Total Skin Electron Irradiation (TSEI)

Total Skin Electron Irradiation (TSEI) relies on the principle of administering a uniform electron field to the entire body. Clinical conditions that are commonly treated with TSEI include, but are not limited to, *mycosis fungoides* and cutaneous T-cell lymphoma. The two most popular methods of administering TSEI are the rotational and Stanford techniques [52]. A specialized linac setting (High Dose Total Skin Electron) sets a large field size ($200 \times 80 \text{ cm}^2$ at the patient treatment plane) and high dose rate (888 MU/min).

The Stanford technique requires that the patient is positioned standing in 6 different poses to ensure full body coverage of the beam. Typically, during each treatment day (often the patient is treated 4 times a week), 3/6 positions are completed. Thus, two full cycles of the Stanford technique are done per week over a series of 6–9 weeks with fractions of 1–2 Gy, depending on the severity of the patient's medical condition. Throughout treatment, the patient's skin surfaces are irradiated such that skin folds and crevices (e.g., armpits) receive adequate dose; sometimes boost doses are required if the disease is present on the soles of the feet, or other areas not easily irradiated by en-face beams. Further specific details, such as energy levels, gantry angles, collimator angles, etc., regarding this treatment modality have been thoroughly described in the literature [53–55].

The rotational TSEI technique necessitates that the patient maintains a single pose (arms raised above head) while standing on a rotating (360°) platform in the path of the beam. Treatment sequences are completed on a regimen similar to the Stanford method described above, specific details regarding the rotational method can also be found in the literature [56, 57]. Regardless of the methodology employed, the goal of

TSEI still remains the same: administering a homogenous electron field to the entire body.

TSEI is a physically taxing procedure and patient fatigue is commonly observed. A substantial amount of time is required for room setup, patient positioning, treatment administration, and postexposure dosimetry processing. Standards set by the American Association of Physicists in Medicine (AAPM) establish that tolerances for variation in the radiation beam are $\pm 8\%$ in vertical and $\pm 4\%$ in horizontal planes within the central $160 \times 60 \text{ cm}^2$ aspect of the composite treatment field. Though, in practice, the variation at the patient has been recorded to be as high as $\pm 15\%$ due to variable self-shielding, differences in patient anatomy (variable skin-beam distance), and patient motion [58]. To note, the European Platform of Cancer Research (EORTC) provides a broader definition of the threshold for dose uniformity: $\pm 10\%$ across the entire body when using TSEI in the management of *mycosis fungoides* [59]. Since the efficacy of TSEI highly depends on uniform coverage across the entire body, there exists a clinical need to verify the homogeneity of administered dose throughout the course of treatment.

Surface dosimetry during TSEI has commonly been accomplished using wired diodes, film, thermoluminescent detectors, and optically stimulated luminescence dosimeters (OSLDs). Recently, a novel method for measuring surface dose during TSEI by capturing light (scintillation) emitted from plastic discs attached to the skin surface has been developed. Custom-machined EJ-212 discs ($1 \text{ mm thick} \times 1 \text{ cm } \varnothing$) are painted with EJ-510 reflective paint (Eljen Technology, Sweetwater, TX) along the read face and edge to better direct light output toward the camera. A clearcoat and adhesive backing enable dosimeter sanitization (via common clinical SaniWipes) and quick attachment/removal, see Fig. 12.2 for the full cross-section of the dosimeters [60].

The imaging setup is composed of an intensified, time-gated, CMOS camera whose image acquisition is synchronized to pulses of the linac [61–63]. During irradiation, images are remotely recorded; upon the completion of treatment, scintillation images automatically undergo processing using a custom MATLAB algorithm and dose values are extracted using external calibration factors [63, 64]. Patient

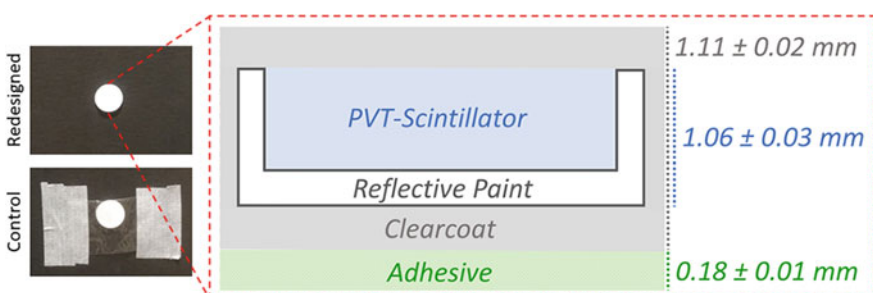


Fig. 12.2 Cross-sectional view of the various layers of the scintillator dosimeter (reproduced from [60] with permission from SPIE)

imaging is conducted with room lights on as detection of ambient background light is suppressed by using a dynamic online background subtraction methodology [65]. Unlike in cases where optical fibers are used, residual Cherenkov signal does not need to be corrected for—the reflective coating on the rear face of the disc prevents mixing of plastic scintillation and Cherenkov light generated from the underlying tissue. Figure 12.3 shows an overview of the imaging setup including sample patient images and surface dose measurements.

Calibration factors are obtained by irradiating the scintillators attached to a flat-faced phantom alongside another standard dosimetry device e.g. OSLD. By exposing the dosimeters to increasing amounts of dose in the TSEI treatment plane, a relationship between light output and administered dose is computed. Human pilot testing has shown that the accuracy of scintillators is comparable to that of OSLDs—percent difference in measuring surface dose during TSET using scintillators vs OSLDs was found to be <5 and <3% for 241/242 and 221/242 anatomically independent dosimetry sites [67].

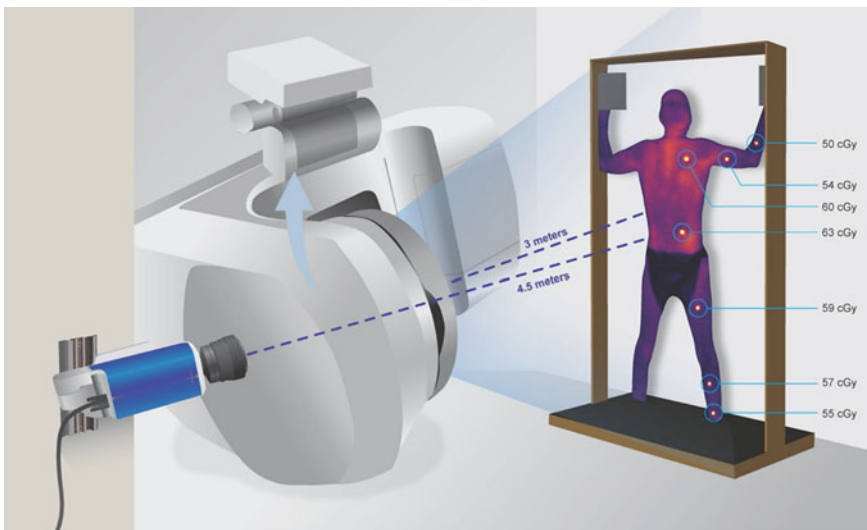


Fig. 12.3 Schematic of the imaging and patient treatment (TSET) setup. Camera-patient and linac-patient (SSD) distances are also provided. Doses measured by scintillators at the seven measured dosimetry sites are provided for a sample posterior-anterior irradiation (300 MU for this single Stanford TSET position, image is a cumulative sum of all frames). To note, each Stanford TSET position required administration of two separate irradiations, one with the gantry at 289.5° and 250.5°; these two angles were optimized to achieve the best vertical dose uniformity and need to be determined from on-site measurements. For illustrative purposes, both fields are shown as a sum with an arrow indicating the trajectory of gantry movement. For phantom imaging, the patient treatment stand was removed and the phantom was placed on a stand 3 m (SSD) away from the linac at the center of the beam, while the gantry was held at 90° (reproduced from [66] with permission from John Wiley and Sons)

Within the scope of TSEI, utilization of scintillator dosimeters does not require correction factors for distance, temperature, and angular correction factors. Furthermore, a bulk calibration factor can be used for converting light output to dose, such that dosimeter-specific calibration factors are not needed. The imaging system can be tuned to detect Cherenkov intensity profiles from the patient during treatment, in turn, providing a unique *en-face* view of the treatment field [67, 68]. Scintillator discs can be cleaned in between uses and are resistant to radiation damage, thus enabling clinical reusability [60]. Surface dosimetry workflow analysis has shown that scintillators can report surface dose nearly twice as fast as OSLDs with substantially less manual work and minimized chances of human error [66, 69]. In addition, constancy quality assurance (QA) measurements are automatically obtained during each image acquisition by permanently attaching constancy scintillator discs to an object in the field of view, such as the patient treatment stand—light emitted from these discs is captured during each irradiation; measurements are automatically compared resulting in day-to-day stability metrics. These TSET-specific QA measurements complement those conducted following standard protocols such as those described in medical linac commissioning documents [70]. Given their linear response to dose and dose rate (irrespective of incident beam energy), scintillator dots have the potential to not only be used as dosimeters for other treatment modalities (whole breast radiotherapy, head and neck treatments, etc.), but as QA dosimetry devices [67, 71, 72, 73].

Total Body Irradiation (TBI)

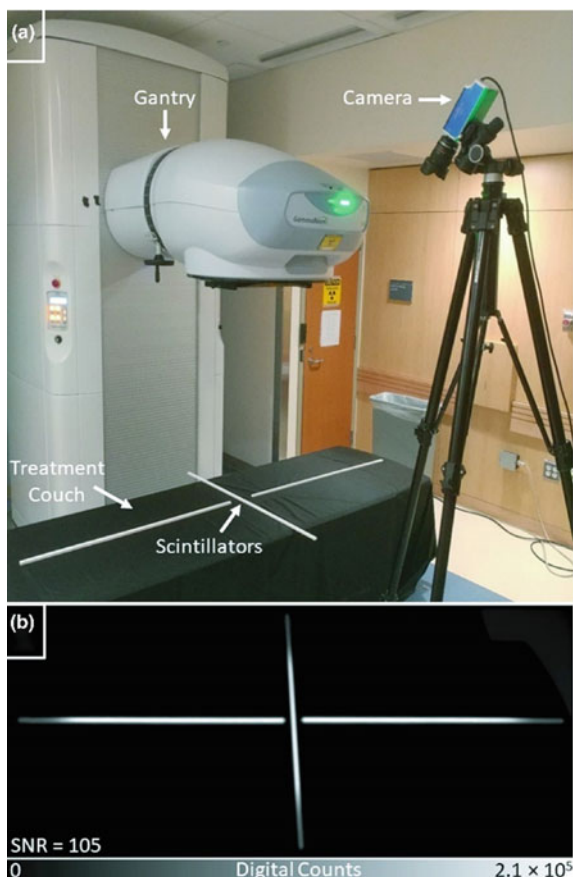
Similar to TSEI, TBI aims to homogeneously irradiate the entire body during treatment, however, the key difference between the two modalities is that TBI utilizes a photon radiation beam (compared to electrons for TSEI). TBI is commonly used for clinical scenarios in which a patient is preparing for bone marrow and stem cell transplantation—TBI simultaneously suppresses the immune system and destroys cancer cells [74].

Commercially available devices, such as the GammaBeam 500 (Best Theratronics Inc., ON, Canada), are designed to act as dedicated ^{60}Co irradiators for TBI patients. QA testing for the GammaBeam 500, and other setups used for TBI (linear accelerator or other ^{60}Co irradiators), often requires time- and resource-intensive point measurements using ionization chambers, or radiographic film for 2D analysis [75]. Imaging of plastic scintillator rods has been demonstrated to be a feasible method for streamlining TBI QA workflow without sacrificing accuracy. Moreover, scintillator imaging produces a single image stack that unlike OSLDs and ionization chambers, does not require postexposure processing or repeat manual measurements, respectively.

Early versions of this dosimetry system involved an intensified CMOS camera mounted on a tripod positioned adjacent to the treatment couch. By recording light emission from rods (EJ-200 plastic coated with EJ-510 paint on all edges except the one facing the camera, $8 \times 15 \times 1000 \text{ mm}^3$, Eljen Technology, Sweetwater, TX) placed along the axis of the treatment couch, beam homogeneity, symmetry, and light-radiation field correspondence can be verified with a single irradiation, see Fig. 12.4a. To note, the homogeneity of the scintillator rods was verified by the

Fig. 12.4 **a** Imaging setup for field homogeneity, light-radiation field correspondence, and symmetry testing featuring tripod-mounted camera, ^{60}Co irradiator, and scintillator dosimeters. **b** Sample cumulative image ($\text{SSD} = 174$) from field symmetry and homogeneity testing, setup shown in **a**, colorbar represents pixel intensities in digital counts (arbitrary units).

Signal-to-noise ratios are also provided for this image. Two separate rods ($2 \times 1 \text{ m}$) are used in the longitudinal direction, a single rod (1 m) is used for the latitudinal axis (reproduced from [76] with permission from John Wiley and Sons)



manufacturer (Eljen Technologies, Sweetwater, TX) during the production of the dosimeter.

Accuracy of all measurements is maintained $<1.5\%$ difference when compared to OSLDs. Effective dose rate can also be measured using this scintillator imaging system by simply raising or lowering the treatment couch from the radiation source and quantifying changes in light output. In this particular case, scintillator rods were able to accurately measure dose rate with $0.7 \pm 0.2\%$ difference compared to an idealized model $\frac{1}{(\text{Source-Surface-Distance})^2}$, ionization chamber measurements resulted in a $0.3 \pm 0.3\%$ difference, see Fig. 12.4b for sample images [76]. To note, verifying the dose *in vivo* during TBI can be accomplished using silicone diodes or thermoluminescent detectors; work is currently in process to assess the feasibility of imaging plastic scintillator for use as *in vivo* surface dosimeters [67, 77, 78].

12.4.2 Proton External Beam Radiation Therapy

12.4.2.1 Optical Scintillating Fibers

Technology Overview

Optical scintillating fibers have been extensively studied for applications as point-dosimeters in photon and electron radiotherapy regimes. The most popular form factor of scintillating fiber detectors within the realm of proton therapy involves irradiating a small organic scintillator that is coupled to a plastic optical fiber. The principle of operation relies on the fact that scintillation light produced in the scintillator tip is directly proportional to the amount of imparted dose. Light generated within this active element travels throughout the length of the fiber and is detected by a receiver; to note, the fiber is designed specifically to enable high fidelity light transport. The incoming light signal is transformed from analog to digital format (often via photodiodes) and then undergoes various processing steps (amplification, filtering, etc.) [9]. There exist numerous methodologies and devices for scintillator-fiber readout, a few examples, include, but are not limited to: thermoelectrically cool CCD array spectrograph, multi-pixel photon counter, PMT-coupled data acquisition system, intensified and electron-multiplying CCD [79–83]. Figure 12.5 shows

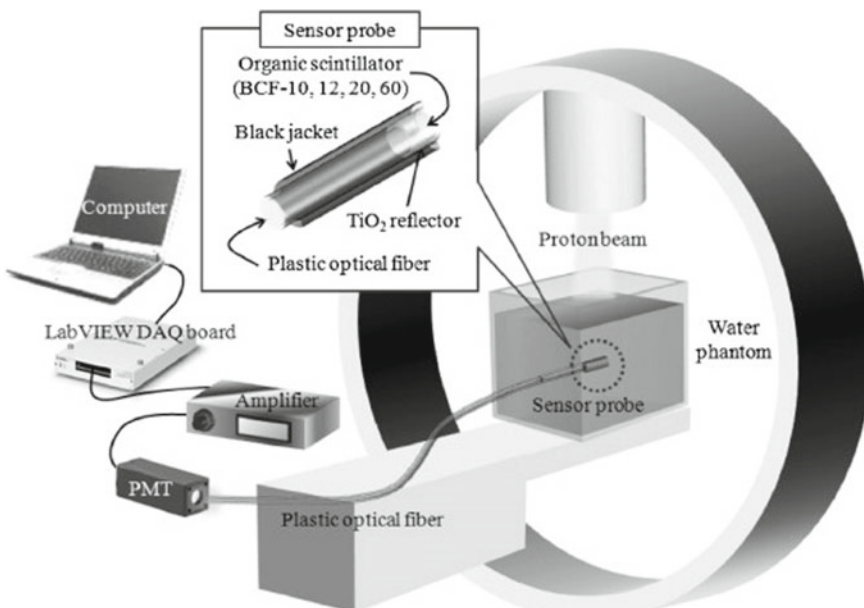


Fig. 12.5 Schematic of a scintillator optical fiber dosimetry setup for QA measurements within a water tank placed in the bath of a clinical proton beam (reproduced from [84] with permission from Elsevier)

a schematic of a scintillator-tip fiber being used for quality assurance testing of a proton beam in a water tank—each portion of the dosimetry is independently labeled: dosimeter, fiber, detector (PMT), amplifier, digital acquisition board, and computer.

One of the greatest drawbacks to this form of dosimetry is that undesirable Cherenkov light is simultaneously generated along the length of the fiber—Cherenkov light generation and other stem effects are discussed in detail in Sect. 12.3.1. Importantly, research effort has shown that other versions of scintillating fibers, such as bare plastic optical fibers, can also act as effective dosimetry devices for proton radiotherapy [85].

Applications to Proton Therapy

Monte Carlo analysis and empirical studies have rigorously shown that scintillator dosimeters do not perturb the proton beam, however, some energy dependencies due to light quenching within the plastic scintillator were observed [17]. For small ($0.5\text{ mm } \varnothing \times 1\text{ mm}$) scintillating fibers, a 5% difference in depth-dose profiles were noted when compared to Markus chamber readings; differences attributed to quenching effects were corrected by using Birks' formula. Multiple studies have independently confirmed that scintillator light response is linear ($R^2 > 0.99$) versus dose [86, 87, 84]. A summary of various scintillator-based optical fiber dosimetry systems is provided in Table 12.2. In conjunction with plastic scintillators, other nonorganic scintillators have been used as active elements within optical fiber dosimetry setups, an example is included within Table 12.2 row 5.

Scintillator materials are specifically chosen to meet certain key performance criteria such as water equivalence, rapid response time, rapid decay time, minimal energy dependence, minimal angular dependence, linear dose response, independence to dose rate, resistance to radiation damage (e.g., radiation-induced polymer/plastic cross-linking), and minimal requirement for temperature correction factors. A thorough description of these various criteria and additional design considerations have been previously summarized [9].

Scintillator Optical Fiber Array

A substantial amount of research effort has been devoted to developing arrays of scintillator fibers for two-dimensional measurements. Arrays of plastic dosimeters, such as those described by Son [88], feature numerous fiber/scintillator tips arranged in a geometrical pattern, see Fig. 12.6a. Simultaneous exposure of many dosimeters not only provides a 2D view—spatial resolution is directly dependent on the number and spacing of dosimeters utilized—but can improve workflow efficiency by minimizing the number of measurements required (when compared to single fiber dosimeters) [87]. Potential applications of this type of technology can be seen in the realm of quality assurance testing and *in vivo* dosimetry. For example, previous work has shown that scintillator arrays can potentially be used for real-time dose monitoring during ocular proton therapy [84, 89], see Fig. 12.6b.

The feasibility of utilizing commercialized products, such as the Exradin W1 PSD, for *in vivo* skin dosimetry for patients undergoing proton therapy has been an area of active research [90]. Results have shown that for passive scattering proton

Table 12.2 Summary of various scintillator optical fiber materials and dimensions

Publication	Dosimeter material and dimensions	Fiber material and length	Additional information
Jang et al. [86, 84]	<ul style="list-style-type: none"> • BCF-10 • BCF-12 • BCF-20 • BCF-60 	15 m, step-index multimode SH-2001	Scintillator and fiber ends were polished and connected using DP-100 + optical epoxy (3 M). TiO ₂ reflector was used to minimize leakage of light from the scintillator
Wang et al. [79]	BCF-12	20 m, super Eska GH2001 PMMA plastic-core optical fiber	Scintillator shielded by black polyethylene jacket and black adhesive—attached to fiber using optical glue
Son et al. [88]	Plastic optical fiber PGS-CD1001-13-E	N/A*	2D array of bare plastic fibers
Darafsheh et al. [85]	15 m with tip exposed, plastic optical fiber SH4001	N/A	Bare optical fiber with PMMA core and fluorinated polymer cladding
Penner et al. [80]	Terbium-activated gadolinium oxysulfide powder UKL65FR1	13.5 m, PMMA plastic core optical fiber with fluorinated polymer cladding	1.9 × 1 mm Φ plastic optical fiber with 1 × 0.5 mm Φ hole drilled and filled with scintillator powder
Hwang et al. [81]	BCF-12	SH 1001 optical fiber	Surface of fiber jacketed with black polyethylene
Alsanea et al. [89]	<ul style="list-style-type: none"> • BCF-12 • PMMA RP-200 • PVT • LS Optiphase HiSafe 3 liquid 	40 m, optical fiber	Solid scintillators coupled to fiber using UV-curing epoxy. The fiber was placed into the liquid scintillator cuboid holder and sealed using black epoxy and head shrink tubing
Alsanea et al. [90]	Exradin W1—polystyrene with ABS plastic enclosure and polyimide stem	Acrylic (PMMA) with polyethylene jacket	Commercialized product manufactured by Standard Imaging

N/A non announced

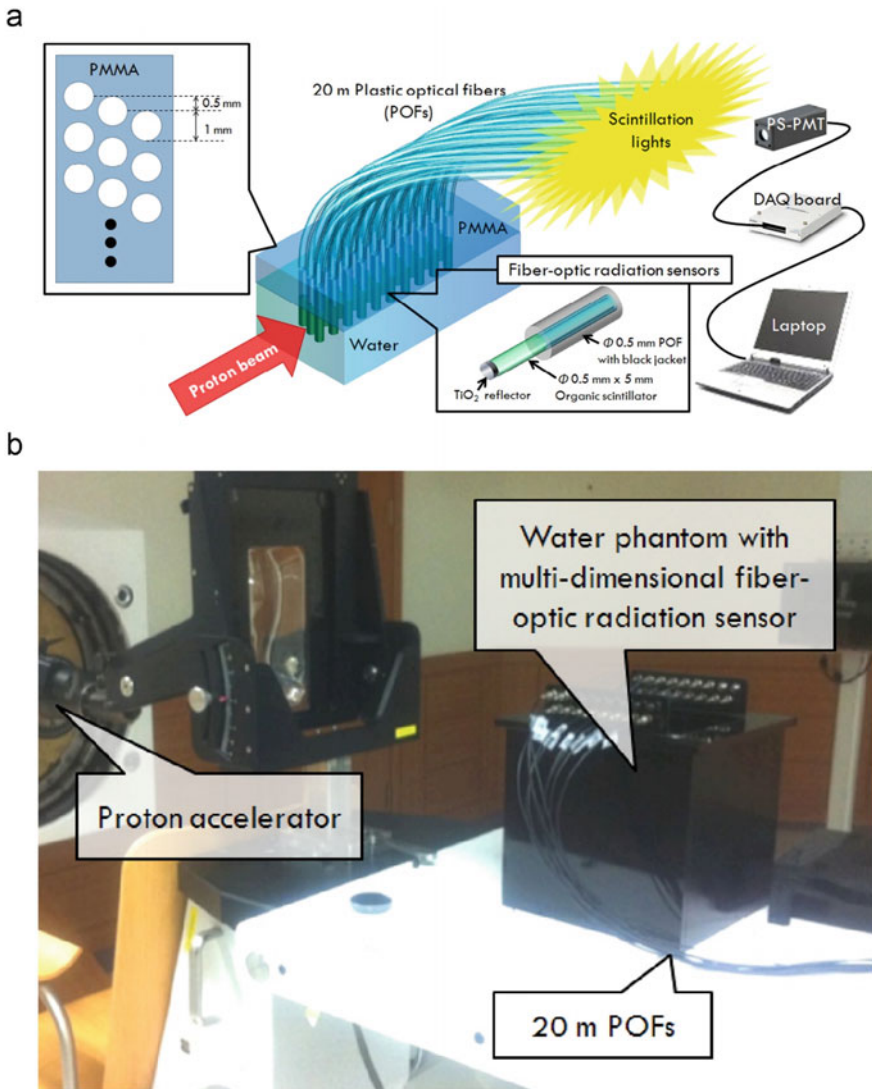


Fig. 12.6 Schematic showing the application of a scintillator optical fiber array applied to a phantom (reproduced from [84] with permission from Elsevier)

treatments, PSD dose response was within $\pm 1\%$ of the expected dose for all patients ($n = 6$), treatment plans test following corrections for ionization quenching ($7.8 \pm 1\%$ under-response) and temperature (4% under-response). Similar results (7% loss of signal at 250 MeV), in terms of under-response due to ionizing quenching were observed when measuring entrance dose using a BCF-12 (Saint-Gobain Crystals and Detectors, Courbevoie, France) scintillating fiber [91].

12.4.2.2 Quenching Effects

The phenomenon of quenching is commonly observed in proton and heavy ion beams as a suppressed scintillation response when ionization density increases with depth. As such, to maintain a linear (or near-linear) light output-to-dose relationship, depth-dependent correction factors are employed when scintillators are used for proton and heavy ion beam dosimetry [17]. Within the scope of scintillator dosimetry in proton radiotherapy, quenching effects can be directly observed as a noticeable decrease in the magnitude of the Bragg peak—it is important to note that the depth of the Bragg peak is not impacted—where linear energy transfer (LET) is the driving force of depth-dose distribution [9]. The physical mechanisms of quenching have been well described; existing explanations include, but are not limited to, saturation of scintillation centers, reduction in primary excitation efficiency of the scintillator (uni-, bi-, and n-molecular, bimolecular, and thermal flash along the ionization track) [92–96].

Numerous studies have explored quenching correction factors for various scintillator form factors, e.g., liquid, fiber, sheet, and solid scintillators. One potential strategy employed focused on determining the first-order Birks model quenching parameter (kB) via Monte Carlo comparison of scintillator response versus LET. Experimentally determined $kB \left[\frac{g \cdot MeV}{cm^2} \right]$ values for scintillators manufactured by Saint-Gobain Crystals and Detectors (Courbevoie, France) were 9.22×10^{-3} , 9.40×10^{-3} , 2.38×10^{-2} for BC-521, BCF-12, and BCF-60, respectively [20, 79, 97]. For reference, the equation for the Birks model [94, 95] is provided below

$$\frac{dS}{dx} = \frac{A \cdot \frac{dE}{dx}}{1 + kB \cdot \frac{dE}{dx}} \quad (12.8)$$

where

$\frac{dS}{dx}$ = scintillation light(s) emitted over a distance (x) in the medium

A = scintillation efficiency of the medium (material property)

$\frac{dE}{dx}$ = energy deposited by protons over a distance (x)

kB = empirical factor for nonscintillation energy loss

Plastic scintillator response was found to be within $\pm 5\%$ difference when compared to ionization chamber readings for >100 MeV proton beams (the width of the Bragg peak becomes narrower at lower energies) [79]. Figure 12.7 shows overlaid views of liquid scintillator measured, corrected, and simulated depth-dose profiles for proton pencil beams ranging from 85.6 to 161.6 MeV. By applying a Birks model-based quenching correction factor, corrected optical imaging data were within $< 1\%$ of their Monte Carlo counterparts; the limiting factor, in this case, was the noise floor of the imaging system [20]. The greatest drawback to this method is that location-specific LET is a required input to the Birks model—alignment of

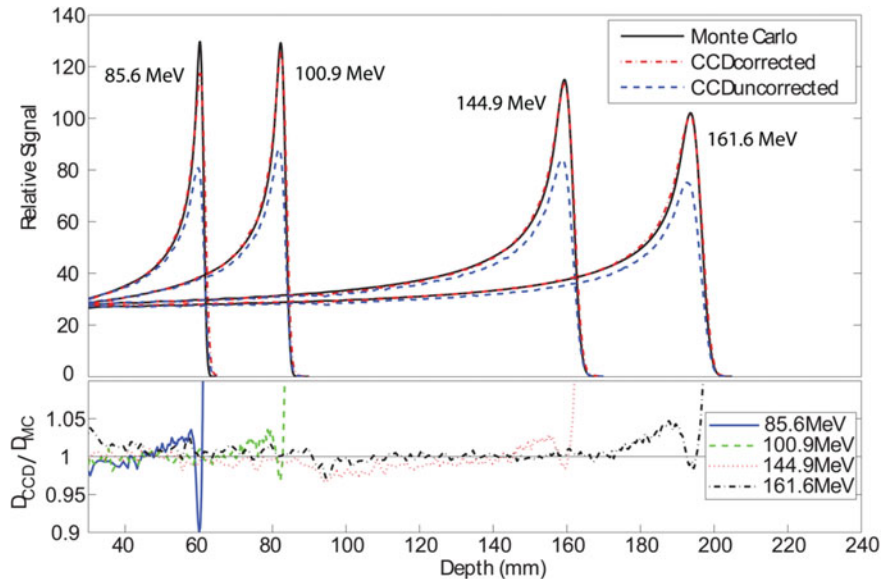


Fig. 12.7 *Upper* panel shows the relative magnitude of measured scintillator light signal for corrected and uncorrected data plotted against Monte Carlo simulations for proton pencil beams of various energies. *Lower* panel shows the ratio of corrected scintillation light signal versus Monte Carlo simulation data (reproduced from [20] with permission from IOP)

measured scintillator data with calculated LET is nontrivial. Considering the sharpness of the Bragg peak (large dose gradient) and LET gradient, minor misalignment between measured and calculated data sets can lead to large discrepancies between scintillator signal and measured dose. An alternative approach to the Birks model operates on the principle of accounting for energy deposition by secondary electrons (EDSE) as a factor of total light output versus energy of the ion beam. Preliminary data has shown that the EDSE method can produce results comparable in accuracy ($\pm 5\%$) to that of the Birks model when for quenching effects in 3D scintillator proton beam dosimetry [98].

12.4.2.3 Large Volume Scintillators for 3D Dosimetry

Scintillation dosimetry in the field of proton radiotherapy can be conducted in one-, two-, and three- spatial dimensions. Section 12.4.2.1 outlined numerous dosimetry techniques utilizing scintillating fibers (1D) and scintillator-fiber arrays (2D). Large volume solid, liquid, and gas scintillators have been shown to be useful tools in capturing 3D profiles of proton beams. Regardless of the physical state of the scintillator used, similar means for image acquisition and processing are used. Attempts at

3D scintillation dosimetry have been made using single- and multi-camera setups—the latter potentially yielding higher spatial resolution, shorter acquisition time, and improved processing speed.

Typically, to obtain images, a camera is aimed at a volume of scintillator positioned within the path of the beam. Cameras with intensifiers (i.e., photocathode technology) have been demonstrated to be effective detectors of large volume scintillator light output [99]. On occasion, light yield can be large enough in magnitude to eliminate the need (thereby lowering cost and simplifying the required hardware) for intensification. As the particle beam transects the scintillator, light is emitted through mechanisms outlined in Sect. 12.2. Often, strategies using materials such as black-out painting, shielding or reflective paint are employed to influence the directionality of light emission from the scintillator in the direction of the camera—in certain cases, mirrors and other optical-based approaches are also used to improve upon detection efficacy of scintillator light. To note, optimal camera positioning and lens/optics choices are key in maximizing light capture efficiency and must be carefully considered for each unique imaging setup [100]. The issue of confounding quenching effects is omnipresent in 3D scintillator proton dosimetry, however, numerous methods for correcting quenching effects exist and are discussed in Sect. 12.4.2.2.

Liquid 3D Scintillators

Liquid scintillators can accurately provide proton radiography, beam characterization, dosimetry, and QA testing of discrete spot scanning systems [9]. Potential downsides to liquid scintillators are often associated with the fact that a large volume of liquid is required for imaging; thought must be given to potential leakage, cleaning of the tank, and management of large volume (and weight) of water.

A CCD-imaged OptiPhase HiSafe 3 (PerkinElmer, Waltham, MA) $20 \times 20 \times 20 \text{ cm}^3$ liquid scintillator dosimetry system was developed for, near-real time QA testing of proton spot scanning beams, see Fig. 12.8 [99]. A tank with a wall thickness of 11.6 mm was used to hold the scintillating volume and three scientific complementary metal oxide semiconductor (sCMOS) cameras were used to image the scintillator along the X, Y, and Z-axis. Multi-dimensional imaging was accomplished by using a head-on view of the scintillator volume (X-axis) and two 45° mirrors (Y- and Z-axes). A custom-manufactured microcontroller trigger solution was developed for image acquisition; images were synchronized to beam spot START/STOP signals such that camera readout time did not overlap with dose-delivery times. The entirety of the delivered beam was simultaneously captured by all three camera views. The camera system has an observed image intensity variability of 2% and background signal varied by 0.6% for exposure times ranging from 1 ms to 1 s [101]. Studies specifically attempting to correct for quenching effects using both Birks and energy deposition by secondary electron (EDSE) models have been previously published, see Sect. 12.4.2.2 for further detail [20, 102].

The previously described imaging system was modified to produce proton radio-graphs using an integrating detector approach [103]. 2D grayscale output from a single camera located along the beam's eye view was converted to water-equivalent-thickness (WET) values using a light intensity-WET calibration curve. Calculated

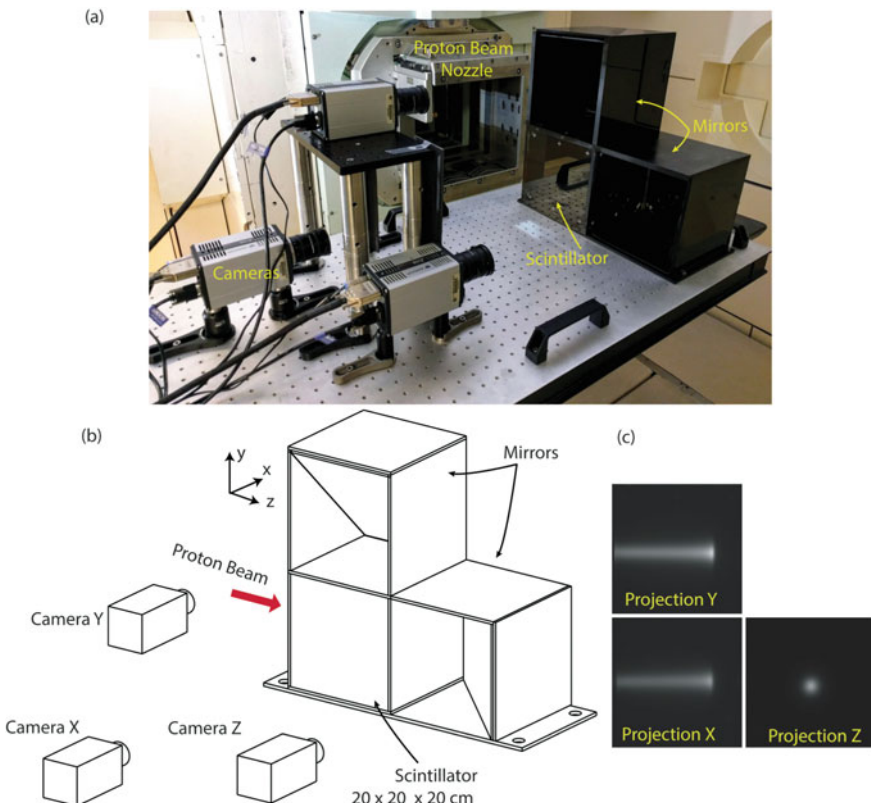


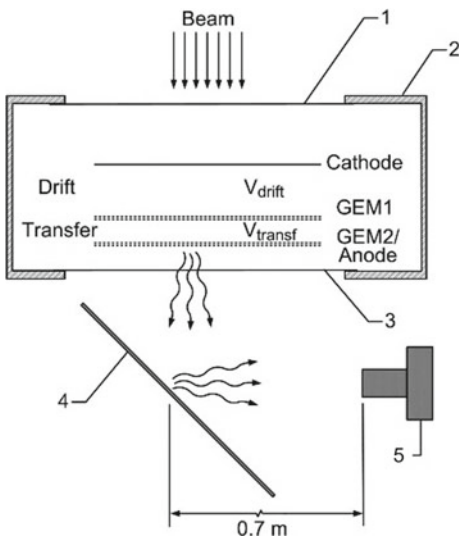
Fig. 12.8 **a** and **b** Photograph and schematic of a 3-camera with proton beam nozzle, mirrors, and liquid scintillator labeled in yellow; **c** 2D projection views shown for each (X, Y, and Z) camera observation axis (reproduced from [101] with permission from Elsevier)

WET values were within 2% difference from actual values for solid water, acrylic, and cortical bone. A filtered back-projection image processing algorithm was used to reconstruct proton CT images from camera outputs of radiographic projections—WET measured by reconstructed CT was within 0.3% of simulated Monte Carlo values. Furthermore, proton beam range and spread-out Bragg peak (SOBP) width were also measured with a maximum difference between the empirical and absolute range of 1.0 mm and 0.1 mm for SOBP, respectively—light output was stable with a standard deviation of 0.14% [104].

Gas 3D Scintillators

Gas scintillator detectors have been designed for high spatial resolution proton beam QA and commissioning. A dual gas electron multiplier (GEM) filled with He/CF₄, and readout via CCD, maintains a near tissue equivalence and has been shown to have a linear response to dose and energy, see Fig. 12.9 [105]. Despite that each detector is

Fig. 12.9 Schematic of a dual-GEM detector placed in the path of a proton beam. To note, additional GEM detectors can be added to this type of imaging setup to increase the 3D spatial resolution. 1. Entrance window 2. Housing 3. Exit window 4. Mirror 5. CCD camera



relatively thin and provides only 2D information, the coupling of multiple detectors is able to provide 3D beam measurements. This system features improvements such as (1) improved detection area footprint (2) higher resolution imaging sensor (3) better matched sensitivity spectrum of the detector and gas mixture, and (4) improved optical throughput [106]. Dual and triple GEM detectors containing CO₂/DME and He/isobutane function with detector stability in the range of $\pm 2\%$ and dose sensitivity within 1% [107]. Another GEM composed of Ar (45%), CO₂ (15%), and CF₄ (40%) was shown to be a promising detector for conducting 3D radiography and energy characterization studies [108]. For all of the above-mentioned detectors, rotation of the detector or beam may be necessary to acquire images from various angles in order to achieve 3D visualizations and measurements. Larger sized ($30 \times 30 \text{ cm}^2$) detectors are currently under development; upon realization and verification of these scintillator detector designs, fewer imaging frames will be required as each image will contain coverage of a larger area of active scintillator volume [109].

Solid 3D Scintillators

3D solid scintillator imaging for proton beam QA is an emerging field of research. Currently, published studies have focused on small volume ($278 \times 355 \times 0.4 \text{ mm}^3$, Blue 800, PJ Xray, NJ, USA) sheets for 2D profiling of pencil beam dose rates measurements [110]. For larger sized solid 3D scintillators, the presence of blurring is a major drawback; light emission in low-dose regions of the beam caused by light re-absorption. Corrections for this phenomenon have been attempted and show an improvement in dosimetric accuracy on the order 10–25% depending on radiation field size [67]. As an aside, solid scintillators ($30 \times 30 \times 30 \text{ cm}^3$, EJ-208, Eljen Technology, Sweetwater, TX) have also been used for quality assurance testing of

photon beams within the presence of a strong magnetic field (0.3 T MRIdian MRI-linac, ViewRay, Cleveland, OH) [67]. Thus, these types of QA techniques would be well suited for future implementation in MRI-guided proton therapy [111].

12.4.3 Brachytherapy

The use of dosimeters in brachytherapy have three main focuses: (1) sourced strength verification, (2) quality assurance (QA), and (3) in vivo dosimetry (IVD). In the first case, a well-chamber is better adapted for the task and leads to very precise source strength measurements [112]. The use of plastic scintillators for QA and IVD are the two applications found in the literature. While IVD implies first and foremost the notion of direct dose measurements during treatment delivery, recent works have demonstrated that scintillator-based signals can also be used for source tracking and in vivo dwell-time measurements, and if possible, all three simultaneously [113–115].

The major challenge for dose measurements in brachytherapy is the dominating effect of the inverse-square law on the energy deposited with distance [116]. At short distances, the dose gradient can be as large as 20%/mm such that a small uncertainty on the dosimeter position or the source-to-dosimeter distance can lead to large deviations in the measured dose relative to the expected one. At large distances from the source, the dosimeter sensitivity (in terms of signal-to-noise—SNR, and signal-to-background—SBR ratios) should be carefully considered since both $1/r^2$ and attenuation in the medium decrease the number of photons interacting with the sensitive volume—if the dosimeter is not sufficiently sensitive, not enough signal will be detected. Therefore, a special effort must be done to optimize the photon collecting efficiency throughout the complete optical chain.

This section tackles separately the application of plastic scintillation dosimetry to low energy brachytherapy source, where photoelectric effect becomes important, the mass energy absorption coefficient becomes different from water (loss of water equivalence) and quenching can also be a factor, from high energy dominated by Compton scattering. Finally, the issue of low SNR/SBR is tackled in the last section dealing with the application of inorganic scintillation dosimeters (ISDs).

12.4.3.1 Applications for LDR

During LDR brachytherapy, the radioactive sources are positioned inside or immediately adjacent to the tumor for a duration going from multiple days to a lifetime (i.e. permanent implant). Common isotopes used for LDR brachytherapy are I-125 ($t_{1/2} = 59.90$ days), Cs-131 ($t_{1/2} = 9.69$ days), and Pd-103 ($t_{1/2} = 16.99$ days). Prostate, gynecological, brain, and ocular cancers are among the anatomical sites treated. Because in these applications dose is deposited locally over a long period of time, one of the challenges for validation through dose measurement is the fact that the dose rates implied are much lower than for other radiotherapy applications. Another

challenge is related to the fact that lower energy photons are used and may therefore imply higher energy dependence from the detectors. A study from Therriault-Proulx et al. showed great promises for plastic scintillation detectors during low-dose-rate (LDR) brachytherapy [117]. Monte Carlo simulations around a I-125 seed allowed in validating that the uncertainty in the detector response was limited to 1% as long as the detector was calibrated using the same type of isotope. An optimized plastic scintillation detector using a cooled-PMT (to reduce thermal background noise, also known as dark counts, and thereby lower the detection limit), longer scintillator with a reflector at the tip, and a shorter transmission fiber with higher numerical aperture allowed for dose measurements up to 4.5 cm from a single radioactive seed. In a typical LDR brachytherapy permanent prostate implant, up to 100 seeds are inserted using multiple needles. In addition to validating the dose expected from the treatment planning system, one interesting application is to measure the deposited dose at multiple positions along the surrounding organs at risk (e.g., urethra, rectal wall) [118]. Figure 12.10 represents the dose measurements performed in phantom at sites mimicking the urethra and the rectal wall after each needle insertion of a typical prostate implant. Figure 12.11 shows the measured dose at different positions along those organs at risk, a measurement that could be performed at the end of the implant and be key in documenting the dose and potentially correlating late secondary effects. It is interesting to note that for LDR applications, integration time for dose measurement can be longer as it is less dynamic. Measurements presented at Figs. 12.10 and 12.11 were obtained over 60 s per point of measurement.

In addition to permanent implants, plastic scintillation detectors have raised some interest toward the dosimetry and validation of the eye plaques used for treating choroidal melanomas [119–122]. Because of the curved geometry of the eye plaques and the other challenges mentioned before, it is a hard task to perform accurate dosimetry and relying on the manufacturers data is not recommended. Common eye plaques used in the clinic involve either radioactive seeds of I-125, Pd-103

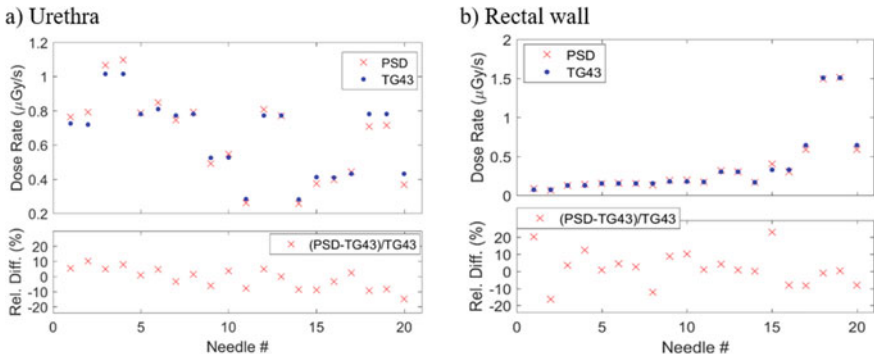


Fig. 12.10 Measurement of dose rate after each of the 20-needle implant of an in phantom typical LDR brachytherapy prostate implant and comparison to the expected values (American Association of Physicists in Medicine (AAPM) Task Group No. 43 (TG-43) [13]) with the plastic scintillation detector placed **a** in the urethra and **b** at the rectal wall

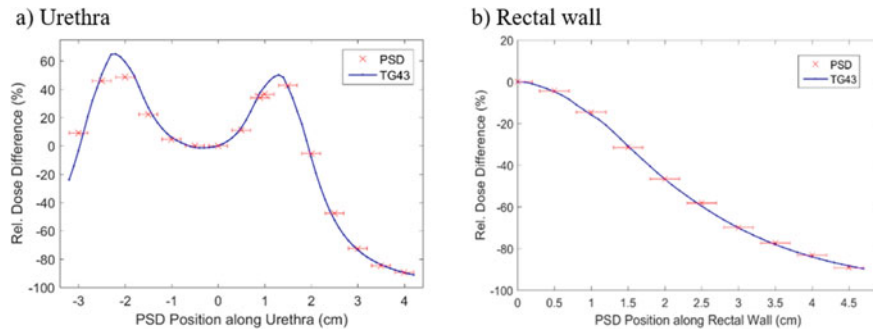


Fig. 12.11 Measurement of the relative dose profile at different positions along **a** the urethra and **b** the rectal wall after a full typical LDR brachytherapy prostate implant in phantom

or Sr-90, or adsorbed distribution of Ru-106. Radiochromic films are currently the state-of-the-art for eye plaque dosimetry in the clinic but require many manipulations (cutting, preparation, and handling) and a significant amount of time from medical physicists [123, 124]. Development of systems using plastic scintillation detectors shows great promises toward providing high-spatial resolution with direct readout, and therefore, decreasing the necessary calibration and validation time [119, 120]. The use of a very precise 3D motorized stage is recommended toward obtaining a precise dose distribution [119, 121]. The use of poly(ethylene naphthalate) scintillator was proposed by Flühs et al. as a replacement for PVT scintillators due to its smaller quenching at low photon energy [122].

12.4.3.2 Applications for High Dose Rate (HDR)

In this energy range, photon interaction with water, soft tissue, and PSDs is dominated by Compton scattering. Therefore, all the properties described previously in this Chapter (energy independence, dose rate independence, water equivalence, etc.) apply. Furthermore, even in the small cavity regime (electron range of a few mm for point-like PSDs) the electron mass-stopping power of the constituents of PSD, either PVT or polystyrene, are essentially constant and within 1–2% of that of water over a very wide range of photon energy [9]. Finally, PSD can be found or made small enough to be inserted inside regular HDR brachytherapy catheters, needles, and applicators (1 mm diameter or less). This enables clinically practical IVD designs [113]. While proposals to use PSD for brachytherapy applications appeared in the 1990s either for 2D dosimetry or in a form factor closer to what is used today for in catheter IVD, there is still no FDA approved commercial system for brachytherapy IVD yet [125, 126]. Furthermore, research systems published in the literature using PSD for brachytherapy in this energy range have been limited essentially to IVD for now [9].

Suchowerska et al. have published the first clinical study using PSD for IVD [127, 128]. As with most clinical studies using a variety of dosimeters, the authors found that dose measurement is severely limited by the accurate knowledge of the dosimeter position also called the source-to-dosimeter distance problem described previously [116]. To go around this problem, Johansen et al. have proposed to invert the problem and extract the estimated source-to-dosimeter distance, now using the advantage of the r^2 dependencies [114]. This allows the experimental extraction of dwell positions and compares to the expected one (from the clinical catheter paths for a given treatment from the treatment plan). Another approach is currently investigated by Tho et al. in which an electromagnetic tracker is integrated into a PSD assembly in order to track in real time the dosimeter position [129]. The expected accuracy was shown to be sufficient to perform IVD within 5% at 1 cm from the source (where the gradient is very large).

Building on a proposal by Therriault-Proulx et al. to place multiple scintillators (mPSD) along a single optical collection line providing multiple dose measurement points in a single assembly, Linares-Rosales et al. have built an optimized three points mPSD in vivo dosimetry system [32, 34]. Decoding of each PSD signal, as well as the simultaneous Cherenkov stem effect removal, is performed using a hyperspectral approach demonstrated by Archambault et al. and Therriault-Proulx et al. [18, 33]. With this system, over 100,000 samples/s are collected during the measurements, enabling a very high SNR as well as exploiting the signal structures as the source moved inside a catheter to independently extract the dwell-time for each dwell-position. Having three measurement points facilitate the triangulation of source position as the treatment delivery proceeds. As such, this system allows for the simultaneous extraction of the dose, source position, and dwell-time providing a redundant in vivo QA system [34].

One of the key remaining challenges for clinical implementation of IVD using PSD is the possible temperature dependence of the light yield observed recently [30, 91, 130]. It also turns out that the hyperspectral approach described above and used for signal unmixing in mPSD can be extended to include temperature effect, and thus may provide a practical method to eliminate this dependency in the near future [29].

12.4.3.3 Inorganic Scintillator Dosimeters

There exists a large body of commercial and research work focused on the development of inorganic scintillators for clinical use within radiation therapy. Unlike the organic plastic scintillators described in previous chapters, inorganic scintillators are commonly crystalline in structure. Within the context of brachytherapy, a key characteristic of inorganic scintillators that provides an advantage over their organic counterparts is higher light yield (up to 1800 \times). Figure 12.12a shows a light yield comparison between common organic (BCF-60, Saint-Gobain Crystals and Detectors, Courbevoie, France) and inorganic scintillators [131, 132]. For therapy regimes using ^{192}Ir , Eu-activated scintillator phosphors ($\text{Y}_2\text{O}_3:\text{Eu}$, $\text{YVO}_4:\text{Eu}$, $\text{Y}_2\text{O}_2\text{S}:\text{Eu}$, and $\text{Gd}_2\text{O}_2\text{S}:\text{Eu}$) were shown to produce 16–134 times more light than

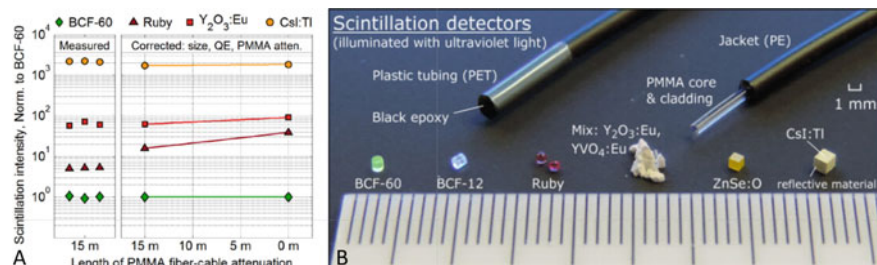


Fig. 12.12 **a** Scintillation intensity (normalized to BCF-60) versus length of PMMA fiber-cable attenuation (reproduced from [131] with permission from IOP). **b** side-by-side photographic comparison of various organic (BCF-XX) and inorganic scintillators (reproduced from [134] with permission from IOP)

an equivalent amount of BCF-12 (Saint-Gobain Crystals and Detectors, Courbevoie France) organic scintillator [133]. Increased light yield is exceptionally important if attempting to utilize scintillators to conduct dosimetry during brachytherapy; the light yield from organic scintillators during lower dose rate and energy treatments can make their use obsolete as an insufficient amount of light is produced. Furthermore, the property of increased luminescence minimizes the need for correcting for Cherenkov and extraneous fluorescence light contamination [134, 135].

The implementation of inorganic scintillators for brachytherapy substantially resembles that of scintillators described in Sect. 12.4.2.1, Optical Scintillating Fibers. Small volume scintillator crystals are coupled to fiber-optic cables and placed within the treatment field. Light generated within the crystal is directed into the fiber, after which the signal processing workflow is similar to PSDs used in photon and electron radiotherapy dosimetry. Popular inorganic scintillator materials used in brachytherapy dosimetry include, but are not limited to, ruby, Zn:Se:O, $\text{Y}_2\text{O}_3:\text{Eu}$ - $\text{YVO}_4:\text{Eu}$ mixture, and CsI:Tl. Figure 12.12b shows a photograph side-by-side comparison of plastic and inorganic scintillators; optical fiber coupling sites are also shown for scale. Previous work has shown that inorganic scintillators also possess the property of reduced optical fiber (PMMA) cable light attenuation when compared to organic scintillators [131].

The design of the scintillator-fiber junction must be carefully considered as light leakage can be a direct cause of reduced light detection by the receiver apparatus. The creation of fiber-optic cables (silica) doped with inorganic scintillator (Yb) can potentially eliminate the need for scintillator-fiber coupling; output is provided in real time without the need for temperature corrections [136].

Clinical data has shown that inorganic scintillators can provide measured dose values for tandem and ovoid brachytherapy within 3 and 1% difference when compared to TG-43 standards and Acuros-BV computations, respectively [137]. A low-cost inorganic scintillator setup composed of a photodetector, data acquisition components, and an interchangeable scintillator crystal ($\text{Al}_2\text{O}_3:\text{Cr}$, $\text{Y}_2\text{O}_3:\text{Eu}$, $\text{YVO}_4:\text{Eu}$, ZnSe:O or CsI:Tl depending on clinical needs of excitation rise/decay time, wavelength of maximum emission, etc.) was shown to provide dosimetrically

accurate (<3% difference compared to standard organic scintillators) without the need for dose-rate corrections [132, 138].

12.5 Conclusion

Because of their almost ideal dosimetric properties, plastic scintillators continue to grow as a popular choice for clinical dosimetry tasks and applications. As more users become familiar with their functionality, it is anticipated that further integration into the modern radiation oncology clinic will occur. Scintillator readout via remote camera imaging or wired optical detectors allows for efficient, real time, dose measurements. Thus, the amount of resources required for conducting dosimetry can be reduced. Point and multi-point detectors are commonly used during mainstream in vivo dosimetry and quality assurance (QA) testing. Flexibility in scintillator form factors allows for further non-traditional QA and dosimetry application for novel treatment modalities such as proton or MR-linac therapies. Future directions in scintillator development will likely be directed toward 2D planar or 3D volumetric detectors—it can be reasonably predicted that there will be additional research effort dedicated to these technologies in the coming decade(s).

References

1. A.S. Beddar, Dissertation, (University of Wisconsin, 1990)
2. T. Murai, T. Nakamura, A. Yamamoto, J. Radiat. Res. **5**(1), 23 (1964)
3. A.S. Beddar, T.R. Mackie, F.H. Attix, Phys. Med. Biol. **37**(10), 1883 (1992)
4. A.S. Beddar, T.R. Mackie, F.H. Attix, Phys. Med. Biol. **37**(10), 1901 (1992)
5. S. Beddar, L. Beaulieu, *Scintillation Dosimetry* (CRC Press, Boca Raton, 2016).
6. A.R. Beierholm, C.F. Behrens, C.E. Andersen, Radiat. Meas. **69**, 50 (2014)
7. P. Carrasco, N. Jornet, O. Jordi, M. Lizondo, A. Latorre-Musoll, T. Eudaldo, A. Ruiz, M. Ribas, Med. Phys. **42**(1), 297 (2015)
8. P.E. Galavis, L. Hu, S. Holmes, I.J. Das, Med. Phys. **46**(5), 2468 (2019)
9. L. Beaulieu S. Beddar, Phys. Med. Biol. **61**(20), R305 (2016)
10. L. Ding, Q. Wu, Q. Wang, Y. Li, R.M. Perks, L. Zhao, EJNMMI Phys. **7**(1), 60 (2020)
11. J.V. Jelley, in *Cherenkov Radiation: Its Properties, Occurrence, and Uses*, ed. by K.C. Smith. Photochemical and Photobiological Reviews, vol. 7 (Springer, Boston, 1983), pp. 275–318
12. A.S. Beddar, T.R. Mackie, F.H. Attix, Phys. Med. Biol. **37**(4), 925 (1992)
13. L. Archambault, A.S. Beddar, L. Gingras, R. Roy, L. Beaulieu, Med. Phys. **33**(1), 128 (2005)
14. P. Andreo, D.T. Burns, A.E. Nahum, J. Seuntjens, F.H. Attix, *Fundamentals of ionizing radiation dosimetry* (Wiley-VCH, 2017)
15. L. Archambault, A.S. Beddar, L. Gingras, F. Lacroix, R. Roy, L. Beaulieu, Med. Phys. **34**(5), 1583 (2007)
16. L. Torrisi, Nucl. Instr. Methods B **170**(3–4), 523 (2000)
17. L. Archambault, J.C. Polf, L. Beaulieu, S. Beddar, Phys. Med. Biol. **53**(7), 1865 (2008)
18. F. Lessard, L. Archambault, M. Plamondon, P. Després, F. Therriault-Proulx, S. Beddar, L. Beaulieu, Med. Phys. **39**(9), 5308 (2012)
19. S. Safai, S. Lin, E. Pedroni, Phys. Med. Biol. **49**(19), 4637 (2004)

20. D. Robertson, D. Mirkovic, N. Sahoo, S. Beddar, Phys. Med. Biol. **58**(2), 261 (2013)
21. M.-C. Vozenin, P. De Fornel, K. Petersson, V. Favaudon, M. Jaccard, J.-F. Germond, B. Petit, M. Burki, G. Ferrand, D. Patin, H. Bouchaab, M. Ozsahin, F. Bochud, C. Bailat, P. Devauchelle, J. Bourhis, Clin. Cancer Res. **25**(1), 35 (2019)
22. J.J.W. Lagendijk, B.W. Raaymakers, A.J.E. Raaijmakers, J. Overweg, K.J. Brown, E.M. Kerkhof, R.W. van der Put, B. Hårdemark, M. van Vulpen, U.A. van der Heide, Radiother. Oncol. **86**(1), 25 (2008)
23. D. Blömkér, U. Holm, R. Klanner, B. Krebs, IEEE Trans. Nucl. Sci. **37**(2), 220 (1990)
24. S. Bertolucci, M. Cordelli, M. Curatolo, B. Esposito, P. Giromini, S. Miscetti, A. Sansoni, Nucl. Instr. Methods A **254**(3), 561 (1987)
25. S. Stefanowicz, H. Latzel, L.R. Lindvold, C.E. Andersen, O. Jäkel, S. Greilich, Radiat. Meas. **56**, 357 (2013)
26. F. Therriault-Proulx, Z. Wen, G. Ibbott, S. Beddar, Radiat. Meas. **116**, 10 (2018)
27. E.A. Simiele, L.A. DeWerd, Med. Phys. **45**(7), 3417 (2018)
28. E. Simiele, R.-P. Kapsch, U. Ankerhold, W. Culberson, L. DeWerd, Phys. Med. Biol. **63**(8), 085001 (2018)
29. F. Therriault-Proulx, L. Wootton, S. Beddar, Phys. Med. Biol. **60**(20), 7927 (2015)
30. S. Buranurak, C.E. Andersen, A.R. Beierholm, L.R. Lindvold, Radiat. Meas. **56**, 307 (2013)
31. J.M. Fontbonne, G. Iltis, G. Ban, A. Battala, J.C. Vernhes, J. Tillier, N. Bellaize, C. Le Brun, B. Tamain, K. Mercier, J.C. Motin, IEEE Trans. Nucl. Sci. **49**(5), 2223 (2002)
32. F. Therriault-Proulx, L. Beaulieu, L. Archambault, S. Beddar, Phys. Med. Biol. **58**(7), 2073 (2013)
33. F. Therriault-Proulx, L. Archambault, L. Beaulieu, S. Beddar, Phys. Med. Biol. **57**(21), 7147 (2012)
34. H.M. Linares Rosales, L. Archambault, S. Beddar, L. Beaulieu, Med. Phys. **47**(9), 4477 (2020)
35. International Atomic Energy Agency, *IAEA TRS 483 Dosimetry of Small Static Fields Used in External Beam Radiotherapy* (2017)
36. H. Palmans, P. Andreo, M. Saiful Huq, J. Seuntjens, K.E. Christaki, A. Meghzifene, Med. Phys. **45**(11), e1123 (2018)
37. I.J. Das, G.X. Ding, A. Ahnesjö, Med. Phys. **35**(1), 206 (2008)
38. A.R. Beierholm, C.F. Behrens, L. Hoffmann, C.E. Andersen, Radiat. Meas. **56**, 290 (2013)
39. J. Morin, D. Béliveau-Nadeau, E. Chung, J. Seuntjens, D. Thériault, L. Archambault, S. Beddar, L. Beaulieu, Med. Phys. **40**(1), 011719 (2013)
40. R. Alfonso, P. Andreo, R. Capote, M. Saiful Huq, W. Kilby, P. Kjäll, T.R. Mackie, H. Palmans, K. Rosser, J. Seutjens, W. Ullrich, S. Vatnistyky, Med. Phys. **35**(11), 5179 (2008)
41. P. Francescon, S. Beddar, N. Satariano, I.J. Das, Med. Phys. **41**(10), 101708 (2014)
42. P. Francescon, W. Kilby, N. Satariano, Phys. Med. Biol. **59**(6), N11 (2014)
43. Y. Kamio, H. Bouchard, Phys. Med. Biol. **59**(1), 4973–5002 (2014)
44. T.S.A. Underwood, B.C. Rowland, R. Ferrand, L. Vieillevigne, Phys. Med. Biol. **60**(17), 6669 (2015)
45. J. Xue, J.D. McKay, J. Grimm, C.-W. Cheng, R. Berg, S.-Y.L. Grimm, Q. Xu, G. Subedi, I.J. Das, Med. Phys. **44**(7), 3815 (2017)
46. M. Pasquino, C. Cutaia, L. Radici, S. Valzano, E. Gino, C. Cavedon, M. Stasi, Br. J. Radiol. **90**(1069), 20160596 (2017)
47. P. Mancosu, M. Pasquino, G. Reggiori, L. Masi, S. Russo, M. Stasi, Phys. Medica **41**, 33 (2017)
48. B. Casar, E. Gershkevitsh, I. Mendez, S. Jurković, M. Saiful Huq, Med. Phys. **46**(2), 944 (2019)
49. G.V. Santurio, Dissertation, (Technical University of Denmark, 2019)
50. F. Therriault-Proulx, R. Pino, J.N. Yang, A.S. Beddar, Phys. Med. Biol. **64**(22), 225007 (2019)
51. S. Lee, T.H. Kim, J.Y. Jeong, J. Son, D.G. Kim, G.-S. Cho, S.H. Choi, H.-T. Chung, Y.K. Kim, Nucl. Eng. Technol. **52**(10), 2334 (2020)
52. T. Piotrowski, P. Milecki, M. Skórska, D. Fundowicz, Adv. Dermatol. Allergol. Dermatol. Alergol. **30**, 50 (2013)

53. K.R. Desai, R.D. Pezner, J.A. Lipsett, N.L. Vora, K.H. Luk, J.Y.C. Wong, S.L. Chan, D.O. Findley, L.R. Hill, L.A. Marin, J.O. Archambeau, Int. J. Radiat. Oncol., Biol., Phys. **15**(3), 641 (1988)
54. Y. Anacak, Z. Arican, R. Bar-Deroma, A. Tamir, A. Kuten, Med. Dosim. **28**(1), 31 (2003)
55. E. El-Khatib, S. Hussein, M. Nikolic, N.J.S. Voss, C. Parsons, Int. J. Radiat. Oncol., Biol., Phys. **33**(2), 469 (1995)
56. M.D.C. Evans, C. Hudon, E.B. Podgorsak, C.R. Freeman, Rep. Pract. Oncol. Radiother. **19**(2), 120 (2013)
57. E.P. Reynard, M.D.C. Evans, S. Devic, W. Parker, C.R. Freeman, D. Roberge, E.B. Podgorsak, J. Appl. Clin. Med. Phys. **9**(4), 123 (2008)
58. C.J. Karzmark, Int. J. Radiat. Oncol., Biol., Phys. **12**(S1), 84 (1986)
59. G.W. Jones, B.M. Kacinski, L.D. Wilson, R. Willemze, M. Spittle, G. Hohenberg, L. Handl-Zeller, F. Trautinger, R. Knobler, J. Am. Acad. Dermatol. **47**(3), 364 (2002)
60. I.I. Tendler, P. Bruza, M. Jermyn, A. Fleury, B.B. Williams, L.A. Jarvis, B.W. Pogue, D.J. Gladstone, J. Biomed. Opt. **24**(7), 075001 (2019)
61. I. Tendler, P. Brůža, J. Andreozzi, M. Jermyn, B. Williams, L. Jarvis, B. Pogue, D. Gladstone, Int. J. Radiat. Oncol., Biol., Phys. **103**(3), 767 (2018)
62. I.I. Tendler, A. Hartford, M. Jermyn, E. LaRochelle, X. Cao, V. Borza, D. Alexander, P. Bruza, J. Hoopes, K. Moodie, B.P. Marr, B.B. Williams, B.W. Pogue, D.J. Gladstone, L.A. Jarvis, Int. J. Radiat. Oncol., Biol., Phys. **106**(2), 422 (2020)
63. P. Bruza, S.L. Gollub, J.M. Andreozzi, I.I. Tendler, B.B. Williams, L.A. Jarvis, D.J. Gladstone, B.W. Pogue, Phys. Med. Biol. **63**(9), 095009 (2018)
64. I.I. Tendler, P. Bruza, M. Jermyn, X. Cao, B.B. Williams, L.A. Jarvis, B.W. Pogue, D.J. Gladstone, Phys. Med. Biol. **64**(12), 125025 (2019)
65. L.A. Jarvis, R.A. Hachadorian, M. Jermyn, P. Bruza, D.A. Alexander, I.I. Tendler, B.B. Williams, D.J. Gladstone, P.E. Schaner, B.I. Zaki, B.W. Pogue, Int. J. Radiat. Oncol., Biol., Phys. (2020). <https://doi.org/10.1016/j.ijrobp.2020.11.013>
66. I.I. Tendler, P. Bruza, M. Jermyn, J. Soter, G. Sharp, B. Williams, L.A. Jarvis, B. Pogue, D.J. Gladstone, J. Appl. Clin. Med. Phys. **21**(6), 158 (2020)
67. I.I. Tendler, Ph.D. thesis, (Dartmouth College, 2020)
68. Y. Xie, H. Petroccia, A. Maity, T. Miao, Y. Zhu, P. Bruza, B.W. Pogue, J.P. Plastaras, L. Dong, T.C. Zhu, Med. Phys. **47**(1), 201 (2020)
69. H. Petroccia, T. Miao, A. Maity, Y. Ong, Y. Zhu, P. Bruza, B.W. Pogue, J. Plastaras, T.C. Zhu, in *Optical Methods for Tumor Treatment and Detection: Mechanisms and Techniques in Photodynamic Therapy XXVIII*, SPIE BiOS 2019, San Francisco, California
70. E.E. Klein, J. Hanley, J. Bayouth, F.-F. Yin, W. Simon, S. Dresser, C. Serago, F. Aguirre, L. Ma, B. Arjomandy, C. Liu, C. Sandin, T. Holmes, Med. Phys. **36**(9), 4197 (2009)
71. D.A. Alexander, I. Tendler, P. Bruza, D.J. Gladstone, P. Schaner, L.A. Jarvis, B.W. Pogue. “Radioluminescence im-aging of dose surrogates for head and neck radiotherapy.” Oral Presentation (YIS). AAPM Spring Clinical Meeting, Kissimmee FL, March 2019. J. Appl. Clin. Med. Phys. **20**(5), 144 (2019)
72. D.A. Alexander, I.I. Tendler, P. Bruza, X. Cao, P.E. Schaner, B.S. Marshall, L.A. Jarvis, D.J. Gladstone, B.W. Pogue, Phys. Med. Biol. **64**(14), 145021 (2019)
73. I. Tendler, P. Bruza, R.L. Hachadorian, D. Alexander, M. Jermy, B.B. Williams, L.A. Jarvis, B.W. Pogue, D.J. Gladstone, Int. J. Radiat. Oncol., Biol., Phys. **105**(1), E697 (2019)
74. C. Wills, S. Cherian, J. Yousef, K. Wang, H.B. Mackley, Appl. Rad. Oncol. **5**(2), 11 (2016)
75. J. Burmeister, A. Nalichowski, M. Snyder, R. Halford, G. Baran, B. Loughery, A. Hammoud, J. Rakowski, T. Bossenberger, J. Appl. Clin. Med. Phys. **19**(3), 131 (2018)
76. I.I. Tendler, J.S. Bredfeldt, R. Zhang, P. Bruza, M. Jermyn, B.W. Pogue, D.J. Gladstone, Med. Phys. **46**(8), 3674 (2019)
77. C.M. Lancaster, J.C. Crosbie, S.R. Davis, Australas. Phys. Eng. Sci. Med. **31**, 191 (2008)
78. E.J. Bloemen-van Gurp, B.J. Mijnheer, T.A.M. Verschueren, P. Lambin, Int. J. Radiat. Oncol., Biol., Phys. **69**(4), 1297 (2007)

79. L.L.W. Wang, L.A. Perles, L. Archambault, N. Sahoo, D. Mirkovic, S. Beddar, Phys. Med. Biol. **57**(23), 7767 (2012)
80. C. Penner, C. Hoehr, S. O'Keeffe, P. Woulfe, C. Duzenli, IEEE Sens. J. **18**(4), 1513 (2018)
81. U.-J. Hwang, D. Shin, S.B. Lee, Y.K. Lim, J.H. Jeong, H.S. Kim, K.H. Kim, J. Korean Phys. Soc. **72**, 1025 (2018)
82. A. Darafsheh, R. Taleei, A. Kassaee, J.C. Finlay, *On the Origin of the Visible Light Responsible for Proton Dose Measurement Using Plastic Optical Fibers*, SPIE BiOS 2017, San Francisco, California
83. F. Lacroix, L. Beaulieu, L. Archambault, A.S. Beddar, Med. Phys. **37**(2), 412 (2010)
84. K.W. Jang, W.J. Yoo, J. Moon, K.T. Han, B.G. Park, D. Shin, S.-Y. Park, B. Lee, Nucl. Instr. Methods A **695**, 322 (2012)
85. A. Darafsheh, R. Taleei, A. Kassaee, J.C. Finlay, Med. Phys. **43**(11), 5973 (2016)
86. K.W. Jang, W.J. Yoo, J.K. Seo, J.Y. Heo, J. Moon, J.-Y. Park, E.J. Hwang, D. Shin, S.-Y. Park, H.-S. Cho, B. Lee, Nucl. Instr. Methods A **652**(1), 841 (2011)
87. J. Son, M. Kim, D. Shin, U. Hwang, S. Lee, Y. Lim, J. Park, S.y. Park, K. Cho, D. Kim, K.W. Jang, M. Yoon, Radiother. Oncol. **117**(3), 501 (2015)
88. J. Son, M. Kim, D. Shin, U. Hwang, S. Lee, Y. Lim, J. Park, S.u. Park, K. Cho, D. Kim, K.W. Jang, M. Yoon, Radiother. Oncol. **117**(3), 501 (2015)
89. F. Alsanea, F. Therriault-Proulx, G. Sawakuchi, S. Beddar, S. Med, Phys. **45**(4), 1782 (2018)
90. F. Alsanea, L. Woottton, N. Sahoo, R. Kudchadker, U. Mahmood, S. Beddar, Phys. Medica Eur. J. Med. Phys. **47**, 58 (2018)
91. L. Woottton, S. Beddar, Phys. Med. Biol. **58**(9), 2955 (2013)
92. J.W. Blue, D.C. Liu, I.R.E. Trans, Nucl. Sci. **9**(3), 48 (1962)
93. R. Gwin, R.B. Murray, Phys. Rev. **131**, 501 (1963)
94. J.B. Birks, Proc. Phys. Soc., London, Sect. A **64**, 874 (1951)
95. J.B. Birks, *The Theory and Practice of Scintillation Counting* (Pergamon Press, Oxford, 1964).
96. M.D. Galanin, Opt. Spektrosk. **4**, 758 (1958)
97. C. Kim, B. Hong, G. Jhang, E. Joo, K.S. Lee, K.S. Lee, S. Lee, S.K. Lee, S.K. Park, H.H. Shim, S.S. Shin, K.S. Sim, H.K. Cha, J. Korean Phys. Soc. **60**, 725 (2012)
98. F. Alsanea, S. Beddar, J. Phys.: Conf. Ser. **847**, 012022 (2017)
99. C.D. Darne, F. Alsanea, D.G. Robertson, N. Sahoo, S. Beddar, Phys. Med. Biol. **62**(14), 5652 (2017)
100. J.M. Andreozzi, R. Zhang, A.K. Glaser, L.A. Jarvis, B.W. Pogue, D.J. Gladstone, Med. Phys. **42**(2), 994 (2015)
101. F. Alsanea, C. Darne, Y. Hojo, S. Beddar, Nucl. Instr. Methods A **939**, 16 (2019)
102. F. Alsanea, C. Darne, D. Robertson, S. Beddar, Phys. Med. Biol. **65**(7), 075005 (2020)
103. C.D. Darne, F. Alsanea, D.G. Robertson, F. Guan, T. Pan, D. Grosshans, S. Beddar, Biomed. Phys. Eng. Express **5**(4), 045032 (2019)
104. T. Henry, D. Robertson, F. Therriault-Proulx, S. Beddar, Int. J. Part. Ther. **4**(1), 1 (2017)
105. D. Nichiporov, L. Coutinho, A.V. Klyachko, Phys. Med. Biol. **61**(8), 2972 (2016)
106. A.V. Klyachko, V. Moskvin, D.F. Nichiporov, K.A. Solberg, Nucl. Instr. Methods A **694**, 271 (2012)
107. P. Radaelli, Dissertation, (Vrije Universiteit Amsterdam, 2015)
108. N. Van der Weiden, Dissertation, (VU University Amsterdam, 2015)
109. J. Yu, E. Baldeolmar, K. Park, S. Park, M. Sosebee, N. Tran, A.P. White, Phys. Procedia **37**, 591 (2012)
110. M. Rahman, P. Brůža, K.M. Langen, D.J. Gladstone, X. Cao, B.W. Pogue, R. Zhang, Phys. Med. Biol. **65**(16), 165014 (2020)
111. A. Hoffmann, B. Oborn, M. Moteabbed, S. Yan, T. Bortfeld, A. Knopf, H. Fuchs, D. Georg, J. Seco, M.F. Spadea, O. Jäkel, C. Kurz, K. Parodi, Radiat. Oncol. **15**, 129 (2020)
112. L.A. DeWerd, G.S. Ibbott, A.S. Meigooni, M.G. Mitch, M.J. Rivard, K.E. Stump, B.R. Thomadsen, J.L.M. Venselaar, Med. Phys. **38**(2), 782 (2011)
113. K. Tanderup, S. Beddar, C.E. Andersen, G. Kertzscher, J.E. Cygler, Med. Phys. **40**(7), 070902 (2013)

114. J.G. Johansen, S. Rylander, S. Buus, L. Bentzen, S.B. Hokland, C.S. Søndergaard, A.K.M. With, G. Kertzscher, K. Tanderup, Brachytherapy **17**(1), 122 (2018)
115. P. Guiral, J. Ribouton, P. Jalade, R. Wang, J.-M. Galvan, G.-N. Lu, P. Pittet, A. Rivoire, L. Gindraux, Med. Phys. **43**(9), 5240 (2016)
116. G.P. Fonseca, J.G. Johansen, R.L. Smith, L. Beaulieu, S. Beddar, G. Kertzscher, F. Verhaegen, K. Tanderup, Phys. Imaging Radiat. Oncol. **16**, 1 (2020)
117. F. Therriault-Proulx, L. Beaulieu, S. Beddar, Brachytherapy **16**(4), 903 (2017)
118. F. Therriault-Proulx, L. Beaulieu, T. Bruno, S. Beddar, Med. Phys. **43**(6), 3463 (2016)
119. D. Flühs, M. Heintz, F. Indenkämper, C. Wieczorek, H. Kolanoski, U. Quast, Med. Phys. **23**(3), 427 (1996)
120. T. Mauceri, J. Turcotte, A. Sliski, Med. Phys. **38**(6), 3576 (2011)
121. M. Eichmann, D. Flühs, B. Spaan, Med. Phys. **36**(10), 4634 (2009)
122. D. Flühs, A. Flühs, M. Ebennau, M. Eichmann, Ocul. Oncol. Pathol. **2**(1), 5 (2016)
123. S. Trichter, C.G. Soares, M. Zaider, J.K. DeWyngaert, L.A. DeWerd, N.J. Kleiman, Biomed. Phys. Eng. Express **4**(4), 045017 (2018)
124. S.-T. Chiou-Tsao, M.A. Astrahan, P.T. Finger, D.S. Followill, A.S. Meigooni, C.S. Melhus, F. Mourtada, M.E. Napolitano, R. Nath, M.J. Rivard, D.W.O. Rogers, R.M. Thomson, Med. Phys. **39**(10), 6161 (2012)
125. H. Perera, J.F. Williamson, S.P. Monthofer, W.R. Binns, J. Klarmann, G.L. Fuller, J.W. Wong, Int. J. Radiat. Oncol. Biol. Phys. **23**(5), 1059 (1992)
126. M.R. Arnfield, H.E. Gaballa, R.D. Zwicker, Q. Islam, R. Schmidt-Ullrich, IEEE Trans. Nucl. Sci. **43**(3), 2077 (1996)
127. J. Lambert, D.R. McKenzie, S. Law, J. Elsey, N. Suchowerska, Phys. Med. Biol. **51**(21), 5505 (2006)
128. N. Suchowerska, M. Jackson, J. Lambert, Y.B. Yin, G. Hruby, D.R. McKenzie, Int. J. Radiat. Oncol. Biol. Phys. **79**(2), 609 (2011)
129. D. Tho, L. Beaulieu, Med. Phys. **46**(5), 2031 (2019)
130. S. Beddar, Med. Phys. **39**(10), 6522 (2012)
131. G. Kertzscher, S. Beddar, J. Phys.: Conf. Ser. **847**, 012036 (2017)
132. G. Kertzscher, S. Beddar, Phys. Medica Eur. J. Med. Phys. **52**(S1), 73 (2018)
133. G. Kertzscher, S. Beddar, Phys. Med. Biol. **62**(12), 5046 (2017)
134. G. Kertzscher, S. Beddar, Phys. Med. Biol. **64**(22), 225018 (2019)
135. G. Kertzscher, S. Beddar, Med. Phys. **43**(6), 3810 (2016)
136. I. Veronese, N. Chiodini, S. Cialdi, E. d'Ippolito, M. Fasoli, S. Gallo, S. La Torre, E. Mones, A. Vedula, G. Loi, Phys. Med. Biol. **62**(10), 4218 (2017)
137. M.D. Belley, A. Faught, B. Moore, E. Subashi, B. Langloss, M.J. Therien, T.T. Yoshizumi, J.P. Chino, O. Craciunescu, Med. Phys. **43**(6), 3809 (2016)
138. M. Alharbi, M. Martyn, S. O'Keeffe, F. Therriault-Proulx, L. Beaulieu, M. Foley, Phys. Medica **68**, 124 (2019)



Sam Beddar is a tenured full professor at the University of Texas MD Anderson Cancer Center, Houston, Texas in the Division of Radiation Oncology, adjunct professor in the Département de physique, de génie physique et d'optique, Université Laval, Quebec, Canada and adjunct professor in the Department of Medical Physics at The University of Wisconsin School of Medicine, Madison, Wisconsin, USA. He is the Director of Clinical Research in the Department of Radiation Physics within the Division of Radiation Oncology at the The University of Texas MD Anderson Cancer Center. He is also the clinical chief of the Gastrointestinal (GI) Service, focusing his clinical attention on developing, SPECT, 4D-CT with and without intravenous contrast for the liver, respiratory-gated modalities and SBRT techniques for GI cancers. He has been the Director of the intraoperative radiation therapy program at MDACC since 2005. Dr. Beddar has served on many National Institutes of Health study section review panels and has been a PI of numerous NIH/NCI grant awards as well as industrial grants. His laboratory research is actively engaged in the rapidly-growing field of scintillation dosimetry and the use of scintillating materials to measure radiation dose. His work ranges from basic research on scintillator properties to detector development, clinical applications, and commercialization. Dr. Beddar's lab is currently using scintillation detectors to perform *in vivo* dosimetry external beam radiation therapy, brachytherapy and proton therapy. His research activities contributed to the EXRADIN W1 and W2 commercial system from Standard Imaging, Inc and the Hyper-Scint commercial system from Medscint, Inc. Recently his lab's is focusing on the 3D dose imaging of proton beams and prompt gamma imaging and proton CT. He has authored 175 peer-reviewed publications and has an h-index of 42 and 9 patents.



Irwin Tendler completed his graduate work in scintillator optical imaging at the Thayer School of Engineering, Dartmouth College. He is currently a medical physics resident at University of Texas MD Anderson Cancer Center. His career interests lie in the field of therapeutic radiation physics and he also aims to conduct research in the field of scintillator-based medical device development. He has authored 24 peer reviewed publications and has an h-index of 7 and 1 patent.



François Therriault-Proulx Since his graduate and post-graduate studies, Dr. Therriault-Proulx has been applying his engineering and medical physics background to the development of scintillation dosimetry devices for several years. His work as a Ph.D. and Odyssey Fellow led to the development of a patented multi-point plastic scintillation dosimetry device using only a single optical probe that has been proven to be valid for multiple fields of application in radiation oncology. His current focus is on optimizing this patented technology for commercially viable applications in the field of radiation oncology and medical physics. He co-founded the company Medscint Inc. (Quebec City, Canada) in 2018 and is the current president and CEO of the company. He has authored 19 peer-reviewed publications and has an h-index of 10 and 1 patent.



Louis Archambault is an associate professor of physics at université Laval and a medical physicist. His main research interests are scintillation detector development for external beam radiotherapy applications, automated treatment planning, radiomics and prediction models. He has authored over 60 peer-reviewed publications and has an h-index of 32 and an i-10 index of 46 and 6 patents.



Luc Beaulieu is a full professor, Director of the CAMPEP graduate program and also Director of the Cancer Research Centre at Université Laval. He served on the Board of the Canadian Organization of Medical Physicists as President Elect, President and Past President (2010–2016). He is a member of the AAPM Brachytherapy Subcommittee as well as three associated Working Groups (Model-based dose calculation, Robotics and Clinical Applications), is the Chair of TG317 on tracking technology for brachytherapy, a member of the ESTRO In Vivo Dosimetry Working Group, was the Chair of TG-186 and until recently led the AAPM/ESTRO/ABG Working Group on Model-Based Dose Calculations in Brachytherapy. He has mentored over 150 trainees from undergraduate to postdoctoral researchers. His research activities constitute the backbone of the W1, W2 and HyperScint commercial scintillation dosimetry systems. He is a recognized expert on topics related to scintillation dosimetry and brachytherapy. He has authored 234 peer-reviewed publications and has an h-index of 52 and 3 patents.

Chapter 13

Plastic Scintillators in Environmental Analysis



Alex Tarancón , Héctor Bagán , and José Francisco García

Abstract Environmental analysis is characterized for being a type of determination in which the amount of radioactivity in the sample is very low, usually more than one radionuclide is present and fast response is frequently constrained by the need for an accurate and precise determination. In the environmental field, plastic scintillators have been mainly used for the analysis of alpha and beta emitting radionuclides. This is because the determination of radionuclides is conditioned by the short path of such particles which makes that detector to be placed at a micrometric distance from the emitting radionuclide. This can be done with plastic scintillators prepared in form of microparticles, fibers or foils which are the shapes most suited for the detection of this type of particles. Moreover, as solids, plastic scintillators permit the flow of liquids among them without consuming them and the surface can be modified to retain selectively a certain radionuclide (PSresin). In the present chapter, the characteristics of the measurements of alpha and beta emitting radionuclides with plastic scintillators in the environmental field are described. Moreover, the preparation of plastic scintillators and resins in form of microspheres and foils is detailed. Finally, various applications of plastic scintillators (i.e., solid sample analysis, sensor and continuous monitoring, alpha/beta screening analysis, and selective analysis of specific alpha and beta emitting radionuclides) are reviewed.

A. Tarancón · H. Bagán · J. F. García

Department of Chemical Engineering and Analytical Chemistry, University of Barcelona,
Barcelona, Spain

e-mail: alex.tarancon@ub.edu

H. Bagán

e-mail: hector.bagan@ub.edu

J. F. García

e-mail: jfgarcia@ub.edu

A. Tarancón

Serra Hunter Fellow, Barcelona, Spain

13.1 Environmental Analysis: Requirements and Characteristics. Contribution of Plastic Scintillators

Radionuclides in the environment originate from both natural and technological processes. As a general rule, natural radionuclides are homogeneously distributed across the different environmental compartments and are compatible with the development of life, with their radioactivity constituting normal background exposure. Their associated activity depends on the specific radionuclide and material involved, but in general it is low. As an example, the mean level of ^{238}U activity in river water in several countries is around 0.01 Bq/L, with the maximum level accepted in drinking water for ^{238}U being 3.0 Bq/L in Europe [1] and 0.75 Bq/L in the USA [2]. Detection of such low activity levels requires a low limit of detection, and therefore, long measurement times. However, in some situations, an accumulation of such radionuclides occurs due to natural reasons (mineral ores) or is enhanced by human activities. NORM (i.e., naturally occurring radionuclides that have become concentrated due to human activity such as the coal industry, oil and gas production, other mining activities, uranium production, or manufacture of phosphates and fertilizers) and artificially produced radionuclides in nuclear plants or particle accelerators, and also present in hospitals and reprocessing plants, may all occur at high concentrations. These may exceed natural levels (reaching from few Bq/kg to thousands of Bq/g in certain samples) and, for artificial radionuclides, can indicate an operational failure or illegal action. As a consequence, they may present a risk for living organisms. In these scenarios, the limit of detection needed is not so low, and therefore, the required measurement time is significantly reduced. Here, fast response to the presence of radionuclides is the key point.

The hazard associated with these materials depends not only on their level of activity, but also on the type of radionuclide and quality factor of the emitted radiation: alpha, beta or gamma. The dose an organism is exposed to by the different types of radiation emitted by these materials can produce biological damage, with the harm it may cause to human beings being particularly worrying. Therefore, from a standpoint of preventive environmental policy, it is good practice to monitor the activity level of any material via all potential pathways that may end up affecting humans.

When considering environmental monitoring, two consequences of the characteristics of gamma radiation need to be borne in mind. First, its low quality factor, resulting from its limited interaction with materials of low atomic number and relatively small effects on organisms. Second, its relatively easy remote detection due to the long distances it travels before it is fully attenuated. This allows for measurement from practically any type of environmental sample without preliminary treatment and with the detector located at a certain distance. Consequently, this type of radiation can be easily monitored in situ and in real time, thus reducing its radioactive threat.

In contrast, alpha and beta emitters are potentially much more harmful, and thus they have become the main issue in environmental radioactivity monitoring. These emitters can cause significant damage to organisms, especially when ingested, even at low activities, due to their short path length; a characteristic that also makes their detection more difficult, since sample and detector must be very close together [3]. Reversely, the same effect is currently used in radiation therapy to destroy cancer cells and tumors (see Chap. 12 for more details).

As already mentioned, the origin of radionuclides determines the activity levels found in the environment. They may come from natural sources, as constituents of rocks, sediments or water reservoirs; from NORM industries; from research centers and hospitals; and from nuclear industries, especially nuclear power plants and reprocessing plants as well as from decommissioning activities. The main dissemination media of radionuclides from the sources to the rest of the environment are water (rain, surface water, rivers, underground water, and the sea) and the atmosphere (wind). Once disseminated, some of the radionuclides are deposited in plants, soil, and sediments. The final distribution of these radionuclides, including their incorporation into the different links of the trophic chain, will depend on the composition and chemical behavior of each material and chemical element.

As a consequence, radioactivity in the environment is caused by different radionuclides, in the form of different chemical species, which are found in several types of samples and at different activity levels. From the set of radionuclides, the main determinations made for environmental monitoring correspond to two screening parameters: total alpha and total beta activity (excluding the contribution from radon, ^{40}K and ^3H), as well as the individual determination of ^3H and ^{222}Rn and other specific radionuclides (^{238}U , ^{232}Th , ^{90}Sr , ^{226}Ra , ^{228}Ra , ^{99}Tc , ^{210}Pb , ^{210}Po , etc.). If screening parameters show values above a certain limit, it is necessary to determine the individual activity of the different alpha or beta emitting radionuclides that can contribute to the total activity value.

In the case of total alpha and total beta screening parameters, both are determined for the same sample. The measurement can be performed by means of proportional gas detectors or liquid scintillation detectors, and alpha and beta emissions can be discriminated by varying the potential applied or the duration of the photon emission, respectively. Treatment of the samples prior to measurement is simple and usually consists of solution concentration or evaporation to dryness.

The activity of a specific alpha or beta emitting radionuclide is mainly determined using semiconductors (alpha) and liquid scintillation or proportional gas detectors (beta). However, in both situations, before measuring, one or more separation steps are required to isolate the radionuclide of interest from other potential sources of interference (radionuclides or stable isotopes) included in the sample, and thus to allow accurate quantification. In the case of alpha emitting radionuclides, in spite of being monoenergetic, other sample components can be deposited on the alpha source together with the alpha emitting radionuclide, attenuating the alpha particle before achieving the semiconductor. For beta particles, they exhibit a continuous distribution of energy from 0 to a characteristic E_{\max} , and consequently spectra in a mixture are overlapped, making difficult their quantification.

Thus, the analytical process includes the dissolution of the sample, separation (using classic techniques such as precipitation, liquid-liquid extraction, solid phase extraction, etc.), and preparation of the isolated radionuclide for measurement. Extensive research has defined new procedures and introduced new reagents to improve these determinations, but the structure of the sequence has remained constant over the last four decades (as we will see in this Chapter).

Thus, the analysis of radionuclides requires time, reagents, and human effort; it needs to be performed in the laboratory, produces mixed waste when using liquid scintillation and the whole procedure introduces an important delay between the moment a sample is taken and when activity data is available. In this situation, the fact that plastic scintillators are solid offers new potential for the design of analytical procedures that improve the determinations in the laboratory but also allow measurements “in situ” and in real time.

These new opportunities can be summarized thus:

- Plastic scintillators can be used for beta and alpha radionuclide determination with the advantages of avoiding the production of mixed waste.
- Plastic scintillators are a solid platform and allow the incorporation of selectivity strategies thereby unifying the separation and preparation for measurement steps. These strategies are mainly based on the addition of compounds or creation of internal structures that permit the selective retention of a defined radionuclide (plastic scintillating resins or extractive scintillators, and plastic scintillating imprinted polymers).
- Plastic scintillators and plastic scintillating resins may be incorporated into a measurement cell for continuous monitoring of the activity of a fluid.

The most critical point for the application of plastic scintillators in the determination of alpha and beta radionuclides (emission with a short path) at the environmental level (with few disintegrations) is the geometrical relationship between the disintegration point and the plastic scintillator surface. This is related to the shape of the scintillator, the assembly of the sample and the scintillator, and the distribution of the radionuclides on the whole system. Those entire variables finally define the distance between the disintegration point and the plastic scintillator.

In plastic scintillation counting, the detection of an alpha or beta disintegration follows a well-known process: Once the particle achieves the scintillator, it transfers its energy to the polymerized solvent, which, in turn, transfers it to the fluors. In response to the energy received, the fluors emit photons which pass through the sample solution, are detected by the photomultiplier tubes, and are registered by the electronic chain. The main difference between plastic scintillation and liquid scintillation for liquid samples concerns the distance between the disintegration point and the scintillator solvent: this is of molecular proportions when the liquid sample is mixed with a scintillation cocktail, but it is much longer when the mixture is heterogeneous and includes solid plastic scintillators. As a consequence of this spatial distribution, disintegration detection via plastic scintillation adds two new quenching phenomena, particle quenching and optical quenching, to the common phenomena observed in liquid scintillation (i.e., chemical quenching, color quenching, and ionization

quenching). While ionization quenching depends on the scintillator, color and chemical quenching are related to the composition of the measured solution, and both particle and optical quenching are related to the geometry, relative refraction indexes and composition of the sample/plastic scintillator mixture.

In environmental analysis, the composition of a sample depends not only on the nature of the initial sample, but also on the chemical treatments applied to separate the radionuclide of interest from interferences. Thus, the measurement solution may incorporate compounds that interfere in the energy transmission between solvent and fluors (usually organic compounds with electronegative atoms), which produce chemical quenching, or compounds that absorb in the UV/VIS range, thereby producing color quenching.

Particle quenching is a consequence of the reduction of the energy of the emitted particle when it passes through the sample solution before reaching the scintillator. Meanwhile, optical quenching is a reduction of the photons that finally reach the photomultiplier tubes due to non-efficient light transmission caused to the successive changes in the refractive index they encounter along their path. These two quenching effects have opposite consequences on the detection of disintegrations and are related to the critical point mentioned above: the distance between radionuclide and scintillator and the shape of the plastic scintillator.

These effects can easily be described by imaging the situation of a vial filled with plastic scintillator microspheres with the sample solution embedded in it. If the diameter of the microspheres increases, the mean distance that the emitted particle has to travel to reach the scintillator increases but the number of changes in the refraction index encountered by the emitted photons before interacting with the photomultiplier tube decreases. Thus, particle quenching increases whereas optical quenching decreases. The detection efficiency and spectrum distribution recorded will depend on the balance between the effects.

It is interesting to note that when the number of changes in the refractive index is very high (for example, due to the use of plastic scintillating microspheres with a very small diameter), the photons are confined within the measurement cell and the detection efficiency is drastically reduced.

Together, particle quenching and optical quenching only have practical consequences for low-energy beta emitter determinations, such as those from ${}^3\text{H}$ ($E_{\max} = 18.59 \text{ keV}$), ${}^{63}\text{Ni}$ ($E_{\max} = 66.98 \text{ keV}$), ${}^{210}\text{Pb}$ ($E_{\max} = 17.0 \text{ keV}$ and 63.5 keV), or ${}^{241}\text{Pu}$ ($E_{\max} = 20.8 \text{ keV}$), where detection efficiency could be reduced to as much as $\frac{1}{4}$ with regard to the value obtained by liquid scintillation. Despite this, even ${}^3\text{H}$ emissions can be determined with plastic scintillators (3–5% efficiency). Detection efficiency for alpha emitters is also reduced depending on the geometrical conditions, with values usually remaining in the 80–100% range.

Special mention is required for procedures in which plastic scintillators are used but in which the radionuclide–scintillator distance is considerably reduced. These procedures include the removal of the solvent by evaporation of the sample solution to dryness on the scintillator and the use of selectivity strategies that retain and bring the radionuclides of interest to the surface of the scintillator. No matter what the shape of the scintillator is, such as microspheres or sheets, in these cases, the effects

on the detection of the different quenching mechanisms can be markedly reduced and practically constant.

The scintillation mechanism of plastic scintillators also allows discrimination of alpha and beta emissions, via the temporal distribution of the pulses. Although the difference between them is not so marked as when liquid scintillation is the technique used, it can be improved by adding a secondary solvent to the polymer composition such as naphthalene or diisopropylnaphthalene.

Thus, the shape and size of plastic scintillators become of paramount importance in the design of detection systems based on these materials. These designs will depend on the considered application.

The first application is the use of plastic scintillators as an alternative to liquid scintillation cocktails to determine total alpha and beta activity in an unknown sample (screening parameter) or to establish the activity of defined beta, and in some cases, alpha emitting radionuclides after a chemical separation process. The most common shape used in this situation is microspheres, although some applications are also based on pellets. This is a logical evolution of particle size from solution, through suspension to a heterogeneous mixture. The diameter of the microspheres should be minimized, balancing the two quenching effects mentioned above for signal optimization. For the plastic scintillation microspheres, the optimum diameter is around 60 microns and the preparation procedure is equivalent to that for liquid scintillation: mixing in a vial the sample solution and plastic scintillator microspheres in such a proportion that, once homogenized, the level of both inside the vial is the same. Homogenization is achieved by sacking using a vortex. The detection efficiencies and distribution spectra for different beta and alpha emitters are presented in Sects. 13.4 and 13.5. The main advantage of plastic scintillators for this application is that, after measurement, the sample solution and plastic scintillator can be segregated by simple filtration, avoiding the production of mixed waste. This characteristic also makes it possible to recover the sample for further determinations and to reuse the microspheres after a cleaning procedure.

The second application of plastic scintillators in environmental analysis is in form of plastic scintillating resins for selective determination of alpha and beta emitting radionuclides. In this application, the plastic scintillator is the support on which the selective strategy is implemented. The most common procedure is to coat the chemical compound that selectively extracts the radionuclide of interest from the sample solution on the surface of the plastic scintillator. For this purpose, any extractant compound used in regular separation can be essayed on the support. Other strategies like imprinted polymers can also be implemented. Ingeniously, the radionuclide is located close to the surface of the plastic scintillator and its disintegration product easily interacts to produce the signal.

Plastic scintillation resins in form of microspheres have the same aspect as other separation resins and therefore they can be packaged into a solid phase extraction cartridge and they can easily be introduced into any laboratory procedure. The significant advantage of radionuclide determination (in both environmental samples and also those from decommissioning processes) is the reduction in resources required,

including time. Plastic scintillating resins have already been developed for several radionuclides, as will be described in Sect. 13.5.

The use of PSsheets for selective analysis is under study and may open up the possibility of designing some quick and easy assays, mainly “in situ”, for materials, solids or solutions, including radionuclides at activity levels higher than environmental values. Their structure is similar to microspheres: the plastic scintillator sheet acts as a support and some extractant, depending on the purpose, is placed on its surface. The idea is that just by contact or rubbing, for solids, or by soaking into a solution, some of the radionuclides are extracted and transferred to the plastic scintillating resin sheet and they can be determined by scintillating techniques. The potential advantage of this development is that it would provide easily applied detection systems to provide information rapidly on the activity of some materials.

The third application of plastic scintillators for environmental analysis is the continuous monitoring of radionuclides in fluids. Although different shapes have been assayed, the most convenient ones for this application are microspheres, for total alpha or beta activity, and resins when searching for a specific radionuclide. Plastic scintillators fill up the measurement cell located inside of a scintillation detector. If the cell has connections for continuous entrance and exit of the fluid, the activity of the dissolved alpha or beta radionuclides can be detected in a way similar to when they are static. The advantages of using plastic scintillators are that no reagents, such as a scintillation cocktail, are consumed and no waste is produced because the same solution goes in and out of the cell. The same design may be used for the determination of specific radionuclides by filling up the cell with plastic scintillating resin. In this case, the activity in the fluid may be gauged by the increase in the signal. However, the continuous use of the plastic scintillating resin presents the drawback of their limited capacity and breakthrough volume.

The capacities of plastic scintillators for the determination of radionuclides in environmental samples will be presented in more details in the next sections, which focus on the preparation of plastic scintillators in their different forms and their applications in surface/soil activity determination, the development of sensors and the analysis of beta and alpha radionuclides.

13.2 Preparation of Plastic Scintillators for Environmental α/β Emitting Radionuclide Analysis

The analysis of alpha and beta emitting radionuclides using plastic scintillators requires their shape and size to be adapted to the short path of some radioactive emissions. Since this path varies from tenths of micrometers for alpha particles or low-energy beta emitters like ${}^3\text{H}$ to a few millimeters for high-energy beta emitters (e.g., ${}^{90}\text{Y}$ ($E_{\max} = 2,278 \text{ keV}$), ${}^{32}\text{P}$ ($E_{\max} = 1,710 \text{ keV}$), etc.) in water or a plastic scintillator, the latter should not be more than 10 mm in diameter. In fact, very small

scintillators, in the micrometer range, or those with a very high volume/surface area ratio, are highly recommended. The most typical shapes are:

- spheres or microparticles with a diameter of nanometers to a few millimeters;
- resins: spheres with an extractant on their surface;
- foils/films/sheets with a width of a few centimeters;
- fibers with a diameter of around one millimeter.

13.2.1 Fibers and Sheets

Fibers and sheets can be acquired from regular commercial producers of plastic scintillators (e.g., Saint-Gobain Crystals and Detectors, Eljen Technology or Kuraray, see Chap. 1) with different compositions and shapes. There is also some literature on the preparation of films with specific capacities. Merín and coworkers describe a procedure to prepare very thin films (from 50 to 150 μm) of polystyrene, polycarbonate or mixtures of both, by the solvent evaporation method. In this method, a solution of the polymers and the fluorescent molecules in dichloromethane is poured into a Petri dish and left to evaporate until all the solvent has gone [4]. Thickness control can be achieved by controlling the amount of polymer solution added or the concentration of polymer in the solution deposited. As an example, a PSfoil with a mean thickness of 94 μm has a thickness variability of 10 μm when it is measured in at least five points along the foil. Regarding homogeneity, PSfoils composed of polystyrene were smooth and homogenous whereas those composed of polycarbonate had pores. This was attributed to the condensation of water microdroplets during the evaporation of the solvent. PSfoils composed of a mixture of polymers were not homogeneous with the polymers clearly segregated, suggesting that polycarbonate and polystyrene were not miscible.

A similar approach was used by Das and coworkers, but in this case, two selective extractants, *tris*-(2-ethylhexyl) phosphate and Aliquat-336, were added to the organic solution. Chavan and coworkers [5] also developed selective extractive films but for actinides. A film of polypropylene or polyethersulfone used as substrate was soaked for 3 h in a solution of the extractant/monomer, bis[2-(methacryloyloxy)ethyl] phosphate (MEP), the organic fluors, and the initiator (2,2'-dimethoxy-2-phenylacetophenone (DMPA) in the suitable solvent (DMF or DMF/methanol respectively). Polymerization was induced by UV light for 15 min. Mass gain achieved after polymerization and SEM images indicate that pores of the membrane were filled with the scintillating polymer.

13.2.2 Plastic Scintillation Particles

Plastic scintillators in the form of spheres of very small size are usually referred to as plastic scintillation microspheres or plastic scintillation microparticles (PSm). PSm

can be acquired on demand from some producers (e.g., Saint-Gobain Crystals and Detectors and Detec) but in limited amounts, and therefore, several procedures to prepare them can be found in the literature following the methods of:

- Swelling,
- Polymerization,
- Membrane emulsification and polymerization,
- Extraction/evaporation,
- Spray-drying,
- Supercritical fluids.

In all cases, except the swelling method, in which the microspheres are already formed, the medium in which the plastic scintillator is formed presents a specific composition that leads to the aggregation of the polymer in the form of particles, which are usually spherical. This medium is composed of a continuous phase (also called the water phase), based on water or another polar solvent with a surfactant dissolved in it, and a disperse phase (also called the oil phase), based on the fluors dissolved in the monomers or the polymer dissolved in a non-polar organic solvent. Since the two phases cannot form a stable single phase when mixed under agitation, spherical micelles or droplets of the dispersed phase are formed inside the continuous one. These droplets are stabilized by the surfactant and the force applied by stirring (which should be vigorous). The size of the droplets depends on the proportion of the phases and the amount of surfactant added. Once the conditions for the formation of the solid polymer occur, the microparticles form. The size and shape of the microparticles are determined by the conditions of the different variables that define the system: amount of continuous phase, amount of disperse phase or monomer, amount of surfactant, rate of agitation, temperature, etc.

13.2.2.1 Swelling

One of the first methods reported for the production of plastic scintillation microspheres consists of swelling for a period of time (from 8 to 24 h) commercial polymer beads in toluene or benzene solutions of the fluorescent solutes [6–10]. The polymer beads should contain a certain amount of divinylbenzene (e.g., 2%). Not too little, to avoid dissolution of the beads; but not too much, to limit the diffusion of the fluors into the polymer chain. The polymer beads developed in these publications were based on:

- acrylic ester macroporous polymer beads (20–50 μm particle size) [6];
- 120 μm -diameter macroporous divinylbenzene cross-linked polystyrene beads (Amberchrom CG-161c) [7, 10];
- poly(chloromethylstyrene) resin cross-linked with 2% divinylbenzene (100–200 mesh and 0.9 mmol Cl/g) [8, 9].

13.2.2.2 Polymerization

Several polymerization procedures have been reported in the literature. Zhu and Jay describe a method to obtain nanosuspensions of polystyrene in water [11]. In their procedure, a disperse phase composed of styrene, divinylbenzene, and the fluors is mixed with a continuous phase composed of sodium dodecylsulfate (100 mg mL^{-1}) and 1-pentanol (0.2% v/v) as surfactants in water and heated for 8 h at 70°C . The fluors used were 2,5-diphenyloxazole (PPO) and 1,4-bis(2-methylstyryl)benzene (bis-MSB) or 2,5-diphenyl-4-(*para*-vinylbenzyl)oxazole. The obtained particles had a diameter of less than 50 nm.

Microparticles of few micrometers were obtained by Bagan and coworkers by thermal polymerization using a mixture of styrene, a cross-linker (divinylbenzene or 1,2-ethylene glycol dimethacrylate), fluorescent solutes (2,5-diphenyloxazole, *p*-terphenyl or (2,5-diphenyloxazol-4-yl)methyl acrylate), and additives (1,2-diisopropylnaphthalene) in a polar organic solvent (methanol, methanol/diethyl ether or methanol/diethyl ether/water mixtures) [12]. Once the mixture was homogenized and purged with N_2 , it was heated to 62°C and then to 75°C and maintained at each temperature for 24 h. In this process, neither surfactant addition nor agitation was used during polymerization. Therefore, the final product obtained, bulk or microparticles, depends on the stability of the droplets of the monomers in the solvent, which, in turn, depends on the proportions and the difference in polarity between them. Figure 13.1a shows the non-spherical microparticles of few micrometers obtained using methanol as the solvent.

Spherical plastic scintillators larger than $100\text{ }\mu\text{m}$ were obtained by DeVol and collaborators using suspension polymerization and reported in different works [8, 9, 13–19]. In the most basic preparation, around 20 mL of the dispersed phase, containing the monomers, the fluorescent molecules and additives, is mixed with

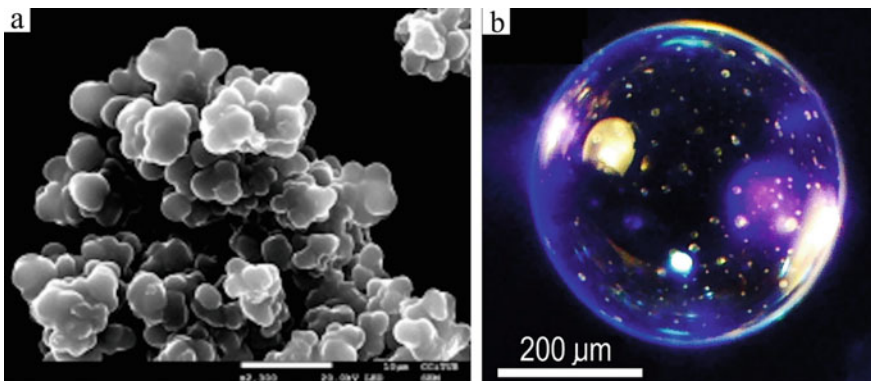


Fig. 13.1 Plastic scintillator particles obtained by polymerization. a Reproduced from [12] and b reproduced from [13] with permission from Elsevier

300 mL of the continuous phase (e.g., 300 mg of poly(vinyl alcohol) as the surfactant, 300 mg of hydroxypropyl methylcellulose for seeding and 2.5 g of sodium chloride in water) and stirred at 200–600 rpm at 75 °C for 12 h. Figure 13.1b shows a typical microsphere obtained when no additives were added. The size of the microspheres usually ranged from 100 to 400 µm. In their work, DeVol and collaborators evaluated different monomers (styrene or 4-methylstyrene), mixtures of monomers (styrene/divinylbenzene, styrene/divinylbenzene/4-vinylbenzyl chloride and 4-methyl styrene/ethyleneglycol methacrylatephosphate/divinylbenzene), additives (toluene, heptane or span-80), and fluorescent solutes ((1-naphthyl)-5-phenyloxazole, 2-(1-naphthyl)-4-allyl-5-phenyloxazole, 2-(1-naphthyl)-4-vinyl-5-phenyloxazole and 2-(4-biphenyl)-5-(4-*tert*-butylphenyl)-1,3,4-oxadiazole). The obtained microspheres vary in size by around 35%, which can be reduced to 15–20% by using membrane emulsification with a 30-µm pore size [20].

13.2.2.3 Extraction/evaporation

Extraction/evaporation is another strategy used to produce microspheres. In this method, the polymer is dissolved in an appropriate solvent together with the fluorescent solutes and the additives. The polymer has to be linear and without any cross-linkers in order to be dissolved. This disperse phase is added to a continuous phase containing a surfactant and the mixture is stirred until the organic solvent evaporates. The organic solvent should have a low solubility in water and a low boiling point. When the phases are mixed, droplets of the disperse phase form in the continuous phase. The organic solvent is dissolved very slowly in the continuous phase, whereas the polymer solidifies on the surface of the droplet forming a crust. Simultaneously, the organic solvent is evaporated and immediately replaced by more solvent from the droplet. The size of the droplet decreases due to the loss of the solvent until no solvent remains in the droplet and only solid polymer remains. Different solvents have been evaluated (e.g., toluene, dichloromethane, and methyl acetate), with dichloromethane providing the best results, thanks to its poor solubility in water (1.3 g L^{-1}) and very low boiling point (39.6 °C) which means that the process is limited by the solubility rate of dichloromethane. In these conditions, the formation of the particles is very gradual and therefore they are spherical (Fig. 13.2a). It should be highlighted that solvent amount in the final product is negligible since it is not detected when analyzed by gas chromatography and no chemical quenching effects are observed when measuring radioactivity.

Tarancón and coworkers studied this process in details by evaluating the influence of the addition of fluorescent solutes on the detection efficiency [21], the addition of naphthalene and 1,2-diisopropynaphthalene for enhancing alpha/beta discrimination [22], and the effect of varying different preparation parameters on the size of the particles [23]. Figure 13.3 shows the diameter of the microspheres for different preparation conditions (Table 13.1).

A low surfactant concentration, high polymer concentration, and small amount of the organic phase lead to large particles since the droplets formed are larger.

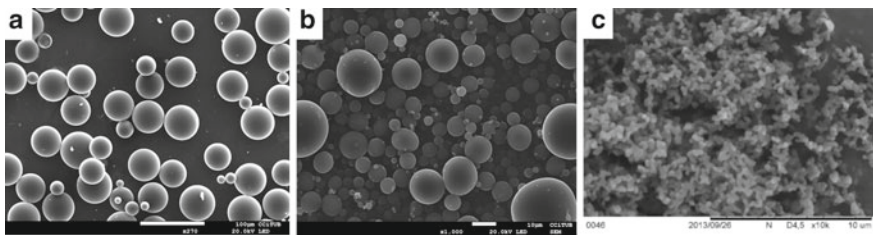


Fig. 13.2 PSm prepared by, **a** extraction/evaporation, **b** spray-drying and, **c** supercritical fluids by anti-solvent precipitation (SAS)

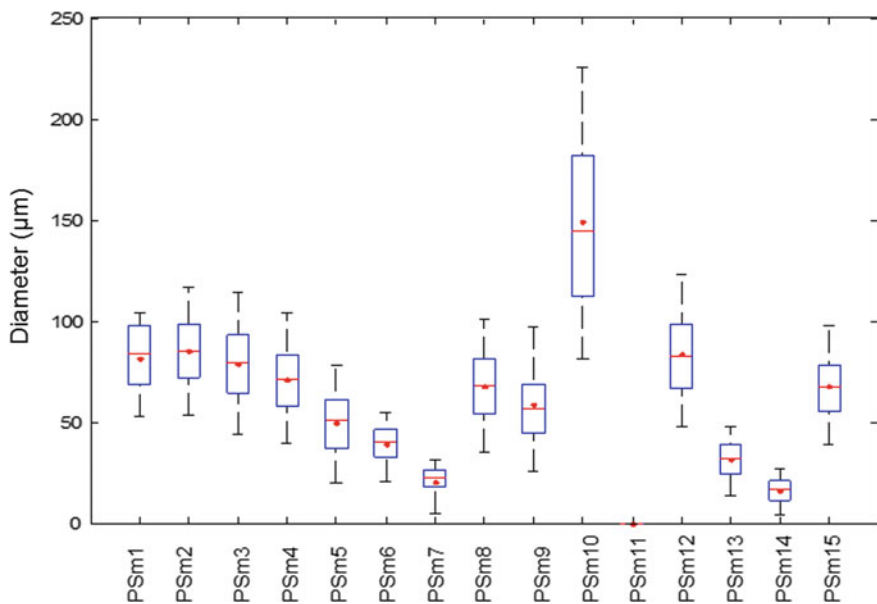


Fig. 13.3 Diameter distribution of the PSm prepared using conditions reported in Table 13.1 (reproduced from [23] with permission from Elsevier)

13.2.2.4 Spray-Drying

When using the spray-drying technique with a MOBILE MINOR™ reactor, the organic solution of the polymer is sprayed through a nozzle, with the help of N_2 , into a chamber at a controlled temperature [24]. Droplets of the organic solution form when it is sprayed and their size depends on the solution flow rate, polymer concentration, and nozzle flow rate. If the solvent evaporates quickly before the droplet reaches the walls of the chamber, particles are formed (Fig. 13.2b). This process depends mainly on the size of the chamber, the range of temperatures between the nozzle and the chamber walls and the solvent used. The larger the chamber is, the larger the particles that are obtained. Regarding the solvent, toluene performs better

Table 13.1 Different parameters employed for PSm synthesis (reproduced from [23])

Synthesis	Polystyrene (g)	DCM (mL)	Temperature (°C)	O:W	PVA (%)	Stirring speed (Hz)
PSm1	10	100	20	1:20	1	16.7
PSm2	10	100	20	1:20	1	8.3
PSm3	10	100	20	1:20	1	13.3
PSm4	10	100	20	1:20	2	16.7
PSm5	10	100	20	1:20	5	13.3
PSm6	10	200	20	2:20	1	16.7
PSm7	10	400	20	4:20	1	13.3
PSm8	20	200	20	2:20	1	16.7
PSm9	40	400	20	4:20	1	13.3
PSm10	10	100	35	1:20	1	16.7
PSm11	10	100	50	1:20	1	16.7
PSm12	10	100	20	1:20	1	16.7
PSm13	30	300	20	3:20	6	11.67
PSm14	30	600	20	6:20	6	11.7
PSm15	25	250	20	2.5:20	1	10.0

O:W organic/water ratio

than dichloromethane since the temperature range is broader, thus avoiding too fast (formation of threads) or too slow (no formation of particles) solvent evaporation. This system works automatically with a range of production of 300 g/day and permits recovery of the solvent. However, it is less robust and produces less spherical particles than the extraction/evaporation method, unless an industrial size reactor is used.

13.2.2.5 Supercritical Fluids by Anti-solvent Precipitation (SAS)

In this technique, the polymer and the fluorescent solutes are dissolved in an organic solvent (ethyl acetate) and the solution is introduced, through a nozzle, into an autoclave of 1 L previously filled with supercritical CO₂ [25]. The rapid extraction of the solvent leads to the formation of microparticles. With this system, submicron nonspherical particles can be obtained (Fig. 13.2c).

13.2.2.6 Porous Scintillating Microspheres

The surface of the microspheres obtained by the procedures described previously is smooth. This results in the lowest surface area per volume of scintillator, which supposes a drawback in applications in which the contact surface needs to be as higher as possible. This can be resolved by the addition of porogen compounds

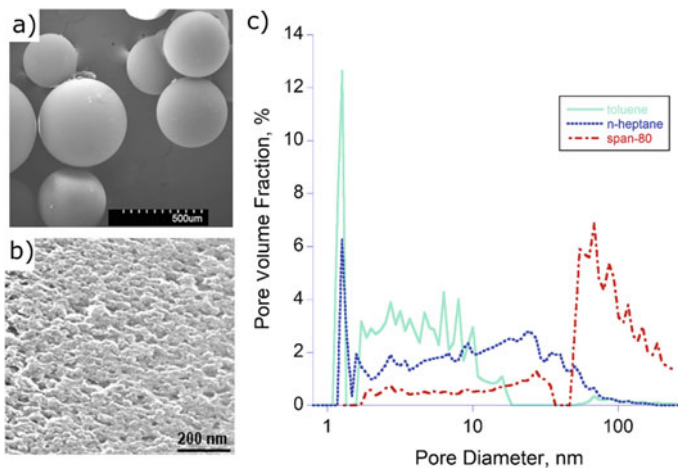


Fig. 13.4 Porous scintillating microspheres obtained by polymerization (reproduced from [13] with permission from Elsevier)

during the synthesis procedure. In the polymerization method [13], the addition of heptane, toluene, methyl ethyl ketone/toluene or span-80 in the disperse phase can lead to the formation of porous surfaces, since these components do not react with the monomer but remain between the polymer chains when the polymer is formed (Fig. 13.4a, b). Pores of different sizes, micro (<2 nm), meso (2–50 nm), and macro (>50 nm), are generated when the porogen is removed during the cleaning process. The pore size distribution depends not only on the porogen used (Fig. 13.4c), but also on the amount of porogen and the proportion of cross-linker used in the synthesis, since the structural distribution and rigidity of the chains of the polymer depend on the presence of cross-linked polymer chains.

Pores can also be introduced using the extraction/evaporation method, but then, a porogen like heptane, which does not dissolve the microsphere, should be used and the pores have larger dimensions (Fig. 13.5).

13.2.3 Stability of Plastic Scintillation Microspheres

One of the issues that arises from the use of scintillators in the form of microspheres is their stability and the potential leaching of fluors from the polymer chain. This is something to take into consideration since plastic scintillation microspheres are usually employed with water samples or different reagents flowing through them for a long period of time. Leaching of fluors has been reported in microspheres prepared by swelling when they are treated with 5,000 pore volumes of a 25% methanol/water solution [8]. However, when prepared by extraction/vaporation, no leaching effect has been observed when the microspheres are cleaned with ethanol

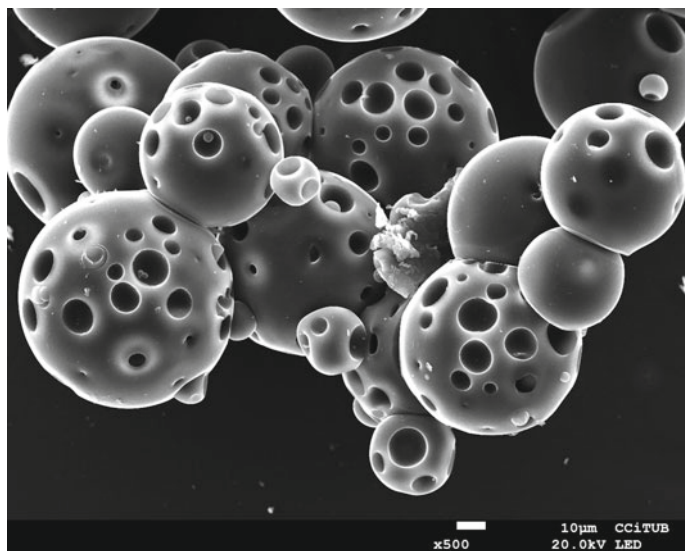


Fig. 13.5 Porous scintillating microspheres obtained by extraction/evaporation

Table 13.2 Polymerizable fluors

2-(1-naphthyl)-4-allyl-5-phenyloxazole [14]	2-(1-naphthyl)-4-vinyl-5-phenyloxazole [14]	2,5-diphenyl-4-(4-vinylbenzyl)oxazole [11]	2-(4-4'(vinylbiphenylyl))-5-(4- <i>tert</i> -butylphenyl)-1,3,4-oxadiazole [17]	(2,5-diphenyloxazol-4-yl)methyl acrylate [12]

or when a water sample flows through the particles for at least 100 hours at a flow rate of 1 mL min^{-1} , since their detection efficiency for ^3H and ^{90}Sr remains constant [26]. The extraction/evaporation method has the advantage that the organic solvent is completely removed during the synthesis process, whereas in polymerization, part of the monomers remain unreactive and trapped inside the polymer chain where they have the capacity to dissolve the fluorescence solute.

A strategy that proved useful to prevent the leaching of fluorescent molecules is the use of polymerizable fluorescent molecules with the polymer monomer. Such compounds are shown in Table 13.2. However, it should be taken into account that the use of this kind of fluors can lead to plastic scintillators that are less efficient in the scintillation energy transmission process than non-polymerizable fluors.

Degradation of the PSm, when treated with high concentrations of nitric acid, was attributed to the nitration of the styrene units of polystyrene scintillators which can later lead to chemical or color quenching. In this situation, the use of poly(vinyltoluene) scintillators seems to reduce this effect due just to a steric effect caused by the methyl group of the aromatic ring [19].

13.2.4 Plastic Scintillation Resins

Plastic scintillation resins can be defined as plastic scintillation microspheres with a selective extractant on their surface. This kind of scintillators are capable of retaining a specific radionuclide on their surface and therefore radionuclides can be separated from interfering compounds and their activity measured online or off-line using the same material.

The simplest strategy is based on a mixture of plastic scintillation microspheres and a commercial solid extractant [27].

Bagán and coworkers extensively used coating methods to add a thin layer of extractant, 4,4'-(5')-di-*t*-butylcyclohexano-18-crown-6 [28] or Aliquat-336 [29], to the surface of plastic scintillation microspheres prepared by extraction/evaporation. In this procedure, the PSm are mixed with a solution of the extractant dissolved in an appropriate solvent (i.e. methanol) and the solvent is then slowly removed in a rotary evaporator.

Trapping the extractant on the plastic scintillator is a strategy that has also been used when PSm are prepared by polymerization method. In some situations, the extractant is an independent compound [15], but in others, it forms part of the polymer chain. This is the case of ethylene glycol methacrylate phosphate (EGMP) resin [16], in which the extractant compound, ethylene glycol methacrylate phosphate, was copolymerized together with 4-methylstyrene, divinylbenzene and a polymerizable fluorescent molecule.

Impregnation has also been used for this purpose. In this approximation, polymers including cross-linkers should be used to avoid the dissolution of the polymer. Roane et al. [30] incorporate *n*-octyl(phenyl)-*N,N'*-diisobutylcarbamoylmethylphosphine oxide (CMPO) in tributyl phosphate (TBP), Bagan et al. [31] use TBP in dodecane, and Egorov et al. [6] aliquat-336 and HDEHP in benzene.

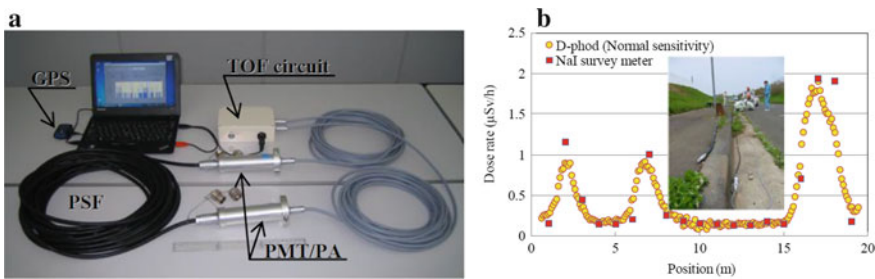
The remaining strategy is to link the polymer and the extractant through a chemical bond. This implies that the surface of the plastic scintillation microspheres should contain molecules with suitable leaving functional groups that can react with the extractant. This has been achieved by adding 4-vinylbenzyl chloride during the polymerization of styrene or 4-methylstyrene, obtaining a copolymer with chloride groups inside the particles and on their surface. Later, the chloride moiety can be substituted by the extractant by using one or more reactions. Duval and coworkers were able to link a methylphosphonic acid group to the surface of a plastic scintillator [18],

while Seliman and coworkers added an *N*-methyldioctylamine through amination of the chloride moiety [14]. Although this strategy is very promising due to the high stability of the resultant resin, some doubts have been raised due to the incorporation of the Cl moiety inside the PSm, potentially causing quenching, and the use of organic solvents during the synthesis that could lead to leaching of the fluors from the PSm.

13.3 Direct Surface and Soil Analysis

Analysis of radionuclides in soils or in solid surfaces is of paramount importance for the characterization of materials potentially contaminated by radionuclides that may be in contact with people. This situation can arise in the decommissioning of nuclear power plants, remediation of soils potentially contaminated by accidents or spills, and in intentioned contaminations. However, this analysis is highly complex for alpha and beta emitting radionuclides since it requires analytical procedures that include sampling, treatment (i.e., sample dissolution and interference removal), and determination. Moreover, often it only provides information on a very small portion of the sample (between 1 and 10 g) and the information has to be extrapolated to the rest of the sample (with a mass of over 1 kg). In this scenario, plastic scintillators have been used to develop methods that permit direct analysis of radionuclides (alpha, beta or gamma) in soil samples or in solid surfaces, with the aim of reducing the time and effort required as well as providing more realistic information. This takes advantage of the fact that plastic scintillators can be prepared as sheets/films/foils or fibers of very different sizes (from cm to m). Some of the systems reported in the literature are only ideas or initial prototypes that do not improve on already existing methodologies [33–36], but others have actually been applied in the field.

Direct analysis of gamma radiation in the field is usually performed using semiconductor detectors, inorganic scintillators or gas detectors in the form of survey meters. However, Gamo and coworkers from Hitachi-GE Nuclear Energy [37] developed a detection system based on a long plastic scintillation fiber and a time-of-flight (ToF) technique, called D-phod, which enables very fast dose rate determinations over large areas. The D-phod detector has a 20 m long plastic scintillation fiber bundle connected to two photomultiplier tubes (PMTs) (Fig. 13.6a). A ToF circuit analyzes pulses detected by the PMTs and is capable of identifying the point along those 20 m at which disintegrations are taking place. The electronics were optimized to weigh less than 0.5 kg and the final weight depends on the bundles used and sensitivity required (from 2.5 to 8 kg). The detector was designed to be waterproof and dustproof, and was used to detect radioactivity from roads, walls, trees or ponds in a scenario in which measurement with an NaI survey meter would be very complex (Fig. 13.6b). The D-phod detector was used to assess the status of environmental contamination and the effect of decontamination associated with the Fukushima Daiichi Nuclear Power Plant accident.



Analysis of pure beta emitting radionuclides (i.e., ^{90}Sr) in contaminated soils was addressed by Venara and collaborators using a PSblock [38] (Fig. 13.7). The thickness of the PSblock and the other components was optimized using Monte Carlo simulations with MCNP6 and PENELOPE. A thickness of 4 mm was chosen as a compromise between maximizing efficiency for ^{90}Y and minimizing sensitivity to gamma emissions. The system was calibrated for two purposes: to provide specific counting windows for ^{90}Y while avoiding signals from ^{137}Cs or other medium-energy

Fig. 13.7 Photograph of the beta spectrometer for measurements on sand samples in direct contact with the sand (reproduced from [38] with permission from Elsevier)



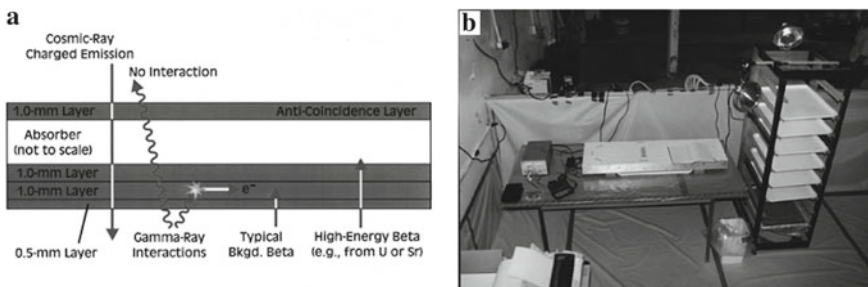


Fig. 13.8 **a** BetaScint principle and **b** detector [42]

beta emitters and to determine the efficiency coefficients according to the density and composition of the soil. An aluminum cover was used to block alpha emissions. The system was validated via analysis of contaminated soil samples (Fontainebleau sand) previously measured by a radiochemical method and containing ^{90}Sr , $^{239+240}\text{Pu}$, ^{238}Pu , ^{237}Np , ^{137}Cs and ^{233}Pa . Samples were measured directly or in polyethylene containers. The measured activities were lower than those obtained using radiochemical methods, with a maximum deviation of 57%, which was attributed to the calibration coefficients used.

A similar approach was developed by Maekawa et al. [39] when they used a 30 × 30 cm block of plastic scintillator coupled to two wavelength shifting (WLS) fibers and two PMTs. Different scintillator thicknesses were evaluated with 1 mm being that at which the beta/gamma ratio was maximum.

Direct analysis of alpha and beta emitting radionuclides was achieved by Schilk and coworkers using a multilayer system of plastic scintillation fibers [40, 41]. That system, known as BetaScint™, has been used by the Department of Energy for the remediation of soils contaminated with ^{238}U and ^{90}Sr with the advantage that it permits characterization of large sample volumes with fewer operations and more cheaply. BetaScint uses an absorber between the different layers of fibers to suppress beta and alpha detection and therefore rejects cosmic rays and gamma emission by anticoincidence counting (Fig. 13.8a). The first layers are not considered for the measurement as low beta emitters deposit their energy on these layers and may interfere with the signal from Sr-90. Taking into account the size of the detector (30 × 60 cm) and typical densities of samples (1.5 g mL^{-1}), it was determined that a sample of 700 g can be measured without self-attenuation (Fig. 13.8b). A detection limit of 0.037 Bq g^{-1} was achieved in 5 min of counting time. The main limitations of the system were that it does not discriminate between alpha and beta radioactivity and that ^{137}Cs can cause interference if activity levels of ^{137}Cs and ^{90}Sr are not comparable or ^{137}Cs activity is higher than 3.7 Bq/g .

Discrimination of alpha and beta emitting radionuclides in the analysis of contaminated surfaces has been achieved using a combination of ZnS(Ag) for the detection of alpha emitting radionuclides and thin layers of plastic scintillators, for the beta emissions [43, 44]. The system is based on a sandwich of a PSsheet (50 × 200 ×

1 mm) and WLS fibers between two 30 μm ZnS(Ag) layers. Discrimination was achieved from the different decay times of the scintillators (200 ns and 2.4 ns for ZnS(Ag) and the plastic scintillator, respectively). Several WLS fiber configurations were evaluated, and that with 9 bent fibers and 3 straight ones provided the best results, with efficiencies (2π) of 70% for alpha emitters (^{238}Pu , ^{241}Am) and 44% (^{137}Cs) to 90% ($^{90}\text{Sr}/^{90}\text{Y}$) for beta emitters (Fig. 13.9).

Finally, some attempts have been made to use plastic scintillators for the analysis of alpha emitting radionuclides in contaminated surfaces [45, 46]. For this application,

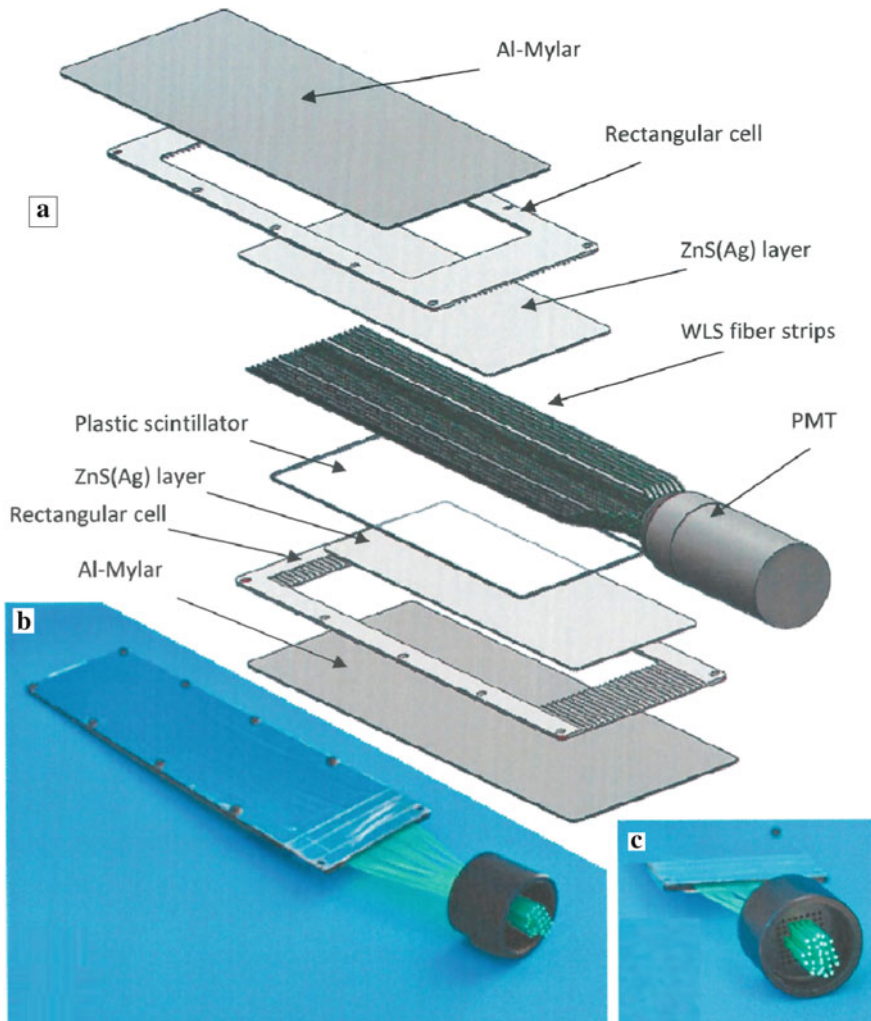


Fig. 13.9 Schema of the prototype detector. **a** Picture of the prototype detector. **b** and **c** Pictures of the WLS fiber holder (reproduced from [43] with permission from Elsevier)

very thin films of less than 20 μm were used since, with this thickness, the energy deposited by beta particles is very low and only alpha emissions are detected. The systems are still at the prototype phase.

13.4 Sensors and Online Analysis of Alpha and Beta Emitting Radionuclides

The use of sensors or online analysis to monitor alpha and beta emitting radionuclides is important in the environmental field as it is the fastest way to detect contamination of water bodies from natural or artificial sources of radioactivity. Flow analysis using liquid scintillators is applied in medicine and radiopharmacy to monitor processes using high activities in small volume samples. However, for environmental or contaminated liquid samples, continuous monitoring using liquid scintillators generates very large amounts of liquid scintillator waste, which means it is not viable in terms of waste generation and management, environmental impact or economics. The use of plastic scintillators makes it possible to avoid these problems since, due to their solid form, no waste is generated and no reagents are needed. Therefore, continuous measurement of several samples is only restricted by the degradation of the plastic scintillator and the analysis time required to achieve the desired limits of detection.

In an online analysis for environmental monitoring, the limit of detection appears to be the crucial parameter since permitted activities are very low. As an example, the European 2013 drinking water directive establishes a threshold of 100 Bq/L for ^{3}H , 1 Bq/L for total beta activity, and 0.1 Bq/L for total alpha activity. According to Currie expression [47], the limit of detection (Eq. (13.1)) depends on four parameters: background signal (B); volume of the sample (V); detection efficiency (Eff); and the counting time (t)

$$LD \left(\text{Bq L}^{-1} \right) = \frac{\frac{2.71}{t} + 4.65\sqrt{\frac{B}{t}}}{V \cdot Eff} \quad (13.1)$$

As a consequence, the design of the detector must minimize B while enhancing V and Eff . While B depends mainly on the quality of the electronics and the use of active or passive shielding and less on the amount of scintillator, V and Eff are highly dependent on the design of the scintillation cell. To achieve a high Eff , especially for particles with less penetrating power such as those emitted by ^{3}H or by alpha emitters, the contact between the liquid sample and the plastic scintillator should be as great as possible. This can only be achieved by maximizing the ratio between the plastic scintillator surface and V , the volume of the sample. The plastic scintillator surface depends on the form and size of the scintillator and V depends on the free volume between the scintillator and the cell walls. This ratio determines the distance probability distribution between the radionuclide and the scintillator, which is critical

if we consider that the mean path length of alpha particles in water is around 50 μm , and it is about a few micrometers for a low-energy beta particle emitted by ${}^3\text{H}$. No particles, beta or alpha, emitted farther away than their maximum path length will be detected, decreasing the detection efficiency of the sensor.

Currently, there is no commercially available detector based on any technique capable of performing online, continuous, and fast monitoring of aqueous samples containing alpha and beta emitters at the environmental level. Since the use of plastic scintillators is one of the techniques whose characteristics appear possible to achieve this, perhaps the principal one, different efforts have been made to develop sensors for tap water surveillance or environmental monitoring of natural waters and contaminated fluids (i.e., waste, lixiviates, etc.).

Taking into account that the most relevant aspect of the performance of a sensor will be derived from its shape, discussion has focused on the types of plastic scintillator available: microspheres, resins, fibers, and plates.

13.4.1 Sensors Based on Plastic Scintillation Microspheres (PSm)

In this type of sensor, the cell is filled with plastic scintillation microspheres that are retained in the cell with frits, while the water sample flows through it. This takes advantage of the fact that the microspheres present a very small diameter, tens or hundreds of micrometers, and therefore, the sample occupies the interstices between the microspheres, maximizing contact between the sample and the plastic scintillator and minimizing the distance between the radionuclide and the scintillator. For example, if we consider a 1 mL cell completely filled with PSm, approximately 0.66 cm^3 of the volume is occupied with PSm and the rest, 0.33 cm^3 , with the water sample (66% packaging). If the PSm presents a mean diameter of 60 μm , the total scintillator surface is around 82.5 cm^2 , which leads to a surface of scintillator/volume of sample ratio of 250 cm^{-1} : considerably higher than the 3 cm^{-1} obtained with a $1 \times 1 \times 0.66 \text{ cm}$ PSsheet (0.66 cm^3 of volume) in contact with 0.33 cm^3 of water sample ($1 \times 1 \times 0.33 \text{ cm}$).

The first efforts to construct a sensor based on PSm included an “alpha–beta chamber” filled with PSm and connected to a bundle of optical fibers, as the aim was to use it in remote monitoring [48, 49]. The chamber was surrounded by a “gamma chamber” made of plastic scintillator and also connected to an optical fiber bundle. The gamma chamber serves as active shielding to reduce the background (Fig. 13.10).

Tests performed using a commercial Wallac 1414 detector showed a background signal of 0.8 cps, detection efficiency of 116 and 3.2% for ${}^{90}\text{Sr}$ (in equilibrium with ${}^{90}\text{Y}$) and ${}^{240}\text{Pu}$, respectively, and a limit of detection of 0.091 and 1.6 Bq mL^{-1} for ${}^{90}\text{Sr} / {}^{90}\text{Y}$ and ${}^{240}\text{Pu}$ for a counting time of 20 min. Spectra obtained for different radionuclides (Fig. 13.11) show that the signals detected were of low energy, which was attributed to the photon losses in the optical coupling between the PSm cell and

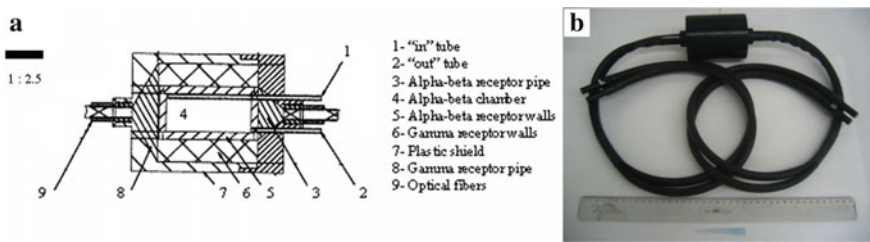


Fig. 13.10 **a** Structure and **b** photograph of the receptor (reproduced from [49] with permission from Elsevier)

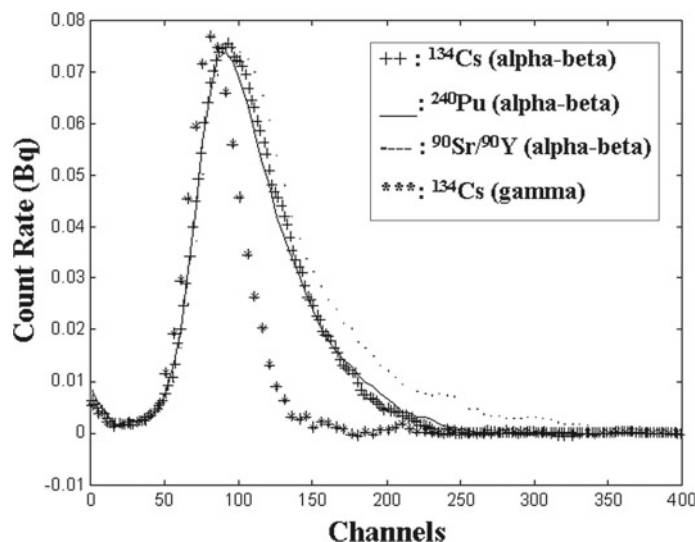


Fig. 13.11 Detection efficiency distribution of $^{90}\text{Sr}/^{90}\text{Y}$, ^{240}Pu and ^{134}Cs , in the alpha–beta receptor, and ^{134}Cs , in the gamma receptor, for a contamination pulse of 20 mL at the effluent volume corresponding to the maxima signals (reproduced from [49] with permission from Elsevier)

the optical fibers, and between the optical fibers and the commercial detector. This factor explained the low efficiencies obtained for alpha emitters.

Explanation

Since ^{90}Sr and ^{90}Y have different energies, an accurate determination of the detection efficiency for each radionuclide cannot be done when both are in equilibrium and the total detection efficiency is lower than the maximum, 200%.

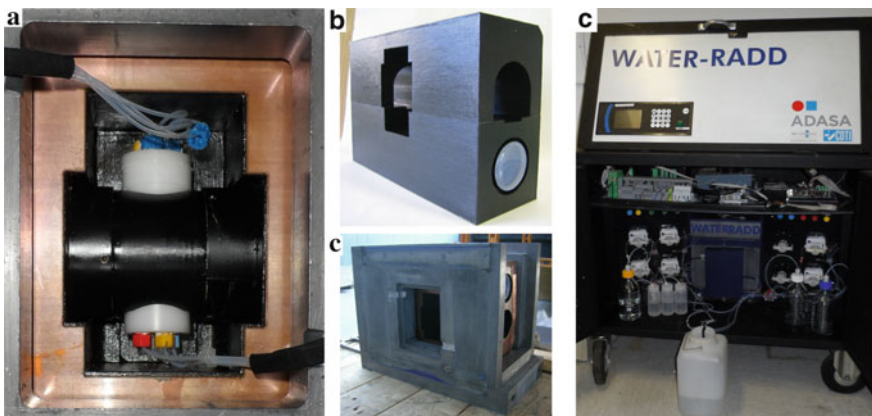


Fig. 13.12 Cell, guard detector, shielding, and hydraulics of the Water-Radd

An improvement of this system, in conjunction with the company Adasa Sistemas, focused on the reduction of the limit of detection. Modifications included increasing the cell size (20 g of PSm and 10 mL of sample), removing the optical fibers, and using a purpose-built detector with lead shielding and four PMTs: two for the cell and two for the guard detector made of plastic scintillator. The detector, called Water-Radd, incorporated FPGA-based electronics, hydraulics, and all the necessary communication equipment to perform the water monitoring in an autonomous way (Fig. 13.12). In normal operation, the cell is filled with the sample and it is measured while static for the desired counting time.

This detector presented a low background of 0.2 cps and a detection efficiency of 0.38%, 142%, and 58.1% for ${}^3\text{H}$, ${}^{90}\text{Sr} / {}^{90}\text{Y}$, and ${}^{241}\text{Am}$, respectively, assuming a sample volume of 10 mL. Detection limits for 5 h counting time were 490 Bq L^{-1} , 2.3 Bq L^{-1} , and 3.0 Bq L^{-1} for ${}^3\text{H}$, ${}^{90}\text{Sr} / {}^{90}\text{Y}$, and ${}^{241}\text{Am}$, respectively. These values are very close to those required for pre-potable water monitoring, especially for tritium and total beta activity. The system incorporated calibration with deionized water and ${}^3\text{H}$, ${}^{90}\text{Sr} / {}^{90}\text{Y}$, and ${}^{241}\text{Am}$ standards, and a cleaning protocol for the PSm with 0.1 M HCl that allowed cell regeneration and multiple sample analysis. Figure 13.13 and Table 13.3 show the results from a sequence of measurements of tap water samples (5 h, 63 samples), deionized water background (19 measurements), and ${}^3\text{H}$, ${}^{90}\text{Sr} / {}^{90}\text{Y}$, and ${}^{241}\text{Am}$ standards (7 measurements) measured for 1 h. The results demonstrate that the system is capable to perform several consecutive measurements with variability below 10% for all parameters and without significant memory effects or cell degradation.

As explained, detection based on the use of PSm presents the advantage of very high detection efficiencies, even making it possible to analyze ${}^3\text{H}$ at low activity levels. However, cell volume is limited by photon transmission (optical quenching), which becomes poorer as the amount of plastic scintillator increases especially

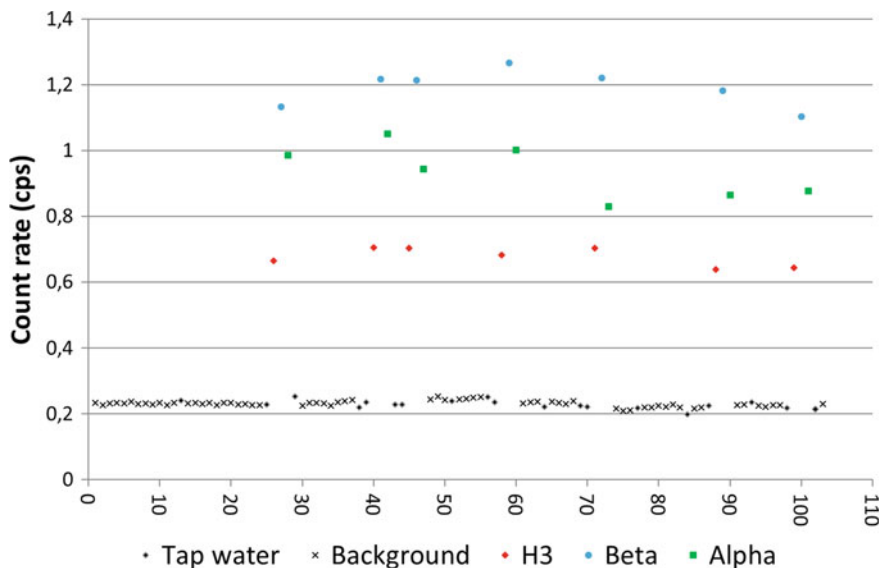


Fig. 13.13 Activity profile of a sequence of measurements in the Water-Radd

Table 13.3 Results of a sequence of measurements in the Water-Radd

Tap water samples count rate (cps)	0.231(0.009)
Background count rate (cps)	0.228(0.013)
$^{3\text{H}}$ efficiency (cps L ¹ Bq ⁻¹)	$1.8 \cdot 10^{-5}$ (0.1·10 ⁻⁵)
^{90}Sr efficiency (cps L ¹ Bq ⁻¹)	$1.7 \cdot 10^{-2}$ (0.1·10 ⁻²)
^{241}Am efficiency (cps L ¹ Bq ⁻¹)	$5.4 \cdot 10^{-5}$ (0.4·10 ⁻⁴)

affecting detection of beta emitting radionuclides and limiting the possibility of applying alpha/beta discrimination.

13.4.2 Sensors Based on Plastic Scintillation Resins

In this strategy, the counting cell is filled with an extractive scintillator capable of selectively retaining the radionuclide of interest. Therefore, as the sample passes through, the radionuclide accumulates in the cell and a progressive increase of the counting rate is observed until the flow stops or the resin becomes saturated. The activity of the sample can be calculated once the count rate achieves a value that is statistically different from the background. In this situation, the activity can be calculated from the slope of the count rate profile during the flow of the sample or from the plateau when the flow stops (Fig. 13.14).

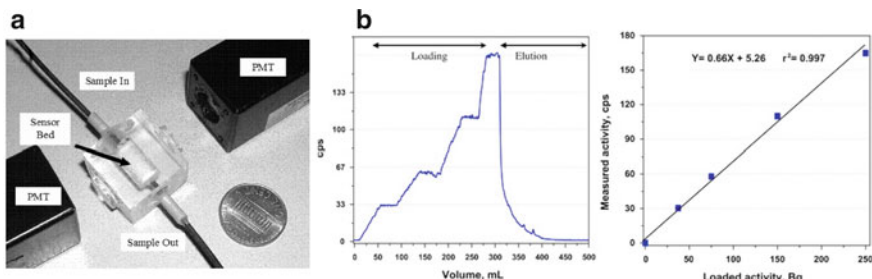


Fig. 13.14 **a** Photograph of a composite bed sensor cell. Cell volume is 385 μL (reproduced from [50] with permission from Springer Nature). **b** Optical detector response to a diethylamine (DOA) column sensor in the response to pertechnetate standards in a well water matrix, using a successive loading technique and the calibration curve resulting from the responses (reproduced from [17] with permission from Elsevier)

As the radionuclide accumulates on the surface of the scintillator, the amount of extractant available and the number of atoms of the radionuclide present in the sample determines the quantity of scintillator needed and the volume of sample that can pass through. Therefore, when non-stable isotopes are measured (e.g., Tc) the amount of extractive scintillator can be very small (below 1 g) or the amount of sample very large. However, when a stable isotope is also present in the sample (e.g., I) or the radionuclide has a very high decay constant (e.g., U), retention becomes limited by the capacity of the extractive scintillator. For example, for the ^{129}I resin [9], the capacity is 7.8 mg of iodide per gram of resin.

Regarding the use of plastic scintillation microspheres, this approach is only valid for the specific radionuclide that is retained in the column. It is, therefore, designed to deal with contaminated water sources or for the monitoring of a specific contaminant rather than for generic radioactivity detector purpose. Most of the reported systems are for the detection of ^{99}Tc , since this is a radionuclide with high mobility in water systems and it is produced in fission reactors as waste. Table 13.4 shows a summary of systems developed for online detection with extractive scintillators.

In off-line measurements using extractive scintillating resins, retention yields can be quantified later using a stable isotope and the activity consequently corrected. However, in online measurements, this correction cannot be made, and therefore, the yield must be quantitative or at least stable and determined previously. In the examples shown, the yields were always quantitative except for iodine, which was around 90%.

The potential absorption of interference should be evaluated previously on the basis of tests with them, or from the reports in the literature referring to the extractant used.

One of the limitations of this approach is related to the need for total regeneration of the extractive scintillator, in terms of both extraction and scintillation. Some of the first attempts based on the mixture of a solid extractant with scintillating beads or impregnated beads showed deterioration of the retention or scintillation capacity

Table 13.4 Summary of sensors based on plastic scintillation resins

Target	Scintillation resin	Cell	Detector	Efficiency	LoD
⁹⁹ Tc [6]	Aliquat-336 acrylic based	212 µL	Radiomatic 515A	25%–44%	6.1 Bq L ⁻¹ (50 mL, 30')
⁹⁹ Tc [10]	Aliquat-336 based	0.5 g in PTFE tube	Radiomatic 515A	56% off-line	6 Bq L ⁻¹ (50 mL, 30')
Alpha emitters [50]	Dipex based	4 cm U shape cell	Triathler (1PMT)	65%–70%	n.d.
⁹⁹ Tc [51]	AG4 × 4/BC400 mixture	385 µL	Custom-built	3.48·10 ⁻³ Hz per Bq/L	6.9 Bq L ⁻¹ (150 mL, 10')
⁹⁹ Tc [52]	TcES	2 mL fountain flow cell	Triathler (1PMT)	10.3%	11.3 Bq L ⁻¹ (200 mL)
¹²⁹ I [9]	MDOA based	0.05 g	LabLogic Beta-RAM	50%	0.4 Bq L ⁻¹ (222 mL, 3.7 h)
⁹⁹ Tc [17]	MDOA based	0.05 g	Flow-one (A-100)	66%	1.45 Bq L ⁻¹ (200 mL)
Uranium [18]	MS-MPA	30 mg	LabLogic Beta-RAM	40% off-line 23% on-line	n.d.

n.d. not determined

due to lixiviation of the extractant or the fluors during the process, or yellowing of the polymers during the cleaning process with nitric acid. The solution proposed for this situation was to attach the extractant to a cross-linked polymer via a covalent bond, as described in Sect. 13.2 of this Chapter.

13.4.3 Sensors Based on Plastic Scintillation Fibers (PSf)

Plastic scintillation fibers have been used, as plastic scintillation microspheres, for continuous online determination of the total amount of radioactivity due to alpha or beta emitters [53]. Compared to PSm, PSf present the advantage that light can be transmitted efficiently over quite large distances, which enables the fabrication of large volume cells suitable for achieving low limits of detection. On the downside, PSf present smaller surface areas than PSm, and consequently most of the designs make use of a high number of PSf and minimizing the interspace between them and the analyte. Moreover, for alpha emitters [54], a cladding of more than 30 µm would attenuate the alpha particles and therefore thinner cladding should be used if the goal is to measure alpha emitters or low-energy beta emitters. Furthermore, thick fibers have better light transmission but a lot of inactive volume, which reduces the

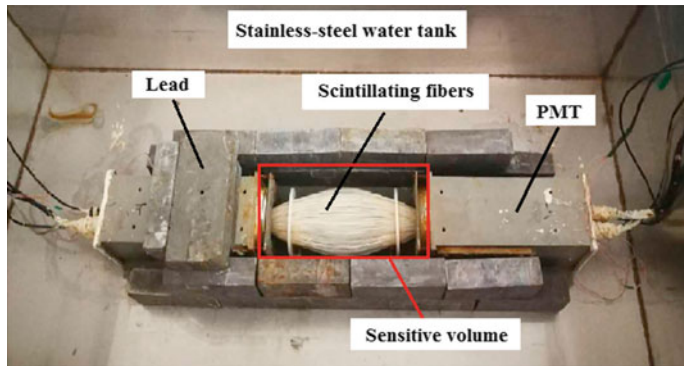


Fig. 13.15 Structure of the scintillating fiber array system (reproduced from [57] with permission from Elsevier)

efficiency of the system, particularly for particles with a short path. In general, the systems reported in the literature are still at the design or prototype phase [55, 56].

The most advanced system [57] is a sensor for real-time monitoring of gross beta radiation in water. It is based on a tank with a capacity of 283 L that contains 1,096 fibers of 1 mm diameter and 500 cm length, the PMTs, and lead shielding (Fig. 13.15).

Detection efficiency was 13.7% for ^{40}K with a background signal of 38.1 cps, and therefore, a detection limit of 1 Bq L^{-1} can be achieved with a measuring time of 2 h. Tap water was measured for 30 days in periods of 2 h. The found activity value ($0.09(0.03) \text{ Bq L}^{-1}$) was in agreement with the reference activity ($0.076(0.009) \text{ Bq L}^{-1}$). However, no description was given of regeneration of the system, analysis of different samples or stability of the system after several measurements.

13.4.4 Sensors Based on Plastic Scintillation Sheets

PS sheets have been used in several attempts to build a sensor for beta emitting radionuclides, especially to monitor tritium. However, in most cases, the limits of detection achieved were not satisfactory. First of all, PS sheets present a low surface/volume ratio and the path of the ^3H beta particles is too short. As a consequence, most of the sample volume is inactive and only betas emitted at the surface are detected [58]. Secondly, very few photons are produced per disintegration and therefore detection of low ^3H activities is only possible using active and passive shielding, and extremely sensitive PMTs.

Hee Reyoung Kim and collaborators designed a ^3H sensor (Fig. 13.16) based on a cell filled with thirteen thin plate plastic scintillators preceded by a PEM electrolytic cell for ^3H pre-concentration [59–63]. This system achieved a limit of detection of 10.3 kBq m^{-3} for air samples and 655 kBq L^{-1} for water samples. These high limits

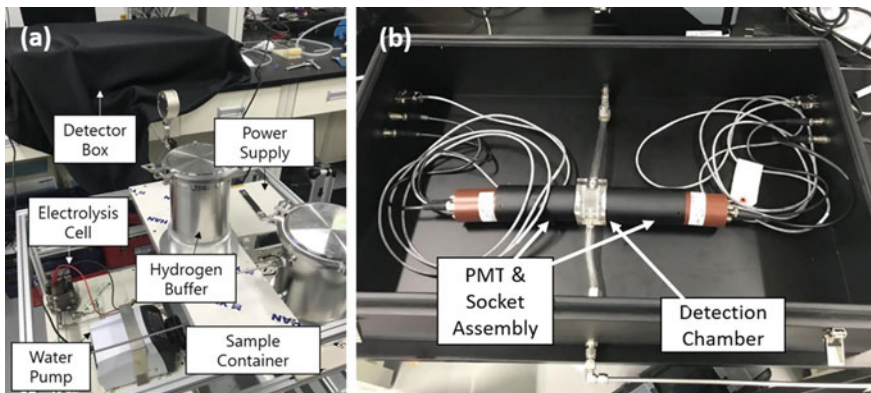


Fig. 13.16 Pictures of **a** the tritium monitoring system developed, and **b** the detection component (reproduced from [61] with permission from Springer Nature)

of detection are mainly due to the low detection efficiency of the device (8.7% for a high-energy beta emitter like ^{90}Sr and $2.7 \cdot 10^{-5}\%$ for ^3H) and the high background level observed (3.7 cps) due to the absence of shielding.

The situation is similar for a ^3H sensor designed to monitor water from a de-tritiation system for fusion reactors [64]. It contains a circular disk of plastic scintillator (29 mm in diameter and 0.5 mm thick) surrounded by the water sample and one PMT. Very high background (904 cps) and low detection efficiency lead to a very high limit of detection (29 MBq L^{-1}) which is higher than the target value.

Measuring ^3H in gas samples was also the objective of a sensor built by creating a channel into a PSblock [65]. The 22-cm long channel had a volume of 0.11 cm^3 and a surface of 2.2 cm^2 . With a detection efficiency of 0.32% and background of 0.6 cps, the limit of detection was $1,430 \text{ Bq mL}^{-1}$ for 10 s counting time: again, too high for regulation purposes.

A device for detecting alpha and beta emitters was built by using a U-shaped tube filled with a melted plastic scintillator (Meltilex, Perkin Elmer) (Fig. 13.17) and connected to a commercial scintillation detector [66]. Detection efficiencies ranged from 3.6% to 73.4% for beta emitting radionuclides, depending on the mean energy; and were no higher than 5% for alpha emitters, due to their short path. Limits of detection were of the order of a few Bq mL^{-1} .

13.5 Plastic Scintillators for Beta Emitting Radionuclide Analysis

The classical measurement of beta emitting radionuclides with plastic scintillators, of whatever shape, can be performed in a simple way similar to other common techniques such as liquid scintillation. The counting vial is filled with the plastic

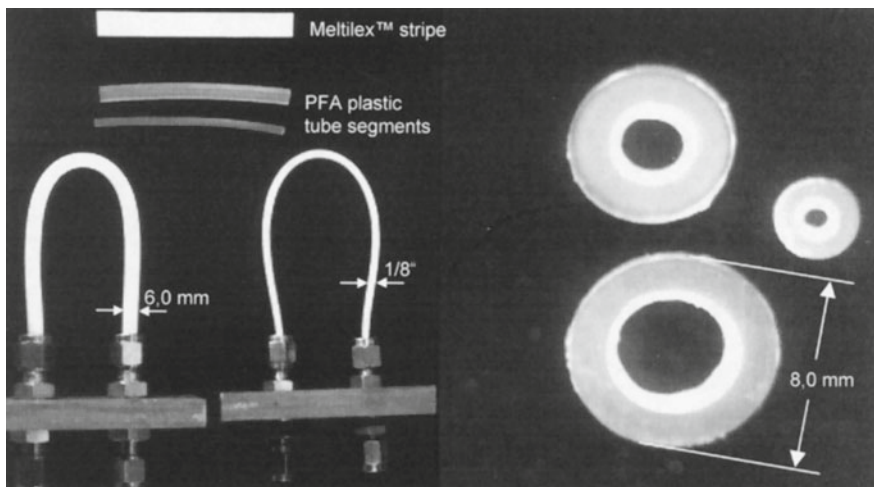


Fig. 13.17 Components of the detector cell. Left: raw materials, coated tubes, and mounted cells. Right: coated tube cross sections (reproduced from [66] with permission from Elsevier)

scintillator and the water solution is added to the vial filling the interstices between the different plastic scintillator pieces, then the vial is measured in a commercial scintillation detector. Usually, as for PSm, it is necessary to apply an additional step to ensure homogeneous distribution of the solution in the PSm interstices. To do this, it is recommended that the vial be shaken in a vortex for 3 min at 3000 rpm. Some examples of measurements with different plastic scintillator shapes are presented in Table 13.5 and Fig. 13.18. The optimized conditions described for the use of plastic scintillators include the use of 16 g of pellets (3 mm diameter) with 8 mL of sample solution, the use of 12 sheets ($0.5 \times 50 \times 13$ mm) with 18–20 mL of sample solution, or the use of 1.5 g of microspheres (60 μm) with 0.625 mL of sample solution [67, 68].

Table 13.5 Detection efficiencies for plastic scintillator measurements under different conditions: pellets, sheets, PSm and PSm-evaporated

Radionuclide	Detection Efficiency (%)					
	Pellets (3 mm)	Pellets (3 mm) without solution	Sheets	Sheets without solution	PSm (57 μm)	PSm (120–180 μm) without solution
^3H (water)	0.25	0.15	0.03	0.027	1.73	–
^3H (organic)	2.6	4.1	3.3	5.7	–	–
^{14}C	22	25	16	17	62.7	80.4
$^{90}\text{Sr}/^{90}\text{Y}$	50 ^a	62 ^a	42 ^a	24 ^a	190.3	192.8

^a Refers just to ^{90}Sr

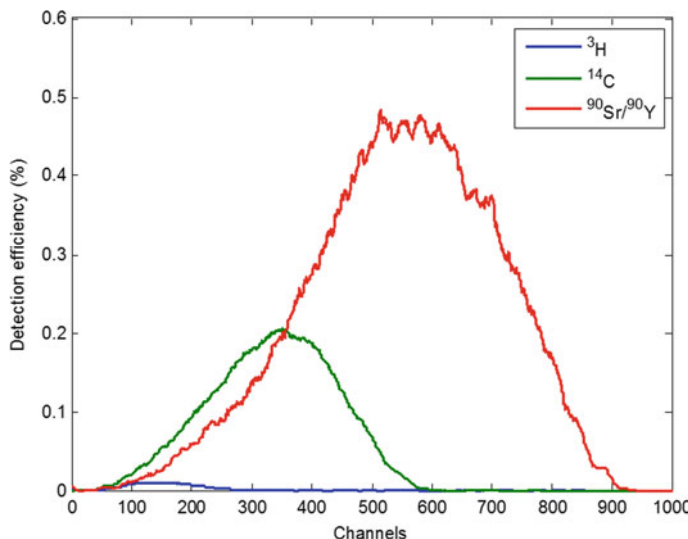


Fig. 13.18 Detection efficiency spectra measured using 1.5 g of PSm (57 μm) mixed with 0.625 mL of solution, for ${}^3\text{H}$, ${}^{14}\text{C}$, and ${}^{90}\text{Sr}/{}^{90}\text{Y}$

In these conditions, taking as an example the PSm, for those radionuclides emitting particles with medium or high energy, the detection efficiencies are high and comparable to those obtained with other techniques, 190% for ${}^{90}\text{Sr}/{}^{90}\text{Y}$ and 63% for ${}^{14}\text{C}$. In contrast, for low-energy beta emitting radionuclides such as tritium, the detection efficiency is quite low: 1.73%. Table 13.6 also reflects the influence of the shape of the plastic scintillator on detection performance. In another example, the ${}^{14}\text{C}$ detection efficiency decreases considerably with the use of pellets or sheets, to 22% and 25%, respectively. In fact, as explained above, this decrease is related to the distance that beta particles need to travel before reaching the plastic scintillator and the composition of the medium. Therefore, in those cases where the distance is reduced or the medium is less dense, such as with the increase of plastic scintillator surface through the decrease of the plastic scintillator size, or the decrease of sample volume between the plastic scintillator pieces, the detection efficiency increases [21].

Table 13.6 Detection efficiencies measured using PSm of different diameters for three radionuclides (reproduced from [69] with permission from Springer Nature)

Size (μm)	Detection Efficiency (%)		
	${}^3\text{H}$	${}^{14}\text{C}$	${}^{90}\text{Sr}/{}^{90}\text{Y}$
17	4.51	74.3	192.9
32	2.69	68.7	189.8
57	1.73	62.7	190.3
79	1.16	54.5	186.7
145	0.81	45.1	184.8

This can be clearly observed in Table 13.6, which shows the influence of diameter on detection efficiency. When the diameter decreases, and therefore, the surface increases, and consequently the mean path that the electrons travel decreases, the detection efficiency increases. This effect is more important for low-energy beta emitting radionuclides such as ^3H than for high-energy emitters such as $^{90}\text{Sr}/^{90}\text{Y}$ which, due to the higher energy, and therefore, higher penetration power, is not greatly influenced by the PSm diameter. However, even when it looks as if the lower the diameter, the better the capabilities, other factors such as light transmission, affected by refractive index successive variations between water and the plastic scintillator, influence the detection capabilities. This means that the use of PSm of $60\ \mu\text{m}$ diameter is the best trade-off [69].

Summarizing, the detection efficiency depends on the mean path that the beta particle has to travel before reaching a plastic scintillator, and therefore, it depends on the shape and size of the plastic scintillator used. However, other approaches can be used to improve detection efficiency such as removing the solvent from the vial, which increases the distance the beta particles can travel, as this is higher in air than in water [70]. Table 13.5 shows two approaches to achieve this. In the first one, the solution is poured out, after absorption of the radionuclide in the plastic scintillator for a 7-day period, and this is used for pellets and sheets. In the second procedure, used for PSm, the solution is evaporated to dryness in an oven at $40\ ^\circ\text{C}$. The first procedure can only be applied to radionuclides that can be absorbed into the plastic scintillator. A good example is organic ^3H (as opposed to tritiated water, which is not absorbed), which shows a high detection efficiency in solution, due to absorption into the plastic scintillator. This efficiency is almost doubled when the solution is removed [68]. The absorption in the plastic scintillator, which changes over time, can be avoided in many plastics through the use of acid media, thereby obtaining a stable signal over time [71]. Meanwhile, the evaporation method can be applied to almost all radionuclides (those that are not volatile) and is easy to control, avoiding the difficulties related to the complete removal of the solvent by pouring it out, especially with pellets. However, this measurement method is affected by any salts eventually contained in the sample which are deposited on the plastic scintillator surface during evaporation and therefore produce quenching [70].

The use of plastic scintillators for the measurement of beta emitter radionuclides shows advantages in two other scenarios: measurements from samples with aggressive media (highly acidic or oxidant conditions) or with high salt concentrations. The possibility of synthesizing resistant plastic scintillators, with the inclusion of a cross-linker in their structure (C-PS), allows measurements to be taken from organic samples or in aggressive media without plastic scintillator degradation (Table 13.7) [12]. In these conditions, the detection efficiencies in organic media are comparable or even higher than those in aqueous media, due to better contact between the C-PS and the sample resulting from their similar polarity.

For salt samples, the intrinsic heterogeneity of the system (plastic scintillator-sample) means that the measurements are not affected by problems such as phase separation that usually occur in liquid scintillation [67].

Table 13.7 Detection efficiency values for ^3H , ^{14}C , and $^{90}\text{Sr}/^{90}\text{Y}$ in some of the organic and aggressive media studied, using 0.6 g of C-PS and 0.25 mL of solution [12]

	Medium			
	Toluene	Methanol	H_2O	HNO_3 (69%)
^3H	—	7.6	1.01	0.32
^{14}C	83.6	80.4	39.5	6.3
$^{90}\text{Sr}/^{90}\text{Y}$	189.4	181.0	175.7	131.2

Another important aspect in the measurement of beta-emitter radionuclides by plastic scintillators is the quenching correction. For color or chemical quenching, the usual procedures for calibrating detection efficiency as a function of a typical quenching parameter, such as the spectral quenching parameter of the external standard SQP(E) in the Wallac detectors, can be performed by measuring a set of standards prepared with different levels of quenching. However, for other quenching sources such as the salt content, different parameters like density must be applied [72]. An example of the combined correction for both kinds of quenching is shown in Fig. 13.19 using SQP(E) for the color quenching correction and density for correction of the salt content. Using this procedure, a relative efficiency was obtained for each quenching effect which, when multiplied by the unquenched detection efficiency, provided the desired correction.

As has been shown throughout this chapter, plastic scintillators allow beta-emitting radionuclides to be measured in different ways and situations. Probably the

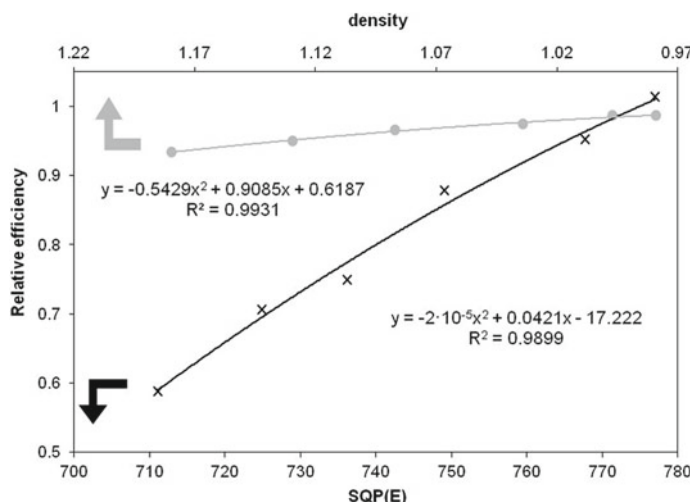


Fig. 13.19 Relative detection efficiencies as a function of SQP(E) for changes in the color quenching and solution density together with changes in the salt content (reproduced from [67] with permission from Elsevier)

most important of these, however, are based on the versatility of plastic scintillators to develop selective strategies for the measurement of specific radionuclides. This is the case of PSresins that include an extractant on the plastic scintillator surface, thereby allowing separation and measurement of the radionuclide using the same plastic scintillator support.

The usual way to work with PSresins is to pack them into a column using frits to constrain them, for example, as in a solid phase extraction (SPE) cartridge, and connect the column to a pump or vacuum chamber that allows the solutions to pass through it. Once the column is conditioned, the sample is passed through it and finally it is rinsed to remove any interference. Usually, the same medium, optimized for the selective retention of the radionuclide, is used in all the steps. However, other media can be used to rinse the column in order to remove specific sources of interference. The column can then be disconnected from the pump or vacuum chamber and measured directly in a commercial scintillation counter, using a 20 mL scintillation vial or a support. Alternatively, it can be continuously measured, as explained in Sect. 13.4.2, by placing the column inside a detector for the whole process. In this scenario, an additional step is applied to the column that consists of the elution of the radionuclide to prepare it for subsequent measurements.

As explained before, the removal of the solvent after mixing the sample with the plastic scintillator allows an increase in detection efficiency compared to measurement in solution; therefore, before PSresin columns are measured, it is recommended to completely empty the column by pumping the solution out, thus increasing the detection efficiency and also the reproducibility.

Another important aspect to be taken into account when working with PSresins is the radionuclide retention yield which, when working with complex matrices, can change from sample to sample. Retention yield can be determined by adding a tracer to the sample. In PSresin separation retention yield is calculated by the difference between two measurements: the amount of tracer in the solution before it passes through the column and its amount in the solution collected afterward. This solution includes the sample but also the rinse solutions passed through the column. This procedure is slightly different from that used with non-scintillating columns, where only one measurement is performed to establish the concentration of tracer in the solution of the eluted radionuclide. This same procedure can also be applied with PSresins if the radionuclide is eluted, for example, in the continuous measurement sensors but only if the elution is quantitative.

Special care has to be taken in retention yield quantification if the stable isotopes of the radionuclide being analyzed are also present on the sample. If the amount of stable isotope is high enough, the initial natural amount of the stable isotopes can be used directly as a tracer. If not, the amount of tracer added has to be at least 20 times higher in order to provide a good determination of the yield.

The final aspect to be highlighted when working with PSresins is that the quenching of the measurements is reduced due to the removal of the matrix solution from the column during the loading and rinsing steps. As a consequence, the usual procedure is to use constant detection efficiency, independent of the sample.

Several PSresins have been developed over the years, especially for radiostrontium and ^{99}Tc . For radiostrontium, three different resins were prepared based on the use of a crown ether as the selective extractant. Two of them used SuperLig 620 commercial resin in the fabrication: in one of them, the resin was mixed with commercial PSm; and in the other, the plastic scintillator monomers were polymerized onto the resin surface [15, 27]. Both resins retained strontium in a low concentrated HNO_3 medium (0.1 M), showing high retentions: 88% and 92%, respectively. The former was lower due to the encapsulation of the binding sites inside the plastic scintillator surface. However, the detection efficiencies were relatively low, 51 and 63%, due to the configuration of these resins. The third resin was prepared by coating the extractant 4,4'-(5')-di-*t*-butylcyclohexano-18-crown-6 (DtBuCH18C6) onto the PSm surface [28]. With this configuration, better properties were achieved: quantitative retention and 83% detection efficiency, using a 6 M LiNO_3 medium. This medium was used to avoid the chemiluminescence of the plastic scintillator produced when high HNO_3 concentrations are used. This resin was successfully applied first in the measurement of spiked water samples at low activity levels for environmental monitoring (drinking, sea and river water) with errors lower than 4%. Then it was used with more complex matrices (e.g., milk, air filters and vegetation) in higher activities like those expected in emergency situations [28, 73, 74]. In those complex matrices, the yield decreased to 70% mean retention, especially for milk due to the low capacity of the column and the high content of calcium and stable strontium of the sample. However, an increase in the detection efficiency was obtained, up to 93%, through the use of SPE cartridges, which allow better light transmission, but especially thanks to the removal of the solution before measurement, which, as explained above, increases detection efficiency. With these samples, errors lower than 7% were achieved for the spiked samples and also for the reference material samples, and the resin also showed a high selectivity for strontium. Furthermore, this PSresin column also allowed the separate quantification of ^{90}Sr and ^{89}Sr , by applying deconvolution methods, with errors lower than 30%.

One of the disadvantages of these radiostrontium PSresin columns is the strong retention of lead, which can interfere in the measurement as ^{210}Pb . Lead can be removed successfully from the solution via previous precipitation with KIO_3 in an acidic medium heating until boiling. In any case, the retention of lead allows the use of these PSresin for the quantification of ^{210}Pb , using a 2 M HNO_3 medium. Under these conditions, 90% retention and 44% detection efficiency were achieved, obtaining errors lower than 10% in the measurement of spiked well water and river water samples [75].

Regarding ^{99}Tc , almost all the resins prepared used quaternary ammonium salts as the extractant, with Aliquat-336 being by far the most commonly used. In almost all the resins developed, a quantitative technetium retention was achieved, using a neutral or slightly acidic medium (HCl or HNO_3). Egorov et al. developed an initial resin using Aliquat-336 by diffusing it, together with the fluorescent molecules, in a plastic support. They obtained 42% detection efficiency, but with losses of fluorescence molecules when the radionuclide was eluted with a 4 M HNO_3 medium. Nevertheless, a method for the renewal of the resin was applied for its use in a continuous detector,

and the method was successfully employed in the analysis of spiked groundwater samples [6]. As an alternative to overcome this fluorescent molecule loss, a mixture of AG 4-X4 resin and PSm was used as the resin, but poorer performance was obtained: 82% retention and 38% detection efficiency, probably due to the increase on the inactive scintillating volume [27]. Meanwhile, DeVol and coworkers developed several resins for application in a continuous sensor, starting with the immobilization of Aliquat-336 and ABEC resin extractant (Eichrom, USA) in PSm, as well as a mixture of TEVA resin (Eichrom, USA) and commercial PSm (but this last one was ruled out due to its low detection efficiency: 7.5%). They obtained detection efficiencies ranging from 50% for the Aliquat-336-based resins to 79% for the ABEC-based resin, with good results in their application to spiked groundwater sample quantification [10].

The intention to apply these resins in a continuous detector led to the further development of resins using covalently bound extractants (triethylamine, TEA, and methyldiethylamine, MDOA) and polymerizable fluorescent molecules, in order to avoid the loss of resin performance while reusing, as observed with previous resins [8, 14]. Whereas the detection efficiencies continued to be acceptable, and the retention was quantitative, reusability was the main challenge in the development of sensors for continuous monitoring, due to other factors such as the difficulty in eluting the radionuclide. In a similar way, Harjula and coworkers prepared different resins with a polymerizable fluorescent molecule and covalently bound extractants (octylamine nOA, diethylamine DOA and triethylamine TOA). They obtained good detection efficiencies for the secondary and tertiary amines, 58% and 68%, respectively, with DOA being capable of eluting the radionuclide (5 M HNO_3), and therefore, being used in a continuous sensor with no influence on the signal with regards to the water matrix (tap, well and river water) [17].

Our group also developed a ^{99}Tc resin by coating Aliquat-336 onto the PSm surface, obtaining quantitative retentions and detection efficiency of 70% and 85% when using 7 mL column vials or SPE cartridge, respectively. This PSresin was applied to the measurement of seawater and urine, as well as to river water, seawater, and reference material using an automatic treatment system, with errors always lower than 10%. The resin showed selectivity among nonradioactive anions and also when faced with sources of radioactive interference, such as uranium or chloride, with the use of HF/ HNO_3 and HCl as rinsing steps, respectively. A slight increase in detection efficiency up to 84% was achieved when 0.1 M HF/0.1 M HNO_3 was used [76, 77] probably due to a modification of the PSresin surface. This PSresin also presented the advantages of having a breakthrough volume higher than 200 mL, and the fact that rhenium can be used as a tracer. Finally, an extractive plastic scintillator membrane, also prepared with Aliquat-336, was developed for ^{99}Tc measurement [78]. In this case, the use of the membrane (2 cm × 1 cm × 900 μm) included its equilibration with the radioactive solution for 4 h beforehand, rinsing with distilled water and drying. This membrane showed 95% retention and 72% detection efficiency, as well as the possibility of being reused after desorbing the technetium with a 2 M HNO_3 medium.

The Tc PS resin developed by our group was in fact initially prepared for the analysis of ^{14}C -labeled thiocyanate used as a radiotracer in the study of the size and behavior of oil reservoirs. As this extractant shows a strong retention for thiocyanate, quantitative retention was obtained with 54% detection efficiency and quantification errors lower than 5%. This PSresin was applied to the analysis of production water from oil reservoir, obtaining the same results as those obtained with the standard quantification method and with no degradation of the resin after processing 100 mL of this sample containing oil residues [29].

Other applications of the ^{99}Tc PSresins were those corresponding to the measurement of ^{129}I , using a covalently bound MDOA extractant on a polymeric support, with the fluorescent molecule diffused inside: 91% retention and 50% detection efficiency were obtained [9]. Also, by using the Aliquat-336 scintillating membrane, 80% retention and 60% detection efficiency were obtained [78].

The last application is a PSresin for the quantification of ^{126}Sn , prepared with tributyl phosphate (TBP), as the extractant, impregnated in a C-PS support, to avoid polymer dissolution by the extractant. Quantitative retention and 84% detection efficiency were achieved when 2 M HCl was used, an optimal media to separate tin from common sources of interference. This PSresin was applied to the quantification of a partially treated reprocessing sample with quantification errors lower than 5% [31].

Tritium is another radionuclide for which specific strategies based on plastic scintillator have been developed. In this case, no PSresins can be developed, due to the nature of the tritiated molecules, but other methods were developed by Furuta et al. [79] based on two different strategies: modification of the plastic scintillator surface and measurement of the volatilized sample. For the former strategy, a plasma flow at atmospheric pressure was used to increase the hydrophilicity of the plastic scintillator surface, supposedly by the formation of carbonyl groups or the unevenness of the surface. After applying the plasma for 2 min, it was possible to analyze 20 μL of tritiated water with an activity of 2 Bq between two PSsheets ($50 \times 15 \times 0.5$ mm) with 48% detection efficiency after 6 h of equilibration [80]. Despite the high detection efficiency, the sample volume was limited and the surface changes on the PSsheets did not seem to be permanent, but at least 1 week under freeze storage. This strategy was continued for the analysis of tritiated organic molecules by evaporating the sample in larger sheets (48 mm diameter) that covered the whole photomultiplier, thereby allowing an increase of the sample volume up to 2 mL with 33% detection efficiency [81].

The latter strategy applied to the measurement of tritiated water involved the volatilization of a small amount of sample in a vial full of 3 mm diameter plastic scintillator pellets (15.5 g in a 20 mL scintillation vial) [82]. Analyzing just 5 μL of volatilized sample, 45% detection efficiency was obtained, since these conditions of measurement reduce the particle quenching and allow more emitted electrons to reach the plastic scintillator pellets. However, this particle quenching dramatically increased with the increase in sample volume, obtaining just 3.1% detection efficiency when 500 μL of sample was analyzed. Again, the method exhibited strong volume limitations. This was partially minimized by the increase of the vial size, which allowed the use of larger volumes of sample, e.g., with 100 mL vials

(72.5 g of plastic scintillator pellets). For 500 μL of sample, 20% detection efficiency was achieved, but this was still limited to a maximum of 1 mL, that yielded 11% detection efficiency. This configuration was applied to a prototype for the measurement of tritium in expired air. The system analyzed 5 L of expired air collected in a bag, recovering around 100 μL of water. However, when the procedure was applied, combined recovery and detection efficiency was just around 5%, showing the difficulties associated with ${}^3\text{H}$ measurements with plastic scintillators [83].

13.6 Plastic Scintillators for Alpha Emitting Radionuclide Analysis

The measurement of alpha emitting radionuclides by plastic scintillator is performed in a similar way to the measurement of beta emitting radionuclides, in which the plastic scintillator is placed in the scintillation vial and the aqueous sample is added, filling the interstices between the different plastic scintillator particles, after the application of a homogenizing procedure. A typical preparation is, in a 20 mL scintillation vial, 1.5 g of PSm with 0.625 mL of solution which is shaken for 3 min at 3000 rpm. The typical detection efficiencies obtained are presented in Table 13.8 [69].

In this case, in spite of the high energy of the alpha particles emitted, due to their low penetration power, the distance that the particles have to travel before reaching the plastic scintillator is still the main variable that influences detection efficiency. In this way, larger diameters PSm such as 416 μm , produce a detection efficiency of 34% for ${}^{241}\text{Am}$ and even lower, 24%, for ${}^{236}\text{U}$, due to the lower energy of its alpha emissions. The detection efficiency increases with the decrease in diameter, reaching values of 89% for ${}^{241}\text{Am}$ and 81% for ${}^{236}\text{U}$ with a diameter of 60 μm .

This phenomenon of energy loss before reaching the plastic scintillator also causes another effect: a “tail” at low energies, as can be observed in Fig. 13.20. The decrease of the size of the plastic scintillator (i.e., the diameter in the PSm) reduces particle quenching, it also reduces the tail at lower energies, which almost disappears when 17 μm diameter PSm are used. It is also interesting to note the shift of the maximum energy of the spectrum to lower energies, with the decrease of the diameter; this

Table 13.8 Detection efficiencies for ${}^{241}\text{Am}$ and ${}^{236}\text{U}$ using PSm of different diameters in solution and after solution evaporated

PSm diameter (μm)	Detection Efficiency (%)			
	${}^{241}\text{Am}$		${}^{236}\text{U}$	
	Solution	Evaporated	Solution	Evaporated
60	89	100	81	96
106	51	99	37	95
327	44	100	29	99
416	34	100	24	98

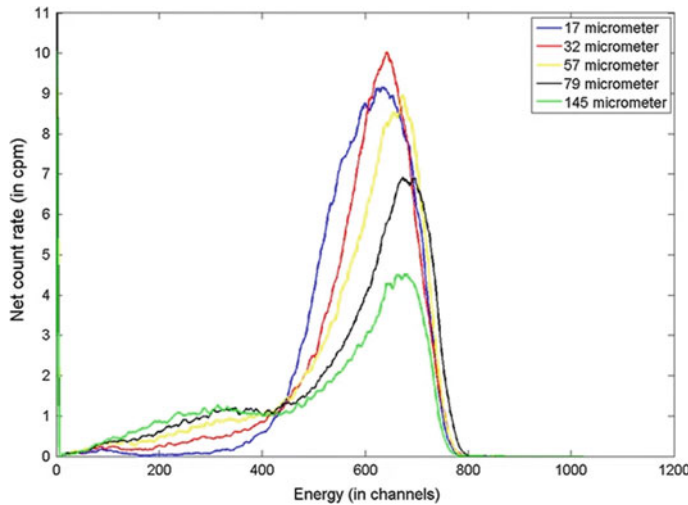


Fig. 13.20 Detection efficiency of ^{241}Am as a function of PSm diameter (reproduced from [69] with permission from Springer Nature)

is, the result of reduced light transmission (i.e., optical quenching) of the photons emitted by the PSm.

Analogously to what happens with beta particles, evaporation to dryness of the sample on the PSm improves detection efficiency by decreasing quenching, as can be observed in Table 13.8. When the sample is evaporated, the detection efficiencies reach around 100%, regardless of the diameter employed or the energy of the alpha particle emitted, as in the ^{236}U case. Sample evaporation also affects the spectra (Fig. 13.21), as the tail at lower energies completely disappears.

All these effects influence the plastic scintillator performance for alpha particle measurement, and particularly the gross alpha index determination. This measurement, as well as gross beta index determination, requires discrimination between the signals generated by alpha and beta particles emitted by the radionuclides in a sample. To this end, a pulse shape discrimination procedure needs to be applied. As can be observed in Fig. 13.22, the misclassification (i.e., the proportion of particles wrongly classified) obtained with PSm in a common measurement, with the liquid sample in the interstices of the PSm, is quite high in certain discrimination conditions (PSA is the pulse shape discrimination parameter of the Wallac detectors), and in particular, for alpha particles. This is related to four different factors: energy propagation in plastic scintillators, the tail of the alpha spectrum at lower energies due to particle quenching, the settings of the scintillation detectors, and the plastic scintillator composition [22, 70, 71].

Regarding the first factor energy propagation in plastic scintillators is very fast, making it difficult to differentiate the light pulses emitted by alpha and beta particles. Moreover, the tail at lower energies, produced by quenching, is usually classified as a beta emission, probably because very few photons are included in the pulse.

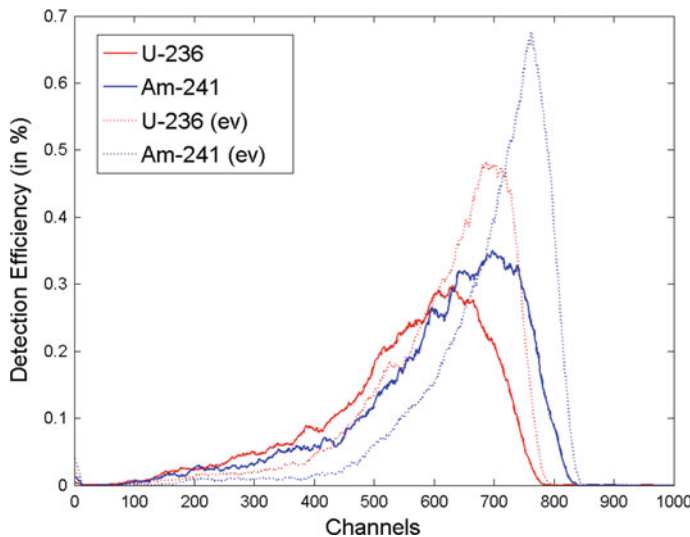


Fig. 13.21 Detection efficiency spectra for ^{241}Am (blue) and ^{236}U (red) in solution for a 3 g PSm of 60 μm in diameter with 1.25 mL and evaporated to dryness (ev) at 40 °C

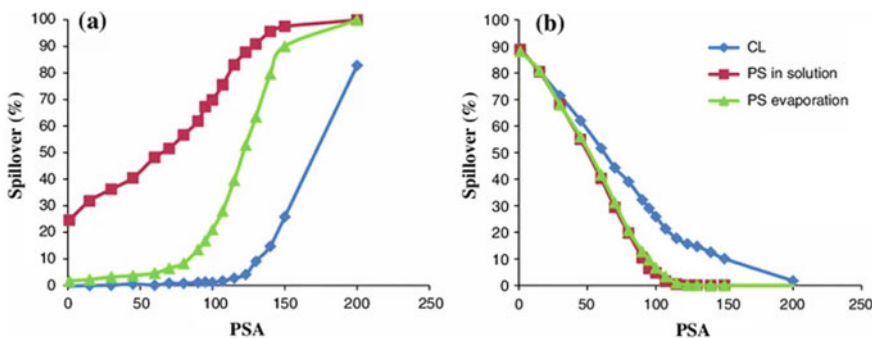


Fig. 13.22 Misclassification for **a** ^{241}Am ; and **b** $^{90}\text{Sr}/^{90}\text{Y}$, obtained by LS (blue), and PSm in solution (red) and after evaporation to dryness (green) as a function of the PSA, the pulse shape discrimination parameter of the Wallac detectors (reproduced from [70] with permission from Springer Nature)

Therefore, the removal of this tail, for example via the evaporation of the sample, produces a considerable improvement of the classification error for alpha emissions, but with little influence on the beta emission classification, as can be observed in Fig. 13.22.

Commercial scintillation detectors, in general, use a configuration for alpha/beta discrimination based on the performance of liquid scintillators. As the plastic scintillator has a faster response, their use in commercial detectors usually leads to greater

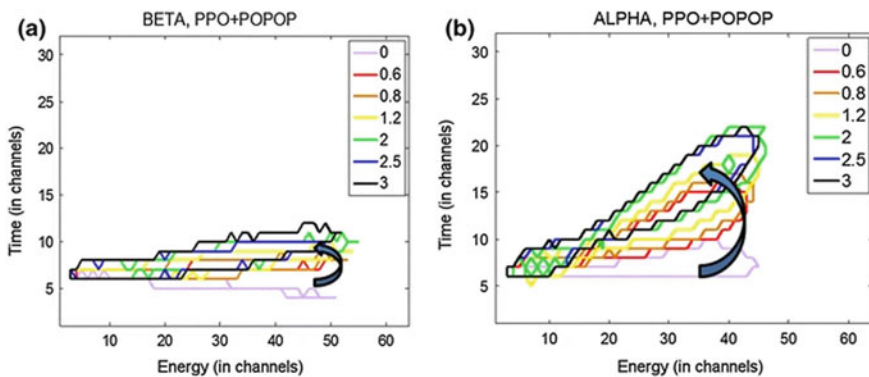


Fig. 13.23 Misclassification using a Triathler detector for **a** $^{90}\text{Sr}/^{90}\text{Y}$; and **b** ^{241}Am , using PSm with different naphthalene content (referred to 10 g of polystyrene) (reproduced from [22] with permission from Elsevier)

errors in the classification of alpha emissions, whereas they are lower for beta emissions. The use of detectors with advanced discrimination configurations, such as Triathler, allows this issue to be avoided (Fig. 13.23).

Finally, plastic scintillator composition affects the duration of the pulse, therefore, the inclusion of secondary solvents, such as naphthalene or diisopropylnaphthalene (DIN), causes a delay in the signals produced by alpha particles, with little influence on the signals produced by beta particles, thus improving the separation, as can be observed in Fig. 13.23.

Taking into account these effects, three procedures have been developed for the measurement of gross alpha/beta indexes using pulse shape discrimination. The first of these uses the common measurement configuration, with the aqueous solution in the interstices of commercial PSm (without a secondary solvent) [71]. In this case, as the use of a compromise PSA value produced high misclassification errors, two PSA values were selected: one without interference from beta emissions in the alpha spectra, and a second with low alpha interference in the beta spectrum, which was then subtracted using the first value obtained. Using this procedure, errors lower than 7% were obtained in the quantification of spiked river water samples.

The second procedure involves evaporating the solvent after mixing the sample and the plastic scintillator, to remove the low-energy tail of the spectra. In this case, the deposition of the sample salts on the plastic scintillator produced quenching, especially when samples with high salt contents or large volumes of sample were analyzed. In this situation, the use of a compromise PSA value still produced high errors. However, when the previous double-PSA system was applied, with a constant salt residue deposited on the PSm, errors lower than 10% were mostly obtained for the quantification of spiked drinking water samples. Using this procedure, even when the errors were not improved, the volume was increased (to around 50 mL) allowing limits of detection within the water directive requirements to be obtained [70].

Finally, a third procedure modifies the PSm composition by adding DIN to its structure and measuring using a Triathler detector. This procedure allowed the use of an integration area in the 3D count rate spectrum, yielding misclassification of 1% and 2% for ^{241}Am and $^{90}\text{Sr}/^{90}\text{Y}$, respectively, but with a decrease in detection efficiency [22].

The measurement of the gross alpha index was also studied with the use of PSresins developed for the selective measurement of actinides, but which have mostly been applied to the measurement of specific radionuclides, especially uranium. Several extractants, immobilized and covalently bound to the plastic scintillator support have been assayed, in almost all attempts using a phosphonic acid group as the basis of the extractant. This allowed separation, usually in weak or moderate nitric acidic media (0.0001 or 2 M), with different retentions and detection efficiencies.

The first resin developed by DeVol and coworkers was prepared by impregnating a cross-linked polystyrene support with the fluorescent molecules and extractant: octyl(phenyl)-*N,N*-diisobutyl-carbamoyl-methylphosphine oxide (CMPO) dissolved in TBP [7]. The retention was quantitative in a 2 M HNO_3 medium, and the detection efficiencies were around 97%. The procedure allowed the sequential elution of ^{241}Am , ^{239}Pu and ^{233}U for individual radionuclide quantification. Even when it is claimed that the different media are used, causing a decrease in the detection efficiency of ^{239}Pu , low errors were obtained for the quantification of high-level waste. However, the loss of the fluorescent molecules did not allow the use of this resin in a continuous sensor, and therefore, others were developed for this application.

The Dipex extractant was tested as a mixture of a non-scintillation resin with commercial PSm (Saint-Gobain Crystals and Detectors) (discarded due to its low detection efficiency), and with two polymeric supports impregnated with the fluorescent molecules. The polystyrene support achieved quantitative retention in a 0.1 M HNO_3 medium, and detection efficiencies of 52 and 66% for natural U and ^{241}Am , respectively. The errors using this resin in the quantification of groundwater samples were lower than 18%, when the activity was high enough [51]. MnO_2 was also tested as an extractant, for the separation of natural U in neutral media, by depositing it on the plastic scintillator surface; however, low retention (25%) and lower detection efficiency (37%) were obtained [84]. A reusable resin was achieved via two strategies: the use of phosphonic acid covalently bound on the plastic scintillator surface; and copolymerization of the plastic scintillator with ethylene glycol methacrylate phosphate, EGMP, also using a polymerizable fluorescent molecule to avoid its loss [16, 18]. The resins obtained showed a certain hydrophobicity which suggested it was necessary to wet the column with ethanol before use. In a pH 4 medium, this setup yielded ^{233}U retentions of around 50% and detection efficiencies around 40%. The resin based on EGMP was preferred because it showed better optical characteristics and retentions as well as being easier to prepare. A similar development was followed for the preparation of extractive scintillation membranes. Using bis(2-ethylhexyl)phosphoric acid (HDEHP) as the extractant, different polymers and plasticizers were used to prepare the membrane by evaporation of the polymer solution. 80% retention and 98% detection efficiency was reported for the measurement of ^{241}Am in a pH 2.5 medium, when cellulose triacetate (CTA) and poly(methyl

methacrylate) (PMMA) were used [85]. This design evolved to use a polymerizable extractant, bis[2-(methacryloyloxy)ethyl]phosphate (MEP) which was polymerized in two support membranes, encapsulating the fluorescent molecules in the process. Using a poly(ether sulfone) support membrane, 99% retention and 81% detection efficiency for ^{241}Am was obtained. This membrane was applied to the quantification of a soil sample spiked with several Pu isotopes, with a 1% error [5].

13.7 Conclusion

Environmental analysis is characterized as being a very complex situation due to the variability and quantity of radionuclides potentially present in the samples and the vast variety of matrices to deal with. Moreover, radionuclides are present at low activities, and therefore, the methodologies employed require complex chemical treatments, long counting times, and highly efficient techniques to perform the analysis. In this scenario, plastic scintillators, especially contribute to addressing those complex situations where classical methodologies for the analysis of beta and alpha emitting radionuclides (liquid scintillation and alpha spectrometry) do not provide adequate information: direct surface analysis; online monitoring; fast and selective determinations.

The adaptation of plastic scintillators for environmental analysis requires polymers with specific shapes and sizes. From the different types of plastic scintillators, those with high surface area allow the maximum amount of sample to be in close contact with the plastic scintillator, such as spherical microparticles, are especially well suited for the analysis of alpha and beta emitters radionuclides. This is because the distance traveled by the particle before reaching the scintillator is low enough (micrometer range) to permit that alpha particles and even low-energy beta particles, as those emitted by ^3H , could be detected. Detection efficiency is correlated with the diameter of the particles and values from 1 to 3% are described for radionuclides as ^3H ($E_{\max} = 18.6 \text{ keV}$); 50–100% for alpha radionuclides and 100% for high-energy beta emitters as ^{90}Y ($E_{\max} = 2.2 \text{ MeV}$).

There are several procedures described to produce plastic scintillators for environmental monitoring purposes, particularly in form of microspheres. Most popular methods are extraction/evaporation and polymerization. Procedures for preparing plastic scintillation microspheres include control of microspheres size (from few micrometers to half a millimeter), but also the incorporation of pores in the structure and the inclusion of reactive functional groups, usually a chlorine moiety, which subsequently can lead to the linkage of an extracting agent in the scintillator surface through a chemical bond.

Online monitoring of liquid effluents is one of the most popular uses of PS for environmental purposes. On one hand, when the sample flows through microspheres of very low diameter ($60 \mu\text{m}$) packaged in a counting cell, limits of detection achieved are very close to drinking water detection levels for alpha and beta screening parameters and ^3H . This is due to the high detection efficiencies observed and the use of

active and passive shielding strategies. On the other hand, online analysis of specific radionuclides in liquid samples has been done by the use of extractive plastic scintillators (PSresins) coupled to online detection. PSresins have been developed by coating the plastic scintillation particles with the corresponding extractant agent and present the advantage that the radionuclide is being accumulated on it with the flow of the solution. Contamination processes of very low activity can be followed using small amounts of PSresin. Other types of PS (sheets or fibers) have been used in several prototypes, however, they are usually limited by the low capacity of such shapes for detecting alpha and low beta emissions or very low activity levels.

Regarding specific analysis of radionuclides in complex samples (from water to milk, vegetation or sludge), the strategy based on the selective deposition of the radionuclide of interest in the surface of the plastic scintillator is the most used. Methods for ^3H , ^{90}Sr , ^{99}Tc , ^{14}C , ^{129}I , ^{126}Sn and uranium isotopes have been described. Usually, extractive scintillating resins are chosen for this purpose but are packed on a plastic cartridge or a tube in a similar way as common resins for solid-phase extraction. This approximation permits a reduction of time analysis and generated waste, as no elution step is required since the extractive scintillator can be used for both separation and measurement. Results obtained with this strategy are very satisfactory since detection efficiencies are usually high as well as the recoveries.

References

1. Council directive 2013/51/EURATOM, OJ L 296, 7.11.2013, p.12 (2013). <https://eur-lex.europa.eu/LexUriServ/LexUriServ.do?uri=OJ:L:2013:296:0012:0021:EN:PDF>. Accessed 25 Oct 2020
2. EPA, U.S. Environmental Protection Agency. Radionuclides in drinking water. Washington DC (2016). <https://www.epa.gov/dwreginfo/radionuclides-rule>. Accessed 13 Oct 2020
3. H. Kang, S. Min, B. Seo, C. Roh, *Chemosensors* **8**, 106 (2020)
4. R. Merín, A. Tarancón, K. Mitev, S. Georgiev, C. Dutsov, H. Bagán, J.F. García, *J. Radioanal. Nucl. Chem.* **319**(1), 135 (2019)
5. V. Chavan, C. Agarwal, A.K. Pandey, *Anal. Chem.* **88**(7), 3796 (2016)
6. O.B. Egorov, S.K. Fiskum, M.J. O'Hara, J.W. Grate, *Anal. Chem.* **71**(23), 5420 (1999)
7. J.E. Roane, T.A. DeVol, *Anal. Chem.* **74**(21), 5629 (2002)
8. A.F. Seliman, A. Samadi, S.M. Husson, E.H. Borai, T.A. DeVol, *Anal. Chem.* **83**(12), 4759 (2011)
9. K.P. Grogan, T.A. DeVol, *Anal. Chem.* **83**(7), 2582 (2011)
10. T.A. DeVol, O.B. Egorov, J.E. Roane, A. Paulenova, J.W. Grate, *J. Radioanal. Nucl. Chem.* **249**(1), 181 (2001)
11. D. Zhu, M. Jay, *Nanotechnology* **18**(22), 225502 (2007)
12. H. Bagán, A. Tarancón, L. Ye, J.F. García, *Anal. Chim. Acta* **852**, 13 (2014)
13. V.N. Bliznyuk, C.E. Duval, O.G. Apul, A.F. Seliman, S.M. Husson, T.A. DeVol, *Polymer* **56**, 271 (2015)
14. A.F. Seliman, V.N. Bliznyuk, S.M. Husson, T.A. DeVol, *J. Mater. Chem. C* **3**(27), 7053 (2015)
15. A.F. Seliman, V.N. Bliznyuk, T.A. DeVol, *J. Radioanal. Nucl. Chem.* **314**(2), 743 (2017)
16. C.E. Duval, W.A. Hardy, S. Pellizzeri, T.A. DeVol, S.M. Husson, *React. Funct. Polym.* **137**, 133 (2019)
17. A.F. Seliman, K. Helariutta, S.J. Wiktorowicz, H. Tenhu, R. Harjula, *J. Environ. Radioact.* **126**, 156 (2013)

18. C.E. Duval, T.A. DeVol, S.M. Husson, *Anal. Chim. Acta* **947**, 1 (2016)
19. C.E. Duval, T.A. DeVol, E.C. Wade, A.F. Seliman, V.N. Bliznyuk, S.M. Husson, *J. Radioanal. Nucl. Chem.* **310**(2), 583 (2016)
20. S.R. Thies, C.E. Duval, T.A. DeVol, S.M. Husson, *J. Appl. Polym. Sci.* **134**(11), 44593 (2017)
21. L.M. Santiago, H. Bagán, A. Tarancón, G. Rauret, J.F. García, *Nucl. Instr. Methods A* **698**, 26 (2013)
22. L.M. Santiago, H. Bagán, A. Tarancón, J.F. García, *Appl. Radiat. Isot.* **93**, 18 (2014)
23. L.M. Santiago, A. Tarancón, J.F. García, *Adv. Powder Technol.* **27**(4), 1309 (2016)
24. L.M. Santiago, A. Tarancón, H. Bagán, J.F. García, *J. Radioanal. Nucl. Chem.* **308**(3), 789 (2016)
25. L.M. Santiago, Y. Masmoudi, A. Tarancón, R. Djerafi, H. Bagán, J.F. García, E. Badens, *J. Supercrit. Fluids* **103**, 18 (2015)
26. A. Tarancón, O. Novella, M. Batlle, M. Pujadas, J. Cros, J.F. García, *Appl. Radiat. Isot.* **114**, 145 (2016)
27. O.B. Egorov, M.J. O'Hara, J.W. Grate, *Anal. Chem.* **78**(15), 5480 (2006)
28. H. Bagán, A. Tarancón, G. Rauret, J.F. García, *Anal. Chim. Acta* **686**(1–2), 50 (2011)
29. H. Bagán, A. Tarancón, L. Stavsetra, G. Rauret, J.F. García, *Anal. Chim. Acta* **736**, 30 (2012)
30. J.E. Roane, T.A. DeVol, *J. Radioanal. Nucl. Chem.* **263**(1), 51 (2005)
31. I. Villarroya, A. Ferradal, H. Bagán, A. Tarancón, J.F. García, *J. Radioanal. Nucl. Chem.* **321**(1), 207 (2019)
32. Y.-T. Qu, H. Wang, Y. Liu, L. Chen, J. Hou, Z. Liu, J.-Z. Ma, *Nucl. Sci. Tech.* **28**(2), 1 (2017)
33. R. Kim, S.B. Lee, J.W. Kim, J.H. Moon, *J. Sens.* **2017**, 1452765 (2017)
34. J.W. Bae, U. Lee, C.W. Lee, H.R. Kim, *IEEE Trans. Nucl. Sci.* **65**(3), 903 (2018)
35. J.W. Bae, H.R. Kim, *Nucl. Eng. Technol.* **52**(6), 1259 (2020)
36. H. Joo, J.W. Kim, J.H. Moon, Feasibility Assessment of a Phoswich Detector for Simultaneous Measurement of a Mixture of Beta-and Gamma-Emitters,, *Progress in Electromagnetics Research Symposium (PIERS-Toyama)*. Toyama **2018**, 1172–1176 (2018)
37. H. Gamo, M. Kondo, T. Hashimoto, R. Tayama, T. Tsukiyama, *Prog. Nucl. Sci. Technol.* **4**, 695 (2014)
38. J. Venara, M. Ben Mosbah, C. Mahé, J. Astier, S. Adera, M. Cuozzo, V. Goudeau, *Nucl. Instr. Methods A* **953**, 163081 (2020)
39. T. Maekawa, A. Sumita, S. Makino, *J. Nucl. Sci. Technol.* **35**(12), 886 (1998)
40. A.J. Schilk, M.A. Knopf, R.C. Thompson, C.W. Hubbard, K.H. Abel, D.R. Edwards, J.R. Abraham, *Nucl. Instr. Methods A* **353**(1–3), 477 (1994)
41. A.J. Schilk, K.H. Abel, D.P. Brown, R.C. Thompson, M.A. Knopf, C.W. Hubbard, *J. Radioanal. Nucl. Chem.* **193**(1), 107 (1995)
42. BetaScint™ fiber-optic sensor for detecting strontium-90 and uranium-238 in soil. Innovative technology summary report (1998). <https://www.osti.gov/servlets/purl/354883>. Accessed 25 Oct 2020
43. Y. Ifergan, S. Dadon, I. Israelashvili, A. Osovitzky, E. Gonen, Y. Yehuda-Zada, D. Smadja, Y. Knafo, D. Ginzburg, Y. Kadmon, Y. Cohen, T. Mazor, *Nucl. Instr. Methods A* **784**, 93 (2015)
44. Y. Ifergan, S. Dadon, A. Ocherashvili, I. Israelashvili, Y. Yehuda-Zada, D. Smadja, L. Carmel, Y. Knafo, D. Ginzburg, A. Osovitzky, R. Atias, Y. Kadmon, Y. Cohen, T. Mazor, *IEEE Trans Nucl Sci.* **63**(2), 634 (2016)
45. S. Yamamoto, T. Iida, *Nucl. Instr. Methods A* **418**(2–3), 387 (1998)
46. Y. Morishita, K. Hoshi, T. Torii, *Nucl. Instr. Methods A* **966**, 163795 (2020)
47. L.A. Currie, *Anal. Chem.* **40**(3), 586 (1968)
48. A. Tarancón, J.F. García, G. Rauret, *Anal. Chim. Acta* **538**(1–2), 233 (2005)
49. A. Tarancón, A. Padró, J.F. García, G. Rauret, *Anal. Chim. Acta* **538**(1–2), 241 (2005)
50. L. Hughes, T.A. DeVol, *Nucl. Instr. Methods A* **505**(1–2), 435 (2003)
51. O. Egorov, M.J. O'Hara, J.W. Grate, M. Knopf, G. Anderson, J. Hartman, *J. Radioanal. Nucl. Chem.* **264**(2), 495 (2005)
52. L.D. Hughes, T.A. DeVol, *Anal. Chem.* **78**(7), 2254 (2006)

53. C.A. Whittaker, C.A.G. Kalnins, H. Ebendorff-Heidepriem, D. Ottaway, N.A. Spooner, *Sens. Actuators, A* **299**, 111573 (2019)
54. C.A. Whittaker, C.A.G. Kalnins, H. Ebendorff-Heidepriem, N.A. Spooner, D. Ottaway, *Sens. Actuators, A* **296**, 101 (2019)
55. C.D.R. Azevedo, A. Baeza, M. Bras, T. Camara, C. Cerna, E. Chauveau, J.M. Gil, J.A. Corbacho, V. Delgado, J. Díaz, J. Domange, C. Marquet, M. Martínez-Roig, A. Moreno, F. Piquemal, A. Rodríguez, J. Rodríguez, C. Roldan, J.F.C.A. Veloso, N. Yahalali, [arXiv:1902.05456](https://arxiv.org/abs/1902.05456) (2018)
56. C.D.R. Azevedo, A. Baeza, M. Brás, T. Cámara, C. Cerna, E. Chauveau, J.M. Gil, J.A. Corbacho, V. Delgado, J. Díaz, J. Domange, C. Marquet, M. Macko, M. Martínez-Roig, A. Moreno, F. Piquemal, A. Rodríguez, J. Rodríguez, C. Roldán, J.F.C.A. Veloso, N. Yahalali, *EPJ Web Conf.* **225**, 03008 (2020)
57. W.H. Lv, H.-C. Yi, T.-Q. Liu, Z. Zeng, J.-L. Li, H. Zhang, H. Ma, *Appl. Radiat. Isot.* **137**, 161 (2018)
58. D. Badocco, D. Cester, D. Filippi, C.L. Fontana, S. Gross, M. Lunardon, G. Mistura, S. Moretto, P. Pastore, M. Pierro, F. Romanini, L. Stevanato, *Nucl. Instr. Methods A* **906**, 50 (2018)
59. K. Kang, J.W. Bae, H.R. Kim, *J. Radioanal. Nucl. Chem.* **322**(3), 1417 (2019)
60. J.W. Bae, U. Lee, H.R. Kim, *J. Radioanal. Nucl. Chem.* **314**(2), 689 (2017)
61. J.W. Bae, K.J. Kang, H.R. Kim, *J. Radioanal. Nucl. Chem.* **322**(3), 1323 (2019)
62. U. Lee, W.N. Choi, J.W. Bae, H.R. Kim, *Nucl. Eng. Technol.* **51**(7), 1828 (2019)
63. U. Lee, W.N. Choi, M.J. Kim, H.R. Kim, *Rev. Sci. Instrum.* **90**(2), 025103 (2019)
64. Z. Kóllő, *Nucl. Instr. Methods A* **798**, 24 (2015)
65. T. Uda, T. Kawano, M. Tanaka, S. Tomatsuri, T. Ito, K. Tatenuma, *Fusion Eng. Des.* **85**(7–9), 1474 (2010)
66. M. Lochny, W. Ullrich, U. Wenzel, *J. Alloys Compd.* **271–273**, 31 (1998)
67. H. Bagán, S. Hartvig, A. Tarancón, G. Rauret, J.F. García, *Anal. Chim. Acta* **631**(2), 229 (2009)
68. E. Furuta, K. Akiyama, H. Inoue, Y. Kataoka, M. Sensui, *J. Radioanal. Nucl. Chem.* **324**(1), 109 (2020)
69. A. Tarancón, H. Bagán, J.F. García, *J. Radioanal. Nucl. Chem.* **314**(2), 555 (2017)
70. H. Bagán, B. Aboudou, A. Tarancón, J.F. García, *J. Radioanal. Nucl. Chem.* **299**(1), 533 (2013)
71. H. Bagán, A. Tarancón, G. Rauret, J.F. García, *Anal. Chim. Acta* **670**(1–2), 11 (2010)
72. H. Bagán, A. Tarancón, G. Rauret, J.F. García, *Nucl. Instr. Methods A* **592**(3), 361 (2008)
73. M. Sáez-Muñoz, H. Bagán, A. Tarancón, J.F. García, J. Ortiz, S. Martorell, *J. Radioanal. Nucl. Chem.* **315**(3), 543 (2018)
74. M. Sáez-Muñoz, H. Bagán, A. Tarancón, J.F. García, J. Ortiz, S. Carlos, S. Martorell, J. Radioanal. Nucl. Chem. **322**(3), 1397 (2019)
75. E. Lluch, J. Barrera, A. Tarancón, H. Bagán, J.F. García, *Anal. Chim. Acta* **940**, 38 (2016)
76. J. Barrera, A. Tarancón, H. Bagán, J.F. García, *Anal. Chim. Acta* **936**, 259 (2016)
77. A. Coma, A. Tarancón, H. Bagán, J.F. García, *J. Radioanal. Nucl. Chem.* **321**(3), 1057 (2019)
78. S. Das, S. Chakraborty, S. Sodaye, A.K. Pandey, A.V.R. Reddy, *Anal. Methods* **2**, 728 (2010)
79. E. Furuta, in *Tritium: Advances in Research and Applications*. ed. by M.M. Janković (Nova Science Publishers, New York, 2018), pp. 1–32
80. E. Furuta, R.-I. Ohyama, S. Yokota, T. Nakajo, Y. Yamada, Y. Watanabe, *J. Radioanal. Nucl. Chem.* **299**(1), 471 (2014)
81. E. Furuta, T. Kawano, *Appl. Radiat. Isot.* **104**, 175 (2015)
82. E. Furuta, Y. Kato, S. Fujisawa, *J. Radioanal. Nucl. Chem.* **314**(2), 701 (2017)
83. E. Furuta, T. Ito, *Appl. Radiat. Isot.* **132**, 151 (2018)
84. B. Ayaz, T.A. DeVol., *Nucl. Instr. Methods A* **505**, 458 (2003)
85. S. Sodaye, Y.M. Scindia, A.K. Pandey, A.V.R. Reddy, *Sens. Actuators, B* **123**(1), 50 (2007)



Alex Tarancón holds a Ph.D. (2007) in Chemistry from the University of Barcelona. Currently, he is associate professor at the Department of Chemical Engineering and Analytical Chemistry at the University of Barcelona. His experience covers topics as development of instrumentation, studies on the scintillation mechanism and optimization of its response, pulse shape discrimination and the complete analysis of samples containing beta and alpha emitting radionuclides in several types of matrices. He has also experience in the preparation of polymers in different shapes and scales of production. His current research is focused on the development of advanced strategies (fast determinations, selective analysis, on-line sensing, in situ measurements, screening methods...) of radioactivity using plastic scintillators. Alex Tarancón has been coauthor of 40 publications in peer-reviewed journals, 1 patent and more than 50 presentations in international conferences. He has been member of the scientific committee of the two last conferences on Advances in Liquid Scintillation Spectrometry.



Héctor Bagán received his Ph.D. in chemistry at the University of Barcelona in 2011 working on the development of procedures to improve the selectivity in radioactivity measurements. He completed his 2-year post-doctorate at Lund University in the field of polymer synthesis for the separation and purification of biomolecules and proteins. Currently, he is associate professor at the Department of Chemical Engineering and Analytical Chemistry at the University of Barcelona. His research focuses on the use and development of analytical methodology for artworks characterization and also on the development of polymeric materials for the selective characterization of radioactive samples. Héctor Bagán has been coauthor of 33 publications in peer-reviewed journals, 2 book chapters and more than 30 presentations in international conferences.



José Francisco García holds B.Sc. in Chemistry, University of Barcelona, 1982; Ph.D. in Analytical Chemistry, University of Barcelona, 1989; Master's degree in Business Administration, ESADE (Barcelona), 1996. Associate professor at the Department of Painting, Conservation-Restoration, University of Barcelona 2001–2005. Since 2005, associate professor at the Chemical Engineering and Analytical Chemistry Department, University of Barcelona. Coordinator of Master in Analytical Chemistry of the University of Barcelona since 2015. Director of the Institute of Water Research of the University of Barcelona since 2019. García works in the development and application of specific analytical methodology to two fields: environmental radiochemistry and cultural heritage. In the area of environmental radiochemistry, the main studies have focused on the development of analytical alternatives based on the use of plastic scintillators to measurements “in situ” and in the laboratory, reducing reagents, residues, manpower and time required to obtain the information. These studies

have included basic research on the scintillation mechanism but also the synthesis of Plastic scintillating materials in different formats, specific Plastic scintillating resins, automated systems and continuous detectors. García has participated on several European and national research projects and technology transfer contracts. García has published more than 80 refereed papers and has presented more than 100 communications at international conferences.

Chapter 14

Use of Scintillators to Study the Earth from Ground to the Radiation Belts



Philippe Laurent, Sébastien Célestin, Vincent Maget, Pablo Caron, and François Trompier

Abstract Scintillators are used in various fields of Earth and atmospheric sciences in order to study high-energy phenomena occurring from ground to the Earth radiation belts. In this chapter, we explore the different scientific domains where high-energy detection is unavoidable, from the study of Earth radioactivity or human nuclear activities to the measure of the particle environment around our planet, including the recent topics on atmospheric gamma-ray processes during thunderstorms.

14.1 Survey of Earth Natural Radioactivity and Potential Nuclear Accidents, Citizen Science

14.1.1 Source of Terrestrial Natural Radioactivity

Natural radiation at Earth's surface comprises cosmic radiation and the radiation arising from the decay of naturally occurring radionuclides. Primary cosmic radiations mainly composed of high-energy proton and He nuclei when interacting with atoms of Earth's atmosphere (mainly N and O) produce in a cascade of reactions secondary particles (pions, kaons, muons, neutrons, electrons, positrons, alpha particles, photons, neutrinos) called air shower. At sea level, the secondary cosmic radiation left are mostly muons and neutrons. In addition, interactions of the primary

P. Laurent (✉)

Laboratoire Astroparticule Et Cosmologie, CEA, IRFU, CEA Saclay, Paris, France

e-mail: philippe.laurent@cea.fr

S. Célestin

Laboratory of Physics and Chemistry of the Environment and Space (LPC2E), University of Orleans, CNRS, CNES, Orleans, France

V. Maget · P. Caron

DPHY - Department of Physics, Instrumentation Environment and Space, ONERA, Toulouse, France

F. Trompier

IRSN, Fontenay-aux-Roses, France

and secondary cosmic radiations with air and soil atoms lead to the production of radioactive isotopes by capture or spallation reactions. These radioactive isotopes are called cosmogenic radioisotopes, the most known being ^{14}C and tritium (^3H), but one could also cite ^7Be , ^{22}Na , ^{85}Kr . In soils, among the long list of cosmogenics formed, one could cite ^{41}Ca . In addition to cosmogenic, natural radionuclides also include the so-called primordial radioactive isotopes in the Earth's crust and their radioactive decay products. From all radioactive isotopes produced in stars billions of years ago and spread over universe and incorporated in the genesis of Earth, only four radioactive elements released from death of stars have survived in the crust of our planet thanks to half-lives measured in billions of years: two isotopes of uranium (^{238}U and ^{235}U), ^{232}Th and ^{40}K .

The three naturally occurring radioactive decay chains include the ^{238}U , ^{235}U , and ^{232}Th , which decay through a series of radioactive elements up to stable Pb isotopes. ^{238}U , ^{235}U , and ^{232}Th are the ancestors, the genitors of three distinct radioactive family trees. These nuclei decay to produce other radioactive nuclei with shorter half-lives, a continuing process which for the sake of clarity is often compared to human genealogy. This "radioactive descendancy" explains why traces of radium can be found alongside uranium inside blocks of granite, for example. ^{226}Ra has a half-life of only 1600 years, and would have completely disappeared from the surface of the Earth unless it is constantly regenerated by its radioactive ancestor, ^{238}U .

Exposure of living organisms to radiation is divided into two categories: external and internal exposure. For the first one, the radiation emission source is located outside the organism, whereas for the second after inhalation or ingestion, for example, is inside the organism making dose deposition by alpha and beta particles also possible in that case. External exposure at ground level from natural source is therefore due on one hand from the secondary cosmic radiation left and from the other hand from the so-called telluric radiations made up of gamma rays emitted by the atoms of thorium, uranium and their descendants, and ^{40}K found in rocks and soils. Internal exposure from natural radionuclides includes mainly ^{40}K , ^{14}C (ingestion), and the radioactive gas ^{222}Rn (inhalation). An adult human body of 70 kg contains about 5000 Bq of ^{40}K . ^{222}Rn occurs from the decay chain of ^{238}U and is actually the principal natural source of exposure to natural radiation. The world average exposure to natural sources of radiation is estimated at 2.4 mSv [1], with a contribution from Radon equal to 1.3 mSv. The external exposure contribution from telluric radiation to this average annual dose is estimated at 0.48 mSv.

Radioelements are not uniformly distributed in the Earth's crust (see Fig. 14.1 for Europe). Concentration of these radioelements in soils and rocks are depending on the process of formation of rocks and the erosion of soils. This radioactivity can be concentrated in some locations, making exposure to these natural radiations dependent on soils and rock composition. Overall, soils in sedimentary basins and limestone formations have less uranium than those of granite massifs. Not all granites have high concentration though. On a local level, specific geological conditions may also lead to unusual levels of uranium, particularly in rivers and ground waters. In Europe, median uranium concentration in soil is estimated to be approximately 2 mg/kg, with a range of variation from less than 0.1 mg/kg to more than 50 mg/kg

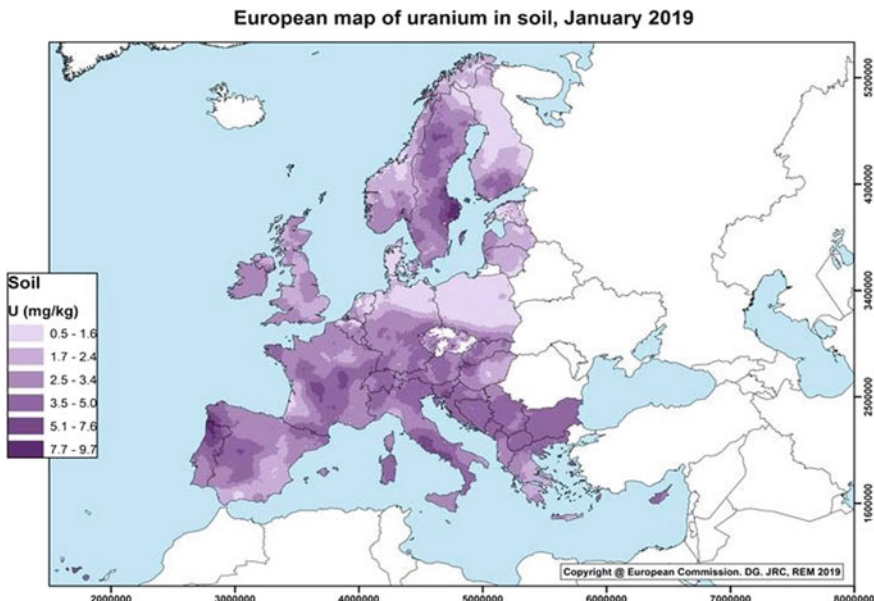


Fig. 14.1 European map of uranium in soil (Credit: <https://remon.jrc.ec.europa.eu/About/Atlas-of-Natural-Radiation/Digital-Atlas/Uranium-in-soil/Uranium-concentration-in-soil->)

[2]. Worldwide, there are a few locations denominated as High Natural Background Radiation Areas (HBNRAs), in which average annual dose and maximal annual doses far exceed those estimated in the Normal Background Radiation Areas (NBRAs). Thus, in Iran, in the city of Ramsar, because of the presence of sulfurous hot springs that contain enhanced ^{226}Ra concentrations, the estimations of the external exposure of inhabitants range between 0.7 and 131 mSv with a mean of 6 mSv [3]. In Kerala state (India), the high level of radioactivity is here due to the presence of thorium and its decay products in the surface soil, mainly in form of monazite. Annual external doses are estimated on average at 4.5 mSv with a maximum reaching 15 mSv [4, 5]. HBRNAs are also found in China (area of Yangjiang County in Guandoung province) and in Brazil (Guarapari) with respective annual external dose of 3.5 and 5.5 mSv and maximal external dose of 5.5 and 35 mSv [6, 7]. After uraninite, thorianite and thorite, monazite and zircons are the most radioactive minerals because of their ability to accept uranium and thorium. High concentration of monazite in the form of much localized hot spots of black sand can be found in river and sand beaches.

Human activities can lead to artificially increase natural radioactivity exposures, sometimes at relatively high levels. Containment of radon in habitats: the use of certain building materials that emit radon, poorly insulated buildings with uranium-bearing soil, and excessively confined habitats can lead to significant exposures. As an example, in the city of Ramsar, estimation of internal dose from exposure to Radon range from 2.5 to 72 mSv [8]. The production processes of certain industrial activities, not related to the nuclear power cycle, can modify the physicochemical balance of the

natural radioactivity contained in the materials used and concentrate it in the produced waste. It represents a possibly increased risk of dissemination in the environment and therefore of human exposure, even after the cessation of industrial activity. One well-known example is the industrial use of radium following its discovery, leaving many places with high levels of contamination. For example, large concentrations of radium were detected on a part of the foreshore at Dalgety Bay in Scotland [9]. It is thought that the contamination originates from the residue of radium-coated instrument panels from military aircraft incinerated and land-filled in the area at the end of World War II. This unintentionally reinforced natural radioactivity can also come from industries extracting minerals and geological resources and from the successive stages of separation, purification, transformation and use of by-products. The main activities are as follows:

- combustion of coal in thermal power stations,
- processing of tin, aluminum, copper, titanium, niobium, bismuth, and thorium ores,
- production of refractory ceramics,
- production or use of compounds including thorium, the production of zircon and baddeleyite,
- production of phosphate fertilizers and the manufacture of phosphoric acid,
- processing of titanium dioxide,
- processing of rare earth elements and the production of pigments containing them,
- treatment of groundwater by filtration for the production of drinking water.

The extraction and processing of uranium ores also generates enhanced natural radioactivity, but in this case, unlike the industrial activities mentioned above, the ore is used for its radioactive properties.

14.1.2 Sources of Radioactive Pollution in the Environment

Sources of radioactive pollution in the environment have various origins but are by definition linked to human activity. They may be naturally occurring radioelements or “artificially” produced by man, either in nuclear reactor or with particle accelerator. Some radio elements artificially produced are also naturally present in the environment such as tritium for example, which finds birth in the release of nuclear power plants and is also a cosmogenic. Some others such as all isotopes of Technetium are produced in stars but are no longer found on Earth because of their relatively short lives. As mentioned in the preceding paragraph, a whole area of human industry, even if it does not aim at the use of radioactivity, generates pollutions during its cycle of use, either at the level of its extraction, such as rare earth, or/and during its use (cf. coal). In these cases, it is a matter of redistributing natural radioactivity present in the soil into the environment.

Human activities related to the nuclear industry, to applications in the field of research, or in the medical field generate radionuclides that are no longer naturally

present. They are either specifically produced for applications (imaging in nuclear medicine: ^{99m}Tc , ^{18}F , for example, radiation sterilization with ^{60}Co sources), or are residues or effluents from industrial processes (nuclear fuel waste, discharges at so-called nuclear electricity production sites or nuclear waste reprocessing sites). In spent nuclear fuel, some of these radioelements can be isolated and used for other applications (^{241}Am for example) or recycled in energy production (^{239}Pu), but many are unusable and considered as waste requiring medium or long-term storage depending on the radioactive periods of the radioelements. During normal operation, certain activities using or generating radioactivity (nuclear industry, radiopharmaceutical production, etc.) emit releases into the environment (gaseous or in the form of effluents), the levels of which are regulated and monitored at different levels: by industrialists, by the authorities, by NGOs using measurement networks specific to each.

To operate, most facilities in the cycle use water taken either from rivers or from the sea. The use of this water leads in part to the production of effluents that are treated to retain most of the activity in solid form (waste). Residual effluents are then discharged by liquid and aerial means after controls to ensure compliance with the regulatory requirements established by the Authorities (flow rate, activities releases, radionuclides present). The radionuclides released by nuclear facilities are numerous and differ according to the type of facility and its operating phase (production, maintenance shutdown, dismantling, etc.). The activities released by these facilities, in normal operation, have also changed over time as a result of the renewal of increasingly restrictive release authorizations issued by the authorities and the implementation of new effluent treatment processes. Today, as an example, releases from French nuclear installations in the fuel cycle are dominated in quantity by three radionuclides: ^{85}Kr , a noble gas, tritium and ^{14}C (here as $^{14}\text{CO}_2$). Other artificial radionuclides are measured in a more punctual manner in continental and marine aquatic environments, as, for example, under the influence of releases from nuclear facilities: ^{54}Mn , ^{58}Co and ^{60}Co , ^{110m}Ag , ^{129}I and very sporadically ^{106}Ru and ^{134}Cs . Releases from nuclear medicine activities are characterized by radionuclides with a very short half-life: 8 days for ^{131}I and 6 h for ^{99m}Tc .

In addition to regulated emissions of radioactivity, the environment is also marked by the presence of radioelements resulting from unauthorized voluntary releases from nuclear facilities, releases related to accidental situations (e.g., accident in 2008 in Fleurus, Belgium with release of 47 GBq of ^{131}I) [10], fallout from nuclear disasters (Three Miles Island, Chernobyl, Fukushima) and nuclear weapons (Hiroshima, Nagasaki, and aerial testing).

^{90}Sr and ^{137}Cs are the two main radioisotopes still detected from nuclear testing and Chernobyl and Fukushima nuclear disasters. Another source of geographically extended radioactive pollution that was detected is ^{238}Pu . The ^{238}Pu was used as a source of energy in the astronautic field (Apollo mission, satellites...), the heat emitted by the Pu in its dioxide form is converted into electricity. The first accident, which occurred on April 21, 1964, was the failure of the launch of the American communication satellite Transit-5BN-3 which burned during its re-entry into the atmosphere in the north of Madagascar. Its 630 TBq of ^{238}Pu was dispersed in the

atmosphere of the southern hemisphere, and because of the dilution in the atmosphere only traces of ^{238}Pu were detected a few months later at ground level but in all continents with higher level in the southern atmosphere. Other detectable radioisotopes of Pu in the environment are mostly due to the fallout of nuclear weapon tests and also in a less extent to some accidental releases of nuclear fuel recycling. Traces of ^{241}Am if not initially present in the fallout is formed by the decay of ^{241}Pu , its activity is steadily increasing and will reach its peak around 2036.

The Reader is encouraged to consult Chaps. 11 and 13 for further information on environmental analysis and Chap. 12 on the use of radioactivity for clinical applications.

14.1.3 Nuclear Activities Survey and Alert in Case of Accident: Description of Official and NGO Networks

Radioactivity in the environment is monitored by different measuring means and methods depending on the medium (atmosphere, aquatic environment, soil, etc.) and the type of radionuclides to be measured. For example, the measurement of the gamma dose rate in air is generally carried out continuously with data reported at regular intervals of about ten minutes, whereas other types of analysis require samples taken at regular intervals (week, month) and measured in the laboratory. In this part, only the monitoring of the dose rate will be discussed, as it may be carried out with gamma-ray spectrometers, in particular scintillators. The measurements in laboratories or filters *in situ* are carried out in the vast majority of cases using high purity Ge diodes type gamma-ray spectrometers or in the case of pure beta or alpha emitters using liquid scintillation counters, alpha spectrometry system (silicon diode) or mass spectrometry.

For dose rate in air, systematic environmental radiation monitoring programs were introduced for more than 60 years. In most cases, national environmental monitoring programs were designed together with the planning of research reactors, Nuclear Power Plants (NPPs), and other nuclear facilities. For example, in most European countries, additional monitoring programs were introduced for civil protection topics. For member states of the EU, it is obligatory to provide data from these networks via EUropean Radiological Data Exchange Platform [11] (EURDEP) data exchange platform. EURDEP makes unvalidated radiological monitoring data available in nearly real-time [12]. The participation of the EU member states is regulated by the Council Decision 87/600 and the Recommendation 2000/473/Euratom. The participation of non-EU countries is possible on a voluntary basis. Countries sending their national data have access to the data of all the other participating countries. In addition, there is a gentlemen's agreement that participating in EURDEP automatically means that data delivery will continue during an emergency but with a higher data transmission frequency.

Complementary to national or regional network of monitoring, local measurement networks are generally deployed around nuclear sites by the operators of these sites and national authorities with probes distributed within a radius of a few kilometers. Data can be shared and made public. In France, for example, all the data measured by the operators are sent to the national database (national environmental radioactivity measuring network (RNM, Réseau National de Mesure de la radioactivité dans l'environnement)). Électricité de France (EDF), for example, as operator of NPPs, takes part in RNM set up by the radiation protection and nuclear safety institute (IRSN) under the auspices of the French Nuclear Safety Authority (ASN). The network makes the results of the regulatory environmental radioactivity monitoring system available to the public [13]. The French national network for environmental radioactivity measurements centralizes all the monitoring data on environmental radioactivity in France and ensures their quality and harmonization through an accreditation procedure. Similar approach is found in many countries: Hungary, South Korea, UK, etc....

Depending on the country and on the nuclear industry activities, the number and the types of detectors vary (Fig. 14.2). Table 14.1 resumes these data for several countries.

Most of these probes are based on gas meters, (Geiger–Müller (GM) counter, proportional, pressurized ionization chamber) and therefore only allow monitoring the dose rate without identifying the nature of the radioactivity (radionuclides). These detectors present a good cost-performance compromise, are robust but have certain limitations. Gas meters have different drawbacks. Many probes have a cut-off at about 60 keV that lead to dose rate underestimation in case of presence of radionuclides emitting low-energy gamma rays. Moreover, their response depends on the energy of the gamma to be measured, which implies additional uncertainties on the reported dose rate values. It is obvious that probes based on gamma-ray spectrometers therefore offer comparatively many advantages: identification of radionuclides, measurement of low-energy gammas and the energy dependence of the response is corrected. For continuous monitoring, scintillators are often preferred, although sometimes when energy resolution is an important criterion solid-state detectors such as CdZnTe semiconductors (CZT) can be considered. The most popular scintillator remains the NaI(Tl) type because of its good trade-off between cost, sensitivity, and energy resolution.

Because energy resolution being sometime an issue, some networks are now considering Cerium-doped Lanthanum Bromide ($\text{LaBr}_3(\text{Ce})$) inorganic scintillator, but due to its higher cost, the number of probes supplied with that scintillator remains limited. $\text{LaBr}_3(\text{Ce})$ has been the reference for excellent energy resolution combined with fast emission and good linearity. The FWHM (full width at half maximum) is below 3% at 662 keV. This type of scintillator presents a significant intrinsic background, mainly because of the natural radioactivity of Lanthanum. This apparent drawback could be turned into an advantage to monitor the temperature effect, for example, and improve the accuracy of the energy calibration. Alternatively, Cerium Bromide (CeBr_3) scintillators are also considered because presenting a very low intrinsic background noise with high light yields and high density properties. CeBr_3

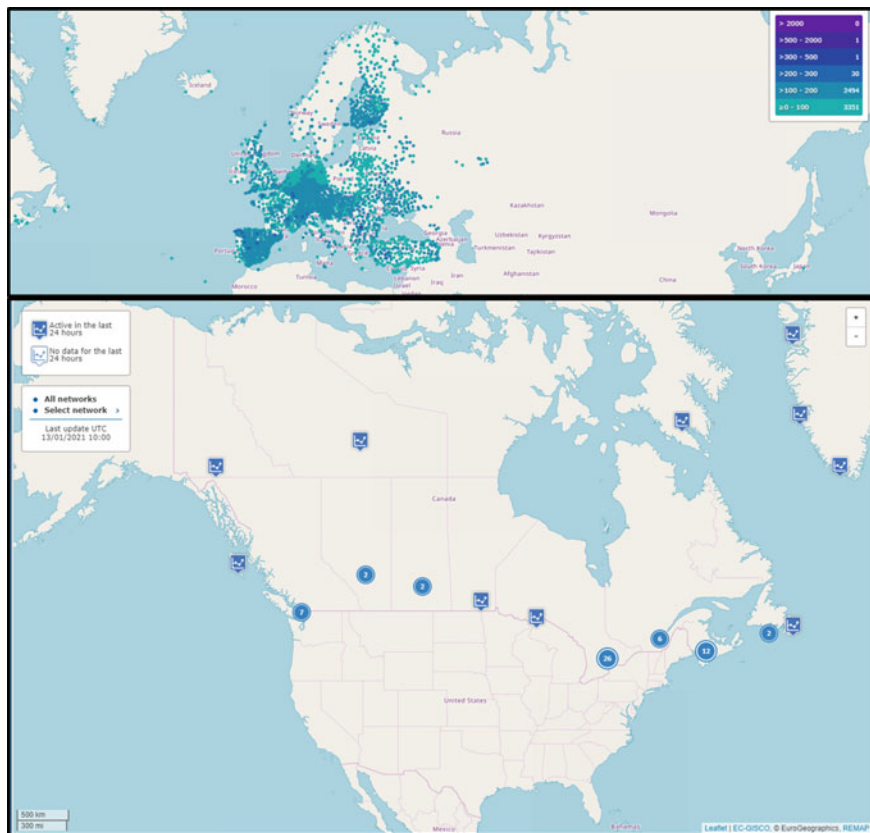


Fig. 14.2 *Top:* screenshot of the EURDEP “expert map” showing the locations of the gamma-dose-rate-monitoring stations. *Bottom:* Map of the real-time dose rate monitoring stations from the Canadian Radiological Monitoring Network, screenshot from the EURDEP “expert map” showing the locations of the Canadian gamma-dose-rate monitoring stations (Credit: European Commission. DG. JRC, REM 2009–2019). Accessible at <https://remap.jrc.ec.europa.eu/Advanced.aspx>

Table 14.1 Number of probes for dose rate monitoring for several countries

Country	Network	Number of probes
France	Teleray	400
United Kingdom	Radioactive Incident Monitoring Network (RIMNET)	91
Switzerland	Automatic Dose Alarm and Monitoring Network (NADAM)	71
USA	US national radiation network (RadNet)	140
Germany	—	1800

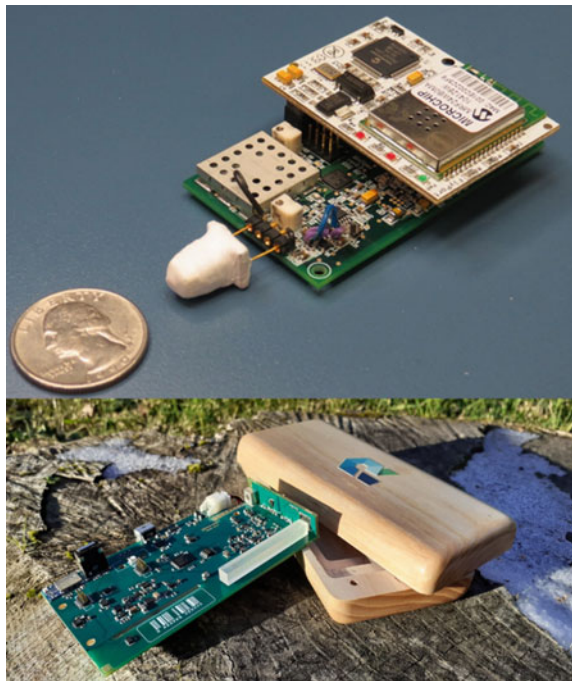
is also fast without any slow components. The typical energy resolution provided by the material is 4 % FWHM at 662 keV.

In the aftermath of the Chernobyl nuclear accident, new NGOs have been created to provide independent information to the public and perform also independent measurements in the environment, mainly based on sampling (water soils). Some of these organizations were able to set up professional systems of dose air and air radioactivity concentration monitoring, but for a rather limited number of system and placed therefore in strategic locations. During the Fukushima Daiichi crisis, university lab supplied with radiation detectors, sometimes gamma-rays spectrometers based on scintillators (mainly NaI(Tl)), shared the measured data through web. For example, the Pachube website allows users to stream various sensor data to the web in real time and was put to use for monitoring radiation by a large number of users after March 2011. There was only one location streaming into Pachube before the accident, but a large number have since started to stream to the site. The community has converged on a standard way to report the information in order to disseminate the large variety of sources, such as detector model. Pachube has become Cosm and now Xively that is an Internet of Things (IoT) platform owned by Google.

Citizen science projects have been established, at first in Japan, to estimate individual doses (e.g., Radiation watch [14], D-shuttle), especially for individuals remaining in contaminated territories or radioactivity mapping (Safecast [15]). The cost of detectors being an issue, mostly photodiode and gas detectors (G.M. and pancake) were considered in these projects. Initially, these projects were considering handy measurements or individual monitoring (with D-shuttle dosimeter), and itinerary measurements when detectors were supplied with a GPS chip (bGeigie Nano from Safecast). In 2017, Safecast released a stationary and autonomous probe based on its pancake-based detector (bGeigie Nano). With recent technological development, detectors can be connected to a smartphone initially via the audio and now via USB and Bluetooth®. Smartphones apps make possible to easily collect and share data into open-access database (Safecast and Openradiation projects). With the development of new technologies like Silicon Photomultiplier (SiPM) and miniaturized FPGA with low cost computers (Raspberry) and communication technology (i.e., Arduino), it has become possible to develop also for public use, low-cost, and good performance radiometers. The RAMESIS project [16], for example, has developed a monitoring probe for stationary and continuous measurements bases on a $\sim 10 \times 15 \times 15$ mm polystyrene-based plastic scintillator [17]. Here, the plastic scintillator has been selected for its high sensitivity and relatively low cost. In those detectors, scintillators are used only in counting mode and do not provide any spectrometric information. On the same principle, some radiometers are based on scintillators, because of the very good cost-sensitivity compromise. The next step was to take advantage of the scintillator to not only use it in counting mode as a radiometer, but also to develop gamma-ray spectrometry system for public at relatively low cost. Oregon State University [18], for example, has developed a low cost and wireless gamma-ray spectrometer based a small CsI scintillator with SiPM and FPGA-based digital pulsed processor for about USD 125 of components [19]. This type of approach is now available to public for few hundred euros. Thus, French start-up Icohup [20] has

developed and proposed a wireless gamma-ray spectrometer connected to a smart-phone app (Rium), with also a CsI scintillator (see Fig. 14.3). New technologies and the reduction in the cost of gamma-ray spectrometers are making these measurement methods more widely available with a very good cost-performance ratio. This opens up new prospects for both citizen science applications, particularly those aimed at measuring radioactivity in the environment, by providing a more extensive network of measurement equipment with more high-performance hardware. The same is true for NGO monitoring programs, which often remain limited due to lack of access to expensive equipment. For institutional networks, which are still mainly made up of gas detectors, the replacement of current detectors by gamma-ray spectrometers is gradually taking place. For these networks, access to gamma-ray spectra is a real added value, especially in the event of crisis nuclear accident. Recent technological progress in the use of scintillators should greatly contribute to the improvement of the measurement network, by offering high-performance and low-cost spectrometric probes.

Fig. 14.3 *Top:* The OSU wireless low-cost gamma-ray spectrometer (reproduced from [21] with permission from Elsevier). *Bottom:* the Icohup Rium wireless gamma-ray spectrometer (courtesy Icohup)



14.1.4 Measuring and Mapping the Radioactivity in the Environment: The Citizen Science Approach

14.1.4.1 OpenRadiation Project

After the Fukushima accident, Japanese citizens wanted to form their own opinion on the radiological risk to which they were exposed using dosimeters available on the market or made available. Systems have also been developed to share the measurements made on sites, in particular through maps. Gradually, the tools for measuring the contamination of territories have multiplied so that everyone could better understand their environment and the level of ambient radioactivity.

This need for transparency and public involvement represents a real paradigm shift in the management of future radiological and nuclear crises. It has become clear that with the development of affordable and reliable consumer devices, social networks and space for sharing measured data, future crises can no longer be managed in the same way as it was in the past. Following this observation, the IRSN and its partners (Institut Français des Formateurs Risques Majeurs et Protection de l'Environnement (IFFO-RMe), Planète sciences, Pierre et Marie Curie University) develop a transparent data sharing tool that enables merging data generated by citizens [22]. In the event of a crisis, it seems obvious that the data reported by the public will also be taken into account. The question then arises as to the reliability of these measurements and their retrieval from the many sites and applications published by manufacturers of measurement equipment. The objective of the project is to improve the reliability of measurements by improving the metrology of measurements (new calibration curves) by offering a single application connectable to the sensors considered as the most reliable and allowing sharing data transparently and immediately on a single data collection site. Comparing to other sharing data site, OpenRadiation [23] adopts a principle of full transparency: data are transmitted live and no data are censored or removed. Besides, a connected radiometer based on a GM tube detector was developed with partners of the OpenRadiation project. This detector is provided as a kit to be mounted. The detector is connected by Bluetooth® to a smartphone application allowing data collection and sharing to the OpenRadiation database. Once a measurement is sent, it can be immediately visualized on the website, without data evaluation or filtration. The OpenRadiation database (in open access) allows a simplified data retrieval especially by the authorities for their own use. The data collected are open data and the main software used is open source. Therefore, it allows anyone to connect his sensor to the database and to transmit data in real time. The project also aims to study and better evaluate the performance of different sensors on the market and to participate in their improvement. Measured data from any sensor can be entered manually via the smartphone application, allowing geolocation of data or uploaded on the website for systems equipped with geolocation (i.e., bGeigie from Safecast). In general, the principle being to have an “open” system, the idea is to have the possibility of carrying out measurements using any kind of dosimeters, based upon gas detector or scintillators. For the moment, the site and the application only allow

to report dose rate data, but spectrometric data, especially those measured by scintillators in the form of time series will soon be taken into account, thus allowing continuous monitoring of radioactivity in the environment.

14.1.4.2 The BELISAMA Project

Atmospheric storms are one of the most important disruptive phenomena in the Earth's environment. Two thousand thunderstorms are permanently active around the world, producing 50 to 100 lightning bolts per second. Recent observations of light emissions in the middle and upper atmosphere and gamma-ray emissions of atmospheric origin indicate a strong coupling of the atmosphere with the ionosphere and the magnetosphere of the Earth above the active storm cells. This coupling can be triggered by cosmic radiation, solar wind, and meteorological and volcanic processes affecting the lower layers of the atmosphere. Current knowledge is limited to that of light emissions observed in the visible spectrum of the ground or from optical detectors on board satellites and oriented toward the horizon. Theoretical studies show that these emissions are only part of a much more complex phenomenon (X-ray emissions, emissions of electromagnetic waves and an atmosphere/ionosphere coupling which leads to the generation of intense electric fields and to the acceleration of electrons up to very high energies).

These events produce flashes of gamma-ray light (Terrestrial Gamma-ray Flashes or TGF) recently discovered by NASA's BATSE satellite, dedicated to the study of cosmic gamma-ray bursts and confirmed by NASA's RHESSI satellite dedicated to the observation of the sun at high energy. These phenomena will be described in more detail in the next paragraph. These flashes were detected from ground in Japan in 2016 by the Japanese GROWTH collaboration [24], but no similar study has yet been carried out in Europe. The BELISAMA project therefore proposes to respond to this problem by bringing into play a network of high schools in France.

The purpose of this project is to introduce students to natural gamma-ray radiation, whether it is of telluric origin or atmospheric (TGF). It will also introduce the means and methods used to detect and analyze these gamma-ray emissions. The high school students will measure the energy of these gamma-ray emissions using a detector specially developed for this project that will be installed e.g. on the roof of their school. High school students will also be able to share their data with other high schools in order to possibly detect simultaneous atmospheric emissions.

The BELISAMA detector consists of a scintillating crystal of Bismuth Germanate (BGO) sensitive to gamma rays of several MeV, readout by a SiPM photodetector (see Fig. 14.4). The SiPM transforms the light emitted by the BGO detector into an electric current which is read by suitable electronics. This electronics has been adapted from that used by the GROWTH collaboration. The whole system is included in a box to ensure thermal and hygrometric insulation.

The data corresponding to the detection of gamma-ray photons (photon energy, arrival date) are processed by a microcontroller and stored on a disk. The data are also

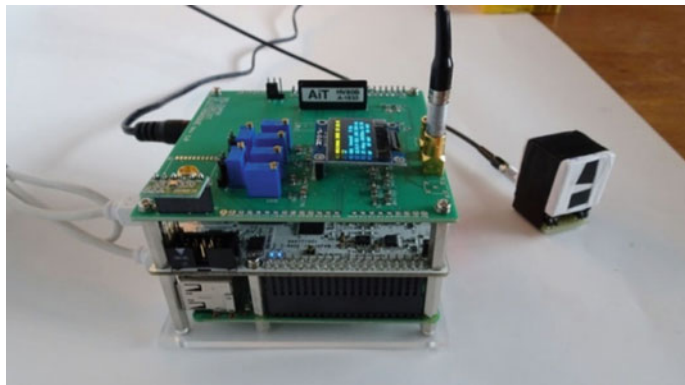


Fig. 14.4 View of the BELISAMA detector to measure gamma-ray radiation. On the right, we see the BGO scintillating detector (Credit: APC)

available via the Internet on computers and smartphones and will be soon transmitted to the OpenRadiation website.

14.2 High-Energy Processes in the Atmosphere, Terrestrial Gamma-Ray Flashes (TGFs), and Gamma-Ray Glows

14.2.1 *Gamma Ray Emissions During Thunderstorms*

Gamma-ray emissions in thunderstorms can be classified by their duration. Some very intense and short events lasting $\sim 100 \mu\text{s}$ are detectable from space and referred to as Terrestrial Gamma-ray Flashes (TGFs) and others, usually named gamma-ray glows are long-duration events (timescale of a few seconds to minutes) detected *in situ* or in the vicinity of the source as high-energy radiation background increases.

Both phenomena have a similar energy spectrum typical of bremsstrahlung with an exponential cut-off at $\sim 7 \text{ MeV}$ [25]. This cut-off is caused by the acceleration and amplification processes of runaway electrons [26, 27]. In a gaseous medium as the Earth's atmosphere, not all electrons are subject to continuous acceleration under a given electric field. Most of the electrons are in the low-energy range and those on average gain as much energy from the electric field than that they lose to collisions with atmosphere molecules, resulting in a slow drift in the opposite direction of the electric field. High-energy electrons, however, may have a low probability of collision and scatter mostly forward, in such a way that they gain more energy from the field than they lose to collisions. As long as the electric field can sustain it, these electrons are continuously accelerated and are referred to as runaway electrons.

That runaway process requires the electric field to exceed a threshold depending on the electron stopping power. In ground-level air density, the threshold is approximately 2.1 kV/cm (in other words, minimum ionizing electrons lose 2.1 keV/cm in ground-level air). In practice, angular scattering needs to be considered and it is the average of the projection of the electric field onto the electron momenta that needs to exceed the stopping-power-based threshold, which makes it increase to about 2.8 kV/cm [28]. In an electric field exceeding 2.8 kV/cm, runaway electrons continuously accelerate, albeit still experiencing collisions, especially ionizing collisions.

Most of the secondary electrons produced in ionizing collisions are in the low-energy range and will rapidly thermalize and slowly drift in the field. On rare occasions, however, a secondary electron might itself be a runaway electron. If the electric field spans over a sufficiently large region, that process might occur many times, and from one initial runaway electron (e.g., produced by the radiation background) one obtains an exponential avalanche of runaway electrons. This process is termed Relativistic Runaway Electron Avalanche (RREA) in the literature. As they gain energy (hence moving forward in the energy spectrum), they may produce many other lower energy runaway electrons. That continuous acceleration combined with the rate of production of new runaway electrons result in the typical above-mentioned 7-MeV exponential cut-off observed in gamma-ray glows and TGFs [29].

14.2.2 Gamma-Ray Glows

Gamma-ray glows have been first observed in the early 1980s using NaI(Tl) scintillators on board airplanes flying through thunderstorms [30, 31]. They were later observed from balloons also using NaI(Tl) crystals [32] and the ground using various kinds of detectors [33, 34]. Although the exact context of their occurrences (geometry, location in thunderstorms, etc.) is not known, these events seem to be frequent. More recent airborne campaigns [35] have reported measurements of an intense glow using two 12.7 cm × 12.7 cm cylindrical plastic detectors, which seems to be consistent with an observation made directly in the avalanche region. Based on their results, Kelley et al. [35] have suggested that the ionization produced by the runaway electrons at the source might be responsible for a significant electric current in the thunderstorm, approaching the conventional charging currents. If confirmed, this would mean that sources of gamma-ray glows may play a role in the large-scale thunderstorm electrodynamics.

More recent observations using a detector made of three BGO scintillator bars (15 cm × 5 cm × 3.2 cm) on board a high-altitude aircraft (ER-2) have shown that gamma-ray glows may occur above cloud tops at a 20-km altitude [36]. The detector and front-end electronics were based on the high-energy detector of the ASIM experiment on board the ISS. The exact mechanisms producing such events remain unknown. The electrostatic field was also measured during the same campaigns and is one order of magnitude below the RREA threshold. Possible mechanisms suggested

are a local enhancement of the cosmic ray background through the electrostatic field produced by the charges in the thundercloud or RREAs inside the cloud. In the latter scenario, the required charge structure in the cloud would be quite complex with large regions having an opposite polarity with respect to others [36].

14.2.3 Terrestrial Gamma-Ray Flashes (TGFs)

Terrestrial Gamma-ray Flashes (TGFs) have been first discovered with the instrument BATSE on board NASA's Compton Gamma ray Observatory (CGRO) [37]. They have later been confirmed and observed in details from space using germanium detectors on board RHESSI (NASA) [38], the CsI(Tl) calorimeter on board AGILE (ASI) [39], and NaI(Tl) and BGO detectors on board Fermi (NASA) [40]. As of writing this chapter, the only instrument especially designed for the observation of TGFs is the MXGS, which is part of the Atmosphere-Space Interactions Monitor (ASIM) installed on the International Space Station. Moreover, TGFs have also been found in the data of the Italian-Dutch satellite BeppoSAX (ASI/NIVR) using the GRBM instrument made of CsI(Tl) scintillator slabs [41]. MXGS is made of two detectors: a low-energy detector consisting of CZT pixels detecting photons from 50 to 400 keV (effective area \sim 400 cm 2 at 100 keV) associated with a coded mask providing imaging capability and a high-energy detector consisting of 12 BGO detector bars (effective area 650 cm 2 at 1 MeV). The TGF detection rate of MXGS is about 0.7 TGF/day [42].

It is also interesting to note that as they propagate through the atmosphere, TGFs produce secondary electrons and positrons through photoelectric effect, Compton scattering, and e $^+$ e $^-$ -pair production. Produced above \sim 30–40 km, as the density of air is very low, electrons and positrons do not scatter much and escape into space while being trapped in the geomagnetic field. These events, usually referred to as Terrestrial Electron Beams (TEB), have first been predicted theoretically and observed by Dwyer et al. [43]. They tend to resemble TGFs but with longer durations (1 to 10 s of milliseconds). Depending on the injection geometry with respect to the geomagnetic field lines, electrons and positrons can mirror in the other magnetic hemisphere, thus forming a lightcurve with two peaks (one on the way forth and one on the way back). TEBs have been observed by all the satellite missions that have reported TGF detections and are of particular interest in that they represent a yet unexplored source of high-energy electrons and positrons (>1 MeV) in the magnetosphere [44].

Recently, a leap forward has been made with the detection of multiple TGFs from the ground using large-area (3 m 2) plastic scintillators of the Telescope Array installed in Utah designed to detect high-energy charged particles in cosmic ray air showers [45, 46]. This type of measurements is very valuable as it enables the use of unprecedented detection area that allows for re-solving source geometries [47] and the simultaneous observation of causative atmospheric discharges using radio measurements such as lightning mapping arrays and interferometers [48].

14.2.4 TARANIS: A Satellite to Study the Effects of Thunderstorms and Lightning

TARANIS was a French CNES satellite specifically designed for the observations of multi-wavelengths signals from Terrestrial Gamma-ray Flashes (TGF), Terrestrial Electron Beams (TEB), and Transient Luminous Events (TLE) occurring during thunderstorms. It was equipped with several instruments to measure the electromagnetic emissions induced by lightning from radio to the gamma-ray wavelengths. Two radio antennas at high frequency and low frequencies, optical light micro-cameras to provide localization of lightning strokes, sprites and Emission of Light and Very low-frequency perturbations from Electromagnetic pulse sources (ELVEs) with a precision of around 1 km, and photometers to provide light curves of lightning and TLE emission with 10 microseconds time resolution were accommodated on the satellite (Fig. 14.5). It also included the X-ray and gamma-ray detector XGRE which measure the time variation and spectrum of TGF and TEB reaching the satellite and the “Instrument DéTECTeurs d’Électrons Énergétiques”, IDEE, to measure the low-energy spectrum and direction of electron beams.

TARANIS was launched on November 17, 2020 from Kourou Space Center. Unfortunately, eight minutes after the launch, the fourth stage of VV17 Vega rocket failed and the mission was lost. A new mission TARANIS-2, with similar instruments as the ones foreseen for TARANIS described above is now under study with CNES and the associated laboratories. If accepted, it should be launched in 2025.

The field of view of the TARANIS instruments was designed to span all the atmosphere observable from the satellite, at 700 km altitude, observing thus around



Fig. 14.5 TARANIS artist view including the X-ray, gamma-ray and electron detectors XGRE, visible light micro-cameras for imaging and photometry (MCP), electric and magnetic field measurement devices IME and IMM (credit: CNES/ill./SATTLER Oliver, 2012)

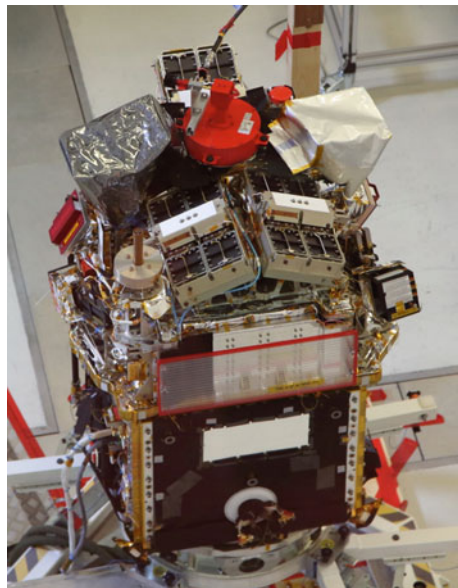
$1000 \times 1000 \text{ km}^2$ on the Earth surface. The combination of all instruments allowed collecting the largest sample of TGF + lightning + TLE events ever measured.

Upon alert of one instrument, after the detection of a TGF, TEB or TLE, all instruments record data prior, during and after the trigger. XGRE is one of the four instruments that have the ability to trigger all the on-board instruments. It was designed to detect photons in the [50 keV, 10 MeV] energy range and electrons in the [1 MeV, 10 MeV] energy range.

The three XGRE instruments, tilted by 20° with regard to the payload baseplate, are shown in Fig. 14.6. The relative counts of the three sensors allow estimating the direction of the gamma-ray flux for bright events with 10° accuracy. Each instrument contains four Detection Units (DU), composed of a 8.7 mm thick Lanthanum Bromide crystal (LaBr_3) scintillator, surrounded by two 5-mm thick plastic scintillators. These three scintillators are connected to two multi-anode photomultipliers to enable redundancy. This sandwich design allows the identification of the triggering event as a photon or a charged particle.

Indeed, plastic scintillators have a low effective atomic number ($Z_{\text{eff}} = 6$) and a low density (1.03 g/cm^3), therefore gamma-rays have a small probability to interact with it and deposit energy. On the other hand, gamma-rays have a much higher probability of interacting with the LaBr_3 due to its high effective atomic number ($Z_{\text{eff}} = 46.9$), its five times higher density (5.08 g/cm^3) and its larger thickness. Thus, the three scintillators are sensitive to charged particles, but only the LaBr_3 is efficient against photons. If a significant amount of energy is deposited in the LaBr_3 only, it will probably be due to a gamma-ray. If some energy is also deposited in the plastic scintillators, it will likely be due to an electron.

Fig. 14.6 Photo of the TARANIS satellite at CNES Toulouse, France. We could see the three XGRE instruments on top of the satellite, inclined at different angles in order to estimate the TGF position (credit: CNES and APC)



The effective area of XGRE for detecting gamma-rays is around 900 cm^2 . This decreases to 190 cm^2 at 1.5 MeV. For higher energies, the pair production probability (by interaction with the detector or the surrounding material) becomes higher, increasing the effective area that reaches 230 cm^2 at 10 MeV. The electrons are detected by the plastic scintillators with an effective area from 100 cm^2 at 600 keV to 720 cm^2 at 20 MeV.

14.2.5 Measure of Gamma Rays and Particles in the Earth Radiation Belts

14.2.5.1 The Radiation Belts

Before the end of the 1950s, scientists agreed on the possibility that charged particles could be trapped in the Earth's magnetic field, but only for short timescales [49]. This was a real revolution when first probes (e.g., Explorer 1 and Sputnik 2) observed such intense radiations in space (associated with complex trapping and interaction processes). This discovery has been recently revisited by Baker et al. [50] who have highlighted how each measurement from early probes and spacecraft in the sixties mapped the global shape of what is now known as the Earth radiation belts (also called Van Allen belts).

Thereby, it has soon been understood that the intensity of the Earth magnetic field was strong enough, and its configuration close enough to a magnetic dipole, to permit that charged particles of high energy remain magnetically trapped, in a continuous quasi-periodic motion as explained in details, for example, by Schulz and Lanzerotti [51]. The trapped particles' lifetime can easily exceed a month or even a year depending on the sub-region of the radiation belts considered. For example, in the 1960s, nuclear tests (Project Starfish) were carried out in the upper atmosphere, thus creating an artificial belt of high-energy particles which has been observed for more than ten years [52]. So close to the atmosphere, i.e., in the inner belt, it is mainly Coulomb-type interactions with residual atmosphere that limit their lifetime, as it has been shown early by Wentworth et al. [53]. At higher altitudes, the mechanisms limiting the lifetime of the trapped particles are more intense and more numerous, in particular due to the decrease of the Earth magnetic field strength.

The Earth radiation belts consequently present a characteristic donut shape (following the near dipolar topology of the Earth magnetic field lines), one for the protons belt, and two for the inner and outer electrons belts. Figure 14.7 illustrates this shape for the electrons belts. The colors reflect the intensity of electron fluxes in the heart of the radiation belts. Typically, the Earth radiation belts extend up to about 7 Earth radii for the trapped protons and between 8 and 10 Earth radii for the trapped electrons. The proton energies range from a few tenth of keV up to more than 500 MeV, while the trapped electrons range from a few tenth of keV up to 5 to 10 MeV.

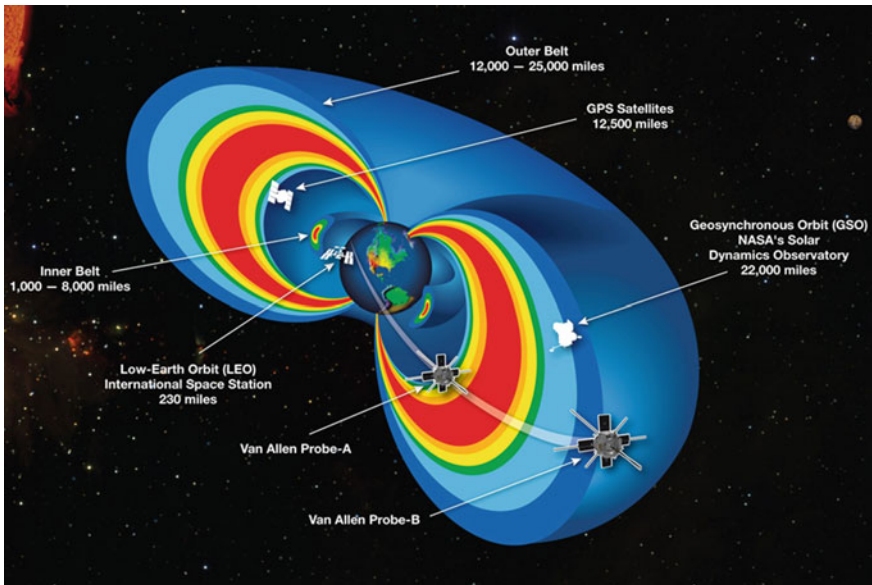


Fig. 14.7 Illustration of the Earth electrons radiation belts shape with over-plotted the location of typical scientific and commercial orbits (credit: NASA)

The major concern promoting the study of this high energetic population close to the Earth is the fact that typical observations and commercial orbits share the same region of Space. Furthermore, highly energetic electrons and protons constrain the design of satellites as they can interact and deposit energy inside on-board materials and electronics, inducing temporary or permanent anomalies and dysfunctions (see recent review by Baker et al. [54]). Figure 14.8 shows average energy spectra of the

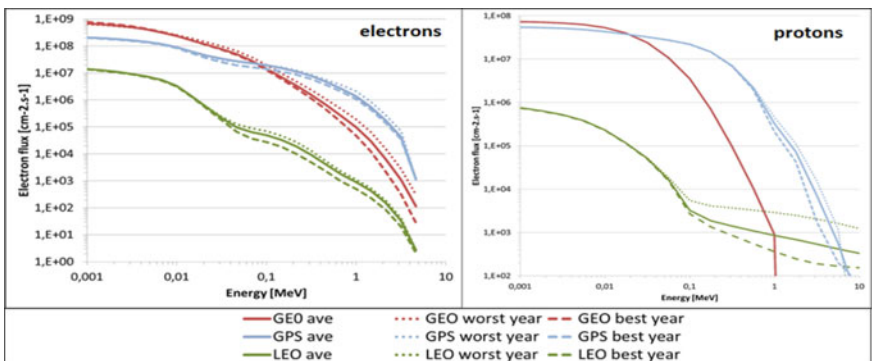


Fig. 14.8 Electrons (left) and protons (right) spectra as estimated by the ONERA-GREEN specification model on typical orbits (LEO, GPS, and GEO). Plotted spectra correspond to solar cycle averages (solid lines), worst year (dotted lines), and best year (dashed lines) (credit: ONERA)

protons and electrons environment encountered by spacecraft along typical orbits, based on the GREEN specification model [55, 56].

The existence of Earth's radiation belts is an interesting paradigm that results from a complex synergy between solar activity and Earth's internal magnetic field. Indeed, on one hand their existence relies on the stability of the Earth magnetic field, while on the other hand their filling requires intensive dynamics. Our Sun is an active medium-sized star that continuously releases a phenomenal amount of energy into the interplanetary medium in the form of three main components:

- a magnetized plasma, the Solar Wind, whose structures (Coronal Mass Ejection and Coronal Interacting Regions) interact with the Earth magnetic field;
- violent emission of very energetic particles called solar flares;
- electromagnetic emissions (from wavelengths in X to radio waves, passing through the visible and infrared).

The first two components induce strong dynamics in the radiation belts, by interacting with the Earth magnetic field and injecting fresh plasma in the region where the Earth magnetic field is dominant (the magnetosphere). This complementary effect induces particle injections, as well as, losses and internal enhanced mechanisms that can energize the trapped population of the Earth radiation belts at different timescales. Figure 14.9 shows these different timescales of dynamics as well as observed dynamics between 2000 and 2015, using the ICARE and ICARE-NG instruments developed by CNES, in cooperation with ONERA and the EREMS company [57, 58]. The groups of Miyoshi [59] and Maget [60] detailed closely these different dynamics as part of the evolving solar cycle activity and Sun-Earth connection. What is of most interest in the perspective of this book is that the dynamics of the Earth radiation belts induce a harsh radiative environment for satellites that can change in hours by more than two or three orders of magnitudes, both for protons and for electrons populations. Moreover, the protons and electrons dynamics are very different, highlighting different behaviors (and related interactions).

As a consequence, it is nowadays still very challenging to forecast and reproduce accurately the shape and evolution of the Earth radiation belts without in situ measurements. Physics-based models lack accuracy and cannot reproduce every different event inducing strong dynamics in the Earth radiation belts. They are indeed commonly and only based on statistical representation of the interactions occurring there [61–64]. In particular, Reeves et al. [65] showed that from one event to another one, the net result induced in the Earth radiation belts may differ a lot, based in particular on the previous history of the population at the event onset. To continue improving the modeling of the dynamics of the Earth radiation belt as well as forecasting its evolution (Space Weather needs) and re-analyzing long-term periods in the past (Specification needs), data assimilation techniques, such as in Meteorology and Oceanography, are developed, combining efficiently physics-based models and in situ data [66, 67]. In conclusion, Earth radiation belts measurements (based on different technology) are still today of prime importance both to mitigate the radiative constraints imposed on spacecraft, and to better characterize and understand the physics behind their dynamics.

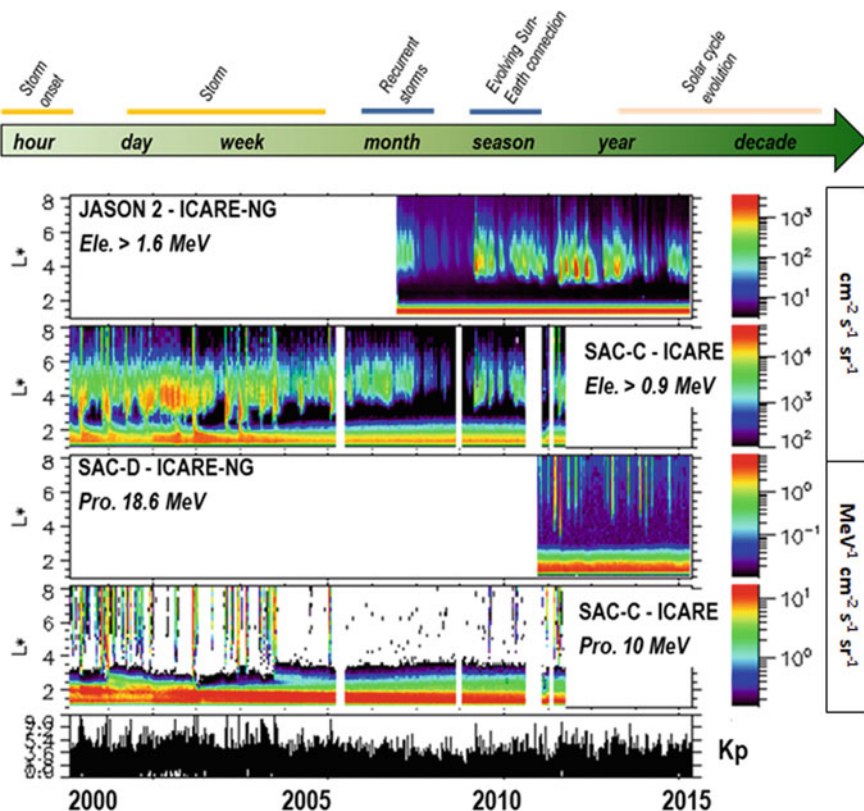


Fig. 14.9 Diagram of the characteristic times of the Earth radiation belts dynamics and related observations made by the ICARE and ICARE-NG instruments (credit: CNES / ONERA / EREMS) from 2000 to 2015. Differential flux are plotted for protons energies (in $\text{MeV}^{-1} \text{cm}^{-2} \text{s}^{-1} \text{sr}^{-1}$) and integral one for electrons energies (in $\text{cm}^{-2} \text{s}^{-1} \text{sr}^{-1}$) as function of the L^* parameter (equivalent to the radial distance in Earth radii, mapped in the magnetic equator)

14.2.6 Measure of Gamma Rays/Particles from the Radiation Belts

Since the presence of charged particles around the Earth has been highlighted, the scientific community have tried to fully understand all the physical mechanisms involved as well as the related dynamics. For this purpose, in situ measurements of particles are paramount. The concept of radiation monitors obviously already existed but the exploration of an unfamiliar environment implied new difficulties:

What are the particles in the radiation belts?

What exactly are the energies involved?

Do these particles have an isotropic distribution?

Added to these questions is the difficulty to address both the needs of the measurement and the constraints inherent to the satellite orbit (unlike ground measurements). Several kinds of radiation monitors associated to space missions have been developed, using different technologies such as EJ-230 fast-timing plastic scintillators [68] and silicon diodes (as ICARENG [57], RADEM [69] and EPT [70]). Detectors using diodes are particularly suitable for measuring high-energy particles (protons > MeV and electrons > 100 keV) [71].

Combination of diodes can be used to explore the information of the radiative environment in which the detector is located. Typically, single-diode detectors can be used to deduce integrated fluxes while detectors using several diodes are particularly adapted to deduce differential fluxes. There are several methods for calculating fluxes from detector measurements [72]. Detectors composed of several diodes can operate with multiple acquisition modes. Indeed, different fields of view are then usable. The coincidence mode describes the case where the incident particle impacts two or more diodes. On the contrary, the anticoincidence mode describes the case where the incident particle impacts only one diode. When the detector consists of only one diode, these modes are obviously not accessible and the acquisition mode is then called single mode.

The behavior of a detector is evaluated by its response function, as shown in Fig. 14.10. Response function makes the link between incident energy and deposited energy for a given environment (electrons, protons, and so on). The color scale is the geometric factor (gef) which can be, for the sake of simplicity, associated to a probability. In the same way, the response functions of all the expected particles of the satellite's environment need to be simulated.

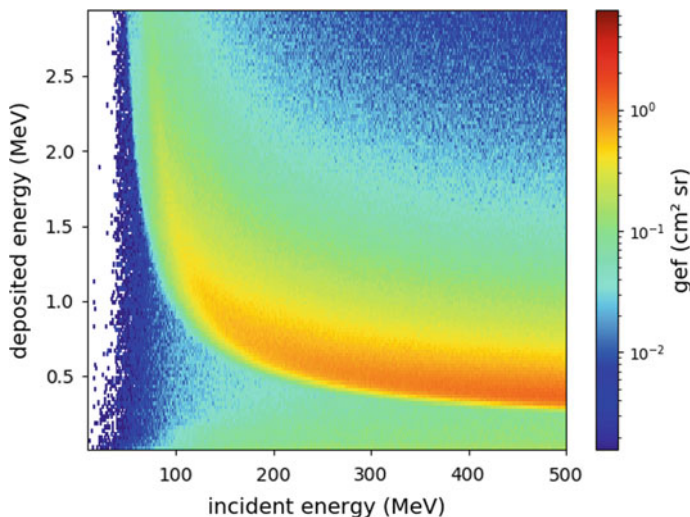


Fig. 14.10 Proton response function of an ICARENG detector (credit: ONERA)

The notion of deposited energy is important because it is very often the basis of particle measurement (in terms of flux). Deposited energies are induced by the interactions produced by the particles as they pass through matter. The proton response function shown in Fig. 14.10 involves mainly two kinds of interactions:

- Coulomb interactions: ionization (which is the dominant contribution in terms of deposited energy in Fig. 14.10) and elastic scattering,
- Nuclear interactions: elastic and inelastic events (whose occurrences are relatively rare).

To describe all these processes and build the response of a detector, Monte Carlo simulations are needed. Several toolkits are available for this purpose, such as GEANT4 [73], FLUKA [74] or MCNPX [75]. In practice, it is not exactly the deposited energy which is measured but a corresponding current. The deposited energy is related to the induced charge by the energy required to create electron–hole pair. In the case of silicon targets, this energy is about 3.6 eV.

For instance, 1 MeV proton deposits all its energy in a silicon diode of few microns and generates more than 250,000 electron–hole pairs on average (which correspond to a charge greater than 40 fC). All the electrons and holes created are then drifting to the electrodes under the field generated by the applied voltage across the sensor. This charge, which is thus in proportion to the energy deposited in the sensor by the incident particle, is then converted into a voltage pulse, or its integral, using a preamplifier.

In addition to the acquisition modes (single, anticoincidence and coincidence modes), the geometry of the detector influences its response. Depending on requirements, the detector will be designed differently by playing with the thickness and nature of the materials used. For instance, by increasing the thickness (or taking high-Z material instead of the aluminum usually used as the sensor housing), the comma that can be seen in Fig. 14.10 will be shifted to higher energies.

Still today, one of the main challenges of radiation monitors is to be able to evaluate with certainty the nature of the incident particle. Indeed, 500 MeV protons have roughly the same LET (Linear Energy Transfer) to 200 keV electrons (up to several tens of microns in silicon material). These particles will therefore deposit, on average, roughly the same quantity of energy (in diodes of these dimensions). Thus, discriminating such particles can be complicated if only deposited energy is recorded. Pulse shape discrimination or appropriate combinations of active regions (with the notion of coincidence) are good candidates to solve this difficulty.

14.2.7 IGOSAT: A Student Nanosat Project to Measure Radiation Belts Gamma Ray/Particles

IGOSAT [76] is a nanosat project from “Université de Paris”, France, which aims at studying gamma-ray and electrons in the ionosphere and radiation belts. Besides its

scientific interests, it has also been conceived as a pedagogical project, where most of the satellite parts has been conceived and realized by students from several Universities and Engineering School during internships. The project, funded by CNES and by the UnivEarthS Labex, is presently in the flight model realization phase for a launch foreseen in 2022. The IGOSAT mission has two main scientific objectives, and thus two payloads:

- To measure the Total Electronic Content (TEC) of the ionosphere (TEC payload),
- To measure gamma ray and electrons spectra in the polar zones and in the South Atlantic Anomaly (SAA, scintillator payload).

14.2.7.1 The TEC Payload

The Ionosphere is a region of the Earth's atmosphere, located between 60 and 800 km in altitude. Free electrons, generated through ionization of the atmospheric molecules by very energetic UV and X-rays radiations, propagate in this medium. Depending on various factors such as the received solar flux intensity, the collision rate between particles and plasma diffusion due to the Earth's magnetic field, ions production occurs more or less simultaneously with recombination of free electrons. The existing equilibrium between ionization, recombination and particle transport determines the global electron density distribution of the ionosphere.

At low altitudes, the density of air molecules is high and the recombination is fast. On the other hand, at higher altitudes, the density of the air is lower, thus the probability of recombination of free electrons with ions decreases. To describe the ionosphere and the variations of free electrons that populate its different layers, a parameter, typically measured during trans-ionospheric investigations, has been defined: the Total Electronic Content (TEC).

This parameter corresponds to the number of free electrons contained in a cylinder of unit section and having as axis the line of sight extending on the path separating on one side, a radio wave receiver and on the other, the emitter of these signals. The TEC, obtained by recording GNSS satellite signals, is a parameter that is measured from data received from several ground station networks (e.g., IGS, UNAVCO, GEONET, SONEL, RENAG). However, these networks cover only continents and islands, and do not cover the entire ionosphere, especially over the oceans. Several space missions have already embarked on-board GPS receivers to measure the TEC from space, producing data that allow surveys around the globe and in particular on areas that are not covered by ground stations. A GPS receiver on a satellite also provides an observation geometry that is not possible from the ground, making possible the observation of the ionosphere in horizontal slices: it is the geometric configuration of the radio occultation technique.

The TEC payload on IGOSAT consists of a double frequency GPS emitter/receiver specially conceived to measure TEC by exchanging signals with other GPS satellites all around the Earth. In collaboration with other space experiments, the TEC payload will thus enable the mapping of the electrons content of the whole ionosphere.

14.2.7.2 The Scintillator Payload

As we have seen above, radiation belts (also known as Van Allen belts) are areas of the Earth's magnetosphere where particles of the solar wind are trapped and propagate from pole to pole spiraling around the field lines. These belts reach very low altitudes at the poles and are in contact with the Earth's atmosphere. Charged particles trapped in the magnetic field lines are thus injected at very low altitudes through these regions, thereby increasing the local density of very high-energy (higher than MeV) electrons and protons. It is here that we can observe polar aurorae (named aurora borealis in the northern hemisphere and aurora australis in the southern hemisphere). The probability of measuring electrons up to ten MeV and gamma photons resulting from the interaction of charged particles with ionospheric air molecules is therefore greater in the polar zones than elsewhere. Another region is characterized by a high particle density: the South Atlantic Anomaly (SAA). Located above Brazil, this anomaly is due to the fact that the Van Allen belt is closer to the surface of the Earth in this region, which is due to the non-alignment between the Earth rotation and magnetic axis.

The scintillator payload aims to observe these zones and is composed of two scintillating materials. The amount of light created when a particle (such as an electron or a gamma-ray photon) enters these detectors is then measured by a photo-sensitive detector, here a SiPM, which converts this amount into an electrical current. This current is then amplified and its intensity is integrated by a dedicated electronic card. This measured charge is also quasi proportional to the primary particle (photon) deposit energy. As in TARANIS/XGRE, two scintillators are used in IGOSAT in order to discriminate between detected photons and charged particles. Indeed, one of the scintillators is made of EJ-200 plastic and is mainly sensitive to charged particles. The other, made of a CeBr_3 crystal, is sensitive, on the other hand, to gamma ray and electrons. The on-board computer will thus tag as electron a "particle" which has made energy deposit in the two detectors, whereas "particle" interacting in the crystal only will be tagged as a photon. The system has been optimized by simulations on ground in order to have a false identification rate as low as possible (less than 10%). The measure of the energy of each detected photon and their flux will enable producing the spectra and light curves of electrons and photons along the IGOSAT orbit, in particular in the SAA and polar regions, that is in highly active regions of the radiation belts.

14.3 Conclusion

As we have seen, scintillators are used in various fields of Earth and atmospheric sciences. They are now widely used on Earth to measure natural radioactivity or monitor possible human-related radioactive emissions, by industries or nuclear accidents. It has become a very hot topic for citizen sciences, illustrated here by the OpenRadiation and Belisama projects, but several other projects exist all over the

world. The study of atmospheric high-energy phenomena during thunderstorms is also a recent scientific topic, starting from the first measurements in the 1990s with scintillating detectors on-board satellites. They are studied in detail by the ASIM experiment on the International Space Station and will be explored by the future TARANIS-2 mission, if accepted by CNES. Going higher in altitude, scintillators are now thought to be used to study the particle environment around Earth (and also the gamma-ray albedo), and get a detailed view of the Van Allen belts. IGOSAT will add a stone to this edifice by measuring the Earth's gamma-ray albedo and by observing charged particles in the South Atlantic Anomaly and at the poles.

References

1. UNSCEAR, Sources and Effects of Ionizing Radiation, UNSCEAR 2008 Report:V. I: Sources - Report to the General Assembly Scientific Annexes A and B. United Nations, United Nations Office, Vienna. ISBN: 13: 9789211422740 (2010)
2. W. De Vos, T. Tarvainen, Geochemical Atlas of Europe. Part 2 – Interpretation of Geochemical Maps, Additional tables, Figures, Maps and Related Publications (2006), <https://weppi GTK.fi/publ/foregatlas/part2.php>. Accessed 22 Jan 2021
3. M. Sohrabi, A.R. Esmaili, Int. Congr. Ser. **1225**, 15 (2002)
4. M.V.Thampi, V.D. Cherian, C.J. Kurien, E.N. Ramachandran, C.V. Karuppasamy, P.K.M. Koya, B. Das, K.P. George, V.KRajan, P.S. Chauhan, Int. Congr. Ser. **1225**, 207 (2002)
5. M.P. Chougaonkar, K.P. Eappen, T.V. Ramachandran, P.G. Shetty, Y.S. Mayya, S. Sadasivan, V.V. Raj, J. Environ. Radioact. **71**(3), 275 (2004)
6. J. Zou, Z. Tao, Q. Sun, S. Akiba, Y. Zha, T. Sugahara, L. Wei, Int. Congr. Ser. **1276**, 97 (2005)
7. I.A. Sachett, Ph.D. dissertation, Universidade do Estado do Rio de Janeiro (2002)
8. M. Sohrabi, M. Babapouran, Int. Congr. Ser. **1276**, 169 (2005)
9. A. Elliott, Committee on Medical Aspects of Radiation in the Environment (COMARE), Radium contamination in the area around Dalgety Bay, 15th report (Public Health England, 2014), https://assets.publishing.service.gov.uk/government/uploads/system/uploads/attachment_data/file/312674/COMARE_15th_Report.pdf. Accessed 22.01.2021
10. C.M. Vandecasteele, M. Sonck, D. Degeldre, Radioprotection **46**(2), 159 (2011)
11. European Radiological Data Exchange Platform website: <https://eurdep.jrc.ec.europa.eu/Entry/Default.aspx>. Accessed 28.12.20
12. M. Sangiorgi, M.A. Hernández-Ceballos, K. Jackson, G. Cinelli, K. Bogucarskis, L. De Felice, A. Patrascu, M. De Cort, Earth Syst. Sci. Data **12**(1), 109 (2020)
13. Réseau national de mesures de la radioactivité de l'environnement website. www.mesure-radioactivite.fr. Accessed 28.12.20
14. Radiation Watch website. www.radiation-watch.org. Accessed 28.12.20
15. Safecast website. <https://safecast.org/>. Accessed 28.12.20
16. Súro website. www.suro.cz/aplikace/ramesis-wiki/. Accessed 28.12.20
17. J. Helebrant, P. Kuča, Radiat. Prot. Dosim. **186**(2–3), 291 (2019)
18. Radiation Detection Group of Oregon State University. <https://research.engr.oregonstate.edu/rddg/wireless-low-cost-gamma-spectrometer>. Accessed 28.12.20
19. E.M. Becker, A.T. Farsoni, A.M. Alhawsawi, B. Alemayehu, IEEE Trans. Nucl. Sci. **60**(2), 968 (2013)
20. Icohup website, RIUM product. <https://icohop.com/en/radiametre-scintillation/>. Accessed 28.12.20
21. E.M. Becker, A.T. Farsoni, Nucl. Instr. Methods A **761**, 99 (2014)

22. J.F. Bottollier-Depois, E. Allain, G., Baumont, N. Berthelot, G. Darley, F. Ecrabé, T. Jolivet, A., Lebeau-Livé, V. Lejeune, F., Quéinnec, C., Simon, F., Trompier, Radioprotection **54**(4), 241 (2020)
23. OpenRadiation website. <https://www.openradiation.org/en>. Accessed 28.12.2020
24. T. Enoto, Y. Wada, Y. Furuta, K. Nakazawa, T. Yuasa, K. Okuda, K. Makishima, M. Sato, Y. Sato, T. Nakano, D. Umemoto, H. Tsuchiya, Nature **551**(7681), 481 (2017)
25. J.R. Dwyer, D.M. Smith, Geophys. Res. Lett. **32**(22), L22804 (2005)
26. J.R. Dwyer, L.P. Babich, J. Geophys. Res.: Space Phys. **116**(A9), A09301 (2011)
27. S. Celestin, W. Xu, V.P. Pasko, J. Geophys. Res.: Space Phys. **117**(A5), A05315 (2012)
28. J.R. Dwyer, Geophys. Res. Lett. **30**(20), 2055 (2003)
29. J.R. Dwyer, D.M. Smith, S.A. Cummer, Space Sci. Rev. **173**, 133 (2012)
30. G.K. Parks, B.H. Mauk, R. Spiger, J. Chin, Geophys. Res. Lett. **8**(11), 1176 (1981)
31. M. McCarthy, G.K. Parks, Geophys. Res. Lett. **12**(6), 393 (1985)
32. K.B. Eack, W.H. Beasley, W.D. Rust, T.C. Marshall, M. Stolzenburg, J. Geophys. Res.: Atmos. **101**(D23), 29637 (1996)
33. A. Chilingarian, L. Vanyan, B. Mailyan, Astropart. Phys. **48**, 1 (2013)
34. Y. Wada, T. Enoto, Y. Nakamura, Y. Furuta, T. Yuasa, K. Nakazawa, T. Morimoto, M. Sato, T. Matsumoto, D. Yonetoku, T. Sawano, H. Sakai, M. Kamogawa, T. Ushio, K. Makishima, H. Tsuchiya, Commun. Phys. **2**, 67 (109)
35. N.A. Kelley, D.M. Smith, J.R. Dwyer, M. Splitter, S. Lazarus, F. Martinez-McKinney, B. Hazelton, B. Grefenstette, A. Lowell, H.K. Rassoul, Nature Comm. **6**, 7845 (2015)
36. N. Østgaard, H.J. Christian, J.E. Grove, D. Sarria, A. Mezentsev, P. Kochkin, N. Lehtinen, M. Quick, S. Al-Nussirat, E. Wulf, G. Genov, K. Ullaland, M. Marisaldi, S. Yang, R.J. Blakeslee, J. Geophys. Res.: Atmos. **124**(13), 7236 (2019)
37. G.J. Fishman, P.N. Bhat, R. Mallozzi, J.M. Horack, T. Koshut, C. Kouveliotou, G.N. Pendleton, C.A. Meegan, R.B. Wilson, W.S. Paciesas, S.J. Goodman, H.J. Christian, Science **264**(5163), 1313 (1994)
38. D.M. Smith, L.I. Lopez, R.P. Lin, C.P. Barrington-Leigh, Science **307**(5712), 1085 (2005)
39. M. Marisaldi, F. Fuschino, C. Labanti, M. Galli, F. Longo, E. Del Monte, G. Barbiellini, M. Tavani, A. Giuliani, E. Moretti, S. Vercellone, E. Costa, S. Cutini, I. Donnarumma, Y. Evangelista, M. Feroci, I. Lapshov, F. Lazzarotto, P. Lipari, S. Mereghetti, L. Pacciani, M. Rapisarda, P. Soffitta, M. Trifoglio, A. Argan, F. Boffelli, A. Bulgarelli, P. Caraveo, P. W. Cattaneo, A. Chen, V. Cocco, F. D'Ammando, G. De Paris, G. Di Cocco, G. Di Persio, A. Ferrari, M. Fiorini, T. Froyland, F. Gianotti, A. Morselli, A. Pellizzoni, F. Perotti, P. Picozza, G. Piano, M. Pilia, M. Prest, G. Pucella, A. Rappoldi, A. Rubini, S. Sabatini, E. Striani, A. Trois, E. Vallazza, V. Vittorini, A. Zambra, D. Zanello, L. A. Antonelli, S. Colafrancesco, D. Gasparrini, P. Giommi, C. Pittori, B. Preger, P. Santolamazza, F. Verrecchia, L. Salotti, J. Geophys. Res.: Space Phys. **115**(A3), A00E13 (2010)
40. M.S. Briggs, G.J. Fishman, V. Connaughton, P.N. Bhat, W.S. Paciesas, R.D. Preece, C. Wilson-Hodge, V.L. Chaplin, R.M. Kippen, A. von Kienlin, C.A. Meegan, E. Bissaldi, J.R. Dwyer, D.M. Smith, R.H. Holzworth, J.E. Grove, A. Chekhtman, J. Geophys. Res.: Space Phys. **115**(A7), A07323 (2010)
41. A. Ursi, C. Guidorzi, M. Marisaldi, D. Sarria, F. Frontera, J. Atmos. Sol.-Terr. Phys. **156**, 50 (2017)
42. N. Østgaard, T. Neubert, V. Reglero, K. Ullaland, S. Yang, G. Genov, M. Marisaldi, A. Mezentsev, P. Kochkin, N. Lehtinen, D. Sarria, B. H. Qureshi, A. Solberg, C. Maiorana, K. Albrechtsen, C. Budtz-Jørgensen, I. Kuvvetli, F. Christiansen, O. Chanrion, M. Heumesser, J. Navarro-Gonzalez, P. Connell, C. Eyles, H. Christian, S. Al-nussirat, J. Geophys. Res.: Atmos. **124**(24), 14,024 (2019)
43. J.R. Dwyer, B.W. Grefenstette, D.M. Smith, Geophys. Res. Lett. **35**(2), L02815 (2008)
44. M.S. Briggs, V. Connaughton, C. Wilson-Hodge, R.D. Preece, G.J. Fishman, R.M. Kippen, P.N. Bhat, W.S. Paciesas, V.L. Chaplin, C.A. Meegan, A. von Kienlin, J. Greiner, J.R. Dwyer, D.M. Smith, Geophys. Res. Lett. **38**(2), L02808 (2008)

45. R.U. Abbasi, M. Abe, T. Abu-Zayyad, M. Allen, R. Anderson, R. Azuma, E. Barcikowski, J.W. Belz, D.R. Bergman, S.A. Blake, R. Cady, B.G. Cheon, J. Chiba, M. Chikawa, T. Fujii, M. Fukushima, T. Goto, W. Hanlon, Y. Hayashi, N. Hayashida, K. Hibino, K. Honda, D. Ikeda, N. Inoue, T. Ishii, R. Ishimori, H. Ito, D. Ivanov, C.C.H. Jui, K. Kadota, F. Kakimoto, O. Kalashev, K. Kasahara, H. Kawai, S. Kawakami, S. Kawana, K. Kawata, E. Kido, H.B. Kim, J.H. Kim, J.H. Kim, S. Kishigami, S. Kitamura, Y. Kitamura, V. Kuzmin, Y.J. Kwon, J. Lan, J.P. Lundquist, K. Machida, K. Martens, T. Matsuda, T. Matsuyama, J.N. Matthews, M. Minamino, K. Mukai, I. Myers, K. Nagasawa, S. Nagataki, T. Nakamura, T. Nonaka, A. Nozato, S. Ogio, J. Ogura, M. Ohnishi, H. Ohoka, K. Oki, T. Okuda, M. Ono, R. Onogi, A. Oshima, S. Ozawa, I.H. Park, M.S. Pshirkov, D.C. Rodriguez, G. Rubtsov, D. Ryu, H. Sagawa, K. Saito, Y. Saito, N. Sakaki, N. Sakurai, A.L. Sampson, L.M. Scott, K. Sekino, P.D. Shah, F. Shibata, T. Shibata, H. Shimodaira, B.K. Shin, H.S. Shin, J.D. Smith, P. Sokolsky, R.W. Springer, B.T. Stokes, S.R. Stratton, T.A. Stroman, T. Suzawa, M. Takamura, M. Takeda, R. Takeishi, A. Taketa, M. Takita, Y. Tameda, H. Tanaka, K. Tanaka, M. Tanaka, S.B. Thomas, G.B. Thomson, P. Tinyakov, I. Tkachev, H. Tokuno, T. Tomida, S. Troitsky, Y. Tsunesada, K. Tsutsumi, Y. Uchihori, S. Udo, F. Urban, G. Vasiloff, T. Wong, R. Yamane, H. Yamaoka, K. Yamazaki, J. Yang, K. Yashiro, Y. Yoneda, S. Yoshida, H. Yoshii, R. Zollinger, Z. Zundel, *Phys. Lett. A* **381**(32), 2565 (2017)
46. R.U. Abbasi, T. Abu-Zayyad, M. Allen, E. Barcikowski, J.W. Belz, D.R. Bergman, S.A. Blake, M. Byrne, R. Cady, B.G. Cheon, J. Chiba, M. Chikawa, T. Fujii, M. Fukushima, G. Furlich, T. Goto, W. Hanlon, Y. Hayashi, N. Hayashida, K. Hibino, K. Honda, D. Ikeda, N. Inoue, T. Ishii, H. Ito, D. Ivanov, S. Jeong, C.C.H. Jui, K. Kadota, F. Kakimoto, O. Kalashev, K. Kasahara, H. Kawai, S. Kawakami, K. Kawata, E. Kido, H.B. Kim, J.H. Kim, J.H. Kim, S.S. Kishigami, P.R. Krehbiel, V. Kuzmin, Y.J. Kwon, J. Lan, R. LeVon, J.P. Lundquist, K. Machida, K. Martens, T. Matuyama, J.N. Matthews, M. Minamino, K. Mukai, I. Myers, S. Nagataki, R. Nakamura, T. Nakamura, T. Nonaka, S. Ogio, M. Ohnishi, H. Ohoka, K. Oki, T. Okuda, M. Ono, R. Onogi, A. Oshima, S. Ozawa, I.H. Park, M.S. Pshirkov, J. Remington, W. Rison, D. Rodeheffer, D.C. Rodriguez, G. Rubtsov, D. Ryu, H. Sagawa, K. Saito, N. Sakaki, N. Sakurai, T. Seki, K. Sekino, P.D. Shah, F. Shibata, T. Shibata, H. Shimodaira, B.K. Shin, H.S. Shin, J.D. Smith, P. Sokolsky, R.W. Springer, B.T. Stokes, T.A. Stroman, H. Takai, M. Takeda, R. Takeishi, A. Taketa, M. Takita, Y. Tameda, H. Tanaka, K. Tanaka, M. Tanaka, R.J. Thomas, S.B. Thomas, G.B. Thomson, P. Tinyakov, I. Tkachev, H. Tokuno, T. Tomida, S. Troitsky, Y. Tsunesada, Y. Uchihori, S. Udo, F. Urban, G. Vasiloff, T. Wong, M. Yamamoto, R. Yamane, H. Yamaoka, K. Yamazaki, J. Yang, K. Yashiro, Y. Yoneda, S. Yoshida, H. Yoshii, Z. Zundel, *J. Geophys. Res.: Atmos.* **123**(13), 6864 (2018)
47. N. Berge, S. Celestin, *Geophys. Res. Lett.* **46**(14), 8424 (2019)
48. J.W. Belz, P.R. Krehbiel, J. Remington, M.A. Stanley, R.U. Abbasi, R. LeVon, W. Rison, D. Rodeheffer, T. Abu-Zayyad, M. Allen, E. Barcikowski, D.R. Bergman, S.A. Blake, M. Byrne, R. Cady, B.G. Cheon, M. Chikawa, A. di Matteo, T. Fujii, K. Fujita, R. Fujiwara, M. Fukushima, G. Furlich, W. Hanlon, M. Hayashi, Y. Hayashi, N. Hayashida, K. Hibino, K. Honda, D. Ikeda, T. Inadomi, N. Inoue, T. Ishii, H. Ito, D. Ivanov, H. Iwakura, H.M. Jeong, S. Jeong, C.C.H. Jui, K. Kadota, F. Kakimoto, O. Kalashev, K. Kasahara, S. Kasami, H. Kawai, S. Kawakami, K. Kawata, E. Kido, H.B. Kim, J.H. Kim, J.H. Kim, V. Kuzmin, M. Kuznetsov, Y.J. Kwon, K.H. Lee, B. Lubsandorzhiev, J.P. Lundquist, K. Machida, H. Matsumiya, J.N. Matthews, T. Matuyama, R. Mayta, M. Minamino, K. Mukai, I. Myers, S. Nagataki, K. Nakai, R. Nakamura, T. Nakamura, Y. Nakamura, T. Nonaka, H. Oda, S. Ogio, M. Ohnishi, H. Ohoka, Y. Oku, T. Okuda, Y. Omura, M. Ono, A. Oshima, S. Ozawa, I.H. Park, M. Potts, M.S. Pshirkov, D.C. Rodriguez, G. Rubtsov, D. Ryu, H. Sagawa, R. Sahara, K. Saito, Y. Saito, N. Sakaki, T. Sako, N. Sakurai, K. Sano, T. Seki, K. Sekino, F. Shibata, T. Shibata, H. Shimodaira, B.K. Shin, H.S. Shin, J.D. Smith, P. Sokolsky, N. Sone, B.T. Stokes, T.A. Stroman, Y. Takagi, Y. Takahashi, M. Takeda, R. Takeishi, A. Taketa, M. Takita, Y. Tameda, K. Tanaka, M. Tanaka, Y. Tanoue, S. B. Thomas, G.B. Thomson, P. Tinyakov, I. Tkachev, H. Tokuno, T. Tomida, S. Troitsky, Y. Tsunesada, Y. Uchihori, S. Udo, T. Uehama, F. Urban, M. Wallace, T. Wong, M. Yamamoto, H. Yamaoka, K. Yamazaki, K. Yashiro, M. Yosei, H. Yoshii, Y. Zhezher, Z. Zundel, *J. Geophys. Res.: Atmos.* **125**(23), e2019JD031940 (2020)

49. C. Störmer, Q.J.R. Meteorol. Soc. **82**(351), 115 (1956)
50. D.N. Baker, M.I. Panasyuk, Phys. Today **70**(12), 46 (2017)
51. M. Schulz, L.J. Lanzerotti, *Particle Diffusion in the Radiation Belts* (Springer-Verlag, Berlin Heidelberg, 1974).
52. L.R. Lyons, R.M. Thorne, J. Geophys. Res. **78**(13), 2142 (1973)
53. R.C. Wentworth, W.M. MacDonald, S.F. Singer, Phys. Fluids **2**(5), 499 (1959)
54. D.N. Baker, P.J. Erickson, J.F. Fennell, J.C. Foster, A.N. Jaynes, P.T. Verronen, Space Sci. Rev. **214**(1), 17 (2018)
55. A. Sicard, D. Boscher, S. Bourdarie, D. Lazaro, D. Standarovski, R. Ecoffet, Ann. Geophys. **36**(4), 953 (2018)
56. A. Sicard, D. Boscher, D. Lazaro, S. Bourdarie, D. Standarovski, R. Ecoffet, IEEE Trans. Nucl. Sci. **66**(7), 1738 (2019)
57. D. Boscher, S.A. Bourdarie, D. Falguere, D. Lazaro, P. Bourdoux, T. Baldran, G. Rolland, E. Lorfèvre, R. Ecoffet, IEEE Trans. Nucl. Sci. **58**(3), 916 (2011)
58. D. Falguere, D. Boscher, T. Nuns, S. Duzellier, S. Bourdarie, R. Ecoffet, S. Barde, J. Cueto, C. Alonso, C. Hoffman, IEEE Trans. Nucl. Sci. **49**(6), 2782 (2002)
59. Y.S. Miyoshi, V.K. Jordanova, A. Morioka, D.S. Evans, Space Weather **2**(10), S10S02 (2004)
60. V. Maget, S. Bourdarie, D. Boscher, R.H.W. Friedel, Space Weather **5**(10), S10003 (2007)
61. D. Herrera, V.F. Maget, A. Sicard-Piet, J. Geophys. Res.: Space Phys. **121**(10), 9517 (2016)
62. S. Lejosne, P. Kollmann, Space Sci. Rev. **216**(1), 19 (2020)
63. K. Orlova, Y. Shprits, J. Geophys. Res.: Space Phys. **119**(2), 770 (2014)
64. A. Sicard-Piet, D. Boscher, R.B. Horne, N.P. Meredith, V. Maget, Ann. Geophys. **32**(8), 1059 (2014)
65. G.D. Reeves, K.L. McAdams, R.H.W. Friedel, T.P. O'Brien, Geophys. Res. Lett. **30**(10), 1529 (2003)
66. S.A. Bourdarie, V.F. Maget, Ann. Geophys. **30**(6), 929 (2012)
67. V. Maget, S. Bourdarie, D. Boscher, IEEE Trans. Nucl. Sci. **55**(4), 2188 (2008)
68. A. Rizzo, L. Narici, R. Messi, P. Cipollone, C. De Donato, L. Di Fino, M. Iannilli, C. La Tessa, C. Manea, G. Masciantonio, M.C. Morone, G. Nobili, D. Pecchi, P. Picozza, E. Reali, M. Rovituso, F. Tommasino, G. Vitali, Nucl. Instr. Methods A **898**, 98 (2018)
69. M. Pinto, P. Gonçalves, A. Marques, J.C. Pinto, W. Hajdas, IEEE Trans. Nucl. Sci. **66**(7), 1770 (2019)
70. M. Cyamukungu, S. Benck, S. Borisov, G. Grégoire, J. Cabrera, J.-L. Bonnet, B. Desoete, F. Preud'homme, C. Semaille, G. Creve, J. De Saedeleer, S. Ilse, L. De Busser, V. Pierrard, S. Bonnewijn, J. Maes, E. Van Ransbeeck, E. Neefs, J. Lemaire, E. Valtonen, R. Punkkinen, M. Anciaux, K. Litefti, N. Brun, D. Pauwels, C. Quevrin, D. Moreau, A. Helderweirt, W. Hajdas, P. Nieminen, IEEE Trans. Nucl. Sci. **61**(6), 15 (2014)
71. D. Boscher, T. Cayton, V. Maget, S. Bourdarie, D. Lazaro, T. Baldran, P. Bourdoux, E. Lorfèvre, G. Rolland, R. Ecoffet, IEEE Trans. Nucl. Sci. **61**(6), 3395 (2014)
72. V. Maget, S. Bourdarie, D. Lazaro, D. Boscher, G. Rolland, R. Ecoffet, E. Lorfèvre, Unfolding JASON-2/ICARE-NG high energy particles measurements using a Singular Value Decomposition approach. Paper presented at 14th European Conference on Radiation and Its Effects on Components and Systems (RADECS), Oxford, United Kingdom, 23–27 Sept. 2013
73. S. Agostinelli, J. Allison, K. Amako, J. Apostolakis, H. Araujo, P. Arce, M. Asai, D. Axen, S. Banerjee, G. Barrand, F. Behner, L. Bellagamba, J. Boudreau, L. Broglia, A. Brunengo, H. Burkhardt, S. Chauvie, J. Chuma, R. Chytracek, G. Cooperman, G. Cosmo, P. Degtyarenko, A. Dell'Acqua, G. Depaola, D. Dietrich, R. Enami, A. Feliciello, C. Ferguson, H. Fesefeldt, G. Folger, F. Foppiano, A. Forti, S. Garelli, S. Giani, R. Giannitrapani, D. Gibin, J.J. Gómez Cadenas, I. González, G. Gracia Abril, G. Greeniaus, W. Greiner, V. Grichine, A. Grossheim, S. Guatelli, P. Gumlunger, R. Hamatsu, K. Hashimoto, H. Hasui, A. Heikkilä, A. Howard, V. Ivanchenko, A. Johnson, F.W. Jones, J. Kallenbach, N. Kanaya, M. Kawabata, Y. Kawabata, M. Kawaguti, S. Kelner, P. Kent, A. Kimura, T. Kodama, R. Kokoulin, M. Kossov, H. Kurashige, E. Lamanna, T. Lampén, V. Lara, V. Lefebure, F. Lei, M. Liendl, W. Lockman, F. Longo, S. Magni, M. Maire, E. Medernach, K. Minamimoto, P. Mora de Freitas, Y. Morita, K. Murakami,

- M. Nagamatu, R. Nartallo, P. Nieminen, T. Nishimura, K. Ohtsubo, M. Okamura, S. O'Neale, Y. Oohata, K. Paech, J. Perl, A. Pfeiffer, M.G. Pia, F. Ranjard, A. Rybin, S. Sadilov, E. Di Salvo, G. Santin, T. Sasaki, N. Savvas, Y. Sawada, S. Scherer, S. Sei, V. Sirotenko, D. Smith, N. Starkov, H. Stoecker, J. Sulkimo, M. Takahata, S. Tanaka, E. Tcherniaev, E. Safai Tehrani, M. Tropeano, P. Truscott, H. Uno, L. Urban, P. Urban, M. Verderi, A. Walkden, W. Wander, H. Weber, J.P. Wellisch, T. Wenaus, D.C. Williams, D. Wright, T. Yamada, H. Yoshida, D. Zschiesche, Nucl. Instr. Methods A **506**(3), 250 (2003)
74. A. Ferrari, P.R. Sala, A. Fasso, J. Ranft, FLUKA: A Multi-Particle Transport Code, SLAC-R-773 (2005)
75. L.S. Waters, G.W. McKinney, J.W. Durkee, M.L. Fensin, J.S. Hendricks, M.R. James, R.C. Johns, D.B. Pelowitz, A.I.P. Conf. Proc. **896**(1), 81 (2007)
76. IGOSat website, <https://igosat.in2p3.fr/fr/page-d-exemple/>. Accessed 28.12.20



Philippe Laurent (58 years) is currently coPI of the INTEGRAL/IBIS mission. He was the head of the French contribution to the Japanese Hitomi X-ray space mission. He spent his thesis in 1992, by studying hard X data sent by the SIGMA telescope on board the Russian-French mission GRANAT. Then, he participated to the realization and calibration of the ISGRI CdTe camera aboard the satellite INTEGRAL. He has managed the IBIS simulation group, and organized the ground calibration of the complete satellite in ESA/ESTEC in 2001. In 2010, he co-leads the French participation to the Japan-French HXI instrument phase A studies for the IXO mission proposal. Since the launch of INTEGRAL, he studied the IBIS data from galactic black holes and neutron stars (such as Cygnus X-1, the Crab pulsar, and Gamma-Ray Bursts), with emphasis on the measure and analysis of the polarization of the gamma-ray light emitted by those sources. He is the author or co-author of 168 publications in peer-reviewed journals, 5805 citations, with an h index of 38, according to the NASA/ADS Website.



Sebastien Celestin received the Ph.D. degree in Physics from École Centrale Paris, France, in 2008. He was then appointed as a Postdoctoral Scholar with The Pennsylvania State University, USA, and subsequently as a Research Associate, in 2011. He has been an Associate Professor in Physics with the University of Orleans (LPC2E, CNRS/CNES) since October 2012. His current research interests include Atmospheric and Space Electrodynamics. He is the author or co-author of over 40 publications, 1 book chapter, with an h-index of 24 according to Google Scholar.



Vincent Maget (41 years) graduated engineer in Space Systems from «Ecole Supérieure de l'Aéronautique et de l'Espace» (ISAE-SUPAERO) and Ph.D. in External Geophysics at Paul Sabatier University of Toulouse. He has worked since 2008 at ONERA, Space Environment Department (DESP) renamed now Department of Physics, Instrumentation, Environment, Space (DPHY) in the field of Radiative Space Environment Modelling. He is currently involved in data assimilation topics dedicated to the Earth radiation belts as well as in their physics-based modelling, and in the development of a miniaturized radiation monitor for a Cubesat mission named CREME. In January 2021, he is the author or co-author of 18 publications, 1 book chapter with a h-index of 9.



Pablo Caron (29 yo) defended his Ph.D. in micronano systems in 2019 at the University of Toulouse (France), on the sensitivity of integrated memories under electron irradiations. He obtained a full position at ONERA in 2019 in the ERS team (space radiation environment) where he is now working on the development of radiation monitors as well as in-flight data processing. In 2020, he is the author or co-author of 6 publications.



François Trompier (49 yo) graduated engineer in Nuclear sciences and Ph.D. in material sciences at Pierre et Marie Curie University (Paris, France). He has worked since 1997 consecutively at the French Atomic Energy and Alternative Energies Commission (CEA) and the Institute of Radiological Protection and Nuclear Safety (IRSN) in the field of ionizing radiation dosimetry. Beside its expertise in the field of electron spin resonance spectrometry, he worked on the use of scintillators in different field such as reactor dosimetry, cosmic radiation, pulsed radiation and citizen science projects. In January 2021, he is the author or co-author of 124 publications, 4 patents, 2 book chapters and 4 reviews, 2 ISO standards, 1 report for international commissions (ICRU) with a h-index 30 according to Scopus and 37 according to google scholar.

Chapter 15

Plastic Scintillator Detectors for Particle Physics



Priscilla Brooks Cushman and David-Michael Poehlmann

Abstract A review of the use of plastic scintillator in large experimental installations for particle physics, with a special emphasis on calorimetry in multi-purpose collider experiments and neutrino physics, is given. The historical developments of the last four decades are summarized. Modern experiments and their design choices are described in the context of the technological and scientific advances which made them possible.

15.1 Introduction

Plastic scintillators have been an integral part of particle physics detector design, starting with the earliest nuclear table-top experiments to the multi-ton scale collider and neutrino detectors seen today. Even as the experiments grew larger and the demands more stringent, advances in scintillator properties and production, as well as new strategies for implementation, have kept plastic scintillator as a popular choice in a variety of applications, due to its good energy resolution, fast timing, and simple and robust construction. The wide variety of geometries and readout options available allow for many different optimizations, from fine segmentation to large low-cost coverage, from simple trigger counters to high-resolution timing, and from charged particle trackers to pulse shape discrimination. For those experiments that require thousands of individual elements, the cost can be reduced by injection-molding and co-extruding the reflective coating. For those experiments that require very low backgrounds, such as dark matter and neutrinoless double beta decay, the plastic base and selected fluorescent compounds can be made radiopure, with casting being the cleaner process. For large particle physics experiments, two measurement regimes drive the technology: (1) high precision measurement of the

P. B. Cushman ()

School of Physics and Astronomy, University of Minnesota, Minneapolis, MN 55455, USA
e-mail: cushman@umn.edu

D.-M. Poehlmann

Department of Physics and Astronomy, University of California, Davis, CA 95616, USA
e-mail: poehlmann@ucdavis.edu

energy–momentum flow of all particles created in a high-energy collision event and (2) detailed particle identification and tracking data used to characterize the interactions of neutrinos produced by reactors, accelerators, the sun, and astrophysical sources. In order to understand the design choices behind modern particle physics detectors for colliders and neutrino physics, we provide a historical review of plastic scintillating calorimetry over the last forty years, since many of the principles are still in play today and many of the technologies developed for early calorimeters are still very useful for smaller installations.

15.2 Principles of Calorimetry in High-Energy Physics

At the high energies available at modern colliders and fixed-target experiments, calorimetry plays a central role. A calorimeter is an instrumented block of material which responds in a manner proportional to the energy of the particle which passes through it. It is therefore primarily an energy-measuring device, but often provides information on timing, position (if appropriately segmented), and particle identification through differing responses to electrons, muons, and hadrons. If the calorimeter is hermetic (i.e., configured to minimize cracks and dead regions), then it can even be used to infer the contribution from undetected particles such as neutrinos, through momentum balance or missing transverse energy.

15.2.1 Electromagnetic and Hadronic Showers

Calorimeters are characterized by the physical process they are designed to observe. Electromagnetic calorimeters (ECAL) measure the interactions initiated by high-energy electrons or photons, which interact with matter principally via bremsstrahlung (incident electron) or pair production (incident photon). These processes create secondary photons and electron–positron pairs which interact similarly, producing a cascade. The number of secondary particles in such an electromagnetic shower continues to grow until their individual energies drop below the threshold dominated by radiation loss, after which they dissipate energy primarily through ionization. The depth at which the largest number of secondary particles occur is called the shower maximum and is parameterized by the radiation length X_0 , defined as the mean distance over which a high-energy electron loses all but $1/e$ of its energy.

The energy (E) of a calorimeter is proportional to the sum of all N charged particle track segments which emerge from the cascade process, so that the intrinsic energy resolution is stochastic, with sigma proportional to \sqrt{N} or \sqrt{E} since the energy is proportional to N . Thus, the energy resolution is usually quoted as

$$\frac{\sigma_E}{E} = \frac{a}{\sqrt{E}} \oplus \frac{b}{E} \oplus c \quad (15.1)$$

where the stochastic term a accounts for statistical fluctuations in the shower development; b is the noise term (mostly from electronic noise) which limits the low E response; and c is the constant term, which dominates at high energy. Sources contributing to the constant term include calibration stability and non-uniformity of signal collection.

Quarks and gluons streaming out from the interaction point clothe themselves with jets of strongly interacting particles called hadrons. Hadrons encountering matter participate in a broad variety of nuclear interactions, but they also create a cascade of secondary particles. This hadronic shower is mostly composed of nucleons and pions. Roughly, a third of the pions are neutral and decay to two photons ($\pi^0 \rightarrow \gamma\gamma$), which then proceed via the electromagnetic channel. Thus, a hadronic shower has a prompt component due to pi-zero production followed by a slower and longer-range component due to the hadronic activity. The size of a hadronic shower roughly scales with the nuclear interaction length λ_0 , defined as the mean distance traveled by a hadronic particle before undergoing an inelastic nuclear interaction. A hadronic calorimeter (HCAL) must therefore be larger than an ECAL in order to contain the shower. It also has larger intrinsic fluctuations in the detected energy, since the shower components can include decay muons and neutrinos, nuclear excitation, spallation, or fission, as well as ionizing tracks.

A hadronic shower is thus composed of both electromagnetic (em) and non-em components. The fraction of energy which is deposited in the em channel fluctuates dramatically from event to event, largely determined by whether or not the pi-zero is one of the early daughters of the hadron-induced shower. If the response of the calorimeter to the em and non-em components differ, then these event-by-event fluctuations in the energy sharing between the components will introduce a broadening in the resolution of the calorimeter. In general, the response of the components *does* differ, since the non-em component of the hadronic shower deposits a sizeable fraction of its energy in invisible channels, degrading its response relative to the em component. Moreover, since the fraction of each component to the whole is also energy-dependent, the resolution of the hadronic calorimeter will not improve at higher energies as $1/\sqrt{E}$.

The left-hand panel of Fig. 15.1 illustrates the overall compensation concept. Clearly, both the size of the signal and the resolution of the calorimeter would be improved by finding a technique that can make visible the invisible, thereby centering the non-em response curve on top of the em response curve in the left-hand panel. Such a calorimeter is called *compensating*. The drive to create calorimeters with better energy resolution focused on compensation during the 1980s and 90s and resulted in a far better understanding of the underlying shower physics, as well as interactions of high-energy particles with the active medium. Plastic scintillator, with its high hydrogen content, was particularly suited to strategies that relied on proton recoils to detect “invisible” energy in the HCAL. The right-hand panel of Fig. 15.1 demonstrates the energy-dependent character of the em fraction with three sample calorimeters from that era, each with different e/h values [2]. WA1 [3] is an example of a sandwich-style lead/plastic sampling calorimeter from the 1970s with $e/h > 1$. A later experiment, HELIOS [4], took advantage of depleted uranium (DU) and tuned

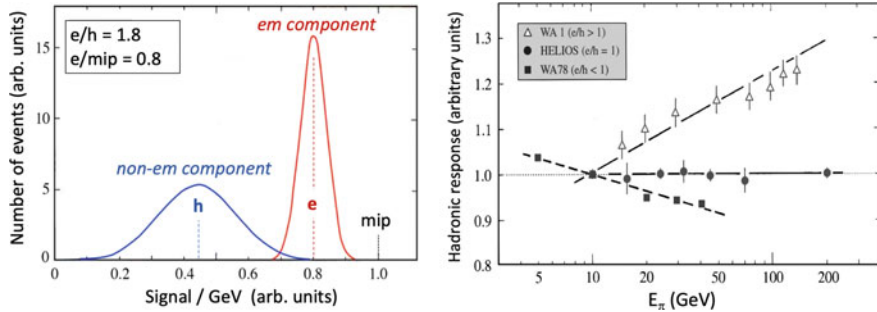


Fig. 15.1 *Left:* The response of an idealized non-compensating hadronic calorimeter to the em and non-em portions of the shower. The distributions are normalized to the response to minimum-ionizing particles (MIPs). The average of the em and non-em distributions corresponds to “e” and “h”, respectively. *Right:* The pion response as a function of energy for three calorimeters with different e/h values. All data are normalized to the pion response at 10 GeV. Figures adapted from Refs. [1, 2]

sampling fractions to achieve compensation: $e/h = 1$, whereas WA78 [5, 6] is an example of a rare over-compensated plastic/DU calorimeter with $e/h < 1$.

15.2.2 Historical Review of Plastic Scintillating Calorimetry

Sampling calorimeters have long used plastic scintillator as the active element. Over the years, the designs have evolved, as has our understanding of the physics of shower development and sampling fluctuations. Advances in photon transport and sensing have enabled new geometries and applications. There is a wide variety in the spectrum and intensity of the produced light, depending on the fluorescent cocktail¹ added to the plastic base. In order to showcase the progress and diversity of the solutions available using plastic scintillator, we have compiled Tables 15.1 and 15.2, which provide, in chronological order, the details of detectors which exemplify the trends in the field. Table 15.1 collects information on the overall progress of sampling calorimeters, whereas Table 15.2 focuses on the tracking calorimeters used primarily in neutrino experiments. The historical narrative that follows establishes the context and provides further details on the forces responsible for the changes.

¹Topological representation and key information of these molecules are given in the Appendix section at the end of the book.

Table 15.1 Large plastic scintillator hadronic sampling calorimeters used in high-energy physics fixed-target and collider experiments

Experiment	Type of Calorimeter	Scintillator	Absorber	Readout	Energy Resolution
WA1 [3] 1979-1983 (CERN)	Sandwich ECAL Sandwich HCAL	5 mm Plexipop	25 mm Fe	Light guide to PMT	$23\%/\sqrt{E}$ $58\%/\sqrt{E}$
MARK J [7,8] 1979-1986 (DESY PETRA)	Sandwich ECAL	5 mm scintillator	5 mm Pb	Light guide to PMT	$12\%/\sqrt{E}$
ATF [9] 1981-1983 (CERN ISR)	Sandwich ECAL	2.5 mm PMMA (10% naphthalene, 1% butyl-PBD)	2 mm DU	BBQ WLS bar to acrylic light guide to PMT	$16\%/\sqrt{E}$
Sandwich HCAL	2.5 mm PMMA (10% naphthalene, 1% butyl-PBD)	3 mm DU, 5 mm Cu	BBQ WLS bar to acrylic light guide to PMT	$36\%/\sqrt{E}$	
UA1 [10-12] 1981-1990 (CERN SpS)	Sandwich ECAL	1.5 mm PS (1% butyl-PBD)	1.2 mm Pb	BBQ WLS bar to acrylic light guide to PMT	$15\%/\sqrt{E} \oplus 3\%$
Sandwich HCAL	1 cm Plexipop (3% naphthalene, 1% butyl-PBD, 0.01% POPOP)	50 mm Fe	BBQ WLS bar to acrylic light guide to PMT	$80\%/\sqrt{E}$	
UA2 [13] 1981-1990 (CERN SpS)	Sandwich ECAL	4 mm PVT (NE-104B)	3.5 mm Pb	Acrylic BBQ WLS light guide to PMT	$16\%/\sqrt{E}$
Sandwich HCAL	5 mm PMMA (10% naphthalene, 1% butyl-PBD, 0.1% POPOP)	15 mm Fe	Acrylic BBQ WLS light guide to PMT	$30\%/\sqrt{E}$	
ARGUS [14-17] 1982-1992 (DESY DORIS)	Sandwich ECAL	5 mm Plexipop (3% naphthalene, 1% butyl-PBD, 0.01% POPOP)	1 mm Pb	Acrylic BBQ WLS bar to light guide to PMT	$7\%/\sqrt{E}$
WA78 [5,6] 1983-1985 (CERN SPS)	Sandwich ECAL	4 mm PS (1% butyl-PDB, 0.02% BDB)	1.57 mm DU	Acrylic Y7 WLS bar to light guide to PMT	$10.2\%/\sqrt{E}$
Sandwich HCAL	5 mm PVT (NE-110)	10 mm DU + 1 mm Fe Back Section: 25 mm Fe	Clear optical fiber bundle to PMT		$51\%/\sqrt{E} \oplus 7\%$
HELIOS [4] 1984-1988 (CERN SPS)	Sandwich ECAL	2.5 mm PMMA plates (10% naphthalene 1% butyl-PBD)	2 mm DU	BBQ WLS bar to acrylic light guide to PMT	$21.5\%/\sqrt{E}$
Sandwich HCAL	2.5 mm PMMA plates (10% naphthalene 1% butyl-PBD)	3 mm DU, 5 mm Cu	BBQ WLS bar to acrylic light guide to PMT	$33.7\%/\sqrt{E}$	

(continued)

Table 15.1 (continued)

Experiment	Type of Calorimeter	Scintillator	Absorber	Readout	Energy Resolution
CDF [18,19] 1985-2011 (FNAL Tevatron)	Sandwich ECAL Sandwich HCAL	5 mm PS (SCSN-38) 10 mm PMMA (0.8% naph, 1% butyl-PBD, 0.01% POPOP)	3.2 mm Pb 25 mm Fe	Y-7 WLS bar to acrylic light guide to PMT WLS bar (Dye 481) to light guide to PMT	13.5%/ \sqrt{E} 33%/ \sqrt{E} + 4%
E-814 [20-22] 1988-1992 (BNL AGS)	Tile-Fiber ECAL Tile-Fiber HCAL	3 mm PVT (BC-408) 3 mm PS (KSTI-430)	10 mm Pb, 16 mm Fe 10 mm Pb, 16 mm Fe	F-201 (1.5 mm) WLS fiber along edge to PMT F-201 (1.5 mm) WLS fiber along edge to PMT	25%/ \sqrt{E} 43%/ \sqrt{E}
DELPHI [23,24] 1989-2000 (CERN LEP)	Spaghetti Beam Monitor	1 mm Scint Fibers (PS, 1% butyl- PBD, 0.02% POPOP)	0.9 mm Pb	Light guide to photodiode	11.4%/ \sqrt{E} ⊕ 1.16%
NA38 [25] 1989-1992 (CERN SPS)	Spaghetti ECAL	1 mm Scint Fibers (PS, H-130)	Pb (50% vol)	Light guide to PMT	30%/ \sqrt{E}
SPACAL [26-36] 1990-1992 (CERN test beams)	Spaghetti Prototype	1 mm Scint Fibers (PS, SCSF-38)	Pb (80% vol)	Acrylic light guide to PMT	12.9%/ \sqrt{E} + 1.2% (em), 30.6%/ \sqrt{E} + 2.2% (had)
WA9 [29,37] 1990-1994 (CERN SPS)	Spaghetti HCAL	1 mm Scint Fibers (PS, SCSF-38)	Pb (80% vol)	Acrylic light guide to PMT	30.6%/ E + 2.2%
JETSET [38] 1991-1996 (CERN LEAR)	Spaghetti ECAL	1 mm Scint Fibers (PS, SU01-S)	Pb (35% vol)	Acrylic light guide to PMT	6.3%/ \sqrt{E}
ZEUS [39-41] 1992-2007 (DESY HERA)	Sandwich ECAL Sandwich HCAL	2.6 mm PS (1% butyl-PDB, 0.02% BDB) 2.6 mm PS (1% butyl-PDB, 0.02% BDB)	3.3 mm DU 3.3 mm DU	Acrylic Y-7 WLS bar to light guide to PMT Acrylic Y-7 WLS bar to light guide to PMT	18%/ \sqrt{E} 35%/ \sqrt{E}
E864 [42] 1993-1998 (BNL AGS)	Spaghetti HCAL	1 mm Scint Fibers (PS, BCF-12)	Pb + 1% Sb (82% vol)	Acrylic light guide to PMT	34.4%/ \sqrt{E} + 3.5%
FOCUS-E-831 [43] 1996-1999 (FNAL fixed target)	Tile-Fiber HCAL	7 mm PS (SCSN-81)	44 mm Fe	Y-11 WLS fiber (0.89 mm) in groove to clear fiber to PMT	85%/ \sqrt{E} + 0.86%
g2 [44] 1997-2004 (BNL AGS)	Spaghetti ECAL	1 mm Scint Fibers (PS, BCF-9-49A)	Pb + 6% Sb (53% vol)	Acrylic light guide to PMT	8.0%/ \sqrt{E} ⊕ 1.7%

(continued)

Table 15.1 (continued)

Experiment	Type of Calorimeter	Scintillator	Absorber	Readout	Energy Resolution
HERA-B [45,46] 2000–2003 (DESY HERA)	Shashlik ECAL	inner: 1 mm PS (PSM-115) outer: 6 mm PS (PSM-115)	2.2 mm W-Ni-Fe alloy 3 mm Pb	Y-11 WLS fiber (1.2 mm) to PMT BCF-91A WLS fiber (1.2 mm) to PMT	Quoted for whole $8.0\%/\sqrt{E} \oplus 1.7\%$
KLOE [47–50] 2000–2006 (DAPNE)	Spaghetti ECAL	1 mm Scint Fibers (PS, SCSF-81)	Pb (42% vol)	Light guide to PMT	$5.7\%/\sqrt{E}$
PHENIX [51,52] 2000–2016 (BNL RHIC)	Shashlik ECAL	4 mm PS (1.5% p -TP, 0.01% POPOP)	1.5 mm Pb	BCF-99-29A WLS fiber (1 mm) to PMT	$8.1\%/\sqrt{E} + 2.1\%$
STAR [53–55] 2000–present (BNL RHIC)	Tile-Fiber ECAL	5 mm PS (SCSN-81)	5 mm Pb	Embedded Y-11 WLS fiber (0.83 mm) to clear fiber to PMT	$14\%/\sqrt{E} + 1.5\%$
ALICE [56,57] 2009–present (CERN LHC)	Shashlik ECAL	1.76 mm PS (1.5% p -TP, 0.04% POPOP)	1.44 mm Pb	Y-11 WLS fiber (1 mm) to light guide to APD	$5.1\%/\sqrt{E} + 11.1\%/\sqrt{E} + 1.7\%$
ATLAS [58,59] 2009–present (CERN LHC)	Tile-Fiber HCAL	3 mm PS (1.5% p -TP, 0.044% POPOP)	5 mm Fe	Y-11 WLS fiber (1 mm) along tile edge to PMT	$52.9\%/\sqrt{E} + 5.7\%$
CMS [60,61] 2009–present (CERN LHC)	Tile-Fiber HCAL	3.7 mm PS (SCSN-81)	505 mm brass	Y-11 WLS fiber (0.94) in groove to clear fiber to HPD	$84.7\%/\sqrt{E} \oplus 7.4\%$
LHCb [62–64] 2009–present (CERN LHC)	Shashlik ECAL	4 mm PS (2.5% p -TP, 0.01% POPOP)	2 mm Pb 10 mm Fe	Y-11 WLS fiber (1.2 mm) to clear fiber to PMT Y-11 WLS fiber (1.2 mm) along tile edge to light mixer to PMT	$8.2\%/\sqrt{E} \oplus 0.87\%$ $69\%/\sqrt{E} \oplus 9\%$
AMS-02 [65,66] 2011–present (ISS)	Spaghetti ECAL	3 mm PS (1.75% p -TP, 0.05% POPOP)	Pb (58 vol%)	Acrylic light guide to PMT	$10.4\%/\sqrt{E} \oplus 1.4\%$
GlueX [67,68] 2014–present (CEBAF)	Spaghetti ECAL	1 mm Scint Fibers (PHT-0044)	Pb (37 vol%)	Acrylic light guide to PMT	$5.4\%/\sqrt{E} \oplus 2.3\%$

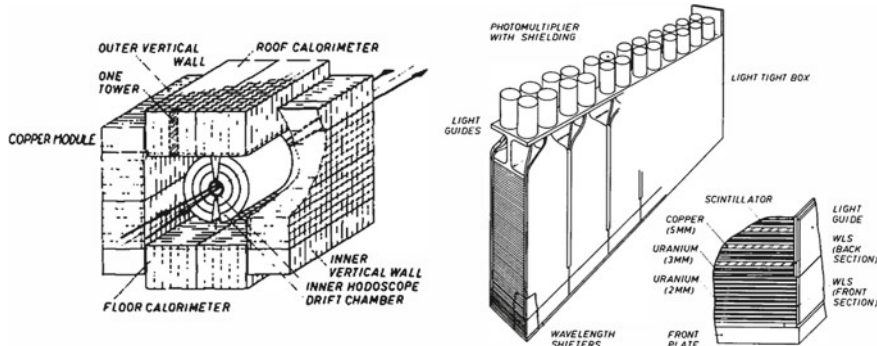


Fig. 15.2 Left: Isometric view of the AFS calorimeter surrounding the central tracking detector. Right: One of the 128 towers, as well as a detail of the ECAL stacking configuration (reproduced from [9] with permission from Elsevier)

15.2.2.1 Compensating Sampling Calorimeters

Since showering hadrons lose a portion of their energy through the release of nucleons from nuclei and the resulting nuclear recoil, the first compensating calorimeters employed nuclear fission processes to contribute the extra needed energy via nuclear de-excitation γ -rays and evaporation neutrons. A sampling calorimeter where the absorber plates are formed from depleted uranium is a practical way to realize this. Depleted uranium (DU) is ^{238}U with $< 0.3\%$ ^{235}U and thus only 60% the radioactivity of natural ^{238}U . The first well-studied demonstration of the principle was a test calorimeter built by Fabjan et al. [69] consisting of two hundred and fifty 1.7 mm-thick DU plates immersed in liquid argon as the active material. The calorimeter was studied using beams of electrons, pions, and protons with variable energies up to 10 GeV and found to give almost the same response to pions as to electrons. Replacing the uranium structure with iron plates and observing the subsequent reduction in pion response relative to the electron response verified that fission processes were responsible for producing compensation.

Following this success, numerous large experiments designed and built depleted uranium sampling calorimeters, mostly using scintillating plastic as the active medium. Enhancement of the non-em component is improved by using hydrogenous materials (typically 5.2×10^{22} atoms/cm 3) such as plastic scintillator. This is because shower neutrons in the energy range between 1 keV and several MeV lose kinetic energy primarily via elastic scattering with the hydrogen nuclei, resulting in recoil protons that contribute directly to the calorimeter signal. Even though the signal is reduced via saturation in the dense solid, all the shower neutrons will produce recoil protons, and you simply need to work harder at improving light collection.

Experiment R807 [70, 71] at the CERN intersecting storage rings (ISR) was a pioneer in these types of hadron calorimeters. A large fine-sampling DU/Cu/scintillator hadronic calorimeter was installed and operated from 1981 to 1983 as part of the axial field spectrometer (AFS) [9]. It was one of the first calorimeters built for a col-

lider experiment and thus consisted of stacked active elements enclosing the beam intersection point, as shown in Fig. 15.2. The active elements were 2.5 mm-thick sheets of Poly(methyl methacrylate), also known as PMMA, plexiglas, or acrylic, with a rectangular cross-section of $1.2 \times 0.2 \text{ m}^2$. Segmentation into six $20 \times 20 \text{ cm}^2$ square cross-sectional towers was achieved by reading out the monolithic scintillator plates with six separate wavelength-shifting strips running up both sides of the stack, mating to acrylic light guides read out by PMTs. ECAL and HCAL were read out separately and had different sampling configurations. In the $6 X_0$ ECAL section, the active element was interleaved with 2 mm-thick depleted uranium plates. In the $3.8 \lambda_0$ HCAL section, the uranium plates alternated with copper plates 5 mm thick in the ratio 2:1 as also shown in Fig. 15.2. Beam tests revealed that the AFS calorimeter was linear to pions over the energy range of 4–200 GeV and its e/h response was close to 1.

The fixed-target experiment HELIOS was installed a few years later at the CERN Super Proton Synchrotron (SPS) to study heavy-ion collisions and lepton production in hadronic interactions. The set of scintillator calorimeter modules built for HELIOS were of similar design (some were actually built from re-used AFS parts), and also demonstrated excellent compensation. For those modules with constrained space (e.g., the calorimetized dipole magnet called MAGCAL), flexible clear fiber bundles were used instead of acrylic light guides.

Unfortunately, not all later DU sampling calorimeters met the expected performance improvements, and compensation proved elusive for some. For example, a hadronic calorimeter built for the WA78 experiment at CERN was strongly over-compensating (see Fig. 15.1). WA78 beam tests [25, 72] were performed for a number of different sampling fractions. The configuration with the lowest $e/h = 0.8$ featured a coarse sampling of 5 mm plastic plates interleaved with 10 and 15 mm-thick uranium plates. A better understanding of the detailed hadronic and nuclear response of layered materials was required before compensating calorimeters could be designed properly from the first principles. Examples of the many sampling uranium and plastic scintillator calorimeters built in the 80s and operated into the 1990s are found in Table 15.1.

By the end of the 1980s, it was recognized that fission-based enhancement of the non-em response was not achieving compensation on its own; a sizeable contribution was coming from suppression of the em response due to the high-Z of the absorber layers, making expensive (and hard to handle) depleted uranium less crucial. The energy deposition mechanism of photons below an MeV is dominated by the photoelectric effect, which goes roughly as Z^5 , meaning that most of the soft photons are removed from the signal by interaction in the passive, high-Z layers. It is still the case that the photoelectrons produced at the outer surfaces of the absorber plates can be detected in adjacent plastic scintillator. Thus, one can further reduce the em response by shielding the active medium with low-Z passive layers, such as thin sheets of iron or the common fiberglass laminate called G-10 that is used for many circuit boards. Highly segmented plastic scintillator near the high-Z absorber can also provide an active measurement of (and correction to) the effect.

Using plastic scintillator as the active medium also increases the non-em contribution, since it is sensitive to soft neutrons via the recoil protons. Given a more nuanced understanding of both the enhancement of the non-em and the suppression of the em signals, it is possible to tune their relative contribution to the observed signal by choosing the appropriate sampling fraction for charged particles. Thus, plastic scintillator sampling calorimeters can achieve compensation for a variety of realistic absorbers, with the advantages of depleted uranium being mostly important for non-hydrogenous active media such as liquid argon. For example, the sampling fraction required for compensation should be $\sim 3\%$ for a Pb/PMMA calorimeter compared to $\sim 10\%$ for DU/PMMA [73]. Thus, Table 15.1 shows a shift away from DU and toward lead as the preferred absorber.

The use of depleted uranium with plastic scintillator also provided an object lesson in radiation damage. The HELIOS experiment incorporated a subset of AFS DU/scintillator modules in their new calorimeter. In testing the modules, they discovered that the optical properties of the scintillator had severely degraded over the modules' four-year lifetime due to continuous exposure to the ^{238}U radioactivity. The effect was found to be due to diffused oxygen in the scintillator, which is broken up into its chemically aggressive atomic constituents when exposed to the UV light [74] induced by particle interactions. Since the diffusion of oxygen is a slow process, the damage is independent of dose rate and is mainly determined by the duration of the exposure. Continued degradation of the modules was avoided by maintaining a slight over-pressure of nitrogen in each individual module.

The ZEUS calorimeter [39] was the last of the depleted uranium calorimeters, having been designed when using DU as an absorber and plastic scintillator as the active material was the only technology known to achieve $e/h = 1$ while maintaining an acceptable resolution for electromagnetic showers. All DU sheets were clad in 0.2 mm of stainless steel to reduce the radioactivity and for ease of handling. Nevertheless, all the scintillator was still continuously bathed in a flux of 10 Gy/year from the DU [75]: 2600 counts/(cm^2s) from β particles above 10 keV and 442 counts/(cm^2s) for γ rays above 60 keV [39]. This radioactivity turned out to be an excellent calibration source and enabled inter-calibration of the scintillator stacks to 1% [76]. It also provided an absolute calibration scale when referenced to the test beam.

Calibration is crucial to maintaining a low constant term in the overall energy resolution, and for the ZEUS experiment, the physics goals demanded that the ratio of the measured signal to deposited particle energy be independent of position and time at the level of 1%. ZEUS also deployed a laser system to monitor the linearity of the photomultipliers and readout electronics, and ^{60}Co source scans for the scintillator system. A computer-controlled trolley moved their 2 mCi ^{60}Co source (1.17 and 1.33 MeV gammas) within a thin stainless steel tube along the tower structure of each module, providing the response of individual scintillator plates, uniformity along the wavelength shifter, and revealing mistakes in stacking or installation. While there have been many incarnations of source-mover systems since ZEUS, the calibration results obtained by their combined uranium and ^{60}Co calibration is still one of the best. As an illustration of what can be achieved, see Fig. 15.3 where the signal from

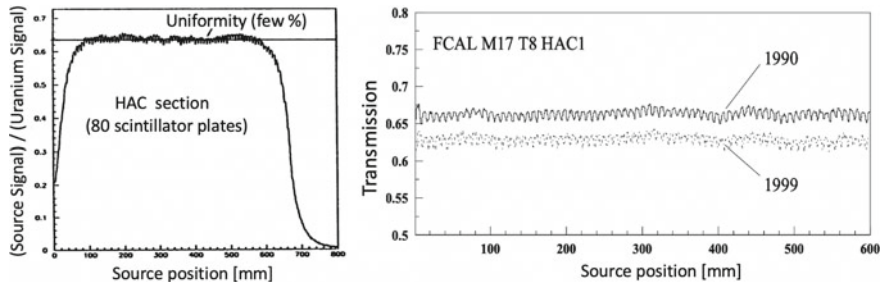


Fig. 15.3 *Left:* Scan with a ^{60}Co source vertically outward along a section of the ZEUS DU/scintillator sampling hadronic calorimeter. *Right:* Aging of the SCSN-38 used in the ZEUS calorimeter. Shown is the transmission parameter of a typical hadronic section (module 17, tower 8) plotted as a function of ^{60}Co source position for two scans 9 years apart (reproduced from [77, 78] with permission from Elsevier and World Scientific)

the gamma source is normalized to the uranium-induced signal [77]. A separate signal is measured for each single scintillator plate, and the uniformity over the whole HAC tower is within a few percent.

Later studies [78] used the ^{60}Co source system to explore long-term aging in the scintillator, finding no significant radiation damage due to operation in the HERA beam, except in the beam pipe calorimeter which was not removed during a period of beam injection and dumping. Although no beam-related damage was discovered, it was found that the transmission of the SCSN-38 scintillator decreased by 3–5% over the 9 years of operation, see Fig. 15.3. Dedicated irradiation tests [78] show that this effect is too large to be caused by the low-level DU radiation and is therefore attributed to aging of the scintillator itself. Thus, operation of DU scintillator calorimeters and dedicated beam studies clearly showed that a robust calibration system can maintain calorimeter performance in the face of both aging and low-dose radiation. With the advent of accelerators of even higher energy and luminosity, however, beam-related radiation damage becomes a much greater challenge. Calibration alone cannot maintain calorimeter performance in the face of seriously degraded photon statistics (see Sect. 15.3.2).

15.2.2.2 Alternate Geometries and Photon Transport

A wide variety of geometrical arrangements can be deployed to arrange the absorber and active elements, as well as many strategies to transport the produced light to a photodetector. Figure 15.4 categorizes the major geometries adopted by the particle physics experiments, as summarized in Table 15.1. This is the signature advantage of plastic scintillator, which can be injection molded, cast, extruded, or machined into a wide variety of shapes.

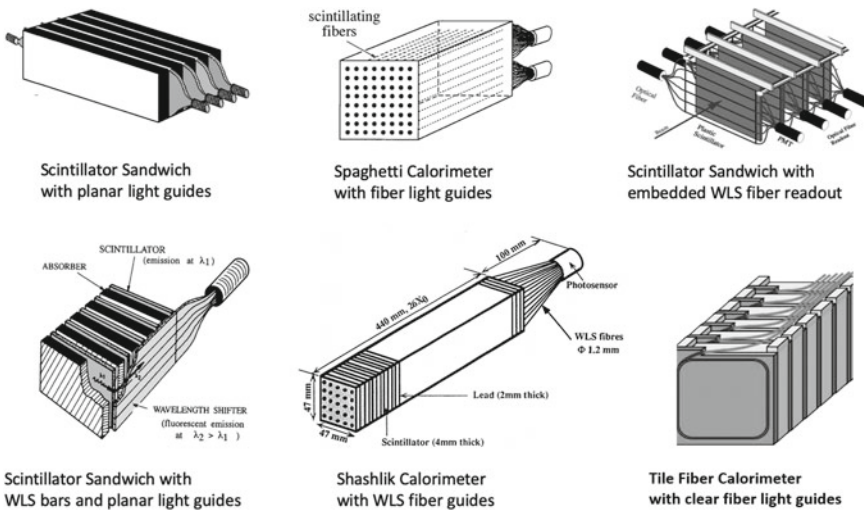


Fig. 15.4 A taxonomy of plastic scintillator sampling calorimeter configurations

Sandwich

Early sampling calorimeters used a simple interleaving of plates of absorber and active element, where the monolithic scintillator elements were read out with acrylic light guides mated to photomultiplier tubes (PMTs). Light guide design requires an excellent coupling at the interfaces using either optical grease or cement and must be well-matched to the index of refraction of both coupling material and scintillator to prevent reflection. Since monolithic light guides present such a large cross-section to intercepting particles and the short-wavelength Cherenkov light they produce, a UV-absorbing acrylic which mitigates this background is a good choice.

Another light guide design criterion is efficient light transport as the cross-section is adiabatically converted from a thin rectangular cross-section at the top of a scintillator plate to the area-filling disk that gets mated to the photocathode of a PMT. The photons are transmitted via total internal reflection, so the acceptance angle is crucial and many clever designs exist. Nonetheless, conservation of phase space (e.g., the flux of photons per unit area and per unit solid angle) dictates that no optical coupling scheme relying on reflection or diffraction alone can transmit photons from a large source to a small detector with full efficiency.

A more compact geometry can be achieved by using wavelength shifting (WLS) technology to redirect the light emitted from the edge of the scintillator and transport it to the photodetector. This is especially important in large sampling calorimeters with tower geometry, where magnetic fields force the PMTs to be located behind the return coils, and curving light guides would create unacceptable gaps in active coverage. Plastic WLS plates run up the side of the tower, optically coupled to the edges of the stack of scintillator tiles. A set of fluorescent compounds in the WLS plates, bars, or plastic fibers shift the wavelength of the intercepted scintillator light

from (typically) blue to green. The 4π re-emission process gives scintillator light striking perpendicular to the long axis of the WLS plate another chance to be captured within the light guide's angle of incidence for total internal reflection. The green light in the WLS element is transmitted efficiently since it has been shifted away from the bluer absorption peak.

Tile–Fiber

With the development of plastic scintillating fibers, other geometries became possible. Depending on the fluorescent compounds used in the doping, these fibers can take the place of either the WLS bar or the scintillator element itself. Typically 0.5–2 mm in diameter, they are composed of a polystyrene core, with one or several thin claddings of lower index of refraction PMMA to enhance total internal reflection. Thus, only light within a specified opening angle (e.g., 45° for multi-clad fibers and considerably less for single-clad) is piped out to the photodetector. Commercially available scintillating fibers have typical attenuation lengths in the range of 1–5 m, although it depends on the type. Non-S type (nomenclature is Kuraray, but has been widely adopted) has a standard polystyrene core with very good attenuation length, but it can develop strain cracks when bent sharply. The molecular chains in the S-type core are oriented along the fiber, allowing for a tighter bend radius at the expense of a shorter attenuation length. The same plastic fiber geometry is also used for clear fiber light guides, which can have attenuation lengths of 10 m or more.

The trapping efficiency of a WLS fiber, defined as the probability that a re-emitted photon will be trapped and guided along the fiber, is only 3–7%,² depending on whether the re-emission occurs near the edge (better trapping) or the center of the fiber. While this is a small fraction of the overall light output from the scintillator, it provides a practical way to effectively concentrate the light into a small area and thus minimizes the overall photodetection area required. In large installations, this is a significant cost driver. WLS fibers can replace the WLS bars that run along the side of scintillator towers. They provide flexible waveguides in constrained spaces. They can also be embedded in the scintillator itself to provide the best coupling and the maximum opportunity for intersecting the primary scintillation light. The CMS HCAL deploys a tile–fiber calorimeter where the embedded WLS fiber loops around the inside of the scintillator in a sigma configuration (see the fiber loop shape in Fig. 15.4 bottom right). Clear fiber with a long attenuation length is used to pipe the light along the length of the tower to multi-channel photodiodes located outside the highest radiation zones. The long scintillator bars used for the MINOS long-baseline neutrino experiment also employ embedded WLS fiber mated to clear fiber to concentrate the light onto a multi-channel PMT.

Shashlik

In a shashlik sampling calorimeter, the scintillation light is read out via WLS fibers running perpendicular to the alternating scintillator and absorber plates, threaded

²<https://www.crystals.saint-gobain.com/sites/imdf.crystals.com/files/documents/fiber-product-sheet.pdf>.

through the middle similar to the Russian kebab it is named after. Shashlik calorimeters are used for high-resolution electromagnetic calorimeters since the sampling fraction is high. The best such detectors can achieve resolutions of 3–5% for 300 MeV gammas by emphasizing the fine sampling. An example of this is the KOPIO prototype detector [79] with a 50% sampling fraction (for MIPs) using 0.275 mm-thick lead foils interleaved with 1.5 mm-thick injection-molded polystyrene plates and penetrated by 1 mm-diameter WLS fibers every 9.3 mm.

The disadvantage of a high sampling fraction calorimeter is its relatively low density. If there is no size restriction, the technology provides a very cost-effective way to build a high-resolution ECAL that is large enough to contain the shower. In large, all-purpose collider detectors, such as ATLAS and CMS, radial space is at a premium and works against this choice. However, shashlik detectors are found in LHC detectors such as ALICE (which studies heavy-ion physics and extreme energy densities) and LHCb (which studies the properties of hadrons containing b-quarks, requiring fine tracking resolution in the forward direction).

Spaghetti

If fine sampling is what you are after, your entire calorimeter can be made of scintillating fibers embedded in an absorber matrix. The plastic sampling is achieved by the fibers themselves, which also pipe the resulting light to the photodetector. In cases where local photodetection is possible, the photodetectors can be mounted directly on the ends of the scintillating fibers, thus minimizing light loss at optical interfaces to clear fibers.

Dubbed spaghetti calorimeters, they rely on early experience building vertex and tracking devices out of scintillating fiber planes. A tracker does not need analog information, but simply a signal above threshold in a matrix of crossed fiber elements to define the particles' passage. When scintillating fibers are elements of a calorimeter, the number of fibers hit becomes a measure of the energy of the shower and thus requires uniformity of response fiber-to-fiber. An irregular fiber lattice leads to sampling non-uniformities, translating into a response that depends on the particle entry point and degrades the energy resolution. This is a different optimization than tracking devices, which require high light yield and long attenuation length.

Early fiber calorimeters were special-purpose, such as the luminosity monitor for DELPHI [23, 24], or small electromagnetic calorimeters like the ones built for NA38 [25] or BNL g-2 [44]. Their advantages as em calorimeters were quickly appreciated, and they are still used now for cost-effective sampling calorimeters that can achieve resolutions of $\sigma_E/E = (6 - 10\%)/\sqrt{E}$, comparable to homogeneous calorimeters, see JETSET [38], KLOE [49], and GlueX [67, 68] in Table 15.1.

The technology for embedding the fibers in the absorber matrix varies widely. A popular approach is to groove lead sheets (usually hardened by a small admixture of antimony) on both sides, glue the fibers in the grooves, and stack the sheets together (DELPHI, JETSET, KLOE, BNL g-2, E864). The resultant modules can be trimmed and the ends fly-cut to produce optically flat surfaces. The fiber ends can then be mated directly to a photodetector or monolithic light guide. Alternatively, a thin disk (or cookie) with well-registered holes can be used to couple individual or bundled

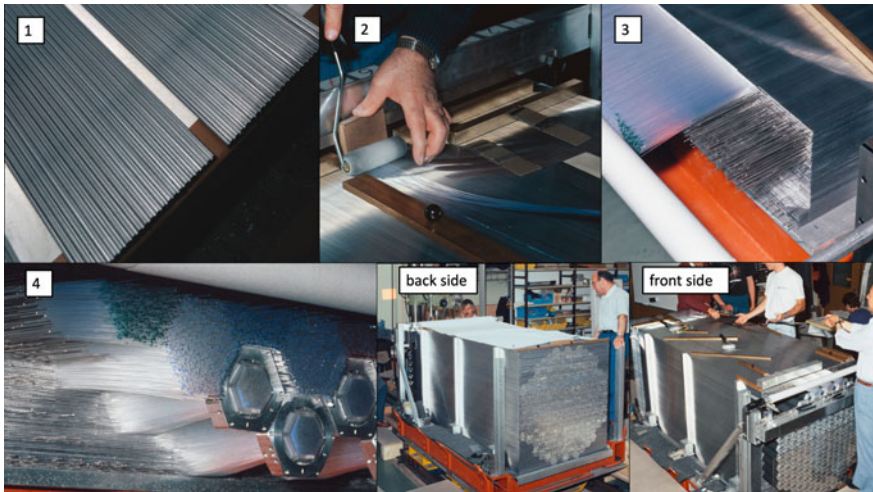


Fig. 15.5 Construction of a spaghetti calorimeter (SPACAL collaboration) at CERN. Stages of construction indicated by the numbered panels (reproduced from [83, 84] with permission from CERN)

scintillating fiber to clear fiber with the segmentation desired for remote sensing. The CERN R&D group [80] successfully built prototype modules by soldering fiber-filled lead sheets together at 70 °C and then replacing the fibers. Casting using low melting point alloys is also possible. The liquefied alloy is poured into a cast where stainless steel tubes are held in position by spacer plates, and the fibers are inserted into the tubes later [26, 81, 82].

With a better understanding of hadronic showers and compensation mechanisms, R&D on hadronic fiber calorimeters was undertaken by the SPACAL [26], RD1 [80], and RD25 [85] collaborations with an eye toward developing this technology for the proposed LHC. A photographic tour of the building of a SPACAL prototype is shown in Fig. 15.5. There are some unique challenges in using fibers for large hadronic calorimeters which surround the intersection point at a collider. The attenuation length of the fibers becomes important, resulting in high-energy tails in the energy spectrum when showers develop late. The em resolution can be deteriorated by channeling, in which a particle travels a long distance inside one individual fiber rather than contributing to the overall shower. Effects of channeling can be mitigated by offsetting the pointing angle slightly or even by curved fiber paths. Longitudinal sampling of projective towers cannot be done by simply bundling the relevant layers together, but must be addressed by starting the fibers at various depths within the tower. This can happen naturally, since the trapezoidal shape slices the outer fibers as it narrows down toward the central axis.

15.2.2.3 Advances in Photodetectors

Over the last 8 decades, the photomultiplier tubes (PMTs) with their robust design and high internal gain have been the main photosensor used in nuclear and particle physics experiments. They continue to be widely used. The development of new PMT designs continues to evolve as the needs of experiments change. However, there are now a large variety of solid-state alternatives to PMTs which have increasingly become favored due to their magnetic-field resistance, radiation hardness, compactness, large dynamic range, and sensitivity and resolution at low light levels.

Photomultiplier Tubes

A PMT is a simple vacuum tube with a photocathode to convert the light to photoelectrons, a set of dynodes arranged to produce gain via a cascade of secondary emission stages, and a resistor divider to provide the accelerating voltage to each of the dynodes in the chain (see chap. 10). The gain depends on the number of dynode stages and exponentially on the applied voltage; gains are typically 10^5 – 10^7 for applied voltages of 1–2 kV. It therefore operates as a nearly perfect current source, with very little Johnson noise. The photocurrent still contains shot noise and the photocathode produces a small, but steady release of single photoelectrons due to spontaneous thermionic emission of electrons (dark counts). General aspects of the technology have improved over the years, such as higher gain and stability due to a better understanding of the internal electric field and the addition of focusing electrodes. Dark current rates have been reduced and photocathode quantum efficiencies have risen to 20–30% with improved vacuum transfer technology and new compound semiconductor coatings.

Other advances have been in response to scientific pressure, e.g., changes in the characteristics of the light produced by a new experimental medium or the environment in which the PMTs are expected to operate. New photocathodes with improved sensitivity in the green were developed in response to the rise in wavelength shifter techniques, and UV applications spurred the development of Cs-Te and Cs-I coatings. Also promoted by experimental demands are special-purpose packaging designs, such as 50 cm-diameter windows for water Cerenkov detectors, compact designs to fit between detector elements, and magnetic-field resistance up to a tesla for use with spectrometers.

Despite the wide variety of available PMTs, there are some applications for which a PMT is not an optimal choice. For sub-nanosecond timing applications, the dynode chain produces an unacceptable spread in the signal width and start time. This can be mitigated somewhat by increasing the relative voltage of the first dynode stage and shaping the field in the gap to be as parallel as possible. If that is not sufficient, then one can replace the dynode structure with stacked microchannel plates (MCPs) made from thin (~ 2 mm), highly resistive material with a regular array of tiny holes densely distributed over the surface. The secondary emission is now confined within each pore (typically 6–20-micron diameter). MCP plates can be stacked together in a chevron or a Z-configuration for increased gain. With rise times <0.5 ns and full widths of <1 ns, these are used for special-purpose applications such as beam triggers, but their expense makes them an unacceptable option for detectors with

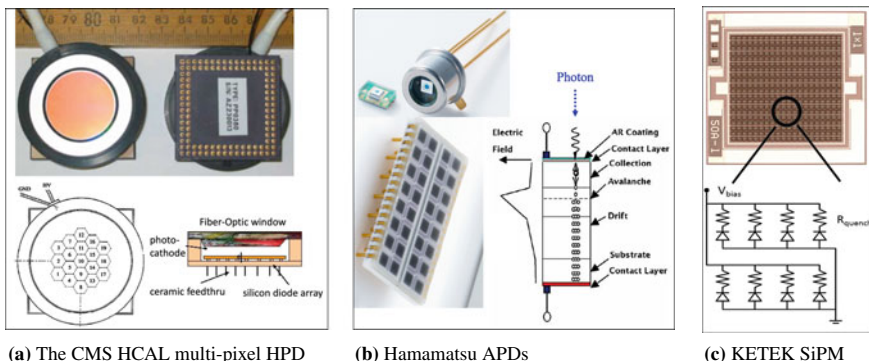


Fig. 15.6 Photodetectors incorporating semiconductor technology (based on figures from [86–88] with permission from CERN, Hamamatsu, and KETEX)

thousands of channels. For large calorimeters needing precision timing, the focus has moved to semiconductors.

Hybrid Tubes

It is possible to skip secondary emission altogether and simply accelerate the photoelectrons from the photocathode onto a semiconductor target. In this case, the gain is provided by the kinetic energy of the accelerated photoelectrons. If the target is a planar silicon diode, the photoelectrons liberate an electron–hole pair for every 3.6 eV of energy delivered to the target. Gains of several thousand can be achieved for applied voltages of 10 kV. If the target is an avalanche photodiode (APD) with its own internal gain, gains comparable to PMTs can be achieved. These devices were developed as novel photodetectors during the design phases of the SSC³ and the LHC to replace PMTs. The driving rationale was the need for compact devices that could operate in a magnetic field and could cover a dynamic range from minimum-ionizing particles to high-energy hadronic showers. The first hybrid tube with a multi-pixel APD as the target was developed in partnership with Litton [89], but languished when funding for the SSC dried up. It was revived more than two decades later, using improved APDs, as a read-out option for large xenon dark matter detectors [90].

Hybrid tubes have excellent linearity across a large dynamic range due to their initial single-step amplification process and the absence of saturation in silicon. They also have far better photon counting statistics than PMTs, with clearly resolved photoelectron peaks. The nuclear counter effect (background caused by charged particles traversing the diode and depositing energy directly in the silicon) is reduced by the additional factor of gain from the internal acceleration in a hybrid tube. For the CMS sampling HCAL, the development of a multi-pixel hybrid photodiode (HPD) [91, 92] was driven by the need to operate the transducer inside a 4 T solenoidal magnet. The cost was also a driver; the HPD was less expensive (due to its multi-pixel

³The superconducting super collider (SSC) was a proposed 40 TeV collider to be built in Texas, canceled by the US Congress in 1993.

configuration matched to multiple fiber bundles) than the individual APDs chosen for the CMS ECAL. The HPDs were also found to be less noisy and more stable against changes in temperature and bias than the APDs available at that time [93]. The design of the CMS HPD is shown in the left panel of Fig. 15.6 as an example of a hybrid tube with a silicon photodiode target.

Disadvantages of hybrid tubes mostly involve issues introduced by the high accelerating voltage across a narrow gap. Without careful HV design and vacuum transfer techniques, the photocathode response can degrade over time due to leakage currents or develop non-uniformities due to sparking or ion feedback. Multi-pixel HPDs must be equipped with a fiber-optic faceplate since optical spread through a borosilicate window would cause unacceptable cross-talk in neighboring pixels. Without an anti-reflective coating on the silicon diode, unconverted photons can reflect back to the photocathode for a second chance at conversion. These secondary photoelectrons can impact the silicon at a location far from the original entrance point causing another source of cross-talk.

Avalanche Photodiodes

Meanwhile, progress on APDs has continued rapidly. With an internal charge amplification of 10–100, these devices are inherently noisier than either PMTs or HPDs, so the focus was on reducing this noise. Older implantation techniques used a “reach-through” architecture, where the junction is on the opposite side of the diode from the illuminated side. With the advent of epitaxial growth production methods, it became feasible to produce highly uniform APDs with the junction on the illuminated side. The junction depth and gain could then be tailored to the wavelength of the scintillation light. Such very low-noise APDs were first used in high-energy physics by the CMS collaboration as the readout of their lead tungstate crystals, in order to reduce the nuclear counter effect. This effect was estimated to be ~ 1 GeV of noise in the energy measurement for a PIN diode, compared to ~ 20 MeV with an APD [94].

Calibration and temperature control are used to control the gain stability of an APD. Their response to radiation is well understood and linear (like all silicon-based devices). When the NOvA long-baseline neutrino detector designed their new liquid scintillator neutrino tracking calorimeter, they decided against the MINOS solution of long fiber bundles mapped to multi-channel PMTs and went instead with APDs mounted directly on the WLS fibers as they emerged from the scintillator channels. They used a segmented version of the CMS APDs with the same vertical structure, but with 32 channels per device. The middle panel of Fig. 15.6 gives examples of APDs, including a schematic of the gain structure. The lower picture in the panel is the 32-channel APD array used by NOvA.

Currently, the form of APD that is preferred by many-particle physics experiments is actually an array of APDs where each pixel is operated in the Geiger mode [95]. For example, this is the upgrade option for the CMS HCAL and the choice for the near detector of the Japanese long-baseline neutrino T2K [96]. These devices go by a variety of names, e.g., silicon photomultiplier (SiPM), multi photon pixel counter (MPPC), or microchannel photodiode (MAPD). One example (out of many comparable devices) is shown in Fig. 15.6. Unlike a conventional APD, the array

is a digital device where the output charge signal is proportional to the number of pixels that fire. Modern SiPMs have quenching resistors associated with each pixel and operate on a common substrate. They can have as much as 10,000 pixels in an area of 1 mm^2 . Gains of up to 10^6 are routinely achieved for a bias voltage under 100 V. At low light levels, the device functions as an excellent photon counter, easily resolving up to 10 photons in individual peaks.

They do have some limitations. They have a finite sensor recovery time due to the Geiger discharge, making them less useful for precision timing applications. At higher light levels, there is an exponential saturation of the SiPM response (Eq. 15.2), which is due to the finite number of pixels.

$$N_{\text{fired}}(N_{\text{pe}}) = N_{\text{pix}} \left(1 - e^{-N_{\text{pe}}/N_{\text{pix}}}\right) \quad (15.2)$$

Like any APD device, their gain and noise are temperature-dependent, so a robust calibration system and temperature control are essential.

15.3 Modern Plastic Scintillator Calorimeter Design

In high-energy physics experiments, the calorimeter, with its ability to measure the energy and direction of particle showers, has become key to understanding the physics of the underlying interaction. The examples presented in the last section illustrate the role of plastic scintillator in these developments. In this section, we cover examples of experiments running now, concentrating on experiments at the large Hadron collider (LHC) at CERN in Geneva, Switzerland, and on modern neutrino experiments. Details of their material and construction are also included in Summary Tables 15.1 and 15.2 for completeness.

15.3.1 Experiments at the Large Hadron Collider

The large Hadron collider hosts four major experiments: two multi-purpose detectors called CMS (Compact Muon Solenoid) [60] and ATLAS (A Toroidal LHC ApparatuS) [58], a heavy-ion physics detector named ALICE (A Large Ion Collider Experiment) [56], and the LHCb (Large Hadron Collider beauty) detector [64] which is used to study baryon asymmetry. Of these detectors, all have some form of plastic scintillator element; plastic scintillator-based HCALs are used by CMS, ATLAS, and LHCb while plastic scintillator-based ECALs can be found in ALICE and LHCb.

ATLAS and CMS

Both CMS and ATLAS made the decision to emphasize excellent energy and position resolution in their ECAL designs, rather than design for the best compensation. This strategy was driven by simulations that indicated that $H \rightarrow \gamma\gamma$ and $H \rightarrow 4e^\pm$ would

produce the cleanest electromagnetic physics signatures most likely to reveal the sought-after Higgs [94, 97]. For their electromagnetic calorimeters, ATLAS chose a finely-sampled liquid argon and lead accordion structure, while CMS installed a homogeneous ECAL built out of blocks of PbWO_4 crystal. When it came to measuring the energy and direction of particle jets and missing energy flow in a hadronic calorimeter, they both chose a sampling calorimeter design using plastic scintillator as the active element, in order to accommodate the inherently larger fluctuations and containment requirements. The scintillator elements of the CMS and ATLAS hadronic calorimeters are shown in Fig. 15.7.

The CMS HCAL is a tile–fiber calorimeter consisting of the barrel (HB), endcap (HE), outer (HO), and forward (HF) subsystems [60]. Inside a 3.8 T, 15 m diameter solenoidal magnet, there are 36 wedge-shaped towers pointing toward the interaction region. Each weighs 26 tons and is formed from 17 layers of 3.7 mm-thick plastic scintillators interleaved with the brass absorber. This corresponds to a sampling fraction of about 7%.

Each tile is cut from the Kuraray SCSN-81 scintillator. A WLS fiber is glued into a sigma-shaped groove machined into each tile. At the exit of the tile, the WLS fiber is coupled to a clear fiber, which is bundled with the rest of the tower fibers and routed to the top of the tower where it is optically summed and read out by multi-pixel hybrid photodiodes (HPDs). Outside the solenoid, the first muon absorber layer is also instrumented with scintillator tiles to ensure adequate sampling depth. Similarly, 36 endcap wedges measure particle energies as they emerge through the ends of the solenoid magnet.

ATLAS also pursued a tile–fiber HCAL, referred to as the TileCal [58], but with a different design than CMS. The scintillator tiles are 3 mm thick, with a steel absorber in a steel-to-scintillator ratio of 4.7 to 1. The tiles use a polystyrene base doped with 1.5% p -TP and 0.044% POPOP and are formed by injection-molding. There are 64 modules arranged in azimuth, partitioned into three layers radially outward from the beam. The tiles themselves are oriented vertically within the module with fibers along one side to minimize cracks.

Calibration is crucial to extracting the best physics from these large plastic scintillator sampling calorimeters. This is especially important for long-lived experimental installations located in high radiation environments, where the scintillator response changes over time. Individual tiles will be affected differently, depending on both their position in the high flux field and any instrumental defects such as degraded optical connections or photodetector issues. Thus, not only does the overall response degrade over time, but so also will the energy resolution, as the variance of the response broadens. Calibration of a subset of the modules is performed in a test beam of high-energy pions, muons, and electrons and is then boot-strapped to the rest of the calorimeter elements by a combination of charge injection or LEDs for the electronics, laser pulses for the photodetectors, and a radioactive source for direct stimulation of the tiles. ATLAS and CMS deployed remotely controlled source-mover systems with a ^{137}Cs source, illuminating all calorimeter cells in situ. ATLAS achieved a singlecell response with a precision of about 0.3%. The error on the mean from individual cells in CMS was similar at 0.2%.

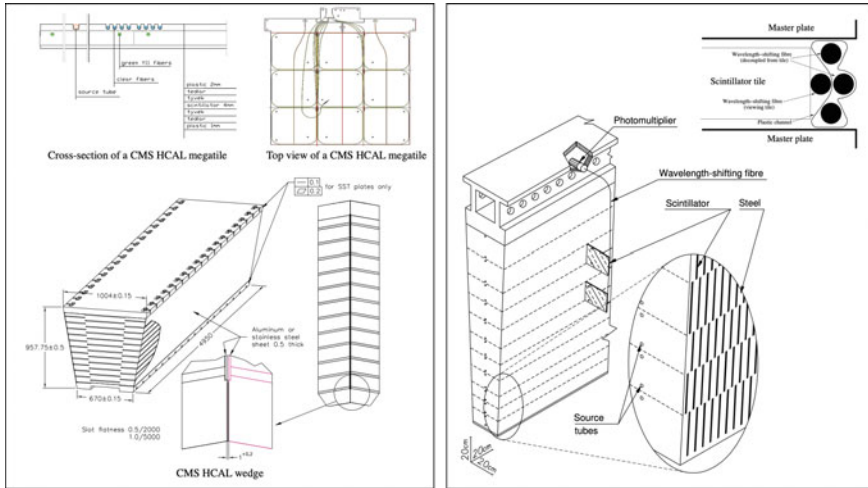


Fig. 15.7 *Left:* Components of the CMS HCAL. Each megatile is formed from an array of several scintillator tiles, with WLS fibers inserted into grooves in a σ shape (shown in green). *Right:* Components of the ATLAS TileCal. The tiles are oriented side-on to the projective axis and a WLS fiber runs along the sides of the tiles, from the center out to the photomultipliers (reproduced from [58, 60, 98] with permission from IOP Publishing and Elsevier)

While radiation damage will reduce the signal from the scintillator, the presence of a magnetic field actually increases the signal. Brightening is due to the polymer base of the scintillator and saturates at about 2 T (well below the CMS field value of 3.8 T) to produce an increase ranging between 5 and 8%. An additional source of signal increase is the curling of knock-on electrons in the magnetic field, which results in an increased path length of the electrons and enhances the signal by 1–2%. Therefore, the signal increase depends on the nature of the particle impinging on the calorimeter, on the geometry, and on the strength of the magnetic field.

At the time of commissioning, the barrel portion of the CMS HCAL was inter-calibrated to 5% for 85% of the channels [60]. The other HCAL channels were inter-calibrated to better than 10% (HE), 12% (HF), and 5% (HO). The presence of the magnetic field resulted in a measured increase of the signal, by 9.4% in HB and 8% in HE, as expected. The ATLAS HCAL was inter-calibrated to better than 3% [58]. An increase in light yield due to the magnetic field was shown to be $\sim 0.6\%$, but was not fully reproducible. Eventually, calibration was improved substantially using proton–proton collision data, as well as cosmic ray muon data collected during the periods when the LHC beams are not present.

ATLAS and CMS have excellent timing properties as well. During commissioning, the modules were synchronized with a laser system and validated using cosmic muons [99], obtaining a precision on the inter-calibration of 2 ns per partition. Once the LHC began running, the machine provided timing calibration by training single beams on a closed collimator located upstream from the detectors. The impact produced a huge number of very energetic particles reaching the detector parallel to

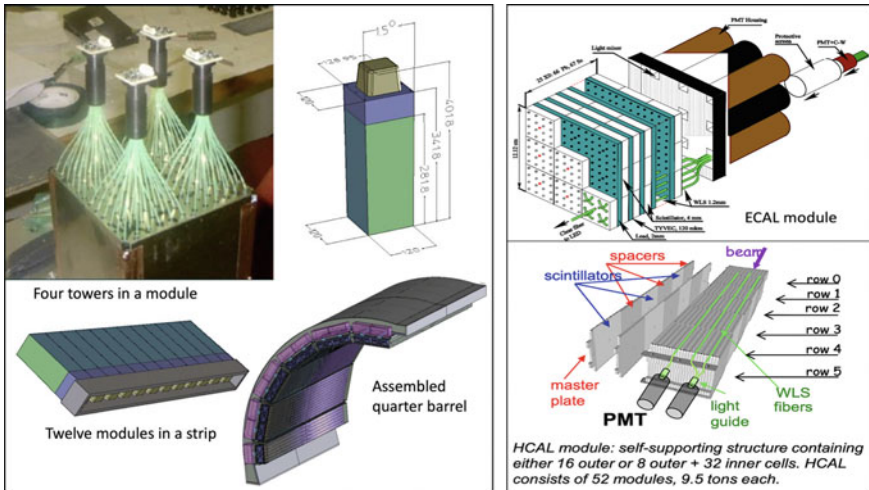


Fig. 15.8 Left: Components of the ALICE shashlik EMCal. Right: The LHCb shashlik ECAL (top) and the LHCb Tile HCAL (bottom) (based on figures from [57, 62, 64, 100] with permission from CERN and IOP Publishing)

the beam axis (“splash events”), depositing a large amount of energy in the entire calorimeter. These studies, augmented by reconstruction of high-momentum jets, resulted in inter-calibration better than 1 ns [59].

ALICE

The ALICE Collaboration studies head-on collisions between heavy nuclei to better understand the quark–gluon plasma, a primordial state of matter which filled the universe until a few microseconds after the Big Bang. As this dense state rapidly cools, it produces up to three orders of magnitude more particles than proton–proton interactions at the same energy. Most of the heavy lifting with respect to disentangling these high multiplicity events is performed by silicon trackers, a giant time-projection chamber, and a finely segmented lead tungstate calorimeter. They are followed by EMCal, a lead-scintillator shashlik design emphasizing efficient, fast triggering, and electromagnetic energy resolution [57]. The EMCal is optimized to measure jet production rates and jet characteristics in conjunction with the charged particle tracking in the other barrel detectors.

Elements of the ALICE EMCal [56] are shown on the left panel of Fig. 15.8. Each tower is made up of alternating layers of 1.44 mm-thick Pb and 1.76 mm-thick scintillator, resulting in a 10.5% sampling fraction. The polystyrene-based scintillator tiles are injection molded and the 1 mm-diameter WLS fibers are threaded through each stack, with one end terminated at an aluminized mirror and the other end read out by an APD. Four towers are combined into a $12 \times 12 \times 24.6 \text{ cm}^3$ module before arranging into long strip modules. The strip modules are mechanically layered into

large arc installments that fit around inside of a 0.5 T solenoid magnet, with 107° azimuthal coverage due to spatial constraints posed by the other detector components.

LHCb

The LHCb detector was built to study rare decays of hadrons composed of b-quarks and to make precision measurements of CP violation in the b-system. Since the b hadrons are predominantly produced at small angles close to the beam pipe (at these high energies), LHCb is a single-arm spectrometer with a forward angular coverage from approximately 10 mrad to 300 (250) mrad in the bending (non-bending) plane [64]. After the silicon vertex and drift chamber tracking system is a set of three plastic scintillator systems: (a) the scintillator pad detector and preshower detector (SPD/PS), (b) the shashlik ECAL, and (c) the iron/scintillator tile–fiber HCAL. All three calorimeters follow the same basic principle: scintillation light from the tiles are converted into WLS fibers, which are then transmitted to a PMT via clear fibers. The single fibers for the SPD/PS cells are read out using multi-anode photomultiplier tubes, while the fiber bundles from the ECAL and HCAL modules require individual PMTs.

The rejection of a high background of charged pions as well as a handle on the π^0 fraction requires longitudinal segmentation of the ECAL and fine-grained lateral sampling before and after a lead converter. This is accomplished by the preshower detector. The SPD/PS detector consists of a 15 mm lead converter that is sandwiched between two planes of polished 15 mm-thick square scintillator pads of high granularity (more than twelve thousand channels). One millimeter diameter Y-11 multi-clad S-type fibers are coiled and placed into a circular groove milled in the tile. The rectangular cross-section of the groove is 4.1 mm deep and 1.1 mm wide and holds three and a half loops of WLS fiber. Each pad is wrapped with 0.15 mm-thick TYVEK14 paper. The two ends of the looped WLS fiber are mated to two clear fibers viewed by a single pixel in a multi-anode PMT.

Since excellent timing and electromagnetic energy resolution are required to study the rapidly oscillating B_s – \bar{B}_s system, a shashlik design was chosen for the ECAL. The ECAL is formed from layers of 2 mm-thick lead and 4 mm-thick scintillator tiles. The tiles are fabricated via high-pressure injection-molding of polystyrene doped with 2.5 wt% *p*-TP and 0.01 wt% POPOP and are wrapped with 120 μm -thick reflective TYVEK sheets. Holes in the molds allowed for 1.2 mm-diameter WLS fibers to be inserted. Each fiber is looped so that it passes through the module twice. Both ends are read out from the same side. Excellent light yield uniformity was achieved with less than 2.5% fluctuation RMS among tiles.

The main purpose of HCAL is to identify a B-meson decay by triggering on a secondary particle with high transverse momentum. While the required energy resolution is a modest $80\%/\sqrt{E}$, the timing has to be very good because the HCAL needs to be able to measure the particle transverse energy at a 40 MHz bunch crossing rate. HCAL is a steel-scintillator tile–fiber calorimeter. It uses the same scintillator mixture as ECAL, but is cast into 3 mm-thick tiles and alternated with 10 mm-thick steel plates. The design is similar to the ATLAS TileCal, with the tiles edge-on to the beam pipe and the WLS fiber running along the edge.

15.3.2 High-Granularity Calorimeters for Particle Flow Strategies

The best single hadron resolution at a collider detector was achieved by the ZEUS plastic scintillator and depleted uranium calorimeter described earlier. The performance for particle jets, however, was considerably worse than one might expect just based on this single hadron resolution. For example, ZEUS quoted a hadronic Z-mass core resolution of 6 GeV [101], which was not sufficient for the separation of W and Z final states. This is because a hadronic calorimeter is not the most precise measuring device for most of the particles in a jet. In a typical jet, 60% of the energy is carried by charged particles, 30% by photons, and only 10% by long-lived neutral hadrons. At modern collider detectors, the energy of the charged particles is best measured with tracking systems, and the photon energies are best measured by high-resolution electromagnetic calorimeters.

Rather than assigning energies to the jet based on depositions independently measured in the early stage (ECAL) and later stage (HCAL) of the shower development, new analyses using “particle flow” techniques image the jet as a whole, identifying and removing the electromagnetic component in the HCAL data using the more precise ECAL and tracking information [102]. What is left in the HCAL data then provides a measurement of the neutral hadron contribution. By using these new paradigms to analyze their data, CMS confirmed the expected gain in performance over standard calorimetric methods, finding improvements from $\sim 30\%$ at 50 GeV down to $\sim 10\%$ at 400 GeV [102–105]. The ATLAS calorimeter, which has inherently better jet resolution, did not see such improvement applying particle flow analysis to their existing data.

In order to fully optimize a detector for particle flow, the detailed topological reconstruction and high granularity of the electromagnetic sector must be extended into the hadronic. Plans for the LHC include an order of magnitude increase in luminosity (the HL-LHC is expected in 2026), creating significant challenges in radiation tolerance and event pileup. At up to 200 interactions per beam crossing every 25 ns, advances in timing performance are also required. Simulations show that the endcap ECAL and HCAL will have to sustain up to 1.5 MGy and 30 kGy of integrated dose, respectively, and a fluence of 10^{16} n/cm². Aging and radiation studies [106] have demonstrated the need to replace the entire calorimetric system in the endcap region by that time. Thus, CMS is proposing to build a new high-granularity sampling calorimeter (HGCAL) with active elements of both silicon and plastic scintillator to replace the endcap calorimeters.

The design draws heavily on almost two decades of research into detector concepts for future electron–positron linear colliders such as ILC and CLIC. Simulations of imaging calorimeters have shown that resolutions around 3–4% can be realized for jet energies from 50–1500 GeV, spurring a broad exploration of the technologies capable of such fine segmentation. Large-scale prototypes have been constructed and tested, organized under the umbrella of CALICE [107–110], and featuring the same fine granularity in three dimensions as used in simulations of jet energy performance

using particle flow techniques. Plastic scintillator is still an element in many of the CALICE designs and also figures in the CMS HGCAL upgrade. Plastic scintillator is still the most cost-effective way to instrument a sampling hadronic calorimeter. Advances in readout technology have created scintillator elements that do not require long fibers in order to keep the phototransducers away from high flux and magnetic fields, thus allowing more compact designs and finer segmentation.

CALICE: ScECAL

The scintillator–tungsten ECAL is an electromagnetic calorimeter whose active elements are scintillator strips with embedded WLS fibers read out at the end with SiPMs (specifically the Hamamatsu multi-pixel photon counter or MPPC). Scintillator layers interleaved with tungsten absorber plates are alternately oriented horizontally and vertically to achieve fine square segmentation. ScECAL underwent several prototyping stages. The final physics prototype [108, 110, 111] was composed of 30 layers with a transverse size of $180 \times 180 \text{ mm}^2$, with a total of 2160 channels. Each layer consisted of 72 scintillator strips with a size of $45 \times 10 \times 3 \text{ mm}^3$. Each strip, produced by an extrusion method, had a hole along its length into which a 1 mm-diameter Kuraray Y-11 WLS fiber was inserted. Each scintillator strip was individually wrapped with reflective foil to increase photon yield and reduce optical cross-talk between strips. This was an improvement over an earlier prototype built with monolithic scintillator plates, grooved to create the individual channels, since even with a plastic film inserted in the grooves, the earlier prototype suffered from 10% cross-talk between neighboring strips. For electrons in the fiducial region, the intrinsic calorimeter resolution for electron beams, after subtraction of the beam momentum spread, was determined to be

$$\frac{\sigma}{E} = \frac{12.8\%}{\sqrt{E}} \oplus 1.0\% \quad (15.3)$$

CALICE: AHCAL

The “Analog HCAL” is a hadronic calorimeter built from planes of small scintillator tiles with the SiPMs embedded directly in the center of each tile and connected to a large printed circuit board that functions both as the SiPM electronics and the supporting structure. An example is shown in Fig. 15.9. The light yield of the $3 \times 3 \text{ cm}^2$ tile shown is >20 photoelectrons. The smaller the tile and the larger the SiPM, the larger the yield of photoelectrons from a MIP. The photoelectron yield can be doubled by wrapping the tile in a VM2000-enhanced specular reflector film. There is a 100 micron-wide zone along the edges of the tile where no light is produced, and a reduction of light yield at the positions of fiber and SiPM, due to reduced scintillator material thickness there. The effects on the response to electrons and pions were found to be negligible.

A prototype [109] deployed 38 layers of 5 mm-thick scintillator tiles interleaved with 17 mm-thick steel absorber plates, which were later replaced by 10 mm-thick tungsten plates [107]. The total thickness corresponded to 5.3 nuclear interaction

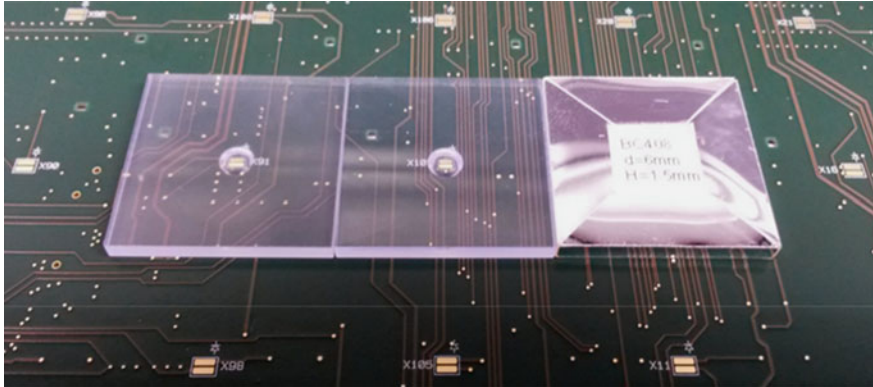


Fig. 15.9 Example of three CALICE $3 \times 3 \text{ cm}^2$ scintillator tiles mounted on a PCB that holds one SiPM per tile. The left two scintillators are unwrapped to show the SiPM within the small dome at the center of the tile, while the right-most tile is wrapped with reflective foil (reproduced from [113] with permission from IOP Publishing)

lengths. The tile dimensions were $3 \times 3 \text{ cm}^3$ in the central region, increasing in size toward the outside.

In total, there were 7608 tiles in the AHCAL, each individually read out via a SiPM produced by MEPhI/PULSAR in Russia [112]. For each SiPM, the over-voltage (reverse bias voltage excess over breakdown voltage) was adjusted to equalize the light yield to about 12 pixels per MIP normally traversing a tile. The response as a function of light intensity is non-linear, but beam tests were used to map out the response and apply the proper corrections.

The AHCAL energy resolution was found to be

$$\frac{\sigma}{E} = \frac{(21.9 \pm 1.4)\%}{\sqrt{E}} \oplus \frac{58 \text{ MeV}}{E} \oplus (1.0 \pm 1.0)\% \quad (15.4)$$

where the second term represents the noise contribution determined by random triggers and was fixed before fitting. The constant term is a measure of calibration uncertainties, non-uniformities, and instabilities. It is so small that it can be neglected for studies with hadrons. As expected from simulation studies, the actual beam tests demonstrated that the version with the tungsten absorber was compensating, whereas the version with a steel absorber yielded 1.2 for e/h.

HGCAL Proposal

The highly granular calorimeter (HGCAL) is the proposed upgrade for the CMS endcap calorimeter. It replaces the homogeneous lead tungstate ECAL and the scintillator sampling HCAL with a highly segmented integrated sampling calorimeter where the inner active layers are silicon and the outer layers are plastic scintillator. Figure 15.10 shows a cut-away of the CMS endcap region and the location of the various HGCAL elements. The radiation environment in the endcap region is much worse than in the barrel region. If the crystal ECAL endcap was to remain in place

during the HL-LHC era, its resolution would degrade significantly. Overall lower light levels would increase the stochastic term, and uneven damage within each crystal and between crystals would increase the constant term. A different technology is required.

Signals from the HCAL scintillator towers, which are less bright than the lead tungstate ECAL to start with, would dip below threshold due to radiation damage. Improved response and local coupling to silicon-based photodetectors are required. In order to retain good overall performance over the ten year lifetime of the project, silicon is used closest to the beam pipe where the radiation is the worst, and a low-cost scintillator is used in those regions where the integrated dose is <3 kGy and the fluence is limited to 8×10^{13} n_{eq}/cm².

The scintillator elements are a design based on the AHCAL prototype work, but are tiled as ring segments to properly fit the endcap geometry. The tiles will vary in size from 4 to 30 cm², comprising 28 longitudinal sampling layers, which must be read

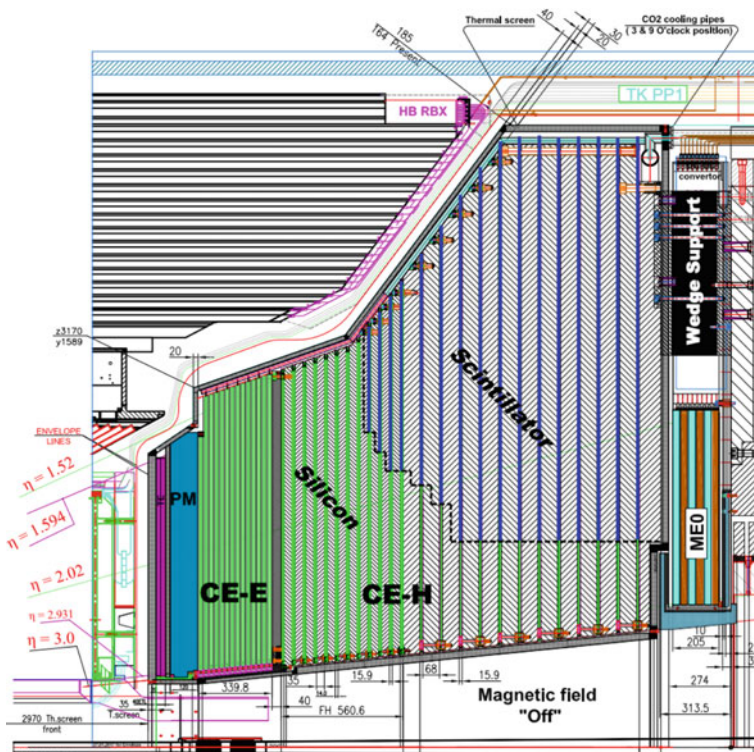


Fig. 15.10 Longitudinal cross-section of the upper half of one endcap calorimeter of the proposed CMS HGCAL. It consists of an electromagnetic compartment (CE-E) followed by a hadronic compartment (CE-H). The green region to the lower left is instrumented with silicon detectors and the blue region to the upper right with scintillator tiles (reproduced from [114] with permission from CERN)

out layer by layer. The absorber in the hadronic compartment will consist of stainless steel plates with a thickness of 35 mm (inner 12 layers) and 68 mm (outer 12 layers). Between these absorber plates sit silicon modules and scintillator tileboards mounted on 6 mm-thick copper cooling plates. This leads to a total calorimeter thickness (both ECAL and HCAL) of 10.7 interaction lengths, including the 120 mm-thick neutron moderator layer in front of the calorimeter.

In order to keep the radiation-induced energy equivalent of electronics noise sufficiently low, SiPMs have to be operated at around -30°C . This is also true for the inner layer silicon sensors, so the whole calorimeter will be operated at that temperature. The high radiation environment, as well as operation at low temperature, require validation studies to prove that plastic scintillator can be used in this new regime. Dedicated studies have been performed in irradiation facilities and have found consistent results between room temperature measurements and those at negative 20°C and below [114]. While no plastic scintillator can remain unchanged over 10 years of such high dose exposure, studies on the rate and amount of signal degradation (even at low temperatures) have established that the overall energy resolution can be maintained by the proposed calibration techniques over the life of the experiment. Both types of commonly available scintillator materials are currently in the running: polyvinyl toluene-based (PVT) scintillator (e.g., EJ-200 from Eljen or BC-408 from Saint-Gobain) or polystyrene-based (PS) scintillators which can be produced economically using injection-molding techniques.

During the design phase of CMS in the 1990s, radiation damage studies were performed on a range of scintillator tiles by exposing them to accelerated aging and high dose fluence tests [115, 116]. It was not fully appreciated that signal degradation is a complicated function of diffusion of oxygen into the plastic during irradiation versus the rate of polymer oxidation in the areas containing oxygen, all of which depend crucially on details of polymer preparation, the presence of additives, environment, and handling. Simple extrapolation from the high flux tests to long-term running at lower dosages underestimated the amount of radiation damage to the HCAL scintillator tiles in the CMS HCAL. Upgrades from the original multi-pixel hybrid tubes (HPDs) to SiPMs [117, 118], first in the endcap region and then more recently in the less-affected barrel, was partly driven by this unexpected loss in scintillator light output.

Extensive in situ data [119] has been accumulated by the CMS collaboration on scintillator response to particles produced in pp collisions at $\sqrt{s} = 13 \text{ TeV}$. While most of the tiles are made of PS-based SCSN-81, layer 0 is a thicker, brighter PVT-based BC-408 designed to mitigate the non-compensating response of ECAL and the intervening dead material. The response of both tile formats was measured as a function of luminosity delivered (fb^{-1}) and average dose rate (Gy/h). The total delivered luminosity determines the doses received by the tiles and the average luminosity delivered per hour controls the dose rates. For any given luminosity, a tile is subjected to a dose and dose rate that depend on its location in the detector: the energy density of the pp collisions varies with pseudorapidity, and the energy deposition profile of the resulting showers varies with depth in the calorimeter. The changing signal response is measured using a laser calibration system, a movable radioactive

source, and the hadrons and muons produced in the pp collisions. The results from the various methods are consistent and indicate that at a fixed dose the damage to the scintillators increases with *decreasing* dose rate. Plots from the laser calibration data are shown in Fig. 15.11.

In a recent upgrade, the HPDs in the endcap were replaced by SiPMs [117, 118] to remedy signal degradation due to radiation damage. This upgrade also provided for a finer longitudinal segmentation, an improved photodetection efficiency (factor of ~ 2.5), and better uniformity (RMS was reduced from 0.22 to 0.07). These same SiPMs are suitable for the new HGCAL and can be purchased from multiple vendors. SiPMs are inherently non-linear since they are made up of individual pixels, but corrections can be applied, especially if each tile is read separately. The nonlinearities are minimized by uniform light illumination, as has been demonstrated for the SiPM-on-tile geometry, and by fast recovery of the SiPM's individual pixels. The properties of these SiPMs reflect how far APD-based technology has come since CMS originally rejected APDs in the late 90s in favor of HPDs. The photodetection efficiency is now at $>30\%$ for a 50% geometric fill factor and the gain is several times 10^5 . Dark counts at room temperature are low at 100 kHz. While the noise rate increases under irradiation, it rises linearly with neutron fluence in a predictable way, which has been tested up to $2 \times 10^{14} \text{ n}_{\text{eq}}/\text{cm}^2$. Lowering the temperature also improves the performance. Noise itself makes only a small contribution to the energy resolution; the more important metric is to maintain inter-calibration within 3%. This requirement demands ongoing calibration of individual tiles with minimum-ionizing particles and drives the decision to use the AHCAL SiPM-on-tile technology.

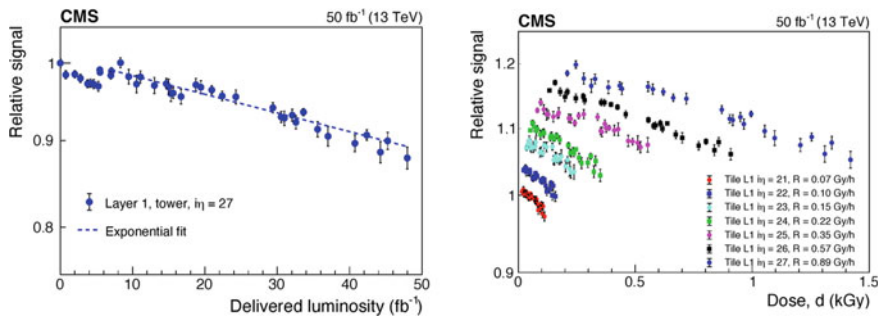


Fig. 15.11 Radiation damage in the SCSN-81 scintillator tiles of the CMS Endcap HCAL, measured using the laser calibration system. The vertical scale is logarithmic (base 10). *Left:* Dependence on delivered luminosity for layer 1 with $i_\eta = 27$ and $i_\phi = 63$. For this tile, the estimated dose at the end of data taking was 1.5 kGy and the average dose rate was 0.89 Gy/h. The dashed line represents a fit to the data to obtain the value of the exponential slope. *Right:* Dependence on accumulated dose for layer 1 with $i_\eta = 2127$. The average dose rates are shown for each set of points. Subsequent sets are shifted up on the vertical scale by a factor of 1.03 relative to the previous set for better visibility. Each set starts at the dose corresponding to an integrated luminosity of 7 fb^{-1} (reproduced from [119] with permission from CERN)

15.3.3 Dual-Readout Solutions

The particle flow approach relies on the integration of momentum (tracking) and energy (calorimeter) with very fine segmentation. Another handle on improved hadronic shower resolution is provided by “dual readout”. This refers to the simultaneous detection of both Cherenkov and scintillation light. While the scintillation channel is sensitive to both components of the shower, the signals from the hadronic fraction are strongly dominated by spallation hadrons produced in nuclear reactions. Spallation hadrons are not sufficiently relativistic to produce the Cherenkov light. Thus, the Cherenkov signal is a measure of the em shower component only. Comparison of the two signals yields a measurement of the shower em fraction on an event-by-event basis, thus providing the information necessary to correct for the large and non-Poissonian fluctuations in the energy sharing between the two components. As we have seen previously, this is key to improving the hadronic energy resolution of an intrinsically non-compensating calorimeter.

The CERN RD52 [120] collaboration is developing dual readout technology for future experiments, concentrating on two avenues: scintillating fibers and inorganic crystals. In a fiber calorimeter, the Cherenkov signal is detected by clear fibers interspersed with the scintillating fibers. The DREAM collaboration, as it is known (Dual-REAdout Module), has built several prototypes over the years. The most recent results are from towers with either lead or copper as the absorber matrix. Each tower is 2.5 m ($10 \lambda_{int}$) long with a cross-section of 46×46 mm². The scintillating fibers are Kuraray SCSF-78⁴ and the clear acrylic fibers are Eska SK-40⁵ with an attenuation length measured to be 6 m. As shown on the left side of Fig. 15.12, the scintillating fibers are bundled to one PMT and the clear fibers to another, one channel of each type per tower. For the scintillator channel, a yellow filter was installed at the entrance to the PMT to improve the longitudinal uniformity of the fiber by removing the blue part of the spectrum attenuated by self-absorption. The towers are stacked four to a module and the modules arranged to make a calorimeter that was tested in a beamline at CERN. Using 40 GeV electrons, the electron energy was measured with an independent resolution of σ_E/E of 3.8% and 4.0% for the scintillation and Cherenkov channel, respectively, to give a combined energy resolution of $\sigma_E/E=2.8\%$ [120].

This new RD52 calorimeter has better electromagnetic energy resolution than the original DREAM prototype, due to the improved sampling fraction. For energies above 20 GeV, it also out-performs the best R&D spaghetti calorimeters built by SPACAL [26]. For pions of 20 GeV, 60 GeV, and 100 GeV, the beam energy was reconstructed from the scintillation channel alone with resolutions of 20%, 15%, and 13%, respectively, but after the dual-readout correction, they became 13.5%, 8.3%, and 7.0%. The 60 GeV results are shown on the right side of Fig. 15.12, providing an explicit demonstration of the compensation principle first shown in Fig. 15.1.

⁴<http://kurarapsf.jp/psf/sf.html>, Kuraray Co. Ltd, Tokyo, Japan.

⁵<http://fiberopticpof.com/pdfs/ProductSpecs/SK40ProductInformation.pdf>, Mitsubishi Chemical Holdings.

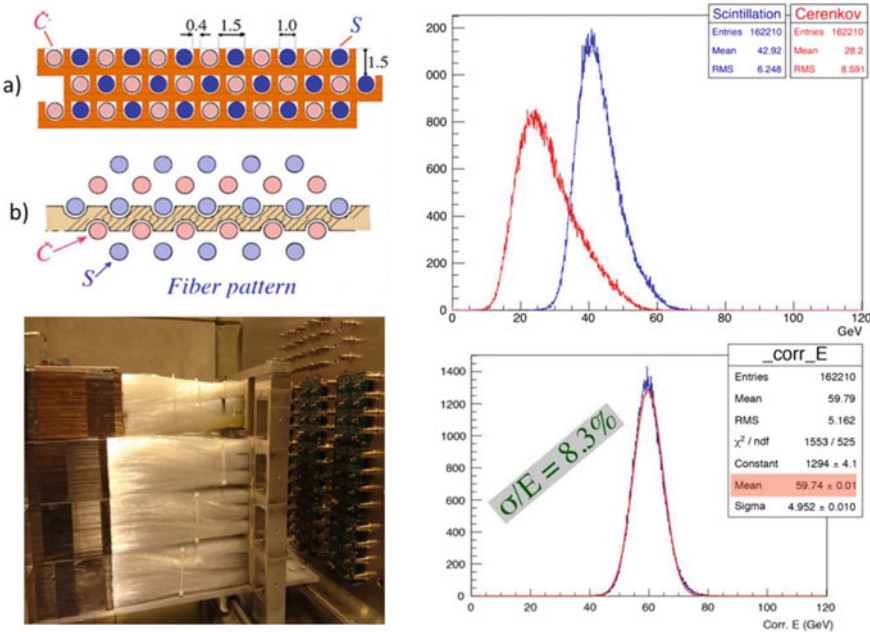


Fig. 15.12 Left: Construction details of the RD52 (DREAM) dual-readout spaghetti calorimeter. At the top is shown the fiber pattern for the copper absorber (**a**) and lead absorber (**b**). The two different colors represent the two different kinds of fibers (C = Cherenkov and S = Scintillator). Right: An example of the improvement in hadronic resolution possible using the dual readout correction to the em fraction in the hadronic shower (data from 60 GeV pions) (reproduced from [120] with permission from World Scientific)

The hadronic shower resolution is dominated by shower leakage fluctuations, since the prototype is too small to contain the whole shower. Simulations indicate that a larger calorimeter with the same design parameters would have a stochastic term of $30\%/\sqrt{E}$ and a constant term $<1\%$. Future upgrades include replacing the PMTs with SiPMs (which will also eliminate the long forest of fibers emerging from the modules), finer transverse segmentation, and industrialization of the fabrication.

15.4 Neutrino Experiments

15.4.1 Optimizing Calorimeters for Neutrino Physics

Large neutrino detectors are optimized differently than the calorimeters used in large multi-purpose detectors at fixed-target and collider facilities. Neutrinos undergo either a charged current interaction where the neutrino converts into the equiva-

lent charged lepton (e.g., inverse beta decay, $\nu_e + p \rightarrow n + e^+$) or a neutral current interaction where the neutrino retains its identity, but transfers momentum to the target, causing a recoil or disintegration. These are weak interactions mediated either by the W^\pm (charged current) or Z^0 (neutral current).

The electrons and muons which are produced in charged current interactions have characteristic tracks that can be used to identify the particle as well as the *flavor* of the parent neutrino, meaning that if an electron (muon, tau) is produced, it came from an electron (muon, tau) neutrino. In order to distinguish between neutrinos and antineutrinos, a magnetic field can be employed to bend charged particles. It is therefore very useful to have both tracking and calorimetry. Unlike most particle physics experiments where the tracking and calorimetry can be handled by separate detectors fanning out from a well-defined interaction point, neutrino detectors need to combine the two functions in one monolithic detector since the interaction can happen anywhere.

When such tracking calorimeters are used for oscillation experiments, there is a focus on combining excellent particle identification (flavor tagging) and energy reconstruction. For neutrino factory experiments especially, charge identification is also required to separate leptons from anti-leptons. Astrophysical neutrinos require improved angular resolution for directional reconstruction and time resolution to study transient signals. All of these properties can be realized using plastic scintillator, as was done by the MINOS long-baseline oscillation experiment [121] and the MINERvA experiment [122]. The sheer size of these detectors demands a sampling calorimeter strategy when using a solid scintillator, with absorbers chosen to optimize tracking resolution rather than shower energy compensation. In addition, the cost must be mitigated by developing cheap methods of producing the scintillator (e.g., factory extrusion) and minimizing the area of the photosensor (WLS fibers and multi-channel PMTs or APD arrays).

15.4.2 Tracking Calorimeters for Neutrinos

MINOS

The MINOS long-baseline experiment [96] observed the disappearance of muon neutrinos (and the appearance of electron neutrinos) at energies between 1–30 GeV, as they traversed the 735 km of distance between production at the Fermilab main injector near Chicago to northern Minnesota. Three steel-scintillator tracking calorimeters were built: a calibration detector (exposed to CERN test beams), a near detector (1 km from the primary proton beam target), and a far detector 705 m underground at the Soudan Underground Laboratory. The detectors were built with the same technology and the same transverse and longitudinal sampling, since the purpose was to reliably compare the rates, energies, and topologies of neutrino events at two different locations, and thereby derive oscillation parameters such as mixing angle and mass difference. The steel absorber plates were 2.54 cm thick, alternating with 1 cm-thick

by 4.1 cm-wide extruded polystyrene scintillator strips read out with WLS fibers and multi-anode PMTs.

The 5,400 metric ton MINOS far detector consisted of 486 magnetized octagonal steel planes, each 8 m in diameter flat-to-flat, interleaved with two crossed planes of 8 m long plastic scintillator strips, providing close to 100,000 channels of tracking and energy information. The 980 metric ton near detector, located 100 m underground at the Fermilab neutrino beam facility, was composed of 282 planes with similar characteristics, but at roughly half the diameter. The first 120 upstream planes of the near detector were fully instrumented as a true tracking calorimeter, capable of defining and characterizing events for the near/far comparison, while the downstream section, with a scintillator only every fifth plane, was operated as a muon spectrometer.

A solid scintillator was chosen over liquid scintillator, proportional wires run in streamer mode (Iarocci tubes), and resistive plate chambers during a 3-year R&D process (see the Technical Design Report [121]), citing good transverse segmentation, fast timing, simple and robust construction, and low maintenance. The MINOS detectors required a significant scale-up in size from previous fine-grained scintillator sampling calorimeters, requiring an investment in new cost-effective extrusion techniques and automated assembly techniques. Polystyrene pellets were mixed in a nitrogen atmosphere with PPO (2,5-diphenyloxazole, 1.0 wt%) and POPOP (1,4-bis(5-phenyloxazol-2-yl) benzene, 0.03 wt%) and melted prior to extrusion. Pellets and TiO₂ were mixed in a second extruding machine to form the thin diffuse reflective coating. The scintillator and coating were co-extruded through two ports in the same forming die in one continuous strip which was cut to length by a traveling saw [123]. At 0.25 mm thick, the 15 wt% concentration of the TiO₂ layer was as thin as could be reliably co-extruded, but thick enough to prevent transmission of UV light. The cross-section of the extruded shape included a 2.3 mm-deep by 2.0 mm-wide groove down the center, which was not coated with TiO₂, into which the WLS fiber could be inserted.

The WLS fiber was 1.20 mm diameter, double-clad polystyrene fiber doped with 175 ppm of Y-11 fluor. The fiber was a custom “non-S” type (long attenuation length) produced by Kuraray Inc. (Japan), but with a lower S-factor of 25 in order to retain flexibility when bent. The fiber was delivered on spools containing 1 km of fiber each to assembly facilities where a semi-automated gluing machine dispensed optical epoxy in the U-shaped groove, inserted the WLS fiber, and covered the groove with reflective tape. The scintillator strips were assembled into aluminum-covered modules of 28 strips each, with a grooved plastic extension to guide the WLS fibers as they exited the strip and glued into the holes of a bulk optical connector. At this point, the fly-cut and polished bulk optical connectors were coupled to bundles of un-doped double-clad fiber. The clear fibers were then mapped to the pixels of a Hamamatsu multi-anode PMT. In the far detector, 8 fibers were bundled to each pixel of a 16-anode PMT, whereas in the near detector with higher flux, each fiber went to an individual pixel of a 64-anode PMT (Fig. 15.13).

Table 15.2 Plastic scintillator tracking calorimeters used in neutrino detectors

Experiment	Tracking Calorimeter	Scintillator	Absorber	Readout	Performance
CHORUS [124-127] 1994-1997 CERN SPS	Spaghetti ECAL	1 mm Scint Fibers (SCSF-81)	Pb + 1% Sb (98 wt%)	Acrylic light guide to PMT	$\sigma_E/E = 13.8\%/\sqrt{E}$, $\sigma_x = 0.350 \text{ mm}$
	Spaghetti HCAL	1 mm Scint Fiber (BCF-12)	Pb + 1% Sb (98 wt%)	Acrylic light guide to PMT	$32.3\%/\sqrt{E} + 1.4\%$, $\sigma_x = 0.350 \text{ mm}$
K2K SciBar [128,129] 1999-2004 J-PARC, Japan	XY planes of strips	1.3 × 2.5 × 300 cm ³ extruded PS strips (1% PPO, 0.03% POPOP)	None	Embedded Y-11 WLS fiber (1.5 mm) to MAPMT	99% reconstruction efficiency for tracks longer than 10 cm
	Spaghetti ECAL	1 mm Scint Fibers (SCSF-81)	Pb + 1% Sb (98 wt%)	light guide to PMT	$\sigma_E/E = 14\%/\sqrt{E}$
MINOS near detector [96] 2005-2012 FNAL, NUMI beam	UVX planes of strips	1.0 × 4.1 × 800 cm ³ co-extruded PS strips (1% PPO, 0.03% POPOP)	25.4 mm Fe plates	Y-11 WLS fiber (1.2 mm) in groove to clear fiber bundle to PMT	$\sigma_E/E = 21.4\%/\sqrt{E} \oplus 4\% \text{ (em)}$, $56\%/\sqrt{E} \oplus 2\% \text{ (had)}$
	UVX planes of strips	1.0 × 4.1 × 800 cm ³ co-extruded PS strips (1% PPO, 0.03% POPOP)	25.4 mm Fe plates	Y-11 WLS fiber (1.2 mm) in groove to clear fiber bundle to PMT	$21.4\%/\sqrt{E} \oplus 4\% \text{ (em)}$, $56\%/\sqrt{E} \oplus 2\% \text{ (had)}$
MINOS far detector [96] 2009-2012 Soudan Underground Lab	UVX planes of strips	1.7 cm-tall 3.3 cm-wide triangular co-extruded PS strips (1% PPO, 0.03% POPOP)	ECAL: 2 mm Pb sheets HCAL: 25.4 mm Fe plates	Embedded Y-11 WLS fiber (1.2 mm) to clear fiber to PMT	$\sigma_E/E = 29.0\%/\sqrt{E} \oplus 13.4\%$, $\sigma_x = 3.1 \text{ mm}$
MINERvA [122] 2009-2019 FNAL	UVX planes of strips	1.7 cm-tall 3.3 cm-wide triangular co-extruded PS strips (1% PPO, 0.03% POPOP)	ECAL: 2 mm Pb sheets HCAL: 25.4 mm Fe plates	Embedded Y-11 WLS fiber (1.2 mm) to clear fiber to PMT	$\sigma_E/E = 29.0\%/\sqrt{E} \oplus 13.4\%$, $\sigma_x = 3.1 \text{ mm}$
T2K near detectors [130-134] 2010-present J-PARC, Japan	ND280 FGD: XY planes of strips ND280 POD: XY planes of strips	0.96 × 0.96 × 184 cm ³ co-extruded PS bars (1% PPO, 0.03% POPOP) 1.7 cm-tall 3.25 cm-wide triangular co-extruded PS bars (1% PPO, 0.03% POPOP)	30 mm water layers (56 wt%) 4.5 mm Pb sheets	Embedded Y-11 WLS fiber (1 mm) to MPPC Embedded Y-11 WLS fiber (1 mm) to MPPC	$\sigma_t = 12.5 \text{ ns}/\sqrt{N}$ $\sigma_E/E = 3.5\%/\sqrt{E} + 10\%$
	ND280 TECal: XY planes of strips INGRID: XY planes of strips	1 × 4 cm ² co-extruded PS bars (1% PPO, 0.03% POPOP) 5 × 1 × 121 cm ³ co-extruded PS bars (1% PPO, 0.03% POPOP)	1.75 mm Pb sheets 65 mm Fe	Embedded Y-11 WLS fiber (1 mm) to MPPC Embedded Y-11 WLS fiber (1 mm) to MPPC	$\sigma_E/E = 7.5\%/\sqrt{E}$ $\sigma_x = 27 \text{ mm}, \sigma_t = 9 \text{ ns}, 95\%$ tracking efficiency for tracks through at least three planes

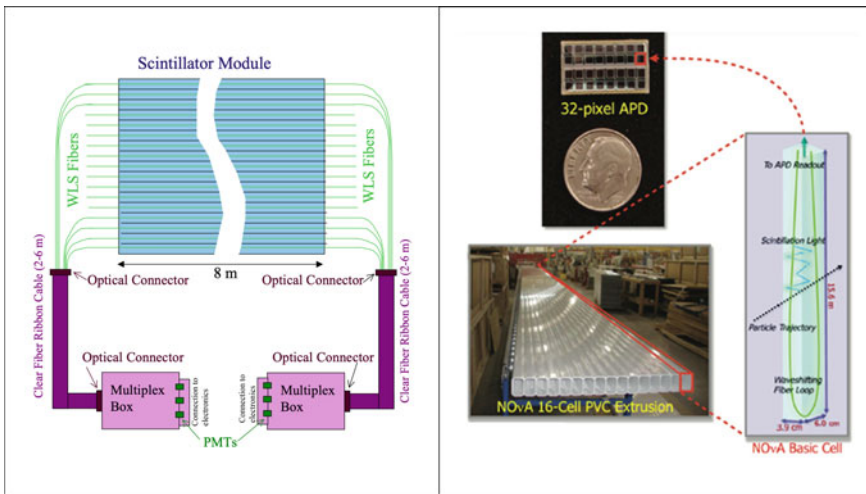


Fig. 15.13 The MINOS co-extruded plastic scintillator strips (*left*) with embedded WLS fiber and multi-channel PMT readout contrasted with the NOvA extruded channels (*right*) filled with liquid scintillator, looped WLS fiber, and APD readout (based on figures in [121, 135] with permission from Elsevier)

NOvA

For the scaled-up NOvA [136] neutrino oscillation experiment (810 km from Fermilab to Ash River, MN), the cost of extruded plastic was too high. Since hydrogen-rich scintillator and the tracking sampling calorimeter concept still provided huge advantages, the new design replaced solid plastic with hollow plastic (PVC) [137] extrusions filled with mineral oil doped with 5.23 wt% pseudocumene. Other advantages included being able to loop the WLS fibers in the liquid to read out all the light at one end, improved optical coupling of the WLS fiber to liquid scintillator, more uniform response, and a higher light output that remained stable over time, in contrast to the aging experienced by the MINOS plastic scintillator.

MINER ν A

The goal of accelerator-based long-baseline experiments is to determine the mass hierarchy of neutrinos and to test for CP violation by comparing the oscillation probabilities for neutrinos and antineutrinos. This requires a detailed understanding of neutrino- and antineutrino-nucleus scattering processes in the energy range from a few hundred MeV to a few GeV. The MINER ν A experiment [122] at Fermilab was designed to make precise measurements of neutrino-nuclei cross-sections in a wide variety of nuclei. This physics goal put very stringent requirements on track reconstruction and particle identification, which drove the design of the tracking calorimeter.

The MINER ν A detector, located 2.1 m upstream of the MINOS near detector in the Fermilab neutrino beamline, employed a forward region with target nuclei (including

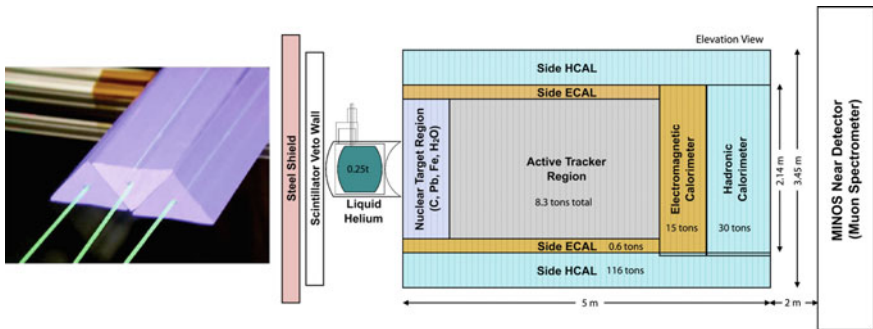


Fig. 15.14 The MINERvA neutrino detector is located upstream of the MINOS near detector in the Fermilab neutrino beam line. The triangular scintillator bars with embedded WLS fiber are also shown (reproduced from [122] with permission from Elsevier)

C, Pb, Fe, and H₂O) followed by an active tracking region composed entirely of plastic scintillator. The tracking region was surrounded by a Pb/scintillator ECAL and a steel/scintillator HCAL. The layout can be seen in Fig. 15.14. The MINOS near detector provided additional muon tracking data, including the muon charge and momentum based on their deflection in the MINOS magnet. Each tracking module consisted of two layers of triangular cross-section scintillator strips nested together to create an interleaved plane. The planes were oriented with the strips running vertically (X-position) and rotated 60° clockwise (U-plane) and counterclockwise (V-plane) from the X-plane in order to avoid ambiguities with reconstructed hit associations from multiple tracks. This geometry provided excellent tracking resolution and the ability to identify final states with multiple particles. Characterization with muons demonstrated a 3.0 ns timing resolution and a 3.1 mm position resolution. The same plane construction was used in the ECAL, but with the addition of 2 mm-thick lead foils. For the HCAL, only one plane of rectangular cross-section scintillator strips was interleaved with the 2.54 cm-thick steel absorber.

All the strips were fabricated using the same scintillator cocktail as MINOS. While the MINOS extrusion process was contracted to a private company (Itasca Plastics, Inc.), Fermilab developed an Extrusion Line Facility [138] for the MINERvA experiment with a continuous process from the vendor-supplied polystyrene pellets to the final extruded strips. The strips were co-extruded with a white reflective coating based on 15% TiO₂ (by weight) in polystyrene and included a central hole into which the WLS fiber would later be inserted. The extrusion line operated under a nitrogen purge from the dryer which used high-pressure nitrogen to dry the polystyrene pellets in the die. The triangular strips measured 33 mm at the base, with a height of 17 mm and were threaded with 1.2 mm diameter Kuraray Y-11 WLS fibers (see Fig. 15.14). The WLS fibers were then coupled to clear fibers arranged in the cable strips of 8 fibers each and read out with a 64-channel Hamamatsu multi-anode PMT.

K2K and T2K Near Detectors

Large experiments specifically designed to detect solar neutrinos (and reactor neutrinos to a lesser degree) require very low energy thresholds and can sacrifice directional information. Because of this, a fully sensitive calorimeter (e.g., water Cerenkov or liquid argon) is a better choice than a plastic scintillator sampling calorimeter, and is also more cost-effective. This bleeds into the design of long-baseline neutrino oscillation experiments as they get ever larger. Not only is plastic scintillator expensive, but there is also a push to provide a wide variety of physics goals in the same facility, with the low thresholds required for non-accelerator neutrino studies and even rare events like proton decay. Thus, liquid argon was chosen for the proposed long-baseline DUNE experiment from Fermilab to the Sanford Underground Research Facility.

The near detectors of neutrino oscillation experiments, however, still require the excellent tracking and time resolution properties of plastic scintillators. This means that when the Super-Kamiokande (SuperK) water Cherenkov detector became the far detector for the neutrino oscillation experiment called K2K (KEK-to-Kamioka), a near detector called SciBar was designed as an upgrade to the original lead glass detector [128]. The tracking calorimeter portion of the SciBar detector is made of over fourteen thousand scintillator bars, each with dimensions $1.3 \times 2.5 \times 300 \text{ cm}^3$, in alternating horizontal and vertical layers. Bars are fabricated using the same scintillator mixture and technique used by MINOS and coated with TiO_2 . WLS fibers embedded in the center of each bar are clustered as they emerge into groups of 64 and read out using multi-anode PMTs. This design allows for a timing resolution of 1.3 ns [129] and identification of particle tracks at least 10 cm long (such as the proton from a sub-GeV charged current quasi-elastic event). After the beam passes through the tracking calorimeter, it encounters the SciBar spaghetti ECAL, re-used from the CHORUS experiment [127], which measures ν_e contamination and π^0 production from neutrino interactions.

The longer baseline T2K (Tokai-to-Kamioka) project deploys two new plastic scintillator detectors, an on-axis interactive neutrino GRID (INGRID) to measure the direction and intensity of the beam, and an off-axis near detector system called ND280 [132]. The 160 ton INGRID detector contains ten 6.5 cm-thick iron layers alternating with 11 scintillator tracking planes. Each plane is formed from 24 horizontal scintillator bars glued to 24 vertical bars, where each bar is $5 \times 1 \times 121 \text{ cm}^3$ [139]. The Fermilab extrusion facility produced the bars using the same scintillator mixture and co-extrusion process developed for MINOS and MINERvA. Kuraray 1 mm-diameter double-clad Y-11 WLS fibers are inserted into a hole in the center of each bar and one end is read out with a SiPM (Hamamatsu MPPC). Detector characterization using cosmic muons measured an average light yield per channel of 10 PE/cm for MIPs and a timing resolution of 3.2 ns. The INGRID detector measured the beam position with a precision better than 0.4 mrad (Fig. 15.15).

ND280 measures the number of muon neutrinos produced along the off-axis beamline in order to compare to the number at the far detector after oscillation. Three components of the ND280 off-axis detector system use plastic scintillator

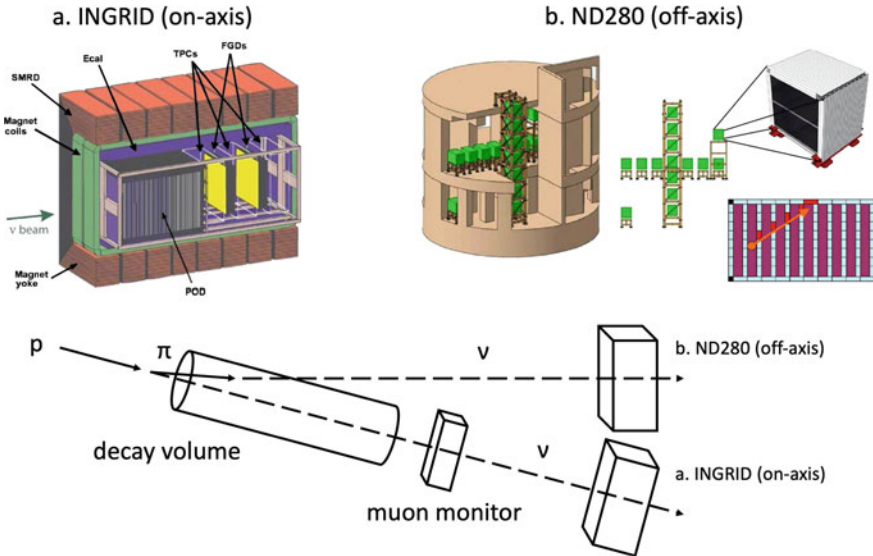


Fig. 15.15 The T2K near detectors. Schematics of the off-axis ND280 detector and on-axis INGRID detectors are shown (reproduced from [132] with permission from Elsevier)

technology: the pi-zero detector (PØD) [131], the fine-grained scintillator detector modules (FGDs) [134], and the ECAL [133]. Like INGRID, the PØD tracking plane elements were extruded at Fermilab. In this case, they use the same triangular scintillator bar die design as MINERvA, alternating with water layers to measure the cross-section of muon neutrinos with oxygen. The upstream and downstream regions are configured as electromagnetic calorimeters providing energy containment and active veto, and the central tracking region provides the π^0 measurements. The central region contains 26 scintillator arrays of tracking, while forward and rear calorimetric regions consist of seven scintillator arrays alternating with 4 mm-thick lead sheets. This design provides an energy resolution of $3.5\%/\sqrt{E} + 10\%$.

The ND280 tracker employs the $\nu_\mu + n \rightarrow \mu^- + p$ interaction to measure the muon and electron neutrino beam fluxes and energy spectra, with two FGDs to detect the proton and three TPCs to measure the muon. The first FGD design is modeled after the K2K SciBar detector, with XY arrays of $0.96 \times 0.96 \times 184 \text{ cm}^3$ extruded scintillator bars read out in the same way as PØD. The second FGD is composed of seven XY sandwiches of scintillator layers alternating with six 3-cm-thick layers of water.

The ECAL consists of two sections. One is coarsely segmented and surrounds the PØD for detecting escaping photons and muons, and the second finely segmented ECAL surrounds the FGDs and TPCs to detect particles leaving the tracking volume. The finely segmented modules are made of 4 cm-wide, 1 cm-thick plastic scintillator bars arranged in 32 layers and separated by 31 layers of 1.75 mm-thick lead sheets.

15.5 Large Plastic Scintillator Detectors in the Future

Plastic scintillator will be used as a major sensitive element in large multi-purpose particle physics collider detectors for the next couple decades. It is featured in the upgrade plans of CMS and represents several design options for a future ILC. A move to silicon-based photodetectors, resistance to magnetic fields, efficient light collection techniques, fine segmentation, and aggressive calibration strategies have extended the competitiveness of plastic scintillator into the high luminosity era. It also continues to be a cost-effective, high-resolution option for small electromagnetic calorimeters.

Due to the sheer size required for the far detectors of the next generation of long-baseline neutrino experiments, even mass-produced extruded plastic is too expensive. This was already true for NOvA, where the substitution of mineral oil-based liquid scintillator in extruded plastic channels was far cheaper than the co-extruded plastic bars developed for MINOS. Signal extraction for both technologies was similar, with embedded WLS fibers and clear fiber light guides to multi-channel photodetectors, see Fig. 15.13. When considering a design for DUNE, the next long-baseline neutrino detector in the US, the technology choice was between water Cherenkov and a liquid argon time-projection chamber (TPC), with the final decision favoring liquid argon. The planned mega-ton Hyper-Kamiokande neutrino detector in Japan's Kamioka mine will have ten times the fiducial volume of the previous Super-Kamiokande neutrino detector, using the very scalable water Cherenkov technology. They will read out the light with banks of improved large-aperture PMTs, augmented by new large-aperture hybrid tubes.

Large detectors built to study neutrinos, dark matter, or even proton decay are therefore more likely to use plastic scintillator as an auxiliary detector rather than the main one or as a near detector for long-baseline neutrino physics. These large, very sensitive experiments are often sited underground to reduce background from cosmic rays. Scintillator provides a signal which can be used to veto high-energy muons which penetrate to that depth. If the scintillator is also able to identify neutrons, a wide variety of new applications become available.

15.5.1 Neutron Sensitivity

New materials that incorporate neutron-sensitive dopants can adjust the neutron-to-charged-particle components by changing their composition ratios. The materials commonly used are salts or compounds containing boron, lithium, or gadolinium. More details about neutron-sensitive plastics and their production can be found in Chaps. 3 and 4 of this book. Acrylic and styrene monomers loaded with gadolinium have been shown to be radiopure [101, 140] and can be fashioned into a variety of shapes and sizes. The resulting capture gamma rays can be detected in a surrounding medium (e.g., liquid argon, un-doped liquid or solid scintillator) or by the Gd-loaded

plastic itself when doped with scintillating fluors. Proprietary chemistry is needed to fully polymerize liquid scintillator when it contains the high concentrations ($>1\%$) of dopants required for efficient neutron detection. We will not discuss the many nuclear experiments that will be enabled by this new technology. Instead, we concentrate on two proposed upgrades in particle physics which depend on this new development.

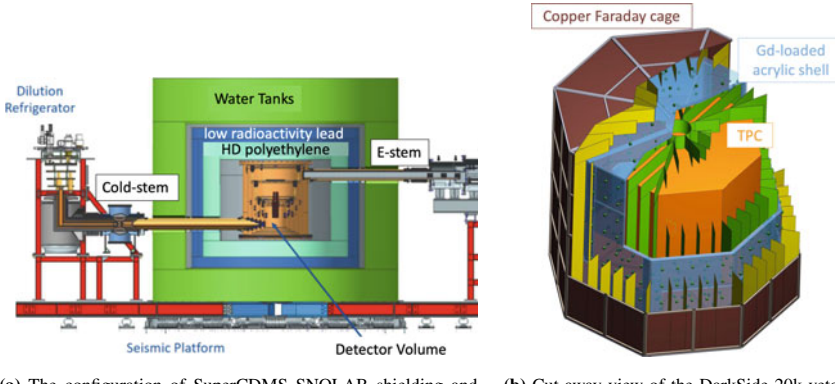
Neutron Veto for Dark Matter

As dark matter experiments explore ever-larger exposures in their search for direct detection of dark matter, background rejection becomes increasingly important. Strategies to reject electron recoils have been effective in reducing gamma and beta backgrounds, but the identification and rejection of residual neutron background remains difficult. An efficient and radiopure active neutron veto surrounding the dark matter detector would enable *in situ* identification and rejection of the residual neutron background, as well as understanding the shield efficiency and identifying internal contaminants.

Neutron-sensitive *liquid* scintillator has already been used as a dark matter neutron veto, completely enclosing the DarkSide-50 [141] liquid argon time-projection chamber. However, a simple, monolithic liquid veto is not possible for experiments featuring a more complicated geometry, in particular for those operating in the mK temperature range and serviced by a dilution refrigerator, such as SuperCDMS [142, 143], see Fig. 15.16a. Attempting to solve this by enclosing the liquid scintillator in multiple small containment vessels complicates readout and increases the risks of leaks. Even for noble liquid experiments such as the DarkSide program, the use of organic liquid scintillators in underground experiments raises site-dependent safety and environmental concerns. Current progress in developing neutron-sensitive solid plastic scintillator would enable a cost-effective neutron veto for cryogenic solid-state dark matter experiments, as well as an alternative for underground experiments which are struggling with the fire hazards and personnel safety risks associated with leaks and dispersion of the primary solvents and dopants underground.

While neutron backgrounds for the first payload of the SuperCDMS SNOLAB experiment will be negligible, a larger payload and longer exposure will begin to observe a small number of single-scatter, neutron-induced nuclear recoil events that cannot be distinguished from a dark matter signal. Some of these neutrons are due to trace contaminants in the shield itself and some are produced by the rare muon that makes it down to the SNOLAB depth.

A GEANT simulation study showed that by replacing the passive polyethylene shield layer with gadolinium-doped plastic scintillator, it is possible to achieve neutron veto efficiencies of 90% with a reasonable choice of veto parameters such as a $100\text{ }\mu\text{s}$ timing window and a 50 keV threshold [140]. Even for a very short $10\text{ }\mu\text{s}$ time window, efficiencies of 80% are possible. The efficiency is defined as the fraction of detected neutron-induced single-scatter events which then scatter back into the neutron veto and deposit energy above threshold in the scintillator within an integration time. The neutron veto studied consisted of trapezoidal scintillator segments in a ring surrounding the outer cryostat of the detector volume with the same thickness



(a) The configuration of SuperCDMS SNOLAB shielding and cryostat. An upgrade could include a Gd-doped plastic scintillator neutron veto in the location of the high-density polyethylene shield. Note the significant penetrations for the He dilution refrigerator (Cold-stem) and the readout electronics (E-stem) which make a liquid scintillator veto very difficult to implement

(b) Cut-away view of the DarkSide-20k veto detector enclosed in a copper Faraday cage. The Gd-loaded acrylic shell (*light blue*) separates the inner and outer veto regions. Reflector panels (*green* and *yellow*) segment the inner and outer veto LAr. SiPMs (*green*) are mounted on both sides of the acrylic

Fig. 15.16 The SuperCDMS (*left*) and DarkSide-20k (*right*) experiments

as the original poly shielding. Embedded WLS fibers piped the signal to radiopure SiPMs on the top surface.

The results quoted above require 1 wt% uniform doping of the scintillator. Efficiency is much lower for an active veto formed from wedges of un-doped scintillator painted with Gd-loaded resin, unless the segmentation is increased significantly or the integration time is long.

The DarkSide-20k experiment [144, 145] will surround its liquid argon time-projection chamber with a veto detector, shown in Fig. 15.16b, to reject neutron backgrounds. The veto consists of two regions of liquid argon, each 40 cm thick, and is separated by a 10 cm-thick Gd-doped acrylic shell. The inner and outer surfaces of the acrylic are instrumented with SiPMs which read out the respective veto regions. The DarkSide-20k veto liquid argon is the scintillator used to detect gammas from neutron captures in the Gd-loaded acrylic, meaning optical clarity of the acrylic is not important, unlike in SuperCDMS. Monte Carlo simulations demonstrated that acrylic loaded with 2 wt% gadolinium is sufficient for achieving the required background limit of <0.1 untagged neutron events expected during a 10 year exposure of DarkSide-20k. Radiopure acrylic with the required Gd concentration has been produced in-house and will be tested in 2022 within a scaled-down prototype of DarkSide-20k.

The DUNE Photon Detection System

The next generation of long-baseline neutrino oscillation experiments will require precision measurements of neutrino interactions in order to determine the neutrino mass ordering and to discover CP violation in the lepton sector. In the US, the flagship experiment is DUNE [146, 147], which would occupy four caverns in the Sanford

Underground Research Facility. Each cavern would house a cryostat containing a liquid argon TPC with a minimum of 10 kt fiducial mass. The nominal plan has two of the caverns housing a single-phase liquid argon time-projection chamber with the third cavern housing a dual-phase (liquid and gas) TPC. In the single-phase design shown in the left panel of Fig. 15.17, the ionization electrons drift horizontally between vertically hung cathode planes (C) and anode plane assemblies (A), submerged in the liquid argon and separated by a distance of 3.5 m. Since the ionization electrons can take milliseconds to cross the drift volume, an auxiliary plastic scintillator system is used to determine the start time using the fast scintillation photons. By comparing with the arrival time of ionization at the anode plane, reconstruction becomes possible in the drift direction. A $1\ \mu\text{s}$ requirement on the timing resolution enables 1 mm position resolution for 10 MeV supernovae neutrino bursts. Good position resolution is also used to reject cosmic-muon-induced background events that occur near the edges of the detector modules, providing a fiducial cut for nucleon decay events.

The scintillator system consists of a set of 209-cm-long photon detection (PD) modules, ten of which are mounted in each anode plane between the wire layers. Each PD module contains 24 X-Arapuca⁶ cells and each cell is a box whose outer layers are dichroic filters transparent to the 127 nm argon scintillation light, but reflective for wavelengths greater than 400 nm. Between these filters is a WLS plate that converts UV photons into the visible spectrum (430 nm). Visible photons emitted inside the WLS plate within the critical angle internally reflect and reach the SiPMs along the edge of the plate. Those photons produced at wider angles escape and reflect off the dichroic filters back into the plates. The PD modules and the 24 X-Arapuca cells that make them up, as well as where they are located within the anode plane, are shown in Fig. 15.17.

If the WLS plate (or even the dichroic filters) were to be doped with gadolinium, then the PD system could operate as a neutron tagger as well as a start time trigger. DUNE will be exposed to wide-band neutrino (antineutrino) beams which have significant antineutrino (neutrino) components. Since the detectors are not magnetized, the relative composition of neutrinos-to-antineutrinos in the beam cannot be determined with simple lepton charge identification. Neutron tagging capabilities would help to quantify beam composition, directly improving the measurements. Neutron tagging would also improve energy reconstruction, making it less dependent on simulation, as energy from these neutral particles is otherwise lost. In its role as a supernova neutrino detector, the addition of neutron detection capability would greatly enhance the ability of DUNE to measure the spectrum and flavor content of supernova neutrinos.

⁶These photon traps are reminiscent of an arapuca, which is a South American bird trap.

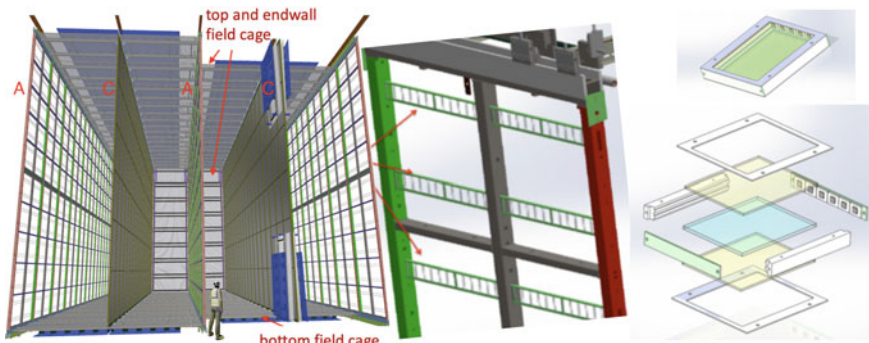


Fig. 15.17 The DUNE far detector single-phase liquid argon TPC is shown on the left with the cathode and anode planes labeled by C and A, respectively. In the middle, the PD modules are shown with their ladder of X-Arapuca cells, shown in more detail to the right with an assembled cell at the top and an exploded view on the bottom. The blue sheet in the middle is the WLS plate with the SiPM array shown on its edge. The yellow sheets on the top and bottom are the dichroic filters. Figure assembled from the DUNE technical design report [147]

15.6 Conclusion

There is an unbroken line of succession from the first sampling calorimeters made with alternating absorber and plastic scintillator to the massive detectors that now surround the intersecting beams at modern colliders like the LHC. Advances have been driven less by improvements in the product itself (e.g., brightness or radiation hardness) and more by enabling technologies and the creative exploitation by scientists of the natural advantages already inherent in solid organic scintillator.

It is the very adaptability of plastic, which can be cut, cast, or extruded, which has provided cost-effective solutions for sampling calorimeters whose wide variety of geometries is dictated by the specific physics process they are designed to study. The use of wavelength shifting fluors as a secondary emission process in a separate plastic element (e.g., WLS bars or WLS fibers) was not an advance in plastic scintillator technology, so much as a very successful strategy developed in response to space constraints and the readout limitations of PMTs. Then, with improved multi-clad plastic fibers, many new configurations appeared. The fibers could be the scintillator elements themselves (spaghetti calorimeters) or operate in tandem with scintillator as WLS fibers (tile–fiber and shashlik configurations). Dual-readout technologies combine scintillating fibers with un-doped fibers to measure the electromagnetic fraction in the shower via the Cherenkov light in the clear fibers.

The exception to this rule is the recent development of neutron-sensitive plastic scintillator. This has the potential to be transformative, opening the door to new applications in nuclear physics and the deployment of auxiliary scintillator detectors in neutrino and rare event experiments which have turned to large volumes of liquid scintillator, water, or noble liquids for cost and channel count reasons.

Of the enabling technologies, the most impactful has been the development of new photon sensors, along with advances in the low-noise preamplifiers that are required to exploit them. Their compact profile and magnetic-field insensitivity have created solutions for collider experiments that require a high degree of hermeticity and operate inside a solenoid. This path has ultimately led to the scintillator pads with their own on-board readout, now being finalized for the CMS Endcap upgrade (HGCal).

References

1. R. Wigmans, Nucl. Instr. Meth. A **259**, 389 (1987)
2. R. Wigmans, Nucl. Instr. Meth. A **265**, 273 (1988)
3. H. Abramowicz et al., Nucl. Instr. Meth. **180**, 429 (1981)
4. T. Åkesson et al., Nucl. Instr. Meth. A **262**, 243 (1987)
5. M. De Vincenzi et al., Nucl. Instr. Meth. A **243**, 348 (1986)
6. M. Catanesi et al., Nucl. Instr. Meth. A **260**, 43 (1987)
7. A. Astbury, Phys. Scripta **23**, 397 (1981)
8. D. Barber et al., Phys. Rep. **63**, 337 (1980)
9. T. Åkesson et al., Nucl. Instr. Meth. A **241**, 17 (1985)
10. M.J. Corden et al., Phys. Scr. **25**, 11 (1982)
11. M. Corden et al., Nucl. Instr. Meth. A **238**, 273 (1985)
12. C. Cochet et al., Nucl. Instr. Meth. A **243**, 45 (1986)
13. A. Beer et al., Nucl. Instr. Meth. **224**, 360 (1984)
14. W. Hofmann et al., Nucl. Instr. Meth. **163**, 77 (1979)
15. W. Hofmann et al., Nucl. Instr. Meth. **195**, 475 (1982)
16. A. Drescher et al., Nucl. Instr. Meth. **216**, 35 (1983)
17. H. Albrecht et al., Nucl. Instr. Meth. A **275**, 1 (1989)
18. L. Balka et al., Nucl. Instr. Meth. A **267**, 272 (1988)
19. S. Bertolucci et al., Nucl. Instr. Meth. A **267**, 301 (1988)
20. J. Simon-Gillo et al., Nucl. Instr. Meth. A **309**, 427 (1991)
21. D. Fox et al., Nucl. Instr. Meth. A **317**, 474 (1992)
22. J. Sullivan et al., Nucl. Instr. Meth. A **324**, 441 (1993)
23. The DELPHI Collaboration, Nucl. Instr. Meth. A **303**, 233 (1991)
24. S. Alvsvåg et al., Nucl. Instr. Meth. A **290**(2–3), 320 (1990)
25. A. Devaux, Nucl. Phys. A **498**, 509 (1989)
26. D. Acosta et al., Nucl. Instr. Meth. A **294**, 193 (1990)
27. D. Acosta et al., Nucl. Instr. Meth. A **302**, 36 (1991)
28. D. Acosta et al., Nucl. Instr. Meth. A **305**, 55 (1991)
29. D. Acosta et al., Nucl. Instr. Meth. A **308**, 481 (1991)
30. D. Acosta et al., Nucl. Instr. Meth. A **309**, 143 (1991)
31. D. Acosta et al., Nucl. Instr. Meth. B **62**, 116 (1991)
32. D. Acosta et al., Nucl. Instr. Meth. A **314**, 431 (1992)
33. D. Acosta et al., Nucl. Instr. Meth. A **316**, 184 (1992)
34. D. Acosta et al., Nucl. Instr. Meth. A **320**, 128 (1992)
35. R. Wigmans, Ann. Rev. Nucl. Part. Sci. **41**, 133 (1991)
36. M. Livan, V. Vercesi, R. Wigmans, Scintillating-fibre calorimetry. CERN yellow report CERN-95-02, CERN, Geneva (1995)
37. M. Beck et al., Nucl. Instr. Meth. A **381**, 330 (1996)
38. D. Hertzog et al., Nucl. Instr. Meth. A **294**, 446 (1990)
39. A. Andresen et al., Nucl. Instr. Meth. A **309**, 101 (1991)
40. G. Drews et al., Nucl. Instr. Meth. A **290**, 335 (1990)
41. M. Derrick et al., Nucl. Instr. Meth. A **309**, 77 (1991)

42. T. Armstrong et al., Nucl. Instr. Meth. A **406**, 227 (1998)
43. V. Arena et al., Nucl. Instr. Meth. A **434**, 271 (1999)
44. S. Sedykh et al., Nucl. Instr. Meth. A **455**, 346 (2000)
45. B. Giacobbe, Nucl. Phys. B (Proc. Suppl.) **150**, 257 (2006)
46. G. Avoni et al., Nucl. Instr. Meth. A **580**, 1209 (2007)
47. D. Babusci et al., Nucl. Instr. Meth. A **332**, 444 (1993)
48. A. Antonelli et al., Nucl. Instr. Meth. A **354**, 352 (1995)
49. F. Ambrosino et al., Nucl. Instr. Meth. A **598**, 239 (2009)
50. M. Adinolfi et al., Nucl. Instr. Meth. A **482**(1–2), 364 (2002)
51. L. Aphecetche et al., Nucl. Instr. Meth. A **499**, 521 (2003)
52. G. David et al., IEEE Trans. Nucl. Sci. **45**, 692 (1998)
53. V. Belousov et al., Nucl. Instr. Meth. A **369**, 45 (1996)
54. M. Beddo et al., Nucl. Instr. Meth. A **499**, 725 (2003)
55. C. Allgower et al., Nucl. Instr. Meth. A **499**, 740 (2003)
56. The ALICE Collaboration, J. Instrum. **3**, S08002 (2008)
57. The ALICE Collaboration, The ALICE electromagnetic calorimeter. Technical design report 1, CERN, Geneva (2008)
58. The ATLAS Collaboration, J. Instrum. **3**, S08003 (2008)
59. The ATLAS Collaboration, Eur. Phys. J. C **70**, 1193 (2010)
60. The CMS Collaboration, J. Instrum. **3**, S08004 (2008)
61. The CMS Collaboration, J. Instrum. **5**, T03012 (2010)
62. I. Machikhiliyan, LHCb calorimeter group. J. Phys. Conf. Ser. **160** (2009)
63. R. Dzhelyadin, Nucl. Instr. Meth. A **494**, 332 (2002)
64. A.A. Alves et al., J. Instrum. **3**, S08005 (2008)
65. G. Gallucci, J. Phys. Conf. Ser. **587** (2015)
66. C. Adloff et al., Nucl. Instr. Meth. A **714**, 147 (2013)
67. B. Leverington et al., Nucl. Instr. Meth. A **596**, 327 (2008)
68. S. Adhikari, et al., [arXiv:2005.14272](https://arxiv.org/abs/2005.14272) (2020)
69. C. Fabjan et al., Nucl. Instr. Meth. **141**, 61 (1977)
70. H. Gordon et al., Nucl. Instr. Meth. **196**, 303 (1982)
71. O. Botner et al., Nucl. Instr. Meth. **196**, 315 (1982)
72. A. Nigro, Nucl. Instr. Meth. A **263**, 102 (1988)
73. R. Wigmans, *Calorimetry: Energy Measurement in Particle Physics*, 2nd edn. (Oxford University Press, Oxford, 2017)
74. Y. Sirois, R. Wigmans, Nucl. Instr. Meth. A **240**, 262 (1985)
75. B. Bicken, U. Holm, T. Marckmann, K. Wick, M. Rohde, IEEE Trans. Nucl. Sci. **38**, 188 (1991)
76. A. Bamberger, J. Lehmann, D. Schäcke, M. Wülker, Nucl. Instr. Meth. A **277**, 46 (1989)
77. J. Krüger, T.Z.C. Group, Nucl. Instr. Meth. A **315**, 311 (1992)
78. I. Bohnet, N. Gendner, F. Goebel, T. Neumann, K. Wick, *Proceedings of the 8th International Conference on Calorimetry in High Energy Physics* (World Scientific, Lisbon, 1999), pp. 639–646
79. G. Atoian et al., Nucl. Instr. Meth. A **584**, 291 (2008)
80. M. Livan, RD1: Scintillating fibre calorimetry. CERN report CERN-PPE-93-22, CERN, Geneva (1993)
81. A. Asmone et al., Nucl. Instr. Meth. A **326**, 477 (1993)
82. H. Blumenfeld et al., Nucl. Instr. Meth. Phys. Res. **225**, 518 (1984)
83. CERN, Spaghetti detector. <https://cds.cern.ch/record/759166> (1990)
84. CERN, Spaghetti calorimeter. <https://cds.cern.ch/record/759262> (1990)
85. G. Anzivino et al., Nucl. Instr. Meth. A **357**, 350 (1995)
86. P. Cushman, B. Sherwood, Lifetime studies of the 19-channel hybrid photodiode for the CMS hadronic calorimeter. CERN report CMS-NOTE-2008-011, CERN, Geneva (2007)
87. Hamamatsu Photonics, Avalanche photodiodes. <https://www.hamamatsu.com/us/en/product/optical-sensors/apd/> (2020)

88. KETEK GmbH, SiPM working principle. <https://www.ketek.net/sipm/technology/working-principle/> (2020)
89. P. Cushman, et al., *Supercollider*, vol. 4, ed. by J. Nonte (Springer, Boston, MA, 1992), pp. 1217–1224
90. A. Teymourian et al., Nucl. Instr. Meth. A **654**, 184 (2011)
91. P. Cushman, A. Heering, A. Ronzhin, Nucl. Instr. Meth. A **418**, 300 (1998)
92. P. Cushman, A. Heering, A. Ronzhin, Nucl. Instr. Meth. A **442**, 289 (2000)
93. P. Cushman et al., Nucl. Instr. Meth. A **387**, 107 (1997)
94. The CMS Collaboration, The CMS electromagnetic calorimeter. Technical design report CERN-LHCC-97-033, CERN, Geneva (1997)
95. D. Renker, E. Lorenz, J. Instrum. **4**, P04004 (2009)
96. D. Michael et al., Nucl. Instr. Meth. A **596**, 190 (2008)
97. H. Wilkens, The ATLAS Collaboration. J. Phys. Conf. Ser. **160** (2009)
98. H.S. Budd, Nucl. Phys. B (Proc. Suppl.) **54**, 191 (1997)
99. L. Fiorini, I. Korolkov, F. Vivès, Time calibration of TileCal modules with cosmic muons. ATLAS note ATL-TILECAL-PUB-2008-010, CERN, Geneva (2008)
100. T. Cormier, C.W. Fabjan, L. Riccati, H. de Groot, ALICE electromagnetic calorimeter: addendum to the ALICE technical proposal. CERN report CERN-LHCC-2006-014, CERN, Geneva (2006)
101. H. Abramowicz et al., Phys. Lett. B **718**, 915 (2013)
102. The CMS Collaboration, Particle-flow event reconstruction in CMS and performance for jets, taus, and MET. CERN report CMS-PAS-PFT-09-001, CERN, Geneva (2009)
103. F. Beaudette, *Proceedings of 35th International Conference of High Energy Physics* (Paris, 2010), p. 1
104. The CMS Collaboration, J. Instrum. **6**, P11002 (2011)
105. The CMS Collaboration, J. Instrum. **6**, P09001 (2011)
106. D. Contardo, M. Klute, J. Mans, L. Silvestris, J. Butler, Technical proposal for the phase-ii upgrade of the CMS detector. Technical proposal CERN-LHCC-2015-010, CERN, Geneva (2015)
107. C. Adloff et al., J. Instrum. **9**, P01004 (2014)
108. The CALICE Collaboration, First stage analysis of the energy response and resolution of the scintillator ECAL in the beam test at FNAL. CALICE analysis note CAN-016, CERN, Geneva (2010)
109. The CALICE Collaboration, J. Instrum. **5**, P05004 (2010)
110. The CALICE Collaboration, Update of the analysis of the test beam experiment of the CALICE ScECAL physics prototype. CALICE analysis note CAN-016c, CERN, Geneva (2014)
111. S. Uozumi, R&D status of the scintillator-strip based ECAL for the ILD (2014)
112. P. Buzhan et al., Nucl. Instr. Meth. A **504**, 48 (2003)
113. Y. Liu, J. Instrum. **12**, C06040 (2017)
114. The CMS Collaboration, The phase-2 upgrade of the CMS endcap calorimeter. Technical design report CERN-LHCC-2017-023, CERN, Geneva (2017)
115. S. Majewski et al., Nucl. Instr. Meth. A **281**, 500 (1989)
116. V. Hagopian et al., Rad. Phys. Chem. **41**, 401 (1993)
117. J. Mans, et al., CMS technical design report for the phase 1 upgrade of the hadron calorimeter. Technical design report CERN-LHCC-2012-015, CERN, Geneva (2012)
118. The CMS Collaboration, Results related to the Phase1 HE upgrade. Detector performance summary CMS-DP-2018-019, CERN, Geneva (2018)
119. The CMS Collaboration, J. Instrum. **15**, P06009 (2020)
120. M. Casella, S. Franchino, S. Lee, Int. J. Mod. Phys. A **31**, 1644024 (2016)
121. I. Ambats, The MINOS Collaboration, The MINOS detectors. Fermilab report NuMI-L-337, Fermilab, Batavia, IL (1998)
122. L. Aliaga et al., Nucl. Instr. Meth. A **743**, 130 (2014)
123. J.C. Yun, A. Para, U.S. Patent 6,218,670, Apr 2001
124. E. Eskut et al., Nucl. Instr. Meth. A **401**, 7 (1997)

125. E. Di Capua et al., Nucl. Instr. Meth. A **378**, 221 (1996)
126. S. Buontempo et al., Nucl. Instr. Meth. A **349**, 70 (1994)
127. P. Annis et al., Nucl. Instr. Meth. A **367**, 367 (1995)
128. K. Nitta et al., Nucl. Instr. Meth. A **535**, 147 (2004)
129. S. Yamamoto et al., IEEE Trans. Nucl. Sci. **52**, 2992 (2005)
130. K. Abe et al., Nucl. Instr. Meth. A **694**, 211 (2012)
131. S. Assylbekov et al., Nucl. Instr. Meth. A **686**, 48 (2012)
132. Y. Kudenko, Nucl. Instr. Meth. A **598**, 289 (2009)
133. D. Allan et al., J. Instrum. **8**, P10019 (2013)
134. P.A. Amaudruz et al., Nucl. Instr. Meth. A **696**, 1 (2012)
135. S. Phan-Budd, Phys. Proc. **37**, 1201 (2012)
136. D. Ayres, et al., The NOvA technical design report. Technical design report FERMI-LAB-DESIGN-2007-01, Fermi National Accelerator Lab, Batavia, IL (2007)
137. S. Mufson et al., Nucl. Instr. Meth. A **799**, 1 (2015)
138. A. Pla-Dalmau, A. Bross, V. Rykalin, B. Wood, *IEEE Nuclear Science Symposium Conference Record, 2005*, vol. 3 (IEEE, Puerto Rico, 2005), pp. 1298–1300
139. K. Abe et al., Nucl. Instr. Meth. A **659**, 106 (2011)
140. D.M. Poehlmann, et al., [arXiv:1812.11267](https://arxiv.org/abs/1812.11267) (2018)
141. P. Agnes et al., Phys. Lett. B **743**, 456 (2015)
142. T.S. Collaboration, Phys. Rev. Lett. **112**, 241302 (2014)
143. The SuperCDMS Collaboration, Phys. Rev. D **95** (2017)
144. C.E. Aalseth et al., Eur. Phys. J. C **133**, 131 (2018)
145. S. Abdelhakim, et al., DarkSide-20k technical design report. DarkSide document 3381, LNGS, Gran Sasso (2019)
146. B. Abi, et al., [arXiv:2002.02967](https://arxiv.org/abs/2002.02967) (2020)
147. B. Abi, et al., [arXiv:2002.03010](https://arxiv.org/abs/2002.03010) (2020)



Priscilla Cushman (65 yr) defended her Ph.D. on hyperon magnetic moments in 1985 at Rutgers University (USA) and then moved to CERN to work on the UA6 experiment. Later, as an assistant professor at Yale, she contributed to the Brookhaven g-2 experiment and developed novel photodetectors for the Superconducting Collider. Her focus shifted to the LHC when the SSC was canceled, and developed the hybrid photodiode readout for the CMS HCAL. She is now a Professor of Physics at the University of Minnesota and spokesperson of the SuperCDMS experiment to detect dark matter. She is a fellow of the APS and the AAAS and has just finished serving as the chair of the APS Division of Particles and Fields. She is co-author of over 300 articles, 4 reviews, and a textbook, with an h-index of 74 (ISIWEB).



David-Michael Poehlmann (24 yo) is pursuing a Ph.D. in physics at the University of California, Davis. His Ph.D. topic is the direct detection of dark matter with the DarkSide program and he expects to defend in 2023. As an undergraduate at the University of Minnesota, he worked with Professor Cushman to develop a neutron veto for the SuperCDMS SNOLAB upgrade.

Appendix

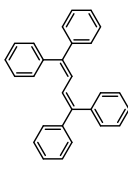
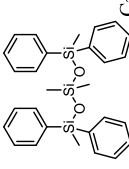
Molecules Cited in the Book

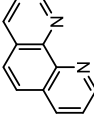
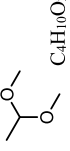
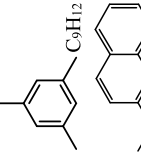
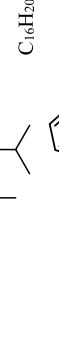
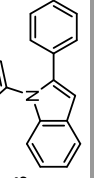
Matthieu Hamel 

This section is provided to give the reader more information about the organic molecules that are cited in this book. Obvious molecules (e.g., water) and inorganics are not included. The following data are given:

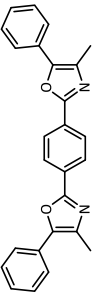
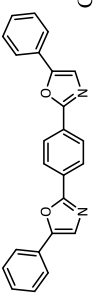
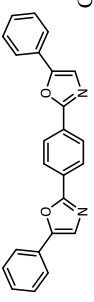
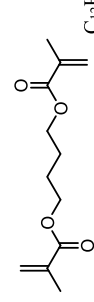
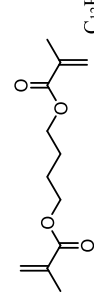
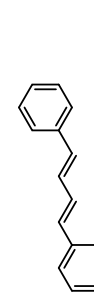
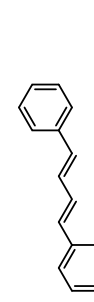
- Full name,
- Abbreviation,
- CAS number,
- Structure,
- Chemical formula,
- Role in scintillation (some molecules may present several roles).

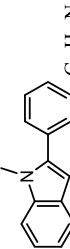
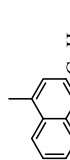
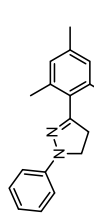
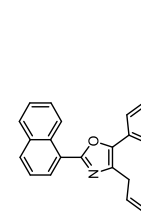
M. Hamel (✉)
Université Paris-Saclay, CEA, List, Palaiseau, France
e-mail: matthieu.hamel@cea.fr

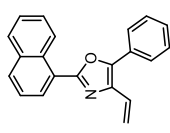
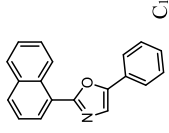
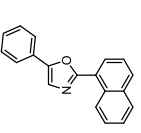
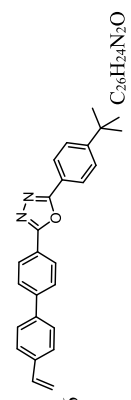
Name	Abbreviation	CAS number	Structure and chemical formula	Role
(9,9-Dimethylfluoren-2-yl)triphenylsilane		1208005-82-6	 C ₃₃ H ₂₈ Si	Organic glass
(Styrene-Ethylene/Butadiene-Styrene) copolymer	SEBS	26835-21-2 (C ₈ H ₈ · C ₄ H ₆ · C ₂ H ₄) _n		Polymer
1,1,4,4-Tetraphenylbutadiene	TPB	1450-63-1		
1,1,5,5-Tetraphenyltetramethyltrisiloxane	TPTMTS	3982-82-9		Solvent

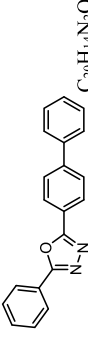
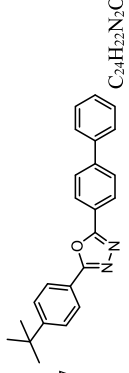
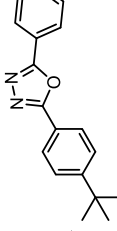
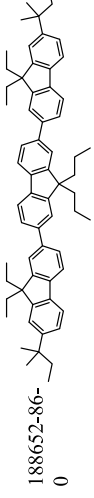
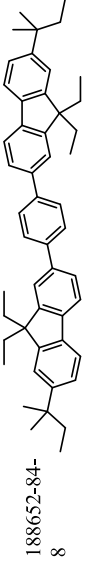
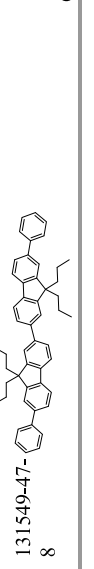
1,10-Phenanthroline	Phen	66-71-7		C ₁₂ H ₈ N ₂	Ligand
1,1-Dimethoxyethane	DME	534-15-6		C ₄ H ₁₀ O ₂	Solvent
1,2,4-Trimethylbenzene	PC	108-67-8		C ₉ H ₁₂	Solvent
1,2-Diisopropylnaphthalene		24157-81-1		C ₁₆ H ₂₀	Solvent, diffusion enhancer
1,2-Diphenyliindole		18434-12-3		C ₂₀ H ₁₅ N	Primary fluorophore

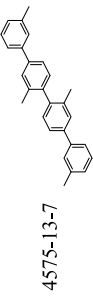
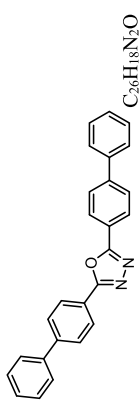
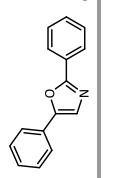
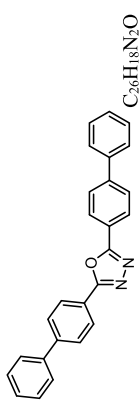
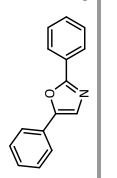
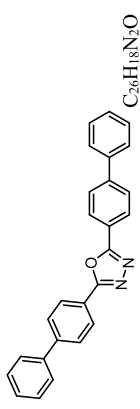
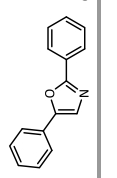
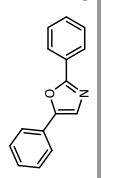
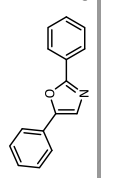
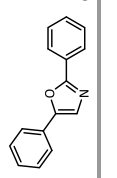
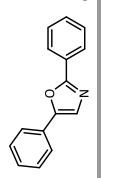
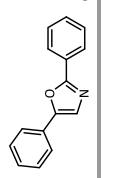
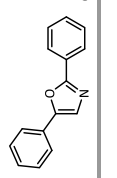
1,2-Ethylene glycol di-methacrylate	EGDMA	97-90-5		C ₁₀ H ₁₄ O ₄	Cross-linker
1,3,5-Tri(2-naphthyl)benzene	TNB	16322-13-7		C ₃₆ H ₂₄	Organic glass
1,3,5-Triphenyl-2-pyrazoline	TPY	742-01-8		C ₂₁ H ₁₈ N ₂	Secondary fluorophore
1,3,5-Triphenylbenzene		612-71-5		C ₂₄ H ₁₈	Organic glass
1,4-Bis(2-methyl(styryl)benzene	bis-MSB	13280-61-0		C ₂₄ H ₂₂	Secondary fluorophore

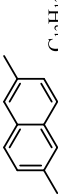
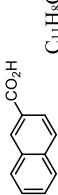
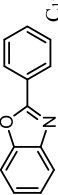
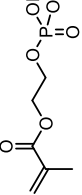
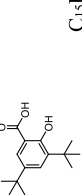
	3073-87-8		3073-87-8	Secondary fluorophore
	1806-34-4		1806-34-4	Secondary fluorophore
	2082-81-7		2082-81-7	Cross-linker
	886-65-7		886-65-7	Secondary fluorophore
	575-43-9		575-43-9	Solvent, diffusion enhancer
	6158-45-8		6158-45-8	Solvent, Diffusion enhancer

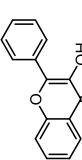
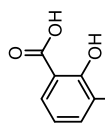
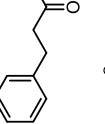
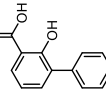
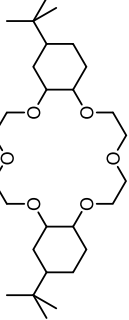
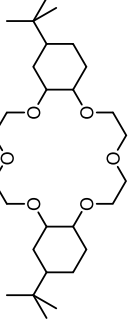
1-Methyl-2-phenylindole	3558-24-5		C ₁₅ H ₁₃ N	Primary fluorophore
1-Methylnaphthalene	90-12-0		C ₁₁ H ₁₀	Diffusion enhancer
1-Pentanol	71-41-0		C ₅ H ₁₂ O	Surfactant
1-Phenyl-3-mesityl-2-pyrazoline	60078-97-9		C ₁₈ H ₂₀ N ₂	Primary fluorophore
2-(1-Naphthyl)-4-allyl-5-phenyloxazole	1799647-68-9		C ₂₂ H ₁₇ NO	Primary fluorophore

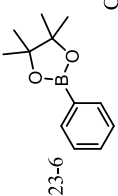
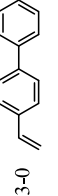
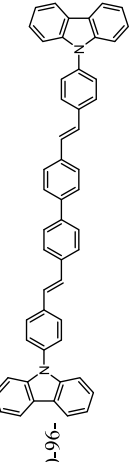
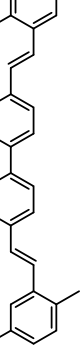
2-(1-Naphthyl)-4-vinyl-5-phenyloxazole 1799647-67-8		C ₂₁ H ₁₅ NO	Primary fluorophore
2-(1-Naphthyl)-5-phenyloxazole 846-63-9		C ₁₉ H ₁₃ NO	Primary fluorophore
2-(1-Naphthyl)-5-phenyloxazole 846-63-9		C ₁₉ H ₁₃ NO	Primary fluorophore
2-(4-Vinylbiphenyl))-5-(4- <i>tert</i> -butylphenyl)-1,3,4-oxadiazole 85884-56-6		C ₂₆ H ₂₄ N ₂ O	Primary fluorophore

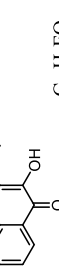
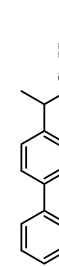
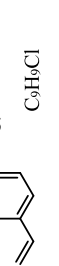
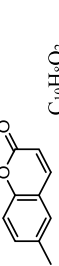
2-(4-Biphenyl)-5-phenyl-1,3,4-oxadiazole	PBD	852-38-0		C ₂₀ H ₁₄ N ₂ O	Primary fluorophore
2-(4- <i>Terf</i> -Butylphenyl)-5-(4-biphenyl)-1,3,4-oxadiazole	Butyl-PBD	15082-28-7		C ₂₄ H ₂₂ N ₂ O	Primary fluorophore
2-(4- <i>Terf</i> -Butylphenyl)-5-phenyl-1,3,4-oxadiazole		17064-48-1		C ₁₈ H ₁₈ N ₂ O	Primary fluorophore
2,2':7,2"-Ter-9 <i>H</i> -fluorene, 7,7"-bis(1,1-dimethylpropyl)-9,9",9",9"-tetraethyl-9",9"-dipropyl	E417	188652-86-0		C ₆₃ H ₇₄	Secondary fluorophore
2,2[Bis(7-(2,2-dimethylpropyl)-9,9-dipropyl)-9 <i>H</i> -fluorophene]-1,4-benzene	E404	188652-84-8		C ₅₀ H ₅₈	Secondary fluorophore
2,2'-Bi-9 <i>H</i> -fluorene, 7,7"-di-phenyl-9,9",9"-tetrapropyl	E411	131549-47-8		C ₅₀ H ₅₀	Secondary fluorophore

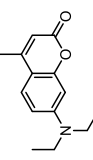
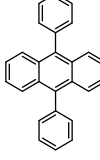
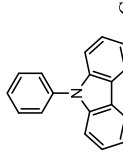
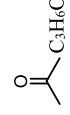
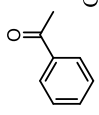
	4575-13-7		7128-64-5		2043-06-3		263403-30-1		92-71-7	C ₂₈ H ₂₆	Primary fluorophore
	7128-64-5		2043-06-3		263403-30-1		92-71-7		92-71-7	C ₂₆ H ₂₆ N ₂ O ₂ S	Secondary fluorophore
	2043-06-3		263403-30-1		92-71-7		92-71-7		92-71-7	C ₂₆ H ₂₆ N ₂ O ₂	Primary fluorophore
	263403-30-1		92-71-7		92-71-7		92-71-7		92-71-7	C ₂₄ H ₁₉ NO	Primary fluorophore
	92-71-7		92-71-7		92-71-7		92-71-7		92-71-7	C ₁₅ H ₁₁ NO	Primary fluorophore

2,6-Diisopropynaphthalene	581-42-0		C ₁₂ H ₁₂	Solvent
2-Naphthoic acid	93-09-4		C ₁₁ H ₈ O ₂	Ligand
2-Phenylbenzoxazole	833-50-1		C ₁₃ H ₉ NO	Primary fluorophore
2-Phosphorylethyl methacrylate	24599-21-1		C ₆ H ₁₁ O ₈ P	Extractant
3,5-Di- <i>tert</i> -butylsalicylic acid	19715-19-6		C ₁₅ H ₂₂ O ₃	Ligand

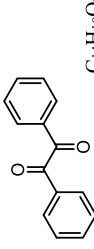
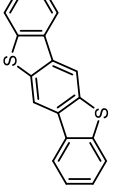
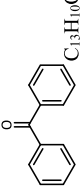
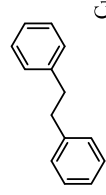
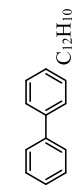
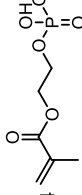
	3-HF	577-85-5		C ₁₅ H ₁₀ O ₃	Primary fluorophore
	3-MeSA	83-40-9		C ₈ H ₈ O ₃	Ligand
	501-52-0			C ₉ H ₁₀ O ₂	Ligand
	3-PSA	304-06-3		C ₁₃ H ₁₀ O ₃	Ligand
		223719-29-7		C ₂₈ H ₅₂ O ₆	Extractant

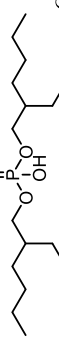
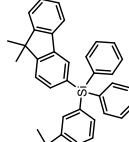
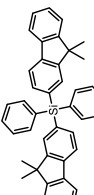
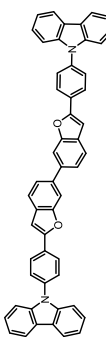
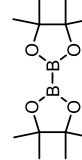
4,4',5-Tetramethyl-2-phenyl-1,3,2-dioxaborolane	MBB		24388-23-6	C ₁₂ H ₁₇ BO ₂	Loading
4,4'-Divinylbiphenyl			4433-13-0	C ₁₆ H ₁₄	Cross-linker, primary fluorophore
4,4'-Bis(<i>E</i> -4-(9 <i>H</i> -carba-zol-9-yl)styryl)biphenyl	9		879220-96-9		Organic glass
4,4'-Bis(2,5-dimethylstyryl)diphenyl	BDB		72814-85-8	C ₃₂ H ₃₀	Secondary fluorophore

4'-Fluoro-3-hydroxyflavone F-3-HF	364-56-7		Primary fluorophore
4-Isopropylbiphenyl	IP		Primary fluorophore
4-Tert-butylbiphenyl	tert-BBP		Primary fluorophore
4-Vinylbenzyl chloride	1592-20-7		Monomer
5-Ethyl-5-methylhydantoin	5394-36-5		Organic glass
6-Methylcoumarin	92-48-8		Primary fluorophore

7-Diethylamino-4-methylcoumarin	MDAC	91-44-1		C ₁₄ H ₁₇ N ₂ O ₂	Secondary fluorophore
9,10-Diphenylanthracene	9,10-DPA	1499-10-1		C ₂₆ H ₁₈	Secondary fluorophore
9-Phenylcarbazole		1150-62-5		C ₁₈ H ₁₃ N	Primary fluorophore
Acetone		67-64-1		C ₃ H ₆ O	Solvent
Acetophenone		98-86-2		C ₈ H ₈ O	Quencher

<p>Acetylacetonatobis(2-phenylpyridinato)iridium(IV)</p> <p>9</p>	<p>Ir(acac)₂(ppy)₂</p> <p>C₂₇H₂₃IrN₂O₂</p> <p>Primary fluorophore</p>
<p>Anthracene</p>	<p>C₁₄H₁₀</p> <p>Primary fluorophore</p>
<p>Benzene</p>	<p>C₆H₆</p> <p>Solvent</p>

Benzil	134-81-6		C ₁₄ H ₁₀ O ₂	Single Crystal
Benzol[1,2-b:4,5-b]bis[b]benzothiophene	241-34-9		C ₁₈ H ₁₀ S ₂	Single Crystal
Benzophenone	119-61-9		C ₁₃ H ₁₀ O	Quencher
Biphenyl	103-29-7		C ₁₄ H ₁₄	Primary fluorophore
Bis(2-(methacryloyloxyethyl) phosphate	92-52-4		C ₁₂ H ₁₀	Primary fluorophore
	32435-46-4		C ₁₂ H ₁₀ O ₈ P	Ligand, extractant

Bis(2-ethylhexyl) phosphateHDEHP	298-07-7		C ₁₆ H ₃₅ O ₄ P	Extractant
Bis(9,9-dimethyl-9 <i>H</i> -fluoren-2-yl)bis(phenyl)silane	1208005-83-7		C ₄₂ H ₃₆ Si	Organic glass
Bis(9,9-dimethylfluoren-2-yl)diphenylsilane	1208005-83-7		C ₄₂ H ₃₆ Si	Organic glass
Bis(9-phenylcarbazoylbenzofuran)	2484840-46-0		C ₅₂ H ₃₂ N ₂ O ₂	Organic glass
Bis(pinacolato)diboron	73183-34-3		C ₁₂ H ₂₄ B ₂ O ₄	Loading

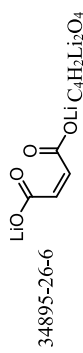
Bismuth hexahydrobenzoate	n.a.	n.a.	
Bismuth tripivalate	130234-54-7		Loading
Bisphenol A	80-05-7		Ligand
Coumarin	91-64-5		Primary fluorophore
Dibutyltin dilaurate	77-58-7		Loading
		<chem>C32H64O4Sn</chem>	

Dimethacrylate (family name)	n.a.		Cross-linker R = alkyl, aryl
Diocylamine	DOA		Extractant C16H35N
Diphenylacetylene	DPAC		Primary fluorophore C14H10
Divinylbenzene (mixture of isomers)	DVB		Cross-linker C10H10
Erythrosin B	15905-32-5		Secondary fluorophore C20H14O5

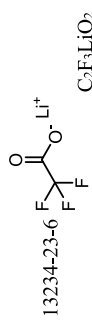
Gadolinium benzoyl acetone	Gd(hba) ₃	n.a.	n.a.	Loading
Gadolinium isopropoxide	Gd(i-PrO) ₃	14532-05-9		
Gadolinium tris(4-phenylvalerate)	Gd(Piv) ₃	2412660-21-8		
Gadolinium, tris(2,2,6,6-tetramethyl-3,5-heptanedionato)-	Gd(TMHD) ₃	14768-15-1		
Hexamethylphosphotriamide	HMPTA	680-31-9		
			C ₆ H ₁₈ N ₃ OP	Solvent

Hydroxypropyl methyl-cellulose		R=H or CH ₃ or Polymeriza-tion seed
Isobutane	75-28-5	
Isopropenyl boron carbohy-dride	n.a.	n.a.
Lead dimethacrylate	1068661-7	
Lithium 3-phenylsalicylate Li-3-PSA	n.a.	3H ₅ LiO ₂ .

Lithium maleate

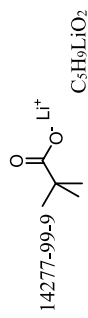
Loading,
monomer

Lithium methacrylate



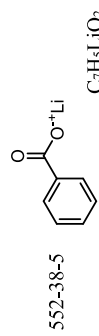
Loading

Lithium pivalate

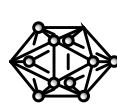
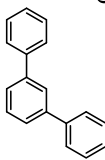


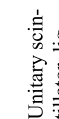
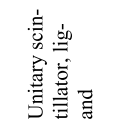
Loading

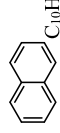
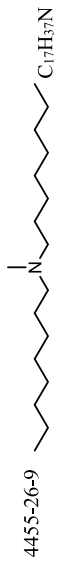
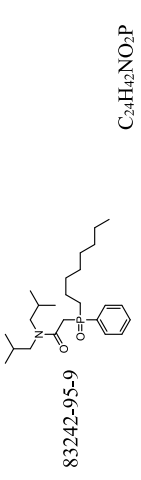
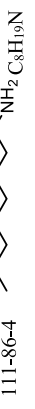
Lithium salicylate

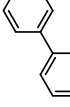
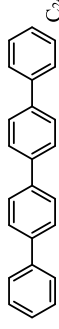
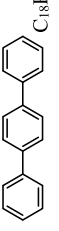
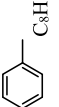


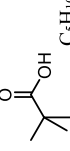
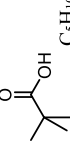
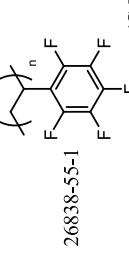
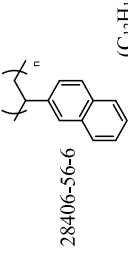
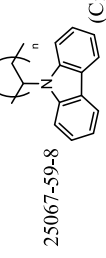
Loading

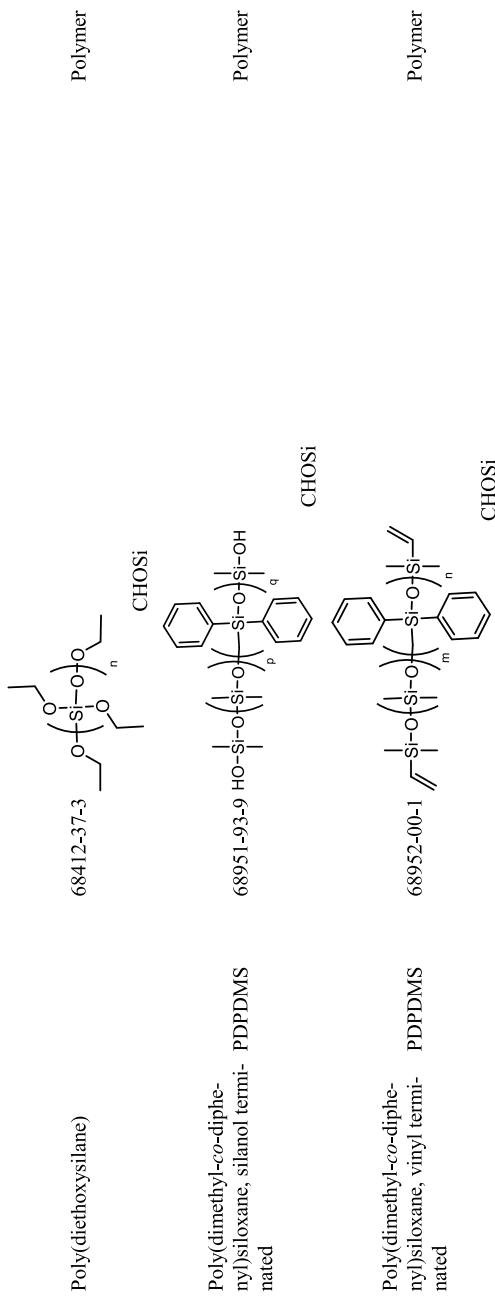
Lithium trifluoroacetate		2923-17-3	$\text{C}_2\text{F}_3\text{LiO}_2$	Loading
Lumogen® F red 330	n.a.	n.a.	Secondary fluorophore	
Lumogen® F violet 570	56148-88-0	n.a.	Secondary fluorophore	
<i>Meta</i> -carborane		16986-24-6	$\text{C}_2\text{H}_{12}\text{B}_{10}$	Loading
<i>Meta</i> -terphenyl		92-06-8	$\text{C}_{18}\text{H}_{14}$	Primary fluorophore

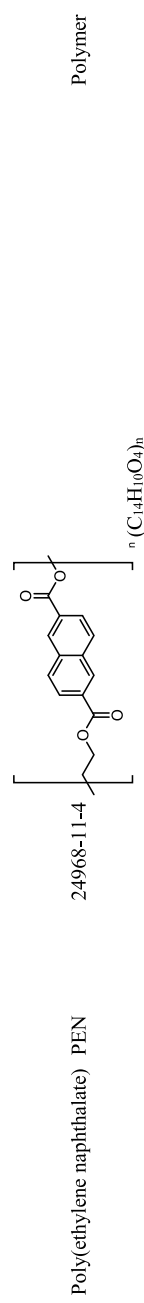
Methacrylic acid	MAA	79-41-4		C ₄ H ₆ O ₂	Monomer
Methyl methacrylate	MMA	79-41-4		C ₅ H ₈ O ₂	Monomer
Methyltriocetyl ammonium chloride	aliquat 336	63393-96-4		C ₂₃ H ₅₄ ClN	Extractant
N-(2-ethylhexyl carbazole)	EHCZ	187148-77-2		C ₂₀ H ₂₅ N	Unitary scintillator, ligand
<i>N,N'</i> -bis(3-methylphenyl)- <i>N,N'</i> -diphenylbenzidine	TPD	65181-78-4		C ₃₈ H ₃₂ N ₂	Organic glass

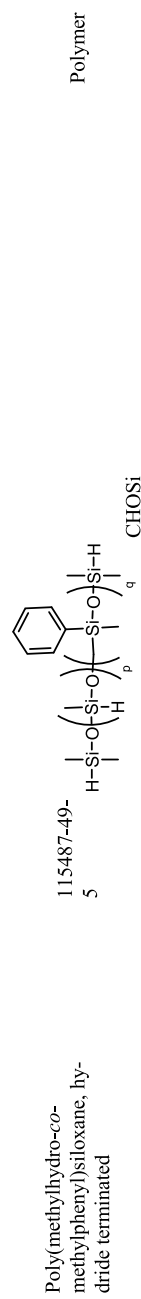
Naphthalene	91-20-3		C ₁₀ H ₈	Primary fluorophore
<i>N</i> -methyldioctylamine	MDOA		4455-26-9	Extractant
n-Octyl(phenyl)- <i>N,N</i> -diisobutylcarbamoylmethylphosphine oxide	CMPO		83242-95-9	Extractant
Octylamine	nOA		111-86-4	Extractant
Oleic acid			112-80-1	Ligand
Oleylamine			112-90-3	Ligand

<i>Ortho</i> -carborane	16872-09-6	Loading
<i>Ortho</i> -terphenyl	o-TP 84-15-1	 $C_{22}H_{16}$
<i>Para</i> -quaterphenyl	p-Q 135-70-6	 $C_{38}H_{28}$
<i>Para</i> -terphenyl	p-T 92-94-4	 $C_{24}H_{18}$
<i>Para</i> -xylene	106-42-3	 C_8H_{10}
		Diffusion enhancer, solvent

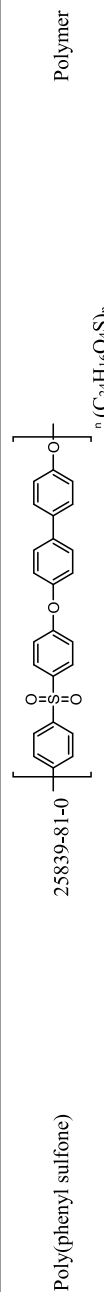
Piperidine	110-89-4		C ₅ H ₁₁ N	Quencher		
Pivalic acid	PA		75-98-9		C ₅ H ₁₀ O ₂	Ligand
Poly(2,3,4,5,6-pentafluorostyrene)	26838-55-1		(C ₈ H ₃ F ₅) _n	Polymer		
Poly(2-vinylnaphthalene)	28406-56-6		(C ₁₂ H ₁₀) _n	Polymer		
Poly(9-vinylcarbazole)	PVK		25067-59-8	(C ₁₄ H ₁₁ N) _n	Polymer	



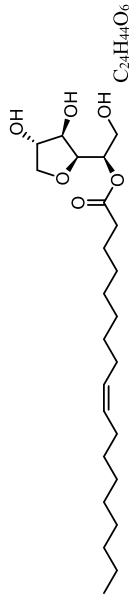
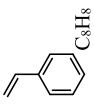
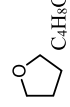
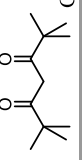


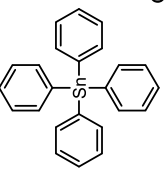
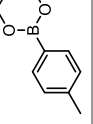


Poly(methylphenyl)siloxane, trimethylsilyl terminated	42557-11-9		Polymer
Poly(methylphenyl)siloxane, vinyl terminated	PMPS100, PM100		Polymer
Poly(<i>N</i> -vinylpyrrolidone)	9003-39-8		Polymer $(C_6H_9NO)_n$



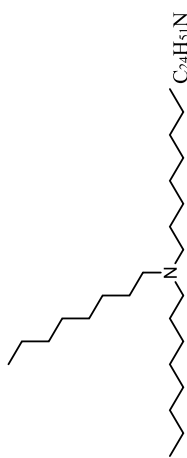
Poly(ether ether ketone)	n.a.		Polymer
Polysiloxanes (family name)	n.a.		Polymer
Polystyrene	PS		Polymer
Salicylic acid	SA		Ligand

Sodium dodecylsulfate	151-21-3		C ₁₂ H ₂₅ NaO ₄ S	Surfactant
Sorbitan monooleate	Span-80		C ₁₂ H ₂₅ NaO ₄ S	Surfactant
Styrene	St		C ₈ H ₈	Monomer
Tetrahydrofuran	THF		C ₄ H ₈ O	Solvent
Tetramethylheptanedione	TMHD		C ₁₁ H ₂₀ O ₂	Ligand

Tetraphenyltin	<chem>SnPh4</chem>	595-90-4		C ₂₄ H ₂₀ Sn	Loading
Toluene	<chem>PhMe</chem>	108-88-3		C ₇ H ₈	Solvent
Toluenehboronic acid 1,3-propanediol ester	TDB	4463-41-6		C ₁₀ H ₁₃ BO ₂	Loading

<i>Trans</i> -stilbene	103-30-0		C ₁₄ H ₁₂	Primary fluorophore
Tributylphosphate	TBP		C ₁₂ H ₂₇ O ₄ P	Extractant
Tributyltin methacrylate	2155-70-6		C ₁₆ H ₃₂ O ₂ Sn	Loading
Triethylamine	TEA		C ₆ H ₁₅ N	Extractant
Trimethoxyphenylsilane	PhTMS		C ₉ H ₁₄ O ₃ Si	Precursor

Extractant

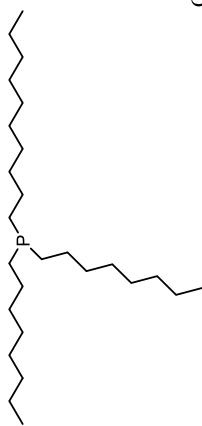


1176-76-3

TOA

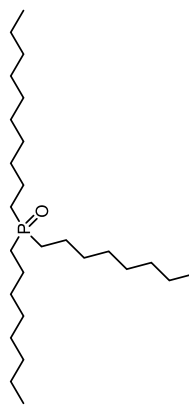
Trioctylamine

Extractant



4731-53-7

Trioctylphosphine



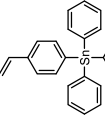
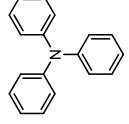
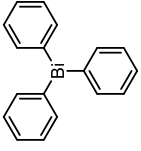
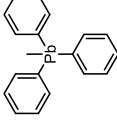
35791-65-2

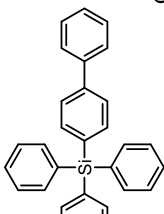
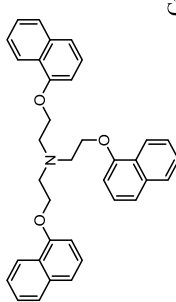
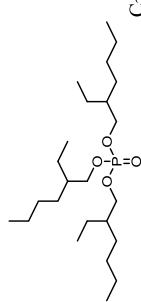
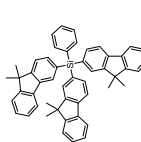
Trioctylphosphine oxide

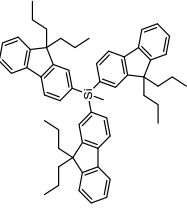
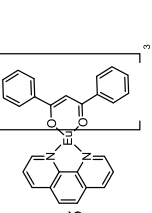
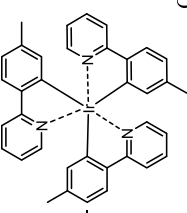
Extractant

 $\text{C}_{26}\text{H}_{55}\text{OP}$

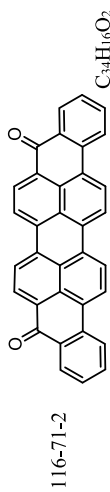
Extractant

			Loading
Triphenyl(<i>para</i> -styryl)tin	2177-14-2		C ₂₆ H ₂₂ Sn
Triphenylamine	603-34-9		C ₁₈ H ₁₅ N
Triphenylbismuth	603-33-8		C ₁₈ H ₁₅ Bi
Triphenylmethyllead	3124-28-5		C ₁₉ H ₁₈ Pb

Triphenyl- <i>p</i> -biphenyl-silane	3172-34-7		Organic glass
Tris(1-naphthoxy)triethylamine	275377-18-9		Organic glass
Tris-(2-ethylhexyl)phosphate	78-42-2		Extractant
Tris(9,9-dimethyl-9 <i>H</i> -fluoren-2-yl)(phenyl)silane	1208005-84-8		Organic glass
			C ₅ H ₄₄ Si

Tris(9,9-dipropylfluoren-2-yl)methylsilane	21699-79-7/3		Organic glass
Tris(dibenzoylmethane)mono(1,10-phenanthroline)europium(III)	Eu(dbm) ₃ (phen) I 7904-83-5		C ₅₇ H ₄₁ EuN ₂ O ₆
Tris[2-(<i>p</i> -tolyl)pyridine]iridium	Ir(mpypy) ₃ 800394-58-5		C ₃₆ H ₃₀ IrN ₃
Vinylnaphthalene (mixture of isomers)	VT 25013-15-4		C ₁₀ H ₁₁
			Monomer

Violanthrone



116-71-2

Secondary
fluorophore

Y 11

Y-11

145687-42-
9 n.a.Scintillating
fiberC₃₄H₁₆O₂

Index

Symbols

- α/β discrimination, 413, 414
- $^{10}\text{Boron-loaded PSD plastic scintillator}$
- $^{131\text{m}}\text{Xe}$, 387–389, 398, 406, 408
- $^{133\text{m}}\text{Xe}$, 386, 387, 398
- ^{133}Xe , 386–388, 391, 397, 398
- ^{135}Xe , 386, 387, 397, 398, 400
- ^{137}Cs , 71, 110, 120, 121, 149, 150, 152, 212, 254, 267, 268, 275, 277, 478–480, 513
- ^{220}Rn , 396, 403
- ^{222}Rn , 388, 394, 396, 402, 403, 405, 406, 408–412, 414, 417, 463, 510
- ^{22}Na , 24, 149, 150, 510
- ^{241}Am , 149, 150, 184, 215, 217, 218, 480, 484, 498, 502, 503, 513, 514
- ^{252}Cf , 40, 47, 69, 72, 77, 78, 93, 97, 98, 109, 117
- ^{37}Ar , 396
- 3D dosimetry, 445
- 3D printing, 11
- ^{57}Co , 149, 152
- ^{60}Co , 20, 110, 120, 121, 149, 186, 438, 513
- 9,10-diphenylanthracene (DPA), 41, 44, 46, 53, 57–59, 64, 69, 73, 76, 80, 85
- ^{85}Kr , 386, 388, 400–402, 406, 408, 510, 513

A

- A Toroidal LHC Apparatus (ATLAS), 554, 559–561, 563, 564
- Absolute neutron detection efficiency, 118
- Accelerated aging, 253, 270, 278, 568
- Acquisition chain, 309–311, 345–347, 359, 364, 365, 369, 372, 373
- Acquisition frontend, 344

- Aging, 244, 245, 255, 262, 282, 283, 409, 551, 575
- Aliasing, 348, 351
- ALICE, 554, 559, 562
- α/β discrimination, 372, 413, 414
- Alpha emitting radionuclides, 463, 479, 480, 498, 503
- Amplitude, 110, 116, 188, 310, 319, 329, 330, 339, 345, 346, 349, 352, 354, 356, 359, 360, 362, 363, 366, 370, 374
- Analog-to-Digital Converter (ADC), 309, 347, 348, 351–355, 357, 359, 364, 368, 440
- Anisotropy, 223, 232
- Anode, 311, 312, 315, 317–319, 321, 322, 324–330, 563, 573, 576, 577, 582, 583
- ARIX, 396, 397, 400
- ARSA, 396, 397
- Artificial Neural Network (ANN), 372

B

- BC-400, 212, 410, 411
- BC-404, 22, 397
- Belisama, 520, 533
- Beta emitting radionuclides, 461, 463, 466, 467, 478, 479, 481, 485, 488, 489, 491, 492, 498
- Bias, 323, 330–333, 335, 338, 340, 342, 388, 558, 559, 566
- Bismuth loading, 148, 151, 152, 156
- Blending, 247, 264, 266, 274
- Boron-containing neutron detector, 277
- Boron loading, 70, 71, 73, 159, 160, 275

Brachytherapy, 425–427, 429, 449–453, 459, 460
 Bulk diffusion, 270

C

Cadmium loading, 4, 161
 Calibration, 22, 145, 183, 324, 365, 368, 425, 432, 433, 436–438, 446, 451, 479, 484, 515, 519, 543, 550, 551, 558–562, 566, 568, 569, 572, 579
 Calorimetry, 22, 266, 541, 542, 544, 572
 Capture-gated detection, 115, 116
 Cathode, 311, 315, 317, 320, 321, 324, 326, 329, 330, 582, 583
 CCD camera, 449
 CdZnTe semiconductors (CZT), 399, 400, 515, 523
 Centroid, 112, 366
 Charge amplifier, 331
 Charge collection, 181
 Charged particle equilibrium, 428
 Cherenkov, 552, 570, 571, 577, 579, 583
 Chernobyl, 388, 513, 517
 Citizen Science, 509, 517–519, 533
 CMOS camera, 436, 438
 CMS, 553, 554, 557–561, 564–569, 579, 584
 Coating, 328, 541, 556, 558, 573, 576
 Coincidence, 18, 318, 330, 356, 365, 366, 372, 388, 390–392, 396–399, 402, 419, 530, 531
 Collection efficiency, 141, 219, 288, 289, 314, 317–322, 410, 411, 415
 Compensation method, 114
 Comprehensive Nuclear-Test-Ban Treaty (CTBT), 238, 386, 387, 396–399
 Compton scattering, 24, 70, 140, 150, 449, 451, 523
 Computing, 309, 357–359, 367, 368, 431
 Configurational disorder, 250
 Constancy, 438
 Constant fraction discriminator, 363
 Consumer, 357, 519
 Convolution, 70, 358, 360, 415, 416, 418
 Correction factor, 433, 434, 438, 441, 444
 Counter, 35, 68, 100, 118, 120, 125, 130, 311, 340, 356, 364, 402, 440, 494, 514, 515, 541, 557–559, 565
 Count rate, 109, 116, 118, 120, 121, 133, 148, 151, 318, 322, 326, 327, 343, 347, 360, 369, 373, 374, 485, 502
 Crystallographic structure, 237

D

Data processing, 137, 310, 366, 368, 369, 419
 Deadtime, 310, 330, 356, 358, 359, 364, 366, 369
 Decay time, 4, 9, 15–19, 112, 144, 179, 188, 189, 207, 218, 226, 230, 253–255, 260, 288, 328, 329, 336, 347, 350, 351, 410, 413, 441, 453, 480
 Deconvolution, 24, 360, 495
 Delayed light, 36, 38, 47, 53, 57, 58, 61, 62, 64, 68, 70
 Delta-sigma, 354, 355
 Density, 14, 25, 57, 64, 95, 103, 105–109, 127, 139, 140, 146, 147, 150, 180, 182, 188–191, 202, 230, 231, 237, 245, 262, 264, 269, 297, 419, 444, 479, 493, 515, 522, 523, 525, 532, 533, 554, 568
 Design strategy, 244, 248, 253
 Detection efficiency, 72, 78, 83, 118, 120, 122, 133, 192, 193, 201, 208, 209, 211, 213, 260, 275, 288, 315, 316, 320, 321, 333, 410, 419, 465, 471, 475, 481, 482, 484, 488, 489, 491–499, 502, 503, 569
 Detector, 3, 6, 11–13, 16, 21–24, 40, 69, 72, 78, 83–85, 89, 91, 100, 109, 110, 112, 114–123, 125, 127, 130–132, 153, 183, 184, 189, 193, 199, 219, 223, 238, 246, 275, 278, 287–289, 299, 302, 304, 307, 310, 311, 331, 340, 343–345, 347, 349, 352, 359, 365, 369, 370, 372, 374, 396–403, 414–417, 419, 425, 427, 428, 430, 434–436, 439, 440, 443, 444, 446–448, 450–452, 454, 459–463, 467–469, 477, 479, 481–484, 486, 489, 490, 493–496, 499, 500, 502, 508, 515, 517–520, 522–524, 526, 530, 531, 533, 534, 541, 542, 544, 548, 552, 554, 556–559, 561–564, 567, 568, 571–583
 Dexter Energy Transfer, 230, 239, 243, 246
 Differentiator, 347
 Diffusion length, 404, 406, 408, 409
 Digital signal processor, 356, 357, 367
 Digitization, 310, 311, 344, 348, 349, 351–354, 360
 Digitizer, 50, 345, 349, 350, 352–354, 373, 411, 412
 Diphenylacetylene (DPAC), 38, 65

- Directional emission, 289, 290, 294–296, 304, 572, 577
Discretization, 349
Disorder, 230, 235, 239, 247, 251, 252, 255, 274
Dose rate, 109, 119–121, 130, 186, 427, 429, 433, 435, 438, 439, 441, 448, 449, 451, 453, 477, 514, 515, 520, 550, 568, 569
DSP, 357, 358, 368, 373
DUNE, 577, 579, 581–583
Dynode, 311–318, 320–324, 326, 329–331, 340, 342, 556
- E**
Effective atomic number, 4, 24, 208, 209, 525
Effective number of bits, 353
EJ-200, 18, 49, 98, 141, 144, 195, 257, 267, 410, 411, 438, 533, 568
EJ-212, 182, 184–186, 195, 292, 294, 399, 410, 411, 436
Elastic neutron scattering, 94, 95
Electromagnetic calorimeter, 542, 554, 560, 564, 565, 578, 579
Electromagnetic showers, 542, 550
Emission wavelength, 9, 12, 18, 180, 206–208, 223, 254, 288, 291, 293–295, 297, 299, 583
Energy, 310, 313, 314, 318, 321–323, 331–333, 338–343, 345–348, 350–352, 355, 360, 365, 368–370, 372–374, 542–545, 548–551, 554, 555, 557–560, 562–564, 566, 568, 570, 572, 573, 575, 577–580, 582
Energy resolution, 13–15, 19, 78, 139, 185, 212, 213, 218, 275, 277, 304, 323, 342, 343, 352, 373, 399, 410, 411, 414, 515, 517, 541–543, 550, 554, 560, 562, 563, 566, 568–570, 578
ENOB, 353
Environmental analysis, 373, 461, 465–467, 503, 514, 580
Europium, 16, 145, 146
Event trigger, 356, 360, 361
Exalite, 53–55, 67, 74, 82, 83
Excimers, 41, 178, 195, 235, 255
Extraction, 4, 15, 287–290, 292–294, 297, 300, 301, 304, 356, 360, 364, 368, 370, 409, 452, 464, 466, 469, 471, 473–476, 486, 494, 503, 504, 512, 579
- F**
Fabrication, 35, 39, 122, 160, 201–206, 212, 219, 223, 244, 269, 278, 287, 487, 495, 571
Fall time, 374
False alarm and true detection rate, 369
Fast-neutron, 4, 9, 16–18, 20, 25, 35, 39, 68, 69, 71, 75–78, 82, 83, 92, 94, 114, 127, 140, 141, 146, 156, 158, 174, 187–191, 194, 213, 214, 257, 275, 277, 412
Feature, 8, 22, 24, 25, 51, 74, 78, 83, 117, 119, 142, 144, 170–173, 176–178, 180, 183, 189, 196, 207, 252, 301, 310, 316, 331, 340, 347, 352, 355, 356, 365, 366, 370–372, 412, 441, 448
Fiber array, 441, 445
Film, 13, 21, 65, 127, 140, 173, 215, 245, 265, 269–271, 299, 400, 434–436, 438, 451, 468, 481, 565
Filter, 18, 110, 225, 326, 327, 346–348, 355, 358–360, 373, 433, 495, 514, 570, 582, 583
Fission products, 132, 385, 400
FLASH, 429
Fluorescence, 15, 18, 35, 36, 46, 47, 54–56, 61, 110, 115, 145, 177–180, 188, 194, 223, 225–231, 235, 237, 239, 253–256, 275, 277, 370, 372, 431, 453, 475, 495
Fluorescence spectroscopy, 180, 194, 343
Förster Resonance Energy Transfer (FRET), 9, 225, 226, 228–230, 235, 243, 253, 268
Fourier, 350
FPGA, 309, 365, 368, 373, 517
Fracture, 237, 238, 263, 265, 266
Fukushima Daiichi, 386, 388, 477, 517
Full widths at half maximum (FWHM), 13, 37, 44, 57, 310, 319, 350, 351, 366, 370, 371, 411, 515, 517
- G**
Gadolinium loading, 158, 160, 579–582
Gain, 71, 92, 152, 315, 317, 318, 321–324, 328, 331–333, 336, 338, 340–343, 345, 346, 352, 353, 373, 426, 468, 521, 522, 556–559, 564, 569
Gamma knife, 434, 435
Gamma-ray spectroscopy, 19, 25, 277, 282
Gas scintillator, 445, 447

Gaussian, 37, 42, 57, 112, 360, 371, 372, 415–418
 Glass transition temperature, 235, 236, 238, 239, 244, 245, 248, 250, 263, 268–270, 301
 Glassy state, 243, 245, 246, 249, 252, 255, 278

H
 Hadronic calorimeter, 543, 544, 548, 549, 551, 555, 560, 564, 565
 Hadronic showers, 542, 543, 555, 557, 570, 571
 Half-value layer (HVL), 108, 110
 Heterogeneous incorporation, 125, 130
 High dose rate, 425, 429, 435, 451, 568
 High-energy physics, 21, 542
 High-pass, 110, 326, 327, 346, 347
 High voltage supply, 323, 325, 326, 330, 331, 343
 Homeland security, 4, 15, 19, 24, 25, 117, 131, 137, 149, 170, 196
 HOMO, 143, 231
 Homogeneous incorporation, 122, 123, 125
 Hybrid photodetector, 311, 340

I
 IAEA, 158, 434
 ICARE-NG, 528
 Identification, 69, 147, 372, 374, 515, 525, 533, 542, 572, 575, 577, 580, 582
 IGOSAT, 531–534
 Imaging, 21, 217, 288, 343, 426, 434, 436–439, 444, 446, 448, 454, 459, 465, 513, 523, 564
 Impedance, 328, 334, 344, 346, 348
 Impurity, 80, 232, 252, 339
 Information processing, 309, 310, 368
 Inorganic, 3, 4, 6, 9–11, 13, 14, 16–18, 21–26, 32, 74, 89, 122, 140, 141, 170, 183, 188, 190, 192, 201–209, 214–216, 219, 244, 289, 297, 299, 302, 304, 338, 419, 426, 449, 452, 453, 477, 515, 570
 Interface, 15, 201–203, 206, 219, 274, 288, 291, 292, 299, 304, 345, 552, 554
 Intermolecular interactions, 177, 264, 270, 274
 Intrinsic neutron detection efficiency, 118, 119, 121, 260
 In vivo, 425–427, 430, 432, 439, 441, 449, 452, 454, 459, 460

Ionization, 92, 141, 143, 146, 156, 180, 182, 183, 188, 208, 218, 223, 224, 230, 231, 236, 331–333, 342, 400, 438, 439, 443, 444, 464, 515, 522, 531, 532, 542, 582
 Ionization recombination, 223
 Iridium, 143, 144, 146, 152
 Isotropic, 235, 238, 243, 244, 277, 299, 529

K
 K2K, 577, 578

L
 La Hague, 386
 Latency, 319, 354
 LHCb, 554, 559, 562, 563
 Light output, 553, 568, 575
 Light extraction efficiency, 289, 290, 300
 Light output, 11, 14–16, 20–24, 69, 70, 125, 127, 146, 154, 156, 169, 170, 173, 190, 194, 196, 224, 230, 232, 260, 287, 288, 304, 410, 428, 429, 432, 436–439, 445–447
 Light scattering, 13, 188, 206, 207, 219
 Light yield, 10, 13–17, 19, 117, 123, 151, 152, 174, 182, 184–186, 189, 208, 209, 211–214, 217–219, 223, 225–227, 229, 232, 234–236, 239, 243, 253–255, 257, 260–262, 267, 268, 275–277, 288, 428, 446, 452, 453, 515, 554, 561, 563, 565, 566, 577
 Limit of detection, 462, 481, 482, 484, 488, 489
 Linearity, 21, 196, 317, 318, 321–324, 328, 331, 337, 342, 343, 360, 365, 368, 429, 435, 515, 550, 557
 Liquid scintillator, 14, 35, 38, 40, 42, 44, 49, 51, 68, 84, 85, 132, 140, 158, 174, 176, 189, 225, 227, 228, 236, 239, 243, 255, 260, 275, 277, 372, 403, 413, 414, 444, 446, 481, 500, 558, 573, 575, 579, 580, 583
 Lithium loading, 158
 Loading, 4, 8, 10, 17, 24, 25, 71, 83, 122, 123, 125, 127, 131, 139, 141, 142, 146–149, 151–156, 158, 160, 162, 173, 189, 190, 208, 236, 239, 268, 494
 Long-term stability, 66, 82, 84, 236, 239, 243, 244, 246, 270
 Low dose rate, 429
 Low-pass, 110, 346–348, 351
 Low Z, 140

LUMO, 143, 231

M

Machine learning, 374

Macroscopic transport cross section, 98

Magnetic field, 23, 24, 185, 317, 318, 321, 322, 331, 340, 430, 449, 526, 528, 532, 533, 552, 556, 557, 561, 565, 572, 579, 584

Makrofol, 406, 408

Mass attenuation coefficient, 108

Mass stopping power, 107

Mean logarithmic reduction, 96, 97

Mechanical properties, 20, 22, 45, 158, 199, 202, 223, 237, 238, 243, 244, 246, 262

Melt-cast, 243, 266, 282

Metaface, 304

Metal-loaded, 24, 275, 282

Microcontroller, 309, 446, 520

Microprocessor, 309, 368

Microscopic cross section, 95, 97, 98, 100–103, 105, 106

Minerva, 572, 575–578

MINOS, 553, 558, 572, 573, 575–577, 579

Moisture, 23, 238, 262, 330

Mold, 170, 255, 257, 294, 299, 301, 302, 563

Molecular design, 231, 243

Molecular mobility, 38, 42, 236, 239, 272

Molecular structure, 171, 223, 230, 248, 255

Molecular weight, 11, 16, 60, 142, 173, 235, 246, 250, 265

Monitoring, 21, 68, 131, 132, 137, 238, 385, 387, 396, 399, 402, 403, 441, 461–464, 467, 481, 482, 484, 486, 488, 495, 496, 503, 514, 515, 517, 518, 520

Monte Carlo, 72, 98, 125, 219, 428, 433, 441, 444, 447, 450, 478, 531, 581

Moving average, 360

Multi-functional additives, 244, 275

Multiplicity-gated detection, 115

N

NaI(Tl), 397, 398, 402, 515, 517, 522, 523

N/ γ discrimination, 21, 40, 46, 67, 78, 110, 112, 116, 119, 176, 189, 194, 412

Nanoimprint lithography (NIL), 287, 297, 299, 301, 302

Nanoparticle, 125, 140, 147, 188, 190, 201–209, 211–217, 219, 297, 304

Nanophotonics, 287, 289, 299, 304, 305, 307

NanoPSD, 412, 415, 417

Natural radioactivity, 19, 109, 114, 511, 512, 515, 533

Neutrino, 12, 83, 132, 315, 509, 541–544, 553, 558, 559, 571–573, 575–579, 581–583

Neutron detection, 4, 35, 39, 52, 68, 70, 71, 78, 79, 82, 89, 99–101, 105, 109, 112, 114, 116, 118–121, 123, 140, 141, 156, 158, 162, 173, 186, 211, 213, 217, 260, 287, 580, 582

Neutron/gamma discrimination, 18, 20, 21, 25, 39, 40, 146, 158, 282, 368, 369, 372, 374, 411, 414

Neutron/gamma rejection ratio, 121

Neutron detection limit, 121, 122

Neutron detection sensitivity, 118

Neutron detector, 35, 91, 93, 107, 109, 117, 119–122, 127, 130–132, 278, 302

Neutron flux monitoring, 131

Neutron mean free path, 106, 107

Neutron moderation, 94, 96–98, 116

Neutrons detectors, 370

Neutron source, 93, 94, 109, 117, 131

Noise, 115, 315, 318, 323, 326–331, 333, 339, 340, 343, 352, 355, 359, 361, 362, 369, 373, 430, 444, 450, 515, 543, 556, 558, 559, 566, 568, 569, 584

Noise reduction, 359, 360

Nova, 558, 575, 579

Nuclear reaction, 570

Nuclear accidents, 517, 518, 533

Nuclear power plant, 132, 385–388, 463, 477, 512, 514

Nuclear reaction, 91–94, 99–102, 105, 119, 186, 208, 213, 385

Nyquist, 349, 351

O

On-line analysis, 481, 504

Openradiation, 517, 519, 521, 533

Operation, 202, 301, 313, 338, 342, 358–360, 367, 551, 568, 402, 440, 479, 484, 513

Optical attenuation length, 223, 227, 229

Optical fiber, 24, 131, 244, 430, 431, 433, 437, 440, 441, 453, 482–484

Optical imaging, 444, 459

Organic scintillator, 309–311, 331, 333, 344, 348, 354–356, 359, 368, 370, 372, 373, 583

Organic crystal, 39, 40, 189, 224, 230–235, 237, 238, 253, 262–264, 270
 Organic glass, 14, 226, 243, 244, 246, 248, 253–257, 262–266, 268–270, 282
 Organic glass scintillator, 253, 255, 265, 266, 268
 Organic-inorganic hybrid, 210
 Organometallic, 4, 14–17, 24, 25, 123, 139–143, 147, 151, 161, 162, 208, 209, 275, 277

P

Parallel, 36, 47, 161, 298, 399, 317, 328, 334, 336, 337, 344, 348, 359, 364, 367, 368, 556, 561
 Particle physics, 373, 541, 542, 551, 556, 558, 572, 579, 580
 Particle Discrimination, 112, 223, 230, 282
 Particle physics, 307
 Particle type, 107, 182, 224, 429
 Partition coefficient, 404, 406, 407, 409
 PERALS, 410, 412, 413, 417
 Percolation, 231–233, 239
 Phosphorescence, 16
 Photocathode, 311–315, 318–321, 326, 328, 330, 331, 340–342, 552, 556–558
 Photocathode, 18, 302, 446
 Photodetection efficiency, 321, 343, 569
 Photodetectors, 21, 22, 288, 289, 311, 331, 340, 427, 428, 453, 520, 551–554, 556, 557, 560, 567, 579
 Photodiode, 18, 311, 331, 332, 334, 336, 440, 517, 553, 557, 558, 560
 Photoelectric, 108, 140, 146, 152, 156, 310, 312, 338, 340, 449, 523, 549
 Photomultiplier Tubes (PMT), 18, 144, 185, 302, 311, 320, 324, 330, 397, 399, 401, 410, 412, 415, 441, 464, 465, 477, 489, 552, 556, 563
 Photonic crystals (PhCs), 16, 287, 289–297, 299–302, 304
 Photophysical properties, 14, 141, 196, 207, 270
 Pipeline, 358, 359, 361
 Plasmonic lattice resonance (PLRs), 287, 289, 297
 Plasticization, 250, 267, 274
 Plastic scintillation sheets, 313, 332, 342
 Plastic scintillation fibers (PSF), 402, 477, 479, 487
 Plastic scintillation microspheres (PSm), 402, 405, 409, 410, 466, 468, 469, 474, 476, 482, 486, 487, 503

Plastic scintillation resins (psresins), 476, 485, 494, 495, 497, 502, 504
 Plastic scintillation sheets, 488
 Plastic scintillator, 3–6, 8, 10, 12–14, 17–19, 22–26, 33, 38, 39, 42–44, 49, 52–55, 61, 65, 67, 68, 74, 81, 83, 88, 89, 96–100, 105–112, 114, 115, 117, 122, 123, 125, 127, 130–133, 137, 139–143, 146, 147, 149, 151, 152, 156, 158, 160, 162, 170, 182, 183, 186, 188, 189, 192, 194–196, 201, 208, 209, 211, 213, 218, 227, 229, 234–236, 238, 239, 243, 253, 255, 257, 260, 262, 267, 270, 275, 277, 278, 282, 283, 287–297, 299–302, 304, 305, 309, 311, 328, 340, 369, 370, 372–374, 385, 396–403, 405, 409–417, 419, 425–427, 429, 430, 432–434, 438, 439, 441, 444, 449, 452, 454, 461, 462, 464–470, 476, 477, 479–482, 484, 488–504, 507, 517, 523, 525, 526, 530, 541, 543–545, 548–552, 559, 560, 563–566, 568, 572–580, 582, 583
 PMT, 311–315, 317–324, 326–331, 338–343, 549, 552, 553, 556–558, 563, 570, 571, 573, 575–577, 579, 583
 Polycarbonates, 15, 244, 406, 409, 468
 Polymerization, 6, 11, 14, 76, 89, 142, 151, 155, 160, 172, 194, 204, 212, 235, 238, 254, 468–470, 474–476, 503
 Polysiloxane, 19, 149, 169, 173, 174, 178, 180, 183–186, 190, 192, 194, 195
 Polystyrene, 4, 11, 12, 19, 22, 25, 96, 142, 149, 154, 170, 189, 209, 211, 213, 215–217, 227, 235, 244, 254, 263, 265, 288, 409, 451, 468–470, 476, 502, 553, 554, 560, 562, 563, 568, 573, 576
 PPO, 4, 35, 38, 40–44, 46, 47, 50–55, 57, 59–62, 64–67, 69, 73–76, 80–83, 85, 154, 156, 172, 173, 182, 184–186, 190, 194, 195, 215–217, 235, 236, 239, 250, 266, 267, 470, 573
 Poly(9-vinylcarbazole) (PVK), 15, 16, 144
 Preamplifier, 344, 348, 353, 531, 584
 Primary fluorophore, 4, 9, 12, 16, 18, 25, 141, 156, 236, 238, 412
 Processing, 11, 97, 112, 137, 196, 278, 283, 309–311, 320, 340, 344, 349, 356–361, 364–368, 373, 374, 396–399, 412, 436, 438, 440, 445–447, 453, 497, 512

- Producer, 18, 357, 468, 469
PSD plastic scintillator, 52, 68, 69, 72, 74, 76, 190, 236, 250, 266
Pulse, 17, 35, 36, 40, 68, 76, 78, 91, 100, 107, 110, 112, 115, 116, 118–120, 141, 144, 146, 152, 184, 188, 189, 212, 213, 215, 217, 224, 230, 260, 307, 310, 313, 315, 317, 319, 321, 323, 324, 326, 328–331, 333, 334, 336, 338–340, 342, 344–353, 356, 358–374, 401, 410, 412, 413, 429, 436, 466, 477, 499, 501, 531, 560
Pulse shaping, 311, 344, 346, 360
Pulse height discrimination (PHD), 110–112, 114–116, 131
Pulse shape discrimination (PSD), 35, 531
Pulse shaping, 4, 14–16, 71, 112, 176, 189, 193, 194, 196, 213, 288, 402, 403, 410–412, 414, 417–419, 499, 501, 507, 531, 541
- Q**
Quantum dots, 10, 25
Quantum yield, 15, 141, 144, 145, 154, 179–181, 225–229, 237, 239, 253, 254, 275, 277
Quenching, 16, 17, 22, 25, 41, 43, 110, 111, 115, 152, 153, 180, 182, 183, 208, 209, 236, 275–277, 334–337, 409, 426, 429, 430, 441, 443–446, 449, 451, 464–466, 471, 476, 477, 484, 492–494, 497, 499, 501, 559
Quenching factor, 25, 78, 110, 111
Q-value, 100, 102, 103, 105, 107, 110, 115
- R**
Radiation damage, 20, 438, 441, 550, 551, 561, 567–569
Radiation detection, 13, 35, 88, 222, 223, 243, 277, 278, 283, 287
Radioactive noble gas, 238, 385, 386, 393, 395, 396, 403
Radon, 385, 388, 393, 395–397, 402, 403, 405, 409, 410, 412, 419, 463, 510, 511
Reactor antineutrino experiment, 132
Reprocessing plant, 385, 386, 400, 462, 463
Resolution, 15, 215, 217, 275, 298, 299, 301, 317, 327, 333, 340, 342, 343, 349, 352, 355, 356, 373, 399, 427, 433, 435, 441, 446–448, 451, 524, 541–543, 550, 554–556, 559, 562–565, 567, 570–572, 576, 577, 579, 582
Rise time, 310, 319, 320, 329, 336, 350, 351, 356, 366, 556
- S**
Sampling frequency, 349, 351, 354, 355
SAR ADC, 354
SAUNA, 396, 398–400
Screening analysis, 461
SCSF-81, 410, 411
Secondary fluorophore, 9, 12, 21, 141
Selectivity, 92, 464, 465, 495, 496, 507
Self-absorption, 10, 12, 15–17, 44, 50, 55, 58, 82, 141, 142, 144, 182, 184, 207, 214, 218, 225, 253, 293, 570
Self-assembly lithography, 287, 299
Sensors, 13, 18, 100, 114, 116, 122, 123, 125, 127, 141, 148, 169, 170, 191, 192, 194, 196, 199, 311, 318, 338, 355, 401, 402, 448, 461, 467, 481, 482, 488, 489, 494, 496, 502, 517, 519, 525, 531, 559, 568, 584
Shannon, 349
Signal to noise, 304, 396
Singlet state, 35, 61, 224, 230
SiPM, 311, 318, 331, 333, 334, 336–341, 343, 399, 411, 412, 517, 520, 533, 558, 559, 565, 566, 568, 569, 571, 577, 581–583
Slow neutron, 91–94, 96, 99–101, 105, 107, 109, 112, 114, 116, 117, 119, 120, 122, 123, 125, 127, 131, 132, 187
Small field, 425, 426, 433, 434
Solid-state photodetectors, 331
South Atlantic Anomaly (SAA), 532–534
SPACAL, 555, 570
SPADS, 331, 333
Spaghetti calorimeter, 554, 555, 570, 571, 583
Spectral unmixing, 372
Spectral overlap, 225, 226, 229, 230, 239, 253, 428
Spectrum, 11, 46, 47, 93, 103, 105, 109, 149, 150, 152, 178–180, 185, 191, 209, 213, 216, 217, 225, 226, 253, 277, 332, 338, 359, 373, 388, 397, 410, 415–417, 428, 431, 432, 448, 465, 498, 499, 501, 502, 520–522, 524, 544, 555, 570, 582
Stem effects, 426, 428, 430, 432, 441, 452

Stereotactic body radiotherapy, 433
 Stereotactic Radiosurgery (SRS), 433, 434
 Stilbene, 38, 65, 88, 231, 403, 411, 412
 Stokes shift, 10, 20, 144, 173, 180, 183, 207, 225
 Stream, 310, 355–358, 360, 368, 454, 517
 Support-vector-machine, 372
 Surface diffusion, 270
 Surface modification, 205, 206, 208
 SVM, 372
 Symmetry, 231–234, 247, 263, 438, 559

T

T2K, 558, 577, 578
 TARANIS, 524
 Terrestrial Gamma-ray Flashes (TGF), 520–525
 Thermal neutron detection, ix
 Thermal properties, 194, 268
 Thoron, 395, 402, 403
 Timing resolution, 179, 260, 304, 343, 576, 577, 582
 Tin loading, 151
 Total Internal Reflection (TIR), 552, 553
 Total body irradiation (TBI), 426, 433, 438, 439
 Total skin electron irradiation (TSEI), 426, 435–438
 Trackers, 452, 541, 554, 562, 578
 Triplet harvesting, 143
 Triplet state, 16, 35, 36, 53, 58, 64, 112, 143, 179, 188, 189, 194, 230, 231
 Triplet-triplet annihilation (TTA), 36, 38, 39, 53, 57–62, 64, 65, 67, 141, 188, 189,

194, 195, 230–233, 235–237, 239, 253
 Tritium, 102, 107, 111, 112, 114, 130, 484, 488, 491, 497, 498, 510, 512, 513

V

Vacuum processing, 272
 Van Allen belts, 526, 533
 Voltage limiter, 347, 348

W

Water, 23, 131, 170, 202, 204, 205, 403, 406, 428, 441, 446, 447, 449, 451, 462, 463, 467–471, 474, 481, 482, 484, 486, 488–490, 492, 495–498, 501–504, 507, 510, 512, 513, 517, 556, 577–579, 583
 Water-equivalence, 441
 Wavelength shifter, 16, 20, 46, 53, 54, 56, 61, 81, 83, 127, 172, 180, 181, 184, 227, 238, 243, 257, 268, 275, 277, 550, 556

X

X-ray, 4, 21, 147–151, 201, 208, 209, 211, 212, 215, 217, 231, 251, 287, 301, 302, 389, 391, 392, 397–399, 429, 520, 524, 532
 X-ray interference lithography (XIL), 301, 302